BNL

NATIONAL SYNCHROTRON LIGHT SOURCE

ACTIVITY REPORT 1997

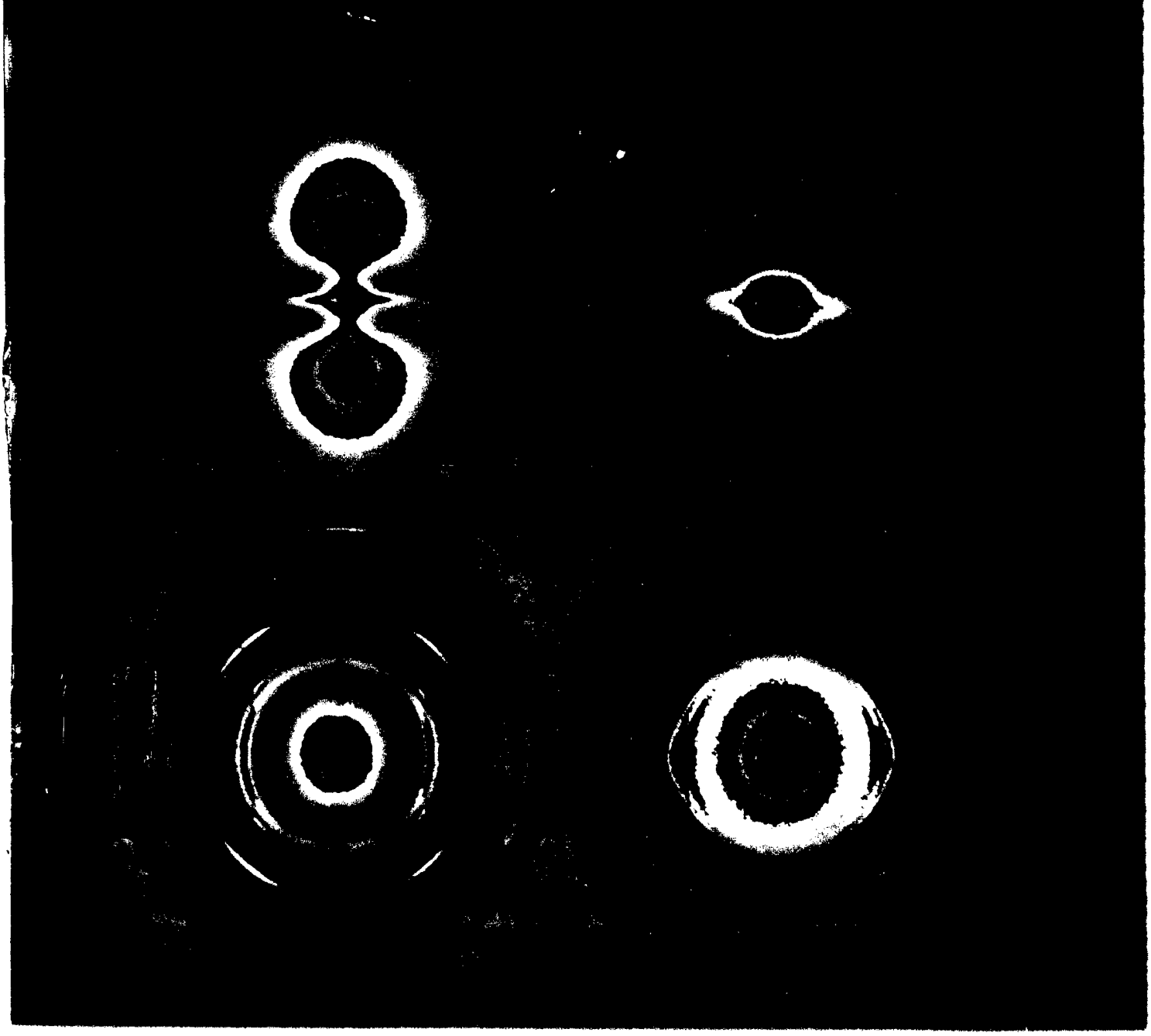

BNL-52540
UC400
(General Energy Research)

The new Advanced Polymers PRT on Beamline X27C: The cover figures are simultaneous small- and wide-angle x-ray scattering patterns of Poly(vinylidene fluoride) (PVDF) fiber collected during deformation at different strains (left:zero strain, right: 140% strain). From these patterns, it is seen that the application of strain not only transforms the PVDF crystal from an alpha-form to a beta-form, but also induces microviods in the stretchedfiber. This study suggests a novel way to produce polymer fibers with nanoscale porosity. This work is funded by a NSF-GOALI grant (DMR-9629825).
J. Wu, J.M. Schultz (University of Delaware), F. Yeh, and B. Hsiao (SUNY at Stony Brook)

DISCLAIMER

Printed in the United States of America
Available from
National Technical Information Service
U.S. Department of Commerce
5285 Port Royal Road
Springfield, VA 22161

BNL--52540

NATIONAL SYNCHROTRON LIGHT SOURCE

For the period October 1, 1996 through September 30, 1997

May 1998

Managing Editor
E.Z. Rothman
Science Editor
J.B. Hastings
Production Assistants
L. Feierabend
L. Rogers
N. Wright

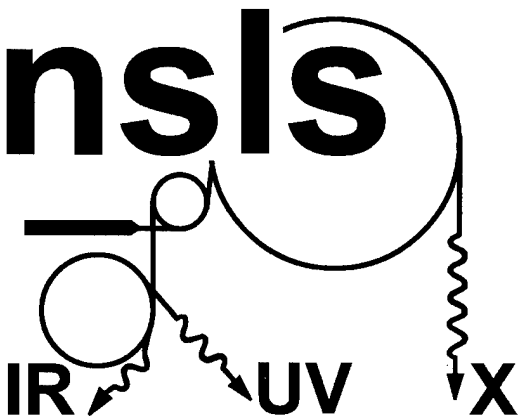

The National Synchrotron Light Source Department
is supported by the
Office of Basic Energy Sciences
United States Department of Energy
Washington, D.C.

MASTER

Brookhaven National Laboratory
Upton, New York 11973
http://www.bnl.gov

INTRODUCTION

SCIENCE HIGHLIGHTS

MEETINGS & WORKSHOPS

OPERATIONS

PROJECTS

ORGANIZATION

ABSTRACTS & PUBLICATIONS

Beamline X20C: The figure at right is an example of silicide phase formation from the reaction of metals with silicon. Time-resolved x-ray diffraction is used to capture the formation sequence during rapid thermal annealing. A resistive heater encapsulated in pyrolytic boron nitride is used together with a linear position sensitive detector allowing for the required time resolution during annealing at ramp rates of up to 35° C/s. Notice that in the figure, as temperature is ramped from 400°C to above 1000°C, at least ten different diffraction peaks representing four distinct silicide phases are present in the ten degree two theta diffraction range. C. Lavoie and C. Cabral, Jr. (IBM Research Division, Yorktown Heights, NY).

ONE
INTRODUCTION

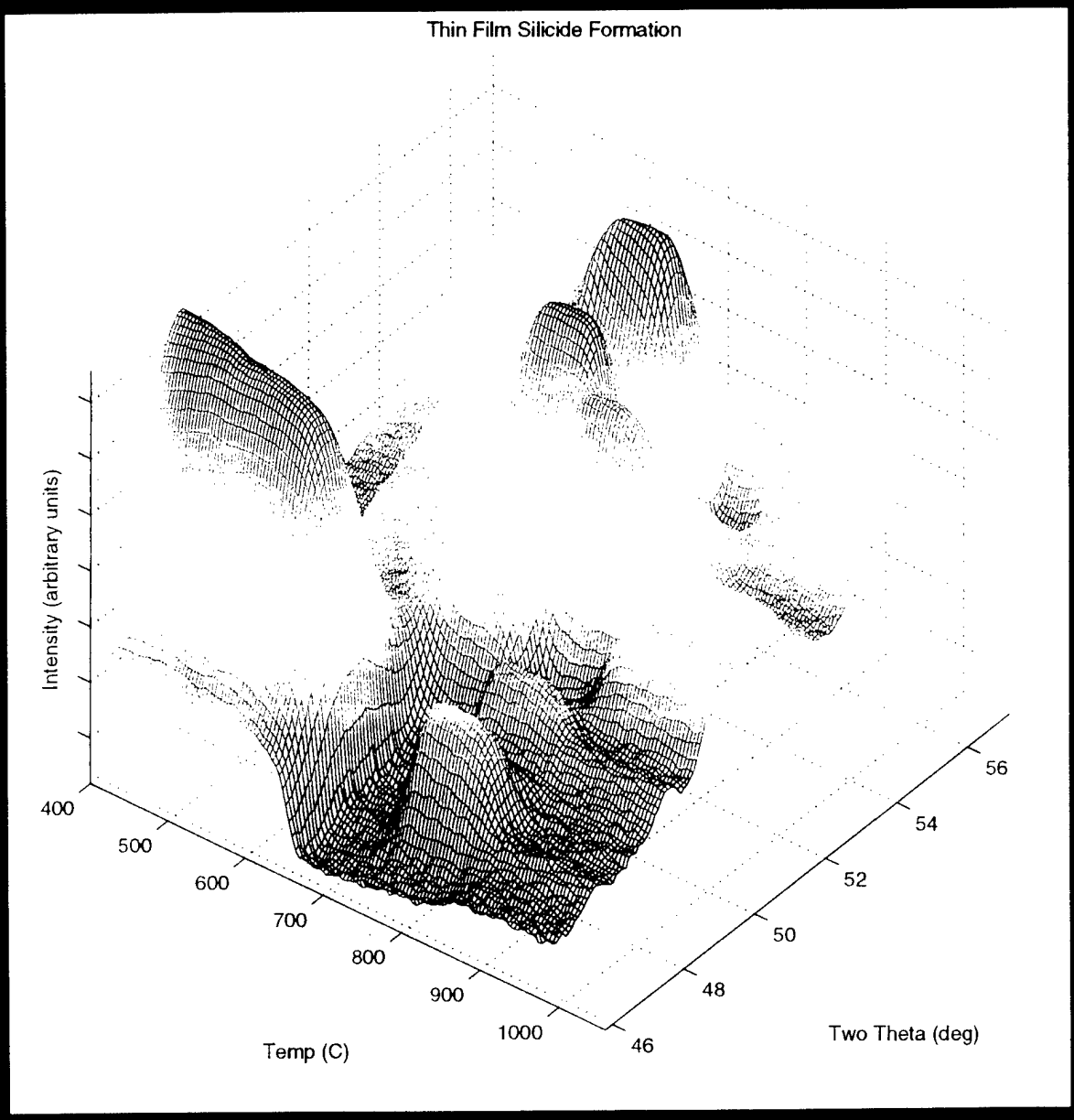

INTRODUCTION

Michael Hart
NSLS Chairman

During FY 1997 Brookhaven National Laboratory celebrated it's 50th Anniversary and 50 years of outstanding achievement under the management of Associated Universities, Inc. The National Synchrotron Light Source and its users' research record are part of that history and, appropriately, since research with light from synchrotron radiation has matured, the scene was set for a major national review of the D.O.E. synchrotron radiation provision.

In the second week of the Fiscal Year the charge was outlined and included both the expected items and the unexpected "What would be the consequences of the shutdown of one or more of the four DOE/BES synchrotron light sources?" A challenge indeed! Within a year the process had run to completion under the Chairmanship of Dr. Robert Birgeneau with a resounding clear message;

"The panel believes that all four D.O.E. synchrotrons are essential to the national scientific and technological enterprise."

"The most straightforward and most important conclusion of this study is that over the past 20 years in the United States synchrotron radiation research has evolved from an esoteric endeavor practiced by a small number of scientists primarily from the fields of solid state physics and surface science to a mainstream activity which provides essential information in the materials and chemical sciences, the life sciences, molecular environmental science, the geosciences, nascent technology and defense-related research among other fields. The user community at U.S. synchrotron facilities continues to grow exponentially, having reached more than 4000 on-site users annually in FY97. The research carried out at the four D.O.E. synchrotron sources is both very broad and often exceptionally deep.

"It is self-evident that research which requires very high brightness will be carried out overwhelmingly at the third generation sources. ..... Nevertheless, most current synchrotron research requires high flux as opposed to high brightness and therefore can be carried out equally well at second and third generation sources.

"The panel was very impressed by the outstanding performance of the second generation facilities (SSRL and NSLS), by the number of users they serve well, by their ability to renew and improve themselves, by their ability to continue cutting-edge research even though the storage rings themselves are not the most advanced, by their commitment to education, and by their abilities to engage new users and address new problems. Given the outstanding track record and clear vision demonstrated by these facilities, the panel expects these facilities to continue to thrive scientifically in a cost-effective manner. These centers are national resources and they should be adequately funded, upgraded and modernized in a timely fashion to serve better the national needs."

The path to at least another decade of outstanding research at NSLS was clearly laid out with appropriate funding recommendations which were accepted in full by the Basic Energy Sciences Advisory Committee (BESAC).

In addition to formal meetings and the collection of statistics, the review included a visit to NSLS at which staff and users had a well-used opportunity to convince the panel of the strength of our program. By the end of FY 1997 NSLS had welcomed its 7000th user. For each of the last five years more than 2200 users came to the light source; almost 800 new users in each year. The strength of their programs in terms of quality and quantity was made clear in the presentations to the panel and by the fact of over 4000 publications in almost 250 different Journals during the 1990s alone. As the bar chart shows, within almost constant total numbers the NSLS user community is not static but represents a thriving and evolving population. The pioneers of research with synchrotron radiation from the physical sciences continue in steady numbers but new communities in the biological and environmental sciences are growing rapidly with a four to five year doubling time. In FY 1997 one third of our users were under the age of 30 and less than one third were over 40. Although about one half come from US universities the whole of the national and international scientific and technological enterprise is strongly represented, as the pie-chart shows.

An outstanding year was overshadowed by the unprecedented early termination of the Associated Universities contract to manage the Brookhaven National Laboratory. The details are well known and some of these are outlined later in this Activity Report (page 1-4) . On 1 March 1998 Brookhaven Science Associates will take responsibility for setting the standards for the second half century of research at Brookhaven. ■

NSLS Users by Institution Type

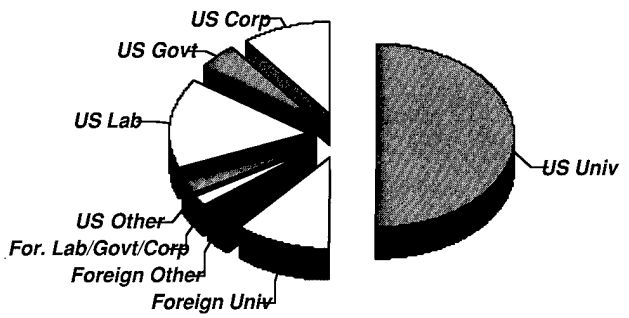

Inst. Type	# Users	Percent
US Univ	1163	50.1
US Other	58	2.5
US Lab	369	15.9
US Govt	113	4.9
US Corp	240	10.3
Foreign Univ	258	11.1
Foreign Other	76	3.3
Foreign Lab/Govt/Corp	43	1.9
Total Users for FY 1997:	2320	100.0

NSLS Users by Field of Research

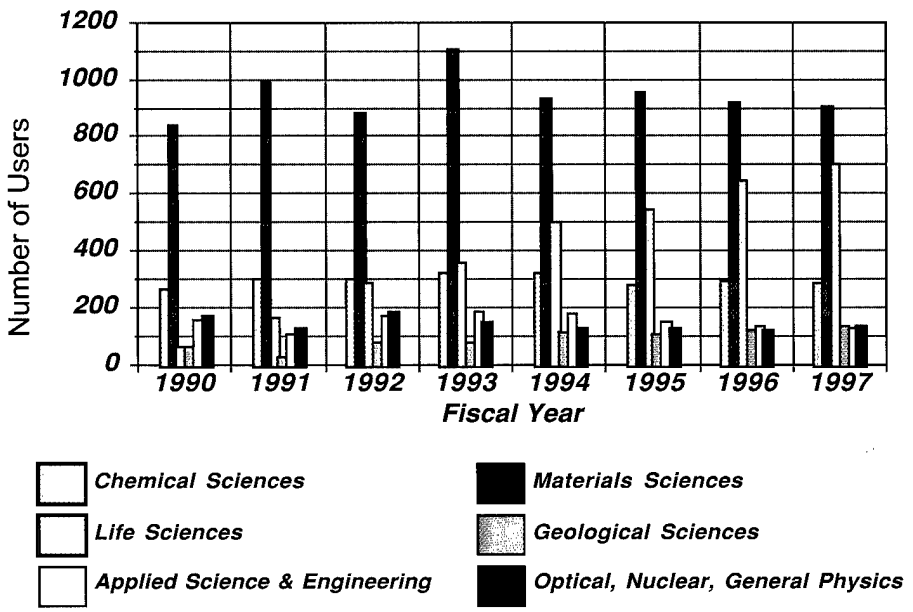

Environment, Safety and Health Update

William Thomlinson
Associate Chairman for ES&H

There is no doubt about this past fiscal year being one of great accomplishments for the NSLS. But it has also been a year largely overshadowed by the chaos surrounding all of BNL with respect to management and ESH issues. Everyone knows that the combination of the discovery of the tritium plume from the spent fuel pool at the HFBR and the extremely negative Integrated Safety Management Evaluation of BNL lead to the current situation. By the time this is published, BNL will have a new contractor and hopefully some measure of stability and reason will be back in vogue. One result is that ESH at BNL, and the NSLS in particular, have taken on a heightened level of priority. At the NSLS, we have participated in all of the ESH activities, both on-going and new, and have overall been extremely pleased to find that our safety programs are solid. In general, we already meet all new standards and have performed in an exemplary fashion throughout all reviews.The coming year will clearly be spent adjusting to new requirements and completing existing initiatives.

At the NSLS, we have participated in all of the ESH activities, both on-going and new, and have overall been extremely pleased to find that our safety programs are solid. In general, we already meet all new standards and have performed in an exemplary fashion throughout all reviews.

The year started with an in-depth ESH Self-assessment. Our dedicated team of NSLS personnel studied key areas such as Training, ALARA, ESH communications, Quality Assurance and Conduct of Operations. A list of findings was developed and prioritized. Our formal report was made to the BNL Directorate and accepted. Some of the findings have been resolved, but we have a ways to go on others. The effort is continuing, but has clearly been hampered by the intense involvement that we have had to have with issues which have arisen this year. In particular, we had to expend a huge amount of resources during the DOE mandated Integrated Safety Management Evaluation through the winter and spring. Many man-months of effort, largely directed by our ESH Coordinator Nicholas Gmür, resulted in the NSLS receiving very good reviews. Our Tier I safety assessments procedures and the tracking of findings developed by John Aloi were highlighted as outstanding procedures. In addition, our appointment of Mike Buckley as our Conduct of Operations Coordinator was timely and effective. The steady, professional safety operations directed by Tom Dickinson were clearly one of the strengths recognized by the assessment team. Some weaknesses in work planning were pointed out in our experimental reviews (corrected with our new experiment Safety Approval Form). Of course, this year the good news was overshadowed by the bad. An electrical safety incident at the NSLS involving a Plant Engineering employee was one of the incidents pointed at by the ISME team in their extremely negative report. At the NSLS, we felt good about how we fared in the evaluation and have already acted on correcting those legitimate weaknesses found during the review.

As a result of the ISME report and the cancellation of the AUI contract, all of BNL turned its attention to ESH and management issues. Directly affecting the NSLS operations has been a revision of the work planning for experiments at BNL. To our credit, we were largely exempt from that process since it was clear that we already are doing most of what is required. In fact, our review of the final standard developed shows that we have only had to formally designate Andrew Ackerman as our Experiment Review Coordinator and give some committee responsibility to our existing ESH Committee to be fully compliant. That is a clear indication that the NSLS continues to be in the forefront of ESH activity at BNL.

Based on some of the recommendations in the ISME report, we decided to modify our Safety Approval

Form for experiments to better capture the safety measures being taken by the experimenters and to document the work control procedures that are agreed to by the NSLS staff and the users. At the same time, we were directly involved in the new Chemical Management System (CMS) at BNL in which all chemicals used at BNL are being logged into a database. At the NSLS we have a specific problem because of the large number of materials brought here by users. If purchased at BNL, the materials are automatically entered into the system and bar coded. However, if brought in from outside the Lab, we have a problem as to how to capture them in the system and how to assure the proper disposal. Andrew Ackerman worked closely with the CMS staff and made arrangements to exclude small quantities if brought to, and subsequently removed from, BNL by the user. That agreement makes it efficient for the users. In order to track those materials, however, we also had to change our Safety Approval Form (SAF).

A third issue recently arose which also impacted our redesign of the SAF. The DOE must receive certain data from the user facilities under its jurisdiction. Items such as user hours, institutional involvement, distribution of resources, etc. are necessary and must be reported. All facilities will uniformly report to DOE each year. At the NSLS, our best way to capture such information is through the SAF since every experiment must have one - whether it is performed on an NSLS or PRT beamline, or by General Users or PRT members. With all of these motivations, we worked rapidly this summer and produced the new, comprehensive and (we hope) more useful form for introduction on October 1, 1997. Our intent is to have a system in place by Spring of 1998 for electronic submissions of the SAF. That will make it very easy for users to submit the comprehensive information now required.

In addition, many new efforts are underway which involve our safety staff. Upgrades at the Accelerator Test Facility and the Source Development Lab require new safety documentation. The shielding of the VUV Ring and the upgraded X-Ray Ring shielding on the beamlines to accommodate 2.8 GeV operations are well underway. The latter is requiring a lot of effort by the users and the NSLS staff. These efforts are being carried out and coordinated by Andrew Ackerman, John Aloi, Tom Dickinson and Nick Gmür with a lot of cooperation from our users and NSLS staff.

The year has not been without problems. A worker at a BNL construction site was killed in an industrial accident. BNL was ordered to stand down for several days, during which the NSLS staff and users met to discuss the general topic of safety in the workplace. I am sure that this was a useful exercise based on the wide range of issues covered and discussed. However, the length of the stand down and its impact on the operations of the rings for users certainly detracted from its full value.

At the NSLS we have had several reportable incidents due to safety issues at the facility. In evaluating these events, the general theme is one of lack of individual responsibility or attention to good work planning and execution. I should note that those are fundamentals of Work Smart Standards which will become pervasive within our operations over the next year. The incidents include the improper use of a coffee thermos as a cryogenic dewar (it exploded and slightly injured two workers), a piece of sheet metal improperly secured during shielding upgrade (it slipped and nearly severed the workers thumb) and untrained users etching material in a hood (the reaction was exothermic and filled the hood and part of the NSLS with acid fumes). Fortunately none of these incidents caused severe injury, but the potential was there in each case.

The NSLS cannot be responsible for training and behavior before a person comes to the facility and we cannot police everyone all the time. Users and staff must realize that their safety and that of their co-workers depend on their own behavior, training, work planning and good execution.

As the new year develops and the NSLS learns what measures it must take to continue to improve and be compliant with any new regulations and standards, the user community will be informed and will be participants with us. We must continue to improve our already outstanding safety program, but we must remain vigilant to ensure that whatever changes are made are in the best interests of, and efficient for, our user community. ■

Users' Executive Committee

Joel D. Brock
Cornell University
UEC Chair

The purpose of the Users' Executive Committee (UEC) is to promote communication between the user community and the NSLS Administration. To this end, the UEC conducts an annual user meeting and three public town meetings each year. The annual meeting serves several functions: to celebrate the scientific and technical accomplishments of the previous year, to obtain the latest news on the support of the U.S. Department of Energy for scientific facilities in general and the NSLS in particular, and to provide an opportunity to visit with old friends and colleagues. Although this year's annual meeting included six workshops and several invited scientific talks, the tone was dominated by the more political talks. The key-note address titled "Future Schlock" by Robert Park was lively and humorous, poking fun at predictions about the future and those who make them. The Interim Director of BNL and President of AUI, Lyle Schwartz then made some short remarks. The U.S. Department of Energy was represented by the Associate Director of Energy Research for the Office of Basic Energy Sciences, Patricia M. Dehmer. In response to Robert Park and Lyle Schwartz, she began her remarks by assuring the audience that during all the upheaval associated with BNL's problems there has been one constant: "the high regard" for the NSLS, its users, and the quality of their science.

The goal of the public town meetings is to provide a venue for discussions between users and to keep communication channels between the NSLS Administration and the users open. Typically, presentations by both the NSLS staff and the UEC on user issues are followed by opportunities for questions and discussion. On the day following the town meetings, the UEC meets with the NSLS and Brookhaven Laboratory staff and management to discuss relevant issues. The current membership of the UEC is listed in the caption of the accompanying photograph. Three general members of the UEC are elected each year at the annual meeting and serve two year terms. Each Special Interest Group (SpIG) also elects (by an e-mail election) a representative. After the general election, the UEC elects one of its general members as Vice-Chair. The Vice-Chair is responsible for organizing the next annual meeting and then becomes the Chair in the following year.

During the past year, although the UEC has dealt with a large number of important issues, our focus was determined by the search for a new contractor to manage Brookhaven National Laboratory and by a review of all four of the DOE supported synchrotron facilities. We attempted, unsuccessfully, to contribute input to the Source Selection Board for use in the selection of a new contractor to manage Brookhaven National Laboratory. Copies of the letters sent by the UEC to the DOE's BNL Source Selection Board can be found on my web page — http://www.msc.cornell.edu/~brock. On the other hand, on June 25th and 26th, the users did assist with presentations to a review panel appointed by the Basic Energy Sciences Advisory Committee (BESAC) and chaired by Professor Robert J. Birgeneau of M.I.T. which reviewed the scientific and technical programs of the NSLS. This panel was charged with reviewing all four of the DOE synchrotron facilities (the ALS at Berkeley, the SSRL at Stanford, the APS at Argonne and the NSLS at BNL) and making recommendations for future funding priorities. The panel was explicitly requested to consider the ramifications of closing one or more of these facilities. Several of the staff and users of the NSLS were called on to discuss the impact synchrotron radiation has had on their particular field of science. It was a very impressive event to witness. In the short time available, leading experts from over a dozen distinct scientific fields presented the impact science done at the NSLS has had on their specific field. Although I have spent a considerable amount of time working on the NSLS X-Ray Ring floor, I got an education about the breadth of the work being done at the NSLS. These talks covered the usual areas associated with synchrotrons, materials science, surface/interface physics, magnetism, lithography, tomography, powder diffraction, macromolecular crystallography, infrared sources, imaging, and so on. But several other talks were given, such as the one by Dr. Barbara Illman (USDA, U. of Madison, and new UEC

member) on the applications of synchrotron radiation to forest science, which illustrated the enormous potential of synchrotron-based measurements to impact non-traditional synchrotron disciplines. The draft of the Birgeneau panel's report (See http://www-als.lbl.gov/als/besac/index.html) was released early this fall and was very favorable towards the NSLS. Patricia Dehmer responded to the report very quickly, releasing additional funds to hire NSLS user support staff and to upgrade user facilities. Due to the increase in funding resulting from the BESAC panel report, the NSLS has asked the UEC for input on how to distribute the additional capital equipment and personnel support funds. Although no less difficult than other issues, this is a welcome departure from the far more frequent request to help determine where to trim.

Looking ahead, now that a new contractor has been chosen to manage BNL, the UEC needs to forge a strong and positive working relationship with the new laboratory management. This will take some time and effort on both sides.

1997 has been another year of very strong scientific output at the NSLS. A cursory look through the abstracts and publication lists in this Activity Report demonstrates the tremendous variety of high quality science being done at the NSLS. The users have come to expect excellent and continuously improving operations at the National Synchrotron Light Source. The NSLS staff have labored hard to ensure that the brightness, stability and reliability of the sources improved steadily over the years. Yet, it is the quality of the science performed by the users which ultimately determines the success or failure of the facility. I am quite optimistic that the NSLS will remain a vital facility long into the future. ■

Users' Executive Committee and Special Interest Group Representatives

(Front, from left to right)
Steven Whisnant (U. of So. Carolina), Malcolm Capel (NSLS-Biology), Elaine DiMasi (BNL-Physics), Joel Brock (Cornell U.), Eva Rothman (BNL-NSLS), and John Parise (SUNY @ Stony Brook).

(Back, from left to right)
Barbara Illman (U. of Wisconsin), G. Lawrence Carr (BNL-NSLS), Michael Dudley (SUNY @ Stony Brook), Peter Stephens (SUNY @ Stony Brook), Ian Robinson (U. of Illinois), D. Peter Siddons (BNL-NSLS), Peter Johnson (BNL-Physics), and Sanjeeva Murthy (AlliedSignal, Inc).

Absent from photo are Thomas Russell (U. of Massachusetts), Paul Stevens (Exxon Research and Engineering), Carl Zimba (MIT), Jon Levin (U. of Tennessee), and Luz Martinez-Miranda (U. of Maryland).

Beamline X26A: A photomicrograph of a tuffaceous rock thin section (A) to which plutonium (Pu) had been sorbed from a solution containing predominantly Pu(V). Micro-X-ray fluorescence imaging isolates Fe rich (B) and Mn rich (C) inclusions. Despite predictions that Pu would preferentially sorb to Fe-oxides, Pu was located only as small inclusions within the Mn-oxides, which are known to associate with smectites in the tuff (D). Micro-XANES (E) conducted at 10 x 15 microns with Kirkpatrick-Baez focussing mirrors indicate the average oxidation state is probably Pu(V) rather than the predicted reduction to Pu(IV). Given tremendous differences in sorption behavior between oxidation states of Pu, this information is vital for the prediction of fate and transport of Pu in the subsurface at nuclear waste repositories.
M.C. Duff, D.B. Hunter (Savannah River Ecology Laboratory), D.T. Reed (Argonne National Laboratory), I.R. Triay, D.T. Vaniman (Los Alamos National Laboratory), and G. Shea-McCarthy (University of Chicago/National Synchrotron Light Source).

TWO

SCIENCE HIGHLIGHTS

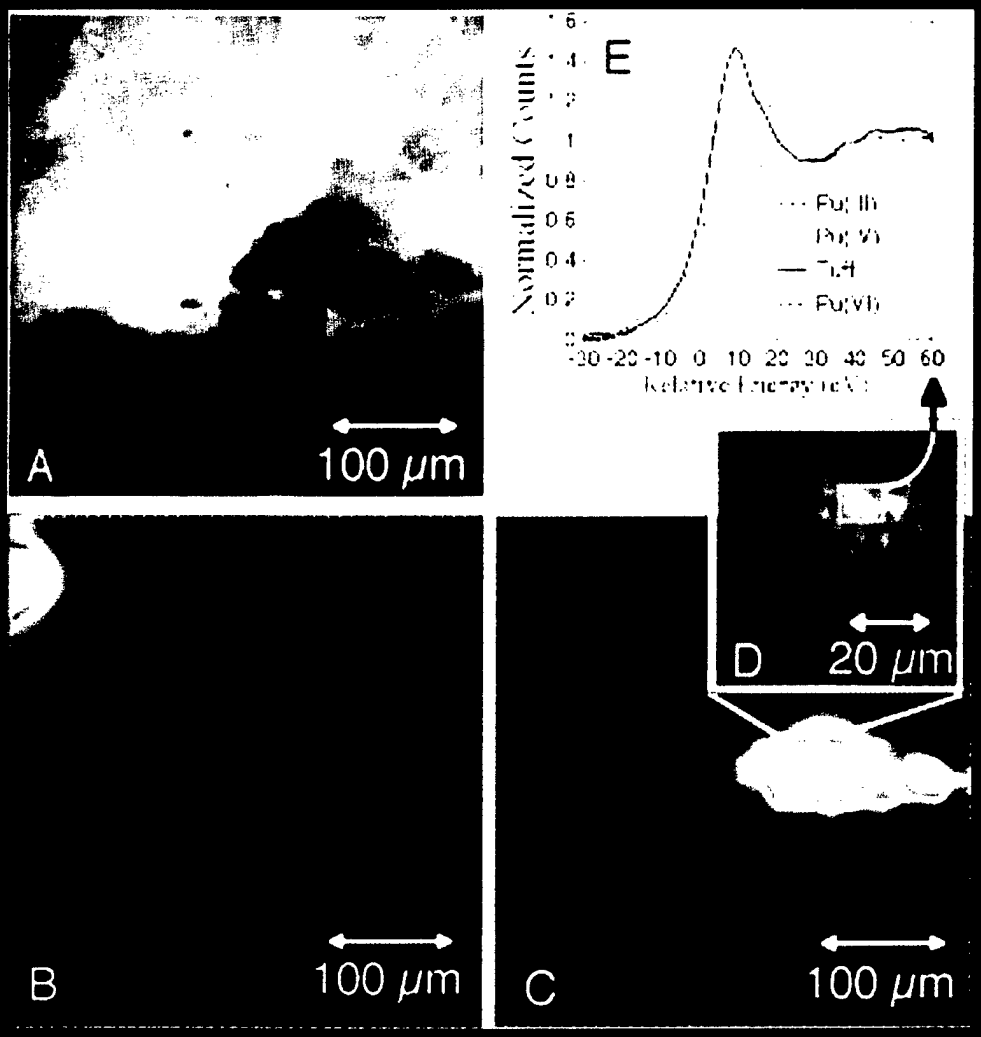

Asbestos Abatement

J. A. Hriljac, C. Eylem, Q. Zhu, R. Sabatini, L. Petrakis (Brookhaven National Lab), R. Hu, and J. Block (W.R. Grace and Co.)

The energy, technology, and environmental research activities which fall into the category of applied science sometimes directly address important problems facing society. Success in such projects can have an immediate positive impact on the public, and thus garner a considerable amount of favorable attention from the general population and press.

A striking example was announced during the fall of 1997 in a press release issued by W.R Grace and Co. The collaborative venture between Grace and BNL resulted in the development of a polymer foam which can be applied to asbestos as part of an abatement strategy. The foam chemically attacks the asbestos crystal structure, leaving behind a residue of minerals which can continue to act as a fire retarder/insulator.

One important aspect leading to the success of the W. R. Grace and Co./BNL CRADA (Cooperative Reasearch and Devlopement Agreement) on Asbestos Abatement was the ability to accurately and reliably determine the quantity of asbestos in treated materials. The current EPA-recommended method is fiber counting using Polarised Light Microscopy. However, at the low levels of asbestos that the Project Team was concerned with, this method was believed to be insufficiently accurate and alternatives were explored.

Quantitative X-ray powder diffraction (QXRPD) is a well-established tool for the analysis of mixtures of crystalline powders. One type of QXRPD analysis is the so-called ratio method, where a known quantity of an internal standard is mixed with the analyte and the intensities of a peak from the phase of interest is compared with that of the added internal standard. An exact weight percent can then be determined by comparison to a calibration curve produced from carefully prepared standard samples. Work led by Dr Ruizhong Hu at W. R. Grace and Co. focussed on the use of this method

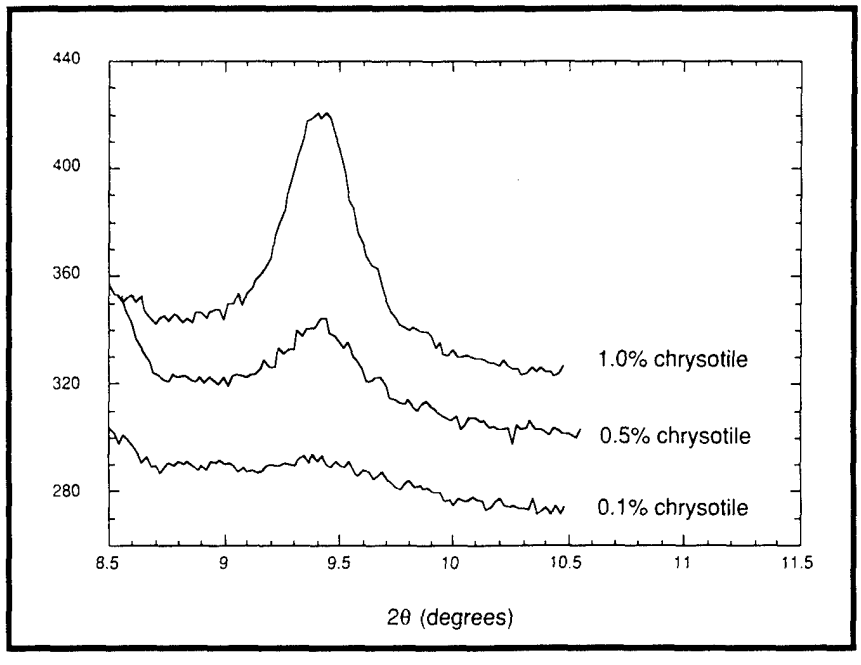

Figure A-1: Diffraction spectra around the chrysotil (0 0 2) peak for low concentration samples of asbestos in alumina.

with a sealed tube X-ray source[1]. A suitable method was developed to quantify low levels of chrysotile absbestos in chrysotile/gypsum/vermiculite (CGV) mixtures, a typical asbestos-containing material.

One potential drawback of this method is that it requires a pre-treatment to remove the gypsum in order to allow accurate quantification at very low (< 1%) levels. Proof that this did not affect the asbestos fibers (and hence complicate the quantification procedure) was achieved, in part, through the use of synchrotron X-ray powder diffraction at beam line X7A. Further work at X7A by Joe Hriljac, Cahit Eylem (then both in DAS), and Qing Zhu (then in Physics) extended the use of QXRPD to allow quantification of low levels (0.25-0.5%) of asbestos in the same CGV mixtures without any pre-treatment[2]. A plot of the diffraction data around the most intense peak of chrysotile in an alumina matrix is in **Figure A-1.** ■

[1] R. Hu, J. Block, J. A. Hriljac, C. Eylem, and L. Petrakis, *Analytical Chemistry* **68**, 3112-20 (1996).
[2] J. A. Hriljac, C. Eylem, Q. Zhu, R. Sabatini, L. Petrakis, R. Hu, and J. Block, *Analytica Chimica Acta* **350**, 221-29 (1997).

NEXAFS Microscopy of Polymers: Phase Separation and Dewetting in Polymer Thin Films and Bilayers

H. Ade, D. A. Winesett, A. P. Smith (Dept. of Physics, NCSU), S. Ge, S. Qu, M. Rafailovich, S. Sokolov (Dept. of Materials Science and Engr., SUNY @ Stony Brook), and D. Slep (Advanced Development and Research, Hilord Chemical Corp., Hauppauge, NY)

In many applications, the physio-mechanical properties of polymeric systems can be tailored by altering the chemical and morphological structure. In most cases, the polymer system of interest is not a homogeneous or single-component system, but is a blend, composite, or copolymer. Sophisticated analytical methods are required for their characterization. Amongst them is the recently developed technique of Near Edge X-ray Absorption Fine Structure (NEXAFS) microscopy. It has an advantage of about three orders of magnitude over the equivalent electron microscopy technique in being able to spectroscopically analyze and image small sample areas of radiation sensitive materials such as polymers[1]. In NEXAFS microscopy, excitations of core electrons into unoccupied molecular orbitals provide sensitivity to a wide variety of chemical functionalities in polymers. This sensitivity complements and resembles that achieved in infrared (IR) spectroscopy. Although NEXAFS spectra are not as specific and "rich" as IR spectra, the spatial resolution achieved in NEXAFS microscopy is about 50 nm[2,3], and thus much superior to that achieved in IR microscopy. In addition, x-ray linear dichroism microscopy can determine orientation of chemical moieties at higher spatial resolution. These inherent advantages of x-ray microscopy have opened up new avenues for the characterization of polymers.

We will exemplify the impact of NEXAFS microscopy to the analysis of polymer systems by focusing our discussion on the characterization of phase separation and dewetting in polymer thin films and thin bilayers. Compared to bulk properties, relatively little is known about the properties of polymer thin films and surfaces, even though polymer films have considerable technological significance and technological applications, such as coatings and dielectric films. A detailed understanding of thin film properties and possible deviations from bulk properties is highly desirable and numerous studies on blends and bilayers have been undertaken in the recent past. While a variety of patterns that evolve during the phase separation process in polymer thin films have been observed, the two dimensional composition has never been directly determined. Often indirect methods, such as the use of selective solvent extraction for one of the phases in conjunction with AFM microscopy is utilized. However, the dissolution process can lead to ambiguities or artifacts. While qualitative details of the subsurface morphology might be revealed with electron microscopy techniques, NEXAFS microscopy provides quantitative equivalent thickness maps of each constituent polymer, which if summed together yield total thickness maps equivalent to AFM topographs. NEXAFS microscopy will thus allow for

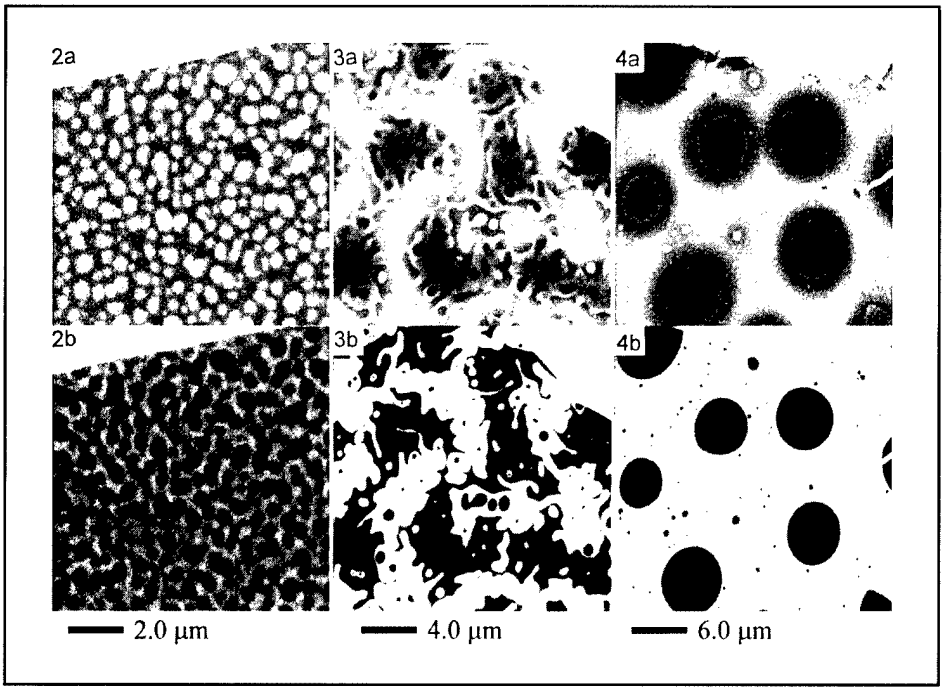

Figure A-2: As cast thin film of 50/50 weight percent PS/PMMA blend imaged at (a) 289.2 eV, and (b) 285.2 eV
Figure A-3: Same as above, but annealed for 10 min.
Figure A-4: Same as above, but annealed for one week.

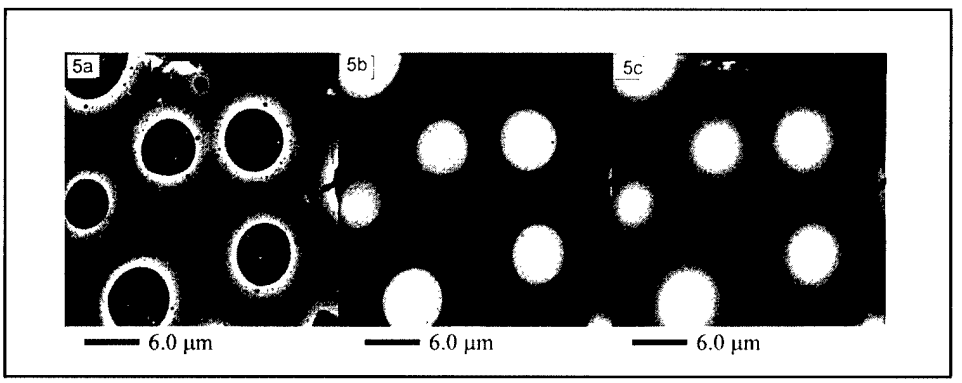

Figure A-5: Quantitative equivalent thickness map of sample annealed for one week. (a) PMMA map, (b) PS map, and (c) total thickness map.

quantitative investigation of the composition of phases and the dynamics of polymer phase separation.

We investigated films composed of a 50/50 weight percent blend of polystyrene (PS) and poly(methyl methacrylate) (PMMA) spun cast onto silicon substrates to a thickness of 146 nm. The films were then annealed for varying times and subsequently transferred to TEM grids for STXM investigation. A series of X-ray micrographs are acquired in the same sample area at energies coinciding with characteristic NEXAFS peaks of the constituent components. For example, **Figures A-2a, A-3a, and A-4a** were acquired at the C 1s to π^* carbonyl peak at 289.2 eV and emphasizes PMMA, while **Figures A-2b, A-3b, and A-4b** were acquired at a photon energy of 285.2 eV, which is almost exclusively absorbed by PS. Darker regions indicate higher x-ray absorption at the particular photon energy and yield qualitative information on the component composition. The samples imaged in **Figures A-2, A-3 and A-4** were annealed for 0, 10 min, and one week, respectively. Initial phase

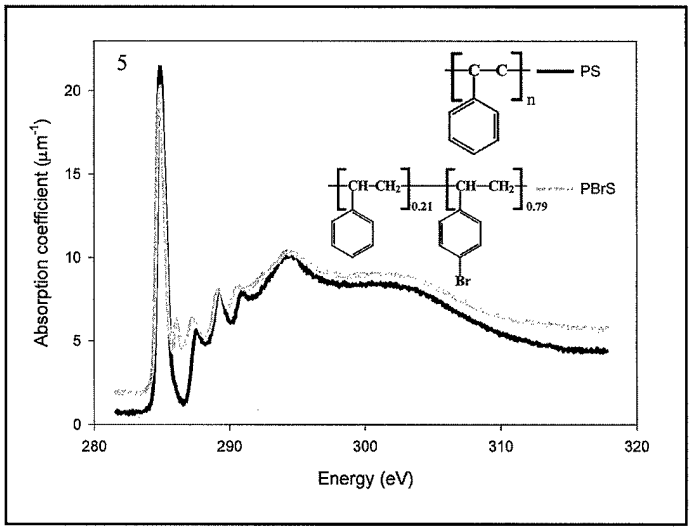

Figure A-6: Linear absorption coefficient of PS and PBrS near the carbon absorption edge.

separation during the spincasting into small domains is observed. After 10 minutes of annealing, intricate filamentary structures and inclusions are observed, with the system evolving towards the formation of large and thick PS domains with a PMMA interconnection layer after one week of annealing. The phase separation process is primarily driven by minimization of the interfacial free energies. In order to differentiate the effects of the relative absorption of the individual polymers, we employ a singular value decomposition method to extract thickness maps of individual components. **Figure A-5** shows the results of using this technique for the sample annealed for one week. **Figure 5a** is the projected thickness map of PMMA, **Figure A-5b** is the map for PS, **and Figure A-5c** is the sum of **5a and 5b**, and provides the total thickness map. The thickness map is equivalent and consistent with AFM topographs of these samples. The NEXAFS micrographs provide insight into the structure of the polymer interface formed.

A related issue to phase separation in thin films of polymer blends is the wetting and dewetting in thin polymer films. We have thus investigated a polystyrene/brominated polystyrene (PS/PBrS) bilayer model system with the Stony Brook STXM and employed the method described above to achieve quantitative thickness maps of PS and PBrS, respectively. The initial structure was a 30 nm thick layer of PBrS on top of a 40 nm thick PS layer prepared by spin casting each film and then floating the PBrS layer on top of the PS layer. After annealing, which initiates dewetting, the sample was transferred to a TEM grid for STXM analysis. Images were acquired of the same sample area at four energies. Each image contains combined information about the PS and PBrS composition and thickness, with the weight governed by the linear absorption coefficient of the two polymers (**Figure A-6.** See inset for chemical structure of PS and PBrS). **Figure A-7** shows the resulting component thickness maps and underlying thickness profiles. Polystyrene has formed thick walls along a network of spines of PBrS that form as PBrS dewets. There is only a pure PS interconnecting thin film between the spines. The total thickness map is consistent with AFM topographs. We attempt to measure the contact angle in these systems as an indirect measurement of the interfacial energies. The NEXAFS data clearly shows thought that a contact angle of the

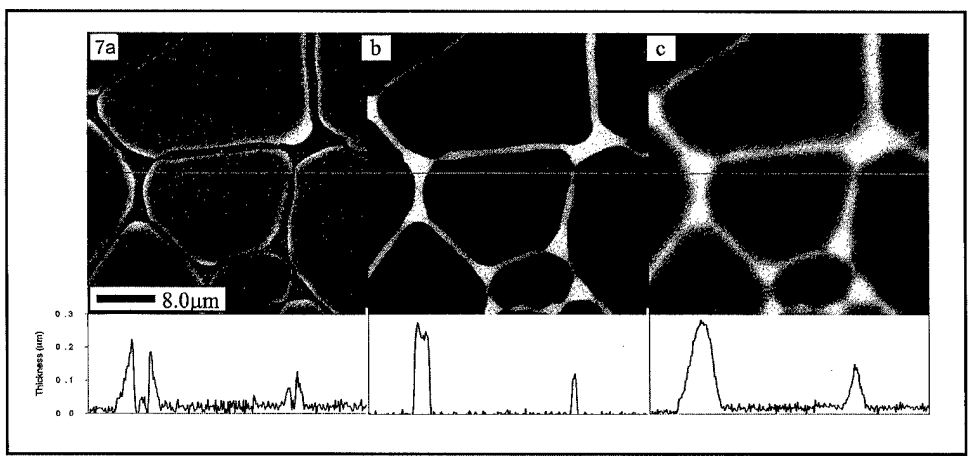

Figure A-7: Quantitative equivalent thickness map of dewetting PBrS/PS bilayer. (a) PS map, (b) PBrS map, and (c) total thickness map.

filamentary structures as measured with the AFM is only indirectly related to the PBrS profiles and the AFM measures primarily the PS walls. The STXM data suggests furthermore that the PBrS is actually completely encapsulated by PS after annealing. This would be consistent with SIMS and Photoelectron Emission Microscopy (PEEM) data that indicate that there is no or little PBrS at the very surface of the sample.

In both cases presented, NEXAFS microscopy provides new quantitative insight into the composition and morphology of the samples investigated, and we believe to be at the very beginning of NEXAFS microscopy making contributions to the science of polymer thin films. A variety of other applications are pursued by some of us and other researchers at beamline X1A. These include the characterization of dispersed phases in complex polyurethane polymers and the initial measurements of the partial miscibility of polycarbonate (PC) and poly(butylene terephthalate) (PBT) in PC/PBT blends. NEXAFS microscopy is also making contributions to polymer materials that were prepared via the non-equilibrium processing technique of mechanical alloying. The morphology of blends produced in this way from polymers such as poly(ethylene terephthalate) (PET), Vectra (75/25 mol% oxybenzoate/2,6oxynaphthoate), ethylene-propylene rubber (EPR) and PMMA can be readily visualized due to the chemical sensitivity of NEXAFS microscopy. NEXAFS microscopy of polymers has matured as a technique and is now systematically applied to a wide variety of materials. ■

[1] E. G. Rightor *et al.*, J. Phys. Chem. B **101**, 1950-1961 (1997).
[2] H. Ade *et al.*, Science **258**, 972 (1992).
[3] X. Zhang *et al.*, Nucl. Instrum. Meth. in Phys. Res. **A347**, 431-435 (1994).
[4] Data acquired with the X1A STXM developed by the group of Janos Kirz and Chris Jacobsen at SUNY@Stony Brook, with support from DOE and NSF. Zone plates made by S. Spector and C. Jacobsen (Stony Brook) and D. Tennant (Lucent Technologies/Bell Labs) with support from NSF. HA, DAW and APS are supported by NSF Young Investigator Award (DMR-9458060). SQ, SG, MR and JS are supported by NSF.

Microbeam Diffraction Studies of Interfacial Strain

I.C. Noyan, J.L. Jordan-Sweet, E.G. Liniger, and S.K. Kaldor (IBM Research Division, Yorktown Heights, NY)

Modern integrated circuits may have millions of transistors and a comparable number of passive circuit elements connected by submicron wide metal lines. The total length of these fine wires may exceed hundreds of meters. In general, this wiring is distributed over several levels, separated by dielectric material to prevent shorts. Millions of metal-filled holes (vias) provide the interconnections between these levels. To achieve (typical) failure rates below one chip per thousand, the on-chip structures must be built to very exacting specifications; a few atoms of a contaminant in the wrong place may cause failure. In addition, significant material problems must be solved, often at a basic level.

The thermal expansion coefficient mismatch between different materials may cause stresses that can result in fractures in the wiring or in the passivation levels that insulate them. In addition, the tremendous current densities seen by the fine metal wires (in excess of 10^6 amps/cm^2) may result in electromigration, where the electron flux knocks atoms from the wiring lattice and sweeps them along, causing voids at the cathode end. The displaced atoms aggregate close to the anode end of the wire (which is terminated by a via with different metallurgy) and cause very large compressive stresses that can actually rupture the passivation. The basic design principles that are used to overcome these problems are based on continuum mechanics with corraborating data from large specimens. These formulations may not be appropriate for the small domains encountered in microelectronic devices; in some cases the material is too close to an edge such that edge effects dominate and, in other cases, there simply are not enough atoms around to yield a continuum. Microdiffraction is used to obtain the basic boundary conditions to develop the deformation mechanics of small domains and, in addition, to yield structure and phase information.

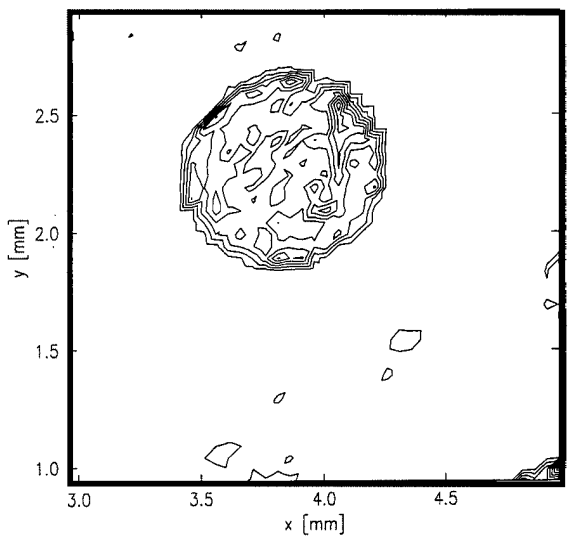

Figure A-8: Contour plot of the variation of Si (004) reflection intensity with position on a 2x2 mm area section of the sample. The circular area in the middle corresponds to the intensity increase observed as the microbeam traversed over one Al dot. The edge of the neighboring dot is seen in the lower right-hand corner. The data was acquired by step-scanning (with 50 micron steps along both axes, 1600 points) and counting for 60,000 monitor counts (about 5 seconds) at each position. The data were then normalized to yield diffracted counts per monitor count (cpmon) and processed to form equi-intenisty contours.

The first monochromatic x-ray microbeam diffraction experiments at Beamline X20A have been made by IBM scientists in Fall 1997. For this purpose a dedicated endstation which had been under construction during 1997 at Beamline X20B was used. This system is based on a two-circle Huber Goniometer and it uses tapered capillary optics for focussing the beam, micrometer precision sample-stages for specimen positioning, and energy-dispersive, linear and/or single channel detectors.

Beam sizes ranging from 2 to 25 microns have been used to characterize the orientation and strain distribution on a variety of thin-film samples. In this first set of experiments, the applicability of continuum equations (which are based on global averages or large homogeneous volumes) to domains containing limited volumes of material was investigated.

One case in particular is the interfacial strain state of patterned thin Al films on

single-crystal Si wafers[1]. In this experiment an array of 1mm-diameter, 850nm-thick Al dots evaporated on a 001 Si substrate was examined. A micro-beam topograph of the Si 004 reflection was constructed by mapping the integrated intensity as a function of position on the wafer. An example is shown in **Figure A-8**. The intensity contours corresponding to the region under the Al dot are 2x higher than the intensity from the bare Si substrate. This intensity enhancement is due to the transition from dynamical to kinematic scattering since the thermal stresses between Al and Si distort the Si under the thin film features[2,3]. A high-resolution scan of the Si 004 reflection across an Al dot (**Figure A-9**) shows multiple maxima and minima on a length scale much larger than the beam size (60-250 micrometers vs. 2x10 micrometers). In contrast, the strain state expected from the continuum "Shear Lag" formulation[4] predicts only two maxima at each end of the film, which decay smoothly down to the base (dynamical) intensity at the "critical length" as one moves closer to the center. The multiple extrema observed experimentally indicate that the strain transfer is periodically interrupted! This result has significant implications in the analysis of adhesion and stress transfer at thin film/substrate interfaces. It also shows that common assumptions about thin film properties may be invalid on a local scale. Microbeam x-ray diffraction provides a tool for testing these assumptions by providing data on a small length scale with minimal sample preparation. ■

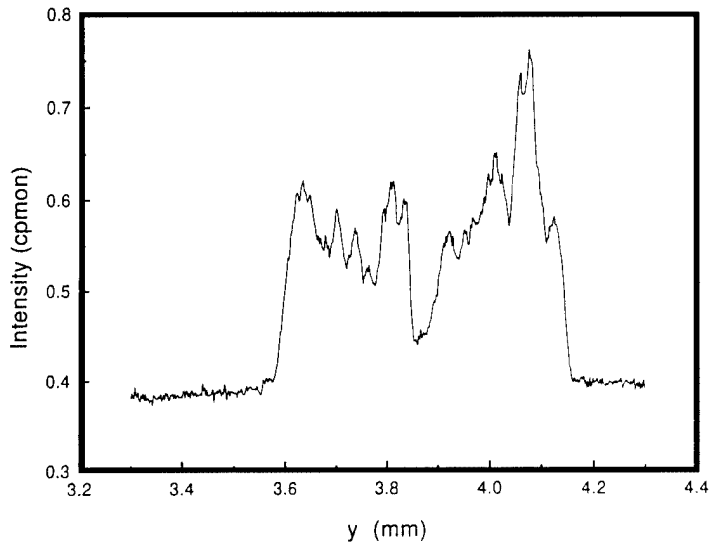

Figure A-9: The variation in Si (004) intensity across an Al dot. The step size is 2 microns. Note that the "baseline" is actually significant intensity from the bare Si wafer. The intensities are normalized to the monitor counts (cpmon). Error bars are not shown because of the high density of data points, but are approximately +/- .006 cpmin.

[1] I.C. Noyan, J.L. Jordan-Sweet, E.G. Liniger, and S.K. Kaldor, *Appl. Phys. Let.* (submitted).

[2] L.V. Azaroff, Elements of X-ray Crystallography, *McGraw-Hill*, pp. 207-227, (1968).

[3] B.D. Cullity, Elements of X-ray Diffraction, 2nd ed., *Addison Wesley*, pp. 268-270, (1978).

[4] W.T. Chen and C.W. Nelson, *IBM J. Res. and Dev.*, **23**, 179 (1979); H.L. Cox, *British J. Appl. Phys.*, **3**, 72 (1952); D. Hull and T.W. Clyne, An Introduction to Composite Materials, 2nd ed., *Cambridge University Press*, pp. 105-121, 143-147, (1996).

The Structure of the GroEL/GroES/ADP Complex

Z. Xu, A. Horwich and P. Sigler (Yale University)

The structure of the molecular chaperone GroEL in complex with a partner assembly GroES in the presence of bound ADP, was determined to a resolution of 3.0 Å using x-ray diffraction data collected at beamline X25 by Z. Xu, A. Horwich, and P. Sigler of Yale U. and the Howard Hughes Medical Institute (HHMI)[1]. The GroEL/GroES complex facilitates the folding of other proteins, and how this is accomplished is an important problem in modern biology. GroEL consists of two back-to-back 7-fold rotationally symmetric rings, that enclose two large, non-contiguous central cavities in which an unfolded protein can be bound. GroES consists of a single 7-fold rotationally symmetric ring, with mobile loops extending from its rim. In the presence of the nucleotide ATP, GroEL and GroES interact via these loops to form an asymmetrical GroEL/GroES complex. The x-ray diffraction data show that the overall structure of this complex undergoes a substantial change upon the binding of the nucleotide, arising from movements of the domain components of one of the GroEL rings (**Figure B-1**). This creates an enlarged cavity from which the bound protein can be released, upon dissociation of the GroES ring from the GroEL. The diffraction data also provide insight to the binding of the nucleotide to the complex. The crystals of this complex have a very large unit cell and diffract x-rays very weakly and anisotropically, and moreover are relatively small. Access to the high beam intensity of X25 was mandatory in order to determine its structure to such high resolution. ■

[1] Z. Xu, A. Horwich, and P. Sigler, *Nature* **388**, 741-750, (1997).

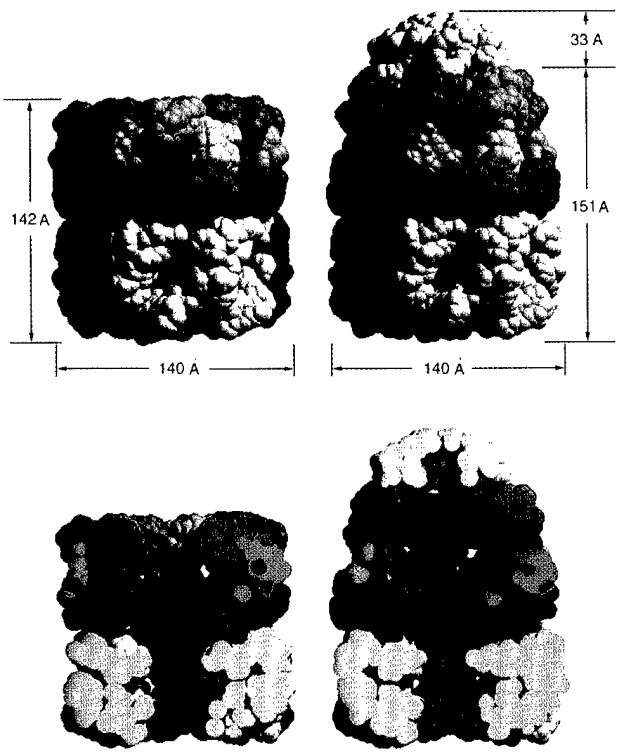

Figure B-1: Overall architecture and dimensions of GroEL and GroEL-GroES-$(ADP)_7$. Van der Waals space-filling models (6 Å spheres around Cα) of GroEL (**left**) and GroEL-GroES-$(ADP)_7$ (**right**). Upper panels are outside views, showing outer dimensions; lower panels show the insides of the assemblies and were generated by slicing off the front half with a vertical plane that contains the cylindrical axis. Various colors are used to distinguish the subunits of GroEL in the upper ring, with shading indicating domains; dark hue, equatorial domain; medium hue, apical domain; lightest hue, intermediate domain. The lower GroEL ring is uniformly yellow. GroES is uniformly gray.

Crystal Structure of Bovine Mitochondrial Cytochrome bc1 Complex, An Essential Component of Cellular Power Plant

D. Xia[1], C. A. Yu[2], H. Kim[1], A. Kachurin[2], L. Zhang[2], L. Yu[2], and J. Deisenhofer[1]

[1] HHMI & Department of Biochemistry, U. Texas, Southwestern Medical Center

[2] Department of Biochemistry, Oklahoma State U.

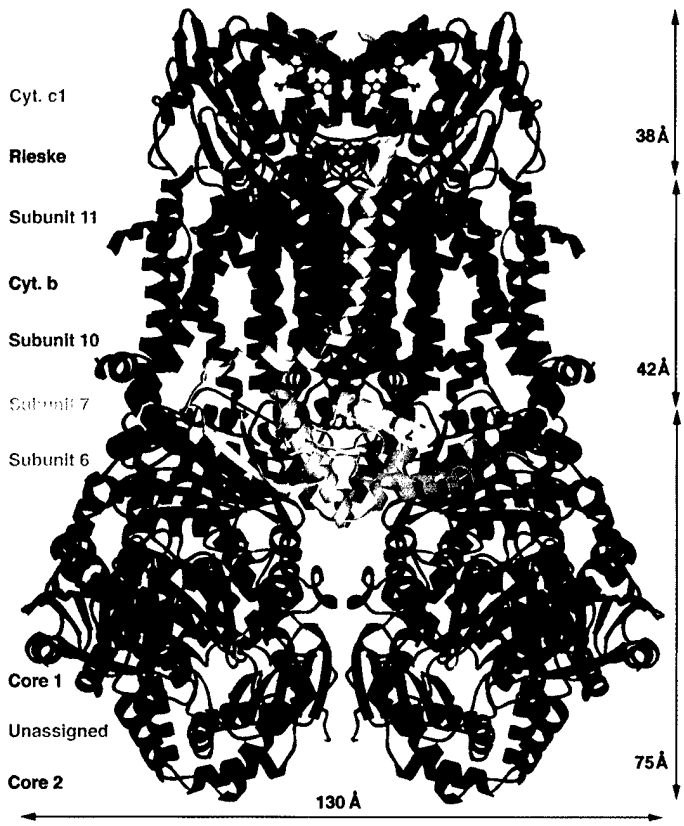

Figure B-2: Partial structural model of the dimeric cytochrome bc1 complex with polypeptides drawn as ribbons, hemes as stick models, and the Rieske iron-sulfur center as balls. Eight of the eleven subunits (core1, core2, cytochrome b, Rieske ISP, subunits 6, 7, 10, and 11) are completely traced and their sequences assigned. The top of the model is in the mitochondrial inter-membrane space, the middle spans the membrane, and the bottom is in the matrix space; approximate dimensions are given for each region.

All living cells use ATP (adenosine 5'-triphosphate) as a form of energy to sustain vital cellular processes essential for survival. ATP is constantly being generated in a cellular organelle called mitochondria — the cellular power plant, and the bc1 complex is one essential component of mitochondria directly involved in ATP synthesis. The bc1 complex performs an intermediate step in cellular respiration which involves a series of chemical reactions that frees energy in the form of ATP from food for use in cellular metabolism.

Cytochrome bc1 complex (ubiquinol-cytochrome c oxidoreductase, bc1) is the middle segment of the respiratory chain in almost all aerobic organisms, and an essential component in the photosynthetic machinery in purple bacteria. Green plants use highly homologous b6f complex as part of their energy photosynthetic apparatus. The bc1 complex is an integral membrane protein; it couples the electron transfer from ubiquinol to cytochrome c to the proton translocation across the membrane to generate a difference in pH and electrostatic potential to drive ATP synthesis. By determining the bc1 complex structure, we will be one step closer to a complete understanding of cellular of ATP generation.

Mitochondrial bc1 complex from bovine heart consists of 11 different subunits, two b- type hemes, one c-type heme and an iron-sulfur cluster with a total molecular weight of 250 Kd. The bc1 complex from bovine heart was purified

and crystallized, and bc1 complex crystals can be cryo frozen for stable data collection; they possess the symmetry of space group I4122 with cell dimensions of a=b=153.7 Å and c=597.5 Å. Synchrotron radiation sources was a critical factor in the successful structure determination. The use of beam time at beamline X12B of NSLS allowed data collection of both native and heavy atom derivatives in a relatively short period of time, a task that would have been impossible with a conventional x-ray source; the tunability of the x-ray wavelength at X4A enabled us to quickly and convincingly identify positions of iron atoms that are associated with redox-active prosthetic groups in the bc1 complex, and detect movement of the Rieske Iron Sulfur Protein (ISP); the high-flux x-ray beam at X25 permitted collection of a complete native data set to 2.7 Å resolution, making the refinement of bc1 structure possible.

The structure of bc1 was determined using MIRAS method with seven heavy metal derivatives. The current atomic model of the bc1 complex contains eight subunits completely sequence assigned, including core1, core2, cytochrome b, Rieske ISP, subunits 6, 7, 10 and 11; three subunits partially sequence assigned, including cytochrome c1, subunits 8 and 9; and four prosthetic groups which include two b-type hemes, one c-type heme and a 2Fe-2S cluster with a total number of amino acids residues in the model near 2000.

The bc1 complex forms a dimer in the crystal, and is 155 Å tall and 130 Å wide (**Figure B-2**). The whole complex can be divided into three regions: The membrane-spanning region is about 42 Å thick with 26 trans-membrane helices for the dimer; the cytochrome b dimer contributes 16 helices, cytochrome c1, the Rieske ISP, subunits 7, 10, and 11 account for the other five pairs of helices, respectively; projecting 38 Å into the inter-membrane space are the water soluble parts of the Rieske ISP and cytochrome c1, as well as subunit 8; the matrix region of the bc1 complex protrudes 75 Å into the mitochondrial matrix space and consists primarily of core1, core2 and subunits 6 and 9.

Taking advantage of the anomalous scattering property of iron atoms in the bc1 complex, we were able to determine the positions of and distances between these iron atoms in the bc1 complex (**Figure B-3**), and to postulate possible routes for electron transfer within the bc1 complex. More importantly, by combining anomalous diffraction experiments with specific inhibitor binding studies, we were able to detect very large conformational changes of the Rieske ISP upon binding of certain classes of inhibitors. These findings indicate a new mechanism for electron transfer from one subunit to another within the bc1 complex. ■

[1] D. Xia, C.A. Yu, H. Kim, J.-Z. Xia, A.M. Rachurin, L. Zhang, L. Yu, and J. Deisenhofer, *Science* 277, 60-66, (1997).

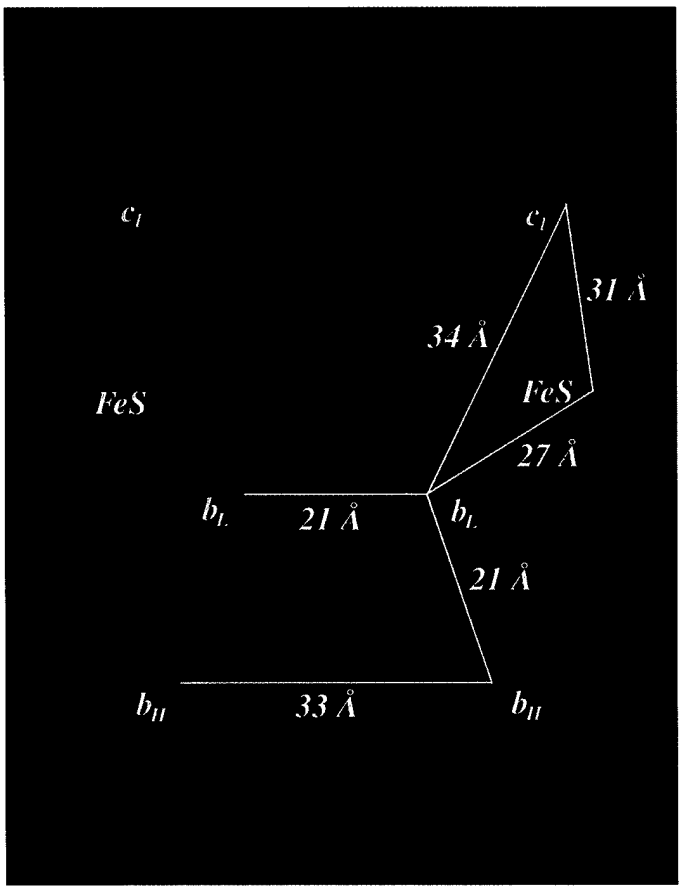

Figure B-3: Anomalous scattering difference-Fourier map contoured at 5.1 σ viewed parallel to the membrane space at the top and the matrix space at the bottom. Peaks were assigned to heme b_H, b_L, and c1 and to the Rieske iron-sulfur cluster, respectively, as shown. Distances between some iron pairs are indicated.

Structural Lyme-ology

C. L. Lawson, H. Li, M. Becker, and W. Ding (BNL Biology Department)

The crystal structure of an antigenic protein from the outer surface of the Lyme disease bacterium has been determined by x-ray diffraction methods. OspA (outer surface protein A) is an abundant immunogenic lipoprotein of the Lyme disease spirochete Borrelia burgdorferi that is being developed as a vaccine to protect humans from being infected after a tick bite. Making use of data from beam lines X12C, X12B, and X25, the crystal structure of a recombinant form of OspA was solved in a complex with the Fab fragment of a mouse monoclonal antibody, and was refined to a resolution of 1.9 Å[1]. OspA is formed from a large antiparallel beta-sheet, with an unusual nonglobular region of "freestanding" sheet connecting globular N- and C-terminal domains (**Figure B-4**). Another unusual feature of the folding pattern in the nonglobular region is arrays of residues with alternating charges. A hydrophobic cavity buried in a positively charged cleft in the C-terminal domain is a potential binding site for an unknown ligand. The binding region of this antibody is biologically interesting because it overlaps with a well conserved surface in the N-terminal domain that is not accessible on the spirochete. This suggests that OspA interacts with other membrane proteins. The other end of OspA, the C-terminal domain, is what is exposed in the spirochete, and this, therefore, is the immunologically interesting part. Recently, native and tungstate-derivative MAD data have been collected at X12C and X25 on crystals of OspA complexed with the Fab fragment of an antibody that inactivates the Lyme spirochete. Preliminary interpretation of these data suggests that the antibody binds to a highly variable region of the C-terminal domain, which would have important implications for world wide effectiveness of OspA-based vaccines. Data also have been collected on the highly homologous OspB lipoprotein, both alone and in a complex with the Fab fragment from an antibody that causes Lyme spirochetes to self-destruct. Multi-wavelength anomalous diffraction (MAD) data will soon be collected on tungstate-derivative OspB crystals. Patterson maps calculated from a single wavelength dataset at the tungstate L-III edge have already pinpointed the heavy-atom binding sites. ■

[1] H. Li, J.J. Dunn, B.J. Luft, and C.L. Lawson, *Proc.Nat. Acad. Sci.USA* 94, 3584-3589, (1997).

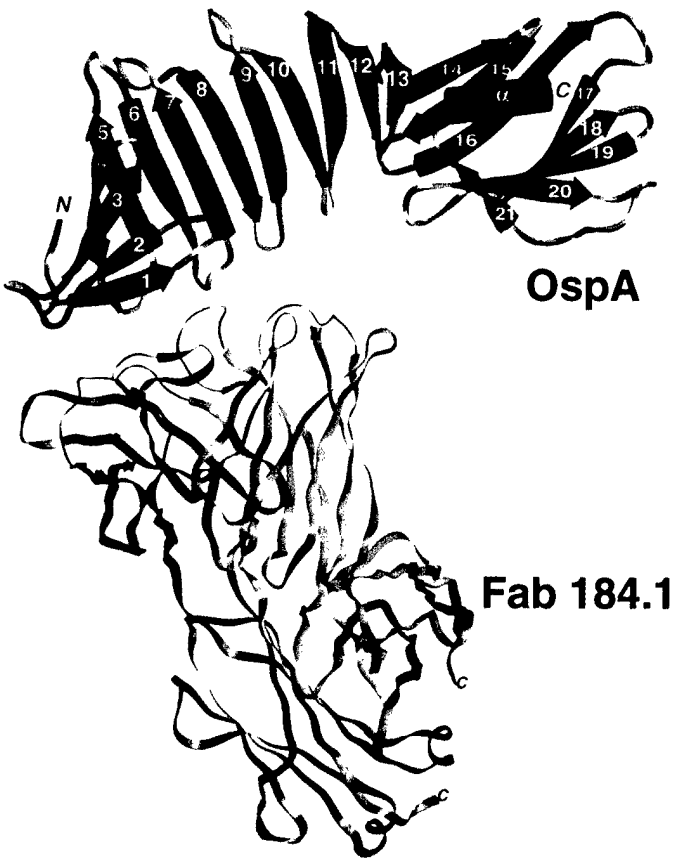

Figure B-4: Ribbon diagram of the first solved complex between OspA and an antibody fragment (Fab), published in Li *et al.*, 1997. OspA is represented by cyan arrows (ß-strands), grey ropes (turns) and a magenta cylinder (α-helix).

The Structure of the Human Natural Killer Cell Inhibitory Receptor

Q. Fan, L. Mosyak, and D.C. Wiley (Harvard University)

Natural killer (NK) cells lyse abnormal cells deficient in class I major histocompatibility complex (MHC) expression. Killer cell inhibitory receptors (KIR) on human NK cells prevent the lysis of target cells bearing specific class I MHC molecules. The x-ray structure of a p58 KIR (p58-cl42) was determined at 1.7 Å resolution using the multiwavelength anomalous diffraction (MAD) method. MAD data of a single selenomethionyl p58-cl42 crystal were collected to 2.2Å with a 300 mm diameter MAR Research image-plate system on the X25 beamline of the NSLS. Based on the x-ray absorption spectrum of the Se-Met p58-cl42 crystal, three wavelengths for data collection were chosen, which included one wavelength at the absorption peak (0.9791 Å), one at the inflection point (0.9794 Å), and a third at a remote high energy point (0.9639 Å). A native data set was collected to 1.7 Å on F-1 beamline at CHESS. MAD phasing was treated as a case of multiple isomorphous replacement. The initial MAD map was improved by density modification. A model of p58-cl42 KIR was traced from both the density modified and unmodified electron density map. The atomic model has been refined against the native data set at 1.7 Å resolution to a crystallographic R-value of 20.6% (R_{free} = 25.4%).

The p58-cl42 KIR structure has tandem immunoglobulin-like domains positioned at an acute, 60 degree angle (**Figure B-5**). Loops on the outside of the elbow between the domains form a binding site projected away from the NK cell surface. The topology of the domains and their arrangement relative to each other reveals a relationship to the hematopoietic receptor family. We propose, by analogy to the hematopoietic receptors, that signalling by KIR may involve receptor dimerization. ■

[1] Q.R. Fan, L. Mosyak, C.C. Winter, N. Wagtmann, E.O. Long, and D.C. Wilery, *Nature* **389**, 96-100, (1997).

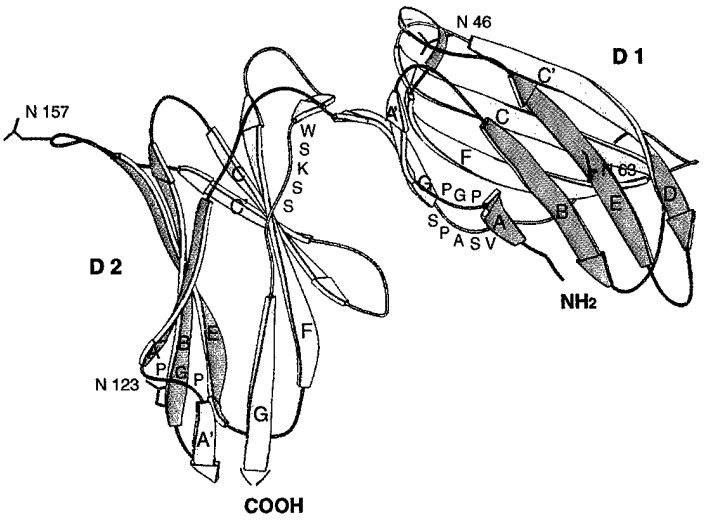

Figure B-5: Structure and topology of p58-42 KIR. KIR domain D1 is N-terminal, and D2 is C-terminal; ABED β-sheet (dark orange) and C'CFGA' β-sheet (light orange); WSKSS and VSAPS motifs (red); potential glycosylation sites at asparagines 46, 63, 123, and 157 (black).

The Structure of the Cre Recombinase/DNA Complex

F. Guo, D.N. Gopaul, and G.D. Van Duyne (University of Pennsylvania)

Genetic recombination involves the breaking and rejoining of DNA strands between two sites to provide a new strand connectivity and therefore an alternative organization of the genetic code. Organisms use DNA recombination for a number of purposes, including the generation of genetic diversity, the repair of damaged DNA, the integration and excision of viral genomes into and out of the host chromosome, the regulation of gene expression, and in ensuring the stable inheritance of circular chromosomes and plasmids. The lambda integrase family of enzymes that mediates recombination in bacteria and yeast recognizes specific DNA sequences and carries out the exchange of DNA strands only at these sites[1]. The bacteriophage P1 Cre recombinase, a member of the lambda integrase family, carries out site-specific recombination between 34-base pair DNA sequences called loxP sites[2]. The simplicity of the Cre/loxP system (no other proteins or DNA sequences are required) has led to a rapid rise in its use as a tool in a number of genetic engineering experiments, particularly those involving the study of gene function in transgenic mice[3].

The work described here involves the recombination reaction between Cre recombinase and its DNA substrate, the loxP site. A cartoon representation of this reaction is shown in **Figure B-6**. Two Cre molecules bind to each of the two loxP substrates and bring the double-stranded helices together to form a recombination synapse. Cre then cleaves two of the four DNA strands in the synapse, using a tyrosine side chain as a nucleophile. Transient phosphotyrosine links between protein and DNA are formed, thereby conserving the energy of the phosphodiester bond. The free DNA strand produced upon cleavage then acts as a nucleophile, attacking the phosphotyrosine linkage located across the synapse on the partner substrate. This results in the exchange of two of the four DNA strands and formation of a Holliday junction intermediate. A complementary set of cleavage and strand exchange steps on the remaining pair of DNA strands then completes the recombination event and gives recombinant DNA duplexes.

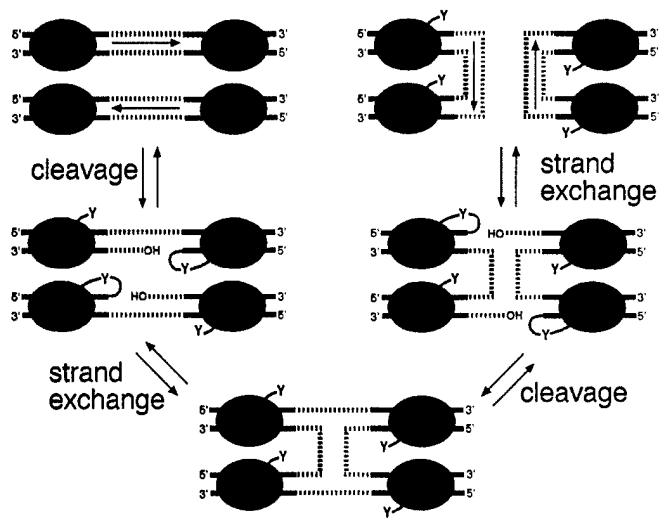

Figure B-6: Representation of the cleavage, exchange, and recombination processes involved in the breaking and rejoining of two DNA double helices, mediated by the bacteriophage P1 Cre recombinase. Two successive cycles of strand cleavage, exchange, and recombination are required to fully carry out the recombination event.

In work carried out at the X25 and X4A beamlines at the NSLS, G. Guo, M. Gopaul, and G. Van Duyne from the University of Pennsylvania School of Medicine have trapped and determined the three-dimensional structure of a Cre-loxP reaction intermediate where the recombinase has cleaved the loxP substrate to form a phosphotyrosine linkage, but is unable to complete the strand exchange step[4]. To accomplish this, they formed and crystallized a 200 kD synaptic Cre-DNA complex using a suicide loxP substrate that loses its attacking nucleotide upon cleavage. Crystals of this Cre-DNA complex diffracted X-rays poorly on home sources and required the wiggler source and optics at X25 in order to obtain the relatively high resolution (2.4 Å) for a structure of this complexity. In addition, the resources of the X4A beamline were used to conduct a multiwavelength

anomalous diffraction (MAD) experiment using selenomethionine-containing Cre recombinase at the Se absorption edge. The anomalous scattering contribution from 22 selenium atoms in the crystallographic asymmetric unit was crucial in obtaining crystallographic phases to interpret the structure.

The Cre-DNA intermediate structure is shown in **Figure B-7**. Four recombinase molecules (green and purple ribbons) form a pseudo-fourfold symmetric tetramer that is held together by a network of protein-protein interactions. The cleaved loxP sites (gold ribbons) have been bent by about 90° and adopt a nearly square planar configuration. The green recombinase molecules have cleaved the loxP site and formed phosphotyrosine bonds to the DNA. The purple recombinase molecules have not cleaved the DNA substrates and one of the interesting questions addressed by this structure involves understanding how the recombinase tetramer coordinates the cleavage reactions. The free ends of the cleaved DNA strands have been pushed towards the center of the synaptic complex, in what appears to be the start of the strand transfer process. The Cre-DNA synaptic intermediate structure has provided the first three-dimensional framework for understanding many aspects of the lambda integrase family site-specific recombination reaction and has both supported a number of recent proposals about how the reaction occurs and has provided a fresh view of other aspects. The structural model also promises to serve as an important starting point for the design of improved recombinases and substrates for use in genetic engineering applications. ■

[1] N.L. Craig, "The Mechanism of Conservative Site-Specific Recombination", *Annual Review of Genetics* **22**, 77-105, (1988).

[2] N. Sternberg, D. Hamilton, S. Austin, M. Yarmolinsky, & R. Hoess, "Site-Specific Recombination and its Role in the Life Cycle of Bacteriophage P1", *Cold Spring Harbor Symposia on Quantitative Biology* **1**, 297-309, (1981).

[3] B. Sauer, "Manipulation of Transgenes by Site-Specific Recombination: use of Cre Recombinase", *Methods in Enzymology* **225**, 890-900, (1993).

[4] F. Guo, D. N. Gopaul, G. D. Van Duyne, "Structure of Cre Recombinase Complexed with DNA in a Site-Specific Recombination Synapse", *Nature* **389**, 40-46, (1997).

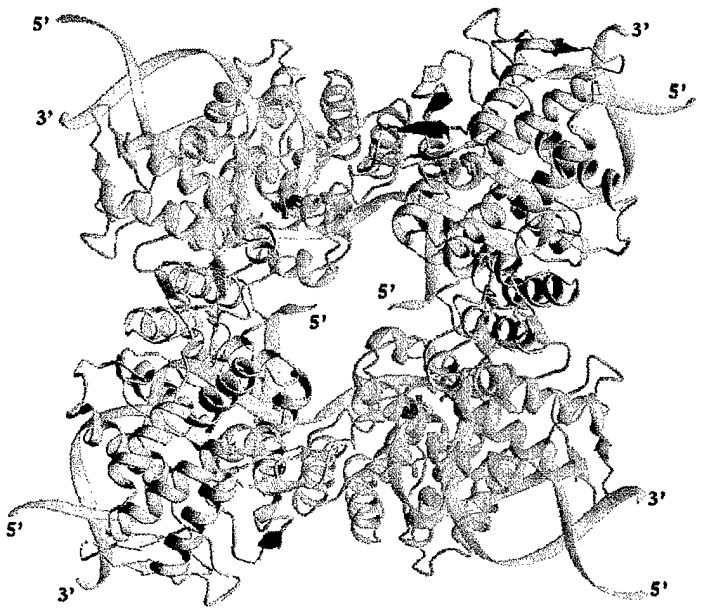

Figure B-7: Ribbon representation, based on x-ray diffraction results, of the Cre-DNA intermediate formed following DNA cleavage, but for which the strand exchange process was not completed. DNA strands are shown as gold ribbons, and the Cre recombinase molecules are shown as green and purple ribbons. The cleaved DNA loxP sites have been bent to form a nearly square planar configuration, and the free ends of the cleaved strands point toward the center of the complex, to strand exchange.

Crystal Structure of the P4-P6 Domain from a Group Ribozyme Reveals Principles of RNA Packing

J. Cate and J. Doudna (Yale University)

The discovery that RNA can function as a biological catalyst, or ribozyme, has raised important questions about the chemistry and evolution of enzymes. Several classes of ribozymes have been identified and characterized, but until recently there was little information about the structure of RNA. The sequences of most families of ribozymes consist of a conserved series of short base-paired stems (helices) connected by "loop" regions. Biochemical experiments suggested that the helices of large RNA molecules often pack into globular structures with solvent-inaccessible cores, much like proteins.

Group I self-splicing introns, the first class of ribozymes discovered, have the remarkable ability to excise themselves from precursor transcripts without the aid of any protein. The structure of the RNA holds the key to understanding the self-splicing mechanism as well as evolutionary relationships among ribozymes. The group I intron from Tetrahymena thermophila has been well characterized biochemically, revealing the ribozyme to be comprised of two structural domains. The domains can be synthesized separately and assembled in trans to produce active ribozymes. The 160-nucleotide P4-P6 domain, containing half of the residues of the catalytic core, is an independently folding structural unit. Following the development of techniques for RNA crystallization, crystals of the P4-P6 domain were obtained that diffracted X-rays to better than 2.8 Å resolution.

The solution of the P4-P6 crystal structure was achieved through an insightful observation by Jamie Cate, then a graduate student working on the project at Yale. Jamie noticed that P4-P6 crystals grew best in the presence of tiny amounts of cobalt hexammine, a small molecule that mimics the geometry of a fully hydrated magnesium ion. Since dramatic effects on crystal growth were seen with stoichiometric amounts of hexammine to RNA, Jamie reasoned that there might be just a few specific hexammine binding sites present in the RNA. To take advantage of such potential sites for making heavy atom derivatives, Jamie obtained from Prof. Henry Taube at Stanford a sample of osmium hexammine, and he soaked this compound into the P4-P6 crystals. An anomalous difference Patterson map calculated using diffraction intensities measured on a laboratory x-ray source showed several strong peaks whose positions could be refined and cross-checked. The osmium derivative was used to solve the P4-P6 crystal structure by multiwavelength anomalous diffraction (MAD) with data measured at NSLS beamline X4A (**Figure B-8**).

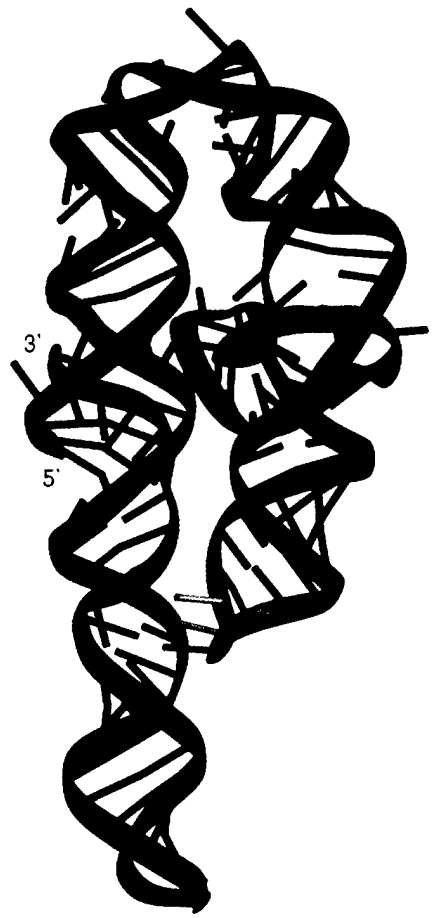

Figure B-8: 2.8 Å crystal structure of the 160-nucleotide P4-P6 of the Tetrahymena self-splicing ribizome. Helices of the conserved catalytic core, in blue and red, pack against helices of an extended region. Tertiary contacts occur between an A-rich corkscrew motif (orange) and the P4 helix (blue), and between a tetraloop (gold) and its receptor (green).

The 2.8 Å crystal structure of the P4-P6 domain is the first crystal structure of an RNA molecule large enough to show side-by-side packing of helices. Such packing is thought to be necessary to form stable active sites as found in self-splicing introns, Ribonuclease P, the ribosome and the spliceosome. In the domain, a sharp bend allows stacked helices of the conserved core to pack against helices of an adjacent region. Two specific long-range interactions clamp the two halves of the domain together: a magnesium-coordinated adenosine-rich corkscrew plugs into the minor groove of a helix, and a GAAA hairpin loop binds to a conserved 11-nucleotide internal loop. Metal- and ribose-mediated backbone contacts further stabilize the close helical packing, giving rise to a solvent-inaccessible interior.

One interesting feature of the P4-P6 structure is the discovery of an unexpected new motif that mediates both intra- and intermolecular interactions. At three separate locations in the P4-P6 molecule, adjacent adenosines in the sequence lie side-by-side, stacking simultaneously on both sides of the helix. This creates an adenosine platform, opening the minor groove for stacking or base-pairing with nucleotides from a distal RNA strand. This motif explains in part the preponderance of adenosines in internal loops of many RNAs.

Most of the contacts that stabilize internal P4-P6 domain structure as well as the packing of arrays of molecules in the crystal lattice involve the minor groove. The wide and shallow minor grooves of A-form helices are generally more accessible than the deep major grooves. However, non-canonical base pairings, loops and bulges in RNA can perturb the geometry of a helix, affecting the shape and electrostatic potential in localized regions. Indeed, local perturbations at tandem G-U "wobble" base pairs in the P4-P6 RNA give rise to specific metal binding pockets in the major groove: the hexammine binding sites used in the structure determination. In two cases these sites are occupied by fully-hydrated magnesium ions in the native structure. The binding sites expand the known repertoire of ligand binding motifs in RNA and may provide a general means of derivatizing appropriately designed RNAs for x-ray crystallographic analysis. Phylogenetic sequence comparisons show that one class of these motifs occurs frequently in ribosomal RNAs, suggesting a possible mechanism for metal binding in the ribosome. ■

[1] J.H. Cate, A.R. Gooding, E. Podell, K. Zhou, B.L. Golden, C.E. Kundrot, T.R. Cech, and J.A. Doudna, "Crystal Structure of a Group I Ribozyme Domain: Principles of RNA Packing", *Science* **273**, 1678-85, (1996).

[2] J.H. Cate, A.R. Gooding, E. Podell, K. Zhou, B.L. Golden, A. Szewczak, C.E. Kundrot, T.R. Cech, and J.A. Doudna, "RNA Tertiary Structure Mediation by Adenosine Platforms", *Science* **273**, 1696-9, (1996).

[3] J.H. Cate, and J.A. Doudna, "Metal Binding Sites in the Major Groove of a large Ribozyme Domain", *Structure* **4**, 1221-9, (1996).

The Structure of a Component of the AIDS Virus: the Carboxyl-Terminal Dimerization Domain of the HIV-1 Capsid Protein

T. R. Gamble, S. Yoo, F.F. Vajdos, U.K. von Schwedler, D.K. Worthylake, H. Wang, .P. McCutcheon, W.I. Sundquist, C.P. Hill (University of Utah)

As reported recently[1] we have solved the x-ray crystal structure of the C-terminal dimerization domain of the capsid protein from the human immunodeficiency virus type 1 (HIV-1). The 26-kD capsid protein (CA) of HIV-1 results from the action of the well-known HIV protease: as the virus buds, a 55-kD polyprotein called Gag is processed by the viral protease to produce three discrete new proteins — one, called matrix, that binds to the viral membrane, the capsid protein which forms the conical viral core structure, and a third called nucleocapsid that helps to organize the viral RNA — as well as several smaller peptides. These are the major structural proteins of HIV, with ~2, 000 copies of each protein present in a single viral particle.

CA performs several essential roles during the HIV life-cycle. Most importantly, CA forms the conical core structure that surrounds the viral genome at the center of the mature virus. Genetic analyses indicate that Capsid also functions during assembly of new virus particles and as the virus enters a new host cell. Our study focused on the COOH-terminal domain of Capsid, residues 146-231 (CA146-231). This domain contains a stretch of 20 amino acids, termed the MHR (major homology region), that is found in all known onco- and lentiviruses, and in the yeast retrotransposon Ty-3. As one might expect, this highly conserved sequence is essential for viral replication, although its precise functions remain unclear. Another feature of special interest is the role of CA146-231 in mediating Capsid dimerization; this domain dimersizes with the same affinity as the full length protein. Capsid dimerization is essential for core formation and infectivity, and the assembly of infectious viral particles.

In an effort to understand the structural basis for Capsid dimerization and MHR conservation, we determined the crystal structures of recombinant selenomethionine-substituted CA151-231 at 1.8 Å. resolution and native (no Se) CA146-231 at 3.1 Å resolution. Diffraction data for the CA151-231

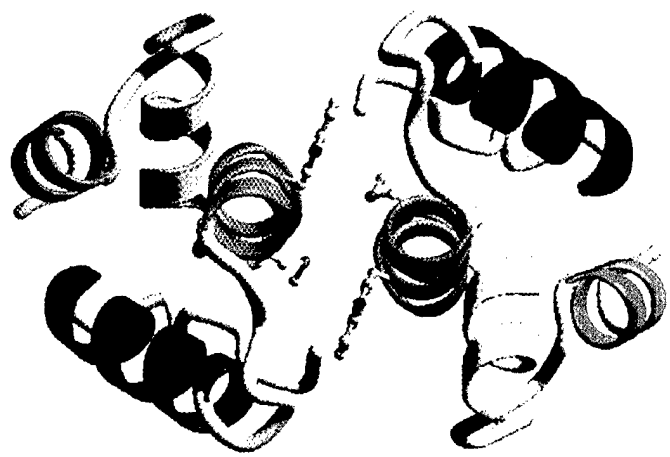

Figure B-9: Ribbon diagram of the structure of the HIV-1 capsid domain CA(146-231) viewed as a dimer. Two residues required for stabilization of the dimer *in vivo* are shown as stick models near the center of the figure.

crystal-structure analysis were taken at NSLS beamline X12C. The structure was solved by the multiwavelength anomalous diffraction method (MAD), based on scattering from Se atoms that had been introduced to the protein in methionine residues. The structure determination was relatively rapid, with an electron-density map produced and an essentially complete model built only 54 hours after data-collection began. Residues 151-219 of CA151-231 formed a well ordered globular domain in this structure. The standard crystallographic R-value is 22.9% and the free R-value (used for cross validation of the result) is 27.4% at the end of the refinement of the structure of CA151-231. Once the CA151-231 structure was known, it was used to determine the CA146-231 structure by the method of molecular replacement.

The CA146-231 and CA151-231 structures are very similar, with each molecule composed of an extended strand followed by four a-helices. **Figure B-9** shows the structure of the biologically relevant CA146-231 dimer that is formed in the crystals. In this figure, the MHR is composed of the helix shown at the lower left (or upper right) and the strand that lies behind it in the figure. The role of the most highly conserved MHR residues is to form a hydrogen-bonding network that stabilizes this structure and links it to the helix that is seen end-on near the center of the dimer. The structure therefore explains the observation that certain "conservative" mutations in the MHR, for example Gln to Asn or Glu to Asp, block HIV-1 replication; even mutational changes as small as the deletion of a single carbon atom appear to disrupt the hydrogen-bonding network within the MHR. A series of four conserved hydrophobic residues also are essential for MHR function; they lie on one surface of this helix and contribute to the hydrophobic core of the protein. Thus, all of the conserved MHR residues perform critical structural roles. Although most of the Gag polyprotein is quite variable among other viruses, the remarkable conservation of this 20-residue segment suggests that the MHR structure mediates an essential interaction with a highly conserved binding partner, such as a cellular factor or an invariant segment of a viral protein.

CA146-231 possesses almost identical dimerization affinity as the full length CA protein. The dimer interface is created by the parallel packing of two helices, to create a hydrophobic core. It is notable that the dimer interface and MHR are distinct non-overlapping structures. Site-directed mutagenesis was used to confirm that the dimer seen in the CA146-231 crystal is also the dimer interface of full-length capsid protein in solution. Two interface residues, Trp184 and Met185 (see **Figure B-9**), were mutated to Ala in the intact CA. In neither case would the mutant protein form dimers in solution, thereby indicating that the crystallographic structure is indeed the authentic dimer. One of these mutations allowed the formation of viral particles in cell cultures, although the particles produced were not infectious. This indicates that the crystallographic dimer is an essential interaction in the assembly and maturation of viral particles, and provides another possible target for the design of drugs to treat AIDS. ■

[1] T.R. Gamble *et al., Science* **278**, 849 - 853 (1997).

Analysis of Model Automotive Exhaust Catalysts: The Oxidation and Reduction of CeO_2

D. R. Mullins, D. R. Huntley and S. H. Overbury (Oak Ridge National Laboratory), G. N. Glavee (Lawrence University)

Modern automotive exhaust catalysts aid in the removal of toxic emissions by converting the harmful gases into more benign substances. In particular CO is oxidized into CO_2 and NO_X is reduced to N_2 and O_2.[1] Current automotive fuel systems are designed to maintain the air to fuel ratio in the proper stoichiometric proportions so that CO and NO_X are almost fully oxidized and reduced, respectively. However, during acceleration and deceleration the air to fuel ratio can move away from the optimal mixture so that the toxic emissions are not fully converted. Various materials have been added to the catalyst formulation in order to widen the air to fuel ratio window in which the catalyst efficiently operates. One important component is CeO_2.[2] Cerium has the ability to readily convert between the +3 and +4 oxidation states, thereby releasing and storing oxygen. In doing so, it is able to assist in the reduction of NO_X under oxidizing conditions.

In order to understand the behavior of CeO_2, the Surface Science and Catalysis Group at Oak Ridge National Lab has been studying the oxidation and reduction of Ce metal foil and single crystal CeO_2 films under UHV conditions and small $Ce_XZr_{1-X}O_2$ particles at atmospheric pressure.

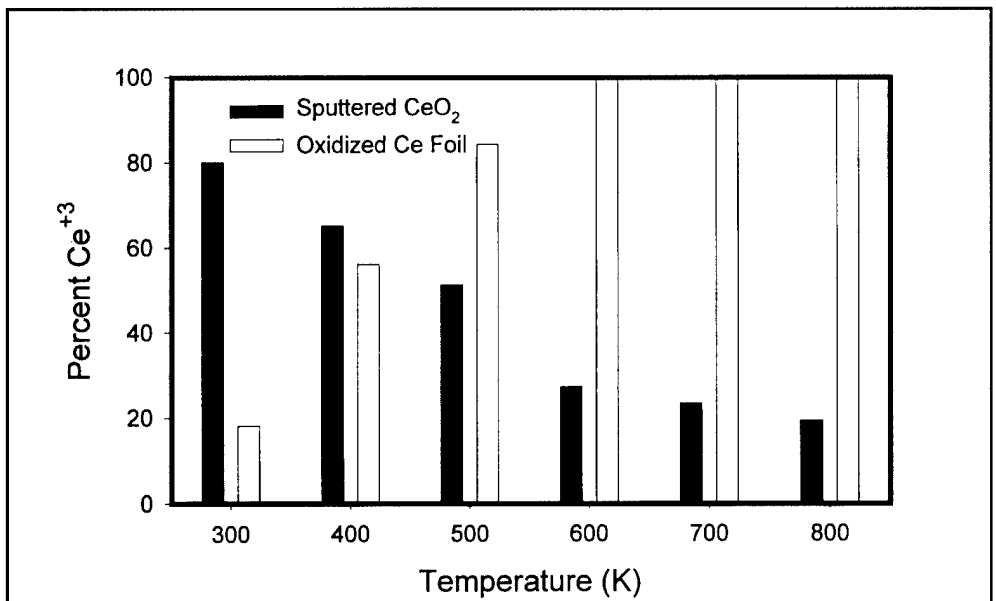

Figure C-1: The percentage of Ce^{+3} in two different CeO_x samples as a function of annealing temperature. Light Bars - Ce metal foil that was oxidized by exposing it to > 1000 L O_2 at 300 K. Dark Bars - CeO_2(110) film that was reduced by sputtering with Ar^+ ions at 300 K.

Ce Metal Foil and Single Crystal CeO_2 Films

Ce metal oxidizes readily and must be stored in an inert gas environment in order to prevent total oxidation to CeO_2. A oxygen free surface can be prepared in UHV and then the degree of oxidation can be varied by controlling the oxygen exposure. Various techniques can be used to monitor the Ce oxidation state. These methods include Ce 4d and valence band photoemission (XPS) and x-ray absorption spectroscopy (XAS) at the O 1s absorption edge.[3] These experiments have been performed on beamline X1B.

At room temperature low exposures of O_2 (< 10 L) produce Ce(III) oxide. This layer is fairly stable and inhibits the uptake of additional oxygen. Large exposures of O_2 (~ 1000 L) are needed to produce Ce(IV) oxide. **Figure C-1** (light bars) shows the relative amount of Ce^{+3} and Ce^{+4} as a function of temperature. The Ce foil is the most oxidized at 300 K. The Ce(IV) oxide layer is themally unstable due to oxygen diffusion and oxidation of the underlying Ce^0. The results indicate that oxygen transport through the Ce substrate is the limiting factor in the oxidation of the Ce bulk. The process is shown schematically in **Figure C-2a.**

The reducibility of fully oxidized CeO_2 was studied by examining single crystal CeO_2 films. These films were very difficult to reduce showing little evidence of Ce^{+3} even after exposure to > 1000 L of H_2 or CO at temperatures up to 800 K. These films could only be reduced in UHV by sputtering with inert gas ions. As shown by the dark bars in **Figure C-1**, the sputtered surfaces re-oxidized as the sample was annealed above room temperature. These surfaces were also thermally unstable due to oxygen diffusion from the bulk. This process is shown schematically in **Figure C-2b.**

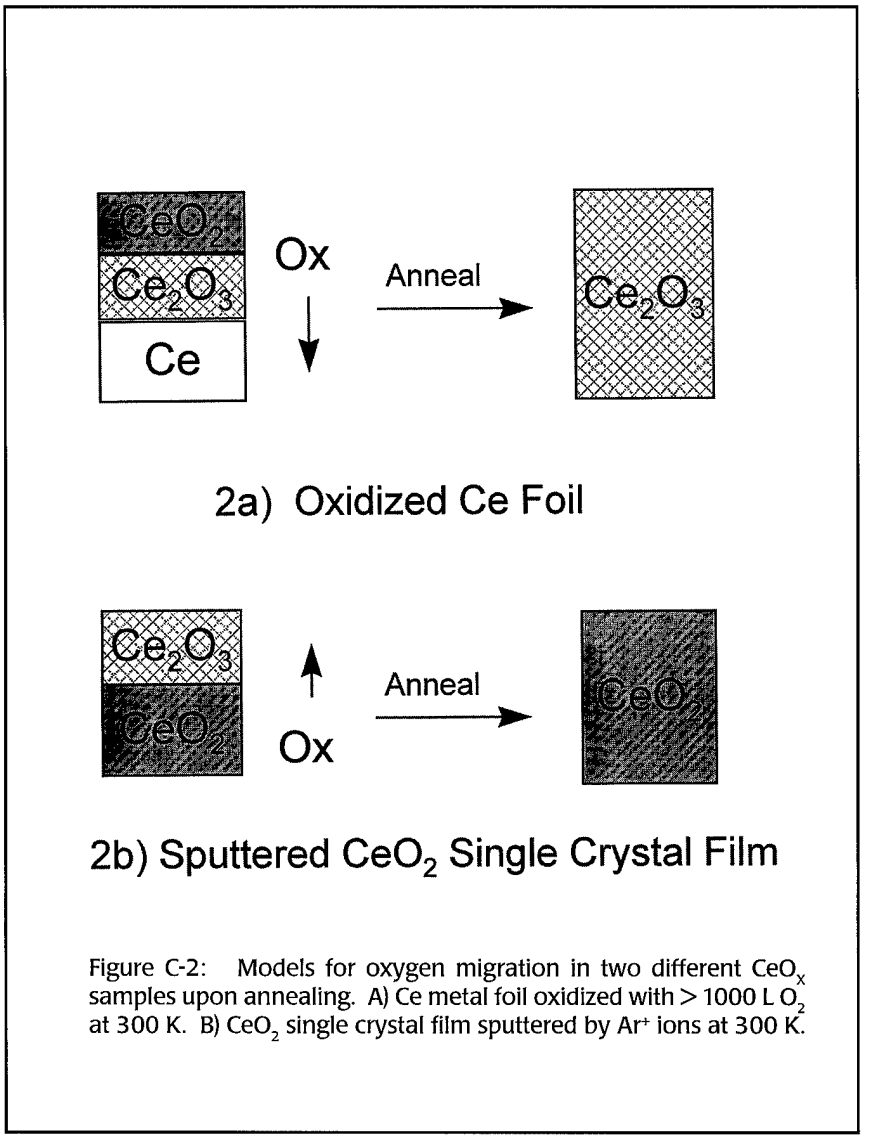

Figure C-2: Models for oxygen migration in two different CeO_x samples upon annealing. A) Ce metal foil oxidized with > 1000 L O_2 at 300 K. B) CeO_2 single crystal film sputtered by Ar^+ ions at 300 K.

$Ce_xZr_{1-x}O_2$ and Rh/ $Ce_xZr_{1-x}O_2$

The oxidation and reduction of small ceria particles at atmospheric pressures were studied by x-ray absorption spectroscopy (XAS) at the Ce L_{III} edge on beamline X19A.[4] Particles with surface areas ~ 100 m^2/g were synthesized using sol-gel techniques and hypercritical drying. In addition to pure CeO_2, mixed oxides were prepared with Zr forming $Ce_XZr_{1-X}O_2$ particles. Some of these oxide were impregnated with 0.5 - 2% Rh, by weight. The oxides were reduced in 4% H_2/He and were oxidized in zero gas air.

The degree of reduction can be determined from several features in the Ce L_{III} XAS.[5] As shown in **Figure C-3a**, Peak C is associated with Ce^{+4} and it decreases as the sample is heated in the H_2/He atmosphere. Peak B_0 is associated with Ce^{+3} and its intensity increases during reduction. CeF_3 and reagent grade CeO_2 were used as standards for Ce^{+3} and Ce^{+4} spectra, respectively.

The reduction of CeO_2, $Ce_{0.5}Zr_{0.5}O_2$ and Rh/ $Ce_{0.5}Zr_{0.5}O_2$ is shown in **Figure C-3b**. It can be seen that the addition of Zr enhances the extent of reduction at a given temperature while the addition of Rh reduces the temperature at which reduction occurs. ■

Acknowledgment

Research was sponsored by the Division of Chemical Sciences, Office of Basic Energy Sciences, U.S. Department of Energy at Oak Ridge National Laboratory, managed by Lockheed Martin Energy Research Corp. under contract number DE-AC05-96OR22464.

[1] K. C. Taylor, *Catal. Rev. - Sci. Eng.* **35**, 457, (1993).
[2] J. G. Nunan, H. J. Robota, M. J. Cohn and S. A. Bradley, *J. Catal.* **133**, 309, (1992).
[3] D. R. Mullins, S. H. Overbury and D. R. Huntley, *Surface Sci.*, submitted.
[4] S. H. Overbury, D. R. Huntley, D. R. Mullins and G. N. Glavee, *Catal. Lett.*, submitted.
[5] J. El Fallah, S. Boujana, H. Dexpert, A. Kiennemann, J. Majerus, O. Touret, F. Villain and F. Le Normand, *J. Phys. Chem.* **98**, 5522, (1994) .

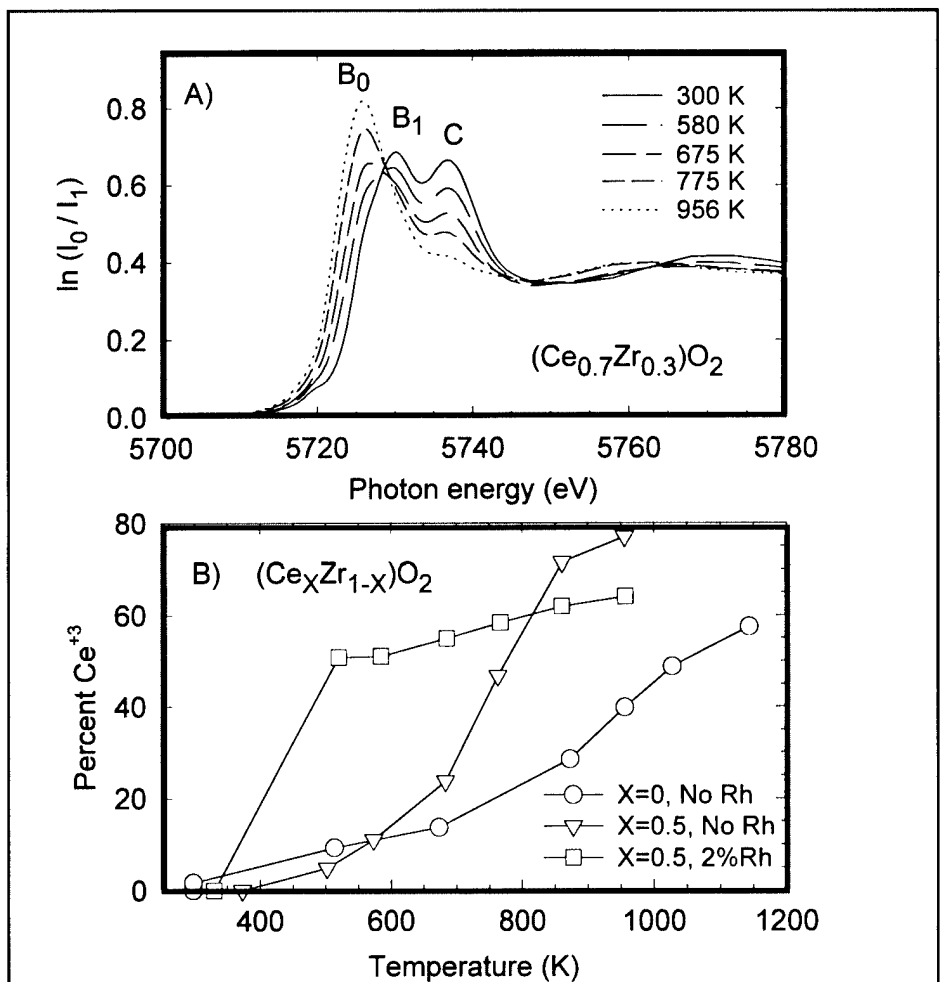

Figure C-3: A) Ce L_{III} absorption spectra for $(Ce_{0.7}Zr_{0.3})O_2$ particles in flowing 4% H_2 / He as a function of temperature. B) Percent Ce^{+3} following reduction in 4% H_2 / He as a function of temperature for $(Ce_XZr_{1-X})O_2$ for sample with no Zr or Rh, 50% Zr and no Rh, and 50% Zr and 2% Rh.

Dynamic Effects in Core Excitation of Small Molecules

B. Kempgens, A. Kivimaki, M.N. Piancastelli, K. Maier, H.M. Koppe, M. Neeb, U. Hergenhahn, and A. M. Bradshaw (Fritz-Haber-Institut, Berlin)

The high resolution capability of X1B has continued to give new insights into dynamic effects in core excitation of small molecules. As reported last year, excitation of the antisymmetric stretching mode by vibronic coupling was observed in the O 1s photoelectron spectrum in CO_2 [1]. A consequence of this effect is that the core hole dynamically localizes on one of the O atoms; the same phenomenon has been recently observed in the photoabsorption spectrum of hydrocarbon molecules containing equivalent C atoms[2]. In the photoelectron spectrum of the ethane molecule (C_2H_2) the intrinsic C 1s bonding-antibonding splitting of ca. 105 meV has been established for the first time[3]. New measurements of the vibrational fine structure of the C 1s and O 1s main lines have been made in CO, as shown in **Figure C-4**. From an analysis of the Franck-Condon factors, the bond lengths of 1.079 Å and 1.167 Å can be determined for the C 1s and O 1s core-ionized states. This shortening and lengthening of the bond with respect to the ground state can be understood from the slightly antibonding and slightly bonding nature, respectively, of the C 1s and O 1s core states in CO[4]. In another study, measurements of the photoelectron spectra above the C 1s threshold in the series C_2H_2, C_2H_4, and C_2H_6 have called into question the existence of shape resonances in the C 1s photoionization of these molecules[5]. Shape resonances can be understood as enhancements of the photoionization cross section by angular momentum transfer to the photoelectron caused by its scattering on the molecular core. This pictures implies that they are

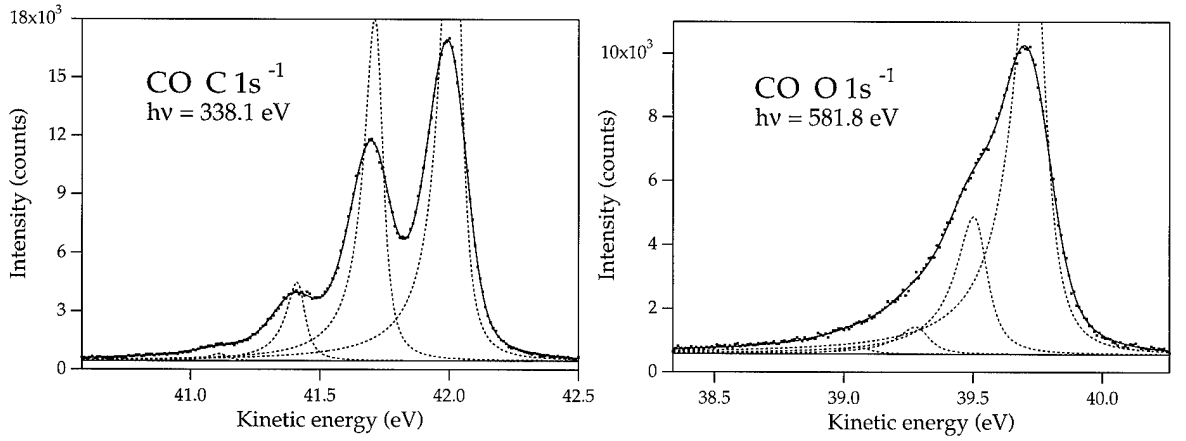

Figure C-4: Photoelectron spectra showing the vibrationally resolved CO C 1s and O 1s main lines. The dashed lines show individual vibrational components before convolution with the instrumental function and with an asymmetric lineshape due to post-collision interaction.

due to a single-particle phenomenon and should be visible in the single hole photoionization cross section. The C_2H_2 photoelectron spectrum in **Figure C-5a** depicts the C_2H_2 C 1s main line and its most prominent satellites, S1 and S0, pertaining to the triplet and singlet states, respectively, due to the valence $1(\pi)u$-to-$1(\pi)^*$ shake-up accompanying the C 1s photoionization. By analyzing a series of these spectra taken at photon energies over the presumed shape resonance position, it is shown that the cross-section of S0 is enhanced at a few eV above its threshold. The same is true for several other satellites, partly due to conjugate shake-up processes which involve the dipole excitation of the C 1s electron and the monopole ionization of a valence electron. Such an enhancement results in the peak around 310 eV in the photoabsorption cross-section in **Figure C-5b**. In contrast to that in the C 1s photoionization main line, no clear enhancement, as would be expected from a shape resonance, is observable. A similar phenomenon leads to a shoulder in the C 1s photoabsorption cross-section of C_2H_4, which was also previously interpreted as a shape resonance by other researchers. This study raises the question as to whether there exists a simple linear correlation between shape resonance position and bond length, as has been proposed earlier both in gas phase spectroscopy and surface science. ■

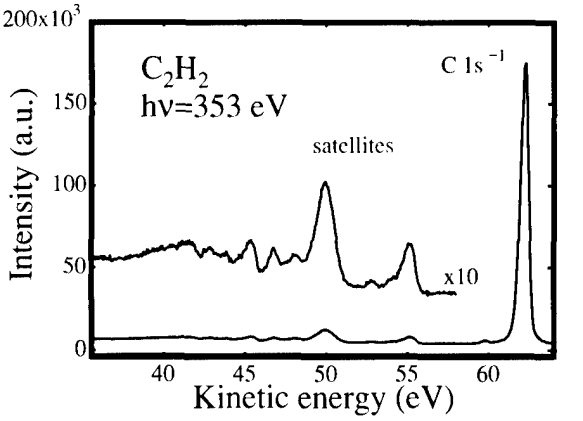

Figure C-5: (a) Photoelectron spectrum of C_2H_2 showing the main line and various satellite lines. (b) The photoabsorption and single-hole cross-sections of C_2H_2 above the C 1s threshold.

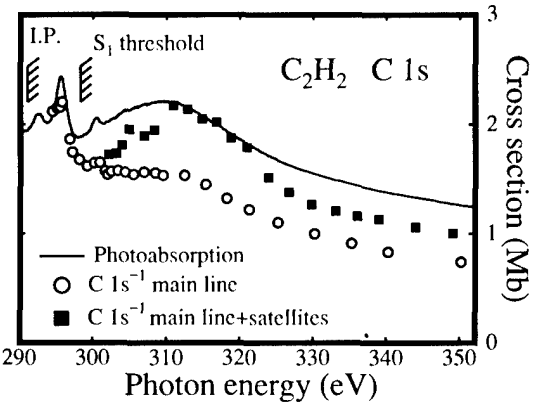

[1] A. Kivimaki, *et al., Phys. Rev. Lett.* **79**, 998, (1997).

[2] B. Kempgens, *et al., Chem. Phys. Lett.* 277, 436, (1997).

[3] B. Kempgens, *et al., Phys. Rev. Lett.* **79**, 3617, (1997).

[4] B. Kempgens, *et al., J. Phys. B* **30**, L741, (1997).

[5] B. Kempgens, *et al., Phys. Rev. Lett.* **79**, 35, (1997).

Monochromatic X-Ray Diffraction and Time-Resolved Measurements at High Pressure and Temperature

J. Chen (SUNY at Stony Brook)

Crystal structure refinements require accurate diffraction intensities. A monochromatic x-ray diffraction has many advantages over an energy dispersive diffraction for the accurate intensity measurements. Traditionally, high pressure *in situ* x-ray diffraction with a large-volume press was carried out in the energy dispersive mode (EDXD) because of the apparatus geometry. The pioneer attempt to acquire monochromatic x-ray diffraction with a large-volume press was made at the Photon Factory[1,2], however, the diffraction from sample surrounding materials remained as a problem for applying imaging plate (IP) detectors to the press. At beamline X17B1, we have developed a translating imaging plate system interfaced with large-volume press SAM85[3], and designed a new high pressure cell coupled with a subtraction data processing[4]. These developments first time allow us to perform time-resolved structure refinements at high pressure and temperature[5].

A experimental setup is schematically shown in **Figure G-1**. The imaging plates are mounted in a specially designed holder held on an optical rail. This can be tilted vertically and horizontally to the incident x-ray direction. The stage is movable along the incident x-ray direction to change the sample-to-IP distance (400 - 870 mm) and along the axis perpendicular to the incident x-ray beam for translating the IP during exposure. The holder can be easily taken off from the guide block to allow the goniometer arm to move down for EDXD measurements. A vacuum ensure two plates, either 200 mm x 250 mm or 200 x 400 mm size, are kept flat to the holder during exposure. When the imaging plate is used to record the diffraction pattern, the goniometer arm is rotated up to +35°. In the time-resolved measurements, a lead screen with a vertical slit in the middle is introduced in the front of the imaging plate to define the dimension of exposure on the detector. Width of the slit is adjusted

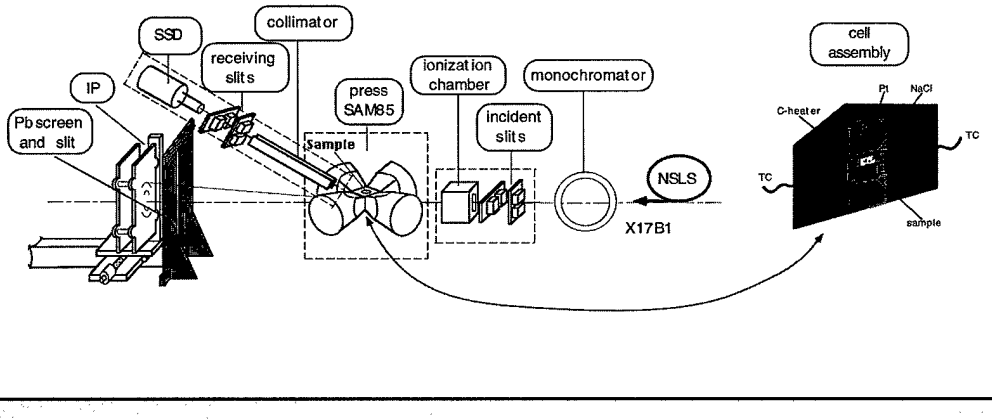

Figure G-1: Schematic layout of the translating imaging plate system for high P-T x-ray diffraction at the X17B1 beamline of the NSLS. The inset on the right shows the high-pressure cell assembly for the large-volume apparatus, SAM85. The monochromator is a Laue-Bragg double-crystal focusing monochromator.

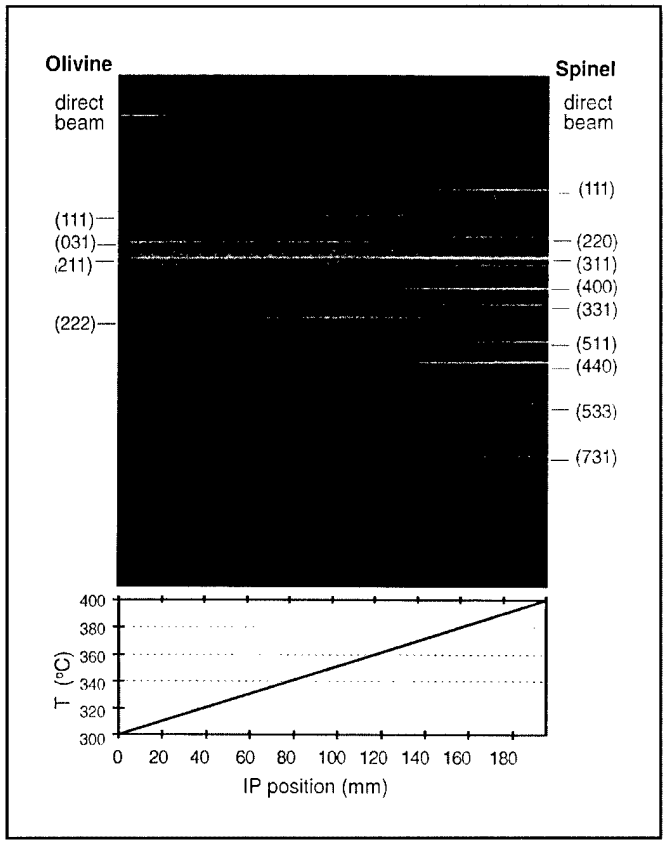

Figure G-2: Time resolved diffraction pattern on the imaging plate showing the olivine-spinel phase transition in fayalite at 5.9 GPa and 370°C. Left indices indicate the diffraction peaks of olivine phase; Right indices indicate those of spinel phase. Bottom curve shows the corresponding relation of sample temperature and imaging plate position.

depending on the beam intensity, IP-to-sample distance and the transporting speed of the imaging plate. A direct beam stop is mounted on the slit. The beam stop blocks most of the intensity of the direct beam, and allows the direct beam to expose the imaging plate with the same intensity as a diffracted beam.

The olivine-spinel transformation mechanism in fayalite was studied by the time-resolved diffraction measurements. The experiment was carried out by compressing the sample at room temperature into the spinel stability field (6.9 GPa) and then heating up the sample. The sample transformed from olivine to spinel during the heating. A time-resolved pattern was recorded when the temperature increased from 300°C to 400°C. The transporting speed of the imaging plate was 3.25mm/min. The heating rate was 1.75 °C/min. **Figure G-2** shows the diffraction pattern taken with an 8 mm front slit and 0.2 mm x 0.2 mm incident x-ray beam. he photon energy of the x-ray was 41.12 keV and the sample-to-IP distance was 812.6 mm. In **Figure G-2**, the sample started with olivine phase (on the left) and ended up with spinel phase (on the right). Indices on the two sides of the pattern indicate major diffraction peaks of olivine and spinel phases respectively. Most of the intensity of the incident beam was blocked by a lead stop, with a thickness about 2 mm, behind the sample; the rest of the intensity made a direct beam marker on the top the imaging plate. Some high background (e.g. those close to spinel (111) peak) were from boron:epoxy pressure medium. The sample temperature was recorded as a function of imaging plate position and plotted at the bottom of **Figure G-2**. Thermal relaxation resulted in the pressure decrease from 6.9 GPa at room temperature to 5.7 GPa at 420°C. It is observed that the spinel phase started growing at 365°C and the olivine phase completely transformed into spinel at 390°C at about 5.9 GPa. Taking account the slit width, there is 52 mm on the imaging plate where the two phases coexist.

The diffraction pattern of two phase coexisting region on the IP was integrated as a function of time. After background subtraction, multi-phase structure refinements were make based on these date. **Figure G-3** shows results of the sequence structure refinements. The emphasis of the refinements focused on the atomic occupancy in the spinel structure. All the occupancy parameters for Fe, Si and O were initially free for fitting. The refinements all resulted in the occupancy parameter for O close to 1. We therefore fixed the O occupancy to 1 for further refinements. The results showed that the occupancy parameters F_{si} and F_{fe} for Si and Fe are only 79% and 82% when the spinel phase is first recognized as amount of 20% of the mixture phases, and with growing of the spinel phase F_{si} and F_{fe} are increase rapidly. This observation indicates that the olivine-spinel transition involves the rearrangement of the oxide sub-lattice of hexagonally close-packed olivine, to form the cubic close-packed arrangement of the spinel structure, followed by the ordering of metals into the octahedral and tetrahedral voids.

Mechanism of the olivine-spinel phase transition has been investigated by several groups. Sung and Burns[6]

proposed a diffusion-controlled process, incoherent nucleation of the spinel phase and subsequent crystal growth; Kronberg [7] and Poirier[8] proposed a shear mechanism, stacking faults in oxygen lattice of olivine accompanying cation reordering coherently. More interesting result reported by Furnish and Bassett[9] from their observation of earlier appearance of some diffraction lines of spinel phase during the phase transition suggested a two-step shear mechanism with stacking faults prior to the cation reordering. However there was no sound evidence such as structure refinement to confirm any of these mechanisms. Our experiments first time provide the reliable data to support the two-step transformation mechanism. ■

Acknowledgments. *All SAM85 team members have contributed to this work, and we wish to thank J. Hastings and P. Siddons at the NSLS for their technical support at the X17B1 beamline. The study is supported by the State University of New York at Stony Brook and the NSF Science and Technology Center for High Pressure Research (EAR 8920329). MPI pub. no. 225.*

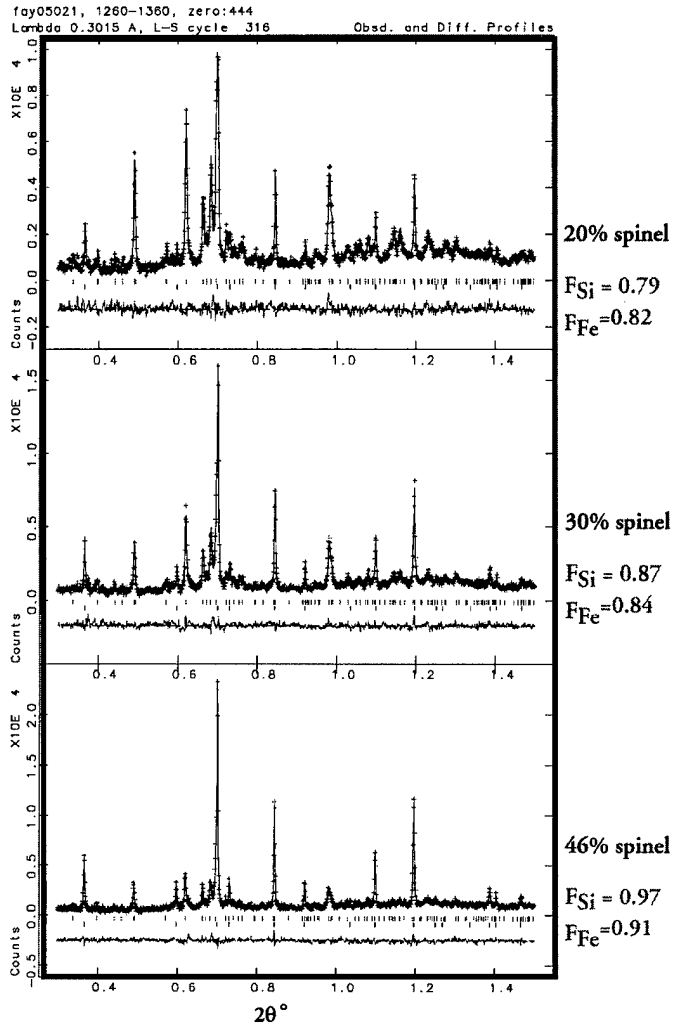

Figure G-3: Full Rietveld refinement of selected patterns in the time sequence through olivine-spinel transformation in fayalite.

[1] T. Kikegawa, J. Chen, Y. Kenichi, & O. Shimomura. *Rev. Sci. Instrum.* 66(2), 1335-1337(1995).
[2] J. Chen, T. Kikegawa, O. Shimomura and H. Iwasaki, *J. Synchrotron Rad.* 4, 21-27(1997).
[3] See abstract of the X17B1 beamline by J. Chen, D. J. Weidner, M. T. Vaughan, R. Li, J. B. Parise, C. C. Koleda and K. J. Baldwin in this report.
[4] J. Chen, J. B. Parise, R. Li, D. J. Weidner, and M. T. Vaughan, in *High-Pressure and Temperature Research: Properties of the Earth and Planetary Materials,* edited by M. H. Manghnani and T. Yagi, AGU Washington D.C., 1998, p129-134.
[5] See abstract of the X17B1 beamline by J. Chen and D. J. Weidner in this report.
[6] C. M. Sung and R. G. Burns, *Earth Planet. Sci. Lett.* **32**, 165(1976).
[7] M. L. Kronberg, *Acta Metall.* **5**, 507(1957).
[8] J. P. Poirier, in *Anelasticity in the Earth, Geodyn.* Ser. vol. 4, edited by F. D. Stacey *et al.* p. 113-117, AGU, Washington D.C. (1981).
[9] M. D. Furnish and W. A. Bassett, *J. Geophys. Res.* **88**, 10333 (1983).

Synchrotron X-radiation, Ultrasonics, and the Composition of the Earth

M. T. Vaughan (Center for High Pressure Research, State University of New York at Stony Brook)

The primary data about the deep interior of the Earth that is relevant to its composition are the travel times of seismic waves. These data are used to determine the compressional and shear acoustic velocity and the density, as functions of depth. To determine the composition of the materials present there (in terms of both chemistry and phase), we need to measure in the laboratory the equivalent parameters of candidate earth materials at equivalent conditions of pressure and temperatures.

Acoustic velocities of many earth materials have been measured at elevated pressures and temperatures using ultrasonic interferometry for several decades now, however only recently have we been able to make these measurements at pressure and temperature conditions equivalent to the Transition Zone at 400 km. (~15 GPa)[1,2]. There has long been a problem of determination of the pressure in these experiments; use of fixed-point calibration has been fairly successful at room temperature, but is much less accurate at high temperatures.

Synchrotron radiation has been used to address some of these issues for over a decade. The change in unit cell volume under increasing pressure and temperature is measured using x-ray diffraction; the known equations of state of various materials such as NaCl and MgO are then used to determine the pressure. With the installation of the DIA multi-anvil high pressure apparatus at the superconducting wiggler beam line at the NSLS in late 1989, we perform these experiments at precisely determined temperatures on fairly large samples (~1mm^3).

In the last two years, we have developed a facility to measure acoustic velocities using ultrasonic interferometry on samples while they are under high pressure and temperature inside the DIA apparatus. The ultrasonic sample is surrounded by NaCl, which can be used to determine the pressure. In **Figure G-4**, we show the acoustic piezoelectric transducer-tungsten carbide anvil arrangement and the high-temperature cell assembly for the DIA. The WC anvil serves as an acoustic buffer rod to transmit the high-frequency signal (20 to 90 MHz) into the cell assembly.

Using this technique, we have measured both the compressional and shear wave velocities of most of the major components of the earth's mantle. These include magnesium silicate in the olivine[3], wadsleyite[4], garnet (majorite)[5], orthopyroxene[6], and perovskite[7] phases. Since these materials exist in the earth as Mg-Fe solid solutions, some of these measurements have been made on samples with some iron in them.

Even though the use of x-ray diffraction to determine the pressure using the equation of state of some known material is a great improvement over earlier, fixed point calibration techniques, it still depends on the knowledge of that equation of state, which was determine earlier using a variety of techniques, not all of which are necessarily very accurate. Measurement of the change in cell volume at elevated pressure (and temperature) while simultaneously measuring the P- and S-wave acoustic velocities on the same sample, provides the ability to determine the pressure absolutely without reference to earlier calibrations. The p- and s-wave acoustic velocities are given by $Vp^2=(K+(4/3)G)/\rho$ and $Vs^2=G/\rho$, where K and G are the bulk and shear moduli, respectively, and ρ is the density. These can be combined to eliminate G, giving $K=\rho[Vp^2-(4/3)Vs^2]$. Because the bulk modulus is also given by $K=VdP/dV$, these two equations can be combined to eliminate the pressure if both acoustic velocities and the cell volume (or density) are independently measured. We have begun a project making these measurements for MgO, with the goal of creating an independent pressure scale[8] ■

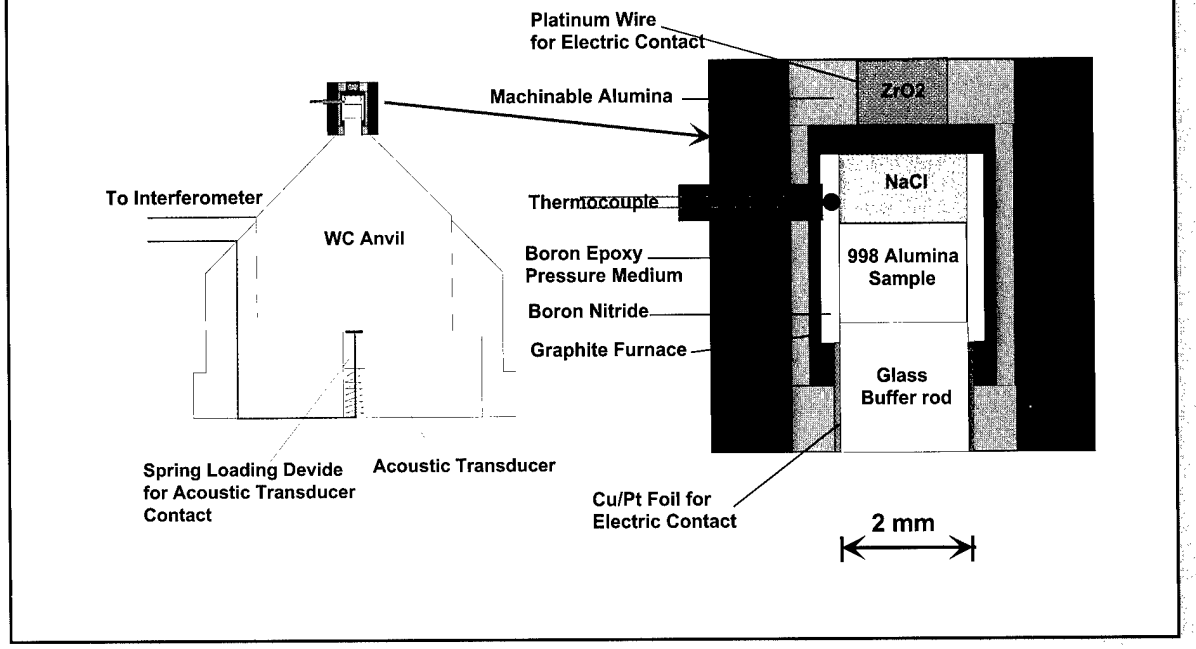

Figure G-4: Diagram of anvil insert and cell assembly for ultrasonic experiments in X17B1.

[1] G. D. Gwanmesia and R. C. Liebermann, High Pressure Research: Application to Earth and Planetary Sciences (ed. by Y. Syono and M. Manghnani), 1992.

[2] G. D. Gwanmesia, B. Li, and R. C. Liebermann, Experimental Techniques in Mineral and Rock Physics, (ed. by R. C. Liebermann and C. H. Sondergeld), PAGEOPH, **141**, 467 (1993).

[3] G. Chen, Y. Sinelnikov, and R. C. Liebermann, this issue; B. Li, J. Liu, L. Flesch, R. C. Liebermann, J. Chen, and B. Savage, this issue.

[4] B. Li, J. Liu, L. Flesch, G. D. Gwanmesia, J. Chen, and R. C. Liebermann, NSLS 1996 Activity Report B-142, 1997

[5] G. D. Gwanmesia, G. Chen, Y. Sinelnikov, J. Cooke, L. Flesch, M. T. Vaughan, and R. C. Liebermann, NSLS 1996 Activity Report B-141, 1997; G. D. Gwanmesia, G. Chen, J. Cooke, L. Flesch, R. C. Liebermann, and M. T. Vaughan, this issue.

[6] L. Flesch, B.Li, J. Zhang, J. Cooke, R. C. Liebermann, and M. T. Vaughan, this issue.

[7] Y. Sinelnikov, J. Zhang, and R. C. Liebermann, NSLS 1996 Activity Report B-144, 1997; Y. Sinelnikov, J. Zhang, and R. C. Liebermann, this issue.

[8] G. Chen, Y. Sinelnikov, J. Cooke, D. J. Weidner, and R. C. Liebermann, NSLS 1996 Activity Report B-138, 1997; G. Chen, Y. Sinelnikov, R. C. Liebermann, and D. J. Weidner, this issue.

Detection of Organic Compounds Associated with Carbonate Globules and Rims in the ALH84001 Meteorite from Mars

G. J. Flynn (Dept. of Physics, SUNY-Plattsburgh), L. P. Keller, M. A. Miller (MVA, Inc.), C. Jacobsen and S. Wirick (Dept. of Physics, SUNY-Stony Brook

In August 1996, D. S. McKay and co-workers[1] reported possible evidence for biological activity on Mars in material along fracture surfaces in the ALH84001 meteorite, believed to be from Mars. They found carbonate globules, which may form by precipitation from water, along the fracture surfaces. Dark rims surrounding the carbonate globules contain magnetite and iron-sulfide grains, similar in size and shape to those produced by terrestrial bacteria[1]. They also detected organic compounds called polycyclic aromatic hydrocarbons (PAHs), frequently produced by the decay of living material, "found in the highest concentrations in the regions rich in carbonates"[1]. While each of the features might have been produced by non-biological processes, their close spatial association suggests they all formed by the same process. They concluded that biological activity, early in the Mars' history, could explain all the features[1].

Other investigators suggest the carbonates formed at high temperatures, inconsistent with precipitation from water[2]. In addition, most meteorites are contaminated by terrestrial organic matter, so the PAHs found associated with the carbonates might be from Earth not Mars. A recent study determined that a majority of the organic matter in ALH84001 is likely to be terrestrial contamination[3], although the same study found some pre-terrestrial carbon after the carbonates had been dissolved. If this carbon is organic, then 10 to 20% of the organic matter in ALH84001 was present prior to its arrival on Earth[3].

The organic measurements by McKay's group were limited by the spatial resolution of the instrument and by their ability to detect only one class of organic compounds. Their instrument has a sampling beamspot 50 microns in size[1], the width of a typical human hair. This is comparable to the size of entire carbonate globules (~50 to 100 microns), and much larger than the dark rims (~5 to 10 microns thick) or the individual magnetite crystals (tens of nanometers in size). In addition, their technique was sensitive only to PAHs, not other (possibly more interesting) organic molecules which are less stable in the laser desorption process they used.

We employed the Scanning Transmission X-Ray

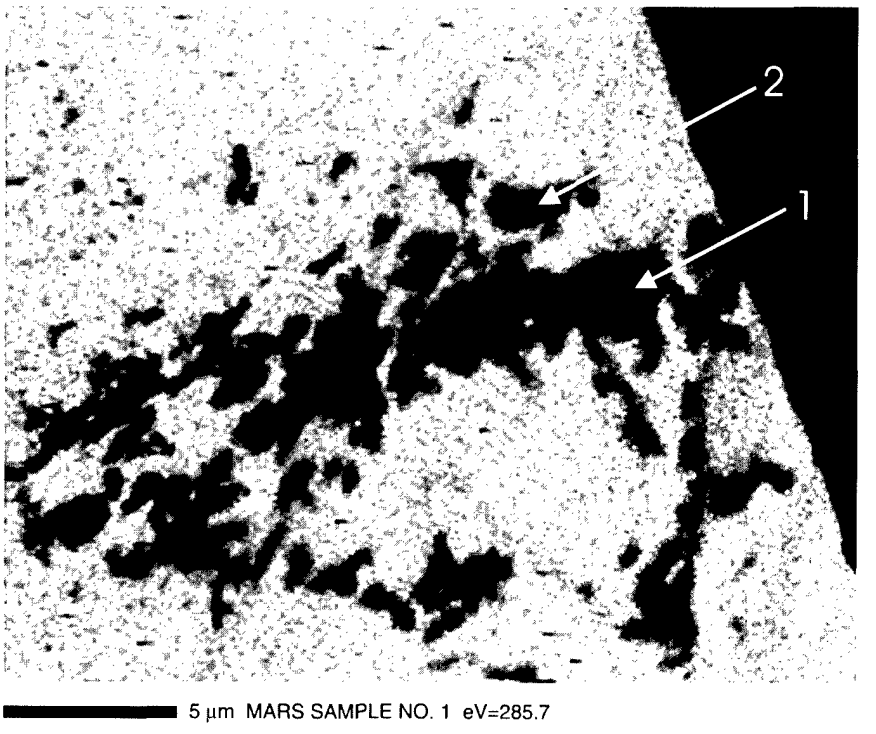

Figure G-5: STXM map of a small section of a carbonate globule from the ALH84001 meteorite. The carbon bonding state was measured at the spots indicated by the arrows.

Microscope (STXM) on beamline X1A at the National Synchrotron Light Source (NSLS) at Brookhaven National Laboratory to determine the bonding states and the spatial distribution of carbon in carbonates and rims from the ALH84001 meteorite[4]. The STXM has a 50 nanometer analysis beamspot, comparable to the size of the individual magnetite and iron-sulfide crystals, which allows the spatial association of carbon bearing compounds to be examined with a resolution about 1000 times better than that achieved by McKay and co-workers[1].

We then examined the samples using a Spectra-Tech Fourier Transform Infrared (FTIR) spectrometer, installed on beamline U4IR at the NSLS, to identify the carbon bonds[5]. Beamline U4-IR produces an intense infrared light beam, providing a sensitivity about 100 times better than the conventional laboratory FTIR instrument[6]. FTIR examination allows identification of a wide range of organic compounds, not just the PAHs detected by McKay *et al.* [1], using analysis spots down to about 3 microns in size.

Samples: Fragments of ALH84001 carbonate and rim were embedded in elemental sulfur, ultramicrotomed to ~200 nanometers thick, and deposited on an SiO substrate. This avoids exposure to the carbon-bearing epoxies and substrates normally used in preparation for Transmission Electron Microscope (TEM) and STXM examination. Thus, we insured that any carbon we detected was indigenous to the samples.

TEM examination of the carbonate samples indicated they consisted mostly of large crystals of Mg-Fe-carbonate with some regions of fine-grained Mg-Fe-carbonate and magnetite. The dark rim samples were dominated by feldspathic glass, but included large (~5 micron) chromite and a few small regions of fine-grained magnetite, sulfide, and Mg-Fe-carbonate similar to the rim material described by McKay *et al.* [1].

STXM Examination: In the STXM mapping mode, the energy of the incident monochromatic x-ray beam is fixed and the sample is scanned beneath the beam. The

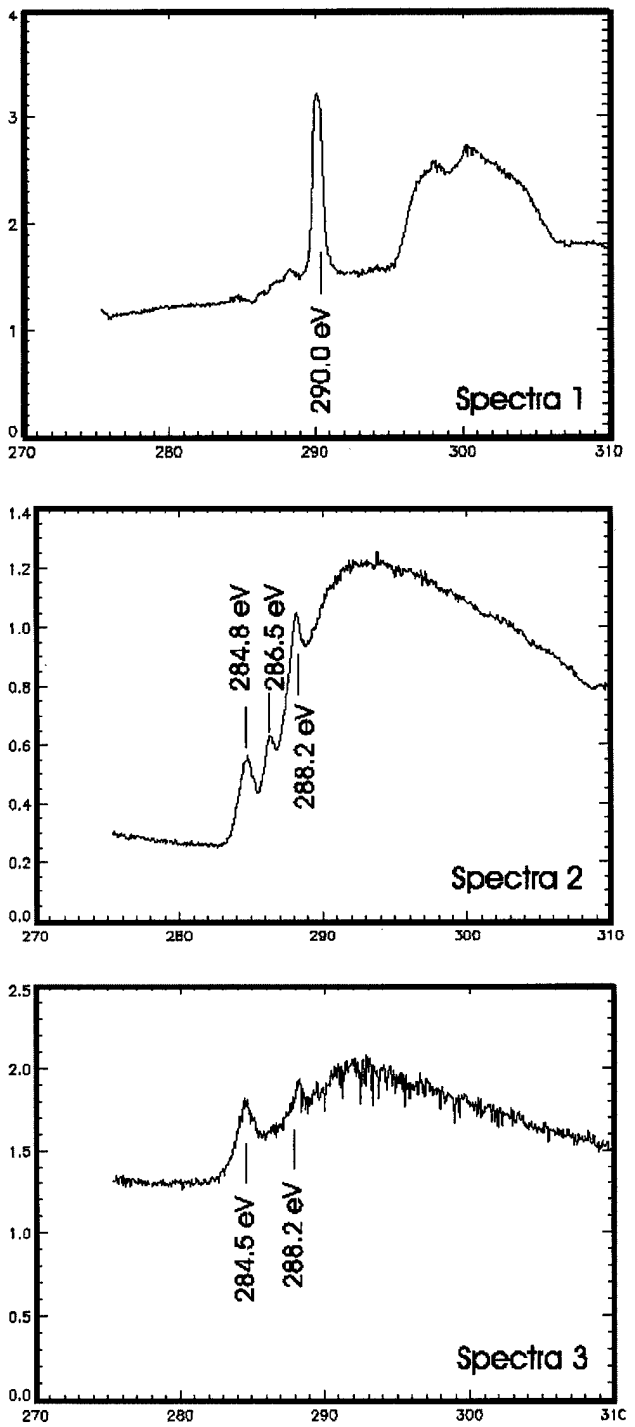

Figure G-6: Carbon-XANES spectra of two spots (shown in Figure G-5) on a carbonate globule from ALH84001. Spot 1 has a strong absorption at 290 eV, indicating the carbon is bound in carbonate, while Spot 2 has three absorptions, at 284.9, 286.5, and 288.2 eV, suggesting the presence of orrganic carbon at this spot. Spot 3 is a carbon-rich spot on the rim sample. It shows strong absorptions at 284.5 and 288.2 eV, indicating the rim contains a different type of carbon than that in the globule.

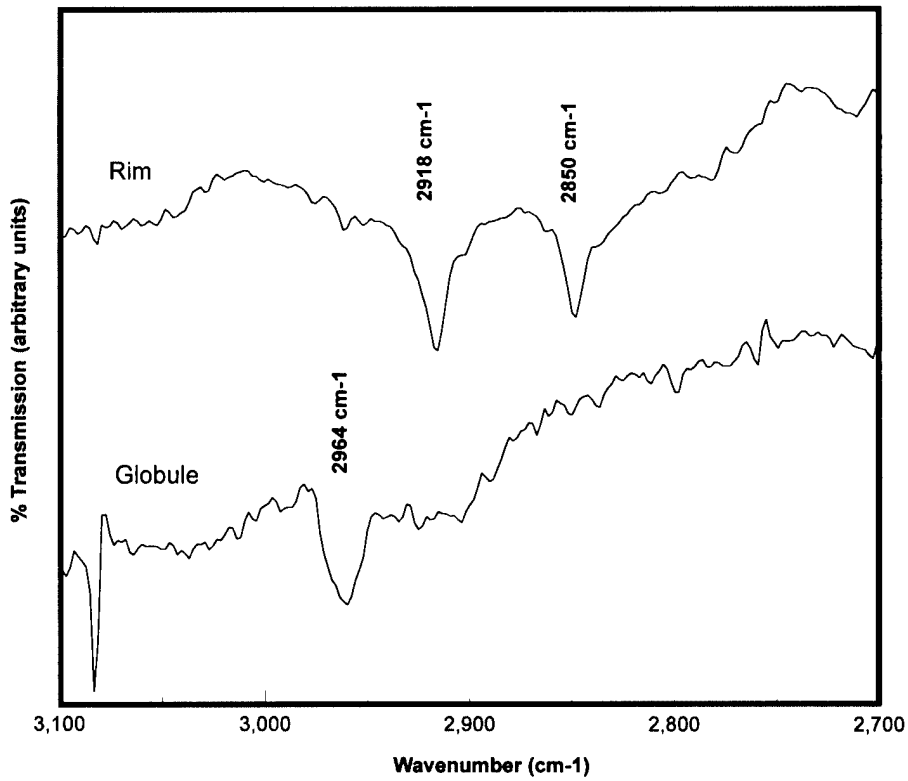

Figure G-7: FTIR spectra of the C-H stretching region of a Rim sample (top) and a Carbonate Globule sample (bottom) from the ALH84001 meteorite. The Rim sample shows two strong absorptions, at 2918 and 2850 cm^{-1}, consistent with the positions and relative intensities of the $C-H_2$ stretching vibrations in an aliphatic hydrocarbon. The Carbonate Globule sample shows a single strong absorption at 2964 cm^{-1}, consistent with a $C-H_3$ stretching vibration, and a weaker, broad absorption from 2900 to 2950 cm^{-1}. This sample may also show a very weak, broad feature from 2990 to 3060 cm^{-1}, possibly associated with PAHs.

absorption of the sample is measured at each pixel. Since the absorption of carbon increases sharply at 290 eV, the carbon K-edge energy, while the absorptions of other elements are approximately constant in a narrow range of energy near the carbon K-edge, a pixel showing an increase in absorption between the map just below the carbon K-edge (e.g., 280 eV) and the map just above the carbon K-edge (e.g., 300 eV) contains carbon (see image in **Figure G-5**).

In Carbon-X-ray Absorption Near Edge Structure (C-XANES) mode the beam hits a fixed position on the sample, and the monochrometer is scanned over the energy range from 270 to 310 eV. Absorptions in this region are characteristic of particular carbon bonds. The C-O bond in carbonate gives rise to a strong absorption near 290 eV but no absorption near 285 eV, while C-C, C=C, and C-H bonds have strong absorptions in the 284 to 287 eV range. Thus, C-XANES is a sensitive technique to detect organic (or graphitic) carbon in a matrix of carbonate, making the STXM particularly well suited to identifying non-carbonate carbon in a matrix of carbonate (as is the case for the ALH84001 carbonate and rim samples).

The C-XANES spectra of the carbonate samples showed a strong absorption at 290 eV, characteristic of the C-O bond in carbonate. These samples also showed weaker absorptions at 284.8 eV, 286.5 eV, and 288.2 eV (see **Figure G-6**). The relative intensities of the latter three absorption peaks were approximately constant (where they could be detected), suggesting that throughout the carbonate samples a single additional carbon-bearing phase dominated the absorption. However these three peaks varied in intensity with position on the sample, ranging from spots showing only

the 290 eV carbonate peak to spots showing strong absorptions at 284.8 eV, 286.5 eV, and 288.2 eV but no detectable 290 eV peak. This indicates the second carbon-bearing phase is distributed inhomogeneously, on the scale of the 50 nm beamspot, within the carbonate. Work is in progress to correlate the locations of this phase with TEM mineralogy.

Most spots on the rim samples showed no absorption at 290 eV, consistent with a low abundance of carbonate. Some spots showed two absorption peaks at 284.5 eV and 288.2 eV, indicating the presence of C-C, C=C, C-O, or C-H bonds. The differences in absorption energies and the absence of the third peak in indicate that the dominant carbon-bearing phase in the rim is different from that in the carbonate globule. Correlation of the STXM carbon map with TEM mineralogy indicates the carbon-rich phase is associated with fine-grained magnetite and sulfide, and may also occur as veins or inclusions in the feldspathic glass.

FTIR Examination: To determine if the dominant carbon-bearing compound is different in the rim samples and the carbonate globule samples and to determine if these phases are organic, the same samples analyzed by STXM were examined by FTIR, a technique routinely used for the laboratory identification of organic compounds. The FTIR spectra of the rim samples showed a broad absorption near 1000 cm^{-1}, characteristic of silicate glass, and two weaker features at 2918 cm^{-1} and 2850 cm^{-1}, consistent in position and relative depths with the stretching vibrations of $C-H_2$ in an aliphatic hydrocarbon (see **Figure G-7**).

The FTIR spectra of the carbonate globule samples showed a narrow absorption at ~1500 cm^{-1}, characteristic of carbonate, and a weaker absorption at 2964 cm^{-1}. The feature at 2964 cm^{-1} is characteristic of the $C-H_3$ asymmetrical stretching vibration. Although a weaker $C-H_3$ symmetrical stretching vibration generally occurs near 2870 cm^{-1}, this feature is absent in the carbonate globule spectrum, and is suppressed in certain compounds containing $C-H_3$ groups. Two even weaker features at 2920 cm^{-1} and 2850 cm^{-1}, consistent with $C-H_2$, were also detected at some spots on the carbonate globule samples. One particularly good spectrum of the carbonate globule sample appears to show a weak, broad absorption over the range 2990 cm^{-1} and 3060 cm^{-1}, where the C-H stretching vibrations (centered at 3030 cm^{-1}) of a mixture of PAHs would occur. Follow-up measurements to determine if we have located the PAHs are planned.

Conclusions: The combined STXM and FTIR measurements confirm, at a much smaller scale than was possible in the work of McKay *et al.* [1], the close spatial association between organic material and the carbonate globules and rims in ALH84001. The carbon detection limit of the STXM is of order percent level. If ALH84001 has a similar bulk carbon content other Mars meteorites (0.04 to 0.07%[7]), then the STXM results demonstrate that compared to the bulk meteorite relatively large concentrations of organic carbon are associated with the carbonate globules and rims. The FTIR measurements indicate the rim material contains an aliphatic hydrocarbon whose absorption is dominated by the $C-H_2$ group, while the carbonate globule is dominated by the $C-H_3$ group absorption. Thus the rim and the globule contain different organic compounds. This results seems to rule out the simplest form of organic contamination of these samples, simple evaporation of an organic-rich fluid, which would be expected to leave the same residue in both the carbonate globules and the adjacent rim material. However, we cannot exclude contamination by selective absorption of different organic species onto the different mineral substrates. ■

[1] D.S. McKay *et al., Science* **273**, 924-927 (1996).

[2] R. Harvey and H.P. McSween, *Nature*, 382, 49ff, (1996).

[3] A.J.T. Jull *et al., Science* **279**, 366-369, (1998).

[4] G.J. Flynn *et al., Meteoritics* **32**, A42, 1997.

[5] G.J. Flynn *et al., Lunar & Planetary Science XXIX, Lunar and Plantetary Institute,* (1998), in press.

[6] J. Reffner *et al., Synchrotron Radiation News* **V. 7**, 30-37 (1994).

[7] A.H. Tremain, *Geochem. Cosmochim. Acta* **50**, 1071-1091 (1986).

Synchrotron Infrared Microspectroscopy: A New Technique for Probing the Chemical Composition of Bone and its Implications for Understanding Osteoarthritis

L. M. Miller, D. Hamerman, and M.R. Chance (Albert Einstein Center for Synchrotron Biosciences), G. L. Carr and G. P. Williams (NSLS), Cathy S. Carlson (Bowman Gray School of Medicine)

Osteoarthritis is the leading cause of disability among people over 65 years old and affects approximately 40 million people in the United States (Center for Disease Control, 1990). It is characterized by a breakdown of the articular cartilage and thickening of the subchondral bone. To date, the cause of osteoarthritis is unknown, but, an extensive study of cynomolgus monkeys has demonstrated that the subchondral bone thickening **precedes** the development of articular lesions.[1] In addition, a recent study on humans determined that the subchondral bone from patients with symptomatic osteoarthritis was hypomineralized compared with that from asymptomatic individuals.[2] These data suggest that the health and integrity of the articular cartilage is dependent upon the mechanical properties of the underlying subchondral bone. In turn, the mechanical properties of subchondral bone are also dependent upon its chemical structure.

Over a lifetime, bone is continuously remodeling itself and the chemical composition of bone is extremely important to this process. Chemically, bone is made up of both organic and mineral components. The organic component is primarily type I collagen, whereas hydroxyapatite, $Ca_{10}(PO_4)_6(OH)_2$, is the mineral component of bone. As bone matures, the size, crystallinity, and stoichiometry of the hydroxyapatite crystals change. Substitutions into the hydroxyapatite crystal lattice are common, where calcium can be replaced by cations such as Na^+, K^+, Mg^{2+}, Sr^{2+}, and Pb^{2+}. Phosphate and hydroxide can be replaced by CO_3^{2-}, HPO_4^{2-}, Cl^-, and F^-. These substitutions into the hydroxyapatite lattice are very important to bone strength, flexibility, and the process of remodeling because they affect crystal size, density, and solubility. Thus, we hypothesize that the bone matrix composition and/or bone mineral content and crystallinity are modified *in situ* in a specific manner as a function of subchondral bone thickness.

We have addressed this hypothesis by examining the chemical composition of subchondral bone using *infrared micro-spectroscopy*. Infrared spectroscopy is an analytical technique that is sensitive to the chemical components in bone. This technique can be used to determine (1) protein structure and concentration, and (2) mineral concentration, crystallinity, and content (e.g. phosphate, acid phosphate, carbonate). The crystallinity results are correlated to hydroxyapatite crystal size and perfection, as determined by x-ray powder diffraction. By putting infrared light through a microscope, infrared spectra can be collected on micron-sized regions of bone *in situ* and compared to visible images of the same region. Thus, we can examine the chemical composition of subchondral bone as a function of subchondral bone thickness, i.e. severity of osteoarthritis.

Inherently, the long wavelengths of infrared light limit the spatial resolution achievable with this technique. We have demonstrated that substantial changes in chemical composition occur within 20 μm of the site of new bone growth.[3,4] This type of spatial resolution can only be achieved with a *synchrotron* infrared source. Beamline U4IR at the National Synchrotron Light Source provides the world's brightest source of synchrotron infrared light — 1000 times brighter than a conventional

infrared source — permitting rapid data collection at the diffraction limit, i.e. 3-5 μm in the mid-infrared region. Recently, we used synchrotron infrared microspectroscopy to examined the subchondral plate of a knee joint from a radiographically normal cynomolgus monkey (Miller *et al.*, 1997a, b). The results can be summarized as follows: (1) Bone crystallinity decreases and (2) the carbonate / phosphate ratio increases as subchondral bone thickens. (3) The phosphate / protein ratio is high where crystallinity is high. (4) The acid phosphate concentration is relatively constant throughout the subchondral bone. Since these results suggest that the chemical composition of subchondral bone varies with thickness, we hope that future experiments as a function of disease severity will continue to provide a chemical understanding of the molecular basis for subchondral bone thickening in osteoarthritis. ■

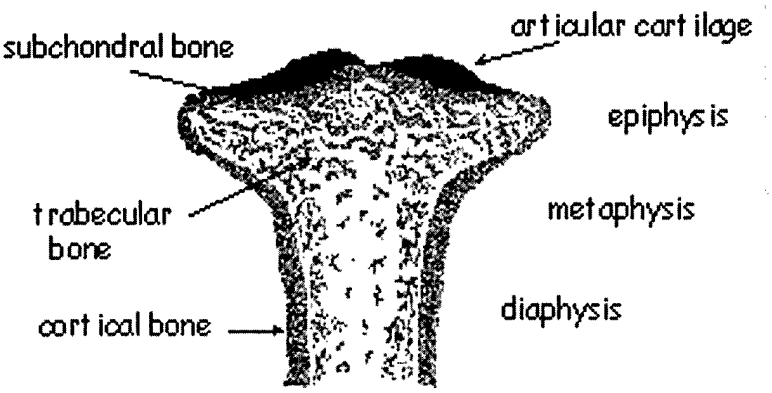

Figure I-1: Schematic drawing of the proximal end of a monkey tibia.

[1] C.S. Carlson, R.F. Loeser, C.B. Purser, J.F. Gardin, C.P. Jerome, "Osteoarthritis in cynomolgus macaques III: Effects of age, gender, and subchondral bone thickness on the severity of disease", *J. Bone & Mineral Res.* **11**: 1209-1217 (1996).

[2] B. Li, R.M. Aspden, "Mechanical and material properties of the subchondral bone plate from the femoral head of patients with osteoarthritis or osteoporosis", *Ann. Rheum. Dis.* **56**: 247-254 (1997).

[3] L.M. Miller, C.S. Carlson, G.L. Carr, G.P. Williams, M.R. Chance, "Synchrotron infrared microspectroscopy as a means of studying the chemical composition on bone: Applications to osteoarthritis", *SPIE*, **3153**: 141-148 (1997).

[4] L.M. Miller, C.S. Carlson, G.L. Carr, M.R. Chance, "A method for examining the chemical basis for bone disease: Synchrotron infrared microspectroscopy", *Cell. and Mol. Biol.*, in press (1997).

Macromolecular Crystallography Area Detectors

L. Berman (NSLS)

During the 1997 fiscal year, the area detectors for all of the macromolecular crystallography beamlines were upgraded, or were in the process of being upgraded. The overall intention was to make the collection of crystallography data to be a less laborious and more user-friendly chore, and to reduce the fraction of users' beam time (dead time) in which no data could be collected at all.

Beamline X4A, operated by HHMI, had installed a Rigaku R-Axis IV automatic imaging plate detector, replacing the manual Fuji imaging plates with off-line readout. The new detector contains two plates, allowing one plate to be read out (in about 3 minutes) while the other is exposing. This allows more efficient use to be made of the available beam time and simultaneously reduces the necessary labor to run the experiment, because manual exchange, readout, and erasure of imaging plates (with the concomitant book-keeping) are no longer necessary. Beamline X4C, also operated by HHMI and undergoing commissioning, will, when operational, use an Area Detectors Systems Corp. (ADSC) Quantum-1 single-module, 1Kx1K CCD detector, which has a readout time of less than 10 seconds.

Beamline X8C, whose PRT was recently reconstituted under the principal auspices of Los Alamos National Laboratory, re-commenced a macromolecular crystallography program using the X-Ray Research (MAR) 300 mm diameter automatic imaging plate system that had been used on the X12C (BNL Biology Dept.) beamline for several years. This single-plate detector has a full-area readout time of about 3 minutes. On beamline X9B, under the joint auspices of the Albert Einstein College of Medicine and the National Institutes of Health, a MAR 345 mm diameter automatic imaging plate system was implemented. This new single-plate detector has a full-area readout time of under 1.5 minutes.

Beamline X12B, operated by the BNL Biology Dept., had earlier in the year removed the MAR 300 mm diameter imaging plate detector, that had been in use there, from its base. It was remounted on the long two-theta arm in the experimental hutch, that was historically employed for small angle x-ray scattering experiments. This upgrade allowed for having a very long detector distance (so that large unit cell crystals could be studied) and, by tilting the two-theta arm, attaining high resolution. An ADSC Quantum-4 four-module CCD detector (1Kx1K per module), funded by the 1996 DOE Basic Energy Sciences Facilities Initiative Program along with some contributions by a few pharmaceutical companies, was also ordered for X12B, and arrived at the start of the 1998 fiscal year.

On X12C, also operated by the BNL Biology Dept., a single-module, 1Kx1K CCD detector, built by a collaboration of Brandeis U. and the BNL Biology Dept., was installed at the start of the 1997 fiscal year. It was presented as an optional alternative to the MAR 300 mm diameter imaging plate detector which had been in use on X12C for several years. The bulk of the macromolecular crystallography experiments on X12C have been serviced by the CCD detector since. At the start of the 1998 fiscal year, a four-module CCD detector was delivered by the Brandeis / BNL Biology collaboration to X12C for commissioning. It will ultimately be made available for use on X25.

On the X25 wiggler beamline, operated by the NSLS, a new MAR 345 mm diameter imaging plate system, provided by the NSLS via Facilities Initiative Program funds, was installed to service macromolecular crystallography experiments. This replaced use of two different MAR 300 mm diameter imaging plate systems, loaned during the past few years to X25 by the BNL Biology Dept. and Cold Spring Harbor Laboratory. The readout time of the new detector (per unit plate area) is 3 times faster than for the old MAR detectors, and it has a finer spatial resolution. In addition, a MAR single-module, 2Kx2K CCD detector, with even finer spatial resolution and a readout time of less than 10 seconds, was also funded by the NSLS via the Facilities Initiative Program, and its delivery is expected in the 1998 fiscal year. It will be able to substitute on X25 for the MAR imaging plate detector, on the same mounting base, when desired. The use of this CCD detector will not be restricted to macromolecular crystallography. Finally, the Brandeis / BNL Biology four-module CCD detector mentioned above that was commissioned on X12C, will become available for use on X25 during early 1998.

Beamline X26C, primarily operated in the past with focussed and unfocussed white x-ray beam capabilities, for Laue macromolecular crystallography and other white beam experimental programs, by the University of Chicago Consortium for Advanced Radiation Sources (CARS) and the BNL Applied Science and Biology

Departments, got an NSLS-sponsored upgrade to give it a standard monochromatic beam capability. Cold Spring Harbor Laboratory and the State University of New York at Stony Brook joined this PRT in the 1997 fiscal year, and began a monochromatic macromolecular crystallography experimental program, based upon a MAR 300 mm diameter imaging plate system provided by Cold Spring Harbor. This system replaced the manual Fuji imaging plates that had been provided by CARS for several years. ■

Nearly Automatic Macromolecular Crystallography at the NSLS

T. Terwilliger, J. Berendzen (Los Alamos National Laboratory),
J. Skinner, R. Sweet (BNL Biology Department)

The pace of protein-structure determination is accelerating rapidly, and synchrotron X-ray sources such as the NSLS are at the center of this action. Structures of protein molecules are in high demand in biotechnology because they are important for applications such as drug discovery and engineering enzymes for commercial use. A structure of a protein molecule can be used to identify what each part of the molecule is doing and makes it possible to design new protein molecules that have improved properties for therapeutic or industrial use. As the genome projects continue to produce thousands of new protein sequences, the demand for structural information on these proteins is increasing. Synchrotron beam lines are a key tool for protein structure determination. The multiwavelength anomalous diffraction (MAD) method takes advantage of the intensity and tuneability of x-rays from synchrotron radiation sources in obtaining x-ray diffraction data that can be used to solve protein structures that contain atoms with accessible x-ray absorption edges.

Until recently, the measurement and analysis of MAD x-ray data has been somewhat difficult owing to the number of steps involved and to the need for an expert to make important decisions about how to handle the data. We have assembled a variety of software and hardware systems to do much of this work for inexperienced users. These include beamline-control and data-collection software, graphical monitoring of data reduction, remote monitoring of beamline operations, and automatic solving of the phase problem to produce an electron-density map of the macromolecule.

The portions of this that involve acquisition of the data, developed by Skinner and Sweet, have been produced for the operation of the synchrotron beamline X12C at the NSLS. These were highlighted in the 1996 NSLS Activity Report. Users of the beamline communicate with all the experimental apparatus, including both the data-collection equipment and the beamline components including the monochromator, through an easy-to-use graphical user interface (GUI). Important features of the system are (1) its modularity, so that different underlying programs or different apparatus can be incorporated easily, (2) its ease of use, minimizing both user errors and training effort, and (3) that most of the experimental operations and parameters are logged automatically, again minimizing errors and facilitating more-or-less automatic reduction of the data. At the time of writing, several different area-sensitive detectors are available (see accompanying article by L. Berman) for mounting on the four-circle diffractometer at the beamline.

The logging of experimental parameters allows the nearly automatic reduction of data. We have constructed a graphical diagnostic routine to display color-coded information about the course of data reduction, neearly all of which is performed while users are present at the beamline. A web-based (Java code) tool monitors much of the information that is displayed on the GUI at the beamline, allowing beamline staff and professors back home to keep track of the course of the data collection at the beamline. Portions of this software package are in use at several beamlines, and we expect to be able to disseminate it further.

To close the loop on the nearly automatic solving of structures, a new software package called SOLVE developed by Terwilliger and Berendzen can carry out all the steps and make all the necessary decisions in the analysis of MAD data automatically, and we have installed

it at beamlines X12C, X8C, and X4A at the NSLS. The SOLVE software has now been run by a number of users at these beamlines and has proven itself capable of solving protein structures in less time than was necessary to collect the x-ray data.

SOLVE is an expert system that automatically produces three-dimensional electron-density maps of protein molecules from x-ray diffraction measurements. For a MAD structure determination, a user at the NSLS will measure diffraction intensities from a single crystal at several x-ray wavelengths spanning an absorption edge for an anomalously scattering atom, such as selenium, incorporated into the protein. These are the raw data needed by SOLVE. The user tells SOLVE where these data are located, what the scattering properties of the selenium atoms are at the x-ray wavelengths used, how many selenium atoms are thought to be in the protein, and how big the protein is. SOLVE takes this information and constructs an electron density map that can be displayed using a graphics program.

The approach used by SOLVE is similar to the one that a protein crystallographer would use. The MAD method for structure determination is a kind of bootstrapping operation in which the positions of the anomalously scattering atoms are first deduced and then used to calculate electron density for the entire structure. The hard part is coming up with likely solutions for the positions of the heavy atoms and evaluating the relative quality of different solutions. These steps often have been done manually in the past, while SOLVE can carry them both out automatically. SOLVE generates a list of likely solutions for the locations of the heaviest atoms in the protein using the program HASSP to analyze an optimized Patterson function derived from the MAD data with MADBST. It then evaluates each solution for internal consistency and it compares characteristics of the electron density map obtained from that solution with those of real electron density maps of proteins. Using the best starting solutions, SOLVE bootstraps to generate improved solutions, and when further improvement is not possible produces a final electron density map of the protein molecule.

Several additional features make SOLVE much faster than it otherwise would be and enable real-time structure solving. One, the MADMRG procedure, is a technique for extracting the three essential pieces of information from a set of up to MAD diffraction measurements. Another, the origin-removed patterson refinement procedure in HEAVY, reduces calculation time by rapidly adjusting a solution to match the x-ray measurements.

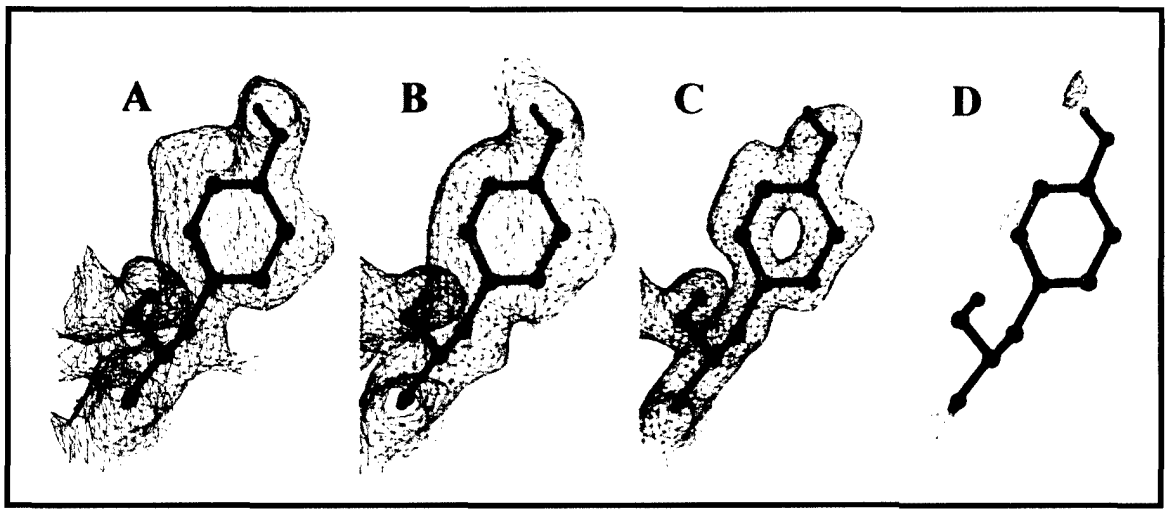

Figure I-2: Electron density maps from MAD-phased MkH data around tyrosine 108. All electron density maps are contoured at 1.5 σ except for D.
(A) 2.0 Å electron density obtained using phases from SOLVE.
(B) 2.0 Å electron density after solvent flattening and histogram matching.
(C) 1.5 Å, 2 fo-fc electron density from current model.
(D) Difference electron density (fo-fc) contoured at 3.0 σ. Positive difference density is contoured in grey and negative density is contoured in black.

Bayesian Correlated MAD Phasing, is a comprehensive way to deal with errors in measurement and to deal with large differences between crystals used in the diffraction analysis. The result of this integration of techniques is a fully automated analysis of x-ray diffraction measurements.

The recent successful structure determination by Richard Fahrner, Duilio Cascio and David Eisenberg (UCLA) at X12C illustrates how useful SOLVE can be. The UCLA group was interested in determining the structure of a histone protein (HMK) from a thermophilic organism. After other methods of solving the structure failed, they used established methods for selenomethionine incorporation to produced selenomethionyl histone protein, and then obtained crystals of the protein. Late in 1997, they came to beamline X12C at the NSLS to collect data for a three-wavelength MAD experiment. Since accurate anomalous information is required for a good MAD experiment, they collected anomalous pairs using the Friedel flip method: for every wavelength there were two datasets, sweeping the same zones, 180 degrees apart. Their MAD experiment consisted of six complete datasets; two at the rising inflection point of the absorption spectrum (0.9798 Å), two at the "white line" peak (0.9799 Å), and two at a distant point (0.9500 Å). Data collection proceeded smoothly and rapidly, employing the automatic MAD data-collection protocols described above. Two factors accelerated high resolution data collection. The size and dynamic range of the new four-module Brandeis CCD-based detector permitted collection of high resolution and low resolution data in a single pass. Also, careful orientation of the crystal with respect to the major zones allowed collection of a large amount of data in a short period of time. The integrated data were about nine-fold redundant, greater than 99% complete to 1.4 Å, with a merging R of 8.1%. Data collection for the complete MAD experiment required about seven hours.

The software package SOLVE was used to perform phase determination and assess the quality of their MAD experiment. The SOLVE package offered several advantages for them. Whereas manual solution of Patterson maps in high symmetry space groups with multiple heavy atom sites is challenging and time consuming, SOLVE offered a simple-to-set-up, automatic phase determination alternative. The three-wavelength unmerged data with Bijovet pairs were input to SOLVE. Using the anomalous and dispersive differences between datasets, SOLVE determined a single solution for four of five Se-Met sites within 78 minutes running on a 500Mhz DC ALPHA workstation. SOLVE was even able to distinguish the correct hand of the structure. The time from placing the crystal into the beam until the structure was solved was an astonishing 11 hours.

The initial electron density maps were easily interpretable (**Figure I-2**). The map quality was then improved through solvent-flattening and histogram-matching routines using the program "dm" in the CCP4 program suite. The solvent-flattened map could be unambiguously traced for 98 of 154 residues. After refinement using XPLOR, the amino acids originally traced were returned in the 2Fo-Fc map and more importantly, most of the remaining residues could be traced. Their current 2.0 Å model includes residues 3 to 154 and 40 water molecules (R=26.3%, R_{free}=33.7%). ■

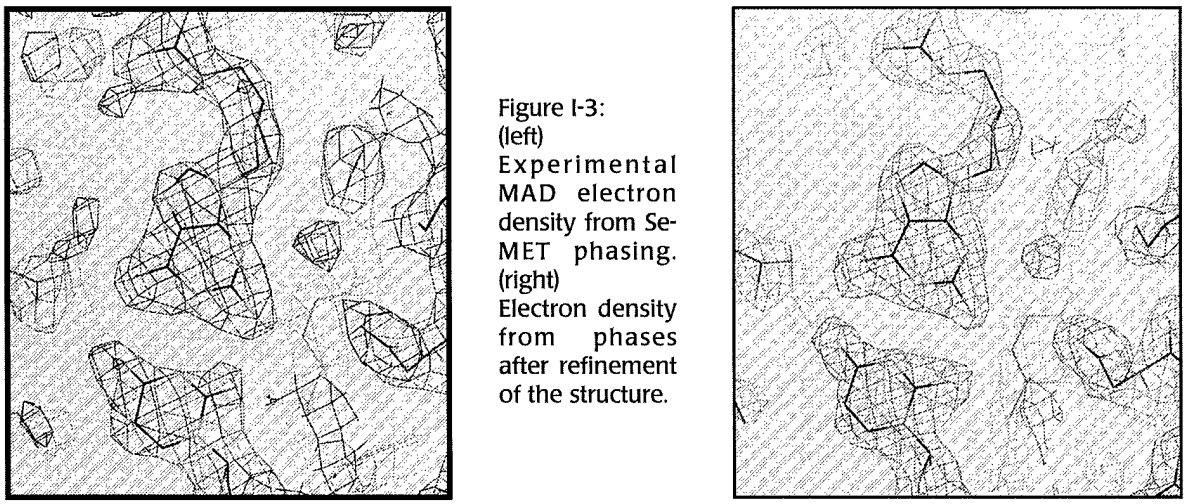

Figure I-3:
(left)
Experimental MAD electron density from Se-MET phasing.
(right)
Electron density from phases after refinement of the structure.

Soft X-Ray Emission Spectroscopy (X1B)

K. Smith *et al.* (Boston U.)

1997 saw the commissioning by Kevin Smith's group from Boston University of a new high resolution soft x-ray emission spectrometer on X1B. There are only a handful of such instruments around the world, and this is the only one dedicated for use at the NSLS. Soft x-ray emission (SXE) spectroscopy allows the bulk electronic structure of complex solids to be measured without regard to the quality or cleanliness of the solid surface. In particular, SXE allows the elementally resolved partial density of states to be measured. SXE also allows the direct measurement of hybrid states, of d-d excitations in transition metal systems, and of changes in electronic structure during metal to non-metal transitions while the sample is in applied electric or magnetic fields.

The BU group is using the spectrometer in the study of three different classes of materials: wide band gap nitride semiconductors, organic superconductors, and transition metal oxides. During two runs in 1997, the BU group calibrated their SXE instrument and began study of each of these materials systems. As an example of the first experiments, **Figure I-4** shows a series of N *K*-emission spectra from the $Al_xGa_{1-x}N$ alloy system. Owing to the magnitude of the bandgap in these materials, they are ideal candidates for optoelectronic devices working in the blue/UV range of the electromagnetic spectrum. The spectra in **Figure I-4** are the result of tuning the incident photon energy to just above the N *K* absorption edge, thus creating holes on the N *1s* level, and measuring the radiative decay of these holes. Dipole selection rules imply that the resulting spectra correspond to the N *2p* partial density of states (PDOS). Thus these spectra show the behavior of the dominant part of the valence band density of states in $Al_xGa_{1-x}N$ as the Al content is varied. The band gap for $Al_xGa_{1-x}N$ varies from 6.2 eV in AlN (x = 1) to 3.4 eV in GaN (x = 0). The motion of the top of the valence band is clearly visible in the spectra, shifting linearly by 1.5 eV as x varies from 0 to 1. This indicates

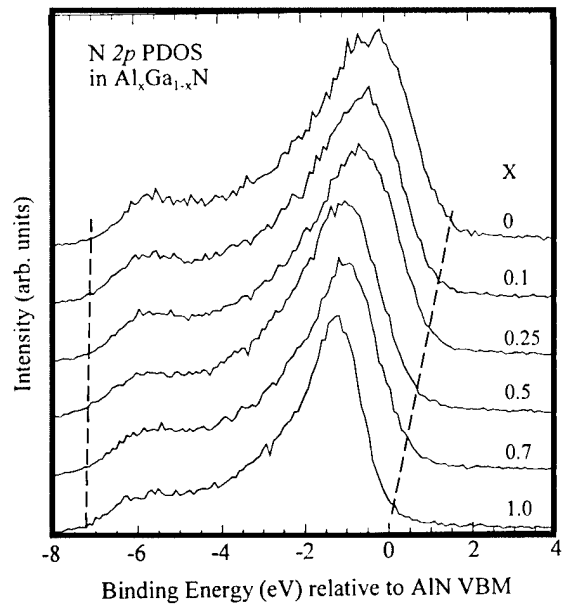

Figure I-4: A series of N *K*-emission spectra from the $Al_xGa_{1-x}N$ alloy system as a function of Al content x ($0<x<1$), excited with a photon energy just above the N *K* absorption edge. The binding energy range shown (0-10 eV) covers the valence bands.

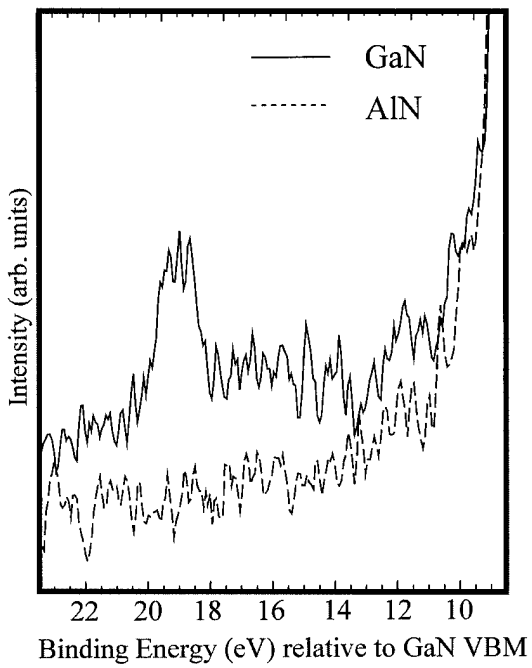

Figure I-5: Same as Figure I-1, except at greater binding energy (14-24 eV).

essentially a symmetric opening up of the band gap. Unlike photoemission, there are no charging problems associated with such measurements, and the surfaces of the films were not atomically cleaned. A further illustration of the power of this spectroscopy is presented in **Figure I-5**. Here the N *K*-emission spectra below the valence band are shown. Clearly visible at 19 eV is a well defined emission feature. This is direct observation of N *2p* states hybridized with the Ga *3d* shallow core level. The interatomic Ga *3d* - N *1s* transition is forbidden, so the emission to the *1s* hole must arise from states with N *2p* character. That the emission at 19 eV is due to these hybrid states is proven by the reduction of the emission with Al content.

Other experiments in the first runs explored the spatially resolved electronic structure of organic superconductors, and changes in *d-d* transitions in transition metal oxides during metal to non-metal transitions. ■

Fermi Surface Mapping in Photoemisson

P.D. Johnson, T. Valla, and A.V. Federov (BNL Physics Department)

Photoemission represents one of the most powerful techniques for the study of the electronic structure of materials. It has seen widespread application to the study of metals, superconductors, surfaces, thin films and, in its spin-resolved form, magnetic systems. In recent years, the development of higher energy resolution in this technique has allowed important contributions to be made to the field of high temperature superconductivity.

Recently, a group in the Physics Department at BNL has commissioned a new photoemission facility based on the use of a Scienta hemispherical analyzer. This instrument has the capability of measuring simultaneously the photoelectron's energy and angle of emission over a wide range of angles. An ultimate energy resolution of 5 meV and an angular resolution of ≤0.2Ῡare anticipated. The momentum resolution of the system is demonstrated in **Figure I-6(a)** where we show the experimentally observed electronic bands of molybdenum dispersing through momentum space in the NH direction of the Brillouin zone. The experimental observations are compared with a tight-binding calculation of the band structure in the same region of the zone. The spectral density plot is obtained with incident photons of energy 390 eV produced by the soft X-ray undulator on the X1B beamline. The center of electron emission corresponds to an angle of 15Ῡ with respect to the surface normal. The experimental parallel momenta, $k_{||}$, are determined from $k_{||} = 0.5123\ (E_{kin})^{0.5} \sin\phi$, where E_{kin} represents the photoelectron's kinetic energy above the vacuum level and j the angle of emission. By using higher incident photon energies, the variation in $k_{\perp}$ of the final state as a function of $k_{||}$ is greatly reduced. However, the question arises as to whether, at these energies, it will still be possible to observe the momentum dependence of the electronic structure. That one can in fact do so is clear from **Figure I-6(a)**. An important point to note is that the experimental observations are obtained with no changes in the voltages applied to the analyzer. One is simply "opening the shutter and taking a picture" of this particular section of the Brillouin zone. In **Figure I-6(b)**

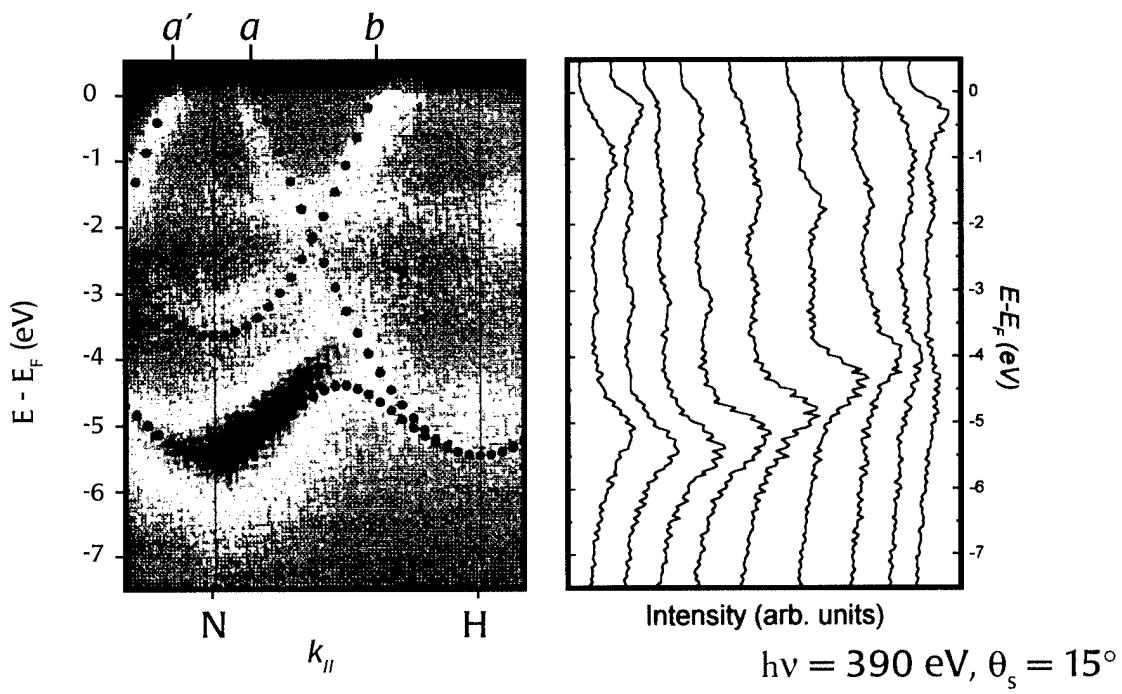

Figure I-6: (a) Spectral density plot recorded from a Mo(110) surface along the NH section of the Brillouin zone. The incident photons from beamline X1B have an energy of 390 eV and the center angle of emission corresponds to 15Ῡ. The dotted lines indicate the results of a tight-binding calculation of the electronic structure in the same region of the zone.
(b) Cuts through the spectral density plot of Figure I-6(a) to produce conventional angle-resolved photoemission spectra in the NH direction.

we show for comparison cuts through **Figure I-6(a)** at well defined spacings in angle in order to provide the traditional angle-resolved photoemission spectra.

A spectral density plot, as shown in **Figure I-6(a)**, allows us to examine in detail the Fermi surface of the material under investigation. This Fermi surface is defined by the points in momentum space at which the electronic bands intersect the Fermi level E_F. Thus, the points labeled a and a' in **Figure I-6(a)** correspond to calipers on an ellipse centered at the N point of the Mo Fermi surface. An interesting observation is that the tunability of synchrotron radiation and the symmetry of the crystal allow the entire surface of such an ellipse to be mapped out without rotating the azimuth of the crystal.

A measurement of the calipers, or spanning vectors, on the Fermi surface of a material is important for our understanding of the oscillatory exchange coupling that is observed in magnetic multilayers. Indeed, **Figure I-7** [1] shows a calculation of the Fermi surface of bulk molybdenum and indicates the relevant spanning vectors for a multilayer grown in the (110) direction with molybdenum as a spacer layer. For comparison, we indicate in **Figure I-7** the points a, a', and b corresponding to the same points in **Figure I-6(a)**. Interestingly, the experimental determination in **Figure I-6(a)** of the spanning vector **q** from a to b would result in an oscillatory period length, $2\pi/q$, 80% of that indicated in the theoretical calculation represented in **Figure I-7**. ■

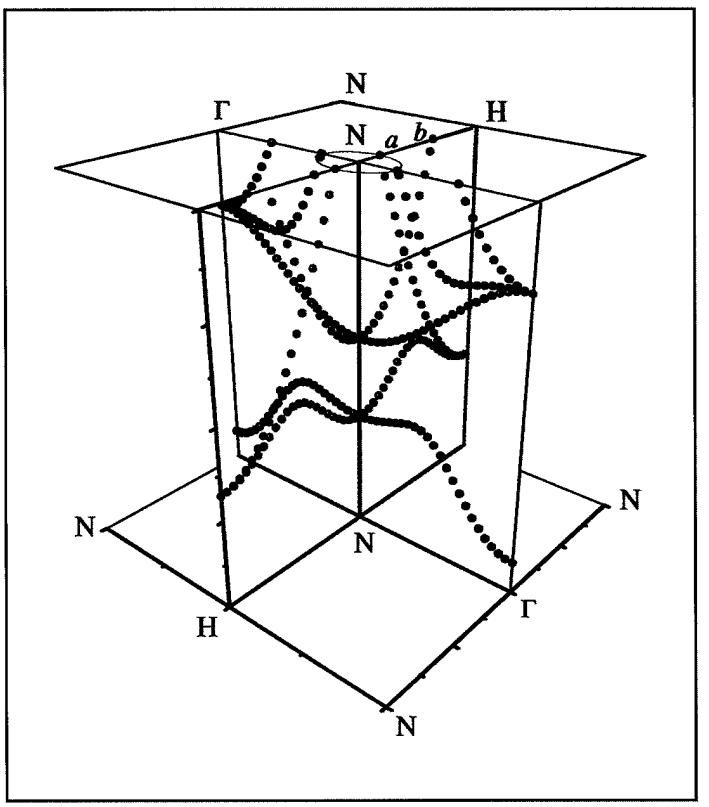

Figure I-7: Calculated Fermi surface of Mo showing the spanning vectors appropriate to oscillatory coupling in the (110) direction from Ref. [1].

[1] M.D. Stiles, *Phys. Rev. B* **48**, 7238 (1993).

Surface Magnetic Ordering: A Spin-Polarized Photoemission Study of Thin Films of Gd

P. Dowben and C. Waldfried (University of Nebraska), E. Vescovo (NSLS)

Perhaps the most remarkable example of the uniqueness of surface magnetic properties is the condition of magnetically ordered surfaces at temperatures where the bulk material is paramagnetic. This is well documented for the rare-earth elements. An enhanced magnetization has also been proposed for chromium surfaces, and the face centered iron phase. This property of the rare earth surfaces is a dramatic example of the different magnetic, as well as electronic, properties that exist at surfaces, as noted, for example, in the recently completed review chapter on the surface magnetism of the rare earth metals by P.A. Dowben *et al* [1].

C. Waldfried and coworkers from the Dowben group have utilized their previous experimental discovery of a localized surface state on the Gd(0001) surface to probe the origin of the different magnetic properties of the surfaces of both "unstrained" and 4% expansively strained gadolinium films. They find that the occupied *bulk* Gd 5d/6s bands for both strained and unstrained Gd exhibit a Stoner-like exchange splitting consistent with theory[2]. However, the strained Gd(0001) surface exhibits a mixture of Stoner-like magnetism and spin-mixing behavior[1], with more rigid band ferromagnetism than the unstrained surface.

During the past year a considerable amount of work focused on a detailed study of the band structure of the 4%-strained Gd(0001) surface using spin polarized electron spectroscopy[3]. An important result of these measurements is that they show very clearly that the exchange splitting, and by extension perhaps the magnetic coupling, is electron wave vector dependent as seen in **Figure M-1**. Finite-temperature many-body band-structure-calculations[2] predict this result, but the extent of this wave vector dependence is surprising. Consistent with the enhanced magnetization of the surface, the exchange splitting and wave vector dependence of the surface is different from the bulk, being dominated by the more localized band structure of the surface.

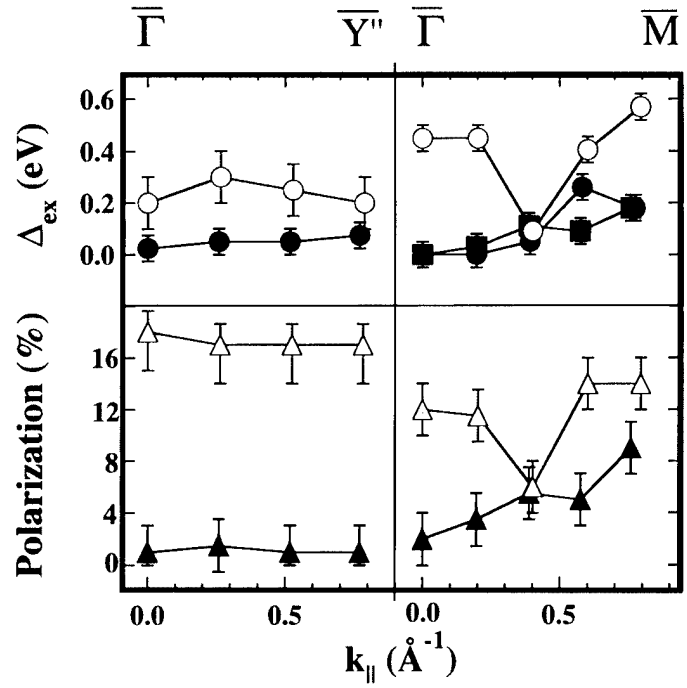

Figure M-1: Wave vector dependence of the exchange splitting and polarization of the Gd surface state (open symbols) and bulk states (filled symbols) for strained Gd(1012) (4ML - left) and strained Gd(0001) (40 ML - right).

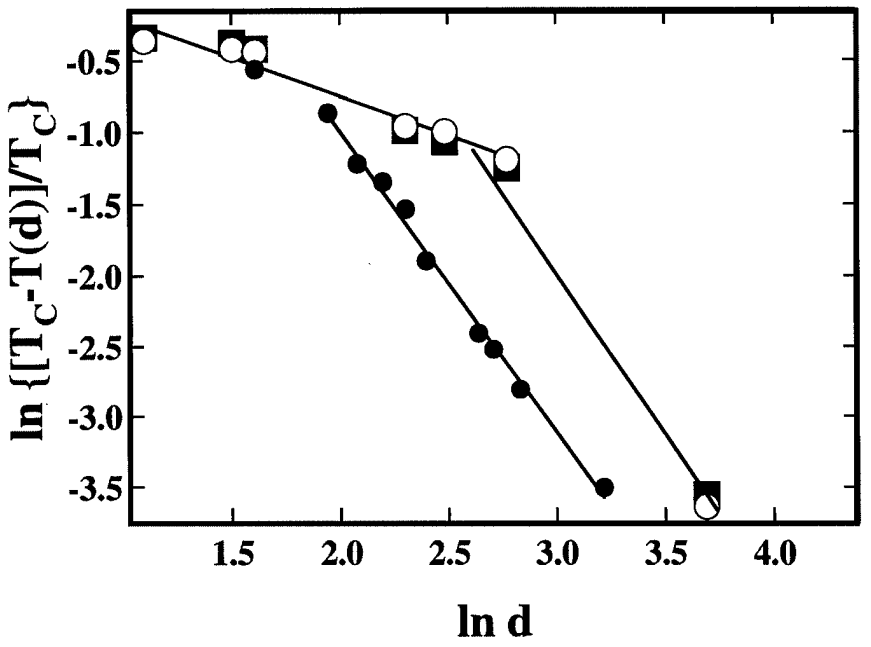

Figure M-2: The logarithm of the reduced Curie temperature for strained gadolinium surface (open circles) and bulk (closed squares) are compared to unstrained gadolinium (closed circles) as a function of film thickness.

A second very important result is that there is direct evidence that the surface Gd 5d exchange splitting, and thus the magnetic moment, is enhanced over the bulk particularly for the expansively strained Gd(0001) surface. The observed surface Curie temperature of these films is 370 K and is much higher than the bulk Curie temperature for expansively strained Gd(0001). Both of these temperatures are much higher than the generally accepted bulk Curie temperature of gadolinium of 293 K. It is very clear that the surface plays the role of an "actor" not a "spectator" and will influence finite size scaling behavior in the ultra-thin film limit[3]. This is indicated in **Figure M-2.** ■

[1] P.A. Dowben, D.N. McIlroy and Dongqi Li, "Surface Magnetism of the Rare Earth Metals", Handbook on the Physics and Chemistry of the Rare Earths, Edited by K.A. Gschneidner and Leroy Eyring, (Chapt. 159) **24**, 1, (1996).

[2] W. Nolting, T. Dambeck and G. Borstel, Z. *Phys. Rev. B* **94**, 409, (1994).

[3] C. Waldfried, D. Welipitiya, T. McAvoy, E. Vescovo and P.A. Dowben, "Wave Vector Dependent Exchange Splitting in a Local Moment System", submitted to *Phys. Rev. Lett.*

C. Waldfried, T. McAvoy, D. Welipitiya, P.A. Dowben, and E. Vescovo, "The Influence of Enhanced Surface Magnetism on Finite Size Scaling", submitted to *Europhys. Lett.*

First Observation of Half-Metallic Behavior: A Spin-Polarized Photoemission Study of Thin Films of $La_{0.7}Sr_{0.3}MnO_3$

J.-H. Park, E. Vescovo, and H.-J. Kim (NSLS)

s mentioned above, a considerable amount of experimental work at U5UA during 1997 was devoted to the study of the electronic structure of a thin film of $La_{0.7}Sr_{0.3}MnO_3$. This material belongs to the class of manganese perovskites, derived from the antiferromagnetic insulating parent-compound $LaMnO_3$ by partial substitution of La with Sr atoms. As is well known, with increasing temperature this material undergoes a complex phase transition from a metallic-ferromagnetic phase at low temperatures to an insulating-paramagnetic phase at high temperature (T_C ~ 350 K). This link between metallic character and ferromagnetic behavior, as opposed to insulating and antiferromagnetism, seems to be a quite general characteristic of transition metal oxides [1] and has been explained, at least in some cases, by the so-called double exchange mechanism[2]. According to this model, substituting divalent Sr atoms for trivalent La ones forces a corresponding number of Mn ions to become tetravalent: the system is now a mixed-valent compound in which both Mn^{3+} (as in $LaMnO_3$) and Mn^{4+} ions are present. The conduction can then be sustained (at no cost, in the ferromagnetic system) by electron hopping from a Mn^{3+} to a neighboring Mn^{4+} site (the two configurations Mn^{3+}-O^{2-}-Mn^{4+} and Mn^{4+}-O^{2-}-Mn^{3+} being obviously degenerate). This transport mechanism is mediated by the O^{2-} ions, which permit a "double exchange" in which an electron is exchanged between a $3d$ orbital of the Mn^{3+} ion and an O $2p$ electron, while at the same time another electron is exchanged from the O $2p$ to the Mn^{4+} ions. However, owing to the strong on-site Mn exchange interaction, this hopping is allowed only if the two neighboring Mn ions are ferromagnetically aligned: i.e. the system can become metallic only if it also ordered ferromagnetically. A very important consequence of this conduction mechanism is that this system should then have charge-carriers all with the same (majority) spins, i.e. it should be a perfect half-metallic system displaying 100% spin-polarization at the Fermi level. In **Figure M-3**, the metal-to-insulator transition of

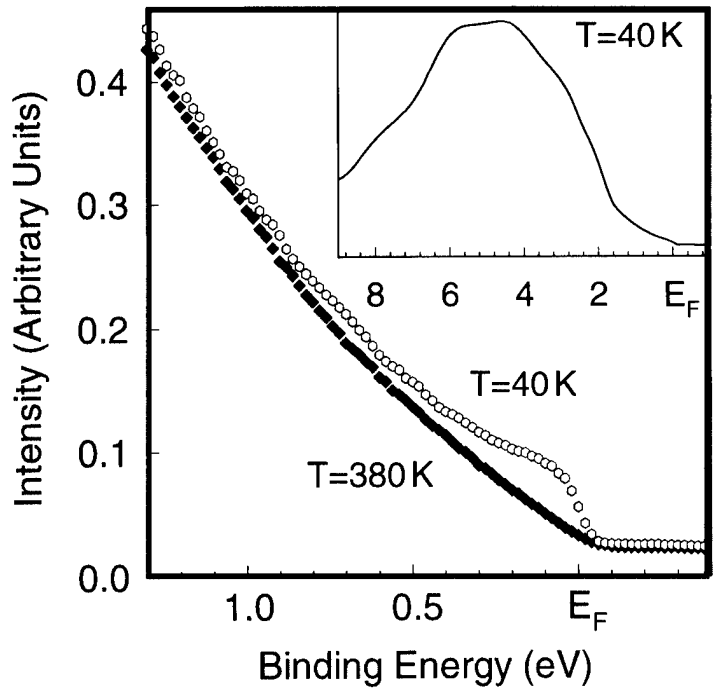

Figure M-3: The metal-to-insulator transition of the $La_{0.7}Sr_{0.3}MnO_3$ thin film is clearly displayed by the change in the density-of-state at the Fermi level. At low temperature (open symbols) the system is metallic while at high temperature (closed symbols) it becomes insulating. The valence band spectrum is shown on a larger binding energy scale in the inset (continuous line).

$La_{0.7}Sr_{0.3}MnO_3$ is clearly displayed: the density-of-state at the Fermi level disappears with increasing temperature. **Figure M-4** instead shows the spin-resolved spectrum of the valence band in a region very close to the Fermi level when the system is kept at low temperature, i.e. in its ferromagnetic-metallic phase. Unambiguously, the predicted 100% spin-polarization is observed close to the Fermi level. The proof of the existence of half-metallic systems[3] is not only important from the fundamental point of view but also has important implications for technological applications. Indeed, the realization of an half-metallic system also implies, for example, the realization of a 100% spin-polarized electron source or the realization of a perfect spin-filter. For this reason, laboratories all over the world are currently testing the magnetic properties of these types of materials. In this connection, the very surface sensitive measurements performed at U5UA on a thin-film surface prepared *in-situ* represent the first measurements available of this kind and do show a largely distinct magnetic behavior on the surface of these materials as compared to their known bulk properties[4]. ■

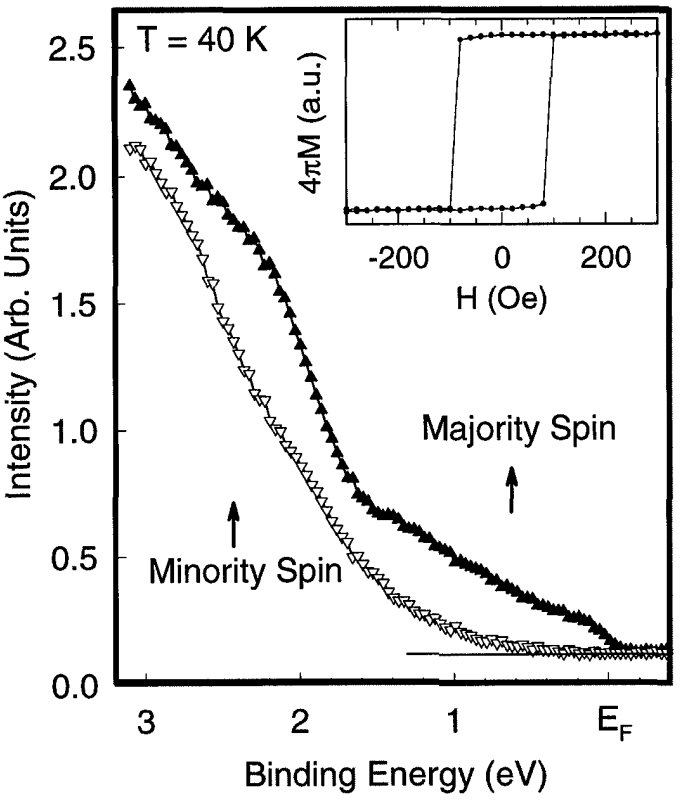

Figure M-4: Contemporary to the metal-to-insulator transition shown in Figure M-3, the $La_{0.7}Sr_{0.3}MnO_3$ system undergoes a ferromagnetic-to-paramagnetic. Below the Curie temperature the thin film shows a very good magnetic remanence (see inset). The spin-resolved spectra (closed up-triangles: majority spin; open down-triangles: minority spin) of the region near to the Fermi level clearly demonstrate that charge-carriers are totally of majority-spin character, i.e.: a 100% spin-polarization is observed. This result represents the first experimental evidence of the existence of an half-metallic system.

[1] D.I. Khomskii, G.A. Sawatzky, *Solid State Comm.* **102**, 87 (1997).

[2] C. Zener, *Phys. Rev.* **81**, 440 (1951).

[3] J.-H. Park, E. Vescovo, H.-J. Kim, C. Kwon, R. Ramesh, and T. Venkatesan, "Observation of a Half-Metallic Ferromagnet", *Nature* (in press, 1997).

[4] J.-H. Park, E. Vescovo, H.-J. Kim, C. Kwon, R. Ramesh, and T. Venkatesan, "Novel Magnetic Properties at Surface Boundary of a Half-Metallic Ferromagnet Manganese Perovskite", submitted to *Science*.

The c-axis Optical Response of $Y_{1-x}Ca_xBa_2Cu_3O_{7-\delta}$ Single Crystals Studied by Far Infrared Ellipsometry

C. Bernhard, R. Henn, A. Wittlin, W. König, and M. Cardona
(Max-Planck-Institut für Festkörperforschung)

The incoherent electronic c-axis conductivity $\sigma_c^{el}(\omega,T)$ of the cuprate high-T_c superconductors has attracted considerable attention. The most peculiar feature is the gap-like suppression of the normal state $\sigma_{1c}^{el}(\omega,T)$ in the far infrared (FIR) regime which has recently been observed in underdoped $YBa_2Cu_3O_{7-\delta}$ (Y-123)[1,2], $YBa_2Cu_4O_8$ [3] and possibly also in $La_{2-x}Sr_xCuO_4$ [4,5]. This observation has raised the question of whether the unusual properties of the FIR c-axis conductivity are related to the pseudogap which depletes the low energy spin- and charge excitations of the CuO_2 planes[6] rather than to the insulating rocksalt layers which separate the metallic CuO_2 planes acting like "blocking layers"[7]. In the former case $\sigma_{1c}^{el}(\omega,T)$ should evolve as a function of the hole doping of the CuO_2 planes, in analogy to the pseudogap which occurs only for underdoped samples and disappears around optimum doping[6]. In the latter case the anomalous features of $\sigma_{1c}^{el}(\omega,T)$ should depend critically on the structural and electronic details of the "blocking layers"[7]. In particular, for Y-123 the CuO chains should have a pronounced influence since they become metallic upon oxygenation and reduce the effectiveness of the "blocking layer".

In order to resolve this question we have performed ellipsometric measurements of the FIR c-axis conductivity on $Y_{1-x}Ca_xBa_2Cu_3O_{7-\delta}$ (Y,Ca-123) single crystals for x=0 and x=0.14 and variable oxygen deficiency δ[8]. The partial substitution of Y^{3+} by Ca^{2+} introduces extra hole carriers into the CuO_2 planes in addition to those that are transferred from the CuO chains as controlled by the oxygen content[9]. This enables us to access almost the entire doping range from underdoped to strongly overdoped. Furthermore, the opposing effects of hole doping due to Ca-substitution and hole depletion due to a deoxygenation of the CuO chains allows us to study samples with a comparable doping state of the CuO_2 planes but a significantly different oxygen content and thus electronic properties of the CuO chains.

The ellipsometry measurements have been performed at the U4IR beamline of the National Synchrotron Light Source (NSLS) at Brookhaven National Laboratory (BNL), using a home-built setup attached to a Nicolet Fourier Spectrometer[5,10]. The high brilliance of the synchrotron allows us to perform accurate measurements on crystals with ac-faces as small as 1∞0.3 mm^2. The ellipsometry technique provides significant advantages over conventional reflection methods. Ellipsometry is self normalizing and does not require a reference sample. The real- and the imaginary part of the dielectric function are obtained directly without a Kramers-Kronig transformation.

Figure M-5 shows $\sigma_{1c}(\omega,T)$ for $Y_{0.86}Ca_{0.14}Ba_2Cu_3O_{7-\delta}$ in order of increasing oxygen content and doping. **Figure M-6** shows the data for Ca-free Y-123 which is more fully oxygenated at a given doping state. The oxygen deficiency of the crystals can be estimated from the spectral weight of the phonon mode at 620 cm^{-1} which increases with the oxygen deficiency of the crystal since it involves the vibration of an apex oxygen next to an empty chain fragment[1,2]. There are five more IR-active modes superimposed on the electronic background which will not be further discussed here.

From **Figures M-5 and M-6** it is evident that a gap-like suppression of $\sigma_{1c}^{el}(\omega,T)$ in the normal state occurs only for the underdoped samples. The normal state gap in $\sigma_{1c}^{el}(\omega,T)$ disappears around optimum doping. In the overdoped regime $\sigma_{1c}^{el}(\omega,T)$ exhibits a metallic T- and ω-dependence. The oxygen content of the CuO chains and the related electronic properties of the "blocking layers" do not affect the characteristic T- and ω-dependence but merely affect the absolute values of $\sigma_{1c}^{el}(\omega,T)$. This finding implies that pseudogap correlations which deplete the low energy spin- and charge excitations of the CuO_2 planes[6] may cause the gap-like suppression of $\sigma_{1c}^{el}(\omega,T)$ and the confinement of the charge carriers in the normal state.

In the overdoped regime this confinement is gradually relaxed while the SC state deteriorates. Both T_c and the SC energy gap 2Δ (as estimated from the onset of the loss of spectral weight in the SC state when the carriers condense into a delta function at zero frequency) are suppressed. In addition a growing fraction of the quasi-particles remains unpaired in the SC state possibly due to strong pair-breaking effects[8,11]. This raises the question whether the pseudogap and the confinement are necessary prerequisites for the occurrence of high-T_c superconductivity in the cuprates. ■

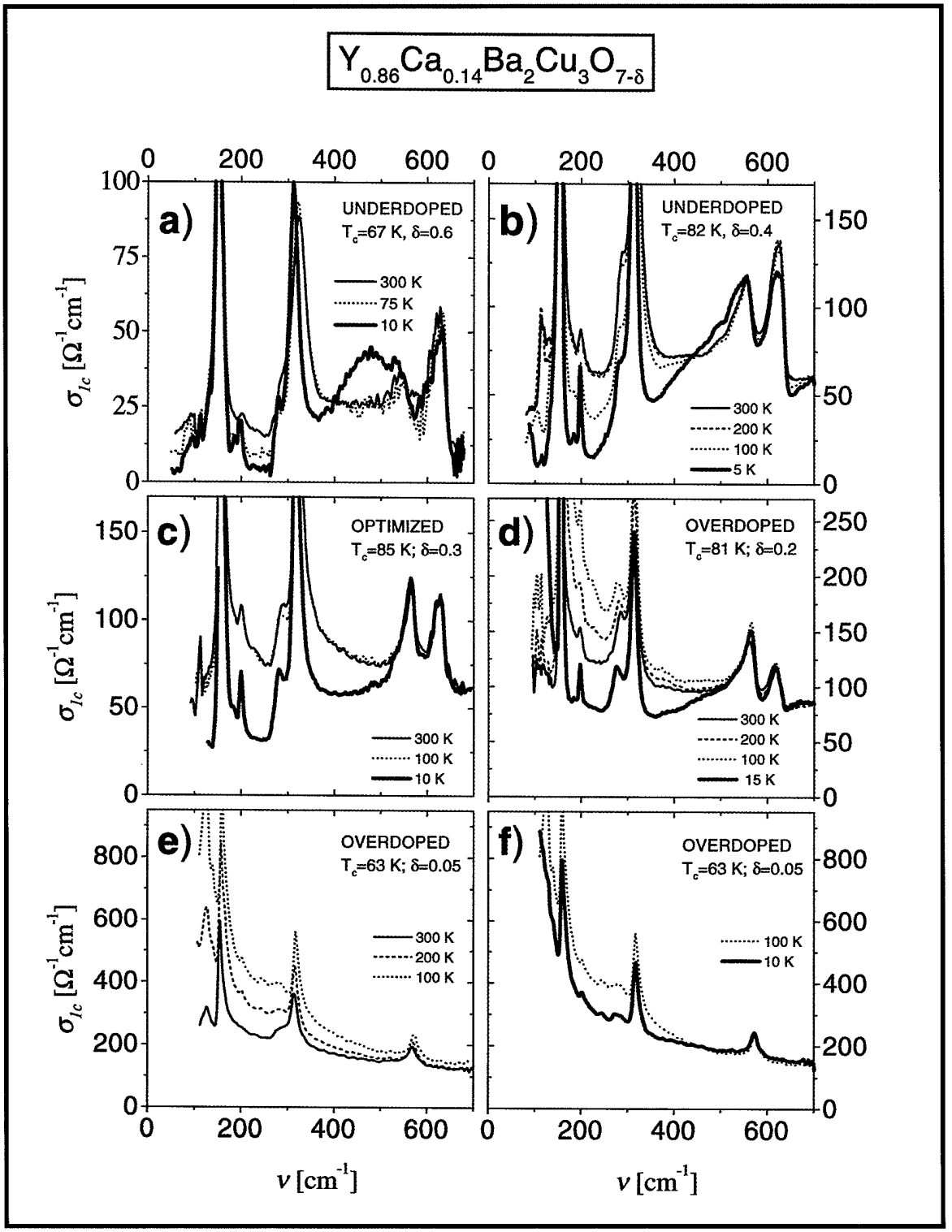

Figure M-5: The real part of the FIR c-axis conductivity $\sigma_{1c}(\omega,T)$ of the $Y_{0.86}Ca_{0.14}Ba_2Cu_3O_{7-\delta}$ single crystals with variable oxygen deficiency d and doping of **a)** $\delta\cup0.6$, T_c=67 K (underdoped); **b)** $\delta\cup0.35$, T_c=82 K (underdoped); **c)** $\delta\cup0.3$, $T_c=T_{c,max}$=85 K (optimally doped); **d)** $\delta\cup0.2$, T_c=81 K (overdoped); and **e,f)** $\delta\cup0.05$, T_c=63 K (overdoped). The data are shown in the SC state by the red solid lines, in the normal state just above T_c by the blue dotted lines, at intermediate temperatures by the green dashed lines and at room temperature by the black solid lines.

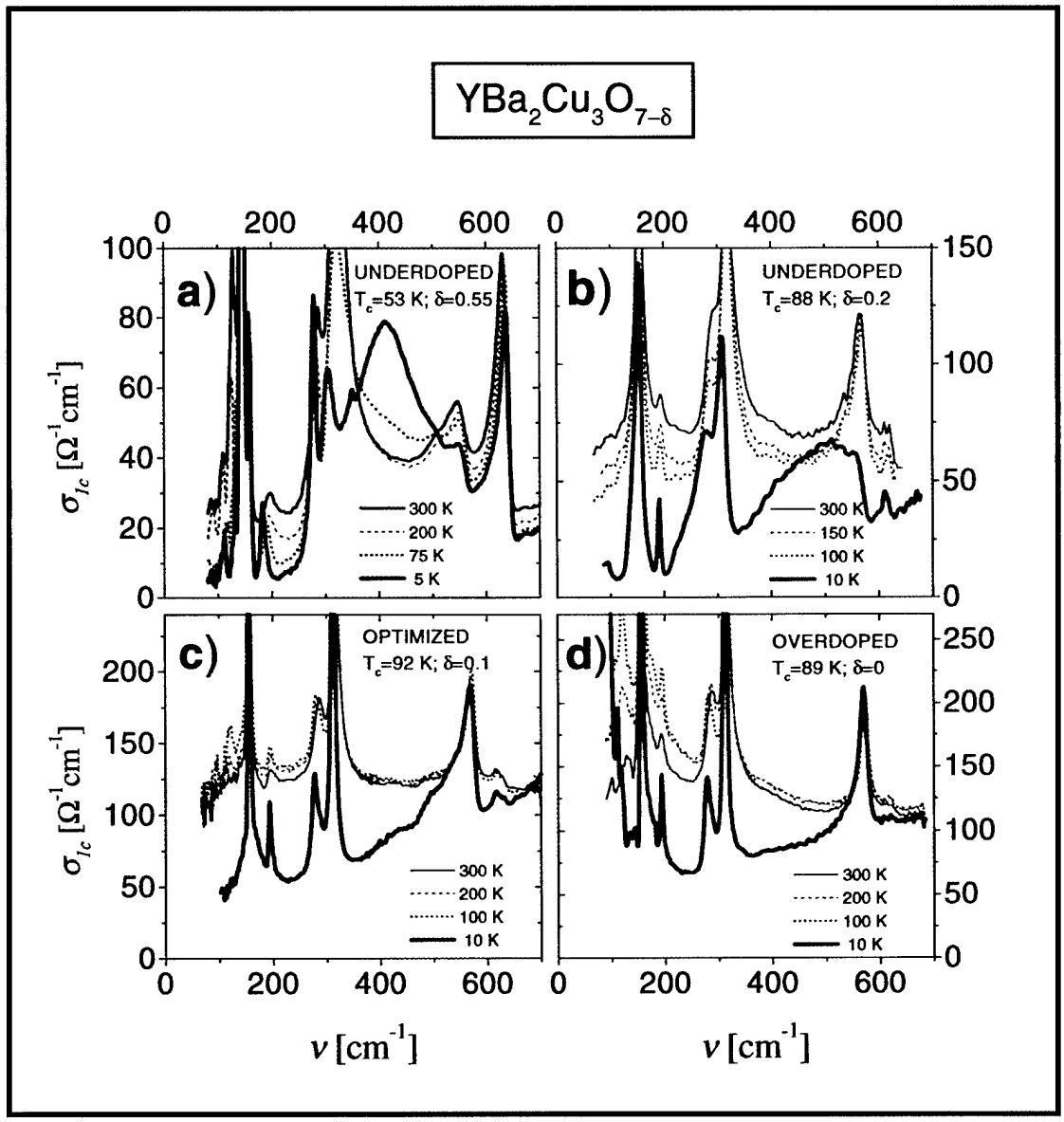

Figure M-6: The real part of the FIR c-axis conductivity $\sigma_{1c}(\omega,T)$ of $YBa_2Cu_3O_{7-\delta}$ single crystals for variable oxygen deficiency and doping of **a)** $\delta\cup0.55$, T_c=53 K (underdoped); **b)** $\delta\cup0.2$, T_c=88 K (underdoped); **c)** $\delta\cup0.1$, $T_c=T_{c,max}$=92 K (optimally doped); and **d)** $\delta\cup0$, T_c=89 K (overdoped). The data are shown in the SC state by the red solid lines, in the normal state just above T_c by the blue dotted lines, at intermediate temperatures by the green dashed lines and at room temperature by the black solid lines.

Acknowledgements. *We are indebted to G.P. Williams and L. Carr for support at the U4IR beamline of the NSLS and acknowledge D. Böhme for technical help. We thank M. Kläser, T. Wolf and C.T. Lin for providing the crystals.*

[1] C.C. Homes *et al., Phys. Rev. Lett.* **71**, 1645 (1993).
[2] J. Schützmann *et al., Phys. Rev.* **B52**, 13665 (1995).
[3] D.N. Basov *et al., Phys. Rev.* **B 50**, 3511 (1994).
[4] K. Tamasaku *et al., Phys. Rev. Lett.* **72**, 3088 (1994).
[5] R. Henn et al., to be published in *Thin Solid Films*; R. Henn *et al., Phys. Rev.* **B 56**, 6295 (1997).
[6] J.W. Loram *et al., Phys. Rev. Lett.* **71**, 1740 (1993); A.G. Loesser *et al., Science* **273**, 325 (1996); G.V.M. Williams *et al., Phys. Rev. Lett.* **78**, 721 (1997).
[7] A.A. Abrikosov, *Phys. Rev.* **B 52** , 7026 (1995); Physica **C 258**, 53 (1996); W.A. Atkinson and J.P. Carbotte, *Phys. Rev.* **B 55**, 3230 (1997).
[8] C. Bernhard *et al.,* to be published in *Phys. Rev. Lett.*
[9] J.L. Tallon *et al., Phys. Rev.* **B51**, 12911 (1995).
[10] J. Kircher *et al., J. Opt. Soc. Am.* **B14**, 705 (1997).
[11] C. Bernhard *et al., Phys. Rev. Lett.* 77, 2304 (1996).

Surface Alloys: An Auger Photoelectron Coincidence Spectroscopy Study

R.A. Bartynski, and Q. Qian (Rutgers University), and S.L. Hulbert (NSLS)

The VUV Ring has seen considerable utilization by a number of novel applications including Auger-photoelectron coincidence spectroscopy (APECS). In this adaptation of photoelectron spectroscopy both the core photoelectron and the Auger electron associated with a given photoexcitation/decay event are detected in time coincidence. Examining the photoemission spectrum with this additional level of discrimination results in higher surface sensitivity and enables site-specific electronic structure studies while eliminating secondary electron background and lifetime broadening.

Perhaps most exciting results are in the field of surface alloys. We have successfully made the first direct measurement of valence band energy shifts in a surface alloy: Ag/Cu(100). In recent years, there has been considerable theoretical and experimental interest in surface alloys (bimetallic systems that intermix only in the first atomic layer) owing to their novel electronic, chemical, and magnetic properties. First principles electronic structure calculations suggest that band narrowing and a systematic shift (as a function of host) in the valence levels of the minority species lead to the

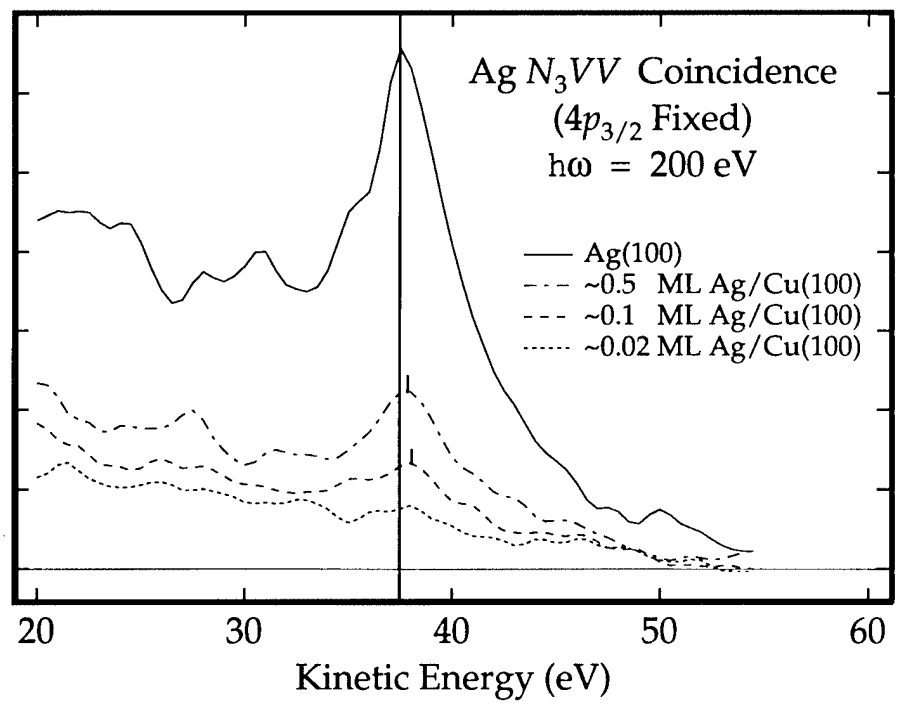

Figure M-7: Auger photoelectron coincidence spectroscopy (APECS) Ag N_3VV Auger spectra from Ag(100) and from the Ag/Cu(100) system for three Ag coverages as indicated. These spectra were taken in time coincidence with Ag $4\mathbf{p}_{3\,2}$ photoelectrons excited with 200eV photons.

unusual physical properties of these systems. Up until now, experimental work has focused on structural aspects, particularly STM measurements exploring phase formation upon intermixing at the surface. Measurements of the electronic structure using conventional photoelectron spectroscopy are extremely difficult because the signal from the minority metal typically is weak and often overlaps spectral features of the substrate.

Our primary result is summarized in **Figure M-7**. Here, APECS spectra of the Ag N_3VV Auger transition from Ag(100) are compared to that of the Ag/Cu(100) system for several Ag coverages. As is clear from the figure, the peak in the coincidence Auger spectrum shifts to higher kinetic energy for low Ag concentrations. This shows that the Ag **d**-levels shift closer to the Fermi level as compared to Ag metal. STM studies indicate that for coverages in the 0.1 monolayer (ML) range, Ag forms a random substitutional alloy in the Cu(100) surface. The calculations predict that in this phase, the centroid of the Ag **d**-band shifts ~ 0.70 eV *away* from the Fermi level.

The origin of the difference between our experimental results and the theory is not yet clear, however the shifts can be understood in terms of relative electron density and the calculations were performed for the closed packed surface, while our experiments examined the more open (100) surface. Upcoming investigations of Pt/Cu(100) and Pt/Ag(100) should prove most interesting.

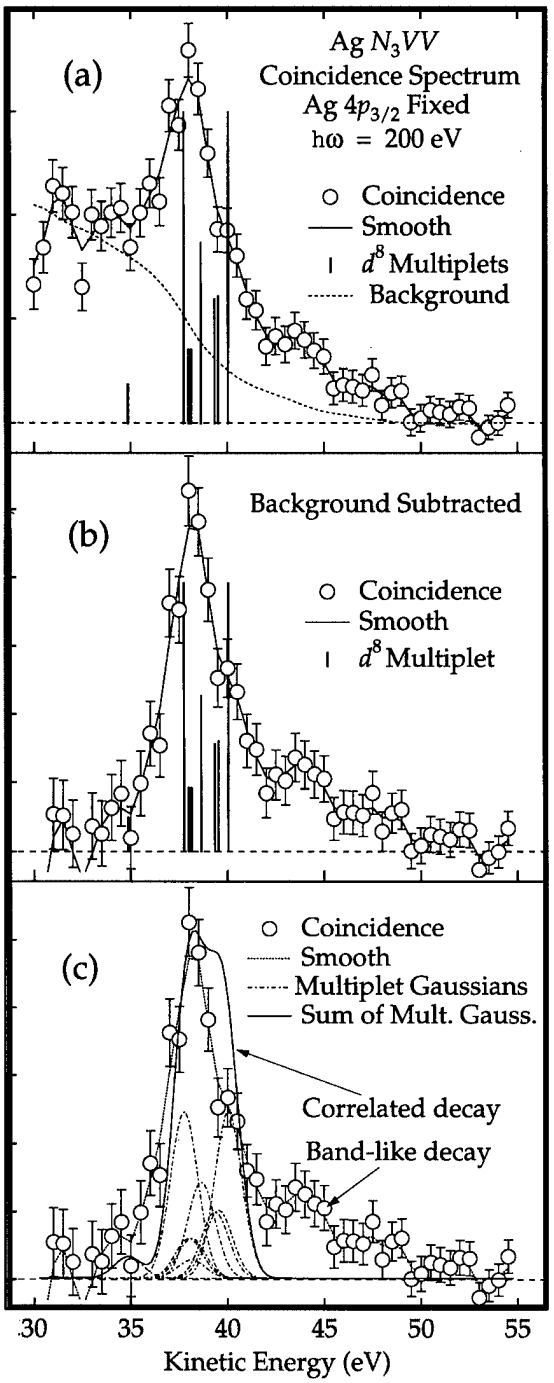

Figure M-8: (a) Ag $N_{2,3}VV$ coincidence Auger spectrum (circles) of the Ag(100) surface taken in time coincidence with Ag $4\mathbf{p}_{3/2}$ photoelectrons excited with 200eV photons. Digital smooth (solid line), multi-electron background (dotted line) and atomic-like $\boldsymbol{d}^8$ multiplets (vertical solid bars) are shown. (b) Background-subtracted (from (a)) Ag $N_{2,3}VV$ coincidence Auger spectrum of the Ag(100) surface. (c) same as (b) except $\boldsymbol{d}^8$ multiplets are Gaussian-broadened. The sum of the broadened multiplets is shown (solid line, labeled "Correlated decay").

To better understand the influence of alloying on the electronic structure of the minority component, we have also performed detailed studies of the Ag 4p core levels and the associated $N_{2,3}VV$ Auger spectra from the single crystal Ag(100) surface. It is well known that the shallow **p**-levels of the late transition metals have very broad and ill-defined spectral line shapes. Owing to strong overlap with the 4**d** bands, the shallow 4**p** levels of Ag have a very short lifetime and hence appear as broad (~5 eV wide) features in photoemission spectra. This width is folded into the conventional Auger spectrum. By measuring Ag $N_{2,3}VV$ Auger electrons in coincidence with Ag 4**p** photoelectrons of a particular kinetic energy, we have eliminated this broadening and revealed the intrinsic lineshape of the Auger transition. These coincidence Ag N_3VV Auger spectra are shown in **Figure M-8**. The majority of the emission is accounted for by an atomic-like d^8 multiplet, but there is a significant band-like component. A comparison of the relative spectral weight contained in each component indicates that the band-like part is larger than is observed in conventional $M_{4,5}VV$ Auger spectra and also larger than is anticipated based on the band width and correlation energies of Ag. ■

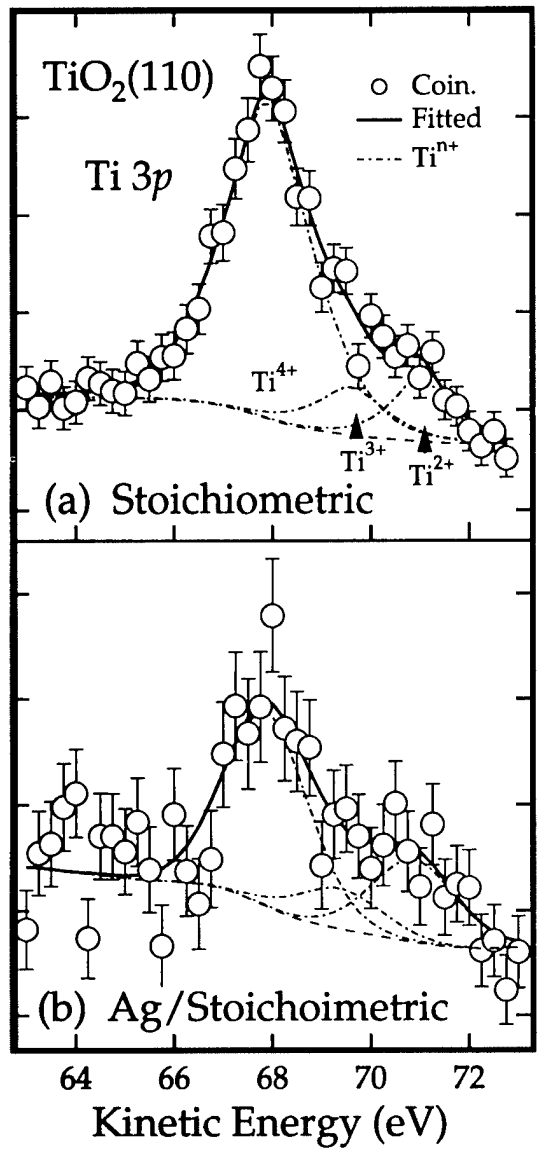

Figure M-9: (a) Ti 3**p** core level spectrum from the clean, stoichiometric TiO_2(110) surface taken in time coincidence with Ti MVV Auger electrons. The Ti^{4+} main peak, and shoulders assigned to Ti^{3+} and Ti^{2+} oxidation states, associated primarily with surface oxygen vacancies and step edges, respectively, are labeled. (b) same as (a), but acquired after ~ 0.2 monolayer (ML) of Ag is adsorbed on the surface.

Large Value of the Electron-Phonon Coupling Parameter λ=1.15 and the Possibility of Surface Superconductivity at the Be(0001) Surface

T. Balasubramanian and E. Jensen (Brandeis University)
X.L. Wu and S.L. Hulbert (NSLS)

The electronic density of states (DOS) at the Fermi level (E_F) at the Be(0001) surface is about four times larger than in the bulk[1]. The E_F DOS is an important parameter for describing many electronic processes. Anomalously large surface core level shifts[2], and giant surface Friedel oscillations[3] have been observed on this surface, and attributed to the large surface to bulk E_F DOS ratio. Electron phonon coupling should also be enhanced. In a typical electron-phonon interaction event, an electron scatters from one state to another with the emission or absorption of a phonon. By simple Fermi golden rule arguments, one expects the probability for this interaction to be proportional to the density of states into which the electron can scatter. Phonon and thermal energies are small on the scale of electronic energies and the final state energy is near to E_F, so the coupling is proportional to the electronic density of states at E_F. The strength of the electron-phonon interaction is conventionally measured by the dimensionless parameter λ, called the mass enhancement or coupling parameter. Accordingly, one should expect λ_s at the Be(0001) surface to be near unity, four times larger than the bulk value λ_b=0.24.

It has been shown that angle resolved photoemission (ARP) can be used to determine λ_s for crystalline metal surfaces[4]. The basic idea is that, under proper conditions, the observed width of a surface state peak is equal to h/τ, where τ is the lifetime of the surface state hole excitation. Since virtually all of the temperature dependence of τ is in the phonon contribution, a measurement of the temperature dependence of the surface state width is effectively a measurement of the temperature dependence of the phonon contribution to the hole lifetime. At high temperatures and small hole energies the temperature dependence of the phonon contribution to the inverse hole lifetime is given by $h/\tau = 2\pi\lambda kT$. In this limit, λ is just $2\pi k$ times the slope of the peak width vs. temperature curve, and is easily measured.

We have used ARP to determine λ_s at the Be(0001) surface and find that λ_s=1.15, more than four times larger

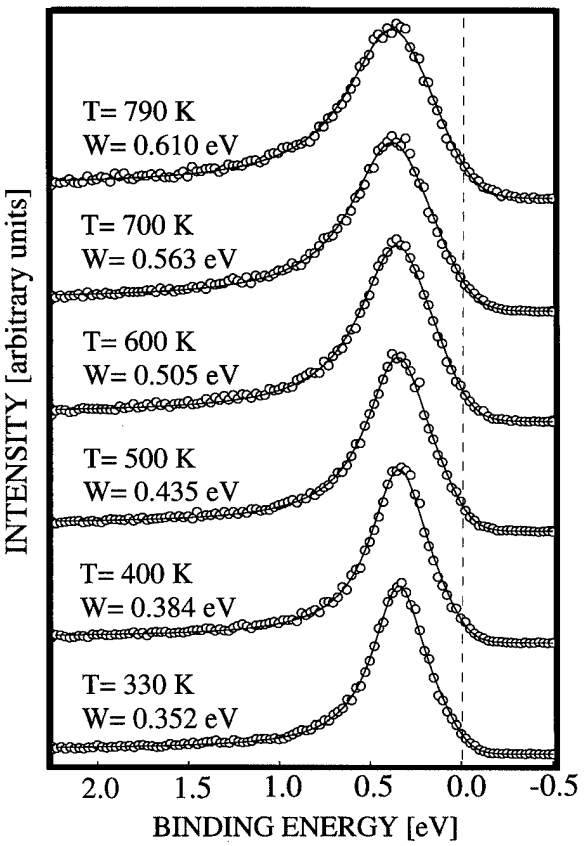

Figure M-10: Surface state spectra at several temperatures. The momentum is 0.89 $Å^{-1}$, the hole energy is 0.35 eV, and the photon energy is 15 eV. The open circles are the experimental data. Typically there are 1500 counts in the peak. The line is a fit to a function of the form lorentzian plus constant times the fermi distribution. Temperatures (T) and widths (W) derived from the fit are as indicated.

than λ_b. The data and analysis are presented in the figure below.

It is common for large values of λ to be associated with high superconducting T_C's, especially in materials such as Be with large phonon energies. If the surface is considered as a thin film with high λ on a thick substrate with low λ, the proximity effect would destroy any observable interesting effects. However, it was shown by Suhl, Matthias, and Walker[5] that different branches of the Fermi surface — for which surface and bulk states qualify — could have different superconducting energy gaps. In the limit of a semi-infinite solid the two branches are essentially uncoupled and the surface states are allowed superconduct independent of the bulk. Application of the McMillan formula using bulk phonons to estimate the superconducting transition temperature yields 70K for the surface transition temperature.

Impurities/defects will likely play a more important role in destabilizing this system than they do in homogeneous superconductors. The problem is that the impurities scatter surface states into bulk states, the one electron eigenstates become linear combinations of surface and bulk states, and the pairing interaction is averaged over surface and bulk. Since the interaction in the bulk is weak, any averaging will quickly destroy superconductivity at the surface. It is known that two band effects are destroyed if the mean free path is shorter than the superconducting coherence length[6]. For the Be(0001) surface, assuming a 70K T_C, ξ_0 is about 300Å. A mean free path as large as this is difficult to achieve on a metal surface. However, only the interband (surface to bulk) scattering should contribute to the averaging. Since the surface state DOS is much larger than the bulk state DOS, surface to surface scattering should be much more common than surface to bulk scattering, and a much smaller mean free path may be adequate.

If the surface states do pair at elevated temperatures, they represent an interesting opportunity to study two dimensional superconductivity for a simple system with a relatively large energy scale. The one electron origins of the many body state are simple and well characterized (parabolic bands, nearly circular Fermi surface), and the pairing mechanism (phonons) is well understood. The superconducting gap energy ought to be resolvable by high resolution ARP spectrometers. Scanning tunneling microscopy should also be able to observe the gap. Simple estimates of the maximum surface current density are of order 10 Å/cm, so the change in resistivity at T_C may be directly observable as well.■

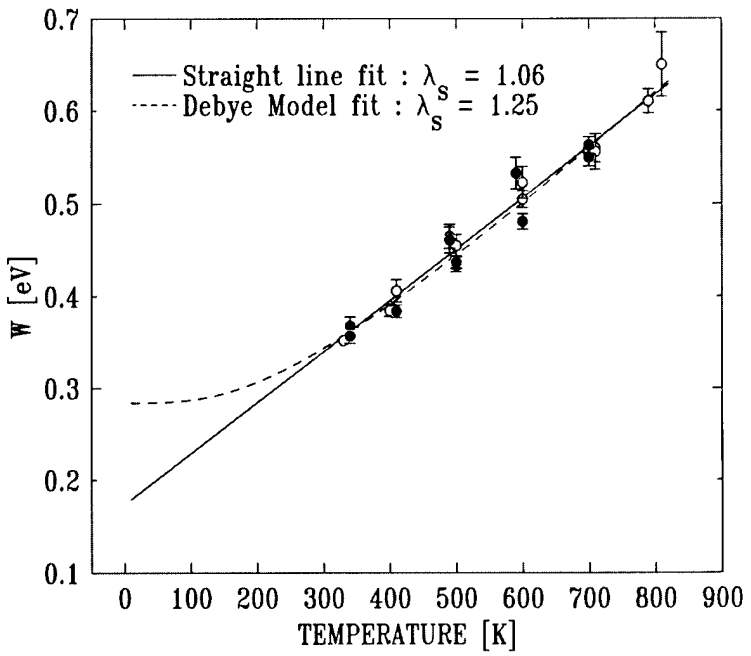

Figure M-11: Surface state widths from fits like those shown in **Figure M-10** vs. temperature. These data include two full cycles from room temperature to 800K and back to room temperature. The error bars on the data are statistical uncertainties from the fits. The open circles are for increasing temperature and the filled circles are for decreasing temperature. This analysis assumes that all of the temperature dependence of the widths comes from phonon creation/annihilation. In the limit of high temperatures, not quite realized for these data, λ is proportional to the derivative of the width with respect to temperature[4]; a more accurate analysis results from a fit to the Debye model.

[1] E.V. Chulkov *et al., Surf. Sci.* **188**, 287, (1987).

[2] L.I. Johansson *et al, Phys. Rev. Lett.* **71**, 2453, (1993).

[3] P.T. Sprunger *et al*, Science **275**, 1764, (1997).

[4] McDougall, Balasubramanian, and Jensen, *Phys. Rev. B* **51**, 13891, (1995).

[5] Suhl, Matthias, and Walker, *Phys. Rev. Lett.* **3**, 552, (1959).

[6] B.T. Gelikman *et al, Sov. Phys. Sol. St.* **9**, 642, (1967).

Characterizing Interfacial Magnetic Roughness

J. Freeland and Y. Idzerda (NRL)

Industrial production of magnetic devices and media (computer hard disks, read/write heads, magnetic memory, etc.) is undergoing an explosion in size similar to that experienced by the semiconductor industry a decade ago. However, many effects that are not well understood plague the behavior of these systems. One of essential importance is the disorder of magnetic moments at the interface (i.e. magnetic roughness). Since these magnetic devices consist of thin layers (~ 10^{-7} cm) of ferromagnetic (FM) and non-magnetic (NM) materials, roughness at the boundary between the FM and NM materials can dramatically alter the magnetic behavior. Recently our group (John Freeland, Varoujan Chakarian, Konrad Bussmann, Yves Idzerda, and Chi-Chang Kao) at the NRL/NSLS Magnetic Circular Dichroism Facility (located at beamline U4B of the NSLS) has been studying the interdependence of magnetic and chemical interfaces.

We find that the magnetic and chemical roughnesses of a NM/FM interface are distinctly different. This means that to obtain a full picture of how roughness influences the magnetic properties, one must obtain information concerning both the magnetic and chemical interfaces. The formalism for the determination of the nature of chemical interfaces and surfaces using specular and off specular (diffuse) scattering is a well established field, but only recently has it become possible to directly probe the magnetic interface. To probe information about a magnetic interface one needs a significant magnetic scattering signal. One way of providing this is through the resonant enhancement of the magnetic and chemical scattering when an incident circular polarized photon is tuned to an absorption edge, known as x-ray resonant magnetic scattering (XRMS). Utilization of a circular polarized photon, like its absorption counterpart Magnetic Circular Dichroism (MCD), generates the magnetic scattering component. By measuring sample rocking curves at the L_3 absorption edge, we can extract information concerning not only the chemical but also the magnetic interface.

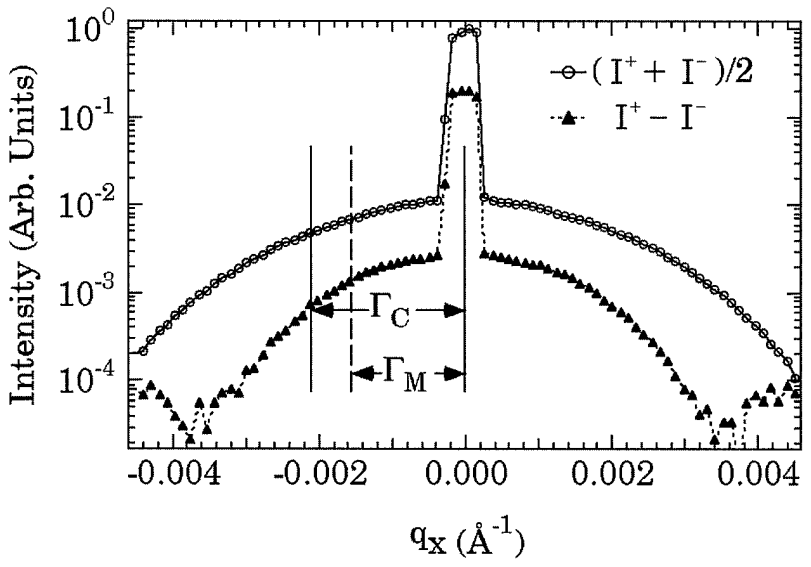

Figure M-12: Sample rocking curve measured at the Co L_3 (778 eV) for chemical and magnetic contributions vs. q_x. This scan was taken at a detector angle 2θ of 90. Notice how the half width if the magnetic diffuse (GM) is smaller than that of the chemical diffuse (GC) indicating a longer correlation length, x, for the magnetic interface.

To explore how an NM/FM interface varies with roughness we utilized a series of CoFe thin films where an increasing chemical roughness was induced through the growth process. **Figure M-12** shows the chemical and the magnetic contributions to a sample rocking (diffuse) scan measured at the Co L_3 edge. From the analysis of these rocking curves we find a distinctly different behavior of both perpendicular (s) and in-plane (x) roughness for the chemical vs. magnetic interfaces. To test the interdependence of the chemical and magnetic roughness we have measured a series of samples with varying chemical roughness, as determined by Atomic Force Microscopy (AFM), where the roughness variation is generated by a thickness variation in Cu growth template prior to magnetic multilayer deposition. As seen in **Figure M-13**, the magnetic roughness in this series of samples typically ~20-30% less than the chemical roughness. The same is seen for the behavior of the chemical vs. magnetic correlation length (bottom panel of **Figure M-13**). This indicates that the magnetic interface is typically much smoother than the chemical interface both perpendicular and in the plane of the film. These results illustrate clearly that one cannot understand the influence of roughness by only exploring the chemical interface. Not all magnetic properties are affected in the same way by interfacial disorder, so only by having the complete picture can we begin to obtain an understanding.

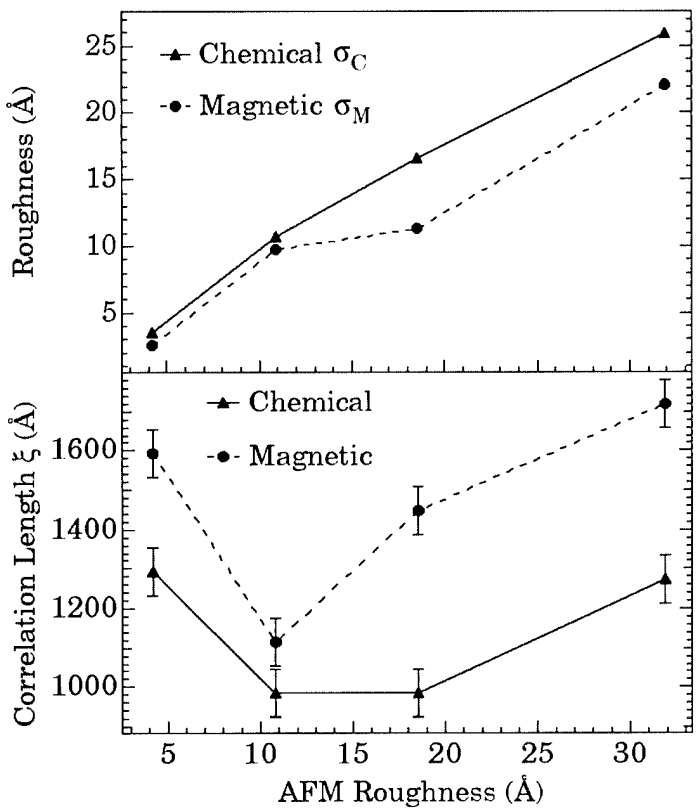

Figure M-13: Perpendicular (s) and in-plane (x) roughness parameters derived from the diffuse scattering data. Top panel: chemical and magnetic rms roughness. Bottom panel: chemical and magnetic correlation lengths.

In addition to our work studying NM/FM interfaces, we are also trying to better our understanding of diffuse XRMS technique. Due the dramatic changes in the scattered intensity near the absorption edge, we undertook a study of the diffuse intensity not only as a function of q_x but also energy of the incident photon. **Figure M-14** shows the results of such a measurement. Notice in particular how by only changing the incident photon by a few eV the shape of the diffuse intensity (both magnetic and chemical) can be altered significantly. While these resonant changes appear very different they contain the same information concerning the interface. Analysis of this data will not only further our understanding of this technique, but will also provide a testing ground for theories of diffuse XRMS.

Our current work has brought our understanding to a point where we stand on the threshold of being able to explore a wide variety of problems related to magnetic heterostructures of extreme interest to many facets of the magnetism community. ■

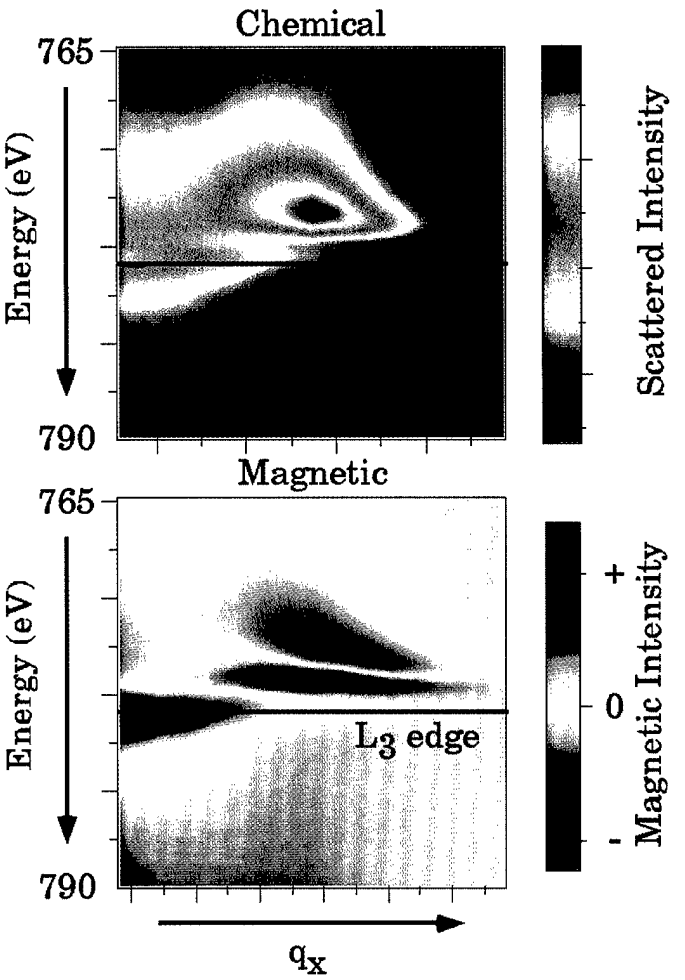

Figure M-14: Diffuse intensity as a function of q_x and incident photon energy. The black line shows the cut along q_x at the Co L_3 edge that yields the data in Figure M-12.

Resonant Inelastic Scattering Studies of 4f rare Earth Compounds

F. Bartolome, J.M. Tonnerre, L. Seve, and D. Raoux (CNRS, France), J. Chaboy and L.M. Garcia (Instituto de Ciencia de Materiales de Aragón, Spain), M. Krisch (ESRF), and C.-C. Kao (NSLS)

A systematic study of the $2p_{3/2}$-$3d_{5/2}$ or $2p_{3/2}$-$4d_{5/2}$ resonant inelastic scattering of 4f rare earth compounds (R = Nd, Sm, Gd, Tb, Dy, Ho, Er, and Tm) was carried out by Bartolome *et al.* [1] An E2 (2p (4f) quadrupolar absorption channel was observed for all the compounds studied. Energy separation between the dominant E1 (2p (5d) dipole absorption energy and the weak E2 absorption energy was also measured systematically. A double-peaked preedge feature was observed for light rare earth ions, and was interpreted as two intermediate states corresponding to the excitations of the two possible spins of the excited photoelectron. Detailed comparison was also made with corresponding x-ray magnetic circular dichroism (XMCD) spectra to show that the origin of the low energy XMCD effect from all rare earth ions is due to E2 absorption channel, and that the sign change in the XMCD signal from light rare earth ions to heavy rare earth ions is due to the doule-peaked pre-edge absorption feature in light rare earth ions. ■

Resonant Inelastic Scattering Study of Nd_2CuO_4

J.P. Hill, C.-C. Kao, W.A.C. Caliebe (BNL), M. Mastubara, A Kotani (ISSP, Tokyo), J.L. Peng and R.L. Greene (University of Maryland, College Park)

Resonant inelastic scattering study of Nd_2CuO_4, the parent compound of the electron doped high temperature superconductor $Nd_{2-x}Ce_xCuO_4$, at the Cu K absorption edge was reported[2]. Resonant enhancement of the charge transfer excitations, similar to the observation in NiO, was observed. An Anderson impurity model which includes both the intra-atomic Coulomb interactions and Cu(3d)-O(2p) interatomic hybridization, was used to interpret the data. The model calculations agree well with both the observed energy loss and the excitation energy dependence of the scattering intensity. And the observed energy loss of 6eV is assigned to excitation from the ground state to the anti-bonding state of the CuO_6 cluster. There is also indication that non-local effects are important in the interpretation of these spectra. ■

[1] F. Bartolome, J.M. Tonnerre, L. Seve, D. Raoux, J. Chaboy, L.M. Garcia, M. Krisch, C.-C. Kao, "Identification of Quadrupolar Excitation Channels at the L III $_{II}$ Edge of Rare Earth Compounds"; *Phys. Rev. Lett.* 79, 3775 (1997).

[2] Hill *et al.*, submitted *Phys. Rev. Lett.*

Bond-length Distortions in Strained Semiconductor Alloys

J.C. Woicik (NIST)

When a macroscopic body is acted upon by small external forces, its deformations are accurately described by the theory of elasticity[1]. Despite the maturity of this branch of theoretical physics, the microscopic distortions ≤ bond length and bond angle ≤ which govern the macroscopic behavior of the body are, in general, not well understood, particularly from an experimental point of view. Because the macroscopic-strain state of semiconductor layers can be accurately determined by bulk-sensitive techniques such as x-ray diffraction, strained-layer semiconductors offer a unique vehicle with which to study these microscopic distortions quantitatively.

In order to address the issue of bond-length strain, we[2] have performed high-resolution extended x-ray absorption fine structure (EXAFS) measurments at the In-K absorption edge (27,940 eV) on a well characterized, buried, 213 Å $Ga_{0.78}In_{0.22}As$ layer grown coherently on GaAs(001). **Figure M-15** shows the EXAFS from the strained layer. These data were recorded at beamline X18B using a Si(111) channel-cut monochromator and a 13 element Ge solid-state detector set to monitor the In-K_α fluorescence yield. Also shown is the EXAFS from bulk InAs, recorded in transmission. Both are plotted with their Fourier-filtered first-shell contributions, which correspond to the In-As bond lengths.

To obtain quantitative information, the data from the layer were fit by the function $k\chi(k)$ using the phase and amplitude functions derived from the bulk InAs standard. The fit determines r'_{InAs} = 2.581 ± 0.004 Å. Because the bond length in bulk InAs is 2.623 Å, the In-As bond length in the strained layer is found contracted 0.042 ± 0.004 Å relative to the In-As bond length in bulk InAs.

In their pioneering study, Mikkelson and Boyce[3] used EXAFS to measure the bond lengths in bulk $Ga_{1-x}In_xAs$ alloys. They found that, instead of following the virtual-crystal approximation (VCA),

$$r_{VCA} = (1 - x) r^0_{GaAs} + (x) r^0_{InAs}, \qquad (1)$$

the In-As and Ga-As bond lengths maintain two chemically distinct values. Although these distinct values do vary linearly with alloy composition, this variation is only about a quarter (~ 0.04 Å) of the natural bond-length difference between bulk InAs (r^0_{InAs} = 2.623 Å) and bulk GaAs (r^0_{GaAs} = 2.448 Å). Using the accurate data of Mikkelson and Boyce[3], the In-As and Ga-As bond lengths in a bulk (cubic) $Ga_{1-x}In_xAs$ alloy with In content 22% are r_{InAs} = 2.596 Å, and r_{GaAs} = 2.455 Å, respectively. The In-As bond length measured in the strained layer, r'_{InAs} = 2.581 ± 0.004 Å, is significantly shorter than this value. In fact, it is even shorter than the In-As bond length measured by Mikkelson and Boyce[3] in the dilute-

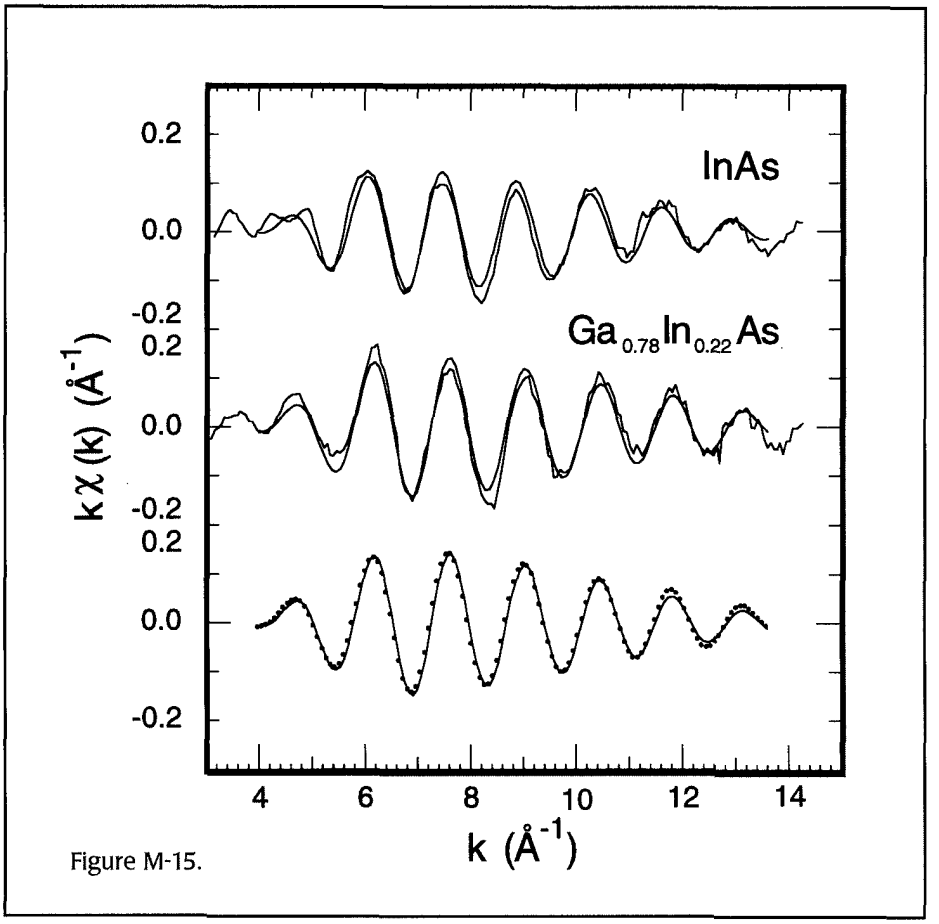

Figure M-15.

alloy limit, r_{InAs} = 2.588 Å for $x \rightarrow 0$; consequently, it must reflect the external compressive strain imposed on the layer by the substrate: $\Delta r = -0.015 \pm 0.004$ Å.

Because the lattice constant of InAs is 7% larger than the lattice constant of GaAs, pseudomorphic growth of a $Ga_{1-x}In_xAs$ alloy on GaAs(001) results in a layer that is compressed bilaterally within the (001) plane of the substrate and Poisson expanded uniaxially along the [001] growth direction. From macroscopic-elastic theory[4], the fractional strain of the film parallel to the interface, $\varepsilon_{//} = (a_{//} - a_f)/a_f$, is related to the fractional strain of the film perpendicular to the interface, $\varepsilon_{\perp} = (a_{\perp} - a_f)/a_f$, through the elastic constants c_{11} and c_{12} of the film, its cubic lattice constant a_f, and the coherency condition $a_{//} = a_{GaAs}$:

$$\varepsilon_{\perp} = -2\,(c_{12}/c_{11})\;\varepsilon_{//}. \qquad (2)$$

Because the layer is tetragonally distorted, the average virtual-crystal bond length is no longer equal to $\tilde{A}3/4 a_f$; however, it may be computed from

$$r' = 1/4\,(\,2\,a_{//}^2 + a_{\perp}^2\,)^{1/2}. \qquad (3)$$

Using $a_{//} = a_f + \Delta a_{//}$ and $a_{\perp} = a_f + \Delta a_{\perp}$, it is easily shown that to first order in ε

$$r' = \tilde{A}3/4\; a_f\,(\,1 + 1/3\,(\,2\,\varepsilon_{//} + \varepsilon_{\perp}\,)\,). \qquad (4)$$

Because equation 4 describes the distortion of the *average* bond length in the layer, a further assumption about the *relative* distortions is needed before the bond lengths can be calculated individually. If we assume that the In-As and Ga-As bond lengths change by the same amount despite their inequivalent bond lengths, Eq. 4 together with macroscopic-elastic theory (Eq. 1) renders r'_{InAs} = 2.582 Å, and r'_{GaAs} = 2.442 Å. This value is indistinguishable from our experimental result: r'_{InAs} = 2.581 ± 0.004 Å.

In order to test the validity of this conclusion, we[5] have performed a random-cluster calculation of the bond lengths in tetragonally distorted, pseudobinary $Ga_{1-x}In_xAs$

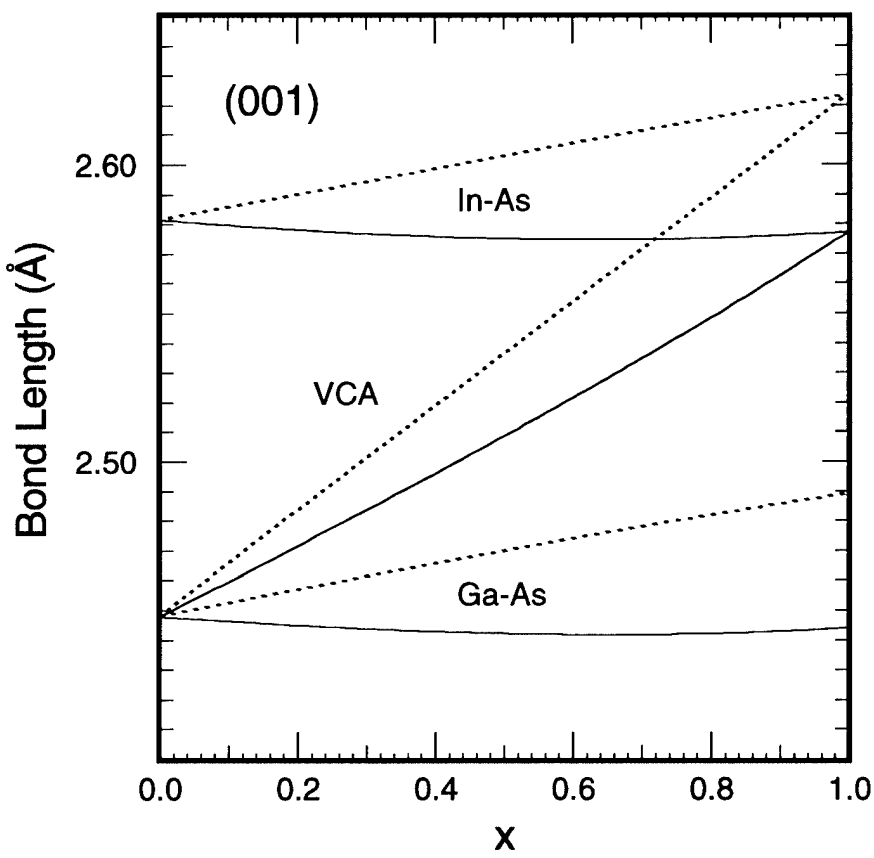

Figure M-16.

alloys on GaAs(001). The calculation was performed by relaxing the atoms within sixteen-bond $Ga_{4-j}In_jAs$ clusters (j = 0,1,2,3,4) embedded in virtual-crystal media. The bond lengths were calculated as a function of medium composition x and then statistically averaged. The Keating valence-force field[6], generalized for the pseudobinary alloy, was used to model the interactions within the clusters:

$$\Delta E = \Sigma_s \, 3/8 \, \alpha_s \left(\frac{r_s^2 - r_{s,o}^2}{r_{s,o}^2} \right)^2 + \Sigma_{s<t} \, \Sigma_t \, 3/8 \, \beta_{s,t} \left(\frac{r_s \cdot r_t - r_{s,o} \cdot r_{t,o}}{r_{s,o} \cdot r_{t,o}} \right)^2. \qquad (5)$$

The α_s's are the two-body radial-force constants, and the $\beta_{s,t}$'s are the three-body angular-force constants. The r_s's are the bond vectors between atoms with equilibrium distance $r_{s,o}$; i.e., the natural In-As and Ga- As bond lengths. **Figure M-16** shows the resulting statistically-averaged In-As and Ga-As bond lengths for cubic clusters (dashed lines) and for clusters that have been tetragonally distorted in accordance with Eq. 1 (solid lines). The results of the calculation are in excellent agreement with the bulk measurements of Mikkelson and Boyce[3] and the results of the present study, thereby confirming the uniform nature of the bond- length distortion. ■

[1] L.D. Landau and E.M. Lifshitz, Theory of Elasticity (Pergamon Press, Oxford, 1970).

[2] J.C. Woicik, J.G. Pellegrino, B. Steiner, K.E. Miyano, S.G. Bompadre, L.B.Sorensen, T.-L. Lee, and S. Khalid, *Phys. Rev. Lett.* **79**, 5026 (1997).

[3] J.C. Mikkelson, Jr. and J.B. Boyce, *Phys. Rev. Lett.* **49**, 1412 (1982).

[4] J. Hornstra and W.J. Bartels, *J. Cryst. Growth* **44**, 513 (1978).

[5] J.C. Woicik, *Phys. Rev. B* 57, 1 (1998).

[6] P.N. Keating, *Phys. Rev.* **145**, 637 (1966).

The N $\rightarrow \Delta$ Transition from Simultaneous Measurements of $p(\vec{\gamma}, \pi)$ and $p(\vec{\gamma}, \gamma)$

The LEGS Collaboration - Beamline X5

The Laser Electron Gamma Source facility (LEGS) provides intense, polarized, monochromatic γ-ray beams by Compton backscattering laser light from relativistic electrons circulating in the X-Ray Ring of the National Synchrotron Light Source at Brookhaven National Laboratory. Such a beam has a high degree of polarization (typically ~90%) with very low background and the energies of the photons are well determined by measuring the loss of energy of the struck electrons($\pm$1%). Photon energies up to 333 MeV can be obtained with the present laser shining on 2.58 GeV electrons. With a new frequency-quadrupled laser that is now being installed and 2.8 GeV stored electrons, photon energies up to 470 MeV will be obtained.

LEGS has its high degree of polarization because the interaction of the laser photons with relativistic electrons preserves the polarization of the photons. By orienting the linear or circular polarization of the laser to give the desired polarization for the γ-rays, measurements can isolate specific contributions to nuclear reaction amplitudes. If the linear polarization (direction of the electric field vector) is in the plane of the reaction, the cross section is sensitive to electric multipole moments. This cross section is denoted as $\sigma_{\parallel}$. If the linear polarization is perpendicular to the reaction plane, the cross section is sensitive to magnetic multipole moments. This cross section is symbolized by $\sigma_{\perp}$. The data is usually presented in terms of $\sigma_{\parallel}/\sigma_{\perp}$ or $\sigma_{\parallel} - \sigma_{\perp}$, or as the asymmetry $\Sigma = (\sigma_{\parallel} - \sigma_{\perp})/(\sigma_{\parallel} + \sigma_{\perp})$. Comparing these cross sections allows for the separation of effects due to static charge distributions from those due to spin and current distributions. Thus, this polarization degree of freedom is extremely important in the understanding of nucleon and nuclear structure.

Since 1990, experiments have concentrated on single polarization observables (polarized beams on unpolarized targets) in nuclear reactions involving the Δ resonance. The Δ resonance is the first excited state of the nucleon with an energy of 294 MeV above the mass of the proton and a width of 120 MeV. It decays with a 99.4% branch to pion-nucleon (πN) final states and a 0.6% branch to γN. By studying photon induced nuclear reactions in the energy region of this excitation, it is possible to measure fundamental quantities such as the deformation of the Δ, to test models describing the internal structure of the nucleon and the Δ and the transition between them, and to study the effects of Δ's produced inside of nuclei. Highlights of this year's results are given below. An updated status of LEGS, including recent publications, is available on the World Wide Web at http://WWW.LEGS.BNL.GOV/~LEGS/ .

The properties of the transition from the nucleon to its first excited state, the $\Delta(1232)$ resonance, serve as a bench mark for models of nucleon structure. An important ingredient in most quark models is a tensor interaction that mixes quark spins with their relative motion. This results in D-wave components which break spherical symmetry, leading to a static deformation for the Δ, and to a small electric quadrupole transition strength, E2, that competes with the dominant magnetic dipole, M1, quark spin-flip transition in N$\rightarrow\Delta$ photo-excitation. This resonance transition is described by two helicity amplitudes, $A_{3/2}$ and $A_{1/2}$, which depend on the E2/M1 mixing ratio (EMR). In simple spherical models of the nucleon their ratio is simply $\sqrt{3}$, while the presence of a D-wave component results in the correction $A_{3/2}/A_{1/2} \cong \sqrt{3}\,(1 - 4\,\mathrm{EMR})$.

The first precision measurements of this ratio were made at the Laser Electron Gamma Source (LEGS)[1], and a fit of these data to the model parameters of Davidson, Mukhopadhyay and Wittman (DMW)[2] gave an EMR of -2.7 %[3]. This EMR was significantly larger than the conventional Particle Data Group (PDG) value of -1.5%[4], and implies a ~10% correction to $A_{3/2}/A_{1/2}$.

At a given energy, a minimum of 7 (and up to 9) independent observables are necessary to specify the photo-pion amplitude[5]. Such complete information is not available and previous analyses have relied almost exclusively on only four, the cross section and the three single polarization asymmetries, Σ (linearly polarized beam), T (target) and P (recoil nucleon). The π^0 and π^+ channels are usually measured separately, introducing the

complication of independent systematic errors. In our current work, $p(\vec{\gamma},\pi^o)$, $p(\vec{\gamma},\pi^+)$ and $p(\vec{\gamma},\gamma)$ cross sections and beam asymmetries have all been measured in a single experiment and a dispersion calculation of Compton scattering has been used to provide two new constraints on the photo-pion multipoles.

Both Compton scattering and π^o-production have a proton and at least one photon in their final states. We have made the first complete separation of these two processes. The two reactions were distinguished by comparing their γ-ray and proton-recoil energies. High energy γ-rays were detected in a large NaI(Tl) crystal, while recoil protons were tracked through wire chambers and stopped in an array of plastic scintillators. By measuring more kinematic parameters than are required to specify the reaction, all detector efficiencies are determined directly from the data itself.

Near the Δ peak ($\approx$ 320 MeV photon energy), the spin-averaged π^o, π^+, and Compton cross sections found here are consistently higher than earlier measurements from Bonn[6-8], while for energies lower than ~270 MeV substantial agreement is obtained. We present here results at 323 MeV and 265 MeV as examples. Angular distributions for $p(\vec{\gamma},\pi^o)$, $p(\vec{\gamma},\pi^+)$ and $p(\vec{\gamma},\gamma)$ are shown with their measurement uncertainties as solid circles in the figure. All cross sections are locked together with a common systematic scale uncertainty, due to possible flux and target thickness variations, of 2%.

In the center panel of **Figure N-1**, π^+ cross sections from Tokyo[9] are shown as cross-hatched squares. These are in good agreement with the present work. In the right panel, two recent Compton measurements from Mainz at 90° and 75° are shown as open circles[11,12]. These data sets are in quite good agreement with the present work over our full energy range. As discussed in Ref. [14], earlier 90° Compton cross sections from Bonn[15] are about 28% too low in the vicinity of the Δ peak. Whatever the error in that early experiment, it is likely to be common to all angles measured with the same detector. The Bonn results are shown here, rescaled by 1.28 (open squares).

To obtain a consistent description of these results we have performed an energy-dependent analysis, expanding the π-production amplitude into electric and magnetic partial waves. Once the (γ, π) multipoles are specified, the imaginary parts of the six Compton helicity amplitudes are completely determined by unitarity, and dispersion integrals can be used to calculate their real parts.

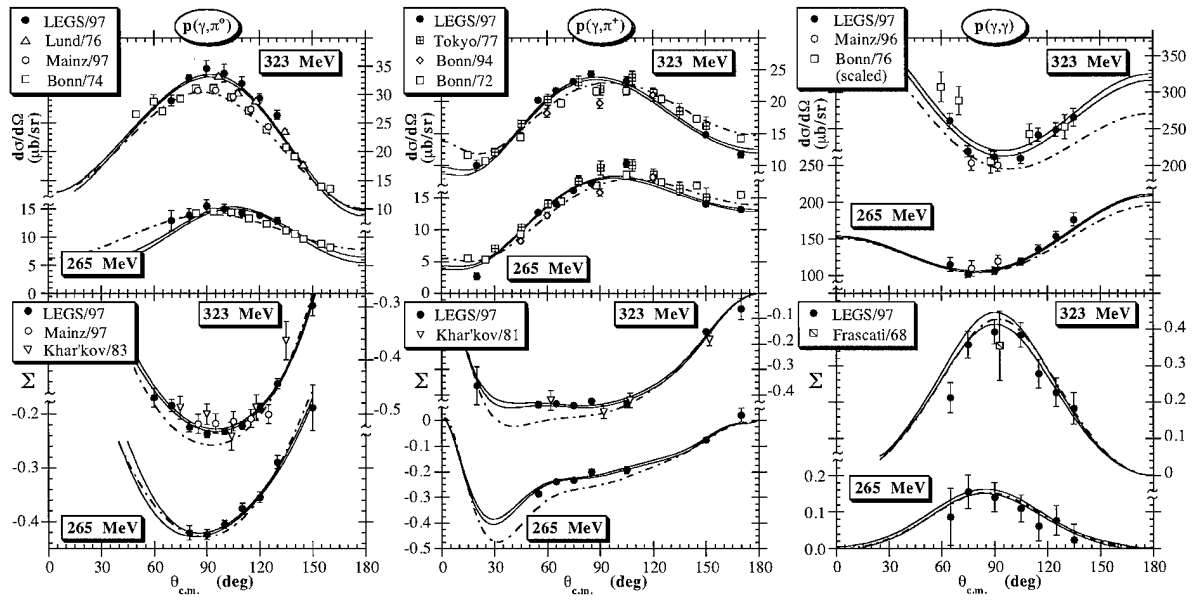

Figure N-1: Cross sections (top row), and polarization asymmetries $\Sigma=(\sigma_{\parallel}-\sigma_{\perp})/(\sigma_{\parallel}+\sigma_{\perp})$ (bottom row), from the present work (•) for $p(\vec{\gamma},\pi^o)$ – left panel, $p(\vec{\gamma},\pi^+)$ – center, and $p(\vec{\gamma},\gamma)$– right panel, together with published data – (γ,π^o): [16-18], (γ,π^+): [9,10,19,20], (γ,γ): [15 (see text),9-11]. Results are shown for 265 MeV (323 MeV) beam energy with scales on the left (right) of each plot. Predictions from our multipole fit are shown with uncertainties as bands bounded by solid curves. Predictions from the VPI[SP97k] multipoles [21] are given by dash-dot curves. The dotted curves in the right panel show the Compton predictions using the prescription in refs. [12, 22].

Quantity	This Experiment	Particle Data Group[4]
$A_{1/2}$	$-137.4\ (\times 10^{-3}\ GeV^{-1/2}) \pm 1.8$ (*stat+sys*) ± 1.8 (*model*)	-141 ± 5
$A_{3/2}$	$-268.9\ (\times 10^{-3}\ GeV^{-1/2}) \pm 2.8$ (*stat+sys*) ± 4.9 (*model*)	-257 ± 8
EMR	-3.0 (%) ± 0.3 (*stat+sys*) ± 0.2 (*model*)	-1.5 (%)± 0.4

Figure N-2: Table.

Fitting the parameters of the (γ,π) multipoles by minimizing χ^2 for both predicted (γ,π) and (γ,γ) observables allows the extraction of the EMR. In this fit we have used $p(\vec{\gamma}, \pi^0)$, $p(\vec{\gamma}, \pi^+)$ and $p(\vec{\gamma}, \gamma)$ cross sections only from the present experiment, since these are locked together with a small common scale uncertainty, and augmented our beam asymmetry data with other published polarization ratios in which systematic errors tend to cancel.

The predictions from the (γ,π) multipoles determined in this fit are shown in the figure as pairs of solid curves to indicate the corresponding uncertainty bands. The reduced χ^2 for this analysis is

$\chi^2_{df} = 997/(644-34) = 1.63$.

The EMR for $N \rightarrow \Delta$ is -0.0296 ± 0.0021. The fitting errors reflects all statistical and systematic uncertainties. Combining *model* uncertainties in quadrature leads to our final results given in **Figure N-2** along with the values accepted by the Particle Data group for comparison.

Other information on the structure of the nucleon can be extracted from these data and this work is in progress. In particular, when placed in a strong static electric or magnetic field, a proton or neutron will experience an internal rearrangement of the quarks and gluons. An electric field will induce a dynamic electric dipole moment by separating the positive and negative quarks and a magnetic field will produce a dynamic magnetic dipole moment by separating the currents and/or spins of the quarks. The measure of the ease with which these internal rearrangements can be done is called the electric, magnetic, or spin polarizability.

Determination of the polarizabilities of the neutron require a neutron target. Since the free neutron is not a stable particle, deuterium the lightest isotope of hydrogen is commonly used to provide a quasi-free neutron. Here the single proton and neutron are bound by only 2.2 MeV, minimizing the corrections necessary to go from the bound neutron to the free neutron.

Since the initial photon and neutron have no charge, a detector is required that has a good efficiency for neutral particle in the final state (π^0 which decays to 2γ's, γ-rays, and neutrons) as will as charged particles. to provide the neutral particle efficiency and the angular coverage for charged and uncharged particles, a new detector has been commissioned. **SASY**, the Spin-**ASY**mmetry detector array provides complete determination of angle, energy, and particle identity for all reactions induced by photons on hydrogen and deuterium over the entire energy range planned for LEGS. SASY will consist of several "layers" designed to fulfill these requirements.

The construction of SASY is being done in two phases. For the first set of experiments to measure the electric and magnetic polarizability of the neutron, only the major calorimetry subsystems will be instrumented: the XTAL BOX (an array of 432 NaI(Tl) crystals) covering all azimuthal angles for scattering angles between about 40° and 130°, the forward neutron wall of plastic scintillator consisting of three layers of 10 cm × 10 cm × 1.6 m bars, and the wall of 176 Pb-glass Cerenkov counters. The second phase will add the capability to track charged particles through a large volume magnetic field thereby permitting the identification of the sign of the charge. This is crucial for the the next phase of LEGS in which double-polarization data will be obtained from the polarized hydrogen and deuterium using the a novel, polarized HD target. This is now in the development stage and initial experiments (without tracking) will begin in the summer of 1998.

Measurement of Compton scattering from the neutron occupied most of calendar 1997. These data are presently being analyzed. ■

[1] LEGS Collaboration, G. Blanpied *et al.*, *Phys. Rev. Lett.* **69**, 1880 (1992).
[2] R. Davidson, N. Mukhopadhyay, R. Wittman, *Phys. Rev.* **D43**, 71 (1991).
[3] M. Khandaker and A.M. Sandorfi, *Phys. Rev.* **D51**, 3966 (1995).
[4] Particle Data Group, L. Montanet *et al.*, *Phys. Rev.* **D50**, 1712 (1994).
[5] I. S. Barker, A. Donnachie and J.K. Storrow, *Nucl. Phys.* **B95**, 347 (1975).
[6] H. Genzel *et al.*, *Z. Physik* **A268**, 43 (1974).
[7] G. Fischer et al., *Z. Physik* **253**, 38 (1972).
[8] K. Büchler, *et al.*, *Nucl. Phys.* **A570**, 580 (1994).
[9] T. Fujii *et al.*, *Nucl. Phys.* **B120**, 395 (1977).
[10] V.A. Get'man *et al.*, *Nucl. Phys.* **B188**, 397 (1981).
[11] C. Molinari *et al.*, *Phys. Lett.* **B371**, 181 (1996);
[12] J. Peise *et al.*, *Phys. Lett.* **B384**, 37 (1996); J. Ahrens, Priv. Comm.
[13] G. Barbiellini *et al.*, *Phys. Rev.* **174**, 1665 (1968).
[14] LEGS Collaboration, G. Blanpied *et al.*, *Phys. Rev. Lett.* **76**, 1023 (1996).
[15] H. Genzel *et al.*, *Z. Physik* **A279**, 399 (1976).
[16] R. Beck *et al.*, *Phys. Rev. Lett.* **78**, 606, 1997; H.-P. Krahn, thesis, U. Mainz (1996).
[17] H. Genzel *et al.*, *Z. Physik* **A268**, 43 (1974).
[18] A. Belyaev *et al.*, *Nucl. Phys.* B**213**, 201 (1983).
[19] G. Fischer *et al.*, *Z. Physik* **253**, 38 (1972).
[20] K. Büchler, *et al.*, *Nucl. Phys.* **A570**, 580 (1994).
[21] *SAID* code (1996), telnet VTINTE.PHYS.VT.EDU {physics,quantum};
R. Arndt, I. Strakovsky and R. Workman, *Phys. Rev.* **C53**, 430 (1996).
[22] A. L'vov, V. Petrun'kin and M. Schumacher, *Phys. Rev.* **C55**, 359 (1997).

Beamline X3B1: The previously unknown compound $Rb_6Pb_5Cl_{16}$ (shown at right, with c axis pointing vertically) was synthesized by melting a stoichiomentric mixture of RbCl and $PbCl_2$ at 700°C and annealing for several weeks at 200°C. Although the metrics could be determined from laboratory powder diffraction patterns, the structure could only be solved by using synchrotron radiation. This new type of structure shows a large variety of different coordination polyhedra for the cations: columns of tetragonal prism and antiprism are mixed with caped trigonal prism and a 6+2+2 polyhedron of a new type. (See also Abstract on page B-47). H.P Beck, M. Schramm, R. Haberkorn (U. of Saarland), R.E. Dinnebier (U. of Bayreuth), and P.W. Stephens (SUNY @ Stony Brook).

THREE

MEETINGS & WORKSHOPS

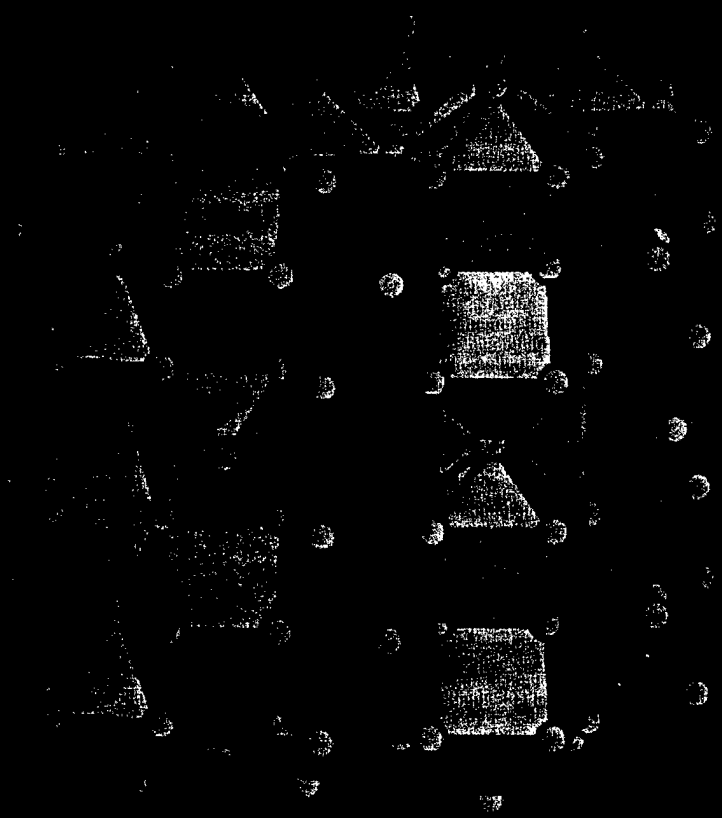

THE 1997 NSLS ANNUAL USERS' MEETING

Joel D. Brock
Cornell University
NSLS Users' Executive Committee Chairman

The users of the National Synchrotron Light Source (NSLS) held their annual Users' Meeting on May 20, 1997, at Brookhaven National Laboratory (BNL). This meeting serves several functions: celebrating the scientific and technical accomplishments of the previous year, obtaining the latest news on the U.S. Department of Energy's support for scientific facilities in general and the NSLS in particular, and providing an opportunity to visit with old friends and colleagues. As in past years, six workshops on scientific and technical topics (descriptions follow this article) were held the day before and the day after the main meeting.

The meeting began with a lively and humorous keynote address titled "Future Schlock" by Robert Park, Professor of Physics at the University of Maryland and author of the WWW news/opinion page "What's New". The main point of Park's address was that one cannot make accurate predictions about the future. He began by pointing out that one year ago, no one was predicting that today we would have budgets before Congress which both balance the budget by the year 2002 and give science annual funding increases. He then continued with several examples of predictions made by various futurists and concluded with the point that no one predicted that scientists would become politically active or how powerful their voice would be.

Robert L. Park (left) of the University of Maryland after his Keynote Speech "Future Schlock" talking with Denis McWhan (center), Associate BNL Director, Basic Energy Science Programs and Lyle Schwartz, Interim BNL Director and President of Associated Universities, Incorporated.

The Interim Director of BNL and President of AUI, Lyle Schwartz, was the next to address the meeting. He began his remarks by addressing recent statements in the press by DOE Assistant Secretary Tara O'Toole (see, for example, *Science News*, Vol. 151, p. 284, May 10, 1997) that the highly publicized deficiencies in Environment, Safety and Health at BNL were the fault of users. Dr. Schwartz strongly defended the users. He then solicited their comments and observations during this time of change at BNL.

The U.S. Department of Energy was represented by the Associate Director of Energy Research for the Office of Basic Energy Sciences, Patricia M. Dehmer. In light of the two previous speakers' remarks, she began her remarks by assuring the audience that during all the upheaval associated with BNL's problems there has been one constant: "the high regard" for the NSLS, its users, and the quality of their science. She then went on to outline the organizational structure of the DOE, pointing out that the Basic Energy Sciences (BES) budget is roughly equal to that of the National Science Foundation, but that BES funds three times the amount of physical science research and most of the major user facilities in the country. She urged the audience to communicate with BES (BES@oer.doe.gov) answering the question, "How has your discipline been affected by synchrotron radiation and how would it be affected by the lack of it?"

Next, Larry Dubois, director of DARPA/DSO, gave an overview of materials research from a DARPA perspective. Emphasizing the potential applications, he cited *in situ* studies of fuel cells, studies of "relaxor" piezo-electric materials, and x-ray patterning of materials as examples of areas where synchrotron x-ray techniques might be of

interest to DARPA.

The last speaker of the morning was Michael Hart, Chairman of the NSLS. His remarks were focused primarily on the BESAC review panel on synchrotron radiation facilities which would be visiting NSLS on June 25 and 26. Part of the review will be presentations by NSLS users. He requested the continued assistance of the user community during this review process.

In dramatic contrast to the morning session, the afternoon was devoted to scientific talks spanning the wavelength spectrum from the far infra-red through the ultra violet into the hard x-ray region. Albert J. Sievers led off, discussing the coherent generation of FIR and describing experiments he has performed using the LINAC at Cornell. In these experiments, he used FIR as a diagnostic probe to measure the profile of the electron bunch. As part of his presentation, he walked the audience through a very clear explanation of how one uses Kramers-Kronig relations to solve the phase problem in time/frequency Fourier transforms.

Robert Bartynski spoke next on his coincidence spectroscopy measurements of TiO_2. The basic idea of the technique is to trigger off of a core level photo-electron and then require the coincidence of a particular Auger electron associated with the death of the core hole. Requiring the coincidence gives the technique both elemental and valence sensitivity and the low background enables one to determine defect densities on the order of 2%. Data illustrating the effects of different surface preparations on the densities of point defects with particular Ti valence states were presented.

From left to right: Susan Barr, APS User Program Administrator; Constance Pittroff, APS Assistant User Program Administrator; Eva Z. Rothman, NSLS User Administrator; and Elizabeth Saucier, ALS User Administrator.

Keith Bowen (left) of the University of Warwick, UK and Bede Scientific Instruments conversing at the User Meeting Poster Session with Michael Hart, Chairman of the NSLS.

Thomas Gog discussed his recent work on Multi-Energy X-ray Holography, presenting reconstructed images of several different systems. Although the technique is still at an early stage of development, the potential to produce atomic resolution real-space images was tantalizing. He discussed several current technical challenges yet to be overcome, including developing a better understanding of the effects of wavelength filtering on the numerical Fourier transform.

The last speaker of the afternoon, Donald Weidner described his work using x-ray diffraction at high pressures and temperatures to study the phase diagram of materials found in the Earth's crust. He related that work to a self-consistent mathematical model which explains an anomaly in the frequency distribution of deep earthquakes.

Two other important features of the Users' Meeting were the scientific poster session, with a reception at the Brookhaven Center, and the equipment exhibit in the Lobby of Berkner Hall. Both were popular with the users, providing an opportunity to get a preview of some of the latest work performed at the NSLS and to see some of the new equipment available from suppliers.

The election of the NSLS UEC occurred during lunch. Paul Stevens, Barbara Illman and John Parise were elected as general members. The SPIG representatives will be elected by e-mail ballot after the meeting. On Wednesday, in executive session, the UEC chose John Parise to be its Vice-Chair (Chair-Elect). ■

The Impact of New Detector Technology on Synchrotron Macromolecular Crystallography

Malcolm Capel
(Brookhaven National Laboratory, Biology)

The goals of the workshop, held on May 19, 1997, was to summarize recent developments in imaging x-ray detector technology (predominantly CCD's) and to discuss issues related to their capabilities and performance in regard to macromolecular crystallography as practiced at x-ray synchrotrons. Leaders in the fields of CCD detector, crystallography software and x-ray beamline development gave presentations to an audience of approximately 45 registered attendees.

Ed Westbrook, director of the Structural Biology Center (SBC) at Argonne National Laboratory discussed the status of the Advanced Photon Source Sector 19 SBC beamline and its 3x3 CCD array detector, developed jointly by the SBC and Steve Naday of ANL's Electronics and Communications Technology division. This detector (known as the APS-1) is constructed from 9 CCD-optical fiber taper cells, and has an active area 20x20 cm in size, with 3000 x 3000 pixels, reads out in 3.3 seconds and is capable of resolving approximately 280 diffraction orders from protein crystals. The SBC beamline presently is capable of producing a beam with a flux of 3×10^{15} monochromatic photons/second/mm^2 (0.01 % bandpass). Complete, fine phi-sliced rotation data sets can be acquired from lysozyme in about 20 minutes with merging statistics around the 2-3% level.

Bob Sweet (NSLS X12C, BNL Biology) provided a synopsis of the design and working principals of the mosaic CCD crystallography detector design and a historical summary of various CCD detectors trialed at the NSLS X12C crystallography beamline. Marty Stanton (Brandeis University) described his group's CCD detector development with special emphasis on a programmable CCD controller/sequencer designed by his group for dynamical diffraction studies with muscle. Eric Eikenberry (Princeton University) discussed design and testing of a prototype solid-state pixel-array detector, the likely successor technology to CCD's in crystallography and synchrotron-based diffraction studies.

The afternoon session of the workshop was dedicated to discussion of software topics. The high speed, resolution and sensitivity of CCD detectors have forced the redesign and optimization of crystallography data collection and reduction software packages, originally written to handle crystallographic data from storage phosphor image plate systems. Jim Pflugrath of Molecular Structures Corporation demonstrated his new display, indexing and integration suite called d*trek, developed under DOE contract with the SBC. Sbeyzek Otwinowski (South Western Medical Center) reviewed the progress of the DENZO data reduction and control package with emphasis on data quality and experimental design. Malcolm Capel (NSLS X12B, BNL Biology) described the Linux/Beowulf clustering system used to produce high-performance (Gflops) low-cost (< $100k) multiprocessor systems for acquisition, reduction and storage of CCD crystallographic diffraction data. ■

Biological and Chemical Applications of EXAFS Spectroscopy

Dr. Mark R. Chance
(Albert Einstein College of Medicine)

A workshop entitled "Biological and Chemical Applications of EXAFS Spectroscopy" was held at the National Synchrotron Light Source on May 21, 1997. EXAFS is one of the most widely used techniques at the NSLS and the presentations highlighted recent research from four of the major groups performing EXAFS at the facility. The first presentation however, was from Dr. Frank de Groot of the University of Gronigen entitled "Multiplet Effects in Core Level Spectroscopies". The interesting initial question answered by Dr. de Groot concerned the necessity of multiplet analysis. It is well known that single scattering can work well in describing spectral data. In the case of L-edge spectroscopy, the 2p-3d interactions are very strong and the single particle approximation breaks down. Dr. de Groot provided a description and an analysis of results using atomic multiplet theory, where electron-electron interactions determine the multiplets and spin-orbit couplings determine the fine structure. Introduction of crystal field splittings provided satisfactory molecular simulations providing values of ligand field strength, high or low spin and valency. Further information on the programs is available at http://vsf1.phys.rug.nl/~degroot.

Professor Dale Sayers from North Carolina State University, gave a talk entitled "XAS Determination of Chemical Speciation of Heavy Metals". Dr. Sayers' presentation highlighted the magnitude of the environmental problem presented by heavy metals and the keen ability of XAS to probe the structure of these metals in soil samples. The first example determined the efficacy of hydroxyapatite treatment in the remediation of lead in soil samples, which can successfully sequester the lead as an insoluble form. A second analysis of lead waste from batteries determined the degree of conversion of lead oxide to lead sulfide forms (the latter being relatively insoluble). XAS was very powerful in determining the metal environment. Dr. Sayers also briefly spoke about the International XAS Society, more information can be found at http://ixs.iit.edu

Professor James Penner-Hahn of the University of Michigan gave a talk entitled "Structural Characterization of Organometallic Reagents", providing interesting results refuting the presumed existence of higher order cuprates and providing a better understanding of phenyl copper complexes with very precise titration data.

Professor Mark Chance from the Albert Einstein College of Medicine illustrated a number of applications of FEFF to analyzing structure in biological systems. A program called AUTOFIT 1.0 was outlined that can automatically iterate crystal structure data, simulate the resultant FEFF spectra, and compare the simulations to experimental data in order to map different possible solutions in an evenhanded fashion. Further information on the programs can be found at http://beam.aecom.yu.edu/phys&bio/csb1.htm

Ms. Lijun Shu from the University of Minnesota finished the talks with a discussion of "Diamond Core" structures (Fe_2O_2) in enzymes like methane monoxygenase and ribonucleotide reductase. The Fe-Fe distances for some of the high valent intermediates were as short as 2.4 Å.

Lastly, Dr. Lars Furenlid of the NSLS provided a demonstration of the 100 element solid state detector that was set up at beamline X9B on the NSLS floor. As the workshop attendees clustered about the beamline we were immensely impressed with the miniaturization of the detector elements (30-40 times smaller than conventional solid state detector elements). ■

X-ray Computed Microtomography : Applications & Techniques

Betsy Dowd
(Brookhaven National Laboratory, NSLS)

The availability of synchrotron X-ray sources to the scientific community sparked the first explosion in the development of the field of X-ray Computed Microtomography (XCMT). More recently, technological advances in two-dimensional detector arrays, combined with the recent boom in available parallel architecture computing technology, have lifted the XCMT field to another level. Talks at this workshop highlighted the impact of these technological advances on a variety of applications of XCMT, from the medical to the metallurgical fields.

A detailed synopsis of the rapid progression of Exxon's X-ray CMT facility at the NSLS over the past 15 years, in parallel with improved detector, processor, and 3-D visualization technology, was given by John Dunsmuir (Exxon Corp.). John and his team now routinely use XCMT to characterize reservoir sandstone pore geometries.

Per Spanne (ESRF) discussed XCMT applications and advances at the ESRF. By parallelizing 16 computers, the group at ESRF has significantly reduced the reconstruction time for tomographic volumes. Per and his colleagues at the ESRF have also used the high coherence of the ESRF X-ray source to make phase contrast CMT measurements.

Chris Jacobsen (SUNY, Stony Brook) presented schemes for soft X-ray submicron resolution tomography. Zhong Zhong (NSLS) and Avraham Dilmanian (BNL, Medical Dept.) proposed a plan for Diffraction Enhanced Computed Tomography for biological tissue characterization.

The present status and recent applications of the XCMT facility developed by the NSLS were reported by Betsy Dowd (NSLS). The versatility of this developing user facility was emphasized by the variety of tomographic volumes generated. Among these are reservoir sandstones (Mobil Corp.), basalts (Sahagian, Univ. of N.H., Song, National Taiwan Univ.), porous metals (Schulte, Northrop-Grumman Corp.), and plasma-spray coatings (Herman, SUNY, Stony Brook). Barbara Illman (USDA/ FS Forest Products Lab., U. of Wisconsin) has obtained CMT volumes of beetles and wood at this facility and spoke about her application of CMT to the study of fungal deterioration of wood. Sheng-Rong Song (Geology Dept., National Taiwan U.) spoke about his investigations into volcanic rock, using CMT data he collected at the NSLS facility.

Brent Lindquist (SUNY, Stony Brook) gave an entertaining and informative tutorial on his 3-D Medial Axis (3DMA) program he developed to characterize the pore geometries from tomographic data of rocks. For the final talk by Ballard Andrews (BNL-Computing & Communications Division) , our group moved to the 3D visualization theater at BNL, where each participant donned a pair of polarized glasses, and relaxed to enjoy a stereo demonstration of some tomographic data collected at the NSLS. In addition to demonstrating this impressive facility, Ballard enlightened us with his knowledge of 3-D visualization and rendering techniques, and applications of IBM Data Explorer to viewing and analyzing tomographic data. ■

Inelastic and Resonant Inelastic X-Ray Scattering

Chi-Chang Kao
(Brookhaven National Laboratory, NSLS)

Inelastic x-ray scattering has long been recognized as a potentially important experimental probe of electron and lattice dynamics in condensed matter systems. Recently, several dedicated high resolution (total energy resolution from 0.1 eV to 1.0 eV) and ultra-high resolution (total energy resolution from 1 meV to 10 meV) inelastic scattering beamlines have become operational around the world. The latest experimental results from these beamlines as well as various theoretical aspects of inelastic x-ray scattering were reported at the workshop.

Denis McWhan (BNL) opened the workshop by giving a brief review of the major steps in the development of inelastic x-ray scattering. The relationship between inelastic x-ray scattering and inelastic scattering of visible light was discussed by Miles Klein (University of Illinois-Urbana/Champaign). Although he found little analogy between the two techniques, he did suggest several areas in which inelastic x-ray scattering might provide new information. He also reported recent visible light scattering studies on high temperature superconductors and related compounds.

Inelastic x-ray scattering studies of many-body correlation effects in simple metals were reported by Ben Larson (Oak Ridge National Lab.) and John Hill (BNL-Physics). Ben Larson found that the measured local-field factors of Al are significantly larger those that obtained from a first principle theoretical calculation. To resolve a long standing controversy over the origin of the double-peak feature in the inelastic scattering spectra of many materials, John Hill reported an inelastic x-ray scattering study of solid and liquid Li and Na, in which spectral features from band structure effects are separated from those due tomany-body effects.

There were also several talks on resonant Raman scattering, or resonant inelastic scattering, studies on highly correlated systems. John Hill along with Eric Isaacs (Bell Laboratories) reported recent Cu K-edge resonant inelastic study of Nd_2CuO_4 and $Sr_2CuO_2Cl_2$, respectively. Trever Tyson (New Jersey Institute of Technology) presented high resolution Mn K-beta emission spectra of a series of doped $LaMnO_3$ compounds. On the theory side, Frank de Groot (University of Groningen, The Netherlands) presented an atomic-multiplet based model calculation for resonant Raman scattering. Very good agreement between theory and experimental results, ranging from soft-x-ray to hard-x-ray, were shown.

In addition to the works done at the NSLS, Francesco Sette of the European Synchrotron Radiation Facility (ESRF) reported an ultra-high resolution inelastic x-ray scattering study of the high frequency collective dynamics of disordered systems, a region in the energy-momentum phase space that cannot be accessed by inelastic neutron scattering. The status of the inelastic scattering beamline at the Advanced Photon Source (APS), and first results were reported by Albert Macrander.■

Materials Characterization with Hard and Soft X-ray Reflectivity

Michael Toney
(IBM Almaden Research Center)
Yves Idzerda (Naval Research Lab)

Specular and diffuse X-ray reflectivity are popular methods for characterizing a variety of materials, including organic thin films, magnetic films and surfaces, and semiconducting materials. This motivated a one day workshop held May 19, 1997 in conjunction with the NSLS Users' meeting. The purposes were to gather together novices and experts to discuss these methods and their applications, to educate newcomers on the power of these methods, and for the NSLS reflectivity community to discuss building an endstation dedicated to reflectivity.

Professor Carol Thompson (ANL and Northern Illinois University) kicked off the workshop with an introduction to X-ray reflectivity, including a description of questions that could (and could not) be addressed and of important experimental requirements, such as spectrometer and sample alignment. She also emphasized that hard x-rays can be used under ambient conditions (e.g., in an electrolyte). Examples were given of layering of smectic liquid crystals on glass and of *in situ* swelling of PMDA-ODA in NaOH.

Paul Mansky (U. of Massachusetts) compared and contrasted x-ray reflectivity with neutron reflectivity as applied to organic thin films. The advantages of isotopic substitution (D for H) were demonstrated, and the complementarity of using both x-ray and neutron reflectivity was illustrated. Data for polymer brushes (polymers bound to a surface at one end) showed how the polymers swelled with increasing temperature, consistent with theory. Paul also described studies of islands in di-block copolymer systems.

This was followed by Eric Chason's (Sandia National Lab.) talk on *in situ* reflectivity studies of the evolution of thin film and surface morphology. Eric described an energy dispersive technique for time resolved measurements (ca. 250sec data collection time). He illustrated several examples, including compound formation during Al deposition on Cr/quartz, the formation of pits in porous silicon, the CVD growth of Fe on Si(100), and the surface roughening (smoothing) of quartz during ion bombardment with Xe (He). There was discussion of the possible advantages of synchrotron radiation for such studies and of the need for detectors with higher throughput.

After a break for an enjoyable lunch and a change in energy range, Jack Rife (Naval Research Lab.) talked about UV and soft x-ray reflectance characterization of semiconductor materials. He explained the technique and described the X24C reflectance setup. He then reviewed the application of this method to GaN and compared the experiments to theory with favorable agreement. This was followed by studies of radiation damage in SiO_2 through bombardment with 5eV neutral oxygen atoms (motivated by etching of surfaces of the space shuttle in low earth orbit).

Gavin Watson returned to the hard x-ray regime with a discussion of x-ray resonant magnetic reflectivity. After describing the technique and emphasizing that it is a resonant method, Gavin described the near-surface, antiferromagnetic ordering in $UO_2(001)$ and how this differs from bulk ordering. Gavin also showed how this method could be used to understand the magnetism on Pt in Co_3Pt, and in a brief excursion to lower energies, showed how the magnetic roughness in Co/Cu multilayers was less than the atomic roughness.

The emphasis on third row transition metals was continued by John Freeland (NSLS, U4B) whose talk was entitled "Materials Characterization with Resonant Soft X-ray Scattering". John explained how this method was related to x-ray circular dichorism and resonant x-ray scattering and how it could be used to obtain magnetic and atomic thickness and roughness. He showed the huge enhancements in cross sections that could be obtained for third row transition elements and described studies of switching in NiFe/Co sandwiches. This was followed by determinations of magnetic and chemical roughness in single Co films and CoFe multilayers.

Near the end of the workshop, there was discussion of a possible endstation dedicated to reflectivity. In this arrangement, the NSLS would provide x-rays up to the hutch and the interested users would fund construction of the endstation. Jerry Hastings (NSLS) explained what had been done by the polymer SAXS community on X27C, and several speakers (Thompson, Watson, Evans-Lutterodt) described what they would like for such a reflectivity endstation. This would cost the interested users approximately $200,000 or more, and with enough support, could be constructed. After much discussion, it seems there is insufficient funding in the user community present at the workshop (either academic or industrial) for the construction of such a beamline/endstation, although some NSLS staff members are actively interested in collaborating on reflectivity experiments and instrumentation. ■

Beamline U9B: The Fluorescence Omnilyzer is a single-photon detector developed to record all of the important parameters of a fluorescence emission spectrum simultaneously. The figure shows the time-wavelength histogram for pyrene in ethanol. The horizontal axis is time after excitation, in nanoseconds, and the vertical axis is the wavelength of the fluorescent light. The intensity (number of photons) recorded for each time-wavelength cell is represented in pseudo-color as a rainbow transformation. Determining all of the important parameters that characterize a fluorescence emission spectrum simultaneously with the Omnilyzer is particularly important in studies of fragile biological and chemical samples that can be damaged by prolonged exposure to the fluorescence excitation beam. (See also Abstract on page A-49.)

In 1997, the Omnilyzer was selected by R&D Magazine as one of the 100 most significant technological developments of the year. A more detailed description of the Omnilyzer is available at http://www.biology.bnl.gov/biodocs/nsls/u9b/omnilyzer.htmlx

Lisa A. Kelly (NSLS/BNL-Biology. Present Address: U. of Maryland, Baltimore County), John G. Trunk, and John C. Sutherland (BNL - Biology).

FOUR

OPERATIONS

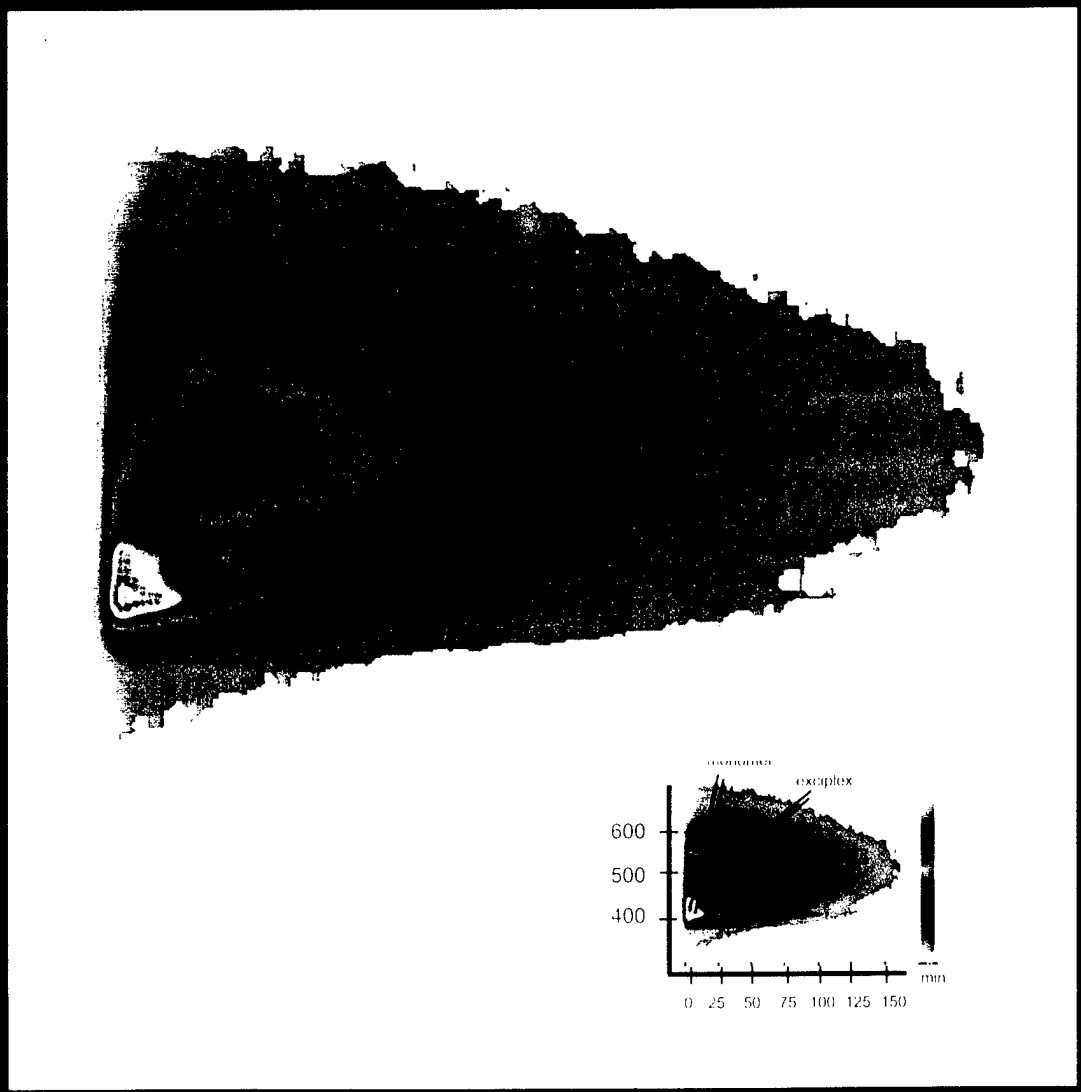

VUV MACHINE

Stephen Kramer
VUV Ring Manager

Figure 1 shows the breakdown of the VUV Ring operating statistics for the Fiscal Year 1997. The monthly breakdown of most significant operational performance statistics are presented in **Figures 2 through 6**. The operational statistics continue to show improvement above the record year of FY 1996. The fraction of the time during the year resulting in unscheduled downtime was only 1.5%. The probability that beam was not available when it was scheduled for operations was only 2.38%. However the total beam time actually delivered to the users was 6 hours greater than was scheduled, or 100.1% of scheduled. This resulted from the early return from maintenance and a reduction in accelerator study hours actually used. The accelerator performance continued to improve with higher injection rates and longer beam lifetimes. Injections are now routinely done in less than 3 minutes with the average approaching 2 minutes. The beam lifetime had been lower due to higher vacuum resulting from the two openings of the ring during the year and due to vacuum leaks. However, from August through the end of the year the lifetime has exceeded the pre-shutdown values by about 8%. This was achieved despite the new gas load introduced by the new U12IR mirror being inserted into the ring vacuum chamber and a leak in the front-ends of two beam ports. To help reduce the impact of these new gas loads, a new beam scrubbing shift (vacuum chamber conditioning shift) was introduced during the owl shift (0:00 to 08:00) of the two day study period that occurs once a month. This shift helps desorb the gas that was introduced by these new sources more rapidly than would occur during normal operations and helps reduce the base pressure of the ring.

The major improvement to the VUV Ring during this fiscal year occurred during the winter shutdown when another large aperture beam port was installed for the U2IR beamline. The ceramic gap just after this beam chamber had started to leak during the fall 1996 and was also replaced during the winter shutdown of the ring. Despite the increased work load from the ceramic gap replacement, the effective planning of the Mechanical Group allowed the ring to be brought on four days early and scrubbing of the vacuum with beam to take place during the three day holiday weekend. This allowed operations to begin on schedule but with longer beam lifetime resulting from the reduced vacuum pressure. During the spring, a front-end valve started leaking in the half of the ring opened during the winter shutdown. This valve was replaced during the May shutdown requiring the same half of the vacuum chamber to be vented again. Recovery to pre-shutdown values of the beam lifetime required about the same integrated current as the winter shutdown, but since this vacuum work had not been anticipated, much of the beam scrubbing had to be done during operations.

Other improvements in the ring resulted from changes in the damping of higher order mode of the main RF cavity and other changes in this RF control system. Testing began on the implementation of a fast RF feedback system on the main RF system. This system should suppress the noise introduced by that RF system on the beam and it appeared to work quite well when operated by itself. However, when the bunch lengthening RF system was also working the beam showed increased fluctuations and will require more work to allow these two systems to work together. Other improvements were in the diagnostics of the electron and photon beams. New extended dynamic range Beam Position Monitor (BPM) receivers were installed on all of the ring's pickups. This will allow measurements of the beam position down to lower values of current. This of little concern for normal operating currents but will help better understand the electron beam model for the ring by allowing measurements at low beam current. A new fast turn-to-turn BPM measurement system was prototyped and the full system should be operational in FY 1998. This BPM will allow modeling of the non-linear properties of the electron beam. Other diagnostic improvements that are planned will help understand the fast beam fluctuations and how to reduce their impact on the users.

The long awaited improvement in the VUV radiation shielding did not take place during FY 1997, as it was originally planned. This was due to the difficulty in finding suppliers of the heavy concrete shielding blocks.

However, this supply difficulty has been overcome and the shielding is planned to be installed around half of the ring during the winter 1997-1998 shutdown. Once the improvement in the radiation levels in that half of the ring is measured the remainder of the shielding will be scheduled for a future shutdown. When the radiation shielding has been installed new studies of the Top-Off Method of Injection (TOMI) will be performed, in order to demonstrate that TOMI offers the users the ultimate improvement in beam stability over long time periods both from the source and the optics points of view. TOMI will also eliminate the age old conflict between longer beam lifetime and higher brightness of the photon beam. To insure that the frequent injection pulses are not seen by the users, new shorter pulse kickers will be installed in FY 1998 to allow the injected beam to be added to the stored beam with minimum disturbance to the stored beam.

During the next fiscal year studies will be carried out to increase the operating beam energy of the VUV Ring. This will continue the improvement in beam lifetime that has dominated the past improvements. In addition, studies are being carried out to develop methods of providing for real-time variation of the undulator gaps in the ring. Although this is common place on the high energy rings, the lower energy of the VUV Ring makes the impact of these gap changes more significant for the other users. The initial studies to control the orbit and betatron tunes proved insufficient and addition correction of horizontal-vertical coupling effects also will have to be compensated. ■

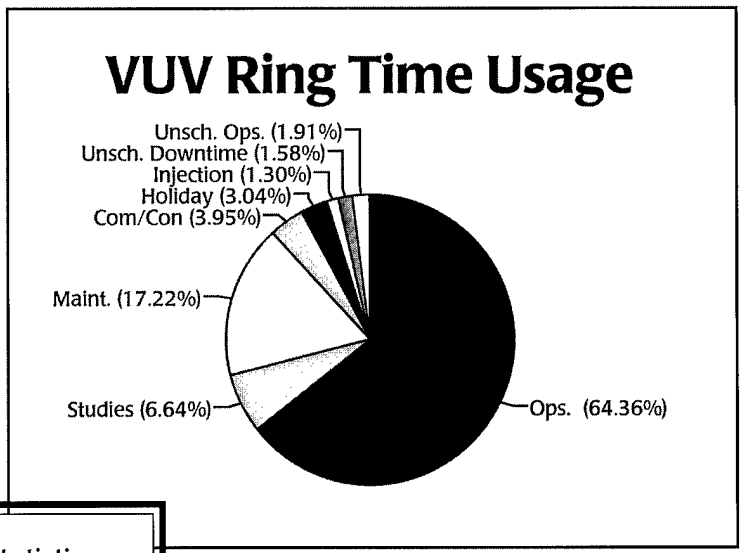

Figure 1: The breakdown of the VUV Ring usage based on total time (not scheduled time) for FY 1997.

FY 1997 Ring Performance Statistics

Ave. fill Current: 848 mA
Ave. Charge Rate: 168 mA/min
Ave. Lifetime at 500 mA: 314 min
Total user integrated current:
2980 A-Hrs (124 A-days)
Total hours of operation: 5752 hours
Average operating current: 518 mA

VUV Ring Performance FY 1997

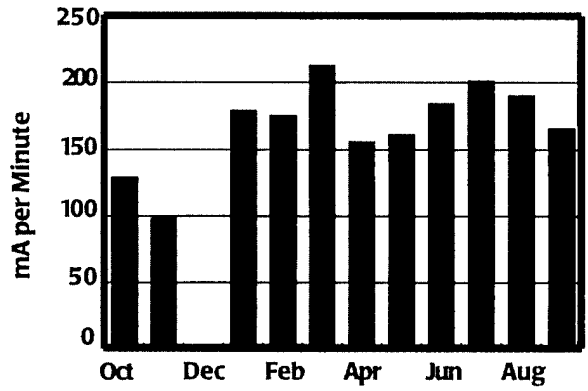

Figure 2: The VUV Ring injection charge rate average over all fills in each month.

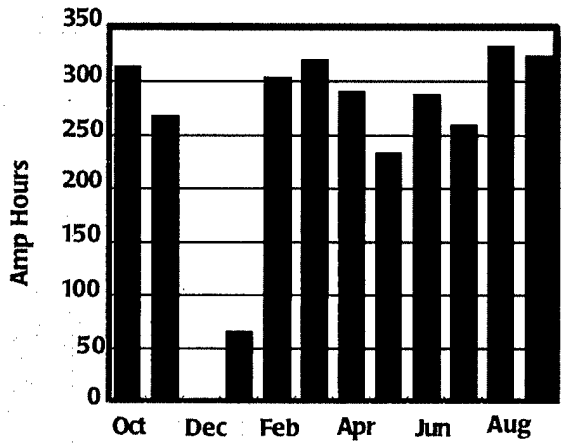

Figure 3: The total integrated current for the VUV Ring accumulated each month.

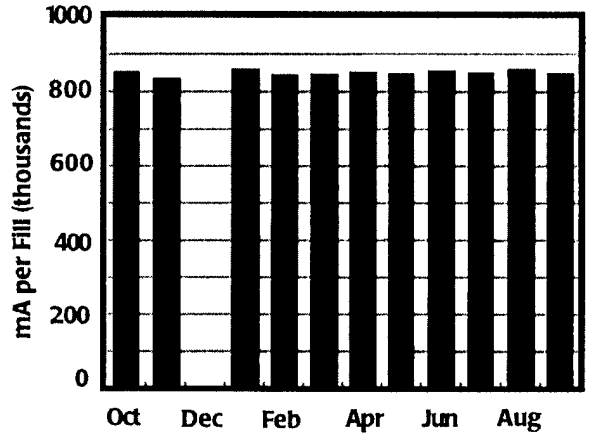

Figure 4: The injection current averaged over all fills in a month for the VUV Ring.

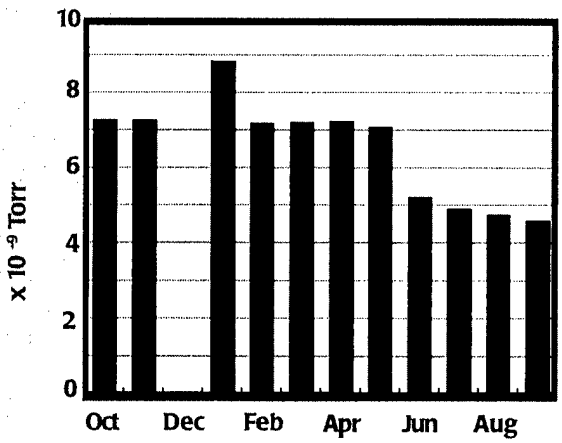

Figure 4: The VUV Ring vacuum pressure at 500 mA beam current averaged over each month.

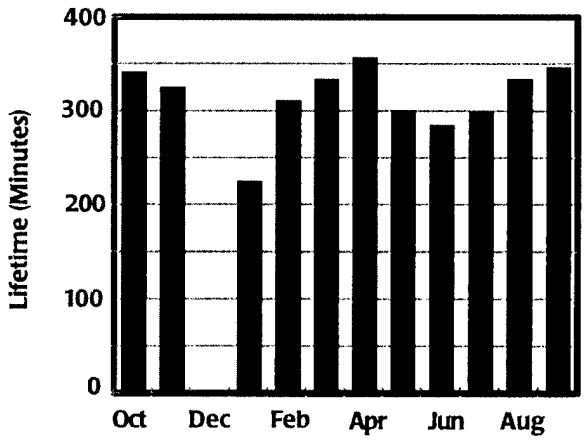

Figure 6: The VUV Ring exponential beam lifetime at 500 mA beam current (seven bunch operation only) averaged over each month.

VUV Storage Ring Parameters as of November 1997

Normal Operating Energy	0.808 GeV
Peak Operating Current (multibunch ops.)	1.0 amp (1.06 x 10^{12}e-)
Circumference	51.0 meters
Number of Beam Ports on Dipoles	17
Number of Insertion Devices	2
Maximum Length of Insertion Devices	~ 2.25 meters
$\lambda_c(E_c)$	19.9 Å (622 eV)
$B(\rho)$	1.41 Tesla (1.91 meters)
Electron Orbital Period	170.2 nanoseconds
Damping Times	$\tau_x=\tau_y=$ 13 msec; τ_ε = 7 msec
Lifetime @ 200 mA with 52 MHz	360 min
(with 211 MHz Bunch Lengthening)	(590 min)
Lattice Structure (Chasman-Green)	Separated Function, Quad, Doublets
Number of Superperiods	4
Magnet Complement	8 Bending (1.5 meters each) 24 Quadrupole (0.3 meters each) 12 Sextupole (0.2 meters each)
Nominal Tunes (ν_x,ν_y)	3.14, 1.26
Momentum Compaction	0.0235
RF Frequency	52.886 MHz
Radiated Power	20.4 kW/amp of Beam
RF Peak Voltage with 52 MHz (with 211 MHz)	80 kV (20kV)
Design RF Power with 52 MHz (with 211 MHz)	50 kW (10 kW)
Synchrotron Tune (ν_s)	0.0018
Natural Energy Spread (σ_e/E)	5.0 x 10^{-4} , I_b< 20 mA
Bunch Length (2σ)	9.7 cm (I_b < 20 mA)
(21_{rms} with 211 MHz Bunch Lengthening)	(36 cm)
Number of RF Buckets	9
Typical Bunch Mode	7
Horizontal Damped Emittance (ε_x)	1.62 x 10^{-7}, meter-radian
Vertical Damped Emittance (ε_y)	$\oplus$ 3.5 x 10^{-10} meter-radian (2.8 x 10^{-9} in normal ops.)*
Power per Horizontal Milliradian (1A)	3.2 Watts

Arc Source Parameters

Betatron Function (β_x,β_y)	1.18 to 2.25 m, 10.26 to 14.21 m
Dispersion Function (η_x,η_x)	0.500 to 0.062 m, 0.743 to 0.093 m
$\alpha_{x,y} = -\beta'_{x,y}/2$	-0.046 to 1.087, 3.18 to -0.96
$\gamma_{x,y} = (1+\alpha_{x,y})/\beta_{x,y}$	0.738 to 0.970 m^{-1}, 1.083 to 0.135 m^{-1}
Source Size (σ_x, σ_y)	536 to 568 μm, >60 to >70 μm (170-200 μm in normal ops.)*
Source Divergence (σ_x,σ_y)	686 to 373 μrad, 19.5 to 6.9 μrad (55-20 μrad in normal ops.)*

Insertion Device Parameters

Betatron Function (β_x, β_y)	11.1 m, 5.84 m
Source Size (σ_x, σ_y)	1240 μm, >45 μm (130 μm in normal ops.)*
Source Divergence (σ_x, σ_y)	112 μrad, >7.7 μrad (22 μrad in normal ops.)*

* ε_y is adjustable

X-Ray Ring

Roger Klaffky
X-Ray Ring Manager

In preparation for the December 1996 shutdown, water lines were installed in Fall 1996 to bring BNL Central Chilled Water Facility (CCWF) water to the NSLS experimental water system in Mechanical Equipment Room A. The control valve/controller installation for this system began. This upgrade was designed to improve temperature regulation, with the present NSLS experimental water system providing redundancy in case the CCWF goes down for maintenance. The BNL CCWF connection to the NSLS experimental water system was completed during the December 1996 shutdown, and temperature control of this system was upgraded. To maintain a redundant NSLS cooling capability in case the CCWF goes down, the old Baltimore cooling tower was replaced and plans were made to upgrade and expand its controls. The experimental water pump capacity was increased and spigots were installed for beamlines requiring enhanced cooling.

A major effort during the December 1996 shutdown was the installation of 20 new beryllium windows to enable 350 mA operation in January 1997. New windows were installed on X3A, X4A, X6A, X12A, X12B, X12C, X13, X14A, X14B, X15A, X19C, X20A, X20C, X21, X22A, X23A, X23B, X25, X26A and X26C. Brazing and welding of the windows was done by Brush Wellman Electrofusion with the pieces being fabricated by BNL Central Shops. An additional 20 windows were also received, which included the remaining windows required for 438 mA operation and at least one spare window for each assembly type. Since the new windows had 5 mm vertical openings (as opposed to 10 mm for the old windows), commissioning shifts were provided in January 1997 to the above beamlines to confirm that the windows were properly surveyed into position.

The dual hybrid RF power amplifier was installed on RF System 2 in December 1996. Two 120 kW amplifiers are combined in this system to enable 438 mA operation and to prevent a beam dump if one of the other

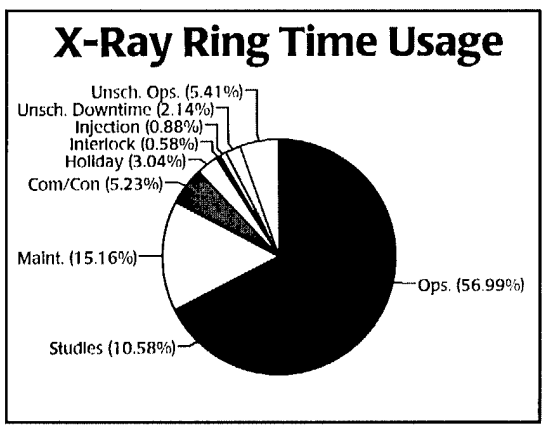

The breakdown of the X-Ray Ring usage based on total time (not scheduled time) for FY 1997.

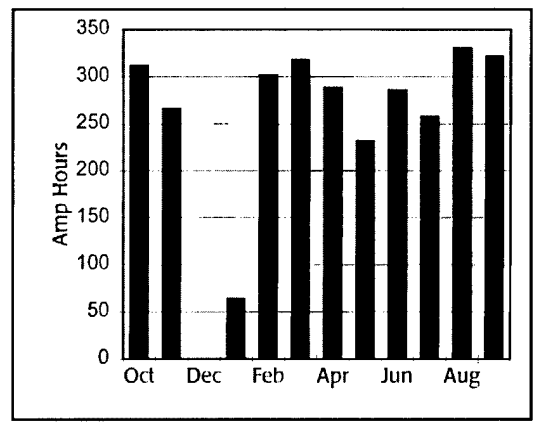

The total integrated current for the X-Ray Ring accumulated each month for FY 1997.

three RF systems drops out. After an initial commissioning period in January, the new dual transmitter on the RF2 cavity became operational. At present each of the transmitters is operating at half power (40-50 kW) with increased reliability. During the Spring 1998 shutdown, a new all-copper cavity will replace the existing copper-clad steel cavity and a new copper coupling loop brazed to a beryllia ceramic window will allow the transmission of more than 150 kW into the cavity. This additional power will enable reliable 438 mA operation at 2.584 GeV or 250 mA operation at 2.8 GeV. Improved windows for the other RF systems were ordered. The new cavity has several desirable features. There are no welded ports or joints, cooling channels are machined in the outside skin, and there is an improved mushroom cooling. The cavity was shipped to the NSLS in September 1997, after an acceptance test in Germany.

Operations commenced on the X-Ray Ring on January 23, 1997 at 350 mA. On February 1, there developed a water-to-vacuum leak in the RF1 cavity, causing the cavity pressure to jump from the 10^{-10} Torr range to the mid 10^{-07} Torr range. Helium leak detection failed to identify which water-cooled component was leaking. At an emergency user meeting the decision was made to replace the RF coupling loop, the most likely defective component, during the February 10 - 11 studies period and to continue operating at 250 mA until that time using the other three RF cavities. The repair was carried out on February 10th, followed by RF and beam conditioning on February 11th. Operations resumed on schedule at noon on February 12th. By February 15th, conditioning with operational beam had lowered the cavity pressure to the 10^{-09} Torr range.

In February 1997, an effort to fully characterize the beamline shielding requirements at 2.8 GeV commenced. Studies periods were utilized for radiation surveys by S&EP personnel to record in detail which beamline components and hutch walls require additional shielding. The initial surveys were completed in April so that users could make use of the May shutdown period to shield. A 21,000 pound shipment of (3'x5'x1/16") sheets was delivered early in May, and a work area was set up outside the NSLS Stockroom for cutting the lead sheet. Procedures for handling the lead and discarding lead scraps, contaminated covering material, gloves and aprons were outlined in the April 16, 1997 NSLS ES&H Highlights. Users were encouraged to begin their shielding efforts early because obtaining final operational approval of the shielding was, in many cases, an arduous process requiring a series of radiation surveys followed by shielding efforts. Beamline personnel continued to use dedicated studies shifts to survey the effectiveness of additional lead shielding for 2.8 GeV operation. To expedite this process, beamlines having sufficiently low radiation levels were put on a list to operate in a "self-monitoring" mode. In this mode users are able to immediately check newly-installed shielding and make required modifications. During the 2.8 GeV operations/ survey week of September 23-29,1997, the X-Ray Ring operated reliably with 230 mA fills. By the end of the week there were 34 beamlines operating in either the self-monitoring mode or in an "approved" mode after a final survey indicated that all beamline components had levels less than 500 cpm on a Ludlum pancake Geiger counter. Self-monitoring lines were expected to continue their shielding efforts to the satisfy the 500 cpm requirement.

During FY 1997 the horizontal and vertical digital feedback systems were prepared for operation. However these systems were not implemented because of a large horizontal chamber motion during a typical fill. To track the chamber motion, sensor stands will be installed and data acquired during operations from high sensitivity LVDT probes mounted on stands at various PUE locations. Carbon fiber tubes for the stands are expected to arrive in January 1998. Data acquired from the horizontal sensors measuring the ring chamber motion at each of the 48 PUEs during X-Ray fills, will be input to the digital feedback system to correct for this motion. During 1997 the algorithm of the global harmonic feedback system was changed to give a factor of two improvement in orbit stability. The programmable boards for the analog global feedback system were received. Initial studies were conducted on the low emittance lattice with the low emittance lattice response matrices successfully downloaded onto these boards. Studies of the new lattice will continue in order to check orbit stability and to increase the fill current to 440 mA.

The major X-Ray Ring task during the May 1997 shutdown was the removal of the PSGU(Prototype Small Gap Undulator) from the X13 straight and the installation of the IVUN(In-Vacuum Undulator) which is a short-period magnet array (30.5 periods, with an 11 mm period length) developed at SPring-8. The associated vacuum chamber and mechanical systems were developed at the NSLS. IVUN is designed to produce 4.6 keV radiation in the fundamental, at a magnet gap of 3.3 mm, with useful photon fluxes in both the 2nd and 3rd harmonics. The magnet gap is adjustable between 2 mm and 10 mm. A number of other shutdown tasks were completed. Upgraded beryllium windows were installed on the X4C and X6B beamlines. The remaining 13 upgraded beamline windows required for high current (438 mA) operation will be installed during maintenance periods and the December 1997 shutdown. Safety metering

transformers were installed on 480 Volt RF and magnet power supplies to verify isolation from source power before carrying out repair work. Also, the full cooling capability of the NSLS high pressure and low pressure copper water systems was restored after heat exchangers for these systems were cleaned out. Finally, the helium cryotransfer line for the X17 superconducting wiggler was replaced, allowing the X17 beamlines to resume operation on June 9th. A leaking transfer line had shut these lines down since the middle of April. Substantial improvements were made on the X17 cryogenic system. The two helium supply and return transfer lines to the refrigerator were totally rebuilt, thereby eliminating an erratic heat leak. Another major problem was solved when a metal chip was removed from the autofill valve seat to the magnet cryostat. After these repairs the system ran smoothly.

Following the installation of the IVUN (In-Vacuum UNdulator) in the X13 straight section during the May 1997 shutdown, there followed a commissioning period. Initial conditioning was carried out at a gap of 10 mm. After 10 amp-hr of conditioning the pressure at 330 mA was 7.1 nTorr which further decreased to 1 nTorr after 230 amp-hr. During studies periods, IVUN operated with magnet gaps between 10 mm and 3.2 mm. At a gap of 3.2 mm the ring lifetime decreased to about 12.7 hr, corresponding to a partial lifetime contribution of over 100 hours. The observed photon spectrum from the IVUN was measured in the X13 hutch using a single crystal spectrometer. The agreement between the observed and theoretical spectrum was good. The brightness at the peak of the 4.6 keV fundamental was 3×10^{17} photons/sec/0.25amp/mm^2/mrad^2 /0.1% bandwidth. Also, during FY 1997 the X13 Elliptically Polarized Wiggler (EPW) was able to operate at 2,23, and 100 Hz with the x-ray orbit compensated so that other beamlines were not affected. ■

X-Ray Storage Ring Parameters as of November 1997

Normal Operating Energy	2.584 GeV
Maximum Operating Current	0.30 amp (10^{12} e-)
Lifetime	~20 hours
Circumference	170.1 meters
Number of Beam Ports on Dipoles	30
Number of Insertion Devices	5
Maximum Length of Insertion Devices	< 4.50 meters
$\lambda_c(E_c)$ at 1.25 T (B)	2.23 Å (5.6 keV)
$\lambda_c(E_c)$ at 5.0 T (W)	0.56 Å (22.2 keV)
B(ρ)	1.25 Tesla (6.875 meters)
Electron Orbital Period	567.2 nanoseconds
Damping Times (2.584 GeV)	$\tau_x = \tau_y = 6$ msec; $\tau_\varepsilon = 3$ msec
Touschek (2.584 GeV, 0.25A)	⊕ 27 hrs ($V_{RF} = 700$ kV)
Lattice Structure (Chasman-Green)	Separated Function, Quad Triplets
Number of Superperiods	8
Magnet Complement	16 Bending (2.7 meters each) 40 Quadrupole (0.45 meters each) 16 Quadrupole (0.80 meters each)
32 Sextupole	(0.20 meters each)
Nominal Tunes (ν_x, ν_y)	9.15, 6.20
Momentum Compaction	0.0056
RF Frequency	52.88 MHz
Radiated Power for Bending Magnets	144 kW/0.25 amp of Beam
RF Peak Voltage	1000 kV
Design RF Power	400 kW
ν_s (Synchrotron Tune)	0.002
Natural Energy Spread (σ_e/E)	8.6×10^{-4}
Natural Bunch Length (2σ)	10.5 cm
Number of RF Buckets	30
Typical Bunch Mode	25
Horizontal Damped Emittance (ε_x)	1.0×10^{-7}, meter-radian
Vertical Damped Emittance (ε_y)	1×10^{-10} meter-radian
Power per Horizontal Milliradian (0.25A)	23 Watts

Arc Source Parameters

Betatron Function (β_x, β_y)	1.0 to 3.8 m, 7.9 to 26.5 m
Dispersion Function (η_x, η_x)	0.47 to -0.11, -0.39 to 0.22
$\alpha_{x,y} = -\beta'_{x,y}/2$	-0.49 to 1.62, -3.4 to 4.5
$\gamma_{x,y} = (1 + \alpha_{x,y})/\beta_{x,y}$	0.952 to 0.962 m^{-1}, 0.81 to 0.52 m^{-1}
Source Size (σ_x, σ_y)	371 to 565 μm, 27 to 49 μm
Source Divergence ($\sigma_{x'}, \sigma_{y'}$)	439 to 324 μrad, 8 to 7 μrad

Insertion Device Parameters

Betatron Function (β_x, β_y)	1.60 m, 0.35 m
Source Divergence ($\sigma_{x'}, \sigma_{y'}$)	260 μrad, 35 μrad

BEAMLINE TECHNICAL IMPROVEMENTS

Roger Klaffky
Beamline Technical Liaison

VUV BEAMLINES

There were a number of technical beamline improvements on the VUV Ring during FY 1997. Rebuilding of the U2A beamline for high-pressure infrared spectroscopy and for infrared micro-spectroscopy was underway. The U1/U2 dipole chamber chamber was modified during the winter 96-97 shutdown to provide a solid angle of 100(H) x 48(V) mradians on the U2 port. Extraction optics consisting of a new mirror box and diamond window were designed and built at the NSLS. A new Bruker IFS 66 V/s FT-IR instrument was purchased and a new Bruker II, IR microscope was tested and implemented for samples in small diamond cells. The optics in both of these instruments was modified for synchrotron radiation measurements. In addition, a new large working distance microscope was designed and built.

Beamline U3A was in an intensive recommissioning phase involving hardware upgrades, monochromator development, beamline calibration and diagnostics. Hardware modification included reconfiguration of the M0 mirror chamber, a beamline computer upgrade, installation of RF reactors for cleaning XUV optics, installation of a new filter assembly, and monochromator operations. Several sets of monochromator crystals and multilayers were mounted and aligned. These included matched pairs of beryl, Na β alumina, Mo/Si and W/Si multilayers. Harmonic content was negligible above 1000 eV. Second order harmonics above 800 eV were controlled with filters. Monochromator motors were replaced and motor translators modified to allow for a programmable holding torque.

The microscope from U2B was moved to U4IR where it was used for several experiments.

As part of the DOE Scientific Facilities Initiative (SFI) spherical gratings and a moveable exit slit will be added to the U4A beamline, replacing the present toroidal gratings and fixed slits. A computer upgrade was in progress and in the ARP chamber, a new cluster of metal evaporators and a thin film thickness monitor were installed.

The U4B SGM-based beamline optics were commissioned, as was the UHV chamber and growth capabilities. The U5UA beamline and its spin-resolved photoemission end station began full operation in January 1997.

A full General User program began at the new U7A S6M soft x-ray photoemission and spectroscopy beamline. Installation and commissioning of a high pressure surface chemistry chamber on top of the chemistry end-station took place.

The former U9A beamline was removed and plans were made to install an NSLS general machine vacuum R&D beamline to measure photon-stimulated desorption of materials and coatings for advanced UHV construction.

Two modified ring vacuum chambers were installed during the Spring 1996 shutdown to provide a 100(H) x 48(V) mradian solid angle IR beam at the U10 port and a 90(H) x 90(V) mradian solid angle IR beam at the U12IR port. The U10A beamline was under construction in FY 1997 and is intended to operate with a rapid Scan Bruker IFS 66V/s FT vacuum spectrometer over the range of 1.2 meV to 3.3 eV. The U12IR beamline was in the final stages of construction with the UHV mirror tank installed on the ring and most of the beam-transport following the diamond window complete. Two IR spectrometers were installed: a far-infrared lamellar grating interferometer for spectra between 2 and 100 cm^{-1} and a Bruker IFS 113V for the 50-10,000 cm^{-1} range.

During 1997 redesign and reconstruction of beamline U12A continued, which will result in a conversion from a TGM into a TGM/SGM beamline covering the 100-800 eV photon energy range. Upgraded electric service was installed. Optics for this conversion will arrive in 1998.

The U13UB beamline was under construction in 1997. This beamline is devoted to UV/VUV spectroscopy in the 5-30 eV range. The U13 undulator/wiggler source can be directed to either: (1) a focused white light branch, or (2) a high energy resolution monochromatic branch. The PRT members acquired DOE SFI funds to design and construct a high resolution ARPES chamber.

At U15 the beamline computer control hardware and software were upgraded as was the vacuum system. The U16B ERG monochromator and refocusing optics were restored to an operating condition.

X-RAY BEAMLINES

The X1A beamline was rebuilt during the second half of 1996 and started operation in the new configuration in February 1997. The rebuilding resulted in two independent branches, improved energy resolution and flux, and additional space. A large effort was directed towards commissioning of the cryo-scanning transmission x-ray microscope (Cryo-STXM) on the inboard branch line. This instrument images frozen hydrated biological specimens at near liquid nitrogen temperature, where radiation damage does not manifest itself even after repeated imaging. Tomography data sets were taken with this apparatus. Cryogenic capabilities were implemented in the x-ray holography chamber, which is also used on the inboard branch line.

Two new experimental facilities were implemented on X1B. A soft x-ray emission (SXE) spectrometer was commissioned as was a new spin polarization facility based on the use of a Scienta hemispherical analyzer and a micro-Mott spin polarimeter. This will allow high resolution spin polarized photoemission studies in the soft x-ray range.

At X3A electric wiring in the monochromator assembly was redesigned to eliminate cross-talk between the A1 and A2 monochromators. Also, new operating software for a Pentium PC was under development in collaboration with the staff of the 15-ID station at the APS.

On X4A a new Raxis-IV automated detector was installed and tested. The X4C beamline approached completion. First light was taken into the hutch in February 1997. The Windows 95 based VME motion control system began operation, controlling close to 30 motors. The horizontal focusing monochromator, based on an NSLS design, was commissioned. In the future, the monochromator will be completely characterized and

The New DOW / NIST Materials Characterization Facility at Beamline U7A.
Back, left to right: Arnie Moodenbaugh (DAS), James Wood (Osmic, Inc.), Raj Korde (IRD), Michael Hart (Chairman, NSLS), Gabrielle Long (NIST), Steve Hulbert, and Qing Yi Dong (NSLS).
Front, left to right: Daniel Fischer (NIST), Benjamin DeKoven (DOW), Stephen Freiman (Chief, Ceramics Division, NIST), Lyle Schwartz (Director, Materials Science & Engineering, NIST), and Robert Bubeck (Synchrotron Coordinator, DOW).

a vertical focusing mirror will be installed.

There were substantial improvements at the X5 Laser Electron Gamma Source (LEGS) beamline. The first phase of the Spin ASYmmetry detector array (SASY) was installed in the X5 experimental area. The detector array comprises the XTAL BOX (an array of Pb-glass Cerenkov counters. A prototype of the in-beam Gas Cerenkov counter for the rejector of electron pair production events online was also implemented. The XTAL BOX provides good photon resolution (~10%) for high energy photons as all azimuthal angles and at polar angles of 70 to 145 degrees in the current configuration. The forward wall of plastic scintillators provides coverage for nucleons from 10 to 35 degrees with a 40% efficiency for the detection of neutrons. The plastic bars and Pb-glass wall are capable of detecting high energy photons with moderate energy resolution, and angular resolution on the order of 6 degrees results in an overall acceptance for reconstruction of neutral pions of 50%. The complete restructuring of the X5 laser hutch was underway in order to accommodate the energy quadrupled laser designed and constructed by Frascati and BNL. This Nd-YLF ring laser delivers 2 Watts of ultra-violet light at 263 nm. The combination of the new ring laser and 2.8 GeV electrons will increase LEGS energies to 470 MeV. The development of the new spin- polarized HD ice target yielded an operable full-size target, albeit in a limited mode, of 51% H polarization and 11% D polarization. After partial aging, the target was disengaged from the dilution refrigerator, raised with the cold-transfer assembly, reinserted and the retained polarization measured. This was a milestone in the target development. The HD production equipment has been improved and operated to produce large amounts of target quality HD with only a single distillation starting from 98% pure commercial HD. The in-beam cryostat was constructed at Orsay.

At X7B it was discovered that the beamline Zerodur fused silica premirror had deteriorated due to exposure to white-beam synchrotron radiation. The beamline was reconfigured to run without a premirror while a new coated silicon crystal mirror was being manufactured for installation during the December 1997 shutdown. There was also progress in addressing monochromator heat-loading problems. Water flow to the crystal holders was improved, and graphite filters were purchased. A new MAR 345 mm image-plate based detector was purchased. Work was in progress on the design and construction of a MAR-based detector system, incorporating a precision, variable sample-to detector-distance table, a new universal sample holder installation and a new set of front-end beam positioning/tracking devices.

On the X9B beamline a MAR image plate detector and a Silicon Graphics computer were purchased to enhance the collection of protein crystallography data. Implementation of a new computer control system and monochromator modifications were also underway. Funding was secured for completion of a state-of-the-art protein crystallography station on the X9A beamline. This work will begin in FY 1998.

A number of upgrades were completed or underway on X11A, largely as a result of DOE SFI funding. A sagitally-focusing system was purchased which will provide at least a three-fold increase in intensity. A Rh-coated vertical ly collimating Si mirror was purchased for installation during the December shut down. A new Huber goniometer was purchased and a new computer-controlled slit assembly was installed in the hutch. Finally, a 13 element solid state detector was obtained.

At X12B a custom built phi-spindle was implemented for the sample goniostat. The spindle mount incorporates a high magnification video microscope. An Oxford Cryosystems Cryostream cools the sample. Funding from DOE SFI funding allowed the purchase of a large aperture Area Detector Systems Quantum-4 CCD array detector. The array generates an image consisting of 2300 x 2300 16-bit pixels, with a readout dead time of approximately 9 seconds. The detector was tested in July 1997, and has become the principal crystallography detector. A MAR scanner is used for experiments requiring greater coverage and readout dynamic range. A series of hoists and surface plates (called the "detector selector") was installed in the hutch roof permitting rapid detector chairs. A Beowulf.Linux computational cluster was installed with a 100 MHz Ethernet connection between X12B, X12C, and X25.

The X13 port uses either the In-Vacuum Undulator (IVUN) or the Elliptically Polarized Wiggler (EPW) as a source. During FY 1997, full orbit compensation was achieved when the EPW changes the photon polarization at a 2,23, or 100 Hz rate. A soft x-ray SGM monochromator was designed and ordered for the X13A branchline using SFI funds. Commissioning will occur in 1998.

Beamline X14A initiated an upgrade of the mirror, monochromator and computer hardware. A new mirror with a factor of three lower surface roughness and insignificant figure error was procured with DOE SFI funds. The improved mirror should deliver about 25% more flux at 10 keV and a factor of 2 lower emittance at the sample. New crystals, with three times the useable surface area for focusing synchrotron radiation, will allow X14A to focus up to 15 mradians of horizontal beam divergence. X14A was designated a test-bed for the development of hardware and software to allow remote

control of major DOE facilities. Towards this end, plans were made for a migration to a PC-based computer system running SPEC, and installation of cameras and telecommunication hardware.

At X16C a front-end white-beam aperture (with slits and a pinhole) was designed and installed for microprobe and micro-XAFS applications. A permanent setup for XAFS experiments was also built.

At X17C a pair of Kirkpatrick-Baez mirrors was set up for focusing white x-ray beams at a glancing angle incidence to a 3-30 micron spot. Clean up slits were used to eliminate the tail of the focusing beam. A 130 element detector was used to permit simultaneous collection of energy dispersive x-ray diffraction at different angles, an important configuration for high pressure elastic properties studies. A new 12 degree cone double receiving slit system was developed for the multi-element detector to reduce background and increase the signal-to-noise ratio. An optical microscope for precise and convenient alignment was integrated into the diffraction system.

At the X19A a white beam damaged Zerodur mirror was replaced with a new silicon mirror. An improvement in throughput of more than a factor of 10 was achieved as well as a significant decrease in focused beam size. Additional diagnostics were installed to facilitate alignment. The successful implementation of InSb crystals took place, and the possibility of using monochromator crystals with larger d spacing to permit studies at the Al edge is under consideration. At X19C an analyzer axis was designed for the defector arm to enable harmonic contamination analysis of white beam topographs. Implementation of the axis was underway.

On the X20A,B, and C beamlines data-acquisition/ analysis computers were replaced with IBM RS/6000 computers running the AIX 3.2.5 operating system. The motor controlling and data acquisition program SPEC was upgraded to version 4.03.01. A UPS for these computers, along with software capable of shutting down the AIX operating system automatically during a power outage, was purchased and installed. At X20B, a computer-controlled monochromator focus and tilt DC-motor problem was solved on the bench and plans were made to complete an X20B monochromator upgrade with the installation of these motors. At X20C a new focusing mirror purchased by the NSLS with DOE SFI funds was installed, improving the vertical focus by a factor of three. A new set of synthetic Si/W multilayers also improved the focused spot size.

Normal maintenance and upgrades were carried out at X22A,B and C including installation of a LINUX operating systems. Pt-coated Si mirrors were purchased for these beamlines using SFI funds with installation to occur in 1998. The X22B slit assembly was upgraded, and SFI funds were used to upgrade the liquid surface spectrometer, including addition of a UHV chamber for liquid metals.

The X23A2 beamline was upgraded with the installation of new ion chambers, a new Macintosh Power PC 8600/200, LABVIEW data acquisition software and a computer driven exit slit. The two-reflection Bense-Hart-type SAXS at X23A3 was temporarily replaced with a four-reflection instrument. Significant reductions in background, and concurrent improvements in signal-to-noise, were observed. Testing of the instrument continues.

At X23B it was discovered that the collimating mirror was not coated with Pt as requested. Investigation into this problem led to the discovery that several mirrors at the NSLS has been mis-coated (sometimes with germanium, rather than platinum). In May 1997 a properly coated mirror was installed resulting in a dramatic increase in flux. The monochromator microstepper controller was replaced to reduce maintenance and correct a problem with missing steps. PZT drivers were added to allow realtime adjustment of chi and a larger theta range. Computer equipment was also upgraded.

There were substantial changes at X24A as new applications using the x-ray standing wave (XSW) technique were added to the previous soft x-ray gas spectroscopy capability. New UHV chambers were made available for back-reflection XSW. DOE SFI funds were used to purchase a hemispherical analyzer for electron spectroscopy. The computer controlling the monochromator was replaced with a PC operating in LINUX or Windows. New two-axis (theta and chi) PZT correctors were installed on several monochromator crystal pairs. This will stabilize the focused beam position. Also, an InSb/KDP crystal pair was added to permit operation down to 1800 eV with a resolution of 0.5 eV or better.

At X25 SFI funds were used to purchase a new 34.5 cm diameter imaging plate system for macromolecular crystallography, and diffraction cryostats for materials and condensed matter x-ray scattering and spectroscopy applications. A new pair of monochromator multilayers was obtained and utilized in several experiments.

During FY 1997 the X-ray Computed Microtomography apparatus was moved from X27C to X27A. A multilayer monochromator was installed inside the X27A hutch to allow microtomography on biological samples in the 4 to 12 keV range. A new cooled CCD camera was integrated into the setup, increasing both the resolution and the size of samples that can be analyzed. The size of data sets that can be acquired grew due to new data collection hardware and software, and the reconstruction time reduced through the use of 8

multiplexed Pentium processors in BNL CCD. In January the newly established Advanced Polymers PRT was given approval to instrument and operate X27C for real time simultaneous small and wide angle X-ray scattering (SWAX) experiments. During the commissioning phase a double-multilayer (silicon/tungsten) monochromator, a three pin-hole SAXS collimation system, and a simultaneous SAXS/WAXD camera were installed. The double-multilayer monochromator increased the x-ray flux by a factor of 10 compared to a conventional double-crystal monochromator. The beamline began initial operations in July.

The x-ray pinhole camera on X28C continued to report data to the Control Room and history programs on a real-time basis. Cooling for stepping motor operation, and a host of signal and pre-amp cables were wired for use. Some components and features of the pinhole camera system were also improved. ■

Beamline X25: The structure of the complex between oncogenic protein Ras and the Ras-interacting domain of RalGDS (RalGDS-RID) has been studied by x-ray crystallography. The structure of the complex will provide crucial information on Ras' interaction with its binding partner at an atomic level. Since the mutant forms of Ras are involved in 30% of human cancer and Ras' function is carried out through its effectors, the spatial location of the key interface residues may assist in identifying small molecules that are capable of disrupting this interaction and thus provide insights for the development of anti-cancer drugs. The crystal has a P212121 space group, with a=75.648, b=78.256, c=87.313 . The complex crystallizes as a heterotertramer with two active Ras molecules and two RalGDS-RID subunits. (See also Abstract on page B-220.)

L. Huang, F. Hofer, G.S. Martin, and S-H. Kim (U. California at Berkeley)

FIVE
PROJECTS

THE NSLS SOURCE DEVELOPMENT LABORATORY

Erik D. Johnson
SDL Project Manager

The Source Development Laboratory (SDL) was created as a project within the National Synchrotron Light Source as a way to serve its user community by developing sources for the next generation of synchrotron radiation based research. The path to the founding of the current SDL was based on a strong interaction between potential users of advanced sources of light, and the NSLS. It is possible due to innovative developments in accelerator physics by NSLS staff and experimental achievements at the Accelerator Test Facility (ATF). Another element that makes the SDL so readily possible is the wealth of infrastructure and equipment already available.

The focus of the SDL is on joint development of both the radiation source and science program based on its capabilities. Generally speaking, the project is developed to fit within the framework of research supported by the DOE office of Basic Energy Sciences. It's sister facility, the ATF, provides significant accelerator expertise employed by the SDL. However the active beam physics experimental program of the ATF precludes its use as a UV FEL source for research. Throughout the SDL project, we have made every possible effort to draw on existing resources and the strengths of collaborators from many interested institutions.

Early on in the process of evaluating alternative source technologies, the vacuum ultraviolet was identified as a promising area for development. Although there are many FEL projects in the world, to date, all the successful user facilities have been based on oscillator designs. This places very great demands on the optical elements of the cavity in terms of reflectivites which would be difficult to routinely achieve in the ultraviolet. An alternative approach would be to run a high current electron beam through a long undulator in a single pass. Many projects have been started based on this Self Amplified Spontaneous Emission (SASE) or startup from noise model.

While SASE may get to shorter wavelength without oscillator optics, it is essentially amplification of noise which, from the standpoint of users of the radiation, may have serious experimental consequences. For this reason, Li-Hua Yu and his collaborators have developed the approach adopted at BNL for creating a seeded amplifier FEL. In addition to providing superior stability, this approach allows the

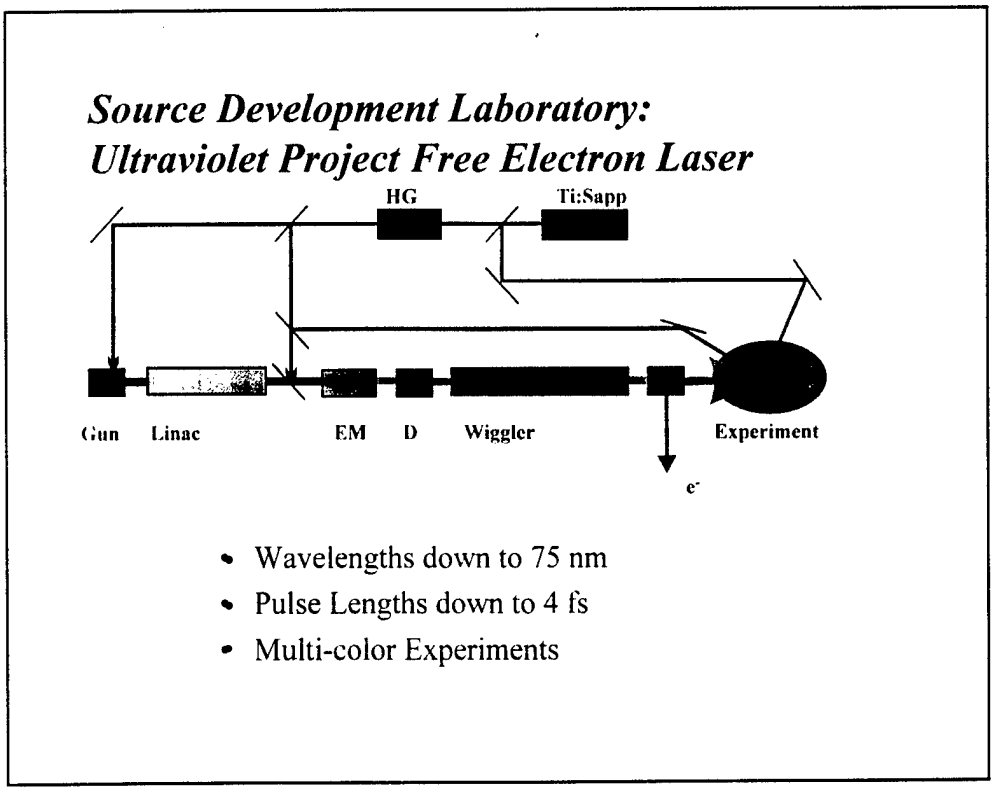

generation of high harmonics of the fundamental radiation used for the seed. This means a visible seed laser (and its properties) may be amplified and frequency multiplied, in principle, well into the ultraviolet.

The figure gives a qualitative picture of how the SDL FEL works, and provides some insight into its potential power as an experimental tool. A "conventional" Ti:Sapp laser system is frequency multiplied to stimulate emission of electrons from the cathode of the RF gun. This gun provides a high peak current, low emittance pulse of electrons which is accelerated by a SLAC type S-band linac. For seeded beam operation, these electrons pass through an energy modulation wiggler (EM) while interacting with a portion of the laser beam from the laser driving the photocathode. In the seeding process an energy modulation is introduced on the electron beam which is converted into a spatial modulation by a dispersive magnet (D). The already microbunched beam is introduced to the amplifier wiggler which may be tuned for gain either at the fundamental seeding energy, or a higher harmonic.

This arrangement can be readily viewed as essentially a high gain amplifier and frequency multiplier for the seed laser. The FEL output will then reflect characteristics of the seed laser such as wavelength, pulse length, bandwidth and energy chirp. This property makes the seeded beam FEL a very high quality tool for research applications requiring stability and short wavelengths. For our long term goal, we have our sights set on performing experiments with an FEL producing UV radiation at wavelengths below 100 nm in pulses as brief as 5 fs with peak power ranging to over 100 GW. There are, of course, a few intermediate steps that need to be taken.

We are working hard on bringing up the SDL accelerator now, and are hoping to have the linac operational in mid 1998. The FEL experiments will come as rapidly after that as time, determination, and budget allow. As the effort has intensified a great deal of work must be pursued in parallel. To make this possible we have formed a management team.

Jim Desmond and Nick Gmür are responsible for finding ways to make sure the project gets done with the budget we have, and meets all the requirements to run in a safe manner; no small tasks these days. For the other team members, the project areas listed are really an inadequate representation of the wide range of contributions and responsibilities within this small project. For example, in addition to specifying and commissioning the SDL Laser systems, Lou DiMauro (with his joint appointment in Chemistry) brings his expertise in atomic physics and the broader knowledge of conducting experiments with lasers to the project. Besides developing new diagnostics and coordinating the rebuilding of the accelerator control system, Bill Graves did extensive simulations of the compression system and beam transport. Through this work, he developed the current linac design that includes pulse compression and a focused interaction point for Thompson scattering studies; enhancements that significantly extend the potential of the machine.

Richard Heese brings extensive experience in linac technology and development to the project. He has also assumed the responsibility for supervising the reconstruction and upgrade of the SDL linac and has taken on the difficult task of coordinating the technical work in bringing the facility up. Xijie Wang brings not only the gun technology to the project, but his experience of coordinating the operation of the ATF. Li-Hua Yu not only developed the basic physics for our planned FEL, he is leading the High Gain Harmonic Generation (HGHG) experiment at the ATF and applies his experience to the development of the SDL program.

We also have a project advisory panel, consisting of Ilan Ben-Zvi, Jerry Hastings, and Sam Krinsky who bring a broad perspective to the problems of bringing up a new accelerator based source. In actually accomplishing anything, the broad participation from every section of the department has been critical. This has been especially true of the electrical and mechanical groups who are responsible for the majority of the visible progress to date. All in all people have been attacking their tasks with an enthusiasm that lifts the whole project. We hope to be seeing some of that work coming to fruition in the next year. To look at the project in more detail or to keep abreast of the latest developments, visit the SDL web page http://www.nsls.bnl.gov/BeamRD/Erik/SDL.html. ■

The SDL Management Team

The following individuals are bringing their expertise to the task of bringing the SDL "on-line".

Jim Desmond	Fiscal Management
Lou DiMauro	Laser Physics
Nicholas Gmür	ES&H
Bill Graves	Diagnostics & Controls
Richard Heese	Linac Systems
Erik Johnson	Project Manager
Xijie Wang	Electron Gun Systems
Li-Hua Yu	FEL Physics

The Accelerator Test Facility

Ilan Ben-Zvi
ATF Head

The interest in Free-Electron Lasers operating in very short wavelengths, down to hard x-rays, is growing. Recently a team of NSLS, MIT, Columbia and Berkeley scientists made a measurement that is deemed important in this context. In the following I will try to provide the background for this measurement that was made at the BNL Accelerator Test Facility.

A key aspect of the mission of Brookhaven National Laboratory (BNL) is to construct, operate and use large facilities for the breadth of scientific disciplines supported by the Department of Energy. An important component of the success of BNL comes from innovative accelerator R&D, since new accelerator technologies hold the key to new achievements in applications and user facilities. We are facing now the emergence of a new technology, that of very high-brightness electron beams. This technology has far reaching implications for x-ray sources and other applications.

Part of the mission of the National Synchrotron Light Source is to develop radiation sources for the future. The NSLS has been the first light source to pursue the development of **Free-Electron Lasers** as the next generation synchrotron light sources. BNL has been a leader in the national effort on FEL development, hosting the workshops "Prospects of a 1 Å FEL" in 1990 and "Towards Short Wavelength FELs" in 1993, as well as developing its Conceptual Design Report and pursuing subsequent efforts to develop a national collaboration in the field. In the past decade, the NSLS made significant contribution to the science of FELs like the theories on Universal Scaling of exponential regime FELs in 3-D, the High-Gain Harmonic Generation and beam conditioning. Experimentally we have led in the development of record high-brightness electron beams and methods of measurements of these and, as has been hinted at earlier, the shortest wavelength measurement of Self Amplified Spontaneous Emission (SASE).

FELs can provide an important tool reaching beyond the capabilities of high brightness synchrotrons. Science that explores non-linear effects at short wavelength, dilute systems or intensity correlation studies, require high peak power and will only become possible when appropriate sources, such as FELs, are available.

The NSLS developed a vision of the next generation of light sources and is assembling the beam physics and technology to make this happen. Emphasizing single-pass FEL amplifiers, which have advantages over oscillators in the short wavelength regime where cavity mirrors are unavailable, the NSLS developed the High-Gain Harmonic-Generation (HGHG) FEL approach as a the best strategy to build a high quality short wavelength FEL. High-brightness electron beams R&D was undertaken in a major way, since this is the key to achieving short-wavelength FELs as well as other significant applications, such as linear colliders, laser accelerators and more. The BNL Accelerator Test Facility (ATF) is the proving ground for these advances.

What is the ATF? First and foremost, it is a User's Facility for accelerator and beam physicists, operated by the NSLS and the BNL Center for Accelerator Physics. There is no other proposal-driven, peer-reviewed facility like the ATF that is dedicated for long range R&D in accelerator and beam physics.

The ATF has a unique combination of a high-brightness electron beam, synchronized-high-power lasers, a well-equipped 3 beamline experiment hall, and advanced diagnostics and control systems. The ATF's program in RF guns is recognized internationally. With its synchronized lasers and electron beams of unprecedented brightness, the ATF is an ideal site for R&D on advanced accelerator concepts, FELs, femtosecond X-ray sources and similar topics. These tools have been crucial to recent ATF record achievements: the measurement of Self Amplified Spontaneous Emission (SASE) at 1 μm and 0.63 μm, and laser acceleration by the Inverse Cerenkov and Inverse FEL mechanisms.

The generation and acceleration of very high brightness electron beams is a key technology for short wavelength FELs as well as other applications, including linear colliders, Compton backscattering for the production of femtosecond x-rays, laser accelerators and more. A high brightness means that the electron bunch

has a high density in 6-D phase space. To achieve high brightness beams, it is necessary to master the production of such beams in special electron guns, to develop diagnostics that provide information of the 6-D distribution of electron bunches on sub-picosecond time scales, to control the 6-D distribution of the bunch in various ways and to be able to accelerate the electrons to high energies without diluting the brightness.

NSLS scientists working at the ATF measured the slice emittance of a 10 ps electron bunch with a 1 ps resolution, achieved an unprecedentedly high 6-D electron phase-space density and directly measured electron bunching on an optical scale. Another diagnostic under development at the ATF is tomographic analysis of the distribution of electrons in transverse phase space. The next step is to pursue non-linear emittance compensation. Laser photocathode RF guns have provided a major improvement in the brightness, which was further enhanced by the introduction of (linear) emittance compensation. The dream of another major improvement by the introduction of non-linear corrections has been brought within reach by the development of the slice-emittance diagnostic and the availability of lasers with longitudinal pulse shaping.

Key to our plans is the development of sub-harmonically seeded FELs in which harmonic generation converts a laser seed to much shorter wavelength radiation. A proof-of-principle High-Gain Harmonic-Generation (HGHG) FEL experiment is planned to be carried out at the ATF in the infrared using a CO_2 laser seed. Both the SASE and HGHG work will be extended into the VUV at the SDL, using the NISUS wiggler. These experiments at the ATF and the SDL are milestones, not just for the BNL program, but also for other projects like the proposed

(Top, from left to right) John Skarita (Mechanical Section), Marc Montemagno (Electronics), and Igor Pogorelsky (Lasers).
(Middle, from left to right) Bob Harrington (Mechanical and Optical Systems), Joe Sheehan (Electrical Section), Robert Malone (Computer and Control), Bill Cahill (Technical Supervisor and Users' Coordinator), and Marcus Babzien (Lasers).
(Bottom, left to right) Xijie Wang (Accelerator, gun, diagnostics), Ilan Ben-Zvi (Head of ATF), and Vitaly Yakimenko (Accelerator, gun, diagnostics).

Linear Coherent Light Source at SLAC and the Tesla Test Facility FEL at DESY, Hamburg. The goal of these efforts is basic experimental research in FEL physics, which has been recommended by numerous panels and review committees as an imperative on the way to developing short wavelength FELs. An initial success in this program has been the ATF measurement of SASE at 1μm and 0.63 μm. At the SDL, it is planned to utilize the output of the FEL to carry out prototype experiments to gain experience in providing FEL beams to users.

One of the special features of the measurement at the ATF is that the short wavelength was reached at a relatively low electron beam energy (34 MeV for the 1 micron measurement). To get gain with an FEL at a lower energy, the beam emittance must be small. It is easy to show that the beam energy required for obtaining a particular FEL wavelength is proportional to the beam emittance. The wiggler length is proportional to something between the emittance and the emittance squared, depending on the wiggler strength parameter. Since the complexity and cost of an electron linac and a wiggler are proportional to the length of these devices, an improvement of one order of magnitude in the electron beam emittance will reduce the cost by one order of magnitude! Such a reduction has taken place in the last decade with the introduction of emittance compensation techniques to laser-photocathode RF guns, and that is the driver behind the recent activity in short wavelength FELs. Another order of magnitude will place an x-ray FEL within reach of every laboratory.

Another feature, made necessary by the low energy, is the use of a very short period undulator. It is clear that to make use of lower emittance electron beams short period undulators must be developed. The SAE measurement at the ATF was made with an undulator built by MIT with a period of 8.8 mm. Another undulator, with the same period but using a superconducting magnet, was developed by the NSLS. These are the shortest period undulators in actual use anywhere.

The ATF and the NSLS are in the center of the national effort to develop short wavelength FELs, and effort that at this time encompasses also SSRL, APS, TJNAF and universities. Whenever possible, we have collaborated with other laboratories, as exemplified by the highly successful "Next Generation Photocathode RF Gun" developed with SLAC and UCLA, the SASE and HGHG experiments at the ATF being developed with ANL using a wiggler from Cornell, as well as collaboration with industry. In the near future, an exciting new experiment is being proposed for the ATF. This is the VISA experiment (short for Visible SASE). It is planned as a collaboration of BNL (NSLS), UCLA, SLAC (SSRL), LLNL and LANL. In this experiment a four meter long wiggler with a period of 1.8 cm will be installed at the ATF to produce SASE to saturation at visible wavelengths. This experiment is considered by SSRL as an important milestone on the way to a hard x-ray FEL. Following the experiment at the ATF the wiggler will be increased in length to six meters and installed at the SDL to extend the experiment to the VUV at about 100 nm.

The FEL community is aware of the large gap that exists between the wavelength at which SASE has been demonstrated and the goal of sub nanometer wavelengths. Until recently the gap was 7orders of magnitude. The consensus reached at many professional workshops and reviews on the subject of short wavelength FELs is that in order to bridge this gap in FELs, a series of experiments at increasingly shorter wavelengths must be undertaken. UCLA and Los Alamos have recently made a good SASE measurement at 12 microns, closing the gap to five orders of magnitude. The ATF measurement closed it to four orders of magnitude and we may expect new records to follow, until x-ray wavelengths will be reached. ■

Beamline U2B: Localization of drug metabolites within human hair is important in determining the pharmacokinetics of drug incorporation in hair. This information is critical to validate drug testing data from hair. Doped hairs compared to reference hairs show spectral differences with bands corresponding to the frequencies of the drug of interest. Analysis of the patient hairs from cocaine and heroin abusers showed that the drug was concentrated in the medulla of the hair. When the patient had non-medullated hair the drug was not present. At right is a topical graph of a hair from the synchrotron infrared microscope, mapped for the primary frequency band for cocaine in a drug abuser's hair. The graph shows the drug to be in its highest concentration in the central portion of the hair and the lack of drug absorption in parts of the central portion of the hair correlates to areas where the medulla was fragmented or not present. This evidence for high binding of the hydrophobic drugs to the central medulla helps explain the hair color and racial bias found in hair drug testing. (See also Abstract on page A-12.)

K.S. Kalasinsky (Armed Forces Institute of Pathology), and D.G. Cameron (DHC Analysis)

ORGANIZATION

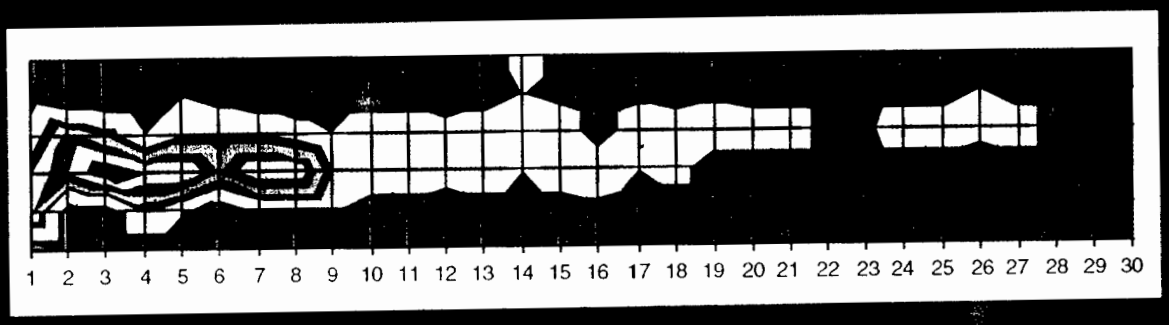

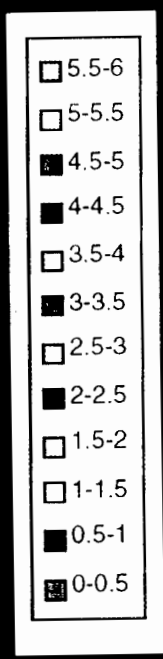

NSLS Advisory Committees

1997-1998
Users' Executive Committee

The Users' Executive Committee (UEC) provides for organized discussions among the user community, NSLS administration, and laboratory directorate. It aims to communicate current and future needs, concerns, trends within the user community to NSLS staff and management, and to disseminate to the users information about NSLS and BNL plans. Members were:

Chairperson: Joel D. Brock, Cornell University
Vice-Chairperson: John Parise, SUNY @ Stony Brook
Past-Chairperson: Peter Stephens, SUNY @ Stony Brook
Secretary: Elaine DiMasi, BNL-Physics
General Members: Thomas Russell (U. of Massachusetts), Barbara Illman (U. of Wisconsin), Ian Robinson (U. of Illinois)
Paul Stevens(Exxon Res. & Engr.)
NSLS User Administrator: Eva Rothman, Ex-Officio
Beamline Support/R&D Head: D. Peter Siddons, Ex-Officio

Special Interest Group Representatives

Special Interest groups in areas of common concern communicate with NSLS management through the UEC. Group representatives were:

Biological Scattering, Diffraction	Malcolm Capel, BNL-Biology
Imaging	Carl Zimba, NIST
Industrial Users	Sanjeeva N. Murthy, AlliedSignal, Inc.
Infrared Users	G. Lawrence Carr, BNL-NSLS
Nuclear Physics	Steven C. Whisnant, U. of So. Carolina
Time Resolved Spectroscopy	Jon Levin, U. of Tenn.
Topography	Michael Dudley, SUNY @ Stony Brook
Students and Post Docs	Elaine DiMasi, BNL-Physics
UV Photoemission, Surface Science	Peter Johnson, BNL-Physics
XAFS	Mark Chance, Albert Einstein Coll. of Med.
X-ray Scattering, Crystallography	Luz J. Martinez-Miranda, U. of Maryland

General User Oversight Committee

The GUOC resolves disputes between General Users, PRTs, and NSLS staff. Members were:

Simon Bare, UPO
Dale Sayers, NCSU
Mark Chance, Albert Einstein Coll. of Med.
Peter Stephens, SUNY @ Stony Brook

Science Advisory Committee

The Science Advisory Committee (SAC) evaluates the science programs at the NSLS and makes recommendations to the Chairman. The SAC met in March of 1997 and its members were:

Boris Batterman, CHESS, Cornell U.
Martin Blume, Brookhaven National Laboratory
Stephen Harrison, HHMI, Harvard U.
Franz Himpsel, U. of Wisconsin, Madison
Jochen Schneider, HASYLAB, DESY
Albert J. Sievers, Cornell U.
Paul Sigler, HHMI, Yale U.
Sunil Sinha, APS, Argonne National Laboratory

General User Proposal Study Panels

The Proposal Study Panels met in November 1996, March 1997, and July 1997 to review and rate General User research proposals for the FY 1997 cycles. PSP members are drawn from the scientific community and usually serve a two year term. Members during FY 1997 were:

UV Panel

Daniel Fischer	NIST
David Hanson	SUNY
Boris Sinkovic	NYU
David Tanner	U. of Florida

X-Ray Imaging/Other Panel

Chris Jacobsen	SUNY
Alastair MacDowell	Lucent Tech./Bell Labs.
Steve Sutton	U. of Chicago

X-Ray Biology

Aneel Aggarwal	Columbia
Jens Birktoft	Hoffmann-LaRoche
Howard Einspahr	Bristol-Myers Squibb
James Hurley	NIH
Thomas Terwilliger	LANL
Gregory Van Duyne	U. of Penn

X-Ray Spectroscopy Panel

Chuck Bouldin	NIST
Bruce Bunker	U. of Notre Dame
Lars Furenlid	NSLS
Steven Heald	APS
William Orme-Johnson	MIT
James Penner-Hahn	U. of Michigan
Linda Powers	Utah State U.
Dale Sayers	U. of North Carolina

X-Ray Scattering/Diffraction Panel

Joel Brock	Cornell U.
Jerome Cohen	NWU
Simon Moss	U. of Houston
Sunil Sinha	ANL
Cullie Sparks	ORNL
Thomas Russell	IBM

Allocation Panel

The Allocation Panel met in November 1996, March 1997, and July 1997 to allocate time on beamlines to each General User proposal for the FY 1997 cycles. Allocation Panel members are drawn from the scientific community and usually serve a two year term. Members during FY 1997 were:

UV Members

Harold Ade	NCSU
David Heskett	U. of R.I.
Jan Hrbek	BNL-Chemistry
Paul Stevens	Exxon
Elio Vescovo	BNL-NSLS

X-Ray Members

Malcolm Capel	BNL-Biology
Mark Chance	Albert Einstein
Alex Darovsky	SUNY-Stony Brook
Lars Furenlid	BNL-NSLS
John Hill	BNL-Physics
James McBreen	BNL-DAS
Gavin Watson	U. of Maryland

NSLS STAFF

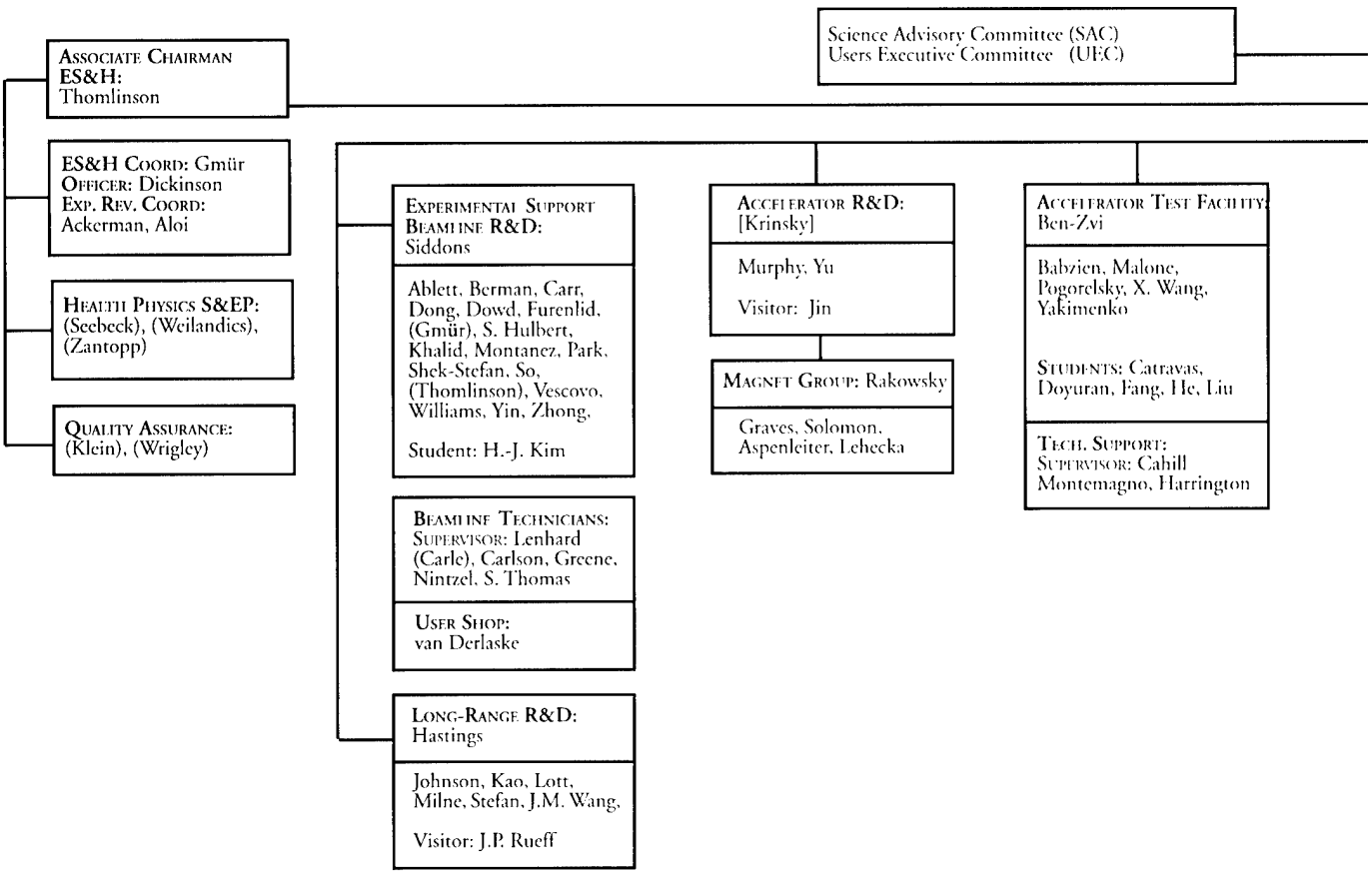

* Temporary

** Reports to Denis McWhan,
BNL Assoc. Dir. for Basic Energy Sciences

[ ] NSLS Personnel with Multiple Functions

( ) PRT personnel or member of non-NSLS division

NSLS Staff

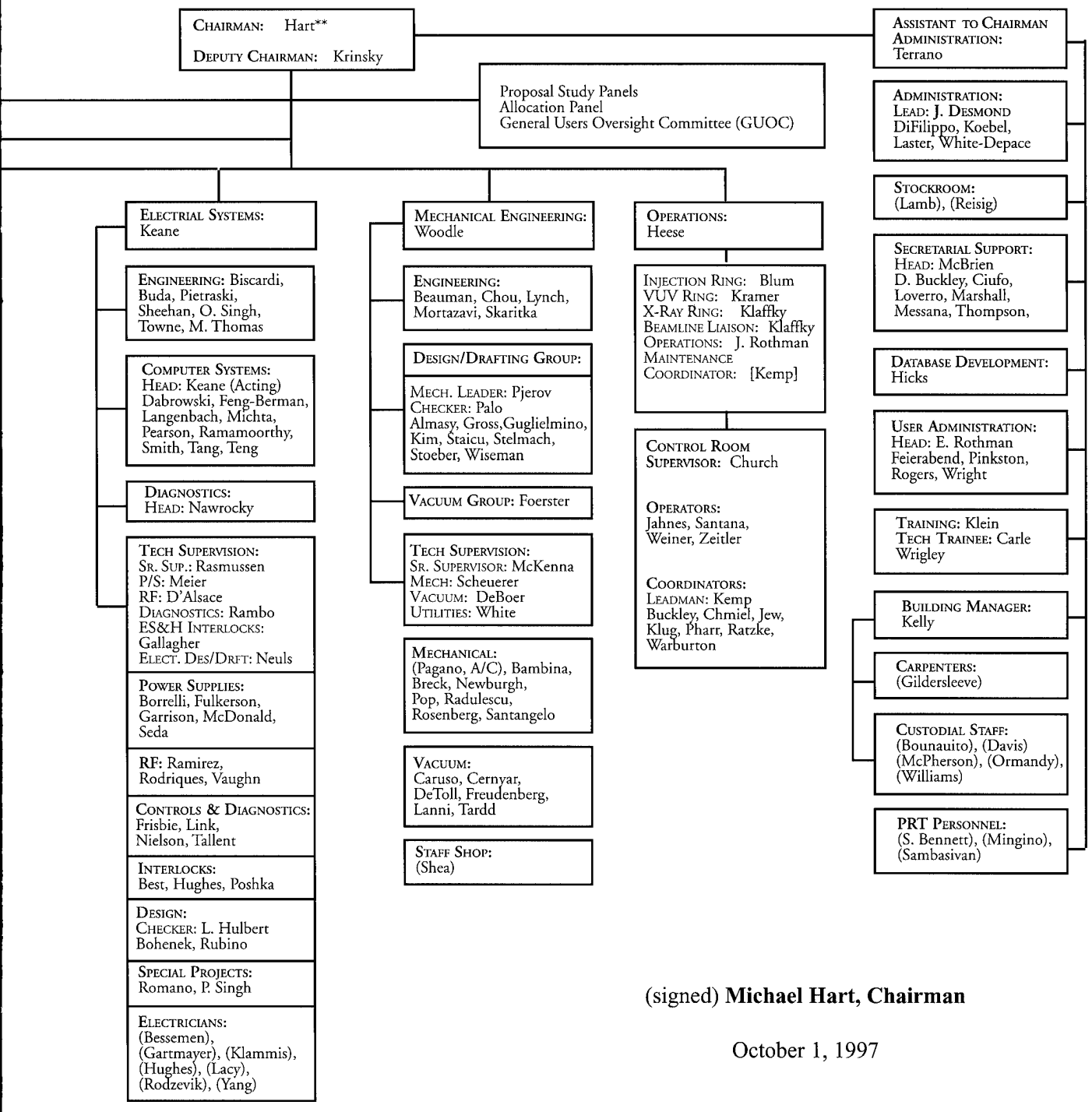

(signed) **Michael Hart, Chairman**

October 1, 1997

NSLS Beamline Guide

October 1997

This table lists the abbreviations appearing in the Beamline Guides.

ARUPS	=	Angle-Resolved Ultraviolet Photoemission Spectroscopy
CD	=	Circular Dichroism
C-T	=	Czerney-Turner
ERG	=	Extended Range Grasshopper
EXAFS	=	Extended X-Ray Absorption Fine Structure
IR	=	Infrared
LEGS	=	Laser Electron Gamma Source
MCD	=	Magnetic CD
MI	=	Michelson Interferometer
NEXAFS	=	Near Edge X-ray Absorption Fine Structure
NIM	=	Normal Incidence Monochromator
PGM	=	Plane Grating Monochromator
SEXAFS	=	Surface EXAFS
SGM	=	Spherical Grating Monochromator
S-N	=	Seya-Namioka
SXES	=	Soft X-ray Emission Spectroscopy
TGM	=	Toroidal Grating Monochromator
TOK	=	Transverse Optical Krystron
UPS	=	Ultraviolet Photoemission Spectroscopy
WB	=	White Beam
WDI	=	Wavefront Dividing Interferometer
XPS	=	X-ray Photoemission Spectroscopy
XAS	=	X-ray Absorption Spectroscopy

VUV Beamline Guide

Beam line	Research Program	Mono.	Affiliation	Local Contact	Spokesperson
U1A	SEXAFS, ARUPS, XPS	8-500 A	Exxon	B DeVries 516-344-5501 516-344-5206	J Chen 908-730-2738
U1B	(Conceptual)	TGM	Exxon	B DeVries 516-344-5501 516-344-5206	J Chen 908-730-2738
U2A	IR		Carnegie Inst. Wash	R Lu 516-344-5502 202-686-2410	R Hemley 202-686-2410x2465
U2B	IR Microscopy, Spectroscopy	MI	Albert Einstein	L Miller 516-344-5502 516-344-3800	M Chance 718-430-4136/2894
U3A	Detector and system calibration; meas. of material optical const.; spectrometeric properties	DC/DG	Smiths Astro Obs Bechtel Nevada Los Alamos Natl Lab	A Burek 516-344-2838 516-344-5503	R Blake 505-466-0566
U3B	(Conceptual)				
U3C	Photoelectron spect.; exp. system and detector calibrations	ERG	Los Alamos Natl Lab Sandia Natl Lab Bechtel Nevada SFA, Inc	M Sagurton 516-344-5503 516-344-5708	R Blake 505-466-0566
U4A	Photoemission spectroscopy to study electronic structure in solids, surfaces	TGM	Boston U No Carolina St U BNL-NSLS Rutgers U	S Hulbert 516-344-5504 516-344-7570	K Smith 617-353-6117
U4B	Soft x-ray and/VUV photoemission spectroscopy and photo absorption	SGM	Naval Res Lab BNL-NSLS SRRC	J Park 516-344-7290 516-344-4744	Y Idzerda 202-767-4481

Beam line	Research Program	Mono.	Affiliation	Local Contact	Spokesperson
U4IR	Grazing incid. Reflectivity in UHV; transmission & normal incidence reflectivity	MI, WDI	BNL-NSLS	G Williams 516-344-3634 516-344-7529	G Williams 516-344-3634 516-344-7529
U5	Diagnostic instrument monitors beam parameters during operations and machine studies		BNL-NSLS	R Nawrocky 516-344-5505 516-344-4449	R Nawrocky 516-344-5505 516-344-4449
U5UA	Spin polarized angle-resolved ultraviolet photoemission	TGM	BNL-NSLS BNL-Physics ANL U of Texas	E Vescovo 516-344-5505 516-344-7399 S Hulbert 516-344-7570	E Vescovo 516-344-5505 516-344-7399
U6	Lithography	WB		516-344-5506	
U7A	XPS and XAS on surface and in bulk, under vacuum and atm.P	TGM	BNL-Physics BNL-Chemistry Dow Chem NIST U of Michigan Rutgers U Texas A&M U	Q Dong 516-344-5507 516-344-5358	D Fischer 516-344-5177
U7B	Photoemission; SEXAFS	PGM	BNL-NSLS	Q Dong 516-344-5507 516-344-5358	S Hulbert 516-344-5507 516-344-7570
U8A	ARUPS NEXAFS	TGM	UCA@Riverside	J Yarmoff 516-344-5508 909-787-5336/3537	R McFeely 914-945-2068
U8B	ARUPS NEXAFS	TGM	IBM	K Zhang 516-344-5508	R McFeely 914-945-2068 M Banaszak-Holl 313-763-2283
U8C	Zone plate monochr. evaluation; reflectivity measurements of thin films and multilayers	ZONE PL.	IBM	R McFeely 516-344-5508 914-945-2068	R McFeely 914-945-2068
U8D	(Conceptual) Scanning soft x-ray microscopy		IBM	R McFeely 516-344-5508 914-945-2068	R McFeely 914-945-2068

Beam line	Research Program	Mono.	Affiliation	Local Contact	Spokesperson
U9A	(Planned) PSD measurements of UHV materials at room temperature	WHTE.LIGHT	BNL-NSLS	C Lanni 516-344-7766 516-344-4100	C Foerster 516-344-4754
U9B	Absorption.;CD;MCD; flores/phosphorescence spectrocpy (incl. times-res. fl.)	C-T	BNL-Biology	J Sutherland 516-344-5509 516-344-3406	J Sutherland 516-344-5509 516-344-3406
U10A	(Commissioning GU {1998} High Brightnes IR measurements on "bad metals"	INFRARED	BNL-NSLS BNL-Physics	C Homes 516-344-5510 516-344-7579	G Carr 516-344-5510 516-344-2237
U10B	IR microspectroscopy	INFRARED	BNL-NSLS Northrop Grumman	G Carr 516-344-5510 516-344-2237	G Williams 516-344-5510 516-344-7529
U11	Gas phase photo-ionization and spectroscopy	NIM	BNL-DAS BNL-Biology BNL-NSLS	J Sutherland 516-344-5511 516-344-3406 S Hulbert 516-344-7570	B Klemm 516-342-4001
U12A	Soft x-ray photoemission (SXPS); XAS; NEXAFS		Oak Ridge Natl Lab BNL-NSLS BNL-DAS	S Hulbert 516-344-5512 516-344-7570	D Mullins 423-574-2796
U12B	(Available)	TGM			
U12IR	IR and far-IR measurement time-resolved (pump/probe IR & far-IR spectroscopy		U of Florida BNL-NSLS	G Carr 516-344-5512 516-344-2237	D Tanner 352-392-4718
U13UA	High res VUV/soft x-ray abs and electron spectr. (incl. spin-polarized photoemission)	SGM	BNL-NSLS	S Hulbert 516-344-5913 516-344-7570	S Hulbert 516-344-5913 516-344-7570
U13UB	UV/VUV spectroscopy; hi resol. Angle resolved photoemission of solid surf.;pump-probe GU-'98	WB	BNL-NSLS BNL-Physics Boston U Brandeis U	S Hulbert 516-344-5513 516-344-7570	E Jensen 617-736-2865
U13UC	Interferometry	WB	Lucent Tech	S Spector 516-344-5513	O Wood 908-582-4457

Beam line	Research Program	Mono.	Affiliation	Local Contact	Spokesperson
U14A	VUV/soft x-ray spectroscopy Auger Photo-Electron Coincidence Spectroscopy (APECS)	PGM	BNL-NSLS Rutgers U	M Shek 516-344-5514 516-344-5930	S Hulbert 516-344-5514 516-344-7570 R Bartynski 908-445-4839
U14B	Diagnostic Instrument: VUV Ring beam position monitoring	WB	BNL-NSLS	J Hastings 516-344-5514 516-344-3930	J Hastings 516-344-5514 516-344-3930
U15	Soft x-ray spectroscopy (solids and gases)	TGM	BNL-NSLS SUNY@Buff SUNY@SB	A Wen 516-344-5515 516-632-7918	D Hanson 516-632-7917 Y Kao 716-645-2576
U16A	(Unassigned)				
U16B	Unassigned - NSLS is handling any GUs who need time here		BNL-NSLS	S Hulbert 516-344-5516 516-344-7570	S Hulbert 516-344-5516 516-344-7570

X-Ray Beamline Guide

Beam line	Research Program	Energy (keV)	Affiliation	Local Contact	Spokesperson
X1A	Soft x-ray imaging	10-80 Å	SUNY@SB No Carolina St U BNL-NSLS LBNL ANL	S Wirick 516-344-5601 516-632-8095	J Kirz 516-632-8106 C Jacobsen 516-632-8093 516-344-4723
X1B	Soft x-ray spectroscopy	10-50 Å	BNL-Physics KFA - Juelich Fritz-Haber-Inst Boston U	P Johnson 516-344-5701 516-344-3705	P Johnson 516-344-5701 516-344-3705
X2A	Surface scattering		Exxon Oak Ridge Natl Lab	S Bennett 516-344-5602 516-344-4719	K Liang 516-344-5602 908-730-3032
X2B	X-ray microtomography	6.5-30, WB	Exxon	S Bennett 516-344-5602 516-344-4719	J Dunsmuir 908-730-2548
X3A1	Short wavelength crystallography, diffration and scattering		SUNY@Buff SUNY@SB Amoco Corp Alfred U	L Ribaud 516-344-5603 716-645-6800x2218 G Wu 516-344-5603	P Coppens 716-645-6800,x2217
X3A2	Diffractometry; x-ray spectroscopy; scattering; crystallography; small angle scattering	3-31	SUNY@SB SUNY@Buff Amoco Corp Alfred U	L Ribaud 516-344-5603 716-645-6800x2218 G Wu 516-344-5603	P Coppens 716-645-6800,x2217
X3B1	X-ray spectroscopy; powder diffraction	4.0-40 KEV	SUNY@SB SUNY@Buff Amoco Corp Alfred U	L Ribaud 516-344-5603 716-645-6800x2218 P Stephens 516-632-8156 516-344-3176/5634	P Coppens 716-645-6800,x2217

Beam line	Research Program	Energy (keV)	Affiliation	Local Contact	Spokesperson
X3B2	Surface science	4-20	SUNY@Buff SUNY@SB Amoco Corp Alfred U	L Ribaud 516-344-5603 716-645-6800x2218 P Stephens 516-632-8156 516-344-3176/5634	P Coppens 716-645-6800,x2217
X4A	Multiwavelength anomalous diffraction analysis of crystalline biological macromolecules	4-30 KEV	Howard Hughes	C Ogata 516-344-5604 516-344-7435	W Hendrickson 212-305-3456
X4B	(Conceptual)				
X4C	Diffraction meas. from biological macromolecules	7-20 KEV	Howard Hughes	C Ogata 516-344-5585 516-344-7435	W Hendrickson 212-305-3456
X5A	Laser Electron Gamma Source (LEGS); medium energy nuclear physics	80-400 MEV	BNL-Physics Norfolk St U Ohio U U of So Carolina SUNY@SB Syracuse U U of Virginia VA Polytech & St U U of Paris U of Mainz Frascati Natl Lab U of Rome II	C Thorn 516-344-5605 516-344-7798	A Sandorfi 516-344-7951
X5B	Diagnostic				
X6A	Time and space resolved dispersive x-ray spectroscopy	4-20	NSLS	M Shek 516-344-5930	D. Peter Siddons 516-344-2738
X6B	X-ray scattering	2.4-21.0	NSLS	M Shek 516-344-5930	D. Peter Siddons 516-344-2738

Beam line	Research Program	Energy (keV)	Affiliation	Local Contact	Spokesperson
X7A	High resolution structural studies through powder diffraction	5-45 KEV	Air Products & Chem BNL-Physics Mobil Carnegie Inst of Was UOP U of Pennsylvania SUNY@SB Chevron UCA@Santa Barbara NIST	D Cox 516-344-5607 516-344-3818 P Woodward 516-344-5065	D Cox 516-344-5607 516-344-3818 P Woodward 516-344-5065
X7B	Crystallography; wide angle scattering	5-21	Swedish Nat Res Coun BNL-Chemistry	J Hanson 516-344-5707 516-344-4381	T Koetzle 516-344-4384 J Larese 516-344-4349 516-344-4438
X8A	Calibration of mirrors & dector systems; material optical constants; spectrometric properties	0.26-5.9	Los Alamos Natl Lab Smiths Astro Obs Bechtel Nevada	M Sagurton 516-344-5608 516-344-5708	R Blake 505-466-0566
X8C	Diffraction from biological macromolecules and detector calibrations AXAF	5-20 KEV	Los Alamos Natl Lab Bechtel Nevada Smiths Astro Obs	M Sagurton 516-344-5608 516-344-5708	G Idzorek 505-667-8848
X9A	Time-resolved x-ray footprinting;	3.4-18.6	Albert Einstein Rockefeller U Sloan-Kettering Inst	M Sullivan 516-344-5609 516-344-3800	M Chance 718-430-4136 718-430-2894
X9B	Small angle scattering; EXAFS; multiple anomalous diffraction (MAD); protein x-ray diffraction	3.2-18.8	Albert Einstein NIH	M Sullivan 516-344-5609 516-344-3800	M Chance 718-430-4136 718-430-2894
X10A	Diffraction; small angle scattering; crystallography; scattering; SAXA; WAXS	6-15.2 KEV	Exxon	S Bennett 516-344-5610 516-344-4719	E Sirota 908-730-3407
X10B	Scattering; crystallography PXD, Reflectivity	8,12 KEV	Exxon	B Zhang 516-344-5710 516-344-3553	E Sirota 908-730-3407
X10C	EXAFS	4.0-24.0	Exxon	M Sansone 516-344-3265 908-730-0100	P Stevens 908-730-2584

Beam line	Research Program	Energy (keV)	Affiliation	Local Contact	Spokesperson
X11A	EXAFS	4.5-35	Naval Res Lab Mobil U of Connecticut No Carolina St U Hoechst Celanese BNL-DAS The DuPont Co U of Washington Rice U Ill Inst Tech (IIT) Naval Surf War Cntr Georgia Inst Tech U of Notre Dame Advanced Fuel NJ Inst of Tech	K Pandya 516-344-5611 516-344-3165	D Sayers 919-515-4453
X11B	EXAFS	1.7-8	Naval Res Lab U of Notre Dame Mobil No Carolina St U The DuPont Co BNL-NSLS U of Connecticut Advanced Fuel Naval Surf War Cntr Hoechst Celanese Ill Inst Tech (IIT) U of Washington Rice U	K Pandya 516-344-5611 516-344-3165	D Sayers 919-515-4453
X12A	Instrument development and x-ray physics		BNL-NSLS	J Ablett 516-344-2738 516-344-5627 P Siddons 516-344-2738 516-344-5627	P Siddons 516-344-2738
X12B	Time-resolved and static x-ray diffr. of macromol. crystallography	6-15	BNL-Biology	M Capel 516-344-5712 516-344-5234	M Capel 516-344-5712 516-344-5234
X12C	Macromolecular crystallography; multi-wavelength anomalous dispersion (MAD)	8-13	BNL-Biology	R Sweet 516-344-5642 516-344-3401	R Sweet 516-344-5642 516-344-3401

Beam line	Research Program	Energy (keV)	Affiliation	Local Contact	Spokesperson
X13	R&D optics development; soft x-ray utilization		BNL-NSLS	E Johnson 516-344-5613 516-344-4603 J Hastings 516-344-3930	E Johnson 516-344-5613 516-344-4603
X14A	Scattering crystallogr. spectroscopy phase ID and resid. strain meas. high temp x-ray diffraction	3.5-40	Oak Ridge Natl Lab Univ of Ill Urb Cham U of Tennessee U of Houston Sandia Natl Lab	J Bai 516-344-5614 516-344-2583	G Ice 423-574-2744
X14B	(Planned) Manuf. res. for hard x-ray lithogrphy exposures for precision microfabrication	WHITE	BNL-NSLS	E Johnson 516-344-5614 516-344-4603 J Milne 516-344-5910	E Johnson 516-344-5614 516-344-4603 P Siddons 516-344-2738, 5627
X15A	X-ray standing waves	3-20, WB	ANL BNL-NSLS Northwestern U	Z Zhong 516-344-5615 516-344-5617	M Bedzyk 630-252-7763
X15B	X-ray absorption spectroscopy of complex, reactive, very dilute systems	1.8-1O	Lucent Tech	P Northrup 516-344-3565 516-344-3565	P Citrin 908-582-5275
X16A	Surface diffraction	4-12	Lucent Tech U of Illinois	W Lehnert 516-344-5616 516-344-3635	K Evans-Lutterodt 908-582-2154
X16B	rapid access for sample characterization; powder characterization;thin film characeterization	7.85	Lucent Tech BNL-NSLS	W Lehnert 516-344-5716 516-344-3635	K Evans-Lutterodt 908-582-2154
X16C	Novel spectroscopy; diffraction	3-16	Lucent Tech U of Illinois	W Lehnert 516-344-5816 516-344-3635	M Marcus 908-582-2749
X17B1	X-ray scattering at high pressure and temperature	20-100, WB	BNL-NSLS SUNY@SB	Z Zhong 516-344-5717 516-344-5617	J Hastings 516-344-3930
X17B2	Medical research: Angiography;Bronchography computed tomography; radiotherapy	27-35	BNL-NSLS BNL-Medical SUNY@SB Ill Inst Tech (IIT) Stanford U	N Gmur 516-344-5617 516-344-2490	W Thomlinson 516-344-3937

Beam line	Research Program	Energy (keV)	Affiliation	Local Contact	Spokesperson
X17C	Hi P research; energy dispersive diffraction from microscopic sample volumes	10-100, WB	Naval Res Lab LLNL Carnegie Inst of Was U of Chicago	J Hu 516-344-5917 202-686-2410	H Mao 202-686-4454 E Skelton 202-767-3014
X18A	Diffuse and surface scattering	4-20	U of Missouri U. of Maryland BNL-DAS U of Illinois Purdue U Penn St U	S Ehrlich 516-344-5618 516-344-7862 J Schwanof 516-344-5618 516-344-5635	G Liedl 317-494-4100 S Ehrlich 516-344-7862
X18B	X-ray spectroscopy	7-40	UOP Chevron AlliedSignal BNL-NSLS Dow Chem PPG Industries General Electric	S Khalid 516-344-5718 516-344-7496	P Siddons 516-344-2738 S Khalid 516-344-7496
X19A	X-ray absorption spectroscopy: EXAFS and XANES	2.1-25.6	BNL-DAS U of Michigan BNL-NSLS U of Kentucky UCA@Davis Rutgers U	F Lu 516-344-5619 516-344-2338 L Furenlid 516-344-5699	L Furenlid 516-344-5699
X19C	Topography; liquid surface scattering	4-25, WB	Johns Hopkins U Army Research Lab SUNY@SB NASA U of Wisconsin Northrop Grumman Dartmouth Coll	Z Huang 516-344-5719 312-702-7229	M Dudley 516-632-8500 M Schlossman 312-996-8787
X20A	X-ray Scattering and diffraction	6.3-12	MIT IBM	J Jordan-Sweet 516-344-5720 914-945-3322	R Birgeneau 617-253-4937 J Jordan-Sweet 914-945-3322 516-344-5192
X20B	Scattering at fixed energy	17.4	IBM MIT	J Jordan-Sweet 516-344-5720 914-945-3322	J Jordan-Sweet 516-344-5720 914-945-3322 R Birgeneau 617-253-4937

Beam line	Research Program	Energy (keV)	Affiliation	Local Contact	Spokesperson
X20C	X-ray scattering and diffraction with high flux by multilayer monochromator	4-11	IBM MIT	J Jordan-Sweet 516-344-5720 914-945-3322	J Jordan-Sweet 516-344-5720 914-945-3322 R Birgeneau 617-253-4937
X21	Inelastic x-ray scattering	5-10	BNL-NSLS	C Kao 516-344-5721 516-344-4494	C Kao 516-344-5721 516-344-4494
X22A	X-ray scattering of thin films, multilayers, catalytic materials, electrochemical interfaces	10 NOM.	BNL-Physics BNL-DAS U of Maryland	B Ocko 516-344-5622 516-344-4299	D Gibbs 516-344-4608
X22B	X-ray scattering and spectroscoppy of liquid surfaces; magnetic stud. under magnetic fields	5-10	BNL-Physics Harvard U ANL	B Ocko 516-344-5622 516-344-4299	D Gibbs 516-344-4608
X22C	X-ray Scattering studies of magnetism; structure and phase behavior of metal surfaces	3-12	BNL-Physics ANL U of Maryland	J Hill 516-344-5622 516-344-3736	D Gibbs 516-344-4608
X23A2	EXAFS	5.4-30	NIST	J Woicik 516-344-5823 Z Fu 516-344-3156 516-344-5059	J Woicik 516-344-5823
X23A3	Topography; small-angle scattering	5-30, WB	NIST	D Fischer 516-344-5623 516-344-5177 Z Fu 516-344-3156 516-344-5059	G Long 301-975-5975
X23B	EXAFS; scattering; crystallography	3-11	Naval Res Lab	J Kirkland 516-344-5723 516-344-2258	T Elam 202-767-3015

Beam line	Research Program	Energy (keV)	Affiliation	Local Contact	Spokesperson
X24A	Atomic, molecular, and optical physics with x-rays	1.8-5.0	NIST BNL-NSLS Northwestern U U of Rhode Island U of Tennessee Brooklyn Coll - CUNY U of Maryland	B Karlin 516-344-7863 516-344-5624	T Jach 301-975-2362
X24C	Photoemission and reflectance spectroscopy	6-1800	Naval Res Lab	J Rife 516-344-5724 202-767-4654 J Kirkland 516-344-2258	M Kabler 202-767-2223
X25	High intensity, high brightness photon beam; high Q-resolution elastic scattering	3-30	BNL-NSLS	L Berman 516-344-5625 516-344-5333 Z Yin 516-344-5625 516-344-5525	L Berman 516-344-5625 516-344-5333
X26A	X-ray Microscopy; structural biology; atomic and molecular physics	4-20, WB	U of Chicago/CARS BNL-DAS BNL-Biology U of Georgia/SREL Cold Spring Harb Lab SUNY@SB	G Shea-McCarthy 516-344-5626 516-344-2229	S Sutton 630-252-0426
X26C	Dev. and applic. of x-ray microscopy techniques; Laue diffraction protein crystallography	4-30, WB	BNL-Biology BNL-DAS U of Chicago/CARS U of Georgia/SREL Cold Spring Harb Lab SUNY@SB	G Shea-McCarthy 516-344-5726 516-344-2229	S Sutton 630-252-0426
X27A	NSLS R&D only; instrument development and x-ray physics		BNL-NSLS	B Dowd 516-344-5738 516-344-7092	P Siddons 516-344-2738
X27B	NSLS R&D only; Develop exposure techniques; matls. char.; and tool development for microfab.		BNL-NSLS	E Johnson 516-344-5627 516-344-4603 J Milne 516-344-5910 516-344-5910	E Johnson 516-344-5627 516-344-4603 P Siddons 516-344-2738 516-344-5627

Beam line	Research Program	Energy (keV)	Affiliation	Local Contact	Spokesperson
X27C	Simultaneious small & wide angle x-ray scattering (SWAX) in real time		AlliedSignal BNL-Physics General Electric Hoechst Celanese Montell Polyolefins NIST SUNY@SB	F Yeh 516-344-5627 516-632-7892 Z Wang 516-632-7928	B Hsiao 516-632-7884 B Chu 516-632-7928
X28A	Instrument development; photon-based diagnostics and detector development for the X-ray Ring		BNL-NSLS	P Stefan 516-344-5728	P Stefan 516-344-2117
X28B	Photon-based diagnostics and detector development for the X-ray Ring		BNL-NSLS	P Stefan 516-344-2117	P Stefan 516-344-2117
X28C	Photon-based diagnostics and detector development for the X-ray Ring		BNL-NSLS	P Stefan 516-344-2117	P Stefan 516-344-2117
X29A	(Available)				
X29B	(Available)				
X30	Diagnostic Instrument		BNL-NSLS		

Beamline X27A: Recent developments in porous materials have demonstrated the potential to achieve ultra-light weightmetal structures at reduced cost using a solid-gas eutectic solidification process known as the Gasar process. The process is capable of producing controlled porosity in metals by influencing the size and shape of pores as well as the pore distributions. The stereo pair at right is a 3-D volume section of an aluminum alloy sample rendered from x-ray microtomography data. (See also Abstract on page B-245.)
R. Schulte, R. Meilunas, A. Tobin, J. Papazian, T. Donnellan (Northrup-Grumman), B.A. Dowd, D.P. Siddons (NSLS), and B. Andrews (BNL - Computing and Communications Division)

SEVEN
APPENDICES

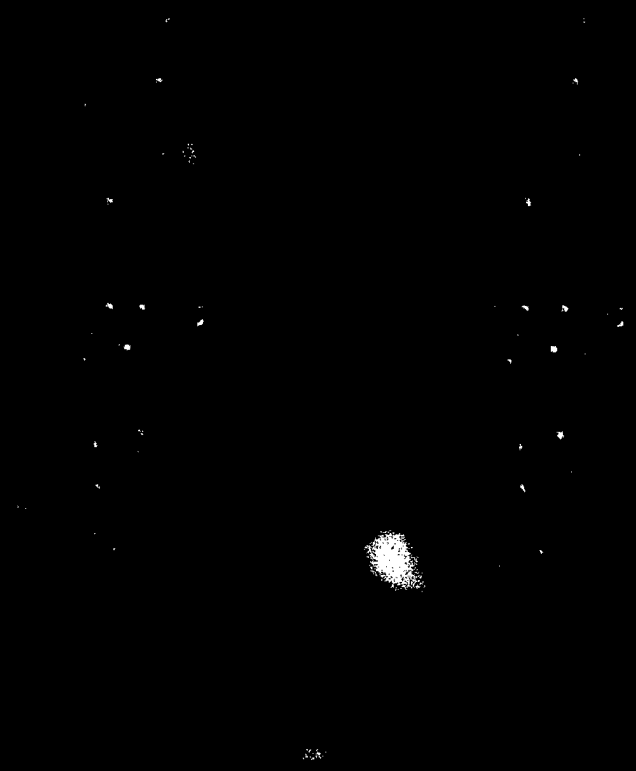

From the Managing Editor

Four years ago, in the FY 1994 Activity Report, the NSLS implemented a new Web-based abstract submission system. After the author enters the information using their Web browser software, the system stores the abstracts in an Oracle database which then allows the NSLS to publish the abstracts in many formats. The abstracts are not only being published in the printed book now, but also on the World Wide Web in both HTML and PDF formats. The past years' Abstracts and Activity Reports can be found at the NSLS Home Page, www.nsls.bnl.gov, under "Science".

For this 1997 edition of the Activity Report, almost 600 abstracts were received (Appendices A and B). This is 100 more than last year and indicates that the NSLS user community is more willing and able to use the system. At the time the abstract submission system was implemented, it was viewed as very experimental and cutting-edge because there were not many such systems in use. Today, however, the scene on the Internet is quite different. Web forms are much more common and browser software has become more standardized, so people are more comfortable using them. In addition, the NSLS abstract system has been fine-tuned and enhanced over the past couple of years, becoming easier to use for both the authors and NSLS Production Staff.

This edition of the Activity Report also contains a higher than usual number of publication references (Appendix C). The reason is that many users submitted more extensive lists to the NSLS this year, with publication dates in some cases dating back to 1990. Production Staff had to check all previous editions of the Activity Report to identify any references which had never before been included. To complete the official record of publications which used synchrotron data taken at the NSLS, the previously unlisted references were added to this year's list. Appendix C therefore contains publication references dating from 1996-1997 as well as a fair number from previous years.

ABSTRACTS

VUV Beamlines

Beamline U1A

Beamline U2B

Beamline U4A

Beamline U4B

Beamline U4IR

Beamline U5UA

Beamline U7A

Beamline U7B

Beamline U8A

Beamline U8B

Beamline U9B

Beamline U11

Beamline U12IR

Beamline U13UA

Beamline U14A

Orientation and Order in Microcontact-Printed, Self-Assembled Monolayers of Alkanethiols on Gold Investigated with NEXAFS	U1A

D. Fischer, A. Marti, and G. Hähner (ETH Zurich, Department of Materials)

The field of self-assembled monolayers (SAMs) has been a research area of increasing interest for more than a decade due to their ease of preparation and large number of potential applications. Particularly alkanethiols, mostly adsorbed on gold, are well characterized and known to establish well-ordered and highly oriented films. The recently developed technique of microcontact-printing (μCP) by Whitesides et al. allows SAMs to be laterally structured down to the (sub)micrometer range. In short, a PDMS stamp that is inked with the thiol solution is used to print the thiol onto the substrate surface.

We have investigated such contact-printed (CP) layers of alkanethiols on gold with NEXAFS and compared them to layers prepared by the conventional immersion technique [1]. We studied the influence on order and orientation of the alkyl chains of both the chain length of the thiols and the concentration of the solution that was used for stamping and for immersion.

Our study shows that the CP process, when performed with a sufficiently concentrated solution of the thiol, can result in monolayers indistinguishable from those established by immersion into solution, independent of the thiol chain length. For lower concentrations, however, CP monolayers show a significant deviation from well-ordered films and have to be classified as mainly disordered. As with SAMs prepared from solution, shorter chains (dodecanethiol) lead to a lower degree of order compared to longer ones (hexadecanethiol) and hence a relatively higher percentage of *gauche* conformations. NEXAFS is capable of detecting this difference of *gauche* defects, which is on the order of 30%. Since we do not observe any difference in our NEXAFS spectra for the different preparation methods for one chain length and sufficiently high concentrations, the upper limit of the difference in the density of defects in the resulting films can be estimated to be 30%.

[1] D. Fischer, A. Marti and G. Hähner, J. Vac. Sci. Technol. A 15 (4), 2173, (1997)

NEXAFS Studies of Benzene on the Si(100)-2x1 Surface	U1A

M.J. Kong, A.V. Teplyakov and S.F. Bent (New York University)

Interaction of benzene with various single crystalline surfaces has served as a reference point in the studies of a variety of processes. Here we present the Near Edge X-ray Absorption Fine Structure (NEXAFS) studies of benzene on Si(100)-2x1. This system is an excellent model for the interaction of hydrocarbons with silicon surfaces and for the formation of silicon-carbon interface, relevant for the manufacturing of electronic devices. Benzene has been studied on silicon surfaces relatively extensively; however, questions still remain about the detailed chemistry. Most importantly, it is still not understood if benzene reacts with the Si(100)-2x1 surface only at room temperature or if this reaction occurs at 100 K as well. Previous studies used thermal desorption spectrometry and HREELS to answer this question, but the obtained results were inconclusive. The use of NEXAFS allows one to determine if benzene is chemisorbed or physisorbed at cryogenic temperature by following its signature split p* transition, which is characteristic of a conjugated system. Furthermore, the nature of the product of the reaction of benzene with the Si(100)-2x1 surface at room temperature can be probed by using the same approach. Fig. 1 presents the spectrum of benzene taken at glancing and at normal incidence for submonolayer coverage adsorbed on the Si(100)-2x1 surface at 100 K. The split p* transition is easily seen at glancing incidence. The average of the spectra taken at glancing and normal incidence of the photon beam is consistent with the multilayer spectra of benzene and with the literature results on benzene physisorbed on unreactive surfaces. The angle between the plane of the benzene molecule and Si(100)-2x1 surface was found to be 30, which is consistent with the strongly corrugated nature of the Si(100)-2x1 surface. Fig. 2 presents the spectra analogous to those described in Fig. 1, but taken at room temperature. These spectra are clearly different from those of the physisorbed benzene. The split p* transition, signature of conjugation, seems to be absent, whereas s*C-H, s*C-C, and s*C=C are clearly seen. All these results suggest that benzene physisorbs on the Si(100)-2x1 surface at 100 K without significant alteration of its electronic structure. At room temperature, however, it reacts with this surface chemically to form an intermediate without conjugated double bonds. One of the possible intermediates is shown in the inset for Fig. 2. Further studies are needed to support this structure.

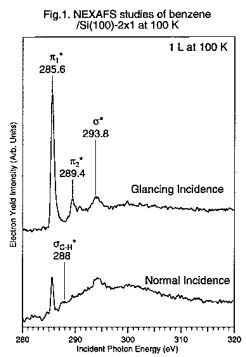

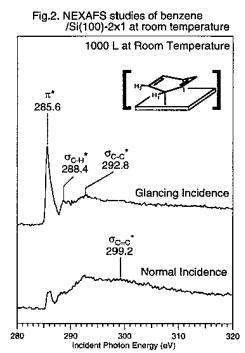

NEXAFS Studies of Diels-Alder Reactions of Butadienes with the Si(100)-2x1 Surface as a Dienophile — U1A

A. Teplyakov, M. J. Kong, S.E. Bent (New York U.)

Over the last few decades, increasing use of semiconductor-based electronic devices has directed serious attention towards the chemical properties of interfaces, specifically, towards the silicon-carbon interface. Directly related to the properties of this interface, is the semiconductor chemistry of hydrocarbons at silicon surfaces. The interaction of simple hydrocarbons (ethylene, acetylene, benzene) has been studied on silicon single crystal surfaces in some detail; however, even for these simple hydrocarbons, the reaction chemistry is still not completely understood. In the studies presented here, we direct our attention to a Diels-Alder type reaction between the 2,3- dimethyl-1,3-butadiene and the silicon dimers of the Si(100)-2x1 surface which was theoretically predicted by R. Konecny and D. Doren.1 Recent vibrational spectroscopic and thermal studies of these systems suggest that the product of this interaction is indeed a Diels-Alder adduct; however, only Near Edge X-ray Absorption Fine Structure (NEXAFS) studies can allow for accurate determination of the geometry of this intermediate, especially the angle between the double bond of the reaction product and the substrate surface. In addition, it allows us to probe the differences between the reaction at high (300 K) and low (100 K) temperatures.

Figure 1 presents the temperature dependent studies of 2,3-dimethyl-1,3-butadiene at glancing incidence of the photon beam. The split π transition present in the spectrum of submonolayer 2,3- dimethyl-1,3-butadiene adsorbed on a Si(100)-2x1 at 100 K, as well as all other transitions, are consistent with the multilayer spectrum of the same compound, suggesting that 2,3-dimethyl-1,3- butadiene does not interact chemically with the Si(100)-2x1 surface at 100 K. At the same time, spectrum of Si(100)-2x1 surface exposed to the submonolayer coverage of 2,3-dimethyl-1,3- butadiene at room temperature is completely different. The single π transition now appears at higher photon energy than in the physisorbed compound, indicating that the molecule is chemisorbed at room temperature.

Figure 2 presents the polarization dependence of the NEXAFS intensities for a submonolayer coverage of 2,3-dimethyl-1,3-butadiene adsorbed on a Si(100)-2x1 surface at room temperature. The calculations based on relative intensities of the π transition at normal and glancing incidence give 41° as the angle between the plane of the double bond in the Diels-Alder adduct and the Si(100)-2x1 surface, which is in agreement with the theoretical predictions.

(1) R. Konecny and D. Doren (submitted to J. Am. Chem. Soc.)

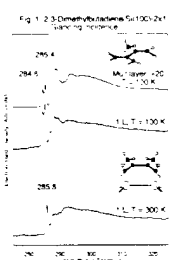

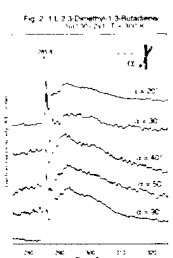

Construction of an Infrared Beamline Dedicated to the Study of Bio-Medical Problems — U2B

M.R. Chance, L.M. Miller, Q. He, M. Sullivan (AECOM) and G. Williams (NSLS)

Beamline U2B at the National Synchrotron Light Source is being designed and built as an infrared beamline dedicated to the study of biological problems. During the winter shutdown of 1996, the horizontal acceptance of the U2B beamline was increased from 10 to 45 milliradians, in order to increase the overall flux of the beamline. The final designs have been approved and the construction has begun for the mirror box, which will accept the infrared light out of the UV ring. The diamond window has been ordered, which will separate the ultrahigh vacuum of the UV ring from the rough vacuum of the beamline. The infrared spectrometer has been purchased, installed, and is running with an internal infrared source until beamline construction is complete. The spectrometer is a Nicolet Magna 560, equipped with interchangeable (1) KBr and silicon beamsplitters and (2) MCT and DTGS detectors. These beamsplitter/detector combinations permit data collection in the mid- (650-4000 cm^{-1}) and far- (10-650 cm^{-1}) infrared regions. Most recently, a NicPlan infrared microscope, equipped with a video imaging camera and motorized x-y sample stage, has just been included in the Nicolet system, adding the capability for infrared microspectroscopy. Finally, 300 ft^2 of laboratory space has been awarded to the biological infrared program for sample preparation and characterization.

Synchrotron Infrared Absorption of Single Crystal Brucite to 20 GPa | U2B

A. F. Goncharov, R. J. Hemley, and H. K. Mao (Carnegie Inst. of Washington)

The high-pressure behavior of brucite, $Mg(OH)_2$, is of great interest because this compound may serve as an analog of complex hydrogen-bearing silicates of the Earth's crust and mantle. In this work we studied for the first time the infrared absorption spectra of brucite single crystals. Measurements were done at U2B NSLS beamline using FT-IR spectrometer and diamond anvil cells. Samples of several micrometers thickness were loaded into the pressure chamber with ruby pressure gauge and KBr or NaCl pressure transmitting medium. Transmission spectra were normalized to the transmission of the cell with the medium at the same pressure.

The infrared spectrum of brucite in the mid-IR consists of O-H fundamental and its combination modes with the low-frequency lattice phonons. The O-H stretching mode is only weakly active in the geometry used (direction of propagation is perpendicular to the basal plane of the crystals) because the transition moment direction is parallel to the wave vector of light. We observe that O-H fundamentals broadens under pressure and at 4 GPa new bands appear at lower frequencies and gain intensity with pressure. These modes soften with pressure. The initial O-H fundamental loses intensity gradually and at approximately 20 GPa becomes almost unobserved. On the pressure release the initial IR spectrum is restored at ambient pressure, but some hysteresis is observed and new bands are seen almost to ambient pressure. The observed phenomena are interpreted as due to the phase transition, which involves displacements of hydrogen atoms from their original axial sites as was also proposed in recent neutron diffraction an Raman studies [1,2].

[1] T. S. Duffy et al., Am. Mineralogist, 80, 222 (1995)
[2] Catti et al., Phys. and Chem. of Minerals.

Synchrotron Infrared Absorption and Raman Spectroscopy in para-Hydrogen to >200 GPa. | U2B

A. F. Goncharov, R. J. Hemley, H. K. Mao, and J. F. Shu

We have studied solid H_2 by infrared and Raman spectroscopy to pressures in excess of 200 GPa and to 8 K. After cooling down to T<25 K we observe a ortho-para conversion in both phases I and II by monitoring the infrared spectra of the pure vibron and the zero-phonon rotation-vibration bands and the Raman spectra of the roton bands with time. We documented nearly complete ortho-para conversion for samples cooled at 33, 76 and 97 GPa, while one, cooled at 110 GPa contained a substantial amount of ortho-species even after 112 hours at 15 K. For pure para-H_2 the transition to the ordered phase (BSP, phase II) recorded at 110-120 GPa and 17 K is characterized by major and previously unobserved changes in rotation and rotation-vibration excitations. The second dramatic change of the low-frequency excitations (librons) occurs at 145-165 GPa, which is associated with the discontinuity in the Raman and infrared vibrons at the transformation to phase III. Librons in the phase III are strongly pressure dependent, indicating an increase in molecular ordering. New vibrons sidebands are observed in all three phases (I, II, and III) of para-H_2.

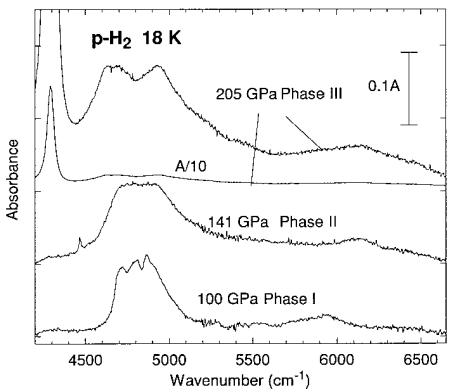

Figure 1. IR absorption spectra of para-H_2.

High-Pressure Synchrotron Infrared Spectroscopy of $Ar(H_2)_2$ and $CH_4(H_2)_2$ Compounds	U2B

A. F. Goncharov, M. Somayazulu, R. J. Hemley, H. K. Mao (Carnegie Inst. of Washington)

The infrared spectra of new hydrogen containing compound $Ar(H_2)_2$ and $CH_4(H_2)_2$ has been measured with synchrotron radiation to 220 GPa and 60 GPa, respectively, to study the ordering phenomena and/or possible metallization/dissociation transitions. The infrared spectra of these compounds consist of a number of IR-active fundamentals and combinational modes with rotational excitations and lattice phonons. All these excitations persist to highest pressures achieved, manifesting the stability of molecular structures under compression. Change of intensities of C-H stretching vibration and hydrogen vibron in $CH_4(H_2)_2$ is interpreted as due to unusual charge transfer between the CH_4 and H_2 molecules above 30 GPa. No Drude-type absorption to 0.3 eV was found for both compounds.

Drug Distribution in Human Hair Determined by Infrared Microscopy	U2B

K.S. Kalasinsky (Armed Forces Institute of Pathology), and D.G. Cameron (DHC Analysis)

Localization of drug metabolites within human hair is important in determining the pharmacokinetics of drug incorporation in hair. This information is critical to validate drug testing data from hair. Previous work at the NSLS had shown the feasibility of this project for resolving the drug incorporation issue on the synchrotron infrared microscope with longitudinally microtomed hair sections. Doped hairs compared to reference hairs showed spectral differences with bands corresponding to the frequencies of the drug of interest. However, patient hairs were obscured due to a contamination arriving form the sample prep process. Corrections were made to the preparation procedure and subsequent work was performed at NSLS this year. Repeat work of the doped hairs versus reference hairs were performed for cocaine and heroin drugs of abuse. The results showed the drug to be in the central medulla of the doped hair. Analysis of the patient hairs from cocaine and heroin abusers showed the same results. The drug was concentrated in the medulla of the hair. When the patient had non-medullated hair the drug was not present. Below is a topical graph of a hair from the synchrotron infrared microscope, mapped for the primary frequency band for cocaine in a drug abusers hair. The graph shows the drug to be in it highest concentration in the central portion of the hair and the lack of drug absorption in parts of the central portion of the hair correlate to areas where the medulla was fragmented or not present. This evidence for high binding of the hydrophobic drugs to the central medulla helps explain the hair color and racial bias found in hair drug testing. The lighter hairs with less medulla retain less hydrophobic drug per dose. The darker hairs typically have greater medulla content and hence heavier loading of drug per dose. Previous studies indicated that melanin was the primary factor for drug retention but this evidence strongly points to additional drug binding to various hair components. This drug distribution and mechanism of incorporation is necessary for determining the binding and transport of the drug to the hair. This information is required before hair testing can be used as a stand alone piece of evidence in court cases. Further studies are needed for the various drugs and hair types.

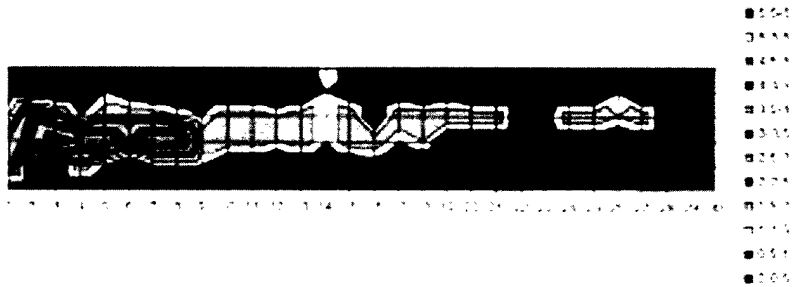

Figure 1. Image of cocaine distribution in hair shaft.

Band Structure of n-type Wurtzite GaN Studied Using Angle Resolved Spectroscopy	U4A

S.S. Dhesi, C.B. Stagarescu, Y.C. Chao, J. Downes and K.E. Smith, (Boston University)

The valence band electronic structure of wurtzite GaN has been determined using angle resolved photoemission spectroscopy. Clean, ordered surfaces were prepared by reapeated cycles of nitrogen-ions bombardment and annealing in ultra-high vacuum. Spectra were recorded along the main symmetry directions of the bulk Brillouin zone. The band dispersion along these high symmetry directions was determined, as were relative critical-point binding energies.

When compared to existing band-structure calculations, our data indicates that local density approximation band-structure calculations using partial-core corrections for the Ga 3d states predict the relative binding energies of the main critical points with a high degree of accuracy.

A similar study, investigating the bulk and surface electronic structure of the p-type GaN is undergoing.

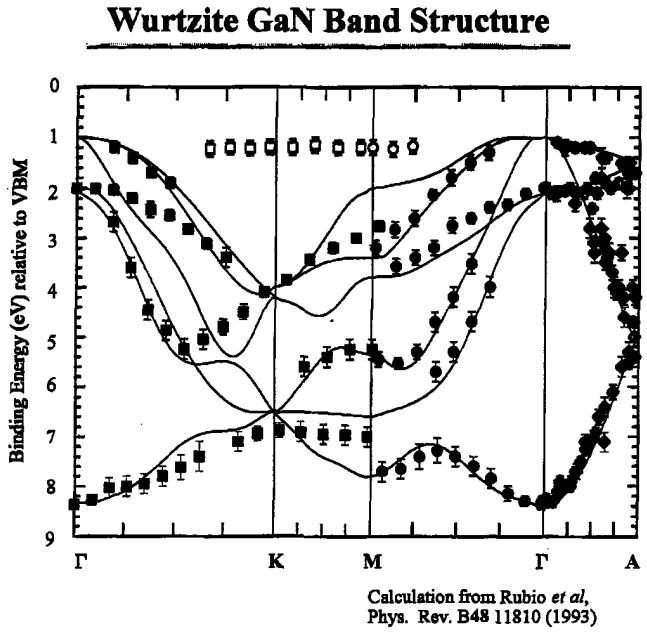

Figure 1.

Surface Electronic Structure of n-type Thin Film Wurtzite GaN	U4A

S.S. Dhesi, C.B. Stagarescu, Y.C. Chao, J. Downes and K.E. Smith (Boston University)

Gallium nitride and related nitride wide band gap semiconductors are an important class of electronic materials due to potential use in optoelectronic devices operating in the blue to ultraviolet spectral range. Consequently, a thorough understanding of the electronic structure of such nitrides is of fundamental importance. At beamline U4A, we have investigated the nature of the substantial band-bending (Fermi level pinning) at the surface of thin film wurtzite GaN by the use of photoemission spectroscopy. Our angle resolved photoemission spectra taken from the in-situ cleaned surface of wurtzite GaN show clearly a non-dispersive emission feature localized near the valence band maximum, in the bulk band gap. Further measurements proved that the associated state does not show any dispersion along the the k_z direction and is destroyed by absorption of oxygen or activated hydrogen, or by ion bombardment of the surface. All this, together with symmetry related arguments and measurements, allowed us to identify this feature with a surface state with sp_z character, consistent with a dangling bond state. A similar study is presently pursued for the surface of the p-type thin film wurtzite GaN.

Resonant Photoemission on VO_2 and V_2O_3 — U4A

E. Goering, M. Schramme, M. Klemm, S. Horn (U. Augsburg), M. L. denBoer (Hunter College CUNY)

V_2O_3, a metallic paramagnet at high temperature and an insulating antiferromagnet below $T_{MI} = 170$ K, undergoes a structural transformation from the high temperature trigonal phase into a monoclinic phase, accomplished by a decrease in the c/a ratio (axes referred to the trigonal phase) and a tilt, by 1.9° with respect to the high temperature phase c-axis, of two of the three V pairs which occupy the octahedral sites. Whether the structural transition drives the electronic one, or vice-versa, is not known, but potentially very important to understanding the mechanism of this metal-insulator transition (MIT). In this context, it is noteworthy that doping V_2O_3 with Cr or Al can also cause a metal-insulator transition, but one which does not change the lattice symmetry.

Recent experiments cast some doubt on the importance of the trigonal to monoclinic distortion for the MIT. O K edge NEXAFS measurements on pure and Cr doped V_2O_3 single crystals in the metallic and insulating phases show the local electronic structure of the Cr doped trigonal insulating phase and the low temperature monoclinic phase are the same, while EXAFS measurements show a monoclinic distortion on a microscopic scale in the room temperature metallic phase of pure V_2O_3 although the average structure is trigonal. There are two possible interpretations: (i) The monoclinic distortion is irrelevant to the MIT in pure V_2O_3, since the trigonal Cr doped insulating phase shows the same local electronic structure, or (ii) a monoclinic distortion is also present in the Cr doped insulating phase.

To decide between these possibilities we have measured the V K edge x-ray absorption spectra of V_2O_3 single crystals, both pure and doped with Al (rather than Cr, to avoid interference with the V edge). On these single crystals, we have measured in fluorescence yield; this may introduce distortions due to self-absorption, which we have corrected by measuring spectra at several sample geometries and comparing to an explicit calculation.We show in Fig. 1 the EXAFS spectra of a V_2O_3 as measured at several exit angles. The apparent amplitude differences caused by self-absorption are removed by the correction procedure.

Although analysis of the extended fine structure is not yet complete, the spectra depend very clearly on the polarization between the incident beam and the single crystal samples. An example is shown in Fig. 2, in which the extended fine structure, transformed into R space, is shown for the incident polarization parallel and perpendicular to the sample c axis.

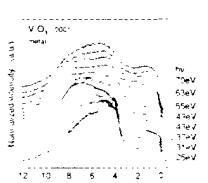

Figure 1. Photoemission spectra of V_2O_3 at various photon energies.

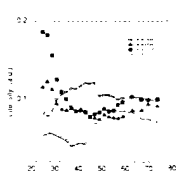

Figure 2. Amplitude of representative regions of photoemission spectrum of V_2O_3 as function of photon energy.

Element Specific Magnetic Hysteresis from XRMS. — U4B

V. Chakarian, J.W. Freeland, Y.U. Idzerda (Naval Research Lab), and N. Unterberry (SJAVS)

Element-specific magnetic hysteresis measurements performed in absorption are an established method for disecting the complex total moment hysteresis curves into their individual components to help understand the interplay between magnetic layers in a magnetic multilayer. Magnetic hysteresis curves performed in reflectivity would allow for a depth selectivity (by changing the incidence angle) not available in absorption. Shown in Fig. 1 is the dependence of the reflected specular intensity at resonance with the Co L_3 edge as a function of applied magnetic field for various incidence angles for a single crystal Co/Cr/Co multilayer (grown on GaAs(100) substrate with an Fe seed layer (4 Å) to promote the bcc Co phase). At first glance, the reflectivity curves seem completely unrelated to each other and to the traditional magnetometry loop (shown in Fig. 2). These different reflectivity loops (normalized to unity and offset for clarity) are generated by the interference of scattering from the four Co interfaces in the trilayer. Changing the incidence angle (and also the magnetic orientation) changes these interference conditions, generating the observed variations in these reflectivity loops. However, these radically different hysteresis curves are related, each displays 2 plateau regions during the field cycle. If the loops are rescaled at these two points, then all the "reflectivity hysteresis" curves look similar (see Fig. 2) and have a qualitative agreement with the magnetometry loop. The remaining differences are due to the failure of achieving complete antialignment of the two films in the plateau region.

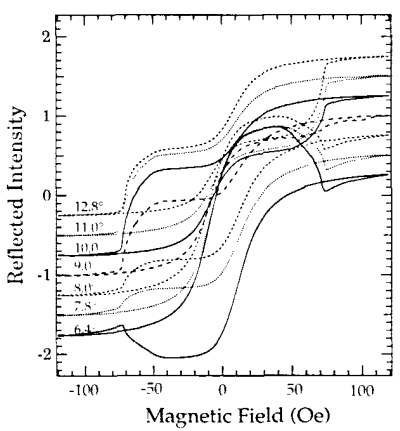

Figure 1. Normalized reflectivity curves at the Co L_3 edge at various angles (offset for clarity).

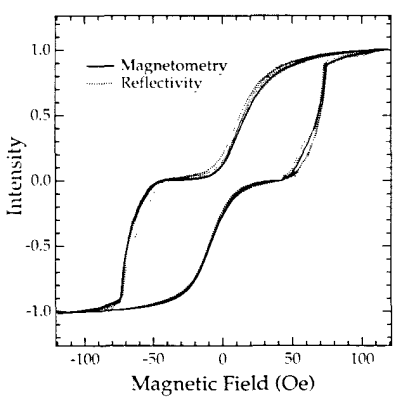

Figure 2. Same reflectivity curves rescaled at two points and compared to a magnetometry loop.

Helicity-Dependent Absolute Absorption Cross-sections of Co and Ni. | U4B

V.Chakarian, Y.U. Idzerda (Naval Research Lab), and C.T. Chen (SRRC, Taiwan).

The extraction of reliable quantitative results from measured X-ray absorption spectra often requires the determination of absolute photoabsorption cross sections. Here, we report on the measured helicity dependent absolute cross sections for hcp Co and fcc Ni measured at their $L_{2,3}$ edges for films deposited in situ at 10^{-10} Torr pressure from e-beam evaporators onto a parylene substrate, $(C_8H_8)_n$, held at room temperature. For these transmission measurements, the attenuation of the soft X-ray flux was determined by measuring the incident flux, I_0, via the photocurrent drain on a highly transmitting Au grid, and measuring the transmitted flux with a Si photodiode. The structural phase of these materials was determined by k-edge EXAFS measurements. The total photoabsorption cross section can be obtained by using $\mu_{Tot} = (\mu_+ + \mu_- + \mu_0)/3$, where μ_+ is the photoabsorption cross section for positive helicity light, μ_- for negative helicity light, and $\mu_0 = (\mu_+ + \mu_-)/2$ for linear polarized light. The data have been corrected for incidence angle, incomplete remnance, and degree of polarization of the beam. The spectra for Co and Ni (shown below) were scaled to calculated cross sections [1] in the pre- and post-edge regions.

[1] J.J. Yeh and I. Lindau, Atomic Data and Nuclear Data Tables 32,1 (1985).

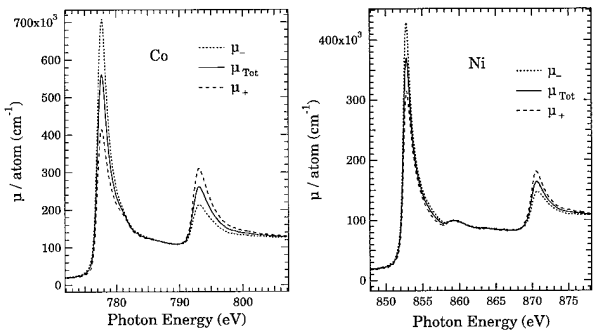

Figure 1. Measured helicity dependent photoabsorption cross section for LEFT: hcp Co and RIGHT: fcc Ni.

Quantitative Evaluation of Magnetic Moment Determination by MCD | U4B

V. Chakarian, Y.U. Idzerda (Naval Research Lab), and C.T. Chen (SRRC, Taiwan)

Using the experimentally determined absolute cross sections, a realistic mean-escape-depth (ξ) for secondary electrons of 10 Å, and a film thickness of 30 Å, we can calculate the expected XAS and MCD spectra at various incidence angles (see Fig. 1) to determine the severity of saturation/self-absorption effects in MCD moment extraction. The calculated XAS and MCD spectral shapes remain nearly unchanged for incidence angles <50° and thereafter visible saturation begins to occur and the white line intensities decrease rapidly. To verify this, we simultaneously measured in TY and in TEY, the helicity-dependent photoabsorption cross sections from a thin 30 Å Fe film as the photon incidence angle is varied from 15°-75°, which corresponds to an effective thickness variation of 31-116 Å (see Fig. 2, TEY data is normalized to TY values so that unity corresponds to no saturation effect). Note that the measured data exhibit saturation effects even near normal incidence and that for incidence angles of <50°, the ratios do not change significantly after which they deviate rapidly. The solid and dashed lines show these same ratios derived from our simulation. Also shown in Fig. 2 are the extracted ml/ms values obtained from TEY data using the energy integral MCD sum rules after normalization to the values obtained from transmission. It is immediately apparent that the resulting errors on the ml/ms values are significantly larger, increasing much more rapidly than the corresponding deviation in the L_3:L_2 intensity ratios.

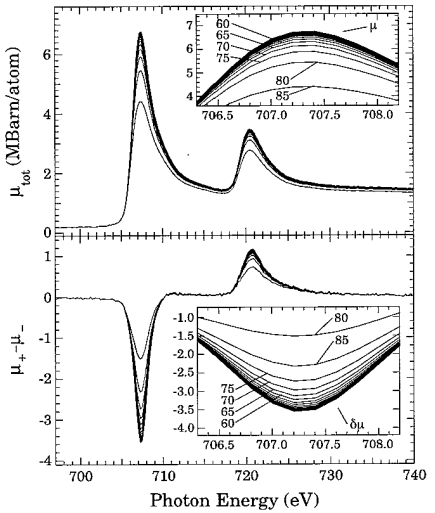

Figure 1. Calculated saturation of XAS (top) and MCD (bottom) for a 30 Å Fe film with ξ=10 Å.

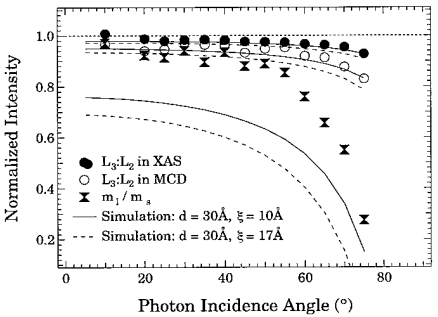

Figure 2. Experimental (points) and simulation (lines) for TEY L_3:L_2 ratios for XAS and MCD as well as the ml/ms ratios for a 30 Å Fe film.

Exploring Magnetic Roughness in CoFe Thin Films — U4B

J.W. Freeland, V. Chakarian, K. Bussmann, and Y.U. Idzerda (NRL), H. Wende (F.U.-Berlin), C.-C. Kao (NSLS)

The influence of roughness on the properties of thin film magnetic structures is a question of current interest to many facets of the magnetism community. Current results have shown that direct measurements of magnetic roughness as compared to measurements of the chemical roughness indicate that these interfaces are compositionaly rough, but magnetically smooth[1-3]. Since the magneto-transport of these structures is strongly affected by interfacial scattering and in particular from magnetic disorder at the interface, chemical roughness may not be the appropriate parameter for correlation with the degradation of the magnetic properties. However, to probe information about a magnetic interface one needs a significant magnetic scattering signal. One way of providing this is through the resonant enhancement of the magnetic and chemical scattering when an incident circular polarized photon is tuned to an absorption edge, known as x-ray resonant magnetic scattering (XRMS). To better understand the variation of magnetic vs. chemical interfaces we have undertaken a study of thin CoFe films where an increasing chemical roughness was induced through the growth process. In particular we have studied the behavior of both in plane and perpendicular roughness via helicity dependent sample rocking curves (i.e. where the detector angle was kept fixed and the sample angle was varied) measured at the Co L_3 edge (see Fig. 1). The extracted rms roughness values for the chemical ($I^+ + I^-$) vs. magnetic ($I^+ - I^-$) interfaces clearly show the magnetic interface is typically smoother (20-30% smoother) than the chemical interface (see Fig. 2). Like the rms roughness, the lateral correlation lengths also are larger for the magnetic interface (not shown here).

[1] J.F. MacKay et. al. Phys. Rev. Lett. **77**, 3925 (1996).
[2] Y.U. Idzerda, et. al., Synchrotron Radiation News **10**, No. 3, 6 (1997).
[3] J.W. Freeland et. al. Submitted to J. Appl. Phys.

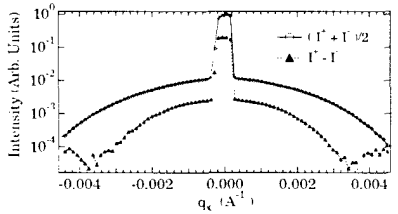

Figure 1. Sample rocking curve measured at the Co L_3 (778 eV) for chemical ($(I^+ + I^-)/2$) and magnetic ($I^+ - I^-$) contributions.

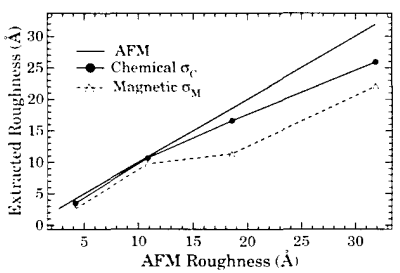

Figure 2. Roughness parameters derived from the diffuse scattering data.

Probing the Magnetic Hysteresis of an Interface with X-ray Resonant Magnetic Scattering — U4B

J.W. Freeland, V. Chakarian, K. Bussmann, and Y.U. Idzerda (NRL), H. Wende (F.U.-Berlin), C.-C. Kao (NSLS)

Interfacial properties play an important role in the behavior of magnetic thin film structures. Effects such as Giant Magneto-Resistance (GMR) and and exchange bias are strongly influenced by the prescence of "loose" spins at the interface (i.e. interfacial spins behaving differently than those in the bulk). One way to probe the behavior of interfacial spins is through the magnetic diffuse intensity[1]. The reflected intensity as a function of applied field can be utilized as a measure of the magnetic hysteresis since the magnetic portion of the scattering tracks with the magnetic moment of the sample. Since the field dependence specular peak intensity gives a measure of the bulk magnetic hysteresis, we can use the diffuse signal, which only comes from the interfaces, to measure the interfacial magnetic hysteresis. In Fig. 1 the clear difference in the coercive and saturation fields of spins at the interface indicates the different nature of the bulk vs. interfacial magnetic environment. This was confirmed by measuring at not only several different points in the diffuse, but also in the specular and diffuse at different detector angles. Combining this measurement with magnetic roughness measurments we can gain a much more complete picture of the behavior of the interfacial spins. It is worth noting that sample indicating the largest difference between specular and diffuse coercive field is also the one exhibiting a roughening of the magnetic interface.

[1] J.W. Freeland et. al. Submitted to J. Appl. Phys.

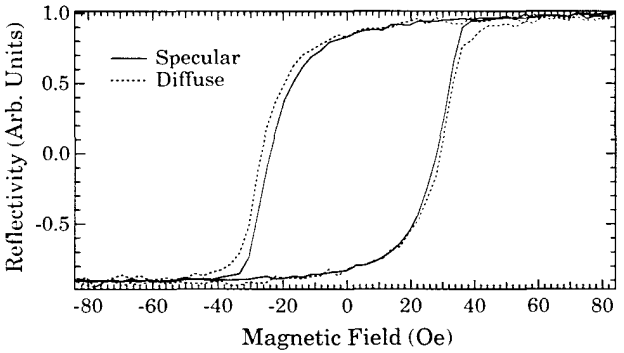

Figure 1. Interface and bulk magnetic hysteresis measured by XRMS.

Directly Identifying the Order of Layer Switching in NiFe/Cu/Co Trilayers	U4B

J.W. Freeland, V. Chakarian, and Y.U. Idzerda (NRL), S. Doherty and J.G. Zhu (Carnegie Mellon Univ.), C.-C. Kao (NSLS)

In order to better understand the dynamics of layer switching, we present a study demonstrating how soft x-ray resonant magnetic scattering (XRMS) can be used to directly probe the layer switching in magnetic multilayers[1]. The behavior of magnetic layer switching critically controls spin-dependent electron transport in heteromagnetic systems. The determination of layer switching is accomplished by monitoring changes in the angular dependence of the magnetic contributions to the reflectivity at the L_3 absorption edge as a function of applied field. The magnetic scattering asymmetry as a function of angle at the Fe L_3 and Co L_3 edges can be compared to directly determine not only the order of the layer switching, but to also extract information about the degree of anti-alignment of the layers. Comparison of the measured asymmetry of the aligned and anti-aligned states clearly shows that the NiFe layer is the first to switch and that the Co layer is never completely anti-aligned to the NiFe layer. The lack of complete anti-alignment is an indication of coupling between the layers probably due to dipolar magnetic coupling and/or film micromorphology. This demonstrates the power of XRMS as a probe of layer switching in magnetic heterostructures.

[1] J.W. Freeland et. al. Appl. Phys. Lett. **71**, 276 (1997).

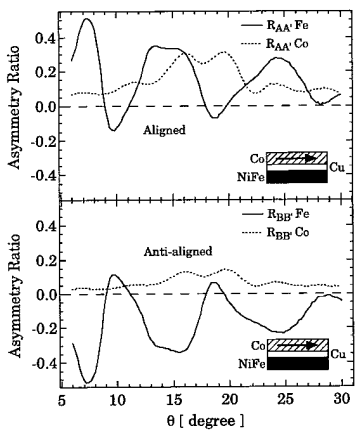

Figure 1. Top panel - Angular dependence of the asymmetry ratio, R, at the Fe and Co L_3 edges for the aligned moment case. Bottom panel - Angular dependence of the asymmetry ratio at the Fe and Co L_3 edges for the anti-aligned moment case. The sign change in the Fe asymmetry is clear demonstration of the NiFe layer switching first.

Layer Switching in a Co/Cr/Co Trilayer	U4B

J.W. Freeland, V. Chakarian, and Y.U. Idzerda (NRL), H. Wende (F.U.-Berlin), C.-C. Kao (NSLS)

Many conditions can effect the switching properties of multilayers, but since standard magnetometry techniques, which measure only the total magnetic response, can only infer the order of the layer switching indirectly, there is need for a direct probe. The determination of layer switching is accomplished by monitoring changes in the angular dependence of the magnetic contributions to the reflectivity at the L_3 absorption edge as a function of applied field[1]. A comparison of the asymmetry ratio R $(=(I^+ - I^-)/(I^+ + I^-))$ for the aligned and near anti-aligned states (see Fig. 1) illustrates the differences caused by the formation of an anti-aligned state. To determine which layer has switched first we examine the behavior at grazing incidence (i.e. small θ). Since the photon mean free path is small at the strongly absorbing L_3 edge, at the low angles the measurement is predominately sensitive to the top layer. The sign change in the asymmetry ratio at low angles is an indicator of the magnetic orientation reversal of the top layer (see Fig. 1). Additional confirmation that the top layer switches first was made from the element specific hysteresis measured in reflectivity. By comparing the Co hysteresis with that of the 7 Å Fe seed layer which is ferromagnetically coupled to the bottom Co layer, we can confirm that the bottom layer is the last to switch. These conclusions are in agreement with a comparison made between the measured data and simulations for the different magnetic layer orientation combinations (aligned, top layer flip, and bottom layer flip). This comparison, not shown due to space limitations, shows that the data can only be reproduced if the top layer is the first to flip.

[1] J.W. Freeland et. al Appl. Phys. Lett. **71**, 276 (1997).

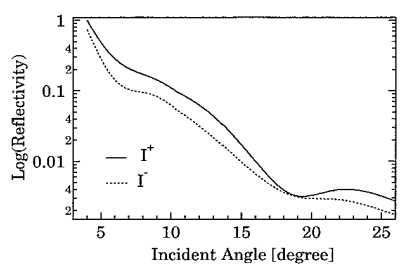

Figure 1. Helicity dependent specular reflectivity at the Co L_3 edge as a function of incident angle.

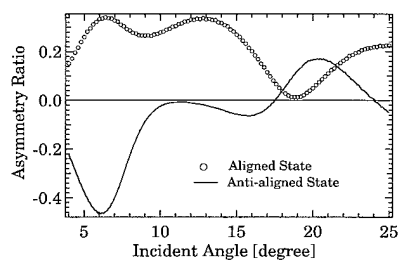

Figure 2. Angular dependence of the asymmetry ratio at the Co L_3 edge for the aligned and anti-aligned states.

Determination of Vertical Correlation of Magnetic Domains in a Multilayer.	U4B

Y.U. Idzerda, J.W. Freeland (Naval Research Lab), and C.-C. Kao (NSLS).

Reflectivity measurements are a sensitive measure of the magnetic orientation of a magnetic film. For multilayer structures, the reflected specular intensity becomes dependent on the relative orientation of each of the magnetic films. Shown in the top of Fig. 1 is the magnetometry curve for a single crystal Co/Cr/Co trilayer grown epitaxially on GaAs(001) taken along its easy axis of magnetization. It is clear from the magnetometry curve that coupling through the Cr interlayer is giving rise to a state where the moments of the two Co layers are nearly anti-aligned at low fields. However, this state will not be in a perfectly anti-aligned due to effects such as diploar coupling caused by roughness, which will reduce the degree of anti-alignment. In order to determine a complete description of the relative orientation of the two Co films the reflected specular intensity is measured as a function of applied field at various incidence angles. From this functional dependence, we can statistically quantify the degree of correlation between the magnetic domains in the magnetic films. This vertical correlation must be generated by coupling through the interlayer.

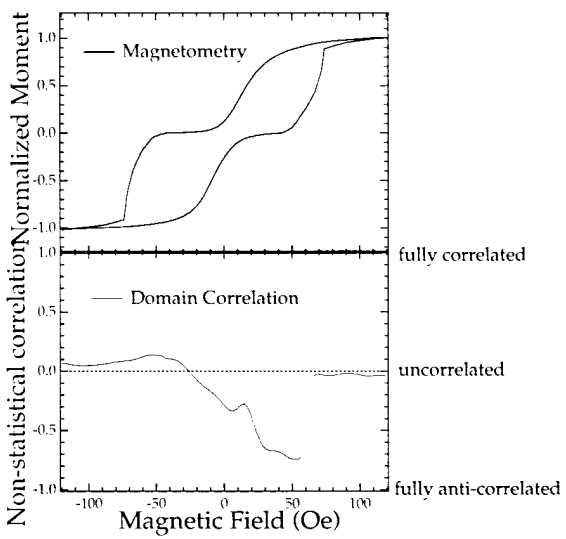

Figure 1. TOP: Magnetometry loop of Co/Cr/Co trilayer. BOTTOM: Vertical correlation of magnetic domains

Separating Chemical and Magnetic Roughness by X-ray Resonant Magnetic Scattering.	U4B

Y.U. Idzerda, V. Chakarian, J.W. Freeland (Naval Research Lab), and C.-C. Kao (NSLS).

A central issue in magnetic thin film research is the correspondence of chemical roughness, the variation of atomic type near an interface, and magnetic roughness, the variation of atomic spin (both magnitude and direction) near an interface. One method which holds promise of selectively characterizing magnetic and chemical roughness is X-ray Resonant Magnetic Scattering (XRMS). By measuring the specularly reflected intensity of a CP soft x-ray from a magnetic film or multilayer as a function of energy, angle, and magnetic orientation, both chemical and magnetic thickness and roughness information can be extracted from the interface, analogous to the hard x-ray θ-2θ scattering. As a demonstration, we have plotted below the asymmetry (difference between scattering using left or right CP soft x-rays normalized by their sum) as a function of photon energy and incidence angle near the L_3 edge of Co for a 37 Å Co film. For comparison, plotted to either side is the calculated asymmetry plot for a 37 Å Co film assuming either no magnetic roughness (LEFT) or assuming a magnetic roughness equal to the experimentally determined chemical roughness (5 Å- RIGHT). It is clear from the comparison that the no roughness spectra agrees with the data better than the 5 Å rough calculation, suggesting that the Co film is magnetically smooth, but chemically rough.

Below are shown the normalized helicity-dependent asymmetry (difference of the two helicity dependent spectra normalized by the sum) for 37 Å Co film as a function of incidence angle and photon energy.

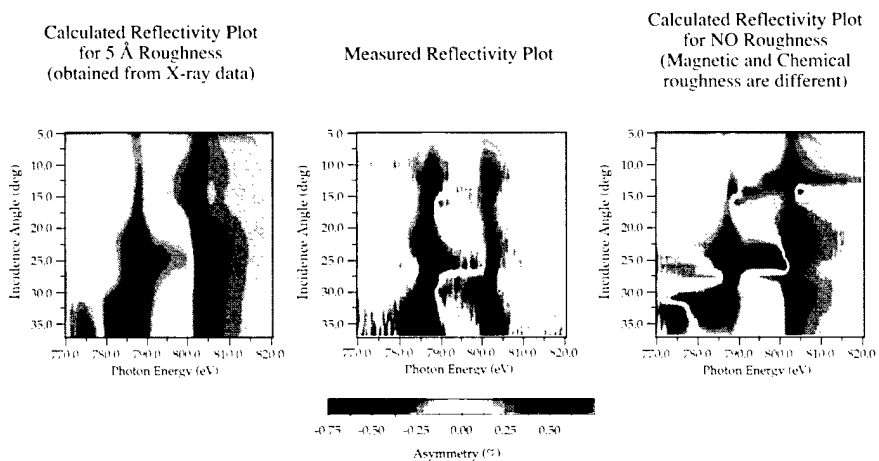

Figure 1.

Magnetic Moment Extraction from Magnetic EXAFS — U4B

Y.U. Idzerda, J.W. Freeland, and V.Chakarian (Naval Research Lab)

Transmission MCD measurements have been extended to the EXAFS region for Fe, Co, and Ni films grown in-situ by e-beam evaporation (250-300 Å) onto $\sim 1\mu$m thick semi-transparent parylene for determination of the L-edge magnetic EXAFS (MEXAFS). The structure of the deposited films were determined by EXAFS measurements at the K-edges of these films, indicating that the Fe, Co, and Ni films are polycrystalline films in the bcc, hcp, and fcc phases, respectively. The combined $L_{2,3}$ spectra can be deconvolved assuming that the L_2 and L_3 oscillations are identical and are offset by the L_2 and L_3 energy separation and that the L_3 edge EXAFS (MEXAFS) is weighted by +2 (-1) compared to the L_2 edge EXAFS (MEXAFS). These weighting factors reflect the relative heights of the L_2 and L_3 edge jumps (quantum degeneracy of 2:1) and the phase relation of the MCD (-1:1). After the L-edge (M)EXAFS is isolated, it is converted to electron wavenumber, k, and fourier transformed (with a k^2 weighting) in the usual way to generate the radial distribution function, shown in Fig. 1. The first shell position is reproduced, but in each case the longer scattering paths are enhanced relative to the first shell for the MEXAFS when compared to the EXAFS. Most interestingly, if the MEXAFS first shell intensity is scaled to the EXAFS first shell intensity, this first shell ratio scales with the spin moment of the material (see Fig. 2).

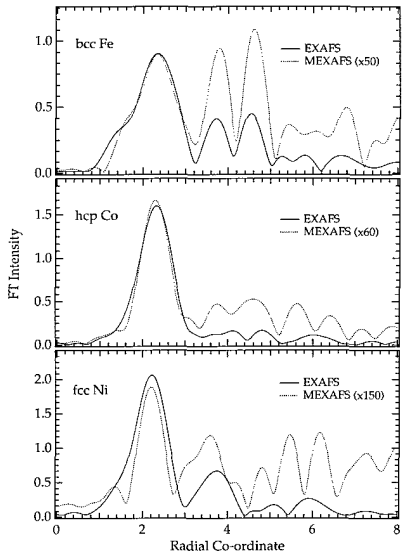

Figure 1. FT Intensities.

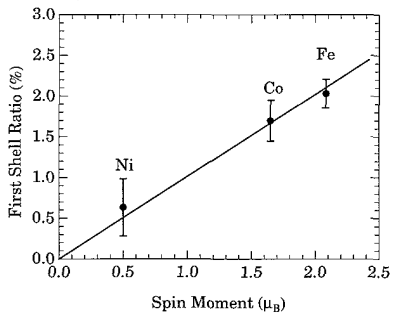

Figure 2. First shell ratio (MEXAFS/EXAFS) for bcc Fe, hcp Co, and fcc Ni as a function moment. Solid line is a linear fit.

Site-Specific NEXAFS of $Y_{1-x}Ca_xBa_2Cu_3O_{7-y}$: Role of Apical Oxygen for High-Temperature Superconductivity — U4B

M. Merz, N. Nücker, P. Schweiss, S. Schuppler (Forschungszentrum Karlsruhe), C. T. Chen (SRRC), V. Chakarian, J. Freeland, Y. U. Idzerda (NRL), M. Kläser, G. Müller-Vogt (U Karlsruhe), and T. Wolf (Forschungszentrum Karlsruhe)

Replacing Y^{3+} by Ca^{2+} in $YBa_2Cu_3O_{7-y}$ (YBCO) is an alternative doping mechanism to the usual O doping. With polarization-dependent O1*s* and Cu2*p* NEXAFS on detwinned (Ca,Y)BCO single crystals, the hole distribution between the CuO_2 planes and CuO_3 chains has been identified and hole counts for the orbitals near E_F have been derived. For a polarization E$\|a$, planar O(2)2*p* orbitals are observed in O1*s* spectra, while E$\|c$ spectra near E_F pick out contributions form the apical O(4) site. For E$\|a$, the spectral weight of the planar Zhang-Rice (ZR) state carrying the superconductivity increases with increasing O or Ca doping (Fig. 1). Here, the electronic structure of the CuO_2 planes for the x=0.23, y=1.0 and the x=0, y=0.5 compounds is very similar – unlike in the corresponding E$\|c$ spectra, where the former exhibits no intensity at the first peak above E_F. In general, E$\|c$ spectra from samples with the same y are similar near E_F and do not depend on x, showing that Ca substitution does not affect the apical site. From considerations like these we conclude that, regardless of the O content, Ca doping introduces holes *exclusively* to the CuO_2 planes, leaving the apical O(4) or the chain O(1) site entirely *unaffected*.

Most significantly, we find that Ca-doped but O-depleted samples exhibit no superconductivity, independent of the hole count on the planes. On the other hand, O doping increases the hole count at the planar *and* the apical (and chain) sites and restores T_c. Thus, for high T_c not only optimally doped planes are needed; the apical hole count is equally important. This result explains the decrease of T_c^{max} with Ca content, questions the validity of "universal" T_c curves [1], and may have more general implications for HTSC, e.g., about the need for theoretical models involving extra-planar hopping.

[1] J. L. Tallon et al., Phys. Rev. B **51**, 12911 (1995).

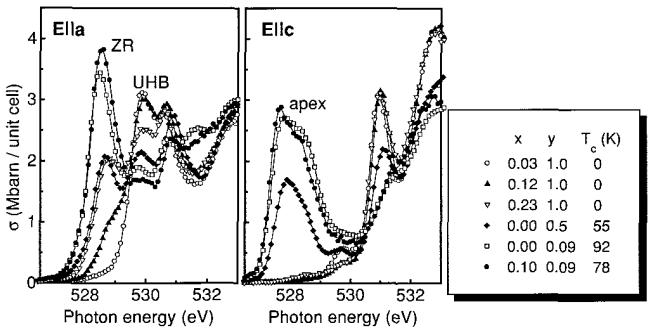

Figure 1.

Pr and Other Rare Earths in REBa$_2$Cu$_3$O$_{7-y}$: A NEXAFS Study | U4B

M. Merz, N. Nücker, P. Schweiss, S. Schuppler (Forschungszentrum Karlsruhe), R. Neudert, M. S. Golden, J. Fink (IFW Dresden), C. T. Chen (SRRC), V. Chakarian, J. Freeland, Y. U. Idzerda (NRL), A. Erb (U Geneva), M. Kläser, G. Müller-Vogt (U. Karlsruhe), and T. Wolf (Forschungszentrum Karlsruhe)

In the family REBa$_2$Cu$_3$O$_{7-y}$ (RE = rare earth, Y), RE=Pr is the only orthorhombic but non-superconducting compound. We showed earlier [1] with polarization-dependent O1s and Cu2p NEXAFS that for RE=Pr, O2p-$RE4f$ ("Fehrenbacher-Rice", FR) hybridization occurs, removing holes from the energetically competing planar O2p-Cu3d "Zhang-Rice" (ZR) states responsible for superconductivity. Now, similar experiments on detwinned REBCO single crystals with RE neighboring Pr (La, Nd) and with substantially smaller ionic radius (Er) were performed to further study the special role of Pr among the RE's and to check if some FR hybridization occurs elsewhere in the RE series.

Spectra with the polarization E$\|a$ (Fig. 1) show for all RE investigated (and for O-rich samples) a prominent ZR state while the upper Hubbard band (UHB) is small; of course, for Pr transfer of spectral weight to the UHB and FR hybridization occurs. Small deviations from this general picture include a tendency for increasing UHB intensity with larger RE radius. This is most obvious for La, but cannot be due to a FR contribution: precisely for La, no further holes can be transferred to a La4f^0 orbital. Also, for decreasing RE ionic radius, the threshold energy moves up (E_F moves relative to the ZR), and an additional structure located at 532-533 eV also moves up. This latter feature is also seen for E$\|c$, appears somewhat isotropic, and is assigned to hybridization effects governed by the RE site. The extra spectral weight $\|c$ for Pr (arrow in Fig. 2) is a signature for the small but existent out-of-plane character of the FR hybrid; it has been confirmed by recent theoretical work.

[1] M. Merz et al., Phys. Rev. B **55**, 9610 (1997); NSLS 1996 Activity Report

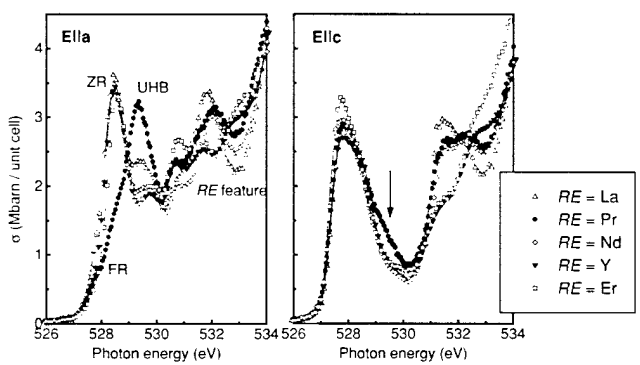

Figure 1.

Temperature Dependence of MCD Anisotropy of La$_{0.7}$Sr$_{0.3}$MnO$_3$ | U4B

J.-H. Park, H.-J. Kim, E. Vescovo (NSLS), C. Kwon, R. Ramesh, T. Venkatesan (U. Maryland)

Soft x-ray magnetic circular dichroism (SXMCD) has been well known to be a powerful tool for studying magnetic properties of ferromagnetic systems. SXMCD utilizes a core level absorption edges, and thus it is element specific. The obtained MCD anisotropy corresponds to the magnetization of the given elements.

Here we present SXMCD study results of a colossal magnetoresistance material La$_{0.7}$Sr$_{0.3}$MnO$_3$ including the temperature dependence of its anisotropy. Figure 1 shows the SXMCD results at Mn L$_{2,3}$ edges obtained at 40K from 1900A thick epitaxial La$_{0.7}$Sr$_{0.3}$MnO$_3$ film on SrTiO$_3$ substrate. Different from the bulk crystal sample, the thin film shows nearly magnetic single domain behavior; low coercive field ($<$ 100 Oe) and $\simeq$ 100magnetic moments. The obtained MCD signal is very large and the anisotropy (difference devided by sum) is as large as $\sim$ 30the line shape of the MCD spectrum can be understood by a model multiplet calculation. More interesting results were obtained in the study of the temperature dependence of the MCD anisotropy presented in Figure 2. The MCD spectra were obtained in a total electron yield mode which has about 50A penetration depth. Thus, the MCD anisotropy reflects the magnetization up to the first $\sim$ 50A, rather than that of the whole sample, which can be obtained by SQUID measurements. Interestingly the temperature dependence of the MCD anisotropy is somewhat different from that of the magnetization obtained by SQUID, indicating that the magnetization near surface is considerably different from that of the bulk.

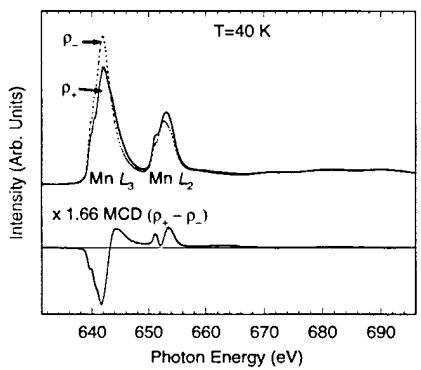

Figure 1. Soft x-ray magnetic circular dichroism at Mn L2,3 edge measured at 40K well below $T_C \simeq$ 360K. MCD signal is multiplied by 1.66 which is a scale factor considering the experimental geometry (cos 45°) and the helicity (85%).

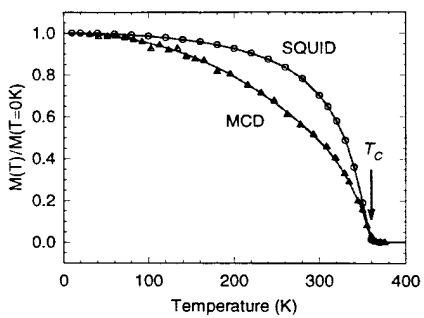

Figure 2. Temperature dependence of the MCD anisotroty $(\rho_+ - \rho_-)/(\rho_+ + \rho_-)$ compared with that of the magnetization obtained by SQUID.

Soft X-Ray MCD Studies of Heusler Alloys, NiMnSb and CoMnSb | U4B

J.-H. Park, H.-J. Kim, E. Vescovo (NSLS), W. Zhu, B. Sinkovic (NYU), C. Tanaka, and J. S. Modera (MIT)

Since theoretical prediction of half-metallic ferromagnets and observation of large magneto-optical Kerr effects in PtMnSb and NiMnSb, interest in Mn-based Heusler alloys have been stimulated theoretically and experimentally. The band structure calculation predicts that the system is metallic for the majority spin but insulating for the minority spin.

Here we present magnetic circular dichroism (MCD) studies of NiMnSb and CoMnSb using soft x-ray absorption spectroscopy (XAS) at Mn $L_{2,3}$ and Ni(Co) $L_{2,3}$ edges. Figure shows the XAS spectra for different helicities and the corresponding MCD spectra. The XAS data were collected in total electron yield mode. As can be seen in the figures, for both systems the XAS spectra exhibit large MCD effects at Mn $L_{2,3}$ edges but very little MCD effects at Ni and Co $L_{2,3}$ edges, indicating that the magnetic moments are mostly induced in the Mn sites. The spectral structure of Mn $L_{2,3}$ edge MCD is very consistent with that expected from Mn_{2+} ions. Most interesting things are observed in the MCD of Ni $L_{2,3}$ and Co $L_{2,3}$ edges, which reflect the unoccupied conduction states. The MCD of the Ni L_3/L_2 edge shows positive/negative signals at the pre-edge while that of the Co L_3/L_2 edge shows opposite signals. These results show that the electron states very near E_F have more majority spin character in NiMnSb but more minority spin character in CoMnSb.

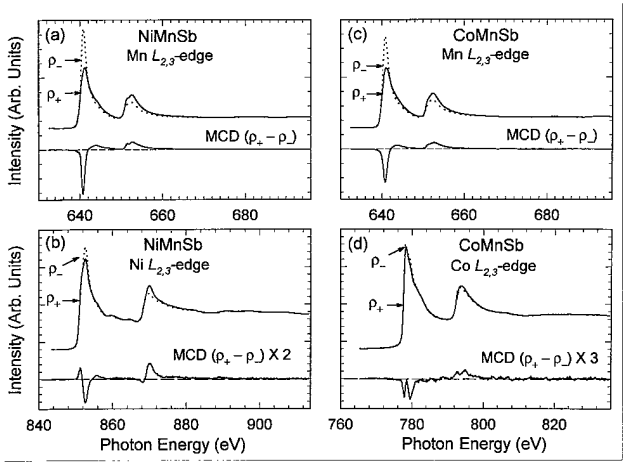

Figure 1. Soft x-ray magnetic circular dichroisms of Heusler alloys, NiMnSb and CoMnSb. at (a),(c) Mn $L_{2,3}$, (b) Ni $L_{2,3}$, and (d) Co $L_{2,3}$ edges.

Characterization of the Charge Carriers in a Double-layered Manganite $La_{1.3}Sr_{1.7}Mn_2O_7$ | U4B

J.-H. Park (NSLS), T. Kimura, and Y. Tokura (U. Tokyo)

Recent success in synthesis of double-layered manganites, $La_{2-2x}Sr_{1+2x}Mn_2O_7$, attracted so much attention scientifically and technologically due to their noble electrical and magnetic properties. Similar to doped manganese perovskites, the double-layered manganites exhibits large negative magnetoresistance. Furthermore, these have intrisic atomic scale magnetic multi-layer tunnel junctions. Each Ferromagnetic metallic MnO_2 bilayers sheet are separated by a nonmagnetic insulating (I) $(La,Sr)_2O_2$ layer, and thus the system forms a virtually infinite arrays of FM/I/FM junctions.

Here we investigate the characteristics of charge carriers of an x = 0.35 double-layered manganite by using polarization dependence O 1s x-ray absorption spectroscopy. The O 1s XAS is well known to present the unoccupied conduction states. To achieve complete polarization geometry and eliminate optical path variations, a single crystal sample in which the sample normal has 45° off from both c-axis and ab-plan, and an azimuthal rotation method was used. The figure shows the O 1s XAS spectra for (a) E_c and (b) E_{ab} at two different temperature, 25K (FM) and 150K (PI), and the differences. The XAS spectra show quite different line shape for different geometries due to the different dipole transition selection rules; O 1s to O $2p_z$ for E_c and to O $2p_{x,y}$ for E_{ab}. The system undergoes PI to FM transition around $T_C \simeq 130$K, and thus the first peak of the difference spectrum reflects the charge carriers at the Fermi level in FM phase, analogous to Drude peak in the optical absorption measurements. The first peak intensity is quite comparable for the two geometries. This result show that the system has comparable in-plane and out-of-plane charge carriers in FM phase. The in-plane and out-of-plane charge carrier ratio is estimated to be 45 : 55.

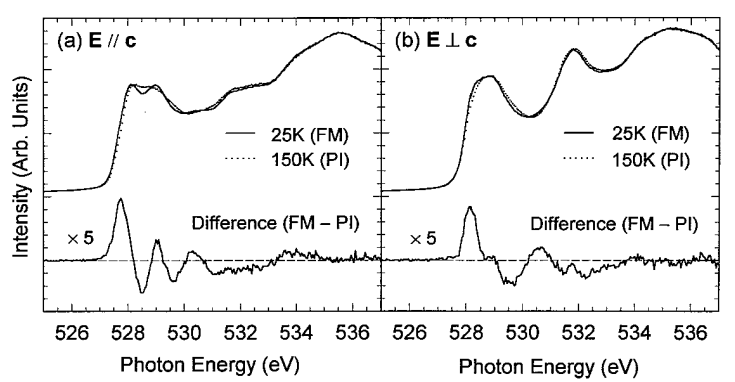

Figure 1. Polarization dependent O 1s x-ray absorption spectra of $La_{1.3}Sr_{1.7}Mn_2O_7$ measured at T = 25K (FM) and at T = 150K (PI). The polarization field of the incoming photon lies (a) out of plane and (b) in plane.

Electronic Structure, Spin State, and Magnetic Properties of $La_{1-x}Sr_xCoO_3$	U4B

E. Pellegrin, O.C. Rogojanu, G.A. Sawatzky (U. of Groningen), M.H.R. Lankhorst, H.J.M. Bouwmeester (U. of Enschede), V. Chakarian, J.W. Freeland, and Y.U. Idzerda (NRL)

The charge-transfer system $La_{1-x}Sr_xCoO_3$ exhibits a wide variety of transport and magnetic properties as a function of temperature and Sr doping. This is partly due to the competition between the crystal field splitting and the Hund's rule exchange interaction on the Co sites leading to strong changes in the Co spin state as a function of the above parameters. In Fig. 1 we show the doping-dependent O K x-ray absorption spectroscopy (XAS) data of (paramagnetic) $La_{1-x}Sr_xCoO_3$ at 300 K. The part of the O K-edge between 527 and 532 eV is in general interpreted as originating from unoccupied O $2p$ states covalently mixed with Co $3d$ states. The dramatic increase of the O K prepeak intensity with increasing Sr concentration gives evidence for a very strong O $2p$ character of the doped charge carriers and for the charge-transfer character of the $La_{1-x}Sr_xCoO_3$ system. The former may indicate the upcoming of a $d^6\underline{L}$-dominated ground state of the Co^{4+} ions as has already been suggested for the fully doped $SrCoO_3$ which would be compatible with the ferromagnetic ordering of $La_{1-x}Sr_xCoO_3$ for $x \geq 0.2$ below 200 K. The temperature dependence of the Mn L-edges of undoped $LaCoO_3$ is presented in Fig. 2. Between 15 K and 150 K significant changes can be observed possibly due to the transition from the low-spin (S=0) d^6 ground state to a mixed-spin (S=0 and S=2) regime. For 150 K$\leq$T$\leq$400 K the systematic changes in the Mn L data suggest an increase of Co^{3+} ions with a high-spin (S=2) ground state.

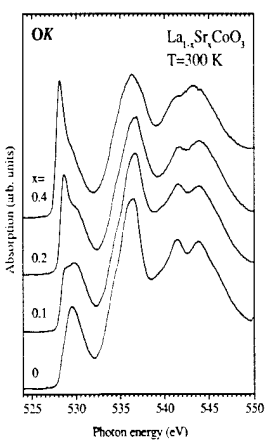

Figure 1. Doping-dependent O K absorption edges of $La_{1-x}Sr_xCoO_3$ measured at 300 K.

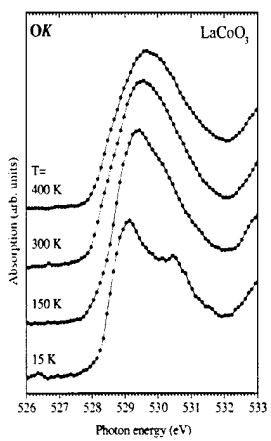

Figure 2. Temperature-dependent Mn L absorption edges of $LaCoO_3$.

Soft X-ray Bragg Scattering study of a Ce/Fe multilayer at the M4 edge of Ce	U4B

L. Sève, F. Bartolomé, J.M. Tonnerre, D. Raoux (LCG-CNRS), V. Chakarian (NRL), C.-C. Kao (NSLS)

X-Ray resonant magnetic scattering (XRMS) experiments have been performed on a metallic multilayer at the M_4 edge ($2p_{1/2} \rightarrow$ 4f transitions) of Ce in a Ce/Fe multilayer, using a linearly polarized soft X-ray beam together with a transverse scattering geometry. A $Ce_{10\mathring{A}}/Fe_{30\mathring{A}}$ was chosen in order to provide a sufficient magnetic asymmetry ratio (the polarization of the Ce 4f shell is assumed to be located at the interface with the Fe layer according to XMCD experiment) and a sufficient number of Bragg peaks orders arising from the multilayered structure. Despite the huge absorption at this edge and the linked large anomalous scattering factors (up to 800 r_o for f" and 400 r_o for f'), we succeeded in measuring the four first Bragg peaks, the 4th order Bragg peak lying right around 45° with still measurable intensity. Rather large asymmetry ratios have been measured : up to 10 % to be compared with the 1.5 % amplitude of the XMCD signal measured on a similar sample. This first resonant magnetic reflectivity experiment on a 4f element ascertains the possibility to study rare earth elements by either soft X-ray magnetic reflectivity or diffraction on multilayers at the M edges of rare earths. The non-constant evolution of the asymmetry ratio (mainly the change in shape) is directly linked to a non-constant profile of the 4f spin polarization across the Ce layer. A quantitative analysis, using the 4 orders of diffraction is underway to determine the 4f polarisation through the Ce layer.

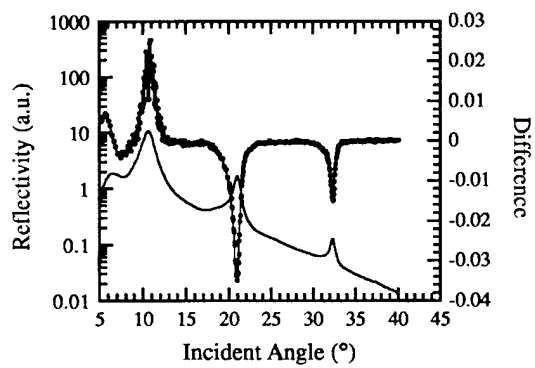

Figure 1. Three first resonant magnetic Bragg orders of a Ce/Fe multilayer at the Ce M4 edge recorded in a transverse geometry. The difference spectra obtained for the two opposite directions of the applied magnetic field is also displayed. Asymmetry ratio is of the order of a few percents.

Soft X-Ray Resonant Magnetic Reflectivity Study of Thin Films | U4B

L. Sève, F. Bartolomé, J.M. Tonnerre, D. Raoux (LCG-CNRS), V. Chakarian (NRL) and C.-C. Kao (NSLS)

Soft X-ray resonant magnetic reflectivity measurements have been performed on thin films. Reflectivity scans have been recorded at the Fe $L_{2,3}$ edges on a $W_{32\mathring{A}}/Fe_{91\mathring{A}}/W_{129\mathring{A}}$ trilayer both versus the beam incident angle on the sample (reflectivity scans) and versus the photon energy (spectroscopic scans). A linearly polarized beam, together with a transverse geometry (magnetic field applied perpendicular to the reflection plane) have mainly been used. In that case both state of light (σ and π polarisation) remain independent polarization states through the sample, easing to introduce the effect of roughness. Thus the resolution of the Maxwell equations for a stratified media, including the calculation of the dielectric tensor using regular Fe XMCD spectra and the various interfacial roughness, allows to simulate accurately the X-Ray Transverse Kerr spectra for both the isotropic intensities and for the magnetic one, through the Asymmetry ratio, R= $(I^+-I^-)/(I^++I^-)$. The asymmetry ratio amplitude are found to be of the order of 5-20 % at the Fe $L_{2,3}$ resonance, to be compared to the typical 1% in conventional TMOKE on 3d transition metals. We also study a Ir / $Fe_{0.9}Mn_{0.1}$ / Ir trilayer, epitaxially grown on a MgO substrate. Asymmetry ratio, up to 25 % measured at the Fe L edges are accurately simulated using the standard bcc Fe XMCD spectra, allowing to ascribe a 2.1 μ_B magnetic moment. A signal of 1 % has been recorded at the Mn L edges ascertaining the magnetic ordering of Mn atoms in such a solid solution. Simulation of the Mn L edges magnetic reflectivity plead for an antiferromagnetic orientation between the Mn net moment and that of Fe, with an equivalent coercitive fields recorded through element specific hysteresis loop measurements in reflectivity mode.

J.M. Tonerre et al, submitted to J. Appl. Phys. (7th Joint MMM Conf. Proc.).
L. Sève et al, to be published.

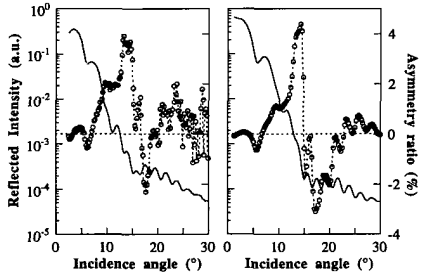

Figure 1. Left : experimental measurement of the reflected intensity for both magnetic field orientations and Asymmetry ratio. Right : calculated ones at the L edges of Fe in a W/Fe/W trilayer as a function of the incident photon energy at a 5 degree incident angle.

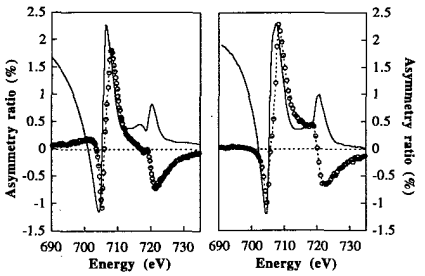

Figure 2. Left : Experimental measurement of the reflected intensity for both magnetic field orientation and Asymmetry ratio. Right : calculated ones at the L edges of Fe in a W/Fe/W trilayer as a function of the incident angle for a 703.2 eV energy.

Temperature Dependence of the Fe L-edge Magnetic EXAFS | U4B

H. Wende, J.W. Freeland, Y.U. Idzerda (NRL), L. Lemke, and K. Baberschke (Freie U.)

This work presents the first systematic investigation of temperature dependence of the Magnetic EXAFS (MEXAFS). We chose a polycrystalline Fe thin film of 500 Å as a model system as it is known that the Debye model describes the temperature dependence of the spin averaged EXAFS reasonably well. The deconvoluted experimental EXAFS data (χ and FT) of the L_3 edge, taken in transmission through the Fe film, are shown in Fig. 1a and 1b. Similarly, the deconvoluted MEXAFS data (chi and FT) are shown in Fig 1c and 1d. A qualitative comparison of the MEXAFS data to EXAFS data shows that the main peak position of the Fourier transforms (Fig. 1b and 1d) is the same for both cases and the temperature dependent damping is comparable. The clear temperature dependence of the experimental data was fitted with the correlated Debye model yielding a Debye temperature of $\theta_D = (520 \pm 40)$K (see Fig. 2) in good agreement with calorimetric measurements for the bulk system (θ_D(calorimetric) = 470K). The Debye model analysis of the MEXAFS temperature dependence results in a value of the 'magnetic' Debye temperature of $\theta_{Dm} = (400 \pm 40)$K, showing that the temperature dependence of the MEXAFS data is even stronger than in the EXAFS. Although the measurment temperatures are far below the Curie temperature of Fe, we have found an even stronger temperature dependence for the MEXAFS compared to the EXAFS. This shows that the temperature dependence of the MEXAFS is not only determined by the temperature dependence of the magnetic moment, which should be constant in the investigated temperature region (70K to 400K), but also by the relative thermal vibrations of the absorbing atom with respect to the backscattering atom.

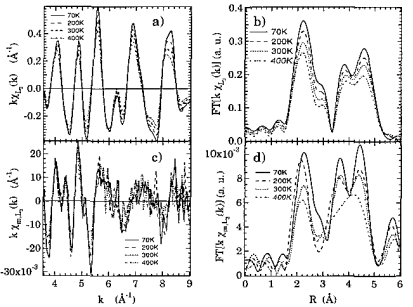

Figure 1. The T dependent deconvolved Fe L_3 EXAFS data (a,b) in comparison to the deconvolved L_3 MEXAFS data (c,d).

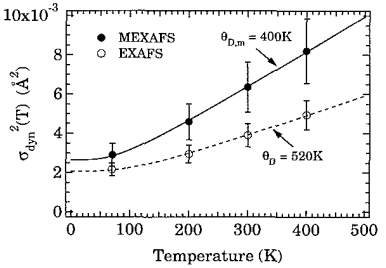

Figure 2. The T dependence for the nearest neighbor distance (R_1) of the EXAFS and MEXAFS data. Also shown is the Debye model (lines).

Characterization of Bitumen-Polymer Mixtures by Infrared Microspectroscopy

U4IR

J-L. Bantignies, G. Fuchs (ELF Atochem, France)

Bitumens are the heavy organic fraction of petroleum products. The main industrial applications of these materials are road surfaces and for such applications polymers are added to the bitumen to improve the mechanical properties, which in turn depend on the homogeneity of the mixture. Any characterization of the mixture using infrared microspectroscopy (IMS) with a conventional (thermal) source is limited to a lateral resolution of about 30 microns, which is inadequate due to the 1 and 50 micron length scale of heterogeneities in the mixture. The situation is much improved using synchrotron radiation, however. To prepare samples for the microscope, the bitumen-polymer mixtures were first heated in a oven at 353K and then spread on 2 mm thick BaF2 pellets. This method does not allow control over the thickness. Fig. 1 shows the IR spectrum of a Bitumen/polymer mixture. The 1377 cm^{-1} band (dCH_2-CH_3) is a signature for the bitumen and the 967 cm^{-1} band (gCH butadiene) is assigned to the polymer. The mapping experiments were made in transmission mode with 2 cm^{-1} resolution with 128 pixels per spectrum using 16x16 micron apertures and 8 micron steps. After mapping, the integrated absorbance (IA) of both bands was calculated as a function of the position. As the thickness of the sample was not homogeneous, the ratios of these values (IA 967 cm^{-1} / IA 1377 cm^{-1}) was calculated for each position and yielded the image in shown Fig. 2. The contours represent increments of 1.1% variation of relative concentration of polymer in the matrix of bitumen (concentration of the polymer in the bitumen mixture of 5 %.). The spatial resolution is limited by the diffraction limit of the wavelength of the polymer band at 10.3 microns and the size of the apertures. Therefore we are able to observe heterogeneity of the relative concentration of the polymer in the bitumen for the mechanically mixed sample of 9%. This scale of heterogeneity (order 15 microns) is impossible to observe by using a conventional source.

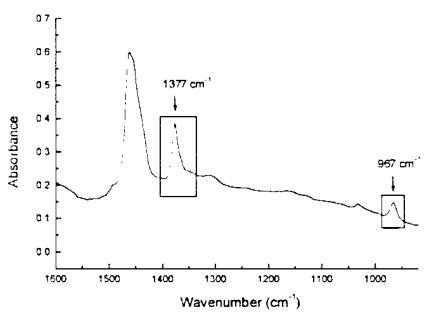

Figure 1. IR spectrum of the mixture of Bitumen-polymer.

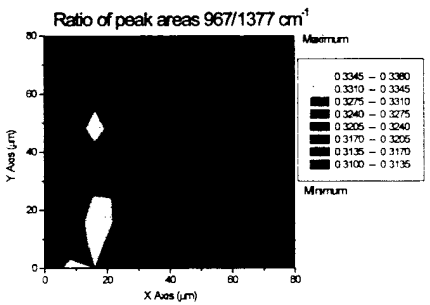

Figure 2. Absorbance contour map of the prepared bitume-polymer mixture for the ratio of the 967 cm^{-1} band (polymer) and the 1377 cm^{-1} band (bitumen). Darker regions represent lower absorption.

Infrared Micro Spectroscopy by Using Synchrotron Radiation Application to Microstructural Hair Characterization

U4IR

J-L. Bantignies, G. Fuchs, (ELF Atochem, France), D. Lutz, S. Marrull (Yves Rocher, France)

Infrared Microspectroscopy (IMS), using thermal sources, is widely employed in the cosmetic industrial environment for the analysis of hair. Nevertheless, the lateral resolution achieved (about 30 microns) does not allow a local characterization (few microns resolution) of the structure of the hair. The IR synchrotron source overcomes this limitation and a chemical imaging of the hair at the micron level is herein presented.

From the morphological point of view, the human hair shaft structure consists of three main components (Fig. 1). The hair is typically composed of an inner core, the medulla (10 microns diameter), which is surrounded by the cortex which constitutes the main part of the bulk of the fiber. The outer layer, which is exposed to the environment, is the cuticle with an average thickness of 5-10 microns.

Chemically, hair mainly consists of keratin, a protein highly cross-linked by the amino acid cystine giving well defined amide signature in the middle infrared.

For the IMS experiments, samples were prepared by embedding hairs in polymer blocks and sectioning them using a microtome. The cross-sectioned cuts were on the order of 6 microns thick (Fig. 1). The polymer was chosen to have bands well away from those of the hair samples.

The hair section shown in Fig. 1 was spectroscopically mapped with a lateral resolution of 6 microns. The integrated absorbance of the amide A band (3290 cm_{-1}) was then extracted and a contour map showing the absorbance of this band as a function of position in the sample is shown in Fig. 2. Since this band is present throughout the hair, but at differing concentrations in the various components, the cuticle, cortex and medulla are all revealed in this map. The variations in absorbance which give the contrast are consistent with the differences in protein composition between these components. The microscope will now be used to study the influence of dyes and cosmetic reagents on the structure of hair samples.

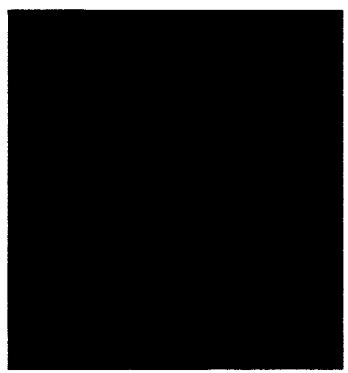

Figure 1. Cross-section of the hair

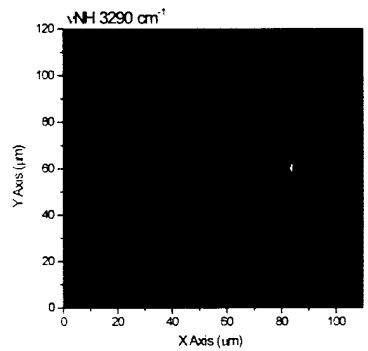

Figure 2. Absorbance contour map of a hair for the amide A band (3290 cm-1). Darker regions represent lower absorbance.

The c-Axis Reponse of $Y_{1-x}Ca_xBa_2Cu_30_{7-\delta}$ Single Crystals Studied by Far-Infrared Ellipsometry	U4IR

C. Bernhard, R. Henn, A. Wittlin, and M. Cardona (Max-Planck-Institut fuer Festkoerperforschung)

We studied the c-axis reponse of $Y_{0.86}Ca_{0.14}Ba_2Cu_3O_{7-\delta}$ crystals by far-infrared ellipsometry. The substitution of Y^{3+} by Ca^{2+} introduces extra hole carriers into the CuO_2 planes. Therfore, the strongly overdoped regime can be explored for Y-123 and the oxygen content and metallic character of the CuO chains can be varied while the doping of the CuO_2 planes is kept constant. This provides a unique possibility to test if the unusual frequency- and temperature dependence of the electronic c-axis conductivity $\sigma_c(\omega,T)$ is determined either by the charge dynamics of the CuO_2 planes or rather by the spacing layers including the CuO chains. Fig. 1a and 1b show $\sigma_{1c}(\omega,T)$ for two optimally doped crystals, a) Ca-free and almost fully oxygenated $YBa_2Cu_3O_{6.9}$ with $T_c=T_{c,max}=92$ K and b) Ca-substituted and oxygen deficient $Y_{0.86}Ca_{0.14}Ba_2Cu_3O_{6.7}$ with $T_c=T_{c,max}=85$ K. The absolute value of the electronic part of σ_{1c} is clearly higher for the Ca-free crystal. The frequency- and temperature dependence of σ_{1c}, however, is very similar for both crystals. Notably, for the Ca substituted crystal there occurs no sign of a "pseudogap-like" suppression of σ_{1c} in the normal state as it has been observed for the oxygen deficient and underdoped Ca-free crystals. This demonstrates that the 'pseudogap-effect' is not related to the electronic properties of the spacing layer (the oxygen deficiency of the CuO chains). Instead, our results imply that the "pseudogap-effect" is intimately related to the underdoped state of the CuO_2 planes, i.e. the charge carriers (in the normal state) are confined to the CuO_2 planes.

A rather different behavior is observed for the strongly overdoped $Y_{0.86}Ca_{0.14}Ba_2Cu_3O_{6.95}$ crystal with $T_c=63$ K for which $\sigma_{1c}(\omega,T)$ is metallic in the normal state (see Fig. 2a). The relaxation of the charge confinment in the normal state is accompanied by two remarkable effects in the SC state (Fig. 2b). Firstly, the the SC gap is strongly reduced since the onset of the reduction of spectral weigth (due to the condensation of the carriers into a delta function at zero frequency) is suppresed to 2Δ=420 cm^{-1} from 2Δ=620-650 cm^{-1} in case of the optimally doped crystals. Secondly, there remains a large fraction of unpaired quasiparticles within the SC gap.

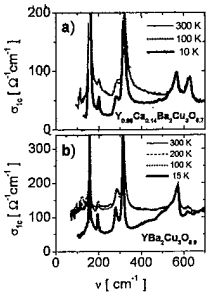

Figure 1.

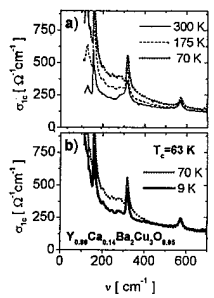

Figure 2.

Infrared Microspectroscopy Studies of Electronic and Electro-Optical Materials	U4IR

L.G. Casagrande (Northrop Grumman Corporation)

The performance of electronic and electrooptical materials and devices is dependent on their physical and chemical quality and uniformity. These materials can be difficult to fabricate, and frequently contain microscopic defects and inhomogeneities such as included secondary phases which can detract from device performance. Understanding the nature of such defects is vital to reducing their formation during fabrication and to determining their effect on device performance. We have used the Fourier-transform infrared microspectrometer originally on the midinfrared beamline at port U2B, now on beamline U4IR, to study these defects in the non-linear optical material $AgGaSe_2$. We have spatially mapped 100 μm $\times$ 100 μm regions of this material containing microscopic defects $\sim$10 to 20 μm across. The infrared beam was shuttered to a 12 μm square and successive spectra were obtained in 10 μm steps. Figure 1 shows spectra obtained from various locations in such a region. The average transmission spectrum is generally representative of this material without an anti-reflection coating, although it deviates slightly from the standard FTIR transmission spectrum of the entire sample. For spectra obtained away from the defect, the spectrum is nearly identical to the average spectrum. However, for spots at or near the surface defect, decreases in transmission occur which may indicate the presence of optically absorbing impurities. The minimum transmission in the spectrum at the second on-defect point occurs at ν=2941 cm^{-1}, and the map of transmission at this frequency vs. location is shown in Figure 2. This shows the unique potential for IR microspectroscopy to correlate microscopic chemical analysis with optical microscopy techniques. Additional work to determine the nature of these defects is underway.

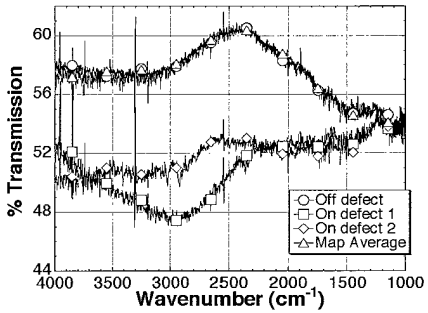

Figure 1. Individual FTIR transmission spectra for different locations in $AgGaSe_2$ map compared to map average.

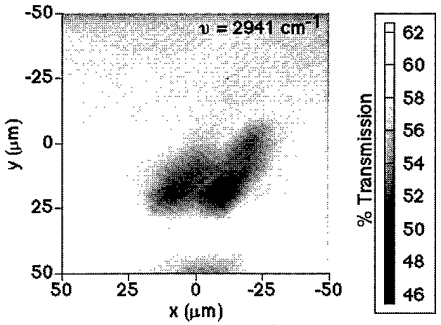

Figure 2. Map of transmission at 2941 cm^{-1} for spectra from region in Fig. 1 showing decrease in T at and around surface defect.

Mapping the Chemical Composition of Subchondral Bone in Osteoarthritis Using Infrared Microspectroscopy	U4IR

M.R. Chance, L.M. Miller, D. Hammerman, R. Stanley (AECOM), and C. Carlson (Bowman-Gray Sch. of Med)

Osteoarthritis naturally occurs in young adult female cynomolgus monkeys and it closely resembles the human disease. In the knee joint, it is characterized by the breakdown of the articular cartilage and marked thickening of the adjacent subchondral bone. There is a strong correlation between the severity of the osteoarthritic lesions and the thickness of the subchondral bone, but it is unclear why this is the case. We question whether the newly-deposited subchondral bone has a different chemical structure/composition compared to the older bone, leading to the development of osteoarthritis. Presently, we are using infrared micro-spectroscopy to study the chemical composition of the subchondral bone as a function of subchondral bone thickness. We are able to map the subchondral bone from the articular cartilage (older bone) to the marrow space (newer bone) and compare their chemical compositions. Bone proteins, primarily collagen, absorb infrared light in the 1450 - 1650 cm^{-1} region. An intense, broad band from 900 - 1200 cm^{-1} and a double-peaked band from 500 - 650 cm^{-1} are attributed to bone mineral, i.e. phosphate ions in hydroxyapatite. A small absorption centered at 875 cm^{-1} arises from carbonate-substituted hydroxyapatite. These bands are sensitive to mineral content (i.e. carbonate, phosphate, acid phosphate), mineral crystallinity, and the content/nature of the organic matrix. They are curve-fit and/or integrated and compared as a function of (1) state of the bone, i.e. thickness of the subchondral plate, and (2) age of bone, i.e. position in the subchondral plate.

Anharmonicity of Low Frequency Vibrational Modes in Amino Acid Polymers	U4IR

M.R. Chance, L.M. Miller, Q. He, and S. Schwartz (AECOM)

Low frequency (collective) modes in proteins ($\approx$10-600 cm^{-1}) have received considerable attention because it is thought that domains or sub-domains in proteins are involved in correlated motions on picosecond timescales. It is clear that motions at these frequencies make an important contribution to the mean-square displacement of atoms from their equilibrium (vibrational) positions. Thus, these motions are the first steps in functionally important motions leading to large-scale conformational changes. Such changes are critical to structural and functional processes like protein folding, cooperativity, and protein-protein or protein-ligand interactions involved in electron transfer, enzyme catalysis, and signaling. Poly-amino acids provide a model system for understanding collective modes in proteins. By polymerizing different amino acid monomers, varying secondary and tertiary structures can be created and studied with far infrared absorption spectroscopy. They provide a controlled method for identifying and characterizing any "breathing modes" attributable to various (α-helical or (β-sheet type structures in proteins. We have also obtained the far-infrared spectra of poly-L-phenylalanine, poly-L-alanine, poly-L-tryptophan, and poly-L-leucine from 10 to 295 K in 20 K increments. The results demonstrate (1) there are several (ranging from 4-10, depending on the poly-amino acid) low frequency modes in the far-infrared region, (2) the bands below $\approx$200 cm^{-1} all increase in frequency with decreasing temperature, and (3) this temperature-dependence increases with decreasing band frequency. These results suggest that these modes are highly anharmonic, consistent with various computational studies. Currently, curve-fitting analysis is being used to aid in the identification of various modes, assignment of their origins, and their sensitivity to temperature.

Chemical Composition of Bone Osteons in Osteoporosis and Osteopetrosis *In Situ*	U4IR

M.R. Chance, L.M. Miller (AECOM), R. Mendelsohn (Rutgers U.), and A. Boesky (Hosp. for Special Surgery)

The unique strength and rigidity of bone arises from a combination of organic components (primarily collagen) and inorganic (mineral) components. Over a lifetime, bone is continuously remodeling itself. Old bone is eroded away in a tunnel-like fashion by osteoclasts and new bone is deposited layer-by-layer in the "tunnel" by osteoblasts. From a cross-sectional view, these new layers of bone, collectively termed an osteon, appear as series of concentric circles through a microscope. A typical osteon measures 200 (μm in diameter, where the youngest bone is at the center. In many diseased states of bone, there is an imbalance between bone production and resorption, resulting in overgrowth (osteopetrosis) or undergrowth (osteoporosis) of bone. To date, it is unclear whether the *chemical composition* of the bone in a diseased state is the same as normal bone. Using infrared micro-spectroscopy, we are able to visibly and chemically image individual osteons in terms of growth-, site-, and age-dependent variations in mineral content (i.e. carbonate, phosphate, acid phosphate), mineral crystallinity, and the content/nature of the organic matrix. A significant advantage of this technique over other chemical methods is that the bone does not need to be homogenized before testing; we are able to study cross-sectional samples of bone *in situ* at a resolution of 3-5 (μm. In this study, we present a comparison of human osteoporotic bone to osteopetrotic bone. Early results show some similarities and also significant differences between osteopetrotic and osteoporotic bone. For both diseased states of bone, the ratios of phosphate-to-collagen and carbonate-to-collagen concentrations are similar and these ratios increases as bone matures (from the center to the periphery of the osteon). Also for both, the phosphate ions (PO_4^{3-}) are replaced by other anions such as carbonate (CO_3^{2-}) as bone ages, i.e. the hydroxyapatite becomes non-stoichiometric. However in contrast, we observe significantly more CO_3^{2-} substitution in osteoporotic bone than osteopetrotic bone as the bone matures.

IR Microspectroscopy of Laser Drilled Graphite/BMI Structural Composite Laminates	U4IR

D. Di Marzio, L. G. Casagrande, and J. Clarke (Northrop Grumman)

Sound attenuation is a major concern in both military and commercial aerostructures. Arrays of microholes drilled into nacelles and other aircraft components can effectively muffle engine noise. The use of advanced composite structural materials present a new challenge for this sound reduction technology. In this project, an automated laser drilling system is used to produce hole arrays in graphite/bismaleimide composite panels. Cylindrical holes have been produced with a uniform diameter of 30 mil and minimal heat damage to the surrounding composite matrix. Reflectance IR microspectroscopy was used to confirm the integrity of the bismaleimide used to hold the graphite fibers together near the laser drilled holes. Cross sections of the laser drilled holes were prepared, and a 50 μm IR beam diameter was used to scan across the cross sectioned holes. Figure 1 shows a schematic of the IR measurements of the cross sectioned panel. Figure 2 shows the dispersion corrected absorbance from a location far from the hole and a location next to the hole. The carbonyl peak near 1750 cm^{-1}, which is an indicator of relative oxidation for the bismaleimide, shows a small increase in integrated area in the region next to the laser drilled hole, as compared to the region far from the hole. A small amount of oxidation is expected next to the hole due to local laser heating. Spectra taken close to, but not next to the hole, exhibit no bismaleimide oxidation. Using IR microspectroscopy, automated laser drilling has been demonstrated as an effective method for fabricating sound attenuating microhole arrays in structural composites.

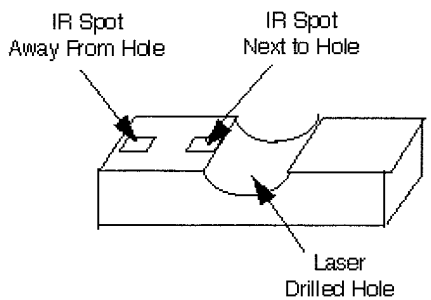

Figure 1. IR sampling schematic for laser drilled composite panel cross section.

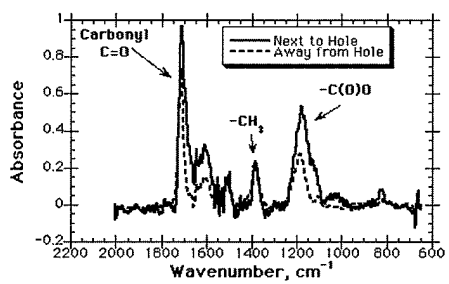

Figure 2. Micro IR spectra of cross sectioned laser drilled composite panel. Regions near the holes show little or no bismaleimide oxidation.

IR Microspectroscopy of Plasma Sprayed Liquid Crystal Polymer Films * | U4IR

D. Di Marzio, L. G. Casagrande, J. Clarke (Northrop Grumman Corporation), J. Brogan, S. Sampath, and H. Herman (SUNY)

Commercial and military marine and aerospace structural materials can experience significant damage due to environmental factors such as oxidation, corrosion, UV exposure, and fouling. Protective coatings are needed to provide a barrier to these damaging environmental effects. We are currently developing a plasma spray process to deposit a coating of liquid crystal polymer (LCP) onto composite structural components. LCP films have been demonstrated to be highly impervious to oxygen and moisture penetration, and they exhibit a high degree of mechanical strength. LCP powder is fed into a plasma spray gun, and the powder particles are melted and propelled at high velocity to the part to be coated. Figure 1 shows a schematic of the plasma spray process. IR microspectroscopy was used to determine the degree of LCP particle oxidation and burning on a local scale as a result of the plasma spray process. Figure 2 shows the IR reflectance spectra of uncharred and charred LCP particles in a plasma sprayed coating developed early in the program. The IR spot size was 50 μm. The uncharred particles exhibit a strong organic vibrational spectrum, especially below 2000 cm^{-1}. The charred particles show a dramatic reduction in the organic signature, and they exhibit a reflectance spectrum more characteristic of pure carbon. Dramatic improvements have since been made in the reduction of particle oxidation and burning in the development of the LCP plasma spray process.

*This work was partially supported by the NSF Materials Research Science & Engineering Center, Center for Thermal Spray Research, SUNY at Stony Brook.

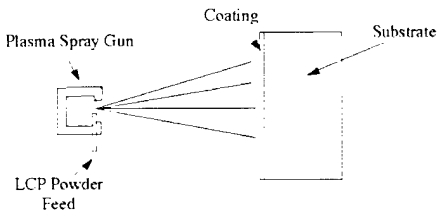

Figure 1. Plasma spray coating process. Liquid crystal polymer particles are partially melted and accelerated by the plasma towards the substrate component.

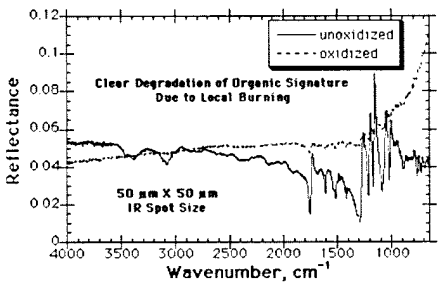

Figure 2. Micro IR spectra of uncharred and charred liquid crystal polymer particles in a plasma sprayed coating. Significant reduction in oxidized LCP particle content has been achieved.

Identification of Organic Compounds in the ALH84001 Meteorite from Mars | X1A, U4IR

G. J. Flynn (SUNY at Plattsburgh), L. P. Keller and M. A. Miller (MVA Inc.)

McKay et al. [1] suggest the ALH84001 meteorite contains evidence of possible ancient biological activity on Mars. One line of evidence is the concentration of polycyclic aromatic hydrocarbons (PAHs), frequently produced by the decay of living material, occuring in close proximity to magnetite and sulfide similar in size and shape to those produced by terrestrial bacteria [1].

We employed the Scanning Transmission X-Ray Microscope on beamline X1A to determine the bonding state(s) and the spatial distribution of the carbon in ultramicrotome thin-sections of carbonates globules and the rims, where the magnetites and sulfides were found, on these carbonates from ALH84001 [2]. Both the carbonate and the rim sections contained carbon-rich regions, but each gave a different C-XANES spectrum, suggesting the major carbon-bearing compound was different in the rim and the carbonate [2]. We then examined the same samples using a Spectra-Tech micro-Fourier Transform Infrared (FTIR) spectrometer, on beamline U4IR, to identify the carbon compounds.

Transmission Electron Microscope (TEM) examination of the rim samples indicated were composed of feldspathic glass and contained micron-size chromite, and regions of fine-grained magnetite and sulfide. The FTIR spectra of the rim samples showed a broad absorption near 1000 cm^{-1}, characteristic of silicate glass, and two weaker features at 2918 cm^{-1} and 2850 cm^{-1}. These two features are consistent in position and relative depths with the symmetric and asymmetric stretching vibrations of the $C\text{-}H_2$ in aliphatic hydrocarbons.

The FTIR spectra of the carbonate globule showed a narrow absorption at about 1500 cm^{-1}, characteristic of carbonate, and a weaker absorption at 2964 cm^{-1}. Two even weaker features appear at 2920 cm^{-1} and 2850 cm^{-1}. The feature at 2964 cm^{-1} is characteristic of the $C\text{-}H_3$ asymmetrical stretching vibration. Although a weaker $C\text{-}H_3$ symmetrical stretching vibration generally occurs near 2870 cm^{-1}, this feature is absent in the carbonate globule spectrum, and is suppressed in certain compounds containing $C\text{-}H_3$ groups. One particularly good spectrum of the carbonate globule sample appears to show a weak, broad absorption over the range 2990 cm^{-1} and 3060 cm^{-1}. Follow-up measurements, to determine if this feature could indicate the detection of C-H stretching vibrations of a mixture of PAHs, which would have an absorption near 3030 cm^{-1}, are in progress.

These preliminary results confirm that high concentrations (of order 1 to 5 percent) of organic carbon are associated with the carbonate globules and rims in ALH84001, and further confirm the STXM observation that the rim and the carbonate globule contain different types of carbon. The latter result seems to rule out the simplest form of organic contamination of ALH84001, simple evaporation of an organic-rich fluid, which would be expected to leave the same residue in both the carbonate globules and the adjacent rim material, although selective, mineral specific, contamination cannot be excluded.

References:

1) McKay, D. S., et al. Science, 273, 924-927, 1996.
2) Flynn, G. J. et al., Meteoritics, 32, A46-A47, 1997.

Experimental Check of the Diffuse Scattering of Conduction Electrons by Adsorbates on Metallic Surfaces	U4IR

M. Hein and A. Otto (U. Duesseldorf, Germany), P. Dumas (LURE and LASIR-CNRS-France) and G.P. Williams (NSLS)

The initial scientific programm at the U4IR beamline was dedicated to the adsorption of molecules on metallic surfaces. It was shown, in the early 90's, that two unexpected features, namely an antiabsorption band accompanied by a broadband IR reflectance change, are related to vibrational dynamics at surfaces. In order to account for these observations, a theory, mainly developped by B.N.J.Persson, suggested that there is a friction force between the collective motion of the adsorbate parallel to the surface, and the substrate conduction electrons, leading to the broadband IR reflectance change (when the frequency of the IR light departs from that of the collective motion), and to a abrupt changes of the reflectivity (antiabsorption band)- when the frequency of the light coincides with the frequency of the collective motion of the adsorbates. This can be viewed as the loss of conduction electron diffuse scattering, (e.g. a change in the resistance of the metallic film) by the adsorbate, which pays the role of a static impurity potential, breaking the translational symmetry at the surface.

Confirmation of the model , and in particular the role of the lifetime of the adsorbate vibrational mode, is of critical importance, and was addressed by simultaneous measurements of the DC resistance and broadband IR reflectance changes for CO, O and Cu on Cu(111) thin epitaxial films, grown on TiO_2. By varying the thickness of the film, and the nature of the adsorbate, we have shown:

1- That the shape of broadband IR reflectance change is well accounted for by the theoretical model (Fig. 1)

2- There is a linear relationship between the IR reflectance change and the resistance change, (Fig2), as predicted by the diffuse scattering model:

$\Delta R_p / R = (4ne^2/mc\cos(\theta))[t \Delta\rho (t)]$

where ($\Delta R_p / R$) is the reflectance change at the asymptotic limit, n is the number of conduction electron per atom, m the electron mass, t the thickness of the film and $\Delta\rho$ the resistivity change.

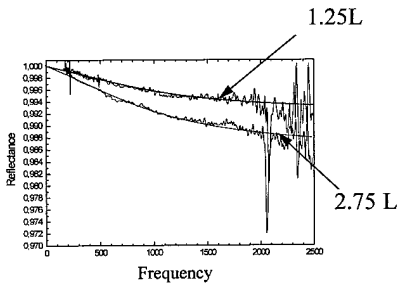

Figure 1. Broadband IR change for CO adsorbed on Cu(111) film, at 80K, as a function of exposure. The line through the data is a fit according to the theory.

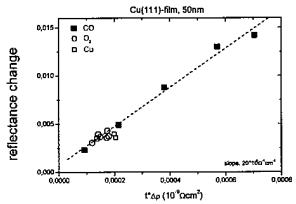

Figure 2. Linear dependence of the broadband IR reflectance change, and the thickness x resistivity change for different adsorbates. The common slope is an additional proof of the validity of the model, as it should depend only on the substrate.

Spatially Resolved Characterization of Coal Heterogeneity with Synchrotron Infrared Microspectroscopy	U4IR

F.M. Hoffmann (SCI-MED), P. Dumas (LURE and LASIR-CNRS, France), G.P. Williams (NSLS) and J. Paul (Bilkent U., Turkey)

Coal is a very complex material consisting essentially of carbon ring structures (coal macerals) and minerals (alumino silicates minerals with attached H2O and OH groups). Each of these groups can contain many different components and elemental compositions. In coal liquefaction the coal component is hydrogenated with different precursors for MoS_2 and other sulfided hydrogenation catalysts. The dispersion and the location of these precursors is an important factor in controlling the activity. The hydrogenation catalyst, which produces hydrogen, should be located in close proximity to the coal macerals to facilitate the reaction of the hydrogen with the coal. Therefore, a spatially resolved characterization of the dispersion and location of the catalytic precursors is of great importance. The difficulty of performing IR spectroscopy on coal samples derives from the high complexity and heterogeneity of the material. The particulate samples of coal used for infrared analysis must be finely ground because of the high absorbance of the coal. Because of the different derivations from biological matter the IR spectra obtained from pulverized samples give average information rather than being characteristic of any individual component in the coal. In the present work we have utilized IR synchrotron radiation on the U4IR beamline to perform Infrared microscopy of coal samples. Coal particles from 20-100 micron in diameter are characterized at a special resolution of 6 x 6 microns. Fig. 1 shows an optical micrograph of a typical coal particle together with an infrared spectrum obtained from the central region of the sample where both maceral and mineral constituents are present. Surface mapping of the entire particle shows a different distribution of the macerals and for the minerals in this particle, as indicated by the intensity profiles of characteristic C-H bands at 2950 cm^{-1} and O-H bands at 3610 cm^{-1}. Further work will investigate the distribution and dispersion of precursors for hydrogenation catalysts on these particles.

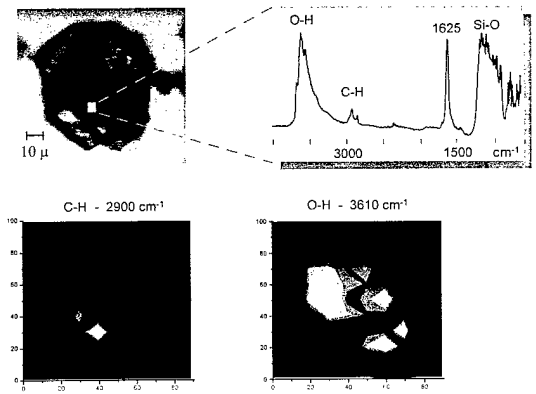

NO_2 Activation and Alkali Compound Formation | U4IR

F.M. Hoffmann, (SCI-MED, New York), G.P. Williams (NSLS) and J. Paul (Bilkent University, Ankara, Turkey).

The activation of CO_2 and NO_2 are important elementary reactions in catalysis and environmental pollution control. Previous work on the activation and compound formation of CO_2 by alkali metals has shown the formation of potassium oxalate $K_2C_2O_4$ and its subsequent decomposition to carbonate [1]. The present work investigates the activation of nitrogen dioxide in the presence of potassium. The experiments were conducted by evaporating potassium in the presence of NO_2. Both the pressure of NO_2 and the evaporation rate of the K could be controlled thus allowing to control the stoichiometry and providing selectivity for certain intermediates. The results presented in Fig. 1 show a typical reaction sequence obtained under NO_2 saturation conditions. The vibrational spectra obtained during evaporation show the formation of N_2O_4 at low temperature (90K). Subsequent annealing of the layer induces decomposition of the layer to nitrate. Changing the K:NO_2 stoichiometry reveals more complex decomposition pathways, which are currently investigated with temperature-programmed time-evolved IR spectroscopy.

[1] F.M. Hoffmann, D.G. Van Campen, G. Williams and J. Paul, Surface Sci., submitted.

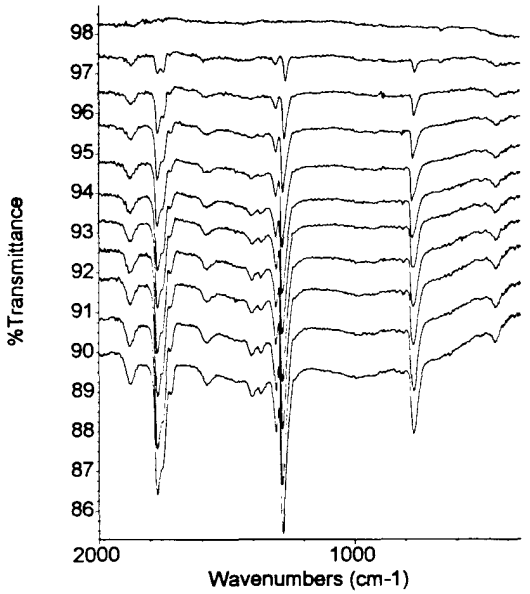

Figure 1. Time evolved vibrational spectra obtained during the reactive evaporation of at NO_2 saturation on Cu(100) (T=90K)

In Situ Synchrotron Far Infrared Spectroscopy of the Electrochemical Interface * | U4IR

C.A. Melendres (ANL), G.A. Bowmaker (U. of Auckland, New Zealand) and J.M. Leger (U. de Poitiers, France)

The objective of this program is to elucidate the structure of the electrode/solution interface, as well as those of electrochemically formed surface films and adsorbed layers. Far infrared spectra of the surface films formed upon anodic oxidation of copper have been obtained "in-situ" for the first time in aqueous solution environments using a synchrotron source. The spectroelectrochemical behavior of copper was studied in NaOH and in a dilute solution of KSCN in perchlorate. The oxide film at -0.05 V vs. SCE in 0.1 M NaOH solution has been identified as Cu2O. In the passive region at 0.3 V, CuO and Cu(OH)2 appear to be present on the surface (Fig. 1a). Vibrational bands observed in 0.025 M KSCN/perchlorate solution are attributed to a surface film of copper (I) thiocyanate (Fig. 1b). The band positions are in good agreement with published data on the corresponding bulk material but some difference in intensity is observed.

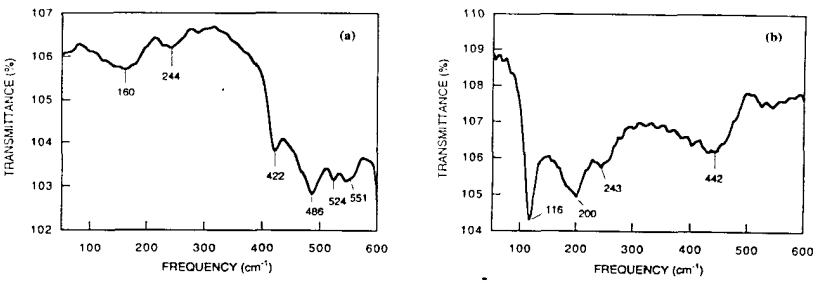

Figure 1. *In situ* far IR spectra of copper in (a) 0.1 M NaOH at 0.3 V vs. SCE (ref. to spectrum a -1.0V and (b) in 0.025 M KSCN + 0.1 M $KClO_4$ at 0.05V vs. SCE (ref. to -1.1V).

* Work supported by the Div. of Matls. Sci., BES Off., USDOE. Co. No. W-31-109-ENG-38

Infrared Materials for Studying Biological Systems With Infrared Microspectroscopy	U4IR

L. Miller (AECOM) and L. Carr (NSLS)

For infrared microspectroscopy, samples such as cells and biological tissues are often supported on or between infrared-transparent window materials such as barium fluoride (BaF_2), potassium bromide (KBr), and zinc selenide (ZnSe). These materials have refractive indices that are frequency dependent, so the focal point that one sees with visible light through the infrared microscope is different than the infrared focal point where the spectrum is taken. In other words, a sample that appears focused with visible light is really out of focus to the infrared light, so that the sample area chosen for data collection is really larger than it visibly appears. The smaller the aperture, the more significant is this focal point "error". Since synchrotron infrared microspectroscopy of biological samples involves apertures of less than 20 (μm, we find that a focus shift correction must be applied in order to obtain spectra with high spatial resolution. Using the frequency-dependence of the refractive indices for BaF_2, KBr, and ZnSe, we have calculated the expected focus shifts for these materials as a function of infrared frequency. Experimentally, we have taken infrared spectra on these materials with a range of focus-shifts from the visible focal point and we find good agreement with our calculated values. For windows with a 2 mm thickness, we find differences of $\approx$ 20, 25, and 60 μm between the visible and infrared focal points of BaF_2, KBr, and ZnSe, respectively. Therefore, after visibly focusing a sample that is mounted on or between the above-mentioned materials, the sample must be "defocused" by translating the sample stage so that the sample is focused for collecting the infrared spectrum.

Characterization of Bone Mineral Model Compounds Through Far-Infrared Spectroscopy	U4IR

L.M. Miller, M.R. Chance, Q. He(AECOM), R. Mendelsohn (Rutgers U.), A. Boesky (Hosp. Special Surgery), and V. Vairavamurthy (Shoreham-Wading River HS)

Hydroxyapatite, $Ca_{10}(PO_4)_6(OH)_2$, is the primary mineral component of bone. Bone growth begins as amorphous calcium phosphate crystallizes into hydroxyapatite. As the bone matures, the size, crystallinity, and stoichiometry of the hydroxyapatite crystals change. For example, the phosphate and hydroxide sites are often substituted by other anions such as acid phosphate (HPO_4^{2-}), carbonate (CO_3^{2-}), and fluoride (F^-). The nature of the phosphate environment in bone can be characterized through analysis of a series of four phosphate bands in the far-infrared region (500 - 650 cm^{-1}). The intensities and peak positions of these modes are sensitive to the hydroxyapatite crystal size, structure, and stoichiometry. Thus, we have grown a series of hydroxyapatite crystals, varying in (1) the initial solution concentration of calcium phosphate, (2) the initial solution concentrations of non-stoichiometric components such a carbonate and fluoride, and (3) the time of crystal growth. The far-infrared spectra of these crystal standards were collected in the form of potassium bromide pellets. Currently, curve-fitting and integration analysis are being used to correlate the peak positions and intensities of these modes as a function of the above-mentioned crystal growth parameters. These results will be valuable for the interpretation of far-infrared spectra from non-synthetic bone samples.

Interchain Hydrogen-Bonding Interactions Between the Filaments of Actin	U4IR

L.M. Miller (AECOM)and B. Chasan (Boston U.)

Hydrogen-bonding interactions are crucial to the function of many biological molecules. The vibrational modes associated with hydrogen bonds fall in the far-infrared region (150-250 cm^{-1}). Actin is the primary component of muscle fibers. The single polypeptide unit is known as G-actin. When G-actin polymerizes to form actin filaments (i.e. muscle fibers), it is called F-actin. F-actin filaments are formed as two G actin monomers are twisted into a helix and it is thought that they are held together by a network of hydrogen-bonding interactions. Thus, a comparison of the far infrared spectra of G- versus F-actin provides a method for studying hydrogen-bonding interactions in proteins. We have grown films of G- and F-actin on polyethylene disks and determined their far infrared spectra. We observe 3 modes (532, 544, and 590 cm^{-1}) in both G- and F-actin. In addition, we observe intense features in the F-actin spectrum at 181 and 254 cm^{-1}, which are absent in the monomeric G-actin, and may be assignable to hydrogen bonding interactions in the F-actin. We plan to continue our studies on G- and F-actin by growing films under different conditions, such as in the presence of D_2O and varying salt concentrations. D_2O is expected to shift the frequency of hydrogen-bonding interactions and various salt conditions provide different levels of polymerization of G-actin into F-actin. In addition, the polarized nature of the infrared light will make it possible to study the orientation of the actin filaments.

Metal-Ligand Stretching Frequencies in Hemeproteins Through Far-Infrared Spectroscopy	U4IR

L. Miller (AECOM), T. Sage and P. Champion (Northeastern U.)

The metal-ligand stretching frequencies in metalloproteins fall in the far-infrared region. The iron atom in the hemeprotein, myoglobin, binds four nitrogen ligands from the heme group, one nitrogen ligand from a histidine residue in the protein, and the sixth coordination position is the oxygen-binding site. Since other ligands such as carbon monoxide and nitric oxide also competitively bind to the oxygen-binding site, it is important to characterize the structural and electronic intermediates that are involved in the ligand-binding process. Since the iron-ligand bond can be photolyzed at 10 K, we are able to use photolyzed/unphotolyzed difference FTIR to probe vibrational modes such as (1) the iron-ligand stretching frequency, (2) the iron-proximal histidine stretching frequency, and (3) heme doming modes, all of which differ in the ligand-bound and photolyzed states. Resonance Raman studies have also been used to identify some of these modes. However, the conditions by which several of them are resonance-enhanced are still unclear, making infrared spectroscopy a necessary alternative. In the past, we have been unsuccessful with myoglobin films in polyvinyl alcohol (PVA) on polyethylene due to (1) the temperature-dependence of the far infrared spectrum of PVA and (2) the optically-opaque nature of polyethylene, making it difficult to photolyze myoglobin at low temperature. Recently, we have shown that solution samples in 75:25 glycerol:water (50 μm pathlength) between sapphire windows are reasonably transparent in the far infrared region below 100 K and completely transparent in the visible. These findings will greatly improve the ability to (1) photolyze the sample, (2) collect high quality difference spectra, and (3) collect far-infrared protein spectra *in solution*-a more biologically relevant state of the protein.

Infrared Microspectroscopy of Small Dust Particles of Astrophysical Origins*	U4IR

G. Quitte, J. Borg, L. d'Hendecourt, J.P. Bibring (Inst. d'Astrophysique Spatiale, Orsay, France), P. Dumas (LURE and LASIR-CNRS, Orsay, France), G.L. Carr and G.P. Williams (NSLS)

One of the main objectives in studying interplanetary dusts is to qualify their physical, chemical, and structural (mineralogical) properties. The ultimate goal is to understand the origin and composition of comets and asteroids, which may carry information about the origin of the Solar System. Such dust particles have been collected from the statosphere or low Earth orbit. Some of these particles are shown in Figure 1.

IR microspectroscopy appears to be a useful technique for characterizing the chemical composition of these dusts due to its fast and reliable analysis. Here we demonstrate how the synchrotron infrared source allows for chemical information to be obtained from particles only a micron or two in size (see Figure 2). The presence of water, silicates, organics (aliphatics) and an olivine mineral phase have been tentatively identified using synchrotron-based spectra. Most of these features can not be detected using the conventional (globar) source, due to its low intrinsic brightness.

*Supported by DOE through contract DE-AC02-76CH00016.

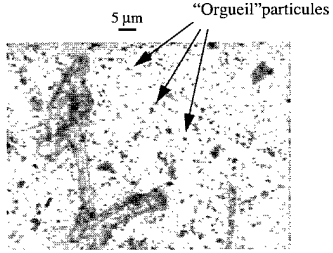

Figure 1. Optical image of "Orgueil" particles.

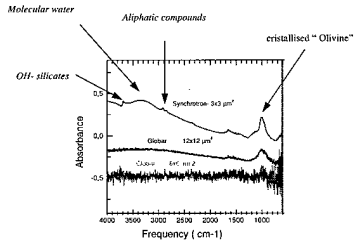

Figure 2. Infrared spectra of individual "Orgueil" particles, taken with a conventional source and with the synchrotron source.

Vibrational Dynamics of C_{60} on Noble Metal Surfaces	U4IR

P.Rudolf (U.Namur, Belgium), R. Raval (U.Liverpool, England), P. Dumas (LURE and ASIR-CNRS-France), and G.P. Williams (NSLS)

Previous experiments by infrared spectroscopy on C_{60} adsorbed on Ag(111) surfaces (see Annual report 1994, 1995), carried out at the U4IR beamline, have shown that C_{60} molecules are chemisorbed on the surface, and that the dominant feature is for a Ag(2) Raman mode, which becomes IR active upon adsorption. The appearance of the Raman active mode was attributed either to a dynamical charge transfer from the silver substrate to the C_{60}, or to a symmetry breaking upon adsorption. Recent experiments have been carried out on two other surfaces: Au(110) and Cu(100) in order: 1- To follow any charge transfer dependence between these surfaces on the frequency of the Ag(2) Raman mode, and 2- To carefully record the broadband infrared change on the three surfaces upon C_{60} chemisorption, and to verify if this changes agrees with the diffuse scattering model of the conduction electron.

We have observed a slight frequency change of the Ag(2) mode for C_{60} on the three surfaces (1450 cm^{-1} for Ag(111) and Au(110) and 1440 cm^{-1} on Cu(100), which apparently does not followed the prediction of the charge transfer hypothesis. More interestingly, the broadband IR reflectance change is well accounted for by the diffuse scattering model (Figs. 1 & 2). According to the friction coefficient model, the lifetime of the collective motion of C_{60}, parallel to the surface, and due to deexciation via electron-hole pair creation, can be determined from the asymptotic limit of the reflectance change. We found values ranging between 170 ps and 220ps for Cu, and Au, Ag respectively. Accounting for the Newns-Anderson model, which states that the lifetime is proportional to the mass of the adsorbate, and depends on the density of states induced by the adsorbed molecule at the Fermi level, the value of the lifetime indicates a high density of states induced by the C_{60} molecules upon chemisorption on noble metal surfaces.

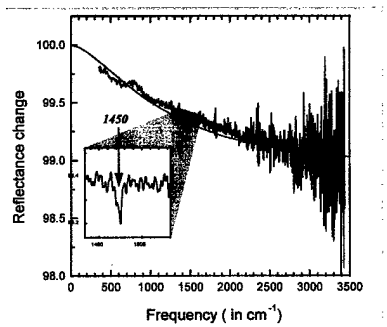

Figure 1. IR spectrum of a monolayer of C_{60} adsorbed on Au(110) surface at room temperature. The solid line is a fit according to the diffuse scattering model theory.

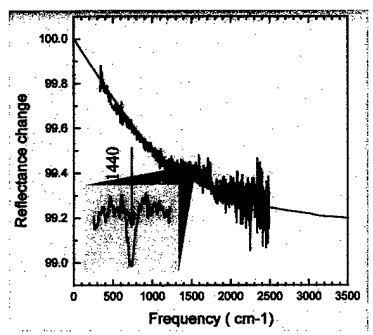

Figure 2. Same as Fig1 , but for C_{60} adsorbed on Cu(100) at room temperature.

Isotope Effects for the Low Frequency Modes of CO/Cu(100) | U4IR

G. P. Williams,(NSLS) and C. J. Hirschmugl, (LBNL)

In order to fully understand the dynamics and lateral potential energy surface of CO molecules chemisorbed onto Cu(100) we undertook a far-IR study of the bonding vibrational modes for all the isotopes. The data will be combined into a paper which also includes helium atom scattering measurements of the lowest frequency frustrated translational mode. The figure shows the changes in reflectance induced by the CO and fits using an expression of Persson and Volokitin (*Surface Science* **310, 314** (1994)) for non-local optics. The data show broadband background changes, a dip corresponding to the carbon-metal stretch mode, and a peak (anti-absorption) corresponding to the frustrated rotational mode. The Persson/Volokitin formula takes into account the the background shape and the hindered rotation mode. Parameters for the fit are all related to and are close to values for bulk Cu and include the Fermi velocity, the plasma frequency, the skin depth and the mean free path. The carbon-metal stretch mode was fitted to a Gaussian line shape.

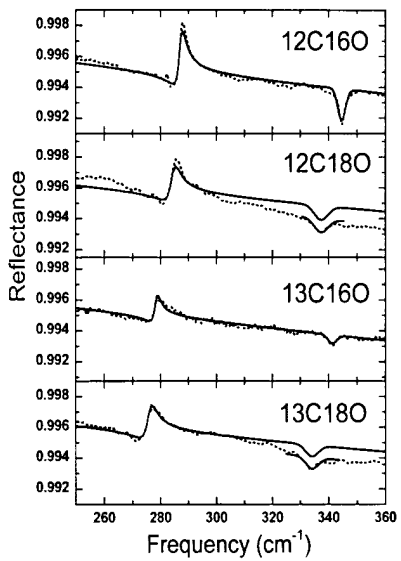

Figure 1. The reflectance ratio of the IRAS spectra obtained with CO to that without CO for a c(2X2) half monolayer (Θ = 0.5) at 90K. The spectra were obtained with a resolution of 0.12meV and a measurement time of 3 minutes. The fits are shown as solid lines. Since the background does not fit well in the vicinity of the carbon-metal stretch mode for the $C^{18}O$ isotopomers, the peaks have been displaced.

Low Frequency Dynamics for mixtures of S and CO on Cu(100) | U4IR

G. P. Williams (NSLS) and C. J. Hirschmugl (U. of Wisconsin)

To understand the behavior of catalysts better, studies of Sulfur and CO coadsorption systems on metals are required. The adsorption of Sulfur /Cu (100) at 300K and CO/Sulfur mixtures /Cu(100) at 90K has been studied by Fourier Transform Infra-red Reflection Absorption Spectroscopy in the 250-2500 cm-1 frequency range using synchrotron radiation. The first system is created by exposing Cu(100) to various amounts of H_2S at 300K. The H_2S dissociates, leaving S atoms adsorbed at 4-fold hollow sites. Subsequently, the S/Cu(100) substrate is cooled and exposed to 2L (2x10-6 torr-s) CO. We have observed a broadband absorption for the S/Cu(100) system, as illustrated in Figure 1. The fit to this curve uses the bulk parameters that have been found in the past for CO/Cu broadband absorptions[1]. The subsequent CO adsorption results in a partial coverage of CO, as confirmed by the appearance of the CO stretch at about 2000 cm^{-1}, but the broadband absorption and concomitant hindered rotation previously observed for CO adsorbed on clean copper are absent. The thermal desorption mass spectroscopy for a 2L CO dose on increasing sulfur precoverages indicates a linear decrease in the CO adsorbed, which correlates to the intensity (triangles and left hand axis) of the CO stretch as shown in Figure 2. The strength of the background absorption for CO/S/Cu ratioed to S/Cu spectra, as a function of increasing preadsorbed S is also shown in Figure 2. Notice that the background change decreases to zero before the CO stretch intensity decreases to zero (corresponding to the spectra in Figure 1.) Appealing to the Persson-Volokitin model that describes the physics which accounts for the appearance of the hindered rotation and broadband absorption, we can attribute the above behavior to the free electrons in the Cu scattering primarily off of the Sulfur adsorbates, exciting the Sulfur parallel modes. The parallel modes of the CO molecules are no longer being driven by this same mechanism. [1] C.J. Hirschmugl and G.P. Williams Physical Review B52 14177 (1995) [2] B.N.J. Persson and A.I. Volokitin Surface Science 310 314 (1994)

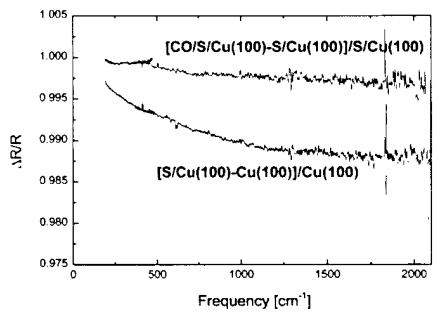

Figure 1. Figure 1

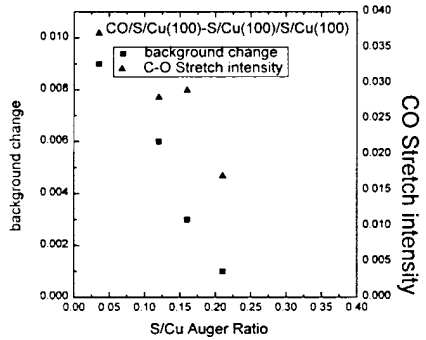

Figure 2. Figure 2

Partial Spectral Weights of Disordered Co-Pd Alloys | U5UA

W.J. Kim, J.H. Park, W.G. Park, S.-J. Oh (Seoul National U.), H.J. Kim, E.Vescovo (NSLS)

Recently, considerable interest is given to the interface formation between magnetic and nonmagnetic materials. Therefore the electronic structures of disordered Co-Pd alloys were investigated by means of turnable photon energies in the soft x-ray region. We made use of the Cooper minimum phenomena of Pd 4d states to deduce the partial spectral weights from photoemission spectra. All alloy samples were made by arc melting method in the Ar atmosphere. Scraped surfaces were cleaned by Ne ion bombardment and anealing at T=400°C in UHV. In order to obtain the partial spectral weight of each component the valence band spectra of pure metals and alloys are measured in the vicinity of the Cooper minimum. The calculated ratio of atomic photoionization cross section between Pd 4d and Co 3d is 0.05 at hv=130eV. But this calculated value is expected to change a little due to the solid state effects. The difference of lattice constants(9%) should also cause some local lattice relaxation and therefore a shift for bonding states and an increase in the intensity of antibonding state is expected. It could be related to the strength of hybridization. Fig.1 shows valence band spectra of the Co-Pd alloys in different at.%-Pd in hv=130eV and the hv-dependence of the photoionization cross section in $Co_{80}Pd_{20}$. At the Cooper minimum of the Pd-4d cross section (about 130eV) it is clearly shown that the intensity of Co 3d emission is the strongest and decreases gradually by changing the photon energy. We expect to find out an influence of photoionization matrix element and take it into account to deduce the accurate partial density of state of Pd. The further analysis in detail, whether the theoretically purposed model can be successfully applied, is in progress.

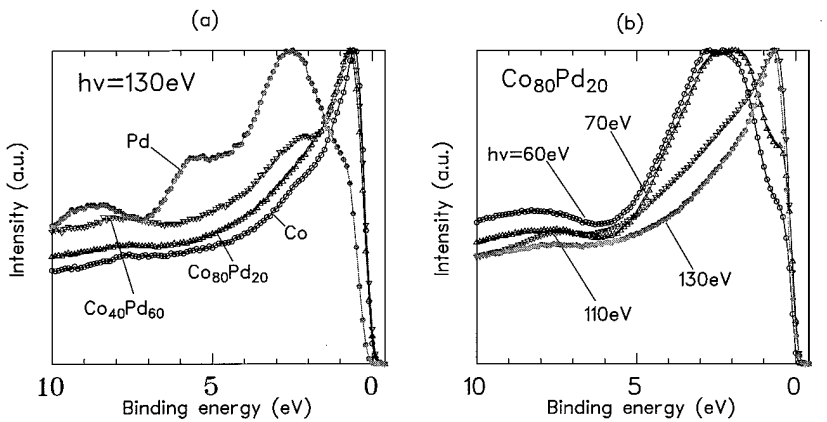

Figure 1. (a) Valence band spectra of the Co-Pd alloys in hv=130eV and (b) photon energy dependence of the photoionization cross section in $Co_{80}Pd_{20}$.

Electronic Structures and Magnetic Ordering of $Fe_{0.52}Al_{0.48}$ Alloy Films | U5UA

Y. P. Lee, K. W. Kim, Y. V. Kudryavtsev (Sunmoon U., Korea), G. S. Chang (Yonsei U., Korea), E. Vescovo (NSLS), and P. D. Johnson (BNL)

Equiatomic β-phase FeAl alloy crystallizes into a CsCl (B2) - type structure. A perfectly ordered stoichiometric FeAl alloy is not ferromagnetically ordered because of an absence of the ferromagnetic nearest neighbors. Even a slight atomic disorder can lead to the occurrence of local magnetic moments. It is widely believed that these magnetic moments are induced from so-called antistructure Fe atoms (Fe-ASA) - Fe atoms at Al sites. The estimated values for the effective magnetic moment of a Fe-ASA spreads widely from 5.4 μ_B to 1.5 μ_B, and it is clear that there is no common point view yet on the nature and value of the magnetic moments of nearly equiatomic FeAl alloys. We investigate the influence of the structural order-disorder transition in the nearly equiatomic FeAl alloy film on the magnetic moments and electronic structures using spin-polarized photoemission spectroscopy at the U5UA undulator beam line of the NSLS. Figure 1 shows the spin-polarized photoemission spectra for the ordered and disordered $Fe_{0.52}Al_{0.48}$ films. The order-disorder transformation enhances the spin polarization doubly in an agreement with our magnetic circular dichroism results[1]. By comparing with the reported magnetic moment and spin polarization of pure Fe[2], we found the spin magnetic moments of the constituent Fe atoms to be 0.25 and 0.55 μ_B for the ordered and disordered states, respectively. These relatively lower values of the spin magnetic moment also indicate a difference in magnetic structure between the top surface layers and the underlying ones.

[1] K. W. Kim et al., J. Appl. Phys. (submitted)
[2] P. D. Johnson et al., Rev. Sci. Instrum. 63, 1902 (1992)

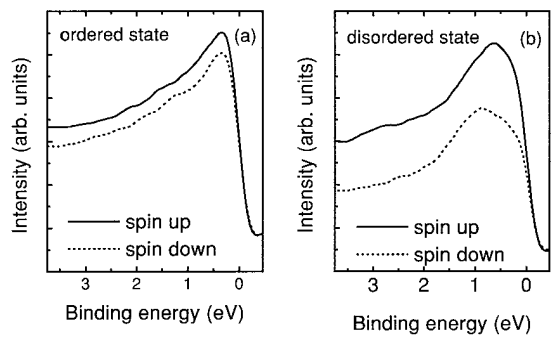

Figure 1. Spin-polarized photoemission spectra of the (a) ordered and (b) disordered $Fe_{0.52}Al_{0.48}$ films.

Observation of a Half-Metallic Ferromagnet — U5UA

J.-H. Park, E. Vescovo, H.-J. Kim (NSLS), C. Kwon, R. Ramesh, and T. Venkatesan (U. Maryland)

Half-metallic systems are new class of materials which are characterized by the coexistence of metallic behavior for one electron spin and insulating behavior for the other. The density of states (DOS) has 100% spin polarization at the Fermi level (E_F), and the conductivity is completely dominated by the metallic single-spin charge carriers. This exotic physical properties could have a significant impact on technological applications of magnetic devices.

Here, we have performed spin-resolved photoemission spectroscopy (SRPES) measurements on $La_{0.7}Sr_{0.3}MnO_3$ which has been known to exhibit large negative magnetoresistance, the so called 'colossal magnetoresistance'. The figure shows valence band spin-resolved photoemission spectra near E_F measured at (a) T = 40K and (b) T = 380K. At T = 40K ($\ll T_C \simeq 350$K), all the Mn $3d$ electron spins are aligned ferromagnetically, and indeed the spectra in figure (a) show considerable difference for the majority and minority spins. The most striking observation is the $half-metallic$ feature. The spectrum for the majority spin extends up to E_F and show the metallic Fermi cutoff, while that for the minority spin falls down at $\sim$ 1eV binding energy and the spectral weight disappears very near E_F, reflecting the insulating gap. In the region of 0 eV to $\sim$ 0.4 eV binding energy, the minority spin states only show spectral noise, and $\sim$ 100% spin-polarization is obtained. This is the first experimental evidence for the existence of a true half-metallic ferromagnet. But above T_c (380K), the spins are disordered, and the spectra in figure (b) show no difference for the two different spins.

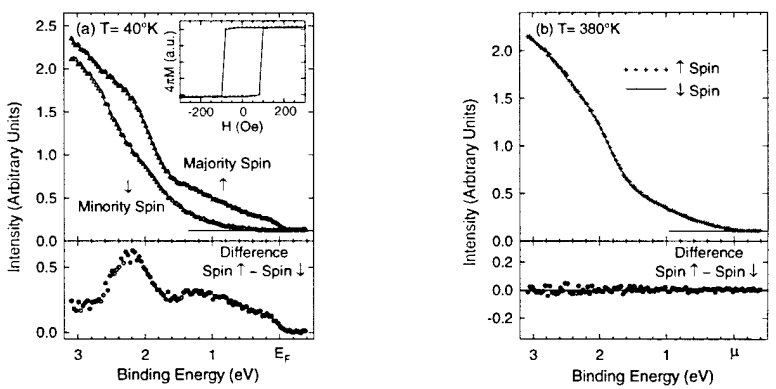

Figure 1. Spin-resolved Photoemission spectra of $La_{0.7}Sr_{0.3}MnO_3$ thin film near the Fermi energy at (a) T = 40K ($\ll T_C$) and at (b) T = 380K ($> T_C$). The photon energy and the experimental resolution were set $h\nu$ = 40eV and ΔE = 0.2eV, respectively. The magnetic hysteresis loop is shown in the inset.

Surface Boundary Magnetizm of Half-metallic Ferromagnet $La_{0.7}Sr_{0.3}MnO_3$ — U5UA

J.-H. Park, E. Vescovo, H.-J. Kim (NSLS), C. Kwon, R. Ramesh, and T. Venkatesan (U. Maryland)

Doped manganese perovskites has been known to exhibita large negative magnetoresistance (MR) near the Curie temperature (T_C), However, the large MR response requires high magnetic fields, which are available only in special environments. Recently, the enhanced low-field MR effects have been reported in manganese perovskite polycrystalline samples and trilayer tunnel-junction devices that a thin insulating layer is sandwiched by the ferromagnetic metallic manganese perovskites layers, and has been known to be originated from the spin-dependent electron tunneling mechanisms, across the gain boundary in the polycrystalline samples and through the insulating layer in the trilayer devices. The tunneling is actually dominated by the charge carriers at the surface (grain) or interface boundaries. Thus, understanding of the magnetization at the surface boundary is necessary for the understanding of the low-field MR effects. Here we have investigated the magnetization at the surface boundary of a half-metallic ferromagnet $La_{0.7}Sr_{0.3}MnO_3$ by using spin-resolved photoemission spectroscopy (SRPES),which has just a few monolayer ($\sim$ 5A) penetration depth. Figure shows the temperature dependence of the spin-anisotropy of the Mn $3d$ states, which represent the magnetization at the surface boundary (M_{sb}), in comparison with that of the bulk magnetization (M_b). Interestingly, the obtained M_{sb} exhibits greatly different temperature dependence behavior than M_b. Upon heating, M_sb decreases rapidly, and shows linear-like (T_C - T)-dependence near T_C. Actually, theoretical studies by using mean field approximation and numerical Monte Carlo simulations based on the Heisenberg spin Hamiltonian predict that the magnetization at the surface has linear (T_C - T)-dependence near T_C, greatly different from the (T_C - T)$^1/2$ or (T_C - T)$^1/3$ dependence of the bulk magnetization.

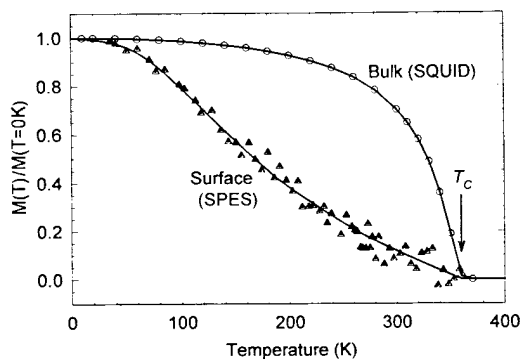

Figure 1. Temperature dependence of the magnetization at the surface boundary of $La_{0.7}Sr_{0.3}MnO_3$ obtained by monitoring the spin-anisotropy of Mn $3d$ states in SRPES spectra is compared with that of the bulk obtained by SQUID measurements.

On Magnetic Instabilities in Fe_xNi_{1-x} Alloys: Spin-polarization Measurements of the Valence Bands Structure of Pseudomorphic Layers	U5UA

F.O. Schumann, R. Zhang, M. Hochstrasser, R.F. Willis (PSU), E. Vescovo, and H.-J. Kim (NSLS)

Recently, it was shown that Fe_xNi_{1-x} films can be grown in the fcc phase as ultrathin films on Cu(100) [1]. At an Fe concentration of 65% bulk Fe_xNi_{1-x} alloys the magnetic moment deviates strongly from the Slater-Pauling curve, dropping quickly to zero as does the Curie temperature, at which point, a structural phase transition from fcc to bcc is observed [2]. Fe_xNi_{1-x}/Cu(100) grows pseudomorphically. Which 'clamps' the Fe_xNi_{1-x} into the fcc phase for Fe concentrations beyond 65% in these ultrathin layers. In particular, at around x∼75% alloy composition, the bulk 'Invar Effect' appears to be suppressed in these metastable thin film alloys and a new 'low magnetization-density, ferromagnetic phase' is stabilized.

The phenomenological Stoner band theory of ferromagnetism informs us that the exchange-energy splitting of $3d$ states reflects this change in magnetization density and varies linearly with the magnitude of the local magnetic moment of the order 1eV per Bohr magneton [3]. Hence, spin-resolved electron spectra of the valence bands in Fe_xNi_{1-x}/Cu(100) give information on a possible 'low spin magnitude, ferromagnetic phase.

Figure 1 shows a spectrum taken in normal emission with 48 eV light at a concentration of x∼60% and Figure 2 a spectrum at a concentration of x∼75%. The copper d-band of the substrate is clearly resolved at around 3 eV below the valence band edge. Also, large changes in the density of states of the alloy valence bands are observed as a function of changing stoichiometry, together with their spin- resolved states. Work is in progress to get more insight into the underlying physics of the electronic structure.

1. F. Schumann et al, Phys. Rev. B, **56**, 2668 (1997).
2. E.F. Wassermann, J. Magn. Magn. Mater., **100**, 346 (1991).
3. F. Himpsel, Phys. Rev. Lett., **67**, 2363 (1992).

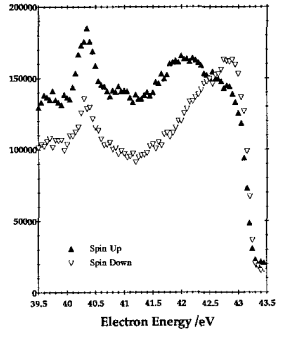

Figure 1. Spin-resolved spectra of an $Fe_{60}Ni_{40}$ alloy.

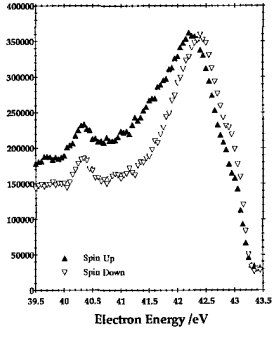

Figure 2. Spin-resolved spectra of an $Fe_{75}Ni_{25}$ alloy

Spin Resolved Photoemission Study of Magnetite	U5UA

E. Vescovo, H.-J.Kim, J.-H. Park (NSLS), H.S. Choi, and T.W. Noh (Seoul National U.)

Magnetite - Fe_3O_4 - is one of the most studied oxides because of its mangetic and electric properties. At variance with the majority of the oxides - which are antiferromagnetic - Fe_3O_4 is a ferrimagnet (T_N = 858 K). Its crystal structure is a spinel structure in which the large oxygen atoms form a close packed fcc lattice with the smaller Fe atoms occupying two inequivalent interstitial positions: tetrahedral A-sites and octahedral B-sites. The A-sites accomodate Fe^{3+} ions while the B-sites contain a mixture of Fe^{3+} and Fe^{2+} ions. The ferrimagnetism is explained assuming that the A and B sublattices are both ferromagnetic but antiparallel oriented with respect to each other: the magnetic moments of the Fe^{3+} ions compensating each other, while the macroscopic magnetization being supported by the unpaired Fe^{2+} ions. Much of the interest in magnetite is connected to its peculiar matal-insulator-like Verwey transition. This is a first-order transition characterized by an abrupt decrease of the conductivity by two order of magnitude below the Verwey temperature of about 120 K. Obviously valuable informations on the electronic structure can be obtained by spin-resolved photoemission experiments. Due to the high surface sensitivity of this technique, it is mandatory to prepare the surface *in-situ*. We started from an Fe_3O_4 thin film (about 1000 A thick) epitaxially grown on an MgO(001) substrate by Pulsed Laser Deposition technique and obtained a magnetic and ordered surface by repeted annealing cycles in oxygen atmosphere. The spin-resolved photoemission spectrum from this film taken at 36eV photon energy is shown in Fig.1. Fig.2 shows the spin polarization. Tentatively the minority feature at 0.5 eV below E_f can be attributed to the t_{2g} state of the Fe^{2+} in the B-site; the majority feature at about 1.8 eV binding energy should originate from the Fe^{3+} in the B-site (e_g state); and finally the minority peak at about 2.9 eV should derive from the antiparallel Fe^{3+} in the A-site.

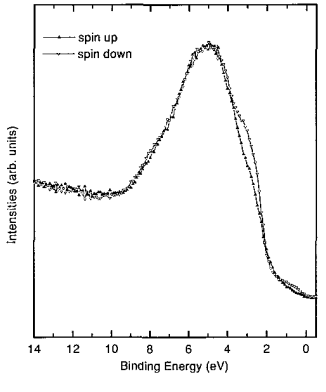

Figure 1.

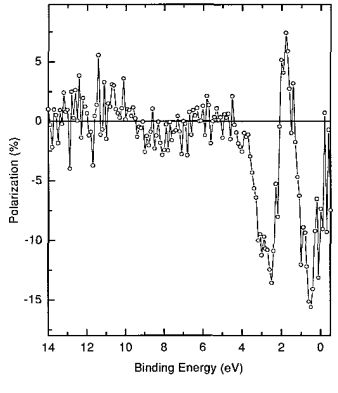

Figure 2.

The Magnetic Structure of Strained Thin Films of Gadolinium	U5UA

C. Waldfried (U. of Nebraska)

The electronic structure of strained thin films of Gd has been studied with spin and angle resolved photoemission. The spin temperature dependent electronic structure is dominated by an admixture of Stoner-like and rigid band magnetism. A very distinct thickness and k-dependence of the exchange splitting can be correlated to electron localization and the band structure. The surface magnetic structure is observed to be different from that of the bulk, as indicated by the different electronic structure and a much higher surface Curie temperature, approximately 10% over the strained bulk. The 4% strain within the Gd films results in an enhanced Curie temperature as compared to the relatively unstrained Gd(0001) by approximately 50 K (a $T_(C)$ in excess of 340 K) and a very different electronic structure. With decreasing thickness the bulk bands of the strained Gd films exhibit increasingly more paramagnetic-like behavior over an increasing volume of the Brillouin zone. The surface magnetic structure dominates the magnetic ordering of the ultra-thin Gd films.

Characterization of Pure and Sulfided $NiMoO_4$ Catalysts using Synchrotron based X-ray Absorption Spectroscopy (XAS) and Temperature Programmed Reduction (TPR)	U7A

S. Chaturvedi, J.A. Rodriguez (BNL) and J.L. Brito (IVIC)

This study aims to characterize the properties of pure and sulfided $NiMoO_4$ catalysts using synchrotron based near edge x-ray absorption fine structure (NEXAFS) and temperature programed reduction (TPR). Mo M_{III}-edge NEXAFS spectra indicate that on reaction with H_2S, the Mo component of $NiMoO_4$ gets partially reduced with the formation of MoS_2 type species. For the beta phase of $NiMoO_4$, the sulfidation of Mo is more extensive than for the alfa-phase, making the former a better precursor for catalysts of hydrodesulfurization (HDS) reactions. The Ni L_{II}-edge features are relatively insensitive to the changes accompanying the partial sulfidation of NiMoO4. The sulfidation of the Ni component is confirmed by analysis of the Ni K-edge extended x-ray absorption fine structure (EXAFS) spectra which show the formation of Ni-S bonds (bond length 2.48) and a NiMoSx phase. The S K-edge NEXAFS spectra show the presence of at least two types of sulfur species, one associated with a formal oxidation state of -2 and another associated with a formal oxidation state of +6. We attribute the former to the presence of metal-sulfur bonds (MoS_x and NiS_y). The latter is associated with the formation of S-O bonds (SO_4^{2-}). The formation of sulfates is also supported by the O K-edge NEXAFS spectra. The partially sulfided $NiMoO_4$ catalysts (both alfa and beta isomorphs) have a much lower thermal stability in a reducing environment than pure $NiMoO_4$ and MoS_2. The sulfided molybdates react with H_2 in TPR producing H_2O and H_2S at temperatures above 400 K.

Reaction of S_2 with ZnO and Cu/ZnO Surfaces: Photoemission and Molecular Orbital Studies	U7A

S. Chaturvedi, J.A. Rodriguez and J. Hrbek (BNL)

The adsorption of S_2 on ZnO and Cu/ZnO has been investigated using synchrotron- based high-resolution photoemission spectroscopy. On dosing a clean ZnO surface with S_2 at 300 K, the molecule dissociates. The S is associated first with Zn and at medium coverages with Zn-O sites. When the sulfur coverage is increased to S= 0.5 ML, evidence is found for sulfur bound purely to the O sites of ZnO. The sulfur species associated with O and the Zn-O sites are unstable at temperatures above 500 K. Possible reaction pathways for the dissociation of S2 on ZnO(0001)-Zn and Zn(10 0) surfaces were studied using ab initio SCF calculations. At low sulfur coverages, an adsorption complex in which S_2 is bridge bonded to two adjacent Zn atoms (Zn-S-S-Zn) is probably the precursor state for the dissociation for the molecule. It is possible to get much higher coverages of sulfur on ZnO (0.7 ML) than on Al_2 O_3 (0.1 ML) at similar S_2 exposures. This, in conjunction with results previously reported for H_2 S adsorption on Cr_2 O_3 and Cr_3O_4, indicates that the reactivity of metal oxides towards sulfur is inversely proportional to the size of their band gap. Oxides with a large band gap (e.g. Al_2 O_3 9.0 eV) are less susceptible to sulfur adsorption than oxides with a small band gap (e.g. ZnO 3.4 eV). The presence of Cu atoms on both metal oxides enhances their respective reactivities towards S_2. Upon dosing Cu/ZnO with S_2 at 300 K, sulfur prefers to attack supported Cu followed by reaction with the Zn sites of the oxide, and at large sulfur coverages the adsorbate bonds simultaneously to metal and oxygen sites on the surface. The sulfur bonded to both the metal and oxygen sites on the surface is relatively weakly bound and desorbs by 500 K. The Cu-S interactions are strong and lead to the formation of copper sulfides that exhibit a distinctive band structure and decompose at temperatures above 700 K.

Chemistry / Orientation of Lubricants on Hard Disk Magnetic Media Substrates Using Near Edge X-ray Absorption Fine Structure	U7A

B. M. DeKoven (Dow), D.A. Fischer (NIST), G E. Potter, T. Richardson, D. J. Perettie (Dow), Singh Bhatia (IBM), T. A. Morgan, (Dow), and S. Hsu (NIST)

In this study we describe the interactions of a lubricant system with carbon overcoat surface typical of a magnetic hard disk. The lubricants used are cyclophosphasene (X-1P) and Fomblin (ZDOL). The following system parameters were studied: effects of surface burnishing; ZDOL alone, X-1P alone, ZDOL/X-1P mixtures, and carbon overcoats (7.5 nm) with varying hydrogen contents (using Ar and Ar / H2 treatments).

Near Edge X-ray Absorption Fine Structure (NEXAFS) was used to probe the reactivity and orientation of applied lubricants on the surface of the various (16) lubricant disk systems combinations. NEXAFS is an ideal non destructive tool for studying the disk lubricant system since it has both elemental and chemically sensitivity, with great selectivity in bond type. The technique can also make direct comparisons between the surface and bulk by measuring simultaneous electron yield (5 nm depth sensitivity) and fluorescence yield (200 nm) spectra. In addition, the average orientation of chemical bonds may be measured via the polarization anisotropy of the soft x-ray absorption spectra. NEXAFS spectra above the Co and Ni L edges as well as C, O, F K edges were recorded. Orientation of the lubricants, thickness, and morphology of the carbon hardcoat and magnetic media are discussed in detail for the samples listed above.

The NEXAFS results suggest little specific orientation of lubricant molecules on COCs, with the exception of X-1P, and only before burnishing. Apparent surface vs. bulk content of Ni may be consistent with the presence of 'cracks' in the COC overlayer or corrosion phenomena. Also, Co appears to be present in the surface region (top 5 nm), unlike Ni. This also suggests cracks or corrosion in the COC overlayer system. For the COC produced without hydrogen we see a systematic reduction in Co upon lubricant application and further reduction upon burnishing.

C-N Bond Activation of Cyclohexylamine on the Ni(100) Surface | U7A

A.M. Gabelnick, S.M. Kane, A.T. Capitano (U. of Michigan), D. A. Fischer (NIST), and J.L. Gland (U. of Michigan)

The effect of hydrogen on carbon-nitrogen bond activation has been studied with cyclohexylamine (CHA) on the Ni(100) surface as a part of continuing research on C-N bond activation on metal surfaces in vacuum and high pressures. Hydrogen has been shown to have a very important role in a wide variety of bond activation processes. Carbon-nitrogen bond activation and the role of hydrogen was studied for CHA on the Ni(100) surface in pressures of hydrogen from vacuum up to 0.02 torr. Temperature Programmed Fluorescence Yield Near Edge Spectroscopy (TP-FYNES) allowed for the determination of surface carbon concentration as the reaction progressed, while Fluorescence Yield Near Edge Spectroscopy (FYNES) anneal sets were used to determine the nature of the surface intermediates.

Using FYNES, the intermediate for C-N bond activation of CHA on the Ni(100) surface was determined to consist of a partially dehydrogenated cyclohexyl ring adsorbed nearly parallel to the surface, as indicated by an increase in the $\pi*$ resonance at bond activation temperatures using normal incidence synchrotron radiation. TP-FYNES experiments taken in 0.02 torr of hydrogen showed a decrease in surface carbon at 220K relative to similar experiments in vacuum. This is indicative of a slightly more facile C-N bond activation process caused by high pressures of hydrogen.

Examination of Ordering in Self Assembled Monolayers and Adsorbed Protein Films with Near Edge X-ray Absorption Fine Structure * | U7A

L. Gamble, D. Castner (U. of Washington), D. Fischer (NIST), P. Stayton, and K. Nelson (U. of Washington)

For many bio-engineered materials the molecules involved in surface modification, such as self-assembled monolayers (SAMs) or proteins, need to be oriented in a specific direction. For example, it may be necessary for functional groups to point away from the surface or proteins may require active sites facing away from the substrate to allow for enhanced reactivity. The orientations of functionalized alkane thiols on gold and adsorbed proteins on alkane thiols have been studied by near edge x-ray absorption fine structure (NEXAFS). Self-assembled monolayers were prepared from biotinylated alkane thiol (BAT), which is an alkane chain with a biotin head group, as well as from methylhexadecand thiol (MHD). Mixed monolayers of BAT and MHD thiols were also prepared. NEXAFS spectra indicates that SAMs made from mixed BAT-alkane thiol solutions are more highly ordered than those made from 100% BAT solutions. NEXAFS spectra (taken in the partial electron yield mode) of SAMs prepared from a solution of 40% BAT and 60% MHD show strong polarization dependence in the C-H$*$ and C-C$*$ resonance. NEXAFS, aided by XPS data, indicates that the MHD "dilutant" helps to order the alkane chain of the BAT to stand relatively perpendicular to the surface, thus orienting the biotin headgroup away from the substrate. When the protein streptavidin (SA) is adsorbed on a MHD monolayer, a small amount of polarization dependence is seen at the N K-edge. Further research includes study of different protein structures on gold and "rubbed" PTFE on gold surfaces. SAMs made with different functionalized alkane thiols and fluorinated thiols are being studied as well.

* This work was supported by University of Washington Engineered Biomaterials (NSF EEC-9529161) and NESAC/BIO (NIH RR01296)

Photoemission of Cleaved and "As-Grown" Surfaces of Pyrite | U7A

J. Guevremont (Temple U.), M.A.A. Schoonen (SUNY-Stony Brook), D. Strongin (Temple U.), and M. Strongin (BNL)

S 2p photoemission on the U7a beamline has been used to investigate the surface composition and stoichiometry of pyrite, FeS_2. Two types of surfaces have been investigated; surface produced by cleavage of a single crystal sample of pyrite and an "as-grown" surface [striated (100)] face, bombarded in UHV with He^+ to remove residual carbon and oxygen contamination. Both surfaces have been annealed to 573 K prior to study. Comparison of these two samples is partly motivated by the need to determine the differences in structure that result when preparing geochemical surfaces for study in UHV. The latter preparation method provides a way to create a reproducible surface that can be then used for surface reactivity studies. Figure 1 exhibits typical S 2p data for the two surfaces. For each surface it is proposed that 4 different S 2p species (denoted by A, B, C, and D doublets) contribute to each spectrum. Contributions A and B are thought to be due to S in the outermost surface region. We tentatively believe that A is, at least due in part, to monosulfide, FeS, and B is due to pyrite S (stoichiometry of FeS_2) that is shifted from the bulk S contribution (i.e., feature C). Finally, feature D is probably due to a more reduced form of S, perhaps similar to polysulfide (this has been proposed to exist on pyrite by other research groups). Assignments for A, B, and C have been independently supported by additional experiments. For example, experiments at U7a have shown that the decomposition of H_2S on pyrite significantly reduces feature A, consistent with the conversion of a monosulfide species into the disulfide that characterizes pyrite. Furthermore, S 2p data obtained with conventional XPS (using 1253 eV radiation) shows only a small contribution from A and B, consistent with these features being due to surface S species. Comparison of the two samples suggests that cleavage results in a more sulfur deficient surface. The surface prepared by gentle ion bombardment results in a more S-rich surface that may be closer to a natural surface then is the surface created by cleavage. Future experiments are planned that will help confirm many of the tentative assignments made here.

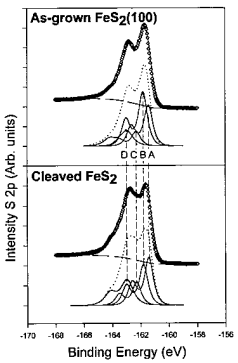

Figure 1. S 2p photoemission of an "as-grown" and cleaved sample of pyrite, FeS_2.

Surfaces of Semifluorinated Block Copolymers Studied Using NEXAFS | U7A

E.J. Kramer, J. Genzer (UCSB), J. Wang, H. Körner, C.K. Ober (Cornell University), B.M. DeKoven, R.A. Bubeck (Dow Chemical Co.), D.A. Fischer (NIST)

We synthesized styrene-isoprene diblock copolymers in which the isoprene block was modified by attaching semifluorinated (-CO-$(CH_2)_x$-$(CF_2)_y$F) side groups. Recent X-ray diffraction measurements demonstrated that these semifluorinated diblock copolymers (SFDs) form highly ordered liquid crystalline (LC) structures whose morphologies are dictated by the combination of x and y. In addition, contact angle measurements revealed that surfaces of thin films made of these SFDs exhibit extremely low surface energies indicating the presence and high ordering of -$(CF_2)_y$F blocks at the surface. In the present study, near-edge X-ray absorption fine-structure (NEXAFS) is used to examine the structure of thin SFD films on a molecular level. By simultaneously detecting both the electron yield (EY) and the fluorescence yield signals whose probing depths are *ca.* 2 and 100 nm, respectively, both the near-surface and "bulk" structures of the SFDs are studied. The use of the EY signal is particularly advantageous because it allows us to examine the molecular orientation within the LC phase and its role on the surface organization of thin films SFDs. Changes in the molecular orientations within the semifluorinated side groups of the SFDs as revealed from the NEXAFS measurements on samples annealed *in-situ* at various temperatures can be correlated with the organization changes (smectic-B - smectic-A - isotropic) previously detected with differential scanning calorimetry.

Hole State Density and Superconductivity in Ca-substituted Yttrium Barium Copper Oxide (Y-1:2:3)	U7A

A. R. Moodenbaugh (BNL) and D. A. Fischer (NIST)

Oxygen K near-edge spectra obtained using fluorescence yield from x-ray absorption were recorded for polycrystalline $YBa_2Cu_3O_7$ (Ca-1:2:3) and $(Y_{0.88}Ca_{0.12})Ba_2Cu_3O_7$ (Y-1:2:3). As oxygen content is increase from x=6.12 in Ca-1:2:3, the superconducting transition temperature rises, reaches a maximum of 80K near x=6.8, then falls at higher oxygen contents. The near edge structure identified with hole density (energy E=529 eV) increases throughout the range of oxygen content. Two additional pre-peaks are observed near 530 and 531 eV, both with maximum intensity at minimum oxygen content, and having similar intensities. Similar peaks are observed for Y-1:2:3.

Direct Observation of the Complete Rehybridization of the Carbon Carbon Double Bond in Chemisorbed Propylene on Supported Silver Materials Using NEXAFS	U7A

J.T. Ranney, D.A. Fischer (NIST), D.H. Parker, R.G. Bowman (Dow Chemical), and J.L. Gland (U. of Michigan)

The room-temperature chemisorption and near-complete rehybridization of propylene on dispersed silver supported on TiO_2 (anatase) has been observed for the first time on a supported material. The thermal chemistry of adsorbed propylene has been characterized on Ag/TiO_2 using fluorescence yield Near-Edge X-ray Absorption Fine Structure (NEXAFS) at the carbon K edges. The intensity of the propylene C 1s to pi* resonance at the carbon K edge is nearly extinguished upon chemisorption of propylene on the material at 300 K. The loss of the pi* resonance indicates substantial rehybridization of the C-C double bond resulting in a reversibly adsorbed di-sigma bonded surface species. When adsorbed at liquid nitrogen temperatures both adsorbed and condensed propylene retain their pi character. No propylene adsorption is seen on the neat TiO_2 support even at 115 K and propylene does not adsorb on silver single crystals above 200 K. Therefore, we propose that the room temperature adsorbed propylene may be related to areas of strong interaction such as the perimeter of the silver particles.

This is the first direct observation of chemisorbed reactant monolayers on a supported materials using fluorescence yield carbon K-edge NEXAFS. These experiments demonstrate an exciting new technique for observing and characterizing adsorbates on supported materials. This technique is element specific and probes the bonding and concentration of the adsorbed species independent of the optical properties of the sample. We have demonstrated that carbon-edge NEXAFS is an ideal technique for the direct characterization of adsorbed reactants, even on porous complex materials.

Tribochemical Reactions of Nanometer Lubricant Films | U7A

Z.F. Yin, S.M. Hsu, D. A. Fischer, X. Zhang and J. Zhang (NIST)

Several lubricants were deposited on Cu, and 52100 steel surfaces by modified dip-coating method to form nanometer scale films. The lubricants chosen for this study were stearic acid and some other simple organic compounds. The films were characterized by using reflectance FTIR spectroscopy and ultra soft x-ray absorption spectroscopy (USXAS). A well designed multi-tips scratcher was employed to execute the tribological treatment. The treatment was done in a very slow motion in order to minimize the effects of flashing heat. For comparison, another set of duplicated samples deposited in the same way were heated in a furnace to induce the thermal reaction. It was found that the tribochemical reaction and thermal reaction between stearic acid and Cu substrate were similar. The chemical change can be detected by reflectance FTIR and USXAS spectroscopies. The results will be discussed and compared with previous works. Tribochemical reactions of other films will also be reported and discussed.

Partial Densities of States in Cu-Pd alloys | U7B

S.L. Qiu, Yang Li and R.G. Jordan (Florida Atlantic University)

We have carried out a series of photoemission measurements from polycrystalline samples of ordered $Cu_{85}Pd_{15}$, $Cu_{75}Pd_{25}$ (with $L1_2$ structure) and ordered $Cu_{58}Pd_{42}$, $Cu_{50}Pd_{50}$ (with CsCl structure) over the photon energy range 40 - 140 eV. Our aim is to determine the Cu- and Pd- contributions to the density of states by exploiting the Cooper minimum in the Pd 4d photoemission cross-section at about 130 eV. In addition, we have also made preliminary investigations on the core level shifts and line-shapes in order to probe the local Cu and Pd environments in these alloys. We show in figure 1 a selection of valence-band spectra from CuPd, and in figure 2 the densities of states of Cu and Pd calculated using the SCF-LMTO-ASA method. Relativistic x-ray photocurrent calculations using the potential functions and density of states from an electronic structure calculation based on the RKKR method are under way for an appropriate comparison with the experimental results.

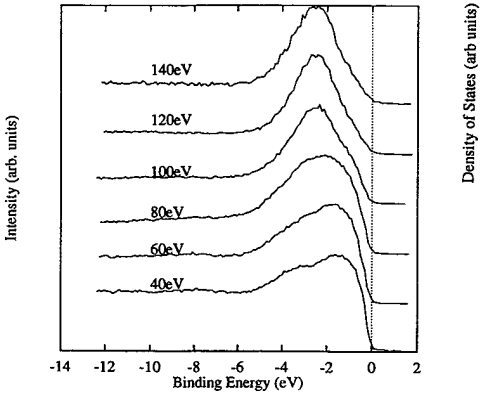

Figure 1. Selection of valence-band photoemission spectra from a polycrystal temperature.

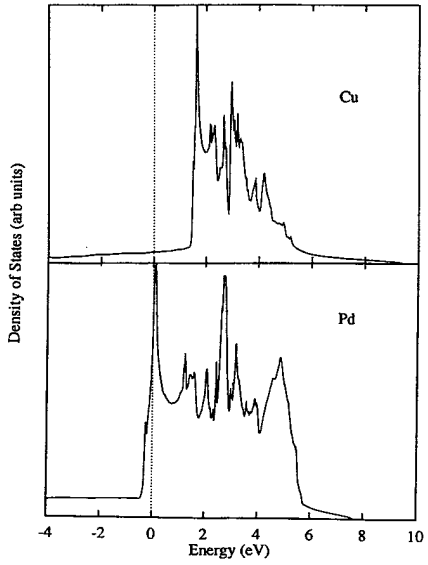

Figure 2. Density of states in Cu and Pd calculated using SCF-LMTO-ASA method.

Photon-Stimulated Desorption of O^+ from Zirconium Oxide * | U8A

W.C. Simpson and T.M. Orlando (PNNL-EMSL), W.K. Wang and J.A. Yarmoff (U.C. Riverside-Physics)

Zirconium-based alloys are commonly used as cladding for nuclear fuel rods and in various components in nuclear power plants, primarily because of the robust nature of the oxide that forms, which is highly resistant to corrosion. Yet, zirconium oxide films break down when submitted to the extreme radiation conditions present in a nuclear reactor. It has been suggested that low-energy electronic excitations generated in the material by the ionizing radiation lead to its degradation, but the exact mechanism is unknown. We are currently conducting a set of controlled experiments to investigate the role of low-energy excitations in the radiation damage of zirconium oxide. Our approach is to take a well-characterized ZrO_2 surface and submit it to bombardment by a monochromatic beam of low-energy photons. Measurements of the O^+ desorption threshold and kinetic energy distribution, coupled with photoemission measurements of the electronic structure of the surface, enable the identification of the excitations that result in oxygen removal from a ZrO_2 surface. For both crystalline and amorphous ZrO_2, the O^+ photon-stimulated desorption thresholds are at 30 eV, corresponding to the removal of a Zr(4p) electron, and the ions have 2 eV of kinetic energy. These findings are consistent with the Knotek-Feibelman mechanism for stimulated ion desorption from metal oxides, in which the ionization of a shallow metal cation core level, followed by interatomic Auger decay, leads to the formation and rapid ejection of O^+ ions from the surface.

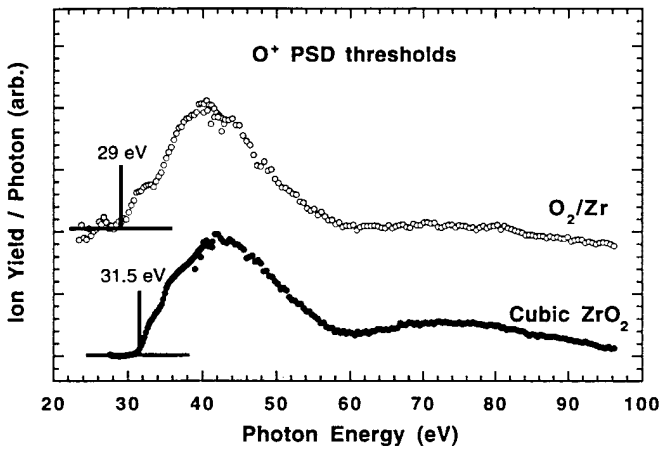

Figure 1. The O^+ PSD threshold for cubic zirconia and oxidized zirconium foil.

* This work was supported by US DOE, Div. Chem. Sci., BES.

Photoemission Studies of the Chemisorption of Chlorine on InAs(001) | U8A

W.K. Wang (U.of California, Riverside and LBNL), W.C. Simpson (EMSL, PNNL) and J.A. Yarmoff (U.of California, Riverside and LBNL)

Reaction of halogens and halogen-containing compounds with III-V semiconductor surfaces are of considerable importance since they play a major role in the fabrication of optoelectronic devices. Previous studies mainly concentrated on the reaction of chlorine with GaAs [1]. It was shown that Cl_2 spontaneously etches GaAs at room temperature under conditions which depend on the initial surface stoichiometry and order. In the present work, we focus on the interaction of Cl_2 with InAs in order to understand the role of surface structure and stoichiometry for this system.

The reactions of Cl_2 with In- and As-terminated InAs(001) surfaces in UHV were investigated with synchrotron-based soft x-ray photoelectron spectroscopy (SXPS) and low energy electron diffraction. An In-terminated InAs(001)-c(8×2) surface was prepared by Ar^+ ion bombardment and annealing. An As-terminated InAs(001)-c(2×8) surface was obtained by adsorbing I_2 on the c(8×2) surface and then removing In iodides by heating [2]. Chlorine was produced from a UHV compatible solid-state electrochemical cell.

High-resolution core-level spectra were collected from the clean and chlorinated surfaces. Representative spectra are given in Fig. 1, which indicate that Cl_2 dissociatively adsorbs, breaking the In-As bonds in a similar manner as with GaAs. The stoichiometry of the near- surface region determines the relative amount of surface reaction products. The bond breaking suggests that the spontaneous reaction itself is a prelude to etching.

[1]. W.C. Simpson and J.A. Yarmoff, Ann. Rev. Phys. Chem. **49**, 527 (1996)
[2]. P.R. Varekamp, M.C. Håkansson, J. Kanski, D.K. Shuh, M. Bjorkqvist, M. Gothelid, W.C. Simpson, U.O. Karlsson and J.A. Yarmoff, Phys. Rev. B **54**, 2101 (1996)

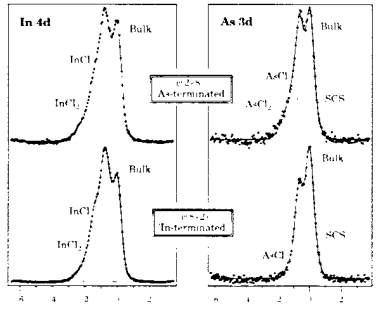

Figure 1. High-resolution In 4d and As 3d core-level spectra collected after a 200 μA•min exposure of Cl_2 shown along with numerical fits to the data. The dots show raw data after background subtraction. The dashed lines are the individual components, while the solid line is the sum of the components.

Chloroethane Physisorbed on Hydrogenated Si(111): A Test System for the Evaluation of Core-Level XPS Assignment Rules *	U8B

F.R. McFeely (IBM), K.Z. Zhang and M.M. Banaszak-Holl (U. of Michigan)

Evidence for Second-Neighbor effects in photoemission on silicon surfaces was presented. The chloroethane molecule, known to exhibit second neighbor effects in the gas phase C 1s spectrum, was physorbed onto a Si(111) surface. No reduction in binding energy shift difference was observed, suggesting that the highly polarizable silicon surface does not cause a diminuition of second-neighbor effects upon binding energies. For a complete description of this study see: *Mat. Res. Soc. Symp. Proc.* **446**, 15 (1997).

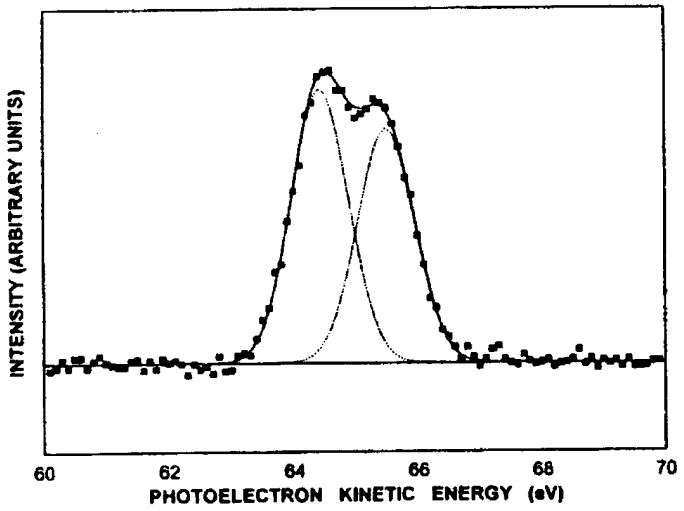

Figure 1. Least-squares fit of the C 1s spectrum of physisorbed chloroethane, illustrating resolution into two components.

* This work was supported by NSF Grant No. DMR-9596208 and IBM.

Photoemission Assignments of H_xSiO_{4-x} Fragments at the Si/SiO_x Interface *	U8B

S. Lee and M. M. Banaszak Holl (Brown U.), W. H. Hung and F. R. McFeely (IBM)

Hydrogenation of the silicon/silicon oxide interface is shown to cause changes in every interface feature spectroscopically discernable by soft x-ray photoemission in additional to depinning the Fermi level. A new feature is observed to grown in at 3.6 eV with respect to bulk Si upon exposure to atomic hydrogen at the expense of interface states intermediate between 0 and 3.6 eV. For a full discussion of this work see: it. Phys. Lett. **68**, 1081 (1996).

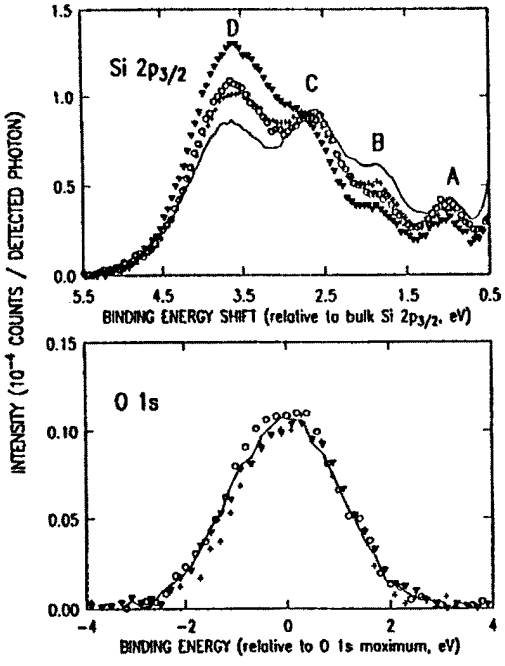

Figure 1. Top: soft x-ray photoemission (Si $2p_{3/2}$ core-levels, 170 eV photon energy) thermal oxide(I, line), 5 min hydrogen radical exposure (II, crosses), 20 (III, triangles), and 670 C anneal (IV, circles).

* This work was supported by NSF grant No. DMR-9596208 and IBM.

Si 2p Core-level Shifts at the Si(100)-SiO_2 Interface: An Experimental Study *	U8B

K. Z. Zhang, M. M. Banaszak Holl (U. of Michigan), J. E. Bender, S. Lee (Brown U.), and F. R. McFeely (IBM)

Si 2p core-level shifts were measured for a model system generated from $HSi(OCH_2CH_2)_3N$ and Si(100)-2x1 (Fig. 1) and compared to the result obtained from a species containing similar coordination about silicon, $HSi(OCH_3)_3$. The dramatic difference in the products obtained was explained in terms of the chelate effect. The results were compared to previous results obtained using spherosiloxane clusters and an empirical, model-compound based core-level shift assignment scheme was compared and contrasted with the conventional formal oxidation state assignment scheme. For a full discussion of this work see: *Phys. Rev. B* **54**, 7686 (1996).

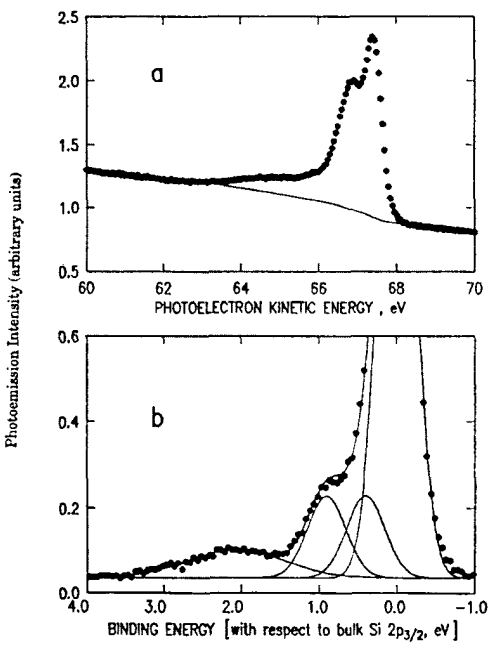

Figure 1. (a) Raw Si 2p core-level spectrum of the silatrane cluster, bound to Si(100). (b) Si $2p_{3/2}$ core-level component peaks.

* This work was supported by NSF Grant No. DMR-9596208 and IBM.

A New Model Silicon/Silicon Oxide Interface Synthesized from $H_{10}Si_{10}O_{15}$ and Si (100)-2x1 *	U8B

K. Z. Zhang, L. M. Meeuwenberg, M. M. Banaszak Holl (University of Michigan), F. R. McFeely (IBM)

A model silicon/silicon oxide interface, synthesized from the spherosiloxane $H_{10}Si_{10}O_{15}$ and Si(100)-2x1, was characterized by study of the Si 2p core-levels and valence band region using soft X-ray photoemission. In addition, the intact $H_{10}Si_{10}O_{15}$ cluster was condensed at -160 C onto Si(111)-H and characterized. The measured photoemission features are in good agreement with the results of previous model studies. These experiments suggest that the formal oxidation state assignment scheme typically applied to the interpretation of Si 2p core-level spectroscopy of Si/SiO_2 interfaces is overly simplistic. For a full discussion of this work see: *Jpn. J. Appl. Phys.* **36**, 1622 (1997).

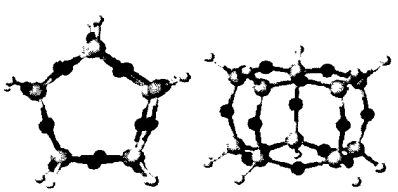

Figure 1. Two views of $H_{10}Si_{10}O_{15}$ highlighting the 2 ten-membered rings and the 5 eight-membered rings.

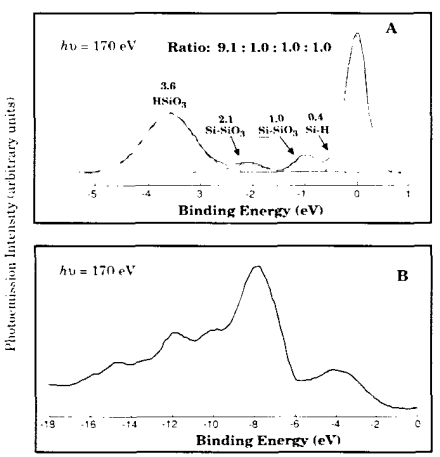

Figure 2. $H_{10}Si_{10}O_{15}$ chemisorbed on Si(100)-2x1 at 25 C. Panel A:Si $2p_{3/2}$ core-levels. Panel B:valence band.

* This work was supported by NSF grant No. DMR-9596208 and IBM.

Soft X-ray Si 2p Core-level Spectra of $H_8Si_8O_{12}$ Physisorbed on Si(111)-H: Additional Experimental Evidence Regarding the Binding Energy Shift of the $HSiO_3$ Fragment *	U8B

K. Z. Zhang and M M. Banaszak Holl (U. of Michigan), F. R. McFeely (IBM)

The hydridospherosiloxane cluster $H_8Si_8O_{12}$ was physisorbed onto Si(111)-H and soft X-ray Si 2p core-level spectra obtained. The results confirmed that $HSiO_3$ units are observed at roughly -3.6 eV binding energy for the intact cluster. Fragments of this type are of considerable interest because of the role of hydrogen in device failure. For a detailed discussion of these experiments and references see: *Mat. Res. Soc. Symp. Proc.* **446**, 241 (1997).

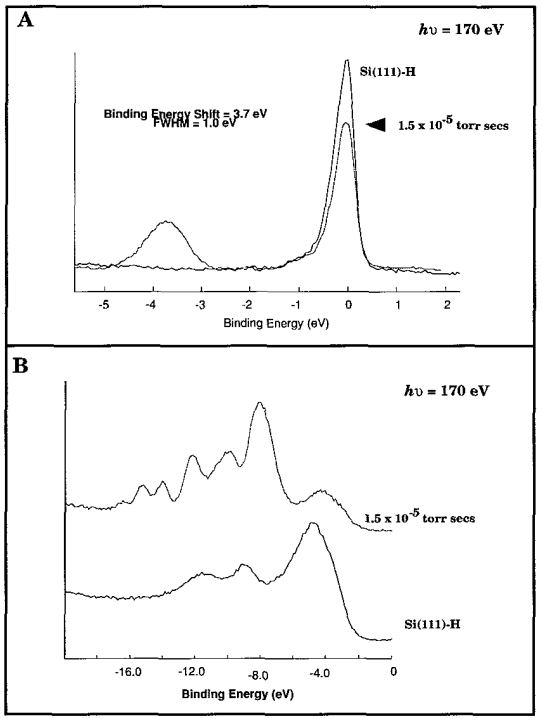

Figure 1. Soft X-ray photoemission spectra of the physisorbtion of $H_8Si_8O_{12}$ onto Si(111)-H at -140 C. Panel A: Si $2p_{3/2}$ core-levels. Panel B: valence band.

* This work was supported by NSF Grant No. DMR-9596208 and IBM.

The Role of Extra-Atomic Relaxation in Determining Si 2p Binding Energy Shifts at Silicon/Silicon Oxide Interfaces *	U8B

K.Z. Zhang, J. N. Greeley, M.M. Banaszak Holl (University of Michigan), F. R. McFeely (IBM)

The observed binding energy shift for silicon oxide films grown on crystalline silicon varies as a function of film thickness. The physical basis of this shift has previously been ascribed to a variety of initial state effects (Si-O ring size, strain, stoichiometry, and crystallinity), final state effects (a variety of screening mechanisms), and extrinsic effects (charging). By constructing a structurally homogeneous silicon oxide film on silicon, initial state effects have been minimized and the magnitude of final state stabilization as a function of film thickness was directly measured. In addition, questions regarding the charging of thin silicon oxide films on silicon were addressed. From these studies, it is concluded that initial state effects play a negligible role in the thickness-dependent binding energy shift. For the first 30 of oxide film, the thickness-dependent binding energy shift can be attributed to final state effects in the form of image charge induced stabilization. Beyond about 30 , charging of the film occurs. For a detailed discussion of this research see: *J. Appl. Phys.* **82**, 2298 (1997).

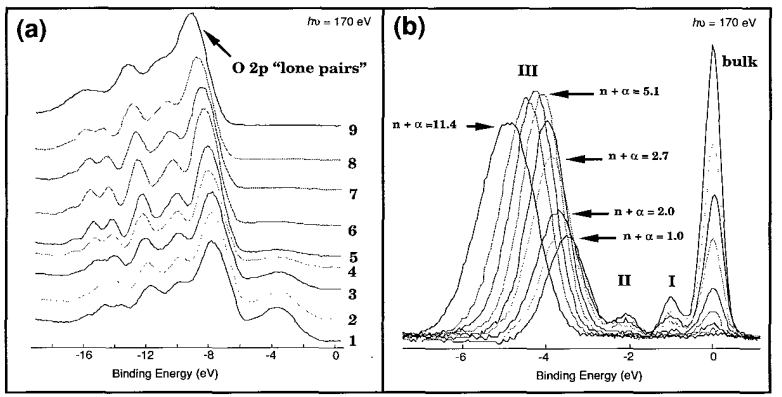

Figure 1. Soft X-ray photoemission spectra of $H_8Si_8O_{12}$ derived films varying in thickness from 0.6 to 7 nm. Panel (a): valence band spectra.Panel (b): Si $2p_{3/2}$ core-level spectra.

* This work was supported by NSF grant No. DMR-9596208 and IBM.

Fluorescence of Paper Filters | U9B

R. Mantauffe (Pall Corporation) and J. Sutherland (BNL- Biology)

The time resolved fluorescence and scattering of UV light from several types of filters with a variety of uses in research and industrial applications was recorded using the Fluorescence Omnilyzer detector. In certain applications, such as the investigation of the composition of aersol samples by fluorescence spectroscopy, it is extremely desirable to have the filter contribute as little fluorescence as possible. Studies of several commercially available filters as well as non-production test samples revealed that some demonstrated considerable fluorescence, while others showed only low levels of fluorescence, albeit detectable levels. Polarization studies showed that fluorophores tended to be tightly bound to the filter (indicated by finite levels of non-depolarization of the fluorescence). Reducing the excited state lifetimes significantly reduces the total intensity of fluorescence from a sample. Thus the fluorescence emmission from a filter can be reduced by incorporating fluorescence quenchers, provided such compounds do not compromise the chemical performance of the filter in its intended role.

For the performance of these experiments, Pall Corp. acquired a sample holder for mounting thin solid samples and viewing fluorescence from near-normal incidence. An angular scale was added to the standard design to permit adjustment of the angle on incidence of the exciting light relative to the normal to the plane of the sample. This holder is being made available to other users of the beamline.

Photoluminescence Study of Simox Buried Oxide | U9B

H. Nishikawa (TMU), J. H. Stathis, (IBM) and R.E. Stahlbush (NRL)

Electrically active defects in the buried oxide (BOX) of SIMOX (Separation by Implantation of Oxygen) wafers, or other SiO_2 films, have been studied mostly with electrical (charge sensing) techniques and with electron spin resonance (ESR). The electrical studies have shown that the buried oxide of SIMOX has a much higher concentration of electron and hole traps than normal thermal oxide and higher concentration of E' centers are observed by ESR measurements in SIMOX than in thermal oxide. These studies concluded that during the high temperature (1300°C) anneal that is necessary to form SIMOX, defects such as oxygen vacancies are formed. In this work, defects in the BOX were studied by photoluminescence which is a complementary technique to electrical and ESR measurements. Electrical measurements provide high sensitivity but no structural information and ESR gives structural information but can only detect the paramagnetic charge state of a defect. Photoluminescence can detect defects in their diamagnetic configuration. Samples used in the present experiments were buried oxide layers produced by the SIMOX technique. Samples included low-dose single-implant (Oxygen dose 0.4-0.6x10^{18} cm^{-2}), double-implant (0.9x10^{18} cm^{-2} total dose) and full-dose single- and triple implant (1.7-1.8x10^{18} cm^{-2} total dose). The implant energy was 180-200 keV and annealing was done in Ar+ 0.5 temperatures in the range 1310-1350°C. One of the full-dose triple-implanted samples received a supplemental dose of 0.1x10^{18} cm^{-2}. After the supplemental implant, the annealing temperature was 1000°C. Example results for full-dose triple-implanted samples with and without the supplemental oxygen implantation are discussed below. Photoluminescence measurements were carried out using the U9B beamline of the National Synchrotron Light Source equipped with an excitation double monochromator (Spex 1680). The PL from the sample was dispersed by a detection monochromator (Chromex) across the 2.5 cm diam bialkali photocathode of an ITT F4146M position sensitive detector. The detection system provides time resolution from 1-15ns and simultaneous recording of PL intensity in the two polarization directions parallel and perpendicular to the excitation polarization. Excitation was done in air at a wavelength of 248 nm (hν=5.0 eV). The surface Si layer was removed for the PL measurement. The spectrum of the BOX (oxide thickness 3550 Angstroms) without the supplemental implant shows a PL peak at 280 nm. On the other hand, the PL at 280 nm in the BOX with supplemental implant was significantly reduced. The decay of the PL follows a single exponential with a lifetime of 4 ns. The PL at 280 nm can be ascribed to a transition from the excited-singlet to ground (S_1-S_0) states at the site of oxygen vacancy . This can be ascribed to a transition from the excited-singlet to ground (S_1-S_0) states at the site of oxygen vacancy. Electrical measurements have shown that SIMOX with a supplemental oxygen dose has less electron and hole traps. PL results from this and a variety of other BOX samples have been accepted for presention at the Semiconductor Interface Specialists Conference to be held Dec 4-6, 1997, in Charleston, SC.

Use of Fluorescence Homotransfer to Monitor BOPIPY-melittin Oligomerization	U9B

S. Scarlata (SUNY at Stony Brook)

Our laboratory has been exploring the possibility of using fluorescence homotransfer (resonance energy transfer between identical fluorophores) to monitor changes in the oligomerization of membrane proteins. Homotransfer is measured by the loss in fluorescence anistropy as the energy is transferred between probes. We have used a stochastic approach to relate the number of subunits in a protein oligomer to the loss in fluorescence anisotropy. We tested this model using fluorescein-labeled melittin which is a small peptide whose monomer to tetramer transition can be easily controlled. Although we found a good correlation between theory and experimental results, a breakdown occurs at higher viscosities or low temperatures since these stabilize the formation of non-fluorescent fluorescein dimers. This problem is also pronounced when the protein is in a membrane. To minimize the dark complex formation, we selected another probe, BODIPY (Molecular Probes, Inc.). This probe has a high probability of homotransfer, but is not expected to form dark complexes. We selectively labeled melittin with this probe on its C-terminus, and found that the homotransfer, as monitored by the loss in fluorescence anisotropy, was obeyed. We then measured the anistropy decays, lifetimes and time-dependent emission spectra of the BODIPY-melittin monomer and tetramer in 50% glycerol at NSLS. We found these time-resolved parameters to be similar, although their initial values differ. These results indicate that the rate of exchange of the excited energy between the probes in the tetramer is faster than the fluorescent lifetime. We are incorporating these results into our model.

Time Resolved Fluorescence Polarization Measurements for Entire Emission Spectra with a Resistive-anode, Single-photon-counting Detector: The Fluorescence Omnilyzer *	U9B

J. C. Sutherland, L. A. Kelly, J. G. Trunk, D. C. Monteleone and K. Polewski (BNL - Biology)

We report a fluorescence analyzer that records simultaneously the temporal profiles for both orthogonal linear polarizations for all wavelengths in a fluorescence emission spectrum. The Analyzer combines a resistive-anode single-photon-counting photomultiplier, imaging spectrograph, Wollaston polarizer, multiparameter analyzer with histogramming memory and standard timing electronics. The spectrograph disperses the fluorescence spectrum across the photocathode of the photomultiplier, and the Wollaston polarizer separates the spectra of the two polarizations in opposite directions from the center of the photocathode perpendicular to the direction of spectral dispersion. The locations at which each photon reaches the photocathode is determined by the ratios of the charges read from the four corners of the resistive-anode. One of the two address coordinates that determine where in histogramming memory each photon is recorded is obtained by measuring the time-of-arrival of the photon at the detector relative to the pulse of light that excites the fluorescence. The second address coordinate is obtained by combining the most-significant bit of the location of the event along the direction on the resistive anode corresponding to the polarization of the photon with the multi-bit digital value indicating photon wavelength. Storing the data directly into histogramming memory permits display of the data-set as it is recorded. Both the spectral and temporal calibrations of the fluorescence analyzer are independent of the polarization of the fluorescence. The 100 ps temporal resolution of the resistive-anode detector is well matched to the 1 ns FWHM pulses of light produced by the synchrotron storage ring that we use as the excitation source, but laser excitation could also be used with this detector. Recording simultaneously all of the data required for the global analysis of the time evolution of both linear polarization components of fluorescent, and thus time-resolved anisotropy, reduces the duration of exposure of the sample to the excitation beam, hence facilitating studies of fragile or photosensitive biological specimens.

* The Fluorescence Omnilyzer was selected by R&D Magazine as one of the 100 most important technical products of the year.

Fluorescence Properties of Recombinant Cardiac Troponin C and its Mutants *	U9B

C. K. Wang (U. of Washington)

The contraction of vertebrate striated muscle is initiated by the binding of Ca^{2+} to the troponin C (TnC) which is the only Ca^{2+} receptor in the thin filaments. TnC obtained from fast skeletal muscle contains four Ca^{2+} binding sites. Of these four sites, sites I and II bind Ca^{2+} specifically, but sites III and IV also bind Mg^{2+} competitively. Cardiac TnC (cTnC) contains only three active Ca^{2+} binding sites (called II, III, and IV). Site I is inactive due to the defect of the binding loop. Previously utilizing cTnC mutants containing single tryptophan (Trp), we studied the effects of Ca^{2+} and Mg^{2+} on Trp fluorescence. The results showed that multiple lifetimes were seen from most of mutants except cTnC(F74W), in which a single lifetime was observed in the presence and absence of divalent cations. We then hypothesized that the observed single lifetime of cTnC(F74W) may result from the electron transfer quenching of Trp fluorescence by the amino acid residue Lys 21 on helix A.

To test this hypothesis we have produced two cTnC mutants, cTnC(F74W,K21A) and cTnC(F74W,K21Q), by replacing the amino acid residue lysine (K) 21 with alanine (A) and glutamine (Q), respectively. Pulsed light from port U9B at the National Synchrotron Light Source (NSLS) was used to excite the Trp on cTnC mutants. Single photon counting techniques were used to measure time-resolved total fluorescence and anisotropy decay. The instrumentation (called fluorescence omnilyzer), data collection, and data analysis procedures have been described in details previously (Kelly, et al., Rev. Sci. Instrum., 1997, 68:2279-2286). Each protein was excited at 295 nm and both parallel and perpendicular polarization components were simultaneously recorded for all wavelengths of a fluorescence spectrum.

With an excitation at 295 nm, at ambient temperature the replacement of K21 by A results in two lifetimes for the fluorescence decay from single Trp at position 74. This finding indicates that the amino acid resiude Lys 21 interacts with Trp 74 on Ca^{2+}-binding loop II. Addition of Ca^{2+} or Mg^{2+} leads to a small change in lifetimes. When K21 is replaced by Q, single lifetime is observed again, however, the lifetime becomes significantly shorter than that of cTnC(F74W). This result suggests that an enhanced quenching of Trp 74 fluorescence by Q. Fluorescence decay of cTnC(F74W,K21Q) is sensitive to the binding of Ca^{2+} and/or Mg^{2+} to the protein. Interestingly the effect of Mg^{2+} on fluorescence of single tryptophan at N-terminal domain is greater than that of Ca^{2+}. It must be emphasized that the two binding sites of cTnC for Mg^{2+} resides at C-terminal region, however, Trp 74 resides at Ca^{2+}-binding loop II which is in the N-terminal half of the protein. These results suggest that indeed Trp 74 on Ca^{2+}-binding loop II interacts with Lys 21 on helix A, and the mechanism for the change in fluorescence is likely to be electron transfer between the two amino acid residues.

* This work is supported in part by NIH Grant No. NIH HL52558.

Large Value of the Electron-Phonon Coupling Parameter $\lambda = 1.15$ and the Possibility of Surface Superconductivity at the Be(0001) Surface	U11, U13UB

T. Balasubramanian, E. Jensen (Brandeis U.), X. Wu, and S.L. Hulbert (BNL)

The electron-phonon coupling parameter at the Be(0001) surface λ_s is measured using angle resolved photoemission from surface states and found to be 1.15 ± 0.1, about four times the bulk Be value $\lambda_b = 0.24$ (see Figure 1). λ_s is determined by assuming that all of the temperature dependence of the surface state width comes from phonon creation/annihilation. In the limit of high temperatures, not quite realized for these data, λ is proportional to the derivative of the width with respect to temperature (see McDougall, Balasubramanian, and Jensen, Phys. Rev. B **51**, 13891 (1995)); a more accurate analysis results from a fit to the Debye model. This result can be understood simply from the large surface to bulk ratio of the Fermi level density of states first noted by Chulkov (Surf. Sci. **188**, 287 (1987)). A large value of λ is often associated with a high superconducting transition temperature. If the surface is considered as a thin film with high λ on a thick substrate with low λ, the proximity effect would destroy any observable interesting effects. However, it was shown by Suhl, Matthias, and Walker (Phys. Rev. Lett. **3**, 552 (1959)) that different branches of the Fermi surface – for which surface and bulk states qualify – could have different superconducting energy gaps. In the limit of a semi-infinite solid the two branches are essentially uncoupled and the surface states can superconduct independent of the bulk. Application of the McMillan formula using bulk phonons to estimate the superconducting transition temperature yields 70K for the surface transition temperature.

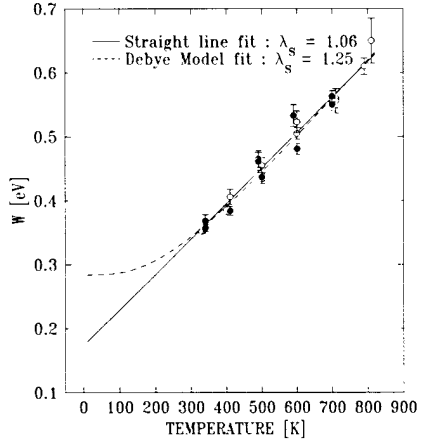

Figure 1. Surface state widths vs.temperature. The error bars on the data are from the fits. The open circles are for increasing temperature.

The VUV Absorption Spectrum of Cold Gas-Phase Methane * | U11

R. Bersohn (Columbia U.) and J.M. Preses (BNL)

The absorption spectrum of cold gas-phase methane in the VUV region from 110 to 140 nm is being measured. The temperature, about 100 K, is approximately the surface temperature of Jupiter and Titan, a moon of Saturn. In this research the absorption of CH_4 will be compared with that of CH_3D. The objectives are a) to try to understand the structure in the spectrum appearing at the shorter wavelengths, b) to compare the absorption with recent *ab initio* calculations of Mebel and Lin and c) to obtain basic data on the most abundant hydrocarbon molecule found in the atmospheres of the heavy planets and their satellites at the temperature of astronomical observation. At low temperatures, barely perceptible features in the absorption spectrum which may be due to vibrational structure could become more pronounced.

* Work supported by NASA Grant No. NAG5-4971 (RB). Research performed at Brookhaven National Laboratory under Contract AE-AC02-76CH00016 with the U.S. DOE and supported by the Div. of Chemical Sciences, Office of Basic Energy Sciences (JMP).

Products of the $O(^3P) + C_3H_6$ Reaction and Branching Fraction for Formation of CH_3 * | U11

R.B. Klemm, S.-C. Kuo, S.K. Ross (BNL) and R.P. Thorn, Jr. (NASA/GSFC)

The reactions of ground state atomic oxygen with olefins are of interest in combustion and atmospheric research because they are fast and because numerous reaction channels are thermodynamically allowed. For the O-atom + propene reaction, there are at least ten exothermic product channels:

(1) $CH_3 + CH_2CHO$
(2) $CH_3 + CH_3CO$
(3) $C_2H_5 + HCO$
(4) $C_2H_4 + H_2CO$
(5) $C_3H_4O + H_2$
(6) $CH_4 + CH_2CO$
(7) $CH_2 + CH_3CHO$
(8) $C_3H_5O + H$
(9) C_3H_6O
(10) $C_3H_5 + OH$

Early mass spectrometric studies by Gutman *et al.* (*Chem. Phys. Lett.* **1972**, *15*, 236) and by Hoyermann *et al.* (*Sixteenth Symposium(Int'l) on Combustion*, The Combustion Institute, Pittsburgh, **1977**, 841) identified channels (2) and (3) as major pathways, however, they differed on the importance of other possible channels. Hoyermann *et al.* were able to distinguish CH_3CO from the ^{13}C isotope of C_3H_6 but neither they nor Gutman *et al.* comment on the CH_2CHO isomer. In later studies with spectroscopic detection, the CH_2CHO radical, was positively identified as a major product of the $O+C_3H_6$ reaction. Moreover, the yield of CH_2CHO was reported by Hunziker *et al.* (*J. Photochem.*, **1981**, *17*, 377) to decrease with increasing pressure of argon, from 0.29 at 40 Torr to 0.19 at 760 Torr. The latest study by Knyazev *et al.* (*Int. J. Chem. Kint.* **1992**, *24*, 545)reported a branching fraction of 0.46 for channel (8) by monitoring H-atom resonance fluorescence.

In the present study, primary products from the $O+C_3H_6$ reaction were generated in a discharge flow reactor under kinetically isolated conditions. Mass spectrometric detection of reactants and products was accomplished via direct photoionization. Qualitative observation of products was accomplished via PIE spectra and/or adiabatic IE's. The following products were positively identified (species (m/z)): CH_3(15); C_2H_3(27); C_2H_4 (28); HCO/C_2H_5 (29); H_2CO(30); C_3H_5 (41); CH_3CO (43); CH_3CHO (44); $CH_3CH{=}CO$ (56); and propylene oxide (and possibly propanal) (58).

Additionally, the branching fraction for the formation of CH_3 ($d[CH_3]/d[O]$) was determined by using calibration experiments coupled with kinetic simulations. The value derived, 0.52 $\pm$0.05, is consistent with the results reported by Hunziker *et al.*, considering the strong pressure dependence of this branching fraction.

* The work at BNL was supported by the Chemical Sciences Division, Office of Basic Energy Sciences, U.S. DOE, under contract No. DE-AC0267CH00016 and by the Laboratory Directed Research and Development Program at BNL. RPT, Jr. thanks the NAS/NRC for the award of a Research Associateship.

Far-vacuum UV Circular Dichroism Spectra of Starch Components * | U11

P. Krzysztof (Agricultural U., Poznan,Poland)

In order to access to higher energy bands the samples have to be prepared as dried gels, films or desolvated samples. Such measurements provide access to transitions located on sugar ring and linkage atoms which may carry the information regarding conformational behavior of the polymer. The vacuum far-UV circular dichroism (CD) spectra of the dried samples of amylose and amylopectin measured up to 120 nm (10 eV), using synchrotron radiation are reported. The fact that the solution CD spectra of amylose and amylopectin are different from solid samples CD indicates that during desolvation the lowest energy transition disappears, which is a mixture of 2p orbitals of oxygen and carbon. The simplest explanation of such behavior is connected with randomization of carboxyl groups orientation relative to glucose ring upon desolvation. At higher energy CD spectra of all solid samples display a broad positive peak in the range 150 -160 nm, which comprise, very probably, few electronic transitions present in the energy range. Positive sign of CD for a-D-glucans suggests that this conformation is independent on molecular conformation and linkage. Studies on the electronic transitions involved in that band are contributions from sugar-ring oxygen containing chromphores, with the excitation originating from the non-bonding n orbital of the oxygen atoms. The highest energy band, 120 nm, observed in this experiment may be ascribed to s s* transitions from 2s orbitals of oxygen and carbon atoms of the glucose ring. The fact that the position remains similar for samples casted from water and DMSO indicates also that those transitions are located inside the sugar ring and are unpertubed by environmental modifications. The changes in CD spectra observed for the samples casted from DMSO very probably display disruption introduced by that solvent. The spectra of amylose and amylopectin are similar regarding the positions and the shape, which we may take as an indication that DMSO interacts with both polymers that final product has this same conformation what should not to be so amazing because both species have this same basic glucosidic ring as a monomer.

* This work was supported by grant from Polish Scientific Committee, KBN Grant 5 PO6G 054 08.

A Discharge Flow-Photoionization Mass Spectrometric Study of HNO: Photoionization Efficiency Spectrum, Ionization Energy and Proton Affinity of NO* | U11

S.-C. Kuo, Z. Zhang, S.K. Ross, R.B. Klemm (BNL), R. D. Johnson III (NIST), P.S. Monks, R. P. Thorn, Jr., and L. J. Stief (NASA/GSFC)

Photoionization efficiency (PIE) spectra of HNO were measured over the wavelength range λ = 110 to 125 nm and in the ionization threshold region, λ = 118 to 124 nm, using a discharge flow-photoionization mass spectrometer apparatus. HNO was generated *in situ* by the reaction sequence: N + NO $\rightarrow$ N_2 + O; O + C_2H_4 $\rightarrow$ CH_3 + HCO; HCO + NO $\rightarrow$ HNO + CO. The PIE spectrum displays step-like behavior near threshold and an HN-O stretching frequency in the cation of 1972 $\pm$ 67 cm^{-1}. A value of $10.18_4 \pm 0.01_2$ eV for the adiabatic ionization energy (IE) of HNO was obtained from photoionization thresholds, which correspond to the $HNO^+(X^2A') \leftarrow HNO(X^1A')$ transition. This result is the first PIMS determination of IE(HNO). Also, an *ab initio* molecular orbital calculation (QCISD(T)/aug-cc-pVQZ) was performed that yields a value for IE(HNO) of 10.186 $\pm$ 0.050 eV. There is good agreement between the experimental and the theoretical values for IE(HNO) reported here and that from a recent photoelectron spectroscopy study. The present experimental value for IE(HNO) was employed along with other, known thermodynamic quantities to obtain values for the heat of formation of the HNO cation and the absolute proton affinity of NO: $\Delta_f H^o_{298}(HNO^+)$ = 1089.73 $\pm$ 1.18 kJ mol^{-1} ($\Delta_f H^o_0(HNO^+)$ = 1092.65 $\pm$ 1.18 kJ mol^{-1}); $PA_{298}(NO)$ = 531.55 $\pm$ 1.26 kJ mol^{-1} ($PA_0(NO)$ = 526.12 $\pm$ 1.26 kJ mol^{-1}).

*Work at BNL was supported by the Chemical Sciences Division, Office of Basic Energy Scienses, U.S. DOE, under Contract No. DE-AC0276CH00016 and by the Laboratory Directed Research and Development Program at BNL. PSM and RPT thank the NAS/NRC for the award of Research Associateships. The work at NASA/GSFC was supported by the NASA Planetary Atmospheres Research Associateships. The work at NASA/FSFC was supported by Planetary Atmospheres Research Program.

Fluorescence Measurements of Indole Photoionization Products | U11

P. LeBreton (U. of Illinois at Chicago)

Preliminary, single-beam, steady-state fluorescence measurements were made of aqueous indole solutions at excitation wavelengths between 250 and 200 nm. Indole is a model compound for tryptophan, which is a primary radiation damage site in proteins. These lie in the energy region of the photoionization conduction-band-edge energy threshold. In these experiments, the same wavelength was employed to photoionize indole, and to excite the photoionization products. In the future, double-beam experiments will be carried out in which the synchrotron beam is used for photoionization and a second conventional light source is used for fluorescence excitiation.

In the past, indole photoionization in aqueous solution has been monitored using electron scavenging analysis and transient absorption of solvated electrons. Electron scavenging analysis only provides information about electron formation. No information is provided about the radical cations which are formed simultaneously with electron emission. Transient absorption detection is of limited sensitivity.

The goal of the present measurements is to determine the feasibility of employing fluorescence detection as a method for monitoring radical cations formed via the aqueous photoionization of indole. Fluorescence detection of photoionization products promises greater sensitvity than that offered by transient absorption measurements. The spectral signature provided by the excitation and emission characteristics of photoionization products will provide information, which will permit identification of the radical cationi products and which cannot be obtained in electron scavening experiments. In these experiments, the challenge will be to discriminate fluroescence associated with small concentratrions of radical cations from fluorescence associated with larger concentrations of neutral indole. This will be accomplished by examining the influence of radical scavengers on fluroescence emission, and by carrying out two-beam, time-resolved fluorescence measurements in which detection is synchronized with the ionizing beam.

Circular Dichroism Evidence for Solution Linkage Flexibility in (1→3)-Linked α-D-Mannopyranoside Residues * | U11

E.S. Stevens (SUNY at Binghamton)

The vacuum UV circular dichroism (CD) spectrum of thyl-3-O-(α-D-mannopyranosyl)-α-D-mannopyranoside in D_2O (175-200nm) is nearly identical to twice the monomer spectrum, both in solution and in films. The lack of a siginificant linkage contribution to the dimer spectrum most likely results from motional averaging among a variety of solution linkage conformations. The CD evidence for significant solution linkage flexibility confirms previous consclusions based on optical rotation, and is in agreement with nmr results of others. In the solid state the dimer CD (145-200nm) differs from the recently proposed quadrant rule to the known dimer crystal structure.

* This work was supported by NIH Grant GM46465.

VUV Spectroscopy of Amide Chromophores | U11

J.C. Sutherland, J.G. Trunk (BNL - Biology), and M.J. Kelley (DuPont Central Research, Experimental Station)

The transformation of polymer surtaces by deep UV light is interesting from both the standpoint of science and potential proactical applications. Good data of all kinds are sparse for UB wavelengths below about 200 nm and are difficult to obtain experimentally. Moreover, polymers are technological materials and can offer more complications than necessary, motivating the modelling, as far as possible. Careful comparisons among whole polymers and molecular model compounds, and between experimental data and computational models are vital to define what "as far as possible" really means.

MATERIALS: hexafluoro isopropanol (HFIP); 6/6 Nylon from "Dartek" film in HFIP; PET from "Mylar" 75 LB film; n-hexyl hexanamide, proxy for monomer; N, N' dihexyl adipamide, proxy for dimer.

METHODS: Absorption spectra were recorded with the apparatus normally used for the detection of circular dichroism using the pseudo-absorption method, which has been described elsewhere.[Sutherland, 1982 186][Sutherland, 1996 595] Auxiliary absorption spectra for wavelengths greater than 200 nm were obtained with a diode array spectrophotometer. Absorption spectra to 185 nm were obtained with a conventional source spectrophotometer at the Du Pont Central Research Laboratory to about 185 nm. Materials were contained in quartz windowed cells with pathlengths of 1.0 and 0.1 mm.

RESULTS: The spectra from U11 were similar to those from the conventional source instruments for the spectral range for which there was spectral overlap, indicating that the pseudo-absorbance method was performing adequately.

The HFIP only blanks were similar when recorded before and after the cells were filled with polymer sample, indicating that the methods used to clean the cells are adequate.

A peak in absorption is observed at about 190 nm that is ascribed to the $\pi_2 \rightarrow \pi_3$ transition.

A shoulder is observed for the nylon compound at about 175 nm that is tentatively ascribed to an $n_0 \rightarrow \sigma_{cO}$ transition.

Beginning about 170 nm the red edge of a strong absorption is observed, presumably due to the $\pi_1 \rightarrow \pi_3$ transition

DISCUSSION AND CONCLUSIONS: The results are generally in line with theoretical expectations. Absorption spectra can be extended to higher photon energies by studying films rather than solutions. Magnetic circular dichroism may confirm the tentative assignments; such experiments are planned for 1998.

[1] J. C. Sutherland, P. C. Keck, K. P. Griffin, and P. Z. Takacs, "Simultaneous measurement of absorption and circular dichroism in a synchrotron spectrometer", Nuclear Instruments and Methods 195, 375-379, 1982.

[2] J. C. Sutherland, "Circular dichroism using synchrotron radiation: from ultraviolet to x-rays," in Circular Dichroism: Conformational Analysis of Biomolecules, edited by Gerald D. Fasman (Plenum Press, New York, 1996), pp. 599-633.

Photoionization Efficiency Spectrum and Ionization Energy of the Cyanomethyl Radical CH_2CN and Products of the $N(^4S) + C_2H_3$ Reaction * | U11

R.P. Thorn, Jr., P.S. Monks, L.J. Stief (NASA/GSFC), S.-C. Kuo, Z. Zhang, S.K. Ross and R.B. Klemm (BNL)

Photoionization efficiency (PIE) spectra of the CH_2CN radical were measured over the wavelength range $\lambda = 115$ to 130 nm using a discharge flow-photoionization mass spectrometer (DF-PIMS). The cyanomethyl radical was produced by the reaction $F + CH_3CN \rightarrow CH_2CN + HF$ and the PIE spectrum displayed step-like behavior near threshold. From the half-rise point of the initial step, a value of $10.28_0 \pm 0.01_0$ eV was obtained for the adiabatic ionization energy (IE) of CH_2CN. This experimental result agrees well with the previous value of 10.1 ± 0.2 that was determined from the difference in the heats of formation of the cation and the neutral by Holmes and Meyer (*J. Phys. Chem.* **1995**, *99*, 1366). It is in even better agreement with a value of 10.20 ± 0.05 eV that was derived from an *ab initio* calculation by Horn *et al.* (*Ber. Bunsenges. Phys. Chem.* **1995**, *99*, 323). The present PIMS study of the CH_2CN radical provides experimental measurements of the adiabatic ionization energy that are simultaneously the most direct and the most precise available. For the reaction $N(^4S) + C_2H_3$, the C_2H_2N radical product exhibits a PIE spectrum that may include CH_2CN along with another species that has a gradual threshold that is at a considerably longer wavelength than the step-like threshold of CH_2CN (derived from $F + CH_3CN$). A possible source of this difference is the contribution from higher energy C_2H_2N isomers and/or from excited CH_2CN. In sharp contrast to the results for the $N(^4S) + C_2H_3$ reaction, no signal attributable to an isomer of the C_2D_2N radical was observed from the $N(^4S) + C_2D_3$ reaction. The C_2H_3N/C_2D_3N adducts from the $N(^4S) + C_2H_3/C_2D_3$ reactions were also studied. The adduct was observed to be solely CH_3CN for the $N(^4S) + C_2H_3$ reaction while for $N(^4S) + C_2D_3$, the PIE spectrum appears to include significant contributions from not only the lowest energy isomer, CD_3CN, but also one or more higher energy isomers.

*The work at BNL was supported by the Chemical Sciences Division, Office of Basic Energy Sciences, U.S. DOE, under contract No. DE-AC02786CH00016 and by the Laboratory Directed Research and Development Program at BNL. PSM and RPT,Jr. thank the NAS/NRC for the award of Research Associateships. The work at NASA/GSFC was supported by the Planetary Atmospheres Research Program.

Discharge Flow-Photoionization Mass Spectrometric Study of HOCl: Photoionization Efficiency Spectrum and Ionization Energy *	U11

R. P. Thorn, Jr., L. J. Stief(NASA/Goddard), S.-C. Kuo, and R. B. Klemm(BNL)

The photoionization efficiency (PIE) spectrum of HOCl was measured over the wavelength range λ = 102 - 115 nm, using a discharge flow- photoionization mass spectrometer apparatus. The PIE spectra displayed steplike behavior near threshold. This study represents the first determination of the HOCl photoionization efficiency spectrum and the photoionization threshold. A value of 11.120 $\pm$ 0.006 eV was obtained for the adiabatic ionization energy (IE) of HOCl from analysis of photoion thresholds, corresponding to the $HOCl^+(X^2A") \leftarrow HOCl\ (X^1A")$ transition. This result compares well with the only previous experimental measurement, a photoelectron spectroscopy study that was complicated by the presence of Cl_2O, Cl_2, and H_2O features in addition to those due to HOCl. The present result is also in good agreement with a recent G2 *ab initio* calculation by Glukhovtsev *et al.*

From the value for IE(HOCl), a value of 999.1 $\pm$ 3.6 kJ mol^{-1} is calculated for $\Delta_f H(HOCl^+)$ and from the latter, the proton affinity of ClO at T = 0 K is determined to be 630.0 $\pm$ 3.6 kJ mol^{-1}.

* The work at BNL was supported by the Chemical Sciences Division, Office of Basic Energy Sciences, U.S. DOE, under contract No. DE-AC0276CH00016 and by the Laboratory Directed Research and Development Program at BNL. RPT, Jr. thanks the NAS/NRC for the award of a Research Associateship. The work at NASA/GSFC was supported by the NASA Upper Atmosphere Research Program.

Radiative Recombination in Rare-Earth Doped Insulating Materials *	U11

A. J. Wojtowicz and J. Glodo (Boston U.)

The aim of the current project was to study carrier capture and recombination processes at structured impurities in wide bandgap materials activated by open *f*-shell (RE) ions which potentially may serve as scintillator materials. A simple model of a scintillator material describes a scintillation pulse in terms of rise and decay times which are determined by radiative (characteristic of the ion, e.g. Ce) and host-to-ion transfer rates. Since the unquenched radiative decay rate is limited by the value of Einstein coefficient, the Hyman theory requires that to achieve the best timing the transfer rate should be infinitely high while decay should be single exponential and as fast as possible. This approach highlights the importance of both emission and transfer processes which determine the intensity, wavelength and pulse shape of the scintillation light. Consequently, we have measured: **1) VUV excitation spectra** of *d-f* and *f-f* luminescences in RE-doped fluorides and Ce-doped aluminates to identify various channels of the host-to-ion energy transfer; **2) luminescence spectra** in order to identify those electronic states which are targets of specific energy transfer channels identified previously; **3) temporal pulse shapes.** In the case of direct excitation into the characteristic band (due to the *f-d* transition) the rise times are practically zero, while decays are largely single-exponential and radiative-rate-determined. The measurement of rise times under excitation favoring some channels of energy transfer identified by VUV spectroscopy (above the bandgap and excitonic) clearly show measurable rise-times, as expected.

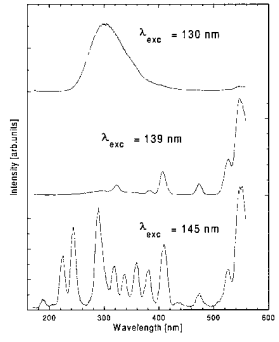

Figure 1. Luminescence spectra of Er-doped BaF_2 under VUV excitation. There is a dramatic change upon relatively small variations in the excitation wavelength. The highly selective nature of monochromatic optical excitation in VUV points to existence of various energy transfer mechanisms like direct excitation, excitonic and charge carrier mediated trapping processes.

* The support and hospitality of Dr. John Sutherland and his group of U11 beamline at NSLS is gratefully acknowledged. This work was funded by the Department of Energy, Grant No DE-FG-02-90ER61033.

Evidence for Coherent Emission from the VUV Ring in the Very Far Infrared*	U12IR

G.L. Carr (NSLS), R.P.S.M. Lobo (U. Florida & NSLS), J. LaVeigne, D.H. Reitze and D.B. Tanner (U. Florida)

We have observed evidence for coherent synchrotron radiation emission, peaked at a wavelength of 7mm (42 GHz), from port U12IR under special operating conditions of the VUV ring. This wavelength is much shorter than the electron bunch length of about 30cm, and therefore does not appear to be due to the intrinsic shape of the electron bunches. The emission appears as quasi-periodic (T ~2ms), short bursts of radiation.

The observed wavelength is comparable to the effective cutoff wavelength for the beamline and spectrometer's lightpipe optics (~8mm) as well as the ring chamber (approx. 30mm). Therefore, our data does not rule out the presence of coherent emission at wavelengths beyond about 10mm. The width of the emission is not quite resolved with the existing instrument, having a spectral resolution of about 0.12mm at 7mm wavelength.

The coherent emission appears to be present only when the current per bunch exceeds a threshold, which depends on the operating conditions of the ring. For example, for operations with E=744MeV and the 4th harmonic cavity at a low (injection level) power, the threshold is about 100ma per bunch. This is observed in 1, 3 and 7-bunch modes. Ramping the electron energy to 800MeV shifts the current threshold to about 160ma. Increasing the power to the 4th harmonic cavity causes a further increase in the threshold value.

*Supported by DOE Contracts DE-AC02-76CH00016 and DE-FG02-96ER45584.

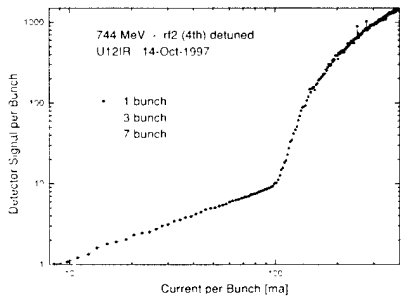

Figure 1. Broadband, long wavelength infrared signal at U12IR, measured versus beam current in the VUV ring. The signal increases linearly with beam current until the 100ma threshold is reached, and then increases approximately as the current squared.

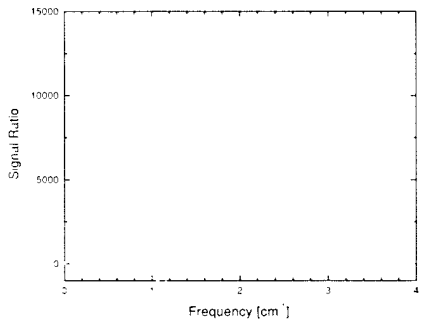

Figure 2. Spectrum of the coherent emission signal, showing a strong peak near 1.4 cm^{-1} (7mm wavelength, or about 42 GHz).

Design of the U12IR Beamline for Solid State Infrared Spectroscopy*	U12IR

G.L. Carr, G.P. Williams and D. Lynch (NSLS)

The new infrared beamline U12IR is designed to serve the solid state physics community's needs for performing IR spectroscopy from wavelengths of a few microns out to several millimeters. The beamline uses a 90x90 milliradian mirror extraction system similar to beamline U4IR (see Figure 1), bringing the light from the ring's UHV environment through a wedged diamond window. However a number of special design features have been incorporated in order to reach such long wavelengths efficiently, such as a large beamline diameter and a tapered light cone preceding the diamond window. When the long wavelength (lamellar grating) interferometer is used, quasi-optic lightpipe is placed immediately after the diamond window and brings the light to this fast interferometer, thus minimizing diffraction losses. Otherwise conventional mirror optics are used collimate the infrared and transport it to the other spectrometer - a Bruker IFS 113v. Figure 2 shows the collimating mirror chamber and spectrometer endstations with the lightpipe in place. The beamline's spectral range is expected to reach from about 1 cm^{-1} up to 40,000 cm^{-1}, although the spectrometer endstations will reach to only 10,000 cm^{-1}. A spectral resolution of ~0.1 cm^{-1} is anticipated.

* Work supported by DOE Contract DE-AC02-76CH00016.

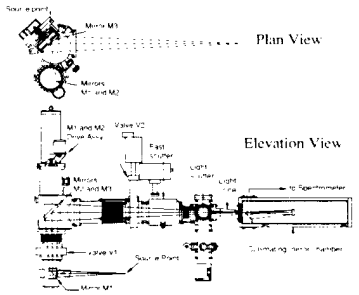

Figure 1. Schematic of the U12IR UHV beamline section. A set of three mirrors extract the beam and focus it onto a wedged CVD diamond window. A cone immediately upstream of the window is used to couple wavelengths beyond 1mm into lightpipe.

Figure 2. Schematic of the two spectrometer endstations. The collimating chamber just downstream of the diamond window is at left. Either lightpipe or conventional mirrors are used to transport the infrared beam to a spectrometer.

Initial Tests of the New Infrared Beamline U12IR	U12IR

R.P.S.M. Lobo, J. LaVeigne, D.B. Tanner (U. of Florida), G.L. Carr (NSLS)

The new infrared beamline U12IR has neared completion, and initial testing of the optical instrumentation has begun. Though the beamline delivers light over the frequency range from ~1 cm^{-1} to 40,000 cm^{-1}, the spectrometer endstations are optimized for the long wavelength region. A Bruker IFS 113v will span the range from 20 cm^{-1} to beyond 5000 cm^{-1}, while a lamellar grating interferometer will be used for the 1 to 100 cm^{-1} range. First measurements have been performed using the lamellar grating interferometer and bolometric detectors operating at T~1.7K and 4.2K. Useful signals down to about 2 cm^{-1} have been obtained. A typical low resolution interferogram is shown in Figure 1, and the resulting spectral signal (obtained by Fourier transform) is shown in Figure 2.

* Supported by DOE through contracts DE-AC02-76CH00016 and DE-FG02-96ER45584.

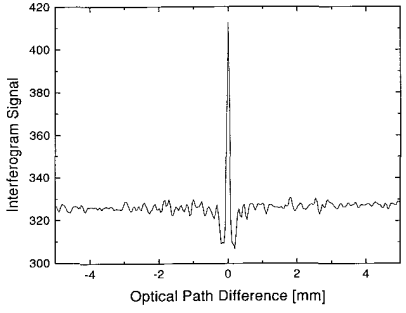

Figure 1. Interferogram obtained with the synchrotron source using the lamellar grating interferometer.

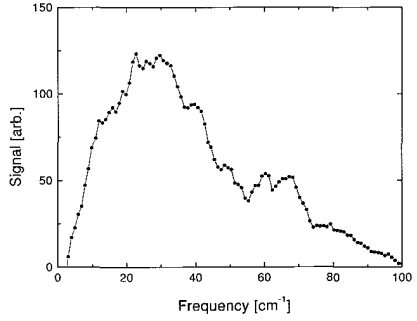

Figure 2. Typical "single beam" spectral signal at a resolution of 2 cm^{-1}.

A Pulsed Synchronized Laser System for Time-Resolved Spectroscopy*	U12IR

D.H. Reitze, J. LaVeigne, D.B. Tanner (U.of Florida), R.P.S.M Lobo (U. Florida & NSLS) G.L. Carr (NSLS)

A custom mode-locked Ti:sapphire laser system has been implemented on the VUV floor. The system is a custom Mira unit from Coherent Laser Group, designed to produce pulses at a 105.76 MHz pulse repetition frequency (PRF) using the 52.88 MHz rf signal from the VUV ring. The system is therefore synchronously locked to the pulse structure of light emitted by this storage ring. The laser is continuously tunable from 0.7 microns to 1 micron wavelengths, and produces up to 10 nJ per 2 ps duration pulse. A pulse selection system, to match special bunch patterns of the ring (i.e., multi-bunch, symmetric 3-bunch, and 1-bunch), has also been developed and tested. Modulation of the Ti:sapphire laser phase will allow lock-in detection of time-dependent signals.

The light will be fed to various experiment stations (U12IR in particular) via fiber optic cable, allowing time-resolved, pump-probe spectroscopy to be performed. The available time resolution is limited by the synchrotron pulse duration, which can be as short as ~100ps under special operating conditions. The longest time between pulses is set by the ring orbital period of 170ns.

* Supported by DOE through Contracts DE-AC02-76CH00016 and DE-FG02-96ER45584.

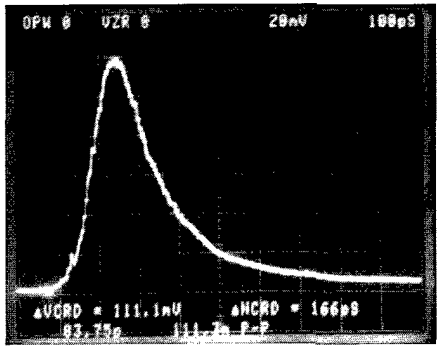

Figure 1. Oscilloscope trace showing a pulse from the synchronized Ti:sapphire laser. The apparent pulse width is limited by the bandwidth of the photodetector and electronics.

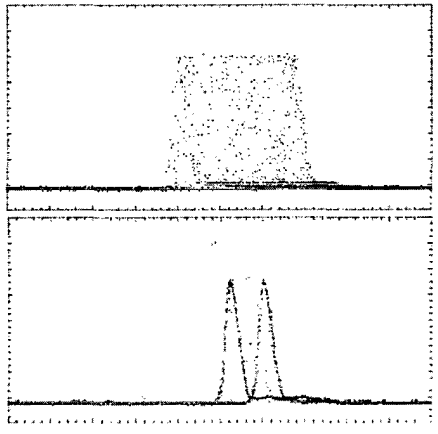

Figure 2. Oscilloscope traces showing both sine and square wave modulation of the Ti:sapphire laser pulse phase (relative to the synchrotron). The horizontal axis is 2ns per major division.

Large Value of the Electron-Phonon Coupling Parameter $\lambda = 1.15$ and the Possibility of Surface Superconductivity at the Be(0001) Surface	U11, U13UB

T. Balasubramanian, E. Jensen (Brandeis U.), X. Wu, and S.L. Hulbert (BNL)

The electron-phonon coupling parameter at the Be(0001) surface λ_s is measured using angle resolved photoemission from surface states and found to be 1.15 ± 0.1, about four times the bulk Be value $\lambda_b = 0.24$ (see Figure 1). λ_s is determined by assuming that all of the temperature dependence of the surface state width comes from phonon creation/annihilation. In the limit of high temperatures, not quite realized for these data, λ is proportional to the derivative of the width with respect to temperature (see McDougall, Balasubramanian, and Jensen, Phys. Rev. B **51**, 13891 (1995)); a more accurate analysis results from a fit to the Debye model. This result can be understood simply from the large surface to bulk ratio of the Fermi level density of states first noted by Chulkov (Surf. Sci. **188**, 287 (1987)). A large value of λ is often associated with a high superconducting transition temperature. If the surface is considered as a thin film with high λ on a thick substrate with low λ, the proximity effect would destroy any observable interesting effects. However, it was shown by Suhl, Matthias, and Walker (Phys. Rev. Lett. **3**, 552 (1959)) that different branches of the Fermi surface – for which surface and bulk states qualify – could have different superconducting energy gaps. In the limit of a semi-infinite solid the two branches are essentially uncoupled and the surface states can superconduct independent of the bulk. Application of the McMillan formula using bulk phonons to estimate the superconducting transition temperature yields 70K for the surface transition temperature.

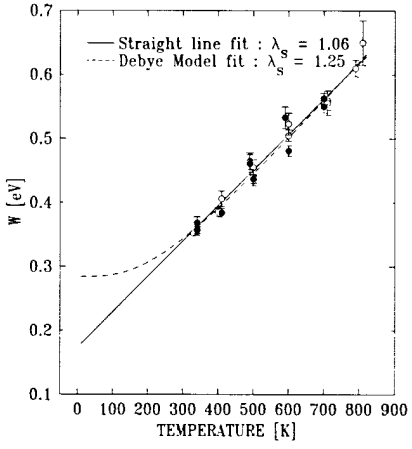

Figure 1. Surface state widths vs.temperature. The error bars on the data are from the fits. The open circles are for increasing temperature.

Line Shape of the Ag $N_{23}VV$ Auger Transition Measured by Auger Photoelectron Coincidence Spectroscopy	U14A

A. Danese, Q. Qian, R.A. Bartynski (Rutgers U.), S.L. Hulbert (NSLS)

It is well known that the shallow p-levels of the late transition metals have very broad and ill-defined spectral line shapes. Owing to strong overlap with the 4d bands, the shallow 4p levels of Ag have a very short lifetime hence appear as broad ($\approx$5 eV wide) features in photoemission spectra. This width is folded into the conventional Auger spectrum. By measuring Ag $N_{2,3}VV$ Auger electrons in coincidence with Ag 4p photoelectrons of a particular kinetic energy, we have eliminated this broadening and revealed the true lineshape of the Auger transition. These coincidence spectra are shown in Figures 1 and 2. As has been seen for the $M_{4,5}VV$ transition, the lineshape appears to include both quasi-atomic and band-like components to its profile. However, in the coincidence spectra, the band-like component is significantly more pronounced. This is most likely because of the elimination of inelastic background in the coincidence measurement. A comparison of the relative spectral weight contained in each component indicates that the band-like part is Ag. In addition to measuring Auger line shapes, extrinsic inelastic background is suppressed in APECS because it has a significantly smaller probing depth. As a result, one can assess the relative contribution of extrinsic (i.e. caused by inelastic scattering on the way to the surface) to intrinsic (i.e. caused by additional excitation in the Auger process) contributions to the secondary electron background. In our coincidence Auger spectra from Ag, we find that a large fraction of the spectral weight appears as inelastic contribution under the primary Auger features. This is in sharp contrast to the equivalent spectra from Cu, where almost no background is found. It is also interesting to note that in Cu, there is no detectable band-like contribution to the Auger spectrum. This suggests that the large intrinsic secondary background, which is presumably dominated by 3- and 4-electron Auger-like transitions, is coupled to the presence of band-like Auger transitions.

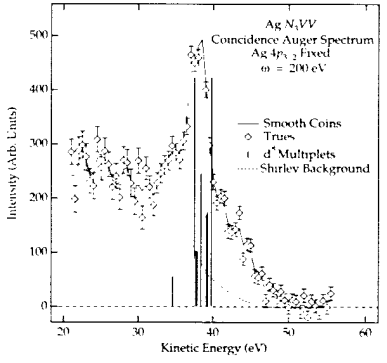

Figure 1.

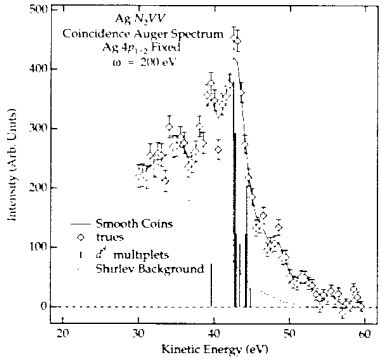

Figure 2.

Adsorption of NH_3 on $TiO_2(110)$ Studied by Auger Photoelectron Coincidence Spectroscopy *	U14A

W.K. Siu, R.A. Bartynski (Rutgers U.), A. Nangia, A.H. Weiss (U. Texas at Arlington), X. Wu, and S.L. Hulbert (NSLS)

We have measured the lineshape of the Ti 3p core level in coincidence with Ti $M_{2,3}VV$ Auger electrons from the stoichiometric and vacuum annealed $TiO_2(110)$ surfaces exposed to saturation doses of NH_3 at room temperature. Fig. 1(a) shows the coincidence photoemission spectrum from the clean stoichiometric surface. Emission from Ti^{3+} and Ti^{2+} ions is associated with residual defects (i.e. steps and isolated oxygen vacancies) on the surface. Fig. 1(b) shows that upon NH_3 adsorption, the relative contribution from the Ti^{4+} ions is significantly reduced. In contrast, Figs. 2(a) and 2(b) show that in the coincidence spectra from the annealed surface, the relative Ti^{4+} signal increases upon adsorption.

We interpret the results from the stoichiometric surface to indicate that NH_3 bonds in-plane to the 5-fold coordinated surface Ti ions but does not interact with residual defects. For the vacuum annealed surface, NH_3 bonds to thermally induced oxygen vacancies and inhibits bonding to in-plane Ti ions. This gives rise to the increase in Ti^{4+} signal for this surface. The signal from Ti^{3+} and Ti^{2+} that survives in Fig. 2(b) is associated with the step edges of the vacuum annealed surface. Using estimates of the defect density for these surfaces to normalize the relative contributions of different Ti-ions in these spectra, we conclude that when NH_3 bonds to thermal defects, it prevents adsorption to slightly less than two in-plane Ti ions on average. These results are able to explain why a reduction in the saturation coverage of NH_3 has been seen for the chemically reduced $TiO_2(110)$ surface.

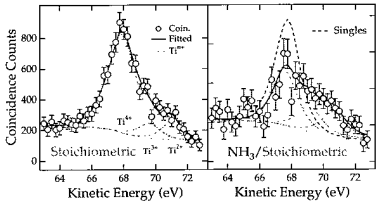

Figure 1.

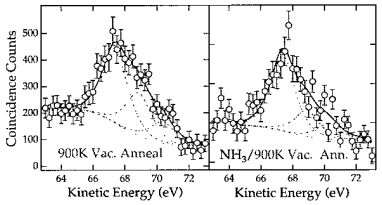

Figure 2.

* Funded under grant number NSF-DMR 94-11610.

ABSTRACTS

X-Ray Beamlines

Beamline X1A

Beamline X1B

Beamline X2A

Beamline X2B

Beamline X3A1

Beamline X3A2

Beamline X3B1

Beamline X3B2

Beamline X4A

Beamline X6B

Beamline X7A

Beamline X7B

Beamline X8A

Beamline X8C

Beamline X9A

Beamline X9B

Beamline X10B

Beamline X11A

Beamline X12A

Beamline X12B

Beamline X12C

Beamline X14A

Beamline X15A

Beamline X15B

Beamline X16A

Beamline X16C

Beamline X17B1

Beamline X17B2

Beamline X17C

Beamline X18A

Beamline X18B

Beamline X19A

Beamline X19C

Beamline X20A

Beamline X20C

Beamline X21

Beamline X22A

Beamline X22B

Beamline X22C

Beamline X23A2

Beamline X23A3

Beamline X23B

Beamline X24A

Beamline X24C

Beamline X25

Beamline X26A

Beamline X26C

Beamline X27A

Beamline X27C

Soft X-ray Imaging and C-XANES Linear Dichroism of Nematic Phase Transitions in Coal Derived Liquids	X1A

G.D. Cody (Carnegie Institute of Washington)

Certain coals, when heated to temperatures > 400°C fluidize. The initially isotropic fluids nucleate microscopic, optically anisotropic, spheres which ultimately coalesce into a highly anistropic fluid. This property has important industrial applications in areas of metallurgical cokes and carbon electrode fabrication. The chemistry of these fluids is dominated by aromatic molecules. As the X-ray beam at X1A is highly polarized, one can use the intensity of the aromatic 1s-$\pi*$ transition to follow the generation of anisotropic regions within quenched samples of the fluids. This is because the 1s-$\pi*$ transition is highly polarized perpendicular to the plane of the aromatic ring. Soft X-ray microscopy and micro C-XANES spectroscopy has been applied to a series of quenched glasses ranging from purely isotropic, to mixed phase, to purely anisotropic. Figure 1 presents images of the highly anisotropic quenched fluid (glass at room temperature). Fine scale anisotropic domains are clearly evident. It has been recognized that the size and topology of the anisotropic domains controls the quality of the material from industrial standpoints, however, details on the physics and chemistry that controls domain size are minimal. Figure 2 presents C-XANES spectra obtained from a single anisotropic domain, but with sample rotation to explore the extent of linear dichroism. Although the dichroism is pronounced, the average degree of preferred orientation parallel to the electric vector of the X-ray beam is on the order of 23 degrees. Comparison of the anisotropic spectra obtained at the magic angle with spectra obtained from the truly isotropic regions reveals minimal differences in the carbon chemistry. This suggests that the isotropic to anisotropic transitions may be purely a second order liquid crystalline phase transition.

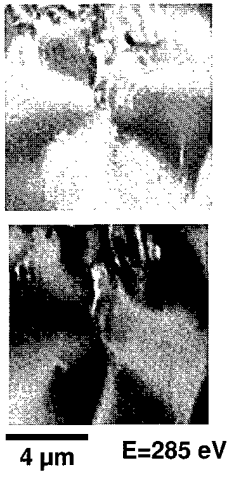

Figure 1.

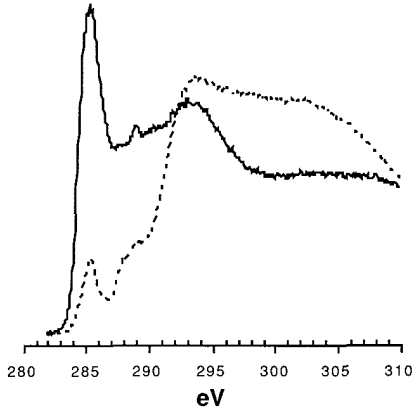

Figure 2.

Carbon and Oxygen XANES and X-ray Imaging of Chemically Differentiated Regions in the Cell Wall Structure of Ancient (40-150 Ma) Wood *	X1A

G.D. Cody (Carnegie Institute of Washington)

The fate of biomacromolecular compounds such as lignin and cellulose in ancient wood is being studied using the unique capabilities of the STXM at X1A. The cell wall of wood is chemically differentiated into several distinct regions, e.g. the middle lamellae, the primary cell wall, the S1, S2, and S3 regions of the secondary cell wall. Mature cells of fresh wood have lignin predominantly located within the middle lamellae and S2 region of the secondary cell wall. Recent studies using the STXM have revealed that the chemical differentiation within the cell wall persists well beyond the stage where the biomacromolecules lignin and cellulose are thermochemically altered into essentially new complex geomacromolecules. Efforts are currently focused on characterizing the chemical reactions that transform these biomacrmolecules, resolved within the discrete regions of the cell wall. High resolution soft X-ray imaging on the carbon (1s) absorption pre-edge, e.g. at 285 eV corresponding to aromatic carbon's 1s-pi* transition reveals that cell wall chemical differentiation persists even after millions of years of preservation (Figure 1). We have observed chemical dif ferentiation in samples as old as 135 million years old. Micro C-XANES reveals significant differences across the discrete regions of the cell well, including variations in the average degree of aromatic ring hydroxylation, variations in lignin and cellulose, and variations in the concentration of oxidized organic functional groups not initially present in pristine lignin or cellulose (figure 1).

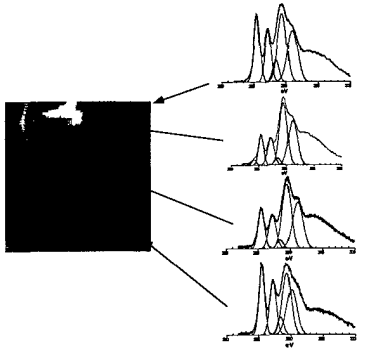

Figure 1. X-ray image of cross section through cell wall of 40 million year old wood. Monochromator fixed at 285 eV; contrast based on concentration of aromatic carbon. Corresponding C-XANES spectra of middle lamellae, primary cell wall, S1 secondary cell wall, and S2 secondary cell wall.

* Financial support by Exxon Education Foundation is gratefully acknowledged

C-XANES Linear Dichroism Studies of Single Crystals of Polycyclic Aromatic Hydrocarbons * — X1A

G. D. Cody (Carnegie Institution of Washington), H. Ade (North Carolina State U.), S. Wirick (SUNY at Stony Brook), and J. Waldbaur (Dartmouth U.)

The recent upgrade of X1A has opened up new opportunities for solid phase characterization of relatively large carbonaceous molecules. In particular we have acquired high resolution near edge spectra of pure polycyclic aromatic hydrocarbons. Single crystals of anthracene (C14), phenanthrene (C14), pyrene (C16), crysene (C18), perylene (C20), and benzo-g-perylene (C22) have been studied to date. In each case pairs of high resolution C-XANES spectra have been obtained with the electric vector of the polarized X-ray beam parallel with the principal optical axes of the crystals (e.g. Figure 1). Anthracene, phenanthrene, pyrene, crysene, perylene, and benzo-g-perylene have manifolds of 7, 7, 8, 9, 10, and 11 $\pi*$ states, respectively; therefore complex spectra are anticipated. The linear dichroism studies clearly allow distinction of pi vs. sigma type polarization; a trivial point at high energies, but a very helpful approach for the low energy (1s-3p/sig*) transitions that occur in the midst of the 1s-$\pi*$ transtions. Extended Huckel molecular orbital calculations including the Z+1 (equivalent core virtual orbital model) approximation fo the photoexcited molecule were used to facilitate assignment of the fine structure in the near edge region (e.g. figure 2). In principal, the fine structure (figures 1 and 2) may result from vibrational splitting as is common for simple molecules. The EHMO Z+1 calculations suggest, however, that small shifts in the energy of various 1s-n$\pi*$ transitions may be due to chemically inequivalent carbons. The results of these studies are providing the key to our understanding of micro- characterization studies of thermally metamorphosed coals; materials with chemistry dominated by polycylcic aromatic hydrocarbons.

* Financial Support from the Exxon Education Foundation is gratefully appreciated.

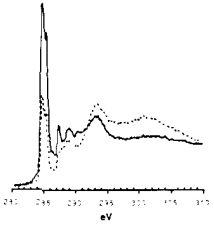

Figure 1. C-XANES spectra of crysene. The pair of spectra correspond to crystal orientations orthogonal to each and alligned along the principal optical axes.

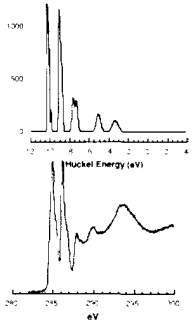

Figure 2. C-XANES spectrum of anthracene (above). Simulated spectrum of anthracene (below) using EHMO methods and the Z+1 (equivalent cores) approximation for the photoexcited carbon.

X-Ray Radiation Damage of PMMA, PC, and Nylon 6 — X1A

T. Coffey and H. Ade (NCSU)

In order to comprehensively understand damage of polymers in X-ray microscopes, we have started to investigate radiation damage in a variety of polymers. Using the Stony Brook Scanning Transmission X-ray Microscope (STXM) on beamline X1A, [1,2] we have compared the radiation damage of three carbonyl containing polymers, poly(methyl methacrylate) (PMMA), polycarbonate (PC), and Nylon 6. We want to ascertain whether the critical dose for damage to the carbonyl functionality depends on the location (main chain vs. side chain) and on the local electronic structure. We use Near Edge X-Ray Absorption Fine Structure (NEXAFS) spectra to monitor both the decay of the carbonyl peak and the mass loss. We quantitate radiation damage by measuring the "critical dose" for the PC and Nylon 6 carbonyl peak decay and PMMA mass loss. The "critical dose" is the radiation dose at which the feature size is decreased by 1/e of its original size. Our critical dose for mass loss in PMMA is 43 eV/nm^3, which compares favorably with the previous result of 56 eV/nm^3 [3]. Previous work separates the mass loss effects and the decay of the carbonyl peak, measuring the critical dose of the PMMA carbonyl peak as 372 eV/nm^3 [3]. We measured the critical doses for the carbonyl peaks in PC and Nylon 6 as 92 eV/nm^3 and 1360 eV/nm^3 respectively. We believe that the differences in the critical doses of the carbonyl functionality can be explained by the local electronic structure. A qualitative relation exists between the critical dose and the ionization potential of the core electron of the carbonyl carbon atom. As the ionization potential of the carbonyl carbon atom increases, the critical dose decreases. In polymers, the ionization potential is a measure of the local electron density which reflects the electronegativity and number of hetero-atoms as nearest neighbors. The ionization potentials of the carbonyl carbon atom are: Nylon 6, 288.01 eV; PMMA, 289.03 eV; and PC, 290.4 eV[4]. This suggests that the critical dose for the carbonyl group is related to the electronegativity of the nearest neighbors of the carbon atom in the carbonyl group, i.e. more electronegative neighbors imply a smaller critical dose.

[1] C. Jacobsen et al., *Optics Communications* 86 (1991), 351.
[2] X. Zhang et al., *Nuclear Instruments and Methods in Physics Research A* 347 (1994), 431.
[3] X. Zhang et al., *J. Vac. Sci. Technol. B* 13(4), 1477.
[4] G. Beamson and D. Briggs, *High Resolution XPS of Organic Polymers*, John Wiley and Sons, New York, 1992.

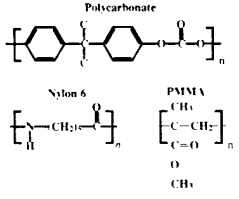

Figure 1. The chemical structures of Nylon 6. PMMA and PC.

Polymer	Critical Dose	Ionization Potential
Nylon 6	1360 eV/nm^3	288.01 eV
PMMA	372 eV/nm^3	289.03 eV
Polycarbonate	92 eV/nm^3	290.4 eV

Figure 2. Summary of results.

A High Rate Gas Proportional Counter For Soft X-Ray Microscopy | X1A

M. Feser (SUNY at Stony Brook), G. Smith, B. Yu (BNL), J. Kirz, and C. Jacobsen (SUNY at Stony Brook)

A multichannel, low pressure gas proportional chamber is being developed and tested for the scanning transmission x-ray microscope (STXM) at beamline X1A, to increase the count rate capability well beyond that of existing single channel detectors.

A schematic layout of the detector with electronics is shown in Fig. 1. The focused monochromatic x-ray beam enters the detector through a thin (120 nm) SiN window. The eight anode wires are connected in groups (from the front) of 1, 1, 2 and 4. Because of the exponential decrease in x-ray photon intensity in the detector (length 5 cm), comparable count rates can be obtained on all four groups when the composition and pressure of the gas are optimized for a specific photon energy. Uncommon low Z gas mixtures such as neon with a CO_2 quench have been tested. Each group of anode wires feeds an electronic channel comprising a high bandwith preamplifier and shaping amplifier.

The detector was studied in the energy range from 270 eV to 800 eV on the STXM at X1A. The principle of spreading photons over more than one channel has been demonstrated with the counter response to photon intensity being quite linear (Fig. 2). Images of a test pattern confirmed the good detector performance in connection with the microscope.

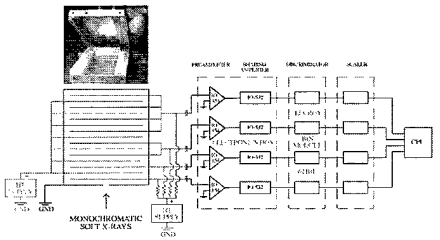

Figure 1. Layout of the detector and electronics.

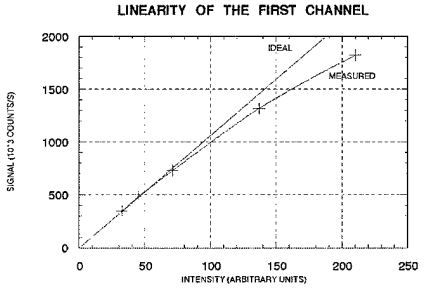

Figure 2. Linearity test of the first channel

The Spatial Distribution and Bonding States of Carbon in the ALH84001 Meteorite from Mars | X1A

G.J. Flynn (SUNY at Plattsburgh), L.P. Keller (MVA, Inc.), C. Jacobsen and S. Wirick (SUNY at Stony Brook)

McKay et al. [1] reported that carbonate globules from the ALH84001 meteorite contain several indicators suggesting ancient biological activity on Mars. One indicator is their detection of polycyclic aromatic hydrocarbons (PAHs) "found in the highest concentrations in the regions rich in carbonates," and associated with magnetites and sulfides similar in size and shape to those produced by terrestrial bacteria [1]. However, the spatial resolution of the PAH measurement (50 micrometers analysis spot) was comparable to the size of individual carbonate globules and far larger than the magnetites and sulfides which occur in thin rims on the globules. We employed the Scanning Transmission X-ray Microscope (STXM) at beamine X1A, using a 50 nanometer analysis beamspot, to determine the spatial distribution and the bonding state(s) of carbon in the ALH84001 meteorite with a spatial resolution about 1,000 times that achieved by McKay et al. [1]. Ultramicrotome sections of the carbonate and of rim material from the AL84001 meteorite were examined.

The C-O bond in carbonate gives rise to a strong absorption near 290 eV [2], while C-C, C=C, and C-H bonds have strong absorptions in the 284 to 287 eV range. Thus, Carbon X-Ray Absorption Near Edge Structure (C-XANES) measurements provide a sensitive technique to detect and map the distribution of organic or graphitic carbon in a matrix of carbonate.

C-XANES spectra of the ALH84001 carbonate globule samples showed strong absorption at 290 eV, characteristic of the C-O bond in carbonate, and weaker absorptions at 284.8 eV, 286.5 eV, and 288.2 eV. The relative intensities of the latter three absorption peaks were approximately constant (where they could be detected) over the sample, however the ratio of these peaks to the C-O peak varied with position. This indicates the presence of a second carbon-bearing phase, distributed inhomogeneously on the scale of the 50 nanometer beamspot, within the carbonate.

C-XANES spectra of the ALH84001 dark rim samples showed no absorption at 290 eV, consistent with the absence of carbonate. Some spots on these sections showed two absorption peaks at 284.5 eV and 288.2 eV, indicating the presence of C-C, C=C, or C-H bonds. The differences in absorption peak energies and the absence of the third peak in the rim sample indicate that the dominant carbon-bearing phase in the rim is different from that in the carbonate globule.

These preliminary results demonstrate the close association of carbon-bearing phases containing C-C, C=C, and/or C-H bonds with the carbonate globules and the rims, confirming, at a much smaller size scale than reported by McKay et al. [1], the association of a carbon-bearing phase with the carbonate globules and the rims on these globules from ALH84001. To confirm that the carbon-bearing phases in the carbonate globule and the rim are different from one another, as indicated by these C-XANES analyses, and to determine if these phases are organic, the same ultra-microtome sections analyzed by STXM were examined by micro-FTIR at beamline U4-IR [see results in 3].

References: 1) McKay, D. S. et al., Science, 273, 924-927, 1996 2) Flynn, G. J. et al., Lunar Planet. Sci. XXVIII, A42, 1997. 3) Flynn, G. J., "Identification of Organic Compounds in the ALH84001 Meteorite from Mars", U4IR Activity Report, this volume.

Identification of Organic Compounds in the ALH84001 Meteorite from Mars	X1A, U4IR

G. J. Flynn (SUNY at Plattsburgh), L. P. Keller and M. A. Miller (MVA Inc.)

McKay et al. [1] suggest the ALH84001 meteorite contains evidence of possible ancient biological activity on Mars. One line of evidence is the concentration of polycyclic aromatic hydrocarbons (PAHs), frequently produced by the decay of living material, occuring in close proximity to magnetite and sulfide similar in size and shape to those produced by terrestrial bacteria [1].

We employed the Scanning Transmission X-Ray Microscope on beamline X1A to determine the bonding state(s) and the spatial distribution of the carbon in ultramicrotome thin-sections of carbonates globules and the rims, where the magnetites and sulfides were found, on these carbonates from ALH84001 [2]. Both the carbonate and the rim sections contained carbon-rich regions, but each gave a different C-XANES spectrum, suggesting the major carbon-bearing compound was different in the rim and the carbonate [2]. We then examined the same samples using a Spectra-Tech micro-Fourier Transform Infrared (FTIR) spectrometer, on beamline U4IR, to identify the carbon compounds.

Transmission Electron Microscope (TEM) examination of the rim samples indicated were composed of feldspathic glass and contained micron-size chromite, and regions of fine-grained magnetite and sulfide. The FTIR spectra of the rim samples showed a broad absorption near 1000 cm^{-1}, characteristic of silicate glass, and two weaker features at 2918 cm^{-1} and 2850 cm^{-1}. These two features are consistent in position and relative depths with the symmetric and asymmetric stretching vibrations of the $C-H_2$ in aliphatic hydrocarbons.

The FTIR spectra of the carbonate globule showed a narrow absorption at about 1500 cm^{-1}, characteristic of carbonate, and a weaker absorption at 2964 cm^{-1}. Two even weaker features appear at 2920 cm^{-1} and 2850 cm^{-1}. The feature at 2964 cm^{-1} is characteristic of the $C-H_3$ asymmetrical stretching vibration. Although a weaker $C-H_3$ symmetrical stretching vibration generally occurs near 2870 cm^{-1}, this feature is absent in the carbonate globule spectrum, and is suppressed in certain compounds containing $C-H_3$ groups. One particularly good spectrum of the carbonate globule sample appears to show a weak, broad absorption over the range 2990 cm^{-1} and 3060 cm^{-1}. Follow-up measurements, to determine if this feature could indicate the detection of C-H stretching vibrations of a mixture of PAHs, which would have an absorption near 3030 cm^{-1}, are in progress.

These preliminary results confirm that high concentrations (of order 1 to 5 percent) of organic carbon are associated with the carbonate globules and rims in ALH84001, and further confirm the STXM observation that the rim and the carbonate globule contain different types of carbon. The latter result seems to rule out the simplest form of organic contamination of ALH84001, simple evaporation of an organic-rich fluid, which would be expected to leave the same residue in both the carbonate globules and the adjacent rim material, although selective, mineral specific, contamination cannot be excluded.

References:

1) McKay, D. S., et al. Science, 273, 924-927, 1996.
2) Flynn, G. J. et al., Meteoritics, 32, A46-A47, 1997.

Carbon Mapping and Carbon-XANES Measurements on Interplanetary Dust Particles	X1A

G. J. Flynn (SUNY at Plattsburgh), L. P. Keller (MVA Inc.), S. Wirick and C. Jacobsen (SUNY at Stony Brook)

Modeling by Anders [1] indicates that interplanetary dust particles (IDPs) may have been an important source of organic matter on the early Earth, providing some of the pre-biotic organic compounds required for the development of life. The IDPs collected from the Earth's stratosphere by NASA are carbon-rich, containing an average of 12 weight percent carbon [2]. However, the ratio of elemental to organic carbon in the IDPs is not well-established. We have previously demonstrated that the Scanning Transmission X-ray Microscope (STXM) on beamline X1A can be used to map the spatial distribution of carbon and to determine the carbon bonding states by Carbon-X-Ray Absorption Near Edge Structure (C-XANES) measurements [3]. The carbon in two of the first three IDPs examined by C-XANES is dominated by poorly graphitized or amorphous elemental carbon rather than organic carbon [3].

In a continuation of that study, ultramicrotome thin-sections (100 to 200 nm thick) of three additional IDPs, L2011*B5, L2009J4, and L2009*F2, have been examined using the STXM. L2009J4 exhibited several distinct morphologies of carbon-rich material: individual micron sized grains, thin regions partially surrounding non-carbonaceous grains (apparently carbon coatings about 100 to 200 nm thick on those grains), and larger regions of carbon-rich material (microns in size) containing non-carbonaceous grains. A C-XANES spectrum of an individual micron-sized carbonaceous grain in L2009J4 showed absorption peaks near 285 eV and 289 eV, consistent with C-C and C-O bonds respectively, and inconsistent with graphite or amorphous carbon. L2011*B5 showed little absorption below the C-edge, indicating that this particle is dominated by carbonaceous material. C-XANES analyses of carbon-rich regions in L2011*B5 are in progress. L2009*F2 showed no obvious carbon-rich areas, indicating the bulk carbon content of this IDP is significantly lower than the other two IDPs in this study and three IDPs previously examined [3] in the STXM. However, C-XANES specta of some spots on L2009*F2 showed an absorption peak near 289 eV, an energy inconsistent with the absorption spectrum of graphitic or amorphous carbon. Thus, the C-XANES analyses of L2011*B5 and L2009*F2 indicate the presence of carbon in a form other than graphite or amorphous carbon. The absorption near 289 eV in each of these samples is indicative of a C-O bond, suggesting an organic phase. The ultra-microtome section of L2009*F2 was subsequently examined by micro-Fourier Transform Infrared (FTIR) spectroscopy at beamline U4IR, and the IR signature of the C-H stretching vibrations in an aliphatic hydrocarbon was detected, confirming the presence of an organic compound in that sample [see results in 4].

These results on L2009*F2 demonstrate that STXM and micro-FTIR can be performed on the same ultra-microtome thin section, using the STXM to map the distribution of carbon in the section, to determine the bulk carbon content, and to identify the graphitic or amorphous elemental carbon, and using the micro-FTIR to determine the types of organic carbon present.

References: 1) Anders, E. Nature, 342, 255-257, 1989. 2) Thomas, K. L. et al., Geochim. Cosmochim. Acta., 57, 1551-1566, 1993. 3) Bajt, S. et al., Lunar Planet. Sci. XXVII, 57-58, 1996. 4) Flynn, G. J., et al., "Identification of Organic Carbon in Interplanetary Dust by FTIR," U4IR Activity Repport, this volume.

Determination of Partial Miscibility in Phase Separated PBT-PC Blends by STXM	X1A

Y. Gao, T. Banach, V. Watkins, G. Hutchins (GE), D. Pierson, A.P. Smith, H. Ade (NCSU)

In partially miscible, phase-separated polymer blends, the amount of miscibility is one of the most important parameters that determine physical and thermal properties. In completely amorphous blends, such miscibilities may be obtained according to the Flory-Fox equation by measuring the glass transition temperatures of the blend. However, this equation does not pertain to blends of semi-crystalline and amorphous materials. Due to solubility differences, it has also not been possible to directly measure it from a single domain. Recently, we have used the X1A SUNY Stony Brook Scanning Transmission X-ray Microscope (STXM) to investigate the partial miscibility in a phase-separated polymer blend consisting of 45C K edge. This particular specimen has lamellar shaped domains with adequate domain size for both PBT and PC rich regions. Since PBT and PC each have their own characteristic spectroscopic features in the vicinity of the C K edge, the observed spectra can be deconvoluted by using the Target Factor Analysis (TFA) method to obtain the percentage of each component given the reference spectra from the pure PBT and PC specimens. We have measured three PBT rich and three PC rich regions using a focused X-ray beam, and then defocused the beam to obtain an average composition from a much larger area. The table below summarizes the weight percentages obtained by TFA analysis.

It appears from the data that PC has a higher degree of miscibility in PBT: two out of three PBT rich regions contain more than 1/3 of PC, while in all the three PC rich region, the amount of PBT is about 1/4. When the defocused X-ray beam was used, the measured composition was 48/52, being very close to the actual composition. It is necessary to mention that these results are still preliminary and the calculated values may contain systematic errors due to the complication from a halo around the incident X-ray micro beam, and variation in specimen thickness. We estimate that the spectral contamination due to the halo is at least several per cent. All these along with the instrumental stability of the X1A-STXM, will be improved in the future experiment.

Sample descriptions	Primary component	weight % of PC	weight % of PBT
45/55 - region 1	PBT	36	64
45/55 - region 2	PC	80	20
45/55 - region 3	PC	76	24
45/55 - region 4	PBT	44	56
45/55 - region 5	PBT	17	83
45/55 - region 6	PC	76	24
45/55 - large area	-	52	48

Figure 1.

X-ray Microscopy of Frozen Hydrated Specimen	X1A

J. Maser, S. Wang, A. Osanna, S. Spector, C. Jacobsen, J. Kirz (SUNY at Stony Brook)

The cryo Scanning Transmission X–ray Microscope (cryo–STXM) at the X1A beamline is capable of imaging frozen hydrated specimens of several micrometer thickness at a temperature of 120 K and below [1]. It allows us to image and analyze biological objects such as cells at sub–100 nm spatial resolution without the need for chemical fixation, staining or sectioning. Spectromicroscopy and microspectroscopy can be performed at a spectral resolution of up to $\lambda/\Delta\lambda = 4000$. The cryo-STXM is designed as a vacuum system. This allows us to make use of the full spectral range of x–rays provided by the X1A beamline.

To demonstrate the increased structural stability of radiation sensitive specimens at low temperatures, we exposed several areas in the nucleus of a 3T3 fibroblast cell to radiation doses in excess of 10^9 Gy. Fig.1 shows the frozen hydrated specimen *after* exposure. Even though ionization and damage from secondary electrons has presumably caused the breakage of a significant number of chemical bonds in the irradiated areas and created radicals, the matrix of frozen water preserves the structural integrity of the cold specimen, and no structural damage is manifest. Fig.2 shows an image of the nucleus after the specimen was slowly warmed in the vacuum chamber to room temperature. Massive mass loss in the areas which have sustained large radiation doses leads to the formation of micrometer–sized holes in the specimen. Less severe mass loss and other artifacts from freeze–drying can be seen in the other areas of the specimen.

We have recently installed a rotary stage to enable tilting of the specimen around an axis orthogonal to the x–ray beam, and started tomographic experiments. We have also embarked upon microspectroscopy of frozen hydrated biological specimens. All images shown have been taken at a wavelength of 2.4 nm using zone plates with an outermost zone width of 60 nm (Rayleigh resolution of 73 nm).

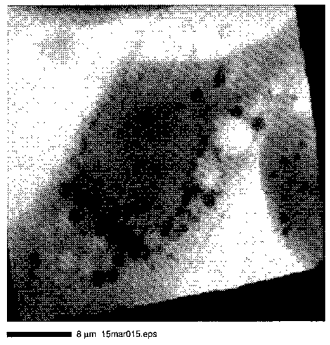

Figure 1. Image of an unfixed, frozen hydrated 3T3 fibroblast cell at a temperature of 114 K. Some spots in the nucleus were exposed to a radiation dose in excess of 10^9 Gy.

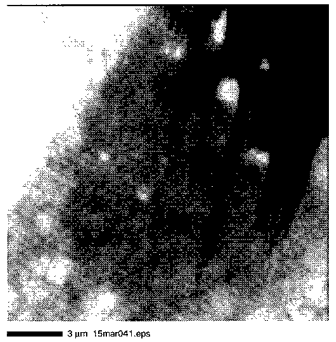

Figure 2. Image of the central area of the fibroblast from fig.1 after warming the specimen. Several holes have formed in the areas which were especially heavily irradiated before.

Lanthanide Polychelate Probes for Scanning X-Ray Microscopy * | X1A

M.M. Moronne (Lawrence Berkeley National Laboratory)

To take advantage of this high resolution now available from x-ray microscopes for biological studies, we have developed multi-residue polychelate lanthanide compounds that are sufficiently bright and radiation stable to be the basis of a family of x-ray excitable biological probes. Luminescent lanthanide compounds can have very large Stokes shifts (more than 100 nm). As a result, their quantum yields are not significantly depressed when assembled into multimeric structures compared with single fluor molecules. This makes it practical to increase probe brightness by building polychelates capable of binding a large number of lanthanides(greater than 80) in a single probe molecule. However, because of their size and surface electrostatic properties, polychelate probes are prone to non-specific background staining. In the past year we have been able to overcome initial problem by the development of biotinylated lanthanide- polychelates (bioLPC) that are virtually free of non-specific labeling artifacts. This approach relies on the tetravalency of avidin/streptavidin. For example, to label actin stress fibers as in Fig. 1, cells are treated with phalloidin-biotin as a primary for filamentous actin, followed by streptavidin, which has four biotin binding site. Only one or two sites is likely to be occupied when bound to phalloidin-biotin leaving two to three available for binding to bioLPC. In this way, as many as 240 lanthanide atoms can be attached to a single molecular target, greatly increasing probe brightness under x-rays. Using a rhodamine tracer on the polychelate probe and fluorescence light microscopy, we have demonstrated that bioLPC is capable of labeling with a specificity fully equivalent to conventional avidin-biotin probes for actin microfilaments, microtubules, nuclear splicing factor, FISH DNA probes, and other antigens. In April'97, we achieved the highest resolution x-ray excited luminescent images to date using bioLPC to label actin filaments in 3T3 mouse fibroblasts (Fig.1). We believe that this data establishes the effectiveness of lanthanide polychelate probes for scanning x-ray microscopy, and fully expect to achieve a five fold improvement in resolution over visible light microscopic methods.

* Data taken using the X1A STXM developed by the group of Kirz and Jacobsen with support from the Off.of Biological and Env. Res., USDOE under contracts DE-FG02-89ER60858, and the NSF under grant DBI-9605045. Probe development supported under DOE contract DE-AC03-76SF00098.

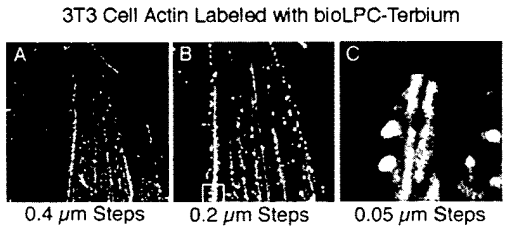

Figure 1. Lanthanide labeled actin filaments viewed at different resolutions. C shows expanded region highlighted by the white square in B.

Soft X-Ray Spectromicroscopy Studies on Aqueous Clay- and Soil Suspensions * | X1A

U. Neuhäusler (SUNY Stony Brook, U. Göttingen), C. Jacobsen (SUNY Stony Brook), D. Schulze (Purdue U.), D. Stott (USDA), S. Abend (U. Kiel)

In clay and soil science, structural properties as well as surface reactions and many other processes of interest depend on water, solutions or other liquids surrounding the actual sample.

In order to start different studies on these fields, a wet specimen cell matched to the special requirements of the X1-A Scanning Transmission X-Ray Microscope has been designed. A section overview of this wet cell is shown in figure 1.

The wet cell consists of two 100 nm thick silicon nitride windows that are pulled together by surface tension forces and form a suspension/solution layer of a few micron thickness, which allows detection of soft x-rays in transmission.

First results show the capability of the cell to be used to take XANES spectra and images from liquid and aqueous samples with sub 100 nm spatial resolution (Figures 2 and 3).

* This work was supported by a fellowship for Ph.D.-research studies (UN) from German Academic Exchange Service (DAAD) and by the Office of Biological and Environmental Research, U.S. DoE under contract DE-FG02-89ER60858.

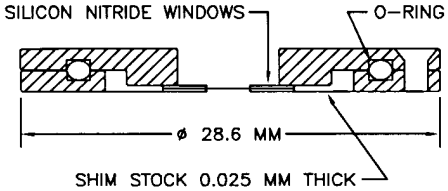

Figure 1. Section overview of the wet specimen chamber.

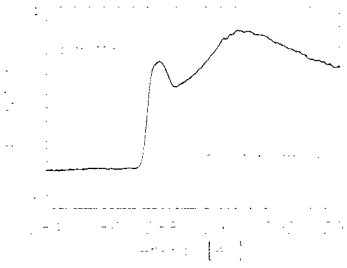

Figure 2. C-XANES spectra of paraffin oil (bulk sample) and hydrated polyacrylamide macromolecules.

Figure 3. A fully hydrated aggregate consisting of 2-0.2 μm kaolinite clay particles and polyacrylamide (PAM), an organic flocculant, suspended in an aqueous solution of 0.01M $CaCl_2$. (The kaolinite is the Clay Minerals Society source clay KGa-1. Clay content is 10 mg/mL. PAM content is 0.005 mg/mL.).

Soft X-ray Spectroscopy of Amino Acids and Peptides * | X1A

A. Osanna, C. Jacobsen, and J. Kirz (SUNY at Stony Brook)

Using the Stony Brook x-ray microscopes, we have continued investigating XANES spectra of amino acids and peptides at the carbon edge [1]. In addition, we have begun to acquire XANES spectra at the oxygen edge. Carbon edge spectroscopy was performed in the ambient environment microscope (STXM); the recently commisioned cryogenic x-ray microscope (CryoSTXM), which operates in high vacuum [2], allowed us to obtain oxygen edge spectra for the first time. For both microscopes, the amino acids were prepared as dry films on SiN windows.

At the oxygen edge, the amino acid spectra show a strong π^* resonance due to the C-O double bond in the carboxyl. The oxygen edge spectrum of Glutamic Acid at 0.2 eV resolution is shown in Fig. 1.

At the carbon edge, we have continued our efforts towards a complete database of the 20 amino acids that make up mammalian proteins. In addition, we have started investigating collagen that consist only of a small number of different amino acids.

[1] J. Boese *et al.*, J. El. Spect. Rel. Phen. **85** (1997)

[2] J. Maser *et al.*, in: X-Ray Microscopy and Spectromicroscopy. Springer Series in Optical Scienes (1997)

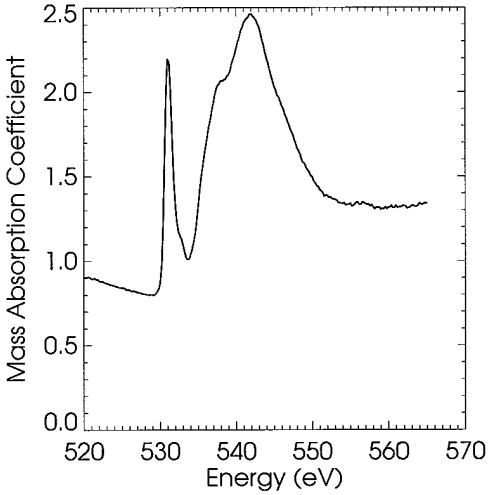

Figure 1. Spectrum of Glutamic Acid at the oxygen edge. The peak at 531 eV is due to the C-O double bond in the carboxyl group.

* Support from the Department of Energy under contract DE-FG02-89ER60858

Soft X-ray Spectroscopy of Frozen Hydrated Specimens * | X1A

A. Osanna, C. Jacobsen, J. Kirz, J. Maser and S. Wang (SUNY at Stony Brook), R. Balhorn (LLNL)

We have begun to use the X-1A cryogenic scanning transmission x-ray microscope to investigate radiation-sensitive specimens in their natural (wet) environment. [1]. We have started imaging human sperm at energies around the oxygen edge to extend our abilities to identify defects in sperm chromatin structure that may be responsible for certain types of male infertility. XANES imaging at the carbon edge has been used to map the DNA and the protein distribution in mammalian sperm heads [2]; however, due to the high dry mass of human sperm heads, it has not been possible so far to determine the DNA and protein distribution for human sperm. DNA is packed inside the nuclei of mammalian sperm by two small proteins, protamine 1 and protamine 2. The protamine 2 content of sperm appears to vary widely among different species of mammals. An increasing number of studies have correlated alterations in the relative proportions of protamine 1 and 2 in the sperm of humans with male infertility. [2]

At the oxygen edge, the increased absorption length of soft x rays compared to the carbon edge has allowed us to image these specimens for the first time. The specimens were prepared in frozen hydrated form by plunge-freezing a suspension of sperm cells on an electron microscope grid. We have begun acquiring protein and DNA spectra at the oxygen edge. In addition, in order to determine if a specimen is embedded in truly vitrified ice, or if the water crystallized, we have started to investigate high-resolution spectra of amorphous and de-vitrified ice.

[1] J. Maser *et al.*, this volume and in: X-Ray Microscopy and Spectromicroscopy. Springer Series in Optical Sciences (1997)

[2] X. Zhang *et al.*, J. Struct. Biol. **116** (1996) 335-344

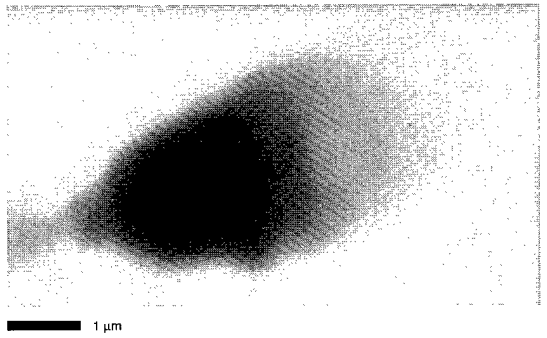

Figure 1. Image of a frozen hydrated human sperm head at 530 eV.

* Support from the Department of Energy under contract DE-FG02-89ER60858

Morphology of Rubber Toughened PMMA Blends with X-ray Microscopy *	X1A

A. P. Smith, H. Ade, R. J. Spontak and C. C. Koch (NCSU)

Toughening of plastics by inclusions of small amounts of rubber has long been recognized as a method to improve the impact properties of brittle polymers. We have begun a study of the rubber toughening of poly(methyl methacrylate) (PMMA) with ethylene-*alt*-propylene rubber (EPR) with the non-equilibrium processing route of mechanical alloying. Determination of the blend morphology for this system with conventional means is prevented due to the absence of a preferential stain. We have therefore employed the Stony Brook Scanning Transmission X-ray Microscope (STXM) and its inherent sensitivity to chemical functionality to ascertain the blend morphology of this system. Three blends were prepared by milling 25/75 w/w EPR/PMMA polymer mixtures at cryogenic temperatures (-180 °C) for 1, 2, and 5 hours respectively. The powders were subsequently melt pressed at 200 °C and 20 MPa for five min. and then quenched. The samples were then cryomicrotomed to form thin sections. Figure 1 contains x-ray micrographs of the blends milled for a) 5 hrs, b) 2 hrs, and c) 1 hr respectively. These micrographs were acquired at a photon energy of 287.6 eV where the EPR appears dark. These micrographs show that fine-scale dispersion of the EPR within the PMMA has been achieved with EPR domain sizes of 3 μm and smaller. The morphology observed in the 1 and 2 hr milling is about the same while the 5 hr milling has started to break the larger EPR domains into smaller pieces. This demonstrates that with increased milling time, the EPR domain size will be smaller and raises the potential of forming submicron particles with increased milling time. Further work will include extending the mechanical alloying time, varying the post alloying processing and correlating the observed morphology to the physical properties of each blend.

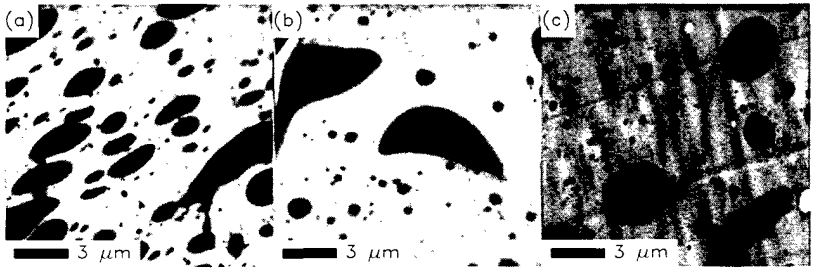

Figure 1. X-ray micrographs of 25/75 w/w EPR/PMMA blends mechanically alloyed for a) 5, b) 2, and c) 1 hours respectively acquired at 287.6 eV where the EPR appears dark.

* Supported by NSF Young Investigator Award (DMR-9458060).

Morphological Characterization of Mechanically Alloyed PET/Vectra Blends with X-ray Microscopy *	X1A

A. P. Smith, C. Bai, H. Ade, R. J. Spontak, C. M. Balik, C. C. Koch (NCSU), and C. Saw (HCC)

We have used high-energy ball milling to form non-equilibrium blends of the highly immiscible polymers poly(ethylene terephthalate) (PET) and Vectra (75/25 mol% oxybenzoate/2,6 oxynaphthoate). Characterization of the blend morphology for this system by conventional TEM is severely hindered by the lack of a preferential stain. Therefore, we have employed the sensitivity to chemical functionality inherent to the Stony Brook Scanning Transmission X-ray Microscope (STXM) to determine the morphology of three separate blends of these polymers. Figure 1 shows micrographs obtained from a)75/25, b)90/10, and c)99/1 w/w PET/Vectra mixtures acquired at a photon energy of 286.7 eV where the Vectra appears dark. These blends were each cryo-milled (-150 °C) for six hours and subsequently melt extruded at 285 °C. The micrographs in Figure 1 show that the Vectra forms dispersions within a PET matrix ranging in size from 0.1 μm to 20 μm, an indication of fine-scale mixing. In addition, the Vectra dispersions possess an internal structure which is potentially due to a) thickness variations, b) chemical variations (PET within the Vectra dispersions), and c) orientation of the liquid crystalline Vectra. Since the STXM is sensitive to all of thickness, chemistry, and orientation, it can be utilized to deconvolve these effects. A series of images of the 90/10 blend acquired at different photon energies show that no PET appears to be within the Vectra dispersions while images acquired with the electric polarization vector rotated by 90° demonstrate that there is a small orientation component to the internal structure. However, most of the internal structure is due to the thickness variation within the sample. These results constitute the first successful morphological characterization of a system containing Vectra.

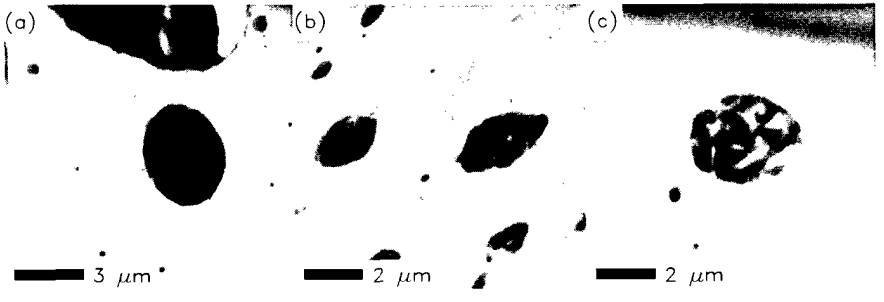

Figure 1. X-ray micrographs of a)75/25, b)90/10, and c)99/1 w/w PET/Vectra blends acquired at 286.7 eV where the Vectra appears dark. The small Vectra dispersions indicate fine-scale mixing has been achieved.

* Supported by NSF Young Investigator Award (DMR-9458060).

NEXAFS Spectromicroscopy of Dispersed Phases in Polyurethane Polymers *	X1A

S.G. Urquhart, H. Ade, A.P. Smith (NCSU), E.G. Rightor (DOW Chemical), and A.P. Hitchcock (McMaster)

We utilize the chemical sensitivity and spatial resolution of the Stoney Brook X1A Scanning Transmission X-ray Microscope (STXM) to chemically analyze sub-micron phase segregation in polyurethane polymers. An understanding of the connections between polymer formulation, the chemical nature of the segregated phases, and the physical properties of the resulting polymer is important in the development of improved polyurethane materials. Chemically sensitive x-ray absorption contrast mechanisms are used to image polymer phase segregation, and Near Edge X-ray Absorption Fine Structure (NEXAFS) spectroscopy are used to chemically characterize sub-micron regions that are inaccessible by other micro-analytical techniques.

We have used x-ray spectroscopy and x-ray microscopy in the STXM microscope to investigate the chemical character of styrene acrylonitrile (SAN) and polyurethane (PIPA) precipitates in a polyether-rich polyurethane matrix. In Figure 1, the Near Edge X-ray Absorption Spectra (NEXAFS) of SAN and the polymer matrix are presented, together with STXM images recorded at specific x-ray energies. In image "A" (recorded at 285.1 eV), both SAN and PIPA precipitates are observed. This x-ray energy corresponds to C 1s $\rightarrow \pi^*_{C=C}$ electronic transitions in phenyl groups, which are in high concentration in the PIPA and SAN precipitates. In image "B" (recorded at 287.1 eV), SAN precipitates are exclusively observed. This x-ray energy corresponds to an acrylonitrile-specific electronic transition (C 1s $\rightarrow \pi^*_{C\equiv N}$). It is also interesting to observe the presence of a "halo" around the SAN precipitates in image "C" (recorded at 289.0 eV), indicating the presence of a chemically distinct region at the precipitate-matrix interface.

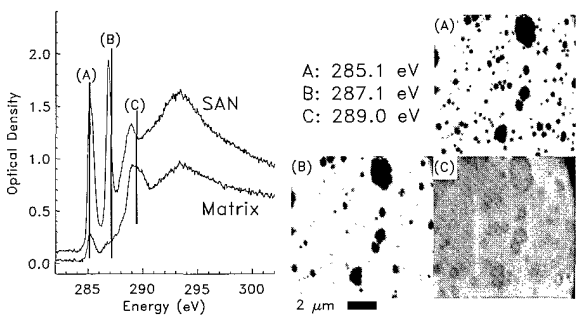

Figure 1. (left) Near Edge X-ray Absorption Spectra of styrene acrylonitrile (SAN) the polyyurethane matrix. Vertical lines indicate image energies. eV), precipitates with high phenyl-group only SAN interface.

* Work supported by NSF Young Investigator Award DMR-9458060

Nano-Tomography with X1A Cryo Scanning X-ray Microscope	X1A

Y. Wang, C. Jacobsen, A. Kalukin, J. Kirz, J. Maser, A. Osanna (SUNY at Stony Brook)

The Cryo Scanning Transmission X-ray Microscope (cryoSTXM) is entering operation at X1A beamline of NSLS[1]. It has produced images of test-pattern and frozen hydrated biological samples at lateral spatial resolution of 70 nm and spectral resolution of $\lambda/\Delta\lambda = 4000$ during commissioning experiments. By using a TEM-type cryo specimen holder, an unfixed biological specimen (3T3 fibroblast cells used for demonstration) is maintained below $-165°$C during imaging, so that it is able to withstand radiation dosage up to about 10^9Gy before structural damage is observable. This level of radiation tolerance allows the acquisition of multiple images with a single biological object for tomography or XANES imaging[2].

The airlock of the cryo specimen holder is mounted on a rotary stage to allow single-axis tilting of the specimen within a $\pm 50°$ angular range. The figure below shows a frozen hydrated 3T3 cell reconstructed from 8 projections in a $\pm 20°$ angular range with algebraic reconstruction technique (ART). Other reconstruction and restoration technique are being explored to improve the image quality. This technique has also been combined with spectroscopy to study chemical composition of a sample in three dimensions. Besides the applications in biology, we have performed experiments to study the possibility of examining defects in materials typically used in semiconductor industries with cryoSTXM. The figure below shows a tear in a copper film.

[1] J. Maser, *et. al.*, this volume

[2] X. Zhang, *et. al.*, Mapping and measuring DNA to protein ratios in mammalian sperm head by XANES imaging. *Journal of Structural Biology*, 116:335-344, 1996.

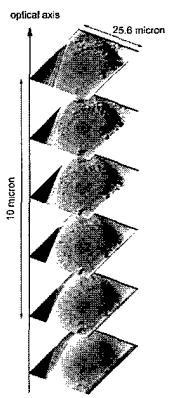

Figure 1. Reconstruction of a frozen hydrated 3T3 fibroblast cell from 8 projections within $\pm 20°$ angular range, using ART.

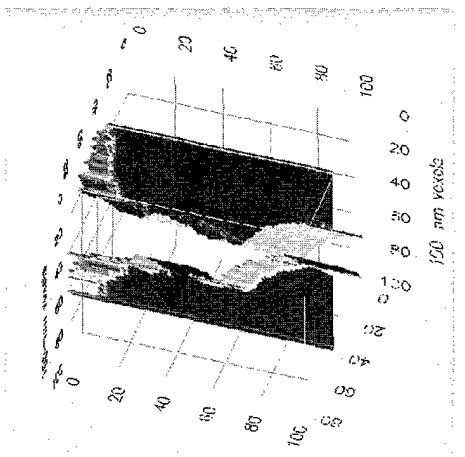

Figure 2. A tear in a 100 nm thick copper film reconstructed from 5 projections in $\pm 20°$ angular range, using a laminography reconstruction technique.

Quantitative Compositional Mapping of Dewetting and Spinodally Decomposing Polymer Films * — X1A

D.A. Winesett, H. Ade, A.P. Smith, (NCSU) M.Rafailovich, S. Sokolov, S. Qu (SUNY at Stony Brook), D. Slep (Hilord Chemical)

We are examining the spinodal decomposition and dewetting in thin polymer films with Near Edge X-Ray Absorption Fine Structure (NEXAFS) imaging utilizing the Stony Brook Scanning Transmission X-ray Microscope (STXM). Our studies of model systems will provide insight into many thin film applications such as dielectric coatings and colloidal paint systems. The primary advantage of NEXAFS imaging is its capability of quantitative compositional analysis. We acquire a series of images of the same sample area at photon energies that are characteristic of each polymer and extract thickness maps of constituent components that are present. This allows for the determination of the overall thickness (analogous to topography with Atomic Force Microscopy) as well as projected thickness mapping of each polymer, results not obtainable by AFM or other techniques. From this, we might be able to determine the three dimensional structure of all components in the resulting systems, and in turn determine important parameters such as interfacial energies.

As an illustration of the present work, we show compositional thickness maps (lighter areas are thicker) obtained from a 1460 nm thick, 50/50 w/w blend of poly(methyl methacrylate) (PMMA) and Polystyrene (PS). Fig. 1 and 2 are for a sample annealed for 10 min and 1 week, respectively. Thickness maps (a), (b), and (c) are the PMMA, PS and total thickness maps, respectively. Annealing causes these two immiscible polymers to phase separate. Initially, we observe smaller domains of mixed PS and PMMA composition, but with time they form larger, separate regions of relatively uniform and pure composition. The images of the sample annealed for one week indicate a thin layer of pure PMMA (Fig. 2a) throughout the sample which grows thicker in areas surrounding the smooth spheroids of PS (Fig. 2b). This configuration is indicative and qualitatively consistent with the encapsulation of PS inside a continuum of PMMA. Overall thickness maps (formed by summing the PS and PMMA maps) are consistent with AFM data acquired from the same samples. We can study the dynamics of decomposition by imaging samples annealed for various lengths of time. We have used similar procedures to study the dynamics and composition profiles of dewetting bilayers of PS and brominated PS.

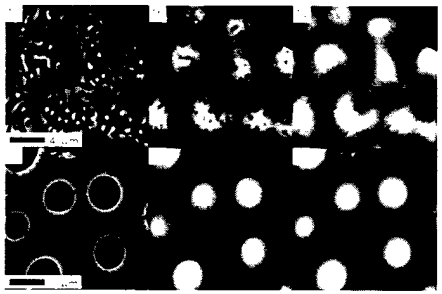

* Work supported by NSF Young Investigator Award (DMR-9458060)

Soft X-Ray Emission and Absorption of $Al_xGa_{1-x}N$ — X1B

L.-C. Duda, C.B. Stagarescu, J. Downes, and K.E. Smith (Boston University)

We performed soft x-ray emission (SXE) and absorption studies at the N-edges of $Al_xGa_{1-x}N$ for various concentrations, x, ranging from 0 to 1. Soft x-ray emission and absorption spectroscopy provide knowledge about the occupied and unoccupied partial density of states, repectively. In the present study we focused on the N 2p states which form an important part of the nitride's valence and conduction band.

The members of the semiconducting nitride alloy family $Al_xGa_{1-x}N$ are particularly interesting to study because they can be epitaxially grown at any concentration x which is important for applications such as blue lasers. The energy gap varies between about 3.5 eV for GaN and 6.2 eV for AlN. The behaviour of the energy gap for the *alloys* is still a matter of debate in current literature. We introduce SXE spectroscopy as a new technique to address this question. Figure 1a shows how the valence band (VB) develops as the concentration is varied from x=0 to x=1. Basically, the bottom of the valence band remains unchanged in energy but the top of the valence band becomes increasingly narrower for increasing x and therefore the VB maximum is found at lower energies (see arrows in Fig. 1a).

In contrast, we find no change in the onset of the N K-absorption edge (Fig. 1b) as the concentration is varied. This surprising result is still under investigation but may have its roots in the fact that the core hole in the final state distorts the energy positions.

SXE spectroscopy can be used to study hybridization phenomena that are obscured in less selective spectroscopies such as VB photoemission. Fig. 1c shows (on a binding energy scale) that N 2p states in pure GaN extend far below the top of the VB and "resonate" with Ga 3d states at about 19eV below the top of the VB maximum. For AlN, however, the situation is different because there are no d-states at this energy and thus N 2p-states do not occur at such high binding energies.

Finally, a comparison of the theoretical partial DOS of pure AlN and experiment shows good agreement (Fig. 1d). For comparison the SXE spectrum of pure GaN is shown (dashed line) illustrating the difference of the gap sizes.

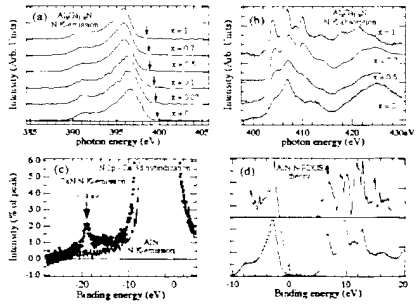

Figure 1. (a) Top left: (b) top right: (c) bottom left; (d) bottom right.

Shape Resonances in the Series C_2H_2, C_2H_4 and C_2H_6 * | X1B

B. Kempgens, H. M. Köppe, A. Kivimäki, M. Neeb, K. Maier, U. Hergenhahn and A. M. Bradshaw (Fritz-Haber-Institut, Berlin)

Local maxima in the photoabsorption spectra of small molecules just above threshold are commonly identified as shape resonances. Their occurrence is explained either by an amplification of the photoionization process via a virtual antibonding orbital, or by scattering of the outgoing photoelectron on the molecular core. In the latter picture, the uptake of angular momentum in the scattering process creates a potential barrier thus trapping the continuum electron. A semi-empirical linear correspondence between bond length and the shape resonance position in the respective near-edge absorption spectrum has been proposed ('bond lengths with a ruler').

We have measured low kinetic energy photoelectron spectra of gaeous C_2H_2, C_2H_4 and C_2H_6 above the C 1s threshold. By integration of the respective peaks we were able to distinguish contributions from the C $1s^{-1}$ single hole state and satellite channels in the photoionisation cross section. Satellite lines in photoionization are due to a simultaneous valence excitation occuring upon removal of the core electron, and are separated from the main line at a lower kinetic energy. Our results show that satellite channels play a much stronger role in above-threshold cross-section enhancement than contributions from the C $1s^{-1}$ single hole state [1]. In C_2H_2 and C_2H_4 this enhancement takes place at photon energies formerly identified as shape-resonance positions from photoabsorption curves. Our results show that care must be taken in the interpretation of photoabsorption measurements, as they provide only indirect information on the underlying processes. Further, we call into question whether there is a simple correlation between shape resonance position and bond length even in polyatomic molecules.

[1] B. Kempgens, H.M. Köppe, A. Kivimäki, M. Neeb, K. Maier, U. Hergenhahn and A.M. Bradshaw, Phys. Rev. Lett. 97 (1997) 35.

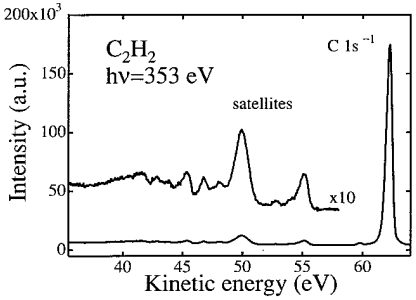

Figure 1. Photoelectron spectrum of ethyne showing the C 1s main line and various satellite lines.

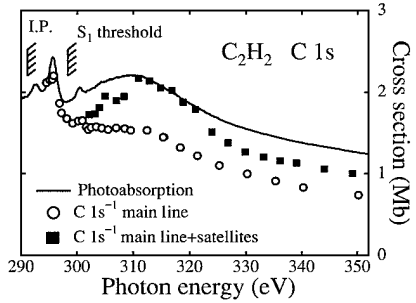

Figure 2. The photoabsorption cross section of ethyne above the C 1s photoionization threshold.

* This work has been supported in part by the Deutsche Forschungsgemeinschaft

Vibrational excitation in C 1s and O 1s photoionization of CO * | X1B

B. Kempgens, K. Maier, A. Kivimäki, H. M. Köppe, M. Neeb, M. N. Piancastelli, U. Hergenhahn and A. M. Bradshaw (Fritz-Haber-Institut, Berlin)

The high resolution of the X1B beamline has enabled us to measure the vibrational fine structure on the C 1s and N 1s level photoelectron lines of several small molecules, e.g. [1,2]. Due to a recent change of grating the O 1s level has now also become accessible, e.g. [3]. Here we report new measurements of both the C 1s and O 1s main lines in the photoelectron spectrum of CO. From Figure 1 it is clear that the vibrational spacing of the O $1s^{-1}$ state is significantly lower than in the C $1s^{-1}$ state: 226(7) meV compared to 300(4) meV. This can be explained by the fact that the 1σ (O 1s) orbital of CO has a slight bonding character, whereas the 2σ (C 1s) orbital is slightly antibonding. Compared to the ground-state equilibrium C-O distance of 1.128 Å, we extract from the analysis of the Franck-Condon factors bondlengths of 1.079(2) Å and 1.167(4) Å for the C 1s and O 1s core-ionized states, respectively.

[1] H. M. Köppe, A. L. D. Kilcoyne, J. Feldhaus and A. M. Bradshaw, J. Electron Spectrosc. Relat. Phen. 75, 97 (1995).

[2] B. Kempgens, A. Kivimäki, M. Neeb, H. M. Köppe, A. M. Bradshaw and J. Feldhaus, J. Phys B: At. Mol. Opt. Phys. 29, 6389 (1996).

[3] A. Kivimäki, B. Kempgens, K. Maier, H. M. Köppe, M. N. Piancastelli, M. Neeb and A. M. Bradshaw, Phys. Rev. Lett. 79, 998 (1997).

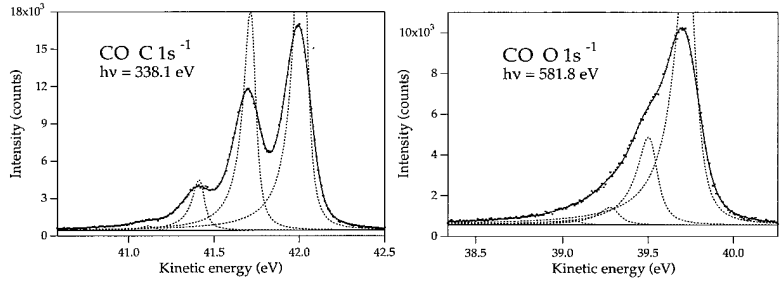

Figure 1. Photoelectron spectra showing the vibrationally resolved CO C 1s (left) and CO O 1s (right) main lines.

* This work has been supported in part by the Deutsche Forschungsgemeinschaft

Energy Dependence of the Multiplet Intensity Ratio in K-level Photoionization of O_2 * — X1B

K.Maier, U.Hergenhahn, B. Kempgens, A.Rüdel, A.M.Bradshaw (Fritz-Haber-Institut, Berlin), and A.Kivimäki (U. of Oulu)

Compared with the wealth of information on core-level photoionization of closed-shell molecules, our knowledge of open-shell molecules is much less profound. As a general feature, the 1s photoelectron spectra of these molecules will show two main lines split by the exchange interaction. Naively, one would expect their branching ratio to be determined by the spin multiplicity. Investigations with an X-ray line source, however, have not shown this expected behaviour in the high energy limit [1].

On X1B we have, therefore, investigated the energy dependence of the K-shell ionization of O_2. This molecule is paramagnetic due to its $^3\Sigma_g$ ground state; on removal of a core electron O ($1s^{-1}$) $^2\Sigma$ and $^4\Sigma$ ionic states can be created (Fig. 1). The two lines are separated by 1.11 eV. The $^4\Sigma/^2\Sigma$ intensity branching ratio would be expected to be two from the ratio of the multiplicities, but Fig. 2 shows that it increases from a minimum at 552 eV steadily towards an asymptotic value of 2.48 at a photon energy of 750 eV which is in good agreement with the value of 2.47 found by Bagus et al [1]. Theoretical investigations of this branching ratio [1] attribute the deviations from two to spin-dependent population differences in the valence shell of the ion. Even for the asymptotic value, however, no quantitative agreement was reached.

[1] P.S. Bagus, M. Schrenk, D.W. Davis and D.A. Shirley, Phys. Rev. A 9 (1974) 1090.

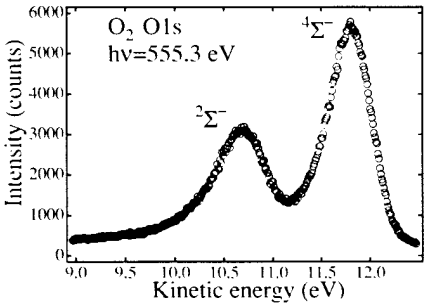

Figure 1. Core-level photoelectron spectrum of O_2.

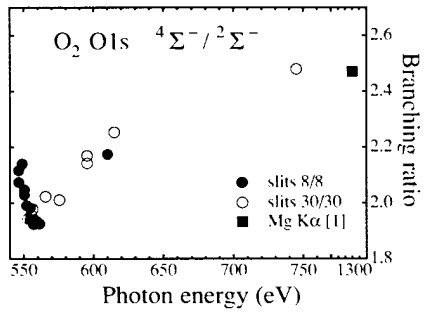

Figure 2. Photon energy dependence of the branching ratio into the $^4\Sigma$ and $^2\Sigma$ O_2^+ ionic states.

* This work has been supported in part by the Deutsche Forschungsgemeinschaft

Adsorption and Reaction of NO on Pt / CeO_2(001) at Low Temperatures * — X1B

D. R. Mullins, D. R. Huntley and S. H. Overbury (ORNL)

Highly crystalline 50 - 100 nm films of CeO_2(001) were prepared *ex situ* by vapor deposition on a rolled Ni foil. This method produced films with small grains having an (001) polar orientation but which were azimuthally disordered. The combination of a thin film thickness and a conductive substrate resulted in oxide samples that showed no evidence of sample charging even when cooled to 100 K. This enabled us to study the adsorption and reaction of NO on CeO_2 at 100 K by XPS and XAS. Previous studies were limited to room temperature and above due to sample charging. The current results also enabled us to assign the binding energies more accurately.

Fig. 1 shows the N 1s spectra from NO adsorbed on sputtered CeO_2(001) at 100 K and 300 K. Six different N 1s signal can be identified. In the 100 K spectrum, the two highest binding energy peaks are associated with N_2O. The highest binding energy peak is assigned to the central N atom and the peak at 404.5 eV is assigned to the terminal N. The presence of N_2O was also indicated by the N k-edge XAS spectra. The large peak 402.5 eV is assigned to NO. When NO is adsorbed at 300 K, three additional peaks are observed and the N_2O peaks disappear. The lowest binding energy peak at 396 eV is assigned to a nitride, N^-, species, while the two other peaks are assigned to atomic N in different states. Only the atomic N peaks persist when the sample is annealed to 900 K.

The adsorption of NO on Pt / CeO_2(001) is similar to what was observed on Rh / CeO_2(001). Deposition of Pt onto a sputtered CeO_2 surface increases the degree of dissociation in subsequently adsorbed NO. When the NO is dosed at 100 K, none of the NO dissociates over Pt on a fully oxidized CeO_2 surface and only partial dissociation occurs upon warming to 300 K. On a sputtered CeO_2 surface, Pt promotes partial dissociation of NO at 100 K and almost total dissociation after warming to 300 K.

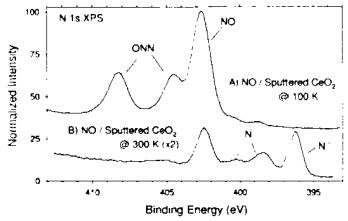

Figure 1. N 1s XPS spectra for NO adsorbed on sputtered CeO_2(001) at A) 100 K and B) 300K.

* Research sponsored by U. S. Department of Energy, Division of Chemical Sciences, Office of Basic Energy Sciences, under contract number DE-AC05-96OR22464 with Oak Ridge National Laboratory, managed by Lockheed Martin Energy Research Corp.

Oxidation of and NO Reactions on Ce Metal Foil * | X1B

D. R. Mullins, D. R. Huntley and S. H. Overbury (ORNL)

The oxidation of polycrystalline Ce metal was studied using O 1s, Ce 4d and valence band photoemission and by O k-edge XAS. Previous studies using single crystal CeO_2 films demonstrated that the CeO_2 was very resistant to chemical reduction by either H_2 or CO in vacuum and could only be reduced by Ar ion sputtering. The aim of the current study was to start with the most reduced form of Ce and then increase the degree of oxidation by exposure to oxygen and then to compare the behavior of the oxidized surface to single crystal CeO_2.

Exposure of Ce metal to 10 - 20 L of O_2 at 300 K was sufficient to oxidize surface Ce from Ce^0 to Ce^{+3}. Exposure to additional oxygen, > 1000 L, resulted in further oxidation from Ce^{+3} to Ce^{+4}. This surface oxide was not thermally stable. Annealing the sample to 600 K resulted in the reduction of the surface Ce back to Ce^{+3}. This is the exact opposite of the behavior of sputtered CeO_2. As shown in the figure, sputtered CeO_2 reoxidizes upon annealing. The behavior of Ce metal and CeO_2 suggests that the oxygen is very mobile and diffuses from regions of high oxygen concentration, i.e. the bulk in CeO_2 and the surface on oxidized Ce foil, to regions of low oxygen concentration.

The adsorption and reaction of NO on oxidized Ce metal was similar to the behavior observed for NO on single crystal CeO_2. If the Ce was highly oxidized to predominantly Ce^{+4}, NO uptake was inhibited and only a small amount of N containing species was observed on the surface by N 1s XPS. Conversely, if the surface Ce was predominantly Ce^{+3}, considerable NO uptake was observed and nearly all of the NO was dissociated. When Rh was deposited on the Ce^{+4} oxide surface, N uptake was observed with some of the NO adsorbing associatively and some dissociating. Addition of Rh to the Ce^{+3} oxide surface promoted additional dissociation of adsorbed NO at 300 K . Heating of Rh deposited on an oxidized Ce foil resulted in the encapsulation of the Rh. Rh deposited on a single crystal CeO_2 film is comparatively stable upon annealing.

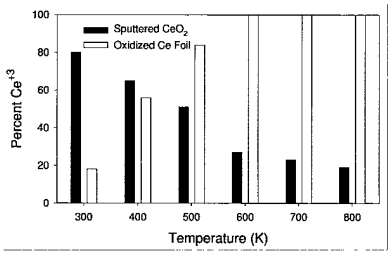

Figure 1. Percent Ce^{+3} vs Temperature for sputtered CeO_2 and oxidized Ce foil. The balance is Ce^{+4}.

* Research sponsored by U. S. Department of Energy, Division of Chemical Sciences, Office of Basic Energy Sciences, under contract number DE-AC05-96OR22464 with Oak Ridge National Laboratory, managed by Lockheed Martin Energy Research Corp.

Non-linear Dispersion in Resonant Auger Decay of Water * | X1B

M.N.Piancastelli, B.Kempgens, K.Maier, U.Hergenhahn, A.Rüdel, A.M.Bradshaw (Fritz-Haber-Institut, Berlin), and A.Kivimäki (U. of Oulu)

The dispersion of a photoelectron line (kinetic energy vs. photon energy) should as a result of energy conservation be a linear relationship with unit slope. For a molecular photoelectron line containing an unresolved vibrational envelope, this statement usually remains valid for the center of gravity. Recently, however, deviations from linear behaviour for the center of gravity-dispersion in resonant X-ray scattering and resonant Auger-decay have been predicted. This means that when the photon energy is tuned over a core-to-bound resonance, there is not necessarily a one-to-one correspondence between the changes in photon energy and in kinetic energy of the center of gravity of some resonantly enhanced photoelectron lines. This can be understood in terms of changes in the vibrational population of the intermediate and final states when different portions of the resonance are excited. Dispersion with a slope larger or smaller than one (the gain in kinetic energy is larger or smaller, respectively, than the gain in photon energy) is possible.

We have measured the resonant Auger decay spectrum of the water molecule at the oxygen K-edge. The first two core-to-bound resonances are usually assigned to O 1s-$4a_1$ and O 1s-$2b_2$ excitations. In the absorption spectrum both resonances are broadened either by an unresolved vibrational fine-structure or by fast dissociation and have widths of about 1.2 eV. The participator decay spectra excited by a photon band much smaller than this resonant linewidth were recorded at different positions along the resonances. (Participator processes involve the electron that has been excited and result in final states with a single hole in the valence shell. The same states are usually populated by direct valence photoionization.) We have determined dispersion relationships for decay into the $3a_1^{-1}$ and $1b_2^{-1}$ final states which demonstrate strong deviations from linear behaviour (Fig. 1). This effect can lead to new insights into the shape of highly excited and ionic molecular potential curves.

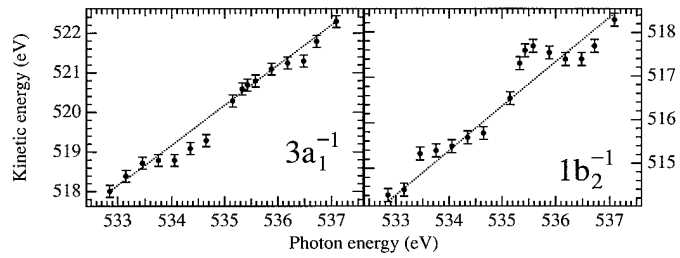

Figure 1. Dispersion curves (center of peak vs. photon energy) for two H_2O participator lines. The straight lines correspond to linear dispersion with unit slope.

* This work has been supported in part by the Deutsche Forschungsgemeinschaft.

Negative Thermal Expansion of Cu(001) — X2A

A. P. Baddorf (ORNL)

State of the art theories, both ab-initio and semi-empirical treatments, are still based on ground state interactions, and do not account for enhanced thermal expansion observed at the surface of a number of metals. Narasimhan and Scheffler have proposed a quasiharmonic model in which entropy contributions to the free energy due to in-plane vibrations lead to large expansions without anharmonicity.[1] A superb test of this quasi-harmonic model can be found in the Cu(001) system, where ion scattering experiments have shown the in-plane vibrational amplitude exceeds the out-of-plane amplitudes, which is rather unusual.[2] We have used XRD to determine the structure of Cu(001) between 300 and 1000 K. At 300 K the results indicate a small contraction in the outermost layer of 1.5% of the bulk spacing. This value is consistent with other surface studies and can be explained by a rearrangement of surface electrons to reduce kinetic energy (Smolouchowski smoothing). As the temperature is increased, the in-plane vibrational amplitudes do dominate. At the same time the outermost interlayer spacing decreases further, reaching a minimum near 800 K (Fig. 1). This thermal contraction is opposite all expectations: current first principles and semi-empirical theories predict an expansion.[1] The quasiharmonic theory exasperates the issue and can only increase the predicted expansion. An additional mechanism, with an inwardly directed force is missing from these theories. One possiblity would be a dynamical application of Smolouchowski smoothing, where the increased surface corrugation induced by excitation of in-plane phonon modes leads to an increased inward relaxation.

[1] S. Narasimhan and M. Scheffler, to be published.
[2] Q. T. Jiang, P. Fenter, and T. Gustafsson, Phys. Rev. B 44, 5773 (1991).

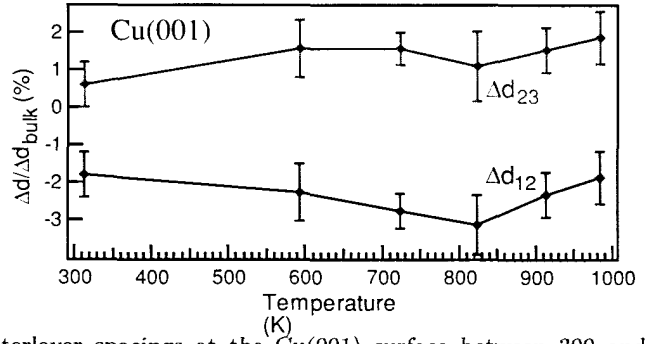

Figure 1. Interlayer spacings at the Cu(001) surface between 300 and 1000 K. Between 300 and 800 K the outermost layer contracts, a result in and semi-empirical theories.

The Periodic Lattice Distortion Accompanying the (3x3) Charge Density Wave Phase of Sn/Ge(111) — X2A

A. P. Baddorf, V. Jahns, Jiandi Zhang (ORNL), J. M. Carpinelli, and E. W. Plummer (ORNL/UT)

Recently we have documented the first clear example of a surface charge density wave (CDW) independent of bulk phenomena.[1,2] Our experimental and theoretical studies of the Ge(111)-(3x3)R30°-M interface, where M is either Pb or Sn, reveal that upon cooling below 255 K (Pb) or 215 K (Sn), the surface reversibly undergoes a symmetry reduction to a (3x3) periodicity. The origin of the CDW in both systems is at present unknown. The structure associated with the PLD provides crucial information for any physical explanation, yet the STM images have shed no light on the nature of the PLD. At NSLS we have utilized XRD to address the issue of the magnitude and character of the lattice distortion that accompanies the CDW. The data indicates that the PLD is confined almost entirely to the Sn and first Ge layer, i.e. no deep reconstruction. Surprisingly (based on STM images) there is little distortion of the Sn atoms induced by the CDW, but three of the nine Ge atoms in the surface plane in the new (3x3) unit cell move laterally 0.22 Åfurther towards the Sn atom that according to STM has an excess of filled states. This result suggests a stronger coupling than indicated by Stumpf's calculations [1], and indicates the origin of the CDW is related to the chemical bond. Specifically, three Ge in the outermost layer give up their nearly ideal sp^3 hybridization, optimized for bonding to the Ge substrate, to better bond to the Sn.

[1] J. M. Carpinelli, H. H. Weitering, E. W. Plummer, and R. Stumpf, Nature 381, 398 (1996). [2] J. M. Carpinelli, H. H. Weitering, M. Bartkowiak, R. Stumpf, and E. W. Plummer, accepted in Phys. Rev. Lett.

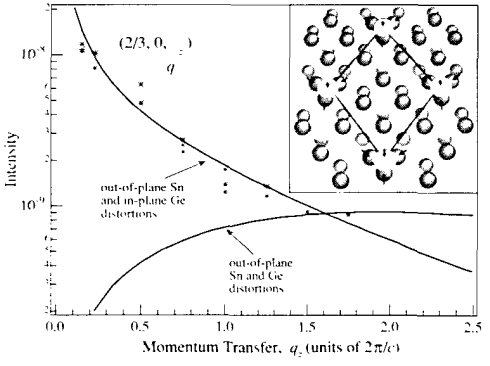

Figure 1. Diffraction from the (3x3) CDW structure with two structural models. The dashed line includes only vertical distortions of Sn and first layer Ge, while the solid line includes lateral displacements of the first layer Ge. A perspective view of the best fit (3x3) structural model is shown in the insert, with arrows indicating displacements relative to the room temperature structure.

In-situ Observation of the Split Diffuse Intensity Maxima of a $Cu_{0.7}Pd_{0.3}$ Single Crystal	X2A

H. Reichert, H. Dosch (U. of Wuppertal, Germany), H.H. Hung, K.S. Liang (SRRC, Taiwan), V. Jahns, and D. Zehner (ORNL)

We have performed measurements of the diffuse x-ray scattering in the disordered phase of a Cu-29.8 at% Pd single crystal exposing a (001) surface. Below the phase transition temperature the crystal exhibits a long-period superstructure producing sattelites along the h,k, and l directions through $L1_2$ superstructure reflections. Crossing the phase transition temperature a subset of the sattelite reflections transforms into diffuse intensity maxima around the positions of $L1_2$ superstructure reflections. Thus, the diffuse maxima exhibit the expected fourfold splitting in the disordered phase, associated with Fermi-surface induced effects. Fig.1 shows the diffuse scattering in the (1+h,0,1+l)-plane together with a textured powder ring from the sample holder.

In this study the total diffuse scattering has been measured in-situ for a set of temperatures along the h and l direction through the (101) position. Fitting the intensity distibution we have determined the temperature dependence of the position of the split diffuse maxima. Fig.2 shows the temperature dependence of the distance between two opposite maxima. Both, the positions of the diffuse maxima and the related temperature dependence differ from predictions of a recent, state of the art first-principles alloy calculation for Cu_3Pd.

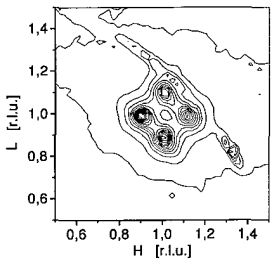

Figure 1. Total diffuse scattering in the (1+h,0,1+l)-plane at $T=T_o+5K$.

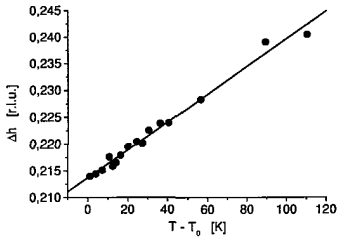

Figure 2. Temperature dependence of the separation distance along the line (h01).

Modeling of Sandstone Permeability from Medial Axis Analysis of 3D Microtomography Images	X2B

D. Coker, W.B Lindquist, W. Zhu,T-F Wong (SUNY), J.H. Dunsmuir(Exxon)

We investigate the scientific usefulness of the medial axis transform (MAT) in characterizing the geometry of the void and grain phases of rock and in predicting bulk flow properties. The MAT is functionally described as the central spine of pixels that remain after a binary object is "burned" inward from the exterior. The pixel value at the spine is the distance to the nearest interface. The MAT preserves the topological and most of the metric information in the image while reducing its dimensionality. The motivation for this work is the accurate description of the network structure of real rock specimens for use in the modeling of fluid transport properties.

We obtained 1024x1024x512 3D microtomographic images at 5μm resolution of six Fontainebleau sandstones with a porosities ranging from 7.5 to 22% and measured permeability. Specimens of Berea sandstone and Danish chalk were also included in the study .Work is ongoing in segmenting the 3D images into pore and grain binary images and computing the MAT.

Computation of Single and Multiple Fluid NMR Relaxation Spectra from Differential Absorption Contrast Microtomography Images	X2B

J.H. Dunsmuir and M. Zhou (Exxon Research and Engineering)

In the petroleum industry an important aspect of modeling fluids in small pores is understanding the signals that arise from instruments that are placed in a drilled borehole to detect hydrocarbons and estimate their producibility. In principle, nuclear magnetic resonance (NMR) tools yield information about fluid saturations, probe local properties of pore fluid geometry and have been used to estimate the pore size distribution of water saturated reservoir rocks near the borehole wall. We have used differential absorption contrast microtomography across the iodine K edge to locally reconstruct in saturated sandstones both the pore geometry and the distribution of two immiscible fluids and apply a simple method for computing the NMR T_2 relaxation spectrum directly from the CT data. Figure 1 shows a 24 micron resolution slice of a large-pore, high porosity sandstone(porosity = 27%, absolute permeability 4.0 Darcy) containing both oil and brine. In this specimen the brine has been labeled with a 5wt% NaI saline solution and the brine distribution is mapped by edge crossing. The specimen has both oil and brine wet pore surfaces and we infer microporous mineral regions by observing regions where segmented iodine and rock overlap.

When diffusion is fast enough to maintain spatial uniformity of the magnetization across a pore, a linear relationship exists between the magnetization relaxation and the surface to volume ratio of the pore space given by $1/\ T_2 = 1/\ T_{2b} + \rho\ S/V$ where T_2 is the observed decay time, T_{2b} is the bulk decay time of fluid, ρ (μm/sec) is the surface relaxivity and S/V is the surface to volume ratio of the pore network. In this work we use a local measurement of the surface to volume ratio around a number of randomly selected points in the tomographically measured pore space to compute the relaxation T_2 at each point. The local measure is taken within a sub-volume of size L^3 selected to lie within the fast diffusion limit $L \ll D_i/\rho$ where D_i is the bulk diffusivity (cm^2/sec) of the fluid i. The algorithm is therefor a simple image processing kernel for the local measurement of S/V.

Tomography specimens are 1cm diameter by 3cm long right cylinders encapsulated in PTFE tubing and are sufficiently large to obtain experimental measurement of the NMR spectrum. NMR spectra acquired at ambient temperature are in good agreement with the computed spectra.

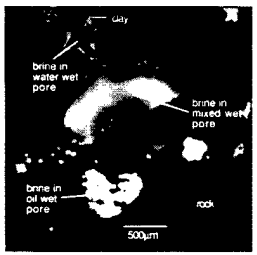

Figure 1. Typical tomographic slice showing fluid and solid distributions.

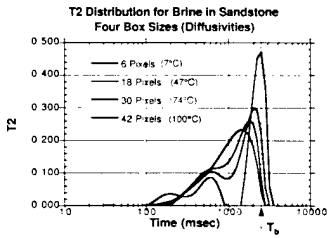

Figure 2. Calculated T_2 magnetization relaxation spectra for the 3D structure at several temperatures (diffusivities)

Structure of the Cyclodextrin/p-nitroaminobiphenyl host/guest Complex *	X3A1

T. Brett (U. of Nebraska), A. Darovsky and P. Coppens (SUNY @ Buffalo)

The "push-pull" compound p-nitroaminobiphenyl (pnab), has a triplet state with a lifetime of 1.4 μs, and is a candidate for the study of photoinduced transient species in crystals, using the time-structure of the synchrotron source. We have synthesized and analyzed crystals of its complex with the host molecule β-cyclodextrin (CD). The measurements were carried out at 13K. The results show that the crystals contain two pnab molecules per CD dimer. The terminal nitro groups of the pnab molecules are in the center of the barrel-shaped host molecules, while the amine groups are at the opening of the host (see Fig. 1). It is of interest that the two pnab molecules have different conformations, the inter-ring torsion angle being $\approx 45^\circ$, and $\approx 38^\circ$ respectively.

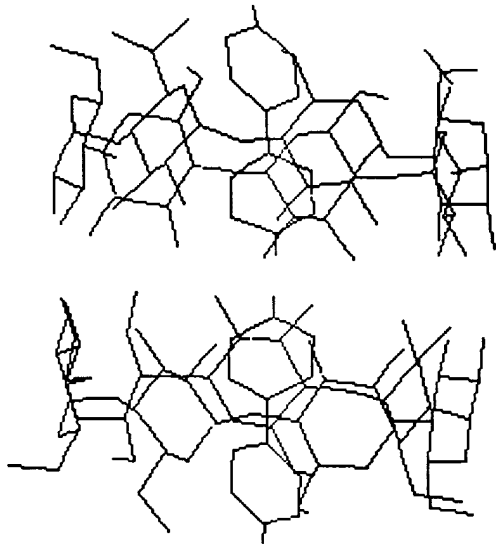

Figure 1. Wire diagram of the structure of p-nitroaminobiphenyl/β-cyclodextrin complex. Hydrogen atoms omitted. The p-nitroaminobiphenyl molecules are vertically aligned. The oxygen atoms of the nitro group, which are in the center of the drawing are not shown.

* This work was supported by DOE Grant No. DEFG0286ER45231 and NSF Grant No. CHE9615586.

Single Crystal Analysis of a New High Pressure Fe-bearing Silicate | X3A1

T. Gasparik, C.L. Cahill, J.B. Parise, (CHiPR, SUNY at Stony Brook)

The synthesis and stability of $Na_2Mg_2Si_2O_7$ (NMS) at high pressures were first reported by Gasparik and Litvin (Eur. J. Mineral. 9, 311, 1997). A crystal chemical investigation of the effects of iron on the properties NMS has been undertaken. Single crystals of Fe-bearing NMS were synthesized at 1550C and 13.5 GPa in a split-sphere anvil apparatus (USSA-2000) from a mix of 1 mol $Na_2Si_2O_5$, 5 mol MgO, 4 mol SiO_2 and 1 mol Fe. Two crystals were screened for data collection at the X3A1 beamline an imaging plate detection system. The first, approximately 100 microns in length, produced split diffraction spots and was subsequently dicounted as being twinned. A second crystal, approximately 30 microns in length, displayed no twinning and was retained for data collection. Preliminary data collection on the larger crystal indicated a hexagonal unit cell: a=4.97, c=6.48 . Data collection and further analysis of the smaller crystal revealed the presence of a supercell of dimensions: a=9.945, c=12.965 . Structure solution and refinement are in progress.

The Electron Density Distribution of MoO3(dipic)(HMPA) at 28 K | X3A1

B.B. Iversen, F. K. Larsen, G. H. K. Madsen, C. Wilson, E. Moeller (U. of Aarhus), D. Young, and A. J. Schultz (Argonne National Laboratory - IPNS)

The field of catalytic oxidation chemistry is of interest both in basic science and from a technilogical point of view. A large number of studies have been devoted to unravelling the mechanisms of various key reactions [1]. In the process of developing fast experimental techniques to determine accurate electron density distributions (EDDs) at very low temperatures using high energy synchrotron radiation, we decided to study catalytic oxidation from a new point of view, namely through analysis of the EDDs of key molybdenum catalysts. We have measured exten- sive 28(1) K Bragg diffraction IP data on MoO3(dipic)(HMPA) , 1, and on MoO5(H2O)(HMPA), 2. Even though the complexes are structurally similar their cata- lytic behaviour is very different. Unfortunately 2 behaves poorly upon cooling to the low temperatures necessary for obtaining accurate diffraction data and at present we have not been able to extract structure factors of sufficient quality for EDD analysis. We can therefore only report results for complex 1, see figure 1. To support the analysis of the X-ray data, time-of-flight neutron diffraction data were collected on 1 at the Intense Pulsed neutron Source at matching temperatures (28K). In Figure 2 experimental details of the synchrotron measurements are shown. To model the electron density full multipole expansions were used to fourth order on Mo and P, to third order on O and N, and to second order on H. Hydrogen positional and thermal parameters were fixed at values obtained from the neutron data. In Figure 2 preliminary refinement residuals are given.

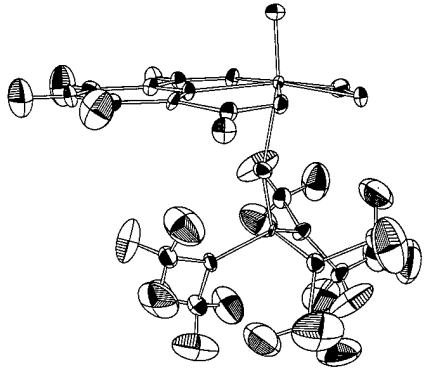

Figure 1. ORTEP drawing of the molecule showing 90% ellipsoids.

Table 1. Crystal data and experimental details for the synchrotron X-ray diffraction study of MoO3(HMPA)(dipic)

Temperature / K	28(1)
Crystal morphology	±(100) 0.075 mm, ±(010) 0.0675 mm, ±(101) 0.125 mm
μ / mm-1	0.92
Unit cell	a = 12.191(3) Å, b = 18.84(1) Å, c = 7.966(2)(1) Å, β = 90.79° (2)
Wavelength / Å	0.394
Transmission (min/max)	0.93-0.95
Image plate data	
Crystal to detector distance / mm	200
Rotation ranges	2θ = 0°: 8° oscillations, 2° overlap (0-182°) 2θ = 10°: 4° oscillations, 1° overlap (180-361°) 2θ = 25°: 5° oscillations, 1° overlap (0-185°)
sinθ/λ / Å^{-1}	0.13 - 1.47
Data collection time	3 days
h, k, l range	-28,35 -50,50 -11,10
Reflections collected	61778
R(int).	0.044 (56588 refs/ 10811 means)
Detector data	
Scan method	ω
Standards	3, measured every half hour
No. reflections measured (excluding standards)	214
Data collection time	1 day
h, k, l range	0,7 -2,11 -0,6
Multipole refinement (sinθ/λ < 1.0 Å)	
Nobs	8702
Npar	897
R(F)	0.033
R(wF)	0.029
R(F^2)	0.041
R(wF^2)	0.057
gof	1.14

Figure 2. Experimental details and preliminary refinement residuals

Single Crystal X-Ray Analysis of a Novel Perovskite $CaMnTi_2O_6$	X3A1

J.-H. Park, C. L. Cahill, and J.B. Parise (CHiPR and SUNY at Stony Brook)

In the investigation of the $CaTiO_3$-$MnTiO_3$ system, a new $CaMnTi_2O_6$ perovskite compound isomorphous to $CaFeTi_2O_6$ was synthesized using a stoichiometric mixture of the $CaTiO_3$-perovskite and $MnTiO_3$-pyrophanite phase(JCPDS29-902). Polycrystalline and single crystal (10x10x20μm) $CaMnTi_2O_6$ perovskite compound was prepared via high pressure-high temperature experiments under 14.5-15 GPa and 1200°C. Synchrotron X-ray diffraction data of a single crystal were collected using the imaging plate system at the X3A beamline. A super-cell of dimensions a, b=7.5339(5) and c=7.6027(6) Å was found. The resulting data is being analyzed in conjunction with previously collected powder diffraction data.

(1) K.Leinenweber et al, J. Solid State Chem., 114, 277 (1994).

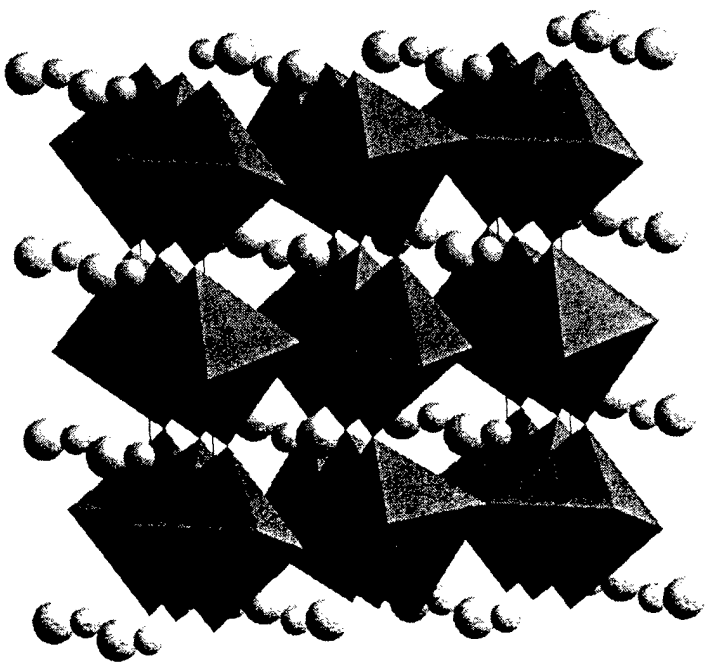

Figure 1. A view of $CaMnTi_2O_6$. TiO_6 and Ca/Mn are represented by octahedra and small/large circles.

The importance of correcting reflection intensities recorded on imaging plates for incomplete absorption in the phosphor layer *	X3A1

J. Zaleski, G. Wu, L. Ribaud and P. Coppens (SUNY@Buff)

When an X-ray beam is incompletely absorbed in the phosphor layer of an imaging plate (IP), a correction for oblique incidence of the beam on the plate becomes essential. Relative to the reflections recorded at normal incidence, it is equal to

$K = (1\text{-}\exp(-\mu d/\cos\alpha))/(1\text{-}\exp(-\mu d)) = (1\text{-}\exp(\ln T\perp)/\cos\alpha))/(1\text{-}T\perp)$ (1)

with $I_{corr} = I_{obs}/K$, and $T\perp$ equal to the transmission of the phosphor layer at the normal incidence. For short wavelengths ($<\approx 1$), the omission of the correction will lead to significant bias in the results, or even a failure of the refinement in the case of very short wavelengths. The correction for oblique incidence is a function of the crystal-to-plate distance, and must therefore be considered separately for each set of conditions. It is likely that a similar correction applies to CCD data. For a flat IP, mounted perpendicular to the incident beam, the correction increases with the 2θ angle of the reflections, but for other orientations of the IP the dependence is more complex. The correction has been tested as illustrated in the figure.

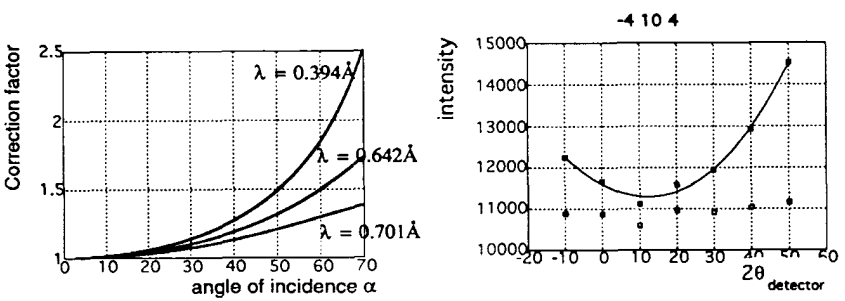

Figure 1. Left: the correction factor for three different wavelengths for Fuji BASIII imaging plates. Right: a reflection measured with 0.394Å photons at several different settings of the detector arm before and after correction.

* This work was supported by DOE Grant No. DEFG0286ER45231 and NSF Grant No. CHE9615586.

Synchrotron Small-angle X-ray Scattering Studies on Crystallization and Structure of Associated Polymer Blends	X3A2

K. Inomata, L.-Z. Liu, B. Chu (SUNY at Stony Brook), and T. Nose (Tokyo Institute of Technology)

Isothermal crystallization of associated polymer blends, consisting of one-end-aminated polystyrene (APS, M_w=5.6×10^3) and one-end-sulfonated poly(ethylene glycol) (SPEG, M_w=5.7×10^3), has been investigated by means of time-resolved synchrotron small-angle x-ray scattering (SAXS).

When APS/SPEG blend (weight fraction of 50/50 percent) prepared by using the freeze-dry method (APS/SPEG-FD) was quenched from a temperature higher than the melting point of SPEG to the crystallization temperature, the SAXS peak intensity (I_{max}) increased with time after quenching, while the peak position (q^*) remained at a constant value as shown in Figure 1. The time dependence of I_{max} and q^* can be explained by the crystallization of SPEG chains in the confined microphase-separated lamellar domain between the glassy PS layer, which is due to the formation of a diblock-copolymer-like structure based on the strong association between the terminal amino group of APS and the terminal sulfonic acid group of SPEG.

On the other hand, the sample prepared by using the solvent-cast method (APS/SPEG-SC) showed a unique time dependence of I_{max} and q^* as shown in Figure 2, i.e., I_{max} increased with time and revealed a maximum before reaching a constant value, and q^* decreased rapidly at the beginning of the crystallization process. Such a change of SAXS profile with time can be explained by assuming a macrophase separation of an APS-rich phase and a SPEG-rich phase, and a formation of dispersed APS microdomains in the SPEG-rich phase. Crystallization of SPEG chains would occur in the matrix phase in the SPEG-rich phase.

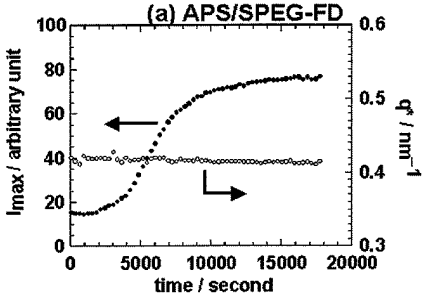

Figure 1. Time dependence of the peak intensity (I_{max}, filled circles) and the peak position (q^*, open circles) obtained from the Lorentz-corrected SAXS profiles of freeze-dry APS/SPEG-FD after quenching from 80°C to 29°C.

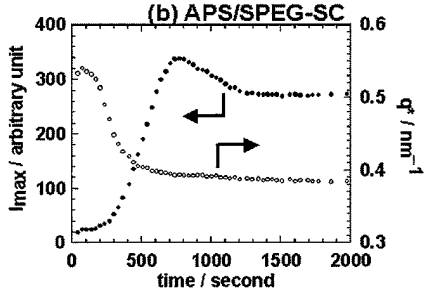

Figure 2. Time dependence of the peak intensity (I_{max}, filled circles) and the peak position (q^*, open circles) obtained from the Lorentz-corrected SAXS profiles of solvent-cast APS/SPEG-SC after quenching from 70°C to 30°C.

Crystalline Structure and Morphology of Microphases in Compatible Mixtures of Tetrahydrofuran-Methyl Methacrylate Diblock Copolymer and Polytetrahydrofuran	X3A2

L.-Z. Liu and B. Chu (SUNY at Stony Brook)

The crystalline structure and morphology of compatible mixtures of tetrahydrofuran-methyl methacrylate diblock copolymers (PTHF-b-PMMA) with a tetrahydrofuran homopolymer (PTHF) were studied with synchrotron X-rays. Wide angle diffraction was used to study the crystalline structures in a confined lamellar region with a thickness ranging from 12.2 to 19.5 nm, and in a PTHF matrix with an interface distance between the PMMA cylinders ranging from17 to 22 nm. As the thickness of the PTHF lamella and the interface are comparable with the long period of PTHF homopolymer ca 17 nm under the crystallization condition used, the crystalline structure has been found to be very sensitive to the average thickness of the PTHF phase. In the case of hexagonally packed cylindrical PMMA microdomains, evidenced by the scattering features shown in Figure 1, the effects of PMMA cylinders on the crystallization morphology in the PTHF matrix, and the effects of the PTHF crystallization on the hexagonally packed structure of PMMA cylinders were also studied. It is shown that only when the interdistance of two neighboring PMMA cylinders is close or larger than the long period of the pure PTHF homopolymer, ordered PTHF stacks can be formed in the PTHF matrix as shown by a scattering peak at q ≈ 0.4 nm-1 in Figure 2.

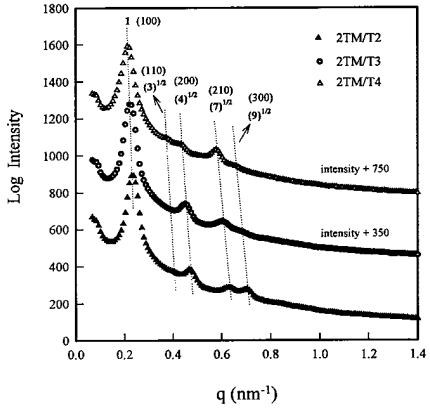

Figure 1. SAXS profiles of the blends in the amorphous state. The blends 2TM/T2, 2TM/T3 and 2TM/T4 contain 20, 30, and 40 wt % of PTHF homopolymer,respectively.

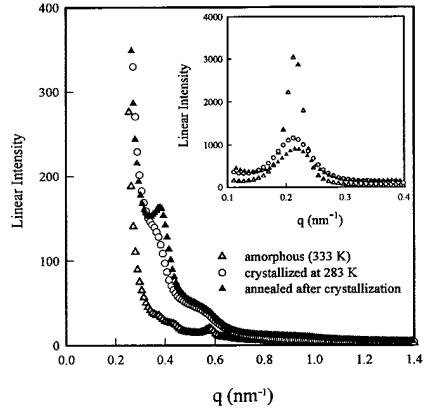

Figure 2. SAXS profiles of the blend 2TM/T4 containing 40 wt % of PTHF homopolymer.

Phase Diagrams and Gelation Structures of $B_5E_{91}B_5$ and $B_6E_{46}B_6$ Triblock Copolymers in Aqueous Solution	X3A2

T. Liu, C. Wu, D. Liang and B. Chu (SUNY at Stony Brook)

Poly(oxybutylene)-poly(oxyethylene)-poly(oxybutylene) (BEB) triblock copolymers are widely used in cosmetic and pharmaceutical industries. It is well known that such kind of block copolymers can form micellar structures in water because of the difference in the solubility of the hydrophobic B block and the hydrophilic E block. Compared with the large amount of studies on their micellization behaviors, the study at high polymer concentrations (< 10 wt%) is less reported and so far no phase diagram of these systems has been published. We used small-angle X-ray scattering technique (SAXS) at the X3A2 beamline of NSLS to study the gelation structures of two triblock copolymers ($B_5E_{91}B_5$ and $B_6E_{46}B_6$). Before the gelation concentration, the scattering peak can be found at high polymer concentrations (50 wt% at room temperature). The relavent q value when the SAXS peaks occued showed a concentration dependence (q value increased with increasing polymer concentration) but no temperature dependence for both polymers, as shown in Figure 1. The gel regions were extremely small when compared with those of EPE (oxyethylene-oxypropylene-oxyethylene) triblock copolymers. For $B_6E_{46}B_6$, this region was so small that we could locate it only at low temperatures (> 6 C) and very high polymer concentrations (< 90 wt%), probably due to the very short E block. SAXS study suggested that both form a fcc (face-centered cubic) packing structure, as shown in Figure 2.

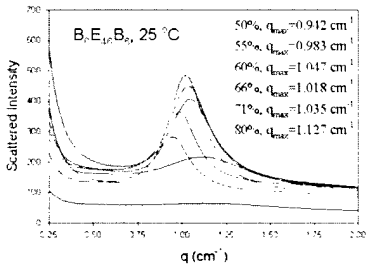

Figure 1. SXAS measurements of $B_6E_{46}B_6$/water systems at different polymer concentrations at 25 C. Larger qmax values were found at higher polymer concentrations. indicating smaller domain-domain distance.

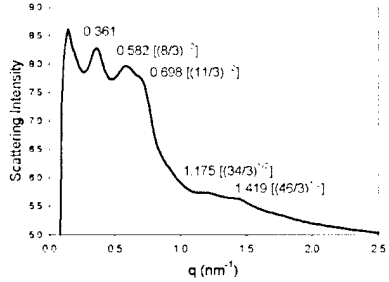

Figure 2. SAXS measurement of 85 wt% $B_5E_{91}B_5$/water system at 6 C. The scattering profile suggested that the micelles form a fcc(face-centerd cubic) structure.

Low-temperature Resonance Scattering of a Mixed-valence Iron Complex with a Distorted-triangular Fe_3O Core *	X3A2

G. Wu, Y. Zhang, L. Ribaud and P. Coppens (SUNY @ Buffalo)

The complex $Fe_3O(OOCCMe_3)_6(py)_3$ (py = pyridine, $(OOCCMe_3)$ = pivalonato) has a distorted O-centered Fe_3O core, indicating a mixed valence complex. We find the distortion, and thus the valence trapping, to increase on cooling. At 50K the three Fe-O bond lengths are 1.983, 1.906 and 1.838Å for Fe(1), Fe(2) and Fe(3) respectively. Site-specific determination of the absorption edge of the three atoms, using resonance diffraction, shows successive differences of about 1-2 eV between the edges, in agreement with the valence-trapped nature of the complex. This is the first time that three different valencies in a single complex have been distinguished by resonance scattering.

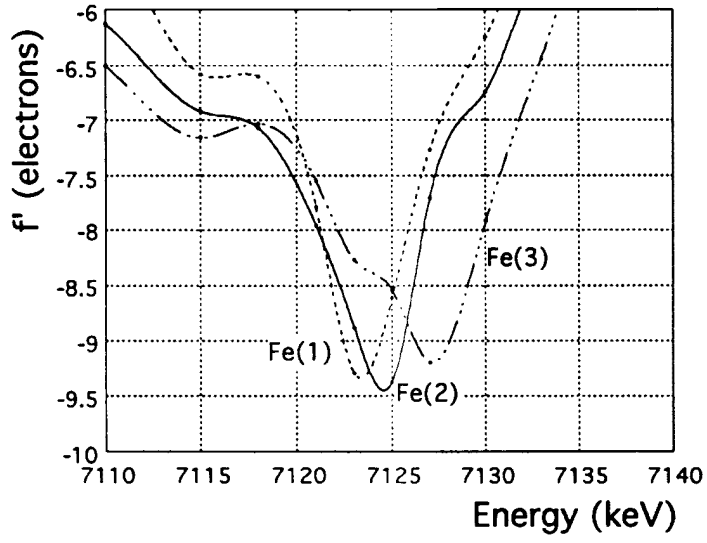

Figure 1. f' for three different Fe atoms as determined by site-specific anomalous diffraction.

* This work was supported by DOE Grant No. DEFG0286ER45231 and NSF Grant No. CHE9615586.

Supramolecular Structures of Complexes Formed by Poly(methacrylate-co-N-isopropylacrylamide) Gels with Hexadecyltrimethylammonium Bromide	X3A2

S. Zhou, F. Yeh, B. Chu (SUNY @ Stony Brook) and C. Burger (Max Plank Institut fur Colloid & Interfaces)

Small-angle X-ray scattering (SAXS) was used to investigate the nanostructure formation by the interaction of slightly crosslinked negatively charged gels of poly(methacrylate-co-N-isopropylacrylamide) (MAA/NIPAM) with hexadecyltrimethylammonium bromide (C16TAB). Three typical polyelectrolyte-surfactant complex (PSC) structures with Pm3n cubic, face-center cubic (FCC), and hexagonal closely packing (HCP) were observed when the charge content in MAA/NIPAM copolymer gel was decreased, namely, Pm3n cubic was formed with gel charge content over 75%, FCC was formed with a charge content of 67%, and HCP was formed at a charge content of 50%. The unit-cell models for the three structures have been suggested. Figure 1 shows a typical Pm3n cubic PSC structure, consisting of spheres at BCC positions and a continuous network, both imbedded in a matrix. Figure 2 shows the three simulation scattering curves from the three different models, which almost matched the experimental scattering curves. The spherical microdomains in various of structures might be formed by the aggregates of C16TAB surfactant, which could be stabilized by the electrostatic and hydrophobic interactions between the surfactants and the gel network chains. With decreasing charge content in the polymer chains, the packing of microdomains became more compact. By decreasing the charge content of the gel to below 33%, no ordered structure was observed due to the weaker electrostatic interactions.

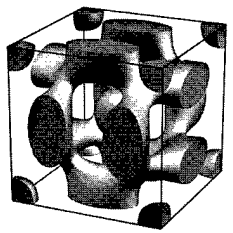

Figure 1. Typical unit-cell model for Pm3n cubic PSC structure formed by the interaction of C16TAB with highly charged MAA/NIPAM copolymer gel.

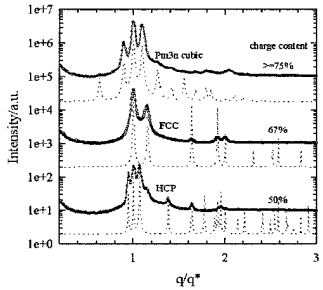

Figure 2. Typical SAXS profiles of the MAA/NIPAM polymer gel/C16TAB complexes. The dotted lines present the simulation curves from ideal models.

The Crystal Structure of $Rb_6Pb_5Cl_{16}$ and its Determination by X-ray Powder Diffraction using Anomalous Dispersion *	X3B1

H. P. Beck, M. Schramm, R. Haberkorn (U. of Saarland), R. E. Dinnebier (U. of Bayreuth) and P. W. Stephens (SUNY at Stony Brook)

The hitherto unknown compound $Rb_6Pb_5Cl_{16}$ was synthesized by melting a stoichiometric mixture of RbCl and $PbCl_2$ at 700°C and annealing for several weeks at 200°C. The metrics could be determined from a powder pattern, taken at a laboratory diffractometer, but the structure could only be solved by using synchrotron radiation.

The compound $Rb_6Pb_5Cl_{16}$ crystallizes in the tetragonal space group P4/mbm with lattice constants a=1171.41(4)pm and c=1103.11(6)pm. A Le-Bail fit enabled to extract about 400 integrated intensities from the powder pattern, which could be used for ab initio determination of the structure. This new type of structure [1] shows a large variety of different coordination polyhedra for the cations: columns of tetragonal prisms and antiprisms, capped trigonal prisms and a 6+2+2 polyhedron of a new type. Because the occupation factors could not be determined unambigously, two additional measurements near the Pb-L_3-edge were performed using anomal dispersion. A statistically distribution of Rb and Pb at only one of the cation sites with a ratio of 1:3 was found. There is no evidence for symmetry reduction by ordering.

[1] H. P. Beck, M. Schramm, R. Haberkorn, R. E. Dinnebier and P. W. Stephens, Z.Anorg.Chem. (accepted).

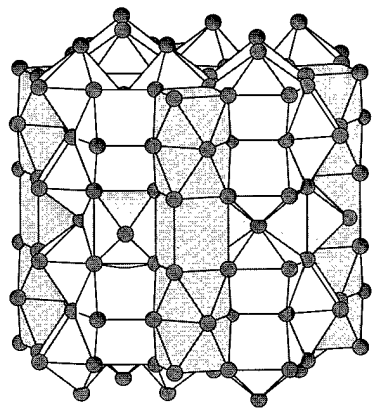

Figure 1. Struture of $Rb_6Pb_5Cl_{16}$ (c axis points vertically).

* Work at the SUNY X3 beamline is supported by the Division of Basic Energy Sciences, U.S. Dept. of Energy (DE-FG0286-ER45231).

Anisotropic Strain of K_4C_{60} at Low Temperatures * | X3B1

G.M. Bendele and P.W. Stephens (SUNY at Stony Brook)

The quadrivalent alkali fulleride salts A_4C_{60} (where A=K,Rb) are non-magnetic insulators with tetragonal crystal structure. We have recently determined that they show no appreciable deviation from exact x=4 stoichiometry [1]. We have performed a low-temperature x-ray powder diffraction study on both K_4C_{60} and Rb_4C_{60}.

The thermal expansion coefficients of the lattices of both compounds are of comparable magnitudes along and perpendicular to the unique axis ($\sim$1.2–2.5$\times10^{-4}$Å/K). Both compounds show an *increase* in the FWHM of Bragg peaks with decreasing temperature and develop an anisotropy, i.e., (00l) peaks along the unique c axis are broader than (hk0) peaks perpendicular to c, indicating anisotropic strain in the lattice that increases as T is lowered. This effect is much stronger in K_4C_{60} than in Rb_4C_{60}, as Fig. 1 illustrates.

Given the recent discovery of a two-dimensional cross-linked polymer phase of Na_4C_{60} [2] we suspect that this anisotropy is evidence of the onset of a phase transition into a similar polymeric phase, possibly at elevated pressure. For steric reasons, we expect such polymerization to become harder with increasing cation size, consistent with the fact that the Na_4C_{60} polymer is stable, K_4C_{60} shows a large degree of anisotropic strain broadening, and Rb_4C_{60} exhibits almost none.

[1] C.A. Kuntscher, G.M. Bendele, and P.W. Stephens, PRB **55**, R3366 (1997).
[2] G. Oszlányi *et al.*, Phys. Rev. Lett. **78**, 4438 (1997).

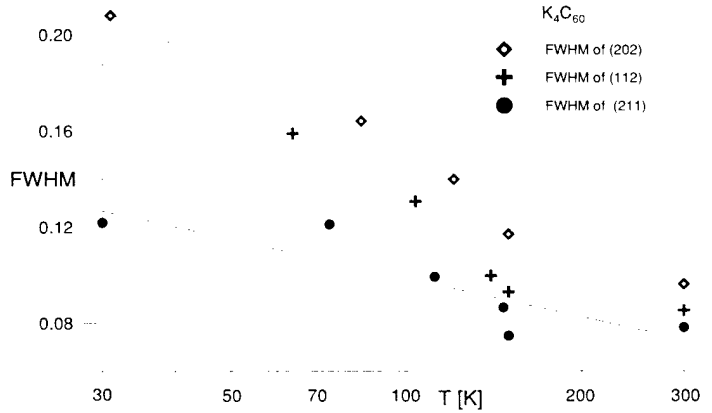

Figure 1.

* Work at the SUNY X3 beamline is supported by the Division of Basic Energy Sciences, U.S. Dept. of Energy (DE-FG0286-ER45231). Research at SUNY is supported by the NSF under grant DMR95-01325.

Na_2KC_{60}: Determining the Orientation of Fullerenes in the Lattice * | X3B1

G.M. Bendele, P.W. Stephens (SUNY at Stony Brook), and L. Forrö (EPF, Lausanne)

Na_2KC_{60} is a cubic alkali fulleride at room temperature and above, but x-ray powder diffraction measurements show that it undergoes a slow phase transition into a symmetry-lowered ground state upon slow cooling. To determine the occurrence and geometry of interfullerene bonding it is crucial to obtain the orientation of the fullerene molecules in the lattice.

After obtaining the monoclinic lattice parameters of the ground state (space group $P2_1/a$, a = 13.714 Å, b = 14.627 Å, c = 9.380 Å, β = 133.91°) we have, without making any *a-priori* assumptions, performed a three-dimensional search over all possible orientations of the C_{60} molecule. We can specify that orientation using just three parameters, which are defined analogous to Euler angles: ϕ and θ specify a point of contact along the shortened c axis and ψ specifies a rotation about c. In searching all (ϕ,θ,ψ) we find only one convincing minimum in the weighted-profile R-factor R_{wp}: a single carbon atom located on the c axis, with a rotation angle about c of ψ = 77°. To illustrate this, Fig. 1 shows R_{wp} vs. ψ for several fullerene points-of-contact.

This compares in an interesting way to the case of isoelectronic Na_2RbC_{60} [1]: For that compound ϕ and θ of the global minimum are identical, but ψ is not, reflecting the fact that the interfullerene bonding geometry is identical, but the arrangement of the chains in the lattice is not.

[1] G.M. Bendele al., submitted to Phys. Rev. Lett.

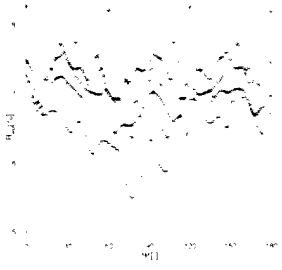

Figure 1. Plots of weighted-profile R-factor R_{wp} vs. rotation angle ψ in Na_2KC_{60} for the following features of the fullerene molecule pointing along the bonding c axis: + Single C atom. ◇ Center of double bond. △ Center of single bond. ◯ Center of pentagon. ▽ Center of hexagon.

* Work at the SUNY X3 beamline is supported by the Division of Basic Energy Sciences, U.S. Dept. of Energy (DE-FG0286-ER45231). Research at SUNY is supported by the NSF under grant DMR95-01325.

Effect of Charge State on Bonding gGometry: Na_2RbC_{60} | X3B1

G.M. Bendele, P.W. Stephens (SUNY at Stony Brook), K. Prassides, K. Vavekis, K. Kordatos (U. of Sussex, UK), and K. Tanigaki (NEC Tsukuba, Japan)

In order to determine the atomic structure of the ground state of the alkali fulleride Na_2RbC_{60} obtained by slow-cooling [1] we have collected x-ray powder diffraction patterns at T=180K and T=20K, with λ=1.15Å and for 2θ=6°–50°.

In short, the unit cell of the low-temperature structure is monoclinic, space group $P2_1/a$, with lattice parameters a=13.711Å, b=14.554Å, c=9.373Å, β=133.53° (at T=180K). In this cell, we find that the fullerenes are connected along c by single carbon-carbon bonds [2], in contrast to the ground state of the otherwise similar RbC_{60} system [3], in which the fullerenes are linked with two bonds via [2+2] cycloaddition. See Figures 1 and 2 for an illustration of the differences.

The question why Na_2RbC_{60} links fullerene molecules with a single bond, while the latter does so with two carbon-carbon bonds is very important. After excluding possible steric and kinetic reasons for this difference in bonding geometry we conclude that it is the charge state of the fullerene that plays a decisive role, causing $(C_{60}^{1-})_n$ to favor cycloaddition and $(C_{60}^{3-})_n$ to favor single carbon-cabon bonds.

Details on both the data analysis and our conclusions with respect to the charge state can be found in [2] or in G.M. Bendele *et al.*, in *Proceedings of the IWEPNM 97 Kirchberg/Tyrol* (World Scientific 1997).

Work at the SUNYX3 beamline is supported by the Division of Basic Energy Sciences, U.S. Dept. of Energy (DE-FG0286-ER45231). Research at SUNY is supported by the NSF under grant DMR95-01325. Work at Sussex is supported by the EPSRC.

[1] K. Prassides *et al.*, J. Am. Chem. Soc. **119**, 834 (1997).
[2] G.M. Bendele *et al.*, submitted to Phys. Rev. Lett.
[3] P.W. Stephens *et al.*, Nature (London) **370**, 636 (1994).

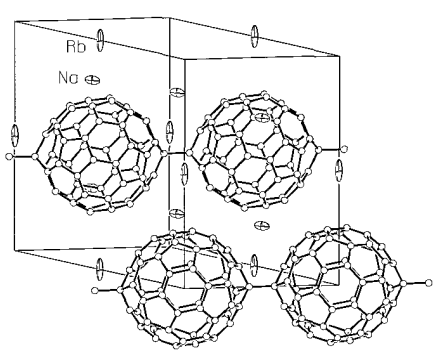

Figure 1. Atomic structure of the Na_2RbC_{60} polymer derived here.

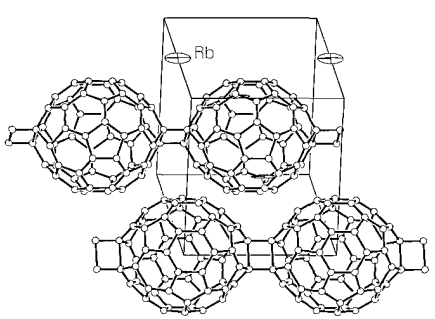

Figure 2. Atomic structure of the RbC_{60} polymer (from [3]).

Powder Diffraction Structure of Fluorenylsodium | X3B1

R. E. Dinnebier (U. of Bayreuth) and F. Olbrich (U. of Magdeburg)

The crystal structure of the organometallic compound fluorenylsodium ($NaC_{13}H_9$) has been solved ab initio. The compound crystallizes in the hexagonal space group P 63/m (No. 176) with a = 9.2828(1), c = 19.1613(2), V = 1429.93(2)Å, and d = 1.197 g cm^{-3}. Data collection was carried out at room temperature using a wavelength of 1.14966 Åfrom double Si(111) monochromator and Ge (111) analyzer. The 2Θ range used for the Rietveld refinement was $5.0 < 2\Theta < 50.0°$. All positions of the carbon and sodium atoms were found by a combination of direct methods, partial Rietveld refinements and difference Fourier analysis. The indenyl ring was refined as a rigid body and the hydrogen atoms were calculated in idealized positions. The actual Rietveld plot yields to R-wp= 5.6%, R-p= 4.3% and R-F2=8.2%. Figure 1 shows part of the coordination spheres around the two different sodium positions of $NaC_{13}H_9$. The $NaC_{13}H_9$ units are connected in two dimensions pependicular to the crystallographic c axis. Within this network, the Na atoms are either hapto5 or hapto6 coordinated by three fluorenyl rings. The layers themselves are connected by van der Waals forces only.

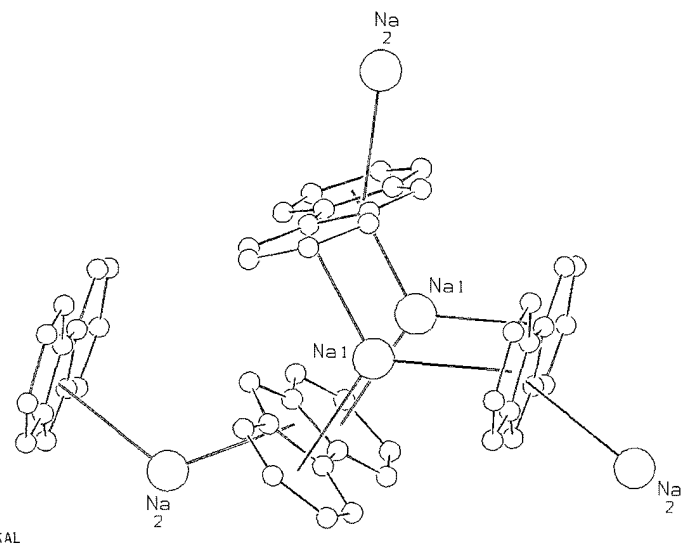

Figure 1. Part of the structure of $NaC_{13}H_9$ showing the two different coordination spheres around the two sodium sites. The two Na1 atoms are aligned along c-axis. Hydrogen atoms have been omitted for clarity.

Study the Phase Diagrams of L64/water/$CdCl_2$ Complex Systems by SAXS	X3A2

T. Liu, C. Wu, D. Liang and B. Chu (SUNY at Stony Brook)

The design of new inorganic materials with special structures has become an important area in materials science. Triblock copolymer micelles can be used as a kind of potential templates for synthesizing inorganic compounds with special nanostructures. To find out proper synthesis conditions, the phase diagrams of polymer/water systems in the presence of specific inorganic salts have been investigated. L64 (poly(oxyethylene)13-poly(oxypropylene)30-poly oxyethylene)13) is a widely used commercial triblock copolymer and the phase diagram of L64/water system has been carefully characterized. In this study, we found that in the presence of $CdCl_2$, a water-soluble salt, the phase diagram of L64/water changed greatly. Cloud-point temperatures and gelation concentrations went down when compared with the pure L64/water system. Also, a two-phase region (thick gel) appeared at high salt concentrations, as shown in Figure 1. Small-angle X-ray scattering (SAXS) at the X3A2 beamline (NSLS) revealed that some new structures, like the bcc (body-centered cubic) strcuture which has not been found in the L64/water system, have been observed due to the introduction of $CdCl_2$, as shown in Figure 2.

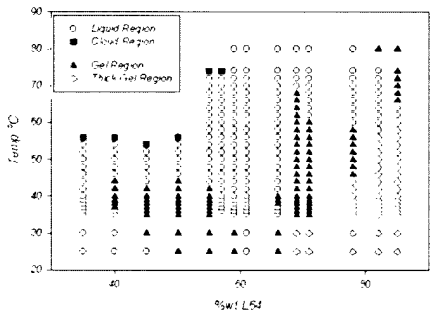

Figure 1. The phase diagram of L64/water/$CdCl_2$ system with molar ratio L64:$CdCl_2$=1:5.76. Several separated gel regions were found.

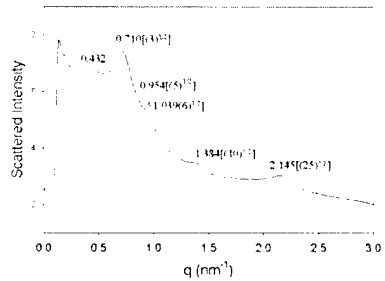

Figure 2. SAXS curve of L64/water/$CdCl_2$ system with molar ratio L64:$CdCl_2$=1:5.76, weight ratio L64:water=82:18. The scattering profile indicates bcc (body-centered cubic)structure.

Formation of Clay Minerals Replacing Diatom Cells in Amazon Delta Sediments	X3B1

P. Michalopoulos, R. C. Aller, P.W. Stephens (SUNY at Stony Brook)

We investigated the potential growth of clay minerals in association with diatom cells found in Amazon delta sediments using x-ray powder diffraction. Processes that lead to the in situ formation of clay minerals in marine sediments are important for global geochemical cycles and the composition of seawater Sample preparation involves separation of individual diatom cells from the sediments, grounding of less than two hundred cells and mounting on a Si (1,0,0) wafer X-ray powder diffraction patterns from these samples (Fig. 1) show the presence of characteristic clay mineral peaks together with pyrite (FeS_2) and gypsum. Pyrite originates from the decomposition of the diatom organic matter through sulfate reduction. Figure 1 shows the 7.17 peak, typical of clay minerals such as kaolinite ($Si_4Al_4O_{10}(OH)_8$). These results indicate that the biogenic silica has acted as a substrate for the formation of new clay minerals. These conclusions have been corroborated with other techniques such as SEM, TEM and electron microprobe studies which show that the new clay minerals are replacing the siliceous frustule of diatoms through dissolution-precipitation reactions. The newly formed 7.17 phase is one of several authigenic mineral phases that form on these substrates. Some phases remain undetected during the X-ray analysis due to poor crystallinity and/or very small crystallite size.

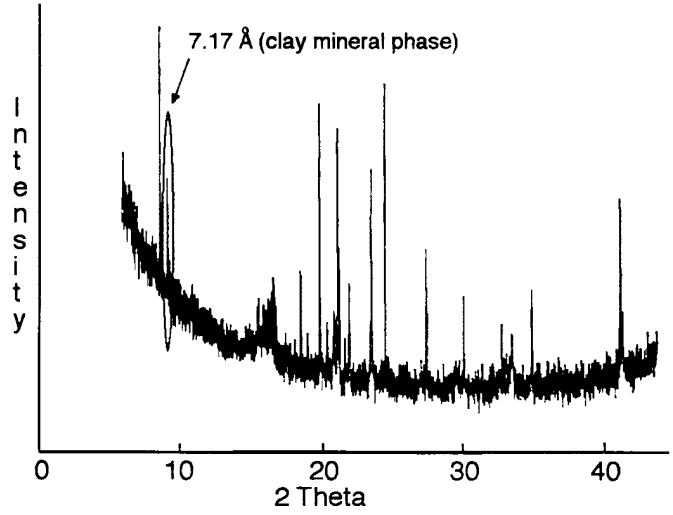

Figure 1. The 7.17 Angstrom peak represents the newly formed clay mineral phase.

Na_4C_{60}: An Alkali Intercalated Two-Dimensional Polymer	X3B1

G. Oszlanyi, G. Faigel (Res. Institute for Solid State Physics) and G. Baumgartner, L. Forro (Ecole Polytechnique Federale de Lausanne)

A remarkable feature of C_{60} molecules is that they may form bonds with each other leading to a variety of crystal structures and physical properties. Initially the Diels-Alder type [2+2] cycloaddition was considered as the exclusive mechanism for bond formation. Recently a different type of interfullerene bond was detected in a metastable dimerized phase of AC_{60} (A=K, Rb) where dimer anions are formed by joining single carbon atoms [1]. This finding suggested that the formation of single bonds is not an isolated example but a general trend at higher charge states of the fullerene anions. In a systematic search, the long-missing Na_4C_{60} phase has been identified by Rietveld analysis of synchrotron powder diffraction data [2]. Its monoclinic structure (space group: I2/m, lattice parameters: a=11.235Å, b=11.719Å, c=10.276Å, β=96.16°) is based on polymer planes of C_{60} where each molecule forms four single bonds within the plane. This compound is not only the first fulleride polymer with such bonds, but also the first two-dimensional polymer which is naturally intercalated with alkali ions and can be synthesized at ambient pressure.

[1] G. Oszlanyi et al., Phys. Rev. B54, 11849 (1996)
[2] G. Oszlanyi et al., Phys. Rev. Lett., 78, 4438 (1997)

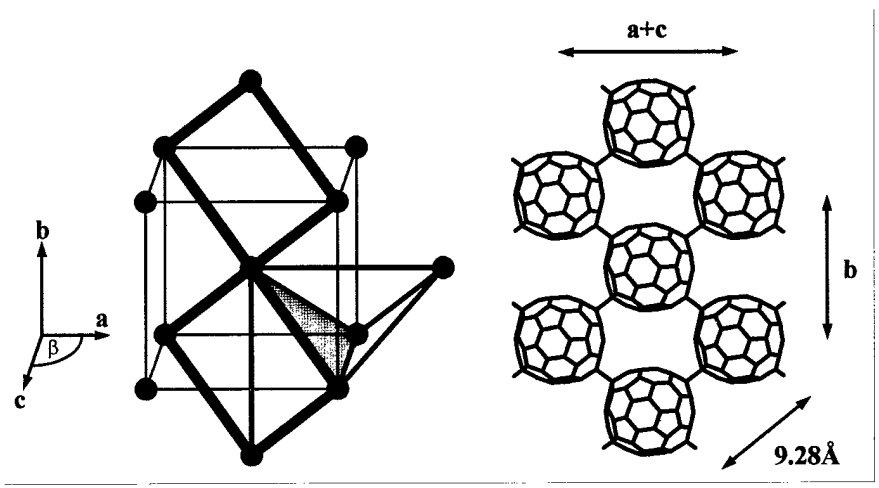

Figure 1.

Measurement of Coherent Scatter Form Factors in Tissues in Support of Monte Carlo Simulation of Mammography *	X3B1

D. E. Peplow and K. Verghese (NC State University)

A team of physicists, engineers and doctors from NC State University, UNC, NSLS and IIT is currently investigating the use of monochromatic synchrotron radiation for mammography to obtain to an image with less scatter and higher contrast than conventional mammograms. In support of these experimental studies, Monte Carlo calculations are being performed to evaluate the new system and investigate its potential performance.

Most Monte Carlo calculations use the free-gas model for determining the coherent scatter angular distributions, which does not include intramolecular or intermolecular interferences. For amorphous materials, this approximation does not hold at low values of x ($x = \frac{E}{hc} \sin \frac{\theta}{2}$). The coherent scattering form factors of these materials show broad peaks and must be measured.

The form factors of five tissues and two plastics materials (relevant to mammography phantoms) were derived from scattering measurements made on the powder diffraction line X3B1 with the assistance of Dr. P. W. Stephens. Due to the difficulties of using human tissues, fresh beef and pork samples were substituted. Shown in Figure 1 is the coherent scattering form factor of water measured at the NSLS with a measurement made by Narten (Report ORNL-4578, 1970) using an X-ray tube spectrum. Figure 2 shows the measured form factor of pork fat with its free-gas approximation. The form factors are being incorporated into the Monte Carlo model to simulate images from the new digital mammography current digital mammography machines and the new synchrotron-based system.

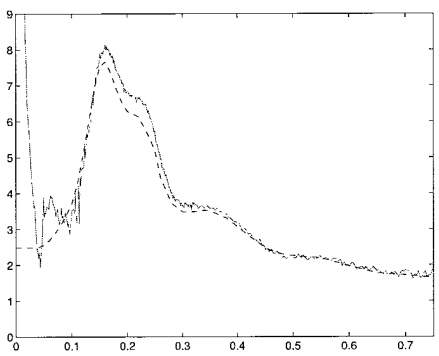

Figure 1. Form factor of water: measured at the NSLS (solid) and Narten's measurement (dashed).

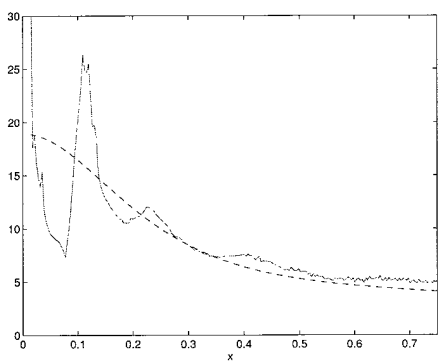

Figure 2. Form Factor of pork fat: measured at the NSLS (solid) and the free-gas approximation (dashed).

* Funding for this research was provided through the US Army Breast Cancer Research Program

Rotational Order in CO Intercalated $C/_{60}$ Crystals * — X3B1

S. vanSmaalen, R. E. Dinnebier (U. of Bayreuth, Germany), I. Holleman, G. von Helden, G. Meijer (U. of Nijmegen, The Netherlands)

The structure of $(CO)_xC_{60}$(x= 0.67) has been determined by high resolution X-ray powder diffraction [1]. Crystallographic data are: space group P a -3, a= 14.0605(1) Å. The data were collected in a closed cycle helium cryostate at 25 K with a wavelength of 1.15030(1) Åusing a double Si(111) monochromator and Ge(111) analyzer in a 2Θ range of $5.0 < 2\Theta < 75.0$ ° for 20 seconds per step. The structure was solved by rigid body Rietveld refinement and difference Fourier analysis. CO is found distributed over six equivalent orientations on the octahedral sites of the cubic closed packed structure of C_{60}. The C_{60} molecules are orientationally ordered in almost exclusively the major orientation. There is evidence for a weak electrostatic interaction between C_{60} and $(CO)_x$.

[1] S. van Smaalen, R. E. Dinnebier, I. Hollemann, G. von Helden, and G. Meijer, submitted.

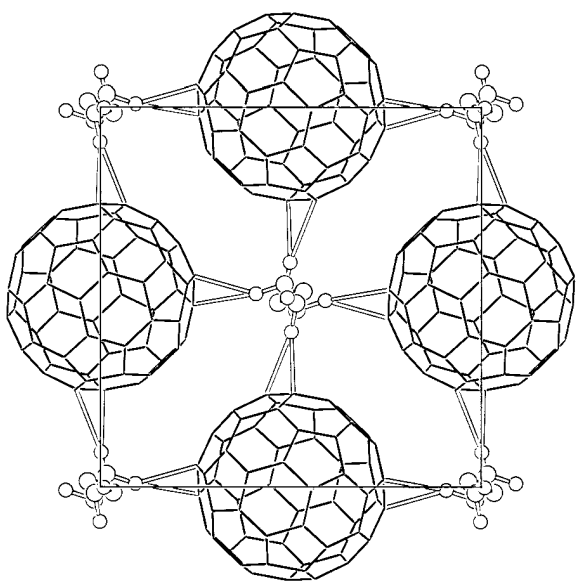

Figure 1. View of the unit cell of $(CO)_xC_{60}$ showing the 6-fold disordered CO molecules near the octahedral sites of the cubic closed packed structure.

* Work at the SUNY X3 beamline is supported by the Division of Basic Energy Sciences, U.S. Dept. of Energy(DE-FG0286-ER45231)

In Situ Diffuse Scattering Studies of Ag(111) During Low Temperature Homoepitaxy * — X3B2

W.C. Elliott, P.F. Miceli (U. of Missouri-Columbia), and P.W. Stephens (SUNY at Stony Brook)

The morphology of a surface during epitaxial growth is determined by the kinetic mechanisms which affect the incorporation of deposited atoms into the crystal substrate. We have studied the lateral structure of a kinetically roughened Ag(111) surface during homoepitaxy at 200K to further understand the effect of a large step-edge barrier to surface diffusion upon the resulting surface morphology.

Measurement of surface diffuse x-ray scattering in reflectivity geometry is a means of obtaining this lateral structure; scans transverse to the specular reflectivity near the out-of-phase position provide excellent sensitivity to the developing lateral structure. As the surface roughens during deposition, the central specular peak diminishes while diffuse scattering appears and broadens with increasing coverage(a).

This diffuse scattering is a measure of the mean terrace length on the surface and can be described by a power-law over two decades in coverage(b). Near 16ML, a second diffuse peak appears which narrows with increasing coverage. This new peak is attributed to the separation between developing mounds which coarsen with increasing coverage.

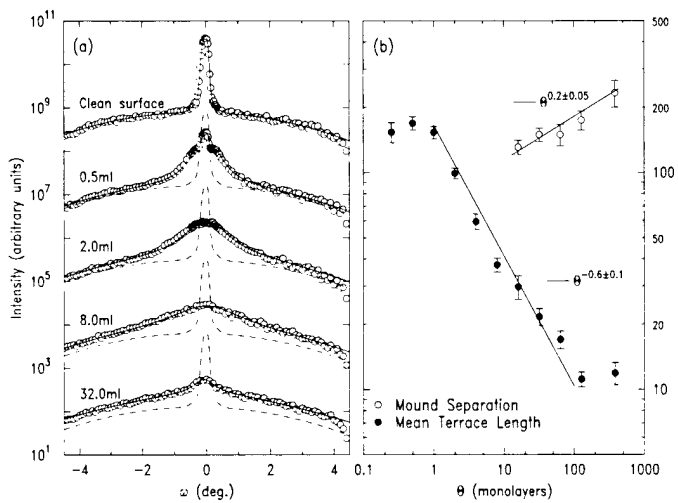

Figure 1.

* Supported by NSF (DMR-9202528 and DMR-9623827). MISCON under USDOE (DE-FG02-90ER45427) and the SUNY X3 beamline is supported by USDOE (DE-FG02-86ER45231).

Structure Of a Cre Recombinase-DNA Site-specific Recombination Synapse	X25, X4A

F. Guo, D. N. Gopaul, and G. D. Van Duyne (U. of Penn.)

Cre recombinase catalyzes the reciprocal exchange of DNA strands between 34-base pair loxP sites during site-specific recombination. Using diffraction data measured at the X25 and X4A beamlines, we have determined the 2.4 A crystal structure of a covalent intermediate in the Cre-loxP reaction, where the recombinase has cleaved and formed 3'-phosphotyrosine linkages to its DNA substrates. Four recombinases and two DNA substrates are arranged in a pseudo-fourfold symmetric tetramer that represents a site-specific recombination synapse.

Parent data and two heavy atom derivative data sets for this structure were measured at the X25 beamline. One derivative was made from selenomethionine-substituted Cre recombinase, with 22 anomalous scatterers in the crystallographic asymmetric unit. Data were measured at a single wavelength corresponding to a maximum of f" and the resulting anomalous diffraction signal led to strong crystallographic phasing power. The second heavy atom derivative made use of an iodine-containing DNA substrate. The selenomethionine derivative was also used for a three-wavelength anomalous diffraction measurement at the X4A beamline. Together, the heavy atom diffraction data from the two beamlines led to a readily interpretable image of the electron density.

In situ Surface X-ray Diffraction Study on $RuO_2(100)$ Single Crystal	X6B

Y. Chu, J. Tanzer, H. You, and Z. Nagy (ANL)

Ruthenium dioxide has been known to exhibit unusually large pseudo-capacitance, and it is appealing candidate material for temporary energy storage device for advance battery applications. This ultra capacitance has been attributed to the change of the oxidation state of the Ru atoms at the electrochemical interface, yet the structural change due to the valency shifting has not been understood well.

In situ surface x-ray diffraction experiment was performed on as-grown $RuO_2(100)$single crystal samples. The cyclic voltammetry of the sample is shown in Fig. 1a. The cathodic peak just before the hydrogen evolution is due to the reduction of Ru atoms from valence 4+ to 3+, and the anodic peak is due to the reverse reaction. The charge transfer obtained from CV indicates the redox reaction is limited to about a single monolayer. Fig. 1b shows that the intensity at (1.5, 0, 0) undergoes a significant change at the same potential where the reduction occurs, suggesting some modification of the surface structure due to the reduction. The reflectivity data shown in Fig 1.c reveal that the reduced surface at -200 mV has a very different surface structure from the oxidized surface at 460 mV (open circuit potential).

Preliminary fitting analysis indicates that the top Ru layer spacing is significantly expanded when reduced, while slightly contracted when oxidized. The expansion of the surface layer spacing may be due incorporation of protons into the lattice to accommodate the shift in the oxidation state of Ru atoms.

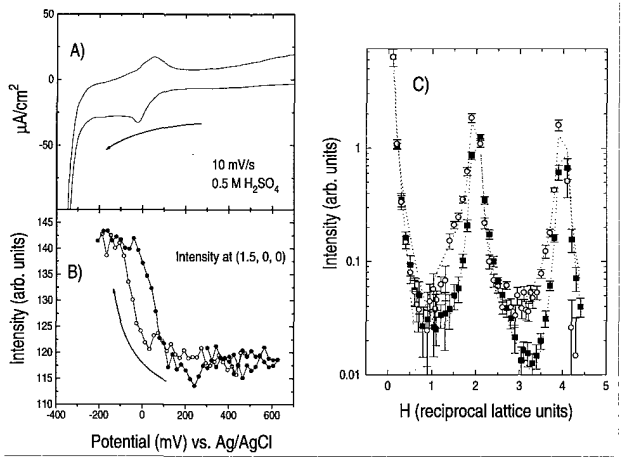

Figure 1. A) Cyclic voltammetry of $RuO_2(100)$ in 0.5 M H_2SO_4. B) Intensity at (1.5, 0, 0) vs. potential. The direction of potential scan is indicated by arrows. C) Reflectivity data at 460 mV (open circuit potential, solid squares) and at -200 mV (open circles). The dotted lines are fits.

Levitation Apparatus for Structural Studies of High Temperature Liquids Using Synchrotron Radiation	X6B, X25

S. Krishnan, J. J. Felten, J. E. Rix, J. K. R. Weber, P. C. Nordine (Containerless Research, Inc.), M. A. Beno, S. Ansell, and D. L. Price (ANL)

A new levitation apparatus coupled to an synchrotron-derived x-ray source has been developed to study the structure of liquids at temperatures up to 3000K. The levitation apparatus employs conical nozzle levitation using aerodynamic forces to stably position solid and liquid specimens at high temperatures. A 270 Watt, CO_2 laser was used to heat the specimens to desired temperatures. Two optical pyrometers were used to record the specimen temperature, heating curves and cooling curves. Three video cameras and a video recorder were employed to obtain and record specimen views in all three dimensions. The levitation assembly was supported on a three-axis translation stage to facilitate precise positioning of the specimen in the synchrotron radiation beam. The levitation system was enclosed in a vacuum chamber with Be windows, connections for vacuum and gas flow, ports for pyrometry, video and pressure measurements. The vacuum system included automatic pressure control and multi-channel gas flow control. A phosphor screen coupled to a high-resolution video microscope provided images of the x-ray beam and specimen shadow which were used to establish the specimen position. The levitation apparatus was integrated with x-ray diffractometers located at X6B and X25 beamlines at the National Synchrotron Light Source. X-ray structural measurements have been obtained on a number of materials including Al_2O_3, Ni, Si, Ge, and other metallic and ceramic materials in the liquid state.

S. Krishnan, et al., *Rev. Sci. Instrum*, **68**, p. 3512 (1997).

X-Ray Investigation of the Transformation of Crystal Structures Induced by Mo Seeding Layers	X6B

C.H. Lee (Tsing-Hua U.,Taiwan), J.C.A. Huang and Y.M. Hu (Cheng-Kung U., Taiwan), and M. Shih (Chung-Hsin U., Taiwan)

Epitaxial permalloy thin films were prepared on the sapphire substrates (1-100) via Mo seeding layer. The structure of the epitaxial permalloy film is stronly related with the thickness of the Mo buffer layer. In details, the permalloy is dominated in (111) in the plane-normal direction when the Mo layer is thinner than 2A. The preferred orientation is switched to (220) when the Mo buffer layer is from 2A to 20A. The permoally thin films are orinetated in (211) directions after 20A of Mo layer is deposited. For the in-plane direction, all the permollay(0-22) surfaces are locked in the Mo(-111)direction or sapphire(0001) directions. For all the good expitaxial films, the permalloy are in a twin fcc structures with a stacking fault along the permalloy(-111)or permalloy(1-1-1) direction and the domain size is 20A to 40A depending on the thickness of Mo layer. The coexistence of permalloy(220) together with permalloy(211) from 2A to 20A can be interpreted by the droplet-like Mo thin film on the surface of sapphire. The edge surface of the Mo droplets stablize the permalloy(220) structure on the surface of sapphire. After 20A of Mo deposition, the Mo islands coalesced and a pure permalloy(211) structure prevails.

In Situ Study of the Growth of OTS Self-Assembled Monolayers on Silicon | X6B

A.G. Richter, M.K. Durbin, C-J. Yu, and P. Dutta (Northwestern U.)

Self-Assembled Monolayers (SAMs) have been extensively studied using many techniques, including X-ray reflectivity and diffraction. Although much is known about the few systems that self-assemble, very little is known about the process of deposition and film formation. Several studies have been made of SAMs of octadecyltrichlorosilane (OTS), and these have given us some insight into this problem, but they have been performed *ex situ*. Recently we have performed in situ experiments on the formation of OTS SAMs using X-ray reflectivity.

X-ray reflectivity requires contrast in the electron density profile, but the densities of most organic materials fall within a narrow range. We used heptane, which has a low density ($\sim$ 0.33 times the density of silicon) as our solvent. Typical monolayer densities are 0.4-0.5 times silicon density. Since the contrast is still low, the reflectivity minima are not as pronounced as for ex situ systems, but the minima are obvious. A solution concentration of 0.0001% was used. Film growth occurred too rapidly at higher concentrations to allow us to study the early stages of growth.

We have found that the film formation has at least three different modes of growth. During the first stage, the film-solution interface is rough and the film thickness is low. This is probably due to the molecules having a range of tilts, most of them large. The second stage of growth begins after about 5 hours at this concentration. During this stage, the film thickness is roughly constant and is about that of a fully extended molecule (2.3nm). However, the modeled density profiles suggest that the film is still loosely packed and that some of the molecules are tilted. Over time, the film becomes denser and more uniform. This most likely occurs because more molecules are deposited, increasing the density and forcing the surrounding molecules to stand up. This stage lasts for about 5 hours, after which the molecules are all mostly untilted. In the last stage, the film changes minimally; only the film-solvent interface becomes slightly sharper.

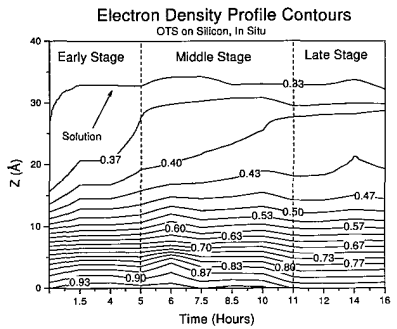

Figure 1. A contour plot of the electron density profile of OTS on silicon over time. Note that 0.33 is the solvent density (in units of silicon = 1.0). The film dioxide layer ranges from 0.75 to 0.37. The silicon dioxide layer ranges from 1 to 0.75.

Strong Negative Thermal Expansion in Siliceous Faujasite * | X7A

M. P. Attfield and A. W. Sleight (Oregon State U.)

Negative thermal expansion has received a lot of interest recently, with the discovery of strong isotropic negative thermal expansion in ZrW_2O_8 (1) over a broad temperature range. An apparent requirement for an oxide material to have strong intrinsic negative thermal expansion is that it has an open framework structure with two coordinate oxygen atoms. Zeolites are a group of compounds whose structures fulfill the aforementioned requirements. Indeed, computer simulations have predicted that some zeolites should exhibit negative thermal expansion (2). The thermal expansion of siliceous faujasite was investigated,thus avoiding the complications associated with the extra-framework cations and greatly reducing the water content of the zeolite.

Synchrotron data were collected on a dehydrated sample of zero defect dealuminated Y (ZDDAY) at seven temperatures between 25.16 and 297.95 K to determine the unit cell constant and structure as a function of temperature. X-ray data above 298 K were collected on a laboratory INEL XRG 3000 diffractometer.

An approximately linear decrease in cell dimension is seen over the entire temperature range (Figure 1)with an overall coefficient of thermal expansion of -4.2 x 10^{-6} K^{-1}. The results from the Rietveld refinements indicate that the bridging Si-O-Si angles display no significant changes over the temperature range analysed and that the constituent SiO_4 tetrahedra of the structure may be considered as rigid tetrahedra over this whole range. These results lead us to believe that the negative thermal expansion of this material is related to the harmonic transverse vibrations of the 2-coordinate bridging oxygen atoms within the structure. These vibrations lead to coupled rotations of the essentially rigid tetrahedra making up the structure of the zeolite. The increased magnitude of these transverse vibrations with temperature results in a decrease in the average Si-Si non-bonding distance and the negative thermal expansion observed.[1] J. S. O. Evans, T. A. Mary, A. W. Sleight and T. Vogt, *Science*, **272**, 90 (1996). [2] P. Tschaufeser and S. C. Parker, *J. Phys. Chem.*, **99**, 10600 (1995).

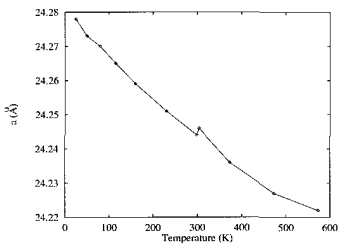

Figure 1. Cell parameter as a function of temperature for siliceous faujasite.

* We thank G. J. Ray, Amoco Chemical Company, for provision of the dealuminated zeolite-Y sample. This work was supported through DOE and through NSF grant No. DMR-9308530.

Structural Changes, Clustering and Photo-induced Phase Segregation in $Pr_{0.7}Ca_{0.3}MnO_3$ * — X7A

D. E. Cox (BNL), P. G. Radaelli (ILL, Grenoble), M. Marezio (MASPEC-CNR, Parma), and S.-W. Cheong (Lucent)

The structural properties of $Pr_{0.7}Ca_{0.3}MnO_3$ were studied by x-ray synchrotron and neutron powder diffraction as a function of temperature ($15 \leq T \leq 300$ K), and as a function of x-ray fluence at 15 and 20 K. The temperature evolution of the lattice parameters and of the superlattice reflections is consistent with the development of charge and orbital ordering below $T_{CO} \sim 180$ K, followed by antiferromagnetic ordering below $T_N \sim 140$ K. Below $T_C \sim 120$ K, the magnetic structure develops a ferromagnetic component along the a axis on the Mn ions. The observation in $Pr_{0.7}Ca_{0.3}MnO_3$ of significant lattice strain below T_{CO}, as well as the development of a ferromagnetic component to the magnetic structure at T_C, can be interpeted in terms of the presence of ferromagnetic clusters with an associated lattice distortion from the average structure. At low temperatures, exposure to the x-ray beam produces a phase segregation phenomenon, whereby the ferromagnetic droplets coalesce into larger aggregates. Further exposure results in a gradual melting of the charge-ordered phase and the formation of the ferromagnetic metallic phase recently reported by Kiryukhin *et al.* (Nature **386**, 813 (1997)). The ferromagnetic phase has a significantly smaller a lattice parameter and unit cell volume ($\Delta V/V \sim 0.4\%$) than that of the charge-ordered phase.

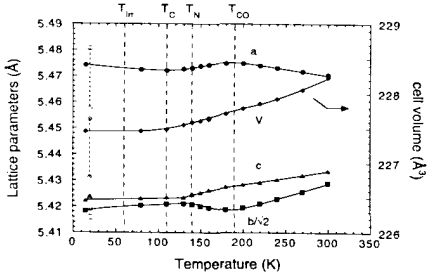

Figure 1. Lattice parameters and unit cell volume vs. temperature

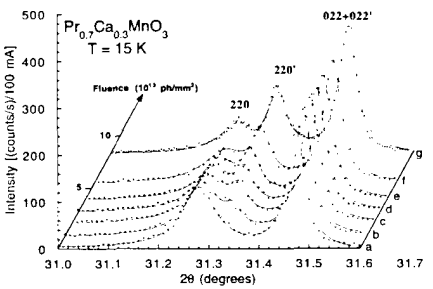

Figure 2. Evolution of the photo-induced ferromagnetic phase with x-ray fluence

* Work at BNL was supported by the U.S. Dept. of Energy, Division of Materials Sciences under Contract No. DE-AC02-76CH00016

High Pressure and Low Temperature Study of the LTO to LTT Phase Transition in $La_{(1.475)}Nd_{(0.4)}Sr_{(0.125)}CuO$ — X7A

M. Crawford, R. Harlow, E. McCarron (DuPont), S. Tozer (Florida State U.), and D. Cox (BNL)

We have continued our high-pressure, low-temperature x-ray diffraction studies of the LTO (B_{mab}) to LTT (P42/ncm) structural transition in doped lanthanum cuprates. $La_{(1.475)}Nd_{(0.4)}Sr_{(0.125)}CuO_4$ undergoes this structural transformation at a temperature of 80 K at ambient pressure, similar to the transition observed in $La_{(1.875)}Ba_{(0.125)}CuO_4$. Results from our previous study of the latter material had shown that a Pccn phase, intermediate to the LTO and LTT phases, was initially stabilized by pressure. The LTO to Pccn transition temperature was observed to decrease slowly with increasing pressure at pressures below 15 kbar, but at pressures greater than 30 kbar only the HTT phase exists from room temperature to 10 K. At pressures near 20 kbar the Pccn phase vanishes and only the HTT phase remains, but the small orthorhombicity in this pressure range precludes precise structural determinations. The suppression of the structural phase transitions under pressure generally correlates with previous reports that the Tc of this material increases under pressure, but only as high as 15 K at pressures of 20 - 25 kbar, where our structural data are consistent with the material still having Pccn symmetry. Since even the ambient pressure orthorhombicity of $La_{(1.875)}Ba_{(0.125)}CuO_4$ is relatively small (making these subtle structural transitions very difficult to follow), we decided to perform the same experiment using a compound with similar Tc characteristics, but with an orthorhombicity twice that of the Ba-doped material: $La_{(1.475)}Nd_{(0.4)}Sr_{(0.125)}CuO_4$. This study was performed using a Merrill-Bassett diamond anvil cell with a 4:1 methanol to ethanol pressure medium. The cell was pressurized to 16 kbar and the study was carried out using a focused monochromatic (0.6967) beam and a position- sensitive detector. Contrary to the results found for the Ba-doped sample, the LTO - LTT transition temperature of the Nd/Sr-doped material was found to increase with pressure. This result is consistent with the observation that the two materials have ambient pressure thermal expansion anomalies of opposite sign at the LTO - LTT transition. It would be interesting to develop a Landau theory for the the temperature/pressure phase diagrams of these materials to qualitatively account for this difference in pressure dependence. Superconducting Tc measurements for the Nd/Sr-doped phase under pressure are now underway.

Energy-dispersive Surface X-ray Scattering Study of Thin Ceria Overlayer on Zirconia *	X7A

W. Dmowski (U. of Pennsylvania)

We have studied the structure of ultra-thin CeO_2 overlayer on single crystals of Y stabilized cubic zirconia (ZrO_2) by energy dispersive surface x-ray scattering [1]. Three different crystallographic surfaces, (001), (011) and (111), were examined. In addition, we performed in-situ temperature study of a sample with (001) surface. We showed that on (001) oriented samples [1,2] CeO_2 formed an epitaxial thin film. The results obtained for the (011) and (111) oriented crystals are qualitatively the same. Fig. 1 shows two dimensional plot of the scattering intensity in the Q_x-Q_z plane. Q_y is offset by 0.05 $\AA^{-1}$ to avoid a strong Bragg peak and Q_x is almost parallel to the [-110] direction. The edge like feature at Q_x=3.4 $\AA^{-1}$ is a truncation rod of a zirconia (-220) reflection. The broad pattern centered at Q_x=3.3 $\AA^{-1}$ and extending well in Q_z corresponds to the (-220) reflection from the ceria overlayer. Depth profiling of Y and Zr fluorescence lines shows depletion of yttrium starting at depth 230 $\AA$ and then surface enrichment. We have studied the surface diffraction from the (001) sample with deposited cerium metal, in-situ, in the temperature range 100-800°C. At the temperature of 420°C we start to see weak diffraction from the (400) ceria peak at Q_x=4.6$\AA^{-1}$ which corresponds well to the ceria lattice constant. The lateral coherence length of the ceria film is only about 20 $\AA$ at this temperature. At 620°C the lateral coherence length is increased to 46 $\AA$. Finally after prolonged annealing above 700°C Ce diffuses into the bulk of the zirconia crystal and the (400) diffraction peak gradually disappears.

[1] W. Dmowski, T. Egami, R. Gorte and J. Vohs, Physica B 221 (1996) 420.
[2] W. Dmowski, S. Fu, T.Egami, R. Gorthe and J. Vohs. MRS , vol. 401, p. 115, (1996).

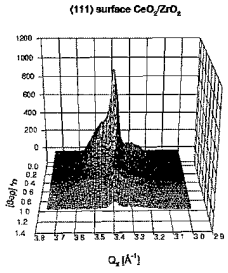

Figure 1. Diffracted intensity in Q_x-Q_z plane for (111) sample oriented with [-110] direction along the scattering vector near the (-220) reflection.

* This research was supported by the U.S. Dept. of Energy and the National Science Foundation through the Automotive Initiative Grant DE-FG02-96ER14682.A000.

X-Ray Diffraction of CMR Sample $La_{1.4}Sr_{1.6}Mn_2O_7$	X7A

W. Dmowski and T. Egami (U. of Pennsylvania)

We have examined powder diffraction of $La_{1.4}Sr_{1.6}Mn_2O_7$ samples. First sample was prepared using "powder" processing while the second one was grown as a single crystal and later crushed to make fine powder. These samples have been examined by neutron diffraction and showed different temperature dependence of lattice parameters. It was observed that metal-insulator transition temperature and charge doping levels were different. This suggested inhomogeneous distribution of Sr atoms such as preferential occupancy of La in (0,0,1/2) position. Since neutron scattering lengths for most elements are very similar we used x-ray diffraction to enhance scattering information from heavy elements. Experiment was done below the absorption edge of strontium in reflection geometry. Intensity was corrected for background and volume changes. We focused on low Q data since they are most sensitive to ordering. The results from GSAS refinement show that for "powder" sample minimum of R-factor is achieved for 0.6 occupancy of La in (0,0,1/2) site (complete disorder corresponds to 0.467). The refinement for "crystal" sample is more complex. The R-factor stays above 28% due to systematic deviations in intensities for (00L) reflection. This is illustrated in the Figure 1. This suggests that "crystal" sample is affected by stacking faults like intergrowths in this layered structure. The intergrowths are likely to localize charge reducing overall doping level. Due to poor R-factor, refinement is not sensitive to La ordering showing similar R-factors between 0.45 and 0.7 of La occupancy in (0,0,1/2) site.

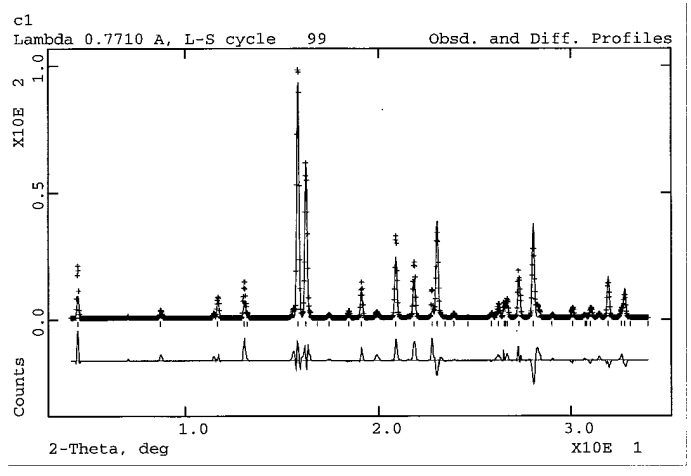

Figure 1. GSAS refinement of $La_{1.4}Sr_{1.6}Mn_2O_7$ powder. Sample was prepared by crushing single crystal sample.

The Crystal Structure of $Bi_4Au_2O_{14}$: The Use of a Siemens CCD Detector with Short-Wavelength Radiation	X17B1

R. Harlow (DuPont), J. Parise (SUNY at Stony Brook), J. Phillips and C. Campana (Siemens), and J. Hanson (BNL)

The determination of the structure of $Bi_4Au_2O_{14}$ presented two difficulties: absorption (mu for MoKa is approximately 1050 cm-1) and the presence of a superlattice which is 4x the sublattice. Three sets of data have been collected on crystals of this compound: with in-house MoKa radiation using a Siemens CCD and a Rigaku image-plate system, and with 0.185 A synchrotron radiation (where mu is reduced to approximately 30 cm-1) at beamline X17B1, also with a Siemens CCD. At this point, the subcell structure (tetragonal, a = 8.676 and c = 5.832 A, in space group P4212) has been solved and refined using the synchrotron data to an R value of 10.3% using 2094 reflections to a resolution of ca. 0.3 A. All of the atoms were refined with anisotropic thermal parameters, with special attention given to those of the oxygen atoms which are the presumable source of the superlattice. One of the oxygen atoms was found to be disordered over two sites: it is believed that this oxygen will be ordered in the supercell where the c-axis is doubled. This type of disorder was expected because the Bi site in the subcell contains a mixture of Bi^{+3} and Bi^{+5}. Presumably, the latter are also ordered in the supercell. The source for doubling the cell along the a-b diagonal has not yet been determined. Using the in-house data, only the heavy atoms could be refined with anisotropic thermal parameters and some of these ellipsoids were not very realistic. Also, the disorder of the one oxygen atom was not visible from the in-house data. Work continues on modelling the supercell structure, but the benefits of using the (almost) absorption-free data from the synchrotron/CCD combination are already clearly evident.

High Pressure Powder Diffraction Studies of Zeolite Na-A	X7A

J. A. Hriljac, I. Gameson and P. P. Edwards (U. Birmingham, UK)

Microporous solids, such as the aluminosilicate zeolites, are characterized by a large and regular pore system of molecular dimensions. They are used widely in several industrial applications including catalysis, ion-exchange, and gas separations. Surprisingly, their structural properties as a function of pressure appear to be mostly unexplored. The only literature reports are for silica sodalite to 1.28 GPa [1], ZSM-5 to 4.0 GPa [2], and scolecite (calcium natrolite) to 10 GPa.

In this work, the high pressure powder X-ray diffraction patterns of the sodium form of zeolite-A were examined. The sample was loaded in a diamond anvil cell with a small amount of NaCl and a ruby chip, and then a 4:1 methanol/ethanol solution added as a pressure transmitting medium. Pressures were measured using the ruby fluorescence technique. The beam line was configured with a sagitally focussing bent silicon (220) monochromator and a PSD. The wavelength was 0.6969(1) Åas determined via calibration against a silicon standard. Diffraction data were measure from *ca.* ambient pressure to 7.85 GPa.

A typical diffraction pattern is shown in Figure 1. Accurate peak positions were determined by the least-squares fitting of individual lines, and the values of the cubic lattice parameter were then determined by least-squares fitting of these values. A graph of the refined lattice parameter *vs.* pressure is shown in Figure 2. From these data a value for the bulk modulus of 57.5(26) GPa has been determined. Further details of the structural changes are difficult to determine from the limited quality data obtained, but these will be further investigated in future studies.

References

[1] K. Futterer, W. Depmeier, F. Altorfer, P. Behrens, and J. Felsch, *Z. Krist.*, **209**, 517 (1994).

[2] S. Y. Zhang, O. Talu, and D. T. Hayhurst, *J. Phys. Chem.*, **95**, 1722 (1991).

[3] X. Y. Liu, W. H. Su, Y. F. Wang, and X. D. Zhao, *J. Chem. Soc., Chem. Commun.*, 902 (1992).

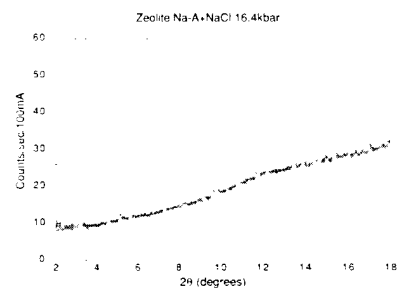

Figure 1. Diffraction Pattern of Na-A at 1.68 GPa

Figure 2. Lattice Constant vs. Pressure

Lattice Parameters and Phase Transitions in $La_{1-x}Sr_xMnO_3$ (x=0.12,0.17) *	X7A

T. Iglesias, D. E Cox, and G. Shirane (BNL), K. Hirota (Tohoku U.)

High-resolution powder data were collected from polycrystalline samples of $La_{1-x}Sr_xMnO_3$ (x = 0.12 and 0.17) obtained by carefully crushing small single crystals grown by the floating zone technique. In the case of the 0.17 sample, a structural transition from a rhombohedrally-distorted perovskite- like phase (R-3c symmetry) to an orthorhombically-distorted phase (Pnma symmetry) was observed below $\approx$ 320 K. The transformation was about 90% complete at 285 K, but a small amount of residual rhombohedral phase persisted down to 210 K. Only small discontinuities were observed in the lattice parameters and unit cell volumes.

The behavior of the 0.12 sample was extremely complex, with two coexisting orthorhombic phases at 300 K, one of which transformed first to a monoclinic phase at $\approx$ 295 K, and then to a triclinic phase at $\approx$ 140 K.

* Work at BNL was Supported by the U.S. Dept. Of Energy, Division of Materials Sciences, under Contract No. DE-AC02-76CH0016

In-situ Ion Exchange Using the Small Environmental Cell for Real Time Study: (SECRETS)	X7A

Y. Lee and J.B. Parise (SUNY at Stony Brook)

In-situ ion exchange experiments were performed on zeolite Na-Y(SRM2850) and clinoptilolite at the X7A beamline using the Small Environmental Cell for REal Time Study(SECRETS). A powdered sample of each material was placed in a 0.7mm capillary while exchange solutions flowed through the SECRETS apparatus. Data were taken by scanning a PSD with a 3° window in steps of 3° and counting times of 20 sec per step. Treatment of zeolite Na-Y with 0.1M solution of $CsNO_3$ showed changes in the relative intensities in the subsequent diffraction patterns which are indicative that ion exchange has occurred and no change was noted after 30 minutes. Similar experiments were undertaken with clinoptilolite powder and $Sr(NO_3)_2$ exchange solution. Detailed study of changes in relative intensities and cell parameters as a function of exchange level will reveal the kinetics of ion exchange for a particular exchange system. These studies are ongoing.

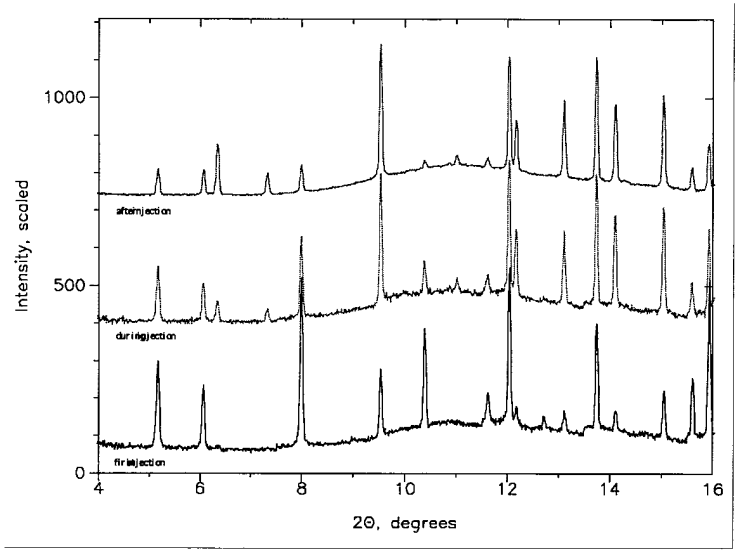

Figure 1. Three of the diffraction patterns taken in-situ while 0.1M of $CsNO_3$ exchange solution flows through the SECRET cell. Changes in the relative intensities of the peaks reveal ion exchange have occured and no more change is noted after 30 minutes (wavelength=0.790012).

Location of CF_3Cl in Partially-hydrated Maximum Aluminum Na,K-X type Zeolites	X7A

Y. Lee, J.B. Parise, and P. Norby (SUNY at Stony Brook)

Rietveld analysis using synchrotron x-ray powder diffraction data collected at 15 K at the X7A beamline reveals that CFC-13 (CF_3Cl; chlorotrifluoromethane) sorbed on Na,K-LSX binds through fluorine to sodium ions around the single 6-ring aperture. There are approximately 33.5 molecules of CFC-13 per unit cell, 4.2 per supercage or close to one CFC-13 molecule around each single 6-ring window. Interactions between individual CFC-13 molecules and extraframework Na atoms are typified by the interatomic distances; 2.49(2)Åfor F(1)-Na(3), and 2.93(4)Åfor F(3)-Na(3). The Na(2) and K(2) sites, which are separated by 0.897(21)Å, are not simultaneously occupied as in the case of K(1) and Na(1) which is close to each other by 2.022(26)Å, and have no interaction with the CF_3Cl molecules. This study reveals some of the structural details of the interactions of CFC-13 molecules with partially hydrated maximum Na,K-X zeolite. Further studies of materials with different loading levels of the chlorofluorocarbon, as a function of hydration level and with different exchangeable cations are required to characterize changes as a function of basicity of the zeolite framework and Lewis acidity of the extra framework cation. These studies are ongoing.

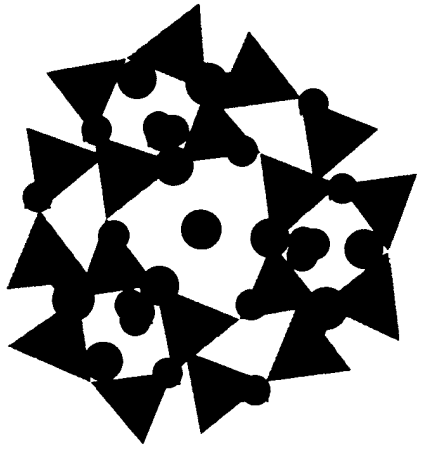

Figure 1. Graphic representation showing the refined position of CFC-13 molecules around the 6-ring window of the supercage. CFC-13 molecules and extraframework cations are represented as circles while Si and Al tetrahedra constitute the framework. The carbon atoms have been omitted for clarity.

Low Temperature X-ray Diffraction Study of $La_{2-x-y}Sr_xNd_yCuO_4$	X7A

A. R. Moodenbaugh, L. H. Lewis, D. E. Cox, and S. Soman (BNL)

The relationship between superconducting transition temperature (T_c) and the low temperature crystallographic phases in $La_{2-x}Ba_xCuO_4$ and $La_{2-x-y}Sr_xNd_yCuO_4$ has been studied for almost 10 years now. The occurrence of a low temperature tetragonal phase (LTT) is associated with a reduced T_c near the x=0.12 composition. However, the relationship is still not completely understood. For example, in the Nd-free system $La_{2-x}Sr_xCuO_4$ the diffraction pattern exhibits the orthorhombic structure (LTO1) which is asssociated with better superconducting properties. Yet T_c is reduced near the x=0.12 composition.

It is well established that this phase transitions (LTO1-LTT) is first order, and there is some temperature range over which the two phases coexist. We undertook a high resolution x-ray diffraction study of some of these materials to carefully monitor the development of the LTT phase as temperature is reduced. We find that in samples which transform to LTT, the LTT phase may begin to form up to 40 K above the acknowledged transformation temperature.

At the composition $La_{1.88}Sr_{0.12}CuO_4$ we studied the 020,022 (LTO1)region as a function of temperature. At low temperatures a two peak fit to the data does not adequately describe the diffraction. A broad third diffraction peak between the two major peaks improves the fit. This peak has a full width at half maximum about three times that of the LTO1 peak, and represents about 10% of the total diffraction at this angle.

While this third peak is relatively broad compared with the LTO1 peaks, its position and breadth are consistent with typical LTT diffraction peak widths. (The broad peaks in LTT probably represent an intrinsic inhomogeneity that has been documented using electron microscopy, both for microstructural and diffraction studies.) In our opinion, this x-ray diffraction data suggests a partial transformation of $La_{1.88}Sr_{0.12}CuO_4$ to the LTT phase.

High Pressure-High Temperature Synthesis of a Novel Perovskite $CaMnTi_2O_6$.	X7A

J.-H. Park and J.B. Parise (CHiPR, SUNY at Stony Brook)

In the investigation of the $CaTiO_3$-$MnTiO_3$ system, a new $CaMnTi_2O_6$ perovskite compound isomorphous with the $CaFeTi_2O_6$[1] was synthesized using a stoichiometric mixture of the $CaTiO_3$-perovskite and $MnTiO_3$-pyrophanite (JCPDS29-902). Polycrystalline and single crystal (10x10x20 μm^3) $CaMnTi_2O_6$ perovskite compound was prepared via high pressure-high temperature experiments under 14.5-15 GPa and 1200°C. Synchrotron powder X-ray diffraction data were collected using PSD[2] at the X7A beamline, NSLS. From the extinction conditions the unique space group $P4_2/nmc$ is found with cell parameters a=7.5339(5) and c=7.6027(6) Å. The structure was refined using $CaFeTi_2O_6$[1] as a starting model (Fig. 1). There are two Mn sites, (1) the one in a tetrahedral site and (2) the other in square planar configuration. Mn(2) prefers sites out of the plane along the [001] axis.

[1] K.Linenweber et al, J. Solid State Chem., 114, 277 (1994). [2] D. E. Cox et al., Aust. J. Phys., 41, 117 (1988); D. E. Cox, High resolution powder diffraction and structure determination, in Synchrotron Radiation Crystallography ed. P. Coppens, Academic Press: London (1992); G.C.Smith, Syn. Rad. News, 4, 24 (1991).

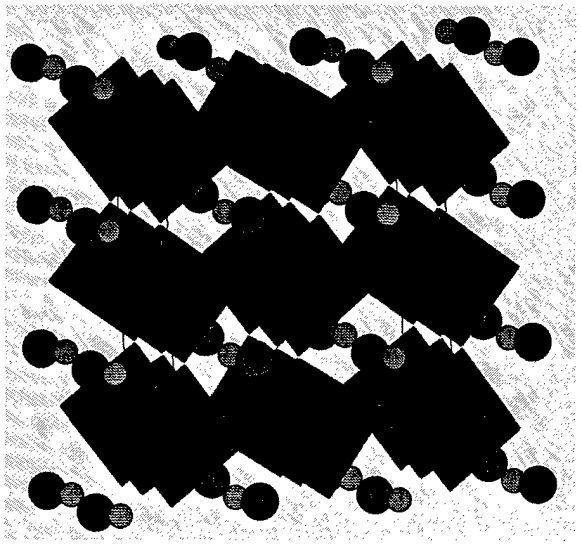

Figure 1. Projection of the structure of $CaMnTi_2O_6$ along [100]. The TiO_6units and Ca/Mn ions are represented by the octahedra and small/large circles.

Ab Initio Crystal Structure Solutions of Metal Phosphonatcs from Synchrotron Powder X-Ray Data	X7A

D.M. Poojary, D. Grohol, F. Gingl, and A. Clearfield (Texas A&M University)

In the September 1996 to present time span we have obtained three data sets at the X7A beamline of the National Synchroton Light Source. One of the data sets involved a drug that exists as two isomers. One is inactive and the other physiologically active. The initial data sets were obtained in house on our rotating anode unit and solved but the active isomer resisted complete solution. The problem was solved with the Synchrotron data . The active isomer has an open structure whereas in the inactive isomer the phenyl rings close in on the active site probably causing steric hinderence. We were not able to publish this study as the sponsor wants to maintain the information private. A second structure, $Zr_2PO_4(O_3PCH_2CH_2(Viologen)CH_2CH_2PO_3)X_3$, was solved entirely from synchrotron data. It has a complex porous structure, is photoactive and behaves as an anion exchanger, X^- being the exchangable ion [Chem. Mater. 8, 2243 (1996)]. The most recent data set is for $U2(O_3PCH_3)_2$. This compound luminesces whereas $UO_2(O_3PCH_2CL)_2$ does not. The quenching process and luminescence properties are under study. The structure solution is in progress.

Certification of Zeolite Standard Reference Materials — X7A

B.H. Toby and N. Khosrovani (NIST)

A group of industrial and academic researchers presented a proposal to NIST requesting that NIST certify and release a series of zeolite reference materials. The result was a decision to obtain three zeolite materials from industrial sources, Na-FAU (Y), Na-LTA and MFI to be certified as SRMs 2850, 2851 and 2852, respectively. Approximately eight additional zeolite materials will be released without certification as reference materials.

Synchrotron diffraction was selected as one of the principal methods for characterizing these materials with respect to the presence of impurity phases lattice parameters and sample-to-sample variations. Since most zeolites absorb large amounts of water and their water loadings change depending on the water partial pressure, care was taken to see that every sample was exposed to a uniform humidity level prior to sealing the sample into a capillary tube. Despite these precautions, larger than expected variations were seen in the obsevered lattice constants. It is not known if these variations are due to the samples being inhomogeneous or due to minor changes in water loading. Further work is planned to see if this can be determined.

Siting of the Structure Directing Agent in Zeolite CIT-1 — X7A

B.H. Toby, N. Khosrovani (NIST) and M. Davis (Caltech)

The zeolite CIT-1 was chosen for study because it can be synthesized nearly free of stacking faults using a particular structure directing agent (template) while similar organic molecules produce a related zeolite, but with up to 30% stacking faults. Crystallography combined with molecular mechanics are being used to study the interaction of the template with the zeolite. Synchrotron and neutron data were collected on samples of CIT-1, as synthesized (with template present) and calcined (without template) using the NIST BT-1 neutron powder diffractometer and the NSLS X7A x-ray powder diffractometer. For the neutron work, two materials were used, one where the amine methyl groups were deuterated and one non-deuterated.

Molecular modeling demonstrated three possible ways that the template can be accomodated in the CIT-1 pores. However, a combined Rietveld refinement of the neutron and synchrotron datasets demonstrated that only two of these orientations actually occur. The template molecules pack very snugly into the pore volume of the zeolite. We are currently investigating the energetics of this packing.

Direct Evidence of Charge Disproportionation in $CaFeO_3$ * | X7A

P.M. Woodward (BNL)

Mossbauer studies of stoichiometric $CaFeO_3$ show the presence of a single line at 300K which evolves into two magnetic hyperfine patterns of nearly equal intensity at 4K [1]. This has been interpreted as being due to $2Fe^{4+} \rightarrow Fe^{3+} + Fe^{5+}$ charge disproportionation. However, attempts to obtain direct crystallographic evidence of this charge disproportionation have not previously been successful. Observation of the charge disproportionation is difficult because the phase transformation involves only small shifts of the oxygen ions. Therefore, in an X-ray diffraction pattern the superstructure peaks are very weak. Neutron diffraction is more sensitive to the oxygen shifts, but interpretation is complicated by the presence of magnetic reflections.

Powder X-ray diffraction data was collected at 300K and 15K on a sample of $CaFeO_3$ synthesized under high oxygen pressure. The structure was refined at both temperatures using the Rietveld technique. At 300K the sample has the $GdFeO_3$ structure, space group Pnma and lattice constants a=5.3445Å, b=7.5292Å, c=5.3193Å. The Fe-O distances are 4x1.919(5)Å and 2x1.930(2)Å. At 15K weak superstructure reflections (the strongest superstructure reflection (110) has an intensity of 0.03% of the strongest peak (121) in the pattern) appear which are consistent with a rock salt ordering of Fe^{3+}/Fe^{5+}. The space group is $P2_1/n$ and the lattice constants are a=5.3100Å, b=5.3470Å, c=7.5185Å, β=90.058°. The Fe-O bond distances are 2x1.872(8)Å, 2x1.894(9)Å, 2x1.88(1)Å for Fe(1), and 2x1.962(8)Å, 2x1.975(9)Å, 2x1.96(1)Å for Fe(2).

[1] M. Takano, et al. *Mater. Res. Bull.* **12**, 923-928 (1977).

* This work was supported by the Division of Materials Sciences, U.S. Department of Energy, under contract No. DE-AC02-76CH00016.

Low Temperature Phase Transitions in $Nd_{0.5}Sr_{0.5}MnO_3$ * | X7A

P.M. Woodward, T. Vogt, D.E. Cox (BNL), C.N.R. Rao (Indian Institute of Science) and A.K. Cheetham (UCSB)

At room temperature $Nd_{0.5}Sr_{0.5}MnO_3$ is reported to be a paramagnetic insulator [1]. Upon cooling single crystals transform into a ferromagnetic metallic state near 250K, and then abruptly transform into an antiferromagnetic insulating state near 160K [1,3]. It is believed that the 250K transition is a consequence of double exchange interactions, while the 160K transition is driven by charge-ordering of Mn^{3+}/Mn^{4+} [1]. Neutron diffraction studies have shown the low temperature phase to have the CE-type antiferromagnetic structure, but no refinement of the crystal structure at low temperature has been carried out to confirm the presence of charge-ordering [3].

We have collected powder X-ray (beamline X7A at NSLS) and neutron (beamline BT1 at NIST) powder diffraction patterns on a ceramic sample of $Nd_{0.5}Sr_{0.5}MnO_3$, over the temperature range 15-300K. At room temperature the sample is single phase (HTO phase), space group Imma (a=5.4245Å, b=7.6226Å, c=5.4682Å) and Glazer tilt system $a^0b^-b^-$. This structure is in good agreement with earlier results [2]. As the sample is cooled a second phase appears between 225K and 200K (LTO1 phase), and a third phase near 150K (LTO2 phase). The LTO1 phase shows a contraction in *b* and an expansion in both *a* and *c* (a=5.4413Å, b=7.5262Å, c=5.4946Å, at 160K), with respect to the room temperature structure. This is thought to be a result of "orbital ordering" of the filled Mn $3d_{z^2}$ orbitals. The LTO2 phase has unit cell constants very similar to the LTO1 phase, but several superstructure reflections are present which can only be indexed by doubling the *a* axis (a=10.8776Å, b=7.5134Å, c=5.5069Å, at 15K). Combined Rietveld refinements of both the X-ray and neutron patterns (using breathing rigid body constraints) at 15K give Mn-O bond distances in the LTO2 phase (space group $P2_1/m$) which directly show Mn^{3+}/Mn^{4+} charge-ordering. Refinements of the neutron data show that the HTO phase is ferromagnetic below 250K, the LTO1 phase has an A-type antiferromagnetic structure, and the LTO2 phase has a CE-type antiferromagnetic structure. There is no indication of charge-ordering in the LTO1 phase.

[1] Kuwahara, et al., *Science* **270**, 173-177 (1996).
[2] Caignaert et al., *Solid State Commun.* **99**, 961-963 (1995).
[3] Kawano et al., *Phys. Rev. Lett.* **78**, 4253-4256 (1997).

* This work was supported by the Division of Materials Sciences, U.S. Department of Energy, under contract No. DE-AC02-76CH00016.

The Influence of Cation Size on the Structural Features of $Ln_{0.5}A_{0.5}MnO_3$ Perovskites at Room Temperature *	X7A

P.M. Woodward, T. Vogt, D.E. Cox (BNL), C.N.R. Rao (Indian Institute of Science) and A.K. Cheetham (UCSB)

Structure determinations have been carried out on samples of $Nd_{1/2}Sr_{1/2}MnO_3$, $Sm_{1/2}Sr_{1/2}MnO_3$, $Gd_{1/2}Sr_{1/2}MnO_3$, $Nd_{1/2}Ca_{1/2}MnO_3$, $Gd_{1/2}Ca_{1/2}MnO_3$, $La_{1/4}Nd_{1/4}Sr_{1/2}MnO_3$, and $Y_{1/2}Ca_{1/2}MnO_3$ at room temperature using high resolution synchrotron (beamline X7A at NSLS) and neutron (beamline BT1 at NIST) powder diffraction. The average Mn-O-Mn bond angles decrease as the average ionic radii of the Ln/A cations, $<r_A>$, decreases. This decrease is more rapid when A=Sr than when A=Ca. The average Mn-O distance increases steadily as $<r_A>$ decreases, indicating a reduction in the overall Mn-O bonding. Both findings are in contradiction to common assumptions made in the literature; that the Mn-O-Mn bond angles are dependent solely on the ionic radii of the Ln/A cations, and that the Mn-O bond distances are independent of the Ln/A cations. Both bond distance and bond angle trends lead to a decrease in the width of the σ^* and π^* bands as $<r_A>$ decreases, destabilizing the ferromagnetic metallic state.

Individual Mn-O bond distances show the onset of a cooperative Jahn-Teller distortion (formation of a large polaron) for $<r_A>$ values below 1.19Å. This effect is mirrored in the behavior of the lattice constants as $<r_A>$ decreases. Quantifying the octahedral tilt angles suggests an $a^-b^+a^- \rightarrow a^-b^0a^- \rightarrow a^-a^-a^-$ evolution of the tilt system in the $Ln_{1/2}Sr_{1/2}MnO_3$ series as $<r_A>$ increases. Relationships between the octahedral tilt anlges, the cooperative Jahn-Teller distortion and the lattice constants were also examined. It was found that in the Pnma setting (tilt system $a^-b^+a^-$) the c lattice constant was very sensitive to octahedral tilting, decreasing rapidly as the tilt angles increase, but relatively insensitive to the cooperative Jahn-Teller disortion. The other two lattice constants were found to be much less sensitive to the octahedral tilting distortion, but strongly dependent upon the Jahn-Teller distortion, with a increasing and b decreasing as the magnitude of the Jahn-Teller distortion increased.

* This work was supported by the Division of Materials Sciences, U.S. Department of Energy, under contract No. DE-AC02-76CH00016.

Structural Analyses of Stuffed Quartz Phases Along the $LiAlSiO_4$-SiO_2 Join	X7A

H. Xu, P.J. Heaney, D.M. Yates (Princeton U.), J. Liu (SUNYat Stony Brook), A. Navrotsky (Princeton U.) and R.C. Liebermann (SUNY at Stony Brook)

Stuffed quartz phases along the $LiAlSiO_4$-SiO_2 join are structural derivatives of quartz, in which tetrahedral Si^{4+} cations are replaced by Al^{3+} and the charge is balanced by the incorporation of Li^+ into the main channels of the structure [1]. This group of compounds is of considerable interest because of their superionic conductivity and near-zero thermal expansion [2,3].

We have investigated the phases with the compositions $Li_{1-x}Al_{1-x}Si_{1+x}O_4$, x = 0, 0.2, 0.33, 0.5 0.7, 0.9, by synchrotron powder X-ray diffraction with a linear position-sensitive detector. Rietveld analysis of unit cell parameters reveals two trend changes in a or c as a function of composition(x): With increasing silica content, a first remains approximately unchanged up to ~0.3 and then decreases with a slope change at ~0.8. In contrast, the cell parameter c first exhibits a linear decrease between x = 0 and ~0.3, remains roughly constant between x = ~0.3 and ~0.8, and decreases between x = ~0.8 and 1.0. Lattice changes at ~0.3 may be related to an Al/Si order-disorder transition. More specifically, the end member β-eucryptite has a completely ordered Al/Si configuration, but as Si substitution for Li+Al increases, this order is gradually lost and disappears at ~0.3. The slope change at ~0.8 probably results from a phase transition that is analogous to the α-β quartz transformation. In other words, for those silica-rich compositions, since there is not sufficient lithium to prop open the β-quartz structure, the aluminosilicate framework tends to collapse to the denser α-quartz modification. As the changes in a and c around ~0.3 cancel each other, there is no discontinuity present in the plot of cell-volume V vs. x up to x = ~0.8, implying a continuous nature of the order-disorder transition. However, the displacive transition at ~0.8 is evident in the V-x plot due to the different densities of the α- and β-quartz frameworks.

[1] Buerger, M.J. (1954) Am. Min., 39, 600-614. [2] Nagel, W. and Böhm, H. (1982) Sol. State Commun., 42, 625-631. [3] Beall, G.H. (1994) in Heaney, Prewitt and Gibbs (ed.), Reviews in Mineralogy, 29, MSA, Washington D.C., 469-505.

Time Resolved *In-Situ* Diffraction Studies of Intercalation Processes: Intercalation of 1,6-Hexanediamine in α-$Zr(HPO_4)_2 \cdot H_2O$. *	X7B

A. M. Krogh Andersen, E. Krogh Andersen, I. G. Krogh Andersen (Odense U., Denmark), P. Norby (SUNY at Stony Brook) and J. C. Hanson (BNL - Chemistry).

Casciola *et al.*[1] showed by batch titration that there exist three intercalates of 1,6-Hexanediamine (HeDA) in α-$Zr(HPO_4)_2 \cdot H_2O$ (α-ZrP), and they determined their composition. We report a continuation of studies of intercalation processes. The experiment was performed at 10° using an INEL CP120 detector. The sample was in a 0.5 mm quartz capillary. In the bottom of the capillary was a plug of quartz wool, then a loose plug of α-ZrP and another plug of quartz wool. A small amount of 10.85 *m* aqueous solution of HeDA was deposited 1-2 mm from the latter quartz plug. Diffractograms were recorded at 1 minute intervals. The intercalation process was started by pressing (4 Atm.) the solution into contact with the α-ZrP. Figure 1 shows a small part of the diffractograms as a 3-D representation, time on the z-axis. The peaks are (from the left):

a) 002 reflection of α-ZrP·HeDA·H_2O b) 002 reflection of α-ZrP·0.5HeDA·1.5H_2O c) 002 reflection of α-ZrP·0.2HeDA·2.5H_2O d) 002 reflection of α-ZrP + 004 reflection of α-ZrP·HeDA·H_2O. That the 002 reflection for the host material (d) does not disappear, is due to that the 004 reflection of α-ZrP·HeDA·H_2O has the same position.

The a and b axes of host and intercalates are nearly the same. From indexing we find: c=30.78(12) A for α-ZrP·HeDA·H_2O, c=25.60(8) A for α-ZrP·0.5HeDA·1.5H_2O, c=21.5 A for α-ZrP·0.2HeDA·2.5H_2O and c=15.461(2) A for α-ZrP.

[1] Casciola, M., Costantino, U., Di Croce, L., and Marmottini, F., *J. Incl. Phenom.* **6** (1988) 291-306.

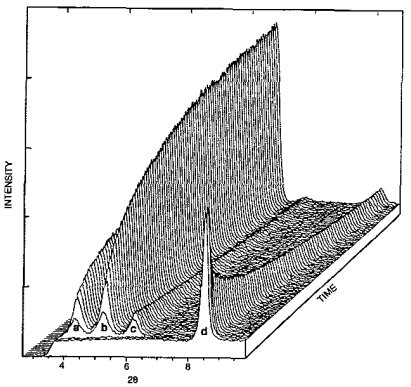

Figure 1. Powder diffraction patterns obtained during the intercalation at 10°C.

* This work was supported by US DOE (DE-AC02-76CH00016, Div. Chem. Sci., BES) and by the Danish Natural Science REsearch Council.

Time Resolved *In-Situ* Powder Diffraction Study of the Process: $LaMnO_{3.00} + La_{0.99}Mn_{1.01}O_{3.14} \rightarrow LaMnO_{3.07}$. *	X7B

A. M. Krogh Andersen, E. Krogh Andersen, I. G. Krogh Andersen (U. of Odense, Denmark), P. Norby (SUNY at Stony Brook) and J. C. Hanson (BNL- Chemistry).

A mixture of equal parts of $LaMnO_{3.00}$ and $La_{0.99}Mn_{1.01}O_{3.14}$ was sealed under vacuum in a 0.5 *mm* quartz capillary. The diffraction data were recorded with a INEL CPS120 detector, the recording time was 120 sec., and 10 sec. were used for data transfer. The sample was heated from 147-868°C in 3 hrs., kept at 868°C for 30 min. and cooled to 147°C.

Figure 1 shows a 3-D representation of diffractograms recorded during heating. Temperature on the z-axis. Diffractograms during cooling are not shown. In diffractogram 1 there are 3 peaks. Two of them, a and b, are the 220 and 004 reflections of the low temperature orthorhombic form of $LaMnO_{3.00}$. The peak marked with c is the 204 reflection of hexagonal $La_{0.99}Mn_{1.01}O_{3.14}$. At 584°C there is a phase transformation. The peaks of orthorhombic $LaMnO_{3.00}$ disappear and one new reflection 204 of hexagonal $LaMnO_{3.00}$ (marked with d) appears. At about 790°C the two peaks of the hexagonal material join as a result of oxidation of $LaMnO_{3.00}$ and reduction of $La_{0.99}Mn_{1.01}O_{3.14}$. At about 820°C the material is a single phase. After cooling to 147°C the material is still a single phase, but now orthorhombic. All the diffractograms can be indexed either as mixtures of two phases (orthorhombic and hexagonal), as mixtures of two hexagonal phases or as one single phase which is hexagonal at high temperature and orthorhombic at low temperature.

Table 1 gives the unit cell volumes of the phases during the heating procedure.

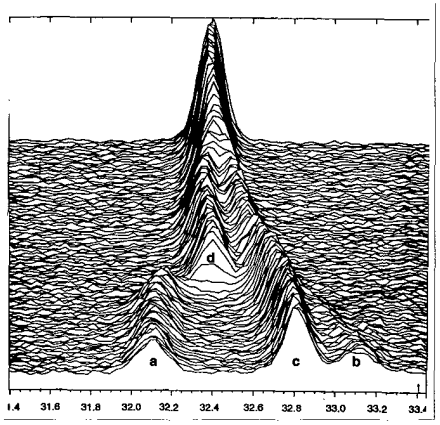

Figure 1.

Table 1. Unit cell volumes i Å^3 at some stages during the heating procedure.

Temperature °C	$LaMnO_{3.00}$	$La_{0.99}Mn_{1.01}O_{3.14}$
	Vol A^{-3}	Vol A^{-3}
147	364.98(5)	353.8(1)
584	365. 59(8)	359.0(1)
	Single phase	
	Vol A^{-3}	
868	367.19(5)	
147	361.44(9)	

Figure 2.

* This work was supported by US DOE (DE-AC02-76CH00016, Div. Chem. Sci., BES) and by the Danish Natural Science Research Council.

Temperature Resolved Diffraction: Lattice Constants and Phase Changes in Lanthanum Manganate	X7B

E. Krogh Andersen, I. G. Krogh Andersen (U. Odense, Denmark), P. Norby (SUNY at Stony Brook) and J. C. Hanson (BNL)

A 0.5 mm quartz capillary with a small amount of $LaMnO_{3.00}$ (prepared according to reference 1) was evacuated, sealed and heated from 25 to 900° during 4 hours and cooled again. Data were collected at beamline X7B using the position sensitive detector INEL CPS120. The wavelength was 1.1143 A and the 2θ range covered was 2-120°. The observed phase transitions orthorhombic - cubic - hexagonal are pictured in Figure 1 and Figure 2. Figure 1 shows the unit cell parameters versus temperature. Figure 2 shows the unit cell volumes during heating. The unit cell volumes are calculated using the program CELLKANT[2]. In order to compare the unit cells for the different phases the unit cell axes were transformed into pseudocubic axes. Similar experiments were performed with $La_{0.98}Sr_{0.02}MnO_{3.00}$, $La_{0.95}Sr_{0.05}MnO_{3.00}$, $La_{0.90}Sr_{0.10}MnO_{3.00}$ and $La_{0.85}Sr_{0.15}MnO_{3.00}$. These data have not yet been processed.

[1] I. G. Krogh Andersen, E. Krogh Andersen, P. Norby and E. Skou, *J. Solid State Chem.* 113, 1994, 320.

[2] N. O. Ersson: *Program CELLKANT*, Institute of Chemistry, Uppsala University, Sweden, 1981.

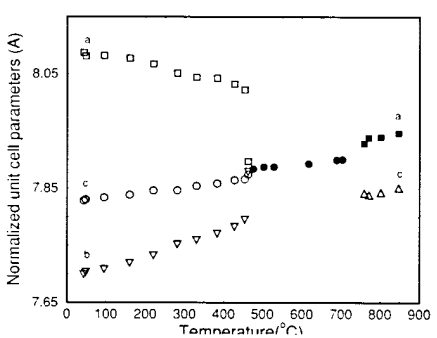

Figure 1. Normalized unit cell parameters versus temperature.

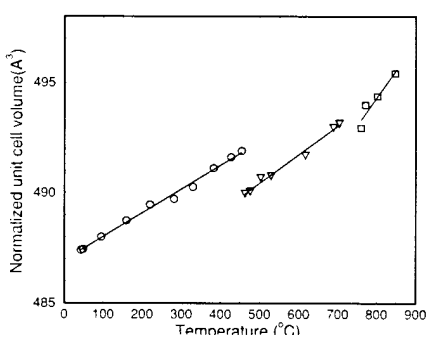

Figure 2. Normalized unit cell volume versus temperature. Circles: orthorhombic form. Triangles: cubic form. Squares: hexagonal form.

A Time-resolved X-ray Powder Diffraction Study of Phase Transformations in the Quinuclidine-Mn-Ge-S System	X7B

C.L Cahill, Y. Ko, J.B. Parise (SUNY at Stony Brook)

Benchtop syntheses in the quinuclidine-Mn-Ge-S system have yielded mixed phase products, both as a function of aging time and uptake of transition metal. A real time x-ray diffraction study was carried out to determine the synthetic pathway for the formation of these open framework materials.

A slurry of starting materials to produce Qui-MnGeS-1 (established nomenclature for synthetic framework materials: organic guest-framework elements-structure type number) was loaded into a glass capillary. The sample was heated to 180C over 90 minutes via an air heater, while hydrothermal conditions were maintained through an over pressure of N_2(g). Real time x-ray diffraction spectra were collected on the X7B Translating Imaging Plate System (TIPS), and the resulting time resolved plot is shown below. The amorphous starting slurry crystallizes to Qui-GeS-10 at approximately 100C. The structure of this material was previously determined and was known to contain no transition metal. At approximately 150C, the type 10 structure proceeds through an amorphous region before re-crystallizing as Qui-MnGeS-1. The type 1 structure was known previously as well, and contains a transition metal species in its framework. Thus a structural rearrangement driven the uptake of a transition metal has been observed.

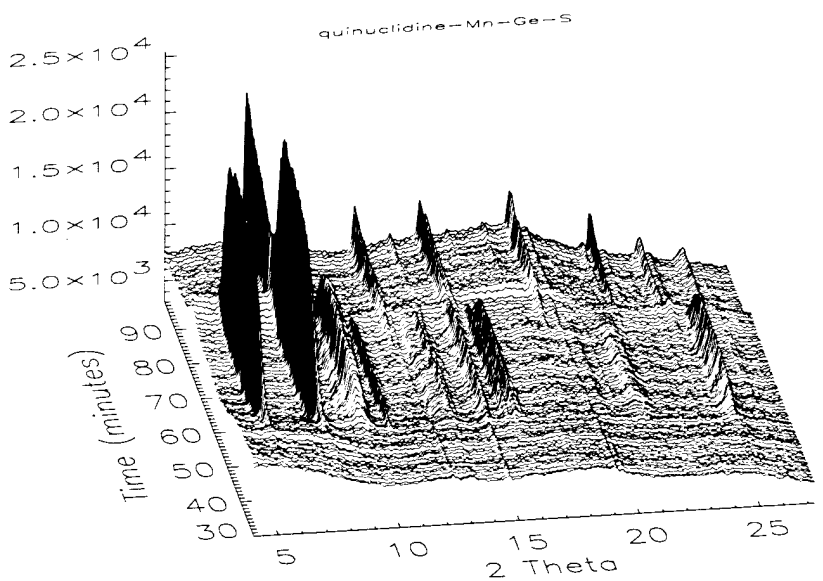

Figure 1.

in situ X-ray Powder Diffraction Study of the Synthesis of DEA-InS-SB1 and DEA-InS-SB2	X7B

C.L. Cahill, Y. Ko and J.B. Parise (SUNY at Stony Brook)

Single crystal x-ray structural analysis of materials in the diethylamine-In-S system [DEA-InS-SB1 and DEA-InS-SB2: (established nomenclature for synthetic framework materials: organic guest-framework elements-structure type number)] have been carried out previously. Their modes of formation or synthetic pathways however, have remained unclear. For example, reaction products in this system often contain mixed phases or vary as a function of aging time; octahedral and plate crystals were obtained depending on how long the reactants aged. A time resolved x-ray diffraction study was carried out in order to elucidate these problems. Elemental indium and elemental sulfur were loaded into a 0.7mm quartz capillary. The solids were then covered with a volume of diethylamine. The sample was heated to 250C over 180 minutes via an air heater, while hydrothermal conditions were maintained through an over pressure of N_2(g). Real time x-ray diffraction spectra were collected on the X7B Translating Imaging Plate System (TIPS), and the resulting time resolved plot is shown below. Powder diffraction spectra were calculated from the known crystal structures of DEA-InS-SB1 (3-D open framework) and DEA-InS-SB2 (2-D layered structure). From these, it was determined that the 3-dimensional structure forms first, and the rearranges to form the 2-dimensional structure.

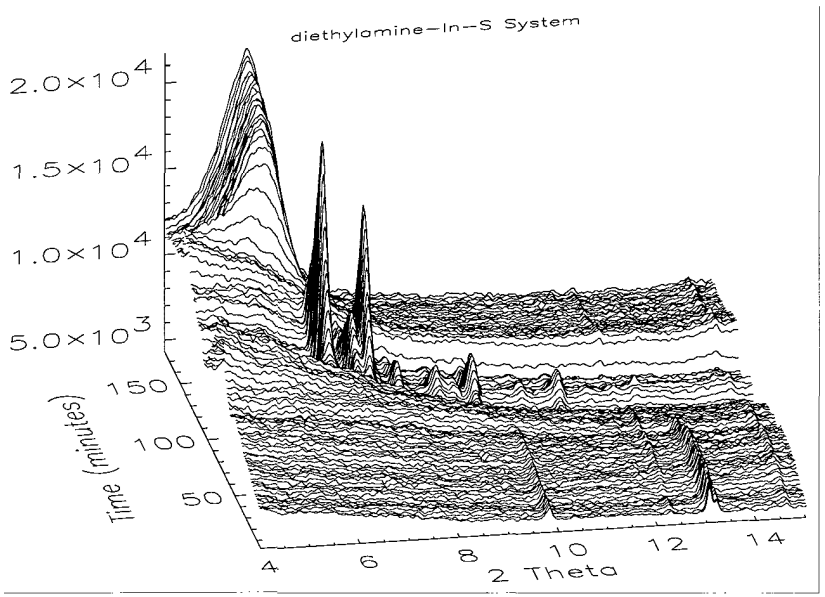

Figure 1.

A Small Environmental Cell for Real Time Studies (SECReTS)	X7B

C.L. Cahill, P. Norby, C. Koleda, J.B. Parise (SUNY at Stony Brook)

We describe here the development of a micro-reaction cell for in- situ powder diffraction studies which can be used for hydrothermal titration, ion exchange, hydrothermal precipitation reactions and to investigate solid/gas phase interactions in real time. The design of the reaction cell is shown in figure 1. Reactions take place in a 1 mm quartz glass capillary (A) which is mounted in a Swagelock tee (B) using a Vespel ferrule. Through the connected tube (C), a pressure can be applied to the surface of the reaction mixture in the capillary. Injection takes place through a 0.3 mm quartz glass capillary (D), which goes through the tee and into the 1 mm capillary. This 0.3 mm capillary is mounted between a Swagelock elbow and the tee with Vespel ferrules, all of which are mounted on a modified goniometer head (F). Injection under pressure through the elbow (E) is possible via a gas chromatography syringe (not shown) mounted in an aluminum holder. A screw connected to the piston of the syringe ensures pressurization. By turning the screw, the piston is depressed and a controlled volume can be injected into the 1 mm capillary through the 0.3 mm capillary. Alternatively, the position of the sample capillary (A) can be plugged, and the assembly extended to expose the injection capillary location to the X-ray beam. Ports (G) and (C) then become supply and exhaust lines respectively for flow-through ion-exchange experiments or solid/gas phase reactions. As a demonstration experiment the precipitation of $BaSO_4$ was studied using the micro reaction injection cell. The experiment was performed at the Chemistry beam line X7B. Time resolved powder diffraction data were collected (λ=1.284) using the Translating Imaging Plate (TIP) camera . The syringe and connecting tube were filled with a saturated Na_2SO_4 solution, and a 0.3mm capillary was mounted between the inner and outer fitting extending approximately 20 mm out from the outer tee. The Swagelock elbow and the capillary were filled with the Na_2SO_4 solution, and the syringe pulled back so that a 2 mm air bubble was formed at the end of the capillary. This prevented contact between the two solutions prior to the injection. A 1 mm capillary was filled with a saturated $BaCl_2$ solution, and was mounted in the outer ferrule. The cell was mounted on the diffractometer so that the X-ray beam was hitting the end of the small capillary, and an oscillation of approximately 45 was used to ensure randomization of the crystallites in the beam.

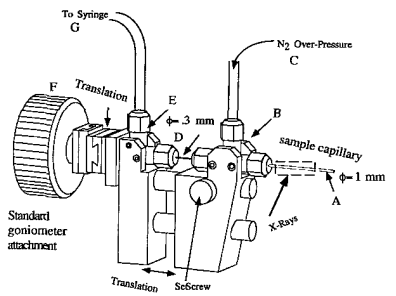

Figure 1.

Reaction Kinetics of the Crystallization of MnAPO-5(AFI) and ZnAPO-47 (CHA) *	X7B

A. Noerlund Christensen (Aarhus U.), T. R. Jensen (U. of Odense), P. Norby (SUNY at Stony Brook), J. Hanson (BNL)

Synchrotron X-ray powder diffraction was used for *in-situ* studies of the crystallization of microporous aluminophosphates and of *Me*-substituted aluminophosphates. The reaction mixtures for the crystallization experiments were gels containing one of the templates, 2-diethylaminoethanol, di-n-propylamine, triethylamine or tripropylamine. The identified reaction products were, $AlPO_4$ (tridymite type), APO-5 (AFI), APO-11 (AEL), MgAPO-5 (AFI), MnAPO-5 (AFI), CoAPO-5 (AFI), ZnAPO-39 (ATN), and ZnAPO-47 (CHA).

The reaction kinetics of the crystallization of MnAPO-5 (AFI) and ZnAPO-47 (CHA) were investigated using isothermal *in-situ* synchrotron X-ray powder diffraction data. The gels were mounted in quartz capillaries with an external pressure up to 25 atm and then the temperature was rapidly raised to the isothermal temperature with a stream of hot air. Time-resolved powder diffraction patterns were measured with a translating image plate detector. Three reflections in each powder pattern were integrated for calculation of crystallization curves. The crystallisation curves of MnAPO-5 formation could be modeled by a first order expression, as shown in Figure 1. Rate constants of the crystal growth under hydrothermal conditions were extracted and allowed calculation of the apparent activation energy. The Arrhenius plot is shown in Figure 2 giving an apparent activation energy of, E_a = 81(6)kJ/mol, for the crystal growth of MnAPO-5. The crystallisation of ZnAPO-47 was more complex and will be further investigated.

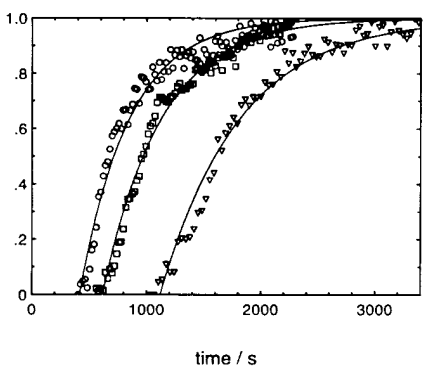

Figure 1. Calculated and observed crystallization curves of MnAPO-5. at 146, 141 and 136°C.

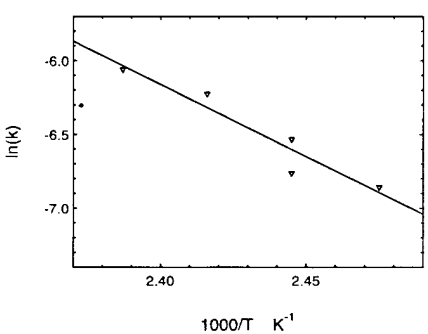

Figure 2. Arrhenius plot

* Supported by DOE BES contract DE-AC02-76CH00016 and Danish Natural Science Research Council.

HFC and HCFC Reactivity and Structure Characterization on Cation Exchanged Faujasites	X7B

M.F. Ciraolo, P. Norby, C.P. Grey (SUNY at Stony Brook), J.C. Hanson (BNL-Chemistry), and D.R. Corbin (Dupont)

Chlorofluorocarbons (CFCs) are believed to be major contributors to the seasonal ozone depletion over Antartica. The synthesis of environmentally friendly hydrofluorocarbons (HFCs) are much more complex than that of the CFC refrigerants since they involve many more steps and unwanted impurities are often produced. Hydrochlorofluorocarbons (HCFCs) are used as temporary replacements for CFCs since only small amounts reach the ozone in the stratosphere. Basic and acidic molecular sieves have been suggested as materials for separating and trapping mixtures of fluorocarbons to remove impurities formed during their synthesis. We have been investigating a series of cation exchanged faujasites(Figure 1) with HCFC-124a(CF_2HCF_2Cl) and HFC-134(CF_2HCF_2H) to determine some of the interactions that are responsible for their adsorption and catalytic properties.

Time resolved diffraction studies were carried out with an image plate detector(IP) to monitor changes as a function of time and temperature. Figure 2 shows the *in-situ* adsorption of HFC-134 on NaX at a partial pressure of 90 Torr. Upon adsorption there is a dramatic decrease in the intensity of the 111 reflection as the HFC is adsorbed in the supercage. Adsorption/desorption cycles were performed with different HFC gases, and by varying the HFC partial pressure, the adsorption temperature and the zeolite.

NaX, RbX and ZnX loaded with HCFC-124a have been studied with both solid state NMR and powder diffraction. Using the IP, *in-situ* high and low temperature studies of bare and preloaded zeolites were performed. Samples were prepared by first dehydrating the zeolites under vacuum at 450°C for 24 hours. Gas adsorption was then carried out with a calibrated vacuum system. Samples were packed in capillaries under dry nitrogen and sealed. Using Rietveld analysis, structures of the bare zeolites have been refined and agree well with NMR data. In order to rationalize the process by which catalytic activity occurs inside the pores an understanding of the binding must first be obtained. We have, therefore, begun the refinement of NaX loaded with HCFC-124a. The preliminary model shows that the cation positions and occupancies do not remain constant. The sodium cations in the supercage move to bind more effectively to the HCFC molecule upon adsorption.

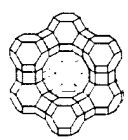

Figure 1. Faujasite framework showing large supercage surrounded by smaller sodalite units.

Figure 2. *In-situ* adsorption of HFC-134 on NaX.

Cation Migration in Zeolites: An *In Situ* Powder Diffraction and MAS NMR Study of the Structure of Zeolite Cs(Na)Y During Dehydration *	X7B

C. P. Grey, P. Norby, F. I. Poshni (SUNY at Stony Brook), A. F. Gualtieri (Modena IT), J. Hanson (BNL)

A knowledge of the positions of the extra-framework cations is fundamental to the understanding of the adsorption and catalytic properties of cation-exchanged zeolites. This is particularly important in the case of zeolites where only partial cation exchange is possible. We have used in-situ synchrotron X-ray powder diffraction and ^{133}Cs MAS NMR to investigate the cation migration and ordering in samples of cesium exchanged zeolite NaY, as a function of temperature, cesium cation exchange level, and during dehydration.1 Figure 1 shows the diffraction pattern collected from a sample of $Na_{18}Cs_{38}Si_{139}Al_{53}O_{384}$ while ramping the temperature (under vacuum) from 90 - 500 °C over 5 hours. The temperature was then held at 500°C for a further 3 hours. Significant changes are initially observed as water is removed; further changes are seen above 300 °C (250 min.) which are predominantly a consequence of the cesium-ion migrations. Rietveld refinement of these time-resolved diffraction patterns was performed, and revealed the temperatures at which the different cation migrations occur. Initially (above 180 °C), sodium cations in the site I' positions in the sodalite cages migrate into the double six rings. This is followed by a migration of the cesium cations, originally only present in the supercages, into the sodalite cages. Migration of sodalite cage sodium cations to the supercages occurs above 300 °C.

Cation positions in both the partially dehydrated and dehydrated material were also observed to be highly sensitive to temperature: at high temperatures, equal numbers of cesium cations were found in the site III' and site II positions in the supercages, while at temperatures close to room temperature, the cesium cations are almost all ordered on site II.

Thus in conclusion, partially exchanged CsY, dehydrated above 300°C, will contain sodium cations in the supercage sites which are, therefore, accessible for gas binding. In addition, the occupancies of the different supercage sites are highly temperature dependent, and the room temperature structure cannot necessarily be assumed to be an accurate model for the high temperature structure.

1. P. Norby, F.I. Poshni, A.F. Gualtieri, J.C. Hanson, and C.P. Grey, submitted to J. Phys. Chem.

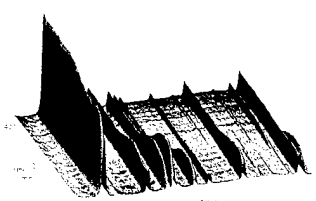

Figure 1. The X-ray powder pattern of Cs(Na)Y during dehydration.

* Support from the NSF through an intra-agency transfer to the US DOE BES.

In situ XRPD Study of the Crystallization of Zeolites from Natural Halloysite *	X7B

A.F. Gualtieri (U. of Modena, Italy), P. Norby (SUNY at Stony Brook), and J.C. Hanson (BNL)

In our previous work at X7B the mechanism of hydrothermal synthesis of zeolite NaA and hydroxysodalite in solution has been investigated (Gualtieri et al., 1997a,b). The precursors utilized for the synthesis experiments were an orderered and a disordered kaolinites activated at 600°C and 800°C, respectively. The results indicate an autocatalytic mechanism for the crystallization of both zeolites species, and dependence upon the thermal history and not upon the degree of disorder (the reaction is much faster from metakaolinite, the precursor activated at 600°C). Since zeolites formed from kaolinite have the same Si:Al ratio (1:1) of the precursor, we are interested in the study of the crystallization process using a precursor with a different Si:Al ratio. A natural halloysite $[Al_2(OH)_4Si_2O_5nH_2O]$ interdispersed in an amorphous silica matrix has been selected. The Si:Al ratio is 4. The sample was activated at 600°C for 5 h and the syntheses were carried out in isothermal mode in the range 70-150°C using a 4M NaOH solution with s:l=1:5. Preliminary data shows that three different zeolites are formed: NaX $[Na_{88}Al_{88}Si_{104}O_{384}16H_{220}O]$ crystallizes first at lower isothermal T and for shorter times, and is progressively replaced by NaP $[Na_7Al_7Si_9O_{32}17H_2O]$ which in turn is replaced by analcime $[Na_{16}Al_{16}Si_{32}O_{96}16H_2O]$ at higher isothermal T and for longer times. The Ostwald's rule is perfectly fulfilled. It is interesting to note that the Si:Al ratio is progressively changing in the forming zeolite as a function of T (from 1.2 in NaX to 1.3 in NaP and finally to 2 in analcime). The analysis of the data is still in progress.

Gualtieri A., Norby P., Artioli G., Hanson J. (1997a) Phys. Chem. Mynerals 24:191-199.

Gualtieri A., Norby P., Artioli G., Hanson J. (1997b) Microporous Materials 9:189-201.

* DOE BES Contract DE-AC02-76CH00016

Preliminary X-ray Reflectivity Study of Interdiffusion in Quantum Well Structures

X7B

S. A. Holt, A.S. Brown (Australian National U.) and D.C. Creagh (U. of Canberra)

The properties of quantum well (QW) devices structures, e.g. lasing wavelength, are strongly dependant upon the interface properties of the structure. This work is at the beginning of a project using x-ray reflectivity to study the interface structure of QW devices. To this end we have performed x-ray reflectivity (XRR) on model structures to study the effects of inderdiffusion on the interface structure, in addition we are also studying the diffusion of defects introduced by anodic oxidation of the capping layer.

Data analysis and modelling are still in progress, however a small subset of the results obtained is shown below. Figure 1 shows the XRR profile from an as-produced sample compared with that from the anodically oxidised equivalent. It is apparent that the structure of the capping layer is quite different as the fine fringe period (due to the total device thickness) has been radically altered. The long period (buried barrier layer) though has remained unchanged by the surface treatment. Rapid thermal annealing at 900°C completely destroyed the fringe structure in comparable samples. In order to highlight different aspects of the sample structure we also recorded XRR profiles close to and far from the gallium edge (1.198 and 0.9991 Å respectively). The effect of this "contrast variation" on the reflectivity profile of the oxidised sample can be seen in Figure 2. As expected the fringe periods are unaffected but the fringe amplitude (related to the scattering length density difference between the layers) has been modified. At the longer wavelength the effective number of electrons of the gallium is reduced, enhancing the contrast of the gallium rich barrier layer.

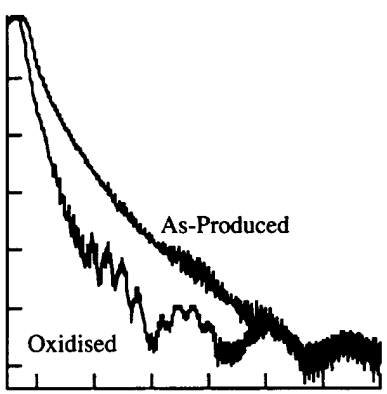

Figure 1. Reflectivity of as-produced and oxidised sample. Maximum Q_z = 0.35 $Å^{-1}$.

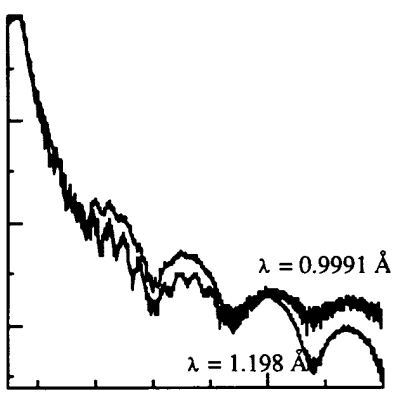

Figure 2. Reflectivity of oxidised sample at two wavelengths. Maximum Q_z = 0.35 $Å^{-1}$.

The Low Temperature Structures of $Tl_6(AlSiO_4)_6$ and $Ag_6(AlSiO_4)_6$ from Image Plate Powder Diffraction Data

X7B

B. B. Iversen, S. Latturner, C. Brown, N. Blake, G.D. Stucky (U. of California at Santa Barbara) and P. Norby and J. Hanson (BNL)

Aluminosilicate sodalites of the general composition $M_{6+y}(AlSiO_4)_6(X)_{yn}H_2O$ form model compounds for more complicated zeolite structures. They consist of space filling polyhedra (beta-cages), formed by a network of alternating, corner-sharing SiO_4 and AlO_4 tetrahedra [1]. The M^+ ions, which compensate for the negative charge of the framework, are located inside the beta-cages together with possible anions and neutral water molecules. The ions serve as spacers preventing the open framework from collapsing. Depending on the exact nature of the cage filling ions and water molecules, the framework can adjust itself in the form of a unit cell reduction, a so-called "partial collapse" [2]. We report here low temperature structures of two dry sodalites, Tl6$(AlSiO_4)_6$ and $Ag_6(AlSiO_4)_6$, based on synchrotron radiation powder diffraction data. In both structures sta- tistical disorder of the six metal atoms distributed over 8 cubic positions crea- tes a pseudo-cubic structure. The data were collected on 200x400 mm Fuji IP's which were scanned off-line using a BAS2000 scanner. Detailed description of the experimental setup at beam line X7B for IP powder diffraction measurements were reported by Norby [3]. In Figure 1 experimental details are shown and in Figure 2 preliminary structural results are given. Some reservation remain about the results for $Tl_6(AlSiO_4)_6$ even though the refinement residuals are very low. For this structure considerable changes in Si-O and Al-O bond lengths are observed, which are very unusual for zeolites. This could possibly be due to a spacegroup error, and work is in pro- gress to clarify this aspect.

[1] G. Engelhardt, J. felsche, P. Sieger, J. Am. Chem. Soc., 1992, 114, 1173-1182 [2] W. Depmeier, Acta Crystallogr. Sect B, 1984, 40, 185-191 [3] P. Norby, J. Appl. Crystallogr., 1997, 30, 21-30

Table 1. Crystallographic data and experimental details.

	$Tl_6(AlSiO_4)_6$	$Ag_6(AlSiO_4)_6$
Temperature / K	100(5)	100(5), 100(5)
Wavelength / Å	0.9341	0.9341, 1.4879
Sample container	Evacuated quartz capilary	Evacuated quartz capilary
Exposure time / min	60	60, 120
Step scan increment (Δ2θ) / °	0.01	0.01, 0.01
Sample to detector distance / mm	218.3	218.3, 365.2
Space group	P-43n (?)	P-43n
a / Å	8.9653(9)	9.1189(9)
Pattern range / °	6 - 57	6 -55, 10-35
No. observations	4948	4369, 2266
No. structural parameters	9	9
No. profile parameters	9	11, 1
No. background parameters	10	8, 7
R_{wp}	0.025	0.048
R_p	0.019	0.037

Figure 1. Crystallographic data and experimental details

Table 2. Bond lengths and angles.

	$Tl_6[AlSiO_4]_6$	$Ag_6[AlSiO_4]_6$
Temperature	**100 K**	**100 K**
Si - O	1.52(1)	1.64(2)
Al - O	1.87(2)	1.70(2)
M- O	2.62(6)	2.36(4)
O - Si - O	107.4(3)	108.9(1)
	114.4(6)	110.6(3)
O - Al - O	109.7(2)	109.3(1)
	109.0(4)	109.9(3)
Al - O - Si	138.3(4)	149.9(2)

Figure 2. Bond lengths and angles

The Structure and Dynamics of Sodium Sodalite as a Function of Temperature	X7B

B. B. Iversen, S. Latturner, C. Brown, N. Blake, G. D. Stucky (U. of California @ Santa Barbara), P. Norby, and J. Hanson (BNL)

The high temperature structure (T=675K) of dry sodium sodalite, $Na_6[AlSiO_4]_6$, was reported previously by Felsche et al [1] based on conventional powder diffraction data. In the high T phase statistical disorder of the six metal atoms distributed over 8 cubic positions create a pseudo-cubic structure with spacegroup P-43n. However as the temperature is lowered an ordering of the sodium atoms takes place leading to one or more phase transitions. In order to solve this challenging structural problem we have measured temperature resolved powder diffraction data in the range 100 - 650 K. As can be seen from Figure 1 the structural changes are complex and the spectra contain many subtle features. The cubic peaks move to higher theta values in the low temperature regime indicating a contraction of the framework with decreasing temperature. Furthermore, numerous well resolved superstructure peaks are present in the low T spectra. Work is in progress to establish the correct spacegroup for the low temperature phase and carry out Rietveld refinements as a function of temperature. This will provide detailed information about the dynamics of metals atoms suspended in a zeolite cage. To assist in the interpretation of the results and to gain insight into the catalytic behaviour of metal atoms in zeolites, ab-initio quantum mechanical calculations are also being carried out on the system [2].

[1] J. Felsche, S. Luger, C. Baerlocher, Zeolites, 1986, 6, 367-372.
[2] N. Blake, V. I. Srdanov, G. D. Stucky, H. Metiu, J. Phys. Chem., 1995, 99, 2127-2133.

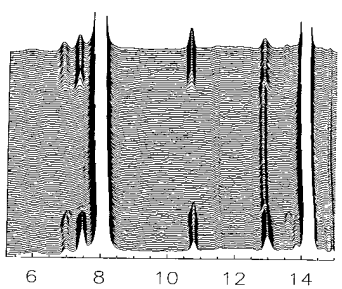

Figure 1. Temperature resolved diffraction pattern of $Na_6[AlSiO_4]_6$ in the low order region. The x-axes depict 2theta and the y-axes the uncalibrated temperature starting at 298 K going to 650 K and returning to 298 K. The temperature scale is non-linear because of a waiting period at the turning point.

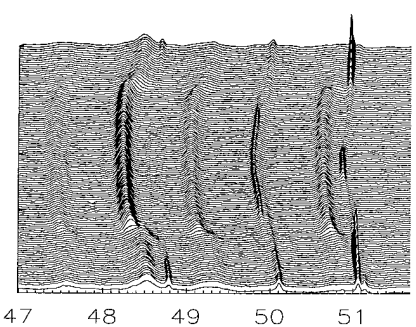

Figure 2. Temperature resolved diffraction pattern of $Na_6[AlSiO_4]_6$ in the high order region. Axes as in Fig. 1.

Structural Origin of the Remarkable Mechanical Properties of Prunus Serrula Bark	X7B

B. B. Iversen, C. Zaremba, X. Xu, F. Wudl, G. D. Stucky, (U. of California)

The bark of Prunus serrula is a natural composite plastic film with remarkable anisotropic mechanical properties. The bark is as strong as Mylar [poly(ethylene-terephthalate)] and as tough as one of the strongest man-made films, Kapton [poly(4,4'-diaminophenyl ether pyromellitamide)]. In a recent communication Xu et al [1] reported detailed mechanical measurements characterising its proper- ties. With the hope of gaining insight into the structural origin of the remark- able mechanical properties we have carried out low temperature (100(5)K) fiber diffraction measurements using the X7B image plate setup. The bark has a low crystallinity, which however can be increased by either stretching and heating the bark or by chemical treatment, see Figure 1. In the treated film not only does the intensity of the inner ring concentrate into fairly discrete peaks, but also a strong new peak appears at a lower d-spacing. In the high order region of the diffraction patterns weaker peaks appear with significant intensity, which are not observable in the untreated sample. Such details were not revealed in diffraction measurements using conventional X-rays and a Siemens SMART ccd de- tector. We are currently analysing the synchrotron patterns with the CCP13 fiber diffraction software [2]. From SEM photos it is clear that the bark consists of 10x10x100 micron rectangular cells packed with their long dimension along the mechanically strong direction of the film. The diffraction patterns reveal that the fiber axis of the system is perpendicular to this direction. It is hoped that the patterns will allow us to establish which forms of cellulose are present in the bark. This may provide an explanation for the unusual properties of this material.

[1] X. Xu, E. Schneider, A. T. Chien, F. Wudl, Chem Mat, 1997, submitted
[2] CCP13 Fiber Diffraction Programs, CCLRC Daresbury Laboratory, Keckwick Lane, Daresbury, Warrington, WA4 4AD, UK

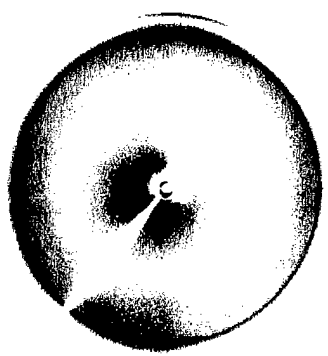

Figure 1. Diffraction patterns of an untreated sample of Prunus serrula bark.Only the high intensity low order region is shown.

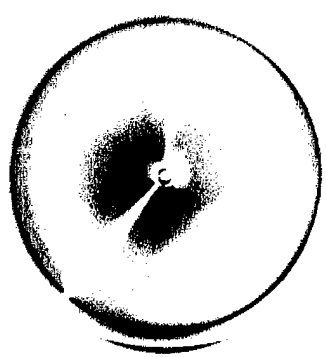

Figure 2. Diffraction patterns of a heated and chemically treated sample of Prunus serrula bark. Only the high intensity low order region is shown.

In-situ Studies of Ethylene Sorption in $CuAlCl_4$ * | X7B

H. Liu, M.F. Ciraolo, C.P. Grey (SUNY at Stony Brook), J. Hanson (BNL), J. Martin and R. Sullivan (NC State)

We have been studying a new class of $CuAlCl_4$ molecular sieves synthesized in one of our laboratories[1] that undergo a phase change on sorption of ethylene and CO. We are able to expose materials to controlled partial pressures of gas and monitor the resultant phase changes (Figure 1) with real-time X-ray diffraction methods. Both $\alpha - CuAlCl_4$[2] and $\beta - CuAlCl_4$ contain large Van der Waals channels which are thought to be important in the reversible absorption of small gasses. As this time, the structure of the material formed on gas loading has not been determined, but must involve a significant rearrangement and opening up of the copper aluminum chloride framework to allow gas molecules to diffuse inside. Use of controlled gas pressures allows to address questions such as: what partial pressure of ethylene is required to force open the structure (and cause the phase change)? The kinetics of the sorption can then be monitored as a function of pressure.

1. J.D. Martin, B.R. Leafblad, R.M. Sullivan, and P.D. Boyle, submitted to Inorg. Chem.

2. K. Hildebrandt, P.G. Jones, E. Schwarzmann, G.M. Sheldrick, Z. Naturforsch, 37b, 1129 (1982).

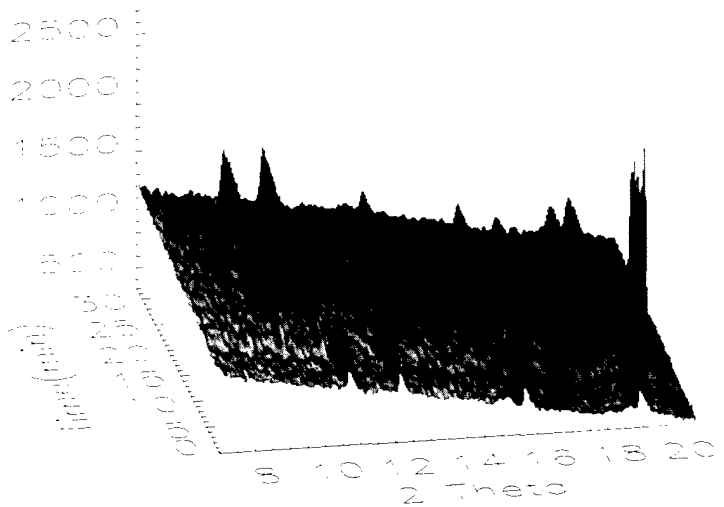

Figure 1. *In-situ* Sorption of ethylene in $\alpha CuAlCl_4$ (Ethylene pressure = 10 psi).

* Thanks to NSF (DMRand CHE) and US DOE BES.

In situ Diffraction Studies of the Akaganeite-hematite Reaction * | X7B

K. Nielsen, K. Stahl (DTU), J.C. Hanson, P. Norby (BNL) J.Z. Jiang (DTU) and J. van Lanschot (School of Conservation)

Akaganeite $FeO_{1-x}(OH)_{1-x}Cl_xyH_2O$, is a commonly encountered corrosion product of iron. This compound is only formed and is only stable in the presence of chloride ions. In the absence of chloride ions, iron is stabilized to prevent further corrosion. In akaganeite the chloride ions are, together with water molecules, enclosed in channels in the structure, and may be released by washing, ion exchange or heating. When heated to temperatures as low as 425 K, akaganeite releases hydrochloric acid, and the transformation to hematite, Fe_2O_3, starts to take place. In order to obtain information on the mechanism of hydrochloric acid release and to obtain a better understanding of the corrosion process, time-resolved X-ray synchrotron powder diffraction studies have been carried out in the temperature range 425 - 525 K, covering the whole transformation region. The structural examination are accompanied by thermogravimetric and differential thermal analyses and by Moessbauer spectroscopy.

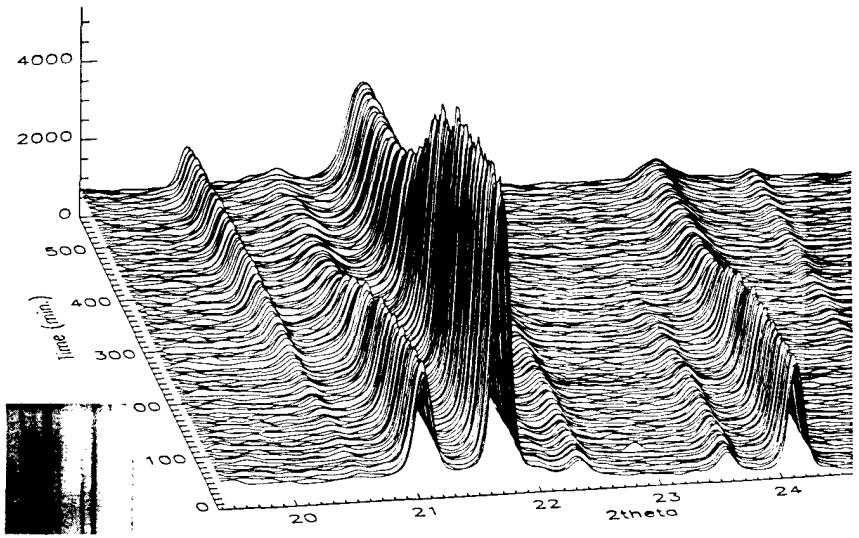

Figure 1. Time-resolved powder pattern taken during 5 hour ramp from 150 to 250C and then held at 250 for 5hr.

* US DOE BES contract DE-AC0276CH00016, Swedish NFR, Danish SNF

Time-Resolved, *In-Situ* X-Ray Diffraction Studies of the Hydrothermal Syntheses of Microporous Gallium Fluorophosphates *	X7B

D. O'Hare, J.S.O. Evans, R. J. Francis, P.S. Halasyamani (Oxford U.) , P.l. Norby, J. Hanson (BNL)

ULM-5 is a microporous oxy-fluorinated gallophosphate containing large 16-membered rings and interconnecting 8-membered rings.[1] ULM-5 is synthesised hydrothermally at 180°C. We have undertaken a study of the formation of ULM-5 under a variety of synthetic conditions in order to gain a greater understanding of the dynamics of crystal growth and nucleation. Early experiments at the SRS, Daresbury Laboratory, UK using time-resolved, *in-situ* energy dispersive X-ray diffraction indicated that a highly crystalline intermediate phase is observed to form which then subsequently reacts to form ULM-5.[2] In an effort to gain a greater understanding of the structural relationships between these phases we undertook an investigation of the synthesis of ULM-5 using monochromatic synchrotron radiation and a translating image plate detector (TIP) available on beamline X7B at the NSLS.

Aliquots of the gel mixture were syringed into 0.7 mm quartz capillaries and heated to 160°C while time-resolved XRD patterns were collected with the TIP detector. The figures show two 3D plots of the evolution with time of the XRD patterns for successive ULM-5 syntheses.

Despite being prepared in the same way, two experiments showed different behaviour. Although in each case ULM-5 was the final product of the reactions, the time taken for complete crystallization was not the same. More dramatically, the behaviour prior to crystallization was completely different in each case. In Fig. 1a a mixture of two intermediate phases was observed which subsequently react to form the final ULM-5 product. In Fig. 1b a single intermediate material is observed.

In conclusion, these it in-situ experiments are a dramatic illustration of the complexity of hydrothermal syntheses, and how subtle changes in the reaction conditions, such as the use of slightly different starting materials or the reaction vessel, can greatly affect the course of these reactions. Nevertheless, be believe are results dramatically illustrate the unique ability of *in-situ* experiments to gain information not available using other techniques.

1. G. Ferey, J. Fluor. Chem., 72 (1995) 187-193.

2. R.J. Francis, S. J. Price, S. O'Brien, A. M. Fogg, and D. O'Hare, Chemical Communications, (1997),521.

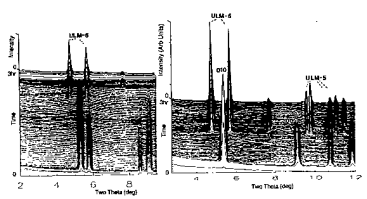

Figure 1. (a) (left)two intermediate (b) (right) one intermediate observed.

* US DOE BES, Leverhulme Trust and EPSRC

Phase Transformations in $CoMoO_4$ and $NiMoO_4$ Catalysts: Time-Resolved Synchrotron XRD Studies	X7B

J.A. Rodriguez, S. Chaturvedi, J.C. Hanson (BNL), J.L. Brito and A. Albornoz (IVIC)

The catalytic properties of cobalt and nickel molybdates have attracted a lot of attention in recent years. These novel materials exhibit interesting relationships between their structural and catalytic properties. At atmospheric presure, two phases of $NiMoO_4$ and $CoMoO_4$ are known to exist, designated as the alfa and the beta phase. The main difference between them is that coordination of Mo^{6+} ions is octahedral in the alfa phase and tetrahedral in the beta phase. In both phases, Co^{2+}/Ni^{2+} ions occur in octahedral sites. The catalytic properties of $NiMoO_4$ are closely related to its structure. The beta phase is almost twice more selective for the dehydrogenation of propane to propene than the alfa phase. In a similar way, sulfided beta-$NiMoO_4$ was found to be a much better catalyst for the HDS of thiophene than the sulfided alfa isomorph. In order to fully understand these catalytic processes, it is essential to understand both, the structural as well as the electronic properties of these molybdates. We carried out a detailed study of these properties using time resolved synchrotron X-ray diffraction. Investigations at X7B have recently established the feasibility of conducting sub- minute, time resolved XRD experiments under a wide variety of sample conditions (-190 C < T < 900 C, P <=45 atm). This important advance results from combining the high intensity of synchrotron radiation with rapid new parallel data-collection devices. Using this approach, we monitored the changes that occur in $AMoO_4.xH_2$ O and alfa-$AMoO_4$ systems (A=Co/Ni) as a function of temperature. The hydrated $CoMoO_4$ and $NiMoO_4$ compounds lose water by 350 and 450 C , respectively to form the pure beta phases. On heating to 550 C, alfa- $NiMoO_4$ starts to transform into the beta isomorph and the transformation is complete by 700 C. The alfa to beta transformation in CoMoO4 occurs around 450 C. The time resolved XRD patterns provide detailed information about the kinetic parameters of these transformations.

Structures from small single crystals of *d,l*-Ir(en)$_3$[Al$_3$P$_4$O$_{16}$]xH$_2$O and Ir(chxn)$_3$[Al$_2$P$_3$O$_{12}$] *	X7B

A. P. Wilkinson (Ga Tech), D. J. Williams (Kennesaw St.), and J. C. Hanson (BNL)

We have been exploring the use of chiral chelate complexes as templates for the preparation of chiral solids. Our early work using simple Co(III) complexes in the synthesis of AlPO and GaPO materials showed that chirality could be induced in a growing framework using templates of this type. However, the range of Co(III) complexes that can be used is limited by their hydrothermal stability. We have examined a number of strategies to produce template species with enhanced stability and found that the use of Ir(III) in place of Co(III) increases the maximum temperature at which the templates can be used by more than 50°C. Initital experiments with Ir(III)containing templates produced two new materials that could not be prepared as single crystals suitable for use with a laboratory based diffractometer.

A hemisphere of data was collected on a 50 × 50 × 50 μm crystal of *d,l*-Ir(en)$_3$[Al$_3$P$_4$O$_{16}$]xH$_2$O using 1.1167Å radiation (Pnna, 8.55, 21.93, 13.94Å). The data was processed using the HKL suite, and the structure was solved and refined using SHELXTL. The material is closely related to *d,l*-Co(en)$_3$[Al$_3$P$_4$O$_{16}$]xH$_2$O.

A hemisphere of data was collected on a 75 × 7 × 7 μm crystal of Ir(chxn)$_3$[Al$_2$P$_3$O$_{12}$] using 1.1167Å radiation (P -1, 9.643, 12.242, 16.222Å, 100.45, 102.64, 105.16°]. The data was processed as above. This material contains a new type of AlPO chain (Fig. 1), related to one previously reported[1] (Fig. 2).

1. I. D. Williams, J. Yu, Q. Gao, J. Chen and R. Xu, Chem. Com. 1273 (1997).

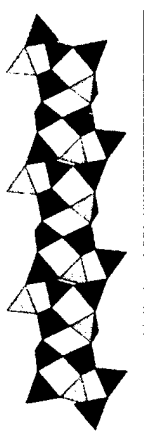

Figure 1. AlPO chain found in Ir(chxn)$_3$[Al$_2$P$_3$O$_{12}$]

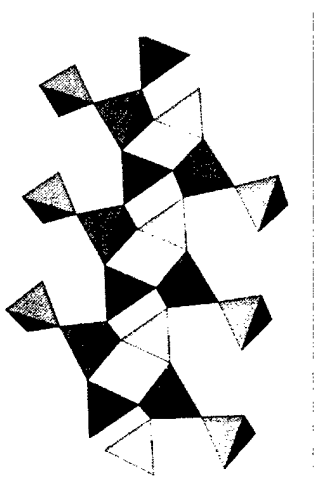

Figure 2. AlPO chain reported by Williams et al.[1]

* Partially supported by DOE under contract DE-AC0276CH00016

AXAF Synchrotron Calibrations over 2010-6200 eV *	X8A

D.E. Graessle, A.J. Burek, A.M. Clark, J.J. Fitch, J.B. Sweeney (Smithsonian Astrophysical Observatory), and R.L. Blake (R&D Services, Prop.)

We report progress in the reflectance calibrations of witness mirrors from the coatings of AXAF. AXAF is an acronym for NASA's Advanced X-ray Astrophysics Facility. The witness mirrors from AXAF are coated with some 350Å of iridium on 100Å of chromium, on Zerodur substrates. Calibrations were completed for four mirrors in the 2010-6200 eV range during November 1996. Problems with adjustments in the X8A monochromator horizontal alignment versus energy resulted in a decision to calibrate only in the limited 2010-2400 eV range after the January restart. The result was the completion of sixteen mirrors in the 2010- 2400 eV range, which includes the iridium M-V and M-IV absorption features. Each calibration was completed within a 24 hour run period. The X-ray beam was extremely quiescent through most of the run period, allowing our gated monitoring mode of operation to provide precision approaching 0.1% for reflectance measurements after normalization. This is as good as we have ever seen on X8A. Calibration results for one mirror over the full X8A Si (111) energy range are given in the figure. The several traces represent data taken at different grazing angles. The M-edge absorption features shown are the most significant features appearing in the AXAF telescope reflecting efficiency. Significant EXAFS appear on the M-IV edge, with 2-3% amplitude oscillations versus energy extending over 300 eV. This remarkable feature occurs in films and coatings of iridium regardless of the quality or density of the film. Further study and analysis of the EXAFS is under way.

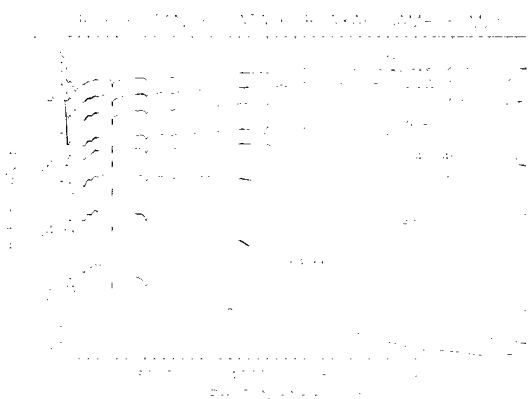

Figure 1. Reflectance calibrations over 2010-6200 eV for a single AXAF witness mirror, taken during the reported run period.

* This work is supported by the US D.O.E. and by NASA (NAS8-40224).

AXAF Synchrotron Reflectance Calibrations 2010-2400 eV – Completion Report *	X8A

D.E. Graessle, A.J. Burek, A.M. Clark, J.J. Fitch, J.B. Sweeney (Smithsonian Astrophysical Observatory)and R.L. Blake (R&D Services, Prop.)

We report the completion of calibrations on a total of 46 witness mirrors in the data range 2010-2400 eV. The final 20 mirrors on the schedule were completed during our second run period of 1997 on X8A. The 2010-2400 eV range includes the M-V and M-IV edges of iridium, two of the most important features in the entire AXAF mirror efficiency spectrum. Our measurements typically obtained 0.2-0.3% experimental noise levels during this run, indicating a very stable and quiescent X-ray ring operation. Years of work on these issues with the NSLS accelerator staff have paid off well. The figure gives the calibration data taken from a typical AXAF witness mirror. The several traces are data taken at different grazing angles. These data are to be reduced to optical constants using a Fresnel equation model with uniform layers and a modified Debye-Waller factor roughness correction. The optical constants will be used in modeling of the AXAF calibration to be compared with data taken from the actual flight optics. Optical constants provide the advantage of removing angular information from the reflectance data, allowing a full calibration versus energy and angle with a minimum of reflectance data.

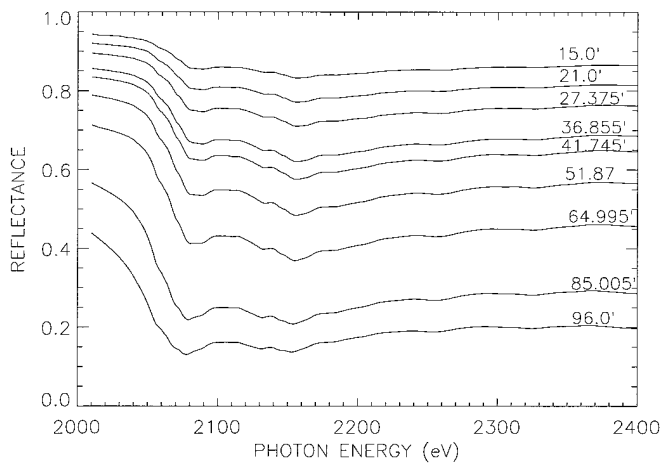

Figure 1. Reflectance calibration for a typical AXAF witness mirror over 2010-2400 eV, showing the M-V and M-IV edges of Ir.

* This work is supported by the US D.O.E. and by NASA (NAS8-40224).

AXAF Synchrotron Reflectance Calibrations over 2010-6200 eV – Year 1 *	X8A

D.E. Graessle, A.J. Burek, A.M. Clark, J.J. Fitch, J.B. Sweeney (Smithsonian Astrophysical Observatory), and R.L. Blake (R&D Services, Prop.)

AXAF witness mirrors are coated with 350 $\AA$ iridium upon 100 $\AA$ chromium, deposited on a Zerodur substrate. We report our first sixteen months' progress on reflectance calibrations of AXAF witness mirrors in the 2010-6200 eV range using beamline X8A (1995-1996). Data quality with 0.2-0.4% precision is nearly always attainable. Noise problems from the source, which are particularly noticeable with the aperturing on this beamline, have largely been cured by the accelerator science staff. At best, data acquistion over four energy ranges which collectively cover 2010-6200 eV, may be completed in four days. Efforts to improve the data acquisition timing are in progress. Included in the efforts are a new data aquisition program based on LabView software from National Instruments, Inc., and some type of semi-transparent flux monitor which can replace the gated PIN diode normalization method we have used during the first year. (Please see adjoining abstracts for progress in these areas.) Through the first sixteen months of the X8A AXAF calibrations, we have calibrated some 13 mirrors. There are 31 mirrors remaining to be calibrated over the full range to meet our calibration goals for AXAF. Iridium optical constants have been derived from some of these data using a Fresnel Equation model with uniform layers and a modified DeBye-Waller factor correction for surface roughness. Figure 1 gives optical constants derived in the 2010-2400 eV range for several of these mirrors. This range includes the iridium M-V and M-IV absorption features. Different mirrors give slightly different optical constants. It appears from the data that a few angstroms of some contaminant are present in varying depths on the several mirrors included.

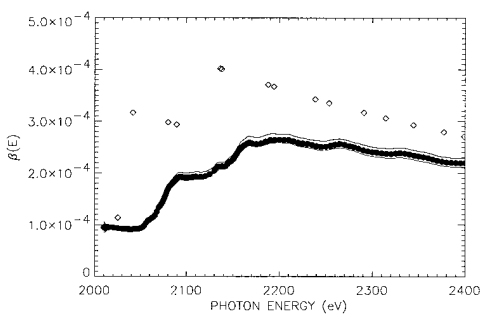

Figure 1. Optical constants $\beta(E)$ determined from reflectances of several mirrors 2010-2400 eV. The black dots are average values of five mirrors. Diamonds give the Henke tables' values.

* This work is supported by the US D.O.E. and by NASA (NAS8-40224).

AXAF Synchrotron Reflectance Calibrations 2250-2900 eV – Completion Report * | X8A

D.E. Graessle, A.J. Burek, J.J. Fitch, J.B. Sweeney (Smithsonian Astrophysical Observatory), and R.L. Blake (R&D Services, Prop.)

We report the completion of calibrations on some 48 iridium-coated witness mirrors in the 2250-2900 eV energy range, which includes the sharp, narrow M-III absorption feature and considerable EXAFS on the M-V and M-IV edges. We have reduced the calibration time to one mirror per eleven-hour shift, using a double-window ionization chamber in the vacuum as a flux monitor, and a new data acquisition program based on LabView. We can now complete the remaining calibrations in approximately 65 eleven-hour shifts on X8A, thereby completing the calibrations slated for this beamline. The relative response between the Si PIN diode which measures the reflected flux, and the double thin-Be-window ionization chamber monitor is constant to within 1% in all cases, but usually is within 0.4% from the start to the finish of any given calibration. The variation in this normalization is currently attributed to the variation in the vertical extent and bifurcation of the X-ray beam. The vertical extent changes as the upstream mirror on X8A cycles thermally during each fill. The data quality, excluding this small slow variation in normalization, is extremely good, and is much less sensitive to temporal instabilities in the X8A intensity, a problem which has occasionally cost our team time when using our old gated Si PIN diode monitoring system. Example data are given in the figure. The precision in the data is at the 0.1% level, the best ever seen from this beamline at these energies.

Figure 1. A typical reflectance calibration over 2250-2900 eV of an AXAF witness mirror, showing the narrow iridium M-III absorption feature.

* This work is supported by the US D.O.E. and by NASA under contract number NAS8-40224.

Scattering Studies of AXAF Witness Mirrors * | X8C

R.L. Blake (R&D Services, Prop.), A.J. Burek, and D.E. Graessle (Smithsonian Astrophysical Observatory)

A preliminary x-ray scattering study has been conducted on one of the AXAF witness mirrors that we are calibrating. The study was intended to determine whether sample scattering can be reliably measured separately from slit scattering and over what range of angles with respect to the specularly reflected beam. The same reflectometer test station was used that is routinely employed for all our reflectivity calibrations at NSLS. Data were taken at 10 keV with the Ir coated witness sample at the critical angle (8.12 milliradians). A 100 micrometer entrance slit upstream of the sample and a 105 micrometer scraper slit between the entrance slit and sample define the beam received by a 25 micrometer detector slit. The detector was scanned through the direct beam with sample removed to get the slit scatter profile, then through the reflected beam to get the combined slit and sample scatter profile. Shown below as the inner, dashed curve is the normalized direct beam profile shifted to be centered on the reflected beam profile (the outer, solid curve). On the direct beam profile one sees the scattering primarily from the entrance slit until it is clipped by the scraper slits at ± 1000 ms from the direct beam centerline. To determine the sample scatter profile without the slit contribution one must invert the direct beam profile around the reflected beam specular peak and then subtract the inverted direct beam profile from the reflected beam profile. Without doing the inversion and subtraction one can see the study goals were met. The sample scatter contribution can be determined to acceptable accuracy to within 300 ms of the specularly reflected peak, or 1.3 milliradians. This preliminary work demonstrates that a full scattering study on AXAF samples is justified.

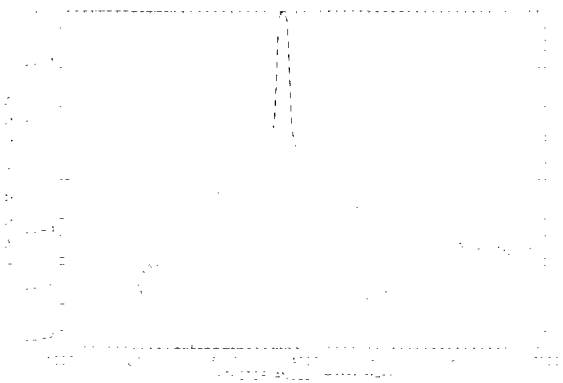

Figure 1. Diffuse X-ray scattering intensity from an AXAF witness mirror.

* This work is supported by the US D.O.E. and by NASA (NAS8-40224).

AXAF Synchrotron Reflectance Calibrations 5-12 keV *	X8C

D.E. Graessle, A.J. Burek, A.M. Clark, J.J. Fitch, J.B. Sweeney (Smithsonian Astrophysical Observatory), R.L. Blake (R&D Services, Prop.)

We report significant progress toward the completion of the 33 scheduled witness mirrors for calibration over 5-12 keV on the X8C beamline. In all, 29 of the orignally slated 33 AXAF witness mirrors have been calibrated successfully in this energy range. A very significant addition to our configuration has made this progress possible. A double-thin-Be-window ionization chamber filled with one atmosphere of Ne has allowed simultaneous monitoring of the incident flux with the detection of the reflected flux by Si PIN diodes. The ion chamber allows data points to be taken in a period of approximately six to eight seconds each, whereas our previous method of gating PIN diodes in and out of the beam required 20-25 seconds per point. This is an improvement of almost a factor of three. Data quality is not only uncompromized, but is in fact improved. (See figure 1 below.) Disparate points frequently occur using the gated monitor because of significant flux variations due to monochromator settling and thermalization which happens at certain energies when the monochromator is initially set or moved to those energies. The change in flux may be as much as 5% at such points, and this ramping may occur up to 10 seconds after the monochromator stepper motor has stopped. The ion chamber essentially eliminates this problem. Hence, we have completed 18 mirrors in the September 1996 data run on X8C. Further progress is reported in the adjoining abstracts.

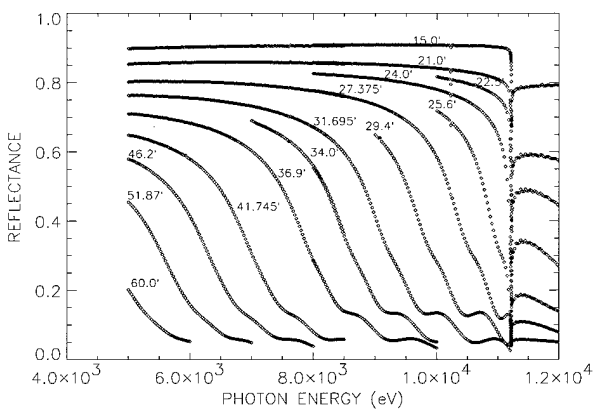

Figure 1. Reflectance calibration data from an AXAF witness mirror using the ionization chamber monitor. The traces give data from different grazing angles.

* This work is supported by the US D.O.E. and by NASA (NAS8-40224).

AXAF Synchrotron Reflectance Calibrations 5-12 keV *	X8C

D.E. Graessle, A.J. Burek, J.J. Fitch, J.B. Sweeney (Smithsonian Astrophysical Observatory), and R.L. Blake (R&D Services, Prop.)

We report the completion of scheduled calibrations on the X8C beamline for AXAF witness mirrors over 5-12 keV. The thin-window ion chamber continues to give consistant normalizations with Si PIN diodes, allowing simultaneous monitoring and reflectance measurements. The final five AXAF witness mirrors originally slated for calibration have been completed during this run. Seven additional angles were added to the procedure for energy scans, which allow better determination of optical constants, particularly in the in the 10-12 keV range. This latter range includes the very sharp, strong L-III absorption feature for iridium. (See Fig. 1.) Optical constants $\beta(E)$ determined from the reflectance data are in Fig. 2, including a comparison with data from Henke, et al., Atomic Data and Nuclear Data Tables, vol. 54(2), p. 181 (1993). (Our fitted $\delta(E)$ is consitently within 2% of the tabulated values.) The β values exhibit a dependence on the roughness of the flat measured, which is not physically reasonable. Further study of our mirror scattering and modeling thereof are in progress.

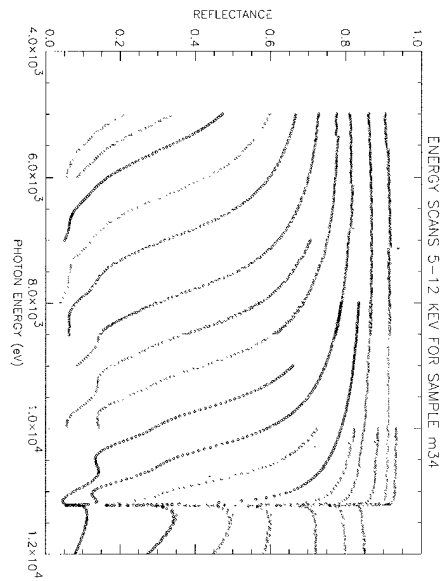

Figure 1. Reflectance calibration over 5-12 keV of a 3Å roughness witness mirror.

* This work is supported by the US D.O.E. and by NASA (NAS8-40224).

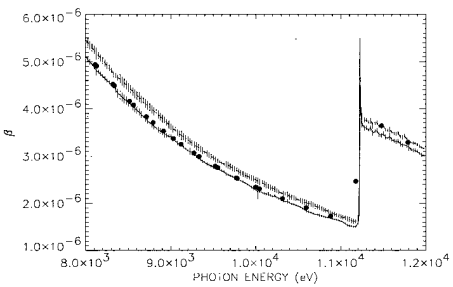

Figure 2. $\beta(E)$ derived from AXAF mirrors with two different surface roughness values.

Structural Studies of Gene 5 Protein-ss DNA Complexes

X25, X8C

T. C. Terwilliger, R. G. Nanni (LANL)

Single-stranded nucleic acid-binding proteins play roles in key cellular processes such as DNA replication, recombination, repair, and control of RNA translation. This project has focussed on determining the crystal structures of complexes between gene V protein and oligonucleotides of lengths from 4 to 16 nucleotides. We have obtained crystals of a number of these complexes and have collected x-ray diffraction data on those that diffract to high resolution. At this point we have collected x-ray diffraction datasets to a resolution of at least 3.5 Å for the 6 different gene V protein-oligonucleotide complexes.

We have used the structure of the wild-type gene V protein that we determined previously to solve the structure of the protein portion of one complex crystal containing a 16-mer oligonucleotide. This complex crystallized in space group R3 and the asymmetric unit of the crystal contains 4 monomers of the protein. The standard R-factor for this structure after rigid-body refinement of the protein portion alone is 0.39, indicating that the solution we have obtained is likely to be correct. We are now in the process of using difference Fourier methods and atomic refinement to determine the location of the bound ssDNA in these crystals.

TATA Binding Protein: Interactions with DNA

X9A

M. Brenowitz, M. Sullivan, B. Sclavi, S. Maleknia, S. Moller, B. Gilden (AECOM)

TBP is a component of the nucleo-protein complexes required for the initiation of transcription by each of the three eukaryotic RNA polymerases. The binding of the "TATA Binding Protein" (TBP) to specific promoter sequences called "TATA boxes" is a key step in the initiation of transcription of genes transcribed by RNA polymerase II. The nucleotide sequence of 'TATA boxes' is variable among naturally occurring promoters. Although promoters containing 'TATA boxes' that bind TBP with high affinity are generally transcribed efficiently, there is not a direct correlation between TBP binding affinity and transcriptional activity.

A mechanism has been proposed for the association of TBP with DNA.

$$TBP + DNA \overset{K_1}{\longleftrightarrow} [TBP - DNA]^* \overset{k_2}{\longrightarrow} TBP - DNA \qquad (1)$$

analogous to that demonstrated for *E. coli* RNA polymerase. The presence of a TBP-DNA intermediate (a rapid equilibrium, K_1, followed by a slow k_2) was inferred by extrapolation to infinite [TBP] by double-reciprocal plotting of k_{obs} versus [TBP]. The hand mixing protocols used in these studies limited the TBP concentrations that could be investigated and hence the accuracy of the extrapolation required for the determination of the value of k_2.

Stopped-flow kinetics studies of TBP promoter interactions conducted at higher TBP concentrations by "footprinting" (E4 promoter) and fluorescence anisotropy (ML promoter) were inconsistent with the presence of significant concentrations of the diffusion-limited intermediate complex of eq. 1. Furthermore, stopped-flow fluorescence resonance energy transfer (FRET) studies of TBP binding to and bending the ML promoter did not reveal a diffusion-limited intermediate. A TBP binding mechanism consistent with these studies is that only a small fraction of the TBP-DNA diffusion-limited "encounter complexes" rapidly progresses to form stable, sequence-specific complexes. This model can be represented as

$$\mathrm{TBP + DNA} \underset{k_{-1}}{\overset{k_1}{\rightleftarrows}} \underset{\text{"}Encounter\text{"}\ complex}{\mathrm{TBP \sim DNA}} \overset{k_2}{\longrightarrow} \mathrm{TBP - DNA} \qquad (2)$$

where the first step of the reaction is the formation of the encounter complex. The encounter complex represents the diffusional encounter of two reactants that become trapped within the same solvent cage during which time they suffer a large number of collisions prior to separating or proceeding down the reaction pathway. It is important to note that in this representation of the binding reaction. K_1 is a quasi-thermodynamic constant depicting the events prior to the chemistry of the reaction and k_2 is the rate constant of the reaction. Time-Resolved hydroxyl radical footprinting will be utilized to test these mechanisms of TBP-DNA interactions.

Single Band Densitometric Analysis Synchrotron X-Ray Footprinting Autoradiograms	X9A

M. Brenowitz, T. Wexler and E. Jamison (AECOM)

A key issue to be resolved for the analysis of synchrotron x-ray "footprinting" kinetics experiments is the development of algorithms for the "band-by-band" densitometric analysis of the gel electrophoresis autoradiograms that are the primary data of these experiments. While the current procedures, in which groups of bands are grouped into "blocks", has been sufficient for the analysis and interpretation of the •OH protections that have been determined in our initial studies of the *Tetrahymena* ribozyme, insight into more subtle changes of structure requires the implementation of "band-fitting" protocols originally developed in our laboratory for thermodynamic studies using •OH and 5-phenyl-phenanthroline as probes of DNA conformation that occur in sequence-specific protein-DNA interactions. Implementation of these protocols have been greatly facilitated through the development by Dr. Thomas Tullius and his co-workers of a band-fitting program (GelExplorer) with an interactive graphical interface interactive that runs within the IRIS Explorer environment. The basic algorithm is that the optical density (OD) of each lane on an autoradiogram is scanned in the direction of electrophoresis across the width of the lane. The OD values determined for each scan are fit to individual curves within the selected lane. The procedure is analogous to spectral deconvolution. Following fitting, the areas of the fitted curves are summed for each band and a histogram can be generated relating relative band density with the nucleotide present at that position in the nucleic acid. The results obtained by this procedure for the DNA containing a 'TATA Box' (the binding site of the eukaryotic transcription factor TBP) shows that the decrease in the relative band densities for the sequence 'AAAA' is consistent with the assumption of a bent configuration by this sequence. Similar data sets obtained at temperatures from 15 - 45 °C are being compared with solvent accessibility calculations of this DNA obtained from molecular dynamics calculations. The goal of this project is to correlate changes in DNA conformation with the temperature dependencies of the thermodynamics and kinetics of DNA binding by TBP. •OH cleavage data sets have been obtained for a number of different 'TATA box' sequences that display unique thermodynamic and kinetic signatures.

A Resource Dedicated to Time-Resolved X-Ray Footprinting	X9A

M. Chance, M. Brenowitz and M. Sullivan (AECOM)

Hydroxyl radicals (•OH) can cleave the phosphodiester backbone of nucleic acids and are valuable reagents in the study of nucleic acid structure and protein-nucleic acid interactions through footprinting studies. Irradiation of solutions by high flux white light x-ray beams based on bending magnet beamlines at the National Synchrotron Light Source (NSLS) yields sufficient concentrations of •OH so that quantitative nuclease protection (footprinting) studies of DNA and RNA can be conducted with a duration of exposure in the range of 10 - 20 milliseconds.

To provide expanded access to this technology, beamline X9A at the National Synchrotron Light Source has been constructed along with a dedicated stopped flow instrument to allow footprinting studies for our expanded group of investigators. The beamline accepts up to 5 milliradians of white beam, with a flux density of 10^9 photons/s/mm^2/0.07% bandwidth over an effective energy range of 3-30 keV. The completion of the beamline has enhanced the productivity of this core project, accelerating both the core and collaborative research programs tremendously. Our Resource is the world leader in this technology and the availability of a dedicated beamline will continue our leadership in this area. We are now routinely conducting footprinting studies on 10-20 milliseconds and longer timescales with our stopped flow device and have made major advances in understanding RNA folding.

The Folding of an Immobile DNA Branched Junction | X9A

M. Chance, B. Sclavi. M. Brenowitz (AECOM), N.C. Seeman, and H. Yan (NYU)

The Holliday junction is a central intermediate in the process of genetic recombination. This is a four-stranded DNA molecule, in which the four strands pair to form four double helical arms that flank a branch point. The site of the branch point in naturally occurring Holiday junctions is unstable, because it is flanked by twofold (homologous) sequence symmetry that permits the junction to relocate through an isomerization known as branch migration. If the symmetry is eliminated in synthetic molecules, the site of the branch point is stable. In the presence of Mg cations, the junction folds into a structure in which the four arms stack on each other pairwise, to form two double helical domains; two strands adopt a roughly helical structure, and the other two strands cross over between the two domains. In the absence of Mg cations, the four arms adopt a fourfold symmetric arrangement. The hydroxyl radical cleavage pattern is sensitive to the folding of the junction in the presence of Mg. Relative to their pattern in linear duplex DNA, the two crossover strands are protected from attack in the two-domain structure. Likewise, four nucleotides 3' to the branch point, the helical strands demonstrate protection, because they occlude each other there. Both protections appear to be lessened in the absence of magnesium. Hence, this is a system whereby the kinetics of the folding of this key intermediate should be measurable through these reporter protection differences.

Time-Resolved Synchrotron X-Ray Footprinting | X9A

M.R. Chance, M. Sullivan, B. Sclavi, M. Brenowitz (AECOM), and S. Woodson (Univ. of Maryland)

Hydroxyl radicals (•OH) can cleave the phosphodiester backbone of nucleic acids and are valuable reagents in the study of nucleic acid structure and protein-nucleic acid interactions through "footprinting" studies. Irradiation of solutions by high flux "white light" x-ray beams based on bending magnet beamlines at the National Synchrotron Light Source (NSLS) yields sufficient concentrations of •OH so that quantitative nuclease protection ("footprinting") studies of DNA and RNA can be conducted with a duration of exposure in the range of 10 - 20 milliseconds. The utility of this timescale for nucleic acid cleavage is demonstrated by synchrotron x-ray time-resolved "footprinting" analyses of the Mg^{2+}-dependent folding of the *Tetrahymena thermophilia* L-21 Sca I ribozyme RNA.

Many macromolecular folding reactions, such as the Mg^{2+}-dependent folding of the P4-P6 domain of the *Tetrahymena thermophilia* group I intron, occur on timescales shorter than one second. Kinetic progress curves describing the millisecond folding of P4-P6 within the L-21 ribozyme have been obtained using a new •OH "footprinting" technique, stopped-flow synchrotron x-ray "footprinting". The folding of P4-P6 is a highly concerted reaction; the regions of •OH protection within the interior of the folded domain appear at rates of $\leq 1.0\ sec^{-1}$.•OH protections within the P5c sub-domain appear at rates of $\approx 2.0\ sec^{-1}$, suggesting that folding of this subdomain is the initial step in the folding pathway. The rates of •OH protection of the "triple helix" junction between P4-P6 and the P3-P7 domain and those protections in P4-P6 ascribed to interaction with the P9 domain at rates of $\approx 0.3\ sec^{-1}$. These results suggest that these tertiary interactions guide the folding of the catalytic core against an extensively folded P4-P6 domain. This stopped-flow approach to "footprinting" will be widely applicable to the kinetic analysis of many nucleic acid folding and protein-nucleic acids binding reactions.

Since RNA folding progress curves over timescales from 20 milliseconds to several minutes have been obtained for nearly 20 regions of the ribozyme, this research provides an unprecedented structural kinetic picture of the folding of a large macromolecule. Synchrotron x-ray "footprinting" is a new approach of general applicability for the study of time-resolved structural changes of nucleic acid conformation and protein-nucleic acid complexes.

Fast Folding of the Tetrahymena Ribozyme: Mutants and P4-P6 Domain Folding	X9A

M.R. Chance, M. Sullivan, B. Sclavi, M. Brenowitz (AECOM), S. Woodson, M. Deras (U. of Maryland), J. Williamson, and M. Rook (MIT)

To further dissect the folding mechanism of the Tetrahymena ribozyme, we have explored two avenues of research. One is to examine the folding of the isolated P4-P6 domain, which is seen to fold on the sub-second timescale in the presence of other ribozyme components. This phase of the research is in conjunction with Dr. Woodson's lab at the University of Maryland. The second approach, in collaboration with Dr. Williamson's lab at MIT, involves examining the folding of several fast-folding mutants of the *Tetrahymena thermophila* group I intron. Dr. Williamson's group is currently characterizing the temperature and urea dependence of folding of these mutants, using their oligo-hybridization method, which probes the formation of helix P3 in the ribozyme. In order to measure the rates of folding of the rest of the 400 bases-long RNA, Martha Rook, a graduate student in Williamson's lab has begun time-resolved x-ray footprinting experiments on these mutants in collaboration with the Resource Center.

Time-Resolved X-Ray Footprinting of Cytochrome c	X9A

I. Kravtsov, S.D. Maleknia and M. Chance (AECOM)

Understanding the folding kinetics of proteins are vital in revealing their biological functions and structures. Spectroscopic methods used to date have been quite helpful in characterizing transient-intermediate structures of proteins, but new methods to investigate tertiary structure changes are needed. Synchrotron x-ray footprinting techniques enable millisecond time-resolved structural changes in nucleic acid conformation and protein-nucleic acid complexes to be studied. This approach in conjunction with mass spectrometric sequencing methods are being used to study folding kinetics of cytochrome c. Hydroxyl radicals generated by x-ray radiolysis of water induce detectable amino acid modifications of cytochrome c within 4 millisecond. Deconvoluted electrospray ionization mass spectra reveal that the prominent modification results in ions at +16 u intervals above the molecular weight of unmodified protein. The nature of these modifications are being identified by proteolysis and mass spectrometric mapping experiments, and are correlated with the solvent accessibility residue map of cytochrome c to reveal the protein structure at various solution conditions. The aromatic, heterocyclic, and sulfur containing amino acid residues are most reactive to hydroxyl radicals.

Synchrotron X-Ray Induced Modifications of Peptides | X9A

S.D. Maleknia and M. Chance (AECOM)

Synchrotron x-ray studies of peptides are being investigated to characterize the reaction mechanisms, and to construct a data base of the reactivity order, for each class of amino acids. These studies include anaerobic and ^{18}O isotope experiments. The order of reactivity of amino acids at various pH conditions or in the presence of denaturing agents (urea, KCl, guanidine hydrochloride) are also being examined. This study provides fundamental information necessary for protein footprinting experiments.

The radiolysis of water by x-rays produces a high flux of free electrons and hydroxyl radicals in a millisecond time scale. Random sequence peptides (10 to 25 mM in water) containing 5 to 20 amino acid residues were exposed to the x-ray beam (X-9B) for 4, 16, 50, or 100 ms. Analysis of these peptides by mass spectrometry using matrix-assisted laser desorption or electrospray ionization techniques revealed modifications to the peptide within 4 ms. The major peptide modification results in ions at +16 u intervals above the molecular ion of the unmodified peptide. Mass spectra of peptides containing phenylalanine residues revealed multiple modifications detected at +16 u intervals after 50 to 100 ms x-ray exposure. Mass spectrometric sequencing identified that the phenylalanine residues were modified by addition of 16 u.

The Structure of an Actin-crosslinking domain from Human Fimbrin | X9B

S. Almo, S. Goldsmith, M. Sullivan, and A. Fedorov (AECOM)

Actin crosslinking proteins organize filamentous (F-) actin into higher order assemblies such as bundles and networks which are important for biological processes including cell motility, cytokinesis and tumorigenesis. Fimbrin is a representative member of the largest superfamily of actin crosslinkers which is characterized by a conserved 275 amino acid F-actin binding domain. We have determined the crystal structure of the N-terminal actin binding domain of human fimbrin (ABD1) to 2.4resolution, which represents the first high resolution structure of an actin-crosslinking domain. Initial characterization of ABD1 crystals was performed using synchrotron radiation at Brookhaven National Laboratory, Beamline X9B, where the crystals diffracted to at least 1.9Åresolution. ABD1 is an ellipsoid molecule of dimensions $\sim$60x40x40Å^3, and has a novel fold composed of two calponin homology (CH) subdomains. CH domains may serve to target a number of proteins) including signaling proteins) to cytoskeletal components. The two CH domains in ABD1 are connected by a central alpha-helix, and are specifically oriented by inter-subdomain hydrophobic and ionic contacts. The crystal structure of ABD1 has allowed for the mapping of peptide segments implicated in F-actin binding, as identified by peptide binding and deletion mutation analysis. The locations of suppressor mutations in the yeast homolog of fimbrin (sac6p) suggest that the interaction between ABD1 and F-actin is mediated by a conformational rearrangement involving the relative orientation of the two CH domains. The crystal structure of ABD1 provides a starting point for the construction of a detailed atomic model of F-actin crosslinking by members of the entire superfamily of proteins.

Synchrotron Crystallography Structural Analysis of Profillin	X9B

S. Almo, N. Mahoney, and M. Sullivan (AECOM)

Profilin is a ubiquitous cytoskeletal protein which binds actin monomers with an equilibrium dissociation constant (Kd) in the 0.1-10 (μM range, and through this interaction regulates the distribution and dynamics of the actin cytoskeleton. Two additional classes of ligand, proline-rich proteins and phosphatidylinositol 4,5-bisphosphate (PIP$-$2) have been shown to interact with profilin *in vitro* and *in vivo*. Proline-rich proteins may serve to localize the actin related activities of profilin. Profilin's ability to bind PIP_2 may link it to signal transduction pathways and suggests the involvement of profilin in phosphoinositide metabolism. Profilin from different organisms have limited sequence homology, but highly homologous three dimensional structures, indicating an evolutionary pressure to maintain the protein fold. It has been the goal of our laboratory to combine crystallography and *in vivo* studies to examine the role(s) of profilin in the cell. Two profilin data sets have been collected at X9B. Crystals of P2 profilin, (a profilin isoform of it Acanthamoeba castellani), which diffracted only to 4.0 Åusing a rotating anode and diffracted to 2.0 Åat X9B, is consistent with the F432 space group with unit cell parameters of a=b=c = 241.28, α=β=γ=90°. The atomic structure of P2 profilin will aid in the creation of mutants with which to study the specific lipid binding activity of this protein. Crystals of *Saccharomyces cerevisae* profilin which diffracted weakly using a rotating anode, diffracted to 3.0 at X9B. The *S. cerevisae* crystals are consistent with the P432 space group with unit cell parameters of a=b=c = 127.66, α=β=γ = 90° and were successfully reduced and scaled. The *S. cerevisae* profilin structure will be vital for the design of rational mutants for *in vivo* structure function studies on profilin in yeast.

Active Site Targeting of Protein Tyrosine Phosphatases by Synchrotron Crystallography	X9B

S. Almo, Y. Puius, M. Sullivan, Z-Y. Zhang, and D. Lawrence (AECOM)

Dr. Steven Almo, an x-ray crystallographer with significant synchrotron experience, has spearheaded a collaborative effort in conjunction with Dr. Zhong-Yin Zhang, an enzymologist, and Dr. David Lawrence, a synthetic chemist. The goal of this project is the structure-based design of potential therapeutic agents which bind to protein tyrosine phosphatases (PTPases), and the elucidation of the structures of novel PTPases. Since data collected on rotating anode sources at AECOM were of insufficient resolution, single-crystal diffraction data collected at beamline X9B has been absolutely essential for current progress.

Using synchrotron methods, Dr. Almo's group has solved the structure of human protein tyrosine phosphatase 1B (PTP1B) in complex with several different substrates, using 1.9A data collected at X9B. The complex of PTP1B and a synthetic high-affinity non-peptide substrate synethesized by the Lawrence group has demonstrated the existence of a novel aryl phosphate binding site, which provides a new paradigm for the design of tight-binding inhibitors. In addition, the recently-solved structure of PTP1B with a bound 11-residue peptide will give insight into determinants of substrate binding. The Lawrence lab is currently synthesizing a second generation of PTP1B ligands based on these findings; in addition, the Zhang lab is involved in the purification and characterization of several novel phosphatases. Therefore, it is anticipated that future diffraction experiments will include the characterization of cocrystals of PTP1B and the new ligands, as well as the structure deteterminination of newly-characterized phosphatases.

Frozen Solutions and Vectorially-Oriented Single Monolayers of Oriented Membrane Herme Proteins	X9B

J.K. Blasie, A. Edwards (U. of Pennsylvania) and K. Zhang (IIT)

Both peripheral (soluble) and detergent-solubilized integral membrane proteins can be tetered to the surface of inorganic substrates via bifunctional organic chain molecules possessing a headgroup specific for the substrate surface and an endgroup specific for one or more residues exposed on the protein's surface. Such tethering can provide a single vectorially-oriented monolayer of the fully-functional protein on the surface of the solid substrate resulting in an ideal form of the protein for closely correlated structural and functional studies, the former employing both x-ray spectroscopy and x-ray diffraction. Over the past year, we have performed polarized Fe-EXAFS studies on such vectorially-oriented single monolayers of cytochrome c in order to determine the utility of such measurements for determining the orientation of the cytochrome's heme group relative to the plans of the monolayer, as compared with that of analogous linear dichroism studies of the heme's optical absorption transitions. These studies have recently been published. In addition, we have performed both Fe-EXAFS and Zn-EXAFS studies on frozen solutions of an entirely synthetic model metalloprotein (or "maquette") based on a four alpha-helix bundle motif containing by design specific binding sites for four either iron porphyrin or zinc porphyrin groups. The analysis of these data are in progress. These studies are essential to establish the precise nature of the actual coordination of the metal atom in such "maquettes" as a prelude to polarized EXAFS studies on vectorially-oriented single monolayers of such model metalloproteins. Overall, these structural studies are essential to understanding the nature of both intramolecular and intermolecular electron transfer phenomena exhibited by these membrane proteins (as well as models and complexes thereof), and the coupling of these phenomena to the generation of transmembrane electrochemical potentials and biological energy conservation.

AUTOFIT 1.0, A New Software for XAS Global Mapping	X9B

M. Chance, E. Scheuring, Wu-Xin Huang (AECOM)

Our global mapping procedure, where crystal structure coordinates are refined to XAS data using the ab initio XAS code FEFF 6.01, continues to be used and updated. In the programs, a grid of hundreds of simulations are directly compared to the experimental data without the use of non-linear least squares fitting procedures to find the interatomic distances. Instead, each simulation is performed with different interatomic distances. The emphasis is on mapping the local and global minima and providing a detailed visual picture and error analysis in the comparison of alternative structures. The three dimensional structural coordinates utilized in the simulations are based on crystal structure models derived from structural databases. Thus, a particular geometry for the metal site is incorporated in this choice. Alternative structures with different geometries can also be selected, processed, and compared. This makes the structural assumptions about the site explicit and they must be justified based on ancillary structural information. Our suite of programs (called AUTOFIT 1.0) vary selected bond distances, compare the resulting *ab initio* simulations to the experimental data, and compute and plot a figure that displays 400-500 alternative solutions simultaneously. These programs are available to outside users free of charge and have been readied for release along with a manual for using the code. In addition, we have recently completed a UNIX based version of the code, along with the original PC based version.

Structural Studies of Optically Rubbed Polymers | X9B

P.A. Heiney, S.S. Ghosh, O.Y. Mindyuk and M. Stetzer (U. of Pennsylvania)

We have measured the X-ray reflectivity of rubbed polyimide films used for liquid crystal alignment. Both mechanically rubbed polyimides and polyimides "rubbed" by linearly polarized UV light were examined. The mechanism for liquid crystal alignment in the optically rubbed films is still unclear; suggested mechanisms include either the formation of large-scale "ripples" due to anisotropic contraction which in turn interact with the liquid crystal, or reorientation of individual polymer molecules. The mechanical rubbing process creates microgrooves on the surface of the polyimide film, which on average run parallel to the rubbing direction. These grooves result in anisotropic off-specular X-ray reflectivity features. The analysis of the specular reflectivities obtained from these films will produce a comparison of the roughness associated with both mechanically and optically rubbed films, parallel and perpendicular to the rubbing direction. We use specular reflectivity, together with the anisotropic character of our resolution function to extract the anisotropy in the roughness along the film surface.

Coordination of Co (II) Protoporphyrin-Substituted Hemoproteins | X9B

C. Lee, E. Scheuring, M. Chance and J. Peisach (AECOM)

Investigations of Co(III) porphyrin complexes have in part been motivated by their use as models for cobalamin species such as coenzyme B_{12}, and in part by their reactivity with nucleic acids. Interactions of Co(III) porphyrins with biomolecules are governed by their axial ligations and no Co(III) porphyrin complex with a single strong field, s-donating axial ligand, such as nitrogen, has been reported. Unlike Co(III) porphyrins, pentacoordinate Fe(III) porhyrins are found in many hemoproteins and have also been synthesized. For example, the met (oxidized, ferric) form of the His64(r)Leu mutant of the oxygen-carrying protein myoglobin [Mb(H64L)] contains a pentacoordinate metal with an axial histidine ligand, whereas in the native protein, the second axial ligand is a water molecule. No water molecule was found near the metal in the mutant. In this study, Co(III) protoporphyrin-substituted Mb and Mb(H64L) are studied by x-ray absorption spectroscopy. The absorption edge energy for both proteins occur near 7729 eV, suggesting that both are hexacoordinate. The sixth ligand of Co(III)-substituted Mb has been suggested to be His64, rather than water as in the Fe(III) protein. Since neither His64 nor water (presumably) are present in the Co(III)-substituted mutant, the current results are surprising. Further studies are being conducted to identify the sixth ligand in Co(III) Mb(H64L).

Biological Metal Clusters — X9B

M. Maroney, S. Choudhury, C. Allan, Z. Gu, G. Davidson, and K. Bose (University of Massachusetts)

Enzyme and protein active sites containing two or more interacting metal centers now figure prominently in metallobiochemistry. Systems containing metal clusters composed of Fe atoms (e.g. ferredoxins, sulfite reductase, hemerythrin, ribonucleotide reductase, methane monooxygenase), Cu atoms (e.g. hemocyanin, tyrosinase, ceruloplasmin, cytochrome oxidase), Mn atoms (photosystem II, catalase) and more than one element, or heteropolynuclear clusters (e.g. nitrogenase-Mo,Fe; cytochrome oxidase-Fe,Cu; hydrogenase and carbon monoxide dehydrogenase-Ni,Fe), have been identified. The ultimate goals of this project are to elucidate the structures of metal clusters in metalloproteins, to determine the roles these clusters serve in the function of the protein, and to understand how nature designs a cluster for a specific purpose. This knowledge will provide a detailed understanding of biological processes and will aid in the design of pharmaceutical enzyme inhibitors and catalysts for various reactions. During the current report period, we have completed studies comparing the structures of the Ni sites in hydrogenases from six different species of bacteria poised in a number of different redox states. These studies reveal the overall similarity of the Ni sites, with the exception of the enzyme from Alcaligenes eutrophus, which undergoes a large change in structure upon redox cycling. We also have examined samples of Chromatium vinosum hydrogenase in eleven distinct states. These studies corroborate and extend the previous studies done on the hydrogenase from Thiocapsa roseopersicina, and specifically confirm the absence of features indicative of CO ligation in the CO-inhibited enzyme.

EXAFS Characterization of the Zinc Binding Site in Cobalamin-Dependent Methionine Synthase * — X9B

K. Peariso, C.W. Goulding, R.G. Matthews, and J.E. Penner-Hahn (U. of Michigan)

Cobalamin-dependent methionine synthase (MetH) from *E. Coli* is an enzyme which catalyzes the transfer of a methyl group from methyltetrahydrofolate to homocysteine to give methionine. Recent studies have shown that the enzyme contains 1 mol zinc/mol protein [1], and that the zinc cofactor is required for methyl transfer to the homocysteine substrate [2]. We have used EXAFS to characterize the zinc binding site in both the native and substrate bound forms of the zinc binding domain, MetH(2-649). Changes observed in the XANES spectrum between the native and substrate bound MetH(2-649) (Fig. 1) demonstrate that addition of homocysteine has a direct effect on the zinc binding site. Fourier transforms of the EXAFS (Fig. 2) clearly show an increase in amplitude of the first-shell scattering peak, in addition to a small shift to longer bond distance in the MetH(2-649) + homocysteine sample. The EXAFS for the MetH(2-649) were best modeled with 1(N/O) at 2.03 A and 3S at 2.32 A, while the MetH(2-649) + homocysteine were best modeled with a single shell of 4S at 2.36 A [2]. These results suggest that the homocysteine substrate binds directly to the zinc cofactor before methyl transfer occurs.

[1] Goulding, C.W. and Matthews, R.G. *Biochem*, **1997**, in press. [2] Peariso, K., Goulding, C.W., Huang, S., Matthews, R.G., and Penner-Hahn, J.E., manuscript in preparation.

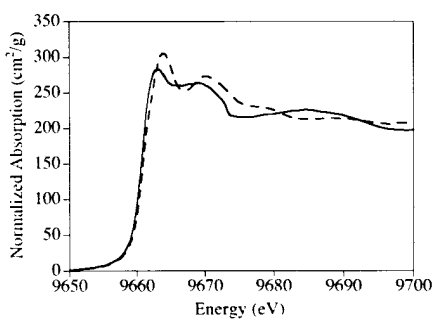

Figure 1. XANES spectra of MetH(2-649)with (dashed line) and without (solid line)L-homocysteine.

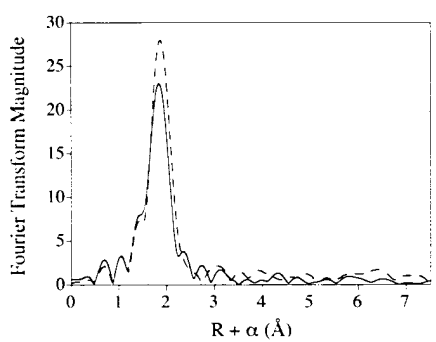

Figure 2. Fourier transforms of MetH(2-649) with and without L-homocysteine.

* Supported in part by the NIH. GM-38047(to JEPH) and GM-24908 (to RGM)

Temporal Speciation of Zinc in Zebrafish (*Danio Riro*) Embryos * | X9B

K. Peariso, F. Su, J. Kuwada, J.E. Penner-Hahn (U. of Michigan)

It has long been recognized that zinc plays a critical role in embryonic development, as evidenced by the teratogenic effects of zinc deficiency. Since the Zebrafish embryo develops without an influx of maternal nutrients, it must contain all of the zinc (and other necessary trace elements) required for development at the time of fertiliation. It has been shown that these embryos contain 1 mM zinc. XANES measurements have been made on five stages of Zebrafish embryos spanning the first eight hours after fertilization to determine whether changes ocurred in the bulk zinc environment during these early stages. Figure 1 shows the absorption differences between the XANES spectra of the later stages and the 1-cell, fertilized embryo. Based on these difference spectra, it is clear that there are significant changes in the bulk zinc environment of the zebrafish embryo during early development. Another intriguing result of these measurements is that the changes appear to be cyclic, demonstrating large differences in the 128-cell and 30% epiboly stages and very small differences in the high and 75% epiboly stages. Efforts are currently being focused on determining the type of zinc environment changes that could produce such differences and measuring the XANES spectrum of more stages within the first eight hours of development to verify the cyclic trend exhibited these measurements.

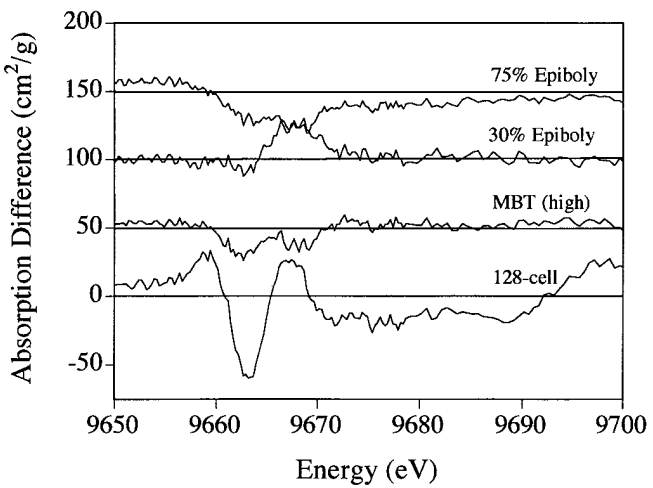

Figure 1. Time-dependent Zinc XANES spectra of developing Zebrafish embryos. Spectra shown are normalized absorption difference spectra relative to a 1-cell, fertilized egg.

* Supported in part by the NIH, GM-38047 (to JEPH).

X-Ray Absorption Spectroscopy of Nucleophilic Zn Enzymes | X9B

J. Penner-Hahn and K. Peariso (U. of Michigan)

Recent work has revealed the existence of a novel class of Zn enzymes, in which the Zn appears to function to activate a coordinated thiolate toward nucleophilic attack. X-ray absorption spectroscopy is being used to study three such enzymes that are involved in various aspects of methyl transfer: cobalamin-dependent and cobalamin-independent methionine synthase and cobamide: coenzyme M methyl transferase. EXAFS measurements on the native enzyme, on site directed mutants, and on enzyme samples with a variety of substrates and substrate analogs are in progress, with the goal of elucidating the three dimensional geometry of the Zn active sites.

Temporal Changes in Zn Speciation During Cell Development	X9B

J. Penner-Hahn and K. Peariso (U. of Michigan)

Zebrafish and *Xenopus* eggs contain ca. 1 mM Zn. Previous measurements have demonstrated that the Zn in these eggs undergoes reproducible, large changes in average structure as a function of time after fertilization. XANES measurements are being used to characterize these changes with improved temporal resolution. The data will be analyzed using the principal component method and selected temporal points will be used for EXAFS measurements.

A Low Angle Diffraction Study of the Structure of the Actomyosin Complex; Effects of ADP Binding	X9B

K. Poole, M. Lorenz, P. Ellison, G. Evans, G. Rosenbaum, P. Boesecke, K.C. Holmes, C.R. Cremo (Max Planck Inst.)

With an atomic model for the actin filament (Holmes et.al. 1990, Nature, 347: 44-49; Lorenz et.al. 1995, *J. Mol. Biol.* **246**, 108-119) and the atomic coordinates for at least one form of the myosin motor protein (Rayment et.al. 1993, *Science* **261**, 50-58) we are in a position to make use of high angle fibre diffraction data from myosin decorated actin filaments to refine a model structure of the complex. Nucleotide-free myosin subfragment-1 (S1) isolated from both chicken skeletal and smooth muscle sources was introduced into overstretched rabbit psoas muscle fibres. In both cases the protein binds tightly to actin and this results in the intensification of the actin based layer lines in the X-ray pattern. Refining an actomyosin atomic model against the nucleotide-free skeletal S1 data produced a best fit which was similar to the model suggested by Rayment et.al. (1993) based on electron microscope evidence. ADP binding had very little effect on the diffraction pattern. The nucleotide-free smooth muscle S1 decorated filaments produced a very different diffraction pattern and the binding of ADP was shown to induce a structural change in the head resulting in a pattern similar to that from skeletal S1 decorated fibres. The Kd for ADP binding was shown to be ca. 2μM. It is most interesting that the two rigor complexes are structurally different. If the rigor structure represents the end of the power stroke then the data imply that at least some part of the power stroke in these two motors is produced by different configuration changes of the actomyosin complex. Alternatively, we must question our interpretation of the rigor structures themselves. We are in the process of refining the model against the smooth muscle S1 data but it is clear that the ADP induced structural change in the myosin head is very large and certainly involves the distal part of the head. We intend to continue our investigation of the actomyosin motor mechanism by looking at the bound structures of myosin motors or parts of motors from different sources, both natural and engineered, with a range of nucleotides or their analogues in the active site.

Escherichia Coli Primase Zinc Structure is Sensitive to the Binding of ATP and High Magnesium	X9B

L.S. Powers and M.A. Griep (Utah State U.)

The structure of the single zinc site in primase from Escherichia coli was studied using X-ray absorption (XAS). XAS provides information about the immediate sphere (radius about 5 Å) of atoms surrounding the metal and has been widely used to characterize metalloproteins. The edge region of the spectrum provides information about the chemical identity of the ligating atom and their coordination geometry while the extended fine structure provides information about the number of ligating atoms and their average distance from the metal. The zinc site in native primase was found to be tetrahedrally ligated by three sulfurs at an average distance of 2.37 $\pm$ 0.02 and one histidine nitrogen located at a distance of 2.11 to $\pm$ 0.02. In the zinc site in high magnesium conformation of primase, one sulfur ligand is lost and one or two oxygen ligands are gained. Finally, when ATP was added to primase, the zinc site structure was altered to octahedral coordination by three sulfur and three oxygen (or nitrogen) ligands, one of which could be a histidine nitrogen. These results and others indicate that the primase zinc site is similar to the PMPS-removable and nonessential-site zinc from Escherichia coli RNA polymerase which can also be coordinated by its initiating nucleotide ATP (Wu, F.Y.H., Huang, W.J., Sinclair, R.B., Powers, L. Journal of Biological Chemistry 267: 25560-25567, 1992. In light of this, the high-magnesium conformation result suggests that high magnesium primase becomes inactive because the zinc is prevented from coordinating ATP.

EXAFS Studies of Nonheme Iron Enzymes	X9B

L.Que, Jr., L.Shu, X.Wang, K.Chen, H.Hsu (U. of Minnesota)

Several metalloproteins containing nonheme diiron centers were investigated in the past year. They include methane monooxygenase (MMO), ribonucleotide reductase (RNR), and purple acid phosphatase. A lot of efforts have been made to study the diiron structure of the high-valent reactive intermediate Q of MMO. XAS data analysis shows an unprecedentedly short Fe-Fe distance of ca. 2.46 angstroms [1]. A similar Fe-Fe distance of 2.46 angstroms has also been observed in intermediate X of RNR, another extensively studied diiron-containing enzyme [2]. These results prompt us to propose a Fe2O2 diamond core structure in both MMO and RNR catalytic cycle and therefore provide essential evidence for the proposed dioxygen activating mechanisms of nonheme diiron-containing enzymes. Data was also collected on an Fe(III)Zn(II) derivative of the purple acid phosphatase from porcine uterus which allows us to look at the Fe(III) and the Zn(II) sites separately. In the phosphate complex of this derivative, the observation of Fe-Zn and M-P (M = Fe, Zn) distances of 3.3 and 3.2 angstroms, respectively, indicates an FeZn(OR)2 core structure and phosphate is proposed to bind to the metal center in a bridging mode [3]. Other oxoanions complexes, such as molybdate and tungstate, have been collected and analyzed as well, and an asymmetric bridging mode is proposed for FeZnUfMoO4 and FeZnUfWO4. The paper is in preparation. Because EXAFS analysis can be a very useful tool for the structure characterization of unstable model complexes, we have also been using EXAFS to study model complexes related to intermediates of metalloproteins along with our investigation of metalloprotein systems. In the past year, data was taken and analyzed on copper model complexes modeling the copper dioxygen chemistry in biological systems [4]. It enabled us to reveal a novel reversible O-O bond cleavage and formation by a dimetallic cluster.

References

[1] L. Shu, J. C. Nesheim, K. Kauffmann, E. MYnck, J. D. Lipscomb, and L. Que, Jr., "An Fe2O2 Diamond Core Structure for the Key Intermediate Q of Methane Monooxygenase", Science, 25, 515-518 (1997).

[2] P. J. Riggs-Gelasco, L. Shu, S. Chen, D. Burdi, B. H. Huynh, L. Que, Jr., and J. Stubbe, "EXAFS Characterization of the Intermediate X Generated During the Assembly of the E. coli Ribonucleotide Reductase R2 Diferric-Tyrosyl Radical Cofactor", J. Am. Chem. Soc., submitted (1997).

[3] X. Wang, C. R. Randall, and L. Que, Jr., "X-Ray Absorption Spectroscopic Studies of an FeZn Derivative of Uteroferrin", Biochemistry, 35, 13946-13954 (1996).

[4] S. Mahapatra, J. A. Halfen, E. C. Wilkinson, G. Pan, X. Wang, V. G. Young, Jr., C. J. Cramer, L. Que, Jr., and W. B. Tolman, "Structural, Spectroscopic, and Theoretical Characterization of Bis(m-oxo)dicopper Complexes, Novel Intermediates in Copper-Mediated Dioxygen Activation", J. Am. Chem. Soc., 118, 11555-11574 (1996).

Metal Cluster Active Sites in Protein — X9B

L. Que, Jr., L. Shu, X. Wang, K. Chen and S. Mandal (U. of Minnesota)

Several metalloproteins containing nonheme-iron centers were investigated in the past year. This class includes methane monooxygenase, ribonucleotide reductase, and purple acid phosphatase. We have collected and analyzed data on methane monooxygenase hydroxylase (MMOH). XAS analysis of MMOH suggests the presence of two Fe-Fe distances of about 3Åand 3.4Å, which are proposed to reflect two populations of MMOH molecules with either a bis (μ-hydroxo) (μ-carboxylato)- or a (μ-hydroxo) (μ-carboxylato diiron(III) core structure, respectively. This novel core flexibility is suggested to be required to accommodate the various intermediates in the catalytic cycle. A lot of efforts have been made to study the diiron structure of the high-valent reactive intermediate Q of MMOH. XAS data analysis shows an unprecedentedly short Fe-Fe distance of ca. 2.46 Å. A similar Fe-Fe distance of 2.46 Åhas also been observed in intermediate X of ribonucleotide reductase (RNR), another extensively studies diiron-containing enzyme. These results prompt us to propose a Fe_2O_2 diamond core structure in both MMO and RNR catalytic cycle and therefore provide essential evidence for the proposed dioxygen activating mechanisms of nonheme iron-containing enzymes. Data was also collected on an Fe(III)Zn(II) derivative of the purple acid phosphatase from porcine uterus which allows us to look at the Fe(III) and the Zn(II) sites separately. In the phosphate complex of this derivative, the observation of Fe-Zn and M-P (M=Fe, Zn) distances of ~3.3 and 3.2 Å, respectively, indicates an $FeZn(OR)_2$ core structure and phosphate is proposed to bind to the metal center in a bridging mode. Other oxoanions complexes, such as molybdate and tungstate, have been collected and analyzed as well, and an asymmetric bridging mode is proposed for $FeZnUf{\bullet}WO_4$. The paper is preparation. Because EXAFS analysis can be a very useful tool for the structure determination of unstable model complexes, we have also been using EXAFS to study model complexes related to intermediates of metalloproteins along with our investigation of metalloprotein systems. In the past year, data was taken and analyzed on copper model complexes modeling the copper dioxygen chemistry in biological systems.

Thermopphillic Alcohol Dehydrogenases — X9B

I. Sagi (Weizmann Institute of Science)

Interconversion of alcohols, aldehydes, and ketones are essential processes in both prokaryotes and karyotes. The oxidoreductases catalyzing these reactions use a variety of different electron acceptors and can be ivided into three main groups: 1) the NAD(P)-dependent alcohol dehydrogenases 2) the NAD(P)-independent alcohol dehydrogenases, which use other cofactors for catalysis; and 3. FAD-dependent alcohol oxidases, which catalyze irreversible oxidation of alcohols. *Thermoanaerobacter* (formerly *Thermoanaerobium*) *brockii* alcohol dehydrogenase (TBADH) is a medium chain, NADP-linked, class A enzyme that reversibly catalyses the oxidation of secondary alcohols to the corresponding ketones.

$$\mathrm{RC(OH)R' + NADP} \overset{TBADH}{\longleftrightarrow} \mathrm{RC(O)R' + NADPH}$$

The ubiquitous alcohol dehydrogenases (ADHs) are found not only in bacteria, but also in yeast, plants, insects and in man. ADH is an oxidoreductase, requiring either NAD(H) or NADP(H) as a coenzyme, that reacts with primary and secondary, linear and branched-chain, aliphatic and aromatic alcohols and with their orresponding aldehydes and ketones. Although some ADHs depend on iron for activation and certain ADHs are known to be metal-free, most ADHs contain zinc at the active site. Zinc-dependent ADHs are either dimers, usually found in higher plants and mammals, or tetramers, such as those present in yeast and bacteria. A monomeric ADH was isolated from *Saccharomyces cerevisiae*, but its metal content is yet unknown.

a) Native TBADH. XAFS data of native TBADH has been collected on zinc and cobalt K-edges. Analysis of EXAFS and edge data of native enzyme and its metal derivatives will provide the ground base for the assigument of coordination environment and accurate metal-ligand distances at the active site. **b) Inhibition Studies.** XAFS measurements on inhibited TBADH were conducted using TBADH-DMSO (dimethyl sulfoxide) complex. DMSO is known to inhibit ALDH in a transition state manner. X-ray crystallography studies of ALDH-DMSO complexes show that the DMSO ligand is directly bound to the catalytic zinc ion. XAFS and edge data will be collected on native TBADH and Cd/Co substituted TBADH complexed with DMSO. Assigning the coordination environment and metal-ligand distances of the active site in TBADH-DMSO complex will provide the structure of the transition state analogue of TBADH and a relevant structural intermediate in the catalytic pathway.

EXAFS of the Low Spin Ferric Center of Nitrile Hydratase	X9B

R.C. Scarrow, B. Strickler, D. Pringle (Haverford College) and M. Nelson (DuPont)

We have been continuing our investigations of the low spin iron center in nitrile hydratase, in collaboration with Mark Nelson and John Cummings of DuPont, who have provided us with frozen protein samples. EXAFS has identified two or three sulfur ligands to the iron center, with the remaining ligands being oxygen or nitrogen scatterers. Some minor changes are seen with binding of inhibitors (to the enzyme-not necessarily to the iron center) such as phenylhydrazine or isobutyronitrile. We are currently in the process of modelling the EXAFS to give bond length distributions to see if this may give insight into the changes which are occuring on the binding of these inhibitors. We have also obtained EXAFS data on model low spin ferric compounds prepared by Henry Jackson and Prof. Julia Kovacs of the Department of Chemistry, University of Washington. These complexes have a ligand with a N3S2 donor set and can be prepared as a binary low spin iron (III) complex (a rare example of five-coordinate iron (III) or as ternary, six-coordinate complexes with a variety of auxilliary ligands including azide and nitric oxide. The EXAFS and edge intensities of these complexes are being compared to those of nitrile hydratase to gain further insight into the coordination of iron in the enzyme.

Global Mapping of XAS Data: Structure of the Active Site of Cobalamin Enzymes	X9B

E. Scheuring, M. Chance (AECOM), R. Banerjee, and R. Padmakumar (U. of Nebraska)

The two available crystallographic structures of cobalamin dependent enzymes, the 27 kDa fragment of the methylcobalamin-dependent enzyme, methionine synthase, from *Escherichia coli* [C. L. Drennan et al. *Science*, **266**, 1669 (1994)] and the 5'-deoxyadenosylcobalamin-dependent enzyme methylmalonyl-coenzyme A mutase from *Propionibacterium shermanii* [F. Mancia et al. *Structure*,**4**, 339 (1996)], show striking similarities despite the differences in reaction mechanism. In particular, the 5,6-dimethylbenzimidazole group is detached and replaced by a histidine group of the enzyme. Here we present an analysis of Extended X-ray Absorption Fine Structure (EXAFS) spectroscopic data for both 5'-deoxyadenosylcobalamin and aquocobalamin bound to methylmalonyl-coenzyme A mutase in the absence of substrate. The analysis is conducted with a suite of programs called AUTOFIT 1.0 [Chance et al., *Biochemistry*, **1996**, 35, 9014], which allows an evenhanded comparison of the goodness-of-fit of the EXAFS data to a varied grid of simulations based on the *ab initio* EXAFS code FEFF 6.01. The x-ray edge data indicate an increase in effective nuclear charge of the metal ion of the enzyme bound 5'-deoxyadeonsylcobalamin compared to the corresponding free cobalamin and the EXAFS results show small decreases in equatorial and no significant change in the Co-C bond length (despite the potential elongation of the Co-N(His) bond) upon cofactor binding to the enzyme. Thus, the change in coordination of the nitrogenous axial ligand engineered by the enzyme does not significantly contribute to a *trans* effect in the ground state. Weakening of the Co-C bond must be initiated by substrate binding. In addition, the global mapping technique resolves discrepancies between previous EXAFS results and crystallographic data on aquocobalamin.

Structure and Thermally Induced Failure of Organic LEDs * | X10B

P. Fenter, F. Schreiber, V. Bulović and S. R. Forrest (Princeton Univ.)

Organic light emitting devices (OLED) represent a new basis for light emissive flat panel displays. We have used x-ray reflectivity to study the structure and thermal degradation mechanism of films and heterostructures consisting of the archetype molecular OLED materials, "TPD", and "Alq3" which were grown on Si wafers by thermal evaporation under high vacuum[1]. The x-ray specular reflectivity of three thin film structures is shown in Fig. 1 (thin and bold lines are experimental data and theoretical fits, respectively). These include (i) TPD on Si, (ii) Alq3 on Si, and (iii) Alq3/TPD on Si. The derived the electron density profiles (shown in Fig. 1b), reveal interface roughnesses of <4.5Å. In Fig. 1c we show the one-dimensional Patterson map for each sample. For the TPD and Alq3 films, a single peak is found corresponding to the film thickness, L(TPD)=306Å, and L(Alq3)=577Å, while the Alq3/TPD heterostructure shows three components corresponding to L(TPD)=296Å, L(Alq3)=518Å, and a total film thickness of L(TPD+Alq3)=813Å. Since the position and intensity of each peak in Fig. 1c is directly related to the layer thickness and the interfacial density discontinuities, respectively, they provide a direct and model-independent means of characterizing the thermally induced failure mechanism of the multilayer device system. Our results indicate that the thermally induced failure of the Alq3/TPD heterostructure is driven by the large thermal expansion coefficient of TPD (independently measured for the TPD film), above its glass transition temperature of 60°C. This thermal expansion is found to induce a strain in the Alq3/TPD heterostructure, and which drives an inhomogeneous strain relief process (e.g., blistering). [1] P. Fenter, F. Schreiber, V. Bulović and S. R. Forrest, Chem. Phys. Lett. 277, 521 (1997).

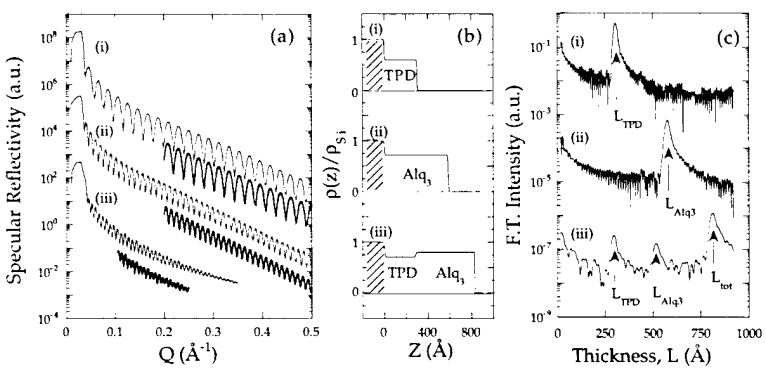

Figure 1.

* This work is supported by the NSF, the AFOSR, and the Universal Display Corporation. F. S. acknowledges the support of the DFG.

Surface X-ray Diffraction Studies of Monolayers of ω-alkenethiol on Au(111) * | X10B

T.Y.B. Leung, P.Fenter, F.Schreiber, P.Eisenberger and G.Scoles (Princeton U.)

We have carried out a surface x-ray diffraction study on monolayers (SAMs) of a series of thiols ω-substituted with the ethylene group, CH_2=$CH(CH_2)_{n-2}SH$ [hereafter abbreviated as C_n], assembled on the (111) face of single crystal gold. Using the self-assembly approach, we have successfully prepared and characterized this system and found that the ethylene endgroups are well-ordered. The thermal behavior of the films was also investigated. Films of thiols on gold are of technologically and scientific importance for several reasons. First of all, they have been extensively studied in the last two decades, and their potential after chemical derivatization has been explored in various technological applications.[1] In order to have a molecular control and tailor the properties of these functionalized SAMs, a detailed understanding of the impact of the endgroups onto the properties and the monolayer structures is needed. Studying the impact of the endgroups reveals the energetic interplay in the self-assembly process. For the particular system presented here, we are also conducting a parallel study on the stereo-dependence of the reactivity of the ethylenic group, which is one of the most important functional groups in industrial chemistry.

We have conducted a series of surface x-ray diffraction studies on films made with molecules where n=9,10,11,17 and 18. The unit mesh of these monolayers was found to be the same as that of the n-alkanethiol SAMs on gold(111). It can be described as a c($4\sqrt{3}$ x $2\sqrt{3}$)R30°C lattice.[2] However, while the tilt angles of C_{10},C_{17} and C_{18} were found to be the same as those of SAMs of alkanethiol of the same chain length, their tilt directions were found to differ somewhat from those of alkanethiol SAMs. For C_{18} monolayers, (the system for which the largest difference was found) the tilt diection is rotated away by 14.1° ± 2.8° with respect to the next-nearest-neighbor(NNN) direction while from an earlier study, this value had resulted to be 8.2° ± 0.5°.[2] An interesting and rather surprising finding is that the tilt direction of the odd-chain monlayers C_{17} is smaller than that of C_{18} and it is rotated only by 5.0° ± 2.9° with respect ot the NNN direction.the observation may be explained by an odd/even effect in π-π interaction of the ethylene endgroups. The thermal properties and the chain length dependence of the thermal properties of these functionalized monolayers were also investigated and found to be very similar to those of alkanethiol monolayers.[3] In conclusion, the impact of the ethylene as endgroups in the self-assembled monolayers of thiol on gold was found to be small. We have also shown that a well-ordered "layer" of ethylene functional groups can be made via self-assembly. In future, we plan to explore the stereoreactivity of these films with beams of atomic oxygen impinging on these surface at variable angles and variable energies.

Reference: [1] A. Ulamn, An introduction to Ultrathin Organic films: From Langmuir-Blodgett to Self-Assembly (Academic, Boston 1991). [2] P. Fenter, P. Eisenberger and K. S. Liang, Phys. Rev. Lett., 70, 2447, (1993). [3] P. Fenter, A. Eberhardt, K. S. Liang and P. Eisenberger, J. Chem. Phys., 106, 1600, (1997).

* We would like to acknowledge Prof. R. Pascal of Princeton Univ. for assisting us in preparation of the thiol and P. V. Schwartz and A. Eberhardt for their participation. This work was financially supported by the Department of Energy

In-situ Studies of the Growth of Coassembled Surfactant/Silica Films	X10B

L. Zhou, P. Fenter, I. Aksay, P. Eisenberger (Princeton U.)

Mesoscopic surfactant/silica thin films have been grown on the surface of mica and silicon under the aqueous condition at pH = 1.6. The molar ratio of the growth solution is TEOS : CTAC : H_2O = 1:2:1000. The structure and the lattice strain of the thin film have been studied [1]. The in-situ growth of the film is studied by following the specular diffraction in real time.

Our results show that there is a 7 hour induction time and the film grows to 1 micron in a few hours after nucleation with a nonlinear growth rate [2]. Similar growth behavior has been found for the films grown on silicon substrate. Therefore the induction time is independent of the nature of the substrate.

We have changed the concentration of CTAC and TEOS to investigate the role that each component plays in the growth process. We have found that the induction time is inversely proportional to the TEOS concentration, and there are at least two growth regimes. At high surfactant concentrations, the induction time depends on the ratio of TEOS to CTAC concentrations. At low surfactant concentrations, the induction time depends on the concentration of TEOS only. The induction time is correlated to the growth rate of the film.

These data suggest that the film growth is a true coassembly process in which the polymerization rate of the silicate, the formation of the surfactant micelles and the interaction between the growth solution and the substrate all play a very important role.

[1] I. A. Aksay, M. Trau, S. Manne, I. Homma, N. Yao, L. Zhou, P. Fenter, P. M. Eisenberger, S. M. Gruner, Science, 273, 892-897 (1996)

[2] L. ZHou, P. Fenter, I. A. Aksay and P. M. Eisenberger, The 43rd National Symposium of American Vacuum Society, October 1996

Local Structure of DiluteTernary 3d Transition Metal Dopants in Ni_3Al *	X11A

M. Balasubramanian, R. Lyver, J. I. Budnick and D. M. Pease (U. of Connecticut)

We have utilized the technique of XAFS to study the local structural order of 3d transition metal (TM) ternary dopants (Ti, V, Cr, Mn, Fe and Co) in $Ni_{75}TM_xAl_{25-x}$. In $\gamma' - Ni_3Al$, the first shell around Al consists of 12 Ni atoms. Ni is surrounded by 8 Ni and 4 Al atoms. In all cases dopant K-edge XAFS results show only Ni backscattering contribution in the first peak of the Fourier transform. Al backscattering contribution is either completely absent or is so weak that it is masked by the strong dopant-Ni bond [1]. The number of Ni near neighbors suggests that for Ti, V, Cr, Mn and Fe absorbers, a majority of the dopants occupy the Al sublattice. However, even in the case of Co dopants where studies by others indicate that the Co atoms occupy the Ni sublattice, no Al backscattering contribution can be detected. A model [2] based on a highly distorted Al sublattice, created by dopant atoms occupying the Ni sublattice, gives a possible explanation for the absence of Al backscattering contributions, and furnishes an explanation for similar studies by others in ternary doped $\gamma' - Ni_3Al$. These investigations are of importance in understanding the effect of dopants on the mechanical properties of such alloys.

[1] M. Balasubramanian, R. Lyver, J. Budnick and D. Pease, J. de Physique **7**, C2-1043 (1997)

[2] M. Balasubramanian, R. Lyver, J. Budnick and D.Pease, Appl. Phys. Lett. **71**(3), 330 (1997)

* Work supported by the U.S. DOE under Grant No. DE-FG05-89-ER45384.

Preferential Co–Si bonding at the Co/SiGe(100) interface * | X11A

B. Boyanov, P. Goeller, D. Sayers, and R. Nemanich (NCSU)

The initial stages of the reaction of Co with $Si_{0.79}Ge_{0.21}(100)$ were studied *in situ* with extended x-ray absorption fine structure spectroscopy (EXAFS) and reflection high energy electron diffraction (RHEED). The first coordination shell of as-deposited 0.7 monolayer (ML) Co films consisted of Si and Ge atoms in approximately 4:1 ratio, similar to the stoichiometry of the $Si_{0.79}Ge_{0.21}$ substrate. After annealing at 450 °C the 0.7 ML film assumed a $CoSi_2$-like structure (Fig. 1) with 6-fold Co–Si first-shell coordination and a $(3\sqrt{2} \times \sqrt{2})$ surface reconstruction. Similarly annealed 1.7 ML films exhibited a $CoSi_2$ structure with the same reconstruction and 8-fold Co–Si coordination. Residual Co–Ge bonding ($\approx$ 1 nearest neighbor) was detected in both the 0.7 and 1.7 ML annealed films. The deviation of the Si:Ge ratio in the first coordination shell of Co from that of the $Si_{0.79}Ge_{0.21}$ substrate indicates preferential formation of Co–Si bonds in the annelaed films. The observed preferential Co–Si bonding has significant implications for the growth of single-crystal $CoSi_2$ template layers on SiGe. Such template layers have been widely used to control the formation of misoriented grains in epitaxial $CoSi_2$/Si(100) heterostructures.

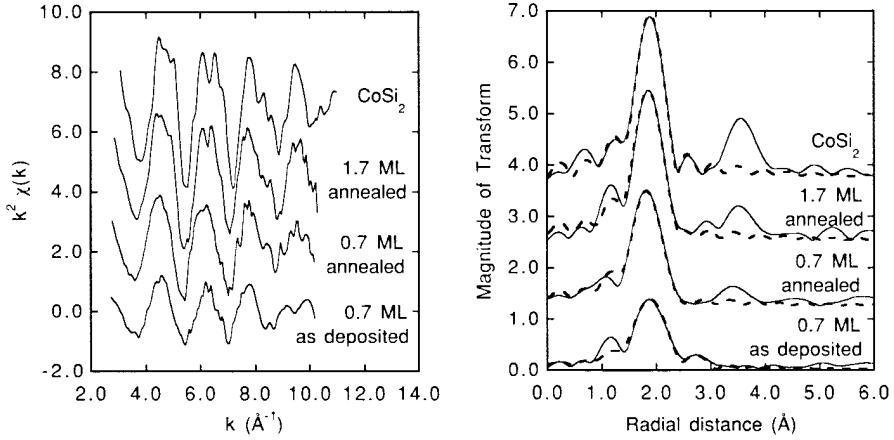

Figure 1. Normalized and Fourier-transformed k^2-weighted EXAFS data (solid line) and fit results (dashed line) for the samples used in this study. The top trace is the data for a 730 Å-thick $CoSi_2$/Si(100) film.

* This work was supported by DOE grants DE-FG05-93ER79236 and DE-FG05-89ER45384.

Co-deposition of Cobalt Disilicide on Silicon-Germanium Thin Films | X11A

P. Goeller (No. Carolina State U.)

The formation of $CoSi_2$ on strained epitaxial $Si_{0.8}Ge_{0.2}$/Si(100) films has been studied as a function of the depositoin method and annealing temperature. Two types of deposition processes were used: a direct method, where 5 nm of pure Co metal were deposited at room temperature onto a strained 80 nm thick $Si_{0.8}Ge_{0.2}$ layer; and a co-deposition method, where 5 nm Co and 18.2 nm Si were simultaneously deposited in a 1:2 ratio onto a strained $Si_{0.8}Ge_{0.2}$ layer at 450 C. Samples were then annealed at temperatures ranging from 500 to 800 C. EXAFS and XRD were used to characterize the structure of the resulting films. It ws found that the samples prepared via the direct depositon method did not convert to $CoSi_2$ at any annealing temperature up to 800 C, while the co-deposited samples formed epitaxial $CoSi_2$ at even the lowest annealing temperature of 500 C. These results are discussed in terms of proposed reaction mechanisms of the different deposition methods, based on consideration of the Co-Si-Ge ternary phase diagram.

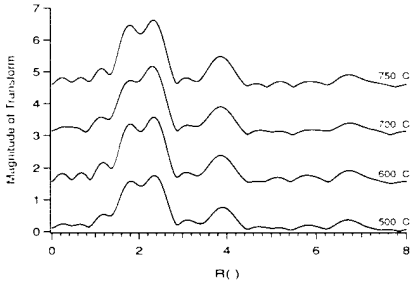

Figure 1. Fourier transforms of k2-weighted EXAFS data for direct deposited samples annealed at 500-800 C for 10 minutes.

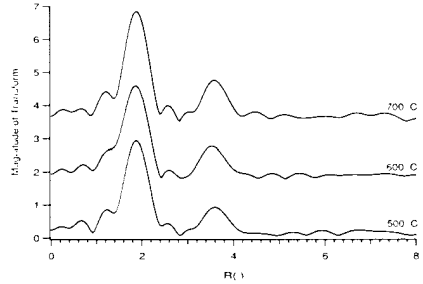

Figure 2. Fourier transforms of k2-weighted EXAFS data for co-deposited samples annealed at 500-700 C for 10 minutes.

Stability of Heavy-Metal Sulfides During Oxidation of Contaminated Soil from a Superfund Site	X11A

P. D. Hansen, D. Hesterberg, W. Zhou, and D. E. Sayers (NC State)

The long-term stability of solid-phase heavy-metal species in soils depend on their resistance to changes in the soil chemical environment. The objective of this study was to determine how exposure to oxidizing conditions affected the speciation of Cu, Zn, and Pb contaminants in samples of reduced soil from a superfund site in the eastern coastal plain of North Carolina. EXAFS analyses of Cu, Zn, and Pb were done at Beamline X-11A on preserved samples collected from four depth intervals (zones) in the soil profile of a waste-disposal site at the Marine Corps Air Station in Cherry Point, NC. Subsamples of this soil were used in a column-flow study to measure metal dissolution under changing redox conditions. After 1 month of continuous exposure to aerated aqueous solution, the soil columns were dismantled and analyzed using EXAFS spectroscopy. The samples contained 1,100 to 1,800 mg Cu/kg, 4,300 to 11,000 mg Zn/kg, and 1,700 to 4,100 mg Pb/kg. EXAFS data showed that metals in the soil samples from Zone 1 (0 to 20 cm depth) and Zone 2 (23 to 47 cm) were predominantly bonded to oxygen in the first shell (Cu-O, Zn-O, and Pb-O bonding). In the Zone 3 (47 to 73 cm) and Zone 4 (73 to 101 cm; the shallow groundwater zone), there was evidence for metal-sulfides for all three metals, with CuS being the dominant Cu phase (Fig. 1). After the column treatment with oxygenated CaCl2 solution, the proportion of metal-sulfides was essentially unchanged, indicating that these minerals were resistant to oxidative dissolution during the course of the column study. A loss of acid volatile sulfide (sulfides converted to hydrogen sulfide gas by an acid treatment) during the column experiment may have helped to stabilize the heavy-metal sulfides, despite the redox potential increasing from -200 to +50 mV (at pH 7.5). The results indicate that the metal sulfides in the deeper zones of the contaminated soil would be resistant to dissolution during short periods of increased redox potential.

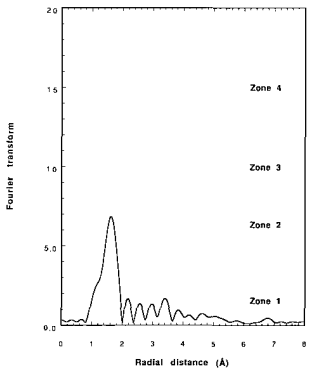

Figure 1. Fig. 1. Radial structure functions (uncorrected for phase shift) of Cu in samples from different depths (zone 1 is shallowest) in the soil profile at the Marine Corps Air Station superfund site.

XAFS Study of Copper Binding with a Sulfur-Rich Humic Acid	X11A

D. Hesterberg, D. E. Sayers, W. Zhou, and K. Hutchison (NC State U.)

The geochemical transformation of heavy metal contaminants into unique mineral phases and adsorbed chemical species in different soil environments is critically important for understanding the long-term stability and fate of these contaminants. Past studies showed that with increasing concentration of certain transition metals bound to soil humic acid (HA), the metal binding affinity decreased. Humic acid is a purified extract of organic matter that typically contains an abundance of reactive carboxylic and phenolic acid functional groups and lesser amounts of nitrogen (e.g., amine) and sulfur (e.g., thiol) groups. The objective of this research was to determine whether Cu(II) preferentially binds to sulfur groups in HA at low adsorbed metal concentrations. A sulfur-rich HA extracted from a soil in a coastal marine wetland was reacted with Cu(II) at pH 5.6 in aqueous background solutions of 0.1 M NaCl or 0.1 M NaNO3. The molar ratio of organic S-to-metal was 4.25, and the total Cu concentration in the suspension was 2 mmol/kg. Sulfur K-XANES data from NSLS Beamline X-19A indicated that about half of the organic sulfur in the samples was in a reduced oxidation state (-II). Copper K-EXAFS spectra showed no evidence for first-shell Cu-S bonding, but Cu bonding was primarily to oxygen or nitrogen atoms. Despite the chalcophilic nature of Cu(II), it does not appear to preferentially bind to organic S groups under the experimental conditions used. This result suggests that our past observations of Cu-S bonding in samples of reduced soil collected from contaminated sites primarily represents inorganic Cu-sulfide species.

XAFS Study of Metal-Sulfide Formation in Contaminated Soil Treated with H2S	X11A

D. Hesterberg (NC State U.), E. C. Thornton (Pacific Northwest National Lab) , W. Zhou, and D. E. Sayers (NC State U.)

The sequestering of potentially-toxic heavy metals as insoluble sulfide minerals under reduced soil conditions may reduce metal mobility and bioavailability. The objective of this study was to determine whether injection of dilute $H_2S(g)$ into a contaminated soil induced the formation of Cu- and Pb-sulfide minerals. The $H_2S(g)$ remediation treatment was originally designed to reduce Cr(VI) to Cr(III) in soil; however, sequestering of heavy metals as sulfides may also be beneficial in certain soils. A column of soil material from the Chemical Waste Landfill at Sandia National Laboratory was treated in the laboratory with a mixture of 0.01% (v/v) $H_2S(g)$ in $N_2(g)$. The sample contained 20 mmol Cu/kg, 186 mmol Pb/kg, and 208 mmol Fe/kg. XAFS analyses were done at Beamline X-11A on untreated and treated soil samples to determine changes in local molecular bonding of Cu(II), Pb(II), and Fe(III) induced by the treatment. Copper(II) was converted from a predominantly 1st-shell oxygen-bonded solid phase to CuS. Although the sample contained considerably more Pb(II) and Fe(III), the $H_2S(g)$ treatment had no discernible effect on the 1st-shell Pb-O and Fe(III)-O bonding structures of these metals. Results were consistent with the greater thermodynamic stability of CuS relative to PbS and FeS. This study demonstrates the utility of XAFS for evaluating the success of in-situ remediation treatments designed to chemically alter contaminants in place.

Electrocatalysis of Methanol and CO Oxidation: An *In situ* XAS Study *	X11A

S. Mukerjee and J. McBreen (BNL)

Elements such as Ru and Sn used as ad-atoms or as alloying elements are known to enhance methanol and CO oxidation. Unlike Ru, enhancement due to Sn additions depend on the nature of interaction of Sn with Pt. Pt alloyed with Sn is marginally active for methanol oxidation in contrast to upd Sn ad-atoms on Pt, but show good activity for CO oxidation. *In situ* XAS studies at the Pt L_3 edge for Pt/C shows that adsorption of hydrogen, oxygenated species and methanol oxydation products (CO and CHO poisons) induce major changes in the Pt L edge XAS. This is evident from the changes in the white line in at 0.0, 0.54 and 0.84 V in the presence of 1 M $HClO_4$ + 0.3 M MeOH. (see J. Electrochem. Soc.,**143**, 2285 (1996) and J. Electroanal. Chem (In Press) for more details. In contrast to this the Pt L_3 edge white line for PtRu/C and PtSn/C show very little variation with potential. Alloying of Ru and Sn to Pt however have very different effects on their electronic and geometric characteristics. In the case of Ru a increased white line (higher Pt *d* band vacancy) and shorter Pt-Pt bond distance is affected in contrast to alloying with Sn. XANES at the Sn and Ru K edges in PtRu/C and PtSn/C alloys as well as upd Sn on Pt/C however provide clear evidence of the presence of oxygenated species even at 0.0 V. The strength and nature of these species are however potential dependent. For upd Sn on Pt/C, the XANES at the Pt L_3 edge in 1 M $HClO_4$ shows behavior similar to those observed previously in the case of Pt/C (see ref. 1), a congruence of white lines for sample and Pt reference foil at 0.54 V (double layer region). This together with the EXAFS results indicate that upd Sn does not significantly effect the electronic and structural charateristics of Pt. The higher Pt *d* band vacancy, shorter Pt-Pt bond distances in the PtRu/C together with the presence of oxygenated species on Ru help explain the higher activity for methanol and CO oxidation. The opposite effects on Pt in PtSn alloy help explain its lack of MeOH activity. In the case of upd Sn the Pt remains unaffected, that together with the presence of oxygenated species on Sn ad-atoms at lower potentials help explain the enhanced methanol oxidation activity.

* This work was supported by the Office of Transportation Technologies, Electric and Hybrid vehicles division of U. S. D. O. E

An XAS Study of Corrosion Characteristics in AB_5 Type Metal Hydride Electrodes *	X11A

S. Mukerjee, J. McBreen, J.J. Reilly, J.R. Johnson and G.D. Adzic (BNL)

The cycle life characteristics of AB_5 alloys depend primarily on the extent of its susceptibility to stress cracking due to volume expansion and contraction during hydriding. However, several alloy substituents such as Ce, Co *etc.*, and presence of zincate in the electrolyte helps improve cycle life without having a direct correlation with changes in volume expansion/cycle. This investigation is aimed at correlating the structural and cycle life characteritics of various AB_5 type alloys with the corrosion of constituent elements in these alloys such as Ni, Co, Mn and Fe. The focus however has been on the Ni due to its relative abundance and catalytic importance in the alloy. Surface (electron yield) and bulk averaged (transmission) XAS were conducted on the electrodes before and after electochemical cycling (150 cycles). The powders used as a part of this study were peractivated in the gas phase to ensure particle sizes 2-5 micro-meters. The electron yield mode probed the first 200-250 angstroms of the surface based on the more energetic KLL Auger electrons with 6.5 KeV electrons at the Ni K edge.

EFFECT OF Ce SUBSTITUTION

Ce substitiution in the A component of the prototype $LaNi_5$ alloy results in reduction of corrosion of the substituent elements such as Ni and hence in lower build up of surface $Ni(OH)_2$. This was evidenced from comparison of the white lines of the Ni K edge XAS in the transmission mode for electrode as a function of cycling. Comparison of the electron yield and transmission spectra at the Ni K edge after 150 cycles for sample with and without Ce showed very little surface build up of $Ni(OH)_2$ in the Ce containing sample in contrast to those without Ce substitution. Independent measurements using *in situ* scanning vibrating electrode technique have shown that Ce passivates the surface reducing surface corrosion.

EFFECT OF Co SUBSTITUTION

Co substitution causes lowering of the molar volume of hydrogen and hence a reduction in stress cracking of the alloy. The Co K edge XANES in the electron yield and transmission modes have also revealed a build up of the more conducting $Co(OH)_2$ on the surface of the electrode negating the effects of resistive build up of surface $Ni(OH)_2$.

EFFECT OF ZINCATE CONTAINING ELECTROLYTE

The presence of ZnO in the electrolyte results in significant imporovement of the cycle life in non Ce substituted samples. This translates itself to lower Ni corrosion and build up of $Ni(OH)_2$ in these samples as evidenced from the electron yield and transmission XANES. In the Ce substituted samples the effect is marginal and agrees with significantly smaller increases in the cycle life.

* Office of Basic Energy Sciences, U.S.D.O.E.

Local Structure of Br in Brominated-YBCO *	X11A

D. Potrepka, M. Balasubramanian, J. Budnick and D. Fenner (U. of Connecticut)

Bromination of deoxygenated YBCO leads to a partial restoration of superconductivity and causes the YBCO lattice to change from a non-superconducting tetragonal structure to an orthorhombic structure [1,2]. In order to understand the mechanism by which superconductivity is restored in these materials it is of interest to understand the local structural properties of Br atoms in the YBCO lattice. Neutron diffraction measurements suggest that Br atoms occupy vacant O(4) sites in the YBCO lattice [2]. Unfortunately, these experiments are hampered by the similarity in the neutron scattering lengths of oxygen and Br. We have performed low-temperature (11 K) Br K-edge XAFS measurements in brominated-YBCO and find that *Br does not occupy the YBCO lattice but rather precipitates out as small $BaBr_2$-like particles.* In conjunction with Cu NQR measurements our results indicate that on bromination the system undergoes an oxygen redistribution within the YBCO lattice. This redistribution probably causes the restoration of superconductivity in these materials [3].

[1] H. B. Radousky et al., Phys. Rev. B **41**, 11140 (1990)
[2] M. Mokhtari et al., Solid State Comm. **93**, 487 (1995)
[3] D. Potrepka et al., to be submitted to Appl. Phys. Lett.

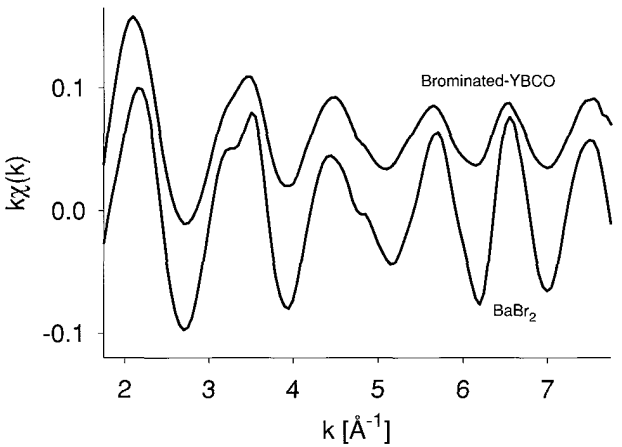

Figure 1. Comparison of the Br- XAFS spectra of brominated YBCO with $BaBr_2$. The similarity in the XAFS clearly reveals the presence of small particles of $BaBr_2$ in brominated-YBCO.

* Work supported by the U. S. DOE under Grant No. DE-FG05-89-ER45384.

Local Coordination of Ba and Pb in Calcite from XAFS Spectroscopy	X11A

R.J. Reeder (SUNY at Stony Brook) and G.M. Lamble (LBNL)

XAFS spectra at the Pb L(III)-edge and the Ba K-edge of Pb- and Ba-doped calcite (CaCO3) were analyzed to reveal that Pb(II) and Ba(II) both substitute for Ca in the unique octahedral metal site in the corner-shared calcite structure. First-shell Pb-O and Ba-O distances are very similar to those predicted for sixfold coordination, however, sixfold coordination for both ions is considered rare because of their large sizes and preference for higher coordination number. For example, PbCO3 and BaCO3 both have the aragonite structure, in which the metal is ninefold coordinated. Fits for higher shells indicate that the local environment is significantly distorted around the Pb(II) and Ba(II) octahedra in the calcite. The dilation of the local structure is proportional to their ionic radii, but Pb-Ca and Ba-Ca distances indicate that the dilation is also highly localized, and most likely accommodated by rotation of rigid structural units.

Previous work has shown that Pb and Ba impurities are incorporated differentially between surface sites that are structurally distinct because of the position and orientation at which they are exposed on growth surfaces of calcite. The present observations demonstrate that despite differences in surface site preferences these large impurity species occupy a unique site in the bulk. The distortion associated with the incorporated metals may affect the stability (and solubility) of the solid in the natural environment.

Kinetics and Mechanisms of Trace Metal Sorption at the Mineral/Water Interface: A Time-Resolved Study	X11A

A. M. Scheidegger, D. R. Roberts, D. G. Strawn and D. L. Sparks (U. of Delaware)

A thorough understanding of the kinetics and mechanisms of metal sorption on soil mineral surfaces is critical in determining the fate, mobility, speciation and bioavailability of metals in aqueous and soil environments. XAFS spectroscopy was used to monitor changes in the local structural environment of Ni and Pb sorbed on clay minerals, metal oxides, and the clay fraction of a soil with increasing reaction time.

XAFS data analysis revealed the appearance of multinuclear Ni complexes in the Ni/pyrophyllite and Ni/gibbsite systems, as shown by the second peak representing the second Ni coordination shell at R $\approx$ 2.8Å in the radial structure functions (Fig. 1a,b), after a reaction time of minutes and hours. These results suggest that adsorption and nucleation processes (mixed Ni/Al hydroxide phase formation) can occur simultaneously over time scales of only minutes. As reaction time progressed, the number of second neighbor Ni atoms (N_{Ni-Ni}) at a distance of $\approx$ 3.05Å increased (N_{Ni-Ni} = 1.7-5.1 for Ni/pyrophyllite and N_{Ni-Ni} = 1.5-5.5 for Ni/gibbsite).

With montmorillonite, a mixed Ni/Al hydroxide phase did not form until after 48 h and the phase continued to grow with increasing reaction time. Although not shown, mixed cation hydroxide phases also occurred on the soil clay surface in minutes. With Ni, our study suggests that three phenomena occur at the mineral/liquid interface: (1) non specific (i.e., outer-sphere complexation) and/or specific adsorption (i.e., inner-sphere complexation), (2) dissolution of Al, (perhaps the rate-limiting step) and (3) nucleation of a mixed Ni/Al phase.

While Pb sorption on mineral surfaces results in similar time-dependent behavior, the retention mechanisms are different. Slow nucleation reactions can be ruled out because analysis of the radial structure function (Fig. 2) does not exhibit any major features (e.g., second peaks indicative of second shell neighbors) beyond the primary Pb-O structural peak at $\approx$1.9Å (uncorrected for phase shifts) with long incubation times (Fig. 2). The biphasic sorption behavior observed with Pb may be related to retention on sites of variable reactivity and/or diffusion limited sorption.

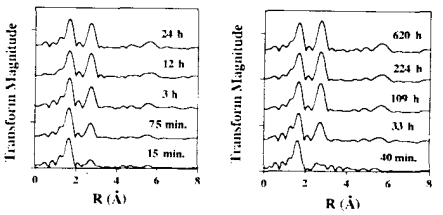

Figure 1. RSF of a) Ni/pyrophyllite and b) Ni/gibbsite. The reaction conditions were: pH = 7.5; $[Ni]_o$ = 3 mM; I = 0.1 M.

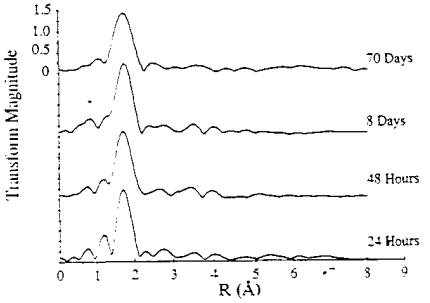

Figure 2. RSF for Pb sorbed on γ-Al_2O_3 incubated for 24 hours to 70 days. Reaction conditions were: pH = 6.5; $[Pb]_o$ = 0.002 M; I = 0.1 M.

Interface Stability of Titanium/Silicon on 6H SiC-(0001) *	X11A

A. J. Stoltz, B. I. Boyanov, D. E. Sayers, and R. J. Nemanich (NCSU)

EXAFS spectroscopy was used to study the interface stability of sequentally deposited titanium and silicon on silicon carbide 6H (0001). Silicon and titanium layers were deposited using a solid source electron beam evaporation system in UHV. All samples were annealed at 500°C, 600°C or 700°C *in-situ* in UHV. EXAFS measurements were performed *ex-situ* at the Ti-K edge, 4966 eV, in total electron yield mode. In samples where only Ti was deposited on SiC, titanium remained mostly unreacted at 500 °C and 600 °C and formed TiC and Ti rich silicide at 700 °C (Fig. 1a). When a sacrificial Si layer was deposited between the SiC and Ti, a $TiSi_2$ (C49)-like structure was formed even after annealing at 500 °C. The formation of C49 $TiSi_2$ is complete at 700 °C (Fig. 1b).

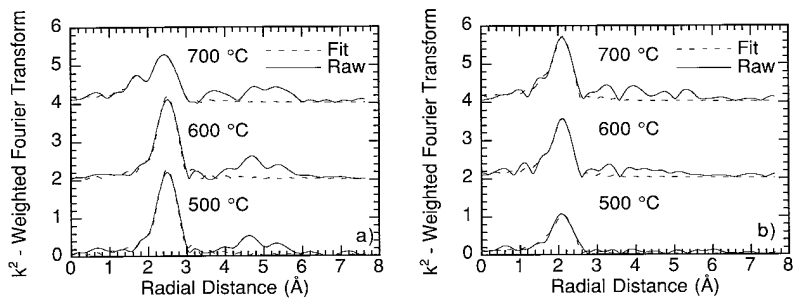

Figure 1. k^2 weighted fourier transform for: a) Ti on SiC and b) Ti/Si bilayer (1:1.2 atomic ratio) on SiC annealed at 500 °C, 600 °C, and 700 °C.

* Supported by DOE Grants No. DE-FG05-93ER79236 and DE-FG05-89ER45384

EXAFS Studies of Sol-gel Processed KTN and PZT	X11A

A. P. Wilkinson, J. Xu and S. Pattanaik (Georgia Tech)

Sol-gel routes are widely used for the preparation of electroactive ceramics such as KTN ($KTa_xNb_{1-x}O_3$)and PZT ($PbZr_xTi_{1-x}O_3$). While it is often stated that this approach delivers compositionally homogeneous solid solutions, in principle, this need not be the case. We have examined a series of KTN and PZT samples using EXAFS at the Nb K, Ta LIII, Zr K, and Pb LIII edges. A preliminary analysis of the data collected for the KTN samples indicates that EXAFS is a sensitive probe of the compositional homogeneity of the solid solution and that the nature of the sol-gel procedure used to prepare the samples does influence the compositional homogeneity of the solid solution. Further data analysis is in progress and additional experiments are planned.

A Tunable Laue/Bent-Laue Monochromator with Fixed Second Crystal for Synchrotron Radiation *	X12A

Z. Zhong, G. Le Duc (NSLS), D. Chapman (CSRRI, IIT), and W. Thomlinson (NSLS)

A Laue/bent-Laue two crystal monochromator has been developed for producing a monochromatic x-ray fan beam with energy tunable over a wide range by adjusting the angle of only the first flat Laue crystal. Bending the second crystal increases the feflection bandwidth, making the the monochromator very stable against vibrations. The monochromator was tuned to above and below the K edge of indium at the X12A beamline at the National Synchrotron Light Source for dual energy subtraction imaging.

The principle for the tunable monochromator is shown in Fig.1. The two crystals are in non-dispersive geometry. The second crystal is strongly bent cylindrically with bending radius ρ_2 in the order of one meter. When the distance s between the crystals is chosen to satisfy: $s = \frac{\rho_2}{2}\cos(\chi \mp \theta_{B0})$, the beam will be reflected by the second crystal for a wide range of energy defined by the Bragg angle of the first crystal. Thus tuning of beam energy can be achieved by adjustment of the first crystal.

With the first crystal tuned to reflect a beam of 27.94 keV, the angle of the second crystal was scanned, Fig.2 shows the rocking curves obtained this way for different beam vertical heights. It is seen that for beam vertical sizes less than 0.6 mm, there exists a flat plateau in the rocking curves. The width $_p$ of the plateau is a good indicator of how stable the monochromator is against vibration. A simple model was proposed which gives $_p = |W - \Delta\theta|$, where W is the FWHM of the bent-crystal reflectivity curve and $\Delta\theta = \frac{h}{\rho\cos(\chi \mp \theta_B)}$. Agreement with experiment is excellent.

In conclusion, a novel monochromator was conceived and tested. Good features include: Tuning of energy by one crystal and stability. Limitations include: the beam height can not exceed about 0.5 mm and a reflectivity of about 0.3 for the second crystal.

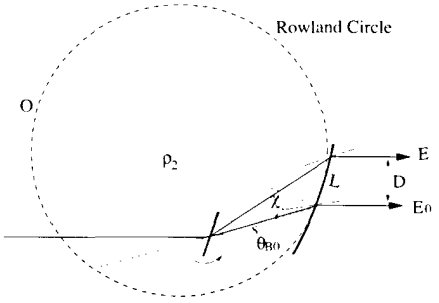

Figure 1. Design considerations

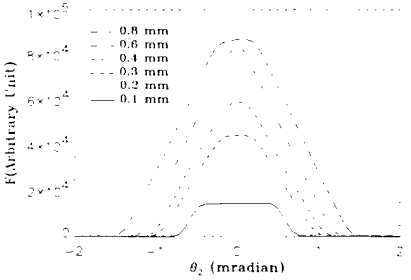

Figure 2. Rocking curves obtained with vertical beam heights of 0.1, 0.2, 0.3, 0.4, 0.6 and 0.8 m

* work supported by US DOE DE-AC02-76CH00016

The Structure Determination of Murine Cytosolic Epoxide Hydrolase	X12B

M. Argiriadi and D. Christianson (U. of Pennsylvania)

Cytosolic epoxide hydrolase's primary function is proposed to be the the hydrolytic cleavage of epoxides to yield vicinal trans diols in the liver cells. This is a critical mammalian detoxification mechanism, e.g., epoxides might otherwise modify protein and/or DNA targets in the cell. They also play a role in the formation or degradation of endogenous chemical mediators. A structure determination of this enzyme might render a better understanding of how particular toxins are metabolized and possibly how cytosolic epoxide hydrolase maintains steady state levels of physiological mediators. Several trips were made to the Brookhaven synchroton. During these trips, native cytosolic epoxide hydrolase crystals were tested which diffracted to 2.8 Å with Rsyms of 6.0%. In comparison, data collected at the University of Pennsylvania diffracted to 4.0 Å resolution at best. On our most recent trip to Brookhaven, heavy metal derivatized crystals were tested. A 3.5 Å (Riso = 15%) uranium derivative was obtained currently bringing the total to three. Preliminary electron density maps have been calculated; however, at this stage they remain uninterpretable. Additional derivatives and anomalous information are necessary to increase phasing power and calculate stronger maps.

X-Ray Structural Studies on OspB, an Immunogenic Outer Surface Protein of the Bacteria *Borrelia burgdorferi*, the Causative Agent of Lyme Disease.	X12B, X12C

M. Becker, B. Lade, H. Kycia, J.J. Dunn, C.L. Lawson (BNL) and B.J. Luft, (SUNY at Stony Brook)

OspB and OspA are lipoproteins expressed on the surface of the spirochete *Borrelia burgdorferi* when the bacteria is dormant in the midgut of a host tick. Each have been shown to ellicit an immunologic response in infected humans, and both are of interest for developing a vaccine against the disease. Recently, the structure of OspA has been solved in complex with an antibody Fab fragment [Li, H., Dunn, J.J., Luft, B.J., and Lawson, C.L. *Proc.Nat.Acad.Sci. USA 94*, 3584-3589.]. The molecule has an unusually long free-standing anti-parallel β- sheet, as well as a putative binding-site for an unknown ligand in the C-terminal domain. Though OspB is highly homologous to OspA, one significant difference is that certain Fabs directed at the C-terminal domain of OspB are bactericidal, even in the absence of complement [Coleman, J.L. *et al.* (1992) *Infec. Immun. 60*, 3098-3104; Sadziene, A. *et al.* (1994) *Infec.Immun. 62*, 2037-2045.]. The 15.6 kDa C-terminal domain of OspB has been cloned, overexpressed, purified, and crystallized in 2 forms. One crystal form has space group $C222_1$ with cell constants $a = 30.8$ Å, $b = 51.7$ Å, and $c = 158.8$ Å, and contains 1 molecule in the asymmetric unit. Diffraction has been observed to at least 1.6-Åresolution at synchrotron beamline X12C of the NSLS, and a data set has been collected with 90% completeness, high redundancy, and an Rmerge of 6.3% to 2.0-Åresolution at 10 °C at beamline X12B. Molecular replacement using MERLOT and XPLOR with a search model based on a homology model to the OspA C-terminus has been used to locate the monomer in the asymmetric unit, but the details of the current model of the OspB C-terminus are unsatisfactory, particularly at the crystallographic interface formed between the artificially truncated molecules. A second crystal form grown in the presence of tungstate has the space group $P2_12_12$ with similar but significantly different axial lengths of $a =$ 167.7 Å, $b = 30.2$ Å, and $c = 50.8$ Å. These crystals diffract similarly well, and a data set has been collected at X12C to a resolution of 2.2 Å with a completeness of 83% and a merging R factor of 6.3% by cooling the crystal to 100 K and using radiation at the anomolous peak of tungstate. The anomolous difference Patterson reveals a 6-σ peak, indicating that tungstate is specifically bound in the crystal, and the Patterson also reveals that these crystals are pseudo-centered. We are currently aiming to collect a full MAD data set at the tungstate edge to provide independant phasing information to solve the structures.

X-Ray Structure of A Six-Finger TGIIIA-DNA Complex	X12B

R.S. Brown, R. T. Nolte, R.M. Conlin and S. C. Harrison (HHMI, Children's Hospital Harvard U.)

The complex containing six zinc fingers of the transcription factor TFIIIA bound to 31 base-pairs of the 5S rRNA gene promoter crystallizes in a triclinic form. We have successfully determined the structure of this complex at 3.1 angstroms resolution. The zinc fingers recognize DNA in two different ways. Fingers 1-2-3 wrap as a unit in a continuous fashion around the major groove of DNA. This mode of binding has been seen in other zinc finger-DNA X-ray structures. In contrast, fingers 4-5-6 extend along the DNA crossing the minor-major-minor grooves respectively. This structure shows how TFIIIA can recognize several separated DNA sequences using fewer fingers than necessary for continuous winding in the major groove.

Triclinic crystals (space group P1) grow as thin plates and diffract weakly. Collection of an X-ray data set takes more than three weeks with a conventional rotating anode source. Using the X12-B beam line at NSLS we were able to obtain data sets in 24 hours from single frozen crystals. The presence of 12 zinc atoms in the unit cell provided an opportunity to use anomalous diffraction as a means to locate them. Data were collected at the Zn K-edge using a wavelength of 1.283 angstroms at X12-B with a MAR image plate. The positions of all of the zinc atoms in the TFIIIA-DNA complex were found in the anomalous Fourier map. These metal sites indicate the correct path and fold of the polypeptide chain.

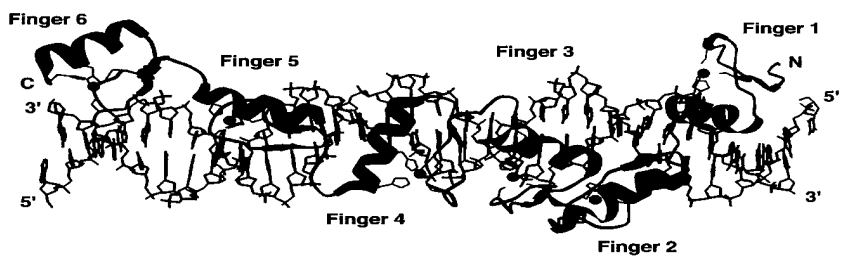

Figure 1.

Real-Time Small Angle X-ray Scattering Study of Isotactic Poly(propylene)	X12B

P. Dai, G. Georgiev, and P. Cebe (Tufts U.),and M. Capel (BNL)

Crystallization and melting of isotactic poly(propylene), iPP, has been studied using real-time small angle X-ray scattering. The iPP used in this study is an experimental product of Hoechst, and was prepared using homogeneous transition metal catalysts (metallocenes). This preparation results in a very narrow molecular weight distribution, with Mw/Mn = 2.3, and Mw = 335,500.

We isothermally crystallized iPP by first, melting at 200°C for 2 min, then cooling to 124.5C or 117°C at 5°C/min, and holding at this temperature for various time. SAXS data were collected during crystallization and subsequent heating. Data were corrected for: sample absorption, changes in incident beam intensity, background subtraction, and thermal density fluctuations. The latter correction was performed by subtraction of the slope of the linear region at high s, in the Is4 vs. s4 plot. Sample-to-detector distance was 1.75m and was determined using cholesterol myristate and collagen fiber. X-ray wavelength was 1.54 Å, and intensity was collected with an integration time of 30 sec.

Analysis of the corrected intensity was done using the one-dimensional electron density correlation function, where the density variation was assumed to occur along a direction normal to the coherently scattering stacks of lamellar crystals. Long period, lamellar thickness, and linear crystallinity of the lamellar stacks were calculated from the correlation function. We find that the long period (distance between adjacent lamellae) decreases during isothermal crystallization at 117°C or 124.5°C. Upon reheating, long period increases dramatically as the melting region is approached. Once the melting peak temperature has been exceeded, long period decreases. Although the melting endotherms observed using thermal analysis show "double melting" behavior, we did not observe any systematic variation of the long period through the temperature region corresponding to the lower melting endotherm.

Mechanical Behavior of Novel Block Copolymer Morphologies	X12B

B.J. Dair (MIT), E.L. Thomas (MIT), M.C. Capel (NSLS)

Novel cubic phases have recently been discovered in copolymer systems, including the ordered tricontinuous double gyroid (DG). DG conforms to the symmetries of the $Ia\bar{3}d$ space group and has a tricontinuous, triply periodic structure, whereby two non-intersecting networks of the minority phase are embedded in the majority. Recently we have identi- fied and obtained triblock copolymers which form cubic morphologies, opening up the possibility of investigating the mechanical properites of these new morphologies. At X12B, we investigate the large strain mechanical properites of styrene-isoprene-styrene triblock copolymers with DG morphology. Tensile samples were prepared from macroscopically oriented, near-single-crystal sheets of DG, which were produced via roll- cast processing and annealing. In-situ X-ray patterns, along with simultaneous load-deformation curves, were taken as specimens were loaded in uniaxial tension. Due to the resulting long-range order, such samples are mechanically anisotropic and scatter anisotropically. Hence, a study of the deformation behavior of this structure via SAXS requires the use of a 2-dimensional detector, and particularly that at X12B.

Glutamine Synthetase from *Mycobacterium Tuberculosis*: Aim Toward Drug Discovery	X12B

H. Gill and D. Eisenberg (UCLA)

Tuberculosis (TB) has re-emerged as a gobal health concern. Previous studies have indicated that Glutamine Synthetase from *Mycobacterium tuberculosis*, the pathogen behind the disease TB, may be involved in a novel role via its secretion from the organism (Harth *et al.*, 1994). Secreted GS is an attractive target for drugs, because the drugs need not penetrate the thick cellular envelope of Mycobacteria in order to combat the disease. We have set out to elucidate the structure of TB-GS as part of the goal to find a drug to selectively inhibit TB-GS over human GS. Synchrotron radiation was a necessary part of this process. As illustrated in Figure 1, approximately 2.6 million reflections were recorded, with 566,370 unique reflections yielding a redundancy of 4.6 and a R_{sym} of 7.5, in a 23 hour time period at the National Synchrotron Light Source X12B Beamline using the new Quantum-4 CCD detector (Area Detector San Diego Company). The space group is $P2_12_12_1$ with unit cell dimension 208 x 255 x 274 Å using the MOSFILM program for data processing to 2.4 Å resolution. Self-rotation functions, calculated on the data set using the program POLARRFN, revealed six aligned and equally spaced non-origin peaks in the appa=180 section and one non-origin peak– 90 degrees away from these 2-folds– in the kappa=60 and 120 sections consistent with the 622 symmetrical architecture of *Salmonella typhimurium* GS. A V_M calculation of 2.89 indicates two dodecamers (24 subunits) in the asymmetric unit. Since only one set of two-fold and six-fold axes are apparent in the rotation function, we conclude that both molecules face each other along the crystallographic axis. The TB-GS model has been solved using an initial model of *S. typhimurium* GS, which has been refined to 2.5 Å resolution in our laboratory. The simulated annealing protocol, thus far, gives a R-factor of 38 percent. Model building is currently in progress using 24 NCS-averaging methods. Hence, synchrotron radiation at beamline X12B and the new CCD detector was crucial to solving the TB-GS structure.

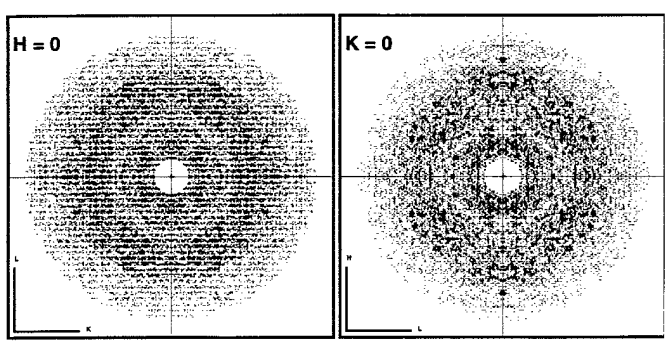

Figure 1. View of the H=0, K=0 sections using the PLOTHKL program G. Pfluegl (UCLA).

2.1 A Structure of the Complex Between Active Ras and The Ras-Interacting Domain of an Effector RalGDS	X25, X12B

L. Huang, F. Hofer, G.S. Martin, and S-H. Kim (U. California at Berkeley)

The structure of the complex bewteen oncogenic protein Ras and the Ras- interacting domain of RalGDS (RalGDS-RID) has been studied by x-ray crystallography. The structure of the complex will provide crucial information on Ras' interaction with its binding partner at an atomic level. Since the mutant forms of Ras are involved in 30% of human cancer and Ras' function is carried out through its effectors, the spatial location of the key interface residues may assist in identifying small molecules that are capable of disrupting this interaction and thus provide insights for the development of anti-cancer drugs. A 2.8 room temperature data set on a native complex crystal was initially taken at BL X12B, which enabled us to solve the structure. A 2.0 frozen data set was later taken at BL X25 in september, which enabled us to refine the structure to a much higher resolution so that we can see the side chain interaction more clearly. The crystal has a P212121 space group, with a=75.648, b=78.256, c=87.313 . The complex crystallizes as a heterotertramer with two active Ras molecules and two RalGDS-RID subunits.

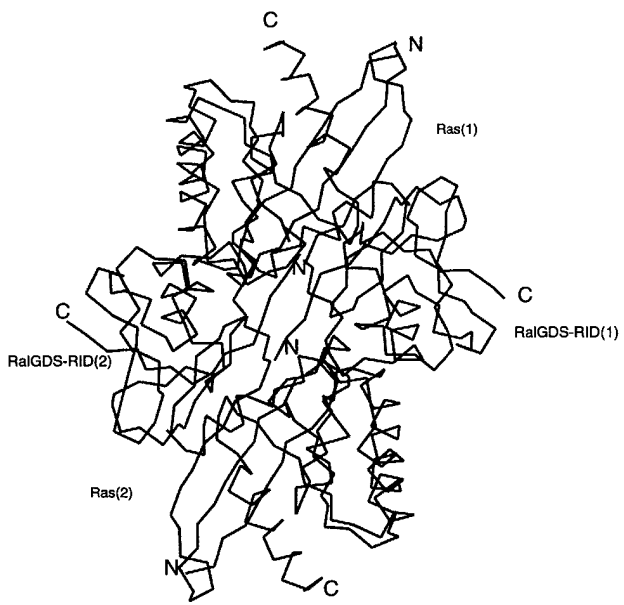

Figure 1.

Vancomycin-Ligand Complex Structures — X12B

P.J. Loll (U. of Pennsylvania)

Structures of complexes of the glycopeptide antibiotic vancomycin with peptide and depsipeptide ligands have been determined at atomic resolution by single-crystal X-ray diffraction methods, using data collected at NSLS and the new direct methods program SnB. These structures reveal asymmetric dimer formation in all complexes, but also show that strong ligands are able to fill both dimer binding sites, whereas weak ligands give complexes with a 2:1 antibiotic:ligand stoichiometry. This structural information is being used in conjunction with simulation methods to understand the molecular basis of target recognition by this class of antibiotics, and will ultimately aid in the design of new agents to combat antibiotic resistance.

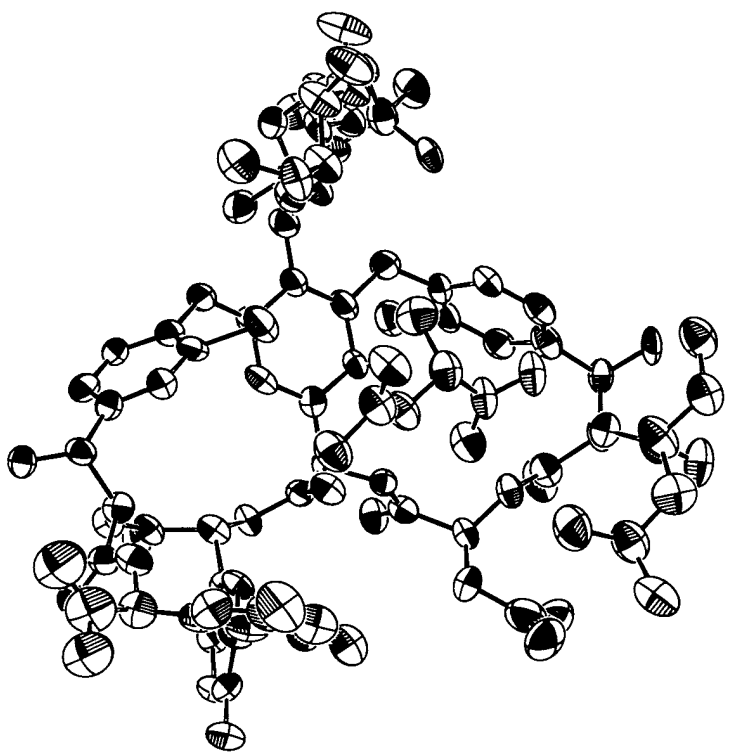

Figure 1. ORTEP drawing of the complex of vancomycin with N-acetyl-D-alanine.

The Crystal Structure of the DNA Binding Domain of the Orphan Nuclear Receptor NGFI-B Complexed to its DNA Target at 2.7 Å — X12B

G. Meinke, P. Sigler (Yale University)

The nuclear receptor superfamily is a large group of proteins which are ligand dependent transcriptional modulators. This family includes receptors for a diverse group of ligands such as steroids, retinoic acid, vitamin D, and thyroid hormone. These receptors bind to a specific DNA sequence termed a hormone response element (HRE). The receptors bind as homo- or hetero-dimers or monomers to a 6 base pair consensus sequence termed a half-site which can be organized as direct, inverted, or everted repeats with variable number of spacer nucleotides or as monomers with a 5′ extension to the half-site.

The X-ray crystal structure of the DNA binding domain (DBD) of the orphan nuclear receptor nerve growth factor induced-B (NGFI-B) complexed to its high affinity DNA target has been refined to 2.7 Å. The structure represents the first example of a nuclear receptor bound as a monomer to its specific DNA target. The DNA target consists of the consensus hexameric half-site AGGTCA with a 5′ flanking sequence of A. The fold of the core DBD is nearly identical to previously solved structures of other members of the nuclear receptor. Residues C-terminal to the core DBD form a stable structure which interact with the minor groove of the DNA via an extended loop. These minor groove contacts occur in the half-site as well as the 5′ flanking basepairs.

Structure Determination of Mitochrondrial Cytochrome bc1 Complex	X12B

D. Xia (HHMI and U. of Texas SW Medical Center) C. A. Yu (Oklahoma State U), H. Kim (HHMI and U. of Texas SW Medical Center), A. Kachurin, L. Zhang, L. Yu (Oklahoma St. U.) and , J. Deisenhofer (HHMI and U. of Texas SW Medical Center)

Cytochrome bc1 Complex (ubiquinol-cytochrome c oxidoreductase, bc1) is the middle segment of the respiratory chain in almost all aerobic organism, and an essential component in the photosynthetic machinary in purple bacteria. Green plants use highly homologous b6f complex as an important part of their energy conservation apparatus. The bc1 complex is an integral membrane protein; it couples the electron transfer from ubiquinol to cytochrome c to the proton translocation across the membrane to generate a pH difference and a membrane potential for ATP synthesis. Mitochondrial bc1 complex from bovine heart consists of 11 different subunits, two b-type hemes, one c-type heme and an iron-sulfur cluster with a total molecular weight of 250 Kd and in excess of 2200 amino acid residues.

The mitochondrial cytochrome bc1 complex from bovine heart was purified and crystallized. bc1 crystals can be cryo frozen for stable data collection at Synchrotron radiation sources. bc1 crystals diffracted X-ray at X12B of NSLS to 3.3 Å resolution and possess symmetry of the space group of I4122 with cell dimensions of a=b=153.7 A and c=597.5 A. Initial phases for the bc1 crystal were determined using MIRAS method with seven heavy metal derivatives, and subsequent phase improvment were carried out with cyclic excutions of density modification and phase combination procedures. Current atomic model of the bc1 complex contains eight completely sequence assigned subunits including core1, core2, cytochrome b, Rieske iron sulfur protein, subunits 6, 7, 10 and 11; three incomplete subunits including cytochrome c1, subuints 8 and 9; two b-type hemes, one c-type heme and one 2Fe2S iron-sulfur cluster with total number of amino acids residues near 2000.

The bc1 structure in crystal is a tightly associated dimer about 155 Å tall and 130 Å wide. It can be divided into three regions, the membrane spanning region, 48 Å thick, has 26 trans-membrane helices in the dimer, sixteen of which belong to cytochrome b dimer. Cytochrome c1, Rieske protein, subunits 7, 10 and 11 each contributes two helices in the dimer. The intermembrane space region of the bc1 complex rises 38 Å into the intermembrane space where the soluble parts of the the Rieske iron-sulfur protein and cytochrome c1 are located. The matrix region of the bc1 projects 75 Å into the mitochondrial matrix where core1, core2, subunit6, parts of Rieske, cytochrome c1, subunits 7, and 9 can be found.

The stuctural information of the bc1 complex has provided significant contribution to our understanding of the redox-coupled proton translocation mechanism.

Structural Studies on the Complex of the C-terminal Domain of Outer Surface Protein B of *Borrelia burgdorferi* with a Bactericidal Fab.	X12C

M. Becker, B. Lade, W. Ding, J.J. Dunn, C.L. Lawson (BNL), J. Bunikis, A.G. Barbour (UC at Irvine), and B.J. Luft (SUNY at Stony Brook)

Outer Surface Protein B (OspB) is a lipoprotein of unknown function found on the surface of *Borrelia burgdorferi*, the causative agent of Lyme Disease. It has been shown that certain antibodies directed at the C-terminal domain of OspB are bactericidal, and surprisingly, that the Fabs alone of these antibodies are bactericidal, even in the absence of complement [Coleman, J.L., Rogers, R.C., and Benach, J.L. (1992) *Infec.Immun. 60*, 3098-3104; Szaziene, A., Jonsson, M., Bergstrom, S., Bright, R.K., Kennedy, R.C. and Barbour, A.G. (1994) *Infec.Immun. 62*, 2037-2045.]. Crystals of a complex of the 15.6 kDa C-terminal domain of OspB with bactericidal Fab H6831 have the space group C2 with cell constants $a = 186.3$ Å, $b = 37.3$ Å, $c = 87.9$ Å, and $\beta = 90.7$ °, contain 1 complex per asymmetric unit, and diffract initially to at least 2.0-Åresolution at 18 ° C. A data set with completeness of 94% and an Rmerge of 7.8% has been collected to 2.6-Åresolution at 18 ° C by merging data from different crystals collected at beamline X12C. Molecular replacement using the program AMORE with the structure of an Fab directed at OspA of *Borrelia burgdorferii* [Li, H., Dunn, J.J., Luft, B.J., and Lawson, C.L. (1997) *Proc.Nat.Acad.Sci. USA 94*, 3584-3589] as a search model provides a clear solution to the location of the Fab in the asymmetric unit, and efforts to determine the structure of the C-terminal domain of OspB in the complex are currently underway. Also, freezing conditions for the crystals are being tested so that data can be collected to higher resolution.

X-Ray Structural Studies on OspB, an Immunogenic Outer Surface Protein of the Bacteria *Borrelia burgdorferi*, the Causative Agent of Lyme Disease.	X12B, X12C

M. Becker, B. Lade, H. Kycia, J.J. Dunn, C.L. Lawson (BNL) and B.J. Luft, (SUNY at Stony Brook)

OspB and OspA are lipoproteins expressed on the surface of the spirochete *Borrelia burgdorferi* when the bacteria is dormant in the midgut of a host tick. Each have been shown to ellicit an immunologic response in infected humans, and both are of interest for developing a vaccine against the disease. Recently, the structure of OspA has been solved in complex with an antibody Fab fragment [Li, H., Dunn, J.J., Luft, B.J., and Lawson, C.L. *Proc.Nat.Acad.Sci. USA 94*, 3584-3589.]. The molecule has an unusually long free-standing anti-parallel β- sheet, as well as a putative binding-site for an unknown ligand in the C-terminal domain. Though OspB is highly homologous to OspA, one significant difference is that certain Fabs directed at the C-terminal domain of OspB are bactericidal, even in the absence of complement [Coleman, J.L. *et al.* (1992) *Infec. Immun. 60*, 3098-3104; Sadziene, A. *et al.* (1994) *Infec.Immun. 62*, 2037-2045.]. The 15.6 kDa C-terminal domain of OspB has been cloned, overexpressed, purified, and crystallized in 2 forms. One crystal form has space group $C222_1$ with cell constants $a = 30.8$ Å, $b = 51.7$ Å, and $c = 158.8$ Å, and contains 1 molecule in the asymmetric unit. Diffraction has been observed to at least 1.6-Åresolution at synchrotron beamline X12C of the NSLS, and a data set has been collected with 90% completeness, high redundancy, and an Rmerge of 6.3% to 2.0-Åresolution at 10 °C at beamline X12B. Molecular replacement using MERLOT and XPLOR with a search model based on a homology model to the OspA C-terminus has been used to locate the monomer in the asymmetric unit, but the details of the current model of the OspB C-terminus are unsatisfactory, particularly at the crystallographic interface formed between the artificially truncated molecules. A second crystal form grown in the presence of tungstate has the space group $P2_12_12$ with similar but significantly different axial lengths of $a =$ 167.7 Å, $b = 30.2$ Å, and $c = 50.8$ Å. These crystals diffract similarly well, and a data set has been collected at X12C to a resolution of 2.2 Å with a completeness of 83% and a merging R factor of 6.3% by cooling the crystal to 100 K and using radiation at the anomolous peak of tungstate. The anomolous difference Patterson reveals a 6-σ peak, indicating that tungstate is specifically bound in the crystal, and the Patterson also reveals that these crystals are pseudo-centered. We are currently aiming to collect a full MAD data set at the tungstate edge to provide independant phasing information to solve the structures.

MAD Studies of the Bacteriophage PRD1 Major Coat Protein, P3 *	X12C

S.D. Benson (The Wistar Instit.), J.K.H. Bamford, D.H. Bamford (U. of Helsinki), and R.M. Burnett (The Wistar Inst.)

PRD1 is an unusual bacteriophage with many structural similarities to the mammalian adenovirus. Both are icosahedral with vertex fibers, have trimeric major coat proteins, and contain linear ds-DNA with terminal proteins. PRD1 is unique in posessing a lipid membrane within its outer capsid, which is composed of two proteins, P3 and P5. P5 lies at the vertices, while P3, a homotrimer of 394 amino acids, forms the facets with its N-termini interacting with the internal viral membrane. The structure of P3 promises an increased understanding of viral capsid assembly and membrane interactions. Crystals of P3 are orthorhombic ($P2_12_12_1$: a = 117.9 Å, b = 121.3 Å, c = 126.4 Å) with a trimer in the asymmetric unit.

Initial heavy atom trials were troubled by crystal disruption and non-isomorphism. A Multiwavelength Anomalous Dispersion (MAD) experiment at the NSLS was designed to overcome these problems. PRD1 was expressed in a bacterial system containing selenomethionine and mass spectrometry showed >90% substitution. Crystals were obtained under the same conditions as the native protein. A three wavelength MAD experiment was performed around the absorption edge of selenium on a single frozen selenomethionine P3 crystal at beamline X12C. The data were collected with a CCD-based detector to 2.2 Å resolution. The positions of the 15 selenium atoms were determined from difference Fourier maps with phasing information from a uranyl acetate derivative. Native data to 1.8 Å resolution also were collected. Crystals of the entire virion, grown in microgravity on the space shuttle, did not diffract but trials continue with a fiberless variant.

Although the P3 trimer is one of the largest structures to be solved with MAD phasing from selenomethionine, the initial electron density map at 2.2 Å resolution was superb. Model building for 81% of the polypeptide chain was unambiguous and refinement of the structure is underway.

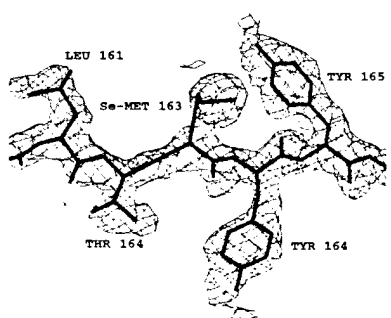

Figure 1. A representative section of the MAD-phased 2σ electron density map for PRD1-P3 containing model residues 161-165.

* Supported by NSF Grant MCB 95-07102 and the Finnish Academy of Sciences.

X-ray Structural Study of Lyme Bacterium Outer Surface Protein A Complexed With a mAb LA2 Fab Fragment by Multiwavelength Anomalous Diffraction Experiment	X12C

W. Ding (SUNY at Stony Brook), B.J. Lufts, X. Yang (SUNY at Stony Brook), J. J. Dunn, and C.L. Lawson (BNL)

Lyme disease is the most common vector borne illness in the United States,caused by spirochete *Borrelia burgdorferi*. Earliest infection is marked by the appearance of erythema migrans. Left untreated, early dissemination may give rise to multisystem illness with dermatologic, rheumatic, cardiac and neurologic manifestions.

Preliminary studies have shown the OspA based vaccine can induce protective immunity in mammals. Protection appears to be serotype specific. In vaccine studies with hamsters, protection was conferred only when hamster's immune response was directed to the epitope defined by the mAb LA2. Subsequent studies have concluded that the mAb LA2 binds to a conformational epitope located near the carboxyl terminus with the stretch of amino acid from 133 to 273. This section of OspA is a hypervariable region. However there is a single conserved tryptophan at amino acid 216, and fragmentation at this point destroys mAb LA2 binding. Studies of a series of OspA fusion proteins, deletion proteins, site-directed mutants, strain chimeric proteins and different strains by Western blot analysis suggests that the mAb LA2 recognizes a 29 amino acid chain on OspA located at a amino acid positions 190 - 217 and supports the theory that epitope is conformationally dependent. Defining this protective epitope is an important consideration in developing an effective vaccine for Lyme disease protection. In order to better define and understand the epitope of OspA, we have initialized a structural study of OspA and LA2 Fab fragment.

Crystals were grown at 4°C by hanging-drop vapour diffusion methods (0.1M Sodium cacodylate, 0.1M sodium Acetate and 10% PEG 3300 at pH 6.15). Crystals were mounted in a glass capillary tubes (0.7 mm in diameter) and data were collected on X12C, NSLS CCD detector (Brandeis University) with crystal temperature maintained at 4°C with a cooling air stream. Diffraction patterns were observed with dmin = 3.0Å. The crystal lattice was determined to be orthorhombic with dimension a =99.5Å b=129.5Å c=144.5Å . Assuming two OspA -LA2 fab protein complex molecular per asymmetric unit with molecular mass 81 kDa, the specific volume (Vm) is 2.9Å /Da, corresponds a solvent content 50%, well inside the observed range for protein crystals.

A complete four-wavelength MAD data set on one Na_2WO_4 derivatized crystal was collected at the X12C with crystal frozen in a stream of gaseous nitrogen held at 100K. The crystal diffracted to 3.2Å and the data set has 96% completeness. The data collection and phasing stragegy of treating MAD as a special case of MIR was applied to obtain phase information. Isomorphous and dispersive patterson maps calculated from the data set showed strong heavy atom binding site peaks (fig 2). The positions were refined and used to calculate the phases. The electron density map is interpretable. We are in the process of the model build-up and refinement.

Crystallization and Analysis of Native and Derivative X-Ray Diffraction Data from Bovine Milk Xanthine Oxidase *	X12C

B. Eger (U. of Toronto), K. Madrid (Aastra, Inc.), K. Okamoto, M. Sato (Nippon Medical School), K. McConville (Aastra, Inc.), T. Nishino (Nippon Medical School), and E.F. Pai (U. of Toronto)

Xanthine oxidase or xanthine dehydrogenase isolated from mammals is a component of the nucleotide catabolism pathway. The active enzyme, a 290kdal homodimer, catalyzes the oxidation of hypoxanthine to xanthine, followed by further oxidation to uric acid. The enzyme, which is synthesized in vivo as xanthine dehydrogenase, contains one FAD, two 2Fe/2S centers, and one molybdopterin group per monomer. Extensive studies on the mechanism of electron transfer between the cofactor sites have been made on both the oxidase and the dehydrogenase forms. Elucidation of the three dimensional structure of the enzyme is an important step in the study of electron transfer between the cofactor and the substrate binding sites. Recently, a purification scheme for xanthine oxidase was developed which yields enzyme preparations of exceptional purity. Large crystals (1.2 x 0.7 x 0.15mm) were obtained using polyethylene glycol 4000 as a precipitant. However, due to the weak diffraction of these crystals, data had to be obtained from a synchrotron radiation source. The lattice type of these crystals was orthorhombic (C2221) with unit cell dimensions of a=118.6, b = 165.4, c = 156.4. From the Matthews parameter, there was one monomer per asymmetric unit and a solvent content of 56%. A native data set was collected which was 95.2% complete to 3.3 with an overall R factor of 9.2% from 107172 measured reflections and 22347 unique reflections. Since no analogous structure has been solved, screening for heavy atom derivatives has begun. Currently, two complete data sets have been collected of possible weak derivatives. In addition, prelimiary diffraction data from five potential derivatives have been screened which show promising results. Each of the five sets diffracts well, has unit cell parameters similar to the native unit cell values, and scale to the native data set with R factors in the range of those expected for a derivative data set. Additional synchrotron beam time will be used for collection of these data sets and screening of additional heavy atoms.

* Supported by National Science and Engineering Council of Canada

Structural Studies of Nucleosomes. * — X12C

J. M. Harp, D. E. Timm (UTK), and G. J. Bunick (ORNL)

Previous data collection done at the NSLS beamline X12C has provided high quality native diffraction data from crystals of nucleosome core particles and of the histone octamer core of the nucleosome. The nucleosomes in that study were prepared using a 146 bp DNA palindrome based on a nucleosome binding sequence in the alpha satellite DNA of the human X-chromosome. The DNA was bound to histones purified from chicken erythrocytes. The DNA palindrome extends the 2 fold symmetry of the octamer core to the entire complex and the use of an alpha satellite sequence provided the highest quality crystals for X-ray diffraction. The histone octamer crystals were grown from the same batches of protein as that used for nucleosome assembly. Recent studies done at beamline X12C have been designed to provide data to be used in solving the phases of the previous native data sets. The nucleosomes were assembled using the same DNA palindrome but with recombinant histone octamers. The recombinant histones were also mutagenized to introduce additional binding sites for heavy atom derivatives. MAD experiments were performed using crystals of the histone octamer derivatized with mercury and a crystal of the nucleosome core particle derivatized with a platinum compound. All data were collected at 100 K and crystals were annealed to lower mosaic spread caused by flash-cooling.

* Research sponsored by the Office of Health Environmental Research, Department of Energy, under contract No. DE-AC05-960R22464 with Lockheed Martin Energy Research Corp., and NIH Grant GM29818

X-ray Structural Study of Equine Infectious Anaemia Virus Capsid Protein p26 — X12C

Z. Jin (SUNY at Stony Brook), A.J. Birkett, L. Jin, D.L. Peterson (VA Commonwealth U.) and C. L. Lawson (BNL)

Equine Infectious Anaemia Virus (EIAV) belongs to the *Lentiviridae* family, which is a subfamily of *Retrovirus*. EIAV is responsible for a chronic, debilitating disease in horses. Infection has been reported world-wide and EIAV is recognized as a livestock pathogen of significant economic importance to the horse industry. There is significant homology between the non-human lentiviruses and HIV-1, which is the most extensively studied member of *Lentiviridae* family. Lentiviral capsid proteins play a crucial role in the maturation of infectious viral particles. Interference with particle maturation would provide an anti-viral mechanism. EIAV and HIV-1 capsid proteins have 30% identity and 55% similarity of their amino acid sequences. The structural study of EIAV core protein will help in understanding the structure of HIV core protein, and in evaluating methods of effective treatment and control of viral infection.

Crystals were grown at room temperature by hanging drop vapor diffusion with 0.1 M Citrate buffer and 10% PEG 3300, 15% isopropanol, at pH 6.5. A complete native data set to 3.6 Å (R_{sym} = 11%) has been collected at the beamline X12C of National Synchrotron Light Source at Brookhaven National Laboratory. Crystals belong to the space group $P6_122$ with a=b=101 Å and c=158 Å.

A complete three-wavelength MAD data set on one Pt derivatized crystal was collected on the X12C beamline using CCD (Brandeis University) detector. The crystal diffracted to 3.11 Å and the data set has 98% completeness. The data collection and phasing strategy of treating MAD as a special case of MIR (V. Ramakrishnan *et al.*, from *Methods in Enzymology* 1997) was applied to obtain phase information. Isomorphous and dispersive patterson maps calculated from the data set showed strong heavy atom binding site peaks (fig 1). The positions were refined and used to calculate the phases. The electron density map is interpretable and the N-terminal and C-terminal domains are intact. The ambiguity of space groups $P6_122$ and $P6_522$ was resolved by examing the the electron density map; the $P6_522$ has the wrong configuration with left-hand helices and was excluded. The crystal contains two p26 protomers per asymmetric unit. We are in the process of the model building and refinement.

Figure 1. Dispersive Patterson map on Harker section z = 1/6

Crystal Structure of Complexes of Human Acetylcholinesterase and Various Nerve Agents	X12C

G. Kryger, I. Silman, J.L. Sussman (The Weizmann Institute of Science, Israel)

Acetylcholinesterase (AChE) is responsible for terminating the action of the neurotransmitter acetylcholine by rapid hydrolysis to choline and acetic acid. AChE is also the target of many insecticides and other reversible and irreversible inhibitors from the organo-phosphate family, of which some have unfortunately been used as nerve agents in chemical warfare. Accurate structural knowledge of the structure of complexes of such inhibitors with human AChE is therefore of great importance in the development and design of more specific insecticides and more important, the development of anti nerve agent treatment. Complexes of recombinant human AChE (rhAChE) with O-ethyl S-(2-diisopropylaminoethyl) methylphosphonothioate (VX), diisopropyl fluorophosphate (DFP) and sarine (SAR) were prepared in solution, then reacted with equimolar amounts of Fasciculin-II (FAS-II) and crystallized. Crystals of about 0.2mm and space group R32 were used for data collection at the BNL-NSLS X12-C X-ray source. Structure determination was carried out by molecular eplacement based on the structure of rhACh/FAS-II obtained at the same beamline and refinement of rhACh/FAS-II/VX, rhACh/FAS-II/DFP and rhACh/FAS-II/SAR is underway.

Ultra High Resolution Protein Structure Studies of the Extracellular Endonuclease from *Serratia marcescens*. *	X12C

M.D. Miller (U. Houston) & K.L. Krause (U. Houston/Baylor Col. Med.)

We are refining and characterizing protein structures at ultra high resolution (>1.0 Å) using data from the extracelluar endonuclease from *Serratia marcescens*[1]. When crystals are cooled to 100 K, diffraction is seen beyond 0.9 Å resolution. One dimer of the endonuclease (53.4 kDa / 490 amino acids) crystallizes in the asymmetric unit of space group $P2_12_12$ with a=106.7 Å, b=74.5 Å, c=68.9 Å. Before our visit to NSLS, data had been collected to 0.92 Å with a MAR image plate system on the EMBL beamline BW7B at DESY ($\lambda = 0.89$ Å).

During our recent trip to the NSLS beamline X12C at BNL, we were interested in extending the resolution and testing the X12C setup for ultra high resolution data collection. Data from a single crystal cooled to 100 K were collected to 0.88 Å resolution (Fig. 1). Three data collection sweeps were used. The two high resolution sweeps differed by 40° in χ and the third sweep was to collect low resolution data. Exposure times were on the order of 12 min/degree for the high resolution data.

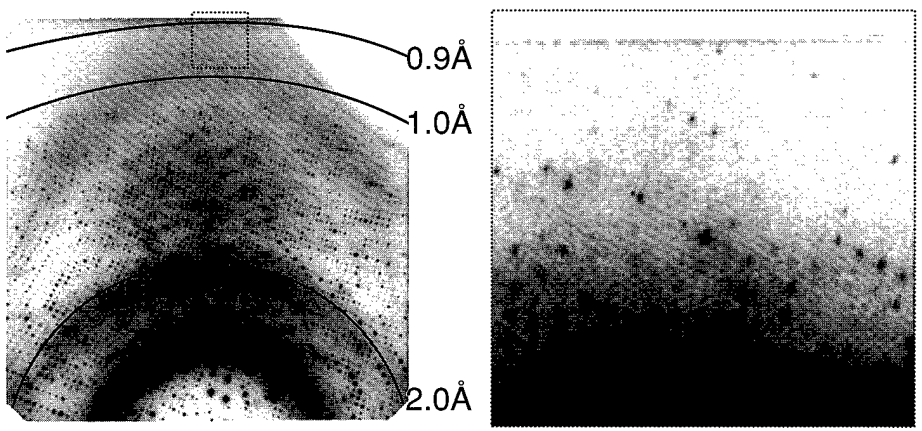

Figure 1. Diffraction image of the *Serratia* endonuclease crystals taken on beamline X12C using the 1K CCD detector ($\lambda = 0.95$ Å). The upper edge of the image is 0.89 Å and the upper left corner is 0.87 Å resolution. The zoomed image (right) shows diffraction to the edge of the detector.

[1]Miller MD & Krause KL. *Protein Sci* **5**, 24-33 (1996); Miller MD, Tanner J, Alpaugh M, Benedik MJ & Krause KL. *Nature Struct Biol* **1**, 461-468 (1994).

* This research is supported by the NIH, The Robert A. Welch Foundation, The Methodist Hospital Foundation, the W.M. Keck Foundation, and the State of Texas ARP

Crystallographic Studies on the Non-enzymatic Plasminogen Activator Streptokinasee	X12C

C. Phillips (LMB, Oxford), G. Spraggon (UCSD) and D.I.Stuart (LMB, Oxford)

Streptokinase (SK) is a bacterial protein from Streptococcus equisimilis that indirectly causes the activation plasminogen (Plg). SK and Plg form an avid 1:1 stoichiometric complex with the subsequent appearance of a serine protease active center from within the Plg moiety; this complex acts in turn as an activator of other Plg molecules. SK has shown itself to be an efficacious agent in the clinical treatment of acute myocardial infarction (heart attack) and has served as a thrombolytic agent for almost three decades. Recently SK has been shown to consist of three domains termed A,B and C, of molecular weight 16K, 17K and 11K respectively. Domain B has been shown to contain the Plg binding site. Data were collected from cryo-cooled crystals of domain B on station X12C using a CCD detector. Several derivative data sets were collected, and a multi-wavelength experiment performed using a promising platinum derivative.

Crystal Structure of the *Rhizomucor miehei* Aspartic Proteinase Complexed with the Inhibitor Pepstatin A at 2.7Å.	X12C

J.W. Quail and J. Yang (U. of Saskatchewan)

The crystal structure of the *Rhizomucor miehei* aspartic proteinase (RMP) complexed with the inhibitor pepstatin A has been determined from 2.7Å data collected at X12C in November, 1996. The crystals were thin and did not diffract to a sufficiently high resolution with a copper tube x-ray source. With the 2.7Å data obtained at NSLS it was possible to see more bonding detail for this complex. The crystals of the RMP-pepstatin A complex form in the orthorhomic space group $P2_12_12_1$. The unit cell dimensions are: a=41.52Å, b=50.82Å and c=172.71Å. The data was refined to an R factor of 19.3% and an R-free of 28.0% at 2.7Å. In the final model, a pepstatin A molecule fits into the large substrate-binding cleft between the two domains of RMP in an extended conformation up to the alanine at the P2' position. The dipeptide analogue statine residue at the P3'-P4' position forms an inverse γ-turn (P3'-P1') with the statine residue at the P1-P1' position, and its leucyl side chain binding into the S1' subsite. The inhibitor interacts with the residues of the substrate-binding pocket by either hydrogen bonds or hydrophobic interactions, or both. The hydroxyl group of the statine residue at the P1-P1' position forms hydrogen bonds with both the catalytic aspartate residues (Asp38 and Asp237). This conformation mimics the expected transition state of the enzyme-substrate interaction. The binding of the inhibitor to the enzyme does not produce large distortions of the active site. No domain movement is observed relative to the native enzyme structure. However, the surface flap region (residues 82 to 88) undergoes a conformational change. It moves toward the inhibitor and becomes rigid due to the formation of hydrogen bonds with the inhibitor. B-factor calculations of the two domains suggests that the C-terminal domain becomes more rigid in the complex than in the native structure.

Structures of UMP Kinase Transition State Analogue Complexes Suggest Mechanism of Phosphoryl Transfer is Associatieve	X12C

I. Schlichting and J. Reinstein (Max Planck Inst. for Molecular Physiology, GE)

Nucleoside monophosphate (NMP) kinases (ATP:NMP phophotransferases) catalyze the reversible transphosphorylation between nucleoside triphosphates and nucleoside monophosphates. NMP kinases play a major role in the regulation of the concentration of nucleoside diphosphates in the cell[1]. To obtain a better understanding of the enzymatic mechanism of NMP kinases we have studied UMP/CMP kinase (UK) from *Dictyostelium discoideum* by kinetic and crystallographic methods. It is difficult to apply time–resolved crystallographic approaches to this class of enzymes as NMP kinases employ an induced-fit mechanism involving large concerted motions that appear to be incompatible with maintainance of a well-ordered crystal lattice. Thus, we determined the three-dimensional structures of UK complexed with ADP, CMP, Mg^{2+} and transition state analogs (aluminum, beryllium and scandium fluoride) of the phosphate being transfered[2]. We measured the kinetic parameters of these analogs and found that all three analogs form rather tight complexes with the enzyme. Diffraction data of the crystals ($P4_12_12$, a=b=78.8 Å, c=100.7 Å) of UK, ADP, CMP, Mg^{2+} grown in the presence of aluminum or beryllium fluoride are 93≈% complete to 1.9≈Å with R_{merge} of 8.7≈% and 90≈% complete to 1.65 Å with R_{merge} of 6.1≈% , respectively. The structures were refined with XPLOR 3.1 using the structure of the UK complexed with the specific and asymmetric bisubstrate inhibitor P^1-(adenosine 5')-P^5-(uridine5')-pentaphosphate (UP5A) as a starting model (omitting the nucleotide, Mg^{2+}, and waters). The positions of the catalytic Mg^{2+} and the highly conserved lysine of the P loop are virtually invariant in the different structures. In constrast, catalytic arginines move to stabilize charges that develop during the phosphyl transfer reaction. The location of the arginines indicates formation of negative charges during the reaction at the transferred phosphoryl group, but not at the phosphate bridging oxygen atoms (see figure). This is consistent with an associative phosphoryl transfer mechanism but not with a dissociative one.

[1] Schlichting, I. & Reinstein, J. (1997) *Biochemistry* **36:** 9290-9296.

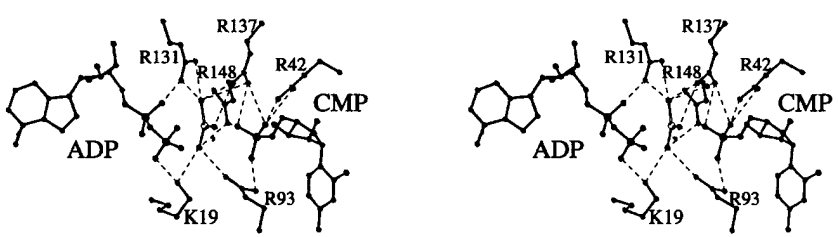

Figure 1. Stereoview of the UmpK.ADP.CMP.AlF_3.Mg^{2+} complex. Interactions between AlF_3 and arginine residues are shown by dashed lines.

Crystal Structure of I-DmoI by MAD Phasing	X12C

G. Silva and P. Van Roey (Wadsworth Center)

I-DmoI is a 22kDa intron-encoded endonuclease from the hyperthermophilic archeaon Desulfurococcus mobilis. Crystals of I-DmoI belong to space group C2, a = 94.2 Å, b = 37.16 Å, c = 55.78 Å, β = 113.3. Previous attempts at determining the structure of I-DmoI by conventional MIR methods have failed because of high mosaicity and non-isomorphism problems. MAD data (3 wave lengths) were measured for a Selenomethionine derivative crystal. For each wavelength, the data within an oscillation range of 160 degrees, and in its Friedel flip, were measured over a 36 hr. period, using one crystal. The data are 99% complete to 2.2 Å, with about 11-fold redundancy. The data were processed with DENZO/SCALEPACK. Rmerge values for each data set are 0.051 to 0.059. Phasing and solvent flatttening, using the package PHASES, has yielded a map that is easily interpretable. Model building is currently in progress.

Structure Determination of Novel Proteins | X12C

W. Smith, X. Qiu, N. Concha, B. Zhao, M. Swairjo, S. Abdel-Meguid (SmithKline Beecham Pharmaceuticals)

Single crystal x-ray diffraction data from several proteins have been collected at NSLS beamline X12C. Resolution extending to 1.7 Angstroms was achieved for small (less than 100 micron) crystals of novel human cysteine protease, bacterial tRNA-synthetases, and viral proteases. Two derivative data sets at 2.8 Angstroms were collected at the Pt and Hg edges to enhance the anomalous scattering signal from crystals of a novel human lipase whose structure is now being determined from this data.

The structures of these proteins are important to drug design efforts in our laboratories. This high resolution diffraction information was not accessible using laboratory radiation with the size crystals available.

Crystal Structure of Crosslinked Fragment D from Human Fibrin * | X12C

G. Spraggon, S.J. Everse and R.F. Doolittle (UCSD)

One of the longest lingering goals in all of blood coagulation research is to understand how fibrinogen units are packed together in fibrin clots. In this regard, the covalent dimer of fragment D known as "double-D" has been isolated from human fibrin, and crystallized in the presence of a Gly-Pro-Arg-Pro-amide peptide ligand simulating the donor polymerization site. These crystals belong to the monoclinic space group $P2_1$ with unit cell dimensions: a=93.82, b=95.5, c=113.76, β=96.08°. An 88.8 percent complete data set to 2.9$\AA$ was collected at beamline X12C of the NSLS. A molecular replacement solution was found using a partially refined model of fibrinogen fragment D.

The 170-kilodalton, end-to-end structure reveals the principle noncovalent interactions between fibrin monomers, including the "knob-hole" interactions between Gly-Pro-Arg and the key residues in the binding cavities on the γ domain, and the "D-D" interactions of abutting molecules. The covalently crosslinked carboxyl-terminal segments extend from one unit to the next on the opposite side of the fibrin dimer to the "knob and holes". These externally situated segments are not clearly delineated, indicating that there is some flexibility even after crosslinking. (G. Spraggon, S.J. Everse and R.F. Doolittle (1997) **Nature** 389:455-462.)

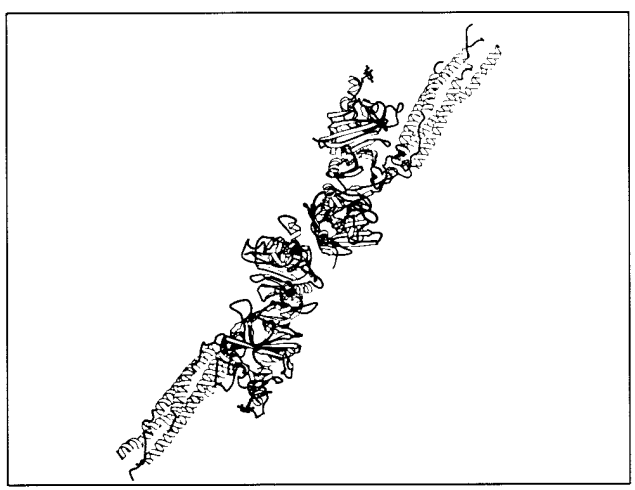

Figure 1. Ribbon representation of the double-D fragment of human fibrin. Color scheme: blue, α-chain; green, β-chain; red, γ-chain. (Figure produced with BOBSCRIPT.)

* This work was supported by NIH Grant HL-26873 and a postdoctoral fellowship to SJE from the American Heart Association, California Affiliate.

Atomic Structure of an $\alpha\beta$ T Cell Receptor (TCR) Heterodimer in Complex with an Anti-TCR Fab Fragment Derived from a Mitrogenic Antibody	X12C

J.H. Wang (Dana Farber Cancer Inst/Harvard), K. Lim (AECOM), A. Smolyar, M.-k. Teng, J-h. Liu, A.G.D. Tse, J. Liu, R. E. Hussey, Y. Chishti, (DFCI), C.T. Thomson (AECOM), R. M. Sweet (BNL - Biology), S.G. Nathenson, (AECOM) H.-C. Chang (DFCI/Harvard), J.C. Sacchettini (AECOM) and E.L. Reinherz, (DFCI/Harvard)

Each T cell receptor (TCR) recognizes a peptide antigen bound to a major histocompatibility complex (MHC) molecule via a clonotypic $\alpha\beta$ heterodimeric structure (Ti) non-covalently associated with the monomorphic CD3 signaling components. A crystal structure of an $\alpha\beta$ TCR/anti-TCR Fab complex shows an Fab fragment derived from a monoclonal antibody (mAb) interacting with the elongated FG loop of the Cβ domain situated beneath the β domain. This loop, along with the partially exposed ABED β-sheet of Cβ and glycans attached to both Cβ and Cα domains, forms a cavity of sufficient size to accommodate a single non-glycosylated Ig domain such as the CD3ϵ ectodomain. That this asymmetrically localized site is embedded within the rigid constant domain module has implications for the mechanism of signal transduction in both TCR and pre-TCR complexes. Furthermore, quaternary structures of TCRs vary significantly even when they bind the same MHC molecule, as manifested by a unique twisting of the V module relative to the C module. These data are the first to define the rigidity of the constant domain module, suggest the basis of structural interaction of the CD3ϵ signaling component with the TCR heterodimer, and define quartenary structural differences among TCRs.

The use of beamline X12C was ideal for our crystallographic problem as the cocomplex crystals were too small for conventional X-ray sources, the unit cell was of significant size with two complexes of TCR-Fab per asymmetric unit, and attempts to obtain conventional heavy atom derivatives for isomorphous replacement was unsuccessful. Consequently based on Friedel flip geometry, we collected data on a single splenomethionine substitute of frozen crystal at the inflection point, peak point and remote point. The integrated data sets were local-scaled together to obtain accurate dispersive differences. Difference-Fourier maps were calculated using the initial phases from the preliminary refined model derived with molecular replacement. Nine out of 12 Se sites showed up in both anomalous and dispersive difference maps, and the sites agree with the methionine positions in the model. The MAD data were treated as a special case of multiple isomorphous replacement and the nine Se sites were refined and used for phasing.

Characterization of Fe Impurities in AlN Using EXAFS *	X14A

T. C. Bruss, S. T. Misture and J. A. Taylor (Alfred U.) and T. R. Watkins (ORNL)

Aluminum nitride is of great interest in the field of electronic ceramics due to its unique combination of a high thermal conductivity and a high electrical resistivity. Direct nitridation of Al is a low cost alternative to traditional sol-gel processing. However, this processing technique typically produces AlN powders with Fe impurities which originate in the Al metal. Metallic impurities have a detrimental effect on the aforementioned properties. A first step in removal of these impurities is identification of the chemical state of the impurities. Since the impurity levels are rather small (¡500 ppm), X-ray diffraction techniques from laboratory instruments were unable to detect Fe or any Fe containing compound, possibly because the phase is amorphous.

Extended X-ray Absorption Fine Structure (EXAFS) is a powerful technique for identification of phases and compounds containing a specific element as well as determination of the local structure (short-range order) about a given atomic center in all states of matter. EXAFS has been used to detect Fe impurities in silicon nitride and Ti impurities in AlN, for example. EXAFS analysis and absorption edge positions were used to unambiguously determine that metallic iron is present in AlN produced by direct nitridation. Based on these results, vapor-phase acid leaching was used to remove the Fe without significant degradation of the AlN.

* Research sponsored by the U. S. Department of Energy, Assistant Secretary for Energy Efficiency and Renewable Energy, Office of Industrial Technologies, Industrial Energy Efficiency Division and Advanced Turbine Systems Program. Research facilities sponsored by the Assistant Secretary for Energy Efficiency and Renewable Energy, Office of Transportation Technologies, as part of the High Temperature Materials Laboratory User Program. Oak Ridge National Laboratory is managed by Lockheed Martin Energy Research Corp. for the U.S. Department of Energy under contract number DE-AC05-96OR22464.

Crystalline Phases of Langmuir Monolayers * | X14A

M.K. Durbin, A.G. Richter, C.-J. Yu, J. Kmetko, P. Dutta (Northwestern U.), and J.M. Bai (ORNL)

Monolayers of alkanoic acids at the air/water interface have a complex phase diagram. Many of the phases are two dimensional versions of phases observed in bulk alkanes. X-ray diffraction experiments have revealed that two of the phases, the CS and L_2'' phases, are two dimensional crystals with molecular packings that are similar to the crystalline packing of long-chain bulk alkanes. Because the crystalline alkane phases are known to have molecules arranged in a herringbone pattern, it has long been assumed that the CS and L_2'' phases must have similar backbone orientational order. Recent IR spectroscopy experiments (M. Li and S.A. Rice, *J. Chem. Phys.* **104**, 1996, 6860) have shown that such orientational order is present. We report the first observation of X-ray diffraction peaks that confirm that the herringbone order is long-range. Figure 1 (top) shows the peaks observed in the CS phase, and their registry according to an orthorhombic lattice with two molecules per unit cell. The peak indexed as (21) would be forbidden if both molecules were equivalent. This situation occurs in the higher temperature S phase, and is shown in the lower half of figure 1. Although the (11), (20), (02), and (31) peak positions in the two phases are similar, there is no intensity maximum at the position where the (21) peak would be in the S phase.

The transition between these two phases is first order. The (21) peak maintains roughly the same intensity as temperature is varied through the CS phase, then vanishes in the S phase. We have found the herringbone peak in the CS and L_2'' phases, but not in the more disordered S, L_2' and L_2 phases.

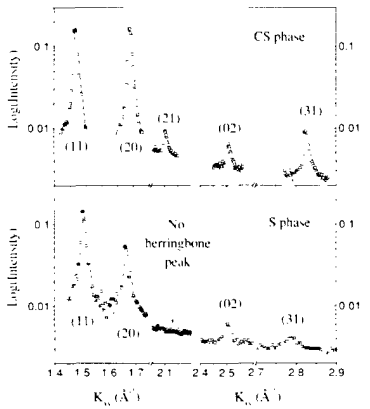

Figure 1.

* Supported by the US Department of Energy Grant DE-FG02-84ER45125.

Characterization of Mo-Ta Films* | X14A

H. J. Holland, G. F. Foster (Corning, Inc), and T. R. Watkins (ORNL)

Sputtered Mo-Ta films were examined by a number of analytical techniques in order to understand the observed asymmetric diffraction peak shapes. The films had been sputtered onto glass substrates in an argon atmosphere at a number of pressures and were between 0.4 and 0.5 microns thick. The composition through the thickness of the films was determined to be constant with depth by secondary ion mass spectroscopy (SIMS). The Mo:Ta weight percent ratio within the films was determined to be 1:3 using inductively coupled plasma spectroscopy (ICP). Residual stresses were determined using x-ray diffraction and photoelastic methods. No residual stress gradient was observed. Pole figures and electron micrographs show the crystallographic texture and morphology of the films. Two alpha bcc phase are believed to exist within these films.

*Research sponsored by the U. S. Department of Energy, Assistant Secretary for Energy Efficiency and Renewable Energy, Office of Industrial Technologies, Industrial Energy Efficiency Division and Advanced Turbine Systems Program. Research facilities sponsored by the Assistant Secretary for Energy Efficiency and Renewable Energy, Office of Transportation Technologies, as part of the High Temperature Materials Laboratory User Program. Oak Ridge National Laboratory is managed by Lockheed Martin Energy Research Corp. for the U.S. Department of Energy under contract number DE-AC05-96OR22464.

Structural Determination of the C_{60}/Ge(111) Interface via X-ray Diffraction	X14A

T. Kidd, H. Hong, T.-C. Chiang (U. of IL, Urbana-Champaign), R. D. Aburano (Cypress Semiconductor), and T. Gog (Argonne Nat. Lab)

An x-ray diffraction study was performed to determine the nature of the C_{60}/Ge(111) interface formed by depositing C_{60} on a Ge(111)- c(2×8)surface at room temperature. In-plane k-scans show a (1×1) periodicity at the C_{60}/Ge(111) interface with no trace of the c(2×8) reconstruction, indicating that the Ge adatoms on the clean c(2×8) reconstructed surface are displaced. Scans along the (10) crystal truncation rod indicate that these adatoms are transferred from the T_4 bonding site to the H_3 site after C_{60} deposition. A model consisting of three relaxed bilayers of Ge and randomly distributed adatoms in the H_3 site best explains the results.

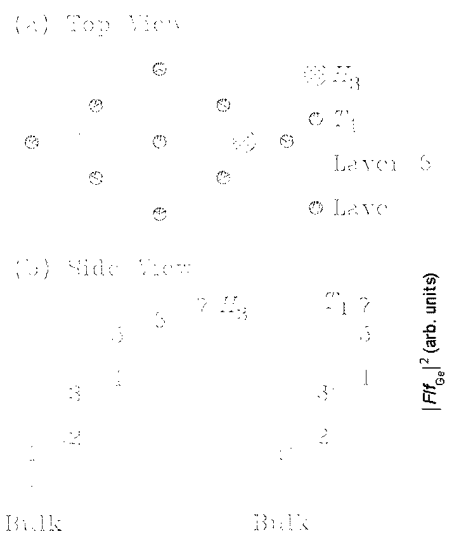

Figure 1. (a) Top view of (2×2) unit cell uncluding uppermost atoms from the model model used to fit x-ray intensities along the (10) rod

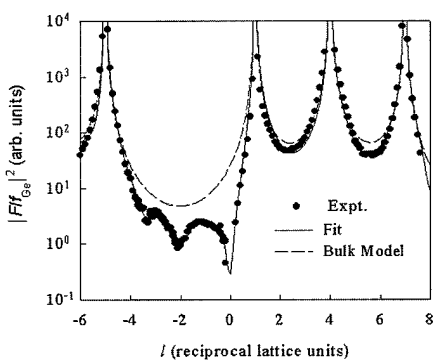

Figure 2. Intensity distribution taken along the (10) rod. The dashed indicates model with in bulk positions. Solid line represents model with adatom coverage and positions.

Anisotropic Behavior and a Second Length Scale in the Critical Diffuse Scattering from the Tricritical System V_2H *	X14A

J. Trenkler, P. Chow, S. C. Moss (U. of Houston), R. Paniago (U. of Munich), J. Bai (U. of Illinois), and R. Hempelmann (U. des Saarlandes)

The tricritical behavior of a single crystal of V_2H at the β_1-β_2-phase transition has been studied by x-ray scattering. Critical diffuse scattering (CDS) in alloys is a major tool for studying critical phenomena since the diffuse scattering data give valuable information on the behavior of thermodynamic parameters like the correlation length and the susceptibility at a phase transition. The sharp increase in long-wave fluctuations of the order parameter near the critical range causes a strong increase in the diffuse scattering of x-rays which directly reflects the thermodynamic behavior in this critical regime.

In this experiment, we mainly focussed on the measurement of the temperature dependence of the CDS above T_C, taking line and area scans in order to deduce the tricritical exponents γ and ν from their "deconvoluted" amplitude and half width at half maximum of the intensity profiles. The sample exhibits a strongly anisotropic CDS in the (Δh, 5/2+Δk, $\bar{5}$/2-Δk) plane measured at T=T_C+1.0 K as shown in fig. 1. Thereby, the correlation length is one order of magnitude larger perpendicular to the hydrogen (H) sheets than within the occupied H-sheets. An analysis of the data is still in progress.

Furthermore, we observed a remarkable change in the line shape of the critical diffuse scattering in the longitudinal [0 1 $\bar{1}$] scan at T=T_C+6.2 K as shown in fig. 2. The measured profile consists clearly of two components, a broad and a narrow one, for temperatures T≥T_C+6.2 K. At T=T_C+7.3 K, the narrow component is very weak. The higher order superstructure peak (0 7/2 $\bar{7}$/2) measured at the same temperature displays the broad component more prominently than the low order superstructure peak (0 5/2 $\bar{5}$/2). However no change in the line shape was observed in the [1 0 0] transverse scans. Further investigation of this issue was done at X18A and X17B1.

*This work was supported by the NSF on DMR92-08450

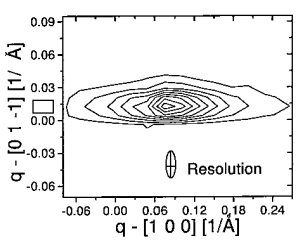

Figure 1. CDS around the (0 5/2 $\bar{5}$/2) superstructure reflection in a heating run in the (Δh,5/2+Δk,$\bar{5}$/2-Δk) plane at T=T_C+1.0 K; this data has not been corrected for resolution. The cross corresponds to the FWHM of the resolution function.

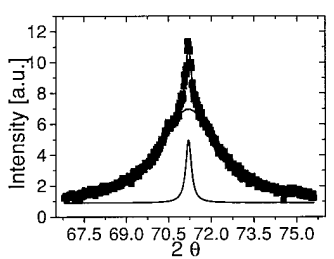

Figure 2. CDS at the (0 5/2 $\bar{5}$/2) position in a heating run in [0 1 $\bar{1}$] at T=T_C+6.2 K, demonstrating two length scales.

High Temperature Residual Stress Measurement in Thermal Barrier Coatings*	X14A

T. R. Watkins and C. R. Hubbard (ORNL)

Thermal barrier coatings (TBC`s) are currently utilized in aircraft and diesel engines to prolong the life of metallic components. TBC failure is typically spallation of the top coat due to oxide scale growth at the bond coat/top coat interface. Understanding the residual stresses of the oxide scale growth is thus critical to enhancing the performance and reliability of TBC systems.

In this study, preliminary characterization of the residual stress state in the bond coat, scale, and substrate was performed. The residual strains are measured in a thermally grown oxide scale and in a PtAl bond coat on top of a Reni N5 superalloy substrate at 1150 0C via x-ray diffraction. Large compressive residual stresses (¿-4 GPa) in the the 2 5m thick alumina scale were observed at high tmperature. The residual stresses decreased at room temperature to -3 GPa, presumbaly due to cracking. Future experimental work is planned.

*Research sponsored by the U. S. Department of Energy, Assistant Secretary for Energy Efficiency and Renewable Energy, Office of Industrial Technologies, Industrial Energy Efficiency Division and Advanced Turbine Systems Program. Research facilities sponsored by the Assistant Secretary for Energy Efficiency and Renewable Energy, Office of Transportation Technologies, as part of the High Temperature Materials Laboratory User Program. Oak Ridge National Laboratory is managed by Lockheed Martin Energy Research Corp. for the U.S. Department of Energy under contract number DE-AC05-96OR22464.

Surface Structure of Zn^{2+} Adsorbed on Calcite $(10\bar{1}4)$ Surface *	X15A

L. Cheng, M. Bedzyk (ANL and Northwestern U.), N.C. Sturchio (ANL) , and J.C. Woicik (NIST)

Divalent metal ions dissolved in aqueous solution interact with ionic mineral surfaces and frequently become adsorbed on the surafce as a result of this interaction. This process effectively acts as a natural means of metal ion transport from the soluble to the solid phase, and has significant implications in fields such as geochemistry and environmental sciences.

Zinc (II) ion (Zn^{2+}) is a typical divalent ion, as is calcite ($CaCO_3$) an abundant mineral on Earth. The interaction of Zn with the calcite $(10\bar{1}4)$ cleavage surface has been a system of rather popular studies [1], in order to obtain quantitative data for use in interpreting geochemical and environmental processes. But a crucial component of these quantitative data—the adsorption structure of Zn on calcite—has not been directly observed at the atomic level.

We have conducted a combined X-ray standing wave (XSW) triangulation and surface-polarized EXAFS study on the structure of Zn ion adsorbed on the calcite $(10\bar{1}4)$ surface from a dilute (10^{-3} M) solution. The XSW triangulation results show a high adsorption coherent fraction, of about 0.7, and the coherent positions P_H have the following values:

Reflection Plane H	Coherent Position P_H
$10\bar{1}4$	0.87 ± 0.01
0006	0.45 ± 0.05
$0\bar{2}24$	0.85 ± 0.03

These positions indicate that Zn substitutes the Ca ion on the surface, but at a lattice position that is displaced appreciably from the undistorted Ca site. The SEXAFS data on Zn show that the Zn-O nearest-neighbor bond length on the adsorption surface is 2.10 ± 0.02 A. This value is within experimental uncertainty comparable to the Zn-O bond length in bulk $ZnCO_3$, which is isostructural with calcite. The combined interpretation of these XSW triangulation and SEXAFS results is that the O atoms bonding to the Zn ion, both in-plane and in the monolayer below, collapses toward the Zn ion.

[1] J.M. Zachara *et. al.* Sorption of divalent metals on calcite. *Geochim. Cosmochim. Acta*, 55, 1549 (1991).

* Work was supported by DOE BES contract No. W-31-109-ENG-38 to ANL.

Polarity Determination of GaN Thin Films on Sapphire(0001) by X-ray Standing Waves	X15A

A. Kazimirov, G. Scherb, J. Zegenhagen (Max-Planck-Inst.-FKF, Stuttgart, Germany), T.L. Lee (NWU), M.J. Bedzyk (NWU and ANL), M.K. Kelly, H. Angerer, O. Ambacher (Walter-Schottky Inst., TU-Muenchen, Garching, Germany)

Thin films of the wide-bandgap semiconductor GaN are important because of their application for short-wavelength, light-emitting LEDs and lasers. In the (0001) crystallographic direction, the non-centrosymmetric wurtzite GaN crystal exhibits no mirror symmetry for the Ga and N atomic planes. As a consequence, for thin films on e.g. sapphire there are two possible stacking sequences. We applied X-ray Standing Wave technique [1] to determine the polarity of thin GaN films grown by MBE on Al_2O_3 single crystals. Different from the standard approach based on the excitation of an XSW field inside a perfect single crystal, we generated an X-ray standing wave by the thin GaN film [2] by X-ray diffracting 10.5 keV photons. The Ga-K_α fluorescence yield was measured as a function of the incidence angle within the range of the GaN(0002) reflection. The experimental result for the $1\mu m$ thick film is shown in Fig.1. The convolution with a Gauss function (σ=0.05 deg.) was used to take into account the broadening of the reflectivity curve due to some growth defects. The static Debye-Waller factor describing the perfection of the film structure was used as the only fitting parameter (Fig.2). Our results unambiguously indicate N-polarity of the MBE grown film (nitrogen atoms occupy the top half of the bilayer) with the static DW-factor $e^{-w} \approx 0.36$. This finding is in contrast with the result of a recent ion-channneling and electron diffraction study for the polarity of thin films on sapphire grown by MOCVD [3].

[1] J.Zegenhagen, Surf. Sci. Rep. 18 (1993) 199.
[2] A.Kazimirov et al., Acta Cryst. B48 (1992) 577; A.Kazimirov et. al., Solid State Comm. 104 (1997) 347.
[3] B. Daudin et al., Appl. Phys. Lett. 69 (1996) 2480.

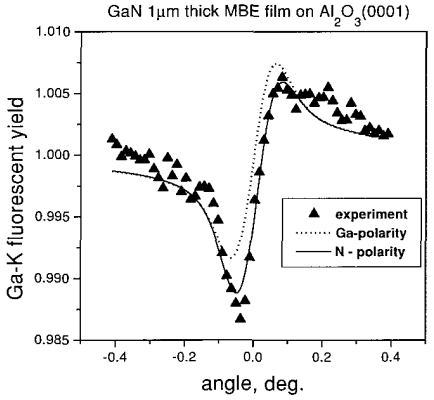

Figure 1.

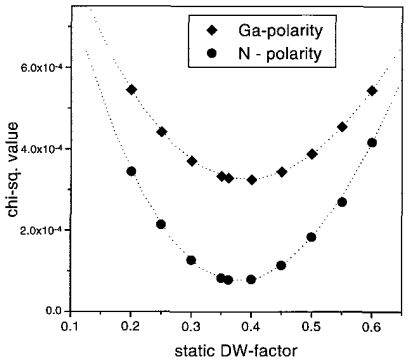

Figure 2.

Dimer Structure of Sb-Terminated GaAs(001)-(2×4) Surface *	X15A

T.-L. Lee (Northwestern U.) and M.J. Bedzyk (Northwestern U. and ANL)

The bonding geometry of the GaAs(001):Sb-(2×4) surface was investigated by the x-ray standing wave technique (XSW) using the (004) and (022) Bragg reflections. The height above the surface (h') and the bond length (L) of the Sb dimer were measured to be 1.72 Åand 2.84 Å, respectively, in good agreement with the previous theoretical calculation [1] and other measurements on related surfaces. The Sb coverage of the (2×4) reconstruction was determined by Rutherford back scattering to be 0.48 ML, consistent with a model having two Sb dimers per unit cell. We then considered two previously proposed structures of a half ML coverage (see figure): one with two Ga dimers in the second layer (Model I), and the other with one As dimer in the third layer (Model II). Theoretical calculation [1] has shown that both structures are energetically stable. We discriminated between these two models by measuring the lateral displacement (Δx) of the Sb dimers, which is expected to be much larger for Model I due to the formation of the Ga dimers. Our (111) XSW measurement revealed a negligible lateral shift and is therefore in favor of Model II.

[1] N. Esser, A.I. Shkrebtii, U. Resch-Esser, C. Springer, W. Richter, W.G. Schmidt, F.Bechstedt, and R. Del Sole, Phys. Rev. Lett. 77, 4402 (1996)

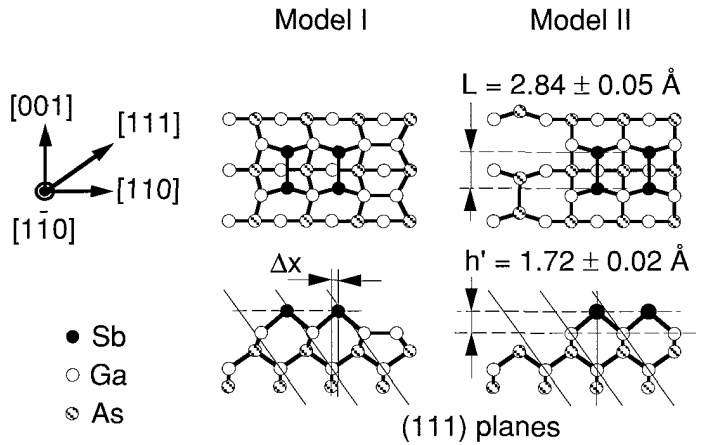

Figure 1.

* This work was supported by the NSF under contract No NMR-9632593 and DMR-9632472 to theMRC at Northwestern U., and by the US DOE under contract No. W-31-109-ENG-38 to ANL.

Surface Structure of Te-Terminated Ge(001) * | X15A

P.F. Lyman (Northwestern U.) and M.J. Bedzyk (Northwestern U. and ANL)

The (001) face of a diamond structure semiconductor exhibits two dangling bonds per surface atom. Therefore, the adsorption a group VI element, which will favor the formation of two bonds, may tie up all available

dangling bonds after adsorption of one monolayer (ML). This will likely result in a low-energy, fully

passivated surface with a (1x1) arrangement of the hexavalent group VI atoms. This phenomenon has been demonstrated previously for the S/Ge(001) system, and, to a lesser extent, for the Te/Si(001) system. Previous to

the present work, we demonstrated using XSW that for Te/Si(001), there is a significant amount of disorder in the Te distribution (coherent fraction = 0.46 to 0.065). We had postulated that this was due to the large size of the Te atom relative to the Si lattice. In the present work, we tested this idea by comparing withthe adsorption of Te on Ge(001), which is similar to Si(001) but has a 4.3

In accordance with our expectations, the adsorbed Te layer exhibited a (principally) (1x1) reconstruction and a much higher coherent fraction (now = 0.85). The XSW data for a sample annealed to 540 K are shown in the lower trace in Fig. 1. This indicates that the Te atoms were able to achieve a nearly perfect de-reconstruction of the native Ge(001) dimerized clean surface in favor of one with a local (1x1) geometry. In addition, the Te exhibited new and surprising behavior upon annealing to 670 K. A clear phase transition occurred, indicated both by a dramatic change in the LEED pattern and a inward motion of the Te adsorption height. The coherent position changed from 0.07 to 0.02, indicated an inward displacement of Te by 0.007 nm. At the same time, the LEED pattern changed to a streaky c(2x2). We hypothesize that appromimately half of the Te has desorbed, and the Ge surface atoms have redimerized; the remaining Te atoms would then sit in long bridge positions, between two dimers.

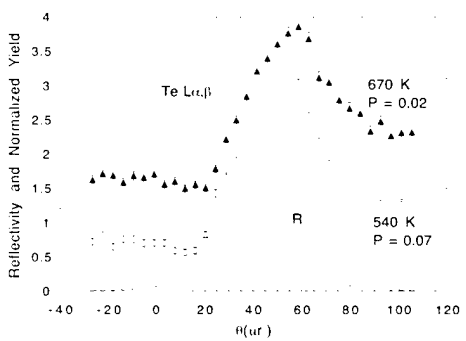

Figure 1.

* This work was supported by NSF Contract No. NMR 9632593 and DMR-9632472 to MRC-Northwestern U. and the US DOE Contract W-31-109-ENG-38 to ANL.

In-As Layer Spacing in Buried InAs/GaAs(001) | X15A

J.C. Woicik and J.G. Pellegrino (NIST) K.E. Miyano (Brooklyn) P.F. Lyman and M.J. Bedzyk (Northwestern)

Utilizing the kinematic theory of x-ray diffraction, we have determined the In-As layer spacing in a buried InAs monolayer grown on GaAs(001). This spacing, 1.62 +/- 0.03 A, coincides with the solution of a Keating valence-force field that explicitly assumes no relaxation of the Ga and As atoms on both sides of the InAs/GaAs interface; it is also consistent with previous extended x-ray absorption fine structure and x-ray standing wave measurements [Woicik et al., Phys. Rev. B 52, 2281 (1995)].

In-Situ X-ray Standing Wave Analysis of Electrodeposited Cu Monolayers on GaAs(001) — X15A

J. Zegenhagen, G. Scherb, A. Kazimirov (Max-Planck-Inst.-FKF, Germany), H. Nogushi, K. Uosaki (Hokkaido U., Japan), T.-L.Lee (NWU), and M.J. Bedzyk (NWU and ANL)

Electrochemical preparation of surfaces is very attractive with the drawback that the majority of the surface characterization tools which are available e.g. for UHV-preparation are not applicable because of the presence of the electrolyte. X-ray techniques are an exception and have been employed increasingly for investigations of metal/electrolyte interfaces. Little work has been done for semiconductor electrodes despite its importance and the scarse information about corresponding structural processes. Recently we reported the first in-situ X-ray structural analysis of this kind employing X-ray diffraction [1]. We studied GaAs(001)/H_2SO_4 as a function of electrode potential and the growth and epitaxy of Cu clusters [1,2]. The first in-situ XSW study of a semiconductor electrolyte interface for GaAs(001)/H_2SO_4(:Cu) is presented here. The GaAs(004) reflectivity and the Cu-K fluorescence yield for 0.6 ML electrodeposited on n-GaAs(001) are shown in the figure. The result shows that (sub)monolayer amounts of Cu adsorb predominantly substitutional before 3-D clusters start to grow. Part of the Cu diffuses a few ten nm into the bulk in an amount different for p- and n-type GaAs. Coherent fractions are always smaller than 0.4, showing that other minority positions are occupied by the Cu. Even if the GaAs is anodically dissolved, the surface Cu is removed only slowly, proving that it is strongly bound to the GaAs **within** the top surface layers, staying at/within the surface even if it is slowly etched away.

[1] J.Zegenhagen et al., Surf. Sci. 352-354 (1996) 346.
[2] D.-M.Smilgies et al., Surf. Sci. 367 (1997) 40.

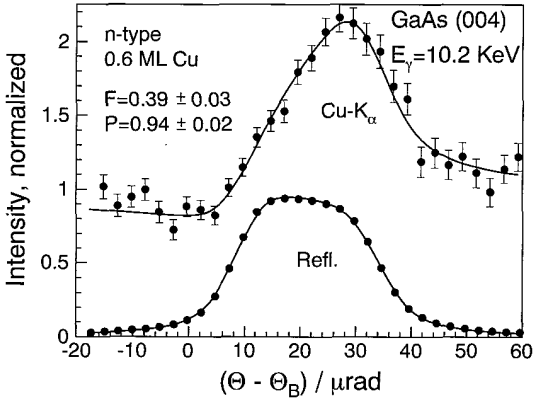

Figure 1.

Fundamental Limit Of Free-Carrier Densities In *n*-doped Si — X15B

D. J. Chadi, C. H. Park (NEC), D. L. Adler, M. A. Marcus, H.-J. Gossmann, and P. H. Citrin (Bell Labs)

A critical factor in the evolution of increasingly small Si-based components is the maximum achievable free-carrier concentration. Electron carrier densities in *n*-type Si are observed to saturate at $\leq 5 \times 10^{20}$ cm^{-3}, a phenomenon generally attributed to the formation of electrically inactive clusters or deactivating dopant defects containing one or more Si vacancies. X-ray absorption measurements and first-principles calculations were used to show that for Group V donors (P, As, Sb) the free-carrier saturation can arise from a very different mechanism, namely, Fermi-level pinning. As the energy of electrons at the Fermi level increases with doping, it becomes energetically favorable to create localized states in a new class of centers called donor-pair (*DP*) defects. Each *DP* center is composed of two nearby, vacancy-free dopant atoms, which capture 2 electrons from the Fermi sea rather than donating 2 electrons into it. The strongly interacting dopant-atom pairs lead to large lattice relaxations with either 3-membered or 5- and 7-membered Si rings. The unusual atomic structure of these defects agrees very well with the x-ray absorption data. and with a variety of other, albeit less direct measurements. A simple model for forming *DP* centers predicts a maximum carrier concentration and dopant dependence that are both in excellent agreement with experiment. This work shows that *DP* defects represent an inherent limitation to the electrical activity of Si doped with Group V donors. That is, while additional vacancy-dopant complexes and/or precipitates may also be formed in amounts that depend on sample preparation conditions (e.g., annealing temperatures and rates), deactivating *DP* defects will always be created – even under the best of circumstances – because they result only from the mutual interaction between nearby Group V dopants. Future work is planned to explore whether analogous defects involving other types of donor, or even acceptor, atoms are equally important in Si.

Trace Metal Contaminants in Optical Silica Preforms | X15B

P. A. Northrup, R. M. Atkins, P. F. Glodis, D. C. Jacobson, and P. H. Citrin (Bell Labs)

The greater transmission losses measured from certain optical silica fibers had been shown by us last year to correlate with the existence of particular metal impurities in the cores of the parent preforms. Surprisingly large amounts of Fe (> 100 ppb) were even found in a fiber preform that had a much lower loss. The results raised concerns about the reliability of the absolute metal concentrations and about the purity of the starting tube itself (supplied by an outside vendor). A new series of calibration standards was therefore studied, and a thorough re-examination was made of two preforms whose fibers yielded very different losses. These more accurate Fe measurements strengthened the conclusions of the earlier study, including the fact that the Fe exists almost exclusively in the relatively benign 3+ state (the concentration of the more absorbing Fe^{2+} species is experimentally obscured by – and clearly scales with – the amount of Fe^{3+} present). Extension of measurements into the outermost shell region showed that the metal impurities do not originate from the starting tube. This was further confirmed by a study of Cu impurities, whose concentration dependence on position and optical loss was essentially identical to that for Fe. The striking spatial variation in metal concentration that was observed suggests the origin of metal contamination in the preform manufacturing process.

Structural Stability of Vacancy-Ordered Rare-Earth Fulleride | X15B

K. M. Rabe (Yale) and P. H. Citrin (Bell Labs)

Superconducting $Yb_{2.75}C_{60}$ is unique among metal-doped fullerene compounds, exhibiting long-range-ordered vacancies, significantly displaced Yb cations (2.4 Å), inequivalently charged and distorted C_{60} anions, and rotationally ordered C_{60} pentagonal faces. A simple electrostatic-energy analysis was used to explain how each of these features stabilizes this apparently exotic crystal structure (2008 atoms/unit cell). The results have general implications for other, more conventional intercalated metal fullerides.

Formation of Copper Silicide using Surface X-ray Diffraction * | X16A

P. Bennett (ASU Physics), I. Robinson and D. Walko (UIUC Physics)

We report an in-situ study of the initial stage of copper silicide formation during deposition of Cu on Si(111) at 300K using surface X-ray diffraction. The practical significance of this system stems from its importance in the VLSI microelectronics industry. From a scientific viewpoint, it is interesting to study how an epitaxial overlayer forms in a large-misfit system [Cu(111) is 5% larger than a RT3 coincidence lattice on Si(111)].

Walker reported in an ex-situ X-ray diffraction study that a 100nm film of Cu on Si(111) contains a buried monolayer of commensurate Cu_3Si, strained 7% to match the substrate. On the other hand, Bootsma reported that only incommensurate silicide forms, based on an in-situ study using RHEED and AES.

We find that the first few Ml of copper forms commensurate Cu_3Si. This is clear from the CTR scan (integrated intensities at points along the substrate truncation rod) shown in the figure (LHS). The new peak near L = -4 corresponds to islanded but commensurate Cu_3Si. Additionally, the overlayer contributes a characteristic +/- asymmetry near the substrate Bragg peaks (L=+1, +4), from which the overlayer registry may be determined (work in progress). At higher coverage, the coherent silicide structure is mostly consumed. Incommensurate copper metal forms at the same time, as evidenced by the incommensurate rod scans Q = (1.65, 1.65, L) shown in the figure (RHS). It is remarkable that this structure begins as hcp Cu (peak near L = 2.2), before adopting the fcc structure (L = 2.2), with marked twinning (L=3.0)

In conclusion, we find that in-situ monitoring of the initial stage of copper silicide formation reveals two "transient" structures that might strongly affect the formation of thicker overlayers.

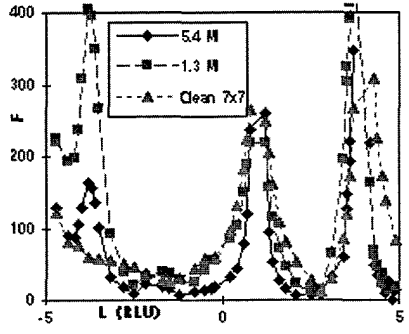

Figure 1.

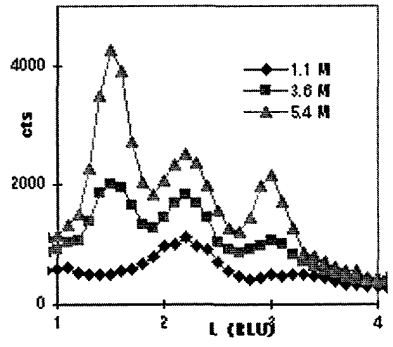

Figure 2.

* Supported by NSF grant MR9528503.

Ultra-High Doping in Si(001): B Pairing and Diffusion | X16A

G. Glass, I. K. Robinson, D. Walko, and J. E. Greene (U. of Illinois)

Ultra-high B doped Si and Si(1-x)Ge(x) films have the potential to drive further miniaturization of microelectronics with minor changes in process technology. Some applications for such layers include source/drain regions in MOS transistors, base layers in SiGe HBT's, and emitter layers in BJT's. Ultra-highly B doped films on Si(001) have generated considerable scientific interest as a tensile strained layer/limited miscibility system. Ultra-high B doped Si(001) samples were grown by Gas-Source MBE to a C_B of $2x10^{20}$ cm^{-3}. The B was determined to be electrically activated from a combination of SIMS and Hall-effect measurements. Samples were isothermally annealed *in-situ* under high vacuum conditions in X16A, at tempertures in the range of 900 to 1100°C until the strain was reduced to ĩ0% of the initial value. The experimental curves show a rapidly decaying separation between the film and substrate (004) peaksas seen in Figure 1. Two exponential terms were needed to fit the data. SIMS measurements after annealing showed B diffusion from the film into the bulk. All films remained coherent, and no precipitates nor misfit dislocations were found by XTEM. *Ab initio* psuedopotential calculations were performed by Zhu* et. al. which revealed that a boron pair on a single Si lattice site is a stable configuration for B in Si. The predicted volume of a cell containing a boron pair bonded to four Si atoms is larger than a pure Si tetrahedron, and therefore would tend to increase the lattice constant of the film. The goal of this experiment was to demonstrate the Arrheneius behavior of the B pairing reaction, and to obtain activation energies for the formation of such pairs. Preliminary results in Figure 2 show the activation energy for the first exponential term attributed to the formation of B pairs to be 1.6 eV. The second activation energy attributable to diffusion is 2.9 eV. This value is lower than the 3.4 eV value typical for lower B concentration material, but it is reasonable considering that B diffusion is enhanced at high concentration. *J. Zhu et al, Phys. Rev. B, 54, 4741 (1996).

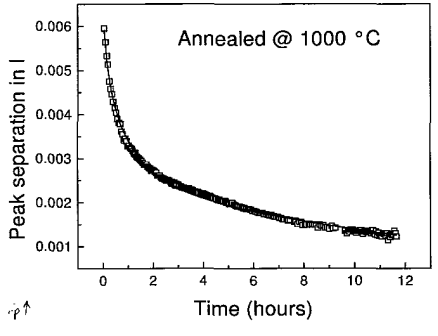

Figure 1. Separation between the Si(004) and Si:B(004) peaks as a function of time at 1000 C. Two exponential terms were used to obtain a good fit.

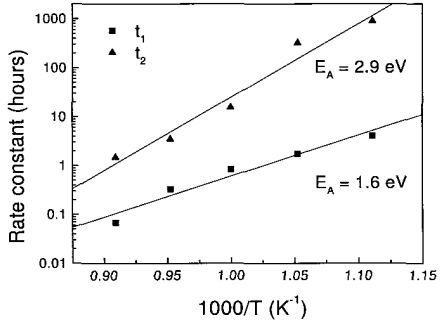

Figure 2. Arrhenius behavior of the two strain reducing mechanisms as a function of 1/T.

Irradiation Induced Strain Relaxation of a Metastable SiGe Film | X16A

C. Kim, T. Spila, J. E. Greene and I. K. Robinson (U. of Illinois)

When SiGe alloy is grown on Si(001), there exists a critical thickness below which the SiGe film can be grown pseudomorphically. The theoretically predicted critical thickness using equilibrium theory is, however, smaller than that measured by experiment because of kinetic effect. A metastable film can therefore exist when its thickness is in the range between the theoretically predicted and experimentally determined critical thicknesses. Since it is not in the state of energy minimum, it might be possible to have the strained film relax by external perturbation such as irradiation.

In our experiment, a metastable SiGe film of 200 Å grown at 500 °C was irradiated with 25 KeV Ga ions in a UHV chamber combined with a diffractometer and strain relaxation was measured *in-situ*. The dose ranged from 8×10^{10} to 3.6×10^{13} (ions/cm^2). Substrate Si unit cell was chosen for indexing Bragg peaks and As shown in Fig.1, a series of index scans through (202) peak of SiGe were made for different doses of irradiation. The maxima of sharp peaks due to coherent diffraction decreased as we increased dose. On the other hand, the intensity of diffuse scattering was oberved to increase. In Fig. 2, the diffuse scattering alone is shown on a linear scale by subtracting the main peaks from the raw data. It is clearly seen that diffuse peaks shifted with increasing dose. The peak shift can be attributed to the misfit dislocations induced by irradiation and is one good evidence of strain relaxation of metastable SiGe film.

The peak position and width convey information about the changes in microstructure of the film during irradiation. For example, the increase of lattice constant with more dose is related to the increase of average dislocation distance. In the meanwhile, peak width, which is inversely proportional to a domain size, decreased as a function of dose. Therefore, if we assume the domain size is determined by average distance between dislocations, information obtained from shift of peak position and width is consistent with each other.

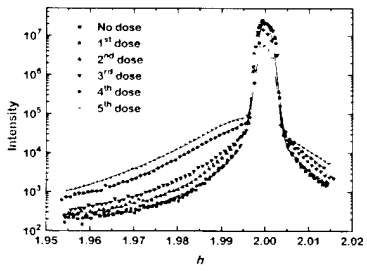

Figure 1. A series of index scans along h direction through SiGe (202) peak after different doses of irradiation.

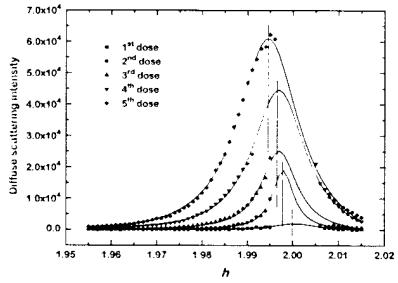

Figure 2. Diffuse scattering intensities for different doses of irradiation. Note that the main peaks due to coherent diffraction were subtracted from the raw data.

Ion Implantation Damage in Semiconductors | X16A

P. J. Partyka, R. S. Averback and I. K. Robinson (University of Illinois)

We studied the diffuse X-ray scattering from defects in Si produced by *in situ* ion implantation, both as a function of dose and as a function of temperature. Fundamentally different behavior was found at temperatures near 100K, which was previously inaccessible for lack of the *in situ* capability.

A typical diffuse scattering profile around an in-plane 440 peak is shown as raw data in Figure 1. This sample was irradiated with 4.5keV He^+ ions at 210K. The lowest trace, marked 'unirradiated' is just due to the thermal diffuse scattering (TDS), measured under the same grazing incidence conditions on the same sample prior to dosing. If the excess scattering were due to the elastic strain field around the ion-beam generated point defects (Huang mechanism), the expected functional form of the scattering would be q^{-2}. Therefore the TDS was subtracted and the vertical axis was rescaled by a factor of q^2 so as to show the deviation from ideal q^{-2} behavior.

The result, shown in fig 2, shows clear deviations from the Huang behaviour. Ideal Huang Diffuse Scattering would appear as a constant value on this graph, which would rise with the dose (or density of defects). There is a clear dip in the intensity near the Bragg peak position in the center of the scan. Our current understanding of this result is that the irradiation causes a roughly equal density of interstitials and vacancies, with approximately the same relaxation volumes, but that they are bound together in an I-V pair. The strain field at large distance is thereby canceled out, and the corresponding small-q diffuse scattering is reduced. We conclude that the defects are spatially correlated. Further modeling of the diffuse scattering is in progress.

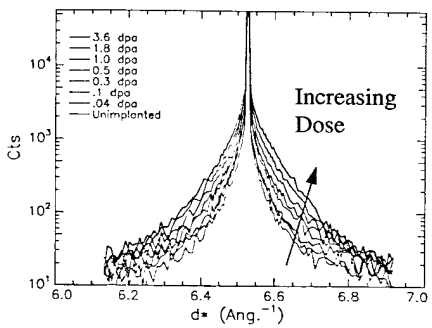

Figure 1. Diffuse scattering around an in-plane Si(440) reflection, plotted as a function of total momentum transfer.

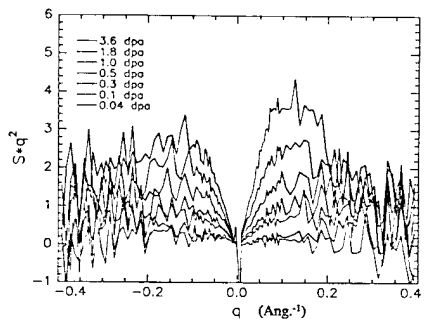

Figure 2. Background subtracted data from figure 1, rescaled by the square of q.

X-ray Investigation of a $Si_{0.9}Ge_{0.1}(001)$ Single Crystal Surface | X16A

H. Reichert (U. of Wuppertal, Germany), S.C Moss (U. of Houston), C.Y. Kim, and K. Evans-Lutterodt (Lucent Technologies)

We have investigated the near surface structure of a $Si_{0.9}Ge_{0.1}(001)$ single crystal. During the cleaning procedure we have performed reflectivity measurements in order to monitor the Ge concentration profile in the near surface region. After cleaning the surface chemically we found a large Ge excess concentration which can be deduced from the oscillations of the reflectivity curve in Fig.1. We have also studied the intensity distibution along integral order crystal truncation rods at this stage of the sample preparation.

Following a short heating treatment at 850°C the quality of the crystal surface degrades quickly. This can be seen by the change in the reflectivity profile in Fig.1. Further heating at 850°C for prolonged times changes the surface morphology in a characteristic way. Fig.2 shows a scanning electron micrograph of the surface after the annealing procedure. A large number of pyramidic holes formed at the surface. The size of the holes depends on the highest temperature reached during the heat treatment. The specular reflected intensity is strongly damped while the off-specular diffuse intensity is increased and structured.

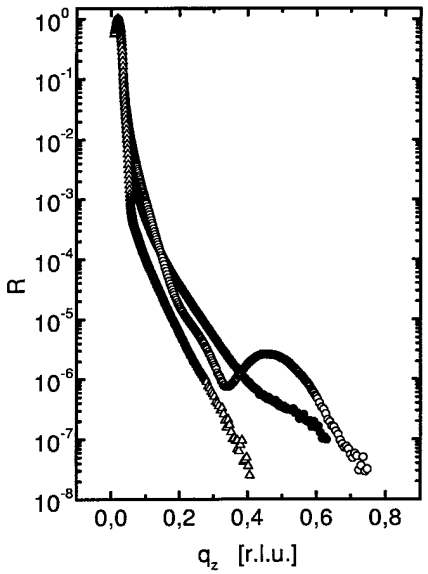

Figure 1. Reflectivity bevor annealing (open circles), after annealing at 850°C for 30 min (filled circles), and after annealing at 850°C for 8 h (triangles).

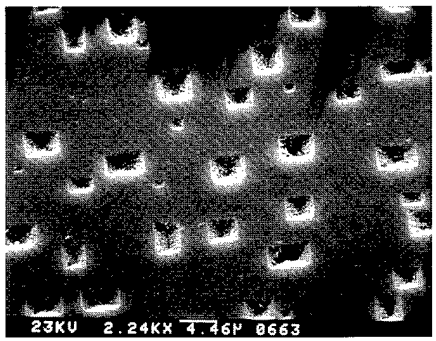

Figure 2. Scanning electron micrograph of the $Si_{0.9}Ge_{0.1}(001)$ surface after annealing.

Evolution of O-Induced Facet Formation on Cu(115) | X16A

D.A. Walko and I.K Robinson (Univ. of Illinois)

We have observed the evolution of the Cu(115) surface during dosing of oxygen. This surface breaks up into three facets after O exposure, whose orientations correspond to (104), the symmetry equivalent (014), and (113). We investigated the dymanics of facetting as well as the static structure of the final surface.

After dosing the Cu(115) surface with several Langmuirs oxygen, the crystal truncation rod corresponding to this surface begins to decay. Rods corresponding to the (104) and (014) facets appear, but the (113) facet does not form immediately. Instead, steps proliferate on the (115) facet and its average orientation slowly changes from (115) to (113). This is seen in Fig. 1 for facetting at two different temperatures. Fig. 1 shows a series of scans passing thru the (115) and (113) facet positions (at h=6.0 and h=6.282, respectively). These scans are 0.8Å^{-1} below the bulk {111} Bragg reflection.

Fig. 2 illustrates the qualitative difference of facet formation above and below T≈310°C, by displaying facet peak position from Fig. 1 as a function of dose. Above this temperature, the peak slides continuously from the (115) to the (113) position. Below T≈310°C, the peak slides about halfway from (115) to (113), then jumps to the (113) position. Apparently, at these lower temperatures, a particular range of facet orientations is thermodynamically unfavorable.

Once the surface was completely facetted, x-ray surface crystallography measurements could be performed on the individual facets. The {104} facets did not show any superstructure, but a 3×1 reconstruction was found on the (113) facets. A structural analysis of the surfaces is in progress.

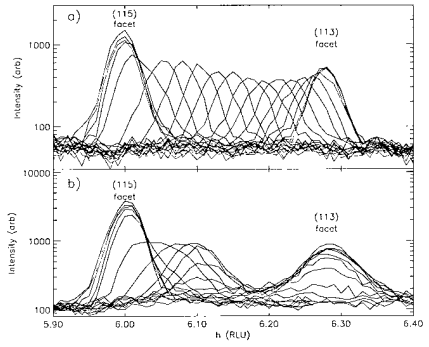

Figure 1. Scans thru the (115) and (113) facet rods, as a function of time during exposure to O_2. As O_2 dosing progresses, the peak moves from left to right. a) T=340°C, $P_{O_2}=4\times10^{-9}$ mbar. b) T=260°C, $P_{O_2}=1\times10^{-8}$ mbar.

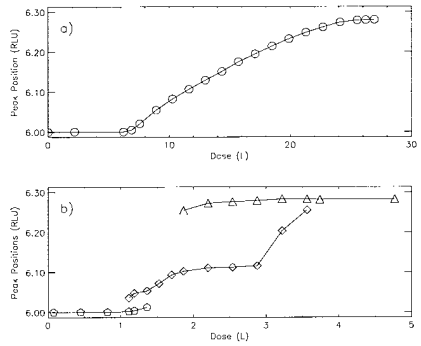

Figure 2. Facet positions (in reciprocal lattice units) as a function of O dose. a) T=340°C; b) T=260°C.

Superstructure Ordering in La Doped PMN Single Crystals | X16C

D. M. Fanning, S. T. Jung, D. A. Payne, I. K. Robinson (U. of Illinois-UC)

Lead magnesium niobate ($Pb[Mg_{1/3}Nb_{2/3}]O_3$) is a classic ferroelectric relaxor, having a very high, frequency dependent dielectric constant near room temperature. It has the perovskite structure, and the mixed B-site is believed to be responsible for its broad transition to the paraelectric state.

Previously [1], we studied pure PMN crystals and found superstructure reflections at the (h+1/2, k+1/2, l+1/2) positions. These were shown to be the result of chemical ordering between the Mg^{2+} and Nb^{5+} ions. The ordered regions were measured to be about 50 Å in size. It is believed that their size is limited due to the non-stoichiometric 1:1 ordering of Mg^{2+} and Nb^{5+}, which results in an average net charge of -0.5e per unit cell. By doping with La^{3+} in place of Pb^{2+}, it is possible to increase the size of the ordered region. In this experiment, we studied the effects of this increased ordering and the feasibility of using La doped PMN for a coherent XRD study.

Single crystals of La-PMN were grown by the flux method. For each crystal,we measured about 100 superstructure reflections. We found the crystal quality was quite good, with no mosaic structure. By averaging the widths of the superstructure reflections, we determined the size of the chemically ordered region using the Scherrer formula. As expected the size increases with La concentration: to 130 Å for 4.5% La-PMN, and 1000 Å for the 10% La-PMN.

We were able to determine the structure of the ordered region by fitting to our model (Figure 1). We assume nearest neighbor unit cells have different B-site ions, alternating between Mg^{2+} and Nb^{5+}. The oxygen atom positions are free parameters that displace towards the smaller Nb^{5+} ions (radius of 0.65 Å vs 0.72 Å for Mg^{2+}). Combined with Debye-Waller factors, this model was used to successfully fit our data for both pure and La doped PMN.

Figure 2 shows the oxygen displacement as well as the measured lattice constant for the 3 crystals. Clearly, the trend in the oxygen displacement and lattice parameter are in a consistent direction. We believe that by chemically ordering, PMN is able to reduce the strain caused by the large Mg^{2+} ion.

A separate DAFS study [2] confirms our value for the oxygen displacement in pure PMN.

[1] D.M. Fanning and I.K. Robinson, NSLS Activity Report, page B-136, 1996.
[2] A.I. Frenkel, D.M. Fanning, D.L. Adler, J.O. Cross and I.K. Robinson, these Proceedings.

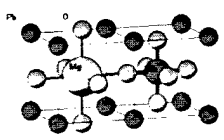

Figure 1. Model of chemical ordering of Mg and Nb ions with oxygen displacements along (100) directions towards Nb.

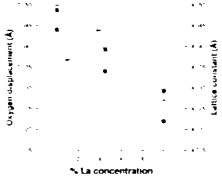

Figure 2. Best fit oxygen displacement and measured average lattice constant.

DAFS Analysis of Local Structure of Ordered Nanodomains in PMN | X16C

A.I. Frenkel, D.M. Fanning, I.K. Robinson (UIUC), D.L. Adler (KLA Instrum.), and J.O. Cross (NRL)

We performed Diffraction Anomalous Fine Structure (DAFS) measurements of the single crystal of relaxor ferroelectric $Pb[Mg_{1/3}Nb_{2/3}]O_3$ (PMN) which has cubic structure at 300 K. Presence of superstructure spots in our X-ray diffraction measurements [1] confirmed the existence of 1:1 Nb:Mg ordered nanodomains in a Nb-rich host lattice. Local structure in the ordered domains has been investigated before by Nb K edge EXAFS measurements [2] where the task of separation between the contributions of the nearest neighbors (NN) to Nb to the total EXAFS signal from the host lattice and nanodomains is very difficult.

DAFS measurements of the peak (-.5, -2.5, 2.5) were taken at the Nb K edge. By using a superstructure peak, we were able to look at only the Nb-NN contributions in the ordered nanodomains. Data were measured using a custom-designed 4-circle Kappa diffractometer and a data acquisition program SUPER. Fluorescence background was measured by moving the 2Θ arm of the diffractometer to an off-peak position. Resultant DAFS data (after fluorescence background was subtracted) are shown in Fig. 1. Smooth background intensity was fit to the DAFS data using Cromer-Liberman theory for f_0' and f_0'' as a first approximation. To extract absorption cross-section $\sigma(E)$ and perform standard EXAFS analysis, iterative Kramers-Krönig transforms procedure [3] was applied to isolate true f' and $f'' \sim E \cdot \sigma(E)$. Resultant EXAFS function $\chi(k)$ was fit with FEFF theory in r space (Fig. 2) in the region mostly contributed by Nb-O pairs. The Nb-O distance in the ordered region was determined to be 0.052(5) Å shorter than half the lattice parameter of PMN, in excellent agreement with our diffraction [1] and previous EXAFS results [2].

[1] D.M. Fanning and I.K. Robinson, these Proceedings.
[2] E. Prouzet et al., J. Phys.:Condens. Matter **5**, 4889 (1993).
[3] J.O. Cross, Ph.D. Thesis, University of Washington, 1996.

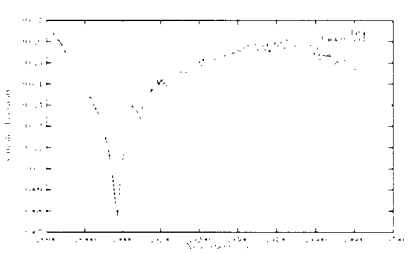

Figure 1. Fluorescence subtracted raw DAFS data (dash) and fit to the background (solid).

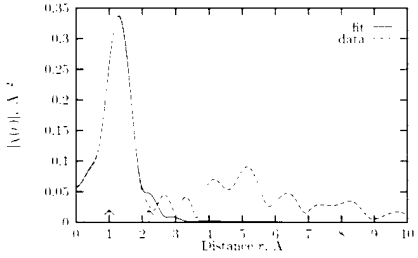

Figure 2. Data (dash) and fit (solid) to the Nb-O nearest neighbor shell. Fitting range is shown by arrows.

In Situ XAFS Study of Pt-Ru Catalysts in Fuel Cell | X16C

A. I. Frenkel, M. S. Nashner, C. W. Hills, J. R. Shapley, and R. G. Nuzzo (UIUC)

In our previous work [1] we reported the results of the preparation and characterization with XAFS of the $PtRu_5$ bimetallic nanoparticles. In the present work, we performed the *in situ* study of a similar system, $PtRu_4$, in a custom designed fuel cell at three different potentials: open circuit, 0.25 and 0.7 V. These potentials correspond to different stages in the methanol oxidation process.

Well-defined Pt-Ru binary particles were prepared from $Pt_2Ru_4(CO)_{18}$ molecular cluster precursor. The solution was then dispersed onto a carbon cloth support and heated under H_2 flow at 400° for an hour. Pt L_3 and Ru K edge XAFS data (Figs. 1 and 2) were collected in these catalysts in a fuel cell in fluorescence at 80°C. Structural refinement was performed simultaneously for the both Pt L_3 and Ru K edges data using UWXAFS programs. We obtained a non-statistical distribution of Pt and Ru atoms in the nanoparticles, consistent with a segregation of the Pt particles in the core of the cluster. While the increase of potential from 0 to 0.7 V led to the decrease of both Pt-Metal and Ru-Metal coordination numbers (Fig. 3), interaction of Pt with low Z atoms (oxygen, CO ligands and C support) was not affected by changes in V (Fig. 1), whereas the number of Ru-low Z bonds increased with V (Figs. 2 and 4).

[1] M. S. Nashner, A. I. Frenkel, D. A. Adler, J. R. Shapley, and R. G. Nuzzo, J. Am. Chem. Soc., **119**, 7760 (1997).

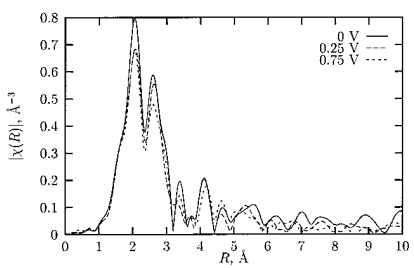

Figure 1. Pt L_3-edge data in R space.

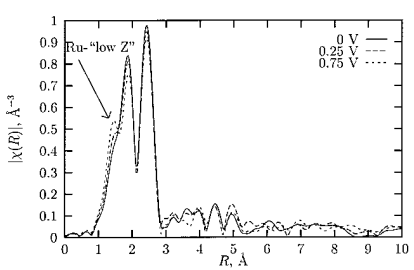

Figure 2. Ru K-edge data in R space.

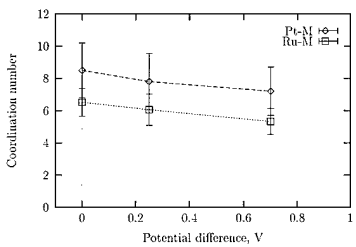

Figure 3. Number of Pt-Metal and Ru-Metal nearest neighbors.

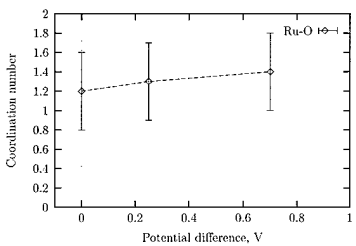

Figure 4. Number of Ru-O nearest neighbors.

Evolution of $PtRu_5C(CO)_{16}$ Molecule into a Pt-Ru Nanoparticle | X16C

A. I. Frenkel, M. S. Nashner, J. R. Shapley, and R. G. Nuzzo (Univ. of Illinois)

In our previous work ([1], see also previous abstract), we analyzed the final product - a bimetallic Pt-Ru supported nanoparticle - as obtained from the precursor $PtRu_5C(CO)_{16}$ by activation at H_2 at 673 K. Here we present the results of *in situ* evolution of the precursor into a bimetallic nanoparticle.

XANES measurements at Pt L_3 edge (Fig. 1) have been performed at different temperatures at H_2 flow. They correspond to different stages of chemical evolution. We found chemical evidence for the loss of CO ligands with temperature as evidenced in dramatic reduction in amplitude of the white line as temperature increases. This amplitude reduction is also consistent with the particle size increase with temperature, observed in STEM measurements. We also observed a shift in the edge position to lower binding energies resulting from the formation of an increasingly metallic state with temperature in the presence of H_2.

EXAFS analysis of Pt L_3 and Ru K edge data confirmed the above XANES results on the fragmentation of the molecular precursors, loss of the CO ligands, and increase of the cluster size with temperature. Over the temperature range 300 - 473 K, the precursor molecules (Fig. 2, left) aggregate into a cherry-like structure with Pt atoms occupying core sites (Fig. 2, center). Upon further temperature increase the structure transforms into its final form (Fig. 2, right) with Pt atoms preferentially occupying surface sites.

[1] M. S. Nashner, A. I. Frenkel, D. L. Adler, J. R. Shapley, and R. G. Nuzzo, J. Am. Chem. Soc. **119**, 7760 (1997).

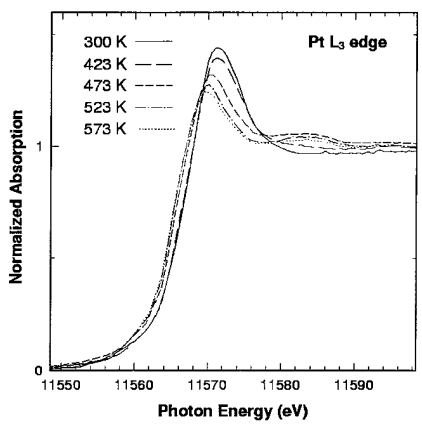

Figure 1. Pt L_3 XANES during activation of the molecular cluster precursor under H_2.

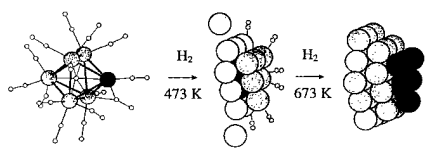

Figure 2. Schematic of the evolution of the molecular cluster precursor into a bimetallic nanoparticle.

XAFS Analysis of Particle Size Effect on Local Structure of $BaTiO_3$ | X16C

A.I. Frenkel and D.A. Payne, (U. Illinois at Urbana-Champaign)

The local structure of several samples of $BaTiO_3$ prepared by solution-gelation method with different particle sizes (less than 0.1 μm) and a sample with $\sim$ 10 μm particle size has been investigated using the X-Ray Absorption Fine Structure (XAFS) technique. Although the macroscopic crystal structure changes from tetragonal to cubic at room temperature when the particle size is less than 0.1 μm, we obtained that Ti atoms are displaced from the center of cubic symmetry for all the samples studied. Both EXAFS (Fig. 1) and XANES (Fig. 2) measurements demonstrate that there is no difference in the local structure around Ti for the reference sample with a macroscopic particle size (10 μm) where it is known that the local structure is off-centrosymmetric and the samples with $d < 0.1$ μm where the local structure is unknown. XANES behavior in the $1s \rightarrow 3d$ transition region (4965-4970 eV) is particularly sensitive to the dispacements of Ti atoms from the center of O octahedron [1] (the area under the peak depends quadratically on the displacement), and our results prove that local displacements are almost the same in all the samples studied.

The existence of different local and macroscopic structures means that the local distortions from the average structure are disordered. This result agrees with previous Raman spectroscopy measurements [2] where the structure of the samples with particles smaller than 0.1 μm was obtained to be non-cubic. In addition to previously obtained evidence of a dominant order-disorder behavior in this and other perovskites, subject to temperature or pressure treatments, this result again demonstrates that the low symmetry structure preserves **locally** while the **average** structure changes during various phase transitions [3].

This work was supported by the DOE Grant No. DEFG0296ER45439 through the Materials Research Laboratory at the University of Illinois.

[1] B. Ravel et al., Ferroelectrics, 1997 (in press).
[2] M.H. Frey and D.A. Payne, Phys. Rev. B **54**, 3158 (1996).
[3] A.I. Frenkel et al., Phys. Rev. B **56**, XXXX (1997).

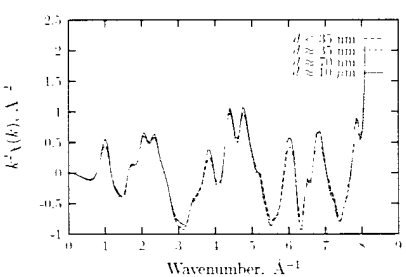

Figure 1. k^2-weighted $\chi(k)$ for the samples with different particle sizes.

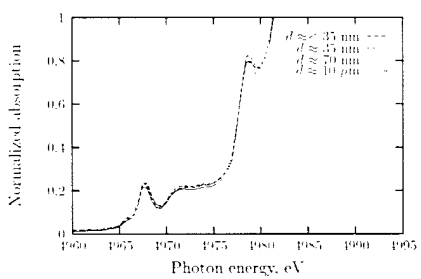

Figure 2. XANES region for the samples with different particle sizes.

Preparation and Characterization of Carbon Supported Pt-Ru Nanoparticle Catalysts | X16C

M.S. Nashner, A.I. Frenkel, D.L. Adler, J.R. Shapley, and R.G. Nuzzo (UIUC)

Bimetallic nanoparticles supported on carbon black were prepared from a $PtRu_5C(CO)_{16}$ molecular cluster precursor by activation at H_2 at 673 K [1]. The narrow compositional distribution, which was found to be centered at 1:5 Pt:Ru ratio, suggests a uniform coalescence of the precursor clusters upon activation. Microdiffraction measurements indicate the formation of nanoparticles with an *fcc* microstructure even though the bulk structure for this composition is *hcp*. The nanoparticles undergo reversible oxidation forming a metal-oxide surface and a core of metal. The Pt L_3-edge and Ru K-edge EXAFS data indicated that bimetallic nanoparticles of $\sim$ 12 Å in diameter were formed where the Pt centers **segregate to the surface** of the *fcc* Ru structure. The hemispherical shape and non-statistical distribution of atoms in the nanoparticle were established using a simultaneous multiple-scattering EXAFS analysis of Pt L_3 and Ru K edge data through the 4th shell around the central atom. In support of the EXAFS measurements, STEM measurements (Fig. 1) demonstrated the formation of an extremely narrow size distribution centered around an average of $\sim$ 15 Å (Fig. 2).

These results provide exciting precedent of the preparation of carbon-supported Pt-Ru nanoparticles with composition that span the binary phase diagram. Further studies of the structure and reactivity of these phases [2] provide insight into the nature of the activity of bimetallic catalysts in Direct Methanol Fuel Cells [3].

[1] M. S. Nashner, A. I. Frenkel, D. L. Adler, J. R. Shapley, and R. G. Nuzzo, J. Am. Chem. Soc. **119**, 7760 (1997).
[2] A. I. Frenkel, M. S. Nashner, J. R. Shapley, and R. G. Nuzzo, these Proceedings.
[3] A. I. Frenkel, M. S. Nashner, C. W. Hills, J. R. Shapley, and R. G. Nuzzo, these Proceedings.

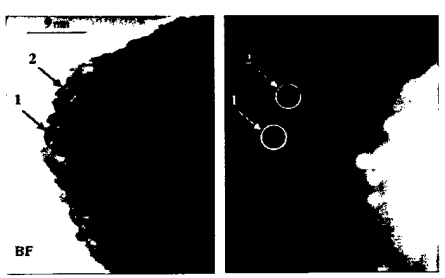

Figure 1. Bright and dark field STEM images showing Pt-Ru nanoparticles (spot 1) and carbon-support (spot 2). Electron beam size is $\sim$ 10Å.

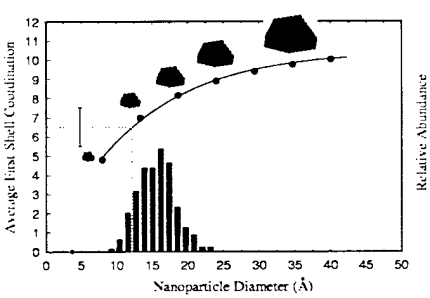

Figure 2. Hisgtogram of the particles size distribution (right axis) measured with STEM. Average coordination number as obtained with EXAFS (left axis).

X-Ray Microprobe Measurements of Patterned InP Multi-Quantum Well Lasers	X16C

E.D. Isaacs, K. Evans-Lutterodt, M.A. Marcus. A.A. Macdowell, W. Lenhart, L.J.P. Ketelsen, J. Vandenberg, S. Sputz, J.E. Johnson and J.A. Grenko (Bell Laboratories)

We have developed a scanning x-ray microprobe (XMP) on beamline X16C. The principal components of the XMP are a horizontally collimating, double Si(111) crystal monochromator with an energy range from 5 - 20 keV, a pair of glancing incidence, elliptically bent mirrors for focusing in the vertical and horizontal, respectively. The mirrors produce a beam of approximately 3 x 20 μm with a flux of 10^8 photons/sec at 8 keV. This represents a gain in flux of 65 over a pinhole with the same area. The diffractometer used with our XMP has a detector arm with two degrees of freedom and micron sample positioning capability.

One of the key applications of the Bell Labs XMP has been in the micro- structural characterization of laterally patterned opto-electronic devices such as the electro-absorption modulator laser (EML). The EML is a monolithically integrated InGaAsP multi-quantum well (MQW) laser and electo-absorption modulator which has been demonstrated to speeds of 10 Gbits/sec. The EML has a 1 μm wide active region and is buried under a few microns of InP. While strain is crucial to the efficient operation of the device, too much strain can cause misfit dislocations which provide non-radiative recombination centers, fatal to laser operation. The XMP is the only probe with which to non-destructively measure the strain in the buried EML device. By measuring radial Bragg scans through the MQW superlattice peaks at several positions on the EML device (see Figure) we are able to make a spatial map of the MQW strain (position of 0^th-order superlattice peak). This microscopic strain map has been crucial in a redesign of the growth masks in order to control the strain in the MQW. The Bragg scans also tell us about the MQW period (superlattice spacing) and composition (relative superlattice intensities). Maps of the period and composition have enabled us to more accurately target lasing wavelengths. Accurate positioning of the wavelengths is becoming more important as wavelength multiplexing, requiring many (8, 16, 32, ...) very closly spaced frequency channels, becomes the norm in high speed lightwave communications.

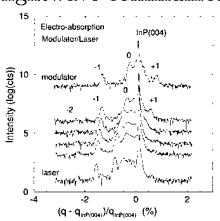

Figure 1. Radial Bragg scans long the InP(004) substrate direction taken at positions inside the laser structure (botton line), through the transition region (middle four lines) and into the modulator region (upper line) taken with 5 um spatial resolution. The variation in MQW period and strain as a function of position is observed as a variation in spacing between superlattice peaks (labeled by order) and the position of the oth order peak, respectively. The data are offset for clarity.

Sound Velocity Measurements at Simultaneous High Pressure and Temperature For Polycrystalline San Carlos Olivine	X17B1

G.Chen, Y. Sinelnikov, R. C. Liebermann (SUNYat Stony Brook) and G. D. Gwanmesia, K. Darling (DSU)

Dense isotropic polycrystalline San Carlos olivine were fabricated at high pressure and high temperature in a Girdle-type high pressure apparatus using hot-pressing techniques developed previously by Gwanmesia and Liebermann (1992; see also Gwanmesia *et al.*, 1993) and crushed natural crystals as starting materials. These specimens have bulk densities within 1% of the X-ray density and exhibit compressional (P) wave and shear (S) wave velocities within 1% of single crystal elastic moduli of Kumazawa and Anderson (1969). Recent technological development in our laboratory has enabled precise interferometric measurements of elastic wave velocities in mienrals to be performed to pressures of 9 GPa and temperatures of 1500 K in a DIA-type, cubic anvil apparatus (SAM85) interfaced with white X-ray radiation from the superconducting wiggler port of the National Synchrotron Light Source at Brookhaven National Laboratory (see Liebermann *et al.*, 1997). We have performed measurements this important mantle mineral (ultrasonic and X-ray) to 7 GPa and 800 K.

Equation of State of NaCl From Simultaneous Ultrasonic and Synchrotron X-ray Diffraction Measurements	X17B1

G. Chen, Y. Sinelnikov, M. T. Vaughan, and R. C. Liebermann (SUNYat Stony Brook,)

Adpatation of the ultrasonic interferometric techniques to be used in a cubic anvil high pressure apparatus installed at the National Synchrotron Light Source (X17B1) of the Brookhaven National Laboratory allows simultaneous ultrasonic and synchrotron X-ray diffraction measurements at high pressure and high temperarure in polycrystalline specimens. Cold-pressed and polished NaCl pellets (with grain size on the order of microns) capable of transmitting high frequency (to 60 MHz) acoustic waves on the bench were used as the specimens. Experimental runs have been attempted to 8 GPa and 700 K with the pressure determined by the X-ray diffraction volume change of the specimen and temperature monitored actively with a W-Re thermocouple. This new development extends the measurement capability of ultrasonic equation of state experiments on NaCl at simultaneous elevated pressure and temperature by a factor of 10 in pressure and at comparable temperature, which is limited at present by the recrystallization of NaCl at higher temperature. Further development in sample handling, e.g., keeping the sample in extremely dry condition, may allow us to reach even higher temperature at high pressure, such as those reached in the MgO experiment (1500 K) reported in a separate NSLS abstract. These new velocity data will allow the determination of he cross pressure and temperature dependence of the elasticity of NaCl, and with the volume data form the basis for refining the pressure scale for this important standard material.

An Experimental Design for Low Pressure and High Temperature	X17B1

J. Chen (CHiPR, SUNY at Stony Brook)

While people are striving for higher and higher pressure to study the physical properties of materials under high pressure, there still are many demands for in situ x-ray diffraction experiments at low pressure (< 1 GPa) and high temperature, for example, phase relation of enstatite and zeolite. Some materials may have a restricted phase stability field below 1 GPa. However, the existing high pressure diffraction designs of a DIA-type press are generally suitable for high temperature experiments at the pressures above 1 GPa. For carrying out a high temperature experiment below 1 GPa, the major problems with a regular 6 mm high pressure cell (Figure 1) is a) unstable electrical contact between anvil and heating component; b) unfavorable pressure control because of the very low required load.

To perform such a low pressure and high temperature experiment, a large anvil truncation high pressure cell was designed (Figure 2). Six steel anvils with the truncation size of 15 mm were used. The size of pressure medium was 20 x 20 x 20 mm. The pressure efficiency was reduced by 1 order so that a good contact was achieved by much higher load at the sample pressure as low as 0.3 GPa. A thermocouple was inserted from one end of the heater to avoid the partial overheating due to the thermocouple hole on the heater sleeve (Figure 1). An experiment was carried out to study the phase boundary between orthoenstatite and protoenstatite. The sample was heated up to 1600 °C at 0.3 GPa. Some diffraction patterns which do not have the characteristics of either phase were observed at the temperature above 1000°C. Further investigation is in progress.

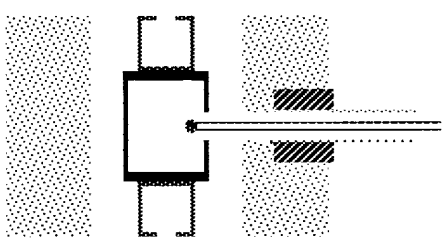

Figure 1. Regular 6 mm high pressure cell assembly for the DIA-type press SAM85.

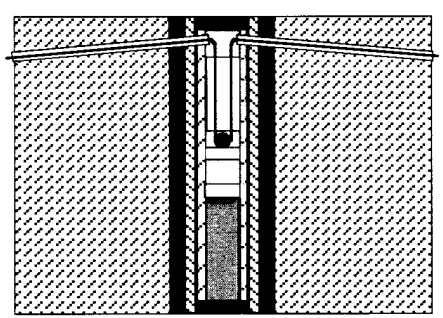

Figure 2. Large volume pressure cell for studies below 1 GPa.

Following Olivine-Spinel Phase Transition in Fayalite with TIPS | X17B1

J. Chen and D.J. Weidner (CHiPR, SUNY, Stony Brook)

The mechanism of the olivine-spinel phase transition has been investigated by several groups. Sung and Burns [1,2] proposed a diffusion-controlled process, incoherent nucleation of the spinel phase and subsequent crystal growth; Kronberg [3] and Poirier [4] proposed a shear mechanism, stacking faults in oxygen lattice of olivine in company with cation reordering. More interesting result reported by Furnish and Bassett [5] from their in situ x-ray diffractions in a diamond anvil cell (DAC) suggested a two-step shear mechanism with stacking faults prior to the cation reordering. Using the newly developed translating imaging plate system(TIPS) for high pressure diffraction at X17B1, we studied the mechanism of the olivine-spinel phase transition in fayalite.

The experiment was carried out by compressing the sample at room temperature into the spinel stability field (6.9 GPa) and then heating the sample. The sample transformed from olivine to spinel during the heating. A time-resolved pattern was recorded when the temperature increased from 300°C to 400°C. The transporting speed of the imaging plate was 3.25mm/min. The heating rate was 1.75 °C/min. Figure 2 shows the time resolved diffraction pattern. Structure refinements were done base on the diffraction patterns during the phase transition. Figure 2 shows an example of the refinement. The result shows that the oxygen framework of spinel structure is formed prior to the ordering of cations into the tetrahedral and octahedral sites.

[1] J. P. Poirier, J. Geophys. Res. 87, 6791(1982).
[2] C. M. Sung and R. G. Burns, Earth Planet. Sci. Lett. 32, 165(1976).
[3] M. L. Kronberg, Acta Metall. 5, 507(1957).
[4] J. P. Poirier, in Anelasticity in the Earth, Geodyn. Ser. vol. 4, edited by F. D. Stacey et al. p. 113-117, AGU, Washington D.C. (1981).
[5] M. D. Furnish and W. A. Bassett, J. Geophys. Res. 88, 10333(1983).

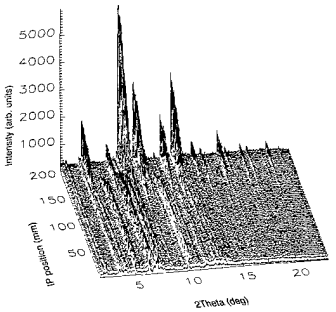

Figure 1. 3-D plot of time resolved diffraction patterns for the olivine-spinel phase transition in fayalite.

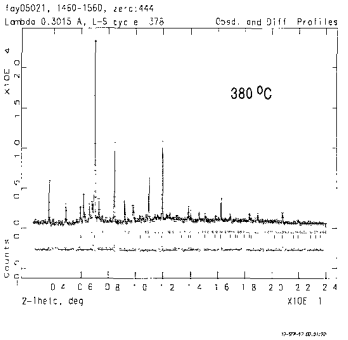

Figure 2. Reitveld refinement of the diffraction pattern at midway of the olivine-spinel phase transition.

Stress Measurement of Anhydrous and Hydrous phase of Ringwoodite | X17B1

J. Chen, D. J. Weidner, T. Inoue, H. Kagi and M. T. Vaughan (CHiPR, SUNY, Stony Brook)

As one of the studies of the rheological properties of mantle minerals, we carried out a stress measurement for anhydrous and hydrous phases of ringwoodite in the T-cup press. In our previous study, we measured the stress of dry and hydrous phase of olivine, wadsleyite as a function of pressure, temperature and time [1]. We observed a difference in water weakening on the rheological property of olivine and wadsleyite. Olivine is weakened dramatically by introducing a small amount (1500 ppm in weight) water. However, hydrous wadsleyite is just slightly weaker than its anhydrous counterpart although the hydrous phase takes as much as 2.2 wt% water.

The samples were synthesized at 19 GPa and 1300°C using the USSA2000 press at Stony Brook. The water content of the hydrous phase was measured to be 3.8 wt% by secondary ion mass spectrometory (SIMS). The result is shown in Figure 1. No data were collected for the anhydrous phase at 400°C because no stress drop is expected based on the previous run for the hydrous phase. The behavior of the ringwoodite is similar to that of the wadsleyite at temperatures up to 400°C although there are somewhat greater experimental errors. Up to 600°C the yield strength drops by 29% and 39% in the anhydrous and hydrous phases respectively, and further drops of the yield strength are observed with further increase of temperature: 29% and 38% from 600°C to 800°C, and 20% and 48% from 800°C to 1000°C in the anhydrous and hydrous phase respectively. Both phases show stress relaxation as a function of time at each temperature. The strength of the hydrous phase at 1000°C is close to zero and the limited instrumental resolution results in larger scatter, and some data are scattered below the base level.

[1] J. Chen, T. Inoue, Y. Wu, D. J. Weidner and M. T. Vaughan, NSLS Report 1996 B-139.

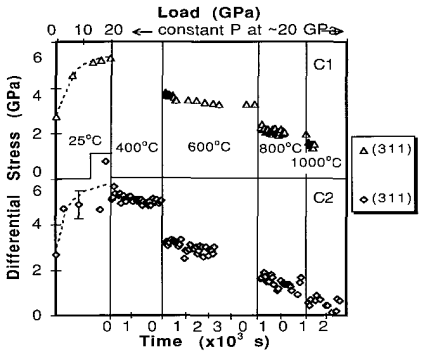

Figure 1. Stress in the anhydrous and hydrous phase of ringwoodite.

Rheological Study of Lower Mantle Minerals, Perovskite and Periclase	X17B1

J. Chen, D. J. Weidner, M. T. Vaughan and H. Kagi (SUNY at Stony Brook)

The lower mantle is considered mainly consisting of (Fe,Mg)SiO_3 perovskite and MgO periclase. As one of the studies on rheological properties of mantle minerals[1,2], we carried out the stress measurement on perovskite and periclase in the T-cup press. In our previous study, we have found that the upper mantle mineral olivine is much weaker than the transition zone minerals, wadsleyite and ringwoodite, especially when water is present. Rheological properties of lower mantle minerals are important for constraining mantle convection and understanding the origin of deep focus earthquakes.

The perovskite sample was synthesized at 26 GPa and 1800°C using the USSA2000 press at Stony Brook. The structure was confirmed by x-ray diffraction before the experiment. The powdered sample was first compressed up to 20 GPa at room temperature and then was heated up to 1000°C stepwise. At each heating step the temperature was held for several tens of minutes during which diffraction data are recorded as a function of time. The results are shown in Figure 1 and Figure 2. The perovskite and periclase have quite different rheological properties, the perovskite is very strong and the periclase is very weak.

Although the perovskite shows very strong rheological behavior, the lower mantle may still have weak characteristics since MgO is much weaker, being comparable to olivine. Results of the rheological study on the mantle minerals, olivine, wadsleyite, ringwoodite, perovskite and MgO may constrain the origin of the deep focus earthquakes in terms of storage of stress.

[1] J. Chen, T. Inoue, Y. Wu, D. J. Weidner and M. T. Vaughan, NSLS Report 1996 B-139.

[2] J. Chen, D. J. Weidner, T. Inoue, H. Kagi and M. T. Vaughan, in this Report (X17B1).

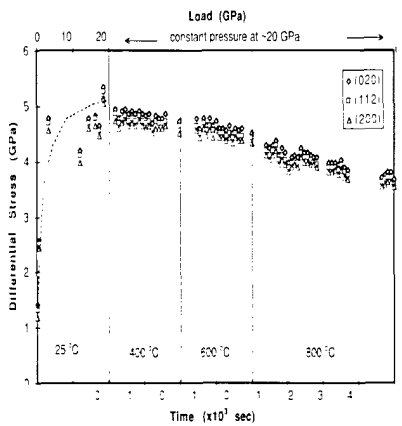

Figure 1. Stress in the perovskite.

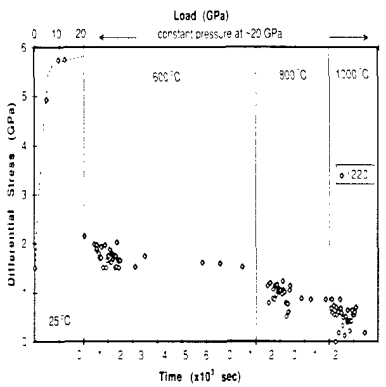

Figure 2. Stress in the periclase.

Time Resolved Diffraction Measurement with an Imaging Plate at High Pressure and Temperature	X17B1

J. Chen, D. J. Weidner, M. T. Vaughan, R. Li, J. B. Parise, C. C. Koleda and K. J. Baldwin (CHiPR, SUNY at Stony Brook)

An imaging plate (IP) has great potential to acquire high quality in situ x-ray diffraction data at high pressure and temperature in both a diamond anvil cell (DAC) [1-2] and large volume apparatus [3-4]. The off-line developing of an imaging plate is a disadvantage for quick data collections. Effords have been made to install an on-lone imaging plate scanner for reducing the operation time. Time resolution in the sequence of consecutive exposures is on the order of tens of minutes. Recently rapid development of a CCD (charge coupled device) provides a good opportunity to perform time resolved data collection. Nevertheless, the current commercial CCD has very limited active detecting area (~50 x 50 mm^2) which results in a relative low resolution when the CCD is used to record a large-range d-spacing pattern. We have developed a translating imaging plate system (TIPS) with the large-volume multi-anvil apparatus SAM85 at the beamline X17B1 to acquire time resolved diffraction.

We introduced a lead screen with a vertical slit in the middle in the front of the imaging plate to define the dimension of exposure on the detector (Figure 1). The imaging plate holder is mounted on a horizontally motor-control stage, and the translation guide block is perpendicular to the incident x-ray beam. A 200 mm x 400 mm imaging plate is used for the data collection. Width of the slit is adjusted depending on the beam intensity, IP-to-sample distance and the transporting speed of the imaging plate. A direct beam stop is mounted on the slit. The beam stop blocks most of the intensity of the direct beam, and allows the direct beam to expose the imaging plate with the same intensity as a diffracted beam (as shown on the top of Figure 2). Olivine-spinel phase transition in fayalite was investigated with this system. Figure 2 shows a time resolved diffraction pattern recorded on the imaging plate during the phase transition. The data enable us to study the sample stresses during the phase transition and the phase transition mechanism.

[1] O. Shimomura, K. Takemura, H. Fujihisa, Y. Fujii, Y. Ohishi, T. Kikegawa, Y. Amemiya, T. Matsushita, Rev. Sci. Instrum. 63(1), 967(1992). [2] R. J. Nelmes and M. I. McMahon, J. Sunchrotron Rad. 1, 69(1994). [3] J. Chen, T. Kikegawa, O. Shimomura and H. Iwasaki, J. Synchrotron Rad. 4, 21(1997). [4] J. Chen, R. Li, J. B. Parise and D. J. Weidner, Am. Min. 81, 1519(1996).

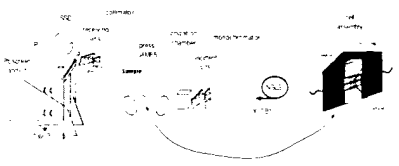

Figure 1. Schematic layout of the translating imaging plate system (TIPS) for high P-T x-ray diffraction at X17B1.

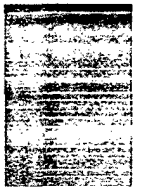

Figure 2. Diffraction pattern of fayalite recorded on an imaging plate while the sample transforms from olivine to spinel.

Sound Wave Velocity Measurements at High Pressure and Temperature for Polycrystalline $MgSiO_3$ Orthopyroxene	X17B1

L. Flesch, B. Li, J. Zhang, J. Cooke, R. Liebermann, and M. Vaughan, (CHiPR, SUNY at Stony Brook)

Polycrystalline samples of $MgSiO_3$-orthopyroxene were hot pressed at pressures of 4 GPa and temperatures of 1250 K in a uniaxial split-cylinder apparatus (USCA-1000). The recovered specimens have a bulk density within 1% of the x-ray density, and compressional and shear wave velocities within 1% of the Hashin-Shtrikman averages of the isotropic velocities calculated from the single crystal elastic moduli. Preliminary acoustic velocity studies were performed on these samples; we have successfully measured P-wave travel times as functions of pressure to 6.5 GPa and temperature to 1300 K in a DIA-type, cubic anvil apparatus (SAM 85) installed on the superconducting wiggler beamline (X17B) at the National Synchrotron Light Source of the Brookhaven National Laboratory.

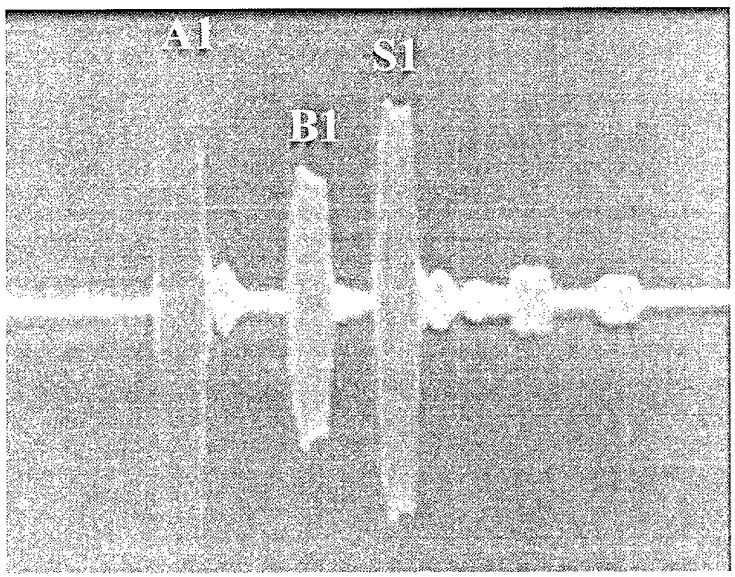

Figure 1. Acoustic signals from an S-wave run on a polycrystalline $MgSiO_3$ speciman at ~6 GPa and 700 C. The first echo represents a reflection off the anvil (A1), the second a reflection off the buffer rod (B1), and third a reflection from the end of the sample (S1).

Comparison of Experimental Electron Spectra with the Integrated TIGER Series (ITS) Simulation	X17B1

N. A. Guardala, D. J. Land, J. L. Price (Naval Surface Warfare Center), Y. Wang, and G. A. Glass (U. Southwestern Louisana)

Measurements have been made on beamline X17B1 of the emitted electron spectra for 58 keV photons incident on a 680 Å titanium target and a 400 Å carbon target. The goal of this work is to examine the prominent features of the electron spectra, such as the Compton-recoil, Auger, and photo-electrons, and to determine how well they are described by current transport models. The measurements were performed at zero degrees with respect to the incoming photon beam. The electrons were energy analyzed using a semihemispherical, double focussing electrostatic analyzer coupled to a channeltron electron multiplier for electron detection.

The results for the Ti data are shown in Fig. 1. The peaks representing the Compton-recoil electrons at 10 keV and the Auger electrons at 4 keV stand out clearly. Also shown are the results of a simulation of 58 keV photons incident on 680 Å Ti performed with the TIGER code, one of the Integrated TIGER Series (ITS) electron/photon transport codes, Ver 3.0 [1]. This curve has been normalized to the area under the experimental Compton peak from 4.5 to 14.0 keV. Overall, the agreement is satisfactory: the ratio of the experimental Compton to Auger yields is 0.91 while the same ratio for the simulated yields is 0.81. However, there are some obvious differences, the most notable of which is the fact the the simulated spectrum does not take account of the broadening of the electron spectrum caused by the internal motion of the electrons, the Compton profile.

[1] J. A. Halbleib, R. P. Kensek, T. A. Mehlhorn, G. D. Valdez, S. M. Seltzer, and M. J. Berger, ITS Version 3.0: The Integrated TIGER Series of Coupled Electron/Photon Monte Carlo Transport Codes, Sandia National Lab. Report No. SAND91-1634, UC-405.

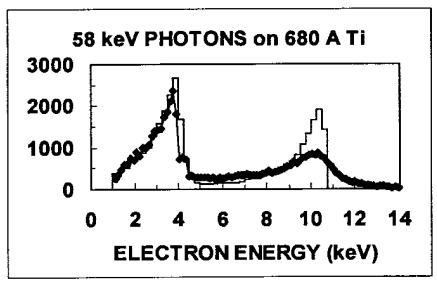

Figure 1. Comparison of the measured electron yield (diamonds) with results from the TIGER code (solid curve) as a function of electron energy for 58 keV photons incident on 682 Å Ti.

Elasticity of Polycrystalline $Mg_4Si_4O_{12}$ Majorite Garnet at P=9 Gpa and T=1000K in a DIA-Type Cubic-Anvil Apparatus Interfaced with Synchrotron X-rays	X17B1

G. Gwanmesia (DSU), G. Chen, J. Cooke, L. Flesch, R. Liebermann, and M. T. Vaughan (SUNY at Stony Brook)

Dense isotropic polycrystalline $Mg_4Si_4O_{12}$ majorite garnet were fabricated at high pressures and temperatures in a 2000-ton uniaxial split sphere anvil apparatus (USSA-2000) using hot-pressing techniques developed previously by Gwanmesia and Liebermann (1992; see also Gwanmesia *et al.*, 1993). These specimens have bulk densities identical to the x-ray density and exhibit compressional (P) wave and shear (S) wave velocities within 0.2% of single crystal elastic moduli of Pacallo and Weidner (1997). Recent technological development in our laboratory has enabled precise interferometric measurements wave velocities in minerals to be performed to pressures of 9 Gpa and temperatures of 1500K in a DIA-type, cubic anvil apparatus (SAM-85) interfaced with white x-ray radiation from the superconducting wiggler port of the National Synchrotron Light Source at Brookhaven National Laboratory (see Liebermann *et al.*, 1997). We have obtained new data on the pressure and temperature dependence of S wave velocity in the $Mg_4Si_4O_{12}$ majorite to 7 Gpa at 1000K. The new data are combined with previous data for P wave and compared with acoustic and PVT data for other compositions in the Pyrope-majorite solid solution series, especially those for a $Py_{62}Mj_{38}$ specimen studies by Rigden, Gwanmesia and Liebermann (1994) and Wang *et al.* (1996).

The Crystal Structure of $Bi_4Au_2O_{14}$: The Use of a Siemens CCD Detector with Short-Wavelength Radiation	X17B1

R. Harlow (DuPont), J. Parise (SUNY at Stony Brook), J. Phillips and C. Campana (Siemens), and J. Hanson (BNL)

The determination of the structure of $Bi_4Au_2O_{14}$ presented two difficulties: absorption (mu for MoKa is approximately 1050 cm-1) and the presence of a superlattice which is 4x the sublattice. Three sets of data have been collected on crystals of this compound: with in-house MoKa radiation using a Siemens CCD and a Rigaku image-plate system, and with 0.185 A synchrotron radiation (where mu is reduced to approximately 30 cm-1) at beamline X17B1, also with a Siemens CCD. At this point, the subcell structure (tetragonal, a = 8.676 and c = 5.832 A, in space group P4212) has been solved and refined using the synchrotron data to an R value of 10.3% using 2094 reflections to a resolution of ca. 0.3 A. All of the atoms were refined with anisotropic thermal parameters, with special attention given to those of the oxygen atoms which are the presumable source of the superlattice. One of the oxygen atoms was found to be disordered over two sites: it is believed that this oxygen will be ordered in the supercell where the c-axis is doubled. This type of disorder was expected because the Bi site in the subcell contains a mixture of Bi^{+3} and Bi^{+5}. Presumably, the latter are also ordered in the supercell. The source for doubling the cell along the a-b diagonal has not yet been determined. Using the in-house data, only the heavy atoms could be refined with anisotropic thermal parameters and some of these ellipsoids were not very realistic. Also, the disorder of the one oxygen atom was not visible from the in-house data. Work continues on modelling the supercell structure, but the benefits of using the (almost) absorption-free data from the synchrotron/CCD combination are already clearly evident.

Strength Measurements of Carbonado, A Natural Polycrystal Diamond.	X17B1

H. Kagi, J. Sweeney, J. Chen and D.J. Weidner (SUNY at Stony Brook)

Carbonado is a natural polycrystal diamond, and its texture can be similar to that of an artificial sintered diamond. Carbonado is expected to be one of the strongest material in terms of hardness, because each micro crystal constituting carbonado polycrystal is arranged without orientation and there exists direct covalent bonding of diamond between micro crystals. In the grain boundaries, it is known that some other minerals are contained as impurities. To obtain information on the strength of carbonado, we observed stress-induced line broadening of X-ray diffraction lines of carbonado diamond at high pressure and high temperature. The cell assembly we used is a typical high pressure cell for a DIA-type, cubic anvil, high pressure apparatus on X-17B1. Carbonado was loaded into a boron nitride capsule after grinding to powder. This was because a chunk sample (carbonado as it is) without powdering cannot be expected to reveal line broadening induced by grain contacts. NaCl powder was also loaded in the cell assembly for a pressure calibration, and a thermocouple was located in the center of the sample. Pressure was increased to around 10 GPa at room temperature, and (111) diffraction peak of diamond (carbonado) broadened and peak position shifted toward the lower d-spacing. At the highest pressure, temperature of the cell was increased to around 1500 degree C and change in the line shape was observed. We are going to compare the results from two different types of carbonado, and the difference from the artificial diamond powder will be considered.

Direct Determination of Pressure-Temperature Paths in the Laser-Heated Diamond Anvil Cell	X17B1

A. Kavner and T. Duffy (Princeton U.), G. Shen (CARS), D. Heinz (U. Chicago), and R. Jeanloz (U.C at Berkeley)

The determination of accurate pressure-temperature equations of state require reliable in-situ standards. To establish a high-pressure high-temperature diamond anvil cell standard, and to investigate the conditions inside the sample chamber at extreme P-T conditions, the behavior of platinum was examined at high pressures and temperatures in the double-sided laser-heated diamond anvil cell. The lattice parameter of platinum normal to the diamond-loading axis was monitored as a function of temperature, and was compared with the pressure-temperature equation of state determined from the shock Hugoniot.

Traditionally, pressure cannot be measured during laser heating, so the pressure at high temperatures is taken to be either the pressure measured before heating, the pressure measured directly afterwards, or a combination of the two. Extensive pressure changes within the sample chamber occur at high temperatures, as recorded by the lattice parameter of platinum, that are not apparent from looking at the difference in the room temperature measurements taken before and after heating (Fig 1). These pressure drops are too large to be accounted for by a thermal pressure or thermal expansion effect, and possibly occur as a result of gasket and cell relaxation at elevated temperatures. The relaxation effect was still present, yet less pronounced during a second heating cycle of the same sample. The experiments were repeated using alumina and NaCl as insulating layers, with alumina showing an enhanced relaxation effect.

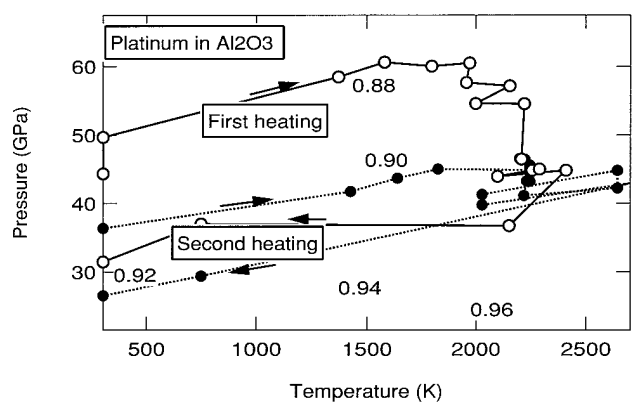

Figure 1. Pressure-Temperature path of platinum in the laser-heated diamond anvil cell. cycles are shown. Contours are of constant V/Vo.

High Pressure High Temperature Behavior of an Iron-Nickel Meteorite	X17B1

A. Kavner and T. Duffy (Princeton U.), G. Shen (CARS), and R. Jeanloz (U.C at Berkeley)

Terrestrial planetary interiors are presumed to be composed of an iron nickel alloy with a range of lighter mass impurities. The behavior of planetary cores helps govern the planetary dynamics, including differentiation, magnetic field effects, and the heat transfer that controls convective properties. Experimental insight into the behavior of core-type alloys is of great interest to dynamicists and mineral physicests. Iron-rich metallic meteorites are thought to be remnants of the differentiated core of a proto-planet; perhaps similar to bodies that coalesced to form the Earth and other terrestrial planets. The high-pressure high-temperature behavior of an iron-nickel meteorite was examined using the laser-heated diamond anvil cell in combnation with *in-situ* x-ray diffraction.

At room pressure and temperature, the iron nickel meteorite is in the bcc structure, and transforms to hcp under pressures above 5 GPa. The hcp sample is heated to about 1000 K at 20 GPa, and immediately transforms to an fcc structured material. With further heating (1000-2500 K) the sample remained in its fcc structure, however there were significant changes in the line intensities, indicating solid-state recrystallization and texturing. Upon quenching to room temperature, the hcp structure is recovered, however there is some residual fcc structure. Heating and diffraction was done with the sample at 20 and at 40 GPa.

Simultaneous Ultrasonic Interferometry and *in-situ* X-ray Studies on Wadsleyite (β-Mg_2SiO_4): P-V-Vp-Vs-T Measurements to 7 GPa 885K	X17B1

B. Li, J. Liu, L. Flesch, R. C. Liebermann, J. Chen (SUNY at Stony Brook), and G. D. Gwanmesia (Delaware State U.)

We have conducted acoustic wave velocities measurements and equation of state (P-V-T) studies on wadsleyite (β- Mg_2SiO_4) using simultaneous ultrasonic interfrometry and in-situ X-ray diffraction techniques in a DIA-type, cubic anvil high pressure apparatus (SAM85) installed at beamline X17B of the National Synchrotron Light Source at the Brookhaven National Laboratory. The polycrystalline specimen (K270) was hot-pressed at 15GPa and 1500 K in a 1000-ton Uniaxial Split Cylinder Apparatus (USCA-1000). The sample was identified as single phase of wadsleyite by X-ray diffraction with a bulk density of 3.470 g/cm3 (0.2% porosity). Compressional and shear wave velocities at ambient P and T agree with single crystal data (Sawamoto et al., 1984) within 0.5%. High P and T ultrasonic measurements in the SAM-85 apparatus are implemented by mounting an acoustic transducer at the back of the WC anvil and enclosing glass as extended buffer rod inside the cubic Boron epoxy pressure medium (see figure below). The sample is surrounded by NaCl and BN to minimize non-hydrostatic stress. X-ray diffraction spectra from both the sample and NaCl were recorded at elevated pressures and temperatures from which the unit cell volumes of the sample and cell pressures were retrieved. The temperatures were measured using thermocouples adjacent to the sample. The experimental P-T path has been designed to minimize non-hydrostaticity and to optimize acoustic signals. Completed P-V-T and Vp and Vs data for the specimen K270 have been collected up to 7 GPa and 885 K with dense coverage in P-T space by performing a few compression/heating and decompression/cooling cycles below these conditions. Combining P-V-T and acoustic data will provide the absolute pressure scale and precise determination of elastic moduli K and G and their pressure and temperature. These data are very important parameters needed for modelling mantle compositions and interpreting the 410 km discontinuity in the Earth's transition zone.

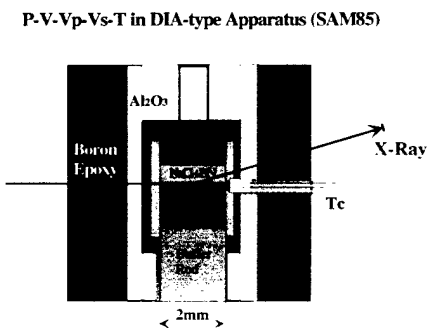

Figure 1.

Simultaneous Ultrasonic Interferometry and in-situ X-ray Studies on Forsterite (Mg_2SiO_4-olivine): P-V-Vp-Vs-T Measurements to 8 GPa and 1300 K	X17B1

B. Li, J. Liu, L. Flesch, , R. C. Liebermann, J. Chen (CHiPR, SUNY, Stony Brook), Brian Savage (UC Berkeley)

We have conducted acoustic wave velocities measurements and equation of state (P-V-T) studies on forsterite (Mg_2SiO_4-olivine) using simultaneous ultrasonic interfrometry and in-situ X-ray diffraction techniques in a DIA-type, cubic anvil high pressure apparatus (SAM85) installed at beamline X17B of the National Synchrotron Light Source at the Brookhaven National Laboratory. The polycrystalline specimen (G717) was hot-pressed at 6 GPa and 1400 K in a girdle- anvil, high-pressure apparatus. The sample was identified as single phase of forsterite by X-ray diffraction with a bulk density of 3.20 g/cm^3 (0.3% porosity). Compressional and shear wave velocities at ambient P and T agree with single crystal data (Kumazawa and Anderson, 1969) within 1%. High P and T ultrasonic measurements in the SAM-85 apparatus are implemented by mounting an acoustic transducer at the back of the WC anvil and enclosing alumina as extended buffer rod inside the cubic boron epoxy pressure medium. The sample is surrounded by NaCl and BN to minimize non-hydrostatic stress. X-ray diffraction spectra from both the sample and NaCl were recorded at elevated pressures and temperatures from which the unit cell volumes of the sample and cell pressures were retrieved. The temperatures were measured using thermocouples adjacent to the sample. The experimental P-T path has been designed to minimize non-hydrostaticity and to optimize acoustic signals. Complete P-V-T and Vp and Vs data for the specimen G717 have been collected up to 8 GPa and 1300 K with dense coverage in P-T space by performing a few compression/heating and decompression/cooling cycles below these conditions. Combining P-V-T and acoustic data will provide the absolute pressure scale and precise determination of elastic moduli K and G and their pressure and temperature. These data are very important parameters needed for modelling mantle compositions and interpreting the 410 km discontinuity in the Earth's transition zone.

Thermal Equation of State of Stishovite	X17B1

J. Liu, J. Zhang, L. Flesch, B. Li, D. J. Weidner, and R. C. Liebermann (SUNY at Stony Brook)

The pressure -volume-temperature (P-V-T) behavior in SiO_2-stishovite has been studied using a DIA-type, cubic-anvil apparatus (SAM 85) and *in situ* synchrotron X-ray diffraction at the superconducting wiggler beamline (X-17B) of the National Synchrotron Light Source at Brookhaven Nationaal Laboratory. Polycrystalline specimens previously hot-pressed in a uniaxial split-sphere apparatus were used to minimize the deviatoric stress which could affect the accuracy of cell parameter determination. The P-V-T data to pressures of 10 GPa and temperatures of 1300 K were analyzed using several approaches, including a temperature-dependent Birch-Murnaghan equation-of-state, isothermal compression, and isobaric expansion. The results obtained from these different approaches show that the entire data set is internally consistent. The bulk modulus (Ko) and axial compressibility of stishovite are compared with values obtained from Brillouin scattering and diamond-anvil cell X-ray studies on single crystal stishovite and ultrasonic studies on polycrystalline specimens. The temperature derivative of bulk modulus at zero pressure (dK/dT) was measured for the first time to be -0.036(11) GPa/K.

Formation of α-eucryptite, $LiAlSiO_4$: An *In-situ* Synchrotron X-ray Powder Diffraction Study of a High Temperature Hydrothermal Synthesis *	X17B1

P. Norby (SUNY at Stony Brook), J. C. Hanson, L. Flaks, J. Hastings (BNL)

Hydrothermal conversion of zeolites is an alternate route for preparation of zeolites and other aluminosilicate materials. Hydrothermal conversion of zeolite Li-A(BW), $LiAlSiO_4$ H_2O, into α-eucryptite, $LiAlSiO_4$, occur at temperatures above 350 C. This is the first in-situ study of a high temperature hydrothermal synthesis using time resolved powder diffraction. Hydrothermal reactions were performed in stainless steel capillaries with a diameter of 1.6 mm. In order to maintain hydrothermal conditions, a hydraulic pressure of 2-300 atm was applied. 35-40 keV synchrotron X-ray radiation was used in order to penetrate the steel capillaries. Angle dispersive time resolved powder diffraction patterns were collected using a Translating Imaging Plate (TIP) camera. Anhydrous Li-ABW, $LiAlSiO_4$ was used as the starting material, and the rehydration into zeolite Li-A(BW) as well as the subsequent conversion into α-eucryptite were observed. Using integrated intensities of a number of diffraction peaks, transformation and crystallization curves were obtained. Figure 1 shows a 3-dimensional representation of a small part of the diffraction pattern as a function of time, and the transformations are clearly visible. An intermediate phase was observed in some of the experiments, and was identified as another polymorph of $LiAlSiO_4$, β- eucryptite. Figure 2 shows an example of transformation and crystallization curves extracted from the patterns.

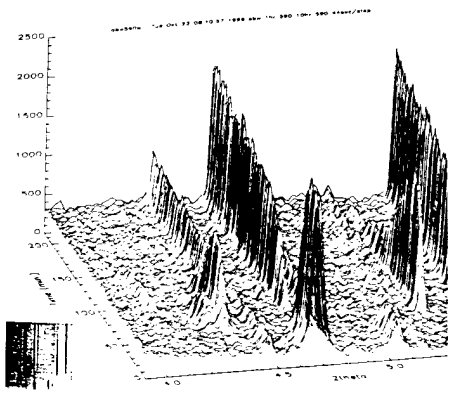

Figure 1.

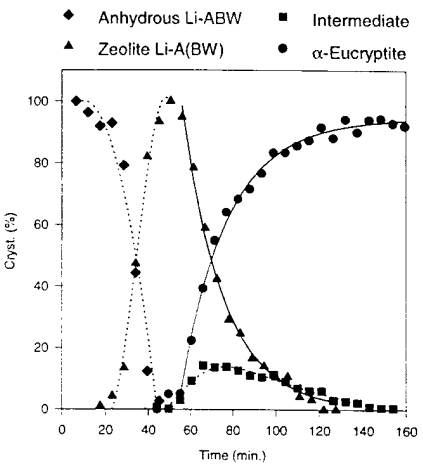

Figure 2.

* DOE BES DE-AC02-76CH00016

Shear Wave Velocity of $MgSi0_3$ Perovskite up to 8 GPa and 400°C	X17B1

Y.D. Sinelnikov, G. Chen, J. Liu, D. Neuville, R. C. Liebermann, and D.J. Weidner (SUNY at Stony Brook)

High quality polycrystalline specimens of the $MgSiO_3$ perovskite have been synthesized in a 2000-ton multianvil split-sphere apparatus (USSA-2000) at 26 GPa and 1350° C using glass as the starting material. The perovskite structure has been confirmed by Raman spectroscopy and X-ray diffraction analyses from the ends of the cylindrical specimens. After polishing the specimens under liquid nitrogen (to protect them from morphization) we performed pilot acoustic experiment at room temperature to the pressures up to 5 GPa in a 1000-ton uniaxial split-cylinder apparatus (USCA-1000) press. The acoustic quality of perovskite specimen was to be excellent at elevated pressure, but the acoustic echoes were barely observable at room pressure, most likely due to the large grain size of synthesized material (up to 50 microns). Two subsequent experiments have been performed in a DIA-type, cubic anvil apparatus (SAM 85) installed on the superconducting wiggler beamline (X17B) at the National Synchrotron Light Source of the Brookhaven National Laboratory. The coustic measurements were performed simultaneously with in-situ X-ray diffraction monitoring of the perovskite sample and NaCl standard, which was used to determine the pressure. (Liebermann et al., 1997, AIRAPT). The temperature was measured by two thermocouples and the gradient determined to be less than 10C/mm. As a result of these experiments, the shear elastic modulus of $MgSiO_3$ perovskite has been measured as a function of temperature and pressure for the first time.

Thermoelastic Properties of $CaTiO_3$-$CaSiO_3$ Perovskites	X17B1

Y. Sinelnikov, J. Zhang, R. C. Liebermann (CHiPR, SUNY at Stony Brook)

Polycrystalline specimens of end-member $CaTiO_3$ and intermediate $CaTi_{0.75}Si_{0.25}O_3$ and $CaTi_{0.5}Si_{0.5}O_3$ perovskites were hot- pressed in a 2000-ton uniaxial split-sphere apparatus (USSA-2000). Intermediate compositons were synthesized at pressures of 15 GPa and temperatures above 1800 K. The pressure -volume-temperature (P-V-T) behavior in these specimens has been studied using a DIA-type, cubic-anvil apparatus (SAM85) and *in situ* synchrotron X-ray diffraction at the superconducting wiggler beamline (X-17B) of the National Synchrotron Light Source at Brookhaven National Laboratory. The P-V-T data to pressures of 8 GPa and temperatures of 1100 K were analyzed using a temperature-dependent Birch-Murnaghan equation-of-state to obtain the isothermal incompressibility/bulk modulus and its pressure and temperature derivatives.

Powder X-ray Diffraction for Anisotropic Compression Measurements at High Pressures	X17B1

M. S. Somayazulu, Y. Z. Ma, J. Z. Hu, J. F. Shu, H.-K. Mao, R. J. Hemley (Carnegie Inst. Washington, CHiPr), M. Rivers (U. of Chicago), T. Duffy (Princeton U.)

Determining the effect of pressure on the elastic properties of materials is essential for understanding mecahnical stability of solids, material strength, seismology and phase transformation mechanisms. We report the setting up of an experimental technique which is capable of measuring the elastic properties of materials at Mbar pressures and temperatures of the order of 2000 K from powder samples.

Elastic constants of the polycrystalline specimen are obtained from evaluating the variation of the d-spacing as a function of Ψ, the angle between the ¿direction and the stress axis of the sample in the diamond anvil cell [1]. Radial x-ray diffraction technique at ultr-high pressures using a high strength Be gasket makes such a measurement possible. However, the diffraction data has to be collected from extremely small sample volumes (typically 5-10 μ^3) enclosed in a relatively thick Be smaple chamber. This requires the use of a high brilliance, white x-ray source available at the wiggler beamlines. To enable data collection from a stationary smaple, an array of detectors are used wherein each detector images a small range of Ψ values so that all the data can be collected at the same time. The diffraction angle and the diffracting volume are fixed by a specially designed conical slit assembly. The advantage of such a technique also being that laser heating of the sample becomes possible to allow studying elastic properties of materials at extreme P. T conditions for which we have installed a double sided laser heating set up using a Nd:YAG laser. Representative data collected from our studies on a geologically important material, FeO are shown below.

[1] A. K. Singh, H-k Mao, J. F. Shu and R. J. Hemley (1997) Phys. Rev. Lett. (in press)

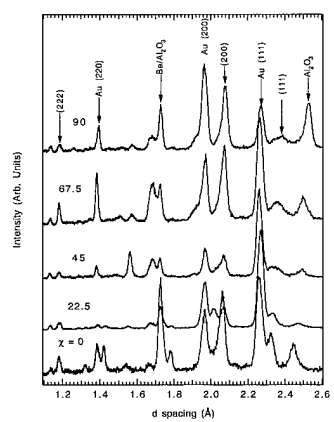

Figure 1.

A High-Energy Diffraction Study of the Bulk Critical Scattering in a V_2H Crystal *	X17B1

J.Trenkler, H. Abe, P. Chow, D. Scarfe, S. C. Moss (U. of Houston), P. Wochner, Z. Zhong, J. Hastings (BNL), R. Hempelmann (U. des Saarlandes)

A sharp quasi-Bragg peak in the critical scattering on top of a broad Lorentzian shaped peak for a $SrTiO_3$-crystal has been recently observed by x-ray scattering. Thereby, the coexistence of two components in the critical scattering suggests the existence of two length scales in the critical fluctuations. Although the origin of the sharp component is not clear, it is believed to be related to surface phenomena such as local distortions around defects close to the surface.

In a recent experiment done at X14A, we observed a similar effect in the line shape of the critical diffuse scattering in a longitudinal [0 1 $\bar{1}$] scan at $T=T_C+6.2$ K in a V_2H crystal. As shown in fig. 1, the measured profile clearly consists of a sharp and a broad component at a temperature of $T=T_C+6.2$ K measured in reflection geometry with a x-ray energy of 11.95 keV. In order to probe whether the two components in the line shape are related to the two-length scale issue or not, we performed a high energy diffraction experiment in transmission geometry at the high energy beamline X17B1 using 44.1 keV photons. A Si-111 analyzer crystal with a Ge-solid state detector was used to increase the q-resolution and suppress the $\lambda/2$-contribution. In this experiment, we measured the "true" bulk behavior and not just the behavior of the first 50 μm below the surface, since the entire crystal volume is probed by the incident beam over the illuminated region. Figure 2 shows a scan measured at $T=T_C+6.5$ K using a x-ray energy of 44.1 keV. Obviously no sharp component on top of the broad one is observed. The measured data can be well-fitted by a single Lorentzian corresponding to the broad component.

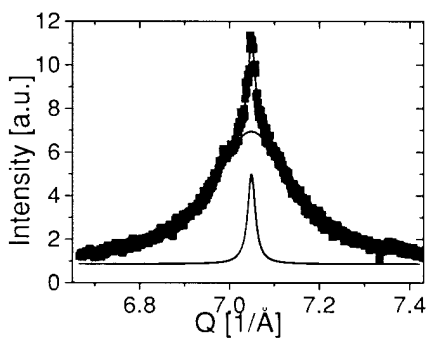

Figure 1. CDS for the (0 5/2 $\bar{5}$/2) superstructure reflection in a heating run in [0 1 $\bar{1}$] at $T=T_C+6.2$ K with a x-ray energy of E=11.95 keV at X14A.

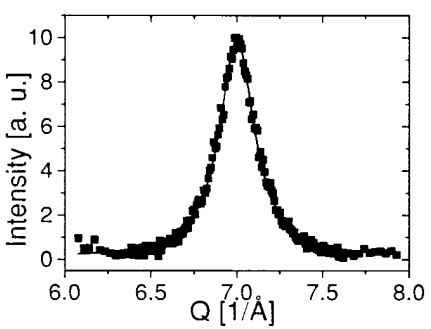

Figure 2. As fig. 1 but at E=44.1 keV measured at X17B1.

* This work is supported by the NSF on DMR92-08450.

Equations of State of $MgSiO_3$ in the Sub-Perovskite Pressure Range *	X17B1

M. T. Vaughan, E. K. Bell, and J. Z. Zhang (CHiPR, SUNY at Stony Brook)

The study of the phase relations of (Mg,Fe)SiO_3 (1996 NSLS Activity Report, B145) is continuing with a measurement of the equation of state (EoS) of the magnesium end member of the Mg-Fe solid solution described above.

The study was going to be the measurement of stress relaxation of the ilmenite phase at about 10 GPa, at various high temperatures. The ilmenite sample studied previously (ibid), was from a natural enstatite and had about 10 mole percent $FeSiO_3$, as well as small amounts of Al. There were several problems, and a reliable EoS has not yet been determined from that data set.

The current, Mg end-member sample, was much less stable, and after a few minutes at 600°C it transformed to a high-pressure form of clinoenstatite. The unit cell volume of the HP-CEn as a function of pressure and temperature is currently being determined. The instability of the ilmenite phase is understandable, because we are operating outside of its stability field, but it is not known why the end-member is so much less stable than the natural sample.

Further work on the $MgSiO_3$ end member will require high temperature measurements within (or closer to) its stability field, *i.e.* > 18 GPa (see Figure 1.)

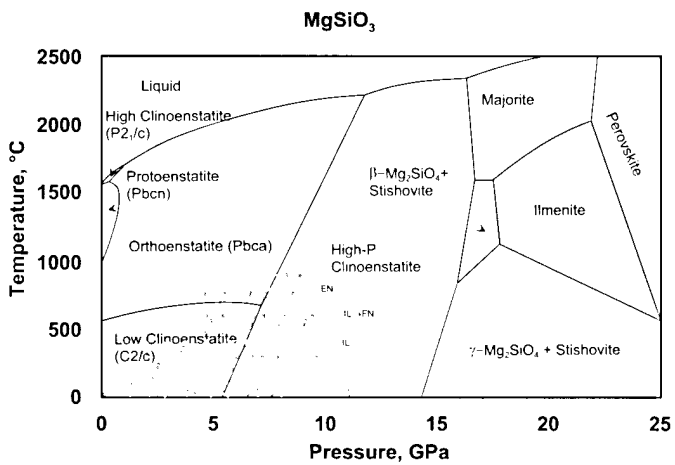

Figure 1. Phase Relations in $MgSiO_3$. Diamond-shaped symbols are the current data set. The two highest-pressure points were ilmenite phase; during the collection of the third data set, the sample transformed to High-pressure clinoenstatite. It remaind in this phase for the rest of the run. The data from last year are the fainter symbols in the background.

* Work supported ty the NSF under a grant to the Center for High Pressure Research and by the DOE under contract number DE-AC02-76CH00016 to the NSLS

Use of Sintered Diamond Anvils in a 6-8 High-Pressure Apparatus * | X17B1

M. T. Vaughan, D. J. Weidner, J. H. Chen, and C. C. Koleda (SUNY at Stony Brook)

The pressure capability of the Tcup apparatus (NSLS Activity Report 1995, B-140; 1996, B-145) has been extended to 22.8 GPa by the use of sintered diamond for the 1 cm cubes used as a second stage (Figure 1). The sintered diamonds were Advanced Diamond Compacts (ADCs). ADC is a natural diamond product hot-pressed with a SiC binder at modest pressure (~2 GPa). We achieved a pressure equivalent to our best tapered anvil run, with a maximum pressure of 22.8 GPa with a load of 110 tons. The untapered ADC pressure-load curve is tangent to the equivalent untapered WC curve at pressures below 5 GPa, but with much less curvature above there. At 110 tons, there is a 6GPa increase. We expect tapered ADC anvils to exhibit similar pressure increases. If we taper the anvils, and extroplate along the best -2° tapered trajectory, we would expect the pressure to reach 30 GPa at 120 tons (Figure 2).

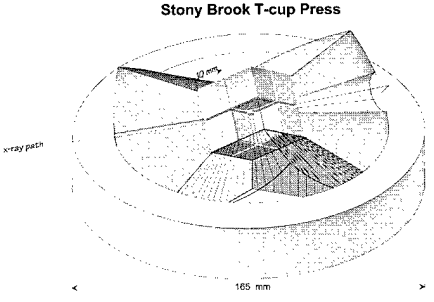

Figure 1. Tcup apparatus, showing eight 10 mm second stage cubic anvils inside three of six first stage anvils, two of which are cut away to allow x-ray passage

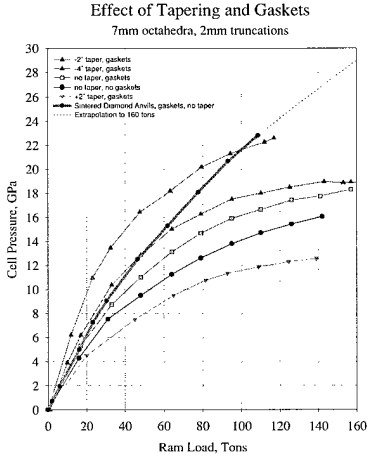

Figure 2. Plot of cell pressure vs. ram load for various anvil and gasket configurations. Heavy line is for the ADC anvils, the rest are WC.

* This work was supported by the NSF under a grant to the Center for High Pressure Research and by the DOE under contract number DE-AC02-76CH00016 to the NSLS.

Phase Transition in Zeolite A at 2 Kbars and 800° C Using SAM-85 | X17B1

Y. Wang (U. Chicago), J. Chen, F. Bejina, (CHiPR, SUNY at Stony Brook), M. C. Hash, L. Leibowitz, M. C. Petri, J. W. Richardson, Jr., (ANL)

We report some preliminary results in an in-situ study on zeolite A, using SAM-85. A large volume BN cell (20x20x20 mm) was used and two samples were packed in the cell: a pure zeolite A, and the other mixed with 5 wt percent glass; they were separated by a layer of NaCl, also used as the pressure standard. Strong diffraction signals were observed at 1 bar for both samples (Figs. 1A and 2A). At 2 kbar and room temperature, diffraction peaks became broad and weak (Figs. 1B and 2B). In the glass-containing sample, close to the sample/NaCl interface (0.1 mm), additional peaks appeared (compare Fig. 2B with 1B); 0.2 - 0.3 mm away from the interface, the spectrum ressembles that of an amorphous material (Fig. 2C). Upon increasing temperature, pure zeolite quickly transformed into sodalite around 800°C (Fig. 1C). For the glass-containing sample, those new peaks persisted (Fig. 2D). These phenomena will be examined further in future experiments.

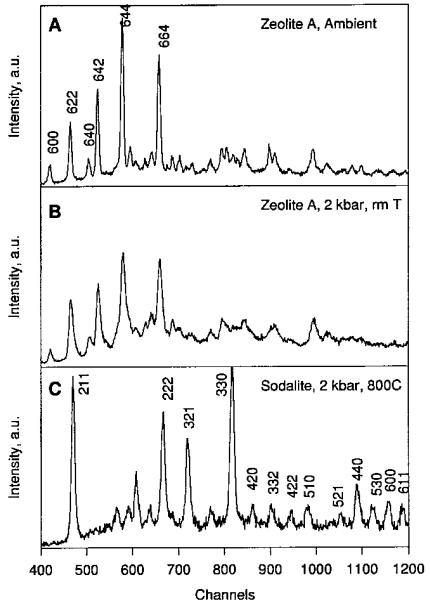

Figure 1. X-ray spectra of pure zeolite A. Major peaks labeled in A. Same intensity scale as in Fig. 2.

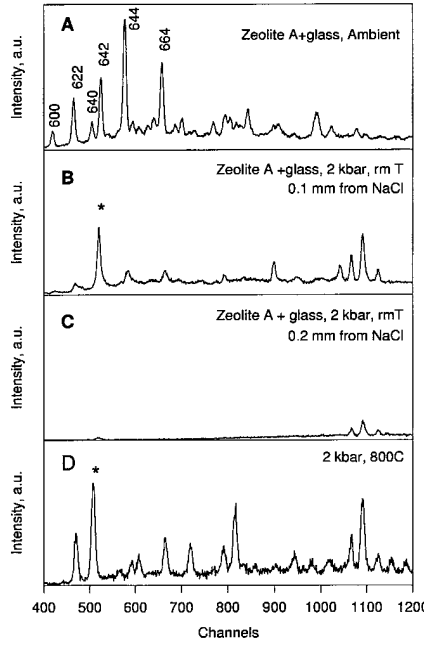

Figure 2. X-ray spectra of zeolite+glass.

Strength of the Subducted Slab: Implications for Deep Focus Earthquakes *	X17B1

D. J. Weidner, J. Chen, J. Ando, and Y. Wu (CHiPR, SUNY at Stony Brook)

The strength of the material of the transition zone at the pressures and temperatures appropriate to subduction have been determined in the laboratory using both the DIA and T-cup multi-anvil pressurizing systems and synchrotron radiation at the X17B1 wiggler port at the NSLS.

The measurement technique consists of several steps: 1. A loose powder sample is used in the study. The deviatoric stress is generated by the stress concentrations between grains. Typically, in the elastic region, (σ_1 - σ_3) = 1.5 times the pressure on loading. As the yield point is obtained, the differential stress falls below this value. 2. The differential stress is monitored as a function of time by recording diffraction spectra every 30 seconds after heating to the desired temperature. This time dependence reflects the effective power law for the stress release process. The time interval varies from an hour to a few days. 3. Several recovered samples are examined with TEM to define the flow mechanism. This methodology is limited to relatively small plastic strains (a few percent) and the threshold deviatoric stress that can be observed is of the order of 0.1 GPa. These data have been obtained for the major phases of the mantle including olivine, wadsleyite, ringwoodite, majorite rich garnet, and perovskite. Both 'wet' and dry samples of the olivine series have been studied.

Requiring a storage capacity of 0.1 GPa for 100 years as a criterion for a seismogenic region, we conclude that olivine cannot sustain earthquakes deeper than 300 km in all but the coldest subducting slabs owing to the temperature induced weakening. Transition zone minerals, on the other hand, being much stronger, can store the necessary strain energies at temperature expected between 400 and 700 km for even relatively hot slabs. These results suggest that the bimodal distribution of earthquake activity with depth is simply a reflection of the strength dependence of the stable phases and thus does not require different triggering mechanism for earthquakes above and below 400 km.

* This work was supported ty the NSF under a grant to the Center for High Pressure Research and by the DOE under contract number DE-AC02-76CH00016 to the NSLS.

The Rheological Study of "Super Dry" Forsterite at High Pressure and Temperature	X17B1

Y. Wu, D. J. Weidner, J. Liu, M. Vaughan and J. Zhang (CHiPR, SUNY at Stony Brook)

The variation of the differential stresses of "super dry" forsterite with pressure, temperature and relaxation time was studied using the DIA type cubic anvil apparatus at the X-17B1 beam line.

Before the experiment, the synthesized polycrystalline forsterite Mg2SiO4 was ground to fine powder, then heated at 1200°C for 20 hours to dehydrate. We call the forsterite after this treatment "super dry" forsterite. Following this treatment, the sample was stored in an oven at 120°C until the experiment. During the experiment, the powder sample was first compressed to 9 GPa at room temperature, then heated up gradully to 800°C. By analysis the peak broadening, we get the differential strains of the sample.

Our priliminary result shows that the "super dry" forsterite reached yield point around 3 GPa at room temperature. The differential stress increased slowly with the increasing pressure. The room temperature behavior is consistent with our earlier results(Wu, Y., etc.,1996). Under the 9.4 GPa confining pressure, we measured the differential strain at 200°C, 400°C, 500°C, 600°C, 700°C and 800°C. We can see the differential strain decreased with the increasing temperature. At the specific temperature, the strain decreased monotonically with the relaxation time, first very fast, the became slower. These behaviors are also similiar to our earlier results (Wu, Y., etc, 1996). However, the "super dry" sample appears to be significantly stronger than the untreated sample. Further data analysis is still in progress.

Figure 1. Strain in "super dry" forsterite as a function of time.

Hard-X-ray Study of Single Crystal Superconducting $La_2CuO_{4+\delta}$ * | X17B1

X. Xiong, D.P. Scarfe, S.C. Moss, A.J. Jacobson, W.J. Zhu, P.H. Hor (U. of Houston), P. Wochner (BNL)

A single crystal of $La_2CuO_{4.08}$, annealed at 110°C was studied in a high energy diffraction experiment at beamline X17B1 using 71keV photons. The crystal was charged by electrochemical intercalation. Two orthorhombic phases were observed within the studied temperature range (180-310K) in this single crystal. The major orthorhombic phase, with ≈90% volume fraction, transforms from a Fmmm phase with random CuO_6 tilts to a stage-4 phase [1,2], where the CuO_6 tilts are ordered along the **c**-axis, at or below room temperature in a second-order fashion. The minor orthorhombic phase shows a larger orthorhombicity with 2(b-a)/(a+b)=0.019 and has, therefore, a higher oxygen content. The integrated intensity of the staging satellites was found essentially to be linearly dependent on temperature from slightly below 300K to 180K as previously found by Ref. 2. Interstitial oxygen layering was observed for the first time in a more straight forward way than through the CuO_6 tilt reversal at oxygen interstitial layers, which is expressed in the Bmab staging satellites. This oxygen ordering was documented by the appearance of (0,0,l±0.65) satellites at room temperature even in the absence of the tilt-staging Bmab satellite peaks. These new satellites are thought to be produced by a periodic lattice expansion in **c**-direction induced by the interstitial oxygens. They are poorly correlated in **c**-direction as can be seen from the broad linewidth of the longitudinal scan of the (0,0,4-0.65) satellite in the inset of Fig.1. The rocking scans (Fig. 1) of the (0,0,6±0.65) satellites are identical to the parent (0,0,6) Bragg peak. The broad FWHM is either due to a small domain size of the ordered regions or a broad distribution of oxygen staging-layer separations or both. A broad distribution would be consistent with our model of the in-plane oxygen ordering [1], which occurs at ≈200K for an oxygen concentration of ≈0.05-0.06. Further experiments will investigate the temperature and Q-dependence of these new satellites. These studies should give new insights in the driving mechanism for this oxygen layering.
References [1] X. Xiong et al., Phys. Rev. Lett. 96, 2997 (1996); P. Wochner et al., J. Superconductivity 4, 367 (1997). [2] B.O. Wells et al., Z.Phys.B 100, 535 (1996).

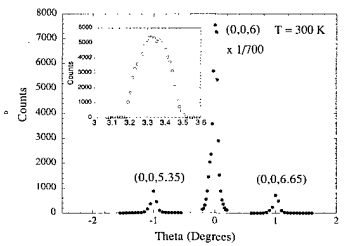

Figure 1. Rocking scans of the (0,0,6±0.65) satellites and the fundamental (006) reflection. The inset shows the longitudinal scan of the (0,0,4-0.65) satellite.

* This work was supported at Houston by the TCSUH, the MRSEC and the NSF on DMR-9208420, at BNL support is from the U.S. DOE Contract No. DE-AC-02-76CH00016.

Room Temperature Compression of CdO | X17B1

J. Zhang (CHiPR, SUNY at Stony Brook)

CdO has the NaCl structure at ambient conditions and at pressures at least up to 30 GPa. From previous compression study of Drickamer et al. (1966), CdO was found to have an anomalously high value of the pressure derivative of the bulk modulus (K_0=9) compared to all other NaCl-type oxides (K_0=3.3-4.1). In addition, compressibility of CdO decreased with pressure more rapidly than would be predicted for ionic compounds, whereas all other NaCl-type oxides were typically ionic in binding.

In view of the fact that the compression data in the work of Drickamer et al. (1966) were considerably scattered in the P-V space, here we carried out in-situ X-ray diffraction on CdO using a DIA-type multi-anvil apparatus. The volume measurements were made up to 8 GPa at room temperature; all data were collected after quench from 800 C to minimize nonhydrostatic stress built up during room-temperature compression or decompression. Due to the limited pressure range of the current experiment, K_0 could not be defined well and was thus fixed in the data analysis. For K_0=4 and K_0=9, we obtained K_0 = 150(2) GPa and K_0= 137(2) GPa, respectively. In comparison, Drickamer et al. (1966) obtained K_0=108 GPa and K_0=9 from the compression data up to 30 GPa. The present results thus show a compressibility that is more than 25 percent smaller than that from previous work. Therefore, one can make a stronger statement that the binding in CdO is not entirely ionic in comparison with the classic Born-Mayer prediction.

Drickamer HG, Lynch RW, Clendenen RL and Perez-Albuerne EA, X-ray diffraction studies of the lattice parameters of solids under very high pressure, Solid State Physics, 19, 135-229, 1966.

Comparative Compressibility of Calcite-Structure Carbonates | X17B1

J. Zhang and R. J. Reeder (CHiPR, SUNY at Stony Brook)

For carbonates of the calcite structure, experimentally measured bulk moduli on $NiCO_3$, $MgCO_3$, $CoCO_3$, $FeCO_3$, $MnCO_3$, and $CaCO_3$ have been found to deviate from empirical predictions, in the sense that substitution of alkaline earth elements by the 3d transition metals yields a different bulk modulus-volume relationship (1., 2.). Here we report new compression data on $ZnCO_3$ and $CdCO_3$ from in-situ X-ray diffraction, which, in combination with our previous results, completes a systematic study of compressibilities for all calcite-structure carbonates. As known from earlier work, the bulk moduli of the 3d transition metal carbonates show an inverse correlation with room-pressure M-O bond length and volume that is linear. $MgCO_3$, however, plots well below the trend, and $CaCO_3$ slightly below. One particular focus of this work is the contribution of the crystal field to the bulk modulus. No crystal field effect beyond that reflected in the ionic radii is observed among the 3d transition metal carbonates, since $ZnCO_3$ and $MnCO_3$ are colinear with $NiCO_3$, $CoCO_3$ and $FeCO_3$. Notably, the bulk moduli of $ZnCO_3$ and $CoCO_3$ are essentially identical, as are their ambient M-O bond lengths and volumes. The bulk modulus of $CdCO_3$, whose ambient M-O bond length and volume are only slightly smaller than those of calcite, is more than 30 GPa greater than that of calcite, and falls about 15 GPa above the trend of the 3d transition metal carbonates. Hence, neither bond-length (or volume) nor crystal-field effect can account for the observed bulk moduli for the complete set of calcite-structure carbonates. Systematic behavior appears to be limited to subsets of carbonates whose metal cations share particular character of their valence electron, e.g., s-type vs. 3d vs. 4d shells.

1. Zhang J and Reeder RJ, Equation of State of Calcite-Structure Carbonates, NSLS Activity Reports, P. B-147, 1996.

2. Zhang J and Reeder RJ, Comparative compressibilities of the calcite-structure carbonates. AGU Spring Meeting, 1997.

Unidirectional Microbeam Radiation Therapy of Rats Bearing Subcutaneous 9L Gliosarcoma Tumors: Relevance to Radiotherapy of Craniospinal Tumors in Humans | X17B2

F. A. Dilmanian, X. Y. Wu, B. Ren, A. Z. Diaz, M. Kershaw, G. Le Duc, D. T. Lombardo, P. L. Micca, M .M. Nawrocky, D. N. Slatkin, F. Telang (BNL), W. C. Thomlinson, Z. Zhong (NSLS), and J. C. Allen (Beth Israel Med. Center)

Microbeam radiation therapy (MRT) is an experimental method that uses parallel arrays of microplanar beams, each about 30 μm wide and millimeters-to- centimeters long, with about 50-100 μm apart center-to-center spacing[1]. MRT studies at the NSLS's X17B1 beamline showed two effects for unidirectional microbeam irradiations. First, they have extraordinary tissue-sparing effects in the normal tissues of rats [1], gerbils, rabbits, and duck embryos; they do not cause necrosis in the brain of rats at doses several times the threshold for direct neuronal death, estimated to be 360 Gy in the cerebrum. Second, they have a preferential tumor-killing effect in rats bearing 9L gliosarcoma (9LGS) brain tumors. The latter effect may reflect important differences in the post-MRT regeneration mechanism in the vascular endothelial cells of normal and tumor tissues.

Eight rats that had been inoculated subcutaneously with 9LGS cells close to their cervical spinal cord twelve days earlier were irradiated with unidirectional microbeams anteroposteriorly through their pharynx and spinal cord; the animals faced the beam with its central anteroposterior body axis at 65 elevation. The in-slice skin-entrance dose was about 200 Gy and the beam's width was 27 m. The center-to-center beam spacing was 75 m. The array's envelope was 20 mm x 20 mm for 6 rats, 23 mm x 23 mm for the 7th, and 26 mm x 26 mm for the 8th. Forty eight days later the tumors had disappeared in 5 rats and were barely visible in two others. One rat died 42 days after irradiation. Necropsy showed hemorrhagic congestion of the lungs and the liver, mainly outside the irradiation field. The tracheal and the esophageal mucosal linings, which were largely in the radiation field, appeared normal. The pericardium also appeared normal. There was no pericardial hemorrhage. The etiology of the pulmonary and hepatic lesions are not known, but might have been cause by congestive heart failure. It is possible that movement of the rat during irradiation precipitated in this condition.

We plan to upgrade the MRT irradiation system at X17B, and expand preclinical MRT studies, preparing for Phase I human studies with the following goals: a) treating children with tumors of the central nervous system, and b) palliating metastases to the spinal cord and brain from primary tumors such as breast or lung. Unidirectional MRT may be appropriate for the following reasons: a) for incident doses below the threshold for direct neuronal-cell killing, it appears harmless, even in developing animals such as duck embryos, which are far more radiosensitive than adults, b) it does not damage the rat's spinal cord, which is more radiosensitive than the cerebrum, c) it appears safe when irradiating large values, d) it is insensitive to the subject's positioning in the beam, e) dose fractionation may prove to be unnecessary, which would be convenient for children and metastatic patients, and f) even with sub-optimal irradiation parameters, MRT's palliative effects are remarkable.

We thank K.A. Bonti, J.A. Coderre, D.D. Joel, C. Rissland, and A.D. Woodhead for assistance. Research supported by the Office of Biological and Environmental Research, DOE.

[1] D.N. Slatkin, et al., Proc. Natl. Acad. Sci. USA 92, 8783-8787, 1995.

Xenon K-edge Imaging With a Monochromatic CT Scanner to Selectively Image Fat in Rats: Relevance to Compositional Imaging of Carotid Atherosclerotic Plaques*	X17B2

F.A. Dilmanian, X.Y. Wu, B. Ren, X. Huang, D.N. Slakin, (BNL), W.C. Thomlinson, Z. Zhong (NSLS); T.M. Button, M.J. Petersen (SUNY at Stony Brook), and L.D. Chapman (ITT)

Carotid artery atherosclerosis is a major cause of stroke. Although carotid artery stenosis is a risk factor, the majority of patients with stenosis do not experience a stroke. Recent evidence suggests that a certain proportion of the main components of carotid atherosclerotic plaques, i.e., fat/cholesterol, fibrous and calcified tissues, carry larger risks of stroke. The monochromatic CT system at X17B2 called MECT (multiple energy computed tomography) [1] may be able to separate these components and allow more accurate selection of patients for carotid endarterectomy. For this, MECT will be used in two energy-selective modes a) a dual-energy quantitative CT (DEQCT), in which 40 keV and 100 keV image are processed to separate the image of the low-Z tissue (the non-calcified one) and the intermediate-Z tissue (the calcified one), and b) xenon K-edge subtraction, that relies on xenon's large solubility in fat and the large gain in contrast in the xenon image obtained by tuning the monochromatic beam energy just above the K-edge [1] to quantify fat.

In the following experiment MECT was operated in the planar (i.e., radiography) mode. A 400-g Zucker rat, was given a mixture of 50% xenon and 50% air for one hour. It then breathed air for an hour to allow the washout of xenon from the lean body mass. The rat was positioned anteroposteriorly in the beam in a prone position, tilted upward (i.e., nose-up), and imaged by moving it vertically in the path of MECT's fan-shaped beam. Images were acquired at two beam energies, 34.40 keV and 34.72 keV, which bracketed the K-edge of xenon (34.56 keV). The spatial resolution was improved by taking two sequential images with the rat shifted laterally by half the detector's element spacing between the two, and combining them. Fig. 1 shows the above the K-edge (left), below the K-edge (center), and subtracted (right). Because of an apparent small movement of the rat between the images at the two energies, they had to be slightly shifted and rotated for the best match. The fat observed in the subtracted picture is the subcutaneous fat under the rat's left shoulder (the rat was imaged in a slightly crooked position)

[1] F.A. Dilmanian, et al., Phys. Med. Biol. 42:371-387, 1997.

*We thank M. Kershaw and A.D. Woodhead for assistance. Research supported by the Office of Biological and Environmental Research, DOE.

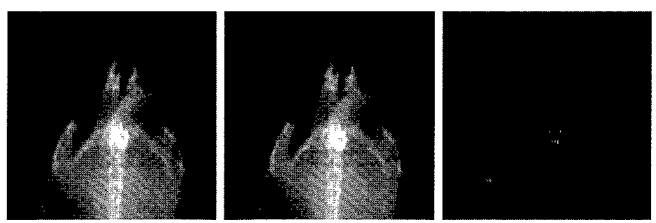

Figure 1. Rat Xe K-edge images.

Preliminary Experiments on a Mammography Imaging System and a Multi-Layer Monochromator for Angiography *	X17B2

K. Hyodo, M. Ando (PF), K. Tanioka, R. Mochizuki (NHK), H. Mori (Tokai Univ.), Z. Zhong and W. Thomlinson (NSLS)

We have been developing a mammography imaging system using a fluorescent screen coupled with a HARP (High-gain Avalanche Rushing amorphous Photo conductor) TV camera, which is a photo-tube camera manufactured by NHK (Japanese Broadcasting Co.). The camera has a dynamic range of larger than 10,000 and high sensitivity. The spatial resolution of 30 microns, with the view size of 30 mm by 20 mm, was achieved during the phantom experiments on X17B using a Hi-vision HARP TV at 20, 25 and 33 keV.

We have been developing a multi-layer monochromator to get larger integral intensity than that of a Si crystal with lapped surface, whose energy resolution, dE/E, is 4.5x10-3. In the case of intravenous coronary angiography using one monochromatic energy at above the K-edge of the contrast material, it is not necessary to use a Si crystal to get monochromatic x-ray photons.

The available photon flux is easily increased without increasing the ring current if we can use a monochromator which can reflect photons in the range of a few keV. We achieved the view size of 30 mm by 60 mm by using a test sample monochromator, whose energy resolution was 2.4x10-2, at 33 keV. However, the intensity of the view area was not uniform. Further investigation will be needed for the monochromator.

* Research suported (in part) by the USDOE, Div. of Materials Sciences and Div. of Chemical Sciences.

Dual-energy subtraction imaging utilizing indium as a contrast agent	X17B2

G. Le Duc, Z. Zhong (NSLS), L. Warkentien, B. Laster (BNL Medical), and W. Thomlinson (NSLS)

The purpose of our current work is to establish the minimum detection limit of indium contrast agent using dual-energy subtraction imaging above and below indium K-edge. Experiments were performed on the X12 and X17B2 beamlines at the National Synchrotron Light Source using the same method but with two different set-ups. Experiments were first carried out on $InCl_3$ solutions, then on V79 Chinese hamster cells and on BALB/c mice excised tumors, labeled with indium. For each experiment, several layers of Lucite were placed in front of the phantom to ensure a 43 mm thickness, close to that of a mammography examination. Results were the same on X12 and X17B2. As expected, indium-free materials dissapeared on subtracted images (water, steel reference and screw). Indium samples were easily distinguishable for the following concentrations: 10-5-2-1 mg/cm^2. Smaller concentrations were not clearly distinguishable and we were unable to see cell samples and tumors. To conclude, the lowest concentration we can image is around 1 mg/cm^2. Such results also suggest that indium concentration in both cells and tumors is lower thatn 0.5 mg/cm^2. Since the current method is close to optimum, we conclude that dual energy subtraction imaging using indium to label tumors is not possible unless the indium uptake is increased by more than an order of magnitude.

Contrast Analysis of 2D Monochromatic X-ray Coronary Artery Images *	X17B2

Y. Oku (U. for Adv. Studies), K. Hyodo, M. Ando (KEK), Z. Zhong and W. Thomlinson (NSLS)

Intravenous SR coronary angiography is relatively simple and safe so that screening looks promising as an application. For clinical use, the construction of a compact source at hospitals is required. In order to design a system, it is necessary to investigate the expected image quality by both simulations and experiments. For example, scattering of x-rays and the presence of higher harmonics in the spectrum may degrade the quality.

A two-dimensional imaging system has been adopted for the intravenous SR coronary angiography program in Japan. It has many benefits such as easier distinction of coronary arteries from pulmonary arteries and soft tissues because of its motion synchronized with the heart beat and the capability of diagnosis of other heart functions such as the rate of blood flow. However, in the 2D mode, scattering of x-rays from the patient may cause significant deterioration of image contrast and visibility. The scattering can be suppressed by x-ray grids which are commmonly used at hospitals, but the inevitable third harmonic cannot be suppressed. Since the higher harmonics and scattering cannot be distinguished on the experimental image, simulations may be effective to identify their influences on the deterioration of the image contrast. We have thus developed a simulation program of II-TV images when 2D monochromatic SR x-rays pass through an acrylic phantom with an artery.

In order to verify the image contrast calculated by the simulation program, experiments have been carried out. The experiment was done at the X17B beamline of the NSLS. An asymmetric, lapped silicon (311) crystal acted as the monochromator. The phantom was an acrylic block with a hole which imitates a coronary artery with diameter 1 - 5 mm containing iodine diluted by water to 1 to 10%. An image intensifier (II) detector was used. Under the same conditions, simulations were carried out while taking into account the response function of the II for the photon energy used. The calculated contrast was compared with the experiment.

* Research supported (in part) by the USDOE. Div. of Materials Sciences and Div. of Chemical Sciences.

A Bent Laue-Laue Monochromator for the Multiple Energy Computed Tomography Project *	X17B2

B. Ren, F.A. Dilmanian, X.Y. Wu, X. Huang (BNL), L.D. Chapman, I. Ivanov (CSRRI), and Z. Zhong (NSLS)

A bent Laue-Laue monochromator is being developed for the multiple energy computed tomography (MECT) program. The present crystal design, a large Czochralski (CZ) Si plate with thick ribs on the top and bottom, was adopted after earlier trials using silicon wafer and smaller, float-zone (FZ), ribbed crystals. The new system was constructed at CSRRI and BNL. The crystals were Si<111> with 35.36° asymmetric angle. Both crystals employed Laue diffraction lower case to eliminate Laue spot contamination. The crystals were bent by a four-rod bender: two fixed and two adjustable. The ends of each adjustable rod was independently held by a compression spring. This four-spring configuration allowed efficient removal of crystal twisting.

The crystals were positioned in the beam such that the diffraction in each crystal came from its vertical center. The bending radius of each crystal was determined by measuring its variation of the Bragg diffraction peak of it against a fixed crystal as the height of the crystal changed stepwise. Furthermore, the horizontal profile of the 14-cm wide diffracted beam was measured at 0.9-mm resolution using the MECT's linear array detector. A 2-dimensional rocking graph was acquired as the angle θ_2 was scanned. The shape of the rocking curve for each horizontal detector channel indicated the degree at which the bending radii of the two crystals matched; the flatness of the gray scale's bright zone in the 2-dimensional display indicated whether there existed twisting, tilting, or 'beam smiling effect' in the system. Much effort were spent to remove the twisting and beam smiling. An example of the 2-dimensional rocking graph is shown in Fig.1. The bending radius was 4.8 m for the first crystal and 4.9 m for the second. The beam size was 140 mm x 2 mm, and the beam energy was 41.7 keV.

The overall shape of the rocking graph was straight except for some small wiggles caused by the local crystals non-uniformities. The 1-dimensional rocking curves, relating to the central and ends positions of the fan beam are plotted in Fig. 2. The flat-top shape in all these three curves, particularly at the relatively large beam height of 2 mm, indicate that the bending radii matched over the entire width of the crystals. The beam stability was tested at the monochromator's tuned configuration. The horizontal beam profile, normalized to that a certain time, was stable within 0.1% for two minutes period. This stability is markedly better than that of the previous flat Laue-Laue monochromator of the MECT system.

* We thank T.S. Dickinson, N.F. Gmür, J.B. Hastings, A. Lenhard, C. Schulze, N.C. Satterley, D.P. Siddons, W.C. Thomlinson, G.M. Vanderleski, S. Wang, and M.H. Woodle for assistance. Research supported by the Office of Biological and Environmental Research, DOE.

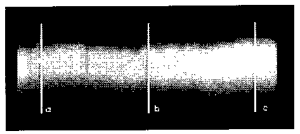

Figure 1. Rocking graph

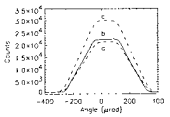

Figure 2. Rocking curves

Beam Harmonics In a Bent Laue-Laue Monochromator	X17B2

B. Ren (Med., BNL), Z. Zhong (NSLS), F.A. Dilmanian and X.Y. Wu (Med., BNL), L.D. Chapman and I. Ivanov (CSRRI)

One advantage of a bent Laue-Laue monochromator over the flat Laue-Laue for the MECT program (see accompanying abstracts) is the lower beam harmonic contamination. The harmonic ratio from two bent-Si<111>-CZ crystal was measured by the Compton scattering method, using a 1/80" thick Be target tilted to $\alpha = 52°$. A Ge detector positioned 90° to the beam measured the scattered beam, while an Ar-filled ion chamber upstream of the Be target monitored incident monochromatic beam, tuned to 41.7 keV. The white beam was filtered with additional 1.6 mm Cu to enhance the harmonic contents.

From the dynamical theory, the fundamental beam yield increases and the harmonic beam decreases at the intermediate bending range (3 - 50 m) as the bending radius is decreased. Our harmonic-ratio results from Ge detector were, about 20% below the predictions, except at ρ= 11 m, where they were 38% higher. The fundamental beam fluxes measured with Ge detector were 0.3-0.5 of the predictions of the code PEPO; the ion chamber results were 0.4-0.6 of PEPO. We suspect that the non-centered vertical position of slits in the white beam's path was one of the reasons for the low harmonic ratios and low beam fluxes. The imperfect alignment of the Ge detector's nozzle could also reduced the beam flux.

Compared with tuned flat-flat Si <111> crystals at this energy, these results showed 5 - 65 fold reduction of the harmonic ratio, and 8-25 fold increased beam flux. These characteristics of the new monochromator should substantially improve MECT's image quality.

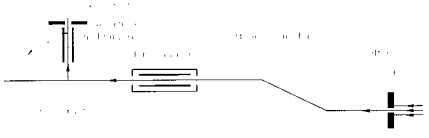

Figure 1. Compton scattering setup.

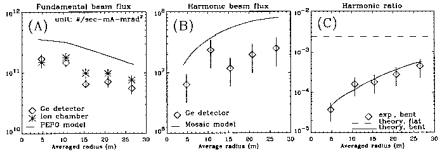

Figure 2. The fundamental and harmonic beam fluxes, and their ratio.

Energy Response Measurements of Dental CCD Sensor Systems Using Monochromatic X-Rays *	X17B2

K. Tokumori, S. Kanda, F. Toyofuku (Kyushu Univ.), K. Hyodo, M. Ando (KEK), Z. Zhong and W. Thomlinson (NSLS)

Several digital dental imaging systems have been developed by manufactureres of intraoral radiology equipment. They have the following advantages: no film development process; reduced radiation dose; digital image processing. This study investigated the energy response of CCD systems by using monochromatic synchrotron x-rays.

The energy responses of two types of CCD digital systems were studied: a Sens-A-Ray system without a scintillator (Regam Medical Systems, Sweden) and a dental visual x-ray imaging system (Matsushita Industrial Eq. Co.) with a scintillator (DVXIS). Monochromatic x-rays were reflected from a Si crystal to expand the beam to about 35 mm (w) x 40 mm (h) at energies of 28.8, 35.5, 45, and 55 keV. The dose rate was varied at each energy by use of Lucite absorbers between 10 and 24 cm thick. The exposure dose was measured with a shallow type ionization chamber (Victoreen). A short exposure time of 0.1 sec was used to minimize the CCD dark current effect.

The pixel values for a series of measurements at varying energies and exposure doses were averaged. The value of the pixel value, for a fixed dose, increased with decreasing energy. As the absorber dose rate decreased with the thicker absorbers, the ratio of the third order to the first order harmonic increased. The ratio estimated from the Lucite linear attenuation coefficient and the known white beam spectrum was very large. However, the influence of the third order harmonic x-rays on the Sens-A-Ray was about 30% at 28.8 keV and less than 5% at other energies. These small ratios were due to the low sensitivity of Si(the main element of the CCD) at the energies of the harmonics.

* Research supported (in part) by the USDOE Div. of Materials Sciences and Div. of Chemical Sciences.

In Situ Identification of Natural Diamond Inclusions with Synchrotron Microdiffraction	X17C

P. G. Conrad, R. J. Hemley, H. K. Mao, L. W. Finger, J. Hu, J. Shu (Carnegie Inst.), B. Harte, M Hutchison (U. of Edinburgh) and J. Harris (U. of Glasgow)

We have used a white synchrotron beam at X17C to obtain energy dispersive x-ray diffraction from natural diamond inclusions *in situ*, i.e., non-destructively. These detrital diamonds, from the São Luiz deposit in Mato Grosso, Brazil, are of geophysical importance because they are thought to have originated in the earth's lower mantle. Electron microprobe analysis (EPMA) on other São Luiz specimens indicates the chemical compositions of lower mantle phases such as (Mg,Fe)O, $MgSiO_3$ and $CaSiO_3$ together with lower pressure phases aluminous garnet and majorite. Because sample preparation for EPMA necessitates destructive polishing of the diamonds to expose the inclusions, any confining pressure signatures within the diamonds will be lost along with textural information. *In situ* structural analysis is an important advance in the study of crystalline inclusions within diamonds and other xenoliths because it enables us to examine samples of the Earth's mantle that are presumably free from alteration or contamination.

Each diamond is mounted on a chi circle, the physical dimensions of which constrain the range of omega values we may search using single crystal procedures. By rotating the two angles χ and ω, we can search for single crystal reflections which will appear as peaks in an energy dispersive pattern for a specific χ and ω when the diffraction condition is satisfied. After aligning the inclusion within the path of the X ray beam, we can adjust the inclusion's position with respect to the detector to optimize intensity of the diffracted beam. With the assistance of two Kirkpatrick-Baez x-ray focusing mirrors, we can achieve a very small beam size (about 11x15 microns). This is useful for searching for diffraction in very small inclusions that are close to one another.

A typical search for diffraction peaks takes us through an interval of $-20<\omega<45$ with $<\chi<180°$. Once peaks are roughly located, they are precisely centered with respect to both c and w. We calculate an orientation matrix for the diamond which is used in two ways: (1) to exclude diamond peaks from the inclusion peak list and (2) to look for epitaxial relationships between diamond and inclusion. Once two or more inclusion peaks are identified and matched with a prospective phase, they may be used to calculate an orientation matrix for the candidate which can, in turn, be used to search for further peaks at predicted diffraction conditions. Because diffraction intensities can vary, one must make frequent adjustments to the vertical and horizontal slits of the Canberra Ge detector , paying strict attention to signs of saturation such as truncated intensities and peak splitting (with respect to ω or χ).

An initial search of inclusions in four diamonds has revealed a range of crystalline character from poorly crystallized to single crystal to polycrystalline (with abundant peaks at a given χ and ω) . One diamond has been probed intensively and five inclusions (four of which share grain boundaries) have been identified using this technique. Three of the inclusions predominantly exhibit the diffraction lines of (Mg, Fe)O with a Mg/Mg+Fe ratio averaging 0.633. The presence of magnetite diffraction peaks epitaxially related to the (111) of the (Mg, Fe)O in all three grains probably implies an exsolution relationship. Two of the inclusions are clinopyroxene, though exact composition may not be inferred without corroborating evidence from some other analytical technique such as EPMA.

Disorder Induced Phase Transition of the Rare Gases in Porous Vycor Glass.*	X18A

D. W. Brown, P. E. Sokol (Penn. State U.) and S. N. Ehrlich (Purdue)

Recently a great deal of effort has been expended to study the effects of finite size and confinement on the properties of simple gases, liquids, and solids, achieved by adsorption into mesoporous materials. Examples of such mesoporous materials include sol-gel glasses, porous Vycor glass, zeolites, and of course rocks and cements. These porous media are of technological interest in fields such rheology, tribology, and materials research. The adsorbed samples provide a platform for fundamental studies of surface effects as well as molecular interactions with surfaces which is unattainable in bulk samples. While many measurements of macroscopic quantities such as the heat capacity of confined materials have been reported few microscopic measurements are available. To explore the effects of confinement on the structure of the rare gas solids we have carried out X-ray diffraction measurements of the structure of Ar and Kr confined to porous Vycor glass as a function of temperature. Bulk Ar and Kr crystallize into the fcc structure at 84 K and 116 K respectively and remain in this phase to absolute zero. At high temperatures confined Kr and Ar solidify into a disordered close packed structure as shown for Ar in figure 1. At low temperature the (200) peak along with sharp (resolution limited) companions to the high temperature peaks appear indicating a solid - solid phase transition that is not present in the bulk phase diagram. W scans reveal the nature of the sample responsible for the low temperature peaks to be large grain poly-crystallites rather than powder as is seen at high temperature. The inset to figure 1 shows the (200) peak with the cell at different orientations exemplifying the non-powder nature of the sample. Similar scans of Kr show analogous behavior. Figure 2 tracks the amplitude of the (200) peak as a function of temperature on warming. The (200) peak, characterizing the fcc structure, is seen to disappear at a reduced temperature of approximately 0.50 for both Kr and Ar. In summary we have shown that disorder induced through confinement of Kr and Ar to the pores of Vycor glass stabilizes a novel structure, disordered close packed, as well as spurs a solid - solid phase transition that is not present in the bulk phase diagram. * (Work was supported by the American Chemical Society Petroleum Research Fund under 31097-AC5 and U.S. DOE under DE-FG02-85ER45183.)

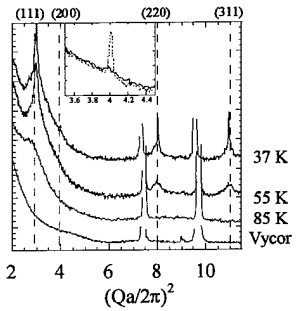

Figure 1.

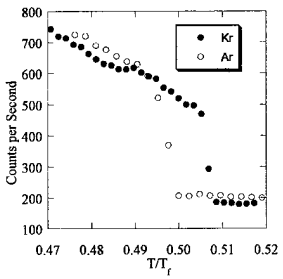

Figure 2.

The Structure of Rare Gases in Porous Vycor Glass *	X18A

D. W. Brown, P. E. Sokol (Penn. State U.) and S. N. Ehrlich (Purdue U.)

Recently a great deal of effort has been expended to study the effects of finite size and confinement on the properties of simple gases, liquids, and solids, achieved by adsorption into mesoporous materials. Examples of such mesoporous materials include sol-gel glasses, porous Vycor glass, zeolites, and of course rocks and cements. These porous media are of technological interest in fields such rheology, tribology, and materials research. The adsorbed samples provide a platform for fundamental studies of surface effects as well as molecular interactions with surfaces which is unattainable in bulk samples. While many measurements of macroscopic quantities such as the heat capacity of confined materials have been reported few microscopy measurements are available. To explore the effects of confinement on the structure of the rare gas solids we have carried out X-ray diffraction measurements of the structure of Ar and Kr confined to porous Vycor glass as a function of temperature. Bulk Ar and Kr crystallize into the fcc structure at 84 K and 116 K respectively and remain in this phase to absolute zero. The freezing points of the confined Ar and Kr, denoted by the appearance of sharp diffraction peaks, were found to be 65 and 100 K respectively, with the melting points of 70 and 106 K being somewhat higher. Figure 1 shows the scattering from the empty cell, liquid Ar and solid Ar at high and low temperature. At high temperature 55 K peaks corresponding to the fcc (111), (220), (311) , and (222) are apparent while the (200) peak is absent. This is characteristic of a disordered close packed structure. The scattering from confined Kr follow a similar pattern. At low temperature the (200) peak along with sharp (resolution limited) companions to the high temperature peaks ppear indicating a solid - solid phase transition that is not present in the bulk phase diagram. W scans reveal the nature of the sample responsible for the low temperature peaks to be large grain poly-crystallites rather than powder as is seen at high temperature. The inset to figure 1 shows the (200) peak with the cell at different orientations exemplifying the non-powder nature of the sample. Figure 2 tracks the amplitude of the (200) peak as a function of temperature on warming. The (200) peak, characterizing the fcc structure, is seen to disappear at a reduced temperature of approximately 0.50 for both Kr and Ar. In summary we have shown that disorder induced through confinement of Kr and Ar to the pores of Vycor glass stabilizes a novel structure, disordered close packed, as well as spurs a solid - solid phase transition that is not present in the bulk phase diagram. * (Work supported by the Amer. Chem. Soc. Petro. Research Fund under 31097-AC5 and U.S. DOE under DE-FG02-85ER45183.)

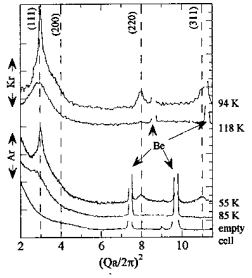

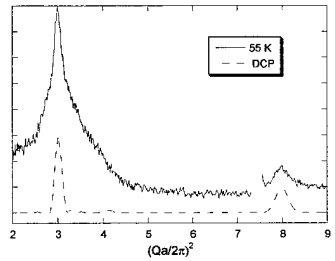

X-ray Scattering Studies of Liquid Crystalline Polymer Structure Under Shear*	X18A

W. Burghardt, D. Cinader, V. Ugaz (Northwestern U.), P. Mather and A. Romo-Uribe (USAF)

We have performed experiments at X18A under two general user proposals; both involve use of x-ray scattering to study th eability of applied shear flows to induce macroscopic molecular orientation in liquid crystalline polymers [LCPs]. This structural information is then used to provide insights into the rheological phenomena in these complex fluids. The first set of experiments focused on the structural origins of so-called "Region I" shear thinning, an anomaly observed in LPCs at low shear rates In one model system, nematic solutions of poly(benzyl glutamate) [PBG] in m-cresol, Region I is only observed beyond a critical concentration. In situ x-ray scattering measurements reveal that Region I is caused by the formation of a hexagonal phase, and is not a characteristic feature of nematic LCP rheology. Figure 1 shows the connection between rheological behavior and structure, showing equitorial scans of scattered intensity obtained during shear flow for four solutions at difference concentrations, as compared with independent measurements of rheology in the same solutions. As concentration increases, a shart peak associated with the hexagonal phase grows at the extense of the diffuse peak attributed to lateral packing correlations in the nematic phase.

In addition to establishing the origins of Region I shear thinning in this system, we have also observed that application of shear at high rates is able to effect a transition from the hexagonal phase back to the nematic phase.

The second set of experiments was targeted at extension of our room temperaure studies on LCP solutions to LCP melts, which require elevated temperatures. In collaboration with our colleagues from Phillips Laboratory, we performed experiments on a number of thermotropic LCPs using a melts shear cell customized for used in x-ray scattering experiments. *Work supported by NSF Grant CTS-9457083 and a DuPont Young Faculty Award.

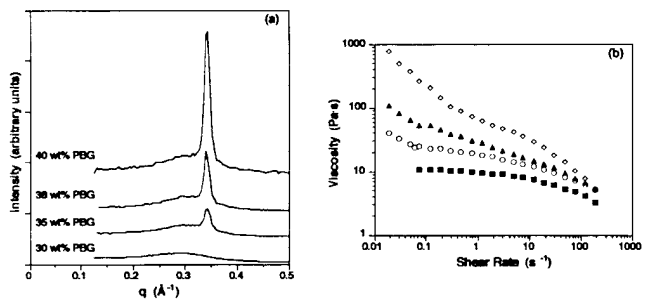

Figure 1. (a) Radial scattered intensity scans along equator measured under shear at a rate of 1 1/s. (b) Steady shear viscosity vs. shear rate for the same solutions as in (a)

Structural Studies of Self-Assembled Alkynyl and Organometallic Thin Film Materials	X18A

Ashok K. Kakkar (McGill U.)

An evaluation of the structure of molecularly self-organized thin films containing long chain rigid-rod alkynyl and dialkynyl chromophores via exclusive pi-pi interactions, is an essential and crucial step for any device applications based on such systems, in the field of optoelectronics, conductivity, photoresists etc. We have now established an efficient synthetic methodology to such supramolecular structures molecularly self-assembled on inorganic oxide surfaces.[1] Monolayers of a variety of alkynyl and dialkynyl chromophores with varied chain lengths and acetylenic microstructures were prepared on single crystal silicon wafers (1" x 3" single side polished, 95-105 mils thick). These thin films were first analyzed by in-house ellipsometry, followed by X-ray reflectivity studies on X18A beamline at NSLS synchrotron facility. In general, there is a good agreement in the thicknesses from X-ray reflectivity and ellipsometry measurements.[1-3] We have begun a study of the surface topochemical polymerization in these oriented alkynyl mono- and multilayered structures. Two of the major requirements for the latter process are orientation of alkynyl chromophores at an angle to the surface, and uniformity. X-ray reflectivity studies in combination with ellipsometry and FTIR-ATR are invaluable techniques to address these issues. We have also been interested in determining the effect of X-rays on the alkynyl thin films, since alkynyl chromophores are subject to radiation damage. In our future trips to BNL, we shall concentrate on the study of the structure of dialkynyl thin film assemblies before and after topochemical polymerization, to understand the mechanistic details of this phenomenon, and to develop a rational approach to materials based on alkynyl thin film. We have also begun to look at the effect of molecular order on the activity and selectivity of heterogenized homogeneous catalysis. A variety of organometallic thin films are self-assembled on flat surfaces and after establishing the degree of order in these thin films, their catalytic activity will be evaluated and compared with solution analogs. Our preliminary work on such thin films has shown that a positive role is played by the orientation of surface bound organometallic species in catalysis.[4-5]

1. C.M. Yam, A.K. Kakkar, J. Chem. Soc., Chem. Commun., 1995, 907-909.
2. C.M. Yam, S. Tong, A. Dickie, A.K. Kakkar, M.A. Whitehead, A. Richter and Pulak Dutta, Can. J. Chem., Special Issue, Invited Paper, 1998.
3. C.M. Yam, S. Tong, A.K. Kakkar, A. Richter, Pulak Dutta, manuscript in preparation.
4. M.G.L. Petrucci, A.K. Kakkar, J. Chem. Soc., Chem. Commun., 1995, 907-909. 5. M.G.L. Petrucci, A.K. Kakkar, Organometallics, submitted for publication.

Role of Oxygen Partial Pressure in Texture Development of Lead Zirconate Titanate Thin Films *	X18A

J.L. Norton, E.B. Slamovich, and G.L. Liedl (Purdue U.)

The formation of a transient lead-platinum intermetallic phase, Pt_3Pb, is found to be instrumental in the development of (111) orientations of $Pb(Zr_{0.60}Ti_{0.40})O_3$ ("60/40 PZT") thin films derived by metallo-organic decomposition (MOD) on (111)-oriented Pt-coated Si substrates. The Pt_3Pb phase is found to form in a (111) orientation, which then enhances the (111) orientation of 60/40 PZT. This phase was investigated by using a combination of slower heating rates (25 °C/min) than those used in "rapid thermal processing" (RTP) processes, and controlled partial pressures of oxygen. It was found, by switching the process atmosphere from oxidizing to reducing (relative to Pb), that it is necessary that the Pt_3Pb phase be present at the time of PZT crystallization but should not be present in such quantity that the growing film is lead-deficient, leading to the formation of a large amount of pyrochlore.

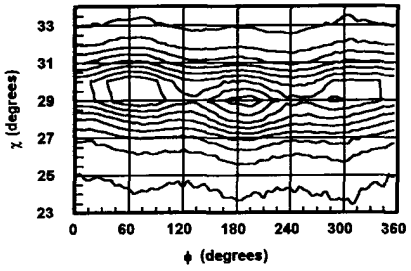

Figure 1. Three fold orientation of the intermetallic phase Pt_3Pb formed on (111) oriented Pt is consistent with (111) orientation of the intermetallic phase. The (311) poles are shown on the left and the (100) poles on the right.

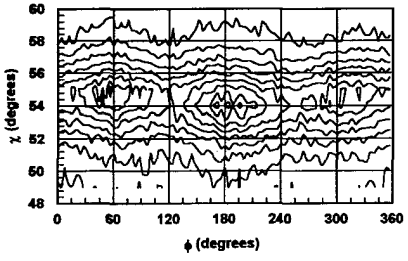

Figure 2.

* This work is supported by U.S. DOE Grant No. DE-FG02-85ER45183

Thermal Diffuse Scattering in Indium *	X18A

A. W. Overhauser, A. S. Bakulin and S. N. Ehrlich (Purdue University)

Single-crystal x-ray diffraction on indium led to the discovery of 118 half-integral *hkl* reflections at room temperature. In order to determine whether these unexpected diffraction peaks arise from a broken symmetry or some other cause, their temperature dependence was measured between 20 and 200K on beam line X18A at the NSLS. It was found that the "satellite" intensities were essentially linearly proportional to T_j so their origin can be attributed to thermal diffuse scattering from the lowest phonon mode near the (1/2,1/2,1/2) points of the Brillouin zone boundary. A complete lattice-dynamics calculation is required (and is in progress) to investigate whether this satellite-like structure requires the presence of a spin-density-wave broken symmetry or not.

* This work is supported by U.S. Department of Energy Grant No. DE-FG02-85ER45183.

Binding Energy of Aligned Glass on Thin Films of Liquid Crystals *	X18A

D. E. Silva, P. E. Sokol, J. S. Patel (Penn. State U.), and S. N. Ehrlich (Purdue U.)

Liquid crystals are vital in industry today, being used for liquid crystal displays in such electronics as calculators and laptop computers. However, the structure, in its various phases, still is not completely known and is worth further study.

We have begun to study the effects of surface preparation on the structure of the Smectic-A (S_A) phase of the liquid crystal, M24. Number 1 glass is spin coated with three parts ACT600 to one part AL1051 and then baked to evaporate the solvent. The glass is rubbed to give a preferred orientation to the glass. The glass is then cut and glued 30 microns apart from one another such that the polymer is on the inside of each piece of glass and oriented in the same direction with respect to one another. The liquid crystal is heated into the liquid phase and the capillary forces of the glass are used to draw the crystal between the two glass plates. Using optical measurements, it is easily seen that surface alignment of the liquid crystals is accomplished.

Our sample was heated into the liquid phase (>360K) and slowly cooled into the S_A phase (327.5K-340.0K). X-ray measurements showed the d-spacing to be approximately 32Åin close agreement with accepted measurements. It was found that as the temperature is decreased within the S_A phase, the layers begin to form a chevron structure (see appropriate progress report). The figure below shows the diffraction peaks as a function of k, where k is the Miller index corresponding to the momentum in the plane, perpendicular to the glass walls. The dotted line is a scan with only the alignment forces of the glass at work, while the solid line is a scan of both the alignment forces of the glass AND a magnetic field. The magnetic field was created by two rare earth magnets, which were positioned such that the field aligned the liquid crystals in the same direction as the glass. Clearly, the shape of the peaks is changed when a magnetic field is introduced.

Future work will include the use of a good electromagnet, so that different magnetic fields can be compared. This will enable the binding energy of the glass to be determined.

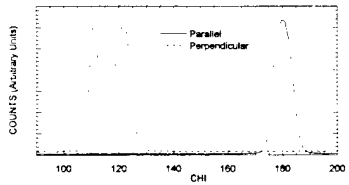

Figure 1. This shows the momentum in the plane, perpendicular to the glass walls. The dotted line is a plot with the liquid crystals aligned solely by the glass. The solid line is a plot with the crystals under surface alignment and alignment from a magnetic field.

* This work supported by the American Chemical Society Petroleum Research Fund under grant No 31097-AC5 and U.S. DOE Grant No. DE-FG02-85ER45183

Chevron Structure in the Smectic-A Phase of the Liquid Crystal M24 *	X18A

D. E. Silva, P. E. Sokol, J. S. Patel (PA. State U.), and S. N. Ehrlich (Purdue U.)

Liquid crystals are vital in industry today, being used for liquid crystal displays in such electronics as calculators and laptop computers. However, the structure, in its various phases, still is not completely known and is worth further study.

We have begun to study the effects of surface preparation on the structure of the Smectic-A (S_A) phase of the liquid crystal, M24. Number 1 glass is spin coated with three parts ACT600 to one part AL1051 and then baked to evaporate the solvent. The glass is rubbed to give a preferred orientation to the glass. The glass is then cut and glued 30 microns apart from one another such that the polymer is on the inside of each piece of glass and oriented in the same direction with respect to one another. The liquid crystal is heated into the liquid phase and the capillary forces of the glass are used to draw the crystal between the two glass plates. Using optical measurements, it is easily seen that surface alignment of the liquid crystals is accomplished.

Our sample was heated into the liquid phase (¿360K) and slowly cooled into the S_A phase (327.5K-340.0K). X-ray measurements showed the d-spacing to be approximately 32Åin close agreement with accepted measurements. It was found that as the temperature is decreased within the S_A phase, the layers begin to form a chevron structure. Figure 1 shows the diffraction peaks as a function of k, where k is the Miller index corresponding to the momentum in the plane perpendicular to the glass walls. If the layers stayed perpendicular to the glass walls, you would expect one peak centered at k=0. The solid line is a scan with the temperature at 340K, just below the nematic phase. Generally, the layers are perpendicular to the glass walls, but multiple peaks can be seen. The dashed line is a scan with the temperature at 334K. The two peaks clearly show an increase in the chevron structure that continues to increase at lower temperatures, especially at 318K (dotted line) where the liquid crystal has supercooled.

More complete analysis will give analytical values to the shape of the momentum curves in all three directions: normal to the planes, in the plane and normal to the glass, and in the plane and parallel to the glass.

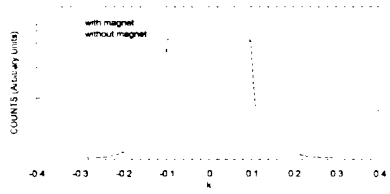

Figure 1. This shows the momentum in the plane, perpendicular to the glass walls for a number of different temperatures. Note the increase in the chevron structure of the layers as the temperature is decreased.

* Work supported by The American Chemical Society Petroleum Research Fund under grant No 31097-AC5 and U.S. DOE Grant No. DE-FG02-85ER45183.

Competition Between Surfaces in Thin Films of Liquid Crystals * | X18A

D. E. Silva, P. E. Sokol, J. S. Patel (PA. State U.), and S. N. Ehrlich (Purdue U.)

Liquid crystals are vital in industry today, being used for liquid crystal displays in such electronics as calculators and laptop computers. However, the structure in its various phases still is not completely known and is worth further study.

We have begun to study the effects of surface preparation on the structure of the Smectic-A (S_A) phase of the liquid crystal, M24. Number 1 glass is spin coated with three parts ACT600 to one part AL1051 and then baked to evaporate the solvent. The glass is rubbed to give a preferred orientation to the glass. The glass is then cut and glued 30 microns apart from one another such that the polymer is on the inside of each piece of glass and oriented normal to one another. The liquid crystal is heated into the liquid phase and the capillary forces of the glass are used to draw the crystal between the two glass plates. Using optical measurements, it is easily seen that surface alignment of the liquid crystals is accomplished.

Our sample was heated into the liquid phase (>360K) and slowly cooled into the S_A phase (327.5K-340.0K). X-ray measurements showed the d-spacing to be approximately 32Åin close agreement with accepted measurements. When rotating the sample, chi is defined as the angle such that the normal of the planes is rotating radially about the x-ray beam. The sample was mounted such that if the liquid crystals aligned themselves to one of the glass slides, one would expect to see a signal at either χ=90° or 180°. As one would expect, the competition between the surface forces of the two pieces of glass should cause the liquid crystals to align themselves somewhere in between these two values. The figure below shows two runs; one with parallel alignment (solid line) and one with perpendicular alignment (dotted line). The parallel glass was prepared such that a peak would be seen at either χ=0° or 180° and indeed, we saw a peak centered at 180°. The perpendicular glass showed multiple peaks centered at 115°. Clearly, there is a competition between the walls which causes the liquid crystals to settle between 90° and 180°. The multiple peaks show that the liquid crystals have not formed into nicely formed layers that stretch from wall to wall. Most likely, the liquid crystals closest to each wall are turned slightly in the direction of the orientiation of the glass.

More complete analysis will give analytical values to the shape of these curves, especially the perpendicular sample where there is, clearly, at least three peaks.

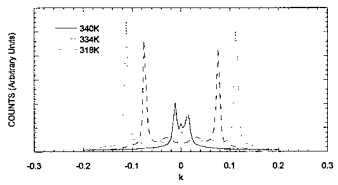

Figure 1. This shows two different scans; one with the glass aligned parallel and one perpendicular. The liquid crystals align nicely with the parallel alignment, but experience a competition between the surfaces of the perpendicular alignment.

* Work supported by the American Chemical Society Petroleum Research Fund under grant No 31097-AC5 and U.S. DOE Grant No. DE-FG02-85ER45183

Long-Range Order and Critical Diffuse Scattering from the Tricritical System V-H near the β_1-β_2-Phase Transition * | X18A

J. Trenkler, P. Chow, U. Klemradt, S. C. Moss (U. of Houston), D. Lott (BNL-NSLS), S. Ehrlich (Purdue U.), R. Hempelmann (U. des Saarlandes)

The tricritical behavior of a single domain single crystal of $VH_{0.525}$ and $VH_{0.547}$ has been studied by x-ray scattering. We first measured the tricritical order parameter exponent β of $VH_{0.547}$ by the temperature dependence of the integrated Bragg-intensity of superstructure reflections below the critical temperature T_C. We found that $VH_{0.547}$ passes a large two-phase coexistence region deduced from the appearance of a second fundamental reflection in the radial intensity distribution around the fundamental reflection (0 3 $\bar{3}$) associated with the β_2-high temperature phase. The existence of the two-phase region is also shown by a sudden drop in the integrated intensity of superstructure reflections as shown in fig. 1. Above the critical temperature, weak critical diffuse scattering (CDS) was measured indicating that the data is taken in the vicinity of a tricritical point.

With another single domain single crystal, $VH_{0.525}$, we recently observed a remarkable change in the intensity line shape of the critical diffuse scattering in the longitudinal [0 1 $\bar{1}$] scan at T=T_C+6.2 K in an experiment done at the NSLS on X14A. At X18A, the Q- and temperature dependence of this profile was investigated at Q=10.64 1/Å with ΔQ=0.14 1/Å between T=T_C+4 K and T=T_C+9 K at a different penetration depth. Fig. 2 gives an example of the measured intensity profile consisting of a sharp and a broad component at T=T_C+6.6 K of the (0 5/2 $\bar{5}$/2)-superstructure reflection.

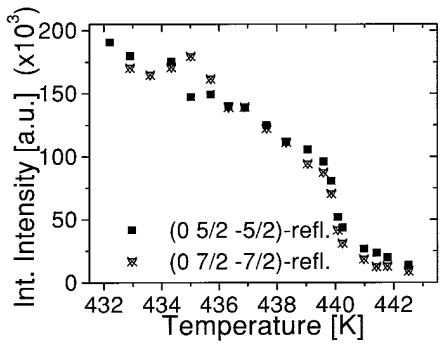

Figure 1. Integrated intensities of the (0 5/2 $\bar{5}$/2) and (0 7/2 $\bar{7}$/2) superstructure reflections in a heating run.

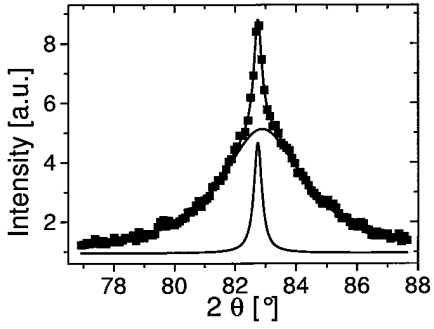

Figure 2. Critical diffuse scattering for the (0 5/2 $\bar{5}$/2) superstructure reflection in [0 1 $\bar{1}$] in a heating run at T=T_C+6.6 K with T_C=444.5 K.

* This work was supported by the NSF on DMR92-08450

Preferred Orientation and Anisotropy of Piezoelectric Materials * | X18A

Shan Wan and Keith J. Bowman (Purdue University)

Piezoelectric materials rely upon development of preferred orientation from the alignment of domains during poling. The poling effect can be eliminated by thermal treatments. Small differences in the relevant (200) and (002) peaks, fine domain structures and modest degrees of orientation in tetragonal piezoelectric materials make four-circle measurements of texture on a conventional diffractometer of only marginal value. In this investigation the preferred orientation of poled and thermally-depoled Navy-II and Navy-VI PZT focusing on (002)/(200) peaks was measured. The longer x-ray wavelength, highly collimated source and the high intensity of synchrotron light enabled reliable measurements of domain orientation.

* This work is supported by U.S. Department of Energy Grant No. DE-FG02-85ER45183.

Structural Evolution of $Li_xMn_2O_4$ in Lithium ion Battery Cells Measured *In situ* Using Synchrotron X-ray Diffraction Techniques* | X18A

X. Q. Yang, S. Mukerjee, X. Sun and J. McBreen (BNL)

With the increased demand for portable devices the commercial and strategic requirements for higher energy efficient batteries are paramount. Among such promising technologies are the lithium ion rocking chair type rechargeable cells. However, cost, cycle life and safety considerations remain a matter of technical concern and need to be addressed based on specific components used. Our interest in the $Li_xMn_2O_4$ cathode material stems from the promise of lower cost (replacement of the currently used $LiCoO_2$) material, however the cycle life characteristics remain irreproducible, showing great sensitivity to preparation conditions. Our studies on the structural and electronic (analogous XAS studies) evolution in these material during intercalation of lithium are aimed at providing answers to these important structure property relationships.

Recent studies on $Li_xMn_2O_4$ prepared at different temperature and annealing conditions have revealed differences in their performance. nevertheless, the conventional x-ray diffraction could not distingiush any differences in the initial structural characteristics. The Li solid state N.M.R studies however revealed differences in lithium site occupancies in samples prepared at different temperatures. The it/ in situ studies on the structural evolution in these material were carried out in the transmission mode at X18A. The preliminary results indicate that both the high (850°C) and low temperature (650°C) show coexistence of two cubic phases when x=0.5 in $Li_xMn_2O_4$. These phases however coalesce into a single cubic phase at the end of charge and discharge. As evident from figure 1, which describes the structural evolution in a sample prepared at 650°C and annealed for 48 hours, the transition from one phase to the other is not smooth and their is evidence of residual lithium remaining after the transition. Example of this behavior is shown in figure 1. Further studies are planned to correlate the effects of other preparation conditions in the strutural evolution of these spinel material. * [Work supported by U. S. DOE contract No. DE-AC02-76CH00016.]

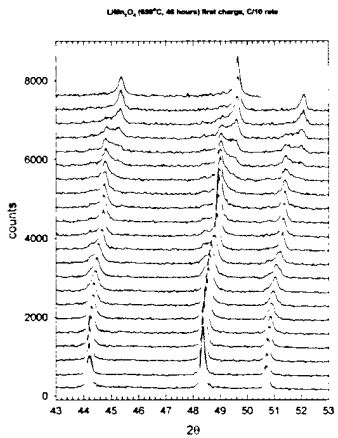

Anomalous Transmission of X-Rays in a Quasicrystal * | X18A

Y. Zhang, S. N. Ehrlich and R. Colella (Purdue U.)

Anomalous Transmission (AT) of x-rays in a quasicrystal was observed for the first time by S.W. Kycia et al. [1]. It is a surprising result, because the absence of periodicity would seem to prevent the conditions needed for the onset of AT. In this work we have determined the absolute value of the AT iffracted beam in a perfect $Al_{71.0}Pd_{20.5}Mn_{8.5}$ quasicrystal, and compared with the theory. The crystal was 0.385 mm thick and the x-ray energy was 9.0 KeV The normal attenuation factor for a beam incident perpendicularly to the surface is about 1.7 x 10^{-9}. The incident beam intensity, at beamline X18A, was evaluated by measuring the (222) reflection with a perfect germanium crystal. The (222) reflection is very weak - it is a forbidden reflection - and its structure factor is well known because it has been measured by several people. The absolute value of the integrated intensity for the (6 4 0 0 4 6) reflection was compared with the value calculated from dynamical theory and found at least one order of magnitude below the theoretical value. Work is in progress to explain the possible reasons for such a discrepancy.

[1] S.W. Kycia, A. I. Goldman, T. A. Lograsso, D. W. Delaney, D. Black, M. Sutton, E. Dufresne, R. Bruning and B. Rodricks, Phys. Rev. B **48**, 3544 (1993).

* This work is supported by U.S. Department of Energy Grant No. DE-FG02-85ER45183.

Debye-Waller Factors in a Quasicrystal * | X18A

Y. Zhang, J. Sutter, S. N. Ehrlich and R. Colella (Purdue U.)

The mean square vibrational amplitude $< U^2 >$ for two reflections located on a twofold axis of an icosahedral quasicrystal $Al_{71.0}Pd_{20.5}Mn_{8.5}$ have been determined between room temperature (RT) and 20 K. The Q values for the two reflections (= 2 $\sin\theta/\lambda$) are: Q1=1.278 $Å^{-1}$ and Q2=2.068 $Å^{-1}$. The integrated intensities of the two reflections were measured as a function of temperature, using the Bragg case of diffraction, on a large polished quasicrystalline slab. The logarithm of the integrated intensity is linear, proportional to temperature, near and below RT, and tends to saturate to a constant value at low temperatures, an effect of the zero point energy. It is assumed that $< U^2 >$ is contributed mostly by low frequency acoustic modes, for which the atoms of Al, Pd and Mn vibrate together. Figures 1 and 2 show that, indeed, $< U^2 >$ is linear with temperature for both reflections above 100 K, but at low temperatures both plots depart significantly from Debye theory. In one case $< U^2 >$ is greater than the theoretical value, in the other case it is smaller. This behavior is reminiscent of that of layered crystals (1) such as graphite or TaS_2, in which the experimental values of $< U^2 >$ are always smaller than those predicted by Debye theory. In the case of layered crystals the anomaly was explained by considering the effect of reduced dimensionality and anisotropy. The same arguments cannot be applied to an icosahedral quasicrystal such as Al-Pd-Mn, supposed to be perfectly isotropic. Work is in progress to measure other reflections, and to understand the physical origin of non-Debye behavior in a quasicrystal.

[1] S.M. Hsieh and R. Colella, Solid State Commun., **63**, 47-50 (1987).

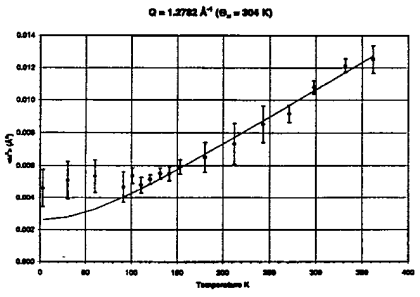

Figure 1.

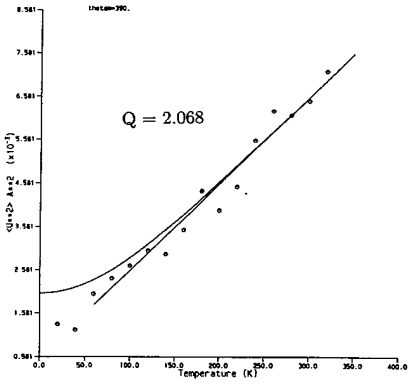

Figure 2.

* This work is supported by U.S. DOE Grant No. DE-FG02-85ER45183.

X-ray Absorption Study of Nickel in FCC Catalysts | X18B

S. R. Bare, A. Z. Ringwelski, F. S. Modica (UOP LLC)

Fluid catalytic cracking (FCC) is a process for the conversion of higher molecular weight hydrocarbons into lighter, more-valuable products through contact with a powdered catalyst at the appropriate process conditions. The reactions are rapid: only a few seconds of contact time is necessary. Simultaneously with the desired reactions, coke is accumulated on the catalyst surface. This coke is combusted to rejuvenate the catalyst. However, cracking of heavy hydrocarbons leads to a problem: the high metal content, mainly nickel and vanadium, of these fractions accumulate on the catalyst with time. Nickel is a catalyst for dehydrogenation reactions, which lead to an increase in coke and hydrogen yields. UOP has used in situ XANES at the Ni K-edge to study the reducibility of Ni in a series of commercial equilibrium FCC catalysts that are heavily contaminated with Ni. Figure 1 shows the Ni K-edge XANES of a commercial REY equilibrium catalysts following in situ reduction in hydrogen at 700°C for 0 min. (as received), 3 min., 15 min., and 45 min. The results indicate that Ni is reducible under these conditions. The Ni K-edge XANES spectrum of the as-received material is similar to that of a nickel aluminate, whereas there are dramatic changes in the in situ reduced spectra which are a combination of Ni metal and Ni aluminate. The authors have studied REY equilibrium catalysts with varying Ni loading and different reduction temperatures in addition to reduction times. These studies illustrate that XANES is a powerful tool for following the in situ oxidation states of Ni in FCC catalysts.

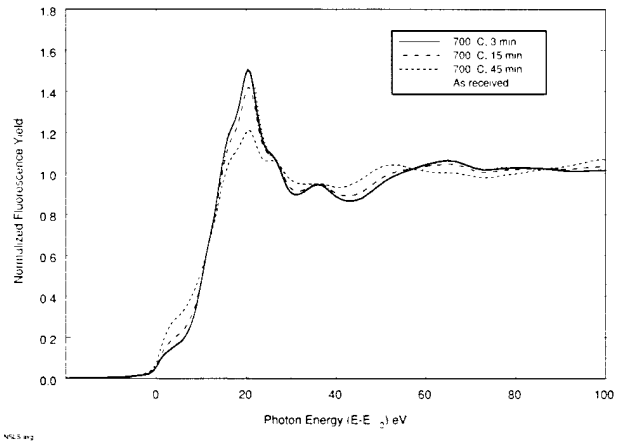

Figure 1. Ni K-edge XANES of a commercial equilibrium FCC catalyst.

Characterization of a Si(Li) Detector for the SIXA Array | X18B

T. Tikkanen, K. Hamalainen, and S. Huotari (U. of Helsinki, Finland)

We have studied the X-ray response of a Si(Li) detector element for the SIXA spectrometer array which is a focal plane detector for the SODART X-ray telescope onboard the Spectrum-X-Gamma satellite. Energy spectra were recorded using monochromatized synchrotron radiation ranging from 7 to 21 keV, yielding the detector lineshapes for the upper part of the detector's energy range (0.5–20 keV). Special attention was paid to the photon energy region above the L_3 absorption edge of gold, because the cathode electrodes of the Si(Li) elements are formed by gold-palladium alloy contact layers and the equivalent thickness of gold can be measured by observing the characteristic L-shell X-rays of gold excited by the primary radiation. The results obtained at 4 different photon energies below the L_2 edge yield an average value of 22.4 ± 3.5 nm which is consistent with the earlier result extracted from detection efficiency measurements.

Bond-length Distortions in Strained-semiconductor Alloys | X18B

J.C. Woicik, J.G. Pellegrino, and B. Steiner (NIST) K.E. Miyano (Brooklyn U.) S.G. Bompadre and L.B. Sorensen (Washington U.) T.-L. Lee (Northwestern U.) S. Khalid (NSLS)

Extended x-ray absorption fine structure performed at the In-K edge has resolved the outstanding issue of bond-length strain in semi- conductor-alloy heterostructures. We determine the In-As bond length in a buried 213 A $Ga_{0.78}In_{0.22}As$ layer grown coherently on GaAs(001) to be 2.581 +/- 0.004 A. This bond length corresponds to a strain- induced contraction of 0.015 +/- 0.004 A relative to the In-As bond length in bulk Ga1-xInxAs of the same composition; it is consistent with a simple model which assumes a uniform bond-length distortion in the epilayer despite the different In-As and Ga-As bond lengths.

XANES Analysis of Ti-V-Silicalites | X19A

S. R. Bare, A. Z. Ringwelski, F. S. Modica, L. Nemeth (UOP LLC)

The partial oxidation of propylene to propylene oxide is an important industrial process. Currently, no direct synthesis route to propylene oxide is practiced commercially. The isomorphous framework titanium-substituted silicalite (MFI) has been shown to be selective for the epoxidation reaction which uses hydrogen peroxide as an environmentally clean oxidant. Research at UOP has focused on synthesizing a more-active epoxidation catalyst with the MFI structure, which contains both Ti and V. These catalysts exhibit an excellent yield of propylene oxide using hydrogen peroxide as the oxidant. UOP has used XANES at the Ti and V K-edges to characterize these materials. Figure 1 shows the Ti K-edge XANES of several reference materials and two Ti-V-silicalite catalysts. The spectra of the catalysts are consistent with all of the Ti being in the MFI framework. Figure 2 shows the V K-edge XANES of two V-silicalite catalysts and several V-containing reference materials with different V oxidation state and symmetry. These data, which are being used to guide the synthesis program, indicate that the V is present in oxidation state +5 and is four fold coordinated.

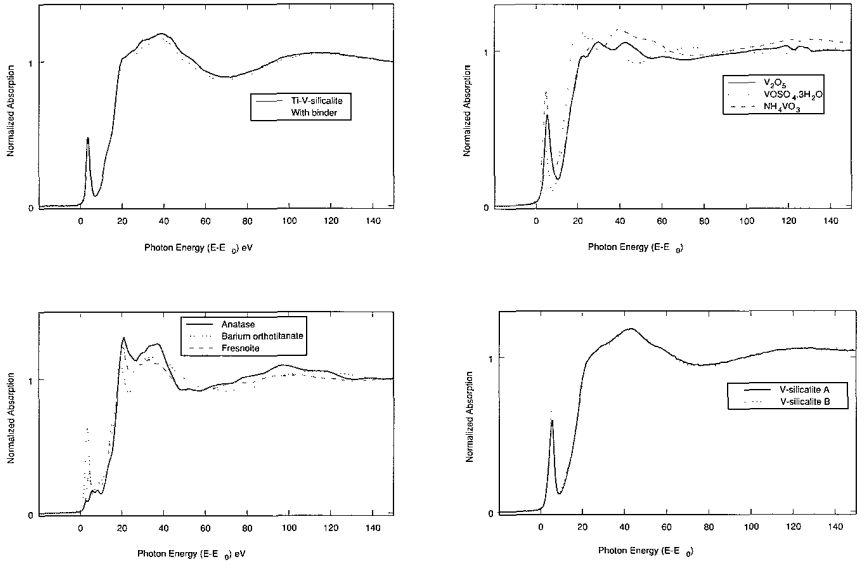

Figure 1. Ti K-edge XANES of Ti-V-silicaltes and reference materials.

Figure 2. V K-edge XANES of V-silicalites and reference materials.

X-ray Absorption Spectroscopy of Cesium Modified Catalysts | X19A

E.J. Doskocil and R.J. Davis (U. of Virginia)

Alkali modified zeolites are materials useful in heterogeneous catalysis in which base strength increases with increasing electropositivity of the alkali cation. Addition of occluded alkali has been found to further increase the surface basicity. Being able to understand how Cs, the most electropositive alkali, interacts with the zeolite framework on a molecular level would aid in understanding how cesium influences the basic character of the zeolite. We have therefore used XAS at the cesium L edges to probe the local environment of cesium for a variety of Cs modified catalysts.

The Cs L_{III} edge occurred within ± 0.5 eV for each compound and catalyst studied, indicating an electronic state of Cs^{+1} for these materials. As seen in Figure 1, the white line intensity for the cesium form of zeolite X exhibits a higher white line intensity than each of the Cs compounds studied. This indicates a larger density of unoccupied 5d states for cesium present in supported samples than in bulk compounds, showing that cesium behaves more like a free-ion in the cesium modified catalysts.

Figure 2 shows the EXAFS spectra for a few of the cesium compounds and catalysts, which is complicated by the presence of a double excitation peak about 100 eV above the edge. The compounds have similar EXAFS spectra. The zeolitic materials contain an additional oscillation in their spectra before the double excitation which is not observed for the compounds studied. The cesium modified carbon catalyst shows an EXAFS spectrum in which the frequency is less than that observed for the zeolite cases, indicating a smaller interatomic distance for cesium in the micropores of carbon than for cesium in the zeolite cages.

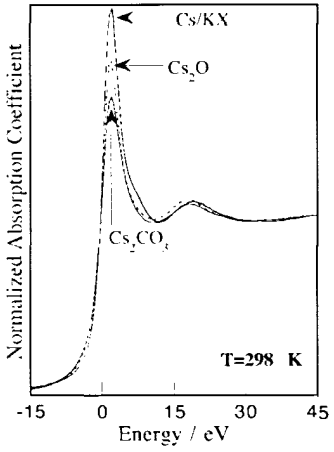

Figure 1. XANES of Cs/KX, Cs_2O and Cs_2CO_3.

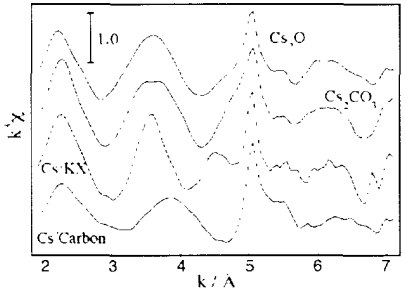

Figure 2. EXAFS of various Cs catalysts and compounds.

XANES Characterization of Soil Phosphorus | X19A

D. Hesterberg, W. Zhou, S. Beauchemin*, and D. E. Sayers (NC State and *Ag-Canada)

Excessive levels of soil phosphorus derived from animal waste applications to agricultural soils are of concern because P discharged from these soils may deteriorate surface water quality. Soils typically have a limited capacity to bind phosphate by surface adsorption. However, thermodynamics predicts that the solubility of solid-phase precipitates is independent of the amount of the precipitate present. Thus, the formation of precipitates such as Ca-, Al-, or Fe-phosphates in soils may serve as a sink for high levels of added P. The objective of this study is to determine whether precipitates of Ca-phosphate (at pH ¿7) or Fe- or Al-phosphates (at pH ¡7) occur in soils containing high levels of phosphorus. Pairs of soil samples collected from different regions of Quebec and having similar total P concentrations (29 to 72 mmol P/kg) but different pH levels were analyzed at the P K-edge at Beamline X19A, along with synthetic Ca-, Fe-, and Al-phosphates and other standards. Phosphorus K-XANES spectra in Fig. 1 show that each of the three mineral standards have distinguishing spectral features, such as a pre-edge feature on the strengite (FePO42H2O) spectrum and a shoulder on the high-energy side of the white-line peak in the amorphous Ca-phosphate spectrum. Soil spectra indicated differences in the average local molecular bonding of phosphorus (Fig. 1). For example, the soil having pH 7.6 (43 mmol P/kg) has a broad shoulder on the white-line peak that may be indicative of Ca-phosphate. This feature is not evident in the spectrum from the soil of pH 6.3 (42 mmol/kg). The soil spectra probably result from multiple P phases that might be resolved by additional XANES analyses coupled with soil fractionation procedures designed to concentrate different phases.

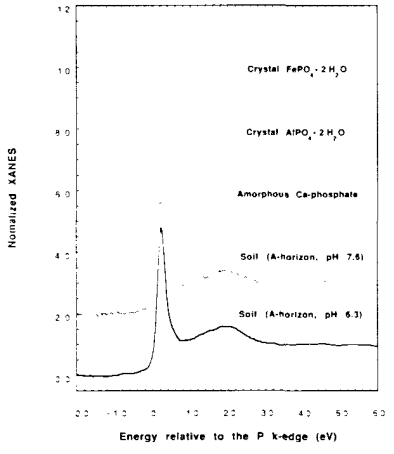

Figure 1. Normalized P K-XANES spectra of samples from the A horizon of soils along with standards of phosphate mineral phases.

In Situ Characterization of the Reduction of Rh / $Ce_XZr_{1-X}O_2$ *	X19A

S.H. Overbury, D.R. Huntley, D.R. Mullins (ORNL) and G. Glavee (Lawrence U.)

In automotive catalysts, ceria is used as an oxygen storage/release media to aid in maintaining high conversions during oscillations in air/fuel ratio. Recently, it has been reported that doping Zr into the ceria enhances the oxygen storage capacity of the oxide [1]. We have measured this enhancement by in situ XANES and find that the presence of Rh further enhances reducibility.

High surface area $(Ce_{1-x}Zr_x)O_2$ where x=0.0-0.5 were prepared by sol-gel techniques and hypercritical drying. Portions of the samples were impregnated with $Rh(NO_3)_3$. After calcining in air at 800 K, the catalysts had surface areas in excess of $100m^2/g$. Samples were suspended in an alcoholic solution and dispersed on the surface of BN pellets. The pellets were placed in a quartz tube reactor under flowing He, hydrogen or air. X-ray absorption at the Ce L_{III} edge was used in transmission mode to distinguish the presence of Ce^{+3} and Ce^{+4}.

Figure 1a shows typical Ce L_{III} edge x-ray absorption spectra of one of the samples as its temperature is increased in H_2/He. Various changes indicative of reduction from Ce^{+4}. to Ce^{+3} are observed including a decrease in the intensity of the peak labeled C. The intensity of this peak above background is indicative of the extent of reduction of the samples. Results are shown in Figure 1b for three different catalysts vs reduction temperature. It is seen that adding Zr to the CeO_2 decreases the temperature required for reduction and increases the extent of achievable reduction. Addition of Rh further catalyzes the reduction process.

[1] P. Fornasiero et al., J. Catal. 164 (1996),173.

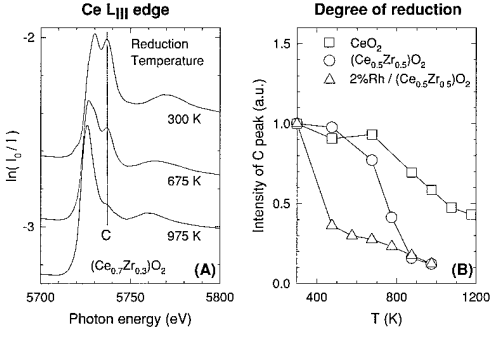

Figure 1. A) Ce L_{III} XAS spectra recorded during the reduction of $(Ce_{0.7}Zr_{0.3})O_2$. B) The degree of reduction vs temperature for several ceria based catalysts.

* Research sponsored by U. S. Department of Energy, Division of Chemical Sciences, Office of Basic Energy Sciences, under contract number DE-AC05-96OR22464 with Oak Ridge National Laboratory, managed by Lockheed Martin Energy Research Corp.

Observation of a Novel 4-Layer Superlattice in a Smectic Liquid Crystal Using Anomalous Diffraction	X19A

R. Pindak (Bell Labs), A.M. Levelut (Orsay), P. Barois (CRPP), P. Mach (Univ. of Minnesota), and L. Furenlid (NSLS)

Classical x-ray diffraction experiments cannot distinguish between variants of the chiral Smectic-C (SmC*) liquid crystal phases since the tilted molecules in the fluid layers of these variants have identical projected electron density profiles with only the tilt direction changing between layers. Nonetheless, by working close to an absorption edge, classical extinction rules no longer hold and it is possible to distinguish between the variants.

To test this hypothesis, we studied the n=11 (C_{11}) member of a sulfur containing thiobenzoate liquid crystal. In bulk samples, C_{11} exhibits the whole sequence of SmC* variants. A 200 layer freely suspended film of C_{11} was prepared in situ in an oven mounted on a two circle diffractometer. Measurements were performed at the maximum of the sulfur absorption peak (Eo). Above 103 degC, in a qz-scan where z is normal to the layers, two diffraction peaks were observed corresponding to the first and second order reflection from the layer planes (qz = qo and 2 qo). At lower temperatures down to crystallization at 90 degC, additional sharp and resolution limited peaks were seen at qz = 0.5 , 0.75 , 1.25 , 1.5 , 1.75 , and 2.25 qo. Fig.2 shows, for the 1.75 qo peak, that the intensity of the satellite peaks decreased as the energy was moved more than 7eV from Eo. The diffraction spectrum observed between 90 and 103 degC is characteristic of a four layer superlattice with a 4_1 or 4_3 symmetry. We propose that this novel superlattice has the following structure shown in Fig.1: in each layer, the molecules are tilted at the same angle with respect to the layer normal but the projection of the molecules forms a helical array of four layers pitch. In conclusion, we unambiguously demonstrated that anomalous scattering can distinguish the SmC* variants as well as observed the occurrence of a novel fourfold helical symmetry.

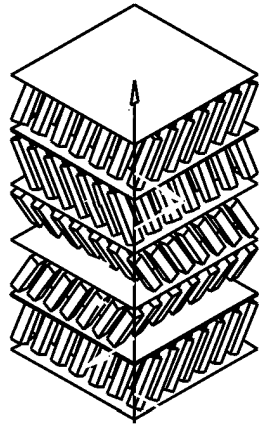

Figure 1.

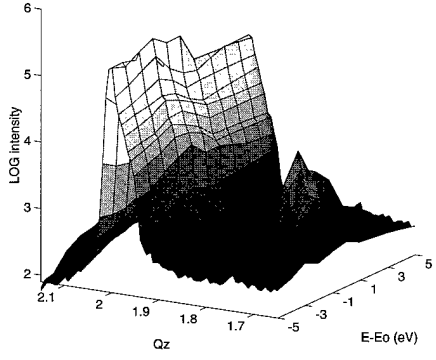

Figure 2.

Characterization of Sulfur Oxidation States in Soil Humic Acid | X19A

W. Zhou, D. Hesterberg, K. Hutchison, and D. E. Sayers (NC State)

Past research indicates that sequestering of heavy metal contaminants by reduced forms of sulfur, especially inorganic sulfides, reduces the toxicity of metals in aquatic sediments. The role of metal sulfur bonding to both inorganic and organic sulfur forms in soils is not well understood, but could impact the chemistry of heavy metals in contaminated soils. The objective of this study was to determine whether chalcophilic metals preferentially bind to organic sulfur functional groups in soil organic matter. Sulfur-rich humic acid (HA) was extracted from soil from a coastal marine wetland and reacted in aqueous solution with Cu(II) or Hg(II) at pH 5.6. The molar ratio of organic S to metal was 4.25, and the total sulfur concentration in the suspensions was 8.5 mmol/kg. Sulfur K-XANES analyses done at Beamline X-19A was used to determine sulfur oxidation states. Initial data showed that organic sulfur in the original, freeze-dried HA sample and in the aqueous metal-HA suspensions was in a highly oxidized form (Fig. 1 - HA Batch 1). Because metal-sulfur binding should occur at reduced sulfur groups, such bonding is unlikely in this system. Sulfur oxidation was considered to be an artifact of highly alkaline or acidic conditions occurring during certain steps of the HA extraction procedure. Therefore, a second batch of HA was extracted using a more restricted pH range. Sulfur K-XANES results from this batch indicated that about half of the organic sulfur in the original HA and the aqueous suspensions was in a reduced oxidation state (Fig. 1). The S K-XANES results will complement EXAFS analyses at Beamline X-11A aimed at determining the molecular-bonding environment of the metals.

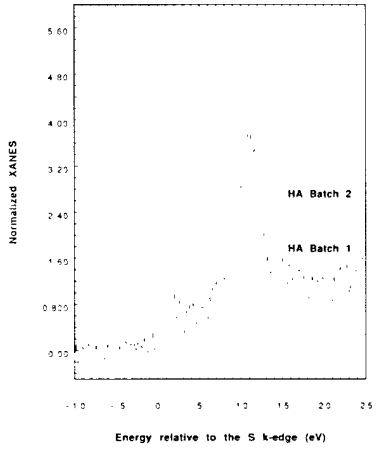

Figure 1. Normalized sulfur K-XANES spectra of aqueous samples of Cu reacted with soil humic acid (HA) from two different extractions: most of the organic S in Batch 1 was oxidized during extraction.

X-Ray Reflectivity of Polymeric Surfactants at the Air-Water Interface. | X19C

A. S. Brown (Australian National U.), S. A. Holt (U. of New South Wales) and G. J. Foran (Australian National Beamline Facility)

At the time these experiments were undertaken our research group was in the process of commissioning a new x-ray reflectometer at the Research School of Chemistry, and were taking the first reliable data using the instrument. Software had been developed in-house for the simultaneous refinement of models against both x-ray and neutron data, from both energy- and angle-dispersive instruments, with or without constraints, but had not yet been proven for use with x-ray data. For this reason we measured x-ray reflectivity data for two simple air-liquid interfaces at beamline X19C using the liquid surface spectrometer, for benchmarking our own reflectometer and for testing the software. The data we collected for air-water and air-hexadecane interfaces yielded interface roughnesses which agreed well with literature values (2.7 ± 0.1 Å for air-water and 3.9 ± 0.3 Å for air-hexadecane). Data subsequently acquired with our in-house reflectometer for these two systems also agreed well with the literature, and confirmed for us that both our reflectometer and software were performing correctly.

Data were also collected for monolayer films of an end-functionalised polystyrene surfactant spread at the air-water interface, compressed to surface pressures of 0.5, 2.0 and 6.0 mNm^{-1}. These data were collected to provide an additional contrast to complement several neutron data sets we have for this material. The neutron data alone are not sufficient to resolve the film structure unambiguously. The x-ray data have provided significant additional information which is currently being used in resolving the film structures by refinement of models against both x-ray and neutron data simultaneously.

Combined SWBXT and HRTXD Studies on Defect Distributions in II-VI Compound Semiconductors I. CdZnTe *	X19C

Y. Guo, H. Chung, J. Su, M. Dudley (SUNY at Stony Brook), H. M. Volz, C. Salles, and R. J. Matyi (U. of Wisonsin-Madison)

Wafers sliced from the microgravity-grown CdZnTe boules (GCRC-1 & GCRC-2) were imaged by SWBXT. Figure 1(a) shows a transmission topograph recorded from a wafer cut from the region of boule GCRC-2 with the best quality. Individual dislocations (D) are clearly resolved. A dislocation density of the order of 5 X 10^2 to 1.2 X 10^3 cm^{-2} is estimated. Note that the dislocations are distributed uniformly and no subgrain structure is observed. Other defects characterized are a few Te precipitates (P). Formation of these precipitates can be attributed to the retrograde solubililty of Te in CdZnTe. Figure 1(b) illustrates the diffracted intensity about the 333 reciprocal lattice point from a similar CdZnTe wafer to the one shown in Figure 1(a). The figure represents a "map" of the distribution of the diffracted intensity in reciprocal space. The presence of a well-defined surface streak is indicative of two qualities of the diffracting crystal: (1) the bulk crystal has sufficient structural perfection in order to diffract dynamically, and (2) the crystal surface is of high enough quality to produce the surface streak. SWBXT and HRTXD results match very well.

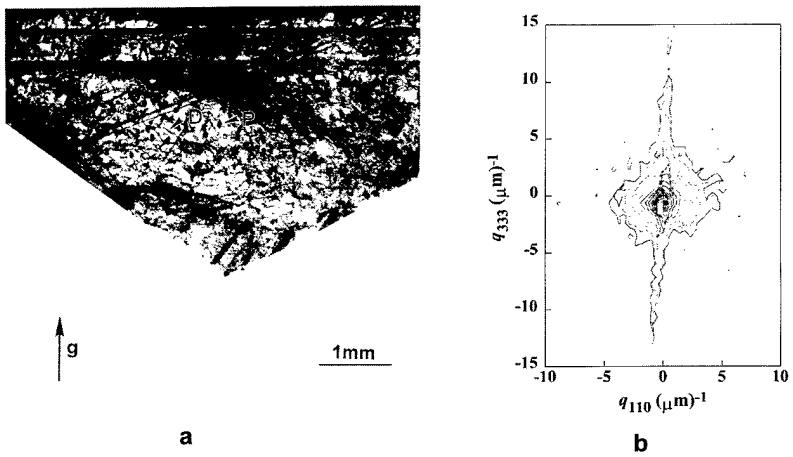

Figure 1. (a)Transmission x-ray topograph (g=113, λ=0.42Å) recorded from a wafer sliced from the most slowly cooled region of GCRC-2. Individual dislocations (D) and precipitates (P) are clearly observed; (b) Triple crystal diffraction scan about the 333 reciprocal lattice point from a similar sample.

* Work performed on the Stony Brook Synchrotron Topography Beamline X-19C and supported by NASA Marshall Space Flight Center

Combined SWBXT and HRTXD Studies on Defect Distributions in II-VI Compound Semiconductors II ZnSe	X19C

Y. Guo, H. Chung, J. Su, M. Dudley (SUNY at Stony Brook), H. M. Volz, C. Salles, and R. J. Matyi (U. of Wisconsin-Madison)

In ZnSe, an even distribution of dislocations was revealed by SWBXT, with no cellular structure being discernible. An example of a topograph recorded from this polished sample, revealing this microstructure is shown in Figure 1(a). Additionally, a few slip bands (S) are also observed. Figure 1(b) is a 220 reciprocal space map from a similar ZnSe sample. The absence of any surface streak and both the intensity and the angular extent of the diffuse intensity is indicative of a highly defective surface region in this sample. This interpretation agrees with SWBXT.

Figure 2(a) shows a reflection topograph recorded from a ZnSe sample with a cleaved (rather than a polished) (110) surface shows a high density of uniformly distributed dislocations and twins. Likewise, HRTXD showed a well-defined surface streak and a large amount of diffuse scatter that was distributed perpendicular to the [110] surface normal direction indicative of a high dislocation density. The uniformity of the diffuse intensity suggested that the dislocations are randomly distributed throughout the crystal and not concentrated in the form of subgrain boundaries. Comparison between the polished and cleaved samples seems to indicate that polishing damage can obscure the true as-grown microstructure in ZnSe.

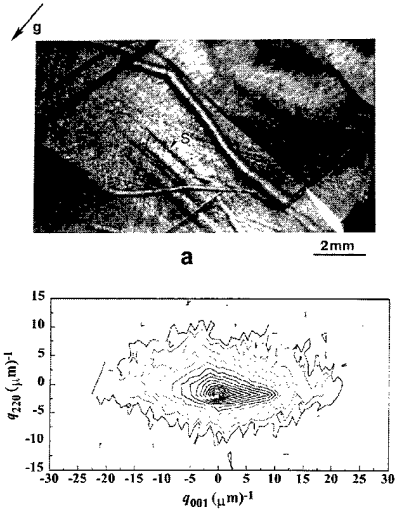

Figure 1.

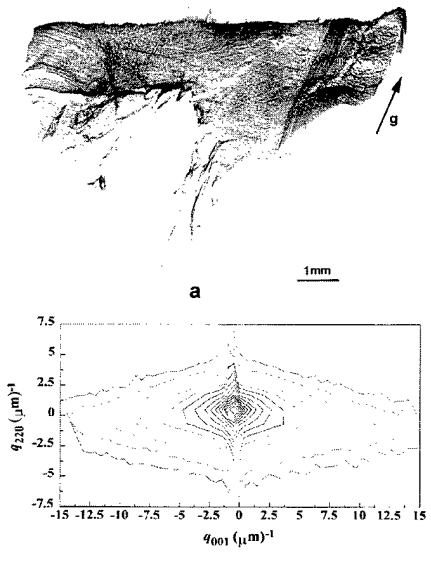

Figure 2.

Characterization of Defects in SiC Devices Using Synchrotron White Beam X-ray Topography and Their Relationship with Device Performance	X19C

W. Huang, M. Dudley (SUNY Stony Brook), P. Neudeck (NASA Lewis Research Center), C. Fazi (Army Research Lab.)

Crystallographic defects such as dislocations in semiconductor crystals can have detrimental effects on the performance of devices. Synchrotron White Beam X-ray Topography (SWBXT) have been used to characterize the defect structures in SiC crystals of various polytype and to determine how these defect structures can influence the performance of various kinds of device manufactured therefrom.Figure 1 is a back-reflection topograph shows the defect structures in a SiC crystal. The device topology can be discerned due to the finite absorption of the metallization layer as well as due to contrast associated with the strain discontinuities at the edges of the metallization layer. Electrical performance of such devices were tested. A I-V curve is shown in figure 2. Correlation with defect map and device performance reveal the detailed influence of the defects present in the crystal on the device performance. Results show that high density and large Burgers vector dislocations decrease and reverse breakdown voltage and increase the leakage current. Microplasma associated with surface morphology and micropipes was observed when voltage is applied.

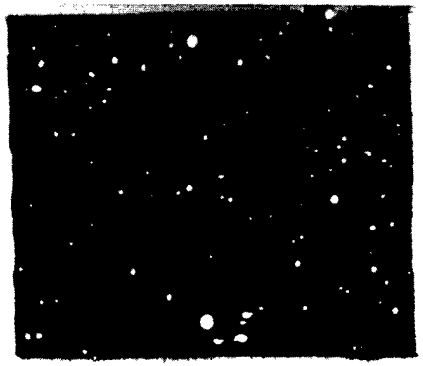

Figure 1. Topograph recorded from a 6H-SiC crystal with devices fabricated upon it. S indicates large Burgers vector screw dislocation (micropipe). E indicates eletrode.

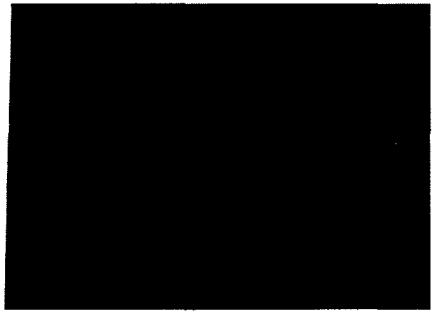

Figure 2. A room-temperature I-V characteristics of a SiC diode.

Contrast Mechanism of Super Screw Dislocations in Back-reflection Synchrotron Topographs *	X19C

X. R. Huang, M. Dudley (SUNY at Stony Brook), C. H. Carter, Jr. (Cree Research, Inc)

As a powerful and efficient diffraction imaging technique for studying crystal defects, synchrotron white-beam x-ray topography (SWBXT) has been investigated extensively in the transmission geometry, but the back-reflection case was seldom used and the corresponding principles and mechanisms of contrast formation are not fully understood. In our systematic experiments, however, it was found that the back-reflection SWBXT (with Bragg angle around 80°) is a particularly useful tool for observation of super screw dislocations (SSDs) in SiC, a wide-bandgap, high-temperature semiconductor material. The typical topographic contrast of an individual SSD perpendicular to a (0001) 6H-SiC wafer surface is shown in Fig. 1(a), where the dislocation image is a black ring encircling a white center. Besides the experimental observation, a new general program based on the ray-tracing principles was established to simulate the dislocation contrast in back-reflection topographs.

The simulated image of a SSD, as plotted in Fig. 1(b), coincides exactly with the recorded image both in dimension and in intensity distribution. Moreover, the simulation demonstrated clearly the strain field of screw dislocations as well as the kinematic diffraction behavior of the deformed lattice. From the simulation, the dependency of the dislocation image size on the magnitude of the Burgers vector was obtained, which provides a direct criterion for quantitative analysis of SSDs. Grazing-reflection topography and the corresponding simulation were also performed to reveal the surface relaxation of SSDs. The detailed contrast mechanisms of back-reflection SWBXT were, thus, obtained from the experiments

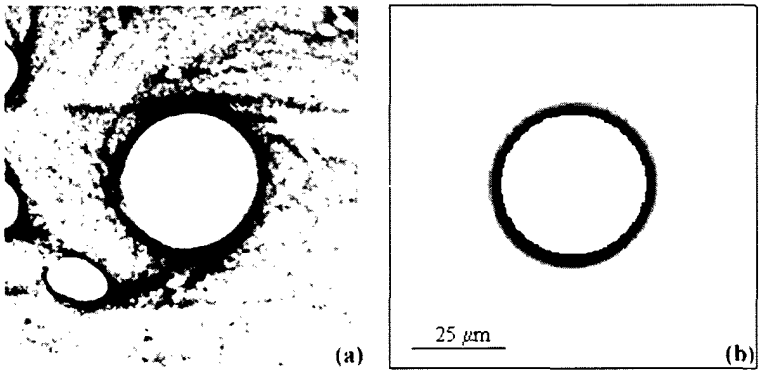

Figure 1. Recorded (a) and simulated (b) images of a SSD (Burgers vector $\mathbf{b} = 8\mathbf{c}$) in 00024 back-reflection topographs (Bragg angle $\theta_B = 81.4°$). Note that the black streaks in (a) correspond to contrast of basal-plane dislocations.

* Work performed on the Synchrotron Topography Project, Beamline X-19C, and supported by ARPA/AFWL under Grant No. FY1457-95-03103.

Determination of Super Screw Dislocation Sense with Synchrotron Back-reflection Section Topography *	X19C

X. R. Huang, M. Dudley, W. M. Vetter (SUNY at Stony Brook), R. Glass, V. Tsvetkov, and C. Carter, Jr. (Cree Research, Inc.)

Synchrotron radiation topography has been widely applied to observe dislocations in single crystals and epitaxial heterostructures. Although the criterion $\mathbf{g}\cdot\mathbf{b} = 0$ can be used to analyze dislocation Burgers vectors, it is still hard to distinguish two dislocations with antiparallel Burgers vectors (opposite senses) from their topographic contrast. In the investigations of super screw dislocations (SSDs) in SiC, we designed a novel technique, namely white-beam back-reflection section topography (WBBRST) which can show clearly the sense of an individual SSD.

In our experiments, the incident synchrotron beam was limited to be 15 μm in width by a slit and was carefully adjusted to cover the core region of a specific SSD for the 00024 back reflection. The topographic contrast of a SSD in a (0001) 6H-SiC wafer is shown in Fig.1(a), in which the dislocation image splits into two disconnected "tails" near the image center. Figure 1(b) represents the simulated image which was calculated on the basis of the strain field of a right-handed SSD. These two patterns indicate that, in addition to the radial shift, the diffracted x rays are twisted around the principle diffraction direction with left-handed screw direction. For a left-handed SSD as shown in Fig. 1(c), the twist of the x rays is naturally right-handed.

Besides the application of dislocation-sense determination, WBBRST can also be used to analyze the local strain field of other crystal defects and is of great help for understanding the contrast mechanisms of back-reflection topography.

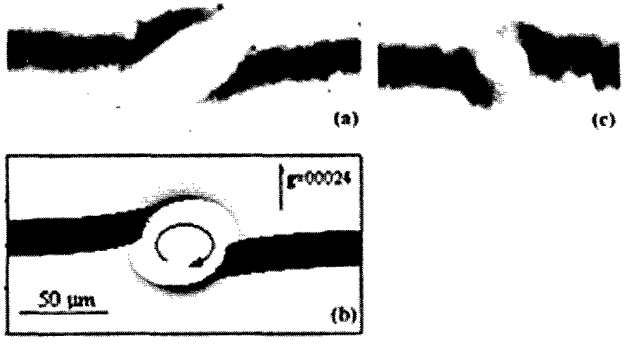

Figure 1. Back-reflection section topographs showing the senses of SSDs in 6H-SiC. (a) and (b) are the recorded and simulated images of a right-handed DDS while (c) corresponds to a left-handed DDS. The curved arrow indicates the twisting direction of the diffracted x rays.

* Work performed on the Synchrotron Topography Project, Beamline X-19C, and supported by ARPA/AFWL under Grand No. FY1457-95-03108.

The Liquid-vapor Interface Structure of Tin:Gallium	X19C

Ning Lei and Stuart A. Rice (U. of Chicago)

The liquid-vapor interface structure of a tin:gallium alloy has been studied by x-ray specular reflectivity and grazing incidence in-plane x-ray diffraction. The reflectivity data are consistent with a model of stratified layers of atoms at the interface, with 100% tin coverage for the outermost layer and ~22% tin in the second outermost layer. In- plane diffraction data reveal that the tin atoms in the interface are in liquid state. Reflectivity and in-plane data show independently that the diameter of the tin atoms in the interface is about 5% smaller than that in its pure 3-d liquid state at the temperature around 40°Celsius. The alloy surface tensions at four different temperatures are deduced from the sample shape measured by x-ray reflection of the sample. The surface tensions measured show clearly that with increasing sample temperature, the surface tension increases. We explain this to be due to the increased solubility of tin in the bulk at a higher temperature and less tin at the interface as shown by the reflectivity data. The tin atom enthaphy difference between that at the interface and that in the bulk is shown to be proportional to the temperature derivative of the surface tension; and thus the enthaphy at the interface is of a smaller value.

Gold Colloid Nano-Structures in Polymer Thin Films | X19C

B. Lin, M. Meron, and P.J. Viccaro (CARS-U. Chicago), S. Williams and M. L. Schlossman (Physics-UIC), T. Morkved, H. Jaeger, and Z. Huang(JFI-U. Chicago)

Materials structured on the nanometer length scale promise to be the next generation of materials for electronics. It may be possible to use the nanometer length scale structures that spontaneously self-assemble in complex fluids as templates to form these nano-structured electronics materials. This methodology has been pursued by Terry Morkved, a graduate student in Heinrich Jaeger's group at the University of Chicago, in preparing a nano-structured system in which gold metal is deposited on and then annealed into a polymer thin film (~50nm thick). Transmission electron microscopy by Morkved revealed that the gold metal is self- assembled and ordered in-plane into spheres or rods of nanometer dimensions inside the polymer films. However, electron microscopy was unable to address the important issue of the distribution of the gold spheres along the normal of the polymer films.

By using x-ray specular reflectivity (not shown) accompanied by x-ray reflection standing wave fluorescence spectroscopy, we measured the electron density and Au atomic density profiles along the surface normal of a gold-sphere-impregnated thin polymer film. This PS-b-PVP diblock copolymer film consists of poly vinyl pyridine (PVP) spheres ($\sim$ 20 nm diameter) embedded in a polystyrene (PS) matrix ($\sim$ 50nm thick). Figure 1 shows x-ray reflection standing wave fluorescence spectrum. For comparison, we also performed the same measurements (shown in Fig.2) on a polymer film of PS homopolymer ($\sim$ 50 nm thick); gold atoms, amount to a layer of $\sim$ 0.5nm, were coated on top of the polymer film and were not annealed. These gold atoms were not spread on top of the polymer film uniformly; instead, they balled up into $\sim$ 8 nm spheres. The solid line in Fig.2 is theoretical calculation for the spectrum using Parratt's formulation.

While a quantitative analysis for the distribution of the gold spheres imbedded in the PS-b-PVP film has yet to be made, the unambiguous qualitative results from both techniques indicate that the gold spheres are smeared along the normal of the film instead of being arranged within a narrow plane in the middle of the film. Although the gold spheres are somewhat ordered into a lattice within the plane of the film, they are not ordered normal to the plane.

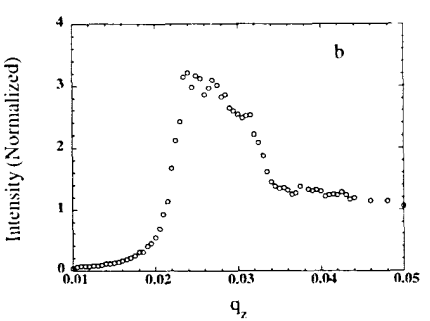

Figure 1.

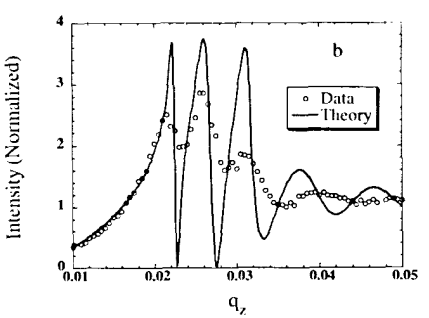

Figure 2.

Effect of Constrained Growth on Defect Structures in Microgravity-Grown CdZnTe Boules I. Nucleation of Grains * | X19C

B. Raghothamachar, H. Chung, M. Dudley, D.J. Larson Jr. (SUNY at Stony Brook)

In order to study the effect of constrained growth on the defect structures in microgravity grown samples, a CdZnTe boule (GCRC-1) was grown in a carbon-coated quartz ampoule by the seeded Bridgman-Stockbarger growth method under constrained conditions aboard NASA space shuttle flight USML-2. Forced wall contact conditions were created by utilizing PBN springs pressed against the molten CdZnTe at the tail end. Synchrotron white beam x-ray topography (SWBXT) was then used to characterize defect structures in the boule by imaging the wafers sliced from it.

Figure 1 shows a diffraction pattern recorded from wafer # OW2 which was sliced from the steady state growth region. Clearly, this is a superposition of several diffraction patterns from regions of different orientations present in the wafer. Detailed studies revealed no definite orientation relationships between the different grains. Nucleation of several grains can be explained in the following way. During growth under constrained conditions, it is observed that generally, maximum stress concentration occurs at the ampoule wall just below the solid-liquid interface where heat extraction occurs. Adhesion reduces the interfacial energy between the solid nucleus and ampoule surface thus favoring the nucleation of new grains at smaller undercooling.

Figure 1. X-ray diffraction pattern in the reflection geometry from wafer #OW2 showing atleast three different large grains (G_1, G_2, G_3) and other smaller grains.

* Work performed on the Stony Brook Synchrotron Topography Beamline X-19C and supported by NASA Marshall Space Flight Center.

Effect of Constrained Growth on Defect Structures in Microgravity-Grown CdZnTe Boules II. Inhomogeneous Strains *	X19C

B. Raghothamachar, H. Chung, M. Dudley, and D.J. Larson Jr. (SUNY, Stony Brook)

Inhomogeneous strains were observed in several regions of the boule grown under constrained conditions on USML-2. A reflection topograph (Fig. 1) ($\mathbf{g} = 551$) taken from the seed transition region shows a highly distorted image indicating presence of heavy inhomogeneous strains. The grain grown from the seed is subjected to high stresses due to forced wall contact especially in the shoulder regions and this must have resulted in high strains. Stress models clearly show that the shouldering operation generated very high stresses and static friction in this region could significantly increase the local stresses. In the steady state growth region, a reflection topograph ($\mathbf{g} = 422$) taken from a grain present in wafer #OW7 is shown in Fig. 2. This topograph shows a distorted image in most regions due to the presence of large inhomogeneous strains. Here, the level of thermal gradient stresses generated by rapid cooling are expected to be much greater than the critical resolved shear stress of CdZnTe. However, because of the constrained conditions forced by the restraining springs, a hydrostatic stress state is created which prevents deformation by shear. Instead the stresses cause large amount of strains.

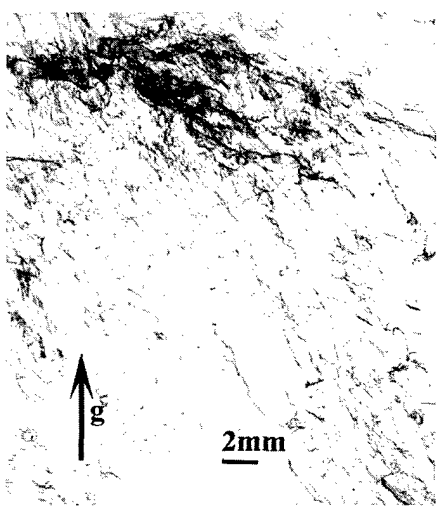

Figure 1.

Figure 2.

* Work performed on the Stony Brook Synchrotron Topography Beamline X-19C and supported by NASA Marshall Space Flight Center.

Effect of Constrained Growth on Defect Structures in Microgravity-Grown CdZnTe Boules III. Twins *	X19C

B. Raghothamachar, H. Chung, M. Dudley, and D.J. Larson Jr. (SUNY, Stony Brook)

The high ionicity of CdZnTe makes it extremely prone to twinning. Nucleation of twins is generally observed to occur at regions of disturbances at the growth interface. Fig. 1 shows a white beam topograph ($\mathbf{g} = 004$) taken in the reflection geometry from a grain showing a relatively good crystalline quality present in wafer #OW7. However, the peripheral regions are still highly strained due to effects related to wall contact. Additionally, this grain also shows the presence of lamellar twins (**T**) which are revealed by orientation contrast. Detailed analysis of back reflection Laue diffraction patterns recorded from these twinned regions reveal that the twins are of the 180° rotation type about the $(1\bar{1}1)$ plane normal. Nucleation of these twins appears to have occurred because of effects related to wall contact. Small angle grain boundaries (**SB**) revealed by orientation contrast are also observed in some regions. Their formation can be attributed to the process of polygonization i.e. stress-induced glide and climb of dislocations introduced in the crystal during solidification. This process occurs during post-solidification cooling.

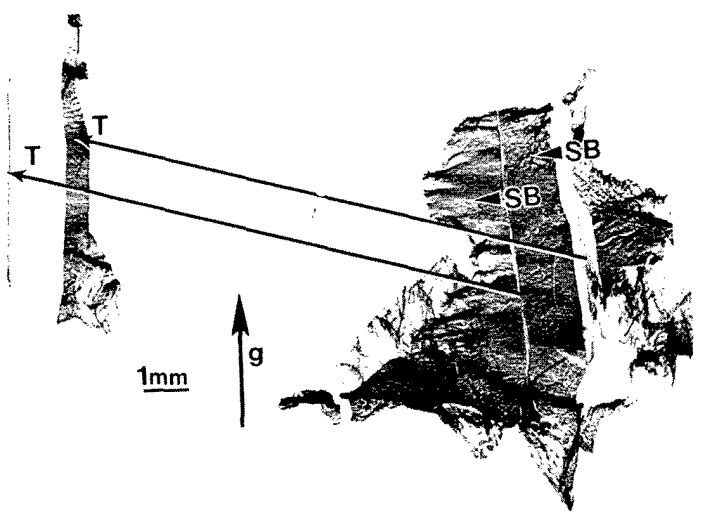

Figure 1.

* Work performed on the Stony Brook Synchrotron Topography Beamline X-19C and supported by NASA Marshall Space Flight Center.

Studies on Interface Demarcation in Bridgman-Stockbarger Grown CdZnTe Single Crystals by SWBXT *	X19C

B.Raghothamachar, M. Dudley, and D.J. Larson Jr., (SUNY, Stony Brook)

A CdZnTe boule grown by the seeded vertical Bridgman-Stockbarger method of crystal growth was subjected to frequent stop and start operations during the course of its growth in order to demarcate the growth interface. Demarcation was expected to be caused by changes in zinc concentration at the solid-liquid interface induced by the applied disturbance. Wafers sliced from this boule were subsequently examined by SWBXT. The wide spectral range of SWBXT allows imaging of crystals with regions of different lattice parameter (produced by segregation or localized strains) that are likely to be introduced during such stop and start operations. Studies of the topographs taken from the wafers revealed no contrast variations due to change in composition. Rather it was observed that twins were nucleated at the stop and start locations. Fig. 1 shows a reflection topograph ($\mathbf{g} = 133$) recorded from a wafer cut from this boule. In this wafer the distorted region **A** revealed by orientation contrast could possibly have been created by a stop and start operation. It is also observed that as soon as growth was recommenced, a twin T_1 (180° rotation type about the (111) plane normal) was nucleated. Lamellar twins T_2 (180° rotation type about the $(1\bar{1}1)$ plane normal) are also characterized. Other defects observed are slip bands (**S**), sub grain boundaries (**SB** and inclusions of Te (**I**).

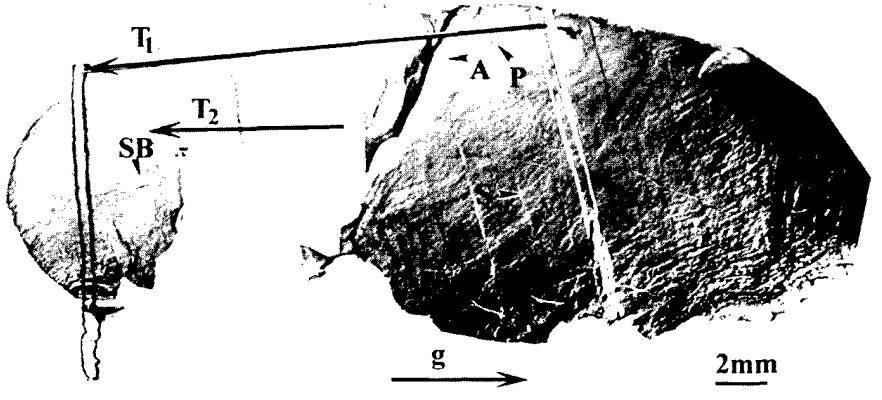

Figure 1.

* Work performed on the Stony Brook Synchrotron Topography Beamline X-19C and supported by NASA Marshall Space Flight Center.

Characterization of Twinning Operations in PVT Grown CdTe Single Crystals by SWBXT *	X19C

B. Raghothamachar, M. Dudley (SUNY, Stony Brook), W. Palosz, D. C. Gillies (NASA Marshall Space Flight Center)

Twinning operations in CdTe single crystals grown by the PVT technique have been characterized by synchrotron white beam x-ray topography. Fig. 1 shows a reflection topograph ($\mathbf{g} = 5\bar{1}\bar{1}$) recorded from a wafer of PVT CdTe. Two twins T_1 and T_2 are identified in this topograph. Twin T_1 is revealed by orientation contrast while twin T_2 is revealed by diffraction contrast. Figures 2(a), (b) and (c) show (110) Laue back reflection diffraction patterns taken from the matrix, twinned region T_1 and twinned region T_2 respectively. We can clearly see that the twin T_1 is rotated in the anticlockwise direction with respect to the matrix by 250° 32 about the [110] tilt axis while the twin T_2 is rotated in the clockwise direction with respect to the matrix by 250° 32' about the [110] tilt axis. Other defects revealed in the topograph are inclusions (possibly Te)(**I**), slip bands (**S**) and lattice distortions (**A**) in some regions.

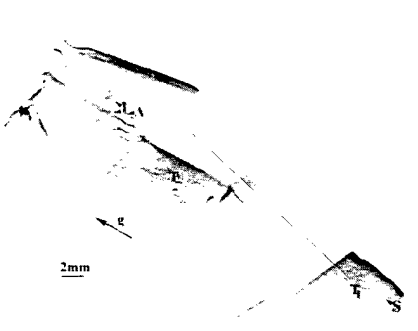

Figure 1.

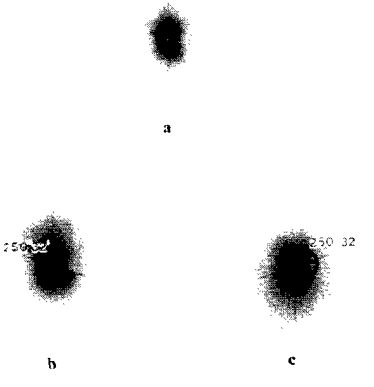

Figure 2.

* Work performed on the Stony Brook Synchrotron Topography Beamline X-19C and supported by NASA Marshall Space Flight Center.

Lamellar Twinning in p-Quaterphenyl Crystals *	X19C

William M. Vetter and Michael Dudley (SUNY Stony Brook)

Flat leaves of p-quaterphenyl with their (001) faces dominant are also common. Most of these are twinned. The twins occur as narrow lamellae, visible by optical microscopy as pairs of parallel lines about 12μm wide, running along [010]. Two of these lamellae are marked T in the x-ray topograph shown in figure 1. Topographic images of the lamellae may be observed as narrow lines displaced from the images of their matrix, or in some reflections, coincident. For one of the lamellae, T_2, all contrast vanishes when $\mathbf{g} = (201)$. The absence of lattice strain associated with this lamella implies that its twin plane is (201). The other lamella, T_1, has another, unidentified twin plane.

The lamellae do not extend continuously along the [010] direction throughout the crystal. Where they terminate, dislocations extend into the matrix. Dislocations also originate at the twinning plane, and either curve back to terminate there, or extend to the crystal's surface. Some of them, D_1, are in maximum contrast in the $\mathbf{g} = (1\bar{1}0)$ reflection shown in figure 1, and extinguish when $\mathbf{g} = (110)$. Those labeled D_2, behave oppositely, extinguishing when $\mathbf{g} = (1\bar{1}0)$. Both D_1 and D_2 have minimal contrast when $\mathbf{g} = (001)$, a reflection almost orthogonal to (110) and $(1\bar{1}0)$. It may be concluded by the $\mathbf{g} \bullet \mathbf{b} = 0$ criterion the Burgers vectors of D_1 and D_2 are $\mathbf{b} = [1\bar{1}0]$ and $\mathbf{b} = [110]$. As their lines roughly follow the same directions, they are mainly screw in character.

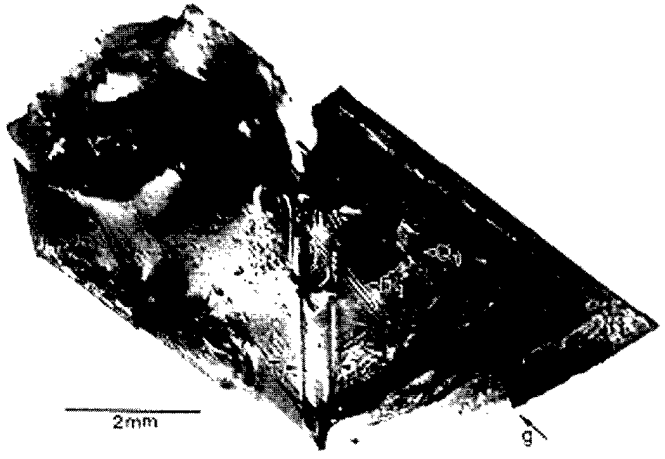

Figure 1.

* Topography was carried out at the Stony Brook Synchrotron Topography Facility, Beamline X19-C, at the NSLS, which is supported by the U.S. Department of Energy.

Macroscopic Twinning in p-Quaterphenyl Crystals *	X19C

W.M. Vetter and M. Dudley (SUNY, Stony Brook)

p-Quaterphenyl crystals form thin, colorless leaves when grown from toluene solution by the temperature gradient method. Macroscopically twinned bicrystalline leaves whose {001} primary faces are inclined to one another by 36.4° (which may be measured by optical goniometry) occur frequently. However, topographs of few such crystals don't show extensive asterism in the region of its twinning plane.

Figure 1 shows a white beam synchrotron Laue pattern of such a specimen. This crystal has one small corner macroscopically twinned in this way, which is free of gross distortion. The (001) face of the larger parent matrix grain is oriented perpendicular to the incident beam. In figure 1, no misorientation between the diffraction spots arising from the matrix and twin occurs for spots of the zone $<\bar{1}02>$ (i.e., $\{4\bar{1}2\}$, $\{2\bar{1}1\}$, $\{2\bar{2}1\}$, etc.), the direction of shear between the twin and matrix lattices. Additionally, the angle between [001] and $[\bar{1}02]$ is 18.2°, half the observed twinning angle in the crystal. Therefore, the twin plane may be assigned as (201).

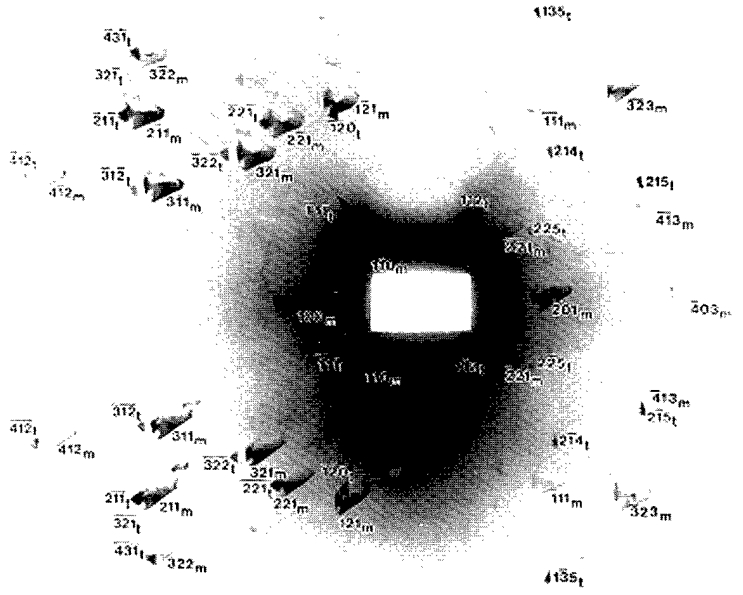

Figure 1.

* Topography was carried out at the Stony Brook Synchrotron Topography Facility, Beamline X19-C, at the NSLS, which is supported by the U.S. Department of Energy.

Surface Scattering From the C_4E_1 Oil-Microemulsion Interface | X19C

S. M. Williams, Z. Zhang, D. M. Mitrinović, M. L. Schlossman (U. of IL-Chicago), and Z. Huang (BNL)

We have made x-ray scattering measurements from the oil-microemulsion interface of a (butoxyethanol)-water-decane mixture at 35°C. The ultra low surface tension of this interface gives rise to strong thermal fluctuations.

No bicontinuous structure has been observed in bulk C_4E_1 microemulsions, enabling us to analyze the effects of these large interfacial fluctuations without the added complexity of layering at the interface. Specular reflectivity data was measured to determine the electron density profile normal to the interface. We also made surface diffuse scattering measurements near the specular condition. This probes the interfacial thermal fluctuations in the plane, which we characterize by capillary waves. Both types of data were analyzed using the distorted wave Born approximation.

Initial analysis of the reflectivity data from the oil/microemulsion interface indicated a roughness of about 54 Å. However, when this value was used in the analysis of the diffuse data, we could not obtain a satisfactory fit. Upon increasing the roughness parameter to 61 Åwe obtained an excellent fit to the diffuse data with a surface tension of about 0.17 dynes/cm.

This discrepancy is a consequence of the low surface tension of the interface. There is both a diffuse and reflected signal at the specular position, but in high surface tension samples, the diffuse signal is much smaller. When the surface tension is low enough, the diffuse signal is of the same order as the reflection, making it necessary to separate the two signals in the analysis of the data. Figure 1 shows the raw reflectivity data (54 Å) and the data after the diffuse signal has been subtracted (60.8 Å). Using the interfacial roughness value obtained from the pure reflected signal, we were able to obtain an excellent fit of the diffuse data with a surface tension of ≈0.22 dynes/cm (figure 2).

This sample demonstrated that the interfacial fluctuations in these ultra low surface tension systems are the result of capillary waves. The interplay that we found between the specular and diffuse signals can now be applied to systems composed of stronger amphiphiles where layering may be present at the interface.

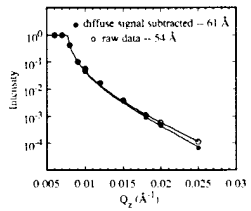

Figure 1. Specular reflectivity data from the oil-microemulsion interface. The raw data yields a roughness of 54 Å. After the diffuse signal is subtracted, the roughness is found to be 61 Å.

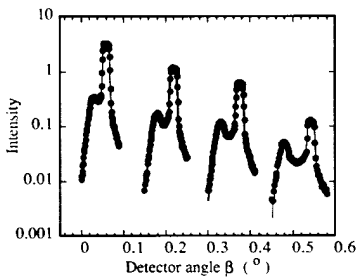

Figure 2. Diffuse scattering data from the oil-microemulsion interface.

Surface Scattering from the $C_{10}E_4$ Oil-Microemulsion Interface | X19C

S. M. Williams, Z. Zhang, D. M. Mitrinovic, M. L. Schlossman (U. of IL-Chicago), and Z. Huang (BNL)

X-ray reflectivity and surface diffuse scattering were measured from the oil-microemulsion interfaces in the 3-phase region in the ternary mixtures $C_{10}E_4$-water-decane and $C_{10}E_4$-water-tetradecane. The ultra low surface tension at these interfaces gives rise to strong thermal fluctuations. In addition, the microemulsion phase in these mixtures is believed to be bicontinuous. This has been predicted to produce interfacial layering at these strongly fluctuating interfaces. The systems studied have interfacial roughnesses ranging from 150 Å to over 200 Å.

Reflectivity and off-specular diffuse scattering data were measured from both samples. While the specular peak tracks incident angle, the surface enhancement associated with the diffuse scattering remains at the critical angle. In smoother samples, for wave vectors at which the magnitude of the specular signal has decayed to the order of the diffuse signal, the two peaks are well separated. In these rough samples, the specular peak falls off so quickly for wave vectors slightly greater than the critical wave vector for total reflection that the specular and diffuse signals are of similar strength at the critical angle, making the reflectivity data difficult to interpret. Initial analysis of the $C_{10}E_4$-water-decane sample established a lower bound on the roughness of 200 Å (Fig. 1).

The specular signal from the$C10E_4$-water-tetradecane interface decays less rapidly. Figure 2 shows the data in the Q_z range from 0.01 to 0.028 Å^{-1}. Below the critical Q_c of 0.01 Å^{-1}, there is only one peak. At Q_z = 0.014 Å^{-1}, the two peaks begin to separate, and at 0.016 Å^{-1} they are resolved. Preliminary analysis of these data indicates a roughness of about 150 Å and a surface tension of 0.01 mN/m. Further analysis of these data will also be useful in separating the diffuse and specular signals in the rougher sample.

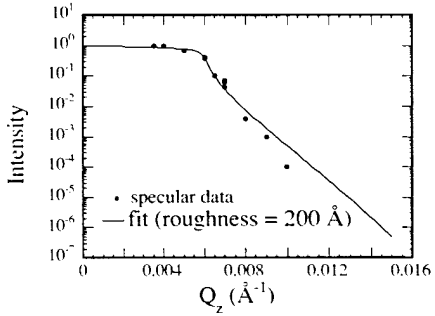

Figure 1.

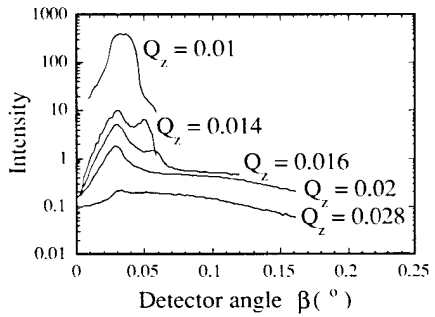

Figure 2.

X-ray Reflectivity From a 1,1,2,2 Tetrahydrohenicosafluorododecanol Monolayer at the Water-Hexane Interface	X19C

Z. Zhang, S.M. Williams, D.M. Mitrinović, M.L. Schlossman (U. of Illinois at Chicago), and Z. Huang (BNL)

Addition of the soluble surfactant 1,1,2,2 tetrahydrohenicosafluorododecanol (denoted $FC_{12}OH$) to hexane (2 mmol concentration) results in the formation of a monolayer of $FC_{12}OH$ at the water-hexane interface. X-ray reflectivity from this water-($FC_{12}OH$)-hexane interface combined with grazing incidence diffraction from an $FC_{12}OH$ monolayer at the water-vapor interface is analyzed to determine that the $FC_{12}OH$ monolayer at the water-hexane interface is a solid at T=32°C. The existence of the solid monolayer at the liquid-liquid interface is due to a delicate balance of solvation and Van der Waals energies in this system. At T=48°C most of the $FC_{12}OH$ molecules are desorbed from the interface.

The two reflectivity curves (at T=48°C and T=32°C) from the water-($FC_{12}OH$)-hexane are shown below. The measurement at T=48°C can be analyzed as a rough interface between two bulk phases. A Born approximation analysis of these data yields a surface roughness, σ=0.38± 0.03 nm.

The data measured at T=32°C were fit using the Born approximation and an electron density profile that models the surfactant monolayer as a simple layer with equal roughness on both sides that is sandwiched between the two bulk phases. The layer thickness determined by the fit to the data is given by L = 1.210±0.085 nm. This thickness is 0.4 nm shorter than the full all-trans length of the surfactant molecule, but is essentially the same as the length of the fluorinated part of the molecule. This indicates that the reflectivity is sensitive only to the fluorinated region of the molecule, most likely because the electron density contrast of the water with the surfactant hydrocarbon headgroup is too small. The electron density of the layer (normalized to the density for bulk water) is 1.96±0.09. This density at the liquid-liquid interface is consistent with the normalized density (2.01) of 2-dimensional crystallites of $FC_{12}OH$ at the water-vapor interface (at the same temperature) as determined by grazing incidence diffraction. Grazing incidence diffraction from the liquid-liquid interface was not possible because the ratio of signal to background was too low. This combined analysis of these two measurements indicates that the monolayer at the liquid-liquid interface is in the solid phase.

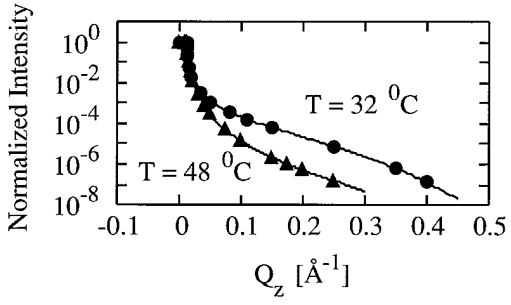

Figure 1. X-ray reflectivities of $FC_{12}OH$ monolayer at T=32°C and 48°C.

X-ray Reflectivity from the Water-Hexane Interface	X19C

Z. Zhang, S.M. Williams, D.M. Mitrinovic, M.L. Schlossman (U. of Illinois at Chicago), and Z. Huang (BNL)

X-ray reflectivity was used to study the roughness of the pure hexane-water interface. To probe this buried interface the x-rays penetrate the upper phase (hexane). X-ray absorption and bulk scattering from the upper interface require that the sample cell be reasonably small. However, since the interfacial tension of this common liquid-liquid interface is similar to the water-vapor interface, the interface will be very curved for a small sample. The cell windows are slanted from the vertical as a gross adjustment to flatten the interface. A fine adjustment is still needed to reduce the macroscopic curvature of the sample to be much less than the angular resolution of the detector (as determined by slits). This is accomplished by rotating the sample cell about an axis collinear with the x-ray beam. Due to non-equilibrium pinning of the contact angle at the cell window, this rotation twists the entire interface and results in a strip of the interface that is very flat. With these two adjustments the measured reflectivity below the critical angle for total reflection is near 100% and reflection measurements can be collected using standard procedures.

The figure below shows the x-ray specular reflectivity versus the wave vector normal to the hexane-water interface at 32.00 ± 0.02 °C (n-hexane from Sigma, 99+%, water produced by a Barnstead Nanopure system). The fit yields an interfacial roughness of 0.33 ± 0.03 nm. Comparison with an earlier measurement of the pure water-vapor interface (at a similar wave vector resolution) for which γ = 72 mN/m and σ=0.27 nm (at T = 20°C) yields $\gamma_{hexane-water} \cong 50 \pm 2$ mN/m, in good agreement with the literature value of 51.4 mN/m obtained from macroscopic interfacial tension measurements.

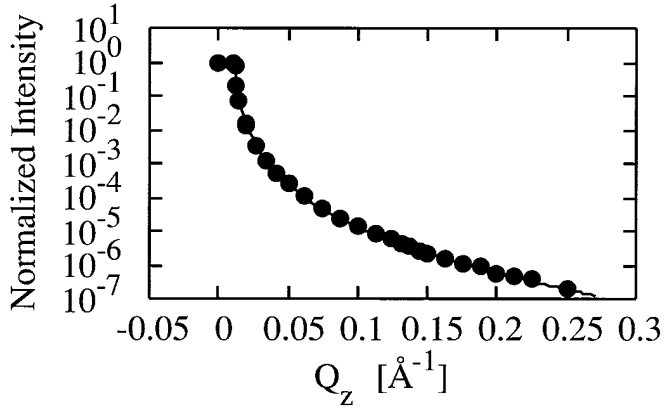

Figure 1. Reflectivity data as a function of wave vector normal to the interface.

Kinetics of Monolayer Electrodeposition | X20A

A.C. Finnefrock, K.L. Ringland, L.J. Buller, H.D. Abruña, J.D. Brock (Cornell Univ.)

In many electrochemical systems, one or two monolayers of an adsorbate may be deposited at a potential less negative than the Nernst potential. The growth mechanisms involved in this so–called underpotential deposition (UPD) have been the subject of intense controversy for over a decade. Static x-ray measurements (Tidswell, *et al.*) on the UPD of copper on Pt(111) in the presence of chloride in an $HClO_4$ solution have noted the existence of a structure ascribed to an adsorbed incommensurate CuCl bilayer.

We have performed a series of voltage-step experiments on this system, simultaneously recording the resultant current transient and time-resolved surface x-ray scattering. The x-ray profiles are fit to a simple trapezoidal form, and the characteristic time scales are shown in Figure 1 (blue). These indicate the ordering of the two-dimensional incommensurate CuCl overlayer in real time. The time for the current transient to fall to 5% of its initial value is also shown in Figure 1 (red). Note that in all cases, the current transient occurs on a shorter time-scale than the emergence of the scattering peak from the two-dimensional overlayer.

The exponential scaling of the time constant for ordering vs. $1/\phi'$ demonstrates that this behavior can be explained as a nucleation process. Furthermore, this nucleation consists of clusters which are two-dimensional and compact (non-fractal).

For a particular voltage transition, we have performed an entire time-dependent q-scan. By monitoring the time-dependent widths of the x-ray peak, we see a narrowing corresponding to the increase in the mean cluster size. We can fit the entire q-$t$scan, as shown in Figure 2, with $\chi^2 = 1.04$. From this analysis, we can extract the rate of cluster nucleation and the growth rate for an individual cluster.

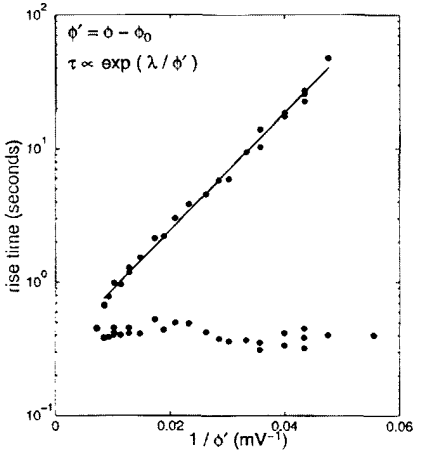

Figure 1. Characteristic rise time versus applied voltage.

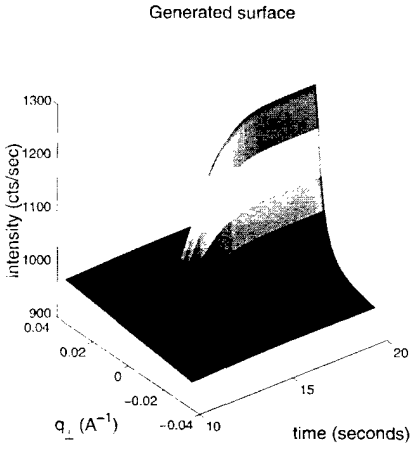

Figure 2. Surface generated from a few-parameter fit to the q-$t$scan.

The Dynamic Evolution of Charge-Density Waves | X20A

K.L. Ringland, A.C. Finnefrock, Y.P. Li, S.G. Lemay, R.E. Thorne, J.D. Brock (Cornell University)

The presence of a charge-density wave (CDW) in a crystal creates x-ray scattering peaks that flank the crystal's Bragg peaks. These CDW peaks exhibit a lineshape that is dependent on the degree of order in the CDW and are significantly different when the CDW slides and when it is stationary. Investigating the evolution of the CDW as it relaxes from the sliding state to the stationary state allows us to better understand the interaction of the deformable CDW with the randomly placed impurities in the crystal.

We applied a continuous square-wave current to a $NbSe_3$ crystal for several temperatures between 80K and 110K. The x-ray scattering in the c^* (transverse) direction was measured by stroboscopic averaging over many periods of the square-wave at each q point. (Fig. 1)

If we use a model for CDW evolution which treats the CDW as an elastic object and the CDW-impurity interaction as a quenched random field, we can derive the equation of motion for the scattering intensity.

$$S(q,t) = S(q,0)e^{-(t/\tau)^\mu/\xi_0} + S(q,\infty)(1 - e^{-(t/\tau)^\mu/\xi_\infty})$$

where ξ_0 and ξ_∞ are the correlation lengths of the CDW phase-phase correlation function at $t = 0$ and $t = \infty$, respectively. In fits to the data (Fig. 2), both the timescale τ and the dynamic exponent μ were varied. It was found that μ was constant over the measured temperature range with a value of $0.23 \pm .01$. The timescale of the CDW evolution was found to vary by four orders of magnitude from 80K to 110K.

Since the measured value of μ excludes the predicted value of 0.5, the proposed model does not describe the CDW evolution and a new model for CDW dynamics is necessary. The very large variation in the evolution timescale suggests that the energies in the evolution process are quite large and may indicate the presence of topological deffects in the CDW system.

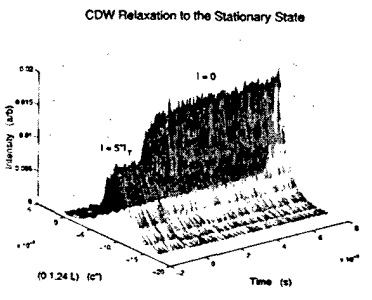

Figure 1. The evolution of the charge-density wave scattering peak is measured as it evolves from the sliding state to the stationary state.

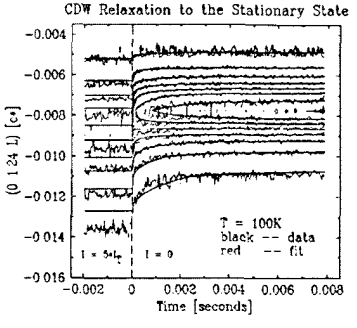

Figure 2. A contour plot showing a fit to the data shown in Fig. 1. The χ^2 is 1.37.

Atomic Structure of the Passive Oxide Film Formed on Iron | X20A

M.F. Toney (IBM Almaden Research Center), A.J. Davenport (UMIST/U. Manchester), L.J. Oblonsky and M.P. Ryan (BNL)

Passivating oxides form on metals and provide corrosion protection. Although the oxide structure largely determines the films protective properties, this structure is often unknown, even for elemental metals. The structure of the passive film on iron has been the subject of particularly intense study [1], but there is still no consensus on questions as basic as to whether the film is amorphous or crystalline, much less on the atomic structure. To resolve this question, we have conducted in-situ and ex-situ X-ray scattering experiments on the passive film formed at high potentials on Fe(110) and (001). The Fe crystals were passivated by potentiostatic polarization for one hour at +0.4V vs. MSE in borate buffer (pH 8.4). Our methodology is to collect a complete data set ex-situ (where the background scattering is small), and then to collect selected in-situ data to compare with the ex-situ experiments. In such a comparison (see Figure) there is excellent agreement, which demonstrates that the passive film formed under these conditions is not altered by emersion.

The data show that the film is crystalline with a small crystallite size of $\approx$ 50Å and has a well defined orientation with the substrate. A quantitative crystal refinement of the integrated diffraction intensities shows that the film structure is **not** one of the bulk forms of iron oxide (see figure). Rather the film structure (LAMM structure) is based on the spinel Fe_3O_4, but with considerable cation vacancies on the octahedral and tetrahedral sites (80% and 66% occupancies, respectively) and with cations occupying octahedral interstitial sites (12% occupancy) [2].

These results resolve the controversy surrounding the film structure and provide a basis for understanding film properties important for corrosion protection, including the behavior of passive films formed on engineering alloys, such as stainless steel.

[1] H. H. Uhlig, in *Passivity of Metals*, edited by R. P. Frankenthal and J. Kruger (The Electrochemical Society, Inc., Princeton, NJ, 1978), p. 1.

[2] M. F. Toney, A. J. Davenport, L. J. Oblonsky, M. P. Ryan, C. M. Vitus, Phys. Rev. Lett. **79**, in press.

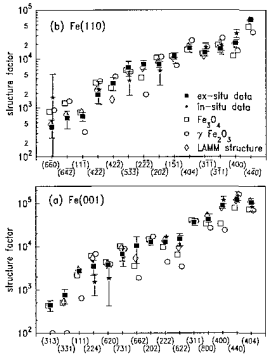

Figure 1. Measured and best fit structure factors for a subset of the diffraction peaks for film grown on (a) Fe(001) and (b) Fe(110).

X-Ray Diffraction Studies of CoPtCr Thin Films for Magnetic Recording Media | X20A

M.F. Toney (IBM Almaden Research Center) and M.F. Doerner (IBM Storage Systems Division)

The areal density in magnetic recording in presently increasing at a 60% compound annual growth rate (CGR). To maintain this rate of increase, the hard disk drive industry must develop magnetic disk media with magnetic properties (e.g., coercivity, signal-to-noise ratio) that are superior to presently used media. One approach to this is through the use of alternative underlayers (i.e., the seed layer beneath the media). This underlayer has an important influence on the structure of the media layer and understanding this relationship (and the consequent effect on the magnetic properties) is a key to developing better magnetic media.

We have used grazing incidence X-ray diffraction to determine the structure of CoPtCr media deposited on several different underlayers. These measurements were made on actual thin film disk coupons. Representative results are shown in the figure for 500Å Cr underlayer (a commonly used underlayer) and 200ÅCrTa/200ÅCr composite underlayer. These data show that the media are both highly (11.0) oriented (although to a greater extent for the CrTa/Cr underlayer), small grained and highly faulted (broad peaks). While the data show these media are hcp, the presence of a weak fcc(200) peak is apparent at Q = 3.45Å^{-1}, particularly for the Cr underlayer. This means that a small fraction of the media forms into the fcc structure. A quantitative analysis of the peak widths shows that in both films the particle size is about 100 by 150 Å, along (100) and (002) directions, respectively. However the stacking fault density (sum of growth and deformation faults) is much higher for the media on the Cr underlayer ($\alpha + \beta = 0.30$) than for the CrTa/Cr underlayer ($\alpha + \beta = 0.18$). Since such faults have localized fcc-like regions in the hcp matrix, the media on the Cr underlayer has a higher percentage of fcc-like regions (about 18% including the regions in the faults and in the fcc part of the crystal) compared with the CrTa/Cr underlayer (about 7%). This structural information provides a better understanding of the media coercivity and magnetic viscosity [1].

[1] P. Dova, K. O' Grady, H. Laidler, M.F. Doerner, and M.F. Toney, paper AB-05, MMM-Intermag Conference 1998.

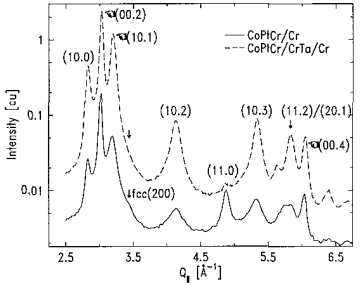

Figure 1. Diffraction pattern from CoPtCr media. Some of the diffraction peaks are indicated.

X-ray Scattering Studies of Thin Ni_xCo_{1-x}, $x \approx 0.25$ Films: Discovery of a Reentrant Phase Transformation — X20A

M.F. Toney and D. Weller (IBM Almaden Research Center), and A. Carl (Gerhard-Mercator U. Duisburg)

Carl et al. found that Ni_xCo_{1-x} films exhibit an $\approx 15\%$ enhanced magnetization for $x \approx 0.25-0.30$ relative to x=0.22 and 0.35 [1]. It was postulated that this is due to an hcp/fcc/hcp sequence of phase transitions as a function of x. To confirm this unusual (reentrant) sequence of phase transitions, we conducted X-ray scattering measurements of these polycrystalline thin films. These measurements are shown in Figure 1. The single peak at $\approx 1.55\text{Å}^{-1}$ shows that for x=31.4 and 24.3% the films are hcp, while the presence of additional peaks at ≈ 1.05 and 2.1Å^{-1} shows that for x=26.2% the film is a mixture of fcc and hcp structures. Measurements on other films showed that for $0.25 < 0.29$, the films had the mixed fcc/hcp structure, while for x outside this range, the films were purely hcp.

It is reasonable to postulate that the formation of the fcc phase in driven by chemical ordering, since a related effect was observed for $CoPt_3$ [2]. To test this idea, experiments were conducted to search for chemical ordering peaks in the mixed fcc/hcp films with the X-ray energy tuned just below the Co K edge (to enhance the contrast between Ni and Co). However, we found no indication of short or long range chemical order. Thus, the driving force for the formation of the hcp phase is still unclear.

[1] A. Carl, D. Weller, R. Savoy, and B. Hillebrands, MRS Symposium Proceedings **343**, 351 (1994).

[2] G. R. Harp *et al.*, Phys. Rev. Lett. **71**, 2493 (1993).

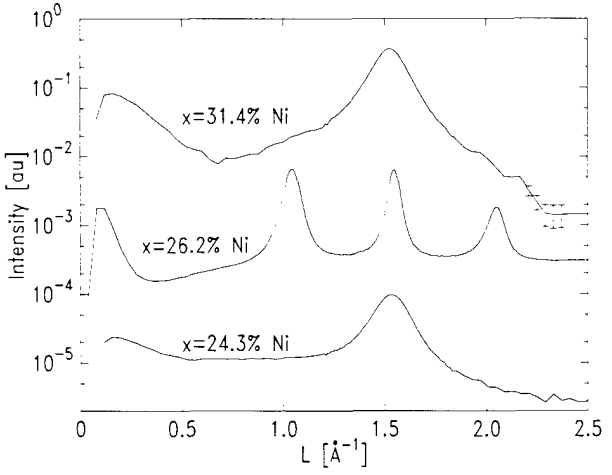

Figure 1. Scans along (10L) (in hexagonal units) for highly (111) textured NiCo have been offset for clarity.

Small Angle X-ray Scattering from Silica Aerogels — X20C

L.B. Lurio, A.R. Sandy, S.G.J. Mochrie (MIT), N. Mulders and M.W.H. Chan (Pennsylvania State University)

Silica aerogel is a highly porous material composed of strands of spheres assembled to form a dilute fractal network up to a length scale ξ, while on length scales greater than ξ, the density is on-the-average uniform. Aerogels have been used to study the effects of quenched randomness on the phase diagram of mixtures by Chan and coworkers who found that their phase diagram differs dramatically in the presence of aerogel from that of the pure mixture[1]. Small angle scattering studies were carried out in order to determine the detailed structure of the aerogels and to investigate the feasibility of structural measurements on aerogels containing mixtures. A model for the scattering was constructed consisting of the product of the structure factors from individual silica spheres, the fractal network, and the packing of networks,

$$S(Q) = \left[\frac{1}{1+\frac{2}{9}Q^4R^4}\right]\left[1+\frac{1}{(QR)^{d_f}}\frac{d_f\Gamma(d_f-1)\sin[(d_f-1)\tan^{-1}(Q\xi)]}{(1+1/(Q^2\xi^2))^{(d_f-1)/2}}\right]\times$$

$$\left[\Theta(QD)\frac{1}{1+8p\Theta(QD)}\right].$$

Here Q is the scattering vector, R the silica sphere radius, d_f the fractal dimension, Γ the gamma function, ξ the correlation length, $\Theta(qD)$ the sphere form factor, D the cluster size and p the packing fraction. Fits using the model above yielded $p = 0.02$, $D = 736$ Å, $\xi = 121$ Å, $d_f = 2.1$ and $R = 15$ Å. The upturn at large Q results from the silica inter-molecular spacing.

[1] S. B. Kim, J. Ma, and M. W. H. Chan, *Phys. Rev. Lett.*, 71:2268, 1993.

[2] D. Posselt *et. al. Journal of Non Crystalline Solids*, 145:128, 1992.

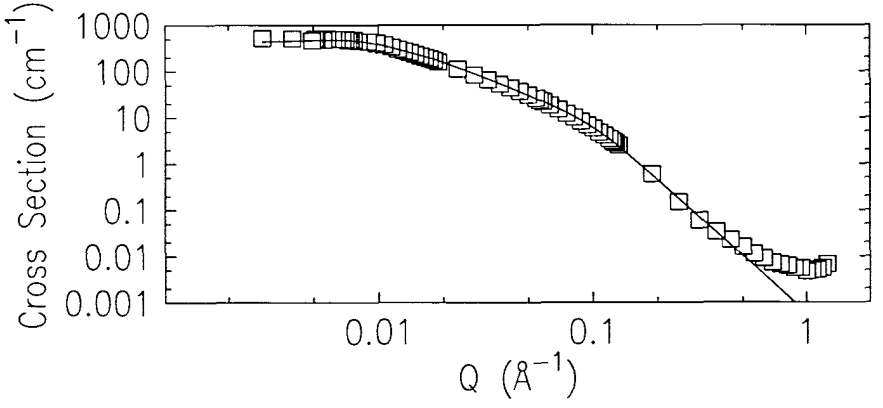

Figure 1. Scattering from a 0.029 g/cc aerogel, (square) data, (line) fit.

Phase Formation Sequence of Nickel Silicides from Rapid Thermal Annealing of Ni on 4H-SiC	X20C

L.D. Madsen (Uppsala U. and U. of Illinois), E.B. Svedberg, H.H. Radamson (Linköping U., Sweden), C. Hallin (Linköping U. and ABB Corp. Research, Sweden), B. Hjörvarsson (Uppsala U., Sweden), C. Cabral, Jr., J.L. Jordan-Sweet and C. Lavoie (IBM T.J. Watson Research Center)

Nickel films were ultra-high vacuum sputter-deposited at 400°C onto 4H-SiC. These films were cubic and highly <111>-oriented with a 6-fold in-plane symmetry. Rapid thermal annealing (RTA) at 3°C/s resulted in the following phase sequence:

$$Ni_{23}Si_2 + Ni_{31}Si_{12} \rightarrow Ni_{31}Si_{12} \rightarrow Ni_{31}Si_{12} + Ni_2Si \rightarrow Ni_2Si$$

The Ni_2Si was orthorhombic and fully formed at 770°C. Rutherford backscattering (RBS) showed that the films had distinct layering in terms of composition with carbon distributed throughout. Atomic force microscopy (AFM) showed a seven fold increase in roughening and in-plane feature size after RTA to 1100°C.

X-ray Scattering Study of Ordering Kinetics in CuAu *	X20C

O. Malis and K. F. Ludwig (Boston Univ.)

In situ x-ray scattering experiments of the kinetics of phase transition in CuAu were performed to investigate the intricate morphologies that emerge during the sublattice ordering of the low temperature ordered phase (CuAuI) following a quench from the disordered phase. The results of this study indicate a subtle competition between the metastable modulated phase (CuAuII) and the stable CuAuI.

The time evolution of the CuAuII modulated and CuAuI superlattice peaks near (110) for quenches from 703K to 653K and 643K is studied (Fig. 1). The experiment shows that CuAuII satellite peaks are generated at early times and that the persistence of these peaks is related to the quench temperature. At shallow quench temperatures or early times the modulated state is favored while at lower temperature or later times the ordered phase dominates.

The ordering kinetics can be strongly altered by changing the prequench state from a disordered phase to a modulated phase. The growth of the ordered state is found to be strongly reduced for a quench from the modulated state. These experimental results were found in qualitative agreement with Langevin simulations based on the effective medium theory (K. R. Elder, O. Malis, K. F. Ludwig, B. Chakraborty and N. Goldenfeld, in preparation).

One interesting feature observed in the experiments and not in the simulations is a shift in position of the x-ray peaks with time. This motion arises from changes in both the lattice spacing and modulation wavelength. Examination of the fundamental (200) peaks indicates that, at the temperatures and time scales discussed above, most of the lattice has already relaxed to its tetragonal shape. More significant is the shifting of the satellite peaks away from the central superlattice peak. These changes are typically quite large and occur in the early to intermediate time scales. For example in the quench to 643K the modulation wavelength decreased from approximately 15.6 to 11.5 lattice constants on a time scale of 300s. We are currently investigating these effects with Monte-Carlo simulations using Embedded-Atom cohesive energy calculations.

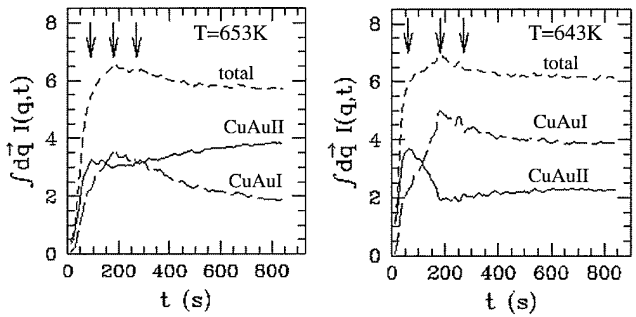

Figure 1. Time evolution of the integrated peak intensities for quenches from 703K to 653K and 643K.

* This work was supported by NSF Grant DMR-9633596.

Determination of Polymer Chain Orientation in Rubbed Polyimide Films	X20C

J. Sands (Pennsylvania State University)

The role of rubbed polyimide films as templates to induce alignment of liquid crystal molecules is an unexplained phenomenon. The near surface orientation of polymer chains produced during buffing is dependent upon the distance over which the films are buffed, applied load, and film thickness. Despite the small macroscopic force applied at room temperature ($\approx$ 200 Pa), a substantial orientation of polymer chain segments at the surface occurs. [†] This is surprising given that the bulk polyimide has high tensile modulus (10.5 GPa), tensile strength (300 MPa), and glass transition temperature (Tg $\approx 400^{o}C$). Grazing incidence x-ray scattering (GIXS) has been used to study the degree of near surface orientation as a function of applied loads. GIXS results indicate that the mechanism for the observed orientation in rubbed polymer films is driven by yielding of polymer chains aligned perpendicular to the rubbing direction. The yielding occurs since microscopically there are large stresses. A model for the measured orientational changes demonstrates that the orientation of the polymer chains is a surface affect that propogates 100Å into the film for a given set of loading conditions.

X-Ray Resonant Raman Scattering Study at the Nd L_3 Edge on Nd_2Fe_{14}	X21

F. Bartolomé, J. M. Tonnerre, L. Sève, D. Raoux (CNRS), and C-C. Kao (BNL)

We report on the work performed during the first week of measurements at X21 beam line, allocated during the 1-4/97 cycle to the General User Proposal 3136, entitled X-ray resonant Raman scattering study at the $L_{2,3}$ edges of Nd in the $Nd_2Fe_{14}B$ permanent magnet system (local contact: Dr. C-C. Kao). Resonant inelastic (Raman) scattering spectra were recorded around the L_3 absorption edge energy, monitoring the $4d_{5/2,3/2} \rightarrow 2p_{3/2}$ radiative decay channel ($L\beta_{2,15}$). About 15 spectra were recorded at different fixed incident photon energies, $\hbar\omega_1$, around the L_3 edge as a function of the scattered photon energy, $\hbar\omega_2$ (IXS scans, four of them are shown in the figure, left panel). Two additional absorption channels (labeled A1,A2 in the figure) besides the strong dipolar 2p$\rightarrow$5d (labeled B) were identified, with excitation energies lying 5–10 eV below the absorption whiteline energy. The quadrupolar origin of these pre-edge features is evidenced by its lower energy position and the qualitative agreement with recent calculations. In order to directly compare the inelastic Raman scattering with XMCD spectra the evolution of the intensity of the dipolar and quadrupolar peaks in the "fixed $\hbar\omega_1$" spectra was monitored as a function energy, thus keeping the energy transfer constant and fixed to the corresponding values of each observed feature (CFS scans). The comparison between X-ray Raman and L_3 XMCD spectra (see figure, right panel) show a one-to-one correspondence. The pre-edge features appearing at the same incident energies in both techniques can be assigned to quadrupolar electric transitions within a simple model. The results of this experiment together with complemetary results have been accepted for publication (F. Bartolomé et al. *Phys. Rev. Lett.* **79** (1997).)

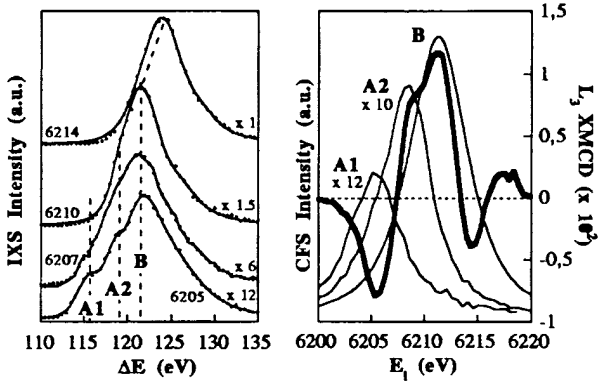

Figure 1. RIXS intensity at four incident energies (left panel) and CFS scans (right panel, thin lines) together with XMCD (thick line) at Nd L_3-edge on $Nd_3Fe_{14}B$. RIXS data are scaled as indicated in both panels.

Inelastic X-ray Scattering from Single Crystal Sodium and Lithium * | X21

P. Chow (U. Houston), J.P. Hill (BNL), C.-C. Kao (NSLS), and B.C. Larson (ORNL)

Advances in synchrotron instrumentation [1] coupled with the capability of ab initio calculations in the last few years [2] provide an opportunity to study the dynamical response the many-electron system in metals. A number of low-Z metals have been investigated in the past decade. Still, reliable experimental S(q,ω) data are required to advance the understanding of many-body physics.

At X21, we have continued our measurement of the dynamical response of single crystal Na, the proto-typical free-electron metal. We grew a 1x1x5 cm^3rod of single crystal of sodium of excellent quality. After determining the orientation of a test piece, we sawed a 1 mm thick slice of Na as our sample, chosing an orientatin such that we could measure S(q,ω) in the [001],[110] and [111] high-symmetry directions. Our aim was to measure the low-q plasmons of single crystal Na and the higher-q response function in Na in those directions. In our recent run, we have made a complete set of measurements of Na in the [110] direction, and a partial set of measurements of the [111] plasmons in Na, including a careful measurement of the empty cell background and the energy resolution. These results are being analyzed, first to account for the scattering that arises from excitations related to the band structure of the crystal, and ultimately to assess the role of the electron-electron correlations in the simple metal Na.

In addition, we have made careful measurements of the excitation spectrum of Na and Li single crystals at large wave vectors in high-symmetry directions, in order to probe many-body local-field effects and off-diagonal contributions to the dielectric function of simple metals. We have performed S(q,ω) measurements of this type on both Na and Li single crystals. The Na measurements required long counting times (due to the high absorption) whereas the Li scattering was relatively strong. *Analysis is in progress.*

[1] C.C. Kao, K. Hamalainen, M. Krisch, D.P. Siddons. T. Oversluizen, and J.B. Hastings, Rev. Sci. Inst. 66(2) 1995.

[2] A. G. Eguiluz, A. Fleszar, and J. Gaspar, Nuclear Inst. and Meth. 96, 550 (1995).

* This work was supported by NSF DMR-9208450 and DOE Div. of Materials Sciences under contract with Lockheed Martin Energy Systems.

The Evolution of the Cu K$\beta_{1,3}$ Spectrum From Threshold | X21

M. Fritsch, M. Deutsch (Bar-Ilan U., Israel), and C.C. Kao (NSLS)

The photoexcited Cu K$\beta_{1,3}$ spectrum was measured near the K edge, complementing previous measurements of the K$\alpha_{1,2}$ lines.

Below the edge, $\leq$ 8980 eV, a resonant Raman behaviour was observed (Fig. 1), showing the characteristic linear dispersion of the peak position, intensity decrease and lineshape distortion with decreasing excitation energy. The expected line narrowing at the edge is also observed.

From the edge up to $\sim$ 15 eV higher the individual lineshape is lorentzian, indicates contributions from the diagram lines only. No other transitions contribute here to the lineshape.

Above 8995 eV increasingly larger changes are observed in the lineshape. Fig. 2 shows the broad shoulder that develops on the low-energy side of the line. The energy threshold for this feature, as well as full-sperctrum fits based on Dirac-Fock *ab-initio* calculations, assign this structure to 3*d* spectator hole transitions. The cross section for this transition rises smoothly and continuously from zero, without any abrupt jumps, showing the 1*s*3*d* two-electron excitation to be a highly pure shake-off process. This is somewhat surprising, since the outer 3*d* orbital is expected theoretically to yield shake-up (rather than shake-off) lines, the cross-section of which changes abruptly at the edge. A detailed analysis is underway.

This work is supported by the Israel Science Foundation, Jerusalem.

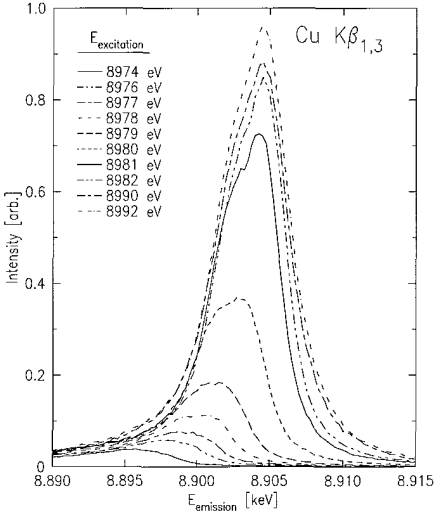

Figure 1. The K$\beta_{1,3}$ evolution near thereshold.

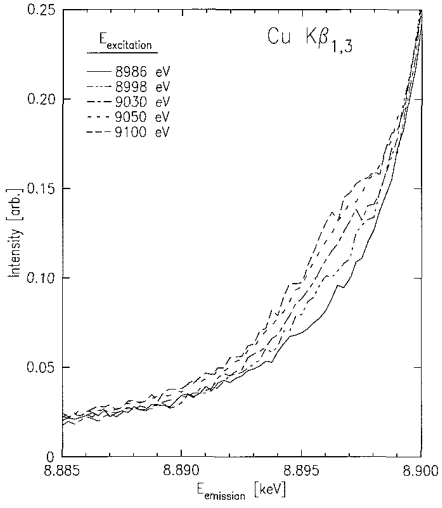

Figure 2. The 3*d* spectator shoulder growth from threshold, 10-15 eV above the K edge.

High Resolution Inelastic Scattering Study of GaN | X21

K. Hämäläinen, S. Huotari, S. Manninen (U. Helsinki, Finland), and C.-C. Kao (NSLS)

We have measured the dynamical structure factor $S(Q,\omega)$ of a single crystal GaN with high energy resolution inelastic X-ray scattering. GaN has relatively large direct bandgap and is a promising semiconductor material for example for blue laser applications. The study concentrated on the verification of the position of the bandgap (Q *and* E), and on the study of the band structure.

The GaN is highly absorbing already at 10 keV and the count rate for the inelastic scattering cross section is extremely low. However, due to the very low background (less than one count in 5 minutes), we were able to clearly separate the bandgap features from the background. We measured the inelastic scattering cross section at several symmetry points. Due to the strong bragg peaks, we could not always examine the transition at all high symmetry points (for example the direct transition), instead we had to study it at the positions of forbidden bragg reflections.

The momentum transfer in the scattering process is relatively high and the dipole approximation starts to fail. This has both a negative and positive impact: it make the calculation of the transition matrix elements more difficult but, on the other hand, it can add more weight on the optically forbidden transitions and makes it possible to study different features of the band structure.

The theoretical analysis of the spectra will be based on band structure calculation including proper matrix elements beyond the dipole approximation. The detailed calculation needs extensive summation over all allowed momentum transfer vectors over the reciprocal space. A detailed analysis of the data and the numerical calculations are in progress.

Resonant Inelastic Scattering in Nd_2CuO_4 | X21

J.P. Hill, C.-C. Kao, W.A.C. Caliebe (BNL), M. Mastubara, A. Kotani (ISSP, Tokyo), J.L. Peng and R.L. Greene (U. Maryland, College Park).

Understanding the normal state electronic properties of the high-Tc copper oxides is important as a prerequisite for a theory of high temperature superconducitivity. In addition, the properties themselves are highly unusual, exhibiting non-Fermi-like behavior and have attracted much interest, both in this context and from a general perspective of understanding electronic behavior in other strongly correlated transition metal oxides (eg the colossal magnetoresistance maganates). Theoretical approaches typically treat the copper oxide planes as the relevant electronic structure within a Hubbard-type model. These correctly predict the antiferromagnetic insulator ground state in the undoped materials, but do less well in calculating excited state properties, in part due to a lack of detailed knowledge of the model parameters. Here inelastic x-ray scattering can make an important contribution because, unlike other spectroscopies, it can measure the excitation spectrum directly without the complicating effects of a core-hole being present in the final state. Further the technique offers bulk-like penetration.

We report resonant inelastic x-ray scattering studies of Nd_2CuO_4, the parent compound of the electron doped high-Tc family, $Nd_{2-x}Ce_xCuO_4$. Resonant scattering provides the additional advantage of being an element specific probe, allowing the excitations associated with the copper orbitals to be preferentially probed. A resonantly enhanced excitation of 2 counts per minute was observed when the incident photon energy was tuned through the Cu K-edge. Our results show that the anti-bonding state in the CuO planes is 6 eV above the ground state. The excitation was identified with the help of numerical calculations of the scattering, using an Anderson impurity model to describe the Cu(3d)-O(2p) hybridization. The 6 eV excitation is only seen at 8990 eV incident energy. The theory also predicts an enhancement at 8983 eV, not seen in the experiment, and we speculate that the absence of a feature at 8983 eV is associated with non-local (solid-state) effects.

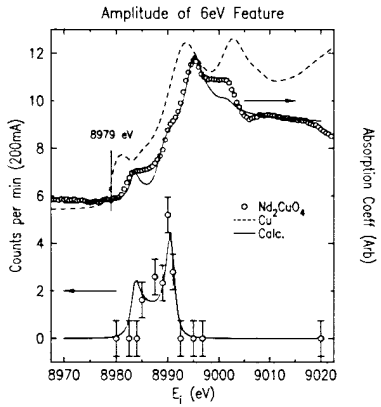

Figure 1.

Impact of Band Structure and Many-Body Effects on the Electronic Response of a Simple Metal Al)*	X21

B. C. Larson, J. Z. Tischler (ORNL), A. Fleszar (U. of Würtzburg), and A. G. Eguiluz (U. of TN & ORNL)

Combined inelastic x-ray scattering and first-principles dynamical response calculations have demonstrated that band-structure effects in electronic energy loss spectra are much more pervasive than generally realized. High-resolution x-ray scattering measurements (~0.75 eV) made on Al using the X-21 beam line at NSLS have shown that band-structure effects have a significant impact on the energy loss spectrum of Al at both small and large wave vectors. In addition to the well-known band-structure and many-body local-field factor (LFF) plasmon energy shifts, zone-boundary collective state resonances, spectral shifts to lower energies, and high energy tails are observed at all wave vectors. Fig. 1 compares calculated non-interacting polarizabilities, $\chi_o(q,\omega)$, for jellium and band electrons. We note that the calculations including the band structure contain a sharp dip at ~8 eV, an overall spectral shift to lower energies, and a high-energy tail; none of these are present in the jellium calculations. The zone-boundary collective state structures (generated by energy gaps at the Brillouin zone boundary) are well known; however, the spectral shift to lower energies and the tail in the dynamical electronic response calculations at high energies are of equal or larger importance for quantitative extraction of many-body effects from the shape of energy loss spectra. The dynamical structure factor calculations, $S(q,\omega)$, in Fig. 1 that include the actual band structure of aluminum are in remarkably good agreement with the measured loss spectrum at a wave vector of 0.71 k_F, in contrast to the poor agreement of the jellium calculations with the measurements.

The effects discussed above relate to diagonal contributions to the dielectric matrix. Measurements along the [001] direction have demonstrated the impact of off-diagonal effects as well, through the interaction of the band structure induced folded-plasmons with single-particle continuum states.

*Research sponsored by U.S. DOE under contract No. DE-AC05-96OR22464 with Lockheed Martin Energy Research Corp.

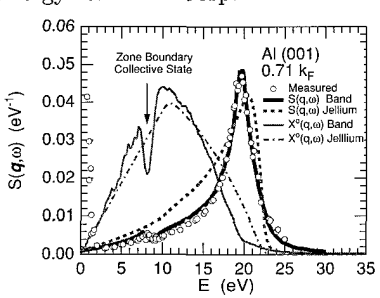

Figure 1. Inelastic x-ray scattering measurements for Al at a wave vector of 0.71 k_F. Jellium model $\chi_o(q,\omega)$ and $S(q,\omega)$ calculations are compared with measurements and first principles calculations including band structure. The (complex) LFF values for $S(q,\omega)$ are (0.5, 0.044) for jellium and (0.2, 0.09) for band calculations.

Inelastic X-ray Scattering around the Metal-Insulator Transition in VO_2	X21

O. Müller, P. Pfalzer, M. Klemm, S. Horn (Univ. Augsburg, Germany), M. L. denBoer (Hunter College CUNY)

The metal insulator transition (MIT) in transition metal oxides has attracted much interest over the last decade. Widely studied examples include V_2O_3 and VO_2, which show an MIT combined with a structural transition. While the transition in V_2O_3 is often considered to be Mott-Hubbard, this probably neglects the role played by the many atomic orbitals near the Fermi surface, and the situation is even less clear for VO_2, which may in fact be "more bandlike than correlated." The high temperature phase of VO_2 is a rutile metal with two molecules per unit cell. Below 340 K the material becomes a monoclinic insulator, with four molecules per unit cell, reached by distortion of the rutile phase and formation of V - V pairs. Photoelectron spectroscopy has been used to study VO_2, and the results differ in important ways from theoretical predictions. To resolve the evident disagreements, and to further study the electronic structure of VO_2 and the changes it undergoes at the MIT, we have carried out inelastic x-ray scattering experiments on well-characterized single crystals of VO_2, both above and below the MIT and as a function of the momentum transfer q. In Fig. 1 we show the energy loss region below 35 eV for the sample in its insulating state at room temperature. Several loss features are apparent, which are found to disperse with the momentum transfer q (not shown). Also shown in Fig. 1 is a preliminary fit to the spectra, showing it is composed of a number of inelastic energy loss excitations, analysis of which is not yet complete. In Fig. 2 the same spectrum is shown with the sample in the metallic state above 340 K. Comparison shows there are important spectral changes associated with the MIT, which will shed light on the electronic states involved in the transition.

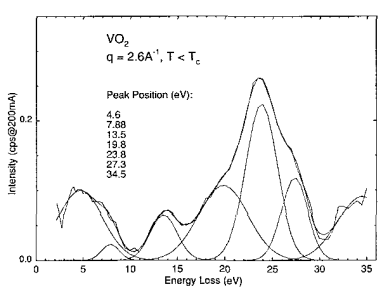

Figure 1. Inelastic loss spectrum of VO_2 at room temperature (insulating) and preliminary fit.

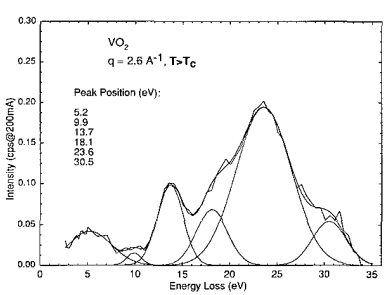

Figure 2. Inelastic loss spectrum of VO_2 above the MIT (conducting) and preliminary fit.

Electronic Excitations in Solid C_{60} by Inelastic X-Ray Scattering | X21

P. W. Stephens, S. Zwerschke (SUNY at Stony Brook), H. Berger (Swiss Federal Institute of Technol, Lausanne), and C.C. Kao (NSLS)

We have measured the dynamical structure factor of a single crystal of C_{60} with an energy resolution of 0.6 eV FWHM for $0.4\AA^{-1} < Q < 1.9\AA^{-1}$, for Q along (111), (110), and (100) directions. The spectra are dominated by an "on-ball" plasmon which disperses from 26 eV at 0.4 $\AA^{-1}$ to 34 eV at 1.9 $\AA^{-1}$.

The lower energy region reveals a more complicated spectrum of electronic transitions. Fig. 1 (left) below shows the evolution of $S(Q,\omega)$ in the (111) direction. The results may be compared with electron energy loss spectra of polycrystalline films recently published in [1].

One might have expected that the excitation spectrum in this energy range would be a property of the single fullerene molecule, but Fig. 2 (right) shows that there is significant dispersion with the *direction* of Q.

[1] M.S. Golden *et al.*, *J. Phys: Condens. Matter* **7** 8219 (1995).

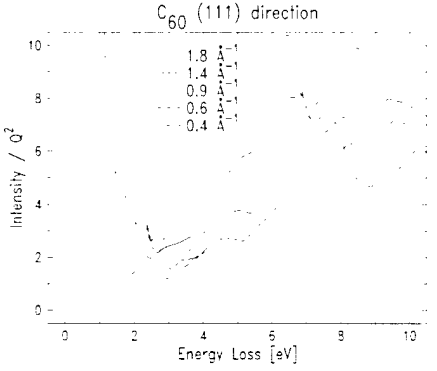

Figure 1.

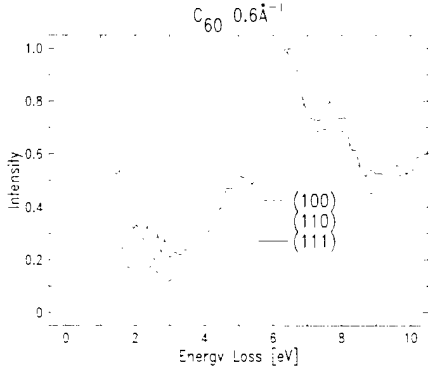

Figure 2.

Structure of Electrode Surfaces in the Course of Electrocatalytic: Br/AU(100) anf Ag/Pr(111) during the course of O_2 | X22A

R.R. Adžić and J.X. Wang (BNL)

Information on the structure of catalytic surfaces, in particular the structure of active phases, obtained during the course of reactions is of paramount important for the areas of electrocatalysis and catalysis. Such information can help designing electrocatalysis with desired properties and increase the understanding of electrocatalytic reactions and these effects are structure-dependent. In this work, the grazing angle incidence x-ray diffraction technique has been applied to study Br and Ag adlayers, during the course of O_2 reduction on Au(100) and Pt(111), respectively.

Structure of Br adlayers was determined on the Au(100) electrodes in the absence and in the presence of O_2 reduction in 0.1 M $HClO_4$ solutions. In both cases, the $c(\sqrt{2} \times 2\sqrt{2})R45°$ and $c(\sqrt{2} \times p)R45°$ phases were found above 0.3 and 0.7 V, respectively, in agreement with previous work in neutral solutions. Oxygen reduction is completely inhibited by the $c(\sqrt{2} \times 2\sqrt{2})R45°$ Br adlayer. It takes place only at potentials negative of the low potential limit of the existence of the $c(\sqrt{2} \times 2\sqrt{2})R45°$ phase (Fig. 1).

Ag forms a hexagonal incommensurate bilayer on Pt(111) at underpotentials. The first monolayer, however, has a commensurate (1×1) structure. A complete inhibition of O_2 reduction on Pt(111) has been observed upon deposition of Ag monolayer. Ag atoms reside in the three-fold symmetry sites on Pt(111). This information allows further analysis of the inhibition of O_2 reduction as a function of the Ag coverage. A statistical analysis of this inhibition shows that during reduction O_2 adsorbs in a bridge configuration on Pt(111). This answers the long-standing question, which of the three models of O_2 adsorption (Pauling's, Griffiths' and "bridge") is operative in O_2 adsorption on Pt during reduction.

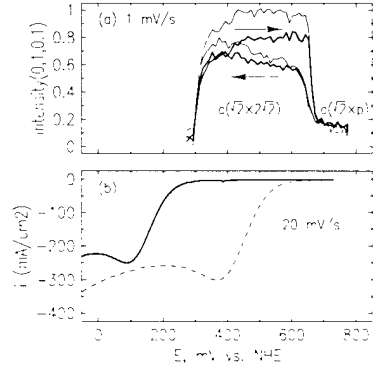

Figure 1. (a) Diffracted x-ray intensity from the $c(\sqrt{2} \times 2\sqrt{2})R45°$(a) Br adlayer as a function of potential for Br/Au(100) in 0.1 M $HClO_4$ containing 20 mMKBr in the absence (thin line) and in the presence (thick line) of oxygen. (b) O_2 reduction on Au(100) in 0.1 M $HClO_4$ in the absence (dashed line) and in the presence of 20 mM KBr (full line).

X-Ray Scattering Study of the Calcite–Water Interface: Surface Structure and Metal Adsorption	X22A

P. Geissbühler, D. Yee*, L. B. Sorensen (U. Washington, Seattle), P. Fenter, N. C. Sturchio (ANL), and E. DiMasi (BNL) *Present address The Boeing Co.

Chemical and physical interactions at mineral surfaces control the transport behavior of metal contaminants in soils and groundwater systems. Atomic-scale structural information on metal speciation and reaction mechanisms at the mineral–water interface is required to achieve a fundamental understanding of these interactions.

Calcite is a ubiquitous mineral and an important metal sorbent. While many powder sorption experiments have been performed on calcite, almost no in-situ atomic-scale structural data is available for adsorbates at the calcite–water interface.

One unresolved question has been the nature of the calcite surface structure in water and air. We have performed X-ray reflectivity measurements of calcite single crystals after cleaving in air, in-situ with a thin water film, and after being blown dry with N_2 gas. In all cases the reflectivity differs from that expected of sharply terminated bulk calcite, and is suggestive of relaxation of the carbonate groups in the surface layer (Fig. 1). Essentially no difference is observed between the air–calcite and water–calcite interfaces.

We have also studied the adsorption of metals from solution, including Pb and Cd. Calcite exposed to Pb solution accumulates a submonolayer of Pb atoms. In combination with previous X-ray standing wave studies, our data indicate that Pb substitutes for Ca in the surface layer [1]. Exposure to solution containing Cd results in a Cd-enriched surface, followed by the appearance of $CdCO_3$ crystallites which are strained by the underlying $CaCO_3$ lattice (Fig. 2) [2].

[1] N. C. Sturchio *et al*, Geochim. Cosmochim. Acta (in press).

[2] R. P. Chiarello, N. C. Sturchio, *Geochem. Cosmochim. Acta* **58** (1994) 5633.

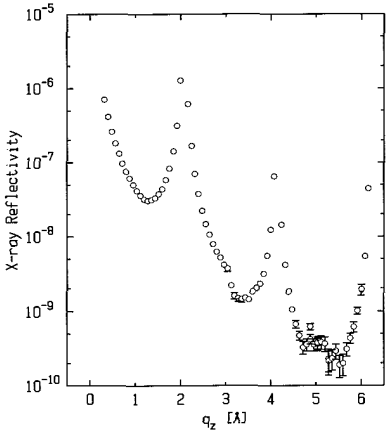

Figure 1. X-ray reflectivity $R(q_z)$ of the calcite–water interface.

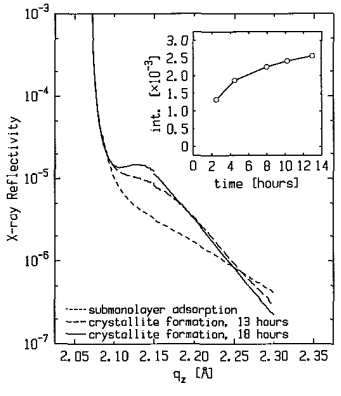

Figure 2. Reflectivity near the $CaCO_3$ Bragg peak during Cd adsorption from solution. Inset: Intensity at the anti-Bragg position during Cd deposition.

Depth-Dependence of Strains in Cu Films on AlN *	X22B, X22A

L. J. Martínez-Miranda, Y. Li (U. of Maryland, College Park), L. K. Kurihara, P. Schoen, and G. M. Chow (NRL)

We have studied the depth dependence of the structure of Cu films deposited on AlN substrates via the polyol method. In this method, Cu particles are believed to precipitate from solution, and aggregate to form a number of reaction interfaces, and a metallic film on the substrate. We have found that this metallic film consists of a bulk polycrystalline Cu film as well as an upper layer of (100) textured Cu. This layer constitutes as much as one third of the film.

We have studied the in-plane structure of this upper layer using 8keV X-rays. We have found that the structure of the films in this region consists of a distribution of lattice spacings that correspond to strains that range between -0.6 and 1 percent, as seen in Figure 1. The observed in-plane peaks are superimposed over a wide diffused background. The in-plane azimuthal texturing depends on the time the solution is left refluxing during film processing as well as the orientation of the substrate during the deposition process. Films deposited on a horizontally oriented substrate are more textured than films deposited on a vertically oriented substrate. Films refluxed for a longer time are less textured than those refluxed at shorter times (compare Figures 1 and 2).

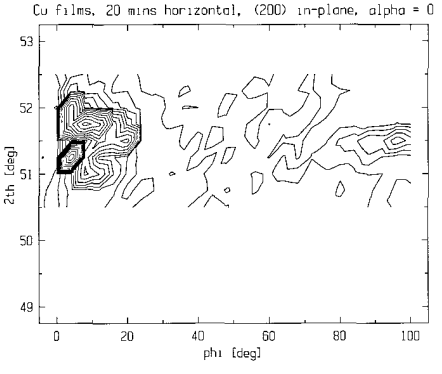

Figure 1. In-plane azimuthal scan of the Cu (200) peak of a 20 min H sample at grazing incidence.

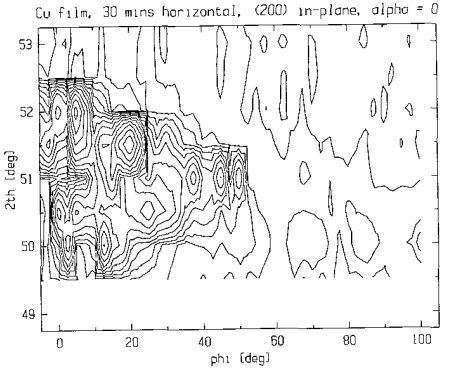

Figure 2. In-plane azimuthal scan of the Cu (200) peak of a 30 min H sample at grazing incidence.

* Work supported by NRL and ONR nanostructured materials programs.

In situ X-ray Diffraction Studies of $LiMn_2O_4$ in Li Ion Battery Cells* | X22A

S. Mukerjee, T. R. Thurston, N. M. Jisrawi, X. Q. Yang and J. McBreen (BNL)
M. L. Daroux, and X. K. Xing (Gould Electronics)

The Structural behavior of layered and spinel lithiated oxides such as $Li_xMn_2O_4$ vary considerably depending on the preparation conditions. The diversity in structural properties in turn affects the behavior of these materials when they are used as cathodes in battery cells. *In situ* x-ray diffraction studies of these materials within operating battery cells offers an excellent method for understanding and improving them, specially with regard to their cycle life characteristics.

Materials studied as a part of this investigation, were from commercial sources. Structural evolution in these spinel compounds could be classified into two groups, A and B. Group A had clear two or three phase coexistence, while group B showed supressed two phase coexistence.Although the exact preparation conditions of the various samples are proprietary, comparison of our experimental results with those of other researchers leads to the conclusion that the group B materials were prepared lithium rich compared to group A. The group B materials consequently show suppressed structural transitions and more importantly better cycle life. This is amply exhibited in figure 1. In contrast to this the group A materials all showed coexistence of two or more phases as evident from figure 2 which shows the coexistence of three phases at x = 0.5 in $Li_xMn_2O_4$. Although all the group B materials have less pronounced structural transitions, we have not measured a single batch where the transitions were completely supressed. It may turn out to be completely impossible to supress this transition in undoped $Li_xMn_2O_4$.

* This work was supported by CRADA grant No , U. S. DOE.

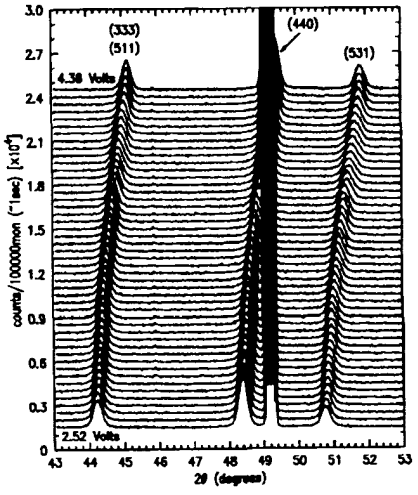

Figure 1.

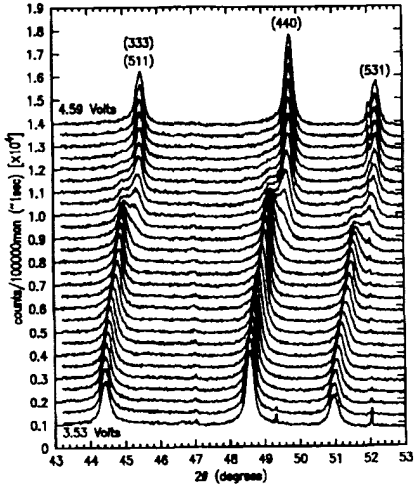

Figure 2.

Epitaxial Growth of Electrodeposited "BCC" Copper on Au(100) | X22A

R. Randler, D.M. Kolb (U. Ulm), I.K. Robinson (U. of Il.), and B.M. Ocko (BNL)

Scanning Tunneling Microcopy studies of copper electrodeposition on Au(100) strongly suggest that the first ten monolayers deposit epitaxially while an instability develops at higher coverages which leads to a buckled film(1). Here we report x-ray scattering results for electrodeposited copper films below ten monolayers. Studies were carried out using a flame annealed single crystal and an in-situ x-ray scattering electrochemical cell. All potentials are with respect to Ag/AgCl electrode.

X-ray specular and nonspecular reflectivities are shown in the figures. The appearance of the broad shoulder/peak at about L=2.8 (Fig. 1) results from a thin copper film with a Cu-Cu layer spacing smaller than the Au(100) layer spacing. The reflectivities were fit to a real-space model which includes the semi-infinite Au(100) lattice terminated by epitaxial copper with a Gaussian thickness distribution. The best fits give 4.2 Cu layers in (c) and 6.5 layers in (d). For all coverages, the extracted copper layer spacing is 2.85 ± 0.03 Å which is very close to the (2.885 Å) Au-Au spacing. The close agreement between the in-plane and out-of-plane lattice constants, along with additional diffraction data (See Fig 2), indicates that the deposited copper is only slightly distorted from BCC.

(1) D.M. Kolb, R.J. Randler, and R.I. Wielgosz, and J.C. Ziegler, in Electrochemical Synthesis and Modification of Materials, Mat. Res. Soc. Symp. Proc. 451 p. 9 (1997).

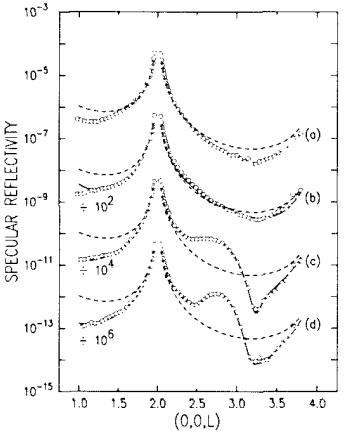

Figure 1. Specular reflectivity from electrodeposited Cu on Au(100). a) no copper (0.5 V). (b) a copper UPD layer (0.1V). and (c.d) copper multilayers with different deposition times (-0.3 V). Dashed lines calculated for ideally terminated Au(100). Solid lines are best fits.

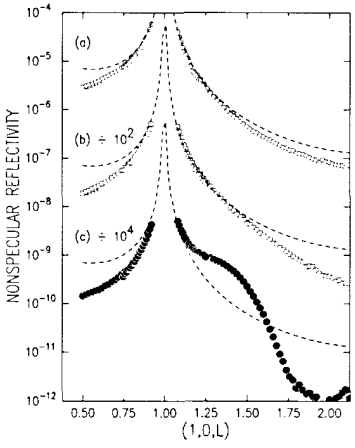

Figure 2. Nonspecular reflectivity (tetragonal coordinates) from electrodeposited Cu on Au(100). a) no copper (0.5 V). (b) a copper UPD layer (0.1V). and (c) copper multilayer (-0.3 V). Dashed lines calculated for ideally terminated Au(100).

Multiple Structures of Tl Adlayers Induced By Coadsorption of Br^- on the Au(111) Electrode Surface	X22A

J. X. Wang and R. R. Adžić (BNL)

The voltammetry curve for the underpotential deposition of Tl on Au(111) in 0.1 M $HClO_4$ solution containing 1 mM TlBr (Fig. 1.) shows rarely observed multitude of reversible peaks. Tl, at potentials negative of peak E, and Br, at potentials positive of peak A, form incommensurate close-packed, hexagonal adlayers as in the absence of the other species. At the intermediate potentials, three superlattice structures are observed which do not exist in the absence of either Tl^+ or Br^-. The phase transitions are shown by the potential dependent diffraction intensities at (9/13,3/13), (0,1/2), and (0.468,0.468) for the $3-(\sqrt{13}\times\sqrt{13})$, $2-(3\times\sqrt{3})$, and $c(2.136\times\sqrt{3})$ phases, respectively. The first two phases are commensurate and well-ordered, existing in the low-current potential regions between peaks B-C and C-D. The diffraction at the (0.468,0.468) position is broad and weak, but does not shift with potential in the region between peak D and E. The integrated intensity has been measured for in-plane diffractions (L=0.2) up to the fifth order for the $3-(\sqrt{13}\times\sqrt{13})$ and $2-(3\times\sqrt{3})$ phases and the part of data are shown in Fig. 2. The integrated intensities (after corrections) agree with the values (listed in Fig. 2) calculated using the models shown in Fig. 1. The $(\sqrt{13}\times\sqrt{13})$ unit cell contains 3 Tl and 6 Br. The hexagonal symmetry and the Tl/Br ratio of 1/2 in this phase can be rationalized by the higher partial charge of Tl than Br at the rather positive potential. As the Tl becomes more discharged at more negative potentials, the Tl/Br ratio becomes 1/1 and the $2-(3\times\sqrt{3})$ phase exhibits quasi-square symmetry. Layer spacings in the coadsorbed phases are proposed on the basis of the ionic radii of Tl^+ (2.98 Å) and Br^- (3.92 Å) and will be determined from surface rod measurements.

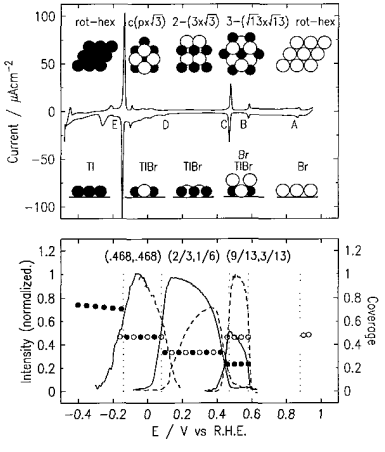

Figure 1.

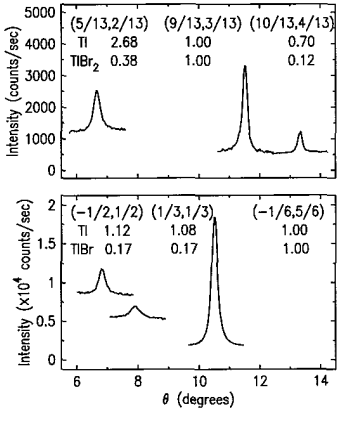

Figure 2.

X-Ray Induced Transitions in Manganites	X22B

D. Casa, V. Kiryukhin, B. Keimer (Princeton U.), J. P. Hill, A. Vigliante (BNL), Y. Tomioka, and Y. Tokura (JRCAT)

Manganites of composition $Pr_{1-x}Ca_xMnO_3$ (x=0.3-0.5) were investigated by synchrotron x-ray diffraction in high magnetic fields. At low temperatures these materials undergo magnetic field induced transitions from charge-ordered antiferromagnetic insulators to ferromagnetic metals. Surprisingly, diffraction experiments on the x=0.3 material revealed that exposure to the x-ray beam itself also diminishes the charge order. At the same time, the electrical conductivity is enhanced by several orders of magnitude[1].

During the past year, we have systematically investigated this novel effect. We found that an applied magnetic field accelerates the x-ray induced transition for x=0.3, and a threshold field has to be applied to induce the transition for larger x (2T for x=0.4, and 8T for x=0.5). The lattice domain structure is altered in a nontrivial manner by x-ray exposure. The transition occurs only at low temperatures and is reversible on thermal cycling. When Ca is partially substituted by Sr, persistent x-ray photoconductivity is observed up to temperatures in excess of 100K. This may facilitate possible applications of the effect in x-ray detection or x-ray lithography.

In analogy to persistent photoconductivity in compound semiconductors doped with DX centers, we argue that the x-ray induced transition is evidence for strong electron-lattice interactions of which the Jahn-Teller effect is a plausible origin. However, the collective nature of the transition in the manganites, and the associated kinetics, require more elaborate models.

[1] V. Kiryukhin, D. Casa, J.P. Hill, B. Keimer, A. Vigliante, Y. Tomioka and Y. Tokura, Nature 386, 813 (1997).

Surface Structure of Liquid Hg/Au Alloys * | X22B

E. DiMasi, B. M. Ocko (BNL), M. Deutsch (Bar-Ilan U., Israel), H. Tostmann, and P. S. Pershan (Harvard U.)

Catalysis at the surface of binary metal alloys is understood to depend on the valence of the two metallic elements, as extra electrons in the dissolved metal act to fill unoccupied surface states. Since the catalyzed reaction proceeds at surface sites, the disorder frozen into the solid metal surface also plays a role [1].

Catalysis at the liquid metal surface has several advantages over that at the solid metal: the surface is smooth, particles are mobile, and active centers can be refreshed on short time scales. Studies of the rate of formic acid decomposition over liquid mercury with different concentrations of dissolved metals have found that the addition of higher-valence metals decreases the activation energy of the reaction. This was interpreted as indicating that electrons are localized in covalent bonds at the alloy surface [1].

To study the effect of dilute alloys on the surface structure of liquid metals, we have performed X-ray reflectivity measurements on liquid mercury alloyed with 0.06, 0.10, and 0.13 weight % Au. The reflectivity for the Hg-Au alloys exhibits one or more minima (Fig. 1), with the surface layering peak somewhat attenuated at high temperatures relative to pure Hg. These data are consistent with a lower density surface region (Au depleted) and a higher density bulk phase (Au enriched). We find a complicated dependence on temperature, concentration, and thermal cycling that may be related to the presence of the passivating H_2 atmosphere in the sample cell.

[1] G.-M. Schwab, "Catalysis on Liquid Metals", Berichte der Bunsen-Gesellschaft **80** (1976) 746.

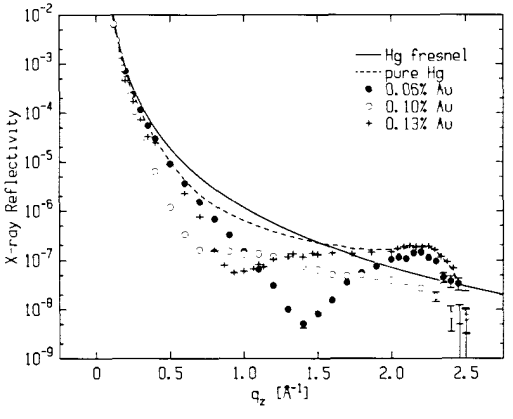

Figure 1. X-ray reflectivity $R(q_z)$ of liquid Hg and Hg-Au alloys at $-23°$C.

* M.D. acknowledges support from the US-Israel Binational Science Foundation.

Temperature Dependent X-ray Scattering from Liquid Metal Surfaces * | X22B

E. DiMasi, B. M. Ocko (BNL), M. Deutsch (Bar-Ilan U.), H. Tostmann, O. G. Shpyrko, and P. S. Pershan (Harvard U.)

Our understanding of the liquid metal surface lags behind that of the solid, due to complications introduced by the lack of long-range order. Features unique to liquid metals, such as surface induced layering, have recently been identified through surface X-ray scattering. Studies at different temperatures reveal characteristics inconsistent with the predictions of capillary wave theory, shown to account well for simple liquids.

We have measured reflectivity and thermal diffuse scattering from liquid Hg and In surfaces. Hg was studied between $-40°$C and $+25°$C in a high vacuum cell equipped with a liquid nitrogen cold finger. A new UHV chamber designed for the Harvard/BNL X22B liquid spectrometer was used for measurements of In at 220°C.

For liquid Hg, the reflectivity $R(q_z)$ is characterized by a peak at $q_z \approx 2.2$ Å with a temperature dependent amplitude that is related to the surface roughness (Fig. 1(a)). Previous studies of liquid Ga [1] revealed that the surface roughness, deduced from fits to $R(q_z)$, has a temperature dependence consistent with thermally excited capillary waves (Fig. 1(b), ◇). Similar analysis of Hg reveals that the surface roughness decreases more quickly with reduced temperature than expected from capillary wave theory.

We have also measured the thermal diffuse scattering for Hg near the specular condition at several q_z by scans over the X-ray exit angle β (Fig. 1(c)). These measurements are expected to reveal information about the length scales affecting surface excitations in the liquid metals.

[1] M. J. Regan *et al*, Phys. Rev. B **54** (1996) 9730.

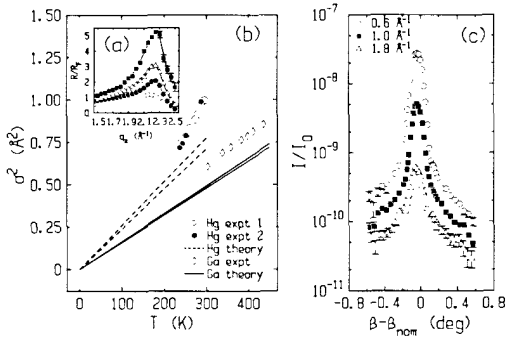

Figure 1. (a) Normalized X-ray reflectivity of liquid Hg at $-36°$C (■), $-15°$C (△), $+6°$C (●), and $+25°$C (○). Solid lines are model fits. (b) Mean-squared surface roughness vs. temperature for liquid Ga and Hg. Lines show the linear capillary wave dependence of $\sigma^2(T)$ for extremal reported values of the surface tension. (c) Thermal diffuse scattering of liquid Hg at several values of q_z.

* M.D. acknowledges support from the US-Israel Binational Science Foundation.

X-ray Scattering Studies of PBLG Monolayers at the Gas/Water Interface | X22B

M. Fukuto, R.K. Heilmann, P.S. Pershan (Harvard U.), J.A. Griffiths, S.M. Yu, and D.A. Tirrell (U. Mass Amherst)

We report x-ray reflectivity and grazing- incidence diffraction (GID) measurements of both mono-and polydisperse PBLG monolayers as a function of area/monomer A. We found no discernible effects on microscopic behavior due to differing dispersity. The area-pressure isotherm shows with decreasing A (I) a surface pressure free region at large A, followed by (II) a steep rise in surface pressure π, (III) a broad coexistence region with fairly constant π, and (IV) a further increase in π at even smaller A. The limiting values for A strongly suggest a mono-to-bilayer transition. In region (I) a single GID peak (inter-helix-distance $d \simeq 13.6$ Å independent of A) indicates parallel alignment of α-helices. Together with reflectivity results and previously taken Brewster angle microscopy pictures this suggests coexistence of macroscopic areas of uncovered water with PBLG monolayer regions. In region (II) the subphase is completely covered by a monolayer and the GID peak shift shows a decrease in d to $\simeq 12.6$ Å, resulting in an average in-plane compressibility of about 8×10^{-3} cm/dyne in the direction perpendicular to the helix axes. In region (IV) the GID pattern shows a narrow ($d_1 \simeq 12 - 12.6$ Å) and a broader peak ($d_2 \simeq 13.5 - 14$ Å). Reflectivity indicates a bilayer with the top layer being less dense. These results suggest that compression through the coexistence region (III) forces α-helices out of the original monolayer into an initially unoccupied second layer on top. The compressibility of the sharp peak in region (IV) is comparable to that of the single peak in region (II), while the broader peak in region (IV) appears less compressible. We believe the broader peak originates from the less dense second layer. (Work supported by NSF-DMR-95-23440 and NSF-DMR-94-00396)

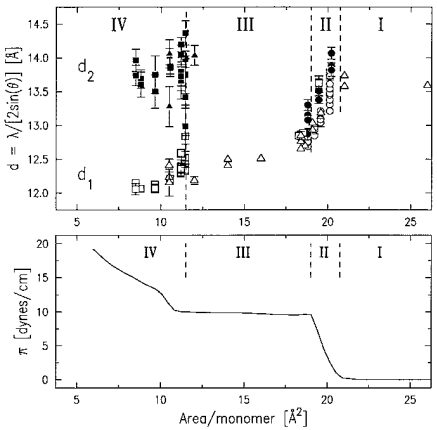

Figure 1. top: d_1 and d_2 vs. A; bottom: continuous $\pi - A$ isotherm.

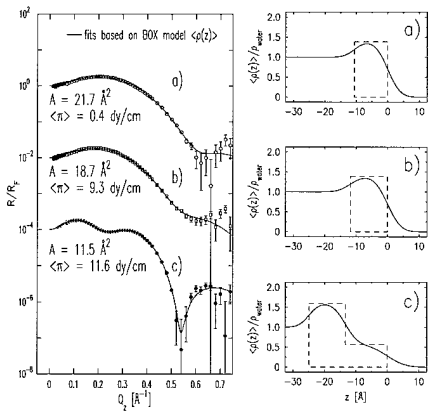

Figure 2. Normalized reflectivities, fits and density profiles at three different A.

Diffuse Scattering from a Langmuir Monolayer of PBLG* | X22B

M. Fukuto, R.K. Heilmann, O.G. Shpyrko, P.S. Pershan (Harvard U.), J.A. Griffiths, S.M. Yu, and D.A. Tirrell (U. Mass. Amherst)

Off-specular diffuse scattering measurements have been carried out on the Langmuir monolayer (LM) formed by polydisperse poly-γ-benzyl-L-glutamate (PBLG) at the water/gas interface. The intensity is measured within the incident plane by scanning the detector angle (β-scan) relative to the surface, for various fixed incident angles (α). The results are shown in Fig. 1 for the *monolayer* at $<\pi> = 7.8$ dy/cm and in Fig. 2 for the *bilayer* at $<\pi> = 8.8$ dy/cm. Each solid line corresponds to the convolution of the known experimental resolution with the differential cross section expected from the presence of thermally excited capillary waves and the surface structure used to model the reflectivity from the homogeneous Langmuir surface layer. Agreement between the measurements and the theory for the PBLG *monolayer* supports the assumptions that the monolayer is microscopically homogeneous and the interfacial height fluctuations on the monolayer surface follow the capillary wave model. However, the data for the *bilayer* is consistently higher than would be expected for a homogeneous bilayer by a factor of 1.5 to 2. The ratio of the measured to the expected intensity is plotted in Fig. 2b for the bilayer, which clearly shows the excess scattering in the off-specular part. The understanding of the bilayer results requires further quantitative analysis. However, the excess scattering must be due to microscopic inhomogeneity in the second layer.

*This work was supported by NSF-DMR-95-23440 and NSF-DMR-94-00396.

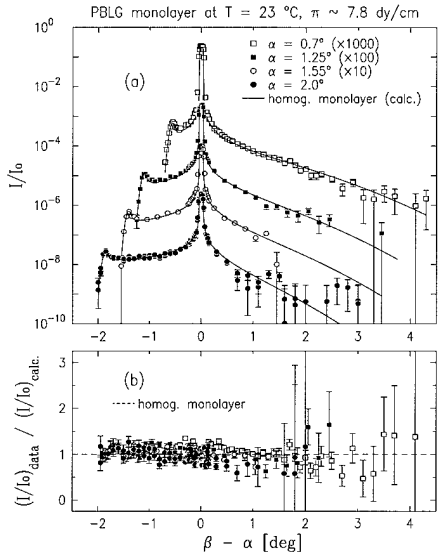

Figure 1. β-scans for PBLG monolayer at $< \pi > = 7.8$ dy/cm.

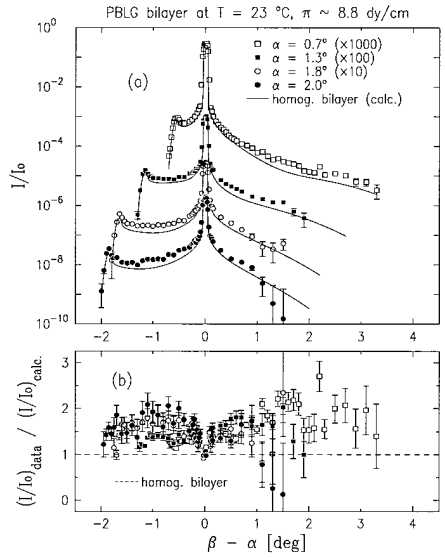

Figure 2. β-scans for PBLG bilayer at $< \pi > = 8.8$ dy/cm.

Surface Phases in Semifluorinated Alkane Melts * | X22B

O. Gang (Bar-Ilan U., Israel), M. Möller (Ulm U., Germany), B. Ocko(BNL), X.Z. Wu (IBM Almaden), E. Sirota (Exxon) and M. Deutsch (Bar-Ilan U.)

The surface structure of melts of diblock n-alkanes $F(CF_2)_m(CH_2)_nH$ (denoted F_mH_n) were investigated for n=12, 16, and 18, and m=12 near the bulk freezing temperature T_f. Unlike simple liquid, including non-fluorinated alkane melts, the X-ray reflectivity (XR) curves of the *liquid* surface (Fig.1a) at ~10K above T_f show modulations for all three compounds, indicating layering at the surface. The shape and wavelength of the modulations are consistent with a first layer of molecules having its hydrocarbon part towards the vapour, and its fluorocarbon part pointing into the liquid.

Upon cooling towards T_f, $F_{12}H_{12}$ and $F_{12}H_{18}$ show surface freezing for $T_f \leq T \leq T_s \approx T_f + 2K$, while $F_{12}H_{16}$ does not. $F_{12}H_{12}$ forms a well-defined, dense crystalline surface monolayer, as indicated by a sharp minimum in the XR (Fig. 1b) and a strong GID peak, both of which remain unchanged down to T_f. By contrast, the surface monolayer formed by $F_{12}H_{18}$ is amorphous in-plane, and varies strongly with temperature below T_s, as shown by the XR curves for different temperatures (Fig. 1c).

These results, in particular the strong dependence of the surface organization near T_s on the length of the hydrocarbon, reflect the strong competition, due to mutual repulsion, between the hydro- and fluoro- parts of the diblock.

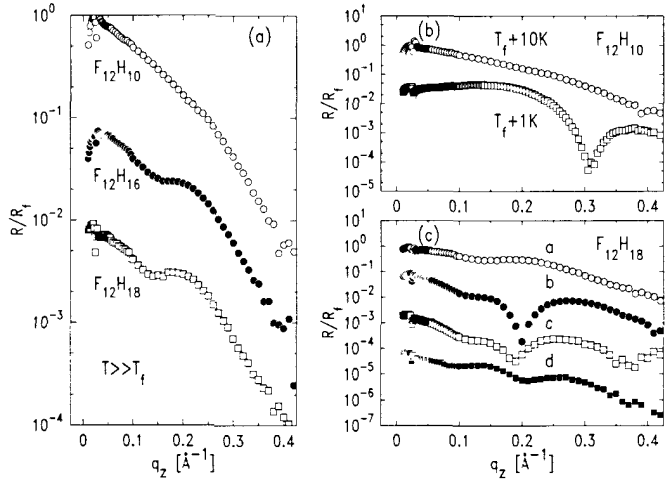

Figure 1. X-ray reflectivity (a) high above melting, (b) in the liquid and crystalline surface phases, and (c) variation with temperature in $F_{12}H_{18}$. Temperature decreases from a to d in the range [T_f, T_s].

* This work was supported by the Israel Science Foundation, Jerusalem.

Structure of Discotic Liquid Crystalline Compounds at the Air-Water Interface* | X22B

D. Gidalevitz, O. Y. Mindyuk, P. A. Heiney, J. Strzalka, J. P. McCauley, Jr., A. B. Smith, III (U. Penn), B. M. Ocko (BNL), P. Henderson, H. Ringsdorf (Mainz), N. Boden, R. J. Bushby, P. S. Martin (Leeds).

We have used grazing incidence X-ray diffraction and X-ray specular reflectivity to study the behavior of platelike hexa-alkoxytriphenylene derivatives **1-4** at the air-water interface [J. Phys. Chem., in press, 1997]. The data are consistent with a two-dimensional columnar mesophase, wherein the molecules are arranged "edge-on" to the water surface, with intercolumnar spacings of 13-19 Å (Fig. 1). We propose a molecular conformation in which hydrophobic tails lie parallel to the water surface so as to allow the hydrophilic oxygen atoms to directly contact the water surface. In equimolar mixtures of two disubstituted amphiphilic isomers of a triphenylene derivative, we see direct evidence for structural self-organization and intercolumnar order, as manifested by a *decreased* intercolumnar distance in the mixtures (bottom 2 panels of Fig. 1). *We thank David Vaknin for the use of his Langmuir trough. Supported by National Science Foundation grants DMR MRL 92-20668 and DMI

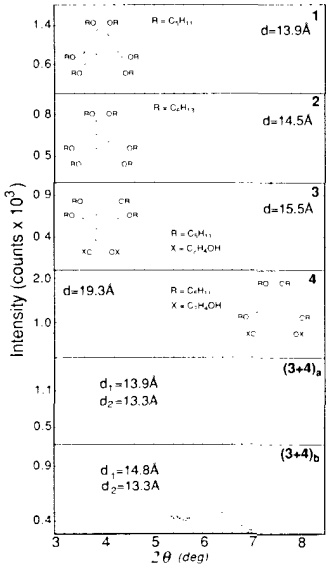

Figure 1. Grazing incidence X-ray diffraction peaks from compounds **1-4** and equimolar mixtures of **3** and **4** on pure water. insets. The **(3+4)**$_a$ and **(3+4)**$_b$ diffraction patterns were measured approximately 2 hr and 0.5 hr after spreading, respectively.

Grazing Incidence X-ray Scattering Study of the Buried Glass-Liquid Crystal Interface * | X22B

Y. Hu, T. K. Misra, and L. J. Martínez-Miranda (U. of Maryland, College Park)

We have used grazing incidence X-ray Diffraction to study the structure of a smectic liquid crystal (LC) film at the buried LC-glass substrate interface. This measurment is done in reflection mode through the glass substrate, which consists of a grating photolithographed onto a 0.22 mm glass slide. The experiment used both 1.38 and 1.34 A X-rays. X-rays in this energy range can penetrate through the glass substrate, which enables the direct study of the LC-glass interface. We varied the incidence angle between 0 and 0.5 degrees in order to obtain depth information on the the in-plane structure of the sample. Two grating depths were used in this study: 1.6 and 0.5 micrometers.

Both the deep as well as the shallow gratings show evidence of in-plane alignment inside the grating grooves. The smectic layers exhibit a compression near the glass interface, as well as deep inside the film. The former result is consistent with previous reflectivity observations of confined LC's in similar gratings. The smectic layers are dilated at intermediate incidence angles. This structure is consistent with a chevron structure. In addition, the in-plane structure at the interface in the deeper gratings shows evidence of a higher azimuthal disordering than the structure observed in the shallow gratings.

* This work was supported by NSF Grant Nos. ECS-9530933 and ECS-96696069.

Charge Density Wave Structure in $NbSe_3$ in High Magnetic Fields | X22B

V. Kiryukhin, D. Casa, B. Keimer (Princeton U.), J.P. Hill (BNL), M.J. Higgins, and S. Bhattacharya (NEC)

$NbSe_3$ undergoes two successive charge density wave (CDW) transitions at 145K and 59K. The magnetic field dependence of the charge density wave structure has been of interest since the discovery of a very large positive magnetoresistance below 59K. On the basis of subsequent narrow band noise and thermopower measurements in transverse magnetic fields, it was attributed to a substantial increase in the number of carriers participating in collective CDW transport, lowering the density of normal carriers in ungapped pockets of the Fermi surface. This would correspond to an increase in the CDW order parameter induced by the magnetic field. Theoretically, this behavior can be understood by considering the orbital response of the electrons to the magnetic field. The transverse field constrains the electronic motion, thereby improving the nesting properties of the quasi-one dimensional Fermi surface and enhancing its propensity for CDW formation. Other transport experiment seemed to suggest a magnetic field induced shift of the CDW wave vector. However, both some of the experiments and the theoretical interpretations were subsequently challenged. A microscopic, equilibrium probe such as x-ray diffraction is necessary to conclusively establish the influence of a magnetic field on the amplitude and periodicity of the CDW.

To this end, a $NbSe_3$ crystal was mounted in a high field superconducting magnet, and scans through superlattice reflections corresponding to the low temperature CDW were taken in a high resolution configuration. Typical data are shown in Figure 1. An upper bound of $\Delta q/q \leq 2.5 \times 10^{-3}$ on the magnetic field induced shift of the CDW wave vector was thus established. The CDW order parameter is also magnetic field independent, to within 10%. These measurements complement transport data taken on the same material and help clarify a long-standing controversy regarding their interpretation.

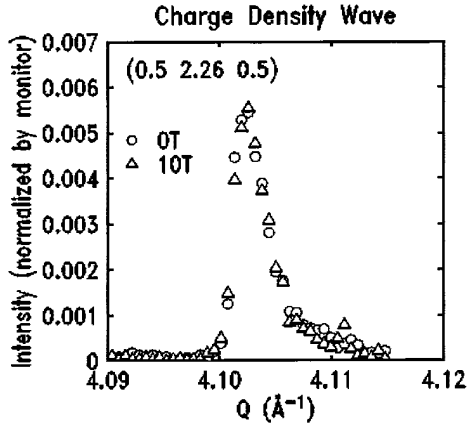

Figure 1. Scans through a CDW superlattice reflection in zero field, and at 10T.

The Surface Structure of Ferrocenyl Surfactants* | X22B

H. Kraack (Bar-Ilan U., Israel), V. Craig, N. Abbott (UC Davis), B. Ocko (BNL), X.Z. Wu (IBM Almaden), and M. Deutsch (Bar-Ilan U.)

Aqueous solutions of the surfactant (15-Ferrocenylpentadecyl)- trimethylammonium Bromide (FeC15) show considerabe surface tension variations with FeC15 concentration (ϕ) and oxidation state[1]. When oxidized, both ends of the molecule are hydrophilic. When reduced, however, only one end is hydrophilic. It has been suggested, therefore, that a conformational transition occurs within the layer adsorbed at the surface. When oxidized a hairpin conformer was suggested, with both ends in the water. When reduced, the usual linear conformation is assumed, with only one end in the water, similar to insoluble Langmuir films. X-ray reflectivity (XR) measurements were undertaken to test these suggestions.

The XR of the reduced molecule shows only weak modulations for all ϕ. The oxidized ones, however, show strong modulations for medium and high ϕ. Fits to the XR curves show a single (medium-ϕ) or two (high-ϕ) high-density layers at the surface. The lowest ϕ shows no modulations and can be fit with a slowly decreasing density profile. Figs. 1,2 show the measured XR and the fit for the high-ϕ oxidized state. These results may indicate surface-induced multilayer ordering, with the number of layers increasing with ϕ. Further analysis is in progress.

*This work is supported by the Israel Science Foundation, Jerusalem,(M.D.) and the U.S. National Science Foundation (N.A.).

1. B.S. Gallardo, K.L. Metcalfe, N.L. Abbott, *Langmuir* **12**, 4116 (1996).

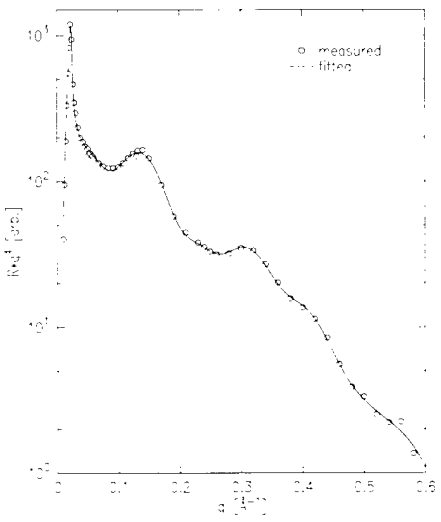

Figure 1. Measured and fitted x-ray reflectivity of 0.6mM solution, oxidized.

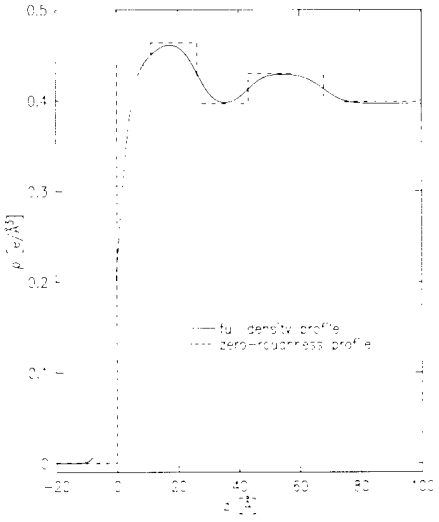

Figure 2. Surface density profile corresponding to the fit in Fig. 1.

Structural Properties of Gramicidin A at the Air/Water Interface | X22B

H. Lavoie, C. Salese, D. Ducharme (U. of Quebec), D. Vaknin (Ames Lab), and B.M. Ocko (BNL)

Valine gramicidin A (VGA) is a known antibiotic polypeptide consisting of fifteen amino acids with D- and -L alternate conformers, and forms specific ion channels for transport of monovalent cations through lipid membranes. The surface pressure isotherm of gramicidin shows some features which are not yet well understood. *In situ* X-ray reflectivity, X-ray GID and ellipsometry were used to characterize the film of gramicidin at the air-water interface. Fig. 1A shows the surface pressure versus molecular area (π-A) isotherm of VGA on pure water at 20°C. Fig. 1B shows the thickness of the molecular film as a function of the molecular area. The thickness values were obtained, *in situ* at the air-water interface, by X-ray reflectivity measurements. Fig. 1B shows the phase shift $\delta\Delta$ in an ellipsometric isotherm which depends on two parameters, the refractive index and the thickness. Using the thickness values from the reflectivity measurements allowed determination of the refractive index of the film, which is shown as a dashed line in Fig. 1B. The gradual change in the refractive index together with the fact that the film thickness is smaller than any dimension of the protein in its crystal form as a dimer, is a clear indication of intra-molecular rearrangement, possibly some degree of protein folding into the dimer tubular form. At lower molecular areas, ($A \leq 300$ Å^2 the refractive index is almost constant and the increase in film thickness is due to the reorientation of the molecules with the pore of the dimer facing the water interface. This is supported by the GID study of VGA shown in Fig. 2B. The 2D Bragg reflection at $Q_{xy} = 0.45$ Å^{-1} is observed only below molecular area of 120 Å^2 ($\pi \approx$ 25 mN/m, or about 240 Å^2 per dimer) and corresponds to the formation of a 2D crystalline phase with a hexagonal lattice having a d-spacing unit cell of 16.09 A.

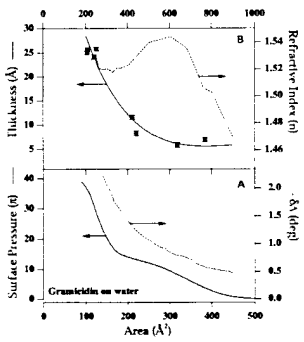

Figure 1. (A) Lateral pressure, ellipsometric phase-shift, (B) film thickness, and refractive index, all versus molecular area of gramicidin monolayer at the air-water interface.

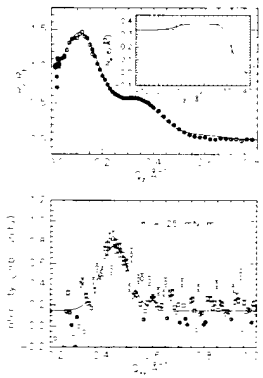

Figure 2. (A) Normalized reflectivity (R/R_F) from VGA monolayer at the air-water interface at 25mN/m. (B) 2D-Bragg reflection from the same monolayer corresponding to the ordering of densely packed tubular proteins.

In-Plane Depth Profile Studies of Strain in PZT and PLZT Thin Films *	X22B

Yiqun Li, A. Dhote, S. Aggarwal, R. Ramesh, and L. J. Martínez-Miranda (U. of Maryland, College Park)

We have performed initial depth dependent studies of the in-plane structure of PZT and PLZT thin films. These films were deposited on lanthanum aluminum oxide (LAO) substrates using the pulsed laser deposition method. Grazing incidence X-ray scattering was used to characterize the in-plane structure of the films, using 1.554A X-rays. The observed in-plane peaks in PLZT consist of a strong signal superimposed on a difused background, as shown in Figure 1. This structure is a-axis oriented, and exhibits compressive stress along the direction of the substrate twinning lines as well as perpendicular to these. The stress along the latter direction is approximately twice as small than the observed stress along the the twinning lines. The in-plane structure of PZT consists of both a-axis and c-axis peaks over a difuuse background. The observed stress is smaller than in PLZT.

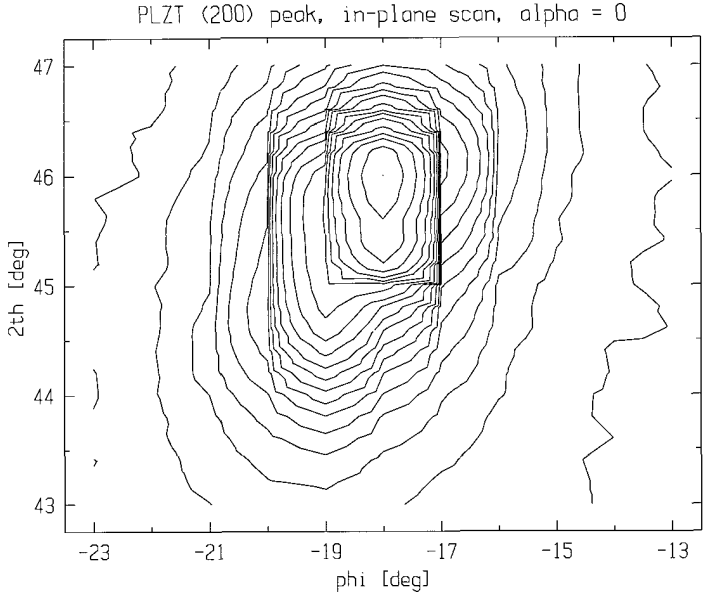

Figure 1. In-plane contour scan of the [200] region for PLZT in the direction perpendicular to the substrate twinning lines.

* Work supported through a NSF-MRSEC Grant No. DMR-9632521.

X-Ray Reflectivity of Diblock Copolymer Monolayers at the Air/Water Interface	X22B

Z. Li, W. Zhao, J. Quinn, M.H. Rafailovich, J. Sokolov, (SUNY at Stony Brook), R.B. Lennox, A. Eisenberg (McGill U.), X.Z. Wu, M.W. Kim, S.K. Sinha (Exxon Research & Engineering Co.), and M. Tolan (U. of Kiel, Germany)

PS_{260}-b-PVP-C_nX_{240}(X=I, Br; n-1,4,8,10) have recently been found to self-assemble at the air/water interface to form circular structures referred to as surface micelles. Synchrotron X-ray reflectivity studies were performed to address the structure relationship between Langmuir Films and the LB Films. Specular reflectance (see Figure 1) reveals that the thickness of the polyelectrolyte layer increases by a factor of 2 as polymer surface density increases 4-fold. No significant hydration of the layer is observed. The off-specular scattering data (Figure 2) are well fit by an exact expression for the scattering intensity from a two-dimensional-ordered hexagonal lattice with a capillary wave contribution. The change in micelle-micelle distance or in the film thickness does not correlate in the pressure-area isotherm for n≥6. A correlation was observed only for the degree of surface ordering and the film stiffness.

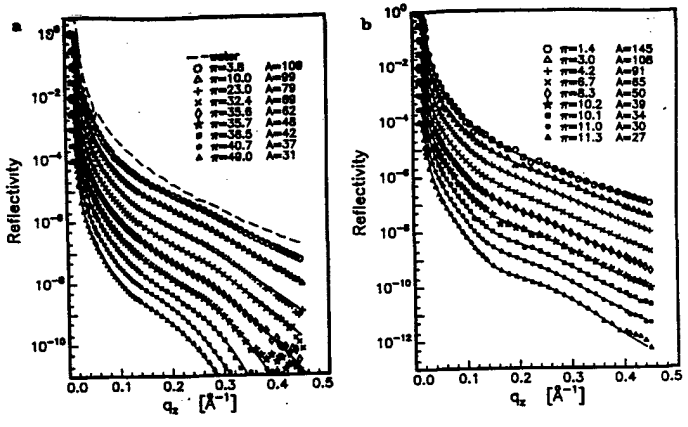

Figure 1. (left) The dashed line is specular reflectivity from the pure water surface. (right) The last curve was obtained after the film was decompressed.

Depth-Dependence of Strains in Cu Films on AlN * | X22B, X22A

L. J. Martínez-Miranda, Y. Li (U. of Maryland, College Park), L. K. Kurihara, P. Schoen, and G. M. Chow (NRL)

We have studied the depth dependence of the structure of Cu films deposited on AlN substrates via the polyol method. In this method, Cu particles are believed to precipitate from solution, and aggregate to form a number of reaction interfaces, and a metallic film on the substrate. We have found that this metallic film consists of a bulk polycrystalline Cu film as well as an upper layer of (100) textured Cu. This layer constitutes as much as one third of the film.

We have studied the in-plane structure of this upper layer using 8keV X-rays. We have found that the structure of the films in this region consists of a distribution of lattice spacings that correspond to strains that range between -0.6 and 1 percent, as seen in Figure 1. The observed in-plane peaks are superimposed over a wide diffused background. The in-plane azimuthal texturing depends on the time the solution is left refluxing during film processing as well as the orientation of the substrate during the deposition process. Films deposited on a horizontally oriented substrate are more textured than films deposited on a vertically oriented substrate. Films refluxed for a longer time are less textured than those refluxed at shorter times (compare Figures 1 and 2).

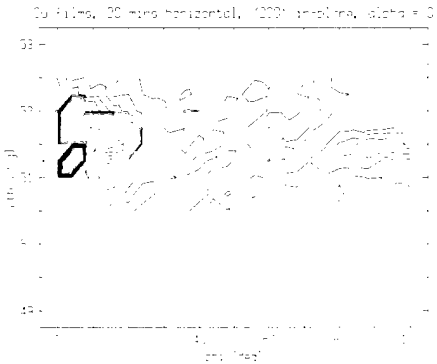

Figure 1. In-plane azimuthal scan of the Cu (200) peak of a 20 min H sample at grazing incidence.

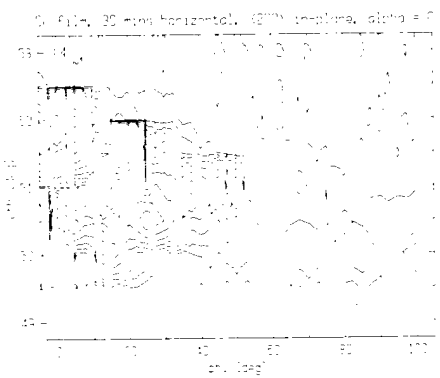

Figure 2. In-plane azimuthal scan of the Cu (200) peak of a 30 min H sample at grazing incidence.

* Work supported by NRL and ONR nanostructured materials programs.

X-Ray Reflectivity Studies of Alkanethiol Coated Gold Nanoparticles | X22B

B. Ocko and D. Nguyen (BNL), C. Clarke and B. Lennox (Mcgill U.), Z. Li (Exxon), M. Rafailovich and J. Sokolov (SUNY at Stony Brook)

Research in the area of "Nanophase Materials" is largely motivated by the unique optical and electronic properties exhibited by the particles as a result of their finite size, shape, and packing configuration. X-ray reflection has been used to study the structure of Langmuir Films of alkanethiol coated gold nanoparticles deposited at the air-water interface. Using the results from this study and Transmission Electron Microscopy (see figure 1) of Langmuir Blodgett Film studies, we are able to obtain information about the molecular architecture (particle size, film thickness, and interparticle spacing) of films produced at different area/molecules, temperatures, and using alkanethiols of varying carbon chain length. Preliminary results indicate that the gold particles assume a prolate structure when spread on the water surface with a thickness of 20 angstroms.

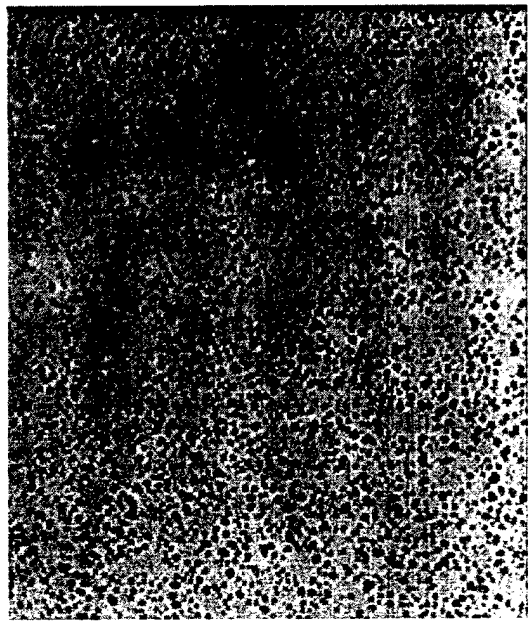

Figure 1. TEM micrograph of Gold Alkanethiol Film lifted from the Air/Water Interface.

Electrodeposited Bromide on Ag(110); Phases and Phase Transition | X22B

B.M. Ocko and J.X. Wang (BNL), and T. Wandlowski (U. of Ulm & Munich)

The structure of electrodeposition of Br on the Ag(110) surface from a NaBr solution has been investigated using surface x-ray diffraction techniques. As shown by the open circles in Fig. 1a, the primitive Ag(110) surface is rectanglar. Above a critical potential, -0.62 V vs. Ag/AgCl in 0.050 mM NaBr, the adsorbed Br forms an incommensurate c(px2) unit cell. As is typical of rectangular electrodeposited adlayers, the bromide adlayer is uniaxially electrocompressive. Diffraction scans through the lowest order peak, (H,0.5), are shown in Fig. 1b. The peak position varies between 0.70 and 0.74 as the potential ranges between -0.60 and -0.20V, respectively. The bromide coverage is exactly equal to the peak position, thus it also varies between 0.70 and 0.74.

Between -0.8 V and -0.62V no diffraction features, besides those from the Ag lattice are observed. However, above -0.80 V there is a large decrease in the scattered intensity at (0,1,0.1) as shown in Figure 2. This results from the adsorbed Br interferring destructively with the scattering from the underlying Ag lattice which occurs when the Br occupies the hollow rows, as indicated by the dashed lines in Figure 1. However, there is no concurrent loss of intensity at (1,0,0.1). This leads to the conclusion that the adsorbed bromide is a novel lattice gas one-dimensional liquid phase (see Figure 1a, left).

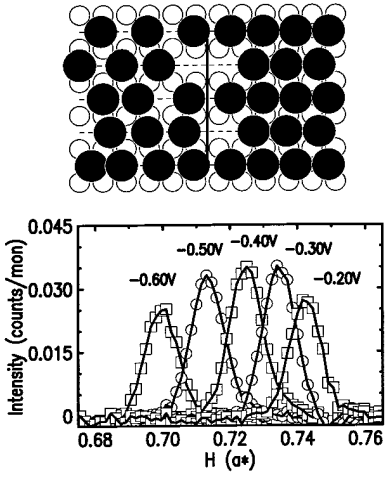

Figure 1. (a) Left: Electrodeposited bromide in the one-dimensional lattice gas phase. Right: Electrodeposited bromide in the uniaxially incommensurate, (px2) phase. (b) Diffraction scans, (H, 0.5), in the (px2) phase.

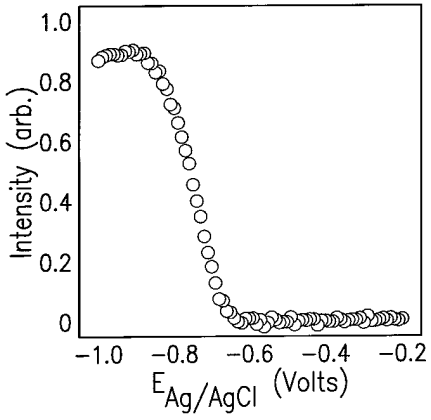

Figure 2. Potential dependent intensity at (1,0,0.1).

X-ray Reflectivity Studies of Phospholipids | X22B

A. Saxena, B. Ocko, D. Nguyen (BNL), C. Clarke (McGill U.), Z. Li (Exxon Research and Engineering), M. Rafailovich, J. Sokolov, and O. Bahr (SUNY at Stony Brook).

Its biological importance (almost half of the human cell membrane is composed of lipids) and its amphipathic nature makes phospholipids prime candidates for Langmuir-Blodgett Film type studies. The viscosity of the lipid is of biological importance because it is the controlling factor of most transport processes and enzyme activities. If the viscosity is too high transport processes will cease which may lead to cell dysfunctions. Phospholipids molecules have a hydrophilic head group and two hydrophobic tail groups (one saturated and the other unsaturated (contains a cis-double bond)). The difference in length of the fatty acid tails influence the manner in which the lipid molecules pack against each other, thus influencing the fluidity of the cell membrane. Lipid fluidity is a function of the temperature and composition.

X-ray reflectivity was used to evaluate a Langmuir film of the phospholipid prepared at 25 C on a water surface (air/water interface). The isotherm developed from this study is shown in figure 1. X-ray Reflectivity data for this study is shown in figure 2. The thickness increases with increasing surface tension and the thickness in the "solid" portion of the isotherm (50mN/m) is 20 angstroms.

Theoretically, the thickness of the layer that forms should not exceed 40 angstroms which was proven in this initial study. More studies in the future will be directed towards varying the chemistry and the temperature of the trough bath in order to obtain biologically inportant information on the viscous properties of phospholipids.

In-situ X-Reflectivity Measurement of Alkylthiolate Formation of Ag Ions and Alkythiol Mmonolayer at the H_2O/Air Interface	X22B

K. W. Shin, M. Rafailovich, J. Sokolov (SUNY at Stony Brook), Z. Li (Exxon Res.& Eng.), A. Gibaud (U. du Maine Faculte des Sciences, France), M. W. Kim (KAIST, Korea) and Y.T. Kim (Yonsei U., Korea)

The interfacial property between the sulfur(n-octadecanethiol) and metal ions(Silver nitrate) has been studied by synchrotron X-ray reflection at the air-water interface using the Langmuir film balace technique. To understand the interfacial chemical and elecronic properties between the sulfur and metal atoms, the isolated metal alkythiolates were prepared. Our previous study of surface pressure-area isotherm measurements show the formation of alkanethiol Langmuir monolayer and the silver thiolates. The monolayers of n-octadecanethiol are well ordered and densely packed(20Å^2 molecular area) at the water/air interface. At pressures where the thiol layer is highly ordered, we inject silver nitrate solution into the water substrate. This subsequent monolayer formation of silver thiolates was monitored by in situ real-time X-ray measurements. After the AgNO3 solution injection, the X-ray reflectivity were measured repeatedly until the Ag ions completed the complex formation with the thiol group at the air/water interface. The reflection curves in Fig. 1 clearly show the process of the silver thiolate formation.

From Figure 1, we see that in the early stage there is no distinct change of the curves. We found that the complete formation of C18S-Ag required approximately 1 hour for the Ag ion diffusion, because silver nitrate solution was injected carefully at the end of the trough to avoid the collapse of packed monolayer. The first oscillation(arrow in Figure 1) is becoming clearly as time goes on. The result was well matched the previous results of BAM and ellipsometry experiments.

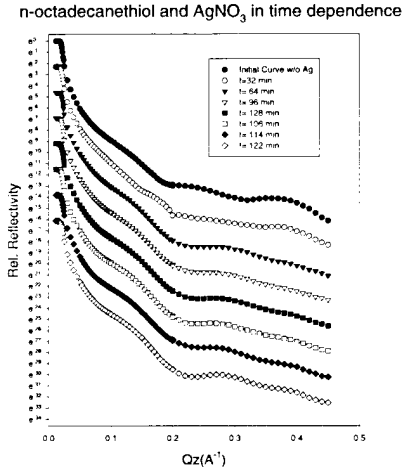

Figure 1. X-ray Reflectivity of Silver thiolate monolayer in time dependence.

The Structure of Polyelectrolyte Block Copolymers in Water/Butanol Mixtures	X22B

K. W.Shin, M. Rafailovich, J. Sokolov (SUNY at Stony Brook), D. Nguyen (BNL), Z. Li (Exxon Res. & Eng.), A. Gibaud, G. Vignaud (U. du Maine Faculte des Sciences), J. Cox, and A. Eisenberg (McGill U., Canada)

Block polyelectrolytes P($S_{260}-b-VP_{240}/C_{10}Br$) and P($S_{260}$-b-$VP_{119}/C_4I$) have been found to self-assemble at air/water interface and to be surface micelles. Eisenberg et al. recently reported that there were three types of surface micelles of block polyelectrolytes, starfish surface micelles, partialy formed jellyfish surface micelles , and jellyfish surface micelles. Our previous studies found P($S_{260}-b-VP_{240}/C_{10}Br$) at water surface formed only starfish surface micelles even under high pressure, due to high energy compensation of such long hydrophobic hydrocarbon chains. To make a jellyfish surface micelle, two scheme were suggested, 1) shortening the hydrocarbon chain length and 2) lowering the surface tension of water by adding butanol. In-situ synchrotron X-ray reflectivity measurements were performed to characterize the structure of surface micelle formation of block polyelectrolytes at Langmuir-Blodgett trough.

The conformational change of surface micelles occurs if there is enough pressure on the surface micelles induced by barriers of LB trough. The conformation of micelles depends on the corona-corona interaction of neighboring micelles lowering the surface energy. The large surface tension of water prevent the polymer chain from entering the subphase. Therefore, adding a certain amount of butanol lessens the surface tension of the air/water interface and the coronas of micelles could diffuse more easily into the water phase. Due to the relatively high electron density of ionic group, X-ray reflectivity experiments are sensitive to the ion distribution near the surface. The oscillations which are clearly visible in pure water (Fig. 1a) disappear when butanol is added(Fig. 1b) indicating that the polymer have formed a more diffuse layer into the subphase. The structure of this polyelectrolyte brush will be further explored with neutron reflection.

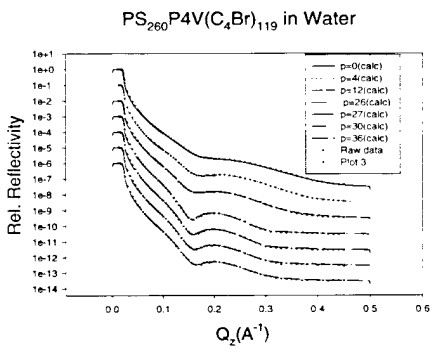

Figure 1.

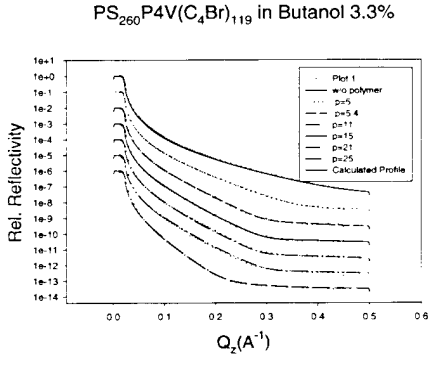

Figure 2.

Magnetic and Structural Measurements of Substrate-Matched Erbium Films	X22C

G. Helgesen (IFE, Norway), D. Gibbs (BNL), M.J. Conover, and C.P. Flynn (U. of Illinois)

The magnetic and structural properties of three erbium films epitaxially grown on a $Lu_{0.6}Y_{0.4}$ alloy substrate have been studied using x-ray magnetic resonant scattering at the Er L_{III} edge. The composition of the substrates was chosen in order to minimize the strain at the Er-substrate interface. The epitaxial relationships in two of the samples were [110] Al_2O_3 || [110] Ta || [001] $Lu_{0.6}Y_{0.4}$ || [001] Er. Their Er film thicknesses were 4000 Åand 1000 Å. A third sample with thickness 4000 Åhaving a [001] Al_2O_3 substrate base layer was also studied. Although the average Er lattice constants of these films were closer to those of bulk Er than those of Er on Y substrates studied earlier, their magnetic behavior for temperatures below 55 K showed clear deviations from that of bulk Er. The conical 5/21 phase found in bulk samples was suppressed in these thin films. At low temperatures the magnetic wave vectors of the 4000 Åfilms locked to 1/4 and 4/15 for [110] and [001] sapphire substrates, respectively. It seems that even for thin film samples with minimal film-substrate interfacial strain the interfacial clamping is sufficient to alter the low-temperature magnetic structure.

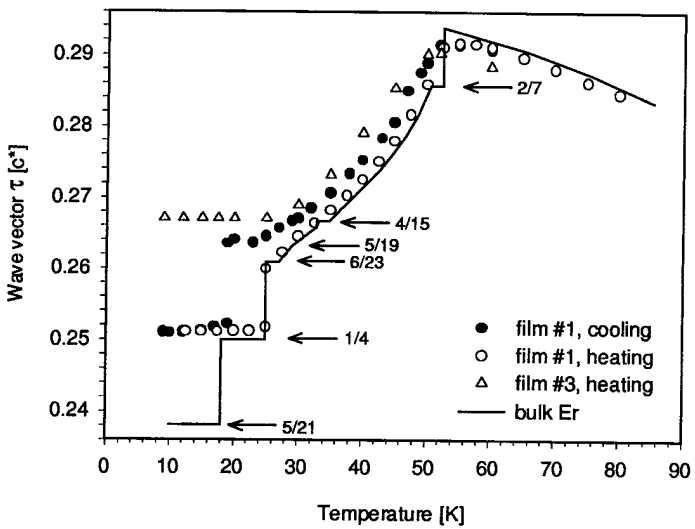

Figure 1. Magnetic wave vector of Er as a function of temperature.

Incommensurate Magnetism In $PrBa_2Cu_3O_{6.92}$	X22C

J.P. Hill (BNL), A.T. Boothroyd (U. Oxford), N.H. Andersen (Risoe), E. Brecht and T. Wolf (Forschungszentrum Karlsruhe)

One strategy for elucidating the mechanism of high temperature superconductivity is to study compounds in which the superconductivity is anomalously suppressed. The absence of superconductivity in $La_{2-x}Ba_xCuO_4$ for example, has been found to be associated with the pinning of incommensurate charge and spin stripe correlations, which may form the basis for a pairing mechanism in the cuprate superconductors. Similarly, $PrBa_2Cu_3O_{6+x}$ has attracted a great deal of interest as an anomalous member of the (RE)$Ba_2Cu_3O_{6+x}$ series, where RE=rare-earth. In addition to the absence of superconductivity, a number of other magneto-transport properties are unique; it is an insulator, exhibiting Cu antiferromagnetism for all x, and the Pr sublattice appears to order at unexpectedly high temperatures, $T_{Pr}(x) = 10 - 20$ K , compared to other members of the series, for which $T_{RE} = 0 - 2$ K. This behavior is particularly puzzling in light of the fact that the hole densities in the CuO planes and chains are very similar to superconducting members of the series.

The role of the Pr site magnetism in these phenomena remains an open question. While neutron scattering studies suggest that the Pr does indeed carry an ordered moment, this interpretation has been called into question by recent NMR work, which suggested that the ordered moment was only 0.017 μ_B. To address this issue we have carried out resonant magnetic x-ray scattering studies of this compound. This technique has the advantage that it is element specific, and offers high reciprocal space resolution. The primary result of this work is shown in the figure below, in which a scan through the (0.5,0.5,8) antiferromagnetic Bragg point is shown. These data were taken with the incident energy tuned to the Pr L_{II} edge and thus demonstrate the existence of an ordered Pr moment. Remarkably the Pr magnetism was discovered to be incommensurate, as illustrated by the existence of two magnetic satellites. The neutron data confirm this result and prove that the modulation is a static one.

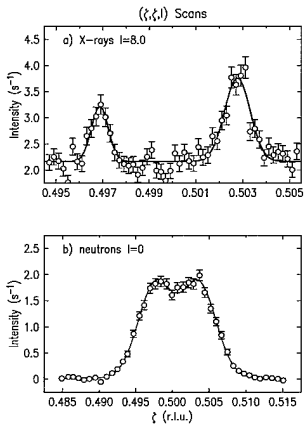

Figure 1.

X-Ray Resonant Exchange Scattering Studies of Magnetic Structures of $EuNi_2Ge_2$ Single Crystal in Zero Applied Magnetic Field	X22C

Z. Islam, C. Detlefs*, A.I. Goldman, S.L. Bud'ko†, P.C. Canfield (Ames Lab.), J.P. Hill and D. Gibbs (BNL)

Magnetic structures of $EuNi_2Ge_2$ (I4/mmm) single crystal was studied using XRES technique at Eu L_{II} edge (E1-resonance). Due to high absorption of neutrons by Eu and small size of these crystals conventional neutron scattering is not feasible. From measurements of bulk magnetization (carried out at Ames Lab.) two transitions were seen ($T_N \approx$34K and $T_t \approx$14K). Paramagnetic moment was found to be consistent with Eu^{+2} ground state ($^8S_{7/2}$). Since there is no orbital moment in this state (as in Gd^{+3}) no CEF effects are expected in first approximation; the anisotropy observed in this material then originates from anisotropic RKKY exchange interaction. So, the study of magnetic structure provides insight into pure exchange effects in this compound.

This compound orders antiferromagnetically with wave vector $\vec{\tau}_m = (001)$ below T_N. $\vec{\tau}_m$ remains the same as the temperature is lowered through T_t. Preliminary measurements of the **Q**-dependence of a series of magnetic peaks at 24K suggests a large Eu moment component in the basal plane whereas at 3.7K the moments seem to be lining up along $\hat{c}$-axis perpendicular to the basal plane. Although this is consistent with magnetization data more accurate measurements of **Q**-dependence of integrated intesities are planned to confirm this behavior.

Current Address : * ESRF, Grenoble, France. † C.B.P.F. Rio de Janeiro, Brazil.

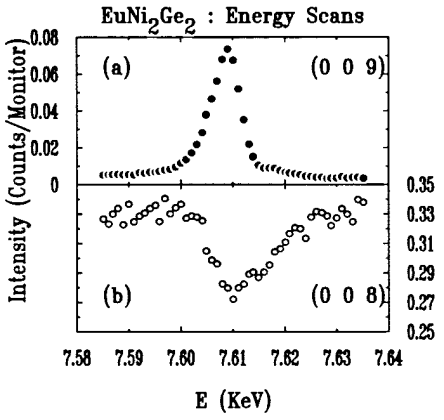

Figure 1. Energy scans through Eu L_{II} edge of (a) magnetic and (b) charge Bragg peaks at 3.7K.

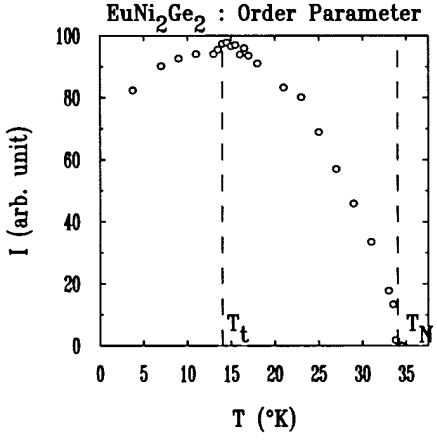

Figure 2. Temperature dependence of integrated intensity (order parameter) of (0 0 7) magnetic Bragg peak.

Structure and Temperature Dependence of Truly Clean Ru(0001)	X22C

V. Jahns, A. P. Baddorf, D. M. Zehner (ORNL), and D. Gibbs (BNL)

A glaring discrepancy exists between experimental values and state-of-the-art first-principles theory in the structures determined for reactive transition metal surfaces.[1] Ru(0001) has received the most attention from this group [2-5], with experiments (electron diffraction) reporting a 2% contraction of the outermost layer and theory predicting a 4% contraction. The disparity has been attributed to contamination of this reactive surface by H, a satisfactory explanation from the theoretical side which predicts a 2% contraction for the H-covered surfaced.[4] We have measured the structure of Ru(0001) using x-ray diffraction, which has capabilities inaccessible to other techniques. The best fit to the data at 300 K involves a first layer (d_{12}) contraction of 2.2±1%, with smaller second and third layer relaxations, in good agreement with electron diffraction results (Fig. 1). To ensure the surface was clean, measurements were repeated with the sample temperature elevated to 490 K, well above the desorption temperature for H. Within the uncertainty the same value was obtained, 2.6±0.8%. With XRD high temperature experiments are accessible; diffraction was measured at 1340 K and again at 1875 K. At these temperatures other contaminants (notably CO) can be ruled out. The relaxation remains near 2%. These temperature dependent measurements reveal a thermal expansion slightly enhanced over the bulk. They also eliminate a second possible origin of the difference between experiment and theory: temperature. Calculations are done at an effective temperature of 0 K. As shown in Fig. 1, a linear extrapolation of the experimental relaxations to 0 K increases d_{12} only to -2.6%. This work provides compelling evidence that the rift between experiment and first-principles calulations is real, and excludes proposed errors in experimental evaluations for Ru(0001).

[1] P. J. Feibelman, Surf. Sci. 360 (1996) 297. [2] G. Michalk, W. Moritz, H. Pfnr, and D. Menzel, Surf. Sci. 129 (1983) 92. [3] G. Held, H. Pfnr, and D. Menzel, Surf. Sci. 271 (1992) 21. [4] P. J. Feibelman, J. E. Houston, H. L. Davis, and D. G. ONeill, Surf. Sci. 302 (1994) 81. [5] D. Menzel, Surf. Sci. 318 (1994) 437.

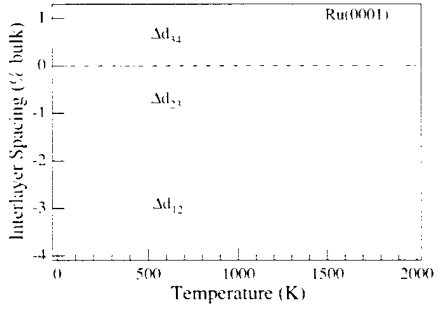

Figure 1. Interlayer relaxations measured on Ru(0001) using XRD. First layer spacings are near -2% relative to the bulk, with a slightly enhanced thermal expansion. Extrapolation to 0 K does not reconcile the first layer relaxation with first-principles calculations.

Surface Relaxation on the Clean and Hydrogen Covered Ru(001) Surface Measured By X-ray Diffraction	X22C

V.Jahns, A.P.Baddorf, D.M.Zehner (ORNL), and D.Gibbs (BNL)

In several previous LEED investigations of the clean Ru(001) surface a 2% contraction of the top layer distance has been determined. On the Hydrogen-covered Ru(001) surface the contraction is removed and even a slight expansion occurs (1-2%). On the other hand, theoretical geometrical structure studies predict a much stronger layer contraction of 4% for the clean Ru(001) surface and also a contraction of 1.5% for the Hydrogen-covered Ru(001). Motivated by the currently ongoing controversy we have measured the X-ray diffraction intensities of the specular and off-specular truncation rods of the clean and Hydrogen-covered Ru(001) surface for temperatures from 300K up to over 2000K. It is observed that the truncation rod intensities for the clean Ru(001)-surface at room temperature and 500K and for the Hydrogen-covered surface at room temperature are not significantly different. Under these conditions the intensity distributions clearly indicate a contraction of the top layer distance. At temperatures of 1890K or 2040K we observe a small change in the modulation of the truncation rod intensities with respect to the low temperature data which can be attributed to a partial release of the contraction. Keeping the momentum transfer fixed at the off-specular truncation rod (Q = 1 0 1) and changing the temperature it is observed that at high temperatures far below the melting point the intensity decrease obeys Debye-Waller behaviour. At highest temperatures close to the melting point a strong decrease of the truncation rod intensity might indicate anharmonic thermal effects.

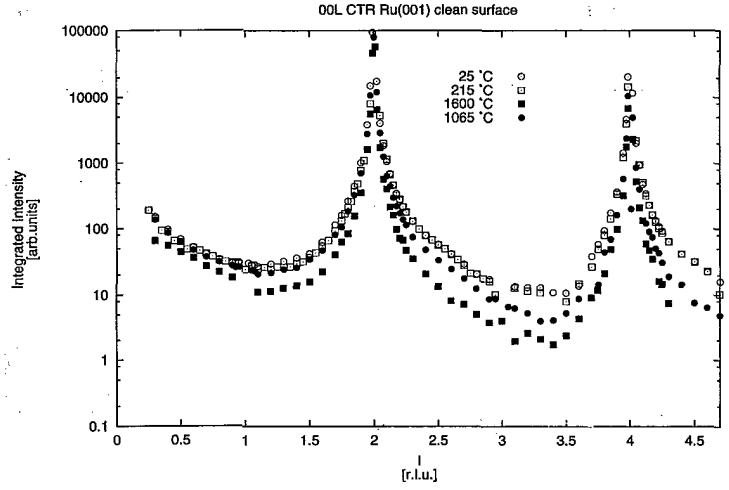

Figure 1. Speculare reflecivity of Ru at different T.

Structure and Phase Behavior of Ir(001)	X22C

V. Jahns, D. M. Zehner (ORNL), G. Watson (UMBC, BNL) and D. Gibbs (BNL)

The structure and phase behavior of the Au(001) surface between room temperature and bulk melting is remarkably similar to that of Pt(001). For example, both surfaces exhibit disordered phases at high temperatures (above 0.9 Tm, where Tm is the bulk melting temperature) and incommensurate quasi-hexagonal reconstructions at lower temperatures. In addition, for temperatures decreasing below about 0.8 Tm, both exhibit surface rotational transitions. However, there are also intriguing differences. The high temperature disordered phase of Pt(001) is rough, while that of Au(001) appears smooth, although disordered within the surface plane. The Pt(001) surface further exhibits a continuous rotational transformation while that of Au(001) is discontinuous. Although some progress has been made in describing the phase behavior of Au(001) using MD simulations and modified elastic theory, these fascinating differences between Pt and Au remain largely unexplained. In the present work, we have undertaken an x-ray scattering study of the structure and phase behavior of Ir(001), the neighbor to the left of Pt in the Periodic Table. We find that at temperatures above 0.7 Tm, Ir(001) apparently roughens in a manner similar to Pt(001) (see Figure 1). Below 0.7 Tm, the surface exhibits a corrugated, quasi-hexagonal reconstruction (see Figure 2), similar to that of Au and Pt (001). However, in constrast to Au and Pt(001), the Ir (001) reconstruction is commensurate with the substrate (possessing a simple (5X1) structure) and exhibits no rotational transformation at any temperature. The absence of a rotational transformation is qualitatively consistent with the theory of Novaco and McTague, who showed that an incommensurate overlayer on a rigid substrate can lower its energy by a small rotation. However, their theory fails to predict the rotation angles observed for Au and Pt (001). In summary, the structures and phases exhibited by Ir, Pt and Au(001) surfaces are qualitatively very similar, yet differ strikingly in their details–in ways which stand outside the predictions of any current theories.

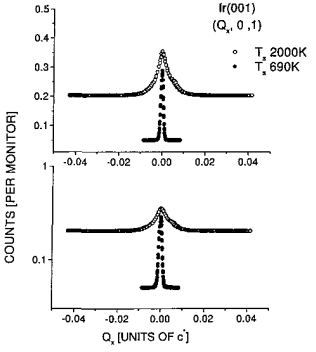

Figure 1. Transverse profiles of the specular reflectivity of Ir (001) at L=1.0c* taken at T=690 K and 2000 K, respectively.

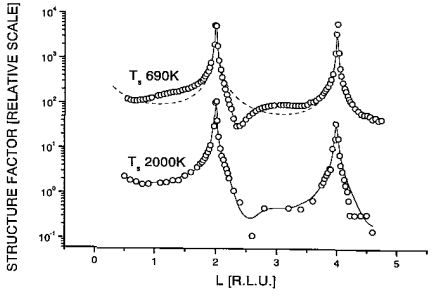

Figure 2. Integrated specular reflectivity profiles taken at T=690 K and 2052 K.

Magnetic Structures and Phase Transitions of $U(As_{1-x}Se_x)$ Solid Solutions	X22C

M.J. Longfield, W.G. Stirling (U. of Liverpool, UK), E. Lidstrom (ESRF, France & EITU, Germany) and G.H. Lander (EITU, Germany)

Continuing our study of actinide antiferromagnets, we have used the X22C instrument to probe the magnetic structures of $U(As_{1-x}Se_x)$ solid solutions with x=0.1, 0.2 and 0.22, at the uranium M_{IV} edge. On cooling, these materials order into incommensurate phases and then undergo first order transitions to a commensurate phase with a multi-q wavevector which depends upon the selenium concentration [1].

We have observed an extra periodicity of the triple-q structure for the x=0.2 sample which has a modulation wavevector, q_m, ~0.44 r.l.u. At low temperature, we have found the x=0.22 crystal to have a similar magnetic structure. The extra modulation for x=0.22 is much weaker than for the x=0.2 sample and does not exist for either the x=0.1 or 0.4 compositions (which do not have the triple-q structure). **Figure 1** shows the formation of the additional magnetic modulation in the commensurate phase of the x=0.2 crystal. By developing the spin-slip description of CeSb [2] we have arrived at a possible model for the extra periodicity, $q_m=q_0(1-1/b)=0.444$. The modulation is described as fraction of the commensurate magnetic wavevector, $q_0=0.5$, which is determined by the number of atomic planes separating the additional spins (b=9 in this case). The additional modulation of the triple-q structure may be an effect confined to the near surface layers, but as yet we have no conclusive evidence of this.

The critical scattering lineshape (above T_N) for the x=0.1 sample is very broad in the specular direction. The transverse direction (H) remains relatively sharp for the (0, 0, 2+q) incommensurate modulation, which is shown in **Figure 2**. This scattering is fitted to a single Lorentzian function. It is not obvious that there is any significant sharp component arising from a second length-scale [3,4] in this material.

[1] Kuznietz et al J. M. M. M. 69 12 (1987); [2] McMorrow et al J. Phys. Condens. Matter 9 1133 (1997); [3] Perry et al Phys. Rev. B54 15234 (1996); [4] Altarelli et al Phys. Rev. Lett. 74 3840 (1995).

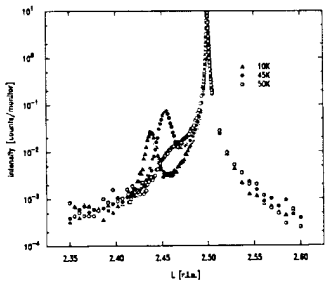

Figure 1. The extra periodicity of the triple-q magnetic structure, for the x=0.2 sample.

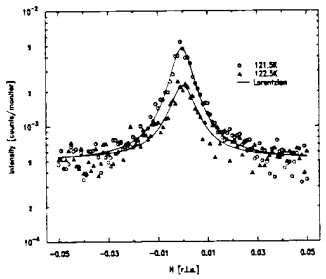

Figure 2. Transverse critical scattering from the x=0.1 sample, near T_N~120K.

Orbital Ordering in a Cubic Perovskite	X22C

Y. Murakami, I. Koyama, M. Tanaka (KEK), J.P. Hill, D. Gibbs and M. Blume (BNL)

There is a great deal of current interest in strongly correlated electron systems, such as the transition metal oxides, which exhibit such diverse phenomena as high-Tc superconductivity and colossal magnetoresistance. The rich physics of these systems results from the fact that the charge, spin and orbital degrees of freedom all play important roles in determining the electronic and magnetic properties. Of these phenomena, the least well understood is the behavior of the orbital degrees of freedom. This is because, until recently, there has been no direct probe of orbital order, though its presence has been inferred indirectly from, for example, lattice distortions associated with cooperative ordering.

X-ray scattering is sensitive to the charge distribution in a solid, and therefore is, in principle, capable of observing orbital ordering directly. However, the sensitivity to the anisotropy in the charge distribution resulting from just one orbital out of the total complement of a given ion is very small. Fortunately, this situation is altered by tuning the incident photon energy to a resonance that couples to that orbital. In this case, the sensitivity may be dramatically enhanced.

We have carried out studies of $LaMnO_3$. Resonant scattering was observed with the incident photon energy tuned to the vicinity of the Mn K-edge, corresponding to a doubling of the periodicity along the (110) direction. We attribute this to an ordering of the Mn^{3+} e_g orbital. This interpretation is supported by the polarization dependence of the scattering, which is dominantly $\sigma \rightarrow \pi$, and the azimuthal dependence, which shows a two-fold symmetry for rotations about the scattering vector. Theoretical calculations describing the scattering process and which predict these dependences are currently underway. The temperature dependence of the orbital ordering was also investigated. The ordering was found to disappear above $T_o \approx 820$ K, coincident with an orthorhombic to rhombohedral strucutral phase transition.

Structure and Magnetism of EuB_6 * | X22C

S. Süllow, M.C. Aronson (U. of Michigan), J.L. Sarrao, Z. Fisk (NHMFL), A. Vigliante, and D. Gibbs (BNL)

Recent experiments on EuB_6 single crystals ($Pm3m$) show the system to undergo *two* instead of the previously reported single ferromagnetic transition. However, the appearance of two FM transitions in a cubic $m3m$ crystal is impossible because of severe symmetry restrictions on the possible magnetic structures for a given crystalline symmetry. Thus, to determine the symmetry of our crystal we performed a detailed x–ray study. In Fig. 1a we present the T dependence of the lattice parameter a of EuB_6, determined from the [100] and [200] Bragg peaks. The overall value of a agrees well with previous reports. At the magnetic transitions no change of the lattice parameter is seen, ruling out massive structural changes accompanying the transitions. In Fig. 1b we plot the intensity distribution in one quadrant of reciprocal space [$h0l$] close to the [300] Bragg peak at 20K; similar results have been found at other Bragg peaks. The intensity distribution of the Bragg peaks is not isotropic in the hl plane. Instead, wings protrude from the side of the Bragg peak. The intensity distribution of the Bragg peaks themselves was well–described by a resolution–limited Lorentzian function, corresponding to a structural correlation length of $\geq$4000Å. The wings at the Bragg peaks are found in all hkl planes, with one wing for each quadrant of the plane. The direction of the wings in [hkl] space is not related to a high symmetry axis of the lattice; for instance, the relative direction of the wing in Fig. 1b is [-302]. The wing intensity decreases slightly as T is increased from 10 to 150K, making thermal diffusive scattering unlikely. Several other explanations for the wings, like strain, lattice disorder or vacancies, are possible, but presently we cannot determine which of these apply to EuB_6. Regarding the symmetry of our crystal, we found a structural anomaly, but cannot conclusively relate this to a lowered crystalline symmetry.

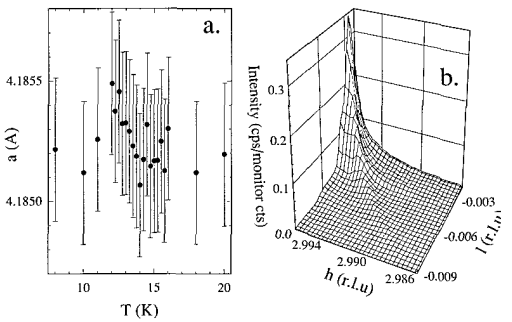

Figure 1.

* Work at U.of Michigan was supported by DOE, Grant 94–ER–45526, and at BNL under contract No. DE AC0276CH00016.

Real-time Relaxation of the Cu/Ru(001) Interface During Growth | X22C

H. Zajonz, D. Gibbs, (BNL), V. Jahns, A.P. Baddorf and D.M. Zehner (ORNL)

Since the discovery of the stripe-phase reconstruction of Au(111), in which partial dislocations separate regions of fcc stacking from hcp stacking, this motif has been found in nearly all heteroepitaxial metal systems studied to date. However, very little is known about the structure of the interface. In this work, we have begun x-ray scattering studies of the structure of Cu layers deposited on Ru(001) substrates during growth and versus substrate temperature. The near-neighbor spacing in bulk Cu is 5.8% smaller than that of Ru, which has an hcp structure. From earlier STM studies, it has been established that the first layer of Cu on Ru adopts a pseudomorphic structure, but that the two-layer film exhibits a stripe-phase reconstruction. Our x-ray experiments involve characterizing the appearance and evolution of the stripe-phase reconstruction peak as a function of Cu coverage and substrate temperature. At 720 K, we confirm a pseudomorphic Cu structure for coverages up to about one monolayer, followed by the growth of a stripe-phase reconstruction between one and two layers (see Figure 2). We find that the average Cu spacing is contracted in the stripe-phase by about 5.3% relative to the near-neighbor spacing of the Ru(001) substrate. At two monolayers coverage, there is an abrupt contraction of the average Cu spacing by an additional 0.5% (see Figure 1). Remarkably, the interfacial lattice then appears to oscillate with a 0.1% amplitude and a three layer period at least for coverages up to ten monolayers. To our knowledge, this phenomenon has not been observed previously for an interfacial reconstruction. Preliminary studies at lower temperatures (300-500 K) suggest that the stripe-phase, interfacial reconstruction is relatively disordered, and that at some temperature there is a cross-over to the ordered, oscillatory behavior. However, this remains to be established.

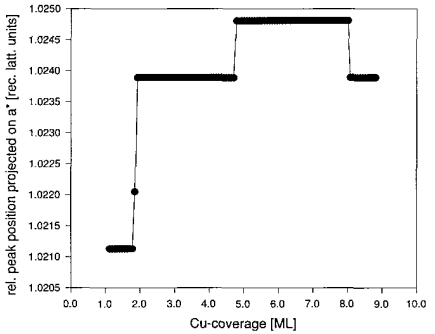

Figure 1. Stripe-phase peak position in reciprocal space versus coverage of Ru(001) by Cu in monolayers (ML). The abrupt change at two monolayers corresponds to a contraction of the average Cu lattice constant of about 0.5%.

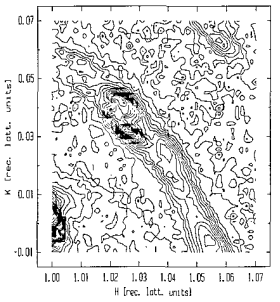

Figure 2. Inplane diffraction pattern of the Cu/Ru(001) interface for 10 monolayers Cu coverage at 720 K. The intense peak located at (H,K)=(1,0) corresponds to the (1,0,0.15) truncation rod of Ru(001). The peak at (H,K)=(1.02,0.04) is the first harmonic of the stripe-phase reconstruction of the Cu. The second harmonic is visible at (H,K)=(1.06,0.06).

In situ X-ray Absorption Studies of Electrodeposited Thin Films *	X23A2

M. Balasubramanian and C. A. Melendres (ANL)

We have performed *in situ* x-ray absorption studies on electrodeposited films of Ni and Cr from aqueous solutions and determined the local atomic and electronic structure of these elements in such films. The films were deposited on a graphite substrate, typically at a constant cathodic current of 5.1 mA/cm^2 for 15 minutes. As can be seen from the XANES, illustrated in Figure (1), the films deposited from solutions containing Cr^{+3} ions do not show a significant pre-edge feature, consistent with the presence of Cr^{+3} in such films (curves a and c). A film formed from a solution containing Cr^{+6} ions shows only a small pre-edge feature, suggesting Cr exists predominantely as Cr^{+3} in this film (curve b). In sharp contrast, the film co-deposited from a solution containing Cr^{+6} and Ni^{+2} ions, suprisingly shows a large pre-edge feature, clearly indicating that Cr in this film exists almost exclusively as Cr^{+6} (curve d). We have performed a systematic study of such films to understand the effect of oxygen by using deaerated solutions as well as by exposing these films to air and measuring them ex-situ. Detailed results will be reported in future. These investigations are of interest in various fields such as electrochromic devices, batteries, corrosion, environmental remediation, etc.

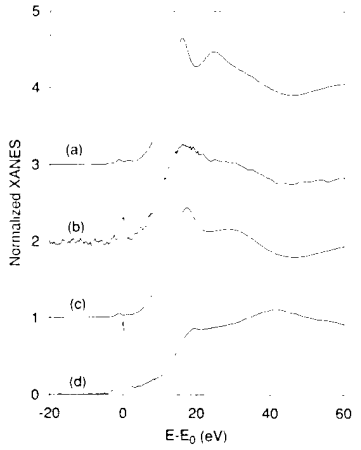

Figure 1. *In-situ* Cr XANES of cathodically deposited films from aqueous solutions: (a) 0.01M $Cr(NO_3)_3$, (b) 0.01M K_2CrO_4, (c) 0.1M $Ni(NO_3)_2$+0.01M $Cr(NO_3)_3$, (d) 0.1M $Ni(NO_3)_2$+ 0.001M K_2CrO_4.

* Research supported by the U.S. DOE under contract W-31-109-ENG-38.

Processing of Pure-Phase MnZn-Ferrite Using High-Energy Ball Milling: An X-Ray Absorption Fine Structure Study	X23B, X23A2

D.J. Fatemi, V.G. Harris(NRL), and J.P. Kirkland(SFA)

$Mn_{.5}Zn_{.5}Fe_2O_4$ ferrites were processed by mechanical alloying a mixture of the elemental oxides MnO, ZnO, and Fe_2O_3 in a high-energy shaker mill. The structure of the milled mixtures was studied via X-ray diffraction (XRD) and extended X-ray absorption fine structure (EXAFS) measurements. Broad diffraction peaks, corresponding with those of the spinel ferrite phase, were detected via XRD after 180 min. of milling (the sample of shortest milling duration), whereupon a pure phase spinel ferrite (as judged by XRD) was measured in the 1260 min. milled sample. The atomic fraction of metal ions existing in the AB_2O_4-type structure, where A and B refer to tetrahedral and octahedral coordinated cations, was measured as a function of milling duration by EXAFS. This analysis reveals that the conversion of metal ions from their elemental oxide structures to the spinel phase occurs near-linear with milling time with 50% of the oxides converted after approximately 500 minutes. Multiple-scattering EXAFS modeling was applied to measure the site distribution of the various cations as a function of milling time. Compared with an equilibrium $Mn_{.5}Zn_{.5}Fe_2O_4$ powder sample, which was prepared by traditional fire and grinding techniques, the mechanically alloyed ferrite samples exhibit a higher fraction of Fe and Mn cations on the A-sublattice, while an unusually high population of Zn cations resides on the B-sublattice. The site distribution can be inferred qualitatively from Fig. 1, in which peaks labeled A and B arise largely from occupation of the absorbing atom on A-sites and B-sites, respectively.

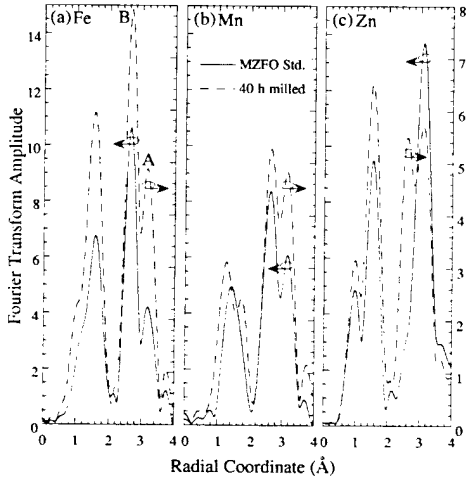

Figure 1. Fourier transformed (a)Fe, (b)Mn, and (c)Zn EXAFS data from MnZn-ferrite formed after 40 hrs of milling and from the standard.

NEXAFS Studies of Ru in the Ternary Skudderudite $Ru_{0.5}Pd_{0.5}Sb_3$	X23A2

V.G. Harris (NRL), G.S. Nolas (Marlow Industries), G.A. Slack (RPI), and T.M. Tritt (Clemson U.)

When the atomic species under consideration exists in a multiple of valence states, the near-edge region of the absorption spectrum will be a superposition of the multiple absorption transitions. In order to measure multiple valence states in a sample of unknown valence one typically makes use of empirical standards of known valence. In the case of the ternary skutterrudite, $Ru_{0.5}Pd_{0.5}Sb_3$, standards of $RuSb_2$ and $RuTe_2$ were employed. These standards where selected because the Ru ions are 4+ and 2+, in $RuSb_2$ and $RuTe_2$, respectively. These prove valuable in 'fingerprinting' the Ru^{4+} and Ru^{2+} valence states in the ternary skutterudite. The first peak in the derivative spectrum corresponds to the inflection point occurring at approximately 50% of the absorption edge step, and is used here to identify the onset of absorption, E_0. This peak is fit using a Gaussian curve to accurately measure E_0 and the half-width at half-maximum (HWHM). Figure 1 is a plot of the isolated first peak data of the derivative versus photon energy for the skutterudite and the two standards. The best fit curves are presented as solid lines and the raw data as symbols.

To accurately measure the relative fraction of the Ru ions we fit the skutterudite data with the best fit Gaussian curves of the standards where the only adjustable parameters are the amplitude of the standards' curves. The relative fraction of the valence states is then given by the ratio of the best fit amplitudes. Using this method we calculate the valence of the Ru in the skutterudite to be 3.1+, or if one were to assume that Ru exists only as 4+ and 2+, 52% of the Ru would be 4+ and 48% is 2+.

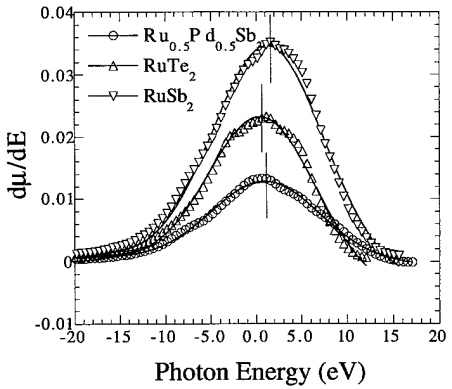

Figure 1. Isolated first peak data from the derivative of the Ru NEXAFS with best fits determined by least-squares fitting using Gaussian curves. Markers indicate the curves centroid. The data corresponding with the $Ru_{0.5}Pd_{0.5}Sb_3$ sample was fit using a combination of best fit curves from the standards.

XAS Studies of Preferential Site Distribution of Ta and Pt in CoCr-Based Films*	X23A2, X23B

K. M. Kemner (ANL), V. G. Harris, W. T. Elam (NRL), Y. C. Feng, D. E. Laughlin (CMU), J. C. Woicik (NIST), and J. C. Lodder (Mesa Research Institute)

CoCr-based alloy films are presently the mainstay mangetic recording media. Numerous studies have shown that these films can be grown in ways to produce a compositional inhomogeneous microstructure having Co- and Cr-enriched regions. The addition of Ta, Pt to these media play an important role in determining the magnetic properties and recording characteristics of the films. In order to better understand the beneficial roles of their addition, we have made XAS measurements on a variety of CoCrX (X=Ta or Pt) films deposited at ambient and 260 C substrate temperatures. Analysis of the Ta and Pt data indicates that no phase separation of the Pt or Ta atoms into clusters has taken place. Further analysis shows that for an increase in substrate deposition temperature, the average coordination number decreases by 0.6 Co/Cr atoms. Figure 2 shows that, with the addition of Ta and Pt, the Fourier peak amplitudes of the Co EXAFS data decrease relative to that of the data for a pure CoCr film. The greater reduction in amplitude of the Fourier peaks when Pt is added than when Ta is added indicates that the Co environment is more disordered by the addition of Pt than by the addition of Ta, suggesting a preferential site distribution of the Pt atoms to the Co atoms. *KMK was supported by a National Res. Council/NRL Fellowship. Research also supported by the U.S. DOE, Office of Basic Energy Sci. & Office of Health & Environmental Res., contract No. W-31-109-Eng-38.

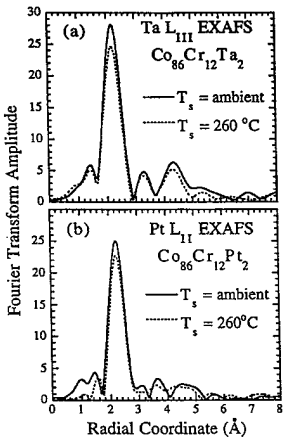

Figure 1. Fourier transformed Ta and Pt EXAFS data for the CoCrX (X=Ta or Pt) samples deposited at ambient and 260°C substrate temperatures.

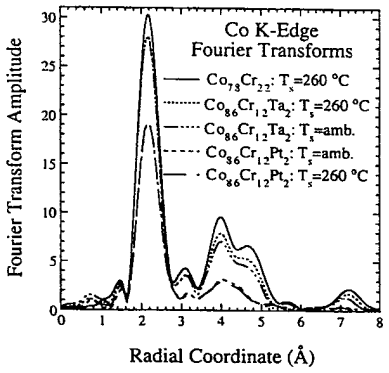

Figure 2. Fourier transforms of Co EXAFS data for the CoCrX (X=Ta or Pt) samples deposited at ambient and 260°C.

XAFS Studies of the Aging of Soils Contaminated With Ethylene Dibromide*	X23A2

K. M. Kemner and S. T. Pratt (ANL)

One of the fundamental issues in environmental remediation and management concerns the time dependence of the bioavailability of toxic chemicals in soils. For many chemicals, this bioavailability decreases dramatically with time, even though destructive analysis of the soil indicates that the chemicals are still present and remain intact; that is, in the times immediately following the application to the soil, the chemical appears to be readily available for degradation, although at much later times, the remaining chemical is essentially unavailable for uptake by microorganisms, fungi, and plants.

Halogenated hydrocarbons make up one of the largest classes of contaminants found in both military and civilian hazardous waste sites, and these solvents have created some of the greatest problems in terms of contaminated drinking water. Brominated hydrocarbons such as ethylene dibromide, which has been used extensively as a fungicide in agriculture, also represent a substantial problem.

One hypothesis for the process responsible for the aging of chemicals in soils is that the chemicals are eventually sequestered in the hydrophobic organic matter within the soil, and another hypothesis suggests that the aging is due to the entrapment of the chemicals in micropores of the soil that are too small to allow access by bacteria. Both proposed mechanisms for the aging of chemicals in soils are based on the hypothesis that changes in the binding or sorption sites of the chemical are responsible for changes in the bioavailability. We have been investigating the utility of using XAS to provide a direct nondestructive means to probe these binding and sorption sites in whole soils and to determine any changes in these sites as a function of time and sample conditions. Initial results of Br K-edge XAS studies of soils treated with ethelyne dibromide are very promising.

*This research was supported by U.S. DOE, Office of Basic Energy Science & Office of Health & Environmental Res., contract No. W-31-109-Eng-38.

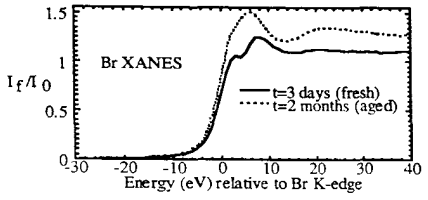

Figure 1. Br K-edge XANES from ethylene dibromide-treated soil 3 days (solid line) and 2 months (dotted line) after treatment.

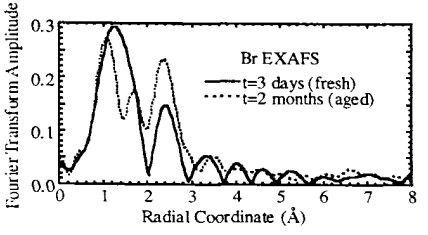

Figure 2. Fourier transformed XAFS data for Br depicting a change in the average local environment of the Br in the soil at 3 days and 2 months after the application of ethylene dibromide.

EXAFS Study of AlGaN Films	X23A2

K.E. Miyano (Brooklyn College), J.C. Woicik, L.H. Robins, C.E. Bouldin (NIST), and D.K. Wickenden (Johns Hopkins)

The III-V nitrides have generated interest as materials for blue and ultraviolet light emitters. Wurzite GaN, the most studied member of this group, has a direct band gap of 3.4 eV, while the AlGaN psuedo- binary alloys provide direct gaps up to 6.2 eV. Though the nitrides are very promising, film structure and quality remain critical issues. We studied the accommodation of the natural Ga-N and Al-N bond lengths in the AlGaN alloys system.

Extended x-ray absorption fine structure (EXAFS) at the Ga-K edge was used to study the local structure of AlGaN films grown by metal organic chemical vapor deposition.[1] The x-ray beam was incident at 45 degrees to the sample normal. Absorption was measured via fluorescence yield, which was detected with a PIN diode covered by a Zn filter. These yield spectra were normalized by an I0 signal measured with a N2-filled ion chamber.

We found that with increasing aluminum content, x, the Ga-N bond length decreases, but much less than the average bond length. This is similar to the effect seen in zincblende AlGaAs alloys.[2] On the other hand, the x dependence of Ga-Ga and Ga-Al distances does follow the variation of the average cation-cation distance. We conclude that bond angle distortions accommodate the differences between the natural Ga-N and Al-N bond lengths.

[1] K. E. Miyano et al., Appl. Phys. Lett. 70, 2108 (1997). [2] J. C. Mikkelsen and J. B. Boyce, Phys. Rev. B 28, 7130 (1983).

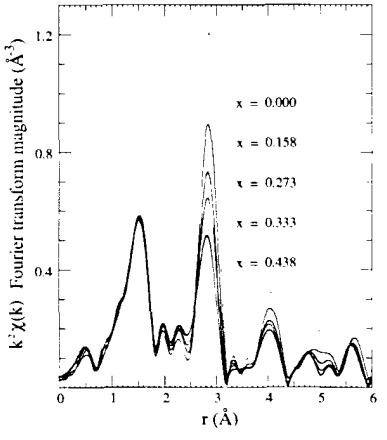

Figure 1. The Fourier transforms of the Ga-K EXAFS from AlGaN are plotted for different values of the aluminum concentration, x.

Structure and Chemistry of FeS_2 Battery Cathodes *	X23A2, X23B

E. Strauss, D. Golodnitsky, E. Peled (Tel Aviv U.) S. Kostov, M. L. denBoer, and S. G. Greenbaum (CUNY, Hunter College)

The Li/CPE/FeS_2 battery (CPE = composite polymer electrolyte) is a promising candidate for energy storage and electric vehicle applications. Its projected specific energy is over 170 Wh/kg (based on 2.5 e/FeS_2), and a recent small laboratory cell demonstrated over 300 full charge-discharge cycles. Using in situ x-ray absorption methods we have investigated the behavior of thin Li/CPE/FeS_2 cells at various stages of charge and discharge cycles. Cells were examined under the following conditions: (i) charged to 1.85 V and x = 0.5, where x represents the number of electrons associated with that particular charge state; (ii) charged to 2.05 V and x = 1.7; (iii) charged to 2.25 V and x = 2.0; (iv) discharged to 1.65 V and x = 1.4; (v) discharged to 1.25 V and x = 0.15, and (vi) discharged to 1.1 V and x = 0.0. Regardless of whether the cell is being charged or discharged, there appear to be only two distinct Fe host environments, a "low-Li" one for conditions (ii), (iii) and (iv) and a dramatically different "high-Li" one for conditions (i), (v) and (vi). At high Li (cathode) concentration a strong pre-edge feature is apparent, which decreases at low Li concentration, as shown in Fig. 1.. This pre-edge feature is dipole-forbidden in octahedral symmetry, and its decrease therefore indicates that the symmetry decreases as Li is removed from the cathode. The EXAFS similarly falls into two distinct categories (Fig. 2). At high Li concentration the Fe environment is ordered, and analysis reveals a combination of metallic Fe and residual unreacted FeS_2. On the other hand, at low Li disorder sets in and only a single broad peak is observed, analysis of which indicates a combination of FeS_2 and Li_2FeS_2. Structural and chemical changes in the Fe environment appear to be highly reversible.

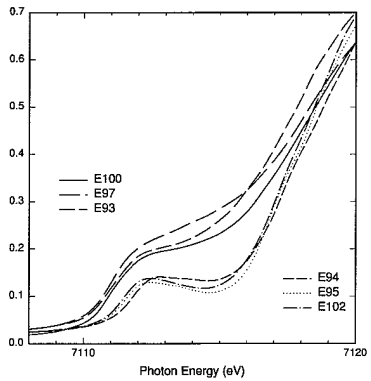

Figure 1. Near-edge x-ray absorption spectrum of cells under various charge conditions as described in the text.

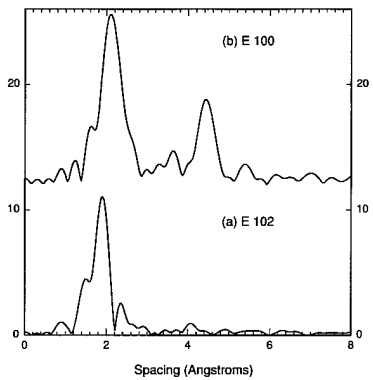

Figure 2. Fourier transform amplitude of representative low-Li and high-Li cathodes.

* Supported by DOE Basic Energy Sciences

Phase-correct Bond Lengths in Crystalline GeSi Alloys	X23A2

J.C. Woicik (NIST), K.E. Miyano (Brooklyn College), C.A. King and R.W. Johnson (Lucent), J.G. Pellegrino (NIST), T.-L. Lee (Northwestern), Z.H. Lu (NRC)

Extended x-ray absorption fine structure performed at the Ge-K edge has determined the Ge-Ge and Ge-Si bond lengths in a series of crystalline GexSi1-x alloys (x¡0.5) to be compositional dependent. This high-accuracy measurement was made possible by utilizing the experimentally determined Ge-Si atomic phase shift from the iso- electronic compounds AlAs and GaP. Strain and Coulomb contributions to the bond lengths are also considered.

The Relationship Between Microstructure Development in Hydrating Cement and the Morphology of Silica Fume Additives	X23A3

A.J. Allen (NIST) and R.A. Livingston (FHWA)

Supplementary cementitious materials like silica fume, which are added to the cement mix and react with calcium ions in the pore solution, enhance the production of calcium-silicate-hydrate gel and modify the microstructure in other ways. By combining ultra-small-angle x-ray scattering (USAXS) experiments on silica fume slurry suspensions with small-angle neutron scattering (SANS) experiments on hydrating cement systems, the effects on the microstructural development during cement hydration of adding silica fume have been studied. The USAXS measurements on the silica fume slurries were performed using 10 keV x-rays and Ge(111) crystal optics. Each fume was slurried in a 4.0 water-to-solids (w/s) weight ratio suspension (fume volume fraction 10%), and sealed into a 1 mm-thick water-cell with x-ray compatible tape windows containing the fume. This concentration of fume gave acceptable (10-15%) x-ray penetration, and negligible multiple scattering. After background subtraction, absolute calibration and desmearing, the effective scattering-vector, h, range was 0.004 - 0.3 nm^{-1}. (Some SANS experiments were also carried out to extend the maximum h achieved.) The USAXS h range was found suitable for determining the main part of the silica particle size distribution which showed very little variation among the fumes. The Porod scattering, which dominates the scattering for h greater than 0.1 nm^{-1}, yields surface areas of around 14 x 10^6 m^{-1} for all of the fume slurries. Since the 4.0 w/s ratio of each slurry implies a solid silica volume fraction of some 10%, the specific surface areas of the solid fumes were deduced to be 60,000 m^2 kg^{-1}, an acceptable value for reasonably well-dispersed silica fumes. Using entropy-maximization methods to determine the volume-weighted particle size distribution, the volume-weighted mean particle diameters are consistent with the expected characteristics of reasonably well-dispersed fumes, and the volume fractions are acceptably close to the nominal concentrations. However, at h below 0.04 nm^{-1}, differences in the USAXS data are discernible among the fumes, with an upturn in the scattering associated with the Porod scattering from coarse features. The coarse features could either be additional volume fractions of independent coarse particles, or, more likely, low-density agglomerates of the particles already characterized in the size distributions. Such agglomerates could not be close-packed, because, if this were so, strong interference effects would appear in the USAXS data. TEM studies and some preliminary laser scattering particle size analyses indicate that the silica fume particles flocculate into large (several μm-diameter) loose assemblages, which, nevertheless, cannot easily be broken up by sonic agitation. In the overall study, a link was established between the existence of such coarse or agglomerated particles in the silica fumes and possible deleterious microstructural evolution during cement hydration. The USAXS studies provided an unique access to the low h values required for the salient agglomeration effects to be discerned in the fumes.

Exploring the Performance Limits of a Bonse-Hart Double-Crystal Ultra-Small-Angle X-Ray Scattering Camera	X23A3

A.J. Allen and G.G. Long (NIST)

Experiments have been conducted to optimize and enhance the resolution, the signal-to-noise ratio, and the range, of a practical Bonse-Hart ultra small-angle x-ray scattering (USAXS) camera. By combining our existing USAXS monolith, the X23A3 monochromating optics, and a new monolith, specifically designed for the use of 100-mm-long crystals, it has been possible to increase the number of crystal reflections to 6 reflections before and 4 reflections after the sample. Each crystal has been surface-etched to eliminate Porod small-angle scattering effects arising from strained regions near the crystal surfaces. The gap between the pair of Ge(111) crystals on each monolith has been reduced to minimize the through-put of parasitically-scattered x-rays. The beam-defining slits and ion chamber for the incident beam normalization have been placed before the monochromating monolith. Thus a truly slitless and windowless instrument geometry has been made possible through the monochromating monolith, the sample position, and the analyzing monolith. The critical air-path through the instrument has also been kept to a minimum. Definition of the beam position within the sample was determined using a magnifying x-ray video camera and a precision sample-stage motion. A 10 decade dynamic-range photodiode x-ray detector was used to measure the x-ray flux transmitted through the instrument as the analyzing monolith was rocked through and then away from the Ge(111) Bragg angle. As in all our USAXS studies, the large dynamic range of the detector enabled an absolute geometric calibration of the SAXS intensity to be made with respect to the incident beam without the need for a secondary standard. Use of the new USAXS configuration at an x-ray energy of 10 keV has resulted in near-theoretical h^{-8} rocking-curve tails down to intensities five decades below the rocking-curve peak. Below this intensity, some small-angle scattering is observed, believed to originate from dust particles in the air. Eight decades below the peak intensity, the scattered intensity becomes dominated by the photodiode dark-current. With a sample present, the minimum scattering-vector reached is close to the theoretical 0.004 nm^{-1} for Ge(111) optics and 10-keV x-rays, and acceptable data statistics can be obtained in a scan taking less than 25 minutes. Further experiments will extend these enhancements to Si(111) optics, in order to take advantage of the high brilliance and small synchrotron opening-angle of a third-generation source.

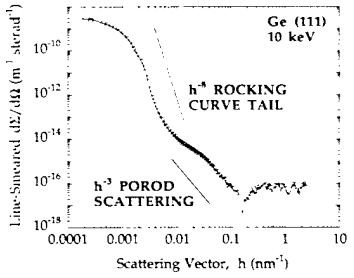

Morphology of Polyethylene/Carbon Black Composites *	X23A3

G. Beaucage, S. Rane, D. W. Schaefer (U. Cinn.) K. Schwartz, M. Wartenberg (Raychem), G. G. Long, D. A. Fischer (NIST) and G. D. Wignall (ORNL)

Carbon black is a common polymer additive that is used for purposes of reinforcement and for enhancing materials properties such as conductivity. This research pertains to a small-angle x-ray scattering (SAXS) study of a conductive grade of carbon black and carbon black/polymer composites. The SAXS from such materials displays a surface-fractal-like power-law decay over many decades of scattering vector, q. While SAXS by carbon blacks can be described in terms of surface-fractal models related to particles with fractally-rough surfaces, the existence of such self-similar surface roughness is not supported by electron microscopy data. It is instead proposed by the present investigators that the scattering represents a more complicated morphology including overlapping structural features and a power-law scaling of polydispersity. We have shown that power-law polydispersity in aggregate size can account for the observed scattering. Moreover, it has been possible to calculate a reasonable heterogeneity index for the aggregates using a power-law polydispersity model. The SAXS from carbon black in an amorphous polymer matrix was used to estimate the primary particle size and other nano-sized structural features of the carbon black, as well as to support a model based on changes in large-scale agglomeration and on aggregate breakup at higher concentrations. When x-ray diffraction data were combined with the SAXS data, it was also possible to identify a scaling regime associated with graphitic layers in the primary particles. Differences in scattering between low and high concentrations of carbon black in polyethylene support a model based on large aggregate breakup and an associated linear agglomeration of aggregates in high concentration carbon black samples. The latter may be critical to understanding conductivity switching in these composites.

Since one application of conductive carbon black composites with polyethylene is in circuit protection devices, where resistive heating leads to a reversible association of carbon black aggregates that controls switching between a conductive and a non-conductive state, these scattering results are very useful as an *in situ* tool to observe the morphological signature of this reversible structural change.

* This work was supported, in part, by the Petroleum Research Fund of the American Chemical Society

USAXS Determination of the Degree of Consolidation of Resin Particles in UHMWPE Components	X23A3

A. Bellare and M. Spector (Harvard U.)

Consolidation of ultra-high-molecular-weight polyethylene (UHMWPE) resin powder particles during processing of UHMWPE components has been a concern in the manufacture of total-joint-replacement prostheses. While UHMWPE resin is beneficial for wear performance in total-joint-replacement prostheses, processing of the resin is difficult since resin particles do not flow, even at temperatures above the melting point of polyethylene crystallites. High pressures and elevated temperatures are required during ram extrusion and compression molding processes to consolidate UHMWPE resin particles. Recently, it has been shown that wear debris retrieved from tissues in cases of failed total hip arthroplasty resemble the size and shape of original resin particles, suggesting that poor consolidation of resin can contribute to wear. It is therefore essential to optimize processing parameters for each type of UHMWPE resin to obtain a high level of consolidation.

In this study, ultra-small-angle x-ray scattering (USAXS) at X23A3 has been used to compare the degree of consolidation of UHMWPE components of various resins. We hypothesize that a lower degree of consolidation leads to a larger number of voids in components. Since voids are usually larger than crystallites of UHMWPE, their presence would lead to scattering at smaller angles. (The only exception is Hylamer in which there are crystallites of sizes comparable to those of voids.)

Fig. 1 shows USAXS data from components that were molded for 5, 10 and 15 minutes. The decrease in scattering with increase in molding times is a direct consequence of lower number of voids and a greater degree of consolidation. Visual inspection revealed the presence of voids in the 5 and 10 minute molded samples, but no significant voids in the 15 minute molded sample. These results show a correlation between USAXS intensity and the number of voids associated with concolidation. In another part of this study, USAXS results from different resins were compared, and a wide variation in the amount of void scattering was observed. For example, it was learned that the 2-million-molecular-weight resins have a lower number of voids, indicating a higher degree of consolidation, compared to the 5-million-molecular-weight resins.

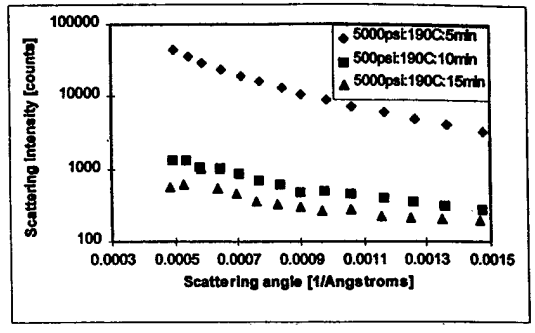

Figure 1. USAXS intensity versus scattering vector for three molding times.

Accelerated Aging of Gamma-Radiation-Sterilized Hylamer Acetabular Components	X23A3

A. Bellare and D.C. Sun (Harvard U.)

Post gamma sterilization aging of UHMWPE components of total joint replacement prostheses has received considerable attention in recent years due to evidence of embrittlement with age. Several accelerated aging protocols have been developed and compared to real time shelf-life aging of UHMWPE. These protocols are useful in the development of new methods of sterilization that aim to prevent embrittlement of UHMWPE with in-vivo age. In this study, we have utilized a previously-developed accelerated-aging protocol to investigate post gamma sterilization (in air) aging of a Hylamer acetabular component. Ultra-small-angle x-ray scattering (USAXS) at X23A3, FTIR, and DSC were used to characterize the degree of oxidation and the accompanying changes in microstructure.

USAXS measurements were performed on the X23A3 beamline at the National Synchrotron Light source. Sampling volumes were 1 mm by 3 mm by 1 mm. Scattering from voids was eliminated by subtracting the scattering curves obtained from melted samples (T = 190°C). The USAXS data measured from as-received and from aged Hylamer revealed the presence of two peaks, one at ultra-low angles (attributed to the presence of large crystallites formed at high pressure) and a broad peak (attributed to crystallites that are similar in size to conventional UHMWPE crystallites. The existence of a bimodal distribution of crystallites is supported by previous DSC observations. The spacing between high-pressure crystallites (approximately 250 nm) did not change with accelerated aging. However, there was a discernable change in the spacing between the crystallites of smaller dimensions. The inter-crystallite spacing changed from 34.5 nm down to 21 nm (±1.5 nm). These results, together with previously-observed changes in intercrystallite spacing in conventionsl UHMWPE, indicates that recrystallization induced by gamma-sterilization (in air) aging occurs by the same mechanism in both types of microstructures. However, due to a much higher degree of crystallinity in aged Hylamer, compared to aged conventional UHMWPE, oxidative aging could be of greater concern in Hylamer from the standpoint of embrittlement and wear.

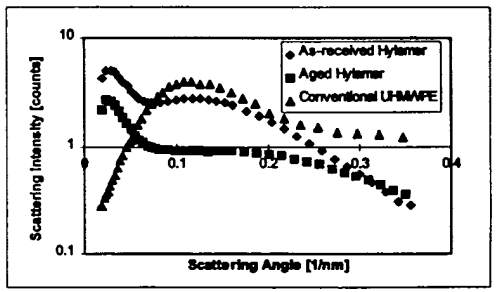

Figure 1. USAXS intensity versus scattering vector for as-received Hylamer, aged Hylamer, and conventional UHMWPE.

Grazing-Incidence X-ray-Diffraction Topography	X23A3

D. R. Black (NIST)

The basic principle of x-ray diffraction topography involves two-dimensional imaging of the x-ray diffracted intensity from a selected set of crystal planes in the sample. The sample diffracts the x-rays in either the reflection geometry to emphasize information on the microstructure near the surface, or in the transmission geometry to emphasize the microstructure of the bulk. Very small variations in the crystalline lattice spacing, Δd, or very small changes in the local crystallographic orientation, $\Delta\theta$, change the diffraction condition and thus the diffracted intensity. Changes in local orientation and the local lattice spacing are the result of crystallographic defects such as dislocations, stacking faults, inclusions, voids, and inhomogeneous strain. Although the best spatial resolution available with x-ray topography is just under a μm, much smaller defects can be detected if there is a strain field around the defect.

As an example, x-ray topographs from single-crystal sapphire typically show long-range inhomogeneous strains or lattice curvature, subgrains, and residual polishing damage. Although such scratches may not be visible optically, they are often visible in the x-ray image if, even after the scratch itself was removed, the lattice below the scratch was disturbed and that damage remains. To further improve the sensitivity to surface microstructures, grazing-incidence topography has been used on X23A3. In this mode, a set of diffracting planes, not parallel to the surface, are chosen to diffract. By adjusting the energy of the incident x-ray beam, one can choose a diffraction angle near the angle for total external reflection of the x-rays. When this occurs, there are no beams entering the sample, only an exponentially-decaying evanescent wave. This condition changes the surface sensitivity of x-ray imaging from tens of μm to tens of nm. In Fig. 1, when the incident energy of the x-ray beam was changed by 100 eV, the incident angle changed by 0.25°, and a much greater sensitivity to surface microstructure of this sapphire crystal was achieved. This microstructure is directly attributable to the fabrication methods.

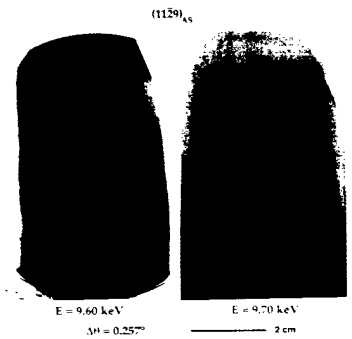

Figure 1. Depth-sensitive observation of the microstructure of single-crystal sapphire. The image on the left was taken using an incident x-ray beam energy 100 eV lower than that in the image on the right.

Small-angle X-ray Scattering Study of the Formation of Colloidal Silica Particles From Alkoxides: Primary Particles or Not?	X23A3

H. Boukari (U. Maryland & NIST), M. T. Harris (U. Maryland) & J. S. Lin (ORNL)

The formation of colloidal silica particles from tetraethyl-orthosilicate (TEOS) in several alcoholic solvents under base-catalyzed conditions was investigated by means of X-ray scattering, SAXS [1] and USAXS. For low concentrations of water, one can follow the dynamics of formation and growth by measuring the scattered intensity profiles at various times following the initiation of hydrolysis and condensation process. The high-q data are analyzed within the concept of fractal geometry and the time-dependent fractal dimension is determined from the power-law region. Furthermore, changes in the radius of gyration are determined from the Guinier low-q regime. Remarkably, we find that, after an induction period, the first particles to appear in the solution are mass-fractals characterized by their polymeric, low-density structure. This stage is followed by an intra-particle densification process and smoothing of the interface leading to the usual compact non-fractal, stable structures. Interestingly, under the same conditions, the initial particles are sizable (radius of gyration is greater than 5 nm) and the initial size depends strongly on the solvent. We are studying these results in light of results predicted by current growth models that have been proposed.

[1] H. Boukari, J. S. Lin, M. T. Harris, *J. Colloid. and Int. Sci.*, (1997) in press.

The Effects of Hydrogen Peroxide and Sterilization on the Structure of Ultra-High-Molecular-Weight Polyethylene *	X23A3

M. Goldman, R. Gronsky, L. Pruitt (U. of C., Berkeley) and G. G. Long (NIST)

Ultra-high-molecular-weight polyethylene (UHMWPE) is an important material for total joint replacement surgeries, and, as such, must be sterilized before placement into the body. It must also perform well as a function of time, or else revision surgeries will be needed. In this research, the effects of hydrogen-peroxide aging and gamma-irradiation sterilization on the structure and morphology of medical-grade UHMWPE were studied. The microstructural changes that were induced via sterilization and accelerated by aging were observed by means of small-angle x-ray scattering (SAXS) measurements on X23A3. Differential-scanning calorimetry, density gradient column measurements, and transmission electron microscopy were also used to characterize the structure. Based on the results, a mechanism for the oxidation of UHMWPE was proposed in which oxygen is incorporated into the amorphous phase of the polymer, leading to strains and breaking of tie molecules, which in turn leads to embrittlement and microcracking within the microstructure.

The SAXS data for four samples aged 11 months are shown in Fig. 1. An interference peak near scattering vector h = 0.0125 $Å^{-1}$ can be seen. This interference peak is associated with the long period in the UHMWPE structure, which is of the order of 515 Å. The sandwich size is the smallest in the untreated sample (n-air) and greatest in the hydrogen-peroxide-aged and gamma-irradiated sample (g-hp). Enhanced scattering at low-h, which is seen in the scattering from some of the samples, is interpreted as Porod scattering from microcracks. Taken together, the lamellar microstructure is best-defined (least tortuous) in the unsterilized sample aged in air (n-air), and this sample shows no evidence of microcracking. The lamellar microstructure is the least well-defined (most tortuous) in the gamma-irradiated sample aged in hydrogen peroxide (g-hp), and this sample shows the most microcracking. This is the first time that microcracking has been observed directly in these samples, and the results are consistent with mechanical properties measurements.

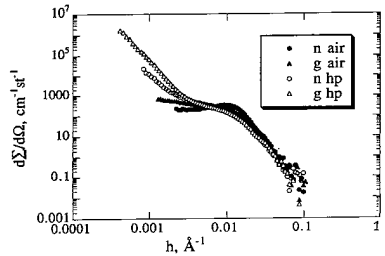

Figure 1. SAXS cross section as a function of scattering vector h for four samples of UHMWPE. n-air = not irradiated and aged in air, g-air = gamma irradiated and aged in air, n-hp = not irradiated and aged in hydrogen peroxide, g-hp = gamma irradiated and aged in hydrogen peroxide.

* This work is supported, in part, by the NSF under Contract No. 44244422178.

Ultra-Small Angle X-Ray Scattering by Single-Crystal Aluminum Deformed In Situ	X23A3

L. E. Levine, G. G. Long and R. Thomson (NIST)

Ultra-small-angle x-ray scattering measurements on single crystal Al, deformed *in situ*, were carried out. Stress-strain data were accumulated simultaneously with the x-ray scattering data to follow the evolution of dislocation structures from 0% strain to 18% strain. Using long-wavelength x-rays, it was possible to follow the development of dislocation structures while avoiding accidental Bragg diffraction. The USAXS results can be understood in terms of scattering by the edge components of the dislocations and of scattering by the dislocation walls in "carpet structures." The scattered intensity is a strong function of the orientation of the scattering vector relative to the configuration of the dislocations. At low strains, it was found that the amount of scattering from the dislocation structures was roughly constant. At higher strains, the scattered intensity increased dramatically. Interestingly, this apparent change in the dislocation configuration does not correspond to any feature in the measured stress-strain curve. Those results are currently being interpreted using a newly-developed theory of small-angle scattering by dislocation structures.

In a companion x-ray topography experiment, also carried out on X23A3, the carpet structures were imaged, and small rotations across dislocation walls were observed and measured. Surprisingly, the grown-in dislocations and the carpet dislocations were sometimes observed to have no measurable influence on one another. The mobile dislocations on the primary slip planes simply cut through the existing immobile dislocations.

Use of Ultra-Small-Angle X-Ray Scattering to Measure Grain Size of Styrene-Butadiene Block Copolymers	X23A3

R. T. Myers, R. E. Cohen (MIT) and A. Bellare (Harvard U.)

It is well-known that appropriate processing techniques can produce essentially perfectly ordered block coplovmer morphologies with a single texture extending throughout the macroscopic dimensions of a specimen. The characteristic repeating length scale, d, of these morphologies is dictated by the molecular weights of the constituent block sequences and is on the order of 100 Å. In the absence of extraordinary processing procedures, a second important length scale appears in the block copolymer. The perfection of the morphology is broken up into grains, each of which contains the ordered morphology of length scale d but with essentially random orientation relative to the specimen boundaries. These large grains typically exhibit a characteristic size, D, which is one or more orders of magnitude larger than the morphological length scale, d. It has been shown that the grainy structure can influence important physical properties of this material such as gas transport.

Conventional small-angle x-ray scattering (SAXS) techniques have been used for decades to characterize block copolymers at the morphological length scale d. Recently, ultra-SAXS (USAXS) measurements at X23A3 have been able to probe significantly larger morphological features, previously observable only through the use of various microscope techniques. The spacing, d, was revealed directly by the data. Although no resolvable peaks appeared as a result of scattering by the grains, an analysis of the Porod tail of the grain scattering, and the use of the scattering invarient, enabled a reliable estimate of the grain size, D. Independent observation of the grains in the bulk specimen by means of transmission electron microscopy corroborated the USAXS analysis. Thus, USAXS can be used to provide a reliable and statistically-significant characterization of bulk specimens of block copolymers simultaneously at both of the above-mentioned length scales.

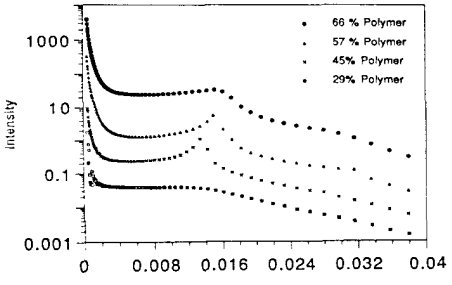

Figure 1. Smeared intensities as a function of scattering vector q for KRO-3 resin diluted with various amounts of cumene. The uppermost plot is at the proper position on the vertical axis. The other curves were shifted successively downward for clarity of presentation. The downward shifts are: 1.0 decade, 1.5 decade and 2.0 decades respectively.

X-ray Topography of Superalloy Single-Crystal Castings	X23A3

R. Napolitano, R. Schaefer and D. R. Black (NIST)

The demand for larger and more complex superalloy single-crystal components in both aerospace and in land-based gas turbines has increased dramatically the degree of process control required for the reliable production of defect-free blades and vanes. The mechanisms responsible for the formation of low-angle grain boundaries is not well understood, and these defects have not been well-characterized in production castings. The objective of this work is to characterize the misorientation in several castings such that the conditions leading to the development of low-angle grain boundaries may be identified, better understood, and ultimately eliminated.

Grain defects are most often observed near mold corners or in other areas of non-uniform cross section. For this reason, several test castings were produced with varying geometries. The castings were made with high-temperature alloy Rene N5. Each casting had one or two regions of non-uniform cross section, which were sectioned and examined by means of monochromatic x-ray topography at X23A3. In some areas, a series of parallel sections were imaged over a large angular range to provide three-dimentional information concerning the crystallographic orientation. With this technique, continuous and discontinuous misorientations can be distinguished and traced through the casting, yielding a qualitative and a semi-quantitative understanding of how they are related to the mold geometry. This is vital information because it can be coupled with thermal analysis of the casting process to provide a complete picture of defect formation at any specific location within the component. In this way, the underlying mechanisms for defect formation may be revealed.

Particle Sizes and Size Distributions in Additives to Polymeric Systems	X23A3

K. C. Sheth and Y. Gao (GE R&D)

The goal of these experiments is to develop techniques to determine average particle sizes and size distributions of additives (such as impact modifiers and flame retardants) in polymeric systems. The USAXS facility at X23A3 has been used to probe particle sizes up to approximately one micrometer in size. Hence this facility fills the gap between conventional SAXS (for the smallest sizes) and light scattering (for the largest sizes).

The conventional approach to particle size analysis is transmission electron microscopy (TEM), but TEM samples only a limited area and it is difficult to obtain a statistically-significant sampling. USAXS, on the other hand, provides a rapid, non-destructive, robust technique for obtaining the required information. We have been studying a variety of polymeric systems, containing a variety of additives. In particular, we have examined isotropic, spherical additives (rubber additives as impact modifiers) and anisotropic additives (such as globular or fibrilar particles). TEM data is available on these systems. The results from the analysis of the USAXS data for spherical particles are in excellent agreement with the TEM data. For example, for a rubber particle dispersion in acrylonitrile-butadiene-styrene, the average particle size is 848 nm, which is in good agreement with the corresponding TEM result of about 800 nm. (TEM is expected to yield smaller numbers than the actual size because there is two-dimensional averaging resulting from the slicing of spheres.) The particle size distribution derived from the USAXS data also correlates well with the TEM results. An analysis of the USAXS from the anisotropic particles is currently in progress.

Characterization of an Er L_{III} Bragg Polarizer Grown by Molecular Beam Epitaxy	X23B

J. O. Cross, B. R. Bennett, M. I. Bell (NRL) and K. J. Kuhn (Intel Corp.)

A wide band linear Bragg polarizer for photon energies around the L_{III} absorption edge of erbium was grown from a ternary semiconductor alloy using molecular beam epitaxy.[1] The active optical element is an 8 micron single crystal film of $In_{.51}Ga_{.49}Sb$ grown on an oriented GaAs (001) substrate. The composition of the alloy was calculated using Vegard's rule, assuming total relaxation of the epitaxial layer, to give maximum linear polarization for the target energy of 8358 eV using the (006) Bragg reflection. The full-width at half-maximum of the energy acceptance was measured to be 27 eV, centered at 8359 eV, by scanning the incident energy with the polarizer and detector held fixed at $\theta = 45$ detrees and $2\theta = 90$ degrees, respectively.

[1] J. O. Cross, et al., Appl. Phys. Lett. **70** (1997) 2224.

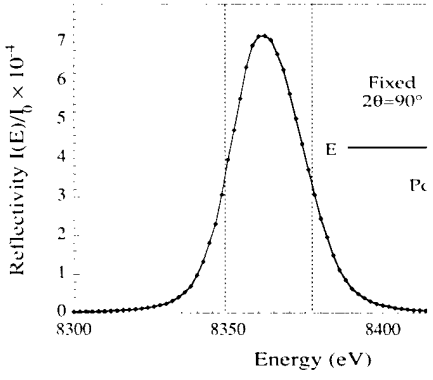

Figure 1. Response of the polarizer as a function of energy in the vicinity of the Er L_{III} absorption edge. The inset shows the experimental arrangement.

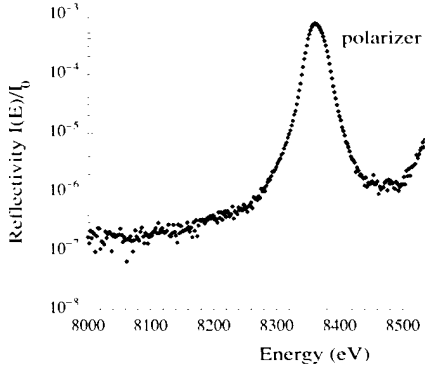

Figure 2. Reflectivity vs. Energy around the (006) Bragg peak. The substrate peak is reduced by the overlayer.

Sample-angle Feedback For Improved Reproducibility in Diffraction Anomalous Fine-structure (DAFS) Spectra	X23B

J. O. Cross, W. T. Elam, V. G. Harris (NRL), J. P. Kirklans (SFA), C. E. Bouldin (NIST) and L. B. Sorensen (U.W.)

Diffraction anomalous fine-structure (DAFS) experiments measure integrated Bragg peak intensities as continuous functions of energy in the vicinity of absorption edges.[1] Often, the peak intensity of the θ rocking-curve is proportional to the integrated intensity over the energy range of the fine-structure (typically 1000 eV), and it is sufficient to track the Bragg peak as the incident energy is scanned. This "peak-tracking" mode of collecting DAFS data significantly reduces the time required for a complete spectrum, however, while the Bragg angle as a function of energy can be calculated easily and given as a command to the diffractometer controller, any systematic error in addressing the goniometer or monochromator motors will result in distorted spectra. One way to insure accurate tracking of the peak is by introducing a small reference oscillation on the sample angle, producing a corresponding fluctuation in intensity at the detector that can be fed to the input of a lock-in amplifier. A piezoelectric actuator-driven sample stage has been designed and tested as part of a sample-angle feedback circuit for locking on to the maximum of the rocking curve as the incident photon energy is scanned during DAFS experiments. Dramatic improvements in reproducibility were observed, as well as a decrease in systematic glitches caused by roundoff errors in the motor addressing.

[1] H. J. Stragier, et al., Phys. Rev. Lett. **69**, 3064 (1992).

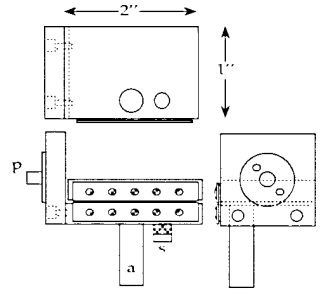

Figure 1. Diagram of the sample stage showing the piezoelectric actuator (a) loading spring (s) to provide the restoring force, and goniometer head mounting post (p).

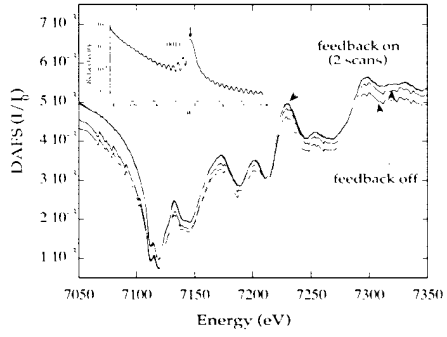

Figure 2. Fe K-shell DAFS. Software peak tracking with and without additional hardware feedback locking. The inset shows the reflectivity around the (Fe 40Å/Si 14Å)×25 (001) multilayer peak.

EXAFS Study of the Local Structure Around Mn in Annealed ZnS:Mn Nanocrystals	X23B

J. O. Cross, W. T. Elam, D. Hsu, H. F. Gray, J. Yang, M. Smith and B. R. Ratna (NRL)

The quantum yield of Mn-doped ZnS nanocrystals grown in the bicontinuous cubic phase (BCP) of a surfactant and water system [1] has been shown to depend on Mn concentration. These crystallites are highly monodisperse, and in the 35Å diameter nanocrystals, a peak in the quantum yield occurs at 0.7 mole percent, or approximately one Mn atoms per particle. Recently, an additional increase in the quantum yield has been shown to follow a structural change induced by annealing the nanocrystals. We have used extended x-ray absorption fine tructure (EXAFS) to study changes in the local environment of the Mn luminescent centers caused by annealing.

The R-space transforms of background subtracted fluorescence EXAFS data from three ZnS:Mn phosphor powders are shown in Figure 1. Background subtraction and R-space fits were performed using AUTOBK and FEFFIT [2], with theoretical χ calculated by FEFF7.[3] The Mn-S distance of 2.409(7)Å determined for the as-grown nanocrystals is approximately 0.03Å shorter than the Mn-S distance of 2.443(6)Å determined for the bulk standard, consistent with a previous EXAFS study of 30-35Å ZnS:Mn grown by precipitation [4]. In the BCP grown samples, however, the amplitude of the Mn-S nearest neighbor shell of the nanocrystals, relative to that of the bulk, is lower than that reported in [4], and the second peak due to the Zn and S next neighbors is absent in the as-grown nanocrystals. The absence of the second peak could be due to disorder in the next neighbor shells, or to the Mn impurities migrating to the surface of the crystallites during growth. X-ray diffraction measurements of BCP grown samples prior to annealing suggest that for particles of ca. 30Å and smaller, the cubic (zinc-blende) lattice distorts tegragonally [5], consistent with disorder in the Zn and S next neighbor distances. After annealing, the EXAFS first shell amplitude remains nearly unchanged and the second peak re-appears. In addition, annealing causes an increase in the first neighbor Mn-S distance to 2.436(8)Å, close to that of the bulk.

[1] J. P. Yang, et al., *J. Phys. Chem.* **100** 17255 (1996). [2] M. Newville, et al., *Phys. Rev. B* **47** 14126 (1993) [3] S. I. Zabinsky, et al., *Phys. Rev. B* **52** 2995 (1995). [4] Y. L. Soo, et al., Phys. *Rev. B* **50** 7602 (1994). [5] S. B. Qadri,et al., *Appl. Phys. Lett.* **70** 1020 (1997).

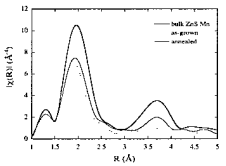

Figure 1. R-space Fourier transform of EXAFS data from bulk standard (heavy solid line) and ZnS:Mn nanocrystals before (dashed line) and after (thin solid line) annealing.

DAFS Study of the Interfaces of an Fe/Si Multilayer	X23B

J.O. Cross, V.G. Harris, W.T.Elam (NRL) and M. Newville (U. Chicago)

Fe/Si multilayers are interesting for their magnetic properties, saturation magnetism (M) and anistropy field (H_k), and as x-ray optical components for magnetic circular dichroism. The boundary between the Fe and Si layers has an intermixing region which which can be disordered, or form an iron silicide. The presence of the crystalline silicide affects the magnetic properties of the multilayers and is therefore of technological interest, however, determining the thickness and structure of the crystalline spacer has so far been unanswerable using diffraction or XAFS.[1]

While XAFS can, in principle, be used to determine the number and distances of Si near neighbors, as well as the presence of order in the Fe and Si next neighbors around the Fe centers, the thickness of the silicide layers are on the order of 10% of the Fe layers, so that XAFS from the interface is lost in the signal from the rest of the film. DAFS gives the same kind of local structural information as XAFS, but also uses the long-range order of the material to select the fine-structure from a subset of the resonant atoms.[2] Since the intensities of the multilayer peaks are proportional to the Fourier components of the electron density normal to the interfaces, the DAFS on each peak samples a different subset of the Fe atoms. Figure 1 shows the reflectivity of (Fe 40Å/Si 14Å)×25 multilayer and Figure 2 shows the Fe K-shell DAFS measured on the (001), (002) and (003) multilayer Bragg peaks of the same sample. Small difference observed in the extended DAFS confirm the presence of at least two different local environments for the resonant Fe atoms. Since the x-ray polarization is confined to x-y plane in these reflectivity measurements, the DAFS is sensitive to the in-plane bond lengths around the Fe sites. The DAFS will be analyzed by solving for the anomalous scattering amplitudes f' and f'' and then combining the χ'' fine-structure from these three reflections and the XAFS subject to a model that is consistent with the reflectivity to isolate the signal from Fe sites at different positions in the bilayer.[3]

[1] J. A. Carlisle, et al., Phys. Rev. B **53**, R8824 (1996). [2] H. J. Stragier, et al., Phys. Rev. Lett. **69**, 3064 (1992). [3] J. O. Cross, et al., J. Phys. IV France **7** (Colloque), C2-745 (1997).

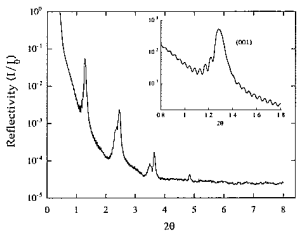

Figure 1. Reflectivity from a (Fe 40Å/Si 14Å)×25 multilayer at 7412 eV. The DAFS measurements were made at the maxima of the (001), (002) and (003) peaks.

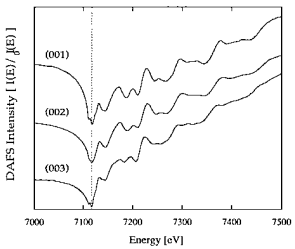

Figure 2. Fe K-Shell DAFS from the (001), (002) and (003) multilayer peaks. Differences between the fine-structure features are visible in the intensity data.

Quantitative Speciation of Cr at ppm Concentrations Using Chemometric Modeling of XANES Spectra	X23B

J. O. Cross, R. E. Shaffer, W. T. Elam, S. L. Rose-Pehrsson (NRL) and J. P. Kirkland (SFA, Inc.)

The ability to differentiate chemical species using x-ray absorption near-edge spectroscopy (XANES) has been demonstrated previously,[1] however, most existing methods require separate measurements of the spectra from model compounds to identify a signature for each species. More recently, soft chemical analysis methods, such as principal components analysis (PCA) and chemometric modeling or partial least- squares regression (PLS), have been applied to determine the number of unknown species present in environmental samples for which laboratory standards may not be available.[2] Based on these ideas, we have set out to determine a lower limit on the quantitative differentiation of Cr species using PCA and chemometric modeling of XANES spectra. In previous studies,[1] the pre-edge feature Figure 1(a) observed in compounds with the Cr(VI) valence has been used to determine the ratio of Cr(VI) to Cr(III) by comparing the integrated peak intensity to the absorption step height. There is an inherent limit to the quantitative accuracy of this method since the peak:step ratio is not the same for all Cr(VI) compounds, e.g., Na_2CrO_4 and $K_2Cr_2O_7$ in Figure 1(inset). Soft modeling methods make use of the entire XANES spectrum, with the strongest weight given to regions such as Figure 1(a), (b) and (c), that change most between samples. The goals of this experiment were 1) to determine the number of species present in a group of samples using PCA and 2) to set a bound on the quantitative accuracy of PLS for determining the amount of known species, i.e., laboratory standards, present in the sample at low total Cr concentration. For this initial study, XANES data were collected from dry mixtures of Cr(VI) and Cr(III) in sand at concentrations from 1000 ppm down to 7 ppm by weight. Figure 2 shows the results of speciation by PLS on mixtures with different ratios of Cr(III) to Cr(VI) and for several total Cr concentrations. PCA determined the presence of two components and speciation using PLS gave a mean error of 3.62% in the Cr(VI) to Cr(III) ratio for total Cr between 300 and 1000 ppm, and 6.59% for 100 ppm and lower.

[1] M. L. Peterson, et al., J. Phys. IV France **7** (Colloque C2, 1997) C2-781.
[2] S.R. Wasserman, J.Phys. IV France **7** (Colloque C2, 1997) C2-203.

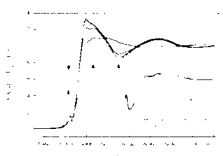

Figure 1. PCA determines the number of species and soft modeling makes use of the entire XANES spectrum, weighted in regions such as (a), (b) and (c) that change most between samples. The ratio of pre-edge peak to step height is not the same for all hexavalent Cr compounds.

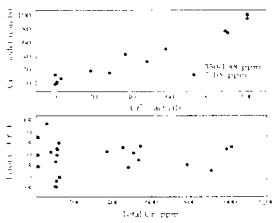

Figure 2. Results of chemometric modeling for mixtures of Cr(VI) and Cr(III) at concentrations from 1000 ppm to 7 ppm (a) predicted ratio vs. actual and (b) error in percent Cr(VI) vs. concentration.

Processing of Pure-Phase MnZn-Ferrite Using High-Energy Ball Milling: An X-Ray Absorption Fine Structure Study	X23B, X23A2

D.J. Fatemi, V.G. Harris(NRL), and J.P. Kirkland(SFA)

$Mn_{.5}Zn_{.5}Fe_2O_4$ ferrites were processed by mechanical alloying a mixture of the elemental oxides MnO, ZnO, and Fe_2O_3 in a high-energy shaker mill. The structure of the milled mixtures was studied via X-ray diffraction (XRD) and extended X-ray absorption fine structure (EXAFS) measurements. Broad diffraction peaks, corresponding with those of the spinel ferrite phase, were detected via XRD after 180 min. of milling (the sample of shortest milling duration), whereupon a pure phase spinel ferrite (as judged by XRD) was measured in the 1260 min. milled sample. The atomic fraction of metal ions existing in the AB_2O_4-type structure, where A and B refer to tetrahedral and octahedral coordinated cations, was measured as a function of milling duration by EXAFS. This analysis reveals that the conversion of metal ions from their elemental oxide structures to the spinel phase occurs near-linear with milling time with 50% of the oxides converted after approximately 500 minutes. Multiple-scattering EXAFS modeling was applied to measure the site distribution of the various cations as a function of milling time. Compared with an equilibrium $Mn_{.5}Zn_{.5}Fe_2O_4$ powder sample, which was prepared by traditional fire and grinding techniques, the mechanically alloyed ferrite samples exhibit a higher fraction of Fe and Mn cations on the A-sublattice, while an unusually high population of Zn cations resides on the B-sublattice. The site distribution can be inferred qualitatively from Fig. 1, in which peaks labeled A and B arise largely from occupation of the absorbing atom on A-sites and B-sites, respectively.

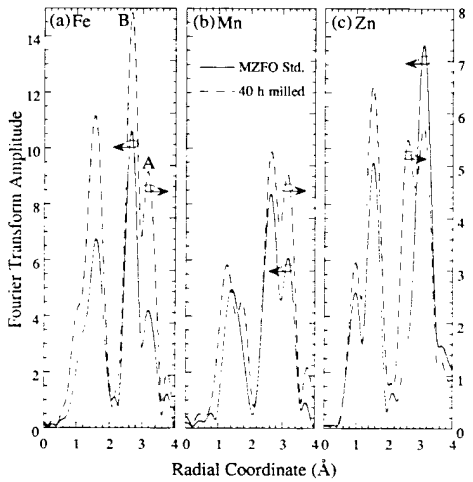

Figure 1. Fourier transformed (a)Fe, (b)Mn, and (c)Zn EXAFS data from MnZn-ferrite formed after 40 hrs of milling and from the standard.

EXAFS Measurements of Non-Superconducting $PrBa_2Cu_3O_{6.9}$: Evidence against Ba Site Pr Substitution	X23B

V. G. Harris, D.J. Fatemi, V. M. Browning, M. S. Osofsky, (Naval Research Laboratory), and T. A. Vanderah (National Institute of Standards and Technology)

Extended X-ray absorption fine structure (EXAFS) measurements on non-superconducting $PrBa_2Cu_3O_{6.9}$ are reported. The EXAFS analysis reported here involves the least-squares fitting of the phase and amplitude of experimental k-space data using a linear combination of simulated Pr(Y)-site and Pr(Ba)-site LII EXAFS data. The simulated Y- and Ba-site Pr L_{II} EXAFS data were generated using the multiple-scattering ab initio FEFF 6 codes of Rehr et al., where the FEFF input files were generated using ATOM 4.2 codes of Ravel. The calculated best fit data contains 0% Pr on the Ba-site. Because the Pr(Ba)-site L_{II} FEFF is nearly$\pi/2$ out of phase over a wide range of low-k values with respect to the Pr(Y)-site L_{II} FEFF the results of the fitting analysis are unambiguous, with the results establishing that only dilute (i.e.< 1%) amounts of Pr can occupy the Ba sites in this compound. It is noteworthy that the substitution of even dilute amounts of Pr on the Ba-site lead to a significant deterioration of the goodness of fit, as judged numerically by the χ^2-fitting parameter and by visual inspection. This is illustrated in Fig. 1 where one sees the appearance of new fine structure peaks at k= 5.15Å^{-1} and 8.05Å^{-1} that do not correspond with the experimental data. This occurs when just 1% of Pr is allowed to occupy Ba sites. A second approach to the fitting analysis involved relaxing the phase constraint. This allows an additional degree of freedom to the fit and would presumably allow a larger fraction of Pr to reside on the Ba-site. In physical terms this is analogous to allowing local dilation or contraction of the local environment by the substitution of the Pr ion on the Ba-site, as might be expected based on the mismatch in atomic radii between Ba and Pr. The best fit obtained in this fitting approach also had 0% Pr on the Ba-site. These results present a serious challenge to models which rely on Ba-site Pr substitution as an explanation for the lack of superconductivity in $PrBa_2Cu_3O_{7-\delta}$.

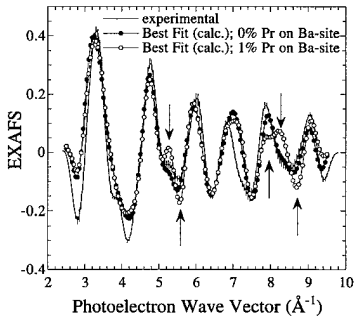

Figure 1. Experimental Pr L_{II} EXAFS and the best fit data for the cases when 0% and 1% Pr ions occupy the Ba-sites. The arrows indicate gross deviations from the experimental data introduced by the inclusion of 1% Pr on the Ba-sites.

Magnet to Volume Effects in $R_2Fe_{17-x}Al_xN_y$ (R=Er,Pr) Compounds Studied via EXAFS	X23B

V.G. Harris, D.J. Fatemi, (Naval Research Laboratory), K.G. Suresh, and K.V.S. Rama Rao, (India Institute of Technology)

Extended x-ray absorption fine structure measurements of the Fe K, and Pr and Er L_{III} absorption edges, were carried out to elucidate the relationship between the local structure and magnetism in Al substituted, nitrogenated $(Er_{0.5}Pr_{0.5})2Fe_{17}$ permanent magnets. Figure 1 is a plot of the FT Fe EXAFS collected from the Al-substituted and nitrided samples, together with data from the parent compound. The inset panel depicts a plot of the average Fe-Fe/Al bond distance ($<r>_{Fe-Fe/Al}$) and the average $_{Fe-Fe/Al}$ Debye Waller Coefficient ($<DWC>_{Fe-Fe/Al}$) calculated for the atoms contributing to the NN peak as a function of x. Because the NN peak of Fe is dominated by other Fe and Al atoms that are distributed on 4 inequivalent sites (i.e. 6c, 9d, 18f, 18h) the environment is described as an average Fe-Fe/Al bond. This simplification reduces the number of adjustable parameters in our fitting analysis from as many as 12 to no more than 3. Upon nitrogenation the $<r>_{Fe-Fe/Al}$ increases 0.86% from that of the parent compound. This result is a direct measurement of the dilation of the Fe coordination sphere and reflects a positive magnetovolume response of the Fe sublattice due to nitrogenation. With the substitution of Al we observe that $<r>_{Fe-Fe/Al}$ decreases abruptly (rel. -0.6%), plateaus, and then continues its decrease. Although, others have reported a positive magnetovolume response to the substitution of Al (x<4) (sans N), we observe in the presence of N that the Al acts to reduce the Fe coordination sphere. This negative magnetovolume effect is consistent with the ME results of Suresh and Rama Rao who found that the T_C and the hyperfine fields of all Fe sites reduce with increased Al content. The $<DWC>_{Fe-Fe/Al}$ increases with increased Al content for 0<x2, and experiences a relative decrease for x=3. The Fe-Al correlation is measured to experience an abrupt decrease of its NN bond for x=3. Taken together, these data and other indicate a preferental redistribution of Al atoms to the 6c site for x_x3.

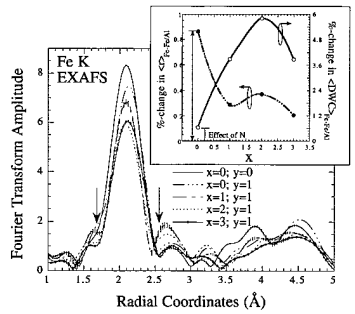

Figure 1. Fourier transformed Fe EXAFS data collected from $(Er_{0.5}Pr_{0.5})2$ $Fe_{17-x}Al-xN_y$ compounds. During Fourier tranformation a k_3-weighting was applied to a k-range of 2.3-13.25Å^{-1}.

XAS Studies of Preferential Site Distribution of Ta and Pt in CoCr-Based Films*	X23A2, X23B

K. M. Kemner (ANL), V. G. Harris, W. T. Elam (NRL), Y. C. Feng, D. E. Laughlin (CMU), J. C. Woicik (NIST), and J. C. Lodder (Mesa Research Institute)

CoCr-based alloy films are presently the mainstay mangetic recording media. Numerous studies have shown that these films can be grown in ways to produce a compositional inhomogeneous microstructure having Co- and Cr-enriched regions. The addition of Ta, Pt to these media play an important role in determining the magnetic properties and recording characteristics of the films. In order to better understand the beneficial roles of their addition, we have made XAS measurements on a variety of CoCrX (X=Ta or Pt) films deposited at ambient and 260 C substrate temperatures. Analysis of the Ta and Pt data indicates that no phase separation of the Pt or Ta atoms into clusters has taken place. Further analysis shows that for an increase in substrate deposition temperature, the average coordination number decreases by 0.6 Co/Cr atoms. Figure 2 shows that, with the addition of Ta and Pt, the Fourier peak amplitudes of the Co EXAFS data decrease relative to that of the data for a pure CoCr film. The greater reduction in amplitude of the Fourier peaks when Pt is added than when Ta is added indicates that the Co environment is more disordered by the addition of Pt than by the addition of Ta, suggesting a preferential site distribution of the Pt atoms to the Co atoms. *KMK was supported by a National Res. Council/NRL Fellowship. Research also supported by the U.S. DOE, Office of Basic Energy Sci. & Office of Health & Environmental Res., contract No. W-31-109-Eng-38.

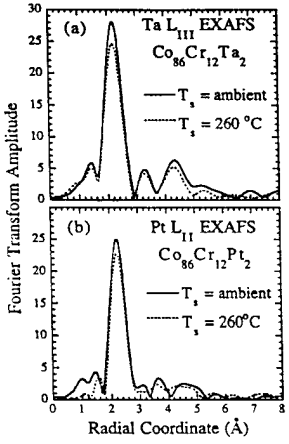

Figure 1. Fourier transformed Ta and Pt EXAFS data for the CoCrX (X=Ta or Pt) samples deposited at ambient and 260°C substrate temperatures.

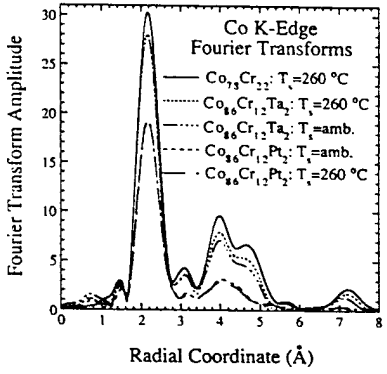

Figure 2. Fourier transforms of Co EXAFS data for the CoCrX (X=Ta or Pt) samples deposited at ambient and 260°C.

Structure and Chemistry of FeS_2 Battery Cathodes *	X23A2, X23B

E. Strauss, D. Golodnitsky, E. Peled (Tel Aviv U.) S. Kostov, M. L. denBoer, and S. G. Greenbaum (CUNY, Hunter College)

The Li/CPE/FeS_2 battery (CPE = composite polymer electrolyte) is a promising candidate for energy storage and electric vehicle applications. Its projected specific energy is over 170 Wh/kg (based on 2.5 e/FeS_2), and a recent small laboratory cell demonstrated over 300 full charge-discharge cycles. Using in situ x-ray absorption methods we have investigated the behavior of thin Li/CPE/FeS_2 cells at various stages of charge and discharge cycles. Cells were examined under the following conditions: (i) charged to 1.85 V and x = 0.5, where x represents the number of electrons associated with that particular charge state; (ii) charged to 2.05 V and x = 1.7; (iii) charged to 2.25 V and x = 2.0; (iv) discharged to 1.65 V and x = 1.4; (v) discharged to 1.25 V and x = 0.15, and (vi) discharged to 1.1 V and x = 0.0. Regardless of whether the cell is being charged or discharged, there appear to be only two distinct Fe host environments, a "low-Li" one for conditions (ii), (iii) and (iv) and a dramatically different "high-Li" one for conditions (i), (v) and (vi). At high Li (cathode) concentration a strong pre-edge feature is apparent, which decreases at low Li concentration, as shown in Fig. 1.. This pre-edge feature is dipole-forbidden in octahedral symmetry, and its decrease therefore indicates that the symmetry decreases as Li is removed from the cathode. The EXAFS similarly falls into two distinct categories (Fig. 2). At high Li concentration the Fe environment is ordered, and analysis reveals a combination of metallic Fe and residual unreacted FeS_2. On the other hand, at low Li disorder sets in and only a single broad peak is observed, analysis of which indicates a combination of FeS_2 and Li_2FeS_2. Structural and chemical changes in the Fe environment appear to be highly reversible.

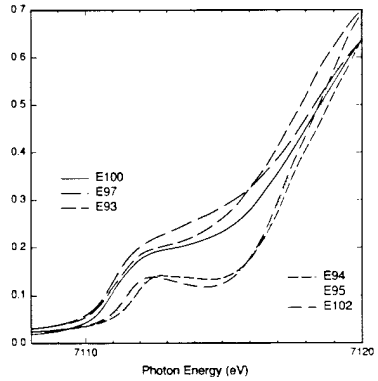

Figure 1. Near-edge x-ray absorption spectrum of cells under various charge conditions as described in the text.

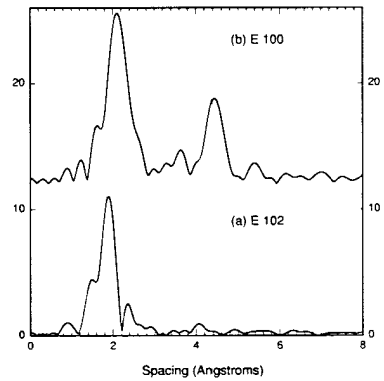

Figure 2. Fourier transform amplitude of representative low-Li and high-Li cathodes.

* Supported by DOE Basic Energy Sciences

XSW Determination of the S/Au Interface Structure in SAMs *	X24A

P. Fenter (Princeton U., & ANL), F. Schreiber and G. Scoles (Princeton U.), L. Berman (NSLS), P. Eisenberger (Columbia U.), and M. J. Bedzyk (Northwestern, & ANL)

While it is widely believed that the S/Au interface structure in self-assembled monolayers (SAM) of thiols adsorbed on Au(111) surfaces consists of sulfur headgroups bound in the Au three-fold hollow site, a recent grazing incidence X-ray diffraction (GIXD) study[1] determined that the GIXD data were inconsistent with this model, and instead required a dimerization of the sulfur headgroups, with a sulfur-sulfur spacing of 2.2Å. To further clarify the bonding in SAMs, we have used X-ray standing waves (XSW) in the back reflection geometry to determine the precise sulfur headgroup positions in this system. Using XSW, we have measured the coherent fraction, f, and position, P for the (111) and (11-1) Au substrate reflections, from which we determine both the vertical and lateral headgroup location. We find that P_{111}=1.10±0.01, f_{111}=0.41±0.01, P_{11-1}=0.25±0.01, f_{11-1}=-0.02±0.01. These measured values are inconsistent with any model which incorporates a unique sulfur bonding site, including the widely assumed three-fold hollow site. Making use of the monolayer symmetry (which incorporates two inequivalent molecules per unit mesh), we derive the full range of sulfur sites which are compatible with the XSW data (shown as dots in Fig. 1). These results clearly show that each sulfur headgroup is located in distinctly different lateral and vertical sites with respect to the Au substrate lattice (large open circles): while one is located near the atop site at a height of 2.21±0.05Å, the other is found in an annulus surrounding the FCC threefold hollow site at a height of 2.97±0.05Å. These results are consistent with the GIXD-derived S-S spacing of 2.2Å, and highlight both our limited understanding of bonding in these complex systems and the related need for quantitative structural probes as the basis for our understanding. [1] P. Fenter, A. Eberhardt and P. Eisenberger, Science **266**, 1216 (1994).

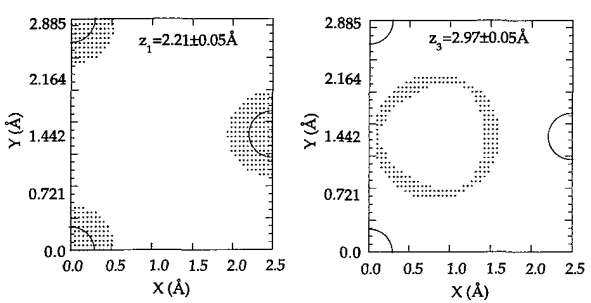

Figure 1.

* This work was supported by DOE grant number DE-FG02-93ER45503, and F.S. acknowledges the support of the DFG

X-ray Standing Wave Determination of Quantum Well Perfection	X24A

J.A. Gupta, E.D. Crozier, S.P. Watkins (SFU) J.C. Woicik, J.G. Pellegrino (NIST), and K.E. Miyano (Brooklyn College)

We have used the x-ray standing-wave technique combined with high-resolution x-ray diffraction to determine the quantum-well perfection in monolayer InAs quantum wells grown on GaAs(001). Preliminary analysis from wells grown at 430, 480, 530, and 580 degrees C find the most organized monolayer to be produced at 480 degree C preceeded by a linear ramp from the 580 degree C buffer layer growth temperature. Apparently, In is desorbed from the growth surface at the higher temperatures, as determined from the ratio of the In versus GaAs fluorescence with the remaining In diffused into the cap. The 430 degree C growth results in a roughened buffer-layer/quantum-well interface.

X-ray Standing Wave Investigation of Hg/Ni(100) — X24A

D. Heskett, J. Warner (Univ. of Rhode Island), L.E. Berman (NSLS-BNL), and P.A. Dowben (Univ. of Nebraska-Lincoln)

We have used the technique of Back-reflection X-ray Standing Waves (BRXSW) to investigate the structure and geometry of mercury on the Ni(100) surface. We prepared these systems by dosing 12-24L of Hg onto the Ni(100) surface at room temperature, which resulted in one layer saturation of the surface. The dosing was then followed by an anneal to 80-100°C., which resulted in the loss of $\approx$ 25 % of the mercury, based on the intensity of the Hg 3d core levels. This procedure has been previously shown to produce a well-ordered (2x2) overlayer LEED pattern.[1]

We next performed x-ray standing wave measurements of this overlayer in both the (200) and (111) Bragg reflection geometries. One set of data taken in the (200) geometry is presented in Fig. 1. Based on the high coherent fractions measured in both geometries, we can conclude that the mercury atoms are very well-ordered both parallel and perpendicular to the Ni(100) surface. Based on triangulation of the coherent positions from both sets of measurements, we can determine that the Hg atoms are bonded in four-fold hollow sites at a distance of 2.36Åabove the (100) Ni planes. This result is in good agreement with a study of this system by Poulsen et al. using the technique of ion transmission channeling.[2] On the other hand, in comparison to another XSW study of this system by Prince et al.,[3] a similar Hg-Ni(100) perpendicular spacing was obtained, however, they concluded that the Hg atoms were bound in bridge sites. In that study, they had not performed triangulation measurements using a different scattering geometry, which in our case conclusively proves hollow site adsorption.

[1] R.G. Jones and A.W.-L. Tong, Surf. Sci. 188, 87 (19987). [2] P.R. Poulsen, I. Stensgaard, and F. Besenbacher, Surf. Sci. 310, L589 (1994). [3] N.P. Prince, N.K. Singh, W. Walter, D.P. Woodruff, and R.G. Jones, J. Phys. Condens. Matter 1, SB21 (1989)

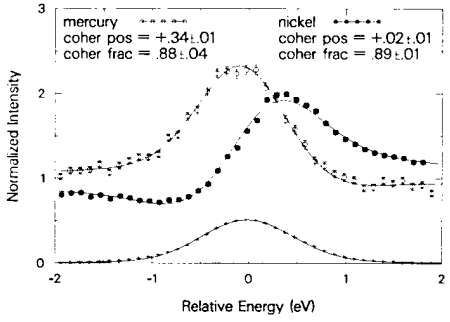

Figure 1. XSW measurements and simulations of the Hg M_V core level and Ni LMM Auger yields for the system Hg/Ni(100) in the (200) Bragg reflection geometry (top curves). The bottom curves are the measured and simulated reflectivity.

X-Ray Standing Wave Measurements from a 5-Fold Symmetry Reflection in the Quasicrystal AlPdMn — X24A

Terrence Jach (NIST), R. Colella (Purdue), A. I. Goldman, T. Lograsso, and D. Delaney (Ames Lab)

We have measured the diffraction peak and the x-ray standing wave in a 5-fold symmetry reflection from a quasicrystal. The $[422222\bar{2}]$ reflection was observed in back reflection ($\theta_B = 90°$) in an energy scan from single-domain AlPdMn around 2860 eV. Al Kα fluorescence observed during the scan displayed distinct x-ray standing wave effects. The observation of x-ray standing waves demonstrates that the dynamical theory applies to aperiodic media The fluorescence from Al is similar to that observed from 2-fold symmetry reflections in that it appears to have a small but non-zero coherent position. This is evidently inconsistent with a centrosymmetric model for the quasicrystal.

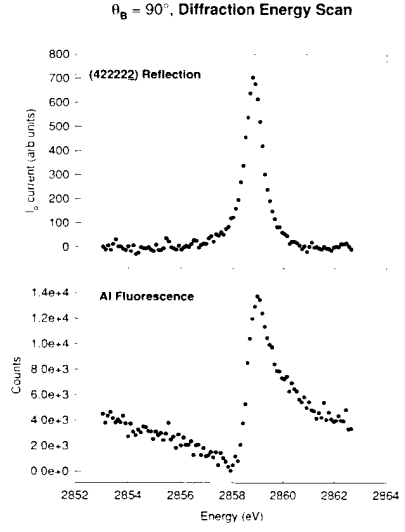

Figure 1. The 5-fold symmetry reflection (above) and Al fluorescence (below) are both shown after subtraction of a linear background.

Grazing Incidence X-Ray Photoemission Spectroscopy of SiO_2/Si | X24A

Terrence Jach and J. Gormley (NIST)

XPS spectra were obtained with collimated incident radiation over a range of angles in the vicinity of the critical angle for total reflection. In addition to the general decrease in the penetration depth which accompanies incidence below the critical angle, the different optical constants of overlayers result in different critical angles. The x-ray fields in each layer change in a non- linear way at each angle and contribute in varying amounts to the photoemission. This allows for fitting the thickness and density of oxide overlayers on Si in a range of 1-10nm. By performing the measurement on X-24A, using an InSb(111)/KDP(111) crystal pair, we have increased the yield by a factor of 100 over what was previously obtained from conventional x-ray sources. We operated in the vicinity of the Si K-edge (1839 eV). We were able to obtain spectra above and below the edge. This allowed us to change the optical constants and observe the resulting effects in photoemission line intensities.

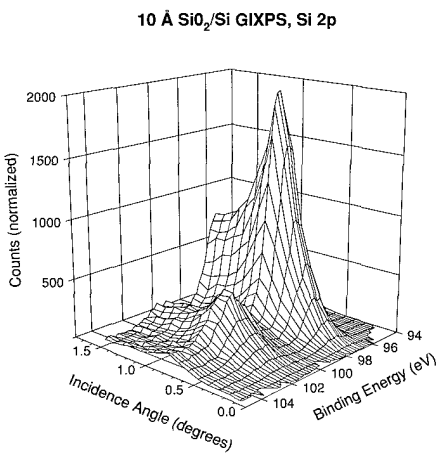

Figure 1. XPS lines from the Si oxide and bulk obtained for E=1820 eV.

Argon Photoion Charge State Distributions | X24A

L. Pibida, R. Wehlitz, J. Levin, and I. Sellin (U. Tennessee at Knoxville)

Using the single-bunch mode of the X-ray ring, we have measured the photoion charge state fractions after photoionization of argon atoms. The experimental setup consist of an ion time-of-flight (TOF) spectrometer, mounted on a XYZ translator together with a hypodermic needle that allow us to align it with respect to the photon beam. The TOF spectrometer was mounted perpendicular to both the photon beam and the electric vector of the monochromatized synchrotron radiation direction. When an Ar atom is photoionized ($h\nu \sim 3206.3eV$) a cascade decay process can occur leaving the Ar ion in different charge states depending on the decay path that occur. The photoion charge state distributions depend on several experimental parameters as the voltage across the microchannel plate detector, the pressure in the experimental chamber, and the threshold of the constant fraction descrimintor used to process the signals. These measurements require a careful control of these parameters. After the optimum experimental parameters were determined we measured the photoion charge state fractions as a function of the photon energy. From where we estimated the fluorescence yield to be 0.115 ± 0.02 and the Auger yield 0.885 ± 0.02. Several measurements of the photoion charge state distributions near the K-edge are available. From these measurements we saw that the value of charge state fractions are sensitive to the variation of the experimental parameters chosen.

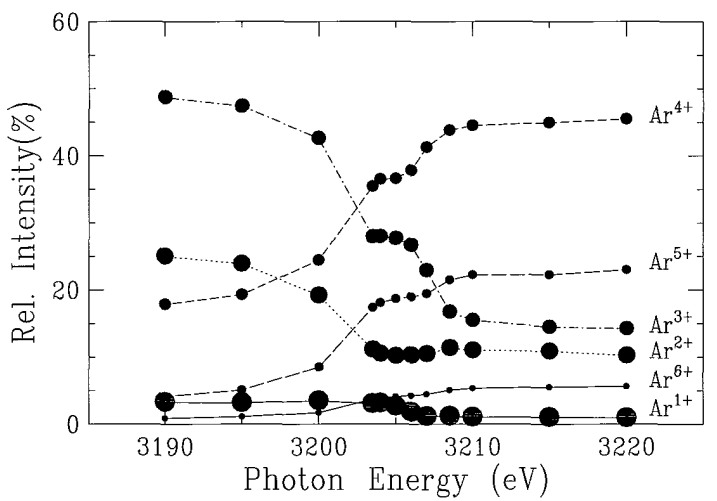

Figure 1. Ion Charge state fractions as a function of the photon beam energy. The error bars are smaller than the size of the symbols.

5 eV Atomic Oxygen Damage to Low Earth Orbit Optical Components — X24C

J.C. Rife (NRL)

We have initiated a study of the effects of 5 eV atomic oxygen (ATOX) bombardment on ultraviolet and soft x-ray optical surfaces. Typical ATOX fluxes for low earth missions such as the shuttle and satellite observatories are 10^{20} to 10^{22} atoms/cm^2-year in the ram direction. ATOX bombardment affects the top surface layers, and is not energetic enough to sputter practically all materials. However, ATOX can quickly erode hydrocarbon compounds and coatings such as osmium that form volatile oxides and can also alter the oxide layers and the surface condition of other materials.

We have measured the reflectance of silicon and fused silica as well as Mo/Si, W/Si, W/B_4C, and W/C multilayers before and after an ATOX dose of 10^{20} atoms/cm^2. Fig. 1 shows the 5 degree grazing reflectance at the oxygen K edge of bulk SiO_2, a silicon wafer with typical native SiO_2 overlayer 1 nm thick, and an equivalent silicon wafer exposed to ATOX. Changes in the absorption edge structure of the dosed wafer indicate an increase in oxide thickness and an admixture of oxygen-oxygen bonds and other bonding states in the damaged oxide.

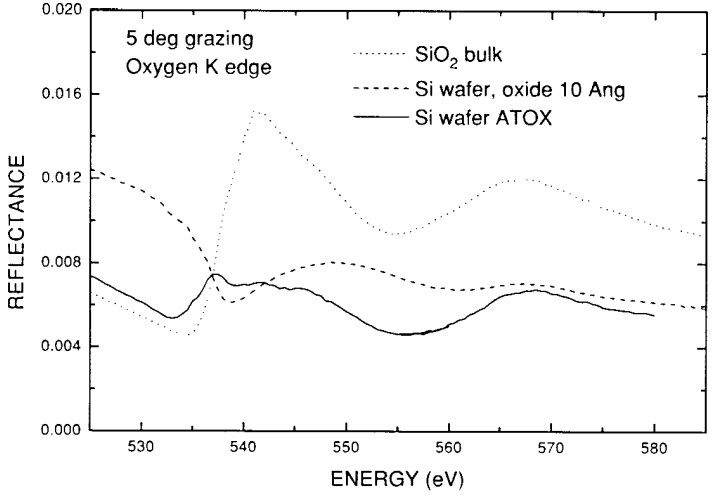

Figure 1.

GaN: Grazing Reflectance XANES at the Nitrogen K Edge — X24C

J.C. Rife (NRL), W.R.L. Lambrecht, S.N. Rashkeev (Case Western Reserve U.), K. Lawniczak-Jablonsha, T. Suski (LBL), and D.K. Wickenden (Johns Hopkins U.)

We have measured the 5 degree grazing reflectance of GaN in its anisotropic wurtzite form at the nitrogen K edge for linearly polarized light with E$\|$c and E$\perp$c. From Kramers Kronig analysis of the data and previous reflectance measurements from 2 eV to 150 eV, we have extracted the polarized absorption coefficient at the nitrogen K edge (see Fig.1). In addition, we have determined the E$\perp$c absorption by total photoyield at the ALS and the unpolarized absorption and reflectance by a first principles LDA band structure calculation at CWRU.

Energy location and shape of the spectral features for the nitrogen absorption derived from reflectance and the total photoyield are in good agreement. A 23.1 eV shift to higher energies was required for the calculated absorption spectrum to match the measured one. The calculated spectrum reproduces all the experimental features well, although the relative magnitudes of peaks vary somewhat. The good agreement of peaks and peak positions implies that the self-energy correction beyond LDA consists primarily of a constant shift up to about 10 eV above the conduction band minimum. This is in disagreement with GW calculations which predict increasing corrections for higher conduction band states.

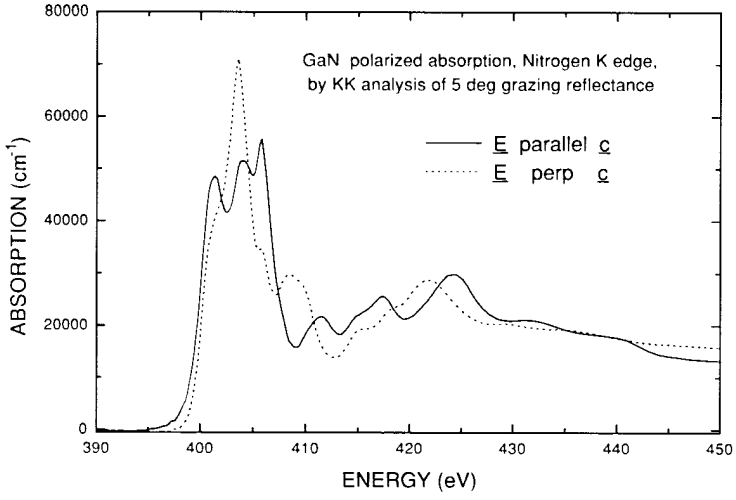

Figure 1.

Characterization of Multilayer Coated Gratings and Mirrors	X24C

J. F. Seely, M. P. Kowalski, J. C. Rife, W. R. Hunter, and R. G. Cruddace (Naval Research Laboratory)

Diffraction gratings and mirrors with multilayer coatings are characterized in the soft x-ray and extreme ultraviolet regions. The multilayer coatings are designed to have high reflectance at wavelengths and angles of incidence that are important for the study of laboratory, solar, and astrophysical plasma emissions. The efficiencies of the multilayer coated gratings, and the reflectances of the mirrors with similar coatings, are measured as functions of the angle of incidence and the wavelength of the incident light. The measured reflectance is compared to model calculations that account for the layer thicknesses, interfacial roughness, interdiffusion layer thicknesses, and the optical constants of the layer materials. The gratings have blazed or laminar groove profiles and are fabricated by the holographic ion-beam etched process. The multilayer coating is matched to the groove profile so that the coated grating has optimal efficiency at the angle and waveband of interest. The measured grating efficiency is compared to the efficiency calculated by a computer code that rigorously models the diffraction process. Multilayer gratings are being developed for a rocket spectrometer that will study the extreme ultraviolet radiation from a white dwarf star. Multilayer mirrors are developed for normal-incidence microscopes that image the soft x-ray emissions from laser-produced plasmas with extremely high spatial resolution.

Structure of Supercooled Liquid Silicon	X25

Stuart Ansell (Argonne National Laboratory), Shankar Krishnan, John J. Felten (Containerless Research, Inc.) and David L. Price (ANL)

We report X-ray diffraction measurements of the structure factor S(Q) and the radial distribution function G(r) of levitated liquid silicon in the stable and supercooled states. Supercooling results in a sharpening of the first peak in S(Q) and a shift to an 8% higher Q value, the appearance of a double shoulder on the high-r side of the first peak in G(r), a sharpening of the first peak in G(r) and a decrease in coordination number. These changes are consistent with a significantly enhanced degree of covalent bonding.

S. Ansell, et al., in Press, *J. Phys. Cond. Matt.*, 1997.

Characterization of Mn Oxidation States in Photosystem II by X-Ray Fluorescence Spectroscopy — X25

U. Bergmann (LBNL), C. R. Horne (LBNL, UC Berkeley), S. P. Cramer (LBNL and UC Davis), P. DeMarois and J. Penner-Hahn (U. of Michigan)

The generation of atmospheric oxygen through photosynthetic water-oxidation is one of the most fundamental processes responsible for the existence of aerobic life forms on earth. The reaction is catalyzed by an oxygen evolving cluster (OEC) located in photosystem II, which contains 4 Mn ions. The catalytic mechanism is proposed to involve 5 intermediate states called the S states of the Kok cycle. In each of the first 4 steps (S0 to S4) a photon is absorbed and the OEC is assumed to be singly oxidized and in the last step (S4 to S0) the oxygen is released. Despite numerous studies over the last 10 years, a controversy about the Mn oxidation states has remained to date, and this information is crucial for the full understanding of the water oxidation. Using the technique of high resolution X-ray fluorescence spectroscopy, we studied the Mn-oxidation states in two S1-states of photosystem II. Fits of the K-beta x-ray emission spectra with that of model compounds are consistent with the following models: 1.) The S1 state of photosystem II contains Mn(III)2Mn(IV)2. 2.) In the hydroquinone-treated S1 state the Mn(III)2 is reduced to Mn(IV)2. The first result confirms one of the currently proposed models, and the second result reveals new information about the chemistry involved in the creation of the OEC. The results demonstrate the potential of this spectroscopic technique, which is complementary to the techniques of XAS and EPR. The study of other S-states of photosysem II is proposed for the future.

Evaluation of Efficacy of New Fixed-Wavelength X25 Side Station — X25

L.E. Berman and Z. Yin (NSLS)

The X25 and X21 hybrid wiggler magnets each radiate a photon fan spanning 5 horizontal mrad (at 2.5 GeV), of which the central 3 consist of useful hard x-rays. For the most part, however, the existing X25 and X21 beam lines make use of no more than the central 1 mrad, containing the brightest x-ray photons, and consequently most of the horizontally off-axis radiation is unused.

The properties of the horizontally off-axis radiation of the X25 wiggler source were studied, in an effort to determine the efficacy of adding a new X25 (or X21) experimental station that would sit aside the existing beam line and make use of the presently unused off-axis photons. In order to make best use of existing floor space, and provide ample enough separation from the present beam line, the optics of a new beam line to support such a station would most likely be based upon a horizontally-focussing, sideways-diffracting bent single crystal monochromator, delivering a fixed wavelength to the station. A subsequent bent mirror could focus the beam vertically and reject harmonics. Such a station could well support a fixed-wavelength crystallography program, which constitutes a large fraction of the demand for the existing X25 station.

There are two handicaps that such a "side station" would suffer, compared with the existing "central station". First, the viewed radiation spectrum is softer because the radiation gets emitted from the gentler-curving segments of the wiggler magnet instead of the tightly-curving ones. This is shown in Fig. 1, which displays the measured X25 wiggler spectrum as a function of horizontal angle across the radiation fan. Second, the wiggler magnet poles, as viewed from a "side station", do not line up (as they would when viewed from the "central station"), and consequently the viewed horizontal source is broadened in proportion to the length of the wiggler magnet. This is shown in Fig. 2, which displays the measured horizontal source size as a function of horizontal angle across the radiation fan. It is concluded that a new "side station", whose central ray is horizontally off-axis by 1 mrad (which is feasible to pursue), could deliver a monochromatic photon intensity that is about 50% of that available in the existing "central station" (based, for instance, on similar optics) at 8 keV, and about 40% at 12 keV.

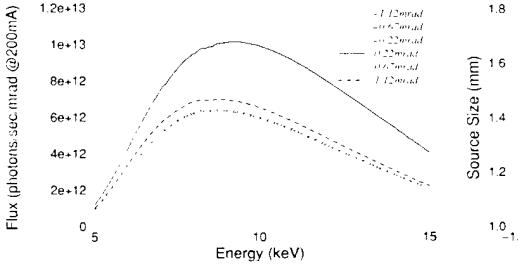

Figure 1. The photon energy spectrum, measured as a function of horizontal angle across the X25 wiggler fan, is shown.

Figure 2. The horizontal source size, measured as a function of horizontal angle across the X25 wiggler fan, is shown.

Characterization of New X25 Double Multilayer Monochromator | X25

L.E. Berman, Z. Yin (NSLS), S.G.J. Mochrie, and O.K.C. Tsui (MIT)

The X25 monochromator has been capable of accomodating a pair of multilayer elements since early 1995. This has been especially useful for x-ray scattering and emission experiments for which high monochromaticity is unnecessary, but high intensity is. A multilayer monochromator has about a 100 times broader bandwidth than a silicon monochromator, and thereby can deliver 100 times as much "monochromatic" intensity to the experiment.

The X25 multilayers are each composed of tungsten-boron-carbide (W/B_4C) multilayer films grown on silicon substrates, and purchased from Osmic, Inc. of Troy, Michigan. Recently, a new pair of (W/B_4C) multilayer elements, each with a d-spacing of 25 Å, was obtained. the new pair has a 30% narrower bandwidth than the original pair. The photon energy dispersion function of the new pair was measured using a Si(111) analyzer crystal, and is shown in Fig. 1. Its main peak has a relative FWHM of 1.1%. The side fringes about the main peak arise from the finite number of bilayers (120) in the multilayers. The calculated reflectivity curve for this multilayer pair, based upon its fabrication parameters and assuming ideal interfaces, is shown in Fig. 1. A better agreement of theory and experiment can be obtained by assuming that an interdiffusion thickness, between layers, was present with a σ of 4 Å, as also shown in Fig. 1.

The efficacy of improving the resolution of the multilayer pair, via angular misalignment (from parallel) of the two elements with repsect to each other, is demonstrated in Fig. 2, which shows the measured dispersion functions for different misalignment angles. A misalignment angle of 1 arcmin reduces the relative FWHM to 0.9%. The main peak sharpens further upon introduction of a 2 arcmin misalignment. However, the neighboring side fringes become comparable in intensity with the main peak in this case, thereby compromising the objective of resolution narrowing.

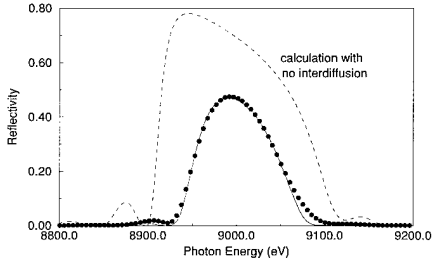

Figure 1. The measured double multilayer dispersion function at 9 keV (dotted curve) is compared with theory, for the ideal case of no interdiffusion at the interfaces (dashed curve) and for the case of an interdiffusion thickness with a σ of 4 Å(solid curve).

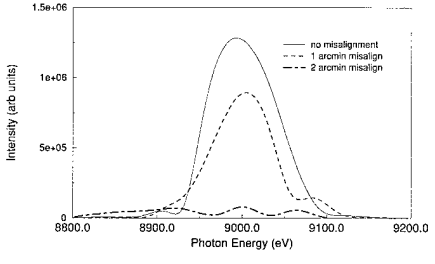

Figure 2. The measured multilayer dispersion functions at 9 keV are shown for the cases of no misalignment of the multilayers (solid curve), a misalignment angle of 1 arcmin (dashed curve), and of 2 arcmin (chain-dashed curve).

Mechanistic Studies of Rat Liver F_1-ATPASE | X25

M. A. Bianchet, J. Hullihen, P. L. Pedersen, and L. M. Amzel (Johns Hopkins U.)

F_1-ATPase is the soluble portion of the F_1F_0-ATP synthetase complex, the protein that carries out the synthesis of ATP in the mitochondria. F_1 by itself exhibits a Mg^{++} dependent ATP hydrolytic activity. Crystals of rat liver F_1-ATPase were obtained using $(NH_4)_2SO_4$ as a precipitant in the presence of ATP, Pi and in the absence of Mg. Under the crystallization condition used, rat liver F1-ATPase is known to be active. F_1 from redissolved crystals has all subunits and hydrolyzes ATP with full activity when Mg^{++} is added. The three dimensional structure of the rat liver F_1-ATPase was determined to 2.8 Å resolution using these crystals. The more symmetrical conformation of the α- and β-subunits observed in the rat liver F_1 *vis-a-vis* the bovine heart enzyme [1] suggests that it may be in another stage of the proposed mechanism or perhaps suggest a different one. A new crystallization condition, without phosphate buffer, allows crystals be formed with Mg present in the crystallization media. Cocrystals of F_1-ATPase with MgAMPPNP (non hydrolyzable analogous to ATP), MgADP.Vi (analogous to the transition state) and MnADP allow the study of different states in the hydrolisis/synthesis of ATP. Data obtained from these three co-crystals at NSLS (X25 beam line) are being analyzed at the present time.

1.- Abrahams et al. Nature **370**, 621-628 (1994).

Crystallographic Studies of Hin Recombinase DNA-binding Domain Bound to Different Binding Sites.	X25

T. K. Chiu, D. Cascio, R. Johnson, and R. E. Dickerson (UCLA)

Hin Recombinase belongs to a family of proteins that catalyses site-specific DNA inversion in enteric bacteria. This family includes Gin from phage Mu, Cin from phage P1, and Pin from phage el4. Hin recognizes a binding site which consists of a highly conserved inverted repeat of 12bp (consensus sequence : A/T G G T T T A/T G G A G/T A A) separated by a central 2 bp 'core.' The crystal structure of a 52 amino acid peptide consisting of the DNA-binding-domain of E.coli Hin bound to the hixL half-site tGTTTTTGATAAGA/aTCTTATCAAAAAC has been solved (Feng et al, Science '94). Two water molecules were observed to mediate contacts between Hin and its binding site and were proposed to be crucial for Hin's site-specific recognition. In order to further characterize this recognition process, we have co-crystallized the Hin Recombinase DNA-binding domain bound to different mutant binding sites, and have collected synchrotron x-ray data at beamline X25 on seven different co-crystals. These crystals are isomorphous (six in space group C2221, with a= 86, b= 82, c= 44; and one in space group C2221, with a=67.5, b=69.7, c=63.6) but diffract to different a extent, with the best one diffracting to 2.2A and the worst one diffracting to 2.9A. Crystallographic refinement and structural analysis are in progress.

OspA-LA2 Fab Complex Structural Study with Molecular Replacement Methods	X25

W. Ding, B.J. Lufts, X. Yang (SUNY at Stony Brook), J. J. Dunn, and C.L. Lawson (BNL)

Lyme disease is a progressive infection resulting from inoculation of the spirochete *Borrelia burgdorferi* into the skin by a feeding tick. OspA (Outer Surface Protein A, 31 kDa) has been shown to be present when the spirochete is dormant in the tick midgut but is no longer detected after rapid division and dissemination to the tick salivary glands during a blood meal. This may explain why the natural immune response to OspA develops only in a minority of Lyme disease patients,and usually only late in the course of the disease. Studies have shown that vaccines based on OspA can induce protective immunity in mammals. Blockage of spirochete transmmison from the tick vector to the mammalian host by anti-OspA antibodies appears to be the main mechanism of the protection. However,the protection appears to be serotype specific. In murine vaccine studies, the protection was conferred only when hamster's immune response was directed to the epitope defined by the mAb LA2. A three dimensional structure of the protein complex of OspA and LA2 Fab will be essential to exactly defining the protective epitope and elucidating protein function. It will provide the invaluable aid in rational vaccine design.

Crystals of the OspA-La2 Fab complex were grown at 4^oC by hanging-drop vapour diffusion methods (0.1M Na Cacodylate, 0.1M Na Acetate and 10PEG 3300 at pH 6.15). They belong to space group $P2_12_12$, with unit cell dimension a = 99.5 b=129.5 c=144.5. Diffraction data were collected at the National Synchrotron Light Source, on the beamline X25 using MAR image plate/scanner systems. The data included 194789 observations of 51741 unique reflection, R_{merge} = 0.048, representing 98% of the observable data to 2.4 Å resoultion. There are two protein complex molecules in a asymmetric unit.

Molecular replacement method was attempted with the data set to determine the orientation and position of LA2 Fab in the crystal lattice. Although the amino acid sequence of LA2 is at present only partially known, the homology to 1gaf is expected to be highest in 17 high resolution Fab structures from the protein data bank by sequence alignment. The molecular replacement program XPLOR (Brunger, 1992) was employed to perform search with the constant plus variable domain of the Fab as a model. The elbow angle was modified with the interval of 5^o. The model with elbow angle of -20^o yielded consistent solutions in each resolution shell. The direct space Patterson search method (Huber, 1985) was employed for roatation search comprised 15 to 4 Å resoultion data. PC-refinements were carried out where the search model was oriented to each of the 191 potential peaks. The first and second peaks gave the potential solution judged by high correliation coefficient. Molecule A was subjected to a translation search with a sampling interval of 1Å in each dimension. The position of molecule B was determined by keeping molecule A fixed to solve the ambiguity on the cell origin. The initial model was refined by the rigid body refinement and energy minimization. The refined R factor is 0.33. The model is cross validated by the difference Fourie map calculated with the protein phase. The electron design map is being interpreted with building OspA model.

Three Dimensional Structure of a Human Natural Killer Cell Inhibitory Receptor at 1.7Å Resolution	X25

Q. R. Fan, L. Mosyak, D. C. Wiley (Howard Hughes Medical Institute), C.C. Winter, N. Wagtmann, and E. O. Long (National Institute of Health)

Killer cell inhibitory receptors (KIR) on human natural killer (NK) cells prevent the lysis of target cells bearing specific class I MHC molecules. The human p58 KIR clone 42 recognizes HLA-Cw4, -Cw2, -Cw5 and -Cw6, but not HLA-Cw3, -Cw1, -Cw7 or -Cw8, which are recognized by p58 KIR clone 43 [1].

We have determined the X-ray structure of a p58 KIR (p58-cl42) at 1.7Å resolution using multiwavelength anomalous diffraction (MAD)[2] method. MAD data of a single selenomethionyl p58-cl42 crystal (hexagonal rod with dimensions of 0.06 x 0.06 x 1.5 mm^3; P61; a=b=92.3Å c=47.0Å were collected to 2.2Å with a 300 mm diameter MAR Research image-plate system at X25 beamline of the National Synchrotron Light Source, Brookhaven National Laboratory. MAD phasing was treated as a case of multiple isomorphous replacement[3]; refinement of anomalous scatterer parameters and phase calculation were performed with MLPHARE[4]. The initial MAD map was improved by density modification using DM[5], assuming 40% solvent content. A model of p58-cl42 KIR was traced from both the density modified and unmodified electron density maps. A high resolution native data set was collected to 1.7Å on the Princeton 2K CCD detector at F-1 beamline of the Cornell High Energy Synchrotron Source (CHESS). The atomic model has been refined against the native data at 1.7Å resolution to a crystallographic R-value of 20.6% (Rfree = 25.4%).

The p58-cl42 KIR structure has tandem immunoglobulin-like domains positioned at an acute, 60° angle. Loops on the outside of the elbow between the domains form a binding site projected away from the NK cell surface. The topology of the domains and their arrangement relative to each other reveals a relationship to the hematopoietic receptor family, with implications for the mechanism of inhibition in NK cells.

[1] Long, E.O., et al. Immunological Reviews, **155**, 135-144 (1997).
[2] Hendrickson, W.A., Science **254**, 51-58 (1991).
[3] Ramakrishnan, V. Biou, V., Methods in Enzymology, **276**, 538-557 (1996).
[4] Otwinowski, Z., Isomorphous replacement etc., (Science & Eng. Res. Council, Daresbury Laboratory, Daresbury, UK, 1991).
[5] The CCP4 suite: Programs for protein crystallography. Acta Crystallographica **D50**, 760-776 (1994).

Structural Studies Of Type I DNA Topoisomerases	X25

H. Feinberg and A. Mondragón (Northwestern U.)

DNA topoisomerases are proteins responsible for controlling and maintaining the topological state of DNA in the cell. They have been found in all cell types of both eukaryotes and prokaryotes and additionally in some viruses. They are involved in DNA replication, transcription, and genetic recombination. Four topoisomerases have been identified in *E. coli* topoisomerase I, gyrase or topoisomerase II, topoisomerases III, and IV. Our work is concerned with type I topoisomerases, which include topoisomerase I and III. The long term goal of our work is to understand in atomic detail the catalytic mechanism of these enzymes, including the protein-DNA interaction, the cleavage and religation reactions, the strand passage, and the conformational changes that occur during the topological manipulations.

We have crystals of a 30 kDa fragment of *E. coli* DNA topoisomerase I. This fragment represents the region that we have speculated that it moves away from the rest of the protein during the topological transformations. The 30 kDa fragment contains the active site tyrosine and has cleavage activity. We have been unable to solve this structure by Molecular Replacement or MIR methods. In order to solve the structure, a four wavelength MAD experiment was conducted at X25 using a MAR CCD detector. For the MAD experiment a platinum heavy atom derivative with two sites per molecule was used. The crystals are monoclinic so 360° of data were collected per wavelength in 1° oscillation steps. A total of 1440 frames were collected in less than 24 hours. The experiment was only feasible thanks to the availability of the MAR CCD detector. The data are excellent and the two sites are clearly visible in an anomalous Patterson. MAD phasing is in progress.

Crystallographic Studies On the Nudix Proteins: Platinum Derivative of *E.coli* dATP Pyrophosphohydrolase *	X25

S. B. Gabelli, M. A. Bianchet, S. F. O'Handley, M. J. Bessman, L. M. Amzel. (JHU)

The E.coli dATP pyrophosphohydrolase is a novel nucleoside triphosphate pyrophosphohydrolase which catalyses the hydrolysis of dATP to produce dAMP and PPi. The enzyme contains the conserved signature sequence GXVEXXETXXXXXXREVXEEXXI that characterizes the "nudix hydrolases". This family of enzymes hydrolyze nucleoside diphosphates linked to different moieties, X. This conserved sequence was previously referred as the MutT pattern.

Crystals suitable for x-ray crystallographic studies have been grown by vapour diffusion and microseeding. The crystals grow in ammonium sulphate and 1crystals were soaked in platinum chloride for 72 hours. They are orthorhombic and diffract to 2.8A resolution. A mixture of 35glycerol with artificial mother liquor was used as cryoprotectant. Data have been collected under cryogenic conditions at beamline X25 at BNLS at a distance of crystal to detector of 225mm, 2 degree oscillation, using the 100 micron slits and 1.1A radiation.

* The author is supported with a NSF graduate fellowship.

Crystallographic Studies on the Nudix Proteins: The Gene Product of the *E.coli* Orf209 *	X25

S.B. Gabelli, M. A. Bianchet, S.F. O'Handley, M. Bessman, L. Mario Amzel (JHU)

The nudix hydrolases are a family of phosphoanhydrases that carry out the hydrolysis of a nucleoside diphosphate linked to several different moieties. Across species, the members of the family contain the consensus sequence GxxExxExxxxxxREVxEExxI. This sequence appears to be a versatile nucleotide binding and catalytic site. Among family members, the gene product of E.coli ORF209, is an enzyme highly specific for ADP-sugars, with its highest activity on ADP-ribose. It catalyzes the hydrolysis of the pyrophosphate linkage: ADP-ribose < AMP+ribose 5-P. Crystals of Orf209 have been grown by vapour diffusion at 18 C using polyethylene glycol as the precipitant. Initial data to 2.9 A resolution were collected on an image plate using a copper rotating anode. Higher resolution native data were collected at beamline X25 at BNLS with 1.1A radiation, using flash frozen crystals with 40the crystal to dectector distance was 225mm and 100 micron slits were used. The crystals are orthorhombic, a=66.9A, b = 67.8A, c=98.07A and diffract up to 1.9A so 345 mm frames were used. The data have been indexed using DENZO, processed using SCALEPACK and the CCP4 suite. In addition, data from a crystal soaked for 72 hours on 1mM K2PtCl4 were collected at a crystal to detector distance of 225 mm, using 1.1A radiation with 100 microns slits. The crystal had an orthorhombic cell, a=66.6A, b = 68.1A, c=96.05A and diffracted up to 2.9A so 180mm frames with 150pixels were used. The data have been processed using DENZO, SCALEPACK and the CCP4 suite.

Crystal	Resolution	Reflections measured	Data completeness % All	Data completeness % outer shell	Rsym% </ All	Rsym% </ outer shell
Native	1.9	248491	87.5	86.9	0.08	0.22
K_2PtCl_4	2.9	62938	87.6	83.5	0.1	0.39

Figure 1. TABLE 1 showing Crystal Resolution Results

* S.Gabelli is supported with a NSF graduate fellowship.

Structure Of a Cre Recombinase-DNA Site-specific Recombination Synapse	X25, X4A

F. Guo, D. N. Gopaul, and G. D. Van Duyne (U. of Penn.)

Cre recombinase catalyzes the reciprocal exchange of DNA strands between 34-base pair loxP sites during site-specific recombination. Using diffraction data measured at the X25 and X4A beamlines, we have determined the 2.4 A crystal structure of a covalent intermediate in the Cre-loxP reaction, where the recombinase has cleaved and formed 3'-phosphotyrosine linkages to its DNA substrates. Four recombinases and two DNA substrates are arranged in a pseudo-fourfold symmetric tetramer that represents a site-specific recombination synapse.

Parent data and two heavy atom derivative data sets for this structure were measured at the X25 beamline. One derivative was made from selenomethionine-substituted Cre recombinase, with 22 anomalous scatterers in the crystallographic asymmetric unit. Data were measured at a single wavelength corresponding to a maximum of f" and the resulting anomalous diffraction signal led to strong crystallographic phasing power. The second heavy atom derivative made use of an iodine-containing DNA substrate. The selenomethionine derivative was also used for a three-wavelength anomalous diffraction measurement at the X4A beamline. Together, the heavy atom diffraction data from the two beamlines led to a readily interpretable image of the electron density.

The CuK$\alpha^h_{1,2}$ Hypersatellites and Correlated Hypersatellites*	X25

K. Hämäläinen, S. Huotari (Helsinki U., Finland), C.C. Kao (NSLS) and M. Deutsch (Bar-Ilan U., Israel)

The hypersatellites (HS) and correlated hypersatellites (CHS) originate in transitions from an initial state having two K holes. Their theoretical intensities in Cu are, respectively, 10^{-3} and 10^{-6} of the K$\alpha_{1,2}$ lines. To date, only a single resolved HS measurement exists. Even there, the Kα^h_1 line is masked by the overlaping WLα_2 line, and a CHS intensity 5000-fold larger than theory is reported.

The measured HS spectrum is shown in Fig. 1. The well-resolved components show the typical asymmetry of all $3d$ transition metal lines, indicating significant contributions from $3d$ spectator hole transitions. They are considerably broader (~7.5eV) than the diagram lines (~3eV), and their separation (~24eV vs. 20 eV) is also larger.

Setting the anlyzer energy at the Kα^h_2 peak and scanning the monochromatic excitation energy yields the HS threshold at 18,380±30 eV (Fig. 2). This agrees well with both the Z+1 approxiamtion (18,380 eV) and our Dirac-Fock calculations (18,400 eV). The intensity rise from zero supports the theoretical prediction of a pure shake-off nature of inner-shell shake processes. The slope change at ~18.6 keV may indicate, however, contributions from yet-unspecified additional modes.

Finally, no indication was found for the CHS lines, to within <1% of the HS intensity, in agreement with the theoretical ~0.1% prediction.

* This work was supported by The Israel Science Foundation, Jerusalem.

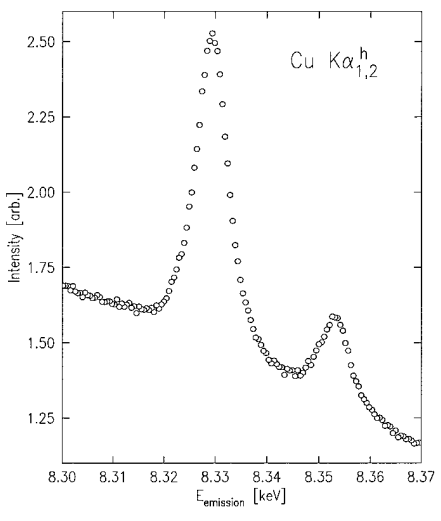

Figure 1. The CuK HS spectrum

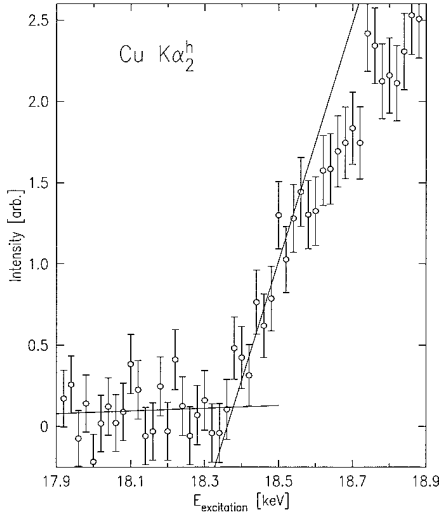

Figure 2. The onset of the Kα^h_2 HS.

Resonant X-ray Magnetic Scattering From an Fe/Gd Multilayer | X25

H. Hashizume, N. Ishimatsu, O. Sakata (Tokyo Inst. of Tech., Japan), N. Hosoito (Kyoto U., Japan), T. Iwazumi (KEK, Japan), K. Namikawa (Tokyo Gakugei U., Japan), and L. Berman (NSLS)

The competing Zeeman and exchange interactions, combined with the distinct thermal coefficients of the Fe and Gd moments, produce various magnetic structures in thin-film Fe/Gd multilayers in an external field. In the aligned states, the Fe and Gd spins are parallel or antiparallel to the applied field. These are reversibly changed, by altering H or T, to the twisted states in which antiferromagnetically coupled Fe and Gd spins make large in-plane angles to the in-plane field. The phase change is expected to be sensitive to the charge and magnetic structures of the layer interfaces. In preparation to explore the spin structures of the Fe/Gd interface, we have measured resonant X-ray magnetic scattering from a 15[Fe(3.5nm)/Gd(5.0nm)] multilayer on a silicon substrate using a circularly polarized beam. The X-ray energy was tuned to the Gd L3 edge and a diamond (100) crystal was used to convert the linear polarization of the X25 wiggler beam to a left circular polarization. A flipping magnetic field of 2.5 kOe was applied parallel to the sample surface and either parallel (ϕ=0°) or perpendicular (ϕ=90°) to the plane of scattering. The sum intensity $I^+ + I^-$ in Fig. 1 shows the charge Bragg peaks of lowest four orders, observed in specular scans at room temperature. The difference signal $I^+ - I^-$, arising from the resonant magnetic-charge interference scattering, shows marked Bragg peaks of alternating signs in the ϕ=90° configuration, while they are absent in the geometry. While this confirms an aligned state, simulations suggest that larger magnetizations are induced in the near- interface region of the paramagnetic Gd layers than at the film centers.

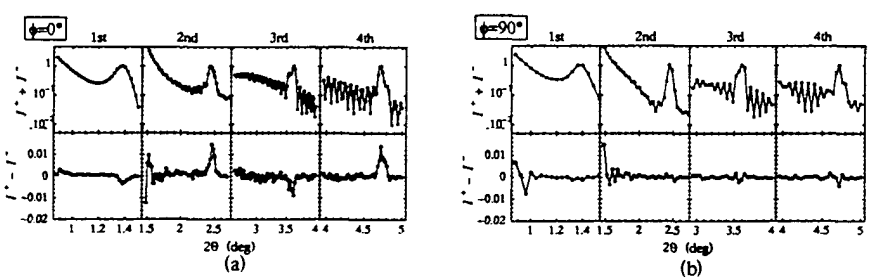

Figure 1. Charge ($I^+ + I^-$) and resonan magnetic-charge interference ($I^+ - I^-$) Bragg peaks observed in a specular scan on a 15[Fe(3.5nm)/Gd(5.0mn)] multilayer at the Gd L3 edge. The applied field is parallel to the plane of scattering in (a) and perpendicular in (b).

2.1 A Structure of the Complex Between Active Ras and The Ras-Interacting Domain of an Effector RalGDS | X25, X12B

L. Huang, F. Hofer, G.S. Martin, and S-H. Kim (U. California at Berkeley)

The structure of the complex bewteen oncogenic protein Ras and the Ras- interacting domain of RalGDS (RalGDS-RID) has been studied by x-ray crystallography. The structure of the complex will provide crucial information on Ras' interaction with its binding partner at an atomic level. Since the mutant forms of Ras are involved in 30% of human cancer and Ras' function is carried out through its effectors, the spatial location of the key interface residues may assist in identifying small molecules that are capable of disrupting this interaction and thus provide insights for the development of anti-cancer drugs. A 2.8 room temperature data set on a native complex crystal was initially taken at BL X12B, which enabled us to solve the structure. A 2.0 frozen data set was later taken at BL X25 in september, which enabled us to refine the structure to a much higher resolution so that we can see the side chain interaction more clearly. The crystal has a P212121 space group, with a=75.648, b=78.256, c=87.313 . The complex crystallizes as a heterotertramer with two active Ras molecules and two RalGDS-RID subunits.

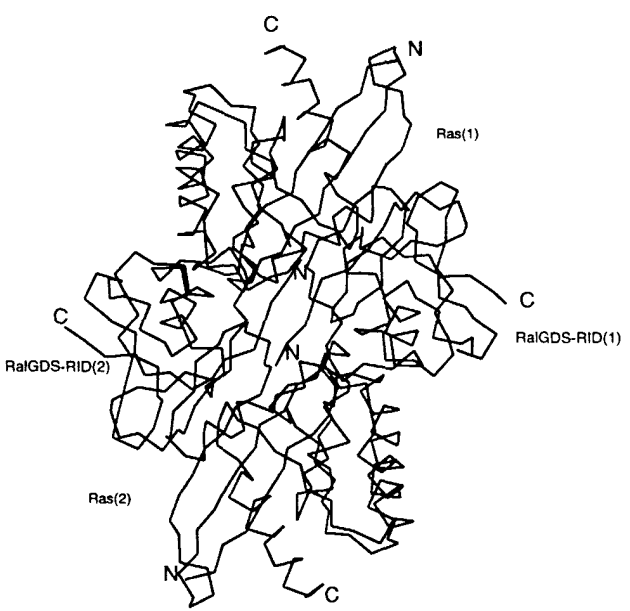

Figure 1.

Structural Studies of the IgE Fc Receptor | X25

T. Jardetzky (Northwestern U.)

We are studying the structure of the high affinity IgE receptor that is involved triggering immediate type hypersensitivities such as allergic reactions. In the past year we have used the NSLS X-25 beamline to study two weakly diffracting crystal forms of the extracellular domains of this receptor. Our first trip in March, 1997 focused on a derivative search for a tetragonal crystal form (P41 or P43), which diffracts to a maximum resolution of ~3.6 Angs. During this trip we used a new MarCCD detector which allowed us to collect 9 different data sets (1 native and 8 potential derivative). Optimal wavelengths for the collection of anomalous data were selected by taking EXAFS scans from metal-soaked crystals. These data were processed and compared to the native data. Although significant differences in intensities were measured for the derivatives compared to the native data, non-isomorphism problems have prevented the successful interpretation of difference patterson maps.

On our second trip to X-25 (September, 1997), we collected seven datasets on a new hexagonal crystal form of the receptor, which diffracts to ~3.2 Angs using synchrotron X-ray sources. These crystals do not suffer from the same non-isomorphism problems as the tetragonal form. During this visit to X-25, we were able to collect two datasets from mercury soaked crystals of a cysteine mutant of the receptor, which show intensity changes when compared to the native protein. In addition, we were able to collect four data sets from heavy atom soaked wild type protein crystals. Tentative heavy atom solutions to the difference pattersons have been identified and are being further evaluated at this time.

The Structure of Liquid Boron | X25

S. Krishnan (Containerless Research, Inc.), J. J. Felten (CRI), S. Ansell, K. J. Volin, and D. L. Price (ANL)

We report the first measurements of the structure factor, S(Q), and the pair distribution function, g(r), for pure liquid boron, in the temperature range 2600-2000K, in the normal and metastable (supercooled) liquid states. The S(Q) data show a weak feature at 2.5 $Å^{-1}$ that resembles the first sharp diffraction peak. The first four peak positions in the g(r) for liquid B occur at 1.78, 3.16, 4.61, 5.98Å respectively, and agree well with the corresponding positions in the g(r) for solid β-rhombohedral boron (B_{105}). Supercooled liquid B shows considerable sharpening and narrowing of the peaks in the g(r) and is indicative of increased ordering of boron atoms. The similarity in the peak positions relative to solid β-boron, a coordination number of about 6, combined with the known stability of boron's covalent bond shows the retention of icosahedral B_{12} units in the liquid state. The number of such icosahedral clusters appears to increase as the liquid is supercooled. The results are discussed in relation to available data on the properties and structure of liquid and solid boron.

S. Krishnan, et al., To be Submitted to *Phys. Rev. B.*, 1997.

Levitation Apparatus for Structural Studies of High Temperature Liquids Using Synchrotron Radiation	X6B, X25

S. Krishnan, J. J. Felten, J. E. Rix, J. K. R. Weber, P. C. Nordine (Containerless Research, Inc.), M. A. Beno, S. Ansell, and D. L. Price (ANL)

A new levitation apparatus coupled to an synchrotron-derived x-ray source has been developed to study the structure of liquids at temperatures up to 3000K. The levitation apparatus employs conical nozzle levitation using aerodynamic forces to stably position solid and liquid specimens at high temperatures. A 270 Watt, CO_2 laser was used to heat the specimens to desired temperatures. Two optical pyrometers were used to record the specimen temperature, heating curves and cooling curves. Three video cameras and a video recorder were employed to obtain and record specimen views in all three dimensions. The levitation assembly was supported on a three-axis translation stage to facilitate precise positioning of the specimen in the synchrotron radiation beam. The levitation system was enclosed in a vacuum chamber with Be windows, connections for vacuum and gas flow, ports for pyrometry, video and pressure measurements. The vacuum system included automatic pressure control and multi-channel gas flow control. A phosphor screen coupled to a high-resolution video microscope provided images of the x-ray beam and specimen shadow which were used to establish the specimen position. The levitation apparatus was integrated with x-ray diffractometers located at X6B and X25 beamlines at the National Synchrotron Light Source. X-ray structural measurements have been obtained on a number of materials including Al_2O_3, Ni, Si, Ge, and other metallic and ceramic materials in the liquid state.

S. Krishnan, et al., *Rev. Sci. Instrum.* **68**, p. 3512 (1997).

Resonant Exchange Scattering in a Co/Ir Superlattice	X25

M. B. Salamon and K. O'Donovan (U. Ill.) and E. Kita and H. Yanagihara (U. Tsukuba, Japan)

The goal of this experiment was to detect the magnetization density induced in the Ir spacer layer of a Co/Ir superlattice by mean of exchange resonant x-ray scattering at the L_{III} edge of Ir. To this end, several superlattices were grown using molecular beam epitaxy, tuned to give antiferromagnetic coupling of successive Co layers. Owing to instabilities in the storage ring during the first 2+ days of the run, only one sample could be examined. In order to separate magnetic dipole scattering from the charge-scattering satellites of the superlattice, the Al(333) Bragg peak was used in the Illinois polarimeter in the σ-π configuration. Numerous additional peaks were detected at positions in reciprocal space that were indexible as one-fourth the distance between superlattice side bands. These were resonant at the Ir L_{III} edge. While these satellites appear to be of magnetic origin, they indicate that the Co layers were arranged in a coherent manner, but with a 90 degree rotation between successive blocks. This could be accomplished by means of dominant biquadratic coupling, but it is suprising that such coupling could give rise to coherent order. Because of the intensity of the beam, the sample was found to degrade during the course of the experiment, presumably due to the absorption within the Ir underlayer when operating close to the Ir L_{III} edge. While data analysis is still underway, we have succeeded in growing new samples that show unambiquous antiferromagnetic order. These will be used in future runs, and some defocussing of the beam will be required to give the necessary intensity while not degradating the samples.

Structural Studies of Gene 5 Protein-ss DNA Complexes

X25, X8C

T. C. Terwilliger, R. G. Nanni (LANL)

Single-stranded nucleic acid-binding proteins play roles in key cellular processes such as DNA replication, recombination, repair, and control of RNA translation. This project has focussed on determining the crystal structures of complexes between gene V protein and oligonucleotides of lengths from 4 to 16 nucleotides. We have obtained crystals of a number of these complexes and have collected x-ray diffraction data on those that diffract to high resolution. At this point we have collected x-ray diffraction datasets to a resolution of at least 3.5 A for the 6 different gene V protein-oligonucleotide complexes.

We have used the structure of the wild-type gene V protein that we determined previously to solve the structure of the protein portion of one complex crystal containing a 16-mer oligonucleotide. This complex crystallized in space group R3 and the asymmetric unit of the crystal contains 4 monomers of the protein. The standard R-factor for this structure after rigid-body refinement of the protein portion alone is 0.39, indicating that the solution we have obtained is likely to be correct. We are now in the process of using difference Fourier methods and atomic refinement to determine the location of the bound ssDNA in these crystals.

Structure Determination of Leukotriene A4 Hydrolase

X25

M.M.G.M. Thunnissen, P. Nordlund (Stocklholm U., Sweden.), and J. Z. Haeggstrom (Karolinska Institute, Sweden)

Leukotrienes are lipid mediators involved in inflammatory and allergic processes. Leukotriene (LT)B4 is a potent chemotactic stimulus for leukocytes and is regarded as an important mediator of inflammation (Samuellson et al, 1987). This compounds is formed from arachidonic acid via the sequential action of two enzymes. 5-lipoxygenase catalyzes the formation of the epoxide intermediate LTA4 which is in turn converted into LTB4 by the enzyme LTA4 hydrolase. In addition to its epoxide hydrolase activity, LTA4 hydrolase also has peptidase/amidase activity towards synthetic substrates.The amino acid sequence for LTA4 hydrolase shows a consensus sequence which is conserved amongs zinc- metalloproteases (Haeggstrom et al. 1990). Site directed mutagenesis studies have shown that His295, His299 and Glu318 are the three Zn binding ligands and that Glu296 is the catalytic amino-acid for the peptidase activity, for which a general base mechanism is proposed (Medina et al., 1991). Tyr383 was identified as the potential proton-donor in this mechanism (Blomster et al., 1995). However much less is known about the epoxide hydrolase activity although mutations at positions 296 and 383 showed that the active sites are not identical but rather overlapping. In view of the potential importance of LTA4 hydrolase as a target for the treatment of inflammatory diseases, novel selective inhibitors have been developed (Yuan, 1993) based on substrate mediated inactivation of the enzyme. The efficiency of these inhibitors has been tested on the epoxide activity of the protein. These new inhibitors are the most potent inhibitors of the enzyme presently available, with IC50 between 2 and 0.2mM. With the help of structural information, these compounds might be used as lead compunds and ultimately be developed into novel anti-inflammatory drugs.

We recently collected MAD data on the L(III) edge of Yb at beamline X25. Three datasets (peak, point of inflection and hard remote) were collected. The data has been processed in a preliminary manner using DENZO. The completeness of these datasets is around 90% to 3.5A with R merges of 10%. Since data was collected very recently no further analysis has been done. Some preliminary Patterson functions show interpretable peaks. We hope that we can use these data for initial phasing and that subsequent two-fold averaging will be sufficient for tracing the peptide chain.

Blomster, M., Wetterholm, A., Mueller, M.J. Haegstrom, J.Z. (1995) Eur. J. Biochem. 231, 528-534.

Haeggstrom, J.Z., Wetterholm, A., Shapiro, R., Vallee, B.L. Samuelsson, B. (1990) Biochem Biophys. Res. Comm. 172, 965-970.

Medina, J.F., Wetterholm, A., Radmark, O., Shapiro, R., Haeggstrom, J.Z., Vallee, B.L. Samuelsson, B. (1991) Proc. Natl. Acad. Sci. USA 88, 7620-7624. Samuelsson, B., Dahlen, S.-E., Lindgren, J.A., Rouzer, C.A. and Serhan, C.N. (1987) Science 237, 1171-1176.

Yuan, W., Munoz, B., Wong, C.H., Haeggstrom, J.Z., Wetterholm, A. Samuelsson B. (1993) J. Med. Chem. 36, 211-220.

X-ray Studies of the Surface Wetting Transition in Liquid Ga–Bi* | X25

H. Tostmann, P. S. Pershan (Harvard U.), E. DiMasi, B. M. Ocko (BNL), and M. Deutsch (Bar-Ilan, Israel)

In contrast to a simple eutectic alloy, such as Ga–In which exhibits Gibbs surface segregation, Ga–Bi has a pronounced miscibility gap. This is a prerequisite for the occurrence of a surface wetting transition. In the case of Ga–Bi, a macroscopically thick Bi rich film completely wets the lighter Ga rich bulk phase if the temperature is raised above the characteristic wetting temperature T_w. Optical ellipsometry studies show that T_w coincides with the monotectic temperature of 220°C.

Using high energy synchrotron radiation, it is possible to monitor the wetting transition from a microscopically thin Bi monolayer to a macroscopically thick Bi film with atomic resolution. An indication for this phase transition can be seen in fig.1. The x-ray reflectivity R from liquid Ga–Bi is shown for three different temperatures, two below and one above T_w. The two reflectivities at 35°C and 95°C can be fitted by a model that assumes a single Bi monolayer on top of the Ga rich bulk (solid line). The principal differences between the 35°C and the 95°C data can be explained by a Debye-Waller type factor associated with the surface roughness due to thermal capillary waves. It is important to note that the basic structural feature — a Bi rich monolayer on top of a Ga rich bulk — is not changed between 35°C and 95°C.

In contrast to this, the difference between the 260°C and the 35°C data in the small wavevector range cannot be explained by thermal roughness and a simple monolayer model does not fit the 260°C data. This indicates a significant change in the surface structure for $T > T_w$. As can be seen in fig.2, at small q the reflectivity for $T > T_w$ (closed triangles) approaches the Fresnel reflectivity expected from a macroscopically thick layer of Bi (dotted line) whereas the reflectivity for $T < T_w$ clearly approaches the Fresnel reflectivity of Ga.

*This work is supported by the DOE grant DE-FG02-88Er45379

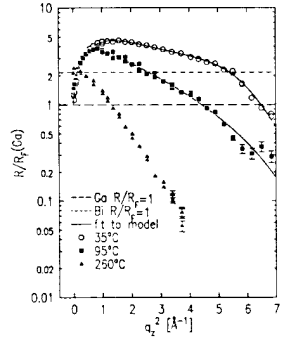

Figure 1. Measured x-ray reflectivity for liquid Ga-Bi at three different temperatures normalized to the Fresnel reflectivity of an abruptly terminated ideal surface. Solid line: fit (see text).

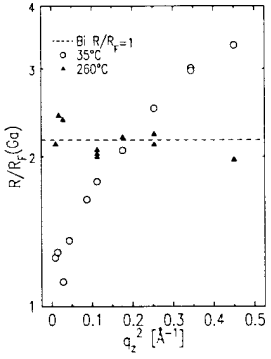

Figure 2. Small angle x-ray reflectivity for liquid Ga-Bi below(35 °C) and above (260 °C) the wetting temperature.

Surface Structure of Liquid Indium* | X25

H. Tostmann, P. S. Pershan, O. G. Shpyrko (Harvard U.), E. DiMasi, B. M. Ocko (BNL), M. Deutsch (Bar-Ilan, Israel)

The surface–normal density profile of liquid metals (LM) is more complex than the relatively simple monotonic decay of density found in dielectic liquids. In the case of LM, the combination of the two-fluid nature, the strong Coulmob interactions and quantum effects give rise to atomic layering normal to the free surface. This has long been predicted by theory and verified recently by our experiments on liquid Hg and Ga. Several features of these density profiles are not explained by theory. To gain deeper insight into the surface strucutre of LM, investigations of additional LM are necessary. Measurements on liquid In are of particular interest since In is more free-electron-like than either Ga or Hg.

The x-ray reflectivity from a liquid In surface is shown in Fig.1. The layering peak at 2.2Å^{-1} is due to interference from the ordered surface layers having a spacing of about 2.7Å. The data can be fitted by a model representing the layer densities by a sequence of Gaussians decaying in amplitude (solid line). The intrinsic density profiles of Ga and In can be compared when the effects of the finite temperature are removed. In this case, the amplitude of the first layer is slightly larger for In than for Ga and the In layering decays faster into the bulk then the Ga layering.

In addition we recorded the off-specular diffuse scattering (Fig.2). The solid lines correspond to the theoretically expected scattering intensity taking into account the surface structure factor, the experimental resolution and the scattering from thermally activated capillary waves. The agreement justifies our proceedure for the separation of capillary induced roughness from the intrinsic surface structure.

*This work is supported by the DOE grant DE-FG02-88Er45379.

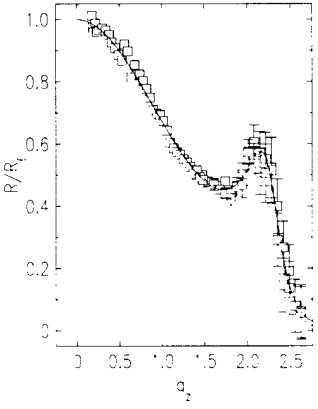

Figure 1. Measured x-ray reflectivity for liquid In at 170°C normalized to the Fresnel reflectivity of an abruptly terminated ideal surface. Solid line: fit (see text).

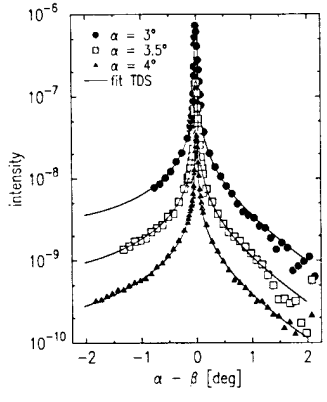

Figure 2. Off–specular diffuse scattering from liquid Indium. For clarity, the data at 3 and 3.5° are multiplied by 4 and 2 respectively (α: incoming angle. β: detector angle).

Non-Brownian Dynamics of Concentrated Colloidal Suspension Probed by X-ray Intensity Fluctuation (XIFS) — X25

O. K. C. Tsui and S. G. J. Mochrie (MIT)

We have performed XIFS measurements of the equilibrium dynamics of suspensions of charge-stabilized Sb_2O_5 spheres of radius $250 \pm 40\text{Å}^{-1}$ in glycerol. Two samples were studied: a dilute sample (sample I) and a concentrated sample (sample II), the latter with an effective hard sphere volume fraction 0.18. Fig. 1 shows the temoral autocorrelation for both samples at different wavevectors. For sample I, the data fit very well to a single exponential (Fig. 1(a)). For sample II, however, this model does not work as well (solid lines in Fig. 1(b)). Therefore, we have adopted a cumulant form up to the third order in order to fit the data. Evidently, it provides a much better description (dashed lines in Fig. 1(b)). In Fig. 2, we have plotted D_0/D vs. Q, where $D = 1/\tau_Q Q^2$ (τ_Q is the characteristic decay time of the autocorrelation) and D_0 is the Stokes-Einstein diffusion coefficient. For sample I, D_0/D is nearly constant versus Q, as expected for a dilute suspension undergoing Brownian motion. The fact that D is a factor of 2.6 bigger than D_0 is probably due to the presence of water impurity in the sample. On the other hand, for sample II, D_0/D increases rapidly with Q, and tends to peak at where $S(Q)$ peaks ($Q_{\max} \sim 0.008\text{Å}^{-1}$). Physically, the particle density wave at $Q_{\max}$ has the optimum interparticle separation, therefore any attempt to move the particle away from this preferred configuration is suppressed. What is the most interesting, however, is that at small Q the asymptotic value of D_0/D is bigger than one. Light scattering results of suspensions with hard sphere or screened Coulomb interactions suggest the opposite. More work is needed to understand the discrepancy.

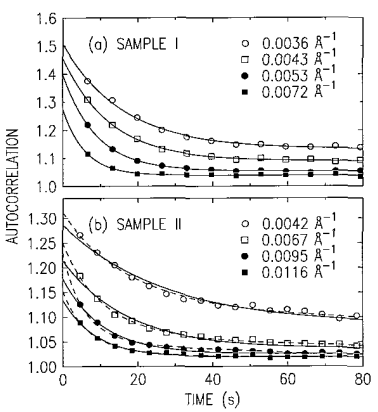

Figure 1. (a) Autocorrelations vs. time for sample I at $-31.5°$C. (b) Autocorrelations vs. time for sample II at $-26.8°$C. Solid lines are fits to a single exponential. Dashed lines are fits to a cumulant form.

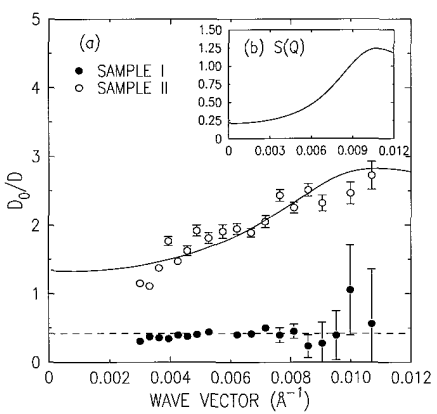

Figure 2. (a) D_0/D vs. wavevector for sample I (solid circles) and sample II (open circles). The lines are guides-to-the-eye. (b) Structure factor, $S(Q)$, of sample II.

Statistical Analysis of X-ray Speckle at X25 — X25

O. K. C. Tsui, S. G. J. Mochrie (MIT), and L. E. Berman (BNL)

A highly coherent x-ray beam was produced at the NSLS wiggler beamline X25 using a rectangular slit 8.9 μm (vertical) $\times 4.2\mu$m (horizontal). By illuminating an aerogel sample (a disordered medium) with the beam, a static speckle pattern was produced (Fig. 1). Statistical analysis was carried out to study the coherence properties of the beam, which may be described by a number M, which may be considered as the number of independent coherent x-ray fields contributing to the observed speckle pattern. We calculated the autocorrelation function and the intensity probability distribution of the speckle pattern at various wavevectors, Q ($0.003 < Q < 0.01\text{Å}^{-1}$) and obtained the Q dependence of M (Fig. 2(a)) and the FWHM of the speckle pattern (Fig. 2(b)). We adopted a model recently developed by Albernathy *et. al.* and found good agreement with the data. Our result showed that the number of coherence areas propagated through the slit, M_0, was 2.3 which is 35% bigger than what one will expect from transverse coherence length considerations. We do not understand the discrepancy although beryllium windows and beamline optics are possible candidates to explain the difference.

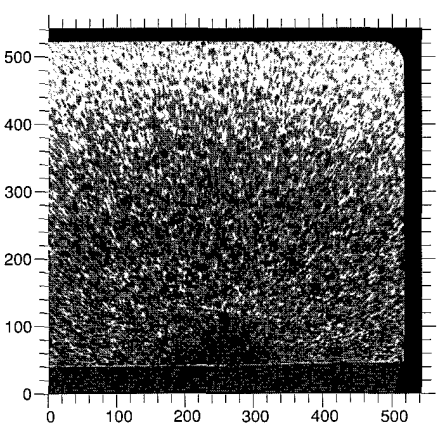

Figure 1. Speckle pattern produced by an aerogel sample. The axes are labelled by the pixel numbers (1 pixel corresponds to $3 \times 10^{-5}\text{Å}^{-1}$).

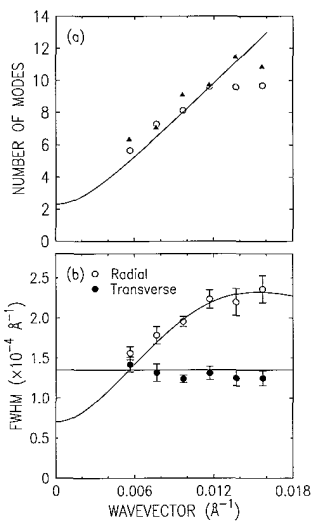

Figure 2. (a) M vs. Q obtained independently from the peak height of the autocorrelations (open circles) and fits to the intensity probability distribution (solid triangles). (b) FWHM of the speckle pattern as a function of Q. Solid lines are best fits of Abernathy *et. al.*s model to the experimental data.

High Resolution Data Collection and Structure Refinement of Mitochondrial Cytochrome bc1 Complex

X25

D. Xia, H. Kim, J. Deisenhofer (HHMI & U. of Texas), C. A. Yu, A. Kachurin, L. Zhang, and L. Yu (Oklahoma St. U.)

Cytochrome bc1 Complex (ubiquinol-cytochrome c oxidoreductase, bc1) is the middle segment of the respiratory chain in almost all aerobic organisms, and an essential component in the photosynthetic machinery in purple bacteria. Green plants use highly homologous b_6f complex as an important of their energy conservation apparatus. The bc1 complex is an integral membrane protein; it couples the electron transfer from ubiquinol to cytochrome c to the proton translocation across the membrane to generate a pH difference and a membrane potential for ATP syntheseis. Mitochondrial bc1 complex from bovine heart consists of 11 different subunits, two b-type hemes, one c-type heme and an iron-sulfur cluster with a total molecular weight of 250 Kd and in excess of 2200 amino acid residues.

The mitochondrial cytochrome bc1 complex from bovine heart was purified and crystallized. Bc1 crystals diffracted X-ray to 3.3 Å resolution and possess symmetry of the space group of $I4_122$ with cell dimensions a=b=153.7 Å and c=597.5 Å. Structure was determined using MIRAS method with seven heavy metal derivatives. Current atomic model of the bc1 complex contains eight completely sequence assigned subunits including core1, core2, cytochrome b, Rieske iron sulfur protein, subunits 6, 7, 10 and 11; three incomplete subunits including cytochrome c1, subunits 8 and 9; and prosthetic groups including two b-type hemes, one c-type heme and one 2Fe-2S iron-sulfur cluster with total number of amino acids residues near 2000.

The diffraction of cryo frozen bc1 crystals is rather weak due to large unit cell volume, high crystal mosaicity and anisotropic distribution of crystal packing contacts. The weak diffraction poses a major obstacle to the refinement of bc1 complex structure. Large bc1 crystals diffract X-ray at high flux beamline such as X25 of NSLS to 2.7 Å resolution or better. We have collected a complete high resolution data set from a single bc1 crystal at beamline X25 to 2.7 Å resolution, which was carried out with multiple passes of high resolution scan by translating the crystal and one pass of low resolution scan. The data set is 95% complete to 2.7 Å resolution with a merge R factor of 8.6%. Structure refinement of the bc1 complex is currently underway.

Structure and Action of Chaperonin: Structure Determination of GroEL/GroES Complexes

X25

Z. Xu, A. Horwich, and P. B. Sigler (Yale U. & Howard Hughes Medical School)

The *E. coli* chaperonin GroEL, a 14-subunit (60k Da each) assembly composed of two back-to-back 7-fold rotationally symmetric rings, requires a partner assembly, GroES, to function. GroES is a 7-fold rotationally symmetric ring of 10 kDa subunits which, with ATP is used to release bound unfolded substrate polypeptide. One GroES 7-mer is thought to form a functional complex with one GroEL 14-mer. In order to understand the interplay of GroES (and nucleotide phosphate) in GroEL-assisted polypeptide folding, we have undertaken the structure determination of GroEL/GroES complex in the presence of stably bound ADP. The crystal structure of GroEL/GroES/$(ADP)_7$ was determined at 3.0 angstrom resolution. The dramatic change in the overall structure of the GroEL/GroES complex can be attributed to the remarkable *en bloc* domain movements in the subunits of the ring to which GroES is bound (the *cis* ring). The movements of these domains more than double the volume of the inside cavity, increase the hydrophilicity of the cavity's lining, and suggest a mechanism for peptide release. These movements also cause significant changes in the nucleotide binding pocket which accounts for the highly asymmetrical binding of ADP to only the seven *cis* subunits and provide plausible links between the binding of GroES and changes in the binding/hydrolysis of ATP.

Refinements to the Two-Beam Diffraction Interference Technique | X25

Y. Yacoby (Hebrew U.), H. Baltes, R. Pindak, L. Pfeiffer, R. Hamm (Bell Labs), R. Clarke (U. of Michigan), and L. Berman (NSLS)

We previously demonstrated that the two-beam diffraction interference technique provided a direct measurement of the phase of the x-ray beam diffracted by a 2D crystal [1]. The experimental results indicated that accurate quantitative measurements required two refinements: a calibration of the diffracted intensity relative to the incident intensity and a direct measurement of the amplitude and phase of the x-ray reflection coefficient for the incident beam.

As our calibration signal we used the powder diffracted beam from a 0.4 μm Au overlayer. We chose this signal rather than a signal proportional to the overall beam intensity because, as illustrated in Fig. 1, this signal is proportional to the intensity of that part of the 20 μm incident beam which is in close proximity to the portion (indicated by dashed lines) participating in the 2D crystal diffraction. The measured intensity of the calibration signal as a function of beam position relative to the Au layer shows that the beam intensity varies continuously within the beam by about 10% confirming the need for calibration.

The absolute value of the reflection coefficient was measured directly as a function of the angle of incidence, α. The results, shown in Fig. 2 (filled circles), are in good agreement with calculations (solid curve). The phase of the reflection coefficient was measured as follows: a monolayer of Ni was evaporated on the 2D crystal prior to evaporating the Pd mirror layer. The intensity of the Ni fluorescence is proportional to the intensity of the standing wave produced by the incident and reflected beams. The Ni fluorescence signal is plotted in the lower right figure (Xs). The results suggest that the phase qualitatively follows calculations (solid curve) for an ideal Pd reflector. In particular, note the increase in fluorescence intensity near the critical angle where the incident and reflected beams are in-phase. Nonetheless, there exist significant deviations in the data suggesting that the GaAs-Pd interface is not a simple one justifying our efforts to measure the phase directly.

[1] H. Baltes et al., Phys. Rev. Lett. **79**, 1285 (1997).

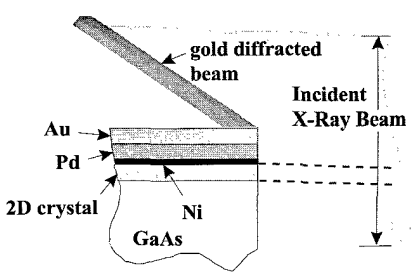

Figure 1.

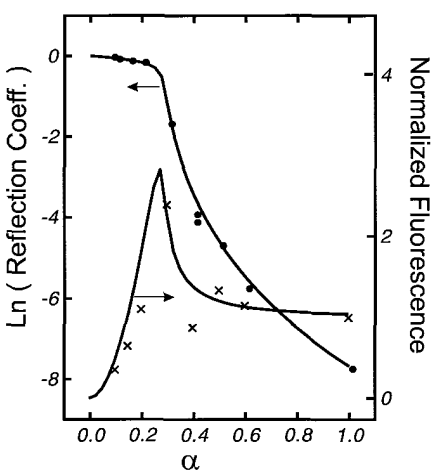

Figure 2.

Structures and Oxidation States of Layers on Platinum Single Crystal Surfaces. | X25

H. You, J. Tanzer, Y. Chu, and Z. Nagy (ANL)

A cyclic voltammetry scan of the Pt(111) surface (not shown) have several prominent features associated with the changes in chemical condition of the surfaces. We will present a set of preliminary data in this report in order to show that the surface resonance scattering through platinum L_3 edge is sensitive to the oxidation or chemical state of the top layer of platinum surface. The precise control of the oxidation state of the surface can be accomplished in electrochemical potential control.

Single crystals of platinum were prepared using the flame annealing followed by an iodine protection scheme. In this way, the surface can be prepared atomically flat. This method has previously used to prepare the surface and proven to work. Now the top surface platinum atoms are oxidized or reduced via electrochemical potential control.

In Figure 1, as a selected set of examples, calculated (left panel) and measured (right panel) x-ray intensities are shown as a function of incident x-ray energy through the Pt L_3 edge for four different conditions. The top panels are for the scan from the bulk platinum. This intensity was measured at the critical angle of platinum where we expect the x-ray evanescent intensity penetrate into the bulk. The rest of the panels are for scans made at the most surface sensitive Q-positions at three different electrochemical potentials (three different oxidation states), i.e., at 0.8, 0.1, and 1.2 V, respectively. At 0.8 V, the surface is under open-circuit potential and very little charge transfer of the top Pt layer is expected. At 0.1 V, the surface is expected to be reduced and at 1.2 V the surface is fully oxidized. It is clear that the x-ray scattering intensity is extremely sensitive to the oxidation state of the top atomic layer of platinum, indicating the feasibility of detecting monolayer-level chemical changes.

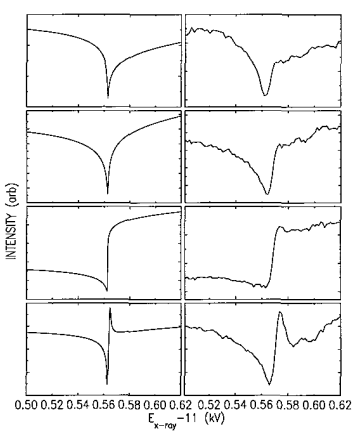

Figure 1. Right panel: Measured intensity at various conditions through Pt L_3 edge. Left panel: Calculated intensity for the experimental conditions.

Partitioning of Ferric and Ferrous Iron Between Coexisting Mafic Silicates from Adirondack Metamorphic Rocks	X26A

P.D. Crowley, R.E. Stamski (Amherst), M.D. Dyar (West Chester U.), R.J. Nevle, J. S. Delaney (Rutgers U.), A.G. Monders, S. Jin Young (Whitman), H.A. Guetschow (Carleton), E.D. Gutmann, (Williams), D.F. Harrington, R. Graham (Union), M. B. Chervasia, (College of Wooster), S. R. Sutton and G.Shea-McCarthy (U. Chicago)

Installation of the focussing mirrors on beamline X26a now allows for the rapid (< 15 minute) acquisition of Fe XANES spectra. Micro-XANES spectra were obtained of garnet, plagioclase, olivine, clinopyroxene, amphibole, and biotite from amphibolite and granulite facies metamorphic rocks from the Adirondacks. Standard petrographic thin sections were analyzed using a roughly 50 x 100 micron beam. After subtraction of the main edge baseline, spectra were fitted to determine the location of the Fe pre-edge relative to a magnetite standard. From the Fe pre-edge position, Fe^{+2}/Fe^{+3} ratios were determined following the procedure of Bajt et al. (1994). Using the Fe^{3+} content of coexisting mafic silicates, partition coefficients for Fe^{3+} were determined. The relative partitioning of Fe^{3+} among mafic silicates was significantly smaller in granulite facies rocks than in lower temperature amphibolite facies rocks.

Coordination Effect on Fe Pre-edge SmX Spectra of Garnet	X26A

P.D. Crowley, R.E. Stamski (Amherst), M. D. Dyar (West Chester U.), R .J. Nevle, J. S. Delaney (Rutgers U.), H. R. Morrison, M. B. Chervasia, (College of Wooster), Z. M. Brown (SUNY at Buffalo), A.G. Monders (Whitman), D.F Harrington, H.A. Guetschow (Carleton), E.D. Gutmann, (Williams), S. R. Sutton and G. Shea-McCarthy (U. Chicago)

Synchrotron micro-XANES spectra of garnet were collected on beamline X26A, during August 1997, after the installation of focussing mirrors just upstream of the sample. The garnet samples came from 13 rocks collected to cover a wide range of Fe^{3+}/Fe^{2+}, including end-member almandine and andradite Mössbauer standards. Measurements were made on thin sections and grain mounts using a roughly 50 x 100 micron beam. Spectra were fitted to determine the location of the Fe pre-edge relative to a magnetite standard and calibration following the procedure of Bajt et al. (1994). After subtraction of the main edge baseline, all of the spectra appear to be composites of two closely overlapped peaks, probably relating to the cubic and octahedral sites in the structure. Fe^{2+} rich garnet has a prominent peak at -1.9 eV (8-fold occupancy) and a smaller peak at +0.5 eV (Fe^{3+} in 6-fold coordination). End-member andradite is a composite of two peaks at -0.2 eV and + 1.3 eV. Thus, the shape and location of the pre-edge is a very sensitive indicator of the Fe^{3+} content of garnet. The composite peaks in the Fe pre-edge were not resolvable prior to the installation of the focussing mirrors.

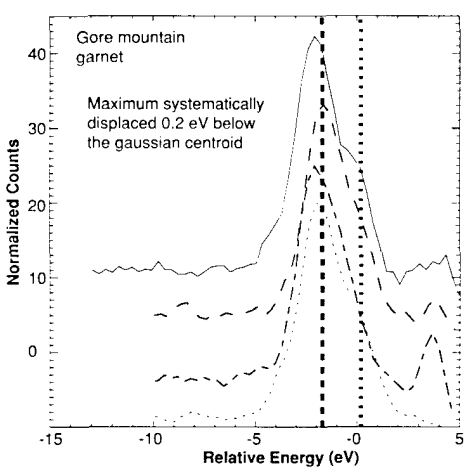

Figure 1. Fe pre-edge after baseline subtraction. This is a composite of two overlapping peaks at -1.8 Ev and 1.0 eV.

Ferric/Ferrous Microanalyses of Geological Glasses by Synchrotron MicroXANES (SmX)	X26A

J. S. Delaney (Rutgers U.), S. Bajt (LLNL), S. R. Sutton (U. Chicago), and M. D. Dyar (West Chester U.)

Fe(III)/Fe(II) in numerous geological glasses, determined by wet chemical and Mossbauer techniques, correlate linearly with variations in the energy of the Fe K-absorption pre-edge measured by synchrotron microXANES (SmX) in fluorescence mode using a 12x15 micrometer beam at X26A. Fe in glass is in 4- and 5-fold coordination, in contrast to the 6-fold Fe of most of the minerals studied. The magnitude of the pre-edge energy change, as a function of Fe(III)/Fe(II), is smaller in glass. The calibration line used for pure glasses is also different from that of minerals because of the different coordination of the Fe. 'Impure' glasses, that contain crystallites or that were slowly quenched have pre-edge peak energies that fall between those of the 'pure' glasses and 'pure' minerals of comparable Fe(III)/Fe(II) ratio. Such 'impure' glasses are typical of geological materials. The impure glass data lie in a continuum between glassy to crystalline states with the average coordination number of Fe probably reflecting the extent of their short vs. long range ordering, or their "crystallinity". The average Fe coordination number of micrometer scale areas of glass may in fact correlate with the cooling rate of the glass.

In SmX, neither a 'pure' glass calibration line nor a 'pure' mineral calibration line can be used for microanalysis of such "real-world" samples because effects of Fe coordination on the measured signal are significant. Fortunately, the coordination of Fe in glassy samples can be determined quantitatively with a combination of XANES and EXAFS technique. The ability to measure simultaneously the XANES and the EXAFS region of a multivalent element, such as Fe, is already in use for the quantitative Fe(III)/Fe(II) microanalysis on minerals and is being explored on coexisting glassy phases.

Preliminary experiments using glass with coexisting minerals are being done to measure the partitioning of Fe(II) and Fe(III) between the phases. These results allow determination of natural crystal growth systematics for materials that were not previous possible.

Redox Ratios with Outrageous Resolution: Solving an Old geological Problem with the Synchrotron MicroXANES Probe.	X26A

J. S. Delaney (Rutgers U.), M. D. Dyar (West Chester U.), S. R. Sutton (U. Chicago), and S. Bajt (LLNL)

In situ measurements of the oxidation state of iron in common minerals have been made using the synchrotron microXANES (SmX) technique. The results compare very well with wet chemical and Mvssbauer spectroscopic analyses of the same samples. Areas of 10 x 20 micrometers have been measured successfully and the results demonstrate that both compositional zoning of Fe3+/(ΣFe) within individual grains and the effect of oxide inclusions on bulk analyses can be quantified. Such sample heterogeneity cannot be detected by conventional bulk analytical techniques. The ability to measure Fe3+/(ΣFe) with spatial resolution comparable to that of the electron microprobe further enhances the importance of microbeam techniques in the earth and planetary sciences. Direct measurements of parameters constrained by oxidation-reduction processes are now possible with the same spatial resolution as traditional compositional analyses derived from electron beam and optical microscopic techniques. The new Kirkpatrick-Baez mirrors on X26A have increased the intensity of the x-ray beam usable for Fe-microXANES, permits rapid analysis and the acquisition of data with the level of spatial detail common to conventional microbeam techniques. Co-ordinated Smx, electron probe and ion probe studies of microvolumes are now feasible and are being done

The Spectroscopic Characterization of U in an Evaporation Basin Sediment, LA-UR-97-3589	X26A

M.C. Duff (LANL), D.B. Hunter, P.M. Bertsch (SREL/UGA), C. Amrhein (UC-Riverside), D.E. Morris (LANL), G. Shea-McCarthy (U. of Chicago)

Evaporation ponds in the San Joaquin Valley (SJV), CA used for the containment of irrigation drainage waters, have elevated levels of U. The ponds support algae which upon evaporation, become incorporated in sediments as depositional sedimentary layers of organic matter (OM). The OM facilitates reducing conditions in the sediments. However, our studies have shown U in one pond sediment exists as primarily the oxidized form, U(VI)–regardless of the presence of oxidizing or reducing conditions. Research was conducted with two pond sediments to characterize U speciation and the influence of various leaching solutions on the U speciation. The research involved spectroscopic techniques such as X-ray Absorption Near Edge Structure (XANES, at the X-26A microprobe beamline) for U oxidation state determinations and (at LANL) basic room and low temperature time-resolved luminescence. These analytical techniques were complemented by wet chemical U extraction methods which involved the use of non-oxidizing carbonate and sulfuric acid solutions and oxidizing solutions. X-ray absorption spectroscopy (XAS) utilizing synchrotron radiation is a non-invasive, in situ method that can be used to distinguish U(VI) and U(IV) oxidation states. The energy of an X-ray absorption edge increases with increasing valence resulting from the reduced shielding of the core electrons from the nucleus. This increase in the binding energy of the core levels is often manifested by shifts in pre-edge and bound-state edge features in a XANES spectrum that can be correlated to differences in the oxidation state of a cationic center. For U-XANES studies with two sediments (Ponds 14 and 16), the surface sediments (0-5 cm) had 69 to 75 per cent U(VI) whereas at depth, the Pond 16 sediments had 46 per cent (5 to 10 cm depth) and 46 per cent (10 to 15 cm). The greater reduction of U in the Pond 16 sediments may be due to differences in the physical and chemical characteristics of the pond surface sediments. This research is currently work in progress.

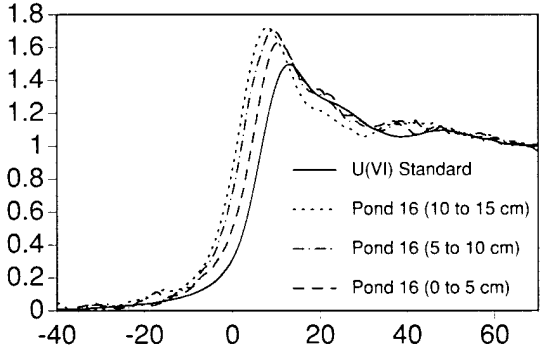

Figure 1.

Factors Influencing U Redox Processes in Saline, Calcareous Sediments, LA-UR-97-3590	X26A

M.C. Duff (LANL), D.B. Hunter (SREL), P.M. Bertsch (SREL), C. Amrhein (UCR), G. Shea-McCarthy (U. of Chicago)

To examine the factors affecting U(VI) reduction in saline pond sediments from the San Joaquin Valley, CA. Sediments were equilibrated with natural and synthetic pond inlet waters containing 10 mg U(VI) L^{-1} and various potential reducing agents. The equilibrations were done under oxidizing conditions (treatments with the algae *Chlorella*) and under O_2-limiting conditions (acetate, sucrose and alfalfa treatments). After three weeks of equilibration, sediment U was characterized for changes in oxidation state (by XANES using the microprobe at X-26A) and the dissolved U concentrations were determined by phospholuminescence spectroscopy. The reduction of U(VI) to the less soluble oxidation state U(IV), was not observed in the *Chlorella*, acetate and sugar treatments. For the treatment with alfalfa (a N and energy source), a loss of 95 percent U from solution occurred along with the generation of volatile sulfides. Additionally, the U(IV) was determined to be the primary U oxidation state in the alfalfa treated suggesting U(VI) reduction to U(IV) and U(IV) precipitation occurred. Under the reducing conditions, the reduction of solution U(VI) to U(IV) most likely occurs after significant SO_4^{2-} reduction has taken place. However, after 4 days under oxidizing conditions, up to 40 per cent of the U(IV) in the alfalfa treated sediments was oxidized to U(VI). Hence, in contrast to some microbial studies which have observed that the reductive precipitation of U(IV) results in a solid which is not easily oxidized, U(VI) reduction followed by precipitation in this system results in a chemically labile U(IV) solid (such as $UO_{2(s)}$, uraninite) that is readily oxidized. Additionally, these results suggest that U reduction in the ponds is a function of nutrient (N and possibly P) availability.

The results of the equilibrations of pond inlet waters with Pond 14 sediment and ~10 mg U L^{-1}. Values in parentheses are after 96 hours of air oxidation. The first 2 rows represent *in-situ* values which were obtained from other studies.

Treatment	pH	H_2S Smell	% U Lost from Solution	% U(VI) in Sediment
Oxidized Sediment	8.3	●	-	85
Anoxic Sediment	8.2	○	-	73
Algae, ONIPW	7.2	●	2	83
Algae, OSIPW	7.5	●	10	77
Alfalfa, ANIPW	6.8	○	95	4.4 (34)
Alfalfa, ASIPW	6.5	○	95	4.0 (48)
Sugar, ANIPW	6.7	●	69	75
Sugar, ASIPW	7.3	●	94	86
Acetate, ANIPW	7.6	●	20	78
Acetate, ASIPW	7.2	●	1	84

O: Oxic; A: Anoxic; N: Natural; S: Synthetic; IPW: Inlet Pond Water
● : No volatile sulfides present by smell;
○ : Volatile sulfides present by smell.

Figure 1.

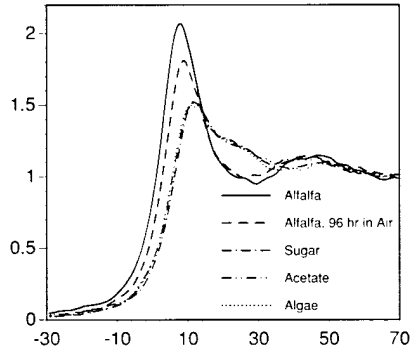

Figure 2.

Redox Speciation of Cr in Contaminated Soils, LA-UR-97-3591 | X26A

M.C. Duff (LANL), D.B. Hunter (SREL), P.M. Bertsch (SREL), P. Longmire (LANL), S. Kung (LANL), G. Shea-McCarthy (U. of Chicago)

At the Los Alamos National Laboratory DOE site, several soils are considered to be mixed-waste due to elevated concentrations of chromium (Cr, a RCRA metal) and radionuclides. At one site, a former research reactor water cooling tower which received over 2 tons of Cr(VI) over a 17 year period was the primary source of soil Cr contamination. The determination of soil Cr(III/VI) ratios is important to the classification of mixed waste because Cr(III) is appreciably less toxic and less mobile than Cr(VI). Soil, plant and groundwater samples were taken and analyzed for Cr content and in most cases Cr oxidation state. Potential factors influencing Cr redox chemistry such as water chemistry, soil Mn oxidation state and concentration, and organic matter (OM) content were also studied. Soils had up to 1000 mg Cr kg^{-1}. Wet chemical soil Cr(VI) extractions determined that Cr(III) was the dominant Cr oxidation state. These findings were further corroborated with in situ XANES studies with the microprobe at beamline X-26A on individual soil particles based on the absence of the pre-edge peak indicative of Cr(VI). Total soil Cr and Cr(VI) values were correlated with soil OM content and based on the XANES spectra, multiple forms of soil Cr(III) species appear to be present. Coarse soil OM had percentage levels of Cr with the dominant Cr oxidation state being Cr(III). According to SXRF studies, species of live plants taken from the cooling tower area have only trace Cr contents relative to the coarse soil OM suggesting the uptake of Cr by the coarse soil OM was postmortem. The Mn-XANES spectra suggest oxidized Mn(IV) is the dominant form of Mn, being greater than 80 per cent of the total soil Mn. However, results from heated acid digestions suggest that only half of the total soil Mn is nitric acid extractable-when it was previously thought that soil Mn(IV) is readily extracted with strong acid. Soil Mn(IV) may be chemically unavailable or in too low a concentration to catalyze significant Cr(III) oxidation to Cr(VI). The inability of Mn(IV) to oxidize Cr(III) to Cr(VI) may also exist because soil Cr is strongly associated with soil OM. Therefore, it is unlikely the Cr(III) will be oxidized to Cr(VI) over the long term. This study provides a strong potential for practical cost savings for mixed-waste characterization and management because it shows that: 1) the majority of Cr in the soil is the environmentally benign Cr(III) species, 2) the oxidation of Cr(III) to the mobile and toxic Cr(VI) is unlikely in this system if it remains fairly undisturbed, and 3) the Cr(VI) content is low enough to make a final recommendation of "no further action" for this site.

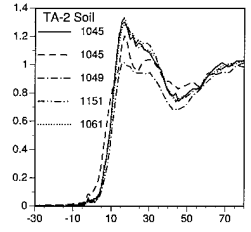

Figure 1.

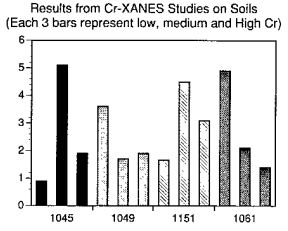

Figure 2.

Chemical Analysis of Interplanetary Dust Particles | X26A

G. J. Flynn (SUNY at Plattsburgh) and S. R. Sutton (U. of Chicago)

Interplanetary dust particles (IDPs), which are fragments of asteroids and comets, are collected from the Earth's stratosphere by NASA aircraft. The element abundance patterns in meteorites have proven useful in inferring their formation temperatures and establishing genetic links between different meteorites. Our prior analyses of over 100 small IDPs (about 10 to 20 microns in size) indicate that the volatile contents ratios separate those IDPs into two groups – one volatile rich and the other having a volatile content similar to the CI carbonaceous meteorites.

The impact collection technique separates the largest IDPs (greater than about 25 microns in diameter) into two groups based on structural strength: strong particles collected intact, and weaker particles which fragment on collection. The latter group are called "cluster particles" because they occur as a localized field of debris on the collector.

We have, thus far, determined element/Fe ratios in 21 large IDPs [1] and 24 cluster fragments from the NASA stratospheric collectors. Although the compositions of individual particles vary widely, the average composition of the large IDPs differs significantly from the average of the cluster fragments. The cluster fragments are enriched in the volatile elements Cu, Ga, Ge, Se, Zn, S, and Br compared to the large IDPs, suggesting the cluster particles may have formed at a lower temperature than the large IDPs. Both types of IDPs have similar contents of the refractory elements, except that Ca is lower, by an average of a factor of 3, in the large IDPs compared to the cluster fragments. Low Ca IDPs generally contain hydrated minerals, while the normal-Ca IDPs are generally anhydrous [2].

Our results indicate the large IDPs collected intact and the cluster IDPs have different chemical compositions, and, thus, may sample different parent bodies of different parts of the same parent body. Previously, Nishiizumi et al. [3], in an examination of larger interplanetary dust particles (greater than 100 microns in diameter) recovered from polar ices, reported a possible correlation between Ca-content and Al^{26} abundance, a measure of space exposure. Their results suggested a higher Al^{26} content, and thus a longer space exposure duration for the normal-Ca than for the low-Ca particles they examined. To determine if the large IDPs and the cluster IDPs from the stratosphere have different space exposure ages, and possibly different sources, we have begun a collaboration with the noble gas mass spectrometry group at Washington University. They will measure noble gas abundances, using the concentrations of solar wind gases and of cosmic ray spallation-produced Ne^{21} to determine space exposure ages, on the same IDPs analyzed for chemical composition at X26A.

References: 1) Flynn, G. J. et al., Meteoritics, 32, A42-A43, 1997. 2) Schramm, L. S. et al., Meteoritics, 24, 99-112, 1989. 3) Nishiizumi, K. et al., Earth Planet. Sci. Lett., 104, 315-324, 1991.

Chemical Analysis of Particle Capture Cells Flown on the MIR Space Station	X26A

G.J. Flynn (SUNY at Plattsburgh), S.R. Sutton (U. of Chicago), T. Bunch (NASA Ames)

When high-speed dust particles impact into a slab of low-density (tens to a a few hundred mg/cc) aerogel the particles generally come to a stop in a distance of about 100 particle diameters, leaving a cone-shaped track with either an intact dust particle or fragments of the particle at the bottom end of the track. If the particle is larger than about 1 micron in size, the entry track can be observed in an optical microscope. However, chemical analysis of the particle has required the removal of the particle from the aerogel, a labor-intensive process. We previously demonstrated that the X-Ray Microprobe at beamline X26A could be used for in-situ chemical analysis of particles captured in aerogel [1]. This capability allows us to perform major and trace element analysis on particles captured in the aerogels flown on earth-orbiting spacecraft, and to distinguish between orbital debris particles (typically metal, paint, or solar cell fragments) and micrometeorites (similar to chondritic meteorites) based on their chemical compositions.

This year, we analyzed an aerogel collector flown on the Russian space station MIR. This 65 cm^2 collector had been exposed to space for three weeks, including one week during Orionid meteor shower in 1995 and two-weeks in early 1996. Based on average micrometeorite flux measurements, the probability of one impact by a particle greater than 10 microns in diameter during a three week exposure is only about 0.3, although it was hoped there might be an enhanced flux during the Orionid shower. Only one "event," corresponding to an object about 10 microns in size, was identified in this collector by optical scanning [2], and degradation of the aerogel surface during the space exposure precluded optical detection of smaller particles. The track measures about 150 microns in length. The X-Ray Microprobe analysis showed high Ca, low Fe and low Ni, a composition distinctly different from chondritic meteorites and from the interplanetary dust collected from the Earth's stratosphere. Further, we found a uniform composition along the length of the track, rather than a chemical "hot spot" corresponding to a particle at the end of the track. Most likely this event is contamination in the form of a fiber cast into the aerogel during manufacture. In the upcoming year, the X-Ray Microprobe will be used to examine a similar collector flown on the space station MIR for more than 6 months, which should have collected a few particles greater than 10 microns in size.

We also performed chemical analyses of aerogels being developed at the Jet Propulsion Laboratory for use on NASA's Stardust mission, scheduled for launching in 1999. Stardust will capture dust particles during a flight through the tail of Comet Wild-2, using aerogel capture cells. The current effort focuses on insuring that the concentration of contaminants in the silica aerogel being developed for the Stardust spacecraft are sufficiently low to allow in-situ chemical characterization of the about 1500 cometary dust fragments greater than 15 microns in size expected to be returned to Earth by the Stardust spacecraft in the year 2006. In-situ chemical characterization will allow efficient curation of the returned comet dust samples, eliminating the necessity for the labor-intensive removal of each particle from the aerogel as part of the sample curation process.

1) Flynn, G. J. et al., Lunar Planet. Sci. XXVII, 369-370, 1996. 2) Nishioka, K. et al., Lunar Planet. Sci. XXVIII, 1029-1030, 1997.

Chemical Analysis and Fe-XANES Measurements on the ALH84001 Mars Meteorite	X26A

G. J. Flynn (SUNY at Plattsburgh), S. R. Sutton (U. of Chicago), L. P. Keller (MVA Inc.), and J. S. Delaney (Rutgers U.)

McKay et al. [1] have reported that carbonate globules and dark rim material surrounding these carbonate globules from the ALH84001 meteorite contain possible indicators of ancient biological activity on Mars. However, the formation temperature of these carbonates and rims is disputed. McKay et al. [1] suggest a low temperature of formation consistent with co-existing biological activity, while Harvey and McSween [2] infer a much higher temperature, inconsistent with biological activity.

We measured the trace element contents and the Fe-XANES spectra of a fragment of a carbonate globule and a fragment of dark rim material from ALH84001 in an effort to understand the origin and formation conditions of the carbonate and the rim and their relationship to one another. We determined the element/Fe ratios for S, Cl, Ca, Ti, Cr, Mn, Ni, Cu, Zn, Ga, Ge, Se, Br, Sr, Y, and Zr at 5 spots on a rim sample and 6 spots on the carbonate globule sample. Individual 10 micron spot analyses of each sample show nearly order-of-magnitude variability of S, Cl, Ga, and Br to Fe ratios, indicating that the most volatile elements in both the carbonate and the rim are distributed quite inhomogeneous at the 10 micron scale. However, the average element/Fe ratios of the rim and the globule are indistinguishable, within analysis errors, suggesting the rim material could be derived from the globule material by a closed system alteration process.

An important question is the degree to which the carbonate globules and rims, which are found along cracks in ALH84001, have been contaminated during their residence on the Earth. Langenauer and Krahenbuhl [3] have demonstrated that all of the Antarctic meteorites they examined showed near surface enrichments in the halogens, attributed to contamination while the meteorites resided on the Antarctic ice. The Cl/Br ratio in the carbonate globule and rim samples we measured is about 10,000, almost two orders-of-magnitude higher than that found in Antarctic ice [4], suggesting these samples have not been significantly contaminated by halogens while in the Antarctic. This may indicate that the carbonates and rims from the interior of ALH84001 have experienced little contamination during their residence in Antarctica.

The Fe-XANES spectra of the rim and the globule are identical, within errors, and consistent with that of Fe bound in carbonate. Although TEM examination of the rim samples described by McKay et al. [1] indicates the rim contains magnetite, Fe-sulfide and Mg-carbonate, Fe bound in carbonate dominates the Fe-XANES spectrum of the rim sample analyzed in this work.

References: 1) McKay, D. S., et al. Science, 273, 924-927, 1996. 2) Harvey, R. and H. P. McSween, Nature, 382, 49ff, 1996. 3) Langenauer, M. and U. Krahenbuhl, EPSL, 120, 431-442, 1993. 4) Spencer, et al., J. Glacialogy, 31, 233ff, 1985.

The Distribution of Zinc in Chondrules of Primitive Meteorites — X26A

G. Herzog, C. Schnabel, and J. S. Delaney (Rutgers U.), G. J. Flynn (SUNY at Plattsburgh), and S. R. Sutton (U. Chicago)

We have begun experiments to determine the microdistribution of the moderately volatile trace element zinc in chondrules from primitive meteorites. Chondrules are a major, millimeter-size structural component of the chondritic meteorites, the most abundant class of meteorites. Information on the microdistribution of zinc is important to the understanding of the geochemical behavior of zinc in chondrules, which is not well known, and for interpreting the published bulk zinc contents of chondrules in the context of various scenarios of meteorite formation. We use the X-ray Microprobe at beamline X26A to measure the zinc content and an electron microprobe to characterize the sample mineralogy and bulk composition. The meteorites to be studied include Allende, Murchison, Semarkona, and several other primitive chondrites.

Traditionally, the bulk zinc content of individual chondrules has been measured by neutron activation analysis. In our preliminary work we have profiled the spatial distribution of zinc in chondrules by exploiting the better than 10-ppm sensitivity and better than 25-micrometer spatial resolution of the X-ray Microprobe at beamline X-26A. We measure the zinc content at points along a line starting in the host matrix and traversing the diameter of the chondrule.

In four Allende chondrules examined thus far, zinc occurs mainly in silicates and to only a limited extent in metal and sulfides. Moreover, both zinc and iron concentrations show clear positive gradients running from the core to the edge of the chondrule. This trend indicates that bulk zinc contents of chondrules, as are typically measured using neutron activation techniques, do not provide a complete picture of the zinc behavior in these chondrules. The zinc gradient from the core to the edge is consistent with diffusion of zinc into the chondrules after formation. At present we favor the interpretation that most of the zinc entered these chondrules after their solidification as a result of interaction with the surrounding zinc-rich matrix. If so, then measured bulk zinc contents of chondrules in Allende represent only upper limits on the compositions of the chondrules immediately after their formation. It follows that the zinc contents at the chondrule interiors offer the best hope of learning the initial chondrule compositions, and constraining the conditions under which the chondrules formed.

Our experimental results require confirmation through further analyses of chondrules from Allende and other primitive meteorites. The technique employed is also applicable to the moderately volatile elements Cu and Ge, and we plan to extend our study of the spatial distribution and abundances of moderately volatile elements in chondrules to these elements as well.

In Situ Investigation of Alloy Element Behavior during Localized Corrosion — X26A

H.S. Isaacs (BNL- DAS), M. Kaneko (Nippon Steel Corp., Japan)

Chlorides and other halides undermine passive oxides and result in localized corrosion of many metals including stainless steels. Once initiated, continued corrosion depends on maintaining the presence of high concentrations of halide corrosion products within the localized corroding site. Hence, both the chemistry and mass transfer processes in pits are extremely important. The halide concentration in a pit is balanced between increases associated with metal dissolution (causing ionic migration into the pit), and diffusion out of the pit. In many cases the concentration attains saturation and a salt layer forms at the metal surface. In situ x-ray microprobe scans across the stainless steel/chloride solution interface in a working electrochemical cell has shown that the salt layer formed was of the order of a micrometers thick and depleted in chromium giving a distinct Fe/Cr maximum. Chloride fluorescence was too weak to penetrate the thin plastic windows and additions of bromide were made to act as a halide marker. Bromide fluorescence intensity gave a maximum intensity just below the region where the Fe/Cr maximum was observed. These results suggest that the salt layer is composed of two layers, an outer chromium depleted ferrous halide layer and an inner layer richer in Br, having a cation stoichiometry of the stainless steel.

Salt Layers Formation on Stainless Steel During Localized Corrosion | X26A

H. S. Isaacs (DAS-BNL) and M. Kaneko (Nippon Steel Corp., Japan)

An in situ study of the chemistry that develops in pits during localized of corrosion of stainless steel in chloride solutions has been carried out using energy dispersive x-ray techniques. An artificial pit was used to maintain a one dimensional diffusion geometry by dissolving back the cross section of a strip of Type 316 stainless steel foil mounted in epoxy resin. A high intensity 8 mm diameter polychromatic x-ray beam at Beamline x26A was scanned across the steel, a salt layer on the steel, and the concentrated dissolution products within the artificial pit. It was previously concluded that the salt layer on the steel was formed mainly by iron chloride, and the other metallic elements were present in significantly lower concentrations relative to the concentration in the steel. In order to obtain more information of the behavior of the halide anion, a fraction of the chloride was replaced with bromide. The fluoresence of this heavier element could be detected whereas the less energetic characteristic x-rays from chlorine which were absorbed by the thin plastic window of the cell. Figure 1 shows the x-ray intensities of Fe and Br across the interface formed between the dissolving steel and the concentrated dissolved products in the pit solution. Also shown is the ratio of the Fe/Cr intensity. The high values for the Br indicate that a salt layer is present over a range of about 0.015 mm. The maximum in the Fe/Cr ratio indicates that a salt layer with a different composition is formed adjacent to the solution and is about 0.006 mm. The results contrast with earlier conclusions where the peak in the Fe/Cr ratio was considered to be the only salt layer present. The present results suggest a duplex salt layer having a cation concentration similar to that of the steel and a high ferrous halide layer adjacent to the solution.

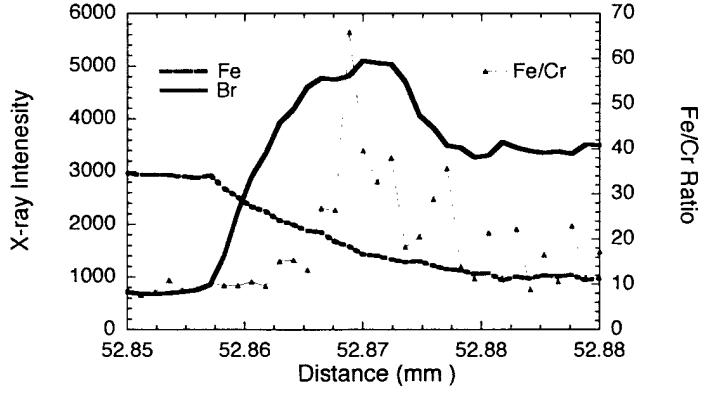

Figure 1. Figure1 Variations of x-ray intensity for Fe and Br across the steel/solution interface at a potential of 1.8 Vsce with a bulk soltion of 0.1 M LiBr and 0.9 M LiCl. The ratio of Fe/Cr intensities are also shown.

Elemental Analysis of Dredged Material From the Port of New York/New Jersey Using Synchrotron Radiation-induced X-ray Emission (SRIXE) * | X26A

K. Jones (BNL) and S.-R. Song (Nat'l Taiwan U. Taipei and BNL)

The Port of NY/NJ is naturally shallow and, as a result, dredging is required in order to ensure the economic viability of the Port. Port operations contribute some 20,000,000,000 dollars and about 200,000 jobs to the regional economy. Loss of shipping volume to other ports could thus have a major impact on the regional environment and its prosperity.

The total volume of dredged material generated each year is on the order of 2,000,000 to 6,000,000 cubic yards. A major portion of the material is contaminated with organic and inorganic compounds which render it unacceptable for ocean disposal. Several alternate disposal methods are now being utilized including use of borrow pits, confined disposal facilities, solidification/stabilization followed by upland disposal. In addition, removal of contaminants using physical/chemical washing techniques, thermal desorption, and high-temperature thermal destruction is of great interest.

The X26A x-ray microprobe is being used to make measurements on individual sediment particles in order to understand the distribution of the contaminants in both the as-dredged materials and in the processed materials. Information on the grain-size distributions can be employed in assaying the effectiveness of the decontamination methods used and in understanding possible long-term environmental impacts resulting from the final disposal site selected. The x-ray probe is able to work with spatial resolutions of about 10 micrometers and detection limits of about 10 fg for the elements of interest.

We are currently carrying on determinations of elemental concentrations as a function of particle size in the as-dredged materials from Newtown Creek and Newark Bay. Measurements are also made using conventional bulk chemistry on size fractions obtained with wet sieving. In addition, we are investigating the changes in the distributions following application of physical washing with high pressure water jets to remove surface organic materials combined with use of a chelator to extract metals in the bulk materials. We find that a substantial number of the particles are highly enriched in one or more contaminant metals. Work is in progress to determine correlations between the metals and to determine whether the enrichments are specific to a particle type and to determine whether there is a surface enhancement to the distributions.

* Work supported in part by the US Department of Energy Contract No. DE-AC02-76CH00016 and by the US Environmental Protection Agency Interagency Agreement Nos. DW89941761-01-0 and DW89937890-01-0.

Secondary Ion Mass Spectroscopy and Synchrotron X-ray Fluorescence in the Study Of the Variation in Metal Content with Time in Tree Rings *	X26A

R. Martin, T. K. Sham (U. Western Ontario, Canada), K. Jones (BNL), and R. Protz (U. of Guelph, Canada)

The study of tree ring patterns, dendrochronology, is a well-established discipline which has been used as a measure of climate variation and other environmental events. Dendrodated tree rings provide ideal sources for radiocarbon calibration. Ring patterns have even been used to study the prehistoric transportation of construction beams.

Analysis of the metal content of tree rings (dendroanalysis or dendrochemistry) has the potential both for identifying pollution events such as metal contamination from mining operations and for providing a long-term chronology of the kinetics of metal deposition and uptake.

Dendroanalysis must be treated with caution since the mechanism of metal deposition in tree rings is poorly understood. Such questions as the mode and kinetics of metal accumulation in trees as well as the possibility of lateral migration of metals with wood have yet to be satisfactorily addressed. Contradictory results appear in the literature. It seems unlikely that the questions posed regarding the usefulness of dendrochemistry will be easily answered. Resolution of the contradictions may depend on obtaining answers to questions on whether or not selected elements are mobile in the soil, air, or the wood itself, or if mobility is concentration dependent.

We have begun an initial investigation of the topic by carrying out measurements on specimens from the Northern Black Spruce, Picea mariana, growing in peat in the Hudson Bay Lowlands. These samples were selected because good data exist on the local soil chemistry and the tree rings are very narrow (of the order of 0.16 mm) because of harsh growing conditions in the form of a short season and low nutrient availability.

The experimental approach has been to apply microbeam analytical methods based on secondary ion mass spectroscopy (SIMS) and synchrotron-radiation induced x-ray emission (SRIXE) to measure metal distributions as a function of radial distance on the wood samples. The two methods have complementary aspects in terms of the sample preparation and the volume of material analyzed.

Results from the two methods show a seasonal pattern for elements such as potassium, calcium, iron, and manganese, with maximum uptake generally at the beginning of the growing season. The patterns are of a nature that suggests that a significant fraction of each of these species is localized with individual growth rings and that if they are diffusing at all, it is at a rate that preserves the local enhancement for periods of at least a century.

* Research supported in part by the US Department of Energy Contract No. DE-AC02-76CH00016.

Energy-Selective Fluorescence Mapping of Zinc in Zebrafish Embryos *	X26A

K. Peariso, F. Su, J. Kuwada, and J.E. Penner-Hahn (Michigan)

Zinc has long been recognized to be an essential element in embryonic development. Zebrafish (*Danio rerio*) embryos have been reported to contain large amounts of zinc at the time of fertilization, approximately 1 mM [Berg, personal communication]. XANES measurements on whole embryos at various stages during early development have shown significant changes in the bulk zinc environment. Using the NSLS X-ray microprobe at X26A, we have performed energy-selective, two-dimensional maps with 45x40 um^2 resolution on zebrafish embryos at four separate stages spanning the first eight hours after fertilization (1-cell, 128-cell, high, and 75% epiboly). Analysis of these maps will allow us to determine the spatial and temporal changes of different zinc environments that give rise to the changes we have observed in the XANES measurements on the whole embryo. Characterization of these changes will aid in our ability to define the role of different types of zinc environments in embryogenesis.

* Supported in part by the NIH, GM-38047 (to JEPH).

Determination of Zinc Content of Poliovirus Protein 2C Expressed in *E. coli* * — X26A

T. Pfister, E. Wimmer (SUNY at Stony Brook), and K. W. Jones (BNL)

The family Picornaviridae includes the genera Enterovirus, Rhinovirus, Aphthovirus, Cardiovirus and Hepatovirus. Each genus contains pathogenic species causing a bewildering array of disease syndromes in humans and animals. In contrast to the diversity of diseases caused by picornaviruses, the molecular mechanisms by which these viruses replicate appear to be similar. Poliovirus, which belongs to the genus Enterovirus is one of the best studied viruses among the picornaviruses and can be considered as the prototype picornavirus in many aspects. The non-enveloped icosahedral capsid of poliovirus contains one molecule of single-stranded positive-sense RNA of 7.5 kb. During infection, the RNA is translated into one polyprotein which is co- and posttranslationally processed to give rise of more than 20 functional proteins. The structural proteins are the building blocks of the progeny virions. The non-structural proteins include three proteinases responsible for polyprotein processing. Most non-structural proteins are involved in RNA replication. Among them, the RNA-dependent RNA polymerase 3Dpol is the best studied protein. Genetic analysis and the use of specific inhibitors have revealed that protein 2C is required for RNA replication. The function of 2C in regard to RNA replication is not known. Several properties of 2C have been demonstrated: RNA binding, ATPase/GTPase activity, and membrane association. It has been proposed that 2C may belong to the superfamily III of RNA helicases. However, no helicase activity of 2C has yet been demonstrated. Protein sequence comparison revealed a conserved cysteine-rich region in the COOH terminus of protein 2C of entero- and rhinoviruses. In poliovirus, the sequence is: 269 CKNCHQPAN-FKRCCPLVC 286. The pattern of cysteine (C) residues in the cysteine-rich region resembles the pattern of the C2C2 type zinc finger motif. In C2C2 type zinc fingers four C residues bind one zinc ion by coordination. Zinc finger motifs have been shown to mediate the binding of a protein with nucleic acids, proteins, or lipids. Methylation of poliovirus protein 2C with iodoacetamide revealed that the C residues are available for methylation and thus neither oxidized nor involved in disulfide bonds in the infected cell. We are using synchrotron x-ray fluorescence in order to find out whether the cysteine-rich region of poliovirus 2C contains zinc. Either full length 2C or the cysteine-rich region of 2C are expressed as fusion proteins with glutathione S-transferase (GST) in E. coli. The fusion proteins are affinity purified using glutathione-charged Sepharose beads (Pharmacia, Uppsala, Sweden). Purified proteins are spotted and dried under vacuum on AP1 membranes (Process Analytics, Orem, Utah, USA). The measurements are done on the X26A x-ray microprobe beam line. Preliminary results indicate that the cysteine-rich region contains zinc. The same region in which all cysteines have been replaced by serines, contains approximately four times less zinc. We are currently determining the sources of zinc and other metal ions by measuring relative metal concentrations in bacterial culture media and buffer solutions used during protein purification. This will allow us to express and purify GST fusion proteins under defined relative metal concentrations leading to a more accurate determination of zinc content in GST fusion proteins expressed in E. coli.

* Research supported in part by US Department of Energy Contract No. DE-AC02-76CH00016.

Elemental Microanalysis and Elemental Mapping on Biological Tissues * — X26A

R. Rizzo and F. Vittur (U.Trieste, Italy)

Alginate gel beads are used to immobilize cells for a number of fermen- tation processes. The suitability of the immobilisation technique depends on the microscopical gel strength. For alginate the above property depends on the calcium distribution. In fact, calcium is the gelling -inducing agent in alginate systems. We investigated gel beads as large as 0.7 mm with a resolution of 20 microns. the data obtained showed that calcium is not homogeneously distributed across bead sections exhibiting the highest concentration at the bead surface. In addition to this, microbeads obtained in different calcium concentration conditions were investigated to get information about the influence of the calcium concentration on the ion distribution into gel. The experimental data were compared with theoret- tical expectations obtained by means of mathematical models of gel formation. Beads obtained in the presence of two different divalent cations were also investigated in order to study the influence of a second cation on the calcium distribution. Preliminary investigations on ion content and distribution in Lichens were per formed with the aim to evaluate these organisms as biological sensors for en vironmental pollution detection.

SRIXE was also used for studies on both porcine articular cartilage and human and porcin osteonic bone. As far as articular cartilage is concerned, sulfur (as sulfate ester) is a minor component of the proteoglycans present in cartilage. In a first set of experiments sulfur distribution was studied in samples of habi tually loaded and habitually unloaded articular cartilage. In the loaded tissues, sulfur concentration increased regularly from the articular surface to the sub- chondral bone while in the unloaded cartilages sulfur concentration gained its maximum in the central part of the sample. These data proved that proteoglycan concentra- tion is not a parameter which could influence the laminar appearance of articular cartilage. In a second set of experiments, sulfur distribution was studied as a probe of a de novo synthesis of proteoglycans by isolated chondrocytes implanted in an alginate gel in experimental chondral defects. A neo-synthesis of proteoglycans during the repair of cartilage was observed.

As far as bone is concerned, we studied the distribution of zinc in human and porcine bones at the level of the Haversian system (osteons), which are the functional elementary units of the secondary bones. We observed a relatively high concentration of zinc in the central part of the osteon near the boundary with the central canal. These results will be compared with hystological detection of zinc in the same tissue i order to obtain a correlation between zinc distribution and the distribution of the enzyme Alkaline Phosphatase, the zinc-containing en- zyme responsible for the initial mineralization of the tissue.

B. Thu, G. Skjak-Braek, F. Micali, F. Vittur, R. Rizzo. Carbohydr. Res. 297 (1997) 101-105.

E. Fragonas, V. Mlynarik, V. Jellus, F. Micali, A Piras, R. Toffannin, R. Rizzo, F. Vittur. Osteoarthritis and Cartilage. In press.

* Work Supported by the Italian Ministero dell'Universita' e della Ricerca Scientifica e Tecnologica and the U. of Trieste.

Reduction Of Soil Mn Oxides During XANES Studies | X26A

D.S. Ross, H. C. Hales (U. of Vermont), and G. Shea-McCarthy (U. of Chicago)

Soil Mn oxide surfaces are important sites for the redox reactions of other metals and organics. XANES spectroscopy is a useful tool for understanding soil Mn oxide behavior. However, sample preparation may affect results. Drying a soil lowers its capacity to oxidize added Cr(III) and increases extractable Mn(II), strongly suggesting drying-induced oxide reduction. To avoid the effects of drying, we wished to examine moist soil samples with XANES spectroscopy. Preliminary studies were undertaken to investigate the effect of x-ray beam exposure on the Mn oxidation state of moist, high-Mn soils. Repeated scans were obtained on one spot using normal analytical conditions. For most soils studied, the absorption edge moved about 1 eV lower within three to four scans. For example, Figure 1 shows repeated scans (35 minutes in length) of a moist, high-Mn soil from Charlotte, Vermont. This same soil showed continuous reduction during ten repeated 8-minute scans. It is interesting to note that, contrary to expectations, dried samples of high-Mn soils were as or more oxidized than their moist counterparts. Research will continue to ascertain the exact cause of the reduction and possible methodologies to avoid it.

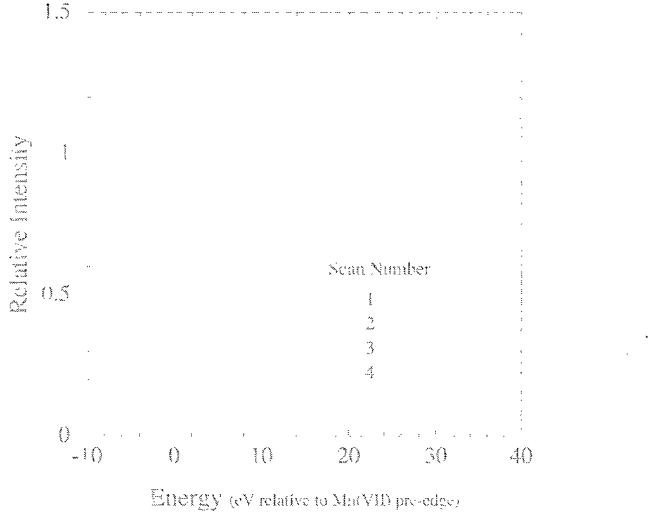

Figure 1. Repeated XANES scans on a moist, high-Mn soil ("supersoil").

Role of Manganese and Associated Trace Element Chemistry in Plant Diseases * | X26A

D. G. Schulze, C. A. Guest, I. A. Thompson, A. Scheinost, and D. M. Huber (Purdue U.)

The redox chemistry of soil manganese plays an important role in Mn uptake by plants, the movement through soil of trace elements absorbed on or occluded in Mn-oxide minerals, and the etiology of some soil-borne plant fungal diseases. We are using micro x-ray absorption near-edge structure (XANES) spectroscopy on beamline X26A to study Mn redox chemistry in situ, both in bulk soils and in the rhizosphere of live plants. Our work this year has focussed on: (1) detecting and quantifying Mn^{2+}, Mn^{3+} and Mn^{4+} in mixed systems, (2) correlating sequential chemical extraction of Mn with changes in the Mn K XANES spectra of soils, and (3) developing techniques for using micro-XANES spectroscopy to measure Mn oxidation state in the rhizosphere of live plants growing in soils.

XANES spectroscopy of mixtures of $MnSO_4$ (Mn^{2+}), a Mn-substituted goethite (Mn^{3+}), and a synthetic Na-birnessite (Mn^{4+}) show that the crest of the x-ray absorption edge for Mn^{3+} occurs between the crest for Mn^{2+} and Mn^{4+}, as expected. We are attempting to develop approaches for quantifying Mn^{2+}, Mn^{3+}, and Mn^{4+} in these mixed systems.

NH_4-acetate, $CuSO_4$, hydroquinone, and dithionite-citrate-bicarbonate were used to sequentially extract increasingly less soluble fractions of manganese from the surface horizon of a soil cropped to wheat. A XANES spectrum of the soil paste was obtained after each step. Initial data analysis suggests a sizable presence of Mn^{3+} in the sample.

Sample cells are being developed to measure XANES spectra in the vicinity of live plant roots growing in soils. We are still testing and evaluating various designs.

* This research is supported by the USDA National Research Initiative, Grant number 96-35107-3183.

Performance of Kirkpatrick-Baez Microfocusing Mirrors on the X26A Microprobe	X26A

S.R. Sutton, M. L. Rivers, P. J. Eng, and G. Shea-McCarthy (U. Chicago)

The microprobe at beamline X26A at NSLS experienced a major upgrade with the installation in May, 1997, of microfocusing Kirkpatrick-Baez mirrors. The Kirkpatrick-Baez optics have the advantage of large working distances (50 mm from the downstream end of the second mirror), achromatic operation (5 - 60 keV), i.e. no refocusing is required as the monochromator energy is scanned, and fixed offset. The dual mirror system consists of trapezoidal, float-glass, Au-coated mirrors (100 mm long) which are dynamically bent to elliptical shapes using a mechanical bender. The complete assembly has a footprint of about 0.1 square meters and is easily accommodated on the 0.7 x 1.0 m breadboard holding the remainder of the x-ray microprobe apparatus (sample stage, optical viewing microscope, x-ray detectors). A long trace profiler was used to measure the RMS surface roughness of the glass prior to coating. The horizontal and vertical mirrors used here gave values of 7 and 9 microradians, respectively. At X26A (9 m from source), these mirrors operated at 5 mrad focused a 400 x 400 micrometer white bending magnet beam down to 10 (vertical) x 15 (horizontal) micrometers (FWHM) resulting in a gain (flux/square micrometer) of about 1000 over a pinhole. This compares with the source size limits for this geometry at X26A of 3 (vertical) and 14 (horizontal) micrometers. Thus, nearly ideal performance was achieved with the horizontal mirror whereas the demagnification of the vertical mirror was somewhat less than ultimately achievable. Further reductions is beam size will be achieved with higher quality mirrors (e.g., polished glass or silicon). This new capability particularly enhances the sensitivity of the microprobe for microspectroscopy applications.

Eng, P. J., M. L. Rivers, B. X. Yang and W. Schildkamp (1995) Microfocusing 4-keV to 65-keV x rays with bent Kirkpatrick-Baez mirrors. Proceedings SPIE 2516, 41-51.

Yang, B. X., M. L. Rivers, W. Schildkamp, and P. Eng (1995) GeoCARS microfocusing Kirkpatrick-Baez mirror bender development. Rev. Sci. Instrum., 66, 2278-2280.

Correlated Synchrotron XRF, MicroXANES and Electron Microprobe Analysis on Individual, $\ll$10 Micrometer, Pb-bearing Particles from Contaminated Soil	X26A

S. R. Sutton, I. M. Steele (U. of Chicago), S. Traina and V. Laperche (Ohio State U.)

The goal of this work is to apply electron and x-ray microprobe techniques to the individual Pb-bearing particles in natural and treated contaminated soils in order to obtain detailed information on mineral associations, elemental associations, and speciation of Pb. To date, we have applied this approach to a Pb-contaminated soil from Oakland CA. The particles consist of mineral fragments and aggregates at the 1-10 micron scale. The analysis procedure was to obtain an electron microphotograph of a 200x200 micron region of the mount, analyze 20 particles at random within this area by electron probe and then obtain trace element measurements and Pb L XANES on these same particles using the x-ray microprobe.

The electron probe results showed that about half of the particles in the 1- 10 micron size range are "pure phases" and about half are aggregates. In the raw soil, Pb occurred in both pure phases and aggregates. Initial, correlated synchrotron XRF (SXRF) and Pb LIII XANES measurements were made on some of these particles using Kirkpatrick- Baez microfocusing mirrors recently installed at X26A (see accompanying abstract). Meaningful XAFS studies (i.e., on pure phases) requires analyses at the micrometer scale which was only possible using the KB mirrors. The figure below shows one such result for particle 9 (5 micrometers) from the untreated soil. Electron probe results showed this particle to be dominated by Pb with minor Si and Ti. The SXRF spectrum shows many other elements are also present at trace levels. The Pb XANES spectrum is qualitatively similar to that of metallic Pb. Detailed data analyses are in progress.

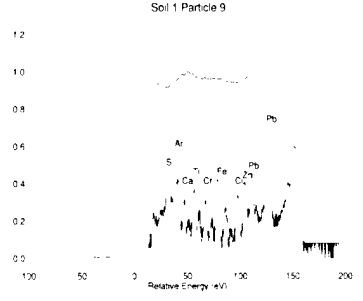

Figure 1. Synchrotron XRF spectrum and associated Pb LIII XANES spectrum for a 5 micrometer particle from a Pb contaminated soil. The XRF spectrum is displayed with a logarithmic vertical scale. The energy scale refers to the XANES spectrum.

Selenium XANES Spectra of Algal Slurries	X26A

T.K. Tokunaga (LBNL), T. Lundquist, M. Zarate, W. Oswald, B. Green (U. California), S.R. Sutton and G. Shea-McCarthy, (U. Chicago), P. Nuessle (U. Georgia)

Elevated concentrations on selenium in agricultural drainage waters in the western San Joaquin Valley of California have been responsible for wildlife deaths and deformities in wetlands receiving such contaminated waters. An algal- bacterial treatment process has been developed by the Applied Algal Research Group, to remove Se from agricultural drainage waters. Knowledge of the speciation of Se among its possible oxidation states is important since its mobility and toxicity are very dependent on its chemical form. The forms of Se accumulated in the reducing algal slurries have not previously been identified by direct methods. In this investigation, X-ray absorption near-edge structure (XANES) spectroscopy was used to determine oxidation states of selenium in algal slurry samples obtained from laboratory chemostats. The XANES of model compounds (elemental Se, seleno-cystine, Se-methionine, sodium selenite, and sodium selenate) were collected for later comparison with algal slurry samples. The XANES of two algal slurry samples showed that Se, which was originally primarily in the +VI oxidation state in drain waters, was reduced to organo-Se and elemental Se forms. Linear combination fits with Se-cystine (R-Se-Se-R) XANES as the dominant component (best fits with 65the two samples), with secondary contributions from Se(0), provided the closest matches to the spectra of algal slurries. Air-drying resulted in algal slurry XANES which were better fit with increased proportions of elemental Se (35and 50algal slurries occurs as a mixture of several organo-Se forms and Se(0). Inclusion of additional model compounds in future comparisons will be useful. The best fit compositions reported here should only be interpreted as showing that Se(VI) was reduced to a mixture comprised primarily of organo-Se forms, with a smaller fraction as Se(0). In future studies, we will examine XANES of algal slurries at various stages along the drainwater treatment process.

Selenium Diffusion and Reduction at the Water-sediment Boundary	X26A

T.K. Tokunaga (LBNL), S.R. Sutton, G. Shea-McCarthy (U. Chicago), S. Bajt (LLNL), and P. Nuessle (U. Georgia)

Mechanistic understanding of trace element cycling between surface waters and sediments can require highly spatially-resolved information at water-sediment boundaries, especially when reactions are involved. Such fine-scale information is not obtainable by conventional sampling and analytical methods. This study demonstrates the application of micro- X-ray absorption near edge structure (micro-XANES) spectroscopy for obtaining such direct, in-situ, spatially- and temporally-resolved information for selenium. The experiments determined the fate of soluble Se(VI) ponded over water-saturated sediments under two different conditions, one oxidizing and the other reducing. One sediment system was maintained oxidizing by the presence of excess nitrate, while the reducing sediment was nitrate-deficient and amended with organic matter. Redox conditions were monitored in each system via arrays of Pt microelectrodes. Scanning micro-XANES analyses showed Se(VI) removal from ponded waters by diffusion into sediments. The oxidizing system exhibited purely diffusive transport, without Se reduction. The diffusion profiles were well-matched by a finite-difference numerical simulation. In the reducing sediment, Se(VI) was transformed to insoluble Se(0) without significant formation of the intermediate Se(IV). Zones of accumulation of insoluble Se(0) were heterogeneously distributed. These results show that the scale over which volume averaging of chemical species is performed at sediment-water boundaries must be selected carefully, and that the spatial resolution offered by micro-XANES is well-suited for these types of investigations. By combining our measurements on these hydrostatic systems with seepage rates characteristic of ponded sediments at Kesterson Reservoir (California), we obtain model predictions of Se distributions in sediments which are consistent with field data from that contaminated wetland.

Electromigration-induced Stress Measured by Real-time X-Ray Microdiffraction | X26C

G. S. Cargill III, P.-C. Wang (Columbia U.), I. C. Noyan, C.-K. Hu (IBM Research)

White beam Laue microdiffraction with a Si(Li) detector has been used for strain measurements on passivated aluminum conductor lines with 10 microns spatial resolution. Real-time measurements were made of strains developed during electromigration using a symmetrical reflection geometry to take advantage of the (111) fiber texture of the aluminum films. On-chip tungsten pads were used as "internal" diffraction standards to correct for angular or energy calibration shifts during the experiments. By measuring differences in d-spacings with time at many locations along 200 micron long lines, the strains developed during electromigration could be measured with greater precision than the absolute d-spacings. The precision of the individual d-spacing measurements was limited by uncertainties in diffraction angles, since only a few grains diffracted into the detector aperature at each location along the line. An example of the d-spacing changes at different locations along a conductor line caused by passing 1.4 x 10^5 A/cm^2 through the line at 260°C for nine hours is shown in Fig. 1, together with the biaxial stresses in grain boundaries deduced from the d-spacings. Values of the stress gradients, e.g. the slope of the dashed line in Fig. 1, were determined for different current densities and times, and these are shown as data points in Fig. 2, together with results from model calculations which are shown as lines for three different values assumed for the effective diffusion coefficient D_{eff}. Good agreement is obtained for the intermediate value of D_{eff}. Electromigration-induced strain measurements are continuing for other line lengths and widths, for other conductor line metals and alloys, and for other passivations.

This work was supported by NSF grants DMR-9530043, DMR-9625887, and DMR-9708003, and by IBM Research.

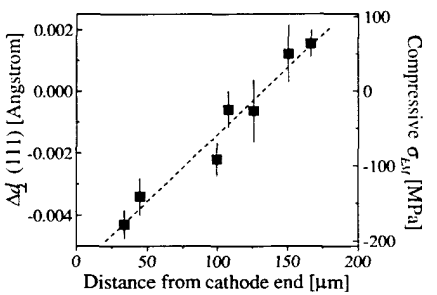

Figure 1. Changes in d-spacing resulting from electromigration-induced stresses, as described in the text. The dashed line is a linear fit to the data points to determine the stress gradient.

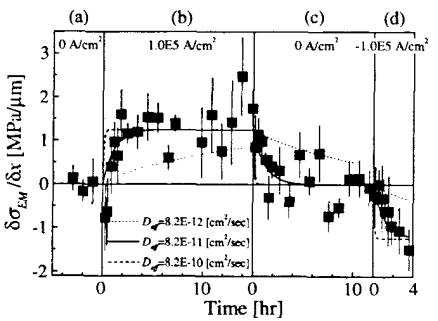

Figure 2. Stress gradient produced by electromigration with different current densities and times, as described in the text. The dotted, solid, and dashed lines are calculations using the different values of $D_{(eff)}$.

X26C Beamline Upgrades for Protien Crystalography | X26C

G. Shea-McCarthy (U. of Chicago)

The X26C protien crystallography program has been expanded to include new PRT members from Cold Spring Harbor Laboratory and the University of Stony Brook. In a collaborative effort with BNL Biology, NSLS RD and Univ. of Chicago BioCARS, the X26C beamline has undergone numerous upgrades.

These upgrades were inclusive of the installation of a water cooled Si(111) monochromator, white beam stop, photon shutter and double exit berillium window. These improvements involved moving the 1:1 focusing mirror further downstream, decoupling the X26C beampipe from the X26A hutch and upgrading lead shielding. This hutch now has the ability to accept a wide white beam (40mm wide x 6mm high), focused white, direct monochromatic, or focused monochromatic beam.

In addition to mechanical upgrades, a MAR detector system has also been installed. Although the BioCARS Fuji scanner is still available for use, the MAR detector has the advantage of using a single image plate which is scanned and erased in a compact pre-aligned unit. The computer system for controlling the X26C beamline has also been upgraded to accomodate the MAR. Two Silicon Graphic Indigo II workstations and one Pentium Pro have been installed to support the MAR software, GRACE (motor control program), and IDL.

Currently a new lift table is also being constructed to support the MAR. Future upgrades will include the addition of a Kappa-goniostat and a better mirror. The existing mirror is coated with Platinum with a high energy cutoff of 11.56 Kev. The possibility of recoating the mirror with Rhodium is being considered. The Kappa-goniastat will permit arbitrary orientation of the sample and two theta inclination of the detector. The new goniometer orientation will also provide a much longer crystal to detector distance, up to one meter.

X-ray Crystallographic Structure of Aminopeptidase from *S. griseus* | X26C

G. Shoham (SUNY at Stony Brook, & Hebrew U., Israel)

Streptomyces griseus aminopeptidase (SGAP) is one of the many enzymes that are present in the extracellular fluid of cultures of this bacterium. It is relatively small (30 kDa), monomeric, heat stable, requires two zinc atoms for activity, and is activated by calcium. The heat stability of the enzyme affords relatively simple isolation from the rest of the enzymes found in Pronase. The enzyme is specific for large hydrophobic amino acids. No cleavage occures if the following residue is proline. These properties make the enzyme an attractive tool for use in two stage assays of other peptidases in diagnistic applications. Low molecular weight, heat stable aminopeptidases like SGAP were proposed as tools for biotechnological applications in processing recombinant DNA proteins and fusion protein products.

The X-ray crystal structure of SGAP has been recently determined by a combination of diffraction studies from both synchrotron and rotating anode X-ray data. The native, double-zinc form of the enzyme has been determined to 1.75A resolution, the apo-enzyme (zinc removed) has been detrmined to 2.1A resolution, and the mercury replaced enzyme has been determined to 2.0A resolution. Data collected on the X26C beamline at BNL/NSLS was especially critical recently in the extention of the structure of the native enzyme to higher resolution as well as to determine the structure of the enzyme with a substrate analoge. This information is unique and extremely important for the determination of the, still unknown, mechanism of catalysis of SGAP as well as other double zinc enzymes.

The protein consists of a central beta-sheet made up of 8 parallel and antiparallel strands, surrounded by helices on either side. The active site is located at the carbonyl ends of two middle stards of the beta-sheet region. The active site contains two zinc cations, each with similar similar ligands, at a distance of 3.6A from each other. A calcium binding site has been identified, consistent with the observations that calcium modulates the activity of the enzyme. The mechanism by which the calcium cation affects enzyme activity is not apparent, since it is located about 25A from the zinc atoms of the active site. This and other mechanistic issues of SGAP are now under study.

Time-resolved Laue Crystallographic Studies of Isocitrate Dehydrogenase | X26C

B. L. Stoddard, J. Bolduc, D. Dyer (FHCRC), W. G. Scott (MRC), M. Brubaker, B. Cohen, A. Mesecar, D. Koshland (UC Berkeley), R.M. Sweet (NSLS)

Obtaining detailed atomic structural information about intermediate states along an enzyme reaction pathway is problematic, because the lifetime of these intermediates are generally several orders of magnitude shorter that the time necessary for collection of a complete data set. Several promising methods are currently being pursued to overcome this limitation. These include the use of cryological temperatures to physically trap specific intermediate states, chemical trapping, and the development of Laue diffraction as a method to decrease the time needed to collect high resolution data sets from protein crystals.

In the previous year we demonstrated the possibility of using site-directed mutagenesis for crystallographic visualization, by trapping specific reaction intermediates formed by isocitrate dehydrogenase in a steady-state complex (Bolduc, et al. (1995) Science 268: 1312; Stoddard et al. (1996) Nature Struct. Biol. 3 (7): 590). We now report time-resolved visualization of the rate-limited intermediate complex formed by the wild-type enzyme. For this experiment, single-turnover events were triggered throughout the crystal using flash-photolysis of a variety of caged substrate and caged cofactor molecules, and data was collected on a millisecond time-scale. Clear difference Fourier maps were produced of the enzymic complex when a caged triggering molecule was used that binds in the active site prior to photolysis.

X-ray Topography and Reciprocal Space Mapping of Protein Crystals	X26C

V. Stojanoff (ESRF, France), T. Boggon, J. Helliwell (U. Manchester, England), and E. Snell (NASA)

A variety of protein crystals were studied using triple-axis diffractometry and monochromatic beam topography. Both space-grown and earth-grown crystals were studied in order to shed light on the potential benefits or otherwise of zero-gravity crystal growth. The experimental arrangement consisted of an unfocussed beam monochromatized by a silicon (111) monochromator, together with a six-circle goniometer. The instrument was operated as a triple-axis spectrometer using a 2-reflection channel-cut analyzer. Diffraction spots to be analyzed were chosen from the resolution shell around 3.5 angstroms, so as to minimize any smearing effects due to wavelength dispersion. Using this setup it was possible to seperate the effects of mosaic spread and d-spacing variations. Indexing of the patterns was achieved by collecting one rotation frame on an imaging plate and indexing the resulting pattern using Denzo. The crystals studied showed a wide range of behaviours, from extremely sharp patterns in both directions of reciprocal space, to very ill-defined peaks broad in both directions. Topographic images were then collected at several points on the omega rocking curve to try and learn something about the nature of the defects giving rise to these properties.

References:

Minor, W. (1993). XDisplayF computer program. Purdue Uninersity, USA.

Otwinowski, Z. (1993a). Oscillation data reduction program, Proceedings of the CCP4 study weekend, edited L. Sawyer, N. Issacs & S. Bailey, pp.56-62. UK: SERC.

Otwinowski, Z. (1993b). Scalepack program. Yale University, USA.

Mosaic Spread and X-ray Topography of Protein Crystals	X26C

V. Stojanoff (ESRF, France), D. P. Siddons (NSLS) and J. Hirschler (Aerospatiale, France)

Turkey Egg White Lysozyme (TEWL) crystals grown under various conditions and containing various impurity levels were studied using monochromatic beam diffraction. Rocking curves were measured and high-resolution diffraction images recorded on film. The diffraction order was identified by recording a single oscilation diffraction pattern on a Fuji image plate. The indexing and integration of this pattern was done with the HKL package (Otwinowski, Z. 1993a; Otwinowski, Z. 1993b; Minor, W. 1993). Preliminary results showed that pure TEWL present a full width of half maximum (FWHM) rocking curve of the order of tenths of miliarcseconds while TEWL with various impurity levels present rocking curves with at least a 10 times higher FWHM. The topographs taken along the rocking curve are in agreement with this result. Multiple domains can be observed in TEWL crystals with different impurity lavels. It is hoped that this type of study will lead to an understanding of the defect structures and mechanisms in macromolecular crystals, and thereby lead to improved growth techniques and improved crystal structures.

References:

Minor, W. (1993). X-DisplayF computer program. Purdue University, USA.

Otwinowski, Z. (1993a). Oscillation data reduction program, Proceedings of the CCP4 study weekend, edited L. Sawyer, N. Issacs & S. Bailey, pp.56-62. UK: SERC.

Otwinowski, Z. (1993b). Scalepack program. Yale University, USA.

Crystallographic Studies of Biological Macromolecules	X26C

R.-M. Xu (Cold Spring Harbor Laboratory)

We have begun the using the newly installed MAR image plate detector system on beamline X26C. Operating in focused monochromatic mode we have been taking single crystal crystallography data over the past year. Numerous data sets from crystals of proteins, nucleic acids and protein-nucleic acid complexes have been collected. These crystallographic projects include structural studies of oligomeric proteases, transcriptional regulators, RNA splicing factors, and novel nucleic acid structures. Determination of several of these structures is currently on-going, using the high resolution and high quality data collected at X26C.

The x-ray energy for monochromatic x-ray crystallography at X26C is presently limited to less than 11.5 kev, due to the platinum coating of the focusing mirror. The mirror will have to be re-coated or replaced before the beamline can be seriously used for multiple anomalous diffraction experiments, which has become a frequently used approach to solve the phase problem in macromolecular crystallography. We hope to remedy the the wavelength limitation soon to allow full-fledged macromolecular crystallography operation at X26C.

X-Ray Computed Microtomography of Laser Drilled Holes in Composite Panels for Acoustic Attenuation in Aerostructures	X27A

D. Di Marzio, J. Clarke (Northrup Grumman); J. Ablett, B. Dowd, P. Siddons, B. Andrews (BNL)

Sound attenuation is a major concern in both military and commercial aerostructures. Arrays of microholes drilled into nacelles and other aircraft components can effectively muffle engine noise. The use of advanced composite structural materials present a new challenge for this sound reduction technology. In this project, an automated laser drilling system is used to produce hole arrays in graphite/bismaleimide composite panels. X-ray computed microtomography was used to nondestructively characterize the structure of an early trial 3 mil (76 m) diameter laser hole array in a 1 mm thick laminate. Figure 1 shows a 7 m thick computed density slice taken parallel to the composite panel surface (parallel to fiber lay-up). Light regions correspond to high density (low void content) and dark regions correspond to low density (high void regions). Each laser drilled hole (dark circle) is surrounded by a dark oval. The long axis of the ovals correspond with the direction of the graphite fibers. The fiber direction can be seen as parallel striations throughout the image (image corresponds approximately to a one-fiber layer). Surprisingly, the high void region (dark oval) induced by the laser drilling is displaced from the hole by approximately 100 m along the oval minor axis. Within the ovals are slightly darker regions suggesting minor laser damage, while at the edge of the holes the density increases. This indicates that at the edge and in the immediate vicinity of the hole the local structural integrity of the composite is maintained. We have demonstrated that x-ray computed microtomography is a highly effective tool for the nondestructive evaluation of processed graphite composite materials.

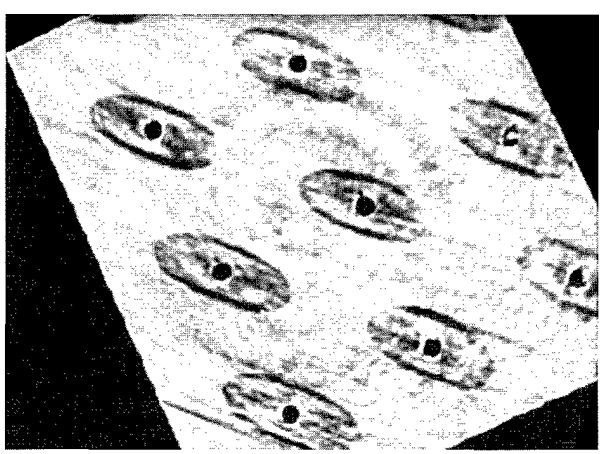

Figure 1. Reconstructed slice showing structural damage around laser-drilled holes: dim. of sample: 2 x 2.5 mm

X-Ray Computed Microtomography Studies on the Biodeterioration of Wood * — X27A

B.L. Illman (U. of Wisc. & Forest Products Lab.), B.A. Dowd (BNL), R.Holaday (BNL, currently at SPring-8, Japan)

Fungal degradation of wood structures causes substantial economic loss worldwide. The exact mechanism(s) of degradation are not clearly understood. X-Ray Computed Microtomography (CMT) is being used to characterize incipient structural changes that occur during the wood degradation process. Microstructures in solid wood were clearly delineated in CMT images with a resolution of 3 microns (Figure 1). The CMT images show well-defined spatial and size distribution of wood fibers. A quantitative measure of the internal microstructure of wood was obtained using the medial axis formalism developed by W.B. Lindquist [1]. Measurements were made of the microgeometry of wood structures to determine the pore spaces (porosity) and connected walls (connectivity) of wood fibers. Preliminary calculations of connectivity curves show that porosity and connectivity of the structures in wood can be measured to quantify changes in wood microstructure that occur during degradation.

[1] W.B. Lindquist,et al., J. of Geophys. Res. Sol. Earth, **B101**, 8297 (1996).

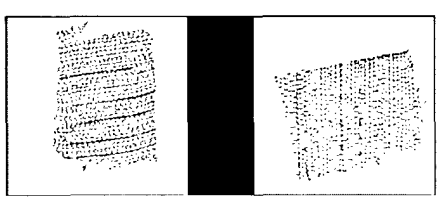

Figure 1. Reconstructed tomographic slices of control(left) and fungal degraded (right) wood.

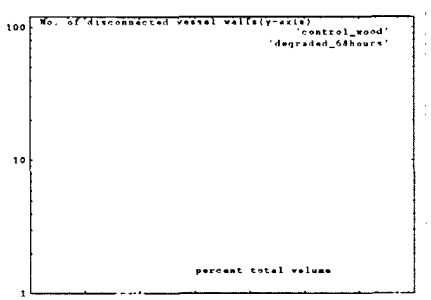

Figure 2. Disconnectivity curves for the vessel walls of control (solid) and degraded (dotted line) wood samples.

* Research supported by USDA grant 94-371031016.

Microtomography of a Boreal Forest Insect * — X27A

B.L. Illman (U. of Wisconsin, Madison, and Forest Products Lab.); B.A. Dowd (NSLS), R. Holaday (presently at SPring-8), and B. Andrews (BNL)

Computed microtomography (CMT) has been used to image one of the most damaging insects affecting North American boreal forests. The spruce bark beetle, Dendroctonus rufipennis (Kirby) has reached epidemic proportions in forests of Alaska. The beetle's ability to exploit the forest resource is augmented by their pheromonally mediated cooperative behavior, and their associations with microbial symbionts. The insect - microorganism complex is responsible for a disease on Alaskan trees that has killed over a million acres of trees. The goal is to use CMT to better understand the internal microstructure of the beetle and the vectoring system used by the insect to transport microorganisms into trees. Especially important is the nature and location of beetle - symbiont fungi. Tree - bark beetle - fungal systems offer an opportunity to evaluate the effects of ecological interactions across multiple spatial and temporal scales, across multiple trophic levels, and among diverse taxa. Understanding these relationships could greatly improve our ability to evaluate and devise appropriate forest management practices, and anticipate the impacts of multiple abiotic, biotic, and anthropocentric stresses. The CMT images provide information about the juxtaposition of circulatory, respiratory, cytoskeleton, and density-determined regions in the beetle.

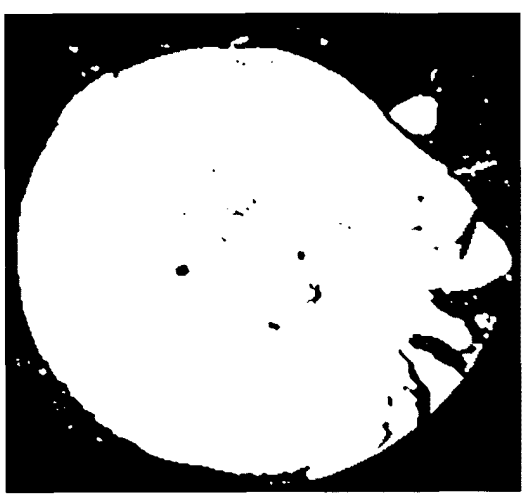

Figure 1. 2-D reconstructed tomographic slice through the eyes of the beetle.

* Research supported by USDA Forest Service.

Applications of Computed Microtomography *	X27A

K. W. Jones, B. Dowd, B. Andrews, A. M. Peskin, and P. Siddons (BNL)

We have carried out several exploratory investigations of applications of synchrotron computed microtomography (CMT). The work has been done at the X27A CMT facility. The equipment provides the capability of measuring tomographic volumes with 10^8 to 10^9 voxels with spatial resolutions down to about 3 micrometers. Four applications are described below.

1. The microstructure of fractures in rocks is important for understanding of fluid transport calculations for petroleum recovery or for transport of pollutants. We are now working on the characterization of a fracture in a 1.3 cm diameter rock. Initial data have been obtained with a resolution of about 10 micrometers. Measurements will also be made using a laser or direct mechanical profiler on the surfaces of the separated rock in order to verify the tomographic results.

2. CMT is being used to determine the microgeometry of sediments taken from the Port of NY/NJ. The sediments are basically a gel with a solids content of about 35sizes less than 3 micrometers. We are making measurements to determine the structure of the particles on the grain-size scale. The results will be used to construct models for the sediments which can be used as the basis for calculations of contaminant transport through the sediments. Experiments to measure fluid transport through the sediments will be initiated shortly.

3. Measurements have been made on glass fragments under study at Pacific Northwest National Laboratory for use in radioactive waste disposal. CMT provides a non-destructive analytical method for following degradation of the glass surfaces resulting to interaction with fluids. Initial results were encouraging and have given insights into improved methods for design of the reaction chamber used in exposing the glass to the liquid.

4. Measurements of structures in organic materials are of interest in several fields. We have carried out one measurement on polymers using a sample of a standard diaper. The polymer structures were clearly resolved and show that CMT should be useful in studying the structures of fibers in a variety of applications. For example, CMT can be combined with x-ray microbeams and secondary-ion mass spectrometry (SIMS) to relate wood morphology to uptake of metals into the growing wood. This is being carried out in collaboration with a group from the University of Western Ontario.

* Research supported in part by the US Department of Energy Contract No. DE-AC02-76CH00016, Office of Energy Research, Advanced Computational Technology Initiative and Office of Basic Energy Sciences Division of Engineering and Geosciences and the US Environmental Protection Agency under Interagency Agreement No. DW89937890-01-0.

Characterization of Ultra-Light Weight Materials, Porous Metals, Using X-Ray Computed Microtomography	X27A

R. Schulte, R. Meilunas, A. Tobin, J. Papazian, T. Donnellan (Northrop Grumman), B.A. Dowd, D.P. Siddons, and B. Andrews (BNL)

Recent developments in porous materials have demonstrated the potential to achieve ultra-light weight metal structures at reduced cost using a solid-gas eutectic solidification process known as the Gasar process. The process is capable of producing controlled porosity in metals by influencing the size and shape of pores as well as the pore distribution. X-ray computed microtomography provides a means to assess the nature of the porosity of samples produced using the Gasar process. Quantitative evaluation of pore distribution, pore size and shape in these materials is important since they are key determinants of the mechanical properties.

Several samples were inspected with X-ray microtomography on the X27A beamline. The figure shows a 3-D volume section of an aluminum alloy sample rendered from the X-ray microtomography data. Information about the porosity such as pore shape, size, and distribution are obtained from the tomographic data and will be used to develop improved processing methods and models for the production of porous metals.

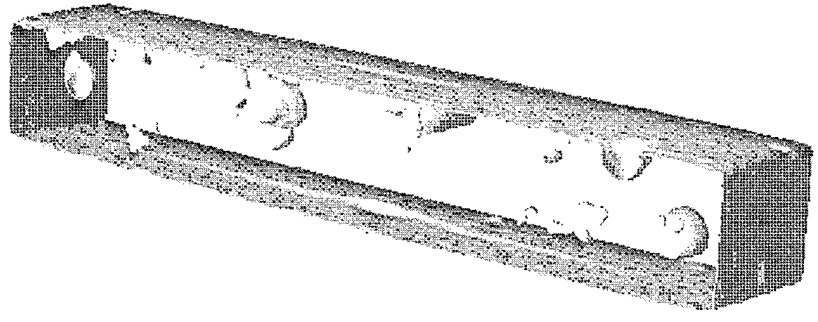

Figure 1. 3-D Rendering of porous aluminum: 1x1x3 mm.

Measurements of Morphology and Physical Properties of Bubble in Vesiculated Basaltic Rocks using X-Ray Computed Microtomography	X27A

S .R. Song (National Taiwan U., Taiwan), W. B. Lindquist (SUNY at Stony Brook), B. A. Dowd, D. P. Siddons, B. Andrews, and K. W. Jones (BNL)

Synchrotron X-ray computed microtomography (CMT) is applied to five pieces of basalt with different occurrences in order to determine the microgeometric structures and physical properties of vesicle. Two (Ba1 and Ba3) and one calcite-filling (Sr5) vesiculated lavas from South Africa and two reticulite tephras (Ba14 and Ba15) from the Lungkuan Volcano Group in northeast China have been examined by CMT on the X27C beam line. The voxel size varies from 10 to 20 microns depending on the chosen field of view of the tomographic instrument. A filtered back-projection algorithm was employed to the tomographic reconstruction, while the medial axis analysis of the tomographic volume to obtain physical properties of the bubble, e.g., vesicularity, size, connectivity, and specific surface area. Two- and three-dimensional images of these rocks clearly show that most of the bubbles are spherical shape, except the sample Ba1, with size ranging from hundreds A3gm to mm. The shapes of bubble in sample Ba1 are significantly irregular and have larger size variation. Original shape and mineral-filling history of bubble in Sr5 can also be clearly identified from the images. Medial-axis statistic analysis show that the vesicularity of these rocks vary from 45These results indicate that synchrotron X-ray CMT with medial-axis statistic analysis is a good nondestructive technique to quickly get the results of the morphology and physical properties of bubble in basaltic rocks. And, it is also a good method to study the properties of original bubbles of which they have been filled with secondary minerals.

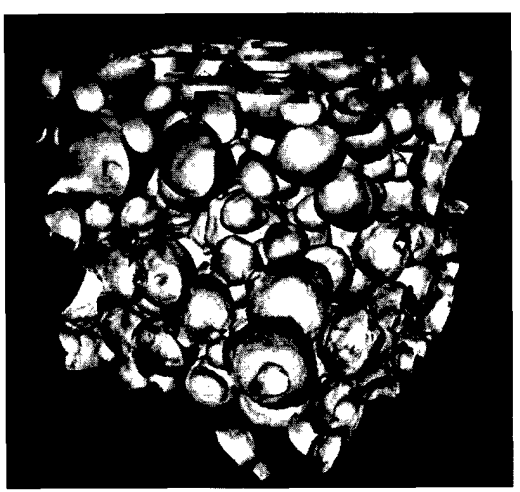

Figure 1. 3-D image of vesiculated basaltic lava: 3x3x3 mm.

X-Ray Computed Microtomography Study on Pumice	X27A

S. R.Song (National Taiwan U., Taiwan), W. B.Lindquist (SUNY at Stony Brook), B. A. Dowd, D .P. Siddons, and K. W. Jones (BNL)

Pumice is highly vesicular silicic to mafic foam, which will commonly float on water. It is a common product of explosive volcanic eruptions and an important component of many pyroclastic deposits and volcanogenic sediments. However, the measurements of physical properties of bubble are still scarce due to the limitation of technique. Synchrotron X-ray Computed microtomography can be used to image the internal structures and determine non-destructively the physical properties of pumice, such as shape, size distribution, deformation of bubble, thickness of bubble wall, vesicularity, connectivity, and specific surface area. The shape, size, deformation, thickness and vesicularity of bubbles are of interest, for example, in studying the mechanism of vesiculation and processes of magma degassing. Connectivity and specific surface area are important in understanding the floating, interaction with water and sedimentary processes. Seven pumice samples with different occurrence from the Changbeishan volcano of northeast China have been obtained to test the value of this approach. Initial CMT images show the well-defined 3D bubble shape, size distribution, deformation, connectivity and preferred orientation in pumice. A typical volume image is shown in the Figure. Further works using 3D medial-axis statistic analysis to quantitatively determine the properties of bubbles, such as vesicularity, connectivity, size distribution and specific surface area.

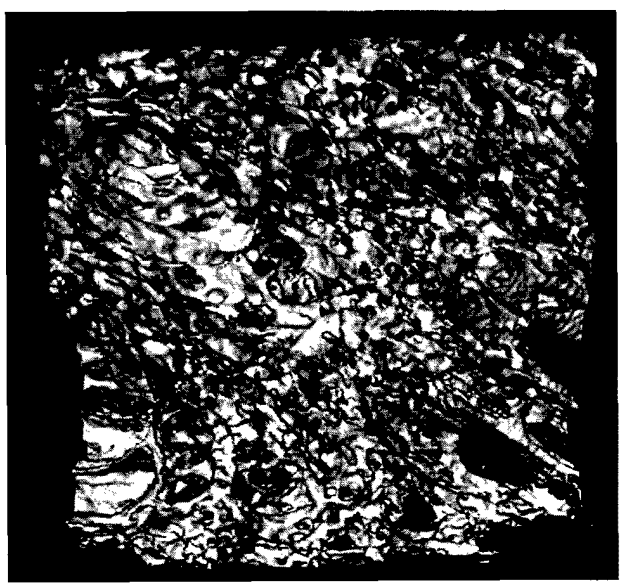

Figure 1. 3-D image of pumice: 3x3x1 mm

Conformational Defects in the Crystals of Low Molecular Weight Two-Arm Poly(ethylene Oxide) Fractions Crystallized from the Melt	X27C

E. Chen, G. Xue, B.-S. Moon, F. W. Harris, S. Z. D. Cheng (U. of Akron), B. S. Hsiao and F. Yeh (SUNY at Stony Brook)

Three two-arm poly(ethylene oxide) (PEO) fractions have been prepared by a coupling reaction. These PEO possess the same molecular weight of 2100 for each arm and the coupling agents used were para-(1,4-), meta-(1,3-) and orth-(1,2-) benzene tetracarboxylic acids. The two arms at the center of PEO molecules form thus an angle of 180, 120 and 60 degree, respectively. The coupling agents are defects at the chain center. They may substantially affect the two-arm PEO overall molecular conformation (OMC) in the crystal state. Differential scanning calorimetry results show that two populations of the crystals exist depending upon the crystallization conditions. Although WAXD powder patterns indicate that the fractions exhibit the same crystal structure disregarding the different coupling agents used, small angle SAXS experiments show two different long spacings corresponding to the two populations of the crystals. One of the crystal populations possesses an extended OMC in these two-arm PEO fractions, and one layer of defects is in between two neighboring lamellae. Another population of the crystals is consisted of an once-folded OMC. Therefore, two layers of the defects are included in between the neighboring lamellae. So the difference of long spacings is caused by the number of layers of the defects in these fractions as well as the phenylene group arrangements on the lamellar surfaces. The crystal with once-folded OMC represents the ultimate stable state compared to the crystal containing the extended OMC. With changing the types of linkage of these two-arms from 1,4- to 1,2-positions at the coupling agents, the population having the once-folded OMC increases in the samples under the same crystallization conditions.

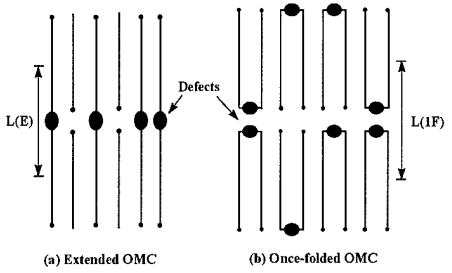

Figure 1. The Schematic diagram for the (a) extended and (b) once-folded OMCs. Note the long spacing L(1F) is larger than L(E).

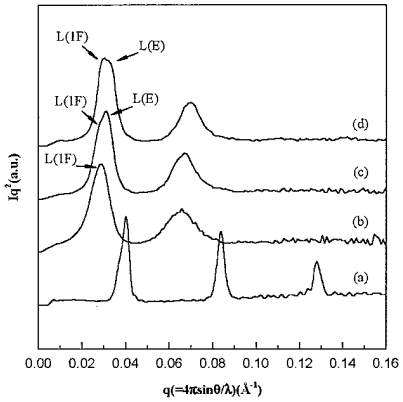

Figure 2. SAXS for the PEO fractions Crystallized at 48C, (a) linear parent PEO, (b) two-arm PEO with orth-linkage, (c)two-arm PEO with meta-linkage, and (d) two-arm PEO with para-linkage.

In-situ Crystallization Studies of Polybutylene Terephthalate (PBT) by SAXS/WAXD	X27C

Y. Gao, K. C. Sheth, S. Talibuddin, Y. Wang (GE), B. S. Hsiao, F. Yeh, Z. G. Wang (SUNY at Stony Brook)

Simultaneous small-angle X-ray scattering (SAXS) and wide-angle X-ray diffraction (WAXD) were used to study the crystallization process of polybutylene terepthalate (PBT) semi-crystalline polymers. Three GE commercial grade PBT materials, Valox195, Valox315 and Valox420, were chosen to study the impact of molecular weight and glass filler under both isothermal and non-isothermal conditions. A dual-cell jump unit was used to effect crystallization at different crystallization temperatures (Tc). At high Tcs (¿180oC), crystallization occurred isothermally whereas non-isothermal conditions similar to those encountered in injection molding were obtained at larger supercoolings. Time-resolved SAXS and WAXD data, at various degrees of supercooling, revealed respectively the morphological (crystalline lamellae) and crystal structure changes as a function of time.

Fig. 1 shows the long period, the average distance between adjacent lamellae, as a function of nominal isothermal temperatures for three PBT materials. These temperatures are equivalent to the wall temperatures in injection molding process. The general trend is that the long periods decrease as the degree of supercooling increases; in other words, thinner crystalline lamellae are formed at lower molding temperatures. At the same wall temperature, both Valox 315 and Valox 420, which have comparable molecular weights but are unfilled and 30Valox 195. Fig. 2 shows the rate of crystallization (as expressed by 1/tc where tc corresponds to the time at which the invariant, Q, plateaus out) as a function of nominal isothermal Tcs. As expected, lower molecular weight Valox 195 crystallized faster than higher MW Valox 315. Valox 420 had the highest crystallization rate, suggesting nucleation by the glass filler.

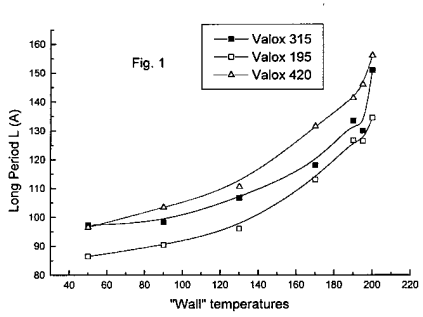

Figure 1.

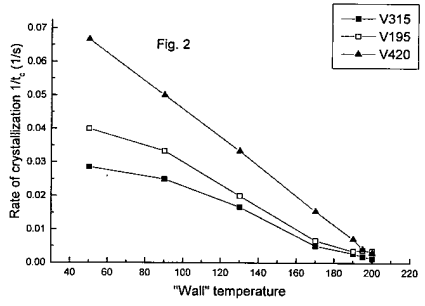

Figure 2.

SAXS Studies of Dendrimer Systems | X27C

T. J. Prosa, B. J. Bauer, and E. J. Amis (NIST)

Two-dimensional small angle X-ray scattering (SAXS) was used to probe the intermolecular and intramolecular structure within various dendrimer solutions. Poly(amidoamine) (PAMAM) and poly(propyeneimine) (DAB-dend-$(NH_2)_X$) dendrimers were examined in both dilute and concentrated solutions confirming reported results regarding molecular size and shape[1]. The availibility of increased accesible q range and incident flux extended both the quality and range of measured particle scattering curves, revealing additional scattering structure for the smaller dendrimer molecules.

The scattering from dilute solutions of dendrimers were used to extract the single particle scattering factors (P(q)) from dendrimers of various generations, resulting in direct information about the molecular size and intramolecular composition of these highly branched materials. For most of the larger generation materials (generation 7 for the PAMAM dendrimers), P(q) has an overall shape that very nearly matches the theoretical scattering curve for a constant electron density sphere.

$$P_{Sphere}(R_g, q) = 9[\frac{sin(v) - vcos(v)}{v^3}]^2, v = qR_g, R_g = \sqrt{\frac{3}{5}}R$$

This function has very distinct minima when $qR_g = \sqrt{3/5}(2n+1)\pi/2$ or when qR_g = 3.650, 6.084, 8.517, 10.951, etc... These minima are expected to disappear quickly when there is sufficient polydispersity in size and/or shape, or when the overall particle composition departs substantially from that of a hard sphere. In order to assess the particle shape of weakly scattering smaller molecules ($R_g \leq 25$ or generations ≤ 6), one needs the combination of large accessible q range and high X-ray flux which X27C provides. Preliminary results reveal higher order features are also present in PAMAM dendrimers of generations 5 and 6 as well as DAB-dend-$(NH_2)_X$ generation 5, suggesting that these dendrimers also take on a hard sphere shape.

[1] T.J. Prosa, B.J. Bauer, E.J. Amis, D.A. Tomalia, and R. Scherrenberg , *J. Polym. Sci.: Part B: Polym. Phys.*, **35(17)** (1997).

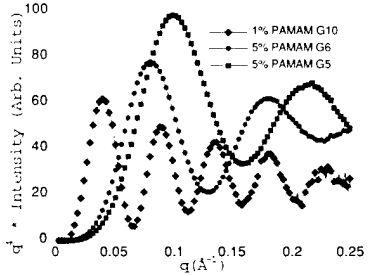

Figure 1. Dendrimer x-ray scattering scaled by q^4 for PAMAM generations 5, 6, and 10. Data has been corrected for empty beam, sample cell, and solution scattering.

Study of Structure and Morphology of PVDF Fibers Under Stress Using Synchrotron Radiation | X27C

J. Wu, J. M. Schultz (U. Delaware), F. Yeh, and B. Hsiao (SUNY at Stony Brook)

Poly(vinylidene fluoride) (PVDF) is a widely used piezoelectric material. Four crystalline forms of PVDF have been reported. The α form, or form II, can be prepared by crystallization from the quiescent melt under normal conditions. The β form, or form I, can be prepared by mechanical deformation of α form. Other crystal structures are prepared under special experimental conditions.

While the film properties of PVDF have been investigated thoroughly, studies on its fiber form are less prevalent. Moreover, the small angle scattering patterns of PVDF fibers have rarely been recorded and analyzed with its wide angle patterns. In this study, simultaneous wide angle and small angle x-ray scattering on PVDF fibers, spun under 4 different speeds, under step-increased strain, were carried out. The experiment was performed at Beamline X27c, NSLS. The 2D WAXD and SAXS patterns are recorded by Fuji^{TM} HR-V image plates(200x250mm) and digitized by a Fuji^{TM} BAS 2000 IP image plate scanner. The drawing unit is based on an Instron^{TM} model 4222. The experiment result will show the effect of strain on structural detail. The enclosed figures are from preliminary data analysis showing the crystal structure and the morphology of the undrawn as well as the fully extended fiber spun under 61m/min. They show the strain induced orientation and possible crystal structure change.

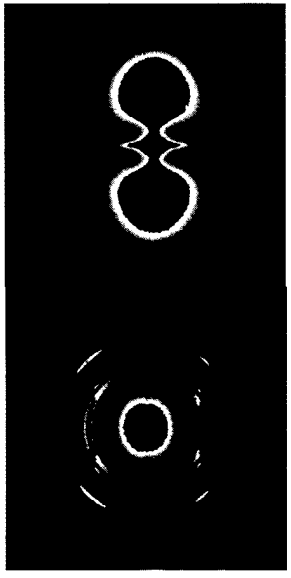

Figure 1. SAXS and WAXD Patterns, Strain=0

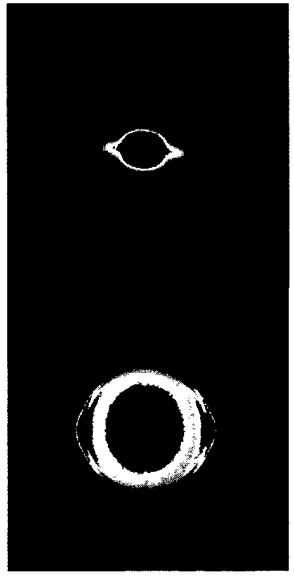

Figure 2. SAXS and WAXD Patterns, Strain=140%

Behavior of Microphase Separation in a Poly(urethane-urea) Film under Deformation	X27C

F. Yeh, B. S. Hsiao, B. Chu (SUNY at Stony Brook), and B. Sauer (DuPont)

Synchrotron small-angle x-ray scattering (SAXS) technique was used to investigate the behavior of a poly(urethane-urea) film containing segmented hard and soft segments under deformation. The film was cast in solvent which showed a clear microphase separation without preferred molecular orientation. Under low level of deformation (<100% strain), the changes in microstructure appears to be completely recoverable. The deformation imposes no permanent effect on the equilibrium of microphase separation from the solvent casting. At large deformation (>100% strain), the stress-induced molecular orientation in some fractions of the microdomains becomes non-recoverable (within the experimental time frame). As a result, after the stretch and relaxation, the recovered microstructure was found to contain multiple populations of domains with different molecular orientation. We attribute this to the stress-induced chain orientation of the hard segment, which is at a new state of dynamic equilibrium.

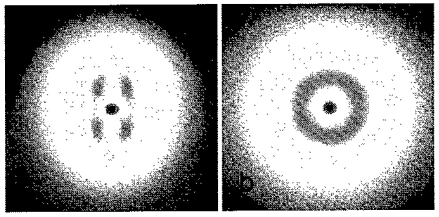

Figure 1. SAXS images of Poly(urethane-urea) film under 75% strain (a) and without strain (b).

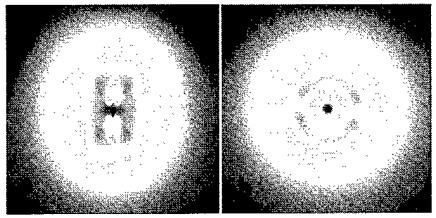

Figure 2. SAXS images of Poly(urethane-urea) film under 200% strain (a) and without strain (b).

Effect of Polymer Diulent on The Lamellar Morphology of Poly(oxymethylene) Blends	X27C

F. Yeh, B. S. Hsiao, B. Chu (SUNY at Stony Brook), and B. Sauer (DuPont)

Poly(OxyMethylene) (POM) and its miscible blends were studied by synchrotron time-resolved small-angle x-ray scattering (SAXS). The blends contain small amount of either poly(vinyl phenol) (PVP) which is a high glass transition (T_g) diluent, or a polyphenol resin low T_g diluent. POM, containing very flexible main chain that could easily fold back and forth, is highly a crystalline polymer. Results indicated that the low T_g polyphenol resin is primarily excluded from the lamellar morphology of POM, while the high T_g diluent is trapped in the lamellar microstructure. The processes of the diulent inclusion and exclusion in the lamellar morphology are determined by the lamellar growth rate of the neat polymer and the mutual diffusion rate of the constituting components. Finally, we observed that the lamellar thickness can be thickened isothermally in both POM neat polymer and blends of low T_g diluent. No sign of isothermal lamellar thickening can be observed in the blends of high T_g diulent.

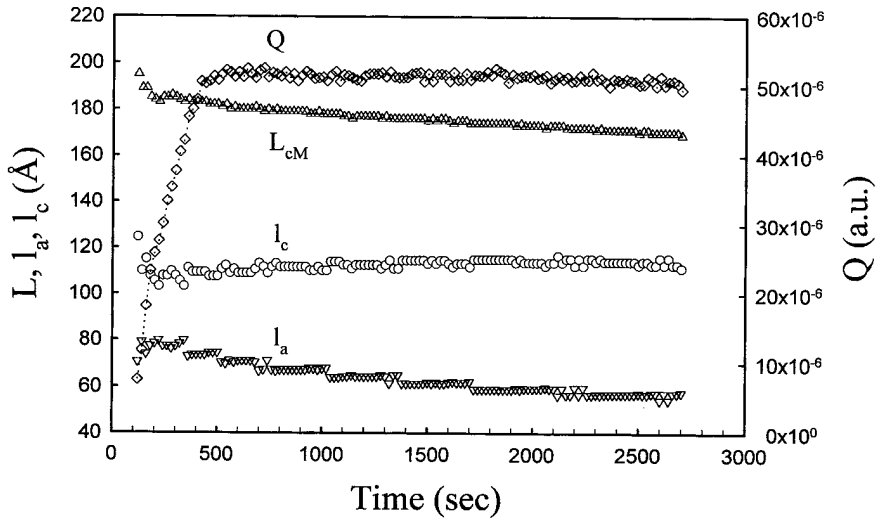

Figure 1. Morphological variables extracted from the SAXS dat of POM at 140°C.

NSLS Users

Beamline U1A

J. Eng, Jr., B.E. Bent, B. Frühberger, and J.G. Chen, "Studies of the Adsorption Geometry and Decomposition Mechanisms of Benzene on Clean and Carbide-Modified Mo(110) Surfaces using Vibrational Spectroscopy", *J. of Phys. Chem.*, **B101**, 4044, (1997).

D. Fischer, A. Marti and G. Haehner, "Orientation and Order in Microcontact-Printed Self-Assembled Monolayers of Alkane-thiols on Gold Investigated with Near Edge X-Ray Absorption Fine Structure Spectroscopy", *J. Vac. Sci. Technol.*, **A4**, 2173, (1997).

B. Frühberger, J. Eng Jr., and J.G. Chen, "Observation of Anomalous Reactivities of Ni/Pt(111) Bimetallic Surfaces", *Catal. Letts.*, **45**, 85, (1997).

R. Kapoor, S.T. Oyama, B. Frühberger, and J.G. Chen, "NEXAFS Characterization and Reactivity Studies of Bimetallic Vanadium Molybdenum Oxynitride Hydrotreating Catalysts", *J. of Phys. Chem.*, **B101**, 1543, (1997).

C.C. Yu, S. Ramanathan, B. Dhandapani, J.G. Chen, and S.T. Oyama, "Bimetallic Nb-Mo Hydroprocessing Catalysts: Synthesis, Characterization and Activity Studies", *J. of Phys. Chem.*, **B101**, 512, (1997).

Beamline U2A

A.F. Goncharov, R.J. Hemley, H.K. Mao, and R. Lu, "Synchrotron Infrared Spectroscopy of Orientationally Ordered Phase of Hydrogen", *Bull. Am. Phys. Soc.*, **42**, 91, (1997).

H. Kagi, T. Inoue, D.J. Weidner, R. Lu, and G.R. Rossman, "Speciation of Hydroxides in Hydrous Ringwoodite", *EOS Trans. Am Geophys. Union*, **78**, S312, (1997).

V.V. Struzhkin, A.F. Goncharov, R.J. Hemley, and H.K. Mao, "Cascading Fermi Resonances and the Soft Mode in Dense Ice", *Phys. Rev. Lett.*, **78**, 4446, (1997).

Beamline U2B

L.M. Miller, G.L. Carr, G.P. Williams, and M.R. Chance, "Synchrotron Infrared Microspectroscopy as a Means of Studying Chemical Composition at a Cellular Level", *Biophysical J.*, **72**, A214, (1997).

A. Xie, Q. He, E.M. Scheuring, B. Sclavi, and M.R. Chance, "Far-Infrared Spectroscopy of Coherent Modes in Proteins", *Prog. In Bioph. & Molecular Biology*, **65**, 42, (1996).

Beamline U3A

B. Harris, A.J. Burek, J.J. Fitch, D.E. Graessle, D.A. Schwartz, R.L. Blake, and E.M. Gullikson, "Determination of Optical Constants for AXAF Mirrors from 0.05-1.0 keV Through Reflectance Measurements", in Grazing Incidence and Multilayer X-ray Optical System, *SPIE*, **3113**, 40, (1997).

Beamline U3C

U. Diebold and N.D. Shinn, "Adsorption and Thermal Stability of Mn/TiO_2(110): 2p X-ray Absorption Spectroscopy and Soft X-ray Photoemission", *Surf. Sci.*, **343**, 53, (1995).

Beamline U4A

K. Breuer, K.E. Smith, M. Greenblatt, W. McCarroll, and S.L. Hulbert, "Dominant Role of the Surface in Photoemission from Quasi-One Dimensional Conductors: $K_{0.3}MoO_3$", *J. Phys. Chem. Solids*, **57**, 1803, (1996).

A. Déchelette-Barbara, J.M. Tonnerre, M.C. Saint-Lager, F. Bartolomé, J.F. Bérar, D. Raoux, H.M. Fischer, M. Piecuch, V. Chakarian, C.C. Kao, M. Gailhannou, S. Lefèvre and M. Bessière "X-ray Anomalous Diffraction and Resonant Magnetic Scattering X-ray Study of Fe_xMn_{1-x}/Ir(001) Multilayers", *J. Magn. Magn. Mater.*, **165**, 87, (1997).

H.-S. Tao, U. Diebold, N.D. Shinn, and T.E. Madey, "Decomposition of $P(CH_3)_3$ on Ru(0001): Comparsion with PH_3 and PCl_3", *Surf. Sci.*, **375**, 257, (1997).

Beamline U4B

V. Chakarian, Y.U. Idzerda, C.T. Chen, G. Meigs, and C.-C. Kao, "Studies of Magnetic Materials with Circularly Polarized Soft X-rays", Applications of Synchrotron Radiation in Industrial, Chemical, and Materials Science, Plenum Press, New York, p. 187, (1996).

V. Chakarian, Y.U. Idzerda, C.-C. Kao, and C.T. Chen, "Circularly Polarized Soft X-ray Resonant Magnetic Scattering Studies of FeCo/Mn/FeCo Multilayers", *J. Magn. Magn. Mater.*, **165**, 52, (1997).

V. Chakarian, Y. U. Idzerda, K. M. Kemner, J. -H. Park, G. Meigs, and C.T. Chen, "Giant Magnetic Effects in the L-edge EXAFS of 3d Transition Metals", *J. Appl. Phys.*, **79**, 6493, (1996).

V. Chakarian, Y. U. Idzerda, H.-J. Lin, C. J. Gutierrez, G. A. Prinz, G. Meigs, and C. T. Chen, "Element-Specific Vector Magnetometry of Buried Layers", *J. Magn. Magn. Mater.*, **156**, 265, (1996).

J. W. Freeland, V. Chakarian, Y.U. Idzerda, S. Doherty, J. G. Zhu, J.-H. Park, and C.-C. Kao, "Identification Layer Switching in Magnetic Multilayers with X-ray Resonant Magnetic Scattering", *Appl. Phys. Lett.*, **71/2**, 276, (1997).

M.M. Grush, J. Chen, T.L. Stemmler, S.J. George, C.Ralston, R.T. Stibrany, A. Gelasco, G. Christou, S.M. Gorun, J.E. Penner-Hahn, and S.P. Cramer, "Manganese L-edge X-ray Absorption Spectroscopy of Manganese Catalase from *L. plantarum* and Mixed Valence Manganese Complexes", *J. Am. Chem. Soc.*, **118**, 65, (1996).

Y.U. Idzerda, V. Chakarian, and J.W. Freeland, "Soft X-ray Magnetic Circular Dichroism at NSLS Beamline U4B", *Syn. Rad. News*, **10**, 6, (1997).

K.M. Kemner, V. Chakrarian, Y.U. Idzerda, and W.T. Elam, "Deconvolution of 3d Transition Metal L-edge EXAFS and Magnetic EXAFS", *Rev. Sci. Instrum.*, **67**, 3365, (1996).

M. Merz, N. Nucker, E. Pellegrin, S. Schuppler, M. Keilwein, M. Knupfer, M.S. Golden, J. Fink, C.T. Chen, V. Chakarian, Y.U. Idzerda, and A. Erb, "X-ray Absorption Spectroscopy of Detwinned $Pr_xY_{1-x}Ba_2Cu_3O_{7-y}$ Single Crystals", *J. of Low Temp. Phys.*, **105**, 347, (1996).

M. Merz, N. Nucker, E. Pellegrin, P. Schweiss, S. Schuppler, M. Keilwein, M. Knupfer, M.S. Golden, J. Fink, C.T. Chen, V. Chakarian, Y.U. Idzerda, and A. Erb, "X-ray Absorption Spectroscopy of Detwinned $Pr_xY_{1-x}Ba_2Cu_3O_{7-y}$ Single Crystals: Electronic Structure and Hole Distribution", *Phys. Rev.*, **B55**, 9160, (1997).

J.-H. Park, S.-W. Cheong, and C.T. Chen, "Double-Exchange Ferromagnetism in $La(Mn_{1-x}Co_x)O_3$", *Phys. Rev.*, **B55**, 11072, (1997).

J.-H. Park, L. H. Tjeng, J. W. Allen, P. Metcalf, and C. T. Chen, "Single-Particle Gap above the Verwey Transition in Fe_3O_4", *Phys. Rev.*, **B55**, 12813, (1997).

J.-H. Park, C. T. Chen, S.-W. Cheong, W. Bao, G. Meigs, V. Chakarian, and Y. U. Idzerda, "Electron Spectroscopic Studies of Colossal Magnetoresistance Material $La_{1-x}Ca_xMnO_3$", *J. Appl. Phys.*, **79**, 4558, (1996).

J.-H. Park, C. T. Chen, S.-W. Cheong, W. Bao, G. Meigs, V. Chakarian, and Y. U. Idzerda, "The Electronic Structure and Metal-Insulator Transition of Perovskite Manganese Oxide Giant Magnetoresistance System", *J. Appl. Phys.*, **79**, 4558, (1997).

Beamline U4IR

P. Dumas, M. Suhren, Y.J. Chabal, C.J. Hirschmugl, and G.P. Williams, "Adsorption and Reactivity of NO on Cu(111): A Synchrotron Infrared Reflection Absorption Spectroscopic Study", *Surf. Sci.*, **371**, 200, (1997).

J. Eng, Jr., K. Raghavachari, L.M. Struck, Y.J. Chabal, B.E. Bent, G.W. Flynn, S.B. Christman, E.E. Chaban, G.P. Williams, K. Radermacher, and S.Mantl, "A Vibrational Study of Ethanol Adsorption on Si(100)", *J. Chem. Phys.*, **106**, 9889, (1997).

R. Henn, J. Kircher, and M. Cardona, "C-Polarized Vibrational Modes in La_2CuO_4 and $La_{1.87}Sr_{0.13}CuO_4$ Determined by Ellipsometry", *Physica,* **C269**, 99, (1996).

R. Henn, J. Kircher, M. Cardona, A. Wittlin, V.H.M. Duijn, and A.A. Menovsky, "Far-infrared C-axis Response of $La_{1.87}Sr_{0.13}CuO_4$ Determined by Ellipsometry", *Phys. Rev.*, **B53**, 9353, (1996).

R. Henn, A. Wittlin, M. Cardona and S. Uchida, "Dynamics of the C-Polarized Infrared Active Modes in $La_{2-x}Sr_xCuO_{4a}$", *Phys. Rev.*, **B56**, 6295, (1997).

J. Hrbek, S.Y. Li, J.A. Rodriquez, D.G. van Campen, H.H. Huang, and G.-Q. Xu, "Synthesis of Sulfur Films from S_2 Gas: Spectroscopic Evidence for the Formation of S_n Species", *Chem. Phys. Letts.*, **267**, 65, (1997).

J. Kircher, R. Henn, M. Cardona, P.L. Richards and G.P. Williams, "Far Infrared Ellipsometry using Synchrotron Radiation", *J. Opt. Soc. Am.*, **B14**, 705, (1997).

L.M. Miller, G.L.Carr, G.P. Williams, and M.R. Chance, "Synchrotron Infrared Microspectroscopy as a Means of Studying Chemical Composition at a Cellular Level", *Biophysical J.*, **72**, A214, (1997).

T. Nanba, and G.P. Williams, "Phase Transitions of CdS Microcrystals Under High Pressure", *J. Phys. Soc. Japan*, **66**, 1526, (1997).

K. Raghavachari, Y.J. Chabal, and L.M. Struck, "Vibrational Interactions at Surfaces: H_2O on Si(100)", *Chem. Phys. Letts.*, **252**, 230, (1996).

A.E. Russell, L. Rubasingham, T.H. Ballinger, and P.L. Hagans, "Thin Layer Effects in *in situ* Far-Infrared Spectroscopy", *J. Electroanalytical Chem.*, **422**, 197, (1997).

L.M. Struck, J. Eng, Jr., B.E. Bent, G.W. Flynn, Y.J. Chabal, S.B. Christman, E.E. Chaban, K. Raghavachari, A.E. White, G.P. Williams, K. Radermacher, and S. Mantl, "Vibrational Study of Silicon Oxidation: H_2O on Si(100)", *Surf. Sci.*, **380**, 444, (1997).

D.L. Wetzel, J.A. Reffner, and G.P. Williams, "Synchrotron Powered FT-IR Microspectroscopy- Single-cell Interrogations", *Mikrochimica Acta*, **S14**, 353, (1997).

G.P. Williams, "IR Spectroscopy at Surfaces with Synchrotron Radiation", *Surf. Sci.*, **368**, 1, (1996).

Beamline U5UA

P.A. Dowben, D.N. McIlroy, and D. Li, "Surface Magnetism of the Lanthanides", Handbook on the Physics and Chemistry of Rare Earths, Edited by K.A. Gschneidner and L. Eyring, North Holland Press, **24**, 159, (1997).

D. Li, J. Pearson, S.D. Bader, D.N. McIlroy, C. Waldfried, and P.A. Dowben, "Spin Polarization of the Conduction Bands and Secondary Electrons of Gd(0001)", *J. Appl. Phys.*, **79**, 5838, (1996).

D.N. McIlroy, C. Walfried, D. Li, J. Pearson, S.D. Bader, D.-J. Huang, P.D. Johnson, R.F. Sabiryanov, S.S. Jaswal, and P.A. Dowben, "Oxygen Induced Suppression of the Surface Magnetization of Gd(0001)", *Phys. Rev. Lett.*, **76**, 2802, (1996).

C. Waldfried, D.N. McIlroy, D. Li, J. Pearson, S.D. Bader, and P.A. Dowben, "Dissociative Nitrogen Chemisorption and Bonding on Gd(00001)", *Surf. Sci. Letts.*, **341**, L1072, (1995).

Beamline U7B

B. Zhao, Photoemission Studies of FeRh, M.S. Degree in Physic, Florida Atlantic University, (1997).

Beamline U8B

F.R. McFeely, K.Z. Zhang, and M.M. Banaszak Holl, "Chloroethane Physisorbed on Hydrogenated Si(111): A Test System for the Evaluation of Core Level XPS Assignment rules at Si/SiO_2 Interfaces", *Mat. Res. Soc. Symp.*, **446**, 15, (1997).

K.Z. Zhang, M.M. Banaszak Holl, J.E. Bender, IV., S. Lee, and F.R. McFeely, "Si 2p Core Level Shifts at the $Si(100)/SiO_2$ Interface: an Experimental Study", *Phys. Rev.*, **B54**, 7686, (1996).

K.Z. Zhang, M.M. Banaszak Holl, and F.R. McFeely, "Soft X-ray Si 2p Core-level Spectra of $H_8Si_8O_{12}$ Physisorbed on Si(111)-H: Additional Experimental Evidence Regarding the Binding Energy Shift of the $HSiO_3$ Fragment", *Mat. Res. Soc. Symp.*, **446**, 241, (1997).

K.Z. Zhang, J.N. Greeley, M.M. Banaszak Holl, and F.R. McFeely, "The Role of Extra-Atomic Relaxation in Determining Si 2p Binding Energy Shifts at Silicon/Silicon Oxide Interfaces", *J. of Appl. Phys.*, **82**, 2298, (1997).

K.Z. Zhang, L.M. Meeuwenberg, M.M. Banaszak Holl, and F.R. McFeely, "A New Model Silicon/Silicon Oxide Interface Synthesized from $H_{10}Si_{10}O_{15}$ and Si(100)-2x1", *Japan J. of Appl. Phys.*, **36**, 1622, (1997).

Beamline U9B

L.A. Kelly, J.G. Trunk, and J.C. Sutherland, "Simultaneous Recording of the Spectral, Temporal and Polarization Properties of Emission Spectra", *Society for Photo-Optical Instrumentation Engineers*, **2980**, 2, (1997).

L.A. Kelly, J.G. Trunk, and J.C. Sutherland, "Time Resolved Fluorescence Polarization Measurements for Entire Emission Spectra with a Resistive-Anode, Single-Photon-Counting Detector: The Fluorescence Omnilyzer", *Rev. of Sci. Instrum.*, **68**, 2279, (1997).

E.S. Stevens, "Carbohydrates", Circular Dichroism: Conformational Analysis of Biomolecules, edited by G.D. Fasman, Plenum Press, pp. 501-530, (1996).

D. Wisniewski, W. Drozdowski, A.J. Wojtowicz, A. Lempicki, P. Dorenbos, J.T.M. De Haas, C.W.E. Van Eijk, and A.J.J. Bos, "Spectroscopy and Thermoluminescence of $LuAlO_3$:Ce", *Acta Physica Polonica*, **A90**, 377, (1996).

A.J. Wojtowicz, "New High Performance Scintillators Based on Re-Activated Insulator Materials", *Acta Physica Polonica*, **A90**, 215, (1996).

A.J. Wojtowicz, A. Lempicki, D. Wisniewski, M. Balcerzyk, and C. Brecher, "The Carrier Capture and Recombination Processes in Ln^{3+}- Activated Scintillators", *IEEE Trans. in Nucl. Sci.*, **43**, 2168, (1996).

Beamline U11

S.-C. Kuo, Z. Zhang, S.K. Ross, R.B. Klemm, R.D. Johnson, III, P.S. Monks, P.T. Thorn, Jr., and L.J. Stief, "A Discharge Flow-Photoionization Mass Spectrometric Study of HNO: Photoionization Efficiency Spectrum andIonization Energy; and Proton Affinity of NO", *J. Phys. Chem.*, **101**, 4035, (1997).

R.P. Thorn, Jr., L.J. Stief, S.C. Kuo, and R.B. Klemm, "The Ionization Energy of Cl_2O and ClO, Appearance Energy of ClO^+ (Cl_2O) and Heat of Formation of Cl_2O", *J. Phys. Chem.*, **100**, 14178, (1996).

Beamline U13UA

S. Conrad, D.R. Mullins, Q.-S. Xin, and X.-Y. Zhu, "Thermal and Photochemical Deposition of Sulfur on GaAs(100)", *Appl. Surf. Sci.*, **107**, 145, (1996).

D.R. Huntley, D.R. Mullins, and M.P. Wingeier, "Desulfurization of Thiophenic Compounds by Ni(111): Adsorption and Reactions of Thiophene, 3-Methyl Thiophene and 2,5-Dimethyl Thiophene", *J. Phys. Chem.*, **100**, 19620, (1996).

D.R. Mullins, "Enhancement of Methane Formation from Methanethiol Adsorbed on a Strained Ni Film on W(001)", *J. Phys. Chem.*, **101**, 1014, (1997).

D.R. Mullins, D.R. Huntley, T. Tang, D.K. Saldin, and W.T. Tysoe, "The Adsorption Site and Orientation of CH_3S on Ni(111)", *Surf. Sci.*, **380**, 468, (1997).

D.R. Mullins, and P.F. Lyman, "The Interaction of Methanethiol with Sulfur Covered W(001)", *Langmuir*, **12**, 6382, (1996).

D.R. Mullins, T. Tang, X. Chen, V. Shneerson, D.K. Saldin, and W.T. Tysoe, "The Adsorption Site and Orientation of Ch_3S and Sulfur on Ni(001) using Angle-Resolved X-ray Photoelectron Spectroscopy", *Surf. Sci.*, **372**, 193, (1997).

S.H. Overbury, and D.R. Mullins, "Geometric and Electronic Structure of Sulfided Ni Films on W(001) Studied by Low Energy Alkali Ion Scattering and Soft X-ray Photoemission", *Surf. Sci.*, **369**, 231, (1996).

Beamline U13UB

A.A. MacDowell, Z. Shen, K. Fujii, J.E. Bjorkholm, R.R. Freeman, L. Fetter, D.W. Taylor, D.M. Tennant, L. Eichner, W.K. Waskiewicz, D.L. White, D.L. Windt, and O.R. Wood, II, "Extreme Ultraviolet 1:1 Ring-Field Lithography Machine", OSA Trends in Optics and Photonics Vol. 4 Extreme Ultraviolet Lithography, edited by G.D. Kubiak and D.R. Kania, Optical Society of America, pp. 192-198, (1996).

K.B. Nguyen, A.A. MacDowell, K. Fujii, D.M. Tennant, and L.A. Fetter, "At-Wavelength Inspection of EUVL Mask Defects with an Offner 1X Offner Ring-Field System", OSA Trends in Optics and Photonics Vol. 4 Extreme Ultraviolet Lithography, edited by G.D. Kubiak and D.R. Kania, Optical Society of America, pp. 49-53, (1996).

D.A. Tichenor, A.K. Ray-Chaudhuri, G.D. Kubiak, K.B. Nguyen, S.J. Haney, K.W. Berger, R.P. Nissen, Y.E. Perras, P.S. Jin, L.I. Weingarten, P.N. Keifer, R.H. Stulen, R.N. Shagam, W.C. Sweatt, T.G. Smith, O.R. Wood, II, A.A. MacDowell, J.E. Bjorkholm, T.E. Jewell, F. Zernike, B.L. Fix, and H.W. Hauschildt, "Progress in the Development of EUV Imaging Systems", OSA Trends in Optics and Photonics Vol. 4, Extreme Ultraviolet Lithography, edited by G.D. Kubiak and D.R. Kania, Optical Society of America, pp. 2-8, (1996).

Beamline U14A

R.A. Bartynski, E. Jensen, S.L. Hulbert, and C.-C. Kao, "Auger Photoelectron Coincidence Spectroscopy using Synchrotron Radiation", *Prog. in Surf. Sci.*, **53**, 155, (1996). BNL 64645.

A.K. See, R.A. Bartynski, A. Nangia, A.H. Weiss, S.L. Hulbert, X. Wu, and C.-C. Kao, "Enchanced Core Level Photoemission from Oxide Surface Defects Using Auger-Photoelectron Coincidence Spectroscopy", *Surf. Sci. Lett.*, **383**, L735, (1997).

Beamline X1A

H. Ade, "Compositional and Orientational Characterization of Polymeric Systems with X-ray Microscopy", *Trends in Polymer Science*, **5/2**, 58-66, (1997).

H. Ade, B. Hsiao, G. Mitchell, E. Rightor, A. P. Smith, and R. Cieslinski, "Chemical and Orientational Imaging of Polymeric Samples", edited by G.W. Bailey and A.J. Garratt-Reed, Proceedings of the 52 Annual Meeting of the Microscopy Society of America, San Francisco, San Francisco Press, pp. 68-69, (1994).

J. M. Boese, X-ray Absorption Near edge Structure of Amino Acids and Peptides, M.A. Thesis, Department of Physics, State University of New York at Stony Brook, (1996).

C.J. Buckley, "The Measuring and Mapping of Calcium in Mineralised Tissues by Absorption Difference Imaging", *Rev. Sci. Instrum.*, **66/2**, 1318-1321, (1995).

C.J. Buckley, "Imaging of Calcium Deposits in Cartilage by Scanning X-ray Microscopy", *Bone*, **13**, 100, (1992).

C.J. Buckley, S.Y. Ali, C. A. Scotchford, M. Rivers, K. L. D'Amico, J. H. Dunsmuir, and S. R. Ferguson, "Imaging of Calcium Deposits in Human Cartilage", *Scanning*, **14**, 27-28, (1992).

C.J. Buckley, S. J. Bellamy, N. Khaleque, S. Downes, and X. Zhang, "Possibilities for Chemical State Imaging of Calcium Compounds", edited by V. V. Aristov and A. I. Erko, X-ray Microscopy IV, Bogorodskii Pechatnik. Proceedings of the 4th International Conference, Chernogolovka, Russia, pp. 207-212, (1994).

C.J. Buckley, R.E. Burge, G.F. Foster, S.Y. Ali, and C.A. Scotchford, "X-ray Probe Mapping of Calcium Deposits in Articular Cartilage", edited by P. B. Kenway, P. J. Duke, G. W. Lorimer, T. Mulvey, I. W. Drummond, G. Love, A. G.Michette, and M. Stedman, X-Ray Optics and Microanalysis, Bristol, IOP Publishing, pp. 621-626, (1992).

C.J. Buckley, S. Downes, N. Khaleque, S. J. Bellamy, and X. Zhang, "Mapping the Density and Mineral Phase of Calcium in Bone at the Interface with Biomaterials using Scanning X-ray Microscopy", edited by G.W. Bailey and A.J. Garratt-Reed, Proceedings of the 52 Annual Meeting of the Microscopy Society of America, San Francisco, San Francisco Press, pp. 44-45, (1994).

H. N. Chapman, "Phase-Retrieval X-ray Microscopy by Wigner-Distribution Deconvolution", *Ultramicroscopy*, **66**, 153-172, (1996).

H. N. Chapman, K. A. Nugent, S. W. Wilkins and A. V. Rode, "Capillary X-ray Optics", edited by C. Jacobsen and J. Trebes, Soft X-ray Microscopy, *SPIE*, **1741**, 40-50, (1992).

H. Chapman, S. Williams, and C. Jacobsen, "Imaging of 30 nm gold Spheres by Dark-field Scanning Transmission X-ray Microscopy", edited by G. W. Bailey and A. J. Garratt-Reed, Proceedings of the 52 Annual Meeting of the Microscopy Society of America, San Francisco Press, pp. 52-53, (1994).

G. D. Cody, R. E. Botto, H. Ade, and S. Wirick, "The Application of Soft X-ray Microscopy to the *in situ* Analysis of Sporinite in Coal", *Intern. J. of Coal Geo.*, **32**, 69-86, (1996).

J. R. Gilbert, Soft X-ray Microimaging of Whole Wet Cells, PhD Thesis, California Institute of Technology, Pasadena, California, (1992).

K. K. Goncz, A Comprehensive Study of the Physical Properties of Isolated Zymogen Granules using Scanning Transmission X-ray Microscopy, PhD Thesis, Department of Biophysics, University of California, (1994).

K. K. Goncz, R. Behrsing, and S. S. Rothman, "The Morphology and Structure of Zymogen Granules", *Cell and Tissue Res.*, **280**, 519-530, (1995).

K. K. Goncz, R. Behrsing, and S. S. Rothman, "A Study of the Properties of Zymogen Granules using X-ray Microscopy", edited by V.V. Aristov and A. I. Erko, X-ray Microscopy IV, Bogorodskii Pechatnik, Proceedings of the 4th International Conference, Chernogolovka, Russia, September 20-24, pp. 256-264, (1994).

K. K. Goncz, M. Moronne, W. Lin, and S. Rothman, "Measuring Changes in the Mass of Single Subcellular Organelles using X-ray Microscopy", edited by C. Jacobsen and J. Trebes, Soft X-ray Microscopy, *SPIE*, **1741**, 342-350, (1992).

K. K. Goncz and S. S. Rothman, "Membrane Protein Transport in Eukaryotic Secretion in Cells", *Membrane Protein Transport*, **3**, 279-293, (1996).

W. S. Haddad, I. McNulty, J. E. Trebes, E. H. Anderson, L. Yang, and J. M. Brase, "Demonstration of Ultra-High-Resolution Soft X-ray Tomography using a Scanning Transmission X-ray Microscope", edited by G.W. Bailey and A.J. Garratt-Reed, Proceedings of the 52 Annual Meeting of the Microscopy Society of America, San Francisco Press, pp. 312-313, (1994).

M. R. Howells, C. J. Jacobsen, and S. Lindaas, "X-ray Holographic Microscopy using the Atomic-Force Microscope", edited by V.V. Aristov and A.I. Erko, X-ray Microscopy IV, Chernogolovka, Russia, Bogorodskii Pechatnik. Proceedings of the 4th International Conference, September 20-24, pp. 413-427, (1994).

A. Irtel von Brenndorff, M. M. Moronne, C. Larabell, P. Selvin, and W. Meyer-Ilse, "Soft X-ray Stimulated High Resolution Luminescence Microscopy", edited by V.V. Aristov and A.I. Erko, X-ray Microscopy IV, Bogorodskii Pechatnik. Proceedings of the 4th International Conference, Chernogolovka, Russia, September 20-24, pp. 337-343, (1994).

C. Jacobsen, "Soft-X-ray Microscopy: Imaging of Biological Systems", edited by E. Burattini and A. Balerna, Biomedical Applications of Synchrotron Radiation, Volume CXXVIII Corso, Amsterdam, IOS Press, pp. 91-109, (1996).

C. Jacobsen, H. N. Chapman, J. Fu, A. Kalinovsky, J. Kirz, J. Maser, A. Osanna, S. Spector, D. Tennant, S. Wang, S. Wirick, and X. Zhang, "Biological Microscopy and Soft X-ray Optics at Stony Brook", *J. of Elect. Spect. and Related Pheno.*, **80**, 337-341, (1996).

C. Jacobsen, E. Anderson, H. Chapman, J. Kirz, S. Lindaas, M. Rivers, S. Wang, S. Williams, S. Wirick, and X. Zhang, "The X-1A Scanning Transmission X-ray Microscope: Optics and Instrumentation", edited by V. V. Aristov and A. I. Erko, X-ray Microscopy IV, Bogorodskii Pechatnik. Proceedings of the International Conference, Chernogolovka, Russia, September 20-24, pp. 304-321, (1993).

C. Jacobsen, J. Fu, Y. Wang, and S. Williams, "Scanning Luminescence X-ray Microscopy: Progress Towards Selective Staining using Microspheres", edited by G. W. Bailey and A. J. Garratt-Reed, Proceedings of the 52 Annual Meeting of the Microscopy Society of America, San Francisco Press, pp. 74-75, (1994).

J. Kirz, H. Ade, R. E. Botto, G. D. Cody, J. Fu, C. Jacobsen, S. Lindaas, W. F. Mangel, W. J. McGrath, V. Oehler, J. van't Hof, S. Williams, S. Wirick, and X. Zhang, "Scanning Transmission X-ray Microscopy at the NSLS", edited by V. V. Aristov and A. I. Erko, X-ray Microscopy IV, Bogorodskii Pechatnik. Proceedings of the International Conference, Chernogolovka, Russia, September 20-24, pp. 41-61, (1993).

J. Kirz, H. Ade, C. Jacobsen, C. H. Ko, S. Lindaas, S. Williams, and X. Zhang, "Soft X-ray Microscopy-Physical Basis and Recent Developments", Proceedings of the Fifth Asia-Pacific Physics Conference, *World Scientific*, **1**, pp. 200-215, (1994).

J. Kirz, C. Jacobsen, S. Lindaas, S. Williams, X. Zhang, E. Anderson, and M. Howells, "Soft X-ray Microscopy at the National Synchrotron Light Source", edited by B. Chance, D. Deisenhober, S. Ebashi, D. T. Goodhead, J. R. Helliwell, H. E. Huxley, T. Iizuka, J. Kirz, T. Mitsui, E. Rubenstein, N. Sakabe, T. Sasaki, G. Schmahl, H. Sturhmann, K. Wüthrich, and G. Zaccai, Synchrotron Radiation in Biosciences, Clarendon Press, Oxford, pp. 563-571, (1994).

C.-H. Ko, Development of a Second Generation Scanning Photoemission Microscope at the National Synchrotron Light Source, PhD Thesis, Department of Physics, State University of New York at Stony Brook, (1995).

S. A. Lindaas, X-ray Gabor Holography using a Scanning Force Microscope, PhD Thesis, Department of hysics, State University of New York at Stony Brook, (1994).

S. Lindaas, C. Jacobsen, A. Kalinovsky, and M. Howells, "X-ray Gabor Holography: Recent Progress", edited by G. W. Bailey and A. J. Garratt-Reed, Proceedings of the 52 Annual Meeting of the Microscopy Society of America, San Francisco, San Francisco Press, pp. 72-73, (1994).

S. Lindaas, M. Howells, C. Jacobsen, and A. Kalinovsky, "X-ray Holographic Microscopy by means of Photoresist Recording and Atomic-Force Microscope Readout", *J. of Opt. Soc. of Am.*, **A13/9**, 1788-1800, (1996).

B. W. Loo, Jr., S. Williams, W. T. Lin, W. H. Love, S. Meizel and S. S. Rothman, "High Resolution X-ray Stereomicroscopy: True Three-Dimensional Imaging of Biological Samples", edited by C. Jacobsen and J. Trebes, Soft X-ray Microscopy, *SPIE*, **1741**, 392, (1992).

K. Maier, Characterization of a Scanning Photoemission Microscope, M.A. Thesis, Department of Physics, State University of New York at Stony Brook, (1995).

I. McNulty, J. Kirz, C. Jacobsen, M. R. Howells and E. Anderson, "First Results with a Fourier Transform Holographic Microscope", edited by A.G. Michette, G.R. Morrison, and C. J. Buckley, X-ray Microscopy III, Springer Series in Optical Sciences, Berlin, Springer-Verlag., **67**, pp. 251-254, (1992).

M.M. Moronne, C. Larabell, P.R. Selvin, and A. Irtel von Brenndorff, "Development of Fluroescent Probes for X-ray Microscopy", edited by G.W. Bailey and A.J. Garratt-Reed, Proceedings of the 52 Annual Meeting of the Microscopy Society of America, San Francisco Press, pages 48-49, (1994).

G. R. Morrison, "X-ray Imaging with a Configured Detector", edited by V. V. Aristov and A. I. Erko, X-ray Microscopy IV, Bogorodskii Pechatnik, Proceedings of the 4th International Conference, Chernogolovka, Russia, September 20-24, pp. 478-486, (1994).

A. Osanna, C. Jacobsen, A. Kalinovsky, J. Kirz, J. Maser, and S. Wang, "X-ray Microscopy: Preparations for Studies of Frozen Hydrated Specimens", *Scanning Microscopy*, **10**, 349-358, (1996).

E. G. Rightor, A. P. Hitchcock, H. Ade, R. D. Leapman, S. G. Urquhart, A. P. Smith, G. Mitchell, D. Fischer, H. J. Shin, and T. Warwick. "Spectromicroscopy of Poly(ethylene terephthalate): Comparison of Spectra and Radiation Damage Rates in X-ray Absorption and Electron Energy Loss", *J. of Phys. Chem.*, **B101/11**, 1950-1960, (1997).

A. P. Smith, Characterization of the Lateral Orientation within Poly(p-phenylene terephthalamide) (Kevlar) Fibers and the Microchemistry of Methylene Diphenyl Diisocyanate (MDI) based Polyurethane foams with X-ray Microscopy, M.S. Thesis, Materials Science and Engineering, North Carolina State University, (1995).

A. P. Smith and H. Ade, "Quantitative Orientational Analysis of a Polymeric Material (Kevlar fibers) with X-ray Microspectroscopy", *Appl. Phys. Letts.*, **69**, 3833-3835, (1996).

A. P. Smith, J. H. Laurer, H. W. Ade, S. D. Smith, A. Ashraf, and R. J. Spontak, "X-ray Microscopy and NEXAFS Spectroscopy of Macrophase-Separated Random Block Copolymer/Homopolymer Blends", *Macromolecules*, **30**, 663-666, (1997).

S. J. Spector, Diffractive Optics for Soft X-rays, PhD Thesis, Department of Physics, State University of New York at Stony Brook, (1997).

Y. Wang and C. Jacobsen, "Modelling of Dissolution and Resolution in Contact X-ray Microscopy", edited by G.W. Bailey and A.J. Garratt-Reed, Proceedings of the 52 Annual Meeting of the Microscopy Society of America, San Francisco, San Francisco Press, pp. 62-63, (1994).

M. Wei, D.T. Attwood, T.K. Gustafson, and E.H. Anderson, "Patterning a 50-nm Period Grating using Soft X-ray Spatial Frequency Multiplication", *J. Vac. Sci. and Tech.*, **12/6**, 3648-3652, (1994).

S. Williams, C. Jacobsen, J. Kirz, S. S. Lamm, J. van't Hof, and X. Zhang, "Metaphase Chromosome DNA Mass Fraction is Independent of Species", edited by G.W. Bailey and A.J. Garratt-Reed, Proceedings of the 52 Annual Meeting of the Microscopy Society of America, San Francisco, San Francisco Press, pp. 46-47, (1994).

S. Williams, C. Jacobsen, J. Kirz and X. Zhang, "Imaging with the Brookhaven Scanning Transmission X-ray Microscope", edited by J.M. Schnur and M. Peckerar, Synthetic Microstructures in Biological Research, Plenum Press, pp. 109-119, (1992).

B. Winn, H. Ade, C. Buckley, M. Howells, S. Hulbert, C. Jacobsen, J. Kirz, I. McNulty, J. Miao, T. Oversluizen, I. Pogorelsky, and S. Wirick, "X1A: Second Generation Undulator Beamlines Serving Soft X-ray Spectromicroscopy Experiments at the NSLS", *Rev. Sci. Instrum.*, **67/9**, 1-4, (1996).

B. Winn, X. Hao, C. Jacobsen, J. Kirz, J. Miao, S. Wirick, H. Ade, C. Buckley, M. Howells, S. Hulbert, I. McNulty, and T. Oversluizen. "Considerations for a Soft X-ray Spectromicroscopy Beamline", edited by L. E. Berman and J. Arthur, Optics for High-Brightness Synchrotron Radiation Beamlines II, *SPIE*, **2856**, 100-109, (1996).

X. Zhang, Development and Applications of Quantitative X-ray Microscopy with Chemical Sensitivity, PhD Thesis, Department of Physics, State University of New York at Stony Brook, (1995).

X. Zhang, R. Balhorn, C. Jacobsen, J. Kirz, and S. Williams, "Mapping DNA and Protein in Biological Samples using the Scanning Transmission X-ray Microscope", edited by G.W. Bailey and A.J. Garratt-Reed, Proceedings of the 52 Annual Meeting of the Microscopy Society of America, San Francisco, San Francisco Press, pp. 50-51, (1994).

Beamline X1B

B. Kempgens, A. Kivimaki, H.M. Kuppe, M. Neeb, A.M. Bradshaw, and J. Feldhaus, "One-Electron vs. Multi-Electron Effects in the Near-Threshold C 1s Photoionisation of Acetylene", *J. Chem. Phys.*, **107**, 4219-24, (1997).

B. Kempgens, A. Kivimaki, M. Neeb, H.M. Kuppe, A.M. Bradshaw, and J. Feldhaus, "A High-Resolution N 1s Photoionization Study of the N_2 Molecule in the Near-Threshold Region", *J. Phys.*, **B29**, 5389-5402, (1996).

B. Kempgens, H.M. Kuppe, A. Kivimaki, M. Neeb, K. Maier, U. Hergenhahn, and A.M. Bradshaw, "A Re-appraisal of the Existence of Shape Resonances in the Series C_2H_2, C_2H_4 and C_2H_6", *Phys. Rev. Lett.*, **79**, 35-38, (1997).

A. Kivimaki, B. Kempgens, K. Maier, H.M. Kuppe, M.N. Piancastelli, M. Neeb, and A.M. Bradshaw, "The Vibrational Resolved O 1s Photoelectron Spectrum of CO_2: Vibronic Coupling and Dynamic Core-hole Localization", *Phys. Rev. Lett.*, **79**, 998-1001, (1997).

A. Kivimaki, M. Neeb, B. Kempgens, H.M. Kuppe, K. Maier, and A.M. Bradshaw, "Angle-Resolved Auger Spectra of C_2N_2 Molecule", *J. Phys.*, **B30**, 4279-91, (1997).

M. Neeb, A. Kivimaki, B. Kempgens, H.M. Kuppe, and A.M. Bradshaw, "The C 1s Auger Decay Spectrum of CF_4: an Analysis of the Core-Excited States", *J. Phys.*, **B30**, 93-100, (1997).

S.H. Overbury, D.R. Huntley, D.R. Mullins, K.S. Ailey, and P.V. Radulovic, "Surface Studies of Model Supported Catalysts: NO Adsorption on $Rh/CeO_2(001)$", *J. Vac. Sci. Technol.*, **A15**, 1647, (1997).

M.N. Piancastelli, A. Kivimaki, B. Kempgens, M. Neeb, K. Maier, and A.M. Bradshaw, "High-Resolution Study of Resonant Decay Following the O 1s π Excitation in CO_2: Evidence for an Overlapping Rydberg Transition", *Chem. Phys. Lett.*, **274**, 13, (1997).

M.N. Piancastelli, M. Neeb, A. Kivimaki, B. Kempgens, H.M. Koppe, K. Maier, and A.M. Bradshaw, "Variation of Cross-Section Enhancement in Decay Spectra of CO under Resonant Raman Conditions", *Phys. Rev. Lett.*, **77**, 4302-4305, (1996).

Beamline X2A

R. Paniago, T.H. Metzger, J. Trenkler, R. Hempelmann, H. Reichert, S. Schmid, P.C. Chow, S.C. Moss and J. Pelsl, "Near-Surface Tricritical Behavior of $V_2H(010)$ at the β_1-β_2 Phase Transition", *Phys. Rev. Brief Reports*, **56**, 16, (1997).

H. Reichert, S.C. Moss, and K.S.Liang, "Anomalous Temperature Dependence of the X-ray Diffuse Scattering Intensity of Cu_3Au", *Phys. Rev. Lett.*, **77**, 4382, (1996).

H. Reichert, S.C. Moss, and K.S. Liang, "Reply to Comment by V. Ozollns, et.al.", *Phys. Rev. Lett.*, **79**, 956, (1997).

H. Reichert, I. Tsatskis, and S.C. Moss, "Temperature Dependent Microstructure of Cu_3Au in the Disordered Phase", NSF/CNRS Workshop on Alloy Theory, *Comput. Mater. Sci.*, **8**, 46, (1997).

Beamline X3A1

R. Bolotovsky, and P. Coppens, "The ϕ-extent of the Reflection Range in the Oscillation Method According to the Mosaicity Cap Model", *J. Appl. Cryst.*, **30**, 65, (1997).

R. Bolotovsky, and P. Coppens, "The "Seed-Skewness" Method for Integration of Peaks on Imaging Plates II: Analysis of Bias due to Finite Size of the Peak Mask and Treatment of α_1-α_2 Splitting", *J. Appl. Cryst.*, **30**, 244, (1997).

C.L. Cahill, and J.B. Parise, "The Synthesis and Structure of $MnGe_4S_{10}.(C_6H_{14}N_2).3H_2O$: A Novel Sulfide Framework Analogous to Zeolite-A(BW)", *Chem. Mater.*, **9**, 812, (1997).

J. Chen, R. Li, J.B. Parise, and D.J. Weidner, "Pressure Induced Ordering in NiMg-Olivine", *Am. Mineral*, **81**, 1519, (1996).

P. Coppens, "Time-Resolved Diffraction in Chemistry and Materials Science: the Developing Field of Photocrystallography", *Synch. Rad. News*, **10/1**, 26, (1997).

A. Darovsky, V. Kezerashvili, P. Coppens, T. Weyhermüller, H. Hummel, and K. Wieghardt, "Temperature-Dependent Electron Transfer in a $Mn^{II}Mn^{III}$(μ-OH) Mixed-Valence Manganese Complex", *Inorg. Chem.*, **35**, 6916, (1996).

C. Eylem, J.A. Hriljac, D.R. Corbin, and J.B. Parise, "Structure of a Zeolite ZSM-5-Bithiophene Complex as Determined by High Resolution Synchrotron X-ray Powder Diffraction", *Chem. Mater.*, **8**, 844, (1996).

M. Kunz, K. Leinenweber, J.B. Parise, T.-C. Wu, W.A. Bassett, K. Brister, D.J. Weidner, M.T. Vaughan, and Y. Wang, "The Baddeleyite-Type High Pressure Phase of $Ca(OH)_2$", *J. High Press Res.*, **14**, 311, (1996).

M. Kunz, D. Xirouchakis, Y. Wang, J. B. Parise, and D.H. Lindsley, "Structural Investigations along the Join $CaTiOSiO_4$ - $CaSnOSiO_4$", *Swiss Bull. Min. Pet.*, **77**, 1, (1997).

J.B. Parise, Y. Wang, G.D. Gwanmesia, J. Zhang, Y. Sinelnikov, J. Chmielowski, D.J. Weidner, and R.C. Liebermann, "The Symmetry of Garnets on the Pyrope ($Mg_3Al_2Si_3O_{12}$)-Majorite ($MgSiO_3$) Join", *Geophys. Res. Lett.*, **23**, 3799, (1996).

K. Prassides, K. Vavekis, K. Kordatos, K. Tanigaki, G.M. Bendele, and P.W. Stephens, "Loss of Cubic Symmetry in Low Temperature Na_2RbC_{60}", *J. Amer. Chem. Soc.*, **119**, 834, (1997).

K. Tan, Y. Ko, J.B. Parise, J.-H. Park, and A. Darovsky, "A Novel Antimony Sulfied Templated by Dimethylammonium: Its Synthesis and Structural Characterization using Synchrotron Imaging Plate Data", *Chem. Mater.*, **8**, 2510, (1996).

Beamline X3A2

T. Dobashi, M. Takenaka, F. Yeh, G. Wu, K. Ichikawa, and B. Chu, "Scattering Studies of Poly(urea-urethane) Microcapsule in Suspension", *J. Coll. & Interface Sci.*, **179**, 640, (1996).

L. Liu, F. Yeh, and B. Chu, "Synchrotron SAXS Study of Crystallization and Microphase Separation in Compatible Mixtures of Tetrahydrofuran-Methyl Methacrylate Diblock Copolymer and Polytetrahydrofuran", *Macromolecules*, **29**, 5336, (1996).

E.L. Sokolov, F. Yeh, A.R. Khokhlov, and B. Chu, "Nano-Scale Supramolecular Ordering in Gel-Surfactant Complexes: Sodium Alkyl Sulfates in Poly(diallydimethylammonium Chloride)", *Langmuir*, **26**, 6229, (1996).

F. Yeh, E.L. Sokolov, A.R. Khokhlov, and B. Chu, "Nano-Scale Supramolecular Structures in Gels of Poly(diallyldimethylammonium chloride) Interacting with Sodium Dodecyl Sulfate", *J. Am. Chem. Soc.*, **118**, 6615, (1996).

Beamline X3B1

D. Balzar, P.W. Stephens, and H. Ledbetter, "Synchrotron X-ray Diffaction Line Profile", *Fizika*, **A6**, 41, (1997).

D. Balzar, P.W. Stephens, H. Ledbetter, J. Li, and M.L. Dunn, "Synchrotron X-ray Diffraction Study of the Surface Layer in Poled Ceramic $BaTiO_3$", Mat. Res. Soc. Symp. Proc., **453**, 715, (1997).

S.D. Bohle, R.E. Dinnebier, S.K. Madsen, and P.W. Stephens, "Characterization of the Products of the Heme Detoxification Pathway in Malarial Late Trophozoites by X-ray Diffraction", *J. Biol. Chem.*, **272**, 713, (1997).

C.L. Cleveland, U. Landman, T.G. Schaaff, M.N. Shafigullin, P.W. Stephens, and R.L. Whetten, "Structural Evolution of Smaller Gold Nanocrystals: The Truncated Decahedral Motif", *Phys. Rev. Letts.*, **79**, 1873, (1997).

C.L. Cleveland, U. Landman, M.N. Shafigullin, P.W. Stephens, and R.L. Whetten, "Structural Evolution of Larger Gold Clusters", *Zeitschrift für Physik*, **D40**, 153, (1997).

R.E. Dinnebier, F. Olbrich, and G.M. Bendele, "Cyclopentadienyl Cesium by High-Resolution X-ray Powder Diffraction", *Acta Cryst.*, **C53**, 699, (1997).

R.E. Dinnebier, F. Olbrich, S. van Smaalen, and P.W. Stephens, "The *Ab Initio* Structure Determination of Two Polymorphs of Cyclopentadienyl Rubidium in a Single Powder Pattern", *Acta Cryst.*, **B53**, 153, (1997).

R.E. Dinnebier, M. Pink, J. Sieler, and P.W. Stephens, "Novel Alkali Metal Coordination in Phenoxides: Powder Diffraction Results on C_6H_5OM [M = Li, Na, K, Rb, Cs]", *Inorg. Chem.*, **36**, 3398, (1997).

W.C. Elliott, P.F. Miceli, T. Tse, and P.W. Stephens, "Temperature and Orientation Dependence of Kinetic Roughening During Homoepitaxy: a Quantitative X-ray Scattering Study of Ag", *Phys. Rev.*, **B54**, 17938, (1996).

S.W. Huang, Z.H. Ming, Y.L. Soo, Y.H. Kao, M. Tanaka, and H. Munekata, "X-ray Scattering and Absorption Studies of MnAs Thin Films Grown by MBE on GaAs(001) Substrates", Evolution of Epitaxial Structure and Morphology, Mat. Res. Soc. Symp. Proc., **399**, 29, (1996).

C.A. Kuntscher, G.M. Bendele, and P.W. Stephens, "Alkali-Metal Stoichiometry and Structure of K_4C_{60} and Rb_4C_{60}", *Phys. Rev.*, **B55**, R3366, (1997).

Z.H. Ming, Y.L. Soo, S. Huang, Y.H. Kao, K. Stair, G. Devane, and C. Choi-Feng, "Structural Ordering in InGaAs/GaAs Superlattices", *J. Appl. Phys.*, **80**, 4372, (1996).

Z.H. Ming, Y.L. Soo, S.W. Huang, Y.H. Kao, K. Stair, G. Devane, C. Choi-Feng, T. Chang, L.P. Fu, G.D. Gilliland, J. Klem, and M. Hafich, "Semiconductor Superlattices Studied by Grazing Incidence X-ray Scattering and Diffraction", Optoelectronic Materials - Ordering, Composition Modulation and Self-Assembled Structures, Mat. Res. Soc. Symp. Proc., **417**, 325, (1996).

T.M. Nenoff, J.B. Parise, G.A. Jones, L.G. Galya, D.R. Corbin, and G.D. Stucky, "Flexibility of the Zeolite RHO Framework: *In Situ* X-ray and Neutron Powder Structural Characterization of Cation Exchanged BePO- and BeAsO-RHO Analogs", *J. Phys. Chem.*, **100**, 14256, (1996).

G. Oszlanyi, G. Baumgartner, G. Faigel, and L. Forro, "Na_4C_{60} an Alkali Intercalated Two-Dimensional Polymer", *Phys. Rev. Lett.*, **78**, 4438, (1997).

G. Oszlanyi, G. Bortel, G. Faigel, L. Granasy, L. Forro, G.M. Bendele, and P.W. Stephens, "Single C-C Bond in $(C_{60})_2^{2-}$", *Phys. Rev.*, **B54**, 11849, (1996).

G. Oszlanyi, G. Bortel, G. Faigel, L. Granasy, P.W. Stephens, G.M. Bendele, and L. Forro, "Single C-C Bond in KC_{60} and RbC_{60}", Fullerenes and Fullerene Nanostructures, edited by H. Kuzmany, J. Fink, M. Mehring, and S. Roth, *World Scientific*, p. 354, (1996).

A.M. Rao, P.C. Eklund, U.D. Venkateswaran, J. Tucker, M.A. Duncan, G.M. Bendele, P.W. Stephens, J.L. Hodeau, L. Marques, M. Núñez-Regueiro, I.O. Bashkin, E.G. Ponyatovsky, and A.P. Morovsky, "Properties of C_{60} Polymerized under High Pressure and Temperature", *Appl. Phys.*, **A64**, 231, (1997).

Y.L. Soo, S.W. Huang, Z.H. Ming, Y.H. Kao, E. Goldburt, R. Hodel, B. Kulkarni, and R. Bhargava, "Investigation of Local Structures Around Luminescent Centers in Doped Nanocrystal Phosphors", Surface/Interface and Stress Effects in Electronic Material Nanostructures, Mat. Res. Soc. Symp. Proc. **405**, 283, (1996).

S. van Smaalen, R.E. Dinnebier, H. Katzke, and W. Depmeier, "Structural Characterization of the High-Temperature Phase Transition in $Ca_8[Al_{12}O_{24}](MoO_4)_2$ Aluminate Sodalite using X-ray Powder Diffraction", *J. Sol. State Chem.*, **129**, 130, (1997).

T. Yilidrim, L. Barbedette, J.E. Fischer, G. Bendele, P.W. Stephens, C.L. Lin, C. Goze, F. Rachdi, J. Robert, P. Petit, and T.T.M. Palstra, "Synthesis and Properties of Mixed Alkali-Alkaline Earth Fullerides", *Phys. Rev.*, **B54**, 11981, (1996).

Beamline X4A

J.C. Boyington, V.N. Gladyshev, S.V. Khangulov, T.C. Stadtman, and P.D. Sun, "Crystal Structure of Formate Dehydrogenase H: Catalysis Involving Mo, Molybdopterin, Selenocysteine and an Fe4S4 Cluster", *Science*, **275**, 1305, (1997).

J.H. Cate, and J.A. Doudna, "Metal-Binding Sites in the Major Groove of a Large Ribozyme Domain" *Structure*, **4**, 1221, (1996).

J. H. Cate, A.R. Gooding, E. Podell, K. Zhou, B. L. Golden, C.E. Kundrot, T.R. Cech, and J.A. Doudna, "Crystal Structure of a Group I Ribozyme Domain: Principles of RNA Packing", *Science*, **273**, 1678, (1996).

D.C. Chan, D. Fass, J.M. Berger, and P.S. Kim, "Core Structure of gp41 from the HIV Envelope Glycoprotein", *Cell*, **89**, 263, (1997).

X. Duan, F.S. Gimble, and F.A. Quiocho, "Crystal Structure of PI-SceI, a Homing Endonuclease with Protein Splicing Activity", *Cell*, **89**, 555, (1997).

R. Gaudet, A. Bohm, and P.B. Sigler, "Crystal Structure at 2.4Å Resolution of the Complex of Transducin βγ and Its Regulator, Phosducin" *Cell*, **87**, 577, (1996).

F. Guo, D.N. Gopaul, and G.D. Van Duyne, "Structure of Cre Recombinase Complexed with DNA in a Site-Specific Recombination Synapse", *Nature*, **389**, 40, (1997).

W.A. Hendrickson, and C.M. Ogata, "Phase Determination by the Method of Multi-wavelength Anomalous Diffraction (MAD)", *Methods in Enzymology*, **276/28**, 494, (1997).

L. Huang, X. Weng, F. Hofer, G.S. Martin, and S.-H. Kim, "Three-Dimensional Structure of the Ras Interacting domain of RalGDS", *Nat. Struct. Biol.*, **4**, 609, (1997).

S. R. Hubbard, "Crystal Structure of the Activated Insulin Receptor Tyrosine Kinase in Complex with Peptide Substrate and ATP Analog", *EMBO J.*, **16**, 5572, (1997).

R. Kovall, and B. W. Matthews, "Toroidal Structure of λ-Exonuclease", *Science*, **277**, 1824, (1997).

Y.-H. Lee, T.W. Olson, C.M. Ogata, D.G. Levitt, L.J. Banaszak, and A.J. Lange, "Crystal Structure of the Phosphoenzyme Intermediate of Fructose-2,6-bisphosphatase Trapped during the Catalytic Reaction", *Nat. Struct. Bio.*, **4**, 615, (1997).

C.D. Lima, K.L. D'Amico, I. Naday, G. Rosenbaum, E.M. Westbrook, and W.A. Hendrickson, "MAD Analysis of FHIT, a Putative Human Tumor Suppressor from the HIT Protein Family", *Structure*, **5**, 763, (1997).

A. Malhotra, E. Severinova, and S.A. Darst, "Crystal Structure of a σ^{70} Subunit Fragment from *E. coli* RNA Polymerase", *Cell*, **87**, 127, (1996).

E. Martinez-Hackert, S. Harlocker, M. Inouye, H.M. Berman, and A.M. Stock, "Crystallization, X-ray Studies, and Site-Directed Cysteine Mutagenesis of the DNA-Binding Domain of OmpR", *Protein Science*, **5**, 1429, (1996).

E. Martinez-Hackert, and A.M. Stock, "The DNA-Binding Domain of OmpR: Crystal Structure of a Winged Helix Transcription Factor", *Structure*, **5**, 109, (1997).

M. Ormo, A.B. Cubitt, K. Kallio, L.A. Gross, R.Y. Tsien, and S.J. Remington, "Crystal Structure of the *Aequorea victoria* Green Fluorescent Protein", *Science*, **273**, 1392, (1996).

S. Raghunathan, C.S. Ricard, T.M. Lohman, and G. Waksman, "Crystal Structure of the Homo-Tetrameric DNA Binding Domain of *Escherichia coli* Single-Stranded DNA Binding Protein Determined by Multiwavelength X-ray Diffraction on the Selenomethionyl Protein at 2.9Å Resolution", *PNAS (USA)*, **94**, 6652, (1997).

L. Shapiro, J.P. Doyle, P. Hensley, D. R. Colman, and W.A. Hendrickson, "Crystal Structure of the Extracellular Domain from P_0 the Major Structural Protein of Peripheral Nerve Myelin", *Neuron*, **17**, 435, (1996).

F. Sicheri, I. Moarefi, and J. Kuriyan, "Crystal Structure of the Src-Family Tyrosine Kinase Hck", *Nature*, **385**, 602, (1997).

J. L. Smith, A. Thompson, and C. M. Ogata, "Crystallography Going Mad?", *Synch. Rad. News*, **9**, 12, (1996).

S.M. Soisson, B. MacDougall-Shackleton, R. Schleif, and C. Wohlberger, "Structural Basis for Ligand-Regulated Oligomerization of AraC", *Science*, **276**, 421, (1997).

L. Tong, S. Pav, D.M. White, S. Rogers, K.M. Crane, C.L. Cywin, M.L. Brown, and C.A. Pargellis, "A Highly Specific Inhibitor of Human p38 MAP Kinase Binds in the ATP Pocket", *Nat. Struct. Bio.*, **4**, 311, (1997).

L. Tong, C. Qian, M.-J. Massariol, P.R. Bonneau, M.G. Cordingley, and L. Lagace, "A New Serine-Protease Fold Revealed by the Crystal Structure of Human Cytomegalovirus Protease", *Nature*, **383**, 272, (1996).

H. Wu, P. D. Kwong, and W. A. Hendrickson, "Dimeric Association and Segmental Variability in the Structure of Human CD4", *Nature*, **387**, 527, (1997).

D. Xia, C.-A. Yu, H. Kim, J.-Z. Xia, A.M. Kachurin, L. Zhang, L. Yu, and J. Deisenhofer, "Crystal Structure of the Cytochrome bc1 Complex from Bovine Heart Mitochondria", *Science*, **277**, 60, (1997).

H. Yamaguchi, and W.A. Hendrickson, "Structural Basis for Activation of a Human Lymphocyte Kinase Lck upon Tyrosine Phosphorylation" *Nature*, **384**, 484, (1996).

F. Yang, L.G. Moss, and G.N. Phillips, Jr., "The Molecular Structure of the Green Fluorescent Protein", *Nature Biotechnology*, **14**, 1246, (1996).

Beamline X5

K. Hicks, H. Baghaei, A. Caracappa, A. Cichocki, G. Davenport, R. Finlay, V. Gladyshev, T. Gresko, S. Hoblit, M. Khandaker, O. Kistner, F.X. Lee, R. Lindgren, M. Lucas, L. Miceli, B. Norum, J. Rapaport, A.M. Sandorfi, R. Sealock, L.C. Smith, C.E. Thorn, S. Thornton, C.S. Whisnant, and L.E. Wright, "Spin Asymmetries from $^{16}O(\vec{\gamma},\vec{\pi}^-)$ near Δ Resonance Energies", *Phys. Rev.*, **C55**, R12, (1997).

Beamline X6B

R.P. Chiarello, N. C. Sturchio, J. Grace, P. Geissbuhler, L. Sorensen, L. Cheng, and S. Tau, "Otavite-calcite Solid-Solution Formation at the Calcite-water Interface Studied *in situ* by Synchrotron X-ray Scattering", *Geochimica et Cosmochimica Acta*, **61**, 1467-1474, (1997).

S. Krishnan, J.J. Felten, J.E. Rix, J.K.R. Weber, P.C. Nordine, M.A. Beno, S. Ansell, and D.L. Price, "Levitation Apparatus for Structural Studies of High Temperature Liquids using Synchrotron Radiation", *Rev. Sci. Instrum.*, **68**, 3512, (1997).

A. Malik, M.K. Durbin, A.G. Richter, K.G. Huang, and P. Dutta, "Order in Langmuir-Blodgett Films of Lead and Calcium Stearate", *Thin Solid Films*, **144**, 284-285, (1996).

Beamline X7A

P. Armand, A. Goldbach, C. Cramer, R. Csencsits, L. E. Iton, D. L. Price, and M.-L. Saboungi, "Semiconductors in the Disordered State: from Bulk to Nanoscale", *J. Non-Cryst. Solids*, **205**, 797, (1996).

P. Armand, M.-L. Saboungi, D. L. Price, L. Iton, C. Cramer, and M. Grimsditch, "Nanoclusters in Zeolite", *Phys. Rev. Lett.*, **79**, 2061, (1997).

C. L. Bowes, W. U. Huynh, S. J. Kirby, A. Malek, G. A. Ozin, S. Petrov, M. Twardowski, D. Young, R. L. Bedard, and R. Broach, "Dimetal Linked Open Frameworks: $[(CH_3)_4N]_2(Ag_2,Cu_2)Ge_4S_{10}$", *Chem. Mater.*, **8,** 2147, (1996).

D. J. Buttrey, T. Vogt, G. P. A. Yap, and A. L. Rheingold, "The Structure of $Bi_{26}Mo_{10}O_{69}$", *Mater. Res. Bull.*, **32,** 947, (1997).

D.G. Castner, P. Favia, and B.D. Ratner, "Deposition of Fluorocarbon Films by Remote RF Glow Discharge", Surface Modification of Polymeric Biomaterials, Edited by B.D. Ratner and D.G. Castner, Plenum Press, New York, pp. 45-52, (1997).

L. Chai, M. A. Akbas, P. K. Davies, and J. B. Parise, "Cation Ordering Transformations in $Ba(Mg_{1/3}Ta_{2/3})O_3$-$BaZrO_3$ Perovskite Solid Solutions", *Mater. Res. Bull.*, **32,** 1261, (1997).

F. C. Chou, A. Aharony, R. J. Birgeneau, O. Entin-Wohlman, M. Greven, A. B. Harris, M. A. Kastner, Y. J. Kim, D. S. Kleinberg, Y. S. Lee, and Q. Zhu, "Ferromagnetic Moment and Spin Rotation Transitions in Tetragonal Antiferromagnetic $Sr_2Cu_3O_4Cl_2$", *Phys. Rev. Lett.*, **78,** 535, (1997).

D. E. Cox, and R. J. Papoular, "Structure Refinement with Synchrotron Data: R-factors, Errors and Significance Tests", *Mater. Science Forum,* **228**, 233, (1996).

Y. Fei, C. M. Bertka, and L. W. Finger, "High-Pressure Iron-Sulfur Compound, Fe_3S_2, and Melting Relations in the Fe-FeS System", *Science,* **275**, 1621, (1997).

C. C. Freyhardt, R. F. Lobo, S. Khodabandeh, J. E. Lewis Jr., M. Tsapatsis, M. Yoshikawa, M. A. Camblor, M. Pan, M.M. Helmkamp, S. I. Zones, and M. E. Davis, "VPI-8: A High-Silica Molecular Sieve with a Novel "Pinwheel" Building Unit and its Implications for the Synthesis of Extra-Large Pore Molecular Sieves", *J. Amer. Chem. Soc.*, **118**, 7299, (1996).

R. L. Harlow, N. Herron, and D. L. Thorn, "The Crystal Structures of some New Forms of Aluminum Fluoride as Determined from Their Synchrotron Powder Diffraction Patterns", Synchrotron Radiation Techniques in Industrial, Chemical and Materials Science, edited by L. J. Terminello, K. D'Amico, and D. K. Shuh, Plenum, New York, p. 37, (1996).

M. Kunz, D. Xirouchakis, Y. Wang, J.B. Parise, and D.H. Lindsley, "Structural Investigations along the Join $CaTi_OSi_{O4}$ - $CaSnSi_{O4}$", *Swiss Bull. of Mineral. and Petro.*, **77**, 1-11, (1997).

K. Leinenweber, and J. B. Parise, "Rietveld Refinement of the Novel Double Perovskite Ca_2TiSiO_6", *Amer. Mineralogist,* **82,** 475, (1997).
L.H. Lewis, C.H. Sellers, and V. Panchanathan, "Annealing-Induced Property Improvements in 2-14-1 Powders Produced by Inert Gas Atomization", *IEEE Trans. Mag.,* **32**, 4371, (1996).

L.H. Lewis, C.H. Sellers, and V. Panchanathan, "Factors Affecting Coercivity in Rare-Earth-Based Advanced Permanent Magnetic Materials", Rare-Earths: Science, Technology and Applications III, edited by R. G. Bautista, C. O. Bounds, T. W. Ellis, and B. T. Kilbourn, The Minerals, Metals and Materials Society, p. 119, (1997).

L.H. Lewis, D.O. Welch, and V. Panchanathan, "Exchange-spring" Nd-Fe-B Alloys: Investigations into Reversal Mechanisms and Their Temperature Dependence", *J. Appl. Phys.*, **81**, 4422, (1997).

R. F. Lobo, S.I. Zones, R.C. Medrud, and T.V. Harris, "Synthesis and Rietveld Refinement of the Small-Pore Zeolite SSZ-16", *Chem. Mater.,* **8**, 2409, (1996).

R.F. Lobo, M. Tsapatsis, C.C. Freyhardt, S. Khodabandeh, P. Wagner, C.-Y. Chen, K.J. Balkus Jr., S.I. Zones, and M.E. Davis, "Characterization of the Extra-Large-Pore Zeolite UTD-1", *J. Amer. Chem. Soc.,* **119**, 8474, (1997).

C. Meingast, G. Roth, L. Pintschovius, R.H. Michel, C. Stoermer, M.M. Kappes, P.A. Heiney, L. Brard, R.M. Strongin, and A.B. Smith, III, "Structure, Dynamics, and Phase Transitions in the Fullerene Derivatives C_{60} and $C_{61}H_2$,",*Phys. Rev.*, **B54**, 124-131, (1996).

J. B. Parise, Y. Wang, G. D. Gwanmesia, J. Zhang, and Y. Sinelnikov, "The Symmetry of Garnets on the Pyrope-Majorite Join", *J. Geophys. Res. Lett.,* **23**, 3799, (1996).

J. B. Parise, K. Tan, P. Norby, Y. Ko, and C. Cahill, "Examples of Hydrothermal Titration and Real Time X-ray Diffraction in the Synthesis of Open Frameworks", Mater. Res. Soc. Symp. Proc., **453**, 103, (1997).

D. L. Price, A. J. G. Ellison, M.-L. Saboungi, R.-Z. Hu, T. Egami, and W. S. Howells, "Short, Intermediate-and Extended-Range Order in Rubidium Germanate Glasses", *Phys. Rev.*, **B55**, 11249, (1997).

P. G. Radaelli, D. E. Cox, M. Marezio, and S.-W. Cheong, "Charge, Orbital and Magnetic Ordering in $La_{0.5}Ca_{0.5}MnO_3$", *Phys. Rev.*, **B55**, 3015, (1997).

M. R. Stetzer, P. A. Heiney, J. E. Fischer, and A. R. McGhie, "Thermal Stability of Solid C_{60}", *Phys. Rev.*, **B55**, 127-131, (1997).

J. Vacinova, J. L. Hodeau, P. Bordet, M. Anne, D. Cox, A. Fitch, P. Pattison, W. Schweggle, H. Graafsma, and Å. Kvick, "Diffraction Anomalous Fine Structure Analysis on $(Bi,Pb)_2PtO_4$ Powders", *Mater. Science Forum*, **228**, 94, (1996).

W. Wang, D.G. Castner, and D.W. Grainger, "Ultrathin Films of Perfluoropolyether-Grafted Polysiloxanes Chemisorbed Via Alkylthiolate Anchors to Gold Surfaces", *Supramolecular Science*, **4**, 83-99, (1997).

P. M. Woodward, A. W. Sleight, and T. Vogt, "Ferroelectric Tungsten Trioxide", *J. Solid State Chem.*, **131**, 9, (1997).

D. Xirouchakis, M. Kunz, J.B. Parise, and D.H. Lindsley, "Synthesis Methods and Unit-Cell Volume of End-Member Titanite ($CaTi_OSi_{O4}$)", *Americna Mineralogist*, **82**, 748- 753, (1997).

Q. Zhu, L. Li, M. S. Masteller, and G. J. Del Corso, "An Increase of Structural Order Parameter in Fe-Co-V Soft Magnetic Alloy after Thermal Aging", *Appl. Phys. Lett.*, **69**, 3917, (1996).

Beamline X7B

J. Aizenberg, J. Hanson, T.F. Koetzle, S. Weiner, and L. Addadi, "Control of Macromolecule Distribution within Synthetic and Biogenic Single Calcite Crystals", *J. Am. Chem. Soc.*, **119**, 881, (1997).

G. Artioli, K. Ståhl, and J.C. Hanson, "The Dehydration Process in the Natural Zeolite Laumontite: A Real-Time Synchrotron X-Ray Powder Diffraction Study", *Mater. Sci. Forum*, **228**, 369, (1996).

R. Bolt, J. Albertsson, G. Svensson, K. Ståhl, and J.C. Hanson, "A Synchrotron X-Ray Study of Ferroelectric Switching, Domain Reversal and Piezoelectric Moduli in $CsTiOAsO_4$ under an Applied Electric Field", *J. Appl. Cryst.*, **30**, 383, (1997)

A. N. Christensen, P. Norby, and J. C. Hanson, "*In Situ* Investigation of Magnesium Aluminophosphate Synthesis by Synchrotron X-Ray Powder Diffraction", *Acta Chem. Scand.*, **51**, 249, (1997).

A.N. Christensen, P. Norby, and J.C. Hanson, "Superconducting Cuprates and Related Oxides. IX. *In Situ* Synchrotron X-Ray Powder Diffraction Investigation of the Oxidation and Reduction of $YBa_2Cu_3O_{7-x}$ in a Flow of Oxygen or of Nitrogen Gas in the Temperature Range 400-725°C", *Acta Chemica Scandinavica*, **51**, 340, (1997).

A. N. Christensen, P. Norby, J. C. Hanson, and S. Shimada, "Phase Transition of KN_{O3} Monitored by Synchrotron X-ray Powder Diffraction", *J. Appl. Cryst.*, **29**, 265, (1996).

M.J. Gray, J.D. Jasper, A.P. Wilkinson, and J.C. Hanson, "Synthesis and Synchrotron Microcrystal Structure of an Aluminophosphate with Chiral Layers Containing λ-Tris(ethylenediamine)cobalt(III)", *Chem. of Mat.*, **9**, 976, (1997).

C.P. Grey, F.I. Poshni, A. Gualtieri, P. Norby, J.C. Hanson, and D.R. Corbin, "Combined MAS NMR and X-ray Powder Diffraction Structural Characterization of Hydrofluorocarbon-134 Adsorbed on Zeolite NaY: Observation of Cation Migration and Strong Sorbate-cation Interactions", *J. Am. Chem. Soc.*, **119**, 1981, (1997).

A. Gualtieri, P. Norby, G. Artioli, and J. Hanson, "Kinetics of Formation of Zeolite Na-A [LTA] from Natural Kaolinites", *Phys. Chem. Minerals,* **24**, 191, (1997).

A. Gualtieri, P. Norby, G. Artioli, and J. Hanson, "Kinetic Study of Hydroxysodalite Formation from Natural Kaolinites by Time-Resolved Synchrotron Powder Diffraction", *Microporous Materials,* **9**, 189, (1997).

A. Gualtieri, P. Norby, J. Hanson, and J. Hriljac, "Rietveld Refinement using Synchrotron X-ray Powder Diffraction Data Collected in Transmission Geometry using an Imaging-Plate Detector: Application to Standard *m*-ZrO_2", *J. Appl. Cryst.*, **29**, 707, (1996).

T. Hänninen, I. Mutikainen, V. Saanila, M. Ritala, M. Leskel, and J.C. Hanson, "[$Ca(Thd)_2$(Tetraen)]: A Monomeric Precursor for Deposition of CaS Thin Films", *Chem. Mat.*, **9**, 1234, (1997).

R.A. Holroyd, J.M. Preses, and J.C. Hanson, "Excited Singlet State Yields in Hydrocarbon Liquids Exposed to X-Rays", *J. Phys. Chem.*, **101**, 6931, (1997).

R.E. Morris, S.J. Weigel, P. Norby, J.C. Hanson, and A.K. Cheetham, "*In Situ* Single-Crystal X-ray Diffraction Study of Crystallization Kinetics in Clathrasil Dodecasil-3C (MTN)", *J. Synch. Rad.*, **3**, 301, (1996).

P. Norby, "Synchrotron Powder Diffraction using Imaging Plates; Crystal Structure Determination and Rietveld Refinement", *J. Appl. Crystall.*, **30**, 21, (1997).

P. Norby, "Hydrothermal Conversion of Zeolites; An *In situ* Synchrotron X-Ray Powder Diffraction Study", *J. Am. Chem. Soc.*, **119**, 5215, (1997).

J.B. Parise, K. Tan, P. Norby, Y. Ko, and C. Cahill, "Examples of Hydrothermal Titration and Real Time X-ray Diffraction in the Synthesis of Open Frameworks", Mat. Res. Soc. Symp. Proc., **453**, 103, (1997).

K. Ståhl, G. Artioli, and J.C. Hanson, "The Dehydration Process in the Zeolite Laumontite: A Real-Time Synchrotron X-Ray Powder Diffraction Study", *Phys. Chem. Minerals,* **23**, 328, (1996).

P. Wochner, X. Xiong, P.C. Chow, and S.C. Moss, "X-ray Study of Two-Phase Coexistence in a C_{60} Single Crystal Through the Cubic-Cubic Phase Transition at 260K", *Phys. Rev.*, **B55**, 5678, (1997).

X. Xiong, Q. Zhu, Z.G. Li, S.C. Moss, H.H. Feng, P.H. Hor, D.E. Cox, S. Bhavaraju, and A.J. Jacobson, "Synchrotron X-ray Study of Interstitial Oxygen Ordering in the Superconducting Phase of $La_2CuO_{4+\delta}$", *J. Mat. Res.*, **11**, 2121, (1996).

Beamline X8A and X8C

J.J. Fitch, R.L. Blake, A.J. Burek, A.M. Clark, D.E. Graessle, B. Harris, D.A. Schwartz, and J.B. Sweeney, "AXAF Synchrotron Witness Mirror Calibrations, 2-12 keV", in Grazing Incidence and Multilayer X-ray Optical System, *SPIE,* **3113**, 30-39, (1997).

D.E. Graessle, A.J. Burek, J.J. Fitch, B. Harris, D.A. Schwartz, and R.L. Blake, "Optical Constants from Synchrotron Reflectance Measurements of AXAF Witness Mirrors, 2-12 keV", in Grazing Incidence and Multilayer X-ray Optical System, *SPIE*, **3113**, 52-64, (1997).

P. J. Loll, A. E. Bevivino, B. D. Korty, and P. H. Axelsen, "Simultaneous Recognition of a Carboxylate-containing Ligand and an Intramolecular Surrogate Ligand in the Crystal Structure of an Asymmetric Vancomycin Dimer", *J. Am. Chem. Soc.*, **119**, 1516, (1997).

Beamline X9A

B. Sclavi, S. Woodson, M.R. Chance, and M.D. Brenowitz, "Examining the Conformational Dynamics of Macromolecules with Time-Resolved X-Ray 'Footprinting' ", *Structure*, **5**, 865-869, (1997).

B. Sclavi, S. Woodson, M. Sullivan, M.R. Chance, and M. Brenowitz, "Time-Resolved Synchrotron X-Ray 'Footprinting', a New Approach to the Study of Nucleic Acid Structure and Function: Application to Protein-DNA Interactions and RNA Folding", *J. Mol. Biol.*, **266**, 144-159, (1997).

B. Sclavi, S. Woodson, M. Sullivan, M.R. Chance, and M.D. Brenowitz, "X-Ray 'Footprinting' Analysis of the Mg^{2+} Dependent Folding of the Tetrahymena Thermophila Ribozyme", *Prog. in Bioph. & Molecular Biology*, **65**, 85, (1996).

B. Sclavi, S. Woodson, M. Sullivan, M.D. Brenowitz, and M.R. Chance, "Kinetics of Folding of the Tetrahymena Thermophila Group I Intron", *Biophysical J.*, **72**, A422, (1997).

David L. Tierney, XAS Characterization of Bacterial Superoxide Dismutase and NMR Characterization of Substrate Binding in Phthalate Dioxygenase, Ph.D. Thesis, University of Michgian, (1996).

Beamline X9B

S.C. Goldsmith, N. Pokala, P. Matsudaira, and S.C. Alom, "Crystallization and Preliminary Crystallographic Analysis of the N-terminal Actin Binding Domain of Human Fimbrin", *Proteins: Structure, Function & Genetics*, **28**, 452-453, (1997).

J.C. Gonzalez, K. Peariso, J. Penner-Hahn, and R.G. Matthews, "Cobalamin-Independent Methionine Synthase from *Escherichia coli:* A Zinc Metalloenzyme", *Biochem.*, **35**, 12228-12234, (1996).

Z. Gu, J. Dong, C.B. Allan, S.B. Choudhury, R. Franco, J.J.G. Moura, I. Moura, J. LeGall, A.E. Przybyla, W.R. Roseboom, S.P.J. Albracht, M.J. Axley, R.A. Scott, and M.J. Maroney, "Structure of the Ni Sites in Hydrogenases by X-Ray Absorption Spectroscopy. Species Variation and the Effects of Redox Poise", *J. Am. Chem. Soc.*, **118**, 11155-11165, (1996).

P. Henderson, D. Beyer, U. Jonas, O. Karthaus, H. Ringsdorf, P.A. Heiney, N.C. Maliszewskyj, S.S. Ghosh, O. Mindyuk, and J.Y. Josefowicz, "Complex Ordering in Thin Films of Di-and Trifunctionalized Hexaalkoxy Triphenylene Derivatives", *J. Am. Chem. Soc.*, **119**, 4740-4748, (1997).

K.C. Holmes, "The Swinging Lever-Arm Hypothesis of Muscle Contraction", *Current Biology* **7**, R112-118, (1997).

K.C. Holmes, "Muscle Proteins: Their Actions and Interactions", *Current Opinion in Structural Biology*, **6**, 781-789, (1996).

H. Huang, Structural Characterization of Organocopper Reagents, PhD. Thesis, University of Michigan, (1997).

H.C. Lee, E.M. Scheuring, J. Peisach, and M.R. Chance, "ESEEM and EXAFS Studies of Models of OxyCo-

Substituted Hemoproteins: Correlating Electron-Nuclear Interactions and Metal-Ligand Bond Lengths", *Biophysical J.*, **72**, A427, (1997).

S. Mahapatra, J. A. Halfen, E. C. Wilkinson, G. Pan, X. Wang, V. G. Young, Jr., C. J. Cramer, L. Que, Jr. and W. B. Tolman, "Structural, Spectroscopic, and Theoretical Characterization of Bis(m-oxo)dicopper Complexes, Novel Intermediates in Copper-Mediated Dioxygen Activation", *J. Am. Chem. Soc.*, **118**, 11555-11574, (1996).

M. J. Maroney, C. B. Allan, S. B. Choudhury, and Z. Gu, "Redox Metalloenzymes with S-donor Ligands. Hydrogenase: A Case Study", Transition Metal Sulfur Chemistry: Biological and Industrial Significance, edited by E. I. Stiefel and K. Matsumoto, *ACS Symposium Series,* **653**, 74-100, (1996).

L.M. Miller, A.J. Pedraza, and M.R. Chance, "Identification of Conformational Substrates Involved in Nitric Oxide Binding to Ferric and Ferrous Myoglobin Through Difference Fourier Transform Infrared Spectroscopy", *Biophysical J.*, **72**, A425, (1997).

M.J. Nelson, L.T. Durney, and R.C. Scarrow, "Nitrile Hydratase from Rhodococcus rhodochorous J1 Contains a Non-Corrin Cobalt Ion with Two Sulfur Ligands", *J. Amer. Chem. Soc.*, **115**, 9194-9195, (1996).

F. Schlunzen, H.A.S. Hansen, J. Thygesen, N. Volkmann, I. Levine, J. Harmes, H. Bartels, A. Bashan, Z. Berkovitch-Yellin, I. Sagi, F. Franceschi, S. Krumbholz, M. Geva, S. Weinstain, I. Agmon, N. Boddejer, S. Morlang, R. Sharon, A. Dribin, M. Peretz, V. Weinrich, and A. Yonath, "A Milestone in Ribosomal Crystallography: The Construction of Preliminary Electron Density Maps at Intermediate Resolution", *Biochem & Cell Biol.*, **73**, 739, (1996).

L. Shu, Y. Liu, J.D. Lipscomb, and L. Que, Jr., "X-Ray Absorption Spectroscopic Studies of the Methane Monooxygenase Hydroxylase Component from Methylosinus Trichosporium OB3b", *J. Bioinorganic Chem.*, **1**, 297-304, (1996).

L. Shu, J.C. Nesheim, K. Kauffmann, E. Münck, J.D. Lipscomb, and L. Que, Jr. "An Fe_2O_2 Diamond Core Structure for the Key Intermediate Q of Methane Monooxygenase", *Science,* **25**, 515-518, (1997).

D.L. Tierney, XAS Characterization of Bacterial Superoxide Dismutase and NMR Characterization of Substrate Binding in Phthalate Dioxygenase, PhD. Thesis, University of Michigan, (1996).

H. Wang, G. Peng, L.M. Miller, E.M. Scheuring, S.J.George, M.R. Chance, and S.P. Cramer, "Iron L-edge X-ray Absorption Spectroscopy of Myoglobin Complexes and Photolysis Products", *J. Amer. Chem. Soc.*, **119**, 4921-4928, (1997).

X. Wang, C. R. Randall, and L. Que, Jr., "X-ray Absorption Spectroscopic Studies of an FeZn Derivative of Uteroferrin", *Biochemistry*, **35**, 13946-13954, (1996).

K. Zhang, A.M. Edwards, J. Dong, J.A. Chupa, and J.K. Blasie, "XAFS on Vectorially-oriented Single Monolayer Protein Samples", *J. de Phys. IV Colloque*, 7, C2-593-C2-597, (1997).

Beamline X10A

P. Fenter, A. Eberhardt, K.S. Liang, and P. Eisenberger, "Molecular Epitaxy and Strain in Self-Assembled Monolayers", *J. Chem. Phys.*, **106**, 1600, (1997).

P. Fenter, F. Schreiber, L. Zhou, P. Eisenberger, and S.R. Forrest, "*In Situ* Studies of Morphology, Strain, and Growth Modes of a Molecular Organic Thin Film", *Phys. Rev.*, **B56**, 3046, (1997).

Beamline X10B

J. Li, and H.D. Abruna, "Coadsorption of Sulfate/Bisulfate Anions with Hg Cations During Hg Underpotential Deposition on Au(111): An *In Situ* X-ray Diffraction Study", *J. Phys. Chem.*, **B101**, 24-252, (1997).

Beamline X10C

P. Schmuki, S. Virtanen, A. J. Davenport, and C. M. Vitus, "*In situ* X-ray Absorption Near-edge Spectroscopic Study of the Cathodic Reduction of Artifical iron Oxide Passive Films", *J. Electrochem. Soc.*, **143/2**, 574-582, (1996).

P. Schmuki, S. Virtanen, A. J. Davenport, and C. M. Vitus, "Transpassive Dissolution of Cr and Sputter-Deposited Cr Oxides Studied by *in situ* X-ray near edge Spectroscopy", *J. Electrochem. Soc.*, **143**, 3997, (1996).

P. Schmuki, S. Virtanen, H.S. Isaacs, A.J. Davenport, H. Böhni, and T. Stenberg, "*In situ* XANES Studies on the Electrochemical Behavior of Thin (Fe,Cr)-oxide Films used as Models for Passive Films", Surface Oxide Films, edited by J. Bardwell, *Electrochemical Soc.*, **96/18**, 234, (1996).

S. Virtanen, P. Schmuki, A. J. Davenport, and C.M. Vitus, "Dissolution of Artificial Iron Passive Films Studied by *in situ* X-ray Absorption near Edge Spectroscopy", *J. Electrochem. Soc.*, **144**, 198, (1997).

S. Virtanen, P. Schmuki, A. J. Davenport, and C.M. Vitus, "Dissolution of Sputter-Deposited Iron Oxide films used as a Model for the Passive film on Iron", Critical Factors for Localized Corrosion II, edited by P.M. Natishan, R.G.Kelly, G.S. Frankel, and R.C. Newman, *Electrochemical Soc.*, **95/15**, 241, (1996).

Beamline X11A

T. Alcacio, XAFS Analysis of Lead Sorption at the Mineral/Water Interface, M.S. Thesis, University of Delaware, (1997).

D. Aldrich, Characterization of the Solid Phase Reaction of Titanium with Silicon Germanium Alloys: Interface Reactions, Phase Formation and Stability, Thesis, North Carolina State University, (1995).

O. Alexeev, M. Shelef, and B.C. Gates, "MgO-supported Platinum-Tungsten Catalysts Prepared from Organo-metallic Precursers: Platinum Clusters Isolated on Dispersed Tungsten", *J. Catal.*, **163**, 1, (1996).

M. Balasubramanian, Studies of Ternary Doped Intermetallics and Nanostructured Materials Using X-ray Absorption Spectroscopy, Thesis, University of Connecticut, (1996).

B. I. Boyanov, Support and Temperature Effects in Platinum Clusters, Thesis, Illinois Institute of Technology, (1995).

D.L. Brewe, S.M. Heald, B. Barg, F.C. Brown, K.H. Kim, and E.A. Stern, "Capillary X-ray Compressor: Principle vs. Practice, X-ray Microbeam Technology and Applications", edited by W. Yun, *SPIE*, **2516**, 197, (1996).

J.-R. Chang, J.-F. Lee, S.D. Lin, and A.S. Lin, "Carbon-Supported Platinum Catalyst Electrode: Characterization by Transmission Electron Microscopy, X-ray Absorption Spectroscopy, and Electrochemical Half-Cell Measurement on a Phosphoric Acid Fuel Cell", *J. of Phys. Chem.*, **99**, 14798, (1995).

Y. Dao, Growth and Characterization of $(Ti_{1-x}Zr_x)Si_2$ Thin Films on Silicon, Thesis, North Carolina State University, (1995).

M.J. Eick, Dissolution Kinetics of Lunar Simulants and Sorption of Oxyanions and Nickel on Secondary Weathering Products, Ph.D. Dissertation, University of Delaware, (1995).

M. Endregard, D.G. Nicholson, M. Stöcker, and G. Lamble, "Cobalticenium Ions Adsorbed on Large-Pore Alumininophosphate VPI-5 Studied by XAS, 13C Solid-state NMR and FT IR", *J. Mat. Chem.*, **5**, 485, (1995).

S.E. Fendorf, Sorption and Oxidation Mechanisms of Hydrolyzable Metal Ions on Oxide Minerals, Ph.D. Dissertation, University of Delaware, (1992).

S.E. Fendorf, M.J. Eick, P.R. Grossl and D.L. Sparks, "Arsenate and Chromate Retention Mechanisms on Goethite. 1. Surface Structure", *Environ. Sci. Technol.*, **31**, 315-320, (1997).

S.E. Fendorf, and D.L. Sparks,. "Application of Surface Spectroscopies and Microscopies to Elucidate Sorption Mechanisms on Oxide Surfaces", *Trans. of Int. Soc. Soil Sci.*, **3a**, 182-199, (1994).

S.E. Fendorf, and D.L. Sparks, "Mechanisms of Chromium(III) Sorption on Silica: II. Effects of Reaction Conditions", *Environ. Sci. Technol.*, **28**, 290-297, (1994).

S.E. Fendorf, D.L. Sparks, and M. Fendorf, "Mechanisms of Aluminum Sorption on Birnessite: Influences on Chromium Oxidation", *Trans. of Int. Soc. Soil Sci.*, **3a**, 129-145, (1994).

S.E. Fendorf, M.J. Eick, P.R. Grossl, and D.L. Sparks, "Arsenate and Chromate Retention Mechanisms on Geothite: Surface Structure", *Environ. Sci. Tech.*, **31**, 315, (1997).

A. Frenkel, B. Barg, S.M. Heald, F.C. Brown, K.H. Kim, and E.A. Stern, "Optimization of Monochromatic Crystal Bending Designs Using Computer Solutions", **67**, 9, (1996).

A.I. Frenkel, E.A. Stern, and F. A. Chudnovsky, "Metal-Insulator Transition and Local Structure of V_2O_3", J. Phys. IV France 7 (Proceedings of the 9th International Conference on X-Ray Absorption Fine Structure), pp. C2-1061-C2-1063, (1997).

A.I. Frenkel, E.A. Stern, and F.A. Chudnovsky, "Local Structure Changes in V_2O_3 Below and Above the Metal-Insulator Transition", *Solid State Comm.*, **102**, 637, (1997).

A.I. Frenkel, E.A. Stern, A. Rubshtein, A. Voronel, and Y. Rosenberg, "Local Structural Distortions in Quenched Au-Cu Alloys", J. Phys. IV France 7, Proceedings of the 9th International Conference on X-Ray Absorption Fine Structure, pp. C2-1005-C2-1006, (1997).

A.I. Frenkel, E.A. Stern, A. Voronel, and S.M. Heald, "Lattice Strains in Disordered Mixed Salts", *Solid State Commun.*, **99**, 67, (1996).

A.I. Frenkel, E.A. Stern, A. Voronel, A. Rubshtein, Y. Ben-Ezra, and V. Fleurov, "Redistribution of La-Al Nearest-Neighbor Distances in the Metallic Glass $Al_{0.91}La_{0.09}$" *Phys. Rev.*, **B54**, 884, (1996).

J.L. Fulton, D.M. Pfund, S.L. Wallen, M. Newville, and E.A. Stern, "Rubidium Ion Hydration in Ambient and Supercritical Water", *J. of Chem. Phys.*, **105/6**, 2161, (1996).

P.R. Grossl, M.J. Eick, S. Goldberg, C.C. Ainsworth, and D.L. Sparks, "Arsenate and Chromate Retention Mechanisms on Goethite. 2. Kinetic Evaluation using a Pressure-jump Relaxation Technique", *Environ. Sci. Technol.*, **31**, 321-326, (1997).

A. Hamid Muhammed Fasihuddin, L-edge X-ray Absorption Study of B-phase Ni_xAl_{100-x} and of the effects of Substitutional Fe Atoms on its Local Electronic Structure, Thesis, University of Connecticut, (1997).

D. Haskel, M. Qian, E.A. Stern, and M. Sarikaya, "Development of EXELFS for Nanoscale Atomic Structure Determination", J. Phys. IV France 7 (Proceedings of the 9th International Conference on X-Ray Absorption Fine Structure), pp. C2-557-C2-560 (1997).

D. Haskel, E.A. Stern, D.G. Hinks, A.W. Mitchell, J.D. Jorgenson, and J.I. Budnick, "Dopant and Temperature Induced Structural Phase Transitions in $La_{2-x}Sr_xCuO_4$", *Phys. Rev. Lett.*, **76**, 439, (1996).

D. Haskel, and E.A. Stern, "Altered Sr Atomic Environment in $La_{2-x}Sr_xCuO_4$", J. Phys. IV France 7 Proceedings of the 9th International Conference on X-Ray Absorption Fine Structure, pp. C2-1177-C2-1178, (1997).

D. Haskel, E.A. Stern, D.G. Hinks, A.W. Mitchell, and J.D. Jorgensen, "Altered Sr Environment in $La_{2-x}Sr_xCuO_4$", *Phys. Rev.*, **B56**, R521, (1997).

S.M. Heald, D.L. Brewe, B. Barg, K.H. Kim, F.C. Brown, and E.A. Stern, "Micro-XAS Using Tapered Capillary Concentrating Optics", J. Phys. IV France 7 Proceedings of the 9th International Conference on X-Ray Absorption Fine Structure, pp. C2-297-C2-301, (1997).

S.M. Heald, D.L. Brewe, K.H. Kim, F.C. Brown, B. Barg, and E.A. Stern, "Capillary Concentration for Synchrotron Radiation Beamlines", Optics for High Brightness Synchrotron Radiation Beamlines #2, edited by Lonny E. Berman and John Arthur, *SPIE*, **2856**, 36, (1996).

J. Kropf, XAFS and Reflectivity Investigations of Solid-Solid Interfaces, Ph.D. Dissertation, Notre Dame University, (1997).

Q. Lu, XAFS Investigations of Structural Properties at Internal Interfaces, Ph.D. Dissertation, Notre Dame University, (1996).

Q. Lu, B. A. Bunker, H. Lou, A. J. Kropf, K. M. Kemner, J. K. Furdyna, and G. C. Hua, "X-ray Study of Atomic Correlations in ZnCdSeTe Epitaxial Thin Films", *Phys. Rev.*, **B55**, 9910, (1997).

A.N. Mansour, and C.A. Melendres, "Chemistry, Structure and Morphology of Native and Passive Oxide films on Aluminum Rich Amorphous Al-Fe-Ce Alloys", Proceedings of the Tri-Service Conference on Corrosion, p. 129, (1994).

J. McBreen, X.Q. Yang, and H.S. Lee, "X-Ray Absorption Studies of $NiBr_2(PEO)_8$ and $ErBr_3(PEO)_{12}$ Complexes", *Macromol. Symp.* **105**, 185 (1996).

A. Moen, and D. G. Nicholson, "Reduction of Copper(II) with Subsequent Disproportionation of Copper(I) During the Hydrothermal Syntheses of Microporous Silicoaluminium Phosphates SAPO-5 and -11", J. *Chem. Soc. Faraday Trans.*, **91**, 3529, (1995).

M. Newville, Local Thermodynamic Measurements of Dilute Binary Alloys using XAFS, Thesis, University of Washington, (1995).

M. Newville, J.L. Fulton, D.M. Pfund, S.L. Wallen, E.A. Stern, and Y. Ma, "XAFS Measurements of Rb-O Bonds in Ambient and Supercritical Water", J. Phys. IV France 7 Proceedings of the 9th International Conference on X-Ray Absorption Fine Structure, pp. C2-1007-C2-1008 (1997).

P. A. Northrup, Topaz: Differential Incorporation and Growth Kinetics Controlled by Detailed Surface Structure, State University of New York at Stony Brook, Thesis, (1996).

K.I. Pandya, K.E. Swider, D.A. Corrigan, and W.E. O'Grady, "*In Situ* Evidence for Quadrivalent Nickel in Nickel Battery Electrodes", *J. Electrochem. Soc.*, **143**, 1601, (1996).

M. Qian, M. Sarikaya, and E.A. Stern, "EXELFS (-Data Renormalization", *Ultramicroscopy*, **68**, 163, (1997).

D.E. Ramaker, H. Sambe, H. Qian, and W.E. O'Grady, "Identification of Resonant, Two Electron, and Interatomic features in K and L23 NEXAFS Spectra", *Physica,* **B208 & 209**, 49, (1995).

B. Ravel, Ferroelectric Phase Transitions in Oxide Perovskites Studied by XAFS, Thesis, University of Washington, (1997).

B. Ravel, and E.A. Stern, "Temperature and Polarization Dependent XANES Measurements on Single Crystal $PbTiO_3$", J. Phys. IV France 7 Proceedings of the 9th International Conference on X-Ray Absorption Fine Structure, pp. C2-1223-C2-1224, (1997).

M. Sarikaya, M. Qian, and E.A. Stern, "EXELFS Revisited", *Micron*, **27**, 449-466, (1996).

A.M. Scheidegger, and D.L. Sparks, "A Critical Assessment of Sorption-Desorption Mechanisms at the Soil Mineral/water Interface", *Soil Sci.*, **161**, 813-831, (1996).

A.M. Scheidegger, and D.L. Sparks, "Kinetics of the Formation and the Dissolution of Nickel Surface Precipitates on Pyrophyllite", *Chem. Geol.*, **132**, 157-164, (1996).

A.M. Scheidegger, M. Fendorf, and D.L. Sparks, "Mechanisms of Nickel Sorption on Pyrophyllite: Macroscopic and Microscopic Approaches", *Soil Sci. Soc. Am. J.*, **60**, 1763-1772, (1996).

A.M. Scheidegger, G.M. Lamble, and D.L. Sparks, "Spectroscopic Evidence for the Formation of Mixed-cation Hydroxide Phases upon Metal Sorption on Clays and Aluminum Oxides", *J. Colloid Interf. Sci.*, **18**, 118-120, (1997).

N. Sicron, Y. Yacoby, E.A. Stern, and F. Dogan, "XAFS Study of the Antiferroelectric Phase Transition in $PbZrO_3$", J. Phys. IV France 7 Proceedings of the 9th International Conference on X-Ray Absorption Fine Structure, pp. C2-1047-C2-1049, (1997).

E.A. Stern, "XAFS and Thermal Averaging", J. Phys. IV France 7 Proceedings of the 9th International Conference on X-Ray Absorption Fine Structure, pp. C2-137-C2-140, (1997).

E.A. Stern, "Development of XAFS into a Structure Determination Technique", Roentgen Centennial: X-Rays in Natural and Life Sciences, Edited by A. Haase, G. Landwehr, and E. Umbach, World Scientific, Singapore, pp. 323-340, (1997).

E.A. Stern, and Y. Yacoby, "Structural Disorder in Perovskite Ferroelectric Crystals As Revealed by XAFS", *J. Phys. & Chem. of Solids*, **57**, 1449-1455, (1996).

R.V. Vedrinskii, V.L. Kraizman, A.A. Novakovich, Ph.V. Demekhin, S.V. Urazhdin, B. Ravel, and E.A. Stern, "Pre-Edge Fine Structure (PEFS) of the K-XAS for the 3d Atoms in Compounds: A New Tool for Quantitative Atomic Structure Determination" J. Phys. IV France 7 Proceedings of the 9th International Conference on X-Ray Absorption Fine Structure, pp. C2-107-C2-110, (1997).

F. Wang, B. Ravel, Y. Yacoby, E.A. Stern, and R. Ingalls, "The Effect of Hydrostatic Pressure on the Local Structure of $K_{1-x}Na_xTaO_3$ and $Kta_{1-x}Nb_xO_3$", J. Phys. IV France 7 Proceedings of the 9th International Conference on X-Ray Absorption Fine Structure, pp. C2-1225-C2-1226, (1997).

K. Xia, W.F. Bleam and P.A. Helmke, "Studies of the Nature of Binding Sites of First-row Transition Elements Bound to Aquatic and Soil Humic Substances using X-ray Absorption Spectroscopy", *Geochim. Cosmochim. Acta*, **61**, 2223-2225, (1997).
K. Xia, W.F. Bleam, and P.A. Helmke, "Studies of the Nature of Cu^{2+} and Pb^{2+} Binding Sites in Soil Humic Substances using X-ray Absorption Spectroscopy", *Geochim. Cosmochim. Acta*, **61**, 2211-2221, (1997).

K. Xia, A. Mehadi, R.W. Taylor, and W.F. Bleam, "X-ray Absorption and Electron Paramagnetic Resonance Studies of Cu(II) Sorbed to Silica: Surface-induced Precipitation at low Surface Coverages", *J. Colloid Interface Sci.*, **185**, 252-257, (1997).

Y. Yacoby, S.M. Heald, and E.A. Stern, "Local Oxygen Octahedra Rotations in $Ba_{1-x}K_xBiO_3$ and $BaBiO_3$", *Solid State Commun.*, **101**, 801, (1997).

Y. Yacoby, S.M. Heald, and E.A. Stern, "Local Oxygen Octahedra Rotations in $Ba_{1-x}K_xBiO_3$", J. Phys. IV France 7 Proceedings of the 9th International Conference on X-Ray Absorption Fine Structure, pp. C2-1081-C2-1083, (1997).

Y. Yacoby, and E.A. Stern, "Structural Disorder in Crystals Undergoing Displacive Type Structural Phase Transitions As Revealed by XAFS", *Comments of Cond. Mat. Phys.*, **18**, 1, (1996).

Y. Zhang, XAFS Research on Biological Systems, M.S., University of Washington, (1995).

A. Zhao, Structurally Well-Defined Supported Iridium cluster Catalysts: Synthesis, Characterization, and Catalysis, University of Delaware, Thesis, (1996).

Beamline X12B

M.A. Canady, S.B. Larson, J. Day, and A. McPherson, "Crystal Structure of Turnip Yellow Mosaic Virus", *Nat. Struc. Biol.*, **3/9**, 771, (1996).

T.R. Gamble, F.F. Vajdos, S. Yoo, D.K. Worthylake, M. Houseweart, W.I. Sundquist, and C.P. Hill, "Crystal Structure of Human Cyclophilin A Bound to the Amino-terminal Domain of HIV-1 Capsid", *Cell*, **87**, 1285, (1996).

L.J. Harris, S.B. Larson, K.W. Hasel, and A. McPherson, "Refined Structure of an Intact IgG2a Monoclonal Antibody", *Biochemistry*, **36/7**, 1581, (1997).

S. Koszelak, J.D. Ng, J. Day, T.-P. Ko, A. Greenwood, and A. McPherson, "The Crystallographic Structure of the Subtilisin Protease from Penicillium Cyclopium", *Biochemistry*, **36**, 6597, (1997).

H. Lin, J.J. Dunn, B.J. Luft, and C.L. Lawson, "Crystal Structure of Lyme Disease Antigen Outer Surface Protein A Complexed with an Fab", *Biochemistry*, **94**, 3584, (1997).

A.J. Malkin, Y.G. Kuznetsov, and A. McPherson, "Defect Structure of Macromolecular Crystals", *J. Struc. Biol.*, **117**, 124, (1996).

A.J. Quantock, N.J. Fullwood, EJ-MA. Thonar, S.R. Waltman, M.S. Capel, M. Ito, S.M. Verity, and D.J. Schanzlin, "Macular Corneal Dystrophy Type II: Multiple Studies on a Cornea with Low Levels of Sulphated Keratan Sulphate", *Eye*, **11**, 57, (1997).

A.J. Quantock, S.M. Verity, and D.J. Schanzlin, "Organization of Collagen in the Lyophilized Cornea", *J. Refract. Surg.*, **13**, 169, (1997).

M.O. Skidmore, and M.R. Sawaya, et al., "Crystallization of the A Alpha Subunit of Protein Phospahtase 2A", *Protein Science*, **5**, 1198, (1996).

R.M. Story, and T.A. Steitz, "Structure of the recA Protein-ADP Complex", *Nature*, **355**, 374, (1992).

R.M. Story, I.T. Weber, and T.A. Steitz, "The Structure of the *E. coli recA* Protein Monomer and Polymer", *Nature*, **355**, 318, (1992).

Beamline X12C

K.M. Barkigia, D. Melamed, R.M. Sweet, K.M. Smith, and J. Fajer, "Self-Assembled Zinc Pheoporphyrin Dimers. Models for the Supramolecular Antenna complexes of Green Photosynthetic Bacteria?", *Spectrochimica Acta*, **53A**, 463, (1997).

V. Biou, F. Shu, and V. Ramakrishnan, "X-ray Crystallography shows that Translational Initiation Factor IF3 consists of two Compact a/b Domains Linked by an α-helix", *EMBO J.*, **14**, 4056, (1995).

H. Blanchard, P. Grochulski, Y. Li, S. Arthur, P. Davies, J.S. Elce, and M. Cygler, "Structure of a Calpain Ca^{2+}-Binding Domain Reveals a Novel EF-Hand and Ca^{2+}-Induced Conformational Changes", *Nat. Stuct. Bio.*, **4**, 532, (1997).

Y. Bourne, P. Taylor, and P. Marchot, "Acetylcholinesterase Inhibition by Fasciculin: Crystal Structure of the Complex", *Cell*, **83**, 503, (1995).

M.A. Canady, S.B. Larson, J. Day, and A. McPherson, "Crystal Structure of Turnip Yellow Mosaic Virus", *Nat. Struct. Bio.*, **3**, 771, (1996).

J. Carey, N. Combatti, D.E.A. Lewis, and C.L. Lawson, "Cocrystals of *Escherichia coli trp* Repressor Bound to an Alternative Operator DNA Sequence", *J. Mol. Biol.*, **234**, 496, (1993).

M.S. Chapman, J. Tsao, and M.G. Rossmann, "*Ab initio* Phase Determination for Spherical Viruses: Parameter Determination for Spherical-Shell Models", *Acta Cryst.*, **A48**, 301, (1992).

X. Cheng, S. Kumar, J. Posfai, J.W. Pflugrath, and R.J. Roberts, "Crystal Structure of the HhaI DNA Methyltransferaase Complexed with S-Adenosyl-L-Methionine", *Cell*, **74**, 299, (1993).

E. Cheung, L. D'Ari, J.C. Rabinowitz, D.H. Dyer, and B.L. Stoddard, "Purification, Crystallization, and Preliminary X-ray Studies of a Bifunctional 5,10-Methenyl/Methyl ene Tetrahydrofolate Cyclohydrolase/Dehydrogenase from Escherichia coli", *Proteins*, **27**, 322, (1997).

J.B. Clarage, M.S. Clarage, W.C. Phillips, R.M. Sweet, and D.L.D.C. Caspar, "Correlations of Atomic Movements in Lysozyme Crystals", *Proteins: Structure, Function, and Genetics*, **12**, 145, (1992).

C. Davies, S.W. White, and V. Ramakrishnan, "The Crystal Structure of Ribosomal Protein L14 Reveals an Important Organizational Component of the Translational Apparatus", *Structure*, **4**, 55, (1996).

L.T.J. Delbaere, R.M. Sweet, and L.J. DeLucas, "Microgravity Improvement of Protein Crystals on STS-62", Spacebound '94 Proceedings, pp. 87-88, (1994).

E.D. Getzoff, K.W. Jones, D. McRee, K. Moffat, K. Ng, M.L. Rivers, W. Schildkamp, P.T. Singer, P. Spanne, R.M. Sweet, T.-Y. Teng, and E.M. Westbrook, "Laue Diffraction Protein Crystallography at the National Synchrotron Light Source", *Nucl. Instrum. and Meth. In Phys. Res.*, **B79**, 249, (1993).

V. Graziano, S.E. Gerchman, A.J. Wonacott, R.M. Sweet, J.R.E. Wells, S.W. White, and V. Ramakrishnan, "Crystallization of the Globular Domain of Histone H5", *J. Mol. Biol.*, **212**, 253, (1990).

M. Harel, G. Kleywegt, R.B.G. Ravelli, I. Silman, and J.L. Sussman, "Crystal Structure of an Acetylcholinesterase-fasciculin Complex: Interaction of a Three-fingered Toxin from Snake Venom with its Target", *Structure*, **3**, 1355, (1995).

P.J. Heath, K. Stephens, R. Monnat, and B.L. Stoddard, "Structure of the I-CreI Intron-Encoded Endonuclease: a Novel Fold that Binds and Cleaves a Long DNA Target Sequence", *Nat. Struct. Bio.*, **4/6**, 468, (1997).

W.-C. Hon, G.A. McKay, P.R. Thompson, R.M. Sweet, D.S.C. Yang, G.D.Wright, and A.M. Berghuis, "Structure of an Enzyme Required for Aminoglycoside Antibioti Resistance Reveals Homology to Eukaryotic Protein Kinases", *Cell*, **89**, 887-895, (1997).

K.Y. Hwang, H.K. Song, C. Chang, J. Lee, S.Y. Lee, K.K. Kim, S. Choe, R.M. Sweet, and S.W. Suh, "Crystal Structure of Thermostable α-amylase from *Bacillus Licheniformis* Refined at 1.7-Å Resolution", *Mol. Cells*, **7**, 251, (1997).

S.C. Johnston, C.N. Larsen, W.J. Cook, K.D. Wilkinson, and C.P. Hill, "Crystal Structure of a Deubiquitinating Enzyme (human UCH-L3) at 1.8Å Resolution", *EMBO J.*, **16**, 3787-3796, (1997).

A.B. Kiyatkin, P. Natarajan, S. Munshi, W. Minor, J.E. Johnson, and P.S. Low, "Crystallization and Preliminary X-ray Analysis of the Cytoplasmic Domain of Human Erythrocyte Band 3", *Proteins: Structure, Function, and Genetics*, **22**, 293, (1995).

P.D. Kwong, S.-E. Ryu, W.A. Hendrickson, R. Axel, R.M. Sweet, G. Folena-Wasserman, P. Hensley, and R.W. Sweet, "Molecular Characteristics of Recombinant Human CD4 as Deduced from Polymorphic Crystals", Proc. Nat. Acad. Sci. USA, **87**, 6423, (1990).

C.L. Lawson, "An Atomic View of the L-Tryptophan Binding Pocket of trp Repressor", *Nat. Struct. Bio.*, **3**, 986, (1996).

H. Li, J.J. Dunn, B.J. Luft, and C.L. Lawson, "Crystal Structure of Lyme Disease Antigen OspA Complexed with an Fab Fragment", *Proc. National Acad. Sci. USA*, **94**, 3584, (1997).

H. Li, and C.L. Lawson, "Crystallization and Preliminary X-ray Analysis of *Borrelia burgdorferi* Outer Surface Protein A (OspA) Complexed with a Murine Monoclonal Antibody **Fab** Fragment", *J. Struct. Bio.*, **115**, 335, (1995).

Y. Lindqvist, W. Huang, G. Schneider, and J. Shanklin, "Crystal Structure of Δ^9 Stearoyl-acyl Carrier Protein Desaturase from Castor Seed and its Relationship to other Di-iron Proteins", *EMBO J.*, **15**, 4081, (1996).

J. Liu, A.G.D. Tse, H.-C. Chang, J.H. Liu, J. Wang, R.E. Hussey, Y. Chishti, B. Rheinhold, R. Spoerl, S.G. Nathenson, J.C. Sacchettini, and E.L. Reinherz, "Crystallization of Deglycosylated T Cell Receptor (TCR) Complexed with an Anti-TCR Fab Fragment", *J. Biol. Chem.*, **271**, 33639, (1996).

M.A. Massiah, D. Worthylake, A.M. Christensen, W.I. Sundquist, C.P. Hill, and M.F. Summers, "Comparison of the NMR and X-ray Structures of the HIV-1 Matrix Protein: Evidence for Conformational Changes During Viral Assembly", *Protein Science,* **5**, 2391-2398, (1996).

A. Mesecar, B.L. Stoddard, and D.E. Koshland, Jr., "Orbital Steering in the Catalytic Power of Enzymes: Small Structural Changes with Large Catalytic Consequences", *Science*, **277**, 202, (1997).

M. O'Gara, S. Klimasauskas, R.J. Roberts, and X. Cheng, "Enzymatic C5-Cytosine Methylation of DNA: Mechanistic Implications of new Crystal Structures for HhaI Methyltransferase-DNA-AdoHcy Complexes", *J. Mol. Biol.*, **261**, 634, (1996).

M. O'Gara, R.J. Roberts, and X. Cheng, "A Structural Basis for the Preferential Binding of Hemimethylated DNA by HhaI DNA Methyltransferase", *J. Mol. Biol.*, **263**, 597, (1996).

V. Ramakrishnan, and S.W. White, "The Structure of Ribonsomal Protein S5 Reveals Sites of Interaction with 16S rRNA", *Nature*, **358**, 768, (1992).

M.R. Redinbo, S.M. Eide, R.L. Stone, J.E. Dixon, and T.O. Yeates, "Crystallization and Preliminary Structural Analysis of *Bacillus subtilis* Adenylosuccinate Lyase, an Enzyme Implicated in Infantile Autism", *Prot. Sci.*, **5**, 786, (1996).

W.G. Scott, B.L. Stoddard, and A. Klug, "Capturing Structures of Catalytic RNA Intermediates: The Hammer-head Ribozyme", *Science*, **274**, 2065, (1996).

D. Shin, K. Hwang, K. Kyeong, S. Kim, R. Sweet, and S. Suh, "Crystallization and Preliminary X-ray Crystallographic Analysis of Phospholipid Transfer Protein from Maize Seedlings", *Proteins: Structure, Function, and Genetics*, **19**, 80, (1994).

H. Song, K. Hwang, C. Chang, and S. Suh, "Crystal Structure of *Bacillus licheniformis* α- Amylase at 1.7Å Resolution", Enzymes for Carbohydrate Engineering II Symposium, pp. 53-62, (1995).

M.G. Strauss, E.M. Westbrook, I. Naday, T.A. Colemen, M.L. Westbrook, D.J. Travis, R.M. Sweet, J.W. Pflugrath, and M. Stanton, "CCD-Based Detector for Protein Crystallography with Synchrotron X-rays", *Nucl. Instrum. and Meth.*, **A297**, 275, (1990).

R.K. Strong, B.L. Stoddard, A.P. Arrott, and G.K. Farber, "Long Duration Growth of Protein Crystals in Microgravity Aboard the MIR Space Station", *J. Cryst. Growth.*, **119**, 200, (1992).

R.M. Sweet, "Review of Handbook on Synchrotron Radiation", Volume 4: Medical, Biological, and Physiological Applications, edited by S. Ebashi, M. Koch, and E. Rubenstein, *Synch. Rad. News*, **6**, 23, (1992).

R.M. Sweet, P.T. Singer, and A. Smalas, "Considerations in the Choice of a Wave-length Range for White-Beam Laue Diffraction", *Acta Cryst.*, **D49**, 305, (1993).

K.S. Thorn, H.E.M. Christensen, R. Shigeta, Jr., D. Huddler, Jr., L. Shalaby, U. Lindberg, N.-H. Chua, and C.E. Schutt, "The Crystal Structure of a Major Allergen from Plants", *Structure*, **5**, 19, (1997).

J. Tsao, M.S. Chapman, H. Wu, M. Agbandje, W. Keller, and M.G. Rossmann, "Structure Determination of Monoclinic Canine Parvovirus", *Acta Cryst.*, **B48**, 75, (1992).

R. Xu, G. Carmel, J. Kuret, and X. Cheng, "Structural Basis for Selectivity of the Iso-quinoline Sulfonamide Family of Protein Kinase Inhibitors", Proc. Natl. Acad. Sci. U.S.A., **93**, 6308, (1996).

R. Xu, L. Jokhan, X. Cheng, A. Mayeda, and A.R. Krainer, "Crystal Structure of Human UP1, the Domain of HnRNP A1 that Contains Two RNA-Recognition Motifs", *Structure*, **5**, 559, (1997).

R. Xu, C. Koch, Y. Liu, J.R. Horton, D Knapp, K. Nasmyth, and X. Cheng, "Crystal Structure of the DNA-Binding Domain of Mbp1, a Transcription Factor Important in Cell Cycle Control of DNA Synthesis", *Structure*, **5**, 349, (1997).

Beamline X13

K. Bane, and S. Krinsky, "Impedance of a Small Gap Undulator Chamber", Proceedings Particle Accelerator Conference, p. 3375, (1993).

A. Friedman, X. Zhang, S. Krinsky, E. Blum, and K. Halbach, "Polarized Wiggler for the NSLS X-ray Ring", Proceedings Particle Accelerator Conference, p. 1599, (1993).

E. Gluskin, I. McNulty, L. Yang, K.J. Randall, Z. Xu, and E.D. Johnson, "Intensity Interferometry at the X13A Undulator Beamline", *Nucl. Instrum. and Meth.*, **A347**, 177, (1994).

E.D. Johnson, and T. Oversluizen, "UHV Photoelectron X-ray Beam Position Monitor", *Nucl. Instrum. and Meths.*, **A291**, 427, (1990).

K.M. Kemner, V.G. Harris, V. Chakarian, Y.U. Idzerda, W.T. Elam, C.-C. Kao, Y.C. Feng, D.E. Laughlin, and J.C. Woicik, "The Role of Ta and Pt in Segregation Within Co-Cr-Ta and Co-Cr-Pt Thin Film Magnetic Recording Media", *J. Appl. Phys.*, **79**, 5345, (1996).

K. M. Kemner, Y. U. Idzerda, V. G. Harris, V. Chakarian, W. T. Elam, C. -C. Kao, E. Johnson, Y. C. Feng, D. E. Laughlin, C. T. Chen, K. -K. Lee, and J. C. Lodder, "Direct Observation of Cr Magnetic Order in CoCrTa and CoCrPt Thin Films", *Rapid Comm. J. App. Phys.*, **81**, 1002, (1997).

T. Oversluizen, W. Stoeber, and E.D. Johnson, "Kinematic Mounting Systems for NSLS Beamlines and Experiments", *Rev. Sci. Instrum.*, **63**, 1285, (1992).

K.J. Randall, Z. Xu, E. Gluskin, I. McNulty, R. Dejus, S. Krinsky, O. Singh, C.C. Kao, E.D. Johnson, C.T. Chen, and G. Meigs, "Characterization of a Novel Elliptically Polarized Wiggler", *J. of Electron Spectroscopy and Related Phenomena*, **80**, 433, (1996).

P.M. Stefan, L. Solomon, S. Krinsky, and G. Rakowsky, "NSLS Prototype Small Gap Undulator", Proceedings Particle Accelerator Conference, p. 1096, (1991).

Z. Yin, L. Berman, S. Dierker, E. Dufresne, and D.P. Siddons, "A Simple X-ray Focusing Mirror using Float Glass", *SPIE*, **2856**, 307, (1997).

Beamline X14A

M.K. Durbin, A. Malik, A.G. Richter, R. Ghaskadvi, T. Gog, and P. Dutta, "Transitions to a new Chiral Phase in Fatty Acid Langmuir Monolayer", *J. Chem. Phys.*, **106**, 8216, (1997).

A. Goyal, M. Paranthaman, Q. He, F.A. List, E.D. Specht, D.K. Christen, D.M. Kroeger, J.E. Tkaczyk, and P. Haldar, "Fabrication, Processing, and Properties of Tl-1223 Conductors", IEEE *Trans. in Appl. Superconductivity*, **5**, 1405, (1995).

H. Hong, R.D. Aburano, K.-S. Chung, D.-S. Lin, E.S. Hirschorn, T.-C. Chiang, and H. Chen, "X-ray Truncation Rod Study of Ge(001) Surface Roughening by Molecular Beam Homoepitaxial Growth", *J. Appl. Phys.*, **79**, 6858, (1996).

S.C. Moss, J.L. Robertson, D.A. Neumann, and L. Reinhard, "Anomalous Static Displacements and their Relation to Lattice Dynamics in $Fe_{0.53}Cr_{0.47}$", *Comp. Mat. Sci.*, **8**, 33, (1997).

J.E. Tkaczyk, J.A. Sutliff, J.A. DeLuca, P.J. Bednarczyk, C.L. Briant, Z.L. Wang, A. Goyal, D.M. Kroeger, D.H. Lowndes, and E.D. Specht, "Texture and Transport in Spray Pyrolyzed $TlBa_2Ca_2Cu_3O_9$ Thick Films", *J. Mater. Res.*, **10**, 2203, (1995).

P. Wochner, E. Isaacs, S.C. Moss, P. Zschack, J. Giapintzakis and D.M. Ginsberg, "X-ray Search for CDW in Single Crystal $Yba_2Cu_3O_{7-\delta}$", Proceedings 10th Anniversary HTS Workshop, Houston TX, World Scientific, p. 425, (1996).

Beamline X15A

M. Bohringer, Q.D. Jiang, R. Berndt, W.D. Schneider, and J. Zegenhagen, "Discommensurations, Epitaxial Growth and Island Formation in Ge(111):Cu", *Surf. Sci.*, **367**, 245, (1996).

L. Cheng, P. Lyman, N.C. Sturchio, and M.J. Bedzyk, "Adsorption and Structure of Selenite Anions on the Calcite (104) Surface", *Surf. Sci.*, **382**, 690, (1997).

R.E. Johnston, D. Washburn, E. Pisano, C. Burns, W.C. Thomlinson, L.D. Chapman, F. Artelli, N.F. Gmür, Z. Zhong, and D. Sayers, "Mammography Phantom Studies with Synchrotron Radiation", *Radiology*, **200**, 659, (1996).

B.H. Laster, W.C. Thomlinson, and R.G. Fairchild, "Photon Activation of Iododeoxyuridine: Biological Efficacy of Augur Electrons", *Radiation Research*, **133**, 219, (1993).

B.H. Laster, W. Thomlinson, J. Kalef-Ezra, V. Benary, E.A. Popenone, V.P. Bond, C. Gordon, L Warkentien, N. Gmür, N. Lazarz, and R.F. Fairchild, "The Biological Efficacy of an Induced Auger Effect: Comparison of Iodine and Bromine as Target Atoms", Biophysical Aspects of Auger Processes, edited by R.W. Howell, V.R. Narra, K.S.R. Sastry, and D.V. Rao, *AAPM Symposium Series*, **8**, 91, (1992).

T.-L. Lee, Y. Qain, P.F. Lyman, J.C. Woicik, J.G. Pellegrino, and M.J. Bedzyk, "The Use of X-ray Standing Waves and Evanescent-Wave Emission to Study Buried Strained-Layer Heterostructures", *Physica,* **B221**, 437, (1996).

W. Lin, T.-L. Lee, P.F. Lyman, J. Lee, M.J. Bedzyk, and T.J. Marks, "Atomic Resolution X-ray Standing Wave Microstructural Characterization of NLO-Active Self-Assembled Chromophoric Superlattices", *J. Am. Chem. Soc.*, **119**, 2205, (1997).

P.F. Lyman, and M.J. Bedzyk, "Local Structure of Sn/Si(001) Surface Phases", *Surf. Sci.*, **371**, 307, (1997).

P.F. Lyman, and M.J. Bedzyk, "Surfactant-Mediated Epitaxy of Metastable SnGe Alloys", *Appl. Phys. Lett.*, **69**, 978, (1996).

Y. Qian, M.J. Bedzyk, P.F. Lyman, T.-L. Lee, S. Tang, and A.J. Freeman, "Structure and Surface Kinetics of Bismuth Adsorption on Si(001)", *Phys. Rev.*, **B54**, 4424, (1996).

Y. Qian, N.C. Sturchio, R.P. Chiarello, P.F. Lyman, T.-L. Lee, and M.J. Bedzyk, "Lattice Location of Trace Elements within Minerals and at their Surfaces with X-ray Standing Waves", *Science*, **265**, 1555, (1994).

N.C. Sturchio, R. P. Chiarello, L. Cheng, P. F. Lyman, M. J. Bedzyk, Y. Qian, H. You, D. Yee, P. Geissbuhler, L. Sorensen, Y. Liang, and D. Baer, "Lead Adsorption at the Calcite-Water Interface: Synchrotron X-ray Standing Wave and X-ray Reflectivity Studies", *Geochimica et Cosmochimica Acta*, **61**, 251-264, (1997).

Beamline X15B

T. Laine, K. Saarinen, J. Makinen, P. Hautojarvi, C. Corbel, L.N. Pfeiffer, and P.H. Citrin, "Observation of Compensating Ga Vacancies in Highly Si-Doped GaAs", *Phys. Rev.*, **B54**, 11050, (1996).

L. Niu, A.R. Kortan, N. Kopylov, and P.H. Citrin, "Local Atomic and Electronic Structure of Heavy-Metal Fluoride ZBLAN Glasses", Optoelectronic Materials: Ordering, Composition Modulation, and Self-Assembled Structures, edited by E.D. Jones, A. Mascarenhas, and P. Petroff, MRS Symposia Proceedings, *Mat. Res. Soc.*, **417**, 175, (1996).

L. Niu, A.R. Kortan, N. Kopylov, and P.H. Citrin, "Local Structure Study of Pb-Induced Instability in ZBLAN Glass", *J. Non-Cryst. Solids*, **213**, 358, (1997).

Beamline X16A

J. Braun, J.P. Toennies, and G. White, "A SPALEED Structural Study of Cesium Adsorption on Stepped Copper Surfaces Cu(211) and Cu(511)", *Surf. Sci.*, **340**, 265-280, (1995).

S. Cundiff, W.H. Knox, F.H. Baumann, K. Evans-Lutterodt, M.T. Tang, M.L. Green, and H.M. van Driel, "Si/SiO_2 Interface Roughness: Comparsion Between Second Harmonic Generation and X-ray Scattering", *Appl. Phys. Letts.*, **70**, 1414, (1997).

R. Felici, I.K. Robinson, C. Ottaviani, P. Imperatori, P. Eng, and P. Perfetti, "The Si(001) 2pl Reconstruction Solved by X-ray Diffraction", *Surf. Sci. Letts.*, **375**, 55, (1997).

H.L. Meyerheim, S. Pflanz, R. Schuster, and I.K. Robinson, "Surface X-ray Diffraction on Clean and Cs-Covered Ag(001)", *Z. Krist. Lett.*, **212**, 327, (1997).

H.L. Meyerheim, I.K. Robinson, and R. Schuster, "Temperature-Dependent Surface X-ray Diffraction on K/Ag(001)-(2x1)", *Surf. Sci.*, **370**, 268, (1997).

H. Reichert, P.J. Eng, H. Dosch, and I.K, Robinson, "Surface-Induced Giant Anisotropy in the Order Parameter Relaxation at $Cu_3Au(001)$", *Phys. Rev. Letts.*, **78**, 3475, (1997).

R. Schuster, and I.K. Robinson, "Reconstruction-Induced Compression of the Cu(110) Surface - Reply to Comment", *Phys. Rev. Letts.*, **78**, 159, (1997).

Beamline X16B

C. A. Burns, and E. D. Isaacs, "Debye-Waller Factor in Solid He-4 Crystals", *Phys. Rev.*, **B55**, 5767, (1997).

Beamline X17B2

F.A. Dilmanian, X.Y. Wu, E.C. Parsons, B. Ren, J. Kress, T.M. Button, L.D. Chapman, J.A. Coderre, F. Giron, D. Greenberg, D.J. Krus, Z. Liang, S. Marcovici, M.J. Petersen, C.T. Roque, M. Shleifer, D.N. Slatkin, W.C. Thomlinson, K. Yamamoto, and Z. Zhong, "Single-and Dual-Energy CT with Monochromatic Synchrotron X-rays", *Phys. Med. Biol.*, **42**, 371, (1997), BNL 62821.

R.H. Menk, W. Thomlinson, N. Gmür, Z. Zhong, D. Chapman, F. Arfelli, W.R. Dix, W. Graeff, M. Lohmann, G. Illing, L. Schildwächter, B. Reime, W. Kupper, C. Hamm, J.C. Giacomini, H.J. Gordon, E. Rubenstein, J. Dervan, H.J. Besch, and A.H. Walenta, "The Concept of Spatial Frequency Depending DQE and its Application to a Comparsion of Two Detectors used in Transvenous Coronary Angiography", *Nucl. Instrum. Meth.*, **398**, 351-367, (1997).

Z. Zhong, Bent Laue Crystal Monochromator for Producing Areal X-ray Beams, PhD., State University of New York, Stony Brook, (1996).

Z. Zhong, D. Chapman, R. Menk, J. Richardson, S. Theophanis, and W. Thomlinson, "Monochromatic Energy Subtraction Radiography using a Rotating Anode Source and a Bent Laue Monochromator", *Phys. Med. Biol.*, **42/9**, 1751, (1997). BNL 64155.

Z. Zhong, D. Chapman, W. Thomlinson, F. Arfelli, and R. Menk, "A Bent-Laue Crystal Monochromator for Monochromatic Radiography with an Area Beam", *Nucl. Instrum. and Meth. in Phys. Res.*, **399**, 489, (1997), BNL 64154.

Beamline X17C

S. Beaver, J. Liu, and Y. K. Vohra, "Phase Transformations in Mo-Ru Alloy Induced by Laser Heating at High Pressures", *J. Phys. Cond. Mat.*, **8**, L647, (1996).

F.P. Bundy, W.A. Bassett, M.S. Weathers, R.J. Hemley, H.K. Mao, and A.F. Goncharov, "Review Article The Pressure-Temperature Phase and Transformation Diagram for Carbon; Updated Through 1994", *Carbon*, **34**, 141, (1996).

L.S. Dubrovinsky, S.K. Saxena, and P. Lazor, "X-ray Study of Iron with *in situ* Heating at Ultra High Pressures", *Geophys. Res. Lett.*, **24**, 1835, (1997).

L.S. Dubrovinsky, S.K. Saxena, P. Lazor, R. Ahuja, O. Eriksson, J.M. Wills, and B. Johansson, "Experimental and Theoretical Identification of a New High Pressure Phase of Silica", *Nature*, **388**, 362, (1997).

T.S. Duffy, Y. Wang, P.J. Eng, S.R. Sutton, and M.L. Rivers, "Development of a High-Pressure Facility at the Advanced Photon Source", German-Japanese Workshop on the use of Ultra-Short Wavelength Photons and Gamma Rays for High-Precision, High-Resolution Analysis of Electronic States of Solids, pp. 12-15, (1996).

A.F. Goncharov, M. Somayazulu, V.V. Struzhkin, R.J. Hemley, and H.K. Mao, "New High-Pressure Low-Temperature Phase of Methane", Fifteenth International Conference on Raman Spectroscopy, edited by S.A. Asher, and P. Stein, pp. 1042-1043, (1996).

A.F. Goncharov, V.V. Struzhkin, M. Somayazulu, R.J. Hemley, and H.K. Mao, "Compression of Ice to 210 GPa: Evidence for a Symmetric Hydrogen Bonded Phase", *Science*, **273**, 218, (1996).

R.J. Hemley, and H.K. Mao, "Static High-Pressure Effects in Solids", *Encyclopedia of Appl. Phys.*, **18**, 555, (1997).

R.J. Hemley, H.K. Mao, A.F. Goncharov, M. Hanfland, and V.V. Struzhkin, "Synchrotron Infrared Spectroscopy to 0.15 eV of H_2 and D_2 at Megabar Pressures", *Phys. Rev. Lett.*, **76**, 1667-1670, (1996).

R.J. Hemley, H.K. Mao, G. Shen, J. Badro, P. Gillet, M. Hanfland, and D. Häusermann, "X-ray Imaging of Stress and Strain of Diamond, Iron, and Tungsten at Megabar Pressures", *Science*, **276**, 1242, (1997).

H. Hua, S. Mirov, and Y. K. Vohra, "High-Pressure and High-Temperature Studies on Oxide Garnets", *Phys. Rev.*, **B54**, 6200, (1996).

E. Huang, A. Li, J. Xu, R. Chen, and T. Yamanaka, "High-Pressure Phase Transition in $Al(OH)_3$: Raman and X-ray Observations", *Geophys. Res. Lett.*, **23**, 3083, (1996).

M.B. Kruger, and C. Meade, "High Pressure Structural Study of GeI4", *Phys. Rev.*, **B55**, 1, (1997).

M.B. Kruger, J.H. Nguyen, W. Caldwell, and R. Jeanloz, "Equation of State of $MgAl_2O_4$ Spinel to 65 GPa", *Phys. Rev.*, **B56**, 1, (1996).

M.B. Kruger, J.H. Nguyen, Y.M. Li, W. Caldwell, M.H. Manghnani, and R. Jeanloz, "Equation of State of α-Si_3N_4", *Phys. Rev.*, **B55**, 3456, (1996).

Y.M. Li, M.B. Kruger, J.H. Nguyen, W.A. Caldwell, and R. Jealoz, "High Pressure X-ray Diffraction Study of β-Si_3N_4", *Solid State Comm.*, **103**, 107, (1997).

P. Loubeyre, R. LeToullec, D. Häusermann, M. Hanfland, R.J. Hemley, H.K. Mao, and L.W. Finger, "X-ray Diffraction and Equation of State of Hydrogen at Megabar Pressures", *Nature*, **383**, 702, (1996).

H.K. Mao, and R.J. Hemley, "Solid Hydrogen at Ultrahigh Pressures", High Pressure Science & Technology-Proceedings of the Joint XV AIRAPT & XXXIII EHPRG International Conference, edited by W.A. Trzeciakowski, pp. 505-510, (1996).

H.K. Mao, J. Shu, Y. Fei, H. Hu, and R.J. Hemley, "The Wüstite Enigma", *Phys. Earth Planet. Inter.*, **96**, 135, (1996).

J.H. Nguyen, M.B. Kruger, and R. Jealoz, "Evidence for 'Partial' (Sublattice Amorphization in $Co(OH)_2$", *Phys. Rev. Lett.*, **78**, 1936, (1997).

S.K. Saxena, L.S. Dubrovinsky, C.S. Yoo, J. Akella, A.J. Campbell, H.K. Mao, and R.J. Hemley, "Detecting Phases of Iron", *Science*, **275**, 94, (1997).

S.K. Saxena, L.S. Dubrovinsky, and P. Haggkvist, "X-ray Evidence for the β-iron at High Temperature and High Pressure", *Geophys. Res. Lett.*, **23**, 2441, (1996).

S.K. Saxena, L.S. Dubrovinsky, P. Lazor, Y. Cerenius, P. Häggkvist, M. Hanfland, and J.Z. Hu, "Stability of Perovskite ($MgSiO_3$) in the Earth's Mantle", *Science*, **274**, 1357, (1996).

W.L. Vos, L.W. Finger, R.J. Hemley, and H.K. Mao, "Pressure Dependence of Hydrogen Bonding in a Novel H_2O-H_2 Clathrate", *Chem. Phys. Lett.*, **257**, 524, (1996).

C.S. Yoo, J. Akella, H. Cynn, and M. Nicol, "Direct Elementary Reactions of Boron and Nitrogen at High Pressures and Temperatures", *Phys. Rev.*, **B56**, 1, (1997).

C.S.Yoo, P. Soderlind, J. Moriarty, and A. Campbell, "Dhcp as a Possible new ε'-Phase of Iron at High Pressures and Temperatures", *Phys. Lett.*, **A214**, 65, (1996).

Beamline X18A

J. Anderson, Atomic Short-Range Order Determination in Au-25at.%Fe and Ni-12.5at.%Si: A Synchrotron X-ray Diffuse Scattering Study, Ph.D., LTV Steel, Cleveland, OH., (1996).

T.E. Burns, Asymmetric Adsorbate and Substrate Interactions in Physisorbed Systems: Nitrogen on Graphite and Dipolar Molecules on Ionic Substrates, Ph.D., Utah State University, (1994).

J. R. Buschert, Time Resolved X-Ray Diffraction Studies of Laser Annealing and Photostriction in Silicon, Ph.D., Faculty Goshen College, (1989).

M.A. Castro, The Pair-Breaking Problem in High Temperature Superconductors: A Study of Magnetic and Nonisovalent Impurities in Yttrium Barium Copper Oxide, Ph.D., Purdue University, (1993).

P. Dai, Synchrotron X-Ray Diffraction Study of Structure and Growth of Adsorbed Layers, Ph.D, Oak Ridge National Laboratory, (1993).

R. Eisenhower, Multiple Bragg Scattering in Decagonal Quasicrystals, Ph.D., NSLS, Brookhaven National Laboratory, (1996).

G.C. Follis, A Novel Theoretical Technique for Quantitative Analysis of X-Ray Diffraction Data, Ph.D., Purdue University, (1993).

R. Goldman, Structural and Electronic Properties of Lattice-Matched Compound Semiconductor Heterostructures, Ph.D., University of Michigan, (1995).

R. S. Goldman, K. L. Kavanagh, H. H. Wieder, V. M. Robbins, S. N. Ehrlich, and R.M. Feenstra, "Correlation of Buffer Strain Relaxation Modes with Transport Properties of Two-Dimensional Electron Gases", *J. Appl. Phys.*, **80**, 6849, (1996).

R. S. Goldman, K. L. Kavanagh, H. H. Wieder, and S. N. Ehrlich, "Modulation-Doped InGaAs/InAlAs Heterostructures Grown on GaAs Substrates Using Step-Graded InGaAs Buffers", *J. Vac. Sci. Tech.*, **B14**, 3035, (1996).

F. Y. Hansen, L. W. Bruch, and H. Taub, "Molecular Dynamics Simulations of the Dynamical Excitations in Commensurate Submonolayer Films of Nitrogen Molecules on Graphite", *Phys. Rev.*, **B54**, 14077, (1996).

S.A. Hoffman, Testing the Response of High Temperature Superconductors to the Presence of Spins: Nickel, Zinc, and Gallium Substitutions if Yttrium Barium Copper Oxide, Ph.D., Purdue University, (1991).

K. Hongladarom, Molecular Orientation and Rheology of Liquid Crystalline Polymers under Shear Flow, Ph.D., Staff GE Plastics on assignment in France, (1995).

J.M. Honig, S.N. Ehrlich, T.P. Hogan, C.R. Kannewurf, G.L. Liedl, T.F. Rosenbaum, J. Spalek, P. Somasundaram, and X. Yao, "Physical Properties of the $NiS_{2-x}Se_x$ System: From Mott Insulator to Paramagnetic Metal, MRS Proceedings, **453**, 291, (1997).

H. Lee, Phase Determination by Multiple Bragg Scattering of X-Rays in an Icosahedral Quasicrystal, Ph.D., University of California at San Diego, (1993).

V. Mahadev, Early Stages of Delta-Prime Precipitation in a Binary Aluminum-Lithium Alloy, M.S., University of Arizona, (1990).

V. Mahadev, Structural Characterization of Pseudo-Insulators for Gallium Arsenide Devices, Ph.D., University of Arizona, (1995).

K. Mahalingam, Precipitation Behavior of δ' (Al_3Li) in a Binary Alumnium Lithium Alloy, Ph.D., Staff Wright Patterson AFB, Dayton, Ohio, (1989).

P. Miller, and K. J. Bowman, "The Relation of Contact and Toughness in Textured Silicon Nitride to Preferred Orientation," Proceedings of the Eleventh International Conference on Textures of Materials, pp.1009-1014, (1996).

J. C. Newton, and H. Taub, "Neutron Diffraction Investigation of the S_2 Monolayer Phase of Ethane Physisorbed on Graphite", *Surf. Sci,.* **364**, 273, (1996).

E. Smela, The Effect of Substrate Topology on Smectic Liquid Crystal Alignment: A High Resolution X-ray Diffraction Study, Ph.D., Likoping Institute of Technology, (1992).

N. Takesue, Thermal Diffuse Scattering and Inpurity Effect on the Para-To-Ferroelectric Transitions of $PbTiO_3$ and $BaTiO_3$, Ph.D., Institute of Solid State Physics, University of Tokyo, Japan, (1996).

V. M. Ugaz, D. K. Cinader, Jr. and W. R. Burghardt, "Origins of Region I Shear Thinning in Model Lyotropic Liquid Crystalline Polymers", *Macromolecules,* **30**, 1527, (1997).

C. Venkatraman, Structural Characterization and Resistivity Variation of Lanthanum Nickelates, M.S., Advanced Refractories Technology, Buffalo, NY, (1990),

C. Venkatraman, Texture Development in YBCO Films Synthesized from Metallo-Organic Precursors, Ph.D., Advanced Refractories Technology, Buffalo, NY, (1994).

S.-K. Wang, Diffraction Studies of the Multilayer Structure Simple Physisorbed Films, Ph.D, Self-employed, (1992).

S.M. Williams, *In Situ* X-Ray Studies of Oxide Thin Films and Multilayers, Ph.D., University of Illinois-Chicago, (1994).

Z. Wu, Diffraction Studies of the Structure and Growth of Films Adsorbed on the Ag(111) Surface, Ph.D., University of Illinois, Urbana-Champaign, (1997).

Z. Wu, B.Matthies, K. W. Herwig, H. Taub, and S. N. Ehrlich ,"Quasiepitaxial Growth of n-Butane on a Ag(111) Surface", *Bull. Am. Phys. Soc.*, **42**, 309, (1997).

Y. Zhang, X-Ray Diffraction Studies of Al-Pd-Mn Quasicrystal. Structural and Thermal Properties, Ph.D., Qualcomm Inc., San Diego, California, (1997).

Beamline X18B

C.J. Dodge, and A.J. Francis, "Biotransformation of Binary and Ternary Citric Acid Complexes of Iron and Uranium", *Environ. Sci. Technol.*, **31**, 3062, (1997).

C.J. Dodge, A.J. Francis, and C.R. Clayton, "X-ray Spectroscopic Studies of Uranium Transformations in Microbial Cultures", In Synchrotron Radiation Techniques in Industrial, Chemical, and Materials Science, Edited by L.J. Terminello, K.L. D'Amico, and D.K. Shuh, Plenum Publishing Co., pp. 159-168, (1996).

E.J. Doskocil, S.V. Bordawekar, and R.J. Davis, "Alkali-Support Interactions on Rubidium Base Catalysts Determined by XANES, EXAFS, CO2 Adsorption, and IR Spectroscopy", *J. Catal.*, **169**, 327-337, (1997).

X. Feng, G. E. Fryxell, L.-Q. Wang, A. Y. Kim, J. Liu, and K. M. Kemner, "Functionalized Monolayers on Ordered Mesoporous Supports (SAMMS)", *Science*, **276**, 923, (1997).

C. C. Freyhardt, R. F. Lobo, S. Khodabandeh, J. E. Lewis, Jr., M. Tsapatsis, M. Yoshikawa, M. A. Camblor, M. Pan, M.M. Helmkamp, S. I. Zones, and M. E. Davis, "VPI-8: A High-Silica Molecular Sieve with a Novel "Pinwheel" Building Unit and Its Implications for the Synthesis of Extra-Large Pore Molecular Sieves", *J. Am. Chem. Soc.*, **118/31**, 7299-7310, (1996).

G. Larson, E. Lotero, L.M. Petkovic, and D.S. Shobe, "Alcohol Dehydration Reactions over Tungstated Zirconia Catalysts", *J. of Catal.*, **169**, 67-75, (1997).

D. E. Resasco, W. E. Alvarez, A. Ali and C. J. Loughran, "Selective Reduction of NO_x with Methane on Zeolite Catalysts", Proc. 15th Iberoamer. Symposium on Catalysis, (Plenary Lecture), Cordoba, Argentina, pp. 59-74, (1996).

Beamline X19A

K. Chae, Y. Lee, C. Whang, Y. Jeon, B. Choi, and M. Croft, "Charge Redistribution in Ion-Beam-Mixed Pd-Ag Alloys", *Nucl. Instrum. and Meths. In Phys. Res.*, **B117**, 123, (1996).

M. Croft, D. Sills, M. Greenblatt, C. Lee, S.-W. Cheong, K.V. Ramanujachary, and D. Tran, "Systematic Mn-d Configuration Change in the $La_{1-x}Ca_xMnO_3$ System: A Mn-K Edge XAS Study", *Phys. Rev.*, **B55**, 8726, (1997).

E. Fujita, L.R. Furenlid, and M.W. Renner, "Direct XANES Evidence for Charge Transfer in Co - CO_2 Complexes", *J. of the Am. Chem. Soc.*, **119**, 4549, (1997).

J. L. Fulton, D.M. Pfund, and Y. Ma, "A Diamond-Window XAFS Cell for Studies of High-Temperature, High-Pressure, Aqueous Solutions", *Rev. Sci Instrum.*, **67**, 1-5, CD-ROM Issue, (1996).

J. L. Fulton, D. M. Pfund, S. L. Wallen, M. Newville, E. A. Stern, and Y. Ma, "Rubidium Ion Hydration in Ambient and Supercritical Water", *J. Chem. Phys.*, **105**, 2161, (1996).

L.R. Furenlid, A. Mayer, and J.P. Kirkland, "NSLS-DAC: A Beamline Control and Data Acquisition Package", *J. de Phys.*, **C2/7**, 335, (1997).

F. E. Huggins, and G. P. Huffman, "Application of XAFS Spectroscopy to Coal Geochemistry", - Mineral Spectroscopy: A Tribute to Roger G. Burns, edited by M. D. Dyar, C. A. McCammon, and M. W. Schaefer, *The Geochem. Soc.*, **5**, 133, (1996).

F. E. Huggins, and G. P. Huffman, "Modes of Occurrence of Trace Elements in Coal from XAFS Spectroscopy", *Int. J. Coal Geol.*, **32**, 31, (1996).

F.E. Huggins, G.P. Huffman, G.E. Dunham, and C.L. Senior, "XAFS Examination of Mercury Capture on Three Activated Carbons", *ACS Div. Fuel Chem.*, **42/4**, 118, (1997).

F.E. Huggins, S. Srikantapura, B.K. Parekh, L. Blanchard, and J.D. Robertson, "XANES Spectroscopic Characterization of Selected Elements in Deep-Cleaned Fractions of Kentucky #9 Coal", *Energy & Fuels*, **11**, 691, (1997).

F. E. Huggins, J. Zhao, N. Shah, F. Lu, G. P. Huffman, L. E. Bool, III, and C. L. Senior, "Investigation of the Oxidation of Arsenical Pyrite in Coal and its Effect on the Behavior of Arsenic During Combustion", Proceedings, ICCS '97, 9th International Conference on Coal Science, edited by A. Ziegler, K.H. van Heek, J. Klein, and W. Wanzl, *P&W Druck and Verlag, Essen*, 1, 381, (1997).

G. Liang, H. Xi, E. Roberts, T. Binford, K. Mochizuki, J. Markert, and M. Croft, "Lattice, Ce-L_3 Valence, Transport, and Magnetic Results on Mixex-Valent/Kondo System $Ce_{1-x}La_xMn_2Si_2$", *J. Appl. Phys.*, **81**, 4924, (1997).

B. J. Palmer, D. M. Pfund, and J. L. Fulton, "Direct Modeling of XAFS Spectra from Molecular Dynamics Simulations", *J. Phys. Chem.*, **100**, 13393, (1996).

J. E. Penner-Hahn, P. J. Riggs-Gelasco, E. Yu, P. DeMarois, and C. F. Yocum, "Structural Characterization of the Manganese Cluster in the Photosynthetic Oxygen Evolving Complex Using X-Ray Absorption Spectroscopy", Photosynthesis: from Light to Biosphere, Vol. II, edited by P. Mathis, Kluwer Academic Publishers, Dordrecht, pp. 214-246, (1996).

A. Pullia, L. Furenlid, H.W. Kraner, G. Bertuccio, P.J. Pietraski, and D.P. Siddons, "High-Resolution Multi-Element Solid State Detectors", *Rev. Sci. Instrum.*, **67/9**, 1, (1996).

M.W. Renner, L.R. Furenlid, K.M. Barkigia, and J. Fajer, "XAFS and Crystallographic Studies of Ni(II) Porphyrins in Single Crystals and Solution", *J. de Phys.*, **C2/7**, 661, (1997).

P.J. Riggs-Gelasco, R. Mei, C.F. Yocum, and J.E. Penner-Hahn, "Reduced Derivatives of the Mn Cluster in the Oxygen Evolving Complex of Photosystem II: An EXAFS Study", *J. Am. Chem. Soc.*, **118**, 2387, (1996).

P. Schmuki, S. Virtanen, H. S. Isaacs, A. J. Davenport, H. Böhni, and T. Stenberg, "*In situ* XANES Studies on the Electrochemical Behavior of Thin (Fe,Cr)-Oxide Films used as Models for Passive Films", Surface Oxide Films, edited by J. Bardwell, *The Electrochemical Soc.*, **96/18**, 234, (1996).

A. Simopoulos, D. Devlin, A. Kostis, A. Jankowski, M. Croft, and T. Tsakalakos, "Structure and Enhanced Magnetization in Fe/Pt Multilayers", *Phys. Rev.*, **B54**, 9931, (1996).

T.L. Stemmler, T.M. Sossong Jr., J.I. Goldstein, D.E. Ash, T.E. Elgren, D.M. Kurtz Jr., and J.E. Penner-Hahn, "EXAFS Comparison of the Dimanganese Core Structures of Mn Catalase, Arginase and Mn-Substituted Ribonucleotide Reductase and Hemerythrin", *Biochemistry*, **36**, 9847, (1997).

David L. Tierney, XAS Characterization of Bacterial Superoxide Dismutase and NMR Characterization of Substrate Binding in Phthalate Dioxygenase, Ph.D. Thesis, University of Michgian, (1996).

S. L. Wallen, D. M. Pfund, J. L. Fulton, C. R. Yonker, M. Newville, and Y. Ma, "A High-Pressure, Capillary XAFS Cell for Studies of Liquids and Supercritical Fluid Solutions", *Rev. Sci Instrum.*, **67**, 2843, (1996).

T. Yamamota, M. Croft, R. Shull, and H. Hahn, "Phase Identification of a Superparamagnetic Iron-Oxide/Silver Nanocomposite", *J. Nano. Mat.*, **6**, 965, (1995).

Beamline X19C

H. Chung, W. Si, M. Dudley, A. Anselmo, D.F. Bliss, A. Maniatty, H. Zhang, and V. Prasad, "Characterization of Structural Defects in MLEK Grown InP Single Crystals using Synchrotron White Beam X-ray Topography", *J. Crystal Growth*, **174**, 230, (1997).

M. Dudley, W. Si, S. Wang, C.H. Carter, Jr., R. Glass, and V.F. Tsvetkov, "Quantitative Analysis of Screw Dislocations in 6H-SiC Single Crystals", *Il Nuovo Climento*, **19D**, 153, (1997).

X. Hu, I. Baker, and M. Dudley, "Temperature Dependence of Dislocations in Notched Ice Crystals", *J. Phys. Chem.*, **B101**, 6102, (1997).

N. Lei, A. Huang, and S.A. Rice, "Structure of the Liquid-Vapor Interface of a Sn:Ga Alloy", *J. Chem. Phys.*, **107**, 4051, (1997).

N. Lei, A. Huang, S.A. Rice, and C.J. Grayce, "In-Plane Structure of the Liquid-Vapor Interfaces of Dilute Bismuth:Gallium Alloys: X-ray Scattering Studies", *J. Chem. Phy.*, **105**, 9615, (1996).

B.M. Park, S.J. Chung, H.S. Kim, W. Si, and M. Dudley, "Synchrotron White Beam X-ray Topography of Ferroelectric Domains in $BaTiO_3$ Single Crystal", *Phil. Mag.*, **A75**, 611, (1997).

D.R. Rhiger, S. Sen, J.M. Peterson, H. Chung, and M. Dudley, "Lattice Mismatch Induced Morphological Features and Strain in HgCdTe Epilayers on CdZnTe Substrates", *J. Elect. Mat.*, **26**, 515, (1997).

M.L. Schlossman, "Surfaces and Interfaces of Fluids, Structure of", *Encyclopedia of Appl. Phys.*, **20**, 311, (1997).

W. Si, M. Dudley, R. Glass, V. Tsvetkov, and C.H. Carter, Jr., "Hollow-Core Screw Dislocations in 6H-SiC Single Crystals: a Test of Frank's Theory", *J. Elect. Mat.*, **26**, 128, (1997).

W. Si, M. Dudley, H.S. Kong, J. Sumakeris, and C.H. Carter, Jr., "Investigations of 3C-SiC Inclusions in 4H-SiC Epitaxial Films Grown on 4H-SiC Single Crystal Substrates", *J. Elect. Mat.*, **26**, 1, (1997).

W.M. Vetter, and M. Dudley, "X-ray Topography of a Single Superscrew Dislocation in 6H-SiC", Defects in Electronic Materials II, edited by J. Michel, T. Kennedy, K. Wada, and K. Thonke, Mat. Res. Soc. Symp. Proc., **422**, 661, (1997).

Beamline X20A

L.J. Buller, Electrochemical and X-ray Studies of the Structure and Dynamics of Deposition of Metal Monolayers, Thesis, Cornell University, (1997).

Q. Feng, Q.J. Harris, R.J. Birgeneau, and J.P. Hill, "Neutron and X-ray Scattering Studies of Field-cooled Ordering in the Three-dimensional Random Field Ising Model", *Phys. Rev.*, **B55**, 370, (1997).

A.C. Finnefrock, L.J. Buller, K.L. Ringland, P.D. Ting, H.D. Abruna, and J.D. Brock, "Time-Resolved Measurements of Overlayer Ordering in Electrodeposition", Mat. Res. Soc. Proc., **451**, 49, (1997).

J.P. Hill, Q. Feng, Q.J. Harris, R.J. Birgeneau, A.P. Ramirez, and A. Cassanhoi, "Phase Transition Behavior in the Random Field Antiferromagnet $Fe_{0.5}Zn_{0.5}F_2$", *Phys. Rev.*, **B55**, 356, (1997).

P.M. Mooney, "Strain Relaxation and Dislocations in SiGe/Si Structures", *Mat. Sci. And Eng.*, **R17**, 105, (1996).

K.P. Rodbell, V. Svilan, L.M. Gignac, P.W. DeHaven, R.J. Murphy, and T.J. Licata, "Film Crystallographic Texture and Substrate Surface Roughness in Layered Aluminum Metallization", Mat. Res. Soc. Proc., **428**, 261, (1996).

F.M. Ross, K.M. Krishnan, N. Thangaraj, R.F.C. Farrow, R.F. Marks, A. Cebollada, S.S.P. Parkin, M.F. Toney, M. Huffman, C.A. Paz De Araujo, L.D. McMilan, J. Cuchiaro, M.C. Scott, C. Echer, F. Ponce, M.A. O'Keefe, and E.C. Nelson, "Applications of Electron Microscopy in Collaborative Industrial Research", *MRS Bulletin*, **21/5**, 17, (1996).

V. Svilan, K.P. Rodbell, L.A. Clevenger, C. Cabral, Jr., R.A. Roy, C. Lavoie, J. Jordan-Sweet, and J.M.E. Harper, "Crystallographic Texture of C54 Titanium Disilicide as a Function of Deep Submicron Structure Geometry", Mat. Res. Soc. Proc., **427**, 53, (1996).

Beamline X20B

V. Kiryukhin, B. Keimer, R.E. Boltnev, V.V. Khmelenko, and E.B. Gordon, "Inert-Gas Solids with Nanoscale Porosity", *Phys. Rev. Lett.*, **79**, 1774, (1997).

Beamline X20C

C. Cabral, Jr., L.A. Clevenger, J.M.E. Harper, R.A. Roy, K.L. Saenger, G.L. Miles, and R.W. Mann, "*In Situ* X-ray Diffraction Analysis of $TsSi_2$ Phase Formation from a Titanium-Molybdenum Bilayer", Mat. Res. Symp. Proc., **441**, 296, (1997).

C. Cabral, Jr., L.A. Clevenger, R.A. Roy, G.B. Stephenson, C. Lavoie, K.L. Saenger, J. Jordan-Sweet, R. Viswanathan, G. Morales, and K.L. Ludwig, Jr., "*In Situ* X-Ray Diffraction Analysis of $CoSi_2$ Phase Formation on Single and Polycrystalline Silicon as a Function of Linewidth and Dopant at Rapid Thermal Annealing Rates", ULSI XI Conference Proceedings, Mat. Res. Soc., p. 439, (1996).

J.R.A. Carlsson, L.A. Clevenger, L.D. Madsen, L. Hiltman, X.H. Li, J. Jordan-Sweet, C. Lavoie, R.A. Roy, C. Cabral, Jr, K.L. Ludwig, G. Morales, K.L. Ludwig, G.B. Stephenson, and H.T.G. Hentzell, "Phase Formation Sequences in the Silicon-Phosphorus System: Determined by *In Situ* Synchrotron and Conventional X-Ray Diffraction Measurements, and Predicted by a Theoretical Model", *Phil. Mag.*, **B75**, 363, (1997).

L.A. Clevenger, C. Cabral, Jr., R.A. Roy, C. Lavoie, J. Jordan-Sweet, S. Brauer, G. Morales, K.F. Ludwig, Jr., and G.B. Stephenson, "Formation of a Crystalline Metal-Rich Silicide in Thin Film Titanium/Silicon Reactions", *Thin Solid Films*, **289**, 220, (1996).

L.A. Clevenger, C. Cabral, Jr., R.A. Roy, C. Lavoie, K.L. Saenger, J. Jordan-Sweet, G. Morales, K.L. Ludwig, Jr., and G.B. Stephenson, "*In Situ* Analysis of the Formation of Thin $TiSi_2$ (< 50 nm) Contacts in Submicron CMOS Structures During Rapid Thermal Annealing", Mat. Res. Symp. Proc., **402**, 96, (1996).

A. Domenicucci, C. Dehm, S. Loh, L.A. Clevenger, C. Dziobkowski, C. Cabral, Jr., C. Lavoie, and J. Jordan-Sweet, "Phase Transformation and Microstructural Properties in Sputtered versus CVD WSix Films", Mat. Res. Symp. Proc., **441**, 3, (1997).

C. Lavoie, C. Cabral, Jr., L.A. Clevenger, J.M.E. Harper, J.L. Jordan-Sweet, K.L. Saenger, and F. Doany, "Light Scattering Measurements of Surface Topography During Formation of Titanium Silicide", Mat. Res. Symp. Proc., **406**, 163, (1996).

B. Park, "Order Re-equilibration Kinetics within the B_2 and DO_3 Phases of Fe_3Al", *Jpn. J. Appl. Phys.*, **35**, L1287, (1996).

R.F. Saraf, C. Dimitrakopoulos, M.F. Toney, and S.P. Kowalczyk, "Near Surface Structure of Solvent-Free Processed Polymide Thin Film", *Langmuir*, **12**, 2802, (1996).

S. Song, M. Yoon, S.G.J. Mochrie, G.B. Stephenson, and S.T. Milner, "Faceting Kinetics of Stepped Si(113) Surfaces: Dynamic Scaling and Nano-Scale Grooves", *Surf. Sci.*, **372**, 37, (1997).

Beamline X21

K. Hämäläinen, S. Manninen, C.-C. Kao, W. Caliebe, J.B. Hastings, A. Bansil, S. Kaprzyk, and P.M. Platzman, "High Resolution Compton Scattering Study of Be", *Phys. Rev.*, **B54**, 5453, (1996).

Beamline X22A

R.R. Adzic, J.X. Wang, O.M. Magnussen, and B.M. Ocko, "The Structure of Tl Adlayers on the Pt(111) Electrode Surface: Effects of Solution pH and Bisulfate Coadsorption", *J. Phys,. Chem.*, **100**, 14721, (1996).

N.M. Jisrawi, T.R. Thurston, X.O. Yang, S. Mukerjee, J. McBreen, M.L. Daroux, and X.K. Xing, "*In Situ* Investigation of Working Battery Electrodes using Synchrotron X-ray Diffraction", Proc. of the 1996 Fall Meeting of the Materials Research Society, Boston, MA, *J. of Mat. Res.*, **451**, 301, (1997).

N.M. Jisrawi, H.Wiesmann, M.W. Ruckman, T.R. Thurston, G. Reisfeld, B.M. Ocko, and M. Strongin, "*In Situ* X-ray Investigation of Hydrogen Charging in Thin Film Bimetallic Electrodes", *J. Mat. Res.*, **12**, 2091, (1997).

L.H. Lewis, D.O.Welch, and T. Thurston, "Texture Determinations in Rare-Earth-Based Permanent Magnets", Proc. 9th International Symposium on Magnetic Anisotropy and Coercivity in Rare-Earth Transition Metal Alloys, Edited by F.P. Missell, H.R. Rechenberg, V. Villas-Boas, and F.J.G. Landgraf, pp. 278-287, (1996).

B.M. Ocko, J.X. Wang, and T. Wandlowski, "Bromide Adsorption on Ag(001): a Potential Induced Two-Dimensional Using Order/Disorder Transition", *Phys. Rev. Lett.*, **79**, 1511, (1997).

B.M. Ocko, and T.H. Wandlowski, "Halide Electroadsorption on Single Crystal Surfaces" Proc. of the Materials Research Society, Electrochemical Synthesis and Modification of Materials, Edited by P. Andricacos, J. Delplancke, S. Corcoran, and T. Moffat, Mat. Res. Soc. Symp. Proc., **451**, 55, (1997).

T.R. Thurston, P. Haldar,Y.L. Wang, M. Suenaga, N.M. Jisrawi, and U. Wildgruber, "*In Situ* Measurements of Texture and Phase Development in $(Bi,Pb)_2Sr_2Ca_2Cu_3O_{10}$-Ag Tapes", *J. of Mat. Res.*, **12**, 891, (1997).

T.H. Wandlowski, O. Magnussen, B.M. Ocko, S. Wu, and J. Lipkowski, "The Surface Structure of Au(111) in the Presence of Organic Adlayers—a Combined Electrochemical and Surface X-ray Scattering Study", *J. Electro. Chem.*, **409**, 155, (1996).

Beamline X22B

P. Bödeker, Effect of Metallic Cap Layers on the Magnetic Properties of Thin Epitaxial Cr[001] Films, Ph.D. Thesis, Ruhr-Universitaet Bochum, (1996).

P. Bödeker, P. Sonntag, A. Schreyer, J. Borchers, K. Hamacher, H. Kaiser, and H. Zabel, "Effect of Fe Cap Layers on the Spin Density Waves in Epitaxial Cr(001) Films", *J. Appl. Phys.*, **81**, 5247, (1997).

P. Bödeker, P. Sonntag. A. Schreyer, H. Zabel, J. Borchers, K. Hamacher, and H. Kaiser, "Spin Density Waves in Epitaxial Fe/Cr Films", *Physica*, **B234**, 464, (1997).

G.M. Bommarito, W.J. Foster, P.S. Pershan, and M.L. Schlossman, "A Determination of the Phase Diagram of Relaxed Langmuir Monolayers of Behenic Acid", *J. Phys. Chem.*, **105**, 5265, (1996).

A. Doerr, X.Z. Wu, B.M. Ocko, E.B. Sirota, O. Gang, and M. Deutsch, "Surface Freezing in Mixtures of Molten Alkanes and Alcohols", *Colls. & Surf. A - Physchem. & Eng. Aspects*, **128/1-3**, 63, (1997).

B.W. Gregory, D. Vaknin, J.D. Gray, B.M. Ocko, P. Stroeve, T.M. Cotton, and W.S. Struve, "Two-Dimensional Pigment Monolayer Assemblies for Light Harvesting Applications: Structural Characterization at the Air/water Interface with X-ray Specular Reflectivity and on Solid Substrates by Optical Absorption Spectroscopy", *J. Phys. Chem.*, **B101**, 2006, (1997).

V. Kiryukhin, D. Casa, J.P. Hill, B. Keimer, A. Vigliante, Y. Tomioka, and Y. Tokura, "An X-Ray Induced Insulator-Metal Transition in a Colossal-Magnetoresistive Manganite", *Nature*, **386**, 813, (1997).

V. Kiryukhin, B. Keimer, J.P. Hill, S.M. Coad, and D.M. Paul, "Synchrotron X-Ray Scattering Study of Magnetic Field Induced Transitions in $Cu_{1-x}(Zn,Ni)_xGe_3$", *Phys. Rev.*, **B54**, 7269, (1996).

O.M. Magnussen, B.M. Ocko, M. Deutsch, M.J. Regan, P.S. Pershan, D. Abernathy, G. Grubel, and J.F. Legrand, "Self-Assembly of Organic Films on a Liquid Metal", *Nature*, **384**, 250, (1996).

O. M. Magnussen, B. M. Ocko, M. Deutsch, M. J. Regan, P.S. Pershan, L. E. Berman, D. Abernathy, J. F. Legrand, and G. Grubel, "Organic Layers on Liquid Metals: An X-ray Reflectivity Study of Thiols on Mercury", *Nature,* **384**, 250, (1996).

R. Moaz, S. Matlic, E. DiMasi, B.M. Ocko, and J. Sagiv, "Self-Replicating Amphiphilic Monolayers", *Nature,* **384**, 150, (1996).

B.M. Ocko, X. Z. Wu, E. B. Sirota, S. K. Sinha, O. Gang, and M. Deutsch, "Surface Freezing in Chain Molecules: Normal Alkanes", *Phys. Rev.*, **E55**, 3164, (1997).

M.J. Regan, O.M. Magnussen, E.H. Kawamoto, B.M. Ocko, N. Maskil, M. Deutsch, S. Lee, K. Penanen, and L.E. Berman, "X-ray Studies of Atomic Layering at Liquid Metal Surfaces", *J. of Non-Crystalline Solids*, **207**, 762, (1996).

M.J. Regan, P.S. Pershan, O.M. Magnussen, B.M. Ocko, M. Deutsch, and L.E. Berman, "Capillary-wave Roughening of Surface-induced Layering in Liquid Gallium", *Phys. Rev.*, **B54**, 9730-9733, (1996).

M.J. Regan, P.S. Pershan, O.M. Magnussen, B.M. Ocko, M. Deutsch, and L.E. Berman, "X-ray Reflectivity Studies of Liquid Metal and Alloy Surfaces", *Phys. Rev.*, **B55**, 15874-15884, (1997).

M.J. Regan, H. Tostmann, P.S. Pershan, O.M. Magnussen, E. DiMasi, B.M. Ocko, and M. Deutsch, "X-ray Study of the Oxidation of Liquid Gallium Surfaces", *Phys. Rev.*, **B55**, 10786-10790, (1997).

E.B. Sirota, X.Z. Wu, B.M. Ocko, and M. Deutsch, "What Drives the Surface Freezing in Alkanes ?", *Phys. Rev. Lett.*, **79**, 531, (1997).

P. Sonntag, Magnetic and Structural Properties of Thin Epitaxial Cr Films, PhD. Thesis, Ruhr-Universitaet Bochum, (1996).

P. Sonntag, P. Bödeker, T. Thurston, and H. Zabel, "Charge Density Waves and Strain Waves in Thin Epitaxial Cr(001) Films on Nb", *Phys. Rev.*, **B52**, 13450, (1995).

Beamline X22C

C. Detlefs, A.H.M.Z. Islam, A.I. Goldman, C. Stassis, P.C. Canfield, J.P. Hill, and D. Gibbs, "Determination of Magnetic Moment Directions using X-ray Resonant Exchange Scattering", *Phys. Rev.*, **B55**, R680, (1997).

G. Helgesen, Y. Tanaka, J.P. Hill, P. Wochner, D. Gibbs, C.P. Flynn, and M.B. Salamon, "Magnetic and Structural Properties of Erbium Films", *Phys. Rev.*, **B56**, 2635, (1997).

J.P. Hill, C.-C. Kao, and D.F. McMorrow, "K-edge Resonant X-ray Magnetic Scattering from a Transition Metal Oxide: NiO",. *Phys. Rev. Rapid Comm.*, **B55**, R8662, (1997).

S.C. Perry, W.J. Nuttall, W.G. Stirling, G.H. Langer, and O. Vogt, "X-ray Scattering Study of the two Magnetic Correlation Lengths in Uranium Antimonide", *Phys. Rev.*, **B54**, 10782, (1996).

J.A. Simpson, R.A. Cowley, D.A. Jehan, R.C.C. Ward, M.R. Wells, D.F. McMorrow, K.N. Clausen, T.R. Thurston, and D. Gibbs, "Co-Existence of Long- and Short-Range Magnetic Correlations in Holmium-Erbium Superlattices", *Z. Phys.*, **B101**, 35, (1996).

A. Stunault, S. Langridge, C. Vettier, D. Gibbs, and N. Bernhoeft, "Near-Surface Effects at the Antiferromagnetic Phase Transition in Uranium Phosphide", *Phys. Rev.*, **B55**, 423, (1997).

Beamline X23A2

M.R. Antonio, and L. Soderholm, "Implications of the Unusual Redox Behavior Exhibited by the Heteroplyanion $[EuP_5W_30_{11}0]^{12-}$", *J. Alloys and Compds.*, **250**, 541, (1997).

M. R. Antonio, and L. Soderholm, "Redox Behavior of Europium in the Preyssler Heteropolyanion $[EuP_5W_30_{11}0]^{12-}$", *J. Cluster Sci.*, **7**, 585, (1996).

M. R. Antonio, L. Soderholm, and A.J.G. Ellison, "Local Environments of Erbiumand Lutetium in Sodium Silicate Glasses", *J. Alloys and Compds.*, **250**, 536, (1997).

M. R. Antonio, L. Soderholm, and I. Song, "Design of Spectroelectrochemical Cell for *in situ* X-ray Absorption Fine Structure Measurements of Bulk Solution Species", *J. Appl. Electrochem.*, **27**, 784, (1997).

S.V. Bordawekar, E.J. Doskocil, and R.J. Davis, "Influence of Support Composition on the Structure and Reactivity of Strontium Base Catalysts", *Catal. Lett.*, **44**, 193, (1997).

C.E. Bouldin, L. Furenlid, and T. Elam, "MacXAFS: An EXAFS Analysis Package for the Macintosh", *Physica,* **B208&209**,190, (1995).

A.C. Carter, C.E. Bouldin, K.M. Kemner, M.I. Bell, J.C. Woicik, and S.A. Majetich, "The Surface Structure of Cadmium Selenide Nanocrystallites", *Phys. Rev.*, **B55**, 13822, (1997).

J.O. Cross, Analysis of Diffraction Anomalous Fine Structure, PhD. Thesis, University of Washington, (1977).

J.O. Cross, M. Newville, L.B. Sorensen, H.J. Stragier, C.E. Bouldin, and J.C. Woicik, "Separated Anomalous Scattering Amplitudes for the Inequivalent Cu sites in $YBa_2Cu_3O_{7-}$ using DAFS", *J. de Phys. IV,* **7**, 745, (1997).

D. Fauteux, A. Massucco, M. van Buren, B. Ouyang, S. G. Greenbaum, S.Kostov, and M. L. denBoer, "A Comparative Study of $LiMn_2O_4$ fromVarious Sources", Mat. Res. Soc. Proc., **369**, 59, (1996).

M.R. Franklin, Structure and Magnetism in Co/X, Fe/Si and Fe/{FeSi} Multilayers, PhD Thesis, Michigan State University, (1996).

M.F. Garcia, J.A. Anderson, and G.L. Haller, "Alloy Formation and Stability in Pd-Cu Bimetallic Catalysts", *J. Phys. Chem.*, **100**, 16247, (1996).

D.M. Giaquinta, L. Soderholm, S.E. Yuchs, and S.R. Wasserman, "The Speciation of Uranium in a Smectite Clay: Evidence for Catalysed Uranyl Reduction", *Radiochimica Acta*, **76**, 113, (1997).

D.M. Giaquinta, S.E. Yuchs, L. Soderholm, and S.R. Wasserman, "The Structure of Uranium in Surface Modified Clays", *J. Alloys and Compds.*, **249**, 142, (1997).

C.J. Gutierrez, R. Selestino, R.A. Mayanovic, and G. Prinz, "Evidence for Loose Spins in Epitaxial Al/Fe/Al", *J. Appl. Phys.*, **81**, 5352 (1997).

V.G. Harris, K.M. Kemner, B.N. Das, J.C. Woicik, P. Crespo, A. Hernando, and A. Garcia Escorial, "Mechanical-alloying and Lattice Distortions in Ball-milled CuFe", *J. de Phys. IV*, **7**, 1151, (1997).

V.G. Harris, K.M. Kemner, W.T. Elam, B.N. Das, N.C. Koon, J. Kirkland, P. Crespo, A. Hernando, A. Garcia Escorial, and J. Woicik, "Near-Neighbor Mixing and Bond Dilation in Mechanically-Deformed CuFe", *Phys. Rev.*, **B54**, 6249, (1996).

K. M. Kemner, W. T. Elam, D. B. Hunter, and P. M. Bertsch, "EXAFS Studies of the Local Environment of Cs in CsBr-dibenzo-18-crown-6 Ether Solutions and Powders", *J. Phys. Chem.*, **100**, 11698, (1996).

K.M. Kemner, D.B. Hunter, W.T. Elam, and P.M. Bertsch, "Cesium XAFS Studies of Solution Phase Cs-Ionophore Complexation", Synchrotron Radiation Techniques in Industrial, Chemical and Materials Science, Plenum Press, pp. 149-158, (1996).

K. M. Kemner, Y. U. Idzerda, V. G. Harris, V. Chakarian, W. T. Elam, C. -C. Kao, E. Johnson, Y. C. Feng, D. E. Laughlin, C. T. Chen, K. -K. Lee, and J. C. Lodder, "Direct Observation of Cr Magnetic Order in CoCrTa and CoCrPt Thin Films", *Rapid Comm. J. App. Phys.*, **81**, 1002, (1997).

A.J. Kropf, XAFS and Reflectivity Investigations of Solid-Solid Interfaces in Superlattices and Thin Films, PhD. Thesis, University of Notre Dame, (1977).

G. Larsen, E. Lotero, L.M. Petkovic, and D.S. Shobe, "Alcohol Dehydration Reactions over Tungstated Zirconia Catalysts", *J. of Catal.*, **169**, 67, (1997).

Q. Lu, XAFS Investigations of Structural Properties at Internal Interfaces, PhD Thesis, University of Notre Dame, (1996).

Q. Lu, B. A. Bunker, H. Lou, A. J. Kropf, K. M. Kemner, J. K. Furdyna, and G. C. Hua, "X-ray Study of Atomic Correlations in ZnCdSeTe Epitaxial Thin Films", *Phys. Rev.*, **B55**, 9910, (1997).

R.A. Mayanovic, Y. Feng, K.W. Groh, Y. Wang, R.E. Giedd, and M.G. Moss, "Local Structure Surrounding Implanted As Ions in Polysulfone Films", Mat. Res. Soc. Proc., **321**, 113 (1994).

R.A. Mayanovic, C.J. Gutierrez, and G. Prinz, "Investigations on Fe Lattice Strain Relaxation in the Al/Fe/Al Trilayer", Mat. Res. Soc. Proc., **437**, 27, (1996).

P. Menacherry, and M.F. Garcia, "An X-Ray Absorption Spectroscopy Determination of the Morphology of Palladium Particles in KL-zeolite", *J. Catal.*, **166**, 75, (1997).

K.E. Miyano, J.C. Woicik, L. H. Robins, C.E. Bouldin, and D.K. Wickenden, "Extended X-ray Absorption Fine Structure Study of $Al_xGa_{1-x}N$ Films", *Appl. Phys. Lett.*, **70**, 2108, (1997).

K.E. Miyano, J.C. Woicik, P. Sujatha Devi, and H.D. Gafney, "Cr K edge X-ray Absorption Study of Cr Dopants in Mg_2SiO_4 and Ca_2GeO_4", *Appl.Phys. Lett.*, **71**, 1168, (1997).

B. Ravel, M. Newville, J.O. Cross, and C.E. Bouldin, "Analysis of DAFS Fine Structure and Background", *Physica,* **B208&209**, 145, (1995).

L. Soderholm, S. Skanthakumar, U. Staub, M. R. Antonio, and C.W. Williams, "The Effect of f-ion Valence on Superconductivity in the Series $Pb_2Sr_2RCu_3O_8$ (R=Ce, Pr, Tb and Am)", *J. Alloys and Compds.*, **250**, 623, (1997).

U. Staub, S. Skanthakumar, L. Soderholm, and R. Osborn, "Magnetic Properties of $Pb_2Sr_2PrCu_3O_8$", *J. Alloys and Compds.*, **250**, 581, (1997).

U. Staub, L. Soderholm, S. Skanthakumar, and M. R. Antonio, "Oxidation States of the Unusual Rare Earths (R=Ce, Pr, and Tb) in Double Layer High-T_c Superconductors", *J. de Phys. IV.*, **7**, 1077, (1997).

U. Staub, L. Soderholm, S. Skanthakumar, S. Rosenkranz, C. Ritter, and W. Kagunja, "Tb Spin Correlations in $Pb_2Sr_2Tb_{.5}Ca_{.5}Cu_3O_8$", *Europhys. Lett.*, **34**, 447, (1996).

J. P. Urbach, O. M. Foller, E. Goering, H. Paulin, M. Klemm, S. Horn, and M.L. denBoer, "Characterization of the Metallic and Insulating Phases of V_2O_3 and $(V,Cr)_2O_3$ by NEXAFS", *J. de Phys. IV.*, **7**, 535, (1997).

H. Wang, Platinum-Tin Bimetallic Catalysts Supported on L-Zeolite: Synthesis and Characterization, PhD. Thesis, Yale University, (1997).

S. R. Wasserman, D. M. Giaquinta, S. E. Yuchs, and L.Soderholm, "The Effects of Surface Modification on the Speciation of Metal ions Intercalated into Aluminosilicates", Mat. Res. Soc. Proc., **465**, 473, (1997).

S.R. Wasserman, S.E. Yuchs, D. Giaquinta, L. Soderholm, and K. Song, "Nanoscale Encapsulation: The Structure of Cations in Hydrophobic Microporous Aluminosilicates", *J. de Phys. IV.*, **7**, 803, (1997).

J.C. Woicik, C.E. Bouldin, K.E. Miyano, and C.A. King, "Unit Cell of Strained GeSi", *Phys. Rev.*, **B55**, 15386, (1997).

Beamline X23A3

W.B. Alexander, P.E. Pehrsson, D. Black, and J.E. Butler, "X-ray Diffraction Analysis of Strain and Mosaic Structure in (011)-Oriented Diamond", III-Nitride SiC and Diamond Materials for Electronic Devices, MRS Symp.Proc., **423**, 305, (1996).

A.J. Allen, G.G. Long, H.M. Kerch, S. Krueger, G. Skandan, H. Hahn, and J.C. Parker, "Sintering Studies of Nanophase Ceramic Oxides using Small-Angle Scattering", Ceramics: Charting the Future, Proc. 8th CIMTEC World Ceramics Congress and Forum on New Materials, edited by P. Vincenzini, *Advances in Sci and Tech.*, **3D**, 1755, (1995).

G. Beaucage, J.H. Aubert, R.R. Lagasse, D.W. Schaefer, T. Reiker, P. Ehrlich, R.S. Stein, S. Kulkarni, and P. Whaley, "Nanostructured Semi-crystalline Polymer Foams", *J. Polymer Sci. and Polymer Phys.*, **34/17**, 3063, (1996).

D.B. Eason, Z. Yu, W.C. Boney, J.W. Cook, Jr., J.F. Schetzina, D.R. Black, G. Cantwell, and W.C. Harsch, "High-Brightness Light-Emitting Diodes Grown by MBE on ZnSe Substrates", *J. Vac. Sci. and Technol.*, **B13/4**, 1566, (1995).

G. Fogarty, B. Steiner, M. Cronin-Golomb, U. Laor, M.H. Garrett, J. Martin, and R. Shrin, "Antiparallel Ferroelectric Domains in Photorefractive Barium Titanate and Strontiuim Barium Niobate Observed by High-Resolution X-ray Diffraction Imaging", *J. Opt. Soc. Am.*, **B13**, 2636, (1996).

S. Han, G. Rodriquez, A. Taylor, M.A. Plano, M.D. Moyer, M.A. Moreno, L.S. Pan, D.R. Black, H.E. Burdette, J. Agers, and A. Chen, "Correlation of Electrical Properties with Defects in a Homoepitaxial Chemical-Vapor-Deposited Diamond Film", MRS Symp.Proc, **416**, 343, (1996).

X. Hu, F. Liu, I. Baker, and D. Black, "The Effect of X-radiation on the Plastic Deformation of Ice", *Phil. Mag.*, **A73/5**, 1355, (1996).

J. Ilavsky, A.J. Allen, G.G. Long, H. Herman, and C.C. Berndt, "Characterization of the Closed Porosity in Plasma-Sprayed Alumina", *J. Mater. Res.*, **32**, 3407, (1997).

J. Ilavsky, A.J. Allen, G.G. Long, S. Krueger, H. Herman, and C.C. Berndt, "Influence of Spray Angle on the Porous Microstructure of Plasma-Sprayed Ceramic Deposits", *J. Amer. Ceram. Soc.*, **80/3**, 733, (1997).

R.A. Livingston, and A.J. Allen, "Application of Small-Angle Neutron Scattering Method to the Study of the Durability of Historic Brick and Mortar", Ceramics in Architecture, Proc. 8th CIMTEC World Ceramics Congress and Forum on New Materials, edited by P. Vincenzini, *Monographs in Materials and Society*, **1**, 573, (1995).

G.G. Long, A.J. Allen, S. Krueger, J. Thomas, D.L. Johnson, and C.J. Hwang, "Small-Angle Scattering Studies of the Microstructure of Silicon Nitride during Processing", High-Performance Materials in Engine Technology, Proc. 8th CIMTEC World Ceramics Congress and Forum on new Materials, edited by P. Vincenzini, *Advances in Sci.and Tech.*, **9**, 129, (1995).

B. Olivier, A. Lagasse, D. Schaefer, J. Barnes, and G.G. Long, "Pore Orientation Periodicity in Porous Polymer and Carbon Structures", *Macromolecules*, **29**, 8615, (1996).

P. Pehrsson, T. McCormick, B. Alexander, M. Marchywka, D. Black, J. Butler, and S. Prawler, "Homoepitaxial Mosaic Growth and Liftoff of Diamond Films", Diamond for Electronic Applications, MRS Symp.Proc., **416**, 51, (1996).

R.Spal, C. Chiang, G. Riley, and C. Christopherson, "Synchrotron Radiation Digital Microradiography of Strained High-Temperature Superconductor Composite Tapes", Proc. ICCE/4 fourth Int'l Conf. On Composite Engineering, pp. 935-936, (1997).

B.L. Steiner, L.E. Levine, M. Brown, and D. Larson, "Residual Disorder in Low-Pressure Low-Thermal-Gradient Liquid-Encapsulated Czochralski Gallium Arsenide Observed in High-Resolution Synchrotron Diffraction Imaging", *J. Cryst. Growth*, **169**, 1, (1996).

L.D. Zhu, J. Zhao, F. Wang, G. Fogarty, P. Lu, S.B. Kang, M. Sinclair, D. Dimos, M. Cronin-Golomb, B. Steiner, P.E. Norris, B. Kear, and B. Gallois, "Epitaxial Electro-Optical SBN Films by Single Source Plasma Enchanced Metaloorganic Chemical Vapor Deposition", *Appl. Phys. Lett.*, **67**, 1836, (1995).

Beamline X23B

J.D. Ayers, V.G. Harris, J.C. Sprague, and W.T. Elam, "Nucleation of the Nanocrystalline Phase in $Fe_{73.5}Cu_1Nb_3Si_{13.5}B_9$", *J. Appl. Phys.*, **75**, 5801, (1994).

J. D. Ayers, V. G. Harris, J. A. Sprague, and W. T. Elam, "The Local Atomic Order of Cu and Fe in Heat Treated $Fe_{73.5}Nb_3Cu_1Si_{13.5}B_9$ Ribbons", *IEEE Trans. on Mag.*, **29**, 2664, (1993).

J. D. Ayers, V. G. Harris, J. A. Sprague, W. T. Elam, and H. N. Jones, "A Model for Nucleation of Nanocrystals in the Soft Magnetic Alloy $Fe_{73.5}Nb_3Cu_1Si_{13.5}B_9$", Proceedings of the 3rd International Conference on Nanostructured Materials, Edited by M. L. Trudeau, V. Provenzano, R. D. Shull, and J. Y. Ying, Kona, pp. 391-396, (1996).

M.I. Bell, K. H. Kim, and W. T. Elam, "Direct Observation of Disorder in Perovskite-Structure Ferroelectrics", *Ferroelectrics,* **120**, 103, (1991).

D. B. Chrisey, G. P. Summers, W. G. Maisch, E. A. Burke, W. T. Elam, H. Herman, J. P. Kirkland, and R.A. Neiser, "Catastrophic Loss of Superconductivity in Ion-Irradiated Films of $Yba_2Cu_3O_{7-\delta}$", *Appl. Phys. Lett.*, **53**, 1001, (1988).

J.O. Cross, B.R. Bennett, M.I. Bell, and K.J. Kuhn, "Synthetic Wide Band-Pass X-ray Polarizers", *Appl. Phys. Lett.*, **70**, 224, (1997).

P.C. Dorsey, V.G. Harris, P. Lubitz, D. Chrisey, and N.C. Koon, "X-ray Absorption Fine Structure Studies of $(Mn_xZn_{1-x})Fe_2O_4$ Films", Mat. Res. Soc. Symp. Proc., **375**, 33, (1995).

J. A. Eastman, M. R. Fitzsimmons, M. Müller-Stach, G. Wallner, and W. T. Elam, "Characterization of Nanocrystalline Pd by X-ray Diffraction and EXAFS", *Nanostruct. Mater.*, **1**, 47, (1992).

A.S. Edelstein, V.G. Harris, L. Kurihara, D.R. Rolison, and F.H. Katz, "Chemical Synthesis and Properties of Nanocrystalline $Cu_{80}Co_{20}$", Processing and Properties of Nanocrystalline Materials, edited by C. Suryanarayana, J. Singh, and F.H. Froes, Proceedings of the Minerals, Metals and Materials Society, pp. 111-122, (1996).

A.S. Edelstein, V.G. Harris, D. Rolison, J.H. Perepezko, and D. Smith, "Nanocrystalline Solid Solutions of Cu/Co and Other Novel Nanomaterials", Mat. Res. Soc. Symp. Proc., **457**, 261, (1997).

A.S. Edelstein, F.H. Kaatz, V.G. Harris, L. Kurihara, D.R. Rolison, and D.J. Gillespie, "Chemically-Prepared CuCo and CuFe Nanoparticles", Clusters and Nanostructured Materials, edited by P. Jena and S.N. Behera, Nova Science Pub., Inc., New York, pp. 41-50, (1996).

W. T. Elam, J. P. Kirkland, R. A. Neiser, E. F Skelton, S. Sampath, and H. Herman, "Plasma Sprayed High T_c Superconductors", *Adv. Cer. Mat.*, **2/3B**, 411, (1987).

J.L. Feldman, W.T. Elam, A.C. Ehrlich, E.F. Skelton, D.D. Dominguez, D.D.L. Chung, and F.W. Lytle, "Polarized X-Ray Absorption Studies of Graphite Intercalated-Bromide Compounds", *Phys. Rev.*, **B33**, 7961, (1986).

C.J. Gutierrez, V.G. Harris, J.J. Krebs, W.T. Elam, and G.A. Prinz, "Magnetic and Structural Characteristics of Epitaxial Fe_xCo_{1-x} Alloy Films on ZnSe(001)", *J. Appl. Phys.*, **73**, 6763, (1993).

C.J. Gutierrez, G.A. Prinz, J.J. Krebs, M.E. Filipkowski, V.G. Harris, and W.T. Elam, "Magnetic and Structural Studies of Epitaxial (001) Fe and (001) Fe_xCo_{1-x} Alloy Film Structures", *J. Mag. and Mag. Mat.*, **126**, 232, (1993).

V.G. Harris, "A Spinning-Stage, Total-Electron-Yield Detector for the Elimination of Diffraction Peaks in X-ray Absorption Spectra", *Rev. Sci. Instrum.*, **68/1**, 23, (1997).

V.G. Harris, K.D. Aylesworth, B.N. Das, W.T. Elam, and N.C. Koon, "Determination of Structural Anisotropy in Amorphous Tb-Fe Alloy Films", *IEEE Trans. on Magn.*, **28**, 2955, (1992).

V.G. Harris, K.D. Aylesworth, W.T. Elam, N.C. Koon, R. Cochoorn, and W. Hoving, "Evolution of Structure in Fe Layer Thickness in Low-Dimensional Fe/Tb Multilayered Films", Mat. Res. Soc. Symp. Proc., **238**, 635, (1992).

V.G. Harris, K.D. Aylesworth, K.H. Kim, W.T. Elam, and N.C. Koon, "EXAFS Studies of IBS Amorphous Fe-Tb Alloy Films", *J. Appl. Phys.*, **70**, 6311, (1991).

V. G. Harris, B. N. Das, M. Rubenstein, J. L. Goldberg, W. T. Elam, and N. C. Koon, "Structural Evolution and Magnetoresistance Properties of Heat Treated $Cu_{80}Co_{15}Fe_5$ Ribbons", *IEEE Trans. on Mag.*, **29**, 2616, (1993).

V.G. Harris and W.T. Elam, "A Miniature Total Electron Yield Detector for Measurement of X-ray Absorption Spectra", *Rev. Sci. Instrum.*, **68/5**, 1972, (1997).

V.G. Harris, W. T. Elam, and N. C. Koon, "Correlation of Magnetic and Structural Anisotropy in Amorphous Tb-Fe Films", *J. Magn. Soc. Jpn.*, **17**, 267, (1993).

V.G. Harris, W.T. Elam, and N.C. Koon, "Structural Origins of Perpendicular Magnetic Anisotropy in Amorphous non-S-state Rare Earth - Transition Metal Alloy Films", High Density Digital Recording, Edited by K.H.J. Buschow, G.J. Long and F. Grandjean, *Appl. Sci.*, **229**, 483-517, (1993).

V.G. Harris, K.M. Kemner, W.T. Elam, B.N. Das, N.C. Koon, J. Kirkland, P. Crespo, A. Hernando, A. Garcia Escorial, and J. Woicik, "Near-neighbor Mixing and Bond Dilation in Mechanically-Deformed CuFe", *Phys. Rev.*, **B54**, 6249, (1996).

V.G. Harris, N.C. Koon, C.M. Williams, Q. Zhang, and M. Abe, "Cation Distributions in Spinel Ferrites Observed via EXAFS Measurements", *J. Appl. Phys.*, **79/8**, 4561, (1996).

V.G. Harris, N.C. Koon, C.M. Williams, Q. Zhang, M. Abe, and J. Kirkland, "Cation Distributions in Spinel Ferrites via EXAFS", *Appl. Phys. Lett.*, **68/15**, 2082, (1996).

V.G. Harris, N.C. Koon, C.M. Williams, Q. Zhang, M. Abe, J.P. Kirkland, and D.A. McKeown, "Direct Measurement of Octahedral and Tetrahedral Site Environments in NiZn-Ferrites", *IEEE Trans. on Magn.*, **31/6**, 3473, (1995).

V.G. Harris, S.A. Oliver, J.D. Ayers, B.N. Das, and N.C. Koon, "Crystallization of Thin Amorphous Fe-B Films Studied via Empirical EXAFS Modeling", *Appl. Phys. Lett.*, **68/15**, 2073, (1996).

V.G. Harris, S.A. Oliver, J.D. Ayers, B.N. Das, and N.C. Koon, "Quantitative Crystallization Studies of Thin Amorphous $Fe_{80}B_{20}$ Films via Empirical Modeling of EXAFS Data", Mat. Res. Soc. Symp. Proc., **375**, 9, (1995).

V.G. Harris, S.A. Oliver, K.H. Kim, W.T. Elam, R. Culbertson, W.B. Nowak, and C. Vittoria, "Magnetic and Structural Investigation of Heat-Treated ion Beam Sputtered Amorphous $Co_{74}Fe_6B_{15}Si_5$ Films", *IEEE Trans.on Magn.*, **26**, 1459, (1990).

V.G. Harris, C.M. Williams, Q. Zhang, and M. Abe, "Multiple-Scattering Extended X-ray Absorption Fine Structure Analysis of Spinel Ferrites", *Coll. C1, Supp. au J. de Phys.*, **7**, 215 (1997).

H.A. Hoff, G.L. Waytena, J.W. Glesener, V.G. Harris, and D.P. Pappas, "Critical Thickness of Single Crystal fcc-Fe on Diamond", *Surf. Sci.*, **326**, 252, (1995).

J.S. Horwitz, P.C. Dorsey, N.C. Koon, M. Rubinstein, J.M. Byers, D.J. Gillespie, M.S. Osofsky, V.G. Harris, K.S. Grabowski, D.L. Knies, E.P. Donovan, and D.B. Chrisey, "The Effect of Oxygen Pressure and Temperature on the Structure and Properties of Pulsed Laser Deposited $La_xCa_{1-x}Mn_Od$ Films", *SPIE*, **2703**, 526, (1996).

J.S. Horwitz, P.C. Dorsey, N.C. Koon, M. Rubinstein, J.M. Byers, D.J. Gillespie, M.S. Osofsky, V.G. Harris, K.S. Grabowski, D.L. Knies, E.P. Donovan, and D.B. Chrisey, "The Effect of Oxygen Pressure on the Structure and Properties of Pulsed Laser Deposited $La_xC_{1-x}Mn_Od$ Films", Mat. Res. Soc. Symp. Proc., **401**, 525, (1996).

F.H. Kaatz, V.G. Harris, L. Kurihara, D.R. Rolison, and A.S. Edelstein, "Slow Oxidation of Cu-Co Nanocrystals", *Appl. Phys. Lett.*, **67/5**, 3807, (1995).

K. M. Kemner, W. T. Elam, V. G. Harris, Y. U. Idzerda, and J. A. Wolf, "Distinguishing the Close-Packed Hexagonal and Face Centered Cubic Phases of the Metallization of Diamond by Polarization-Dependent Extended X-ray Absorption Fine Structure", *J. Vac. Sci. Technol.*, **B14**, 3207, (1996).

K. M. Kemner, D. B. Hunter, W. T. Elam, and P. M. Bertsch, "Cesium XAFS Studies of Solution Phase Cs-Ionophore Complexation", Synchrotron Radiation Techniques in Industrial, Chemical and Materials Science, Plenum Press, pp. 149-158, (1996).

K. M. Kemner, Y. U. Idzerda, V. G. Harris, V. Chakarian, W. T. Elam, C. -C. Kao, E. Johnson, Y. C. Feng, D. E. Laughlin, C. T. Chen, K. -K. Lee, and J. C. Lodder, "Direct Observation of Cr Magnetic Order in CoCrTa and CoCrPt Thin Films", *J. App. Phys.*, **81**, 1002, (1997).

K. H. Kim, W. T. Elam, and E. F. Skelton, "Extended X-ray Absorption Fine Structure Study of Potassium Niobate", Mat. Res. Soc. Symp. Proc., **172**, 291, (1991).

J. P. Kirkland, R. A. Neiser, H. Herman, S. Sampath, E. F. Skelton, D. Gansert, and H. G Wang, "Thermal Spraying of Superconducting Oxide Coatings", *Adv Cer. Mat.*, **2/3B**, 401, (1987).

R.A. Neiser, J.P. Kirkland, W.T. Elam, and S. Sampath, "Optical Performance of the Naval Research Laboratory's Materials Analysis Beam Line at the NSLS", *Nucl. Instrum. & Meth.*, **A266**, 220, (1988).

R.A. Neiser, J.P. Kirkland, W.T. Elam, H. Herman, S. Rangaswamy, V.M. Letourneau, and M. Osofsky, "Electrical, Chemical, and Structural Properties of Plasma Sprayed Y-Ba-Cu-Oxide Superconducting Coatings", Proceedings of MRS Symp. On High Temperature Superconductors, **99**, 689-693, (1988).

R.A. Neiser, J.P. Kirkland, H. Herman, W.T. Elam, and E.F. Skelton, "Plasma Sprayed Superconducting Oxide Coatings", *Mat. Sci. and Engin.*, **91**, L13, (1987).

G.S. Nolas, V.G. Harris, G.A. Slack, D.T. Morelli, and T.M. Tritt, "Low-Temperature Transport Properties of the Mixed-Valence Semiconductor $Ru_{0.5}Pd_{0.5}Sb_3$", *J. Appl. Phys.*, **80/11**, 6304, (1996).

S.A. Oliver, V.G. Harris, C.Vittoria, W.T. Elam, K.H. Kim, H.H. Hamdeh, and M. Alhabash, "Magnetic Properties and Local Ordering During Thermal Annealing of Amorphous $Fe_{75}Ni_5B_{15}Si_5$ Films", *J. Appl. Phys.*, **70**, 5842, (1991).

D.P. Pappas, J.W. Glesener, V.G. Harris, Y.U. Idzerda, J.J. Krebs, and G.A. Prinz, "Growth of FCC-Fe Films on Diamond", *Appl. Phys. Lett.*, **64**, 28, (1994).

D.P. Pappas, J.W. Glesener, V.G. Harris, J.J. Krebs, Y.U. Idzerda, A.A. Morrish, and G.A. Prinz, "Epitaxial Growth of FCC Fe and Cu Films on Diamond", Proc. Of Mat. Res. Soc. **313**, 369, (1993).

D.P. Pappas, V.G. Harris, H.A. Hoff, and G. Waytena, "Stabilization of Single Crystal FCC Fe on Diamond", Mat. Res. Soc. Symp. Proc., **339**, 241, (1994).

S.B. Roscoe, A.K. Kakkar, T.J. Marks, A. Malik, M.K. Durbin, W. Lin, G.K. Wong, and P. Dutta, "Self-Assembled Chromophoric NLO Monolayers: X-ray Reflectivity as a Probe of Building Block-film Microstructure Relationships", *Langmuir*, **12**, 4218, (1996).

A. Shih, C. Hor, W. Elam, J. Kirkland, and D. Mueller, "Surface Geometry of BaO on W(100): A Surface-Extended X-ray-Absorption Fine-Structure Study", *Phys. Rev.*, **B44**, 5818, (1991).

P. Skeath, W. T. Elam, W. K. Burns, F. A. Stevie, and T. H. Briggs, "Concentration Dependence of the Octahedral Ti^{4+} Center in $LiNbO_3$: Its Effect on Refractive Indices", *Phys. Rev. Lett.*, **59**, 1950, (1987).

E.F. Skelton, W.T. Elam, D.U. Gubser, S.H. Lawrence, M.S. Osofsky, L.E. Toth, and S.A. Wolf, "Temperature-Dependent X-Ray Studies of the High T_c Superconductor $La_{1.9}Ba_{0.1}CuO_4$", *Phys. Rev.*, **B35**, 7140, (1987).

J.E. Snyder, V.G. Harris, J.W. Harrell, F.T. Parker, and S. Kitahata, "Local Structure of as-fabricated and Partially-Reduced Co,Ti,Sn-Substituted Ba-hexaferrite Powder", *J. Appl. Phys.*, **81/5**, 3824, (1997).

J. E. Snyder, V.G. Harris, N.C. Koon, X. Sui, and M.H. Kryder, "Local Structure of the Amorphous Precursor to Ba-Hexaferrite Thin Films: An Anisotropic Octahedral Fe-O Glass Network", *Phys. Rev. Lett.*, **77**, 3383, (1996).

J. E. Snyder, V.G. Harris, N.C. Koon, X. Sui, and M.H. Kryder, "Determination of Local Structure in the Amorphous Precursors to Ba-Hexaferrite Thin Films", *J. Appl. Phys.*, **79/8**, 4891, (1996).

J. E. Snyder, V.G. Harris, N.C. Koon, X. Sui, and M.H. Kryder, "Local Anisotropic Structure in Amorphous Ba-Fe-O Films and its Role in Determining Magnetic Anisotropy in Crystallized Ba-Hexaferrite Films", *IEEE Trans. on Magn.*, **31/6**, 3844, (1995).

X. Sui, M. Scherge, M.H. Kryder, J.E. Snyder, V.G. Harris, and N.C. Koon, "Barium Hexaferrite Thin Film Recording Media", *J. Mag. Mag. Mater.*, **155**, 132, (1996).

R. Swineford, D. Pappas, and V.G. Harris, "Structure of C-Stabilized fcc Fe on Diamond: The Growth of Single Crystal Austenite", *Phys. Rev.*, **B52**, 7890, (1995).

Beamline X24A

B. Armen, S.H. Southworth, J.C. Levin, U. Arp, T. LeBrun, and M.A. MacDonald, "Xenon Spectator and Diagram L_3-$M_{4,5}M_{4,5}$ Auger Intensities near the L_3 Threshold", *Phys. Rev.*, **A56**, R1079, (1997).

U. Arp, J.W. Cooper, T. LeBrun, S.H. Southworth, M. Jung, and M.A. MacDonald, "Angular Correlation Between Kα Photons and $L_{2,3}$-$M_{2,3}M_{2,3}$ Auger Electrons Following Argon 1s Photoionization", *J. Phys. B: at Mol. Opt. Phys.*, **29**, L837, (1996).

U. Arp, T. LeBrun, S.H. Southworth, M.A. MacDonald, and M. Jung, "X-ray Fluorescence and Auger-Electron Coincidence Spectroscopy of Vacancy Cascades in Atomic Argon", *Phys. Rev.* **A55**, 4273, (1997).

J.D. Mills, J.A. Sheehy, T.A. Ferrett, S.H. Southworth, R. Mayer, D.W. Lindle, and P.W. Langhoff, "Nondipole Resonant X-ray Spectroscopy: Polarized Inelastic Scattering at the K Edge of Cl_2", *Phys. Rev. Lett.*, **79**, 383, (1997).

K.E. Miyano, Y. Ma, S.H. Southworth, P.L. Cowan, and B.A. Karlin, "Resonant Raman Scattering in Potassium and Chlorine Kβ X-ray Emission from KCL", *Phys. Rev.*, **B54**, 12022, (1996).

Beamline X24C

M.P. Kowalski, R.G. Cruddace, J.F. Seely, J.C. Rife, K.F. Heidemann, U. Heinzmann, U. Kleineberg, K. Osterried, and D. Menke, "Efficiency of a Multilayer-Coated, Ion-Etched Laminar Holographic Grating in the 14.5-16.0-nm Wavelength Region", *Optics Letts.*, **22**, 834, (1997).

M.P. Kowalski, R.G. Cruddace, J.F. Seely, J.C. Rife, W.R. Hunter, and T.W. Barbee, Jr., "The EUV Performance of an Ion-Etched Blazed Diffraction Grating", *J. Electr. Spectro. Rel. Phenom.*, **80**, 473, (1996).

W.R.L. Lambrecht, S.N. Rashkeev, B. Segall, K. Lawniczak-Jablonska, T. Suski, E.M. Gullikson, J.H. Underwood, R.C.C. Perera, J.C. Rife, I. Gregory, S. Porowski, and D.K. Wickenden, "X-Ray Absorption, Glancing-Angle Reflectivity, and Theoretical Study of the N K- and Ga $M_{2,3}$-Edge Spectra in GaN, *Phys. Rev.*, **B55**, 2612, (1997).

J.F. Seely, M.P. Kowalski, R.G. Cruddace, J.C. Rife, T.W. Barbee, Jr., and W.R. Hunter, "High Resolution Spectroscopy using Normal-Incidence Multilayer Gratings", UV and X-ray Spectroscopy of Astrophysical and Laboratory Plasmas, edited by K. Yamashita and T. Watanabe, Universal Academy Press, Tokyo, p. 225, (1996).

J.F. Seely, M.P. Kowalski, W.R. Hunter, and G. Gutman, "Reflectance of a Wideband Multilayer X-ray Mirror at Normal and Grazing Incidence", *Appl. Optics*, **35**, 4408, (1996).

Beamline X25

H. Baltes, Y. Yacoby, R. Pindak, R. Clarke, L. Pfeiffer, and L.E. Berman, "Measurement of the X-Ray Diffraction Phase in a 2D Crystal", *Phys. Rev. Lett.*, **79**, 1285, (1997).

D.C. Boisvert, J. Wang , Z. Otwinowski, A.L.Horwich, and P.B.Sigler, "The 2.4 Å Crystal Structure of the Bacterial Chaperonin GroEL Complexed with ATP Gamma S", *Nat. Struct. Bio.*, **3/2**, 170-7, (1996).

K. Braig, Z. Otwinowski, R. Hegde, D.C. Boisvert, A. Joachimiak, A.L. Horwich, and P.B. Sigler, "The Crystal Structure of the Bacterial Chaperonin GroEL at 2.8 Å", *Nature*, **371**, 578, (1994).

Q.R. Fan, L. Mosyak, C.C. Winter, N. Wagtmann, E.O. Long, and D.C. Wiley, "Structure of the Inhibitory Receptor for Human Natural Killer Cells Resembles Haematopoietic Receptors", *Nature,* **389**, 96, (1997).

J.M. Gulbis, Z. Kelman, J. Hurwitz, M. O'Donnell, and J. Kuriyan, "Structure of the C-Terminal Region of $p21^{WAF1/CIP1}$ Complexed with Human PCNA", *Cell*, **87**, 297, (1996).

F. Guo, D.N. Gopaul, and G.D. Van Duyne, "Structure of Cre Recombinase Complexed with DNA in a Site-Specific Recombination Synapse", *Nature*, **389**, 40, (1997).

J.P. Hill, C.-C. Kao, and D.F. McMorrow, "K-Edge Resonant X-Ray Magnetic Scattering from a Transition-Metal Oxide: NiO", *Phys. Rev.*, **B55**, R8662, (1997).

S. Krishnan, J.J. Felten, J.E. Rix, J.K.R. Weber, P.C. Nordine, M.A. Beno, S. Ansell, and D.L. Price, "Levitation Apparatus for Structural Studies of High Temperature Liquids using Synchroton Radiation", *Rev. Sci. Instrum.*, **68**, 3512, (1997).

H. Li, J.J. Dunn, B.J. Luft, and C.L. Lawson, "Crystal Structure of Lyme Disease Antigen Outer Surface Protein A Complexed with an Fab", *Proc. Nat. Acad. Sci.*, **94**, 3584, (1997).

J.L. Libbert, J.A. Pitney, and I.K. Robinson, "Asymmetric Fraunhofer Diffraction from Roller-Blade Slits", *J. Synch. Rad.*, **4**, 125, (1997).

O.M. Magnussen, B.M. Ocko, M. Deutsch, M.J. Regan, P.S. Pershan, D. Abernathy, G. Grübel, and J.-F. Legrand, "Self-Assembly of Organic Films on a Liquid Metal", *Nature*, **384**, 250, (1996).

M.J. Regan, O.M. Magnussen, E.H. Kawamoto, P.S. Pershan, B.M. Ocko, N. Maskil, M. Deutsch, S. Lee, K. Penanen, and L.E. Berman, "X-Ray Studies of Atomic Layering at Liquid Metal Surfaces", *J. Non-Cryst. Solids*, **205**, 762, (1996).

M.J. Regan, P.S. Pershan, O.M. Magnussen, B.M. Ocko, M. Deutsch, and L.E. Berman, "Capillary-Wave Roughening of Surface-Induced Layering in Liquid Gallium", *Phys. Rev.*, **B54**, 9730, (1996).

M.J. Regan, P.S. Pershan, O.M. Magnussen, B.M. Ocko, M. Deutsch, and L.E. Berman, "X-Ray Reflectivity Studies of Liquid Metal and Alloy Surfaces", *Phys. Rev.*, **B55**, 15874, (1997).

M.J. Regan, H.C. Tostmann, P.S. Pershan, O.M. Magnussen, E. DiMasi, B.M. Ocko, and M. Deutsch, "Oxidation of Liquid Gallium Surfaces: X-Ray Reflectivity Study", *Phys. Rev.*, **B55**, 10786, (1997).

F. Sicheri, I. Moarefi, and J. Kuriyan, "Crystal Structure of the Src Family Tyrosine Kinase Hck", *Nature*, **385**, 602, (1997).

J.A. Simpson, R.A. Cowley, D.A. Jehan, R.C.C. Ward, M.R. Wells, D.F. McMorrow, K.N. Clausen, T.R. Thurston, and D. Gibbs, "Co-Existence of Long- and Short-Range Magnetic Correlations in Holmium-Erbium Superlattices", *Z. Phys.*, **B101**, 35, (1996).

M. Sriram, J. Osipiuk, B.C. Freeman, R.I. Morimoto, and A. Joachimiak, "Human Hsp70 Molecular Chaperone Binds Two Calcium Ions Within the ATPase Domain", *Structure*, **5**, 403, (1997).

Y. Wang, Y. Jiang, M. Meyering-Voss, M. Sprinzl, and P.B. Sigler, "Crystal Structure of the EF-Tu·EF-Ts Complex from Thermus Thermophilus", *Nat. Struct. Biol.*, **4**, 650, (1997).

H. Wu, P.D. Kwong, and W.A. Hendrickson, "Dimeric Association and Segmental Variability in the Structure of Human CD4", *Nature*, **387**, 527, (1997).

Z. Xu, A.L. Horwich, and P.B. Sigler, "The Crystal Structure of the Asymmetric GroEL-GroES-$(ADP)_7$ Chaperonin Complex", *Nature*, **388**, 741, (1997).

Beamline X26A

P.M. Bertsch, D.B. Hunter, P.R. Nuessle, and S.B. Clark, "Molecular Characterization of Contaminants in Soils by Spatially Resolved XRF & XANES Spectroscopy", *J. de Phys. IV*, **7**, C2-817, (1997).

J.S. Delaney, S. Bajt, S.R. Sutton, and M.D. Dyar, "*In Situ* Microanalysis of $Fe^{3+}/\Sigma Fe$ Ratios in Amphibole by X-ray Absorption Near Edge Structure (XANES) Spectroscopy", *Mineral Spectroscopy, Roger Burns Memorial*, **5**, 165, (1996).

W.P. Gates, D.B. Hunter, P.R. Nuessle, and P.M. Bertsch, "A Time Resolved XANES Study of an Organo-Clay Redox System", *J. de Phys. IV*, **7**, C2-785, (1997).

D.B. Hunter, P.M. Bertsch, K.M. Kemner, and S.B. Clark, "Distribution and Chemical Speciation of Metals and Metalloids in Biota Collected from Contaminated Environments by Spatially Resolved XRF, XANES and EXAFS", *J. de Phys. IV*, **7**, C2-767, (1997).

H. S. Isaacs, and S.-M. Huang, "Behavior of Dissolved Molybdenum during Localized Corrosion of Austenitic Stainless Steel", *J. Electrochem. Soc.*, **143/12**, L277, (1996).

R.A. Mayanovic, A.J. Anderson, and S. Bajt, "Microbeam XAFS Studies on Fluid Inclusions at High Temperatures", *J. de Phys. IV*, **7**, C2-1029, (1997).

J. Rakovan, and R.J. Reeder, "Intracrystalline Rare Earth Element Distributions in Apatite: Surface Structural Influences on Incorporation During Growth", *Geochimica et Cosmochimica Acta*, **60**, 4435, (1996).

T. Tokunaga, G.E. Brown, Jr., I.J. Pickering, S.R. Sutton, and S. Bajt, "Selenium Redox Reactions and Transport Between Ponded Waters and Shallow Sediments", *Environ. Sci. & Technol.*, **31**, 1419, (1997).

A. Zappalà, S. Bajt, G.E. Gigante, and A.L. Hanson, "Applications of EDXRF in the Conservation of Acid Papers using a Synchrotron Light Microbeam", *Nucl. Instrum. and Meths. in Phys. Res.*, **B117**, 145, (1996).

Beamline X26C

U.K. Genick, G.E. Borgstahl, K. Ng, Z. Ren, C. Pradervand, P.M. Burke, V. Srajer, T.Y. Teng, W. Schildkamp, D.E. McRee, and et al., "Structure of a Protein Photocycle Intermediate by Millisecond Time-Resolved Crystallography", *Science*, **275**, 1471, (1997).

J.L. Jordan-Sweet, K. Evans-Lutterodt, G.S. Cargill, III, M.A. Marcus, and I.C. Noyan, "Microbeam Diffraction at NSLS", NSLS July Newsletter, p.7, (1997).

K. Moffat, and Z. Ren, "Synchrotron Radiation Applications to Macromolecular Crystallography", *Current Opinion in Struct. Bio.*, **7**, 689, (1997).

V. Stojanoff, D.P. Siddons, L.A. Monaco, P. Vekilov, and F. Rosenberger, "X-ray Topography of Tetragonal Lysozyme Grown by the Temperature-Controlled Technique", *Acta Cryst.*, **D53**, 588, (1997).

P.-C. Wang, G. S. Cargill III, I. C. Noyan, E. G. Liniger, C.-K. Hu, and K. Y. Lee, "Real- Time Measurements of Thermal and Electromigration Strains on Individual Al Interconnects by X-Ray Microdiffraction", International Electron Devices and Materials Symposium Proceedings, **A1/10**, 63, (1996).

P.-C. Wang, G. S. Cargill III, I. C. Noyan, E. G. Liniger, C.-K. Hu, and K.Y. Lee, "X-Ray Microdiffraction for VLSI", Mat. Res. Soc. Symp. Proc., **427**, 35, (1996).

Beamline X27A

B.A. Dowd, "Workshop on X-ray Computed Microtomography: Applications & Techniques", *Synch. Rad. News*, **10**, 5, (1997).

B.L. Illman, and B.A. Dowd, "Synchrotron Applications in Forestry and Forest Products", *Synch. Rad. News*, **10**, 1, (1997).

Beamline X27C

D. Chapman, W. Thomlinson, F. Arfelli, N. Gmür, Z. Zhong, R. Menk, R.E. Johnston, D. Washburn, E. Pisano, and D. Sayers, "Mammography Imaging Studies using a Laue Crystal Analyzer", *Synch. Rad. Instrum.* **67**, 9, (1995), BNL 62394.

R.E. Johnston, D. Washburn, E. Pisano, C. Burns, W. Thomlinson, L.D. Chapman, F. Arfelli, N.F. Gmür, Z. Zhong, and D. Sayers, "Mammography Phantom Studies with Synchrotron Radiation", *Radiology*, **200/3**, 659, (1996), BNL 62733.

NSLS STAFF

M. Babzien, I. Ben-Zvi, P. Catravas, J. M. Fang, A. Fisher, W. S. Graves, X. Z. Qui, Z. Segalov, and X. J. Wang, "Optical Alignment and Diagnostics for the ATF Microundulator FEL Oscillator", *Nucl. Instrum. and Meths. In Phys. Res.*, **A375**, 420, (1996), BNL 63811.

M. Babzien, A. Fisher, I. Pogorelsky, and T. Srinivasan-Rao, "A High Stability Nd: YAG Photocathode Drive Laser", Technical, Digest Conference Proceedings, **15**, 218, (1995), BNL 63263.

H. Baltes, Y. Yacoby, R. Pindak, R. Clarke, L. Pfeiffer, and L. Berman, "Measurement of the X-ray Diffraction Phase in a 2D Crystal", *Phys. Rev. Lett.*, **79/7**, 1285, (1997), BNL 64710.

K. Bane, S. Krinsky, and J.B. Murphy, "Longitudinal Potential well Distortion due to the Synchrotron Radiation Wakefield", Micro Bunches Workshop AIP Conference Proceedings, American Institute of Physics Press, **367**, 191-98, (1996), BNL 63852.

R. A. Bartynski, E. Jensen, S. L. Hulbert, and C.-C. Kao, "Auger Photoelectron Coincidence Spectroscopy Using Synchrotron Radiation", *Progr. Surf. Sci.*, **53/2**, 155, (1996), BNL 64645.

K. Batchelor, M. Babzien, I. Ben-Zvi, J. Fischer, I. Fisher, R. Malone, I. Pogorelsky, T. Srinivsan-Rao, J. Sheehan, and X.J. Wang, "Operational Experience on the Brookhaven National Laboratory Acceleration Test Facility", Proceedings of the 4th European Particle Accelerator Conference, London, England, edited by V. Suller, and C.H. Pette-Jean-Genez, World Scientific Publishing Co., Vol. 1, pp. 736-738, (1994), BNL 60739.

L. Berman, "SPIE Conference on Optics for High-Brightness Synchrotron Radiation Beamlines II", *Synch. Rad. News*, **10/1**, 122, (1997), BNL 63691.

E.B. Blum, M. Dienes, and J.B. Murphy, (Editors), Micro Bunches Workshop AIP Conference Proceedings 367, American Institute of Physics Press, NY, (1996), BNL 63824.

E. Bozoki, S. Ramamoorthy, O. Singh, Y. Tang, and A. Friedman, "Operations with the Digital Orbit Feedback System in the NSLS X-ray Ring", Proceedings of the Fifth European Particle Accelerator Conference, **3**, 1911, (1996), BNL 62947.

P. Catravas, R. Stoner, J. Blastos, D. Sisson, I. Mastrovsky, G. Bekefi, X.J. Wang, and A. Fisher, "MIT Microwiggler for Free Electron Laser Applications", Proceedings of 1995 Particle Accelerator Conference, pp. 192-194, (1995), BNL 61957.

D. Chapman, W. Thomlinson, R. E. Johnson, D. Washburn, E. Pisano, N. Gmür, Z. Zhong, R. Menk, F. Arfelli, and D. Sayers, "Diffraction Enhanced X-ray Imaging", *Phys. in Med. and Biol.*, **42**, 2015, (1997), BNL 64698.

T.T. Chou, C.N. Yang, and L.H. Yu, "Momentum Distribution for Bosons with Positive Scattering Length in a Trap", *Phys. Rev.*, **A55/2**, 1179, (1997), BNL 63778.
C.L. Cleveland, U. Landman, T.G. Schaaff, M.N. Shafigullin, P.W. Stephens, and R.L. Whetten, "Structural Evolution of Smaller Gold Nanocrystals: The Truncated Decahedral Motif", *Phys. Rev. Lett.*, **79/10**, 1873, (1997), BNL 64783.

F.A. Dilmanian, X.Y. Wu, E.C. Parsons, B. Ren, J. Kress, T.M. Button, L.D. Chapman, J.A. Coderre, F. Giron, D. Greenberg, D.J. Krus, Z. Liang, S. Marcovici, M.J. Petersen, C.T. Roque, M. Shleifer, D.N. Slatkin, W.C. Thomlinson, K. Yamamoto, and Z. Zhong, "Single-and Dual-Energy CT with Monochromatic Synchrotron X-rays", *Phys. Med. Biol.*, **42**, 371, (1997), BNL 62821.

P. Dumas, M. Suhren, Y. J. Chabal, C. J. Hirschmugl, and G. P. Williams, "Adsorption and Reactivity of NO on Cu(111): A Synchrotron Infrared Reflection Absorption Spectroscopic Study", *Surf. Sci.*, **371**, 200, (1997), BNL 64673.

C. L. Foerster, C. Lanni, I. Maslennikov, and W. Turner, "Photon Desorption Measurements of Copper and Copper Plated Beam Tubes for the SSCL 20 TeV Proton Collider", *J. Vac. Sci. Technol.*, **A12/4**, 1673, (1994), BNL 64720.

W. S. Graves, "Gain and Startup Conditions for the BNL Visible FEL Oscillator Experiment", *Nucl. Instrum. and Meth. in Phys. Res.*, **A393**, 210, (1997), BNL 63986.

W.S. Graves, L. Solomon, and I. Lehrman, "End Fields in the Harmonic Generation Superconducting FEL at BNL-NSLS", *Nucl. Instrum. and Meths. in Phys. Res.*, **A358**, 414, (1995), BNL 63809.

K. Hämäläinen, S. Manninen, C.-C. Kao, W. Caliebe, J.B. Hastings, A. Bansil, S. Kaprzyk, and P.M. Platzman. "High Resolution Compton Scattering Study of Be", *Phys. Rev.*, **B54/8**, 5453, (1996), BNL 63773.

M. Hart, "Powder Diffraction", Röntgen Centennial, X-rays in Natural and Life Sciences, edited by A. Haase, G. Landwehr, and E. Umbach, World Scientific Publishing Co., pp. 647-658, (1997), BNL 62630.

J. Kircher, P.L. Richards, R. Henn, M. Cordona, and G.P. Williams, "Far Infrared Ellipsometry Using Synchrotron Radiation", *J. Opt. Soc. Am.*, **B14/4**, 705, (1997), BNL 61880.

Y. Liu, S.A. Bogacz, D.B. Cline, X.J. Wang, I.V. Pogorelsky, and W.D. Kimura, "Micro Bunching Diagnostics for the ICA by Coherent Transition Radiation", Micro Bunches Workshop, AIP Conference Proceedings 367, pp. 445-454, (1995), BNL 62387.

Y. Liu, D. Cline, I. Ben-Zvi, X.J. Wang, J. Sheehan, K. Batchelor, R. Malone, and M. Issapour, "A Modified Feed-Forward Control System and the ATF", *Rev. of Sci. Instrum.*, **68/2**, 1137, (1997). BNL 63384.
D.R. Lynch, L. Berman, P. Montanez, S. Pjerov, P. Stefan, and M. Woodle, "Beryllium Windows for Synchrotron Light Sources" *SPIE*, **2855**, 119, (1996), BNL 63637.

R.H. Menk, W. Thomlinson, N. Gmür. Z. Zhong, D. Chapman, F. Arfelli, W.R. Dix, W. Graeff, M. Lohmann, G. Illing, L. Schildwacher, B. Reime, W. Kupper, C. Hamm, J.C. Giacomini, H.J. Gordon, E. Rubenstein, J. Dervan, H.J. Besch, and A.H. Walenta, "The Concept of Spatial Frequency Depending DQE and it's Application to a Comparison of two Detectors Used in Transvenous Coronary Angiography", *Nucl. Instrum. and Meth. In Phys. Res.*, **A398**, 351, (1997), BNL 64757.

J. B. Murphy, S. Krinsky, and R. L. Gluckstern, "Longitudinal Wakefield for an Electron Moving on a Circular Orbit", *Particle Accelerators*, **57**, 9, (1997), BNL 63090.

T. Nanba, Y. Nodake, M. Muneyasu, G. P. Williams, and S. Hayashi, "Size-Dependence of Phase Transition of Cds Microcrystals", *J. Phys. Soc. Japan,* **66/5**, 1526, (1997), BNL 64671.

D. Robin, J. Safranek, G. Portmann, and H. Nishimura, "Model Calibration and Symmetry Restoration of the Advanced Light Source", Proceedings of the European Particle Accelerator Conference, p. 971, (1996), BNL 64140.

J. L. Rothman, "Ultra-fast Monocycle Generator", *Electronic Design*, **522**, 102, (1996), BNL 64006.

J. Safranek, "Experimental Determination of Storage Ring Optics using Orbit Response Measurements", *Nucl. Instrum. and Meths.*, **A388**, 27-36, BNL 63382.

J. Safranek, "Performance Optimization of Synchrotron Light Sources", *SPIE*, **2856**, 2-15, (1996), BNL 64139.

J. Safranek, and P.M. Stefan, "Emittance Measurement at NSLS X-ray Ring", Proceedings of the European Particle Accelerator Conference, p. 1573, (1996), BNL 64141.

O. Singh, S. Krinsky, P.M. Ivanov, and E.A. Medvedko, "Orbit Compensation for the Time Varying Elliptically Polarized Wiggler", *Rev. Sci. Instrum.*, **67/9**, 1, (1996), BNL 63952.

L. Solomon, W. S. Graves, and I. Lehrman, "Magnetic Field Measurements of the Harmonic Generation FEL Superconducting Undulator at BNL-NSLS", *Nucl. Instrum. and Meths. in Phys. Res.*, **A358**, 411, (1995), BNL 63810.

L. H. Tjeng, B. Sinkovic, N. B. Brookes, J. B. Giedkoop, R. Hesper, E. Pellegrin, F.M.F. de Groot, S. Altieri, S. L. Hulbert, E. Shekel, and G. A. Sawatzky, "Spin-Resolved Photoemission on Anti-Ferromagnets: Direct Observation of Zhang-Rice Singlets in CuO", *Phys. Rev. Lett.*, **78**, 1126, (1997), BNL 64219.

X.J. Wang, and I. Ben-Zvi, "High-Brightness Electron Beam Diagnostics at the ATF", AIP Conference Proceeding, **390**, 232-239, (1996), BNL 63151.

X.J. Wang, I. Ben-Zvi, and Z. Segalov, "Experimental Characterization of ATF Beam Position Monitor", Proceeding of the Fifth European Particle Accelerator Conference, pp. 1576-1578, (1996), BNL 63214.

X.J.Wang, X. Qiu, and I. Ben-Zvi. "Experimental Observation of Micro-Bunching in a Photocathode RF Gun Injector", *Phys. Rev. Letts.*, **B54**, R3121, (1996), BNL 62820.

D. L. Wetzel, J. A. Reffner, and G. P. Williams, "Synchrotron-Powered FT-IR Microspectroscopy: Single Cell Interrogation", *Mikrochim. Acta*, **14**, 353, (1997), BNL 64672.

B. Winn, H. Ade, C. Buckley, M. Howells, S. Hulbert, C. Jacobsen, J. Kirz, I. McNulty, J. Miao, T. Oversluizen, I. Pogorelsky, and S. Wirick, "X1A: Second-Generation Undulator Beamlines Serving Soft X-ray Spectromicroscopy Experiments at the NSLS", *Rev. Sci. Instrum.*, **67/9**, 3359, (1996), BNL 64279.

Z. Yin, L. Berman, S. Dierker, E. Dufresne, and D. P. Siddons, A Simple X-ray Focusing Mirror using Float Glass", *SPIE*, **2856**, 307, (1996), BNL 63583.

L. H. Yu, "Quantum Tunneling in a Dissipative System", *Phys. Rev.*, **A54/5**, 3779, (1996), BNL 64041.

L.H. Yu, and I. Ben-Zvi, "High Gain Harmonic Generation of Soft X-rays with the Fresh Bunch Technique", 18th International Free Electron Laser Conference, *Nucl. Instrum. And Meths. In Phys. Res.*, **A393**, 96, (1997), BNL 63639.

Z. Zhong, D. Chapman, R. Menk, J. Richardson, S. Theophanis, and W. Thomlinson, "Monochromatic Energy-Subtraction Radiography using a Rotating Anode Source and a Bent-Laue Monochromator", *Phys. in Med. and Biol.*, **42**, 1751, (1997), BNL 64155.

Z. Zhong, D. Chapman, W. Thomlinson, F. Arfelli, and R. Menk, "A Bent-Laue Crystal Monochromator for Monochromatic Radiography with an Area Beam", *Nucl. Instrum. and Meth. in Phys. Res.*, **A399**, 489, (1997), BNL 64154.

BNL Formal and Informal Reports

I. Ben-Zvi, R. Fernow, J. Gallardo, M. Hart, J. Hastings, E. Johnson, S. Krinsky, R. Palmer, and L.-H. Yu, "Lepton Accelerators and Radiation Sources: R&D Investment at BNL", BNL 64214, March 1997.

J. Dunsmuir, P. Spanne, C. Jacobsen, A. Dilmanian, Z. Zhong, B. Dowd, B. Illman, B. Lindquist, S.R. Song, and B. Andrew, "X-ray Computed Microtomography Workshop 1997", BNL 64772, September 1997.

S. Krinsky, "Storage Ring Working Group Report", Micro Bunches Workshop, Upton, NY, BNL 63987, September 1995.

E.Z. Rothman, and J.B. Hastings, (Editors), "1996 Activity Report", National Synchrotron Light Source, BNL 52517, November 1996.

X.J. Wang, and D. Kehne, "Measurements of Emittance Growth Through the Achromatic Bend at the BNL Accelerator Test Facility", BNL 64646, July 1997.

Report Number (14) BNL--52540

Publ. Date (11) 199805

Sponsor Code (18) DOE/ER, XF

UC Category (19) UC-400, DOE/ER

DOE